THE 1980 ERUPTIONS OF Mount St. Helens, WASHINGTON

GEOLOGICAL SURVEY PROFESSIONAL PAPER 1250

THE 1980 ERUPTIONS OF MOUNT ST. HELENS, WASHINGTON

Edited by PETER W. LIPMAN
and DONAL R. MULLINEAUX

Early results of studies of volcanic events in 1980, geophysical monitoring of activity, and studies of volcanic deposits, effects, and potential hazards

GEOLOGICAL SURVEY PROFESSIONAL PAPER 1250

THE 1980 ERUPTIONS OF MOUNT ST. HELENS, WASHINGTON

UNITED STATES DEPARTMENT OF THE INTERIOR
James G. Watt, Secretary

UNITED STATES GEOLOGICAL SURVEY
Dallas L. Peck, Director

UNITED STATES GOVERNMENT PRINTING OFFICE
Washington, D.C.: 1981

For sale by the Superintendent of Documents, U.S. Government Printing Office
Washington, D.C. 20402

LIBRARY OF CONGRESS CATALOG NUMBER 81-600142

First printing 1981
Second printing 1982

Editors' notes:

Because of the preliminary nature of some of the work reported in this volume, two informal names for geographic features have been used and retained in several reports, as being the clearest way to refer to these features. The names are Coldwater Ridge, applied to an east-west ridge 9–10 km north to northwest of Mount St. Helens, and Harrys Ridge, used for a 1.6-km-long ridge trending north-south, immediately west of Spirit Lake.

Any use of trade names is for descriptive purposes only and does not imply endorsement by the U.S. Geological Survey.

DEDICATION

David Johnston, 30-year-old volcanologist with the U.S. Geological Survey, was swept away by the catastrophic eruption of Mount St. Helens on the morning of May 18, 1980. As one of the first members of the U.S. Geological Survey monitoring team to arrive at Mount St. Helens and the scientist in charge of volcanic-gas studies, Dave spent long hours working on and close to the mountain. Ironically, he was caught at an observation post that was considered relatively safe. From his experience with active Alaskan volcanoes, Dave understood better than most the hazards of explosive volcanism. At the same time, he repeatedly voiced the conviction that adequate hazard assessments require accepting the dangers of on-site monitoring of active volcanic processes. The volcano-monitoring effort of which Dave was part helped persuade the authorities first to limit access to the area around the volcano, and then to resist heavy pressure to reopen it, thereby holding the May 18 death toll to a few tens instead of thousands.

Born and raised in Illinois, Dave Johnston was graduated in 1971 from the University of Illinois, Urbana, with "Highest Honors and Distinction" in geology. His strong interest in volcanism began with his first geologic project studying Precambrian volcanic rocks in the Upper Peninsula of Michigan. This interest in volcanic phenomena intensified with subsequent work in the San Juan volcanic field of southwestern Colorado and on Augustine Volcano in lower Cook Inlet, Alaska. The Augustine study was the basis for his doctoral dissertation, completed in 1978 at the University of Washington, Seattle.

Following his Ph.D., Dave increasingly focused on the fundamental role of volatiles in volcanic processes, as he continued his studies on Augustine and began work on Katmai Volcano, Alaska. His work on volcanic gases brought him in 1978 to the U.S. Geological Survey, where he was assigned to expand the program for monitoring volcanic emissions in Alaska and the Cascade Range. A specific objective of such monitoring is to test whether or not changes in gas geochemistry might provide precursory clues of impending eruptive activity. Thus, it was natural that, when Mount St. Helens reawakened in March 1980, Dave Johnston was one of the first geologists on the volcano.

DAVID A. JOHNSTON, 1949–1980

Dave Johnston was an exemplary scientist, and his approach to his work was a model for all: dedicated and hardworking, with meticulous organization and observation followed by careful evaluation and interpretation. At the same time, Dave was unaffectedly genuine, with an infectious curiosity and enthusiasm. But perhaps his most essential quality was the ability to dissipate cynicism; he looked for, saw, and thereby encouraged the best in all of us. Dave would have expected us to carry on without him, learning all we could from the Mount St. Helens catastrophe. In that spirit this volume is dedicated to his memory.

FOREWORD

The reawakening of Mount St. Helens volcano in March 1980, and its catastrophic eruption of May 18, surely will rank among the most significant geologic events in the United States in the 20th century. The debris avalanche, explosive eruption, and associated mudflows and floods resulted in the loss of about 60 lives—including our own David Johnston—and property damage and destruction totaling billions of dollars. We in the U.S. Geological Survey are proud of the role we played in helping to minimize these losses.

By its Organic Act of 1879, the Geological Survey was charged with "classification of the public lands, and examination of the geological structure, mineral resources, and products of the national domain* * *." Under that charge, volcanoes and volcanic processes—ancient and contemporary—have been studied to advance the knowledge of the geology in our country. Within the last several decades, attention has been directed increasingly toward assessment of the risks to life and property posed by geologic hazards, including volcanic eruptions, earthquakes, and ground failures. The passage of the Disaster Relief Act of 1974 (P.L.93-288) led to the responsibility of the Geological Survey "to provide technical assistance to State and local governments to ensure that timely and effective disaster warning is provided" for all geologic hazards.

Earth scientists can contribute to the reduction of geologic hazards through improvement in the basic understanding of the phenomena involved—by (1) describing the nature and geographic distribution of possible effects and (2) developing a capability to predict hazardous events. Fortunately, Dwight Crandell, Donal Mullineaux, and their colleagues had spent nearly 20 years studying the eruptive histories and associated volcanic hazards of the Cascade volcanoes. From their research, they concluded that Mount St. Helens was the youngest and most active of the Cascade volcanoes. Indeed as early as 1975, in a paper published in *Science*, which was later expanded with additional information into U.S. Geological Survey Bulletin 1381-C published in 1978, Crandell, Mullineaux, and colleagues predicted that Mount St. Helens, the most active and most explosive Cascade volcano, would erupt again, "perhaps before the end of this century." This prediction, of course, has come true. Equally important, the descriptions and locations of the potential hazards associated with an eruption proved accurate, with few exceptions.

The volcanic hazards assessment by Crandell and Mullineaux provided a key element in reducing hazards to life and property. Another key element was the development—in cooperation with the University of Washington—of a seismograph network and the capability for analysis of local earthquake activity. A week of premonitory earthquake activity under Mount St. Helens sounded the earliest warning of the eruptive sequence that began on March 27.

How will Mount St. Helens behave in the coming months or years? Which other Cascade volcano might erupt next? When will it occur and what might be the effects? These are questions that earth scientists cannot yet answer with precision, but current studies on Mount St. Helens and other Cascade volcanoes may provide clues to the answers. In 1981, the U.S. Geological Survey established a facility in Vancouver, Washington, to serve as a field headquarters for monitoring and investigations of Mount St. Helens as well as other Cascade volcanoes.

Science advances by careful documentation and interpretation of observations, formulation of hypotheses, and the testing of interpretations and hypotheses by new observations and experiment. The reports in this volume represent a vital part of the scientific process. Earth scientists—and we in the Geological Survey in particular—have a responsibility to document and understand the current eruptive activity at Mount St. Helens in as much detail as possible. We are embarking on an exciting epoch in volcanology, during which we can anticipate major advances in deciphering the early warning signals of stirring dormant volcanoes and in understanding the fundamental mechanisms of volcanism. This tremendous scientific opportunity and challenge must be matched with commensurate, increased obligation to apply the research results for the mitigation of volcanic hazards and related ecologic and socio-economic impacts.

The lessons of Mount St. Helens must not—and will not—be forgotten.

Dallas L. Peck
Director,
U.S. Geological Survey

PREFACE

The 1980 eruptions of Mount St. Helens, although neither the most voluminous nor the greatest in released energy among recent eruptions, are unusual among historic worldwide volcanic activity, in having occurred close to a major industrialized urban area. Mount St. Helens in 1980 was therefore remarkable for a high degree of national attention, public interest, and social and physical disruption. In addition, exceptional opportunities were presented for scientific observation of infrequently occurring volcanic processes.

When renewed activity was heralded on March 20, 1980, by the first strong earthquake at shallow depth beneath the volcano, it was felt on site and also recorded instrumentally by a joint University of Washington–USGS group in Seattle who had seismometers in operation near the volcano as a part of studies of potential geothermal resources. Within the next 2 days, the unusual character of the seismic activity became clear, and more instruments were set out. A striking increase in earthquakes emphasized the likelihood of an eruption, and warning was given to Federal and State authorities responsible for the land surrounding the volcano.

With the advice of USGS scientists who had been evaluating volcanic hazards of the Casade Range, access to the volcano and adjacent areas was restricted on March 26. A center was established at the U.S. Forest Service headquarters in Vancouver, Wash., for hazards evaluation, monitoring activity, coordination of activities of the agencies involved, and press briefings and public information.

On March 27, hydrothermal explosive activity began at the summit of Mount St. Helens, accompanied by formation of a small crater, ground fracturing, and beginning of a topographic bulge on the upper north flank of the volcano. Strong seismic activity and relatively mild steam-blast eruptions continued intermittently into mid-May. During that time, the new crater gradually enlarged and the north-flank bulge became visually conspicuous. At the same time, the USGS was developing an extensive program of geophysical monitoring and volcanic hazards analysis; especially helpful was the ability to bring in equipment, staff, and experienced former staff from the Survey's Hawaiian Volcano Observatory on short notice. The continued high rate of seismic energy release, intermittent steam-blast eruptions, and remarkable ground deformation all pointed toward the possibility of a significant volcanic event in the near future; these factors also helped provide justification for Federal and State authorities to continue to limit access to areas near the volcano, despite heavy pressure to relax restrictions. Monitoring techniques were developed that, it was hoped, could provide a short-term warning of any major impending eruption, but the catastrophic eruption on the morning of May 18 commenced without any additional precursory signs that were recognized either in advance or by hindsight.

After May 18, studies began on the deposits and effects of the eruption: the debris avalanche that formed by landsliding of the bulge on the north flank, the northward-directed volcanic blast triggered by the massive landslide, mudflows generated by melting of snow and ice, and the pumiceous pyroclastic flows and extensive ash falls. Updated assessments of the status of the volcano and potential hazards received constant attention. Continued monitoring generally provided warnings a few days to a few hours before additional pyroclastic eruptions on May 25, June 12, July 22, August 7, and October 16–18, and before lava domes were emplaced or enlarged in June, August, October, and December.

This report summarizes early results of wide-ranging studies of the volcanic activity and eruptive products at Mount St. Helens in 1980 by the USGS, including some contributions by other participating government, university, and industry scientists. The papers collected here were mostly written in October and November, 1980, with some revisions and updating as late as January 1981. They accordingly constitute initial, in part preliminary, reports and interpretations of the 1980 activity; time constraints on publication have precluded full analysis and interpetation of some data, especially those related to the later events of 1980. More detailed discussions of some aspects of the volcanic activity summarized here can be expected in the future.

Peter W. Lipman
Donal R. Mullineaux, Editors

CONTENTS

ILLUSTRATIONS

TABLES

VOLCANIC EVENTS

VOLCANIC EVENTS

Although Mount St. Helens apparently had been dormant since 1857, geologic studies of deposits around the flanks of the volcano indicate that it erupted frequently in the past and that the modern cone has grown largely during the past 2,500 yr (Mullineaux and Crandell). Eruptions of dacite as pyroclastic flows, ash falls, and viscous lava domes have alternated with lava flows of andesite and basalt. During most eruptive periods, pyroclastic flows and mudflows built fans of fragmental material around the base of Mount St. Helens and partly filled valleys leading away from the volcano. Before 1980, Mount St. Helens was considered by some volcanologists to be the most likely of all Cascade volcanoes to erupt in the near future, and among the most hazardous because of the likelihood of explosive activity and proximity to populated areas.

The 1980 activity of Mount St. Helens (Christiansen and Peterson) began on March 20 with an intensifying swarm of earthquakes. The first steam-blast eruption, a week later, was associated with continued high levels of seismic activity, formation of a summit crater, and beginning of deformation of the north flank of the volcano. These processes continued intermittently through April up to the climactic eruption on the morning of May 18. The May 18 eruption was apparently triggered at 0832 PDT by a magnitude-5+ earthquake, not appreciably different from many preceding quakes, that caused multiple failures of the bulging north flank and produced great avalanches of rock debris. Unloading of the volcano by these failures led to a northward-directed lateral blast, partly driven by hydrothermal steam explosions, that devastated an area of nearly 600 km^2. These events in turn triggered an explosive eruption of dacitic magma that drove a vertical column more than 25 km high, producing visible ash fall for more 1,500 km to the east, and pumiceous pyroclastic flows on the volcano's north flank. Catastrophic mudflows and floods were generated in part by rapid melting of snow and ice. Smaller magmatic eruptions occurred on May 25, June 12, July 22, August 7, October 16–18, and in late December, producing pyroclastic flows, ash falls, and several lava domes. Through December 1980, the eruptions tended to become progressively smaller in volume, slightly more mafic in composition, and less explosive.

The 1980 Mount St. Helens eruptions were especially well documented, because proximity to major population centers offered opportunities not commonly available for monitoring volcanic events in remote areas. An aircraft equipped with USGS large-format fix-mounted cameras, previously used for monitoring glaciers in the Pacific Northwest, was available throughout 1980 (Krimmel and Post). A selection from hundreds of high-quality photographs thus obtained documents surface deformation, crater enlargement, and ash and snow cover before May 18. On May 18, the castastrophic eruption was photographed from about at 1100 PDT until dark. Subsequent photographic coverage documents changes on the volcano later in 1980.

Remarkable documentation of the May 18 eruption also comes from ground-based photography and eyewitness accounts (Rosenbaum and Waitt). Because the eruption occurred under excellent weather conditions in daylight hours on a weekend, observers were present on all sides of the volcano. Observed phenomena of importance to subsequent scientific studies include small rock and ice avalanches that marked the 0832 PDT earthquake, the massive avalanches of the volcano's north flank, the subsequent laterally directed blast, development of the vertical eruption column, timing of mudflows, and the fall of early eruptive products.

A remarkable sequence of photographs taken from the northeast by Gary Rosenquist at intervals of 1–2 s is especially useful in documenting events at the beginning of the May 18 eruption (Voight). Analysis of these photographs provides a time scale for the beginning of the debris avalanche and directed blast, as well as velocity estimates for these events. The avalanche began 10–20 seconds after the 0832 earthquake, and near-source velocities of the directed blast ranged from 50 to more than 200 m/s.

THE 1980 ERUPTIONS OF MOUNT ST. HELENS, WASHINGTON

THE ERUPTIVE HISTORY OF MOUNT ST. HELENS

By DONAL R. MULLINEAUX *and* DWIGHT R. CRANDELL

ABSTRACT

The eruptive history of Mount St. Helens began about 40,000 yr ago with dacitic volcanism, which continued intermittently until about 2,500 yr ago. This activity included numerous explosive eruptions over periods of hundreds to thousands of years, which were separated by apparent dormant intervals ranging in length from a few hundred to about 15,000 yr. The range of rock types erupted by the volcano changed about 2,500 yr ago, and since then Mount St. Helens repeatedly has produced lava flows of andesite, and on at least two occasions, basalt. Other eruptions during the last 2,500 yr produced dacite and andesite pyroclastic flows and lahars, and dacite, andesite, and basalt airfall tephra. Lithologic successions of the last 2,500 yr include two sequences of andesite-dacite-basalt during the Castle Creek period, and dacite-andesite-dacite during both the Kalama and Goat Rocks periods. Major dormant intervals of the last 2,500 yr range in length from about 2 to 7 centuries.

During most eruptive periods, pyroclastic flows and lahars built fans of fragmental material around the base of the volcano and partly filled valleys leading away from Mount St. Helens. Most pyroclastic flows terminated within 20 km of the volcano, but lahars extended down some valleys at least as far as 75 km. Fans of lahars and pyroclastic flows on the north side of the volcano dammed the North Fork Toutle River to form the basin of an ancestral Spirit Lake between 3,300 and 4,000 yr ago during the Smith Creek eruptive period, and again during the following Pine Creek eruptive period.

INTRODUCTION

Mount St. Helens (figs. 1–4) is a young volcano by comparison with its neighbors in the Cascade Range, and it has been characterized by intermittent explosive behavior since its birth about 40,000 yr ago. Before the May 18, 1980, eruption, the volcano was as large as or larger than at any previous time in its history, much of its bulk and shape having been acquired during just the last 2,500 yr. This report summarizes the eruptive behavior of the volcano throughout its lifetime in order to provide a perspective for the eruptive events of 1980 which so drastically modified the shape of the volcano and devastated broad areas beyond it.

Modern studies of Mount St. Helens started with Verhoogen (1937), who outlined the general geologic history of the volcano. He noted that the volcano is young, that it consists of a wide variety of rock types, and that the modern cone overlies an older volcano. Lawrence (1939, 1954) was able to date, by growth-ring studies of trees on the flanks of the volcano, a major pumice eruption of Mount St. Helens that occurred about A.D. 1800, as well as another such eruption nearly 300 yr earlier. The two pumice deposits he dated are now known as layers T and Wn, respectively (Mullineaux and others, 1975, p. 329, 331).

Carithers (1946, p. 16, 18) described two thick pumice layers from Mount St. Helens, a coarse, light-yellow layer and an overlying coarse, light-gray deposit. In addition, he noted scattered pumice granules that are younger than the light-gray deposit. These three deposits have since been designated layers Yn, Wn, and T (Mullineaux and others, 1975, p. 329, 331).

Our studies began in the late 1950's, with an investigation of the origin and age of mudflow and

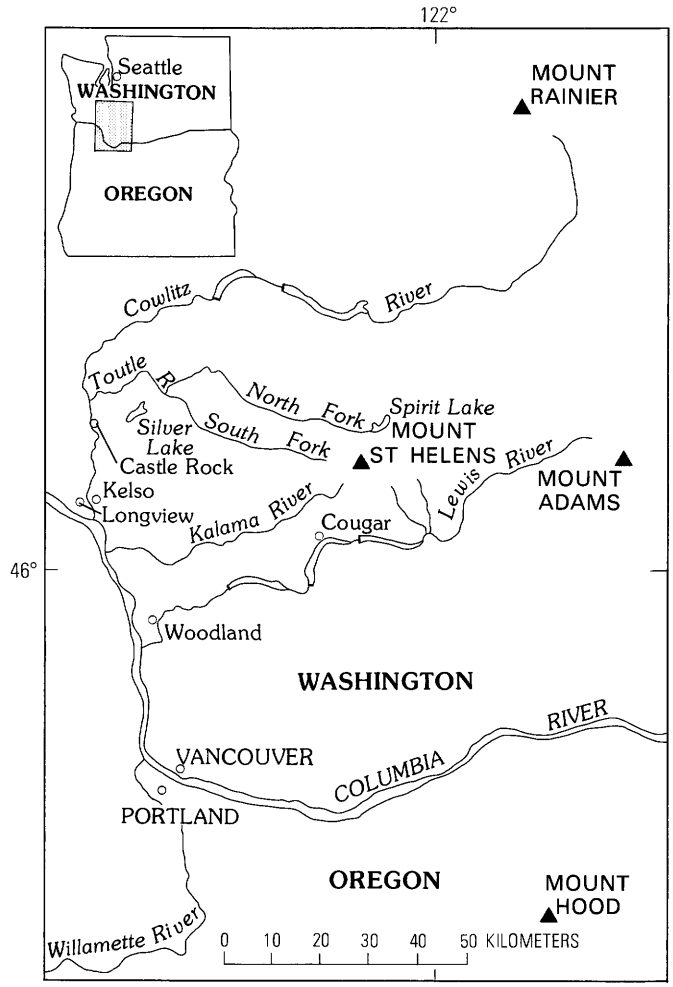

Figure 1.—Location of Mount St. Helens relative to nearby volcanoes in the Cascade Range.

fluvial deposits that dammed Silver Lake, 50 km west-northwest of the volcano (Mullineaux and Crandell, 1960, 1962). These studies confirmed the relative youth of Mount St. Helens, inasmuch as the youngest rocks of Verhoogen's "old Mount St. Helens" were found to be only about 2,000 yr old. Shortly thereafter, we discovered that two conspicuous layers of volcanic ash in Mount Rainier National Park came, not from Mount Rainier, but from Mount St. Helens (Crandell and others, 1962, p. D64). These deposits, the tephra layers Yn and Wn, have been subsequently identified in Canada by Fulton and Armstrong (1965, p. 89) and Smith and others (1977, p. 209), respectively.

In the late 1960's, Hopson (1971) began to prepare a geologic map of the volcano, and to study evidence for possible cyclic eruptive behavior of the modern volcano. Also in the late 1960's, Hyde (1975; Greeley and Hyde, 1972) started a detailed investigation of volcanic deposits on the southern flank of Mount St. Helens.

We began detailed stratigraphic studies in 1970 in order to reconstruct the eruptive history of Mount St. Helens. Our chief objective was to gather data for a volcanic-hazards assessment that could serve as a data base for long-range land-use planning; a second goal was to collect information useful for hazards mitigation, should an eruption occur. Although these studies dealt with the entire history of the volcano, we (Crandell and Mullineaux, 1978) based an assessment of potential hazards on the events of the last 4,000 radiocarbon years (about 4,500 calendar years) because this time span included a representative variety of kinds and scales of eruptions. Furthermore, this time span was preceded by an interval of similar length of little or no activity. We concluded that Mount St. Helens had been frequently active and highly explosive during the last 4,000 yr and could erupt within the next 100 yr—possibly even before the end of the 20th century (Crandell and others, 1975, p. 438; Crandell and Mullineaux, 1978, p. C25).

A study by Hoblitt (Hoblitt and others, 1980), which was virtually complete before eruptions began in March, examined the stratigraphic sequences of rock types produced during the last 1,500 yr and evaluated the evidence for cyclicity or other systematic trends in the eruptive behavior of the volcano.

Information presented here concerning deposits more than 4,000 yr old is largely summarized from in-part unpublished work done by Crandell and by Mullineaux. Ages of eruptive events and eruptive periods are based primarily on 65 radiocarbon dates determined in the radiocarbon laboratory of the U.S. Geological Survey under the supervision of Meyer Rubin.

ACKNOWLEDGMENTS

We thank the many members of the Gifford Pinchot National Forest staff, USFS, who helped during our investigations at the volcano. Some information presented here was acquired working with J. H. Hyde, Tacoma Community College, and R. P. Hoblitt, USGS, and we have benefited from numerous discussions with R. E. Wilcox, USGS, and C. A. Hopson, University of California at Santa Barbara.

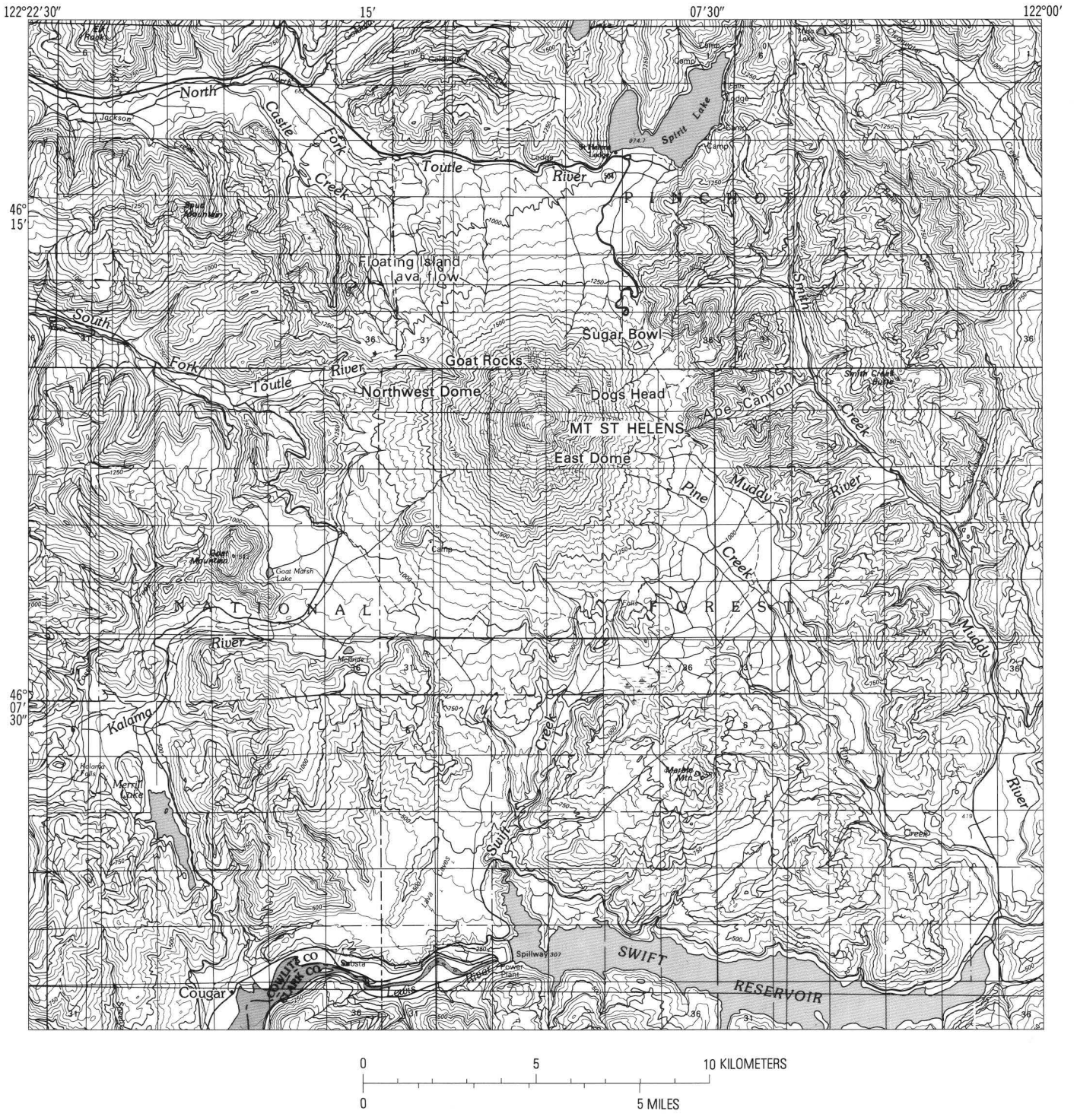

Figure 2.—Pre-1980 cone of Mount St. Helens, showing major topographic features and drainages leading from the volcano.

Figure 3.—Mount St. Helens from the northeast, showing relatively smooth, uneroded profile prior to 1980, the fan of debris that dammed preexisting valleys to form Spirit Lake, and the following plug domes that studded its northern flank: Dogs Head (D), Sugar Bowl (S), Goat Rocks (G).

ERUPTIVE PERIODS AT MOUNT ST. HELENS

The eruptive history of Mount St. Helens is subdivided here into nine named eruptive "periods," which are clusters of eruptions distinguished by close association in time, by similarity of rock types, or both (table 1). The term "eruptive period" is used in an informal and largely arbitrary sense to divide the volcano's history into convenient units for the purpose of discussion. The periods are as much as several thousand years in duration, and include what may have been a single group of eruptions as well as extended episodes of volcanism, during which there were tens or possibly hundreds of eruptions. Eruptive periods are separated by apparently dormant intervals, which are inferred chiefly from buried soils and absence of eruptive deposits. However, some dormant intervals may span times of minor activity that did not produce deposits which can now be recognized. Fine-grained, air-laid volcanic detritus was deposited during some dormant intervals (table 2), but these deposits are not known to have originated directly from eruptions; they might be material reworked from the flanks of the volcano.

The stratigraphic record of eruptive activity during the last 13,000 yr is believed to be reasonably complete. Parts of the older record, however, apparently are missing because of glacial and stream erosion

Figure 4.—Mount St. Helens from the southwest. Dark andesite flows of Kalama age include a lava-flow complex on the southeast flank of the volcano, and single flows on the southwest flank. Dacite of the summit dome forms the slopes above the lava flows. Photograph by R. P. Hoblitt, 1979.

during the last major glaciation (the late Pleistocene Fraser Glaciation) of the region.

APE CANYON ERUPTIVE PERIOD

The first stratigraphic evidence of the existence of Mount St. Helens consists of voluminous dacitic (table 3) deposits of slightly vesicular to pumiceous air-fall tephra and pyroclastic flows, and at least one pumice-bearing lahar. These deposits overlie extensively weathered glacial drift formed during the next-to-last alpine glaciation of the Cascade Range. The volcanic deposits were formed during at least four episodes, separated by intervals during which very weak soils developed (table 2). The entire eruptive period may have extended over a time span as long as 5,000 yr. One pumiceous tephra deposit produced during the period probably had a volume as great as that of any subsequent tephra erupted at Mount St. Helens.

The Ape Canyon eruptive period was followed by a dormant interval which may have lasted from about 35,000 to 20,000 yr ago. Most of this 15,000-yr interval coincided with climates which, at times, were evidently somewhat cooler than those of the present (Alley, 1979, p. 233).

COUGAR ERUPTIVE PERIOD

The second eruptive period probably began about 20,000 yr ago, and was characterized by the eruption of small volumes of pumiceous dacite tephra; it also produced lahars, pyroclastic flows of pumiceous and lithic dacite, a few lava flows of dacite or high-silica

Table 1.—Summary of eruptive history of Mount St. Helens

[d, dacite; a, andesite; b, basalt; >, greater than]

Eruptive periods or dormant intervals	Approximate age, years before 1950[1]	Tephra unit		Other eruptive products[2]
		Set	Layer	
Goat Rocks	150-100			Dome (d).
				Lava flow (a).
			T (d)	
Dormant interval of about 200 yr[3]				
Kalama	450-350			Pyroclastic flows (d).
				Dome (d).
				Pyroclastic flows (a).
				Lava flows (a).
		X (a)		
				Pyroclastic flows (d).
		W (d)		
Dormant interval of about 700 yr				
Sugar Bowl	1,150			Dome (d), pyroclastic flows (d), deposits of lateral blast (d).
Dormant interval of about 600 yr				
Castle Creek	>2,200-1,700		Bu (b)	Lava flows (b).
			Bi (d)	
		B		Pyroclastic flow (a), lava flow (a).
			Bo (a)	
				Lava flow (b).
				Pyroclastic flow (d).
			Bh (a)	
				Lava flow (a).
Dormant interval of about 300 yr				
Pine Creek	3,000-2,500	P (d)		Pyroclastic flows and domes (d).
Dormant interval of about 300 yr				
Smith Creek	4,000-3,300	Y (d)		Pyroclastic flows (d).
Dormant interval of >4,000 yr				
Swift Creek	13,000->8,000	J (d)		
				Pyroclastic flows (d) and domes (d).
		S (d)		Pyroclastic flows (d).
Dormant interval of about 5,000 yr				
Cougar	20,000-18,000	K (d)		Pyroclastic flows (d), domes (d), and a few lava flows (d).
		M (d)		
				Pyroclastic flows (d).
Dormant interval of about 15,000 yr				
Ape Canyon	~40,000(?)-~35,000	C (d)		Pyroclastic flows (d).

[1]Ages of Goat Rocks and Kalama periods are in calendar years; ages of older periods are in radiocarbon years.

[2]Lahars were formed during many eruptive periods but are not included here.

[3]Dormant intervals are intervals during which no unequivocal eruptive products from Mount St. Helens have been recognized.

Table 2.—Partial sequence of air-fall tephra deposits at Mount St. Helens

Eruptive periods or dormant intervals	Tephra unit Set	Tephra unit Layer	Fe-Mg phenocrysts[1]	Other air-laid deposits (d)[2] and soils (s)
Goat Rocks		T	hy, hb, ag	
Dormant interval				
Kalama	X	We	hy, hb	
	W	Wn	hy, hb	
Dormant interval				s
Sugar Bowl[3]				
Dormant interval				
Castle Creek	B	Bu	ol	
		Bi	hy, ag	
		Bo	ol, ag	
		Bh	hy, ag	
Dormant interval				d
Pine Creek	P		hy, hb	
Dormant interval				s d
Smith Creek	Y	Ye	cm, hb	
		Yn	cm, hb	
		Yb	cm, hb, bt	
Dormant interval				s
Swift Creek	J		hy, hb	
				d
	S	So	cm, hb, hy	
		Sg	cm, hb, hy	
Dormant interval				s d
Cougar	K		cm, hb	
				s
				d
	M	Mm	cm, hb, hy	
		Mp	cm, hb, hy	
		Mo	cm, hb, ol	
Dormant interval				s d s d
Ape Canyon	C	Cy	cm, hb, bt	
				s
				d
				s
				d
		Cw	cm, hb, bt	
				s

[1]Minerals used for identification of tephra units: ag, augite; bt, biotite; cm, cummingtonite; hb, hornblende; hy, hypersthene; ol, olivine.

[2]These fine-grained deposits are interbedded with tephra, but their origin has not been determined.

[3]Air-fall tephra deposits associated with the Sugar Bowl eruptive period have not been recognized.

Table 3.—Percentage of SiO_2 in eruptive products of Mount St. Helens

[Calculated water free and to sums of 100 percent]

Eruptive period	Product	SiO_2 (nearest whole percent)
Goat Rocks-----	Dome----------	63
	Andesite lava flow----------	60
	Tephra layer T----------	64
Kalama---------	Dome----------	64
	Andesite pyroclastic flow------	57
	Andesite lava flow----------	58
	Tephra set X (base)----------	58
	Dacite pyroclastic flow--------	64
	Tephra layer We----------	66
	Tephra layer Wn----------	68-65
Sugar Bowl-----	Dome----------	69
	Blast deposit----------	69
Castle Creek---	Tephra layer Bu----------	50
	Tephra layer Bi----------	67
	Basalt lava flow----------	50
	Tephra layer Bo----------	57
	Tephra layer Bh----------	59
Pine Creek-----	Dacite pyroclastic flow--------	64
	Tephra set P (base)----------	66
Smith Creek----	Tephra set Y (top)----------	69
	Lithic pyroclastic flow--------	65
	Tephra layer Yn----------	66
Swift Creek----	Tephra set J----------	62
	Dacite pyroclastic flow (pre-J, post-S).	65
	Tephra layer Sg----------	63
	Dacite pyroclastic flow (pre-S)	67
Cougar---------	Dacite pyroclastic flow--------	62
	Dacite pyroclastic flow--------	62
Ape Canyon-----	Dacite pyroclastic flow--------	68

andesite (C. A. Hopson, written commun., 1974), and perhaps one or more dacite domes. Several different eruptive episodes can be identified during the period. At least one pumiceous pyroclastic flow moved southward to at least 16 km from the center of the present volcano about 20,350 yr ago (Hyde, 1975, p. B11–B13). Two sequences of air-fall tephra that followed (sets M and K) are separated by a two-part deposit of fine air-laid sediment that locally is a meter or more thick, and that contains at least one weakly developed soil (table 2). After another quiet interval during which there was a small amount of soil development, at least two more pyroclastic flows moved south and southeast from the volcano between about 19,000 and 18,000 yr ago. The Cougar eruptive period occurred during the Fraser Glaciation when alpine glaciers in the Cascade Range were at or near their maximum extents, and the products of eruptions generally are poorly preserved.

One lahar that apparently occurred early in the Cougar period is of special interest because of some similarities to the debris avalanche of May 18, 1980, that swept down the North Fork Toutle Valley. The lahar of Cougar age consists of an unsorted and unstratified mixture of gray dacite fragments in a compact matrix of silt and sand as much as 20 m thick. Locally, it contains discrete texturally similar masses of red dacite many meters across. The iron-magnesium mineral content of rocks in the lahar is similar to that of the Ape Canyon period (table 2), suggesting that the lahar might have been derived from older parts of the volcano. The lahar was recognized in the Kalama River drainage 8 km southwest of the center of the modern volcano, and on both walls of the Lewis River valley near Swift dam (Hyde, 1975, p. B9–B11). It has not been recognized elsewhere; thus, little is known of its original extent. Its local thickness and heterolithologic character suggest that the lahar might have originated in a large slope failure on the south side of the Mount St. Helens of early Cougar time.

There is no known stratigraphic record of volcanism at Mount St. Helens between about 18,000 and 13,000 yr ago.

SWIFT CREEK ERUPTIVE PERIOD

The third eruptive period was characterized by repeated explosive eruptions that initially produced many pyroclastic flows as well as pumiceous air-fall tephra deposits (table 2, set S), some of which had large volumes and extended at least as far east as central Washington. These eruptions of dacite pumice were followed by many lithic pyroclastic flows, which are believed to have been derived from domes; at least one of these pyroclastic flows reached a point 21 km from the center of the present volcano. The pyroclastic flows were followed, in turn, by another series of explosive eruptions that produced the voluminous tephra set J (table 2). One coarse pumice layer of set J extends west-southwest from Mount St. Helens, and is as much as 20 cm thick as far as 20 km from the volcano. This layer represents the only coarse and thick pumice known to have been carried principally in a westerly direction. The sequence of explosive eruptions that formed set J apparently ended the Swift Creek eruptive period sometime before 8,000 yr ago, and was followed by a quiet period of at least 4,000 yr.

SMITH CREEK ERUPTIVE PERIOD

Multiple explosive eruptions of the Smith Creek eruptive period, which began about 4,000 yr ago, initiated at least 700 yr of intermittent and at times voluminous eruptive activity. Three coarse pumice layers at the base of tephra set Y are overlain by layers of denser, somewhat vesicular tephra. Deposition of these units was followed by an interval during which a soil began to develop on the tephra. The next eruption of the period produced the most voluminous and widespread tephra deposit of the last 4,000 yr; it is one of the largest, if not the largest, in the history of the volcano, and has an estimated volume of at least 3 km^3. The resulting pumice layer, Yn, has been found nearly 900 km to the north-northeast in Canada (Westgate and others, 1970, p. 184). The formation of this layer was followed shortly by another voluminous eruption of tephra, which resulted in layer Ye (Mullineaux and others, 1975, p. 331), then by a pumiceous pyroclastic flow and a coarse lithic pyroclastic flow. The lithic pyroclastic flow was accompanied by clouds of ash that spread at least a kilometer beyond the sides of the flow and as much as 2 km beyond its front. Many smaller eruptions of lithic and moderately vesicular ash and lapilli followed, perhaps within a few years or tens of years.

Lahars and pyroclastic flows of Smith Creek age formed a fan north of the volcano, and lahars extended down the North Fork Toutle River at least as

far as 50 km downvalley from Spirit Lake. An ancestor of the lake probably came into existence at this time, dammed in the North Fork valley by the fan of lahars and pyroclastic-flow deposits. It is not known if the lake ever existed before Smith Creek time.

A dormant interval of apparently no more than a few hundred years followed the Smith Creek eruptive period.

PINE CREEK ERUPTIVE PERIOD

Although only a short time elapsed between the Smith Creek and Pine Creek periods, eruptive products of Pine Creek age contain an iron-magnesium phenocryst assemblage that is distinctly different from those of Smith Creek age (table 2). During the Pine Creek eruptive period, large pumiceous and lithic pyroclastic flows moved away from the volcano in nearly all directions. The lithic pyroclastic flows, some of which extended as far as 18 km from the present center of the volcano, are believed to have been derived from dacite domes. Eruptions of dacitic airfall tephra were of small volume, but at least four formed recognizable layers as far away as Mount Rainier (Mullineaux, 1974, p. 36).

During this time, lahars and fluvial deposits aggraded the valley floors of both the North and South Fork Toutle River, and created the basin of Silver Lake 50 km west-northwest of the volcano by blocking a tributary valley (Mullineaux and Crandell, 1962). Similar deposits also formed a continuous fill across the floor of the Cowlitz River valley near Castle Rock (fig. 1) that was about 6 m above present river level; this fill probably extended 20 km farther to the mouth of the Cowlitz River. Lahars and fluvial deposits formed a similar fill in the Lewis River valley which, near Woodland, was about 7.5 m higher than the present flood plain (Crandell and Mullineaux, 1973, p. A17–A18).

The eruptions of Pine Creek time extended over a period of about 500 yr. No single eruption of very large volume has been recognized from deposits of Pine Creek age, and the period seems to have been characterized by many tens of eruptions of small to moderate volume and the growth of one or more dacite domes. Some radiocarbon dates on deposits of Pine Creek and Castle Creek age overlap, and if the two eruptive periods were separated by a dormant interval, it must have been short.

CASTLE CREEK ERUPTIVE PERIOD

The next period of activity marked a significant change in eruptive behavior and variety of rock types being erupted at Mount St. Helens (tables 1, 3). During the Castle Creek eruptive period, both andesite and basalt were erupted as well as dacite, and these rock types evidently alternated in quick succession. The overall sequence includes, from oldest to youngest, andesite, dacite, basalt, andesite, dacite, basalt (table 1).

Thus, the stratigraphic sequence of Castle Creek time is complex, and not all stratigraphic units are represented on all sides of the volcano. Northwest of Mount St. Helens, in the Castle Creek valley, the sequence preserved includes the following:

Lava flow of olivine basalt (youngest)
Lava flow of hypersthene-augite andesite
Tephra deposit of olivine-augite andesite scoria (layer Bo)
Pyroclastic-flow deposits of hypersthene-dacite pumice
Tephra deposit of hypersthene-augite andesite scoria (layer Bh)
Lava flow and lahars of hypersthene-augite andesite (oldest)

The pumiceous pyroclastic-flow deposits have a radiocarbon age of 2,000–2,200 yr. Deposits and rocks of Castle Creek age on the south and east flanks of the volcano include pahoehoe basalt lava flows whose radiocarbon age is about 1,900 yr, and pumiceous dacite tephra whose age is about 1,800 yr (layer Bi, fig. 5; tables 1, 2). East of the volcano, layer Bi overlies a pyroclastic-flow deposit of pyroxene andesite, and directly underlies thin olivine basalt lava flows which probably are correlative with the uppermost unit in the Castle Creek valley. The Dogs Head dacite dome was extruded before those thin olivine basalt flows, probably during the Castle Creek eruptive period. Layer Bu is the youngest tephra of Castle Creek age; it underlies a deposit whose radiocarbon age is about 1,620 yr. This tephra is basaltic and probably was formed when thin olivine basalt lava flows were erupted near the end of the Castle Creek period.

Castle Creek time marked the start of eruptions that built the modern volcano. It is interesting to note that the change in eruptive behavior from that of the preceding 35,000–plus years did not follow a long


W
Bu
Bi
Bo
Bh
P
Y

period of dormancy like several that occurred during Mount St. Helens' earlier history. The dormant interval that followed Castle Creek time apparently lasted about 600 yr.

SUGAR BOWL ERUPTIVE PERIOD

During the next 1,200 yr, the only eruptions recorded at Mount St. Helens are those associated with the formation of Sugar Bowl, a dome of hypersthene-hornblende dacite at the north base of the volcano. During extrusion of the dome, a directed blast carried rock fragments laterally northeastward in a sector at least 50° wide and to a distance of at least 10 km. The resulting deposits are as much as 50 cm thick and consist of ash, lapilli, and breadcrusted blocks of dacite from the dome, fragments of charcoal, and stringers of material eroded from the underlying soil. A single fragment of charcoal from within the deposit has a radiocarbon age of about 1,150 yr, whereas a sample of wood charred and buried by the deposit has an age of about 1,400 yr (Hoblitt and others, 1980, p. 556). We provisionally assign an age of about 1,150 yr to the blast deposit; the older date may have been obtained from a fragment of a mature tree that was overridden by the blast.

A pyroclastic-flow deposit of breadcrusted blocks, as well as prismatically jointed blocks of dacite of the same composition as the dome, was found on the north slope of Mount St. Helens downslope from Sugar Bowl; this pyroclastic flow may have occurred at the time of the lateral blast. Three lahars containing breadcrusted blocks of similar dacite were formerly exposed in the North Fork Toutle River valley west of Spirit Lake. These lahars may have been caused by melting of snow by the lateral blast or by the pyroclastic flow.

East Dome, a small dome of hypersthene-hornblende dacite at the east base of the volcano, may have been formed at about the same time as the Sugar Bowl dome. East Dome is overlain by tephra of the Kalama period but not of the Castle Creek period, and could have been formed anytime between the Castle Creek and Kalama eruptive periods, a time span of about 1,200 yr.

Figure 5.—Young tephra sequence 8 km southeast of the former summit. Pale dacite tephras (sets Y and P) are overlain by tephras of Castle Creek and younger periods that include dark andesite tephras of layers Bh and Bo, pale dacite pumice of layer Bi that is about 1,800 yr old, dark basalt tephras of layer Bu, and white dacite pumice of set W.

KALAMA ERUPTIVE PERIOD

Most of the rocks visible at the surface of the volcano before eruptions began in 1980 were formed during the Kalama eruptive period. Although the range in radiocarbon dates and ages of trees on deposits of Kalama age suggest that the eruptive period lasted from nearly 500 to 350 yr ago, all the events described here probably occurred during a shorter time span, perhaps less than a century.

The Kalama eruptive period began with the explosive eruption of a large volume of dacite pumice (layer Wn), which forms the basal part of tephra set W (table 2). Layer Wn was deposited northeastward from the volcano across northeastern Washington and into Canada (Smith and others, 1977, p. 209) and was followed by additional pumice layers. At about the same time, pyroclastic flows of pumiceous and lithic dacite moved down the southwest flank of the volcano. The relative timing of these events is poorly known because most of the air-fall tephra was carried eastward and northeastward, whereas the pyroclastic flows have been found only on the southwest flank of Mount St. Helens.

A short time later, scoriaceous tephra of andesitic composition (table 2, set X) was erupted. In addition, andesite lava flows extended down the west, south, and east slopes of the volcano, and andesite pyroclastic flows moved down the north, west, and south flanks.

These eruptions of andesite were followed by the extrusion of the dacite dome that formed the summit of the volcano (fig. 4) before the May 18, 1980, eruption. Avalanches of hot debris from the dome spilled down over the upper parts of the preceding lava flows, and some of this hot debris partly filled channels between levees of the andesite lava flows on the south side of the volcano (Hoblitt and others, 1980, p. 558). Late in this eruptive period, a pyroclastic flow of pumiceous dacite moved northwestward from the volcano down the Castle Creek valley and covered lahars of summit-dome debris. Charcoal from the pyroclastic-flow deposit has a radiocarbon age of about 350 yr (Hoblitt and others, 1980, p. 558).

The Kalama eruptive period was characterized by frequent volcanism of considerable variety; rock types being erupted alternated from dacite to andesite and back to dacite, and the volcano grew to its pre-1980 size and shape. The eruptive period was followed by a dormant interval of about 200 yr.

GOAT ROCKS ERUPTIVE PERIOD

The Goat Rocks eruptive period began about A.D. 1800 with the explosive eruption of the dacitic pumice of layer T. This pumice was carried northeastward across Washington to northern Idaho (Okazaki and others, 1972, p. 81) and apparently was the only eruptive product of that time. Many minor explosive eruptions of the Goat Rocks period were observed by explorers, traders, and settlers from the 1830's to the mid-1850's. The Floating Island Lava Flow (andesite) (fig. 2) was erupted before 1838 (Lawrence, 1941, p. 59) and evidently was followed by extrusion of the Goat Rocks dacite dome on the north flank of the volcano (Hoblitt and others, 1980, p. 558).

The last eruption of the Goat Rocks eruptive period was in 1857, when "volumes of dense smoke and fire" were noted (Frank Balch, quoted in Majors, 1980, p. 36). A recent study of old records has suggested that minor eruptions of Mount St. Helens also occurred in 1898, 1903, and 1921 (Majors, 1980, p. 36–41). The published descriptions of these events suggest that they were small-scale steam explosions, and none produced deposits that were recognized in our studies.

DISCUSSION

One of the most interesting features of Mount St. Helens' history is the change in eruptive behavior that occurred about 2,500 yr ago. Eruptions of dacite had characterized the volcano for more than 35,000 yr. Then, with virtually no interruption in eruptive activity, andesite and basalt began to alternate with dacite, and not always in the same order. The chemical composition of eruptive products changed gradually during some episodes and abruptly during others. Thus, basalt followed dacite and dacite succeeded basalt; andesite followed dacite of considerably different SiO_2 content, and vice versa (table 3). Some of these changes in composition of eruptive products are not adequately explained as results of eruption of cyclic sequences of compositionally different magmas derived from successively deeper levels in a larger magma body that differentiated at shallow depth, as proposed by Hopson (1971) and Hopson and Melson (1980). An alternative explanation that fits the stratigraphic record better, suggested by R. E. Wilcox (oral commun., 1974), is that some changes resulted from repeated contributions from more than one magma body, or from different parts of an inhomogeneous magma.

Explosive eruptions of volumes on the order of 0.1 to 3 km^3 have occurred repeatedly at Mount St. Helens during some eruptive periods in the past. This record suggests that a similar sequence could occur during the present period of activity and could result in one or more explosive magmatic eruptions of similar or larger volume than the eruption of May 18. If the lengths of the last two eruptive periods are a valid guide to the future, we might expect intermittent eruptive activity to continue for several decades.

REFERENCES CITED

Alley, N. F., 1979, Middle Wisconsin stratigraphy and climatic reconstruction, southern Vancouver Island, British Columbia: Quaternary Research, v. 11, no. 2, p. 213–237.

Carithers, Ward, 1946, Pumice and pumicite occurrences of Washington: Washington Division of Mines and Geology Report of Investigations 15, 78 p.

Crandell, D. R., and Mullineaux, D. R., 1973, Pine Creek volcanic assemblage at Mount St. Helens, Washington: U.S. Geological Survey Bulletin 1383-A, 23 p.

_____1978, Potential hazards from future eruptions of Mount St. Helens volcano, Washington: U.S. Geological Survey Bulletin 1383-C, 26 p.

Crandell, D. R., Mullineaux, D. R., Miller, R. D., and Rubin, Meyer, 1962, Pyroclastic deposits of Recent age at Mount Rainier, Washington, *in* Short papers in geology, hydrology, and topography: U.S. Geological Survey Professional Paper 450-D, p. D64–D68.

Crandell, D. R., Mullineaux, D. R., and Rubin, Meyer, 1975, Mount St. Helens volcano; recent and future behavior: Science, v. 187, no. 4175, p. 438–441.

Fulton, R. J., and Armstrong, J. E., 1965, Day 11, *in* Schultz, C. B., and Smith, H. T. U., eds., International Association (Union) of Quaternary Research Congress, 7th, 1965, Guidebook of Field Conference J, Pacific Northwest: p. 87–98.

Greeley, Ronald, and Hyde, J. H., 1972, Lava tubes of the Cave Basalt, Mount St. Helens, Washington: Geological Society of America Bulletin, v. 83, no. 8, p. 2397–2418.

Hoblitt, R. P., Crandell, D. R., and Mullineaux, D. R., 1980, Mount St. Helens eruptive behavior during the past 1,500 years: Geology, v. 8, no. 11, p. 555–559.

Hopson, C. A., 1971, Eruptive sequence at Mount St. Helens, Washington: Geological Society of America Abstracts with Programs, v. 3, no. 2, p. 138.

Hopson, C. A., and Melson, W. G., 1980, Mount St. Helens eruptive cycles since 100 A. D. [abs.]: EOS, v. 61, no. 46, p. 1132-1133.

Hyde, J. H., 1975, Upper Pleistocene pyroclastic-flow deposits and lahars south of Mount St. Helens volcano, Washington: U.S. Geological Survey Bulletin 1383-B, 20 p.

Lawrence, D. B., 1939, Continuing research on the flora of Mount St. Helens: Mazama, v. 21, no. 12, p. 49-54.

_____1941, The "floating island" lava flow of Mount St. Helens: Mazama, v. 23, no. 12, p. 56-60.

_____1954, Diagrammatic history of the northeast slope of Mount St. Helens, Washington: Mazama, v. 36, no. 13, p. 41-44.

Majors, H. M., 1980, Mount St. Helens series: Northwest Discovery, v. 1, no. 1, p. 4-51.

Mullineaux, D. R., 1974, Pumice and other pyroclastic deposits in Mount Rainier National Park, Washington: U.S. Geological Survey Bulletin 1326, 83 p.

Mullineaux, D. R., and Crandell, D. R., 1960, Late Recent age of Mount St. Helens volcano, Washington: U.S. Geological Survey Professional Paper 400-B, p. 307-308.

_____1962, Recent lahars from Mount St. Helens, Washington: Geological Society of America Bulletin, v. 73, no. 7, p. 855-870.

Mullineaux, D. R., Hyde, J. H., and Rubin, Meyer, 1975, Widespread late glacial and postglacial tephra deposits from Mount St. Helens, Washington: U.S. Geological Survey Journal of Research, v. 3, no. 3, p. 329-335.

Okazaki, Rose, Smith, H. W., Gilkeson, R. A., and Franklin, Jerry, 1972, Correlation of West Blacktail ash with pyroclastic layer T from the 1800 A.D. eruption of Mount St. Helens: Northwest Science, v. 46, no. 2, p. 77-89.

Smith, H. W., Okazaki, Rose, and Knowles, C. R., 1977, Electron microprobe analysis of glass shards from tephra assigned to set W, Mount St. Helens, Washington: Quaternary Research, v. 7, no. 2, p. 207-217.

Verhoogen, Jean, 1937, Mount St. Helens, a recent Cascade volcano: California University, Department of Geological Sciences Bulletin, v. 24, no. 9, p. 263-302.

Westgate, J. A., Smith, D. G. W., and Nichols, H., 1970, Late Quaternary pyroclastic layers in the Edmonton area, Alberta, *in* Symposium on pedology and Quaternary research, Edmonton, 1969, Proceedings: Alberta University Press, p. 179-187.

THE 1980 ERUPTIONS OF MOUNT ST. HELENS, WASHINGTON

CHRONOLOGY OF THE 1980 ERUPTIVE ACTIVITY

By ROBERT L. CHRISTIANSEN *and* DONALD W. PETERSON

ABSTRACT

Mount St. Helens, which had been dormant since 1857, became active in late March 1980 with a swarm of earthquakes that increased quickly to extremely high rates. Eruptions began on March 27 with a short crater-forming event. Steam-blast eruptions of lithic-crystal ash continued intermittently from the summit crater through April 22, paused until May 7, then recurred through May 14. Throughout the period from March 27 through the morning of May 18, rapid major deformation of the north flank gave dramatic indications of magmatic intrusion into the volcano.

The climactic eruption began at 0832 PDT on May 18, probably triggered by an earthquake of magnitude 5 that caused failure of the bulging north flank as a 2.3-km^3 rockslide-avalanche. This failure rapidly unloaded the volcanic edifice, and probably caused the water in its hydrothermal system to flash to steam, initiating a series of northward-directed hydrothermal blasts that devastated an area of 600 km^2. These events in turn triggered a 9-hr dacitic magmatic eruption that drove a Plinian column more than 20 km high, producing ash fallout for more than 1,500 km to the east as well as pumiceous ash flows on the volcano's north flank. Catastrophic mudflows and floods were generated from rapid melting of snow and ice and water derived from the avalanche.

Smaller but significant magmatic eruptions occurred on May 25, June 12, July 22, and October 16–18; each lasted as long as several hours and produced eruption columns more than 10 km high, dacitic fallout, and pumiceous ash flows. A dacitic dome emplaced during or after the June eruption was partially reamed out in the pyroclastic eruption of July 22. Another dome emplaced after the August eruption was removed and then replaced by a third dome during the mid-October eruption. During the times that they remained intact, each of these domes appeared to act as a leaky plug to gas emissions through the volcano's central crater vent. Occasional violent gas emissions between major eruptions produced brief eruption plumes to heights of a few kilometers. Beginning in late December and continuing through the end of 1980, a new dome was emplaced and grew rapidly to the accompaniment of increased seismicity and gas emissions.

INTRODUCTION

The Mount St. Helens eruptions of 1980 included a variety of events—swarms of earthquakes, premagmatic steam-blast eruptions, a massive rockslide avalanche that triggered a low-angle directed blast and a voluminous vertical eruption column, destructive mudflows and floods, pumiceous pyroclastic flows, and lava domes. This report gives a brief summary of the most important events and provides a chronologic framework into which topical papers that follow can be fitted. Photographs are by R. L. Christiansen unless otherwise noted.

ACKNOWLEDGMENTS

This report draws upon the data of many people, far too numerous to acknowledge individually. Because the material presented is based upon so many observations rather than on published materials, it contains no reference citations other than to a few individuals whose observations were unique.

Among the many contributors of data, none was more essential to the systematic reconstruction of the events of 1980 at Mount St. Helens than David Johnston, to whose memory this report is dedicated.

Dave, who was present through all of the activity up to the climactic eruption and who lost his life in that eruption, provided far more than data. His insights and his thoroughly scientific attitude were crucial to the entire effort; they still serve as a model for us all.

INITIAL PERIOD OF SEISMIC AND STEAM-BLAST ACTIVITY

On March 27, 1980, Mount St. Helens, in the Cascade Range of southern Washington (figs. 1, 3) erupted for the first time in about a century and a quarter. This volcanic eruption, the first in the conterminous United States since the end of a long series of eruptions at Lassen Peak in California that lasted from 1914 to 1917, afforded the first opportunity to study an erupting Cascade volcano since the advent of modern volcano-monitoring techniques. Mount St. Helens itself had not erupted since 1857, at the end of a decades-long period of intermittent activity.

The first major event of the 1980 activity was an earthquake of magnitude 4.0+ at 1547 PST[1] on March 20 (day 80:23:47 UT). The swarm of earthquakes increased rapidly to a climax in the late afternoon of March 25, when 24 earthquakes of magnitude 4 and greater occurred during an 8-hr period. Overflights on March 24 had indicated no major changes in the appearance of Mount St. Helens other than avalanches of snow and ice. Additional overflights on March 25, during the peak of seismic activity, revealed several new fractures through glaciers high on the mountain and numerous additional large rockfalls and avalanches. None of the new fractures, however, coincided with the larger fractures that later formed across the summit area; the fractures that formed on March 25 probably resulted directly from ground shaking and the accelerated downslope movement of glacial ice on the volcanic edifice. After March 25, seismicity declined somewhat but remained at a high level, with about 30 events per day having a magnitude of 3 or greater (6/day of magnitude 4 or greater).

The first eruption occurred in the early afternoon of March 27. Although extensive cloud cover had hidden the volcano from the air since the morning of March 25, a loud boom was widely heard at 1236 PST on March 27. Aerial observers reported a dark dense column of volcanic ash rising through the clouds, eventually to a height of 2,000 m above the volcano.

With clearing weather later in the afternoon, several changes were conspicuous on the mountain. A new crater about 60–75 m across had formed in the northern part of the old 400-m-wide ice-filled summit crater, and snow on the southeast sector of the volcano was covered by dark ash emitted from the new crater (fig. 6). The summit area was bisected by an east-trending fracture nearly 1,500 m long that extended from high on the northwest flank, across the old crater, down the upper northeast flank. Another less continuous fracture system paralleled this master fracture just north of the old crater rim and bounded the south side of a newly uplifted block, or bulge, on the volcano's north flank. These changes clearly had occurred during the period of extremely high seismicity and initial eruption, between observations on the morning of March 25 and the afternoon of March 27. One observer, David Gibney—an aerial spotter of the U.S. Forest Service (oral commun., 1980)—reported seeing the large fractures open and close and the uplifted north flank continue to break and rise during the few hours after the first eruption.

A second explosive eruption, beginning at about 0200 on March 28 and lasting nearly 2 hr, was observed from the air. Ash from that eruption spread for many kilometers to the east of the volcano. By nightfall on March 28, at least a dozen more eruptions had occurred, many of them lasting only a few

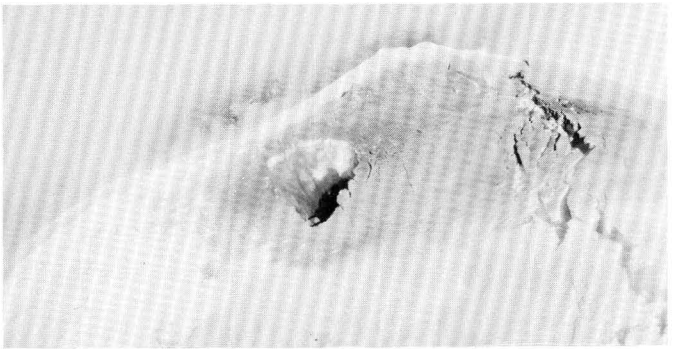

Figure 6.—Summit area of Mount St. Helens. Aerial view on the afternoon of March 27 looking east, showing newly formed crater, swath of dark new ash mainly to southeast of new crater, an east-west fault across middle of summit area, and an uplift or bulge on upper north flank of the volcano. Photograph by David Frank.

[1]Times in this volume are local times and are expressed on a 24-hr scale. Before April 27 and from October 26 through the end of the year, they are Pacific Standard time (PST), which is Universal Time (UT) less 8 hr; between April 27 and October 25, they are Pacific Daylight Saving time (PDT), which is UT less 7 hr.

minutes but some for nearly an hour. Poor weather hampered observations on all of these days. By March 29, however, clear views of the summit revealed the presence of a second larger crater west of the one first seen on March 27 (fig. 21). A septum about 10 m wide separated the two craters. Pale-blue flames were first observed on the night of March 29 and were subsequently observed in each of the two craters.

On April 1, a weak burst of harmonic tremor lasted for about 5 min, but stronger tremor bursts the next day were recorded by seismometers as far away as 100 km. Sporadic harmonic tremor continued until April 12, but these tremor bursts could not be correlated directly with the visible character or intensity of eruptive events. The frequency, duration, and intensity of eruptive blasts gradually decreased until April 22, when eruptions temporarily ceased. Eruptions had declined in frequency from an average of about 1/hr in March to about 1/day by the end of this first period of activity.

The eruptions of this first period produced only lithic-crystal ejecta, composed of fragments of preexisting rocks. All of this material was emitted from vents in the new summit craters, which were repeatedly reamed. By April 7, the septum separating the two craters had broken down entirely, and the enlarged single crater grew to about 500 m from west to east and about 300 m north to south (fig. 7). By late in the month, the crater was about 100–250 m deep. (Its rim was highly irregular in elevation.)

As eruptive activity declined slowly through early and mid-April, earthquakes continued at still impressive rates, generally more than 30/day of magnitude 3 or greater. Many of these earthquakes were large enough to be felt strongly on and immediately adjacent to the volcano. All were very shallow, however, and few were felt very far from the volcano. The epicenters were confined to a small area that coincided with the uplift or bulge on the volcano's north flank. These frequent shallow earthquakes triggered numerous avalanches, which were concentrated around the northern sector of the mountain. Most avalanches started on the upper slopes of the volcano where ashfall was heaviest; because they involved dark ash-laden snow, the avalanche deposits stood out prominently and were at first mistaken for mudflows.

After eruptive activity ceased temporarily on April 22, fumaroles vented continuously within the

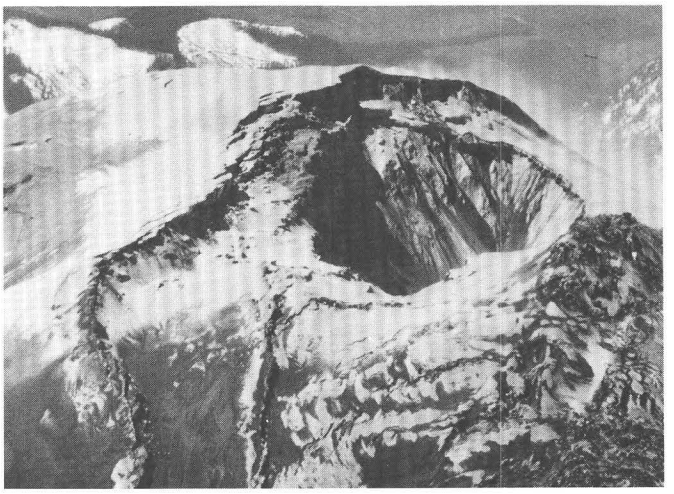

Figure 7.—Summit area of Mount St. Helens. Aerial view, April 12, looking southwest, showing enlargement and coalescence of crater complex and further increase in relief on east-west fault.

crater, in contrast to earlier conditions, when the crater generally was clear between eruptions. The most continuous and generally largest fumarole was on the south wall just above the eastern part of the crater floor. The fumaroles could not be sampled because of frequent ice avalanches from the crater wall above, but a water sample was collected from a small pond on the eastern crater floor. Chemical analysis of the water indicated high chloride, sulfate, and ammonia, relative to local snowmelt, suggesting a contribution to its composition by fluids of deeper origin.

Small eruptions resumed on May 7 and continued sporadically through May 14; these eruptions were similar to those of March and April. A general description can be applied to all of the pre–May 18 eruptions. In a few events, columns of ash and condensed steam rose as high as 3,000 m above the crater floor. Generally, however, the gas-driven bursts of ash-laden material rose less than 500 m above the vents, above which condensed steam billowed in white clouds. Collected samples of distal ejecta consisted entirely of lithic-crystal ash; at the crater rim, the ejecta also included abundant blocks of dacite from the summit dome and sparse blocks of more mafic rock types from the volcanic edifice. The eruptions consisted of intermittent blasts at intervals of a few minutes to several hours that varied greatly in size and duration. The smaller eruptions were confined to the crater; some consisted of only a single blast. Larger ones lasted as long as several hours, with individual pulsating blasts

occurring up to several times per minute, emitting clouds that reached 1,500–3,000 m above the crater. Varying winds carried ash to all flanks of the volcano, entirely mantling its upper slopes.

Close examination of especially the smaller eruptions showed many of them to consist of three parts: (1) a lower, fingerlike ash column, (2) a gray-brown, ash-laden cloud above, and (3) an upper white cloud. The fingerlike ash column was nearly black and had spiked tops similar to the "cockstail" eruptive columns commonly described elsewhere from steam-blast eruptions (fig. 8). These fingerlike columns rose vigorously from the crater bottom; several clearly rose through small, temporary crater lakes and others through collapse pits in the ice-block talus on the crater walls and floor. Many of these columns were dark probably because the ash they carried was wet; ash on the surface became lighter after it dried out over several days. Other evidence suggests that the columns had a high water content: many of them were emitted from lakes; large amounts of water fell from the columns and coursed down the crater slopes; and new lakes commonly formed or preexisting lakes were fullest immediately after such blasts.

Figure 8.—Fingerlike ash column in initial burst of a steam-blast eruption from one of the summit craters of Mount St. Helens, March 28. Height of visible part of the column is approximately 50 m. Photograph by James G. Moore.

Roiling, gray-brown, ash-laden clouds developed from the tops of the ash-finger columns and commonly obscured them (fig. 9). These clouds expanded rapidly as blocks of rocks and ice trailing white vapor-condensate were blasted through them. The upper white clouds were formed by continued expansion of the gray-brown ash cloud and by the condensation of water vapor, growing on calm days to great heights. Under normal windy conditions, however, they blew nearly horizontally, dropping thin, nearly vertical veils of ash.

Downslope winds commonly generated sweeping clouds of ash down the volcano's flank. Although these ground-hugging clouds were first regarded as possible pyroclastic flows, further observations showed them to be driven by the wind rather than by the eruption column itself. Further movement downslope, however, apparently occurred as density flows. Typically, the ash swept up in rising air currents from the lower flanks of the volcano. The deposits left by these flows commonly were very thin, some of negligible thickness; where conspicuous, their downslope limits were marked on new snow by a sharp scalloped boundary of black ash. Occasionally these dust-laden density currents in their downward sweep produced spectacular displays of lightning parallel to the volcano slope.

Fumarolic activity continued after eruptions resumed in early May, and it appeared to increase gradually. A large pitlike steam vent opened high on the Shoestring Glacier about May 11 and remained open and active during the succeeding week. More new steam vents appeared to open in the upper part of the bulging north flank during the first half of May, and thermal infrared scanning at about mid-month revealed numerous areas of thermal emission in the ice crevasses of that area.

The prominent topographic bulge that had been noted on the north flank of the volcano on the first day of eruption continued for nearly 2 mo to become larger and more conspicuous. Ground ruptures at the 5,400-ft level on the north flank were first noted on April 3 and provided early evidence that the bulge affected a large part of the cone. The first detailed photogrammetric measurements, completed in mid-April and compared with contours based on photography of August 1979, revealed the startling dimensions of this bulge. By May 12 (the date of the last con-

Figure 9.—Steam-blast eruption from summit crater of Mount St. Helens. Aerial view, April 6, looking southwest, showing a roiling, gray-brown, ash-laden cloud that envelops and almost completely hides an initial fingerlike ash column, and an upper white cloud formed by atmospheric condensation of water vapor in the convectively rising top of the eruptive column. Photograph by James G. Moore.

tour map predating the climactic eruption of May 18), the high point north of the old crater rim stood 150 m above a corresponding point on the former north slope, and the Goat Rocks area low on the bulge had been displaced northward by 106 m. Geodetic measurements showed that displacement was only slightly upward near the top of the bulge; it was mainly outward—nearly horizontally—at consistent rates of about 2 m/day. No appreciable change occurred in this rate of displacement, even up to 1½ hr before the climactic eruption. Photogrammetric evidence suggests that no appreciable bulging of the north flank occurred before the events of 1980. Comparison of maps made from aerial photographs of 1952 and 1979 indicates that if any bulging did occur before August 1979, the amount was close to the resolution possible with the 80-ft (24.4-m) contour interval of the maps—an order of magnitude less than that which occurred between late March and mid-May 1980.

During late April and early May, the upper part of the bulge changed in general appearance. A high point that had formed in late March (north peak 1) just north of the crater stagnated and subsided during April as a second high point (north peak 2) began to form farther north (fig. 10). An east-west line between these two points appeared to be a fracture zone that delimited areas of differing rates and styles of deformation. In early May, old fractures and disturbed segments of the north and west rims of the summit crater south of the fracture zone were partly filled by snow and drifted volcanic ash and appeared to be parts of a coherent graben block that moved downward with the crater. By contrast, the surface of the actively bulging main part of the north flank continued to break and distort,

indicating persistent internal deformation as well as outward bodily displacement.

By mid-May, earthquakes of magnitude 3 or greater continued to occur at a rate of 20–40/day, including 5–10 of magnitude 4 or greater. Two magnitude-5.0 earthquakes occurred, on May 8 and 12. On May 8, the day following a resumption of eruptions, two periods of harmonic tremor were recorded, each lasting only a few minutes. No further harmonic tremor occurred until after the beginning of the May 18 eruption.

In summary, throughout an initial 2-mo period, ejecta consisted entirely of fragmental material derived from the volcanic edifice, most of it generated by shattering and pulverization at shallow levels within the 350-yr-old summit dome. A moderate amount of this ash was distributed 50 km away and some was reported as far as 100 km to the east, but most fell within a few kilometers of the volcano's summit. Evidence for the involvement of water was abundant, and the eruptions apparently all resulted from a steam-blast mechanism that reflected internal heating of the volcano by a shallow intrusion that also produced localized, but very high, seismicity and a rapidly and continuously bulging north flank.

THE CLIMACTIC ERUPTION

The situation at Mount St. Helens in the early morning hours of May 18 was much as it had been for the preceding month. There had been no eruptions for 4 days; fumaroles remained active in the summit and north flank areas; seismicity was high but no greater than it had been for many weeks; deformation continued at an awesome rate, but the rate had neither increased nor decreased significantly since detailed measurements began on April 25.

Figure 10.—Mount St. Helens. Aerial view, May 16, looking east, showing bulge on north flank having two high points in its upper portion. Mount Adams on the horizon.

At 0832 PDT (day 139:15:32 UT), with no known immediate precursors, a magnitude-5+ earthquake triggered a rapid series of events. As seen by Keith and Dorothy Stoffel (written commun., 1980) from a small aircraft at low level directly above the summit crater, the earthquake caused avalanching from the walls of the crater and, only a few seconds later, triggered a sudden instability of the north flank. The entire north flank was described as "quivering" and appeared to almost liquefy. The slope failed along a surface intersecting the northern of the two high points on the north flank, near the east-west fracture separating the active bulge from the crater block. As the north flank began to slide away from this surface, a small, dark, ash-rich eruption plume rose directly from the base of the scarp and another from the summit crater rose to heights of about 200 m. As virtually the entire upper north flank slid off the cone and became a massive debris avalanche, a blast broke through the remainder of the flank, spewed ash and debris over a sector north of the volcano (fig. 11), overtook the massive avalanche, and devastated an area nearly 30 km from west to east and more than 20 km northward from the former summit of the volcano. In an inner zone extending nearly 10 km from the summit, much of which had been densely forested, virtually no trees remained. Beyond, nearly to the limit of the blast, all standing trees were blown to the ground, and at the blast's outer limit the trees were left standing but thoroughly seared. The devastated area of 600 km^2 was blanketed by a deposit of hot debris carried by the blast.

The sole of the debris avalanche was nearly at the base of the steep volcanic cone on the north side; the avalanche moved down the lower gradients of the volcano's outer flank and was nearly blocked by a ridge 8 km to the north. Part of the avalanche rounded the east end of that ridge and displaced the water from Spirit Lake, raising the bed in its southern part by more than 60 m. The bulk of the avalanche, however, turned westward down the valley of the North Fork Toutle River to form a craggy and hummocky deposit, part of which crossed the ridge to the

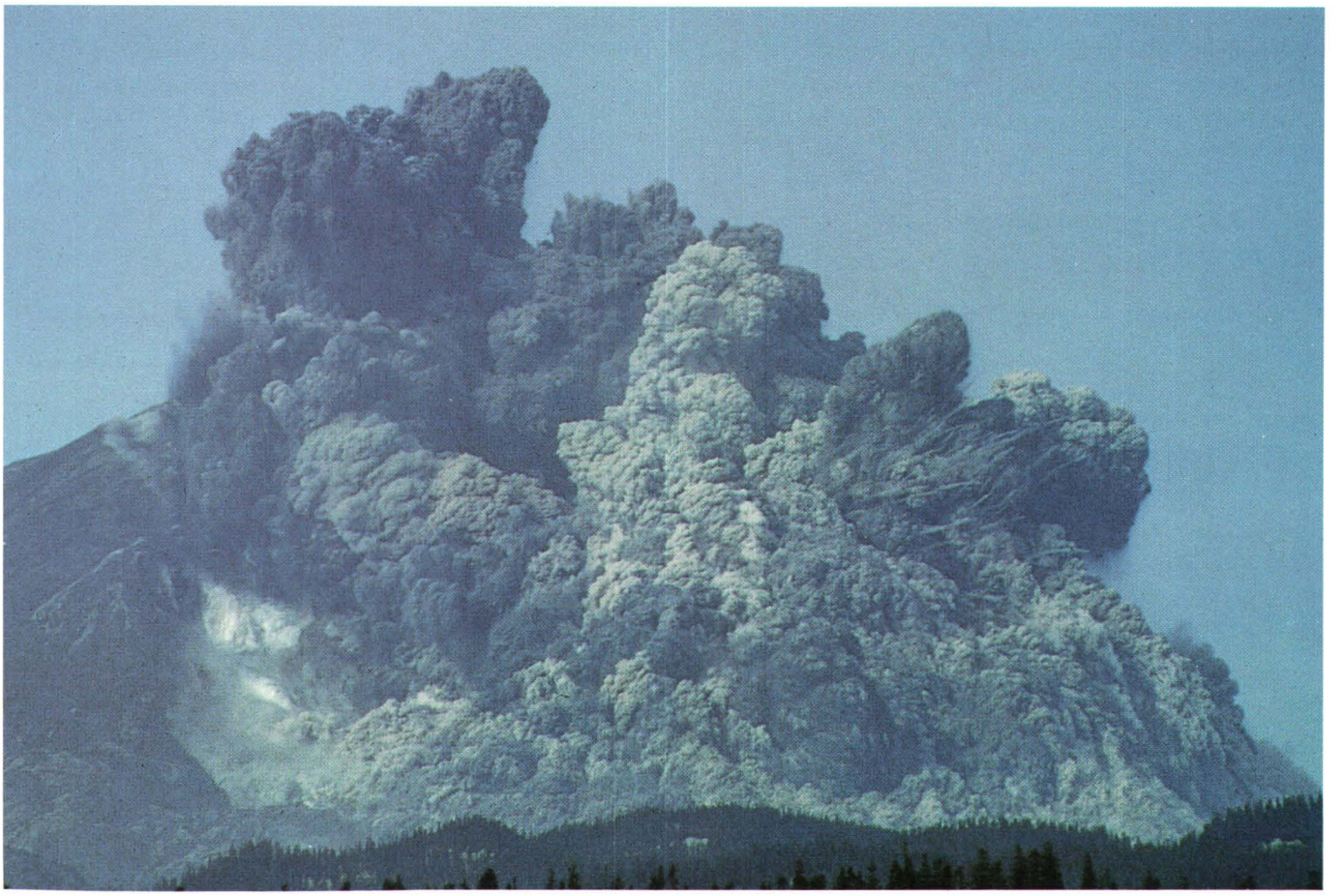

Figure 11.—Hydrothermal-magmatic blast of Mount St. Helens; view from Bear Meadow, 17 km northeast of summit, May 18, about 14 s after initial detachment of the landslide at 0832 PDT. Blast is directed laterally from center of volcano through scar left by landslide removal of volcano's north flank. Copyrighted photograph by Keith Ronholm, 1980, published with permission.

north, but most of which flowed as far as 23 km down the North Toutle. The total volume of the avalanche in place is about 2.8 km^3, and its length makes it one of the largest on record.

Water incorporated by the avalanche from the North Fork Toutle River and possibly from Spirit Lake combined with melting blocks of ice from the torn-out glaciers of the volcano's north flank and melting snow and ice from the volcano's remaining slopes to produce mudflows that later in the day coursed across the avalanche and down the North Fork Toutle River, sweeping up thousands of logs from timbering operations in the valley and destroying most bridges across the river. The mudflows continued downstream, depositing sediment in the Cowlitz River channel and also obstructing the deep-water navigation channel of the Columbia River. Smaller mudflows were produced from the east flank of the volcano and went down the valleys of Muddy River and Pine Creek into Swift Reservoir (pl. 1). Yet other mudflows and floods went from the volcano's northwest flank down the South Fork Toutle River; smaller floods occurred in the Kalama River on the southwest.

The initial events of the eruption—the rockslide avalanche, the northward blast of ash and debris, and the mudflows—caused most of the casualties and destruction in the immediate region of the volcano. However, within a few minutes a Plinian eruption column (fig. 12) began to rise from the position of the former summit crater and within less than 10 min had risen to a height of more than 20 km. Ash from this eruption cloud was rapidly blown east-northeastward, producing lightning and starting hundreds of small forest fires, causing darkness eastward for more than 200 km, and depositing ash for many hundreds of kilo-

meters. Major ash falls occurred as far east as central Montana, and ash fell visibly as far eastward as the Great Plains of the Central United States, more than 1,500 km away. As this Plinian eruption column grew, it reamed out the volcanic conduit. The eruptive crater, along with the upper 300 m of the cone that was entirely removed by the initial slide and blast, formed a great amphitheater 1½ × 3 km across, enclosed by the

Figure 12.—Plinian eruption column rising from the central crater of Mount St. Helens, 1330 PDT May 18. Aerial view looking northeast showing cauliflower-like structure of eruptive column and a pall of dust rising from area north of amphitheater-shaped crater. Photograph by J. G. Rosenbaum.

volcano's former east, south, and west flanks (fig. 16).

The Plinian phase of the eruption continued vigorously for 9 hr and produced numerous ash flows. Some of these were thin flows that spread out over much of the upper surface of the volcano and were generated by fallback from the expanding eruption column in the vicinity of the summit. Most of the flows were directed out through the large northward breach of the crater to form a fan of pumiceous ash flows over the avalanche, extending to Spirit Lake and part way down the North Fork Toutle River valley. Ash flows continued to be emplaced at least until dark on May 18. The hot blast deposits, the avalanche, and these ash flows were frequently disrupted in the vicinity of Spirit Lake and its former drainage into the North Fork Toutle River by large secondary steam-blast eruptions that formed craters as large as 20 m across and drove columns of ash to heights as great as 2,000 m above the surface.

The Plinian eruption began to decrease in intensity at about 1730 on May 18 and by the next morning had decreased to a very low level. Minor eruptive emissions persisted almost continuously until May 21 from a smaller vent crater near the center of the large amphitheater, but observations of their size and character were restricted by poor weather. Weak steam and ash eruptions continued intermittently for about a week.

The magma tapped during the major eruption of May 18 was dacitic. The principal juvenile material was a light-colored hypersthene-hornblende dacitic pumice having a range of silica content of about 63–64.5 percent. A texturally different rock type—the first magmatic material erupted—was incorporated into the initial blast deposits. It was a denser, and therefore, darker dacite whose composition is at the silicic end of the range of the pumice compositions. A total of about 0.2 km^3 of magmatic material (as reduced to the equivalent volume of dense rock) was erupted on May 18.

In summary, although no precursory changes in seismicity or in the rate of deformation on the north flank had provided immediate warning of an impending major slope failure, the longer term likelihood of such failure suggested the possibility that it could trigger a major volcanic eruption. The bulge probably had nearly reached the point of instability and might have been almost ready to begin creeping more rapidly toward failure when a magnitude-5+ earthquake at 0832 on May 18 intervened to push the mass over its stability threshold. The earthquake triggered the rockslide-avalanche, which in turn unloaded the hydrothermal system in the volcano that had driven intermittent steam-blast eruptions for the previous 2 mo. This abrupt release of confining pressure on hot water in the system caused a massive flashing to steam, initiating a hydrothermal blast that was directed laterally through the landslide scar. This sequence of events in turn caused further unloading of magma in the shallow body that was intruding the volcano, causing it to de-gas and to drive the Plinian eruption column that continued for the next 9 hr.

PERIOD OF SUBSEQUENT PYROCLASTIC ACTIVITY AND LAVA DOMES

A series of increasingly energetic ash eruptions on the Saturday night following the eruption of May 18 led to the second large eruptive event, on Sunday, May 25, from the vent crater within the amphitheater. That eruption began at about 0230 PDT during a period when winds were blowing in different directions at different altitudes. Although the eruption was an order of magnitude less voluminous than that of May 18, windblown ash was dispersed over wide areas of western Washington and Oregon and affected several metropolitan areas that had not experienced ash falls in the May 18 eruption.

For the next 2½ weeks, the volcano continued to emit large quantities of gas that rose in plumes of steam condensate to altitudes of 3–5 km above sea level. Sulfur emissions, monitored since late March, had remained low until the eruption of May 18. After that eruption, sulfur gases were emitted at a higher rate, but relatively little ash was carried in the gas plumes and appreciably none fell more than a few kilometers beyond the volcano. During this time, no lava appeared at the surface, but there were several night observations of incandescent rock, probably caused by hot gases streaming through the vents from a magma body not far below. Also during this time, small steam blasts continued to erupt through the avalanche and ash-flow fill in the former North Fork Toutle River valley north of the volcano. Some of the craters formed by those eruptions were enlarged considerably by repeated blasts and by the coalescence of smaller craters.

A third magmatic eruption took place on June 12. This eruption was preceded by several hours of harmonic tremor that began around midday and gradually grew in intensity throughout the afternoon. A marked increase in tremor amplitude was noted at 1905 PDT, and an eruption drove an ash column to at least 4 km above sea level by 1910. Tremor amplitude decreased markedly immediately after this brief eruptive pulse and fluctuated at moderate levels for more than 2 hr. The temporary lull was broken by a rapid, large increase in tremor amplitude at 2111, and by 2118 an eruption column had risen to 15 km above sea level. The height of the column fluctuated between 5 and 12 km above sea level until 0043 on June 13, when it decreased abruptly.

Prevailing winds carried the ejected ash south-southwest, allowing centimeter-sized pumice fragments to fall in Cougar, Wash., about 16 km downwind. Portland, Oreg., and Vancouver, Wash., received moderate ash falls beginning at about 2250.

Several new ash flows issued from the vent crater and descended the volcano's north flank during the June 12 activity. These flows nearly reached the south shore of Spirit Lake and overrode and locally ponded within steam-blast craters in the ash flows of the May 18 eruption. Like the May 25 deposits, the June 12 material contained some dark-gray, dense pumice as well as lighter colored and more vesicular pumice.

A lava dome (fig. 13) probably began to rise in the vent crater shortly after the explosive eruptions of June 12, but because of poor visibility it was not sighted until June 15. Several features suggest that the dome was close to the surface before and during the June 12 eruption. At the time of the last previous good view of the crater amphitheater on June 11, a large elliptical lake about 300–400 m long and 50–75 m wide occupied much of the southern crater floor. Its elliptical shape resulted from a broad flat topographic high in the center of the crater at the location of the subsequent dome. This mound, completely mantled by gray ash, may have represented the early rise of a magma plug nearly to the crater floor. Also, in contrast to the ash flows erupted on May 18 and 25, the ash flows of June 12 contain not only pumice but also abundant blocks of dense, gray dacite, as much as 2 m in diameter. The June 12 deposits thus resemble "block-and-ash" flows emplaced as a result of dome collapse on other volcanoes and may contain parts of the solidified margins of a cryptodome prior to its arrival at the surface.

Repeated observations from a hovering helicopter documented steady dome growth at a rate of 2–3 m/day from June 15 through the late afternoon of June 19. No observations were possible during poor weather from June 20 through June 27, but observations on June 28–29 suggested a stabilization after June 19 or even a slight collapse.

In mid-July, measurements showed an apparent northward expansion of the rampart north of the vent crater of about 5 cm/day. Mount St. Helens again erupted at 1714 PDT on July 22 (fig. 14) after a small swarm of shallow local earthquakes that began about 1000 that morning. From 1400 to 1500 there were 4 earthquakes, followed by 9 more from 1500 to 1600, and by 20 from 1600 to 1700. The first ash eruption lasted about 6 min and a pyroclastic column reached 14 km above sea level. A second ash cloud erupted at 1825 and lasted about 22 min, reaching a height of more than 18 km. The third and longest ash eruption began at 1901 and lasted about 2 hr and 40 min (fig. 14); maximum column heights fluctuated (the highest at 14 km at 1907) and from a distance gave the appearance of several separate eruptions. Winds blew the main ash cloud northeastward, and satellite images showed it to cross from Idaho into Canada. Pumiceous ash flows were erupted on the north flank of the volcano, especially during the second and third eruptive bursts. No harmonic tremor accompanied the earthquake swarm prior to the 1714 eruption, but tremor did occur during the periods of ash emission.

The July 22 eruption blasted a new crater through the center of the June lava dome. The walls of the new crater, which had a diameter of about 300 m and a tail-like southward extension of about 400 m, were in the still-hot June dome, which was mantled by several meters of new ash from the July eruption. No new dome was produced, and this new crater remained intact until an eruption in early August.

Following the explosive eruption of July 22, the crater area fumed—copiously at times—and columns of condensing water vapor rose to elevations as high as 3,000–3,500 m above sea level. A dull red incandescence was observable in dim light on the walls of the vent crater. The walls of the larger amphitheater around the vent crater produced numerous rock falls and avalanches. Once again, measurements in early August suggested northward expansion of the northern rampart of the vent crater by one to several centimeters per day. The principal measured gas emissions, CO_2 and SO_2, were moderately high at the

Figure 13.—Lava dome plugging June 12 vent crater. Aerial view, July 18, looking southwest. Average diameter of dome is 365 m. Photograph by Maurice and Katia Krafft, Centre de Volcanologie, Cernay, France, published with permission.

end of July but decreased somewhat in early August, and the ratio CO_2:SO_2 declined markedly on August 6.

Just after noon on August 7, harmonic tremor began, and it continued to increase in amplitude for several hours. The combination of changing gas fluxes, harmonic tremor, and occasional small earthquakes suggested an impending eruption, and ash emission started at 1623, growing rapidly to full eruption by 1627. This first burst produced an ash-laden eruptive column that rose to an elevation of more than 13 km. A small pumiceous ash flow swept the area below the breach on the north side of the amphitheater (fig. 15). The flow reached part way to Spirit Lake, leaving a thin lobate deposit. Smaller eruptions continued through the late afternoon and evening, with one major sequence around 1930. A culminating burst, nearly as large as the first one, began at 2232. The intensity of harmonic tremor decreased and small deep earthquakes occurred during the period following this last eruptive burst, which ended before midnight.

A dome began to rise in the vent crater on the morning of August 8, filling it to about half its former depth of 90 m by the end of the day and stopping growth just below crater-rim level by August 10. For several weeks following, the volcano remained relatively quiet; there were few earthquakes and no major eruptions. Some incandescence could still be seen in the walls of the vent crater and in cracks on the surface of the new lava dome. Gas emissions fluctuated from moderate to low levels.

Following the August 7 eruption, the volcano generally remained very quiet for more than 2 mo (fig. 16), and seismicity dropped to its lowest levels since before the reawakening of the volcano in March. A slow outward movement of the unstable sector on the north flank, however, indicated that

Figure 14.—Third pulse of eruption of July 22. Aerial view taken at 1907 PDT looking south, showing spreading mushroom top on convectively rising column and cloud of ash rising from an ash flow that has swept northward out of volcano's crater amphitheater. Northwest slope of volcano visible at lower right. Column height about 15 km. Photograph by James Vallance.

Figure 15.—Pumiceous ash flow of August 7 eruption, viewed from Coldwater Ridge, 8 km north of volcano. The fully developed ash flow was moving down lower north flank of volcano at about 1629 PDT. Speeds in excess of 100 km/hr were measured from carefully timed 35-mm still photographs and from 16-mm motion pictures. Photograph by Peter W. Lipman.

magma within the volcano remained active. During the second week of October, small shallow earthquakes resumed at the rate of one to a few per day. On October 16, their frequency gradually increased to several per hour, and at 1902 PDT a magnitude-3 earthquake occurred. The small earthquakes continued, and a pyroclastic eruption began at 2158, lasting between 5 and 10 min. Shallow seismicity continued, and other eruptive pulses followed at 0928 and 2112 on October 17 and 1235 and 1428 on October 18. Each of these events lasted from about 5 min to nearly an hour, although the most vigorous activity during each of them took place in the first few minutes. The pyroclastic eruption columns reached maximum heights of about 14 km. Small pyroclastic flows occurred during two of the events, descended the north flank of the cone, and reached lengths of about 5 km. The wind was variable throughout these events but blew generally from a sector between northwest and northeast; light ash falls occurred in a southern sector extending from the volcano to the Portland-Vancouver area and as far east as The

Dalles, Oreg. Following the final pyroclastic eruption on October 18, a new lava dome emerged from the floor of the crater and grew at a dramatic rate through the afternoon and evening. By the following morning it had obtained its ultimate size of more than 200 m in diameter and 40 m in height.

During the intervals between the major eruptions after May 18, occasional emissions of gas and some ash broke the general quiet; the ash probably was entrained, being derived from ejecta in and near the vent crater. Some of these events were accompanied by brief pulses of harmonic tremor and produced small perforations in the domes or crater floors. Significant events of this type occurred on July 28, August 15, and several times in September and October. After the mid-October eruption, the volcano returned to a very quiet state that persisted until late November, with very few earthquakes, rare episodes of harmonic tremor, little ground deformation, and only slow rates of gas emission. Beginning in late November, a new pattern began to develop. Low-level seismic events of uncertain character preceded or accompanied episodes of low-amplitude harmonic tremor. Accompanying some of these events were weak to moderate gas emissions, some of which carried entrained ash. On December 13, a small crater formed and a wedge-shaped sector of the dome was blasted away in one of these gas-emission events. Beginning during a period of increased seismicity between December 25 and 28, a new dome was extruded alongside the October dome. The new dome continued to rise and expand rapidly through the end of 1980, accompanied by frequent small, shallow earthquakes, harmonic tremor, and heavy gas emissions.

During the period of intermittent volcanic and seismic activity that followed the climactic eruption

Figure 16.—Mount St. Helens in repose, August 29, looking south from Harrys Ridge, 8 km north of the volcano. Shows amphitheater left by removal of north flank, collapse of summit, and eruptive enlargement of crater on May 18. A light fume cloud rises from vent crater within the amphitheater, which is partly plugged by dome emplaced after August 7 eruption.

of May 18, there were significant adjustments of the drainage system to the changes wrought by that eruption. The drainage that was disrupted and blocked by the massive avalanche of May 18 quickly began to reestablish itself across the hummocky surface of the avalanche in the North Fork Toutle River valley. The river course along the lower part of the avalanche had already been reestablished on the south side of the avalanche before the end of the day on May 18. One event illustrates in part how the establishment and integration of drainage continued to occur through the summer months. During the last 2 weeks of August, water from Maratta Creek, which had been impounded by an avalanche levee on the north side of the valley, was released suddenly onto the surface of the avalanche and filled a small depression. The water was retained temporarily in a deep pond a few kilometers above Camp Baker. On the afternoon of August 27, the rising pond overtopped its rim and eroded its outlet as it drained downvalley. Much of the water was retained by a check dam under construction by the U.S. Corps of Engineers, but some spilled over, destroying some temporary bridges and portions of access roads along the North Fork Toutle River as far downvalley as the town of Toutle.

In summary, a possible pattern of volcanic behavior may be evident in the post-May 18 events at Mount St. Helens. A magma column seems to be slowly and intermittently rising; sometimes it is entirely confined beneath the surface and at other times its upper portion emerges as a lava dome. The outer solidified shell of this magma column is an imperfect seal, and fluctuating amounts of gas continuously escape to the atmosphere. At irregular intervals, pressure within the column exceeds the confining strength, and gas is released violently, blasting out new craters and giving rise to pyroclastic flows and to high eruption columns that deposit new ash. Renewed rise of the magma column after each eruption replugs the vent and may produce a new dome.

THE 1980 ERUPTIONS OF MOUNT ST. HELENS, WASHINGTON

OBLIQUE AERIAL PHOTOGRAPHY, MARCH-OCTOBER 1980

By ROBERT M. KRIMMEL *and* AUSTIN POST

ABSTRACT

Oblique aerial photographs offer many advantages over vertical photographs for documentation of volcanic events; these include more natural perspective, greater areal coverage from low altitude, greater flexibility in aircraft operation, coverage of specific localities during periods of partial cloud or ash obscuration, and lower cost. Generally, large-format cameras, such as 241 mm, give better results than small-format cameras, such as 35 mm. In light aircraft the large-format cameras are usually fix mounted.

The USGS (U.S. Geological Survey) Glaciology Project Office documented the eruption of Mount St. Helens from March through October 1980 using large-format oblique black-and-white photography. From March until May 17, 1980, the progression of surface deformation, crater enlargement, ash and snow cover, and avalanching was documented. On May 18, the catastrophic eruption was photographed, and from May 19 through October 1980 the results of the eruption and subsequent events were photographed. These photographs can be purchased from the EROS Data Center, Sioux Falls, S. Dak., 57198, and can be seen at U.S. Geological Survey offices, Tacoma and Vancouver, Wash.

OBLIQUE AERIAL PHOTOGRAPHY, MARCH-OCTOBER 1980

Oblique aerial photography can be used to simply and rapidly document visible change due to any large volcanic event. The resulting photographs differ from vertical aerial photographs because they generally cannot be used for precise cartography. Oblique photographs, however, offer the advantage of a more natural perspective; generally cover large areas, simplifying qualitative observations; often can accentuate a particular feature; and sometimes offer a qualitative documentation of a feature before the process of photogrammetry can show the same thing from vertical photographs. Oblique photographs often offer a flexibility impossible to achieve with vertical photographs, oblique cameras are less expensive to acquire and operate than vertical equipment, and very useful oblique photographs can be taken when volcanic eruptions or weather conditions do not permit vertical photography to be effective.

The USGS Glaciology Project Office uses a number of different cameras. High-quality 35-mm format cameras offer convenience, availability, large lens selection (including high-quality zoom lenses), and rapid color processing. For detailed study, however, small transparencies or negatives may not have the necessary resolution, and high-quality enlargements are difficult to obtain. The next larger format uses the 120/220 film size, providing either 57×57 mm ($2\frac{1}{4} \times 2\frac{1}{4}$ in.) or 6×7 cm negatives. These cameras offer handling convenience similar to that of the 35-mm cameras; they are more expensive and film and processing are generally less available; however, negative detail is improved. For most of our photography, large-format cameras are used. A standard large-format aerial camera uses 241-mm ($9\frac{1}{2}$ in.) roll film, which gives excellent resolution and the convenience of more than 300 frames per roll. These cameras are not readily available and are so bulky that they are

Table 4.—Missions for large-format oblique aerial photographs, Mount St. Helens, March-October 1980

[Roll number: first two numerals indicate year, letter indicates Mount St. Helens, final numeral indicates roll sequence. Frames are numbered consecutively. Time is approximate and is given when considered significant. Photographer noted in description]

Roll	Frame	Date and time (1980)	Description
80S1	001-138	Mar. 30	Scattered to broken clouds, cloud tops to 2,500 m. Minor eruption plumes. Distant views of Mount St. Helens: one-half covered with clean snow, one-half covered with ash. Details of summit, crater, and bulge. Post.
80S1	139-263	Mar. 30	Scattered clouds. Intermittent eruption plumes. Distant and close views of Mount St. Helens from all sides. Krimmel.
80S1	264-276	Apr. 1	Scattered to broken clouds. Much of the summit obscured in clouds. Post.
80S1	277-360	Apr. 1	Scattered to broken clouds. Much of the summit obscured in clouds. Krimmel.
80S2	001-053	Apr. 10	Broken clouds, cloud tops to 2,500 m. Eruption plume; details of summit, crater, and bulge. Post.
80S2	054-127	Apr. 25	Clear. Views of volcano from most sides; details of summit, crater, bulge, lower flanks, and Spirit Lake. Post.
80S2	128-207	May 1	Clear. Distant views of Mount St. Helens; details of Spirit Lake, lower flanks, upper cone from most sides, summit, crater, and bulge. David R. Hirst, USGS.
80S2	208-241	May 4	Clear. Views of cone from all sides; details of summit, crater, and bulge. Krimmel.
80S3	001-046	May 11	Scattered to broken clouds. Mount St. Helens mostly obscured from the west and northwest. Views looking northwest, west, southwest, and south. Details of summit and bulge. Krimmel.
80S3	047-109	May 17 (1100-1200)	Scattered clouds to clear. Distant views to south; closer views of cone from all sides. Details of summit, crater, bulge, and Forsyth Glacier ice avalanche. Krimmel.
80S3	110-200	May 18 (1100-1230)	High overcast, and ash from eruption. Distant views of eruption plume looking south and east; closer views of eruption plume looking east and north. Details to north and east, eruption plume, and ash flows. Krimmel.
80S3	201-268	May 18 (1200-1400)	High overcast, ash from eruption. Views of eruption plume; details to south and west of volcano, plume, and ash flows. Post.
80S3	269-310	May 18 (1900-2030)	High overcast, and ash from eruption. Distant views of eruption plume looking southeast, east, and northeast. Details of plume, ash flows, and crater rim, looking east and north. Krimmel.
80S4	001-273	May 19	High overcast, some lower clouds, dust and ash from Mount St. Helens. Details of blast area, debris avalanche, tree blowdown, phreatic eruptions in ash flows, and views of cone to north and east. Details of cone and mudflows to north and east. Post.
80S5	001-056	May 30	Scattered to broken clouds at 2,100-2,500 m. Steam plume about 300 m above crater rim. Views of Spirit Lake and portions of the blast area. Post.
80S5	057-312	June 4	Scattered clouds. Mount St. Helens obscured above 2,300 m. Low-level views of the fringes of the blast area, North Fork Toutle River and debris avalanche, Camp Baker, and Spirit Lake. Details of debris avalanche, blast area, ash blanket, and tree blowdown. Post.
80S6	001-156	June 19	Scattered clouds. Clouds and plume over Mount St. Helens to 3,400 m altitude. Distant views of North Fork Toutle River, blast area, debris avalanche, flanks of volcano, and Spirit Lake. Details of Harrys Ridge (ridge south of St. Helens Lake), St. Helens Lake, Spirit Lake, partially obscured crater and lava dome, crater rim, rampart, post-May 18 eruption lake formed at junction of South Coldwater and Coldwater Creeks, and blast area. Lowther,[1] Post.
80S7	001-319	June 30	Clear to about 3,000 m altitude. Distant views of volcano and blast area. Panoramas of blast area from several locations. Views from south side of volcano; Muddy River, Swift Reservoir, Pine Creek, and Swift dam. Views from west side of Mount St. Helens: South Fork Toutle River, North Fork Toutle River. Details of Camp Baker, debris avalanche, tree blowdown, Spirit Lake, Mount Margaret, and the post-May 18 eruption lake formed at the junction of South Coldwater and Coldwater Creeks. View into crater, partially obscured rampart, and lava dome. Lowther, Post.
80S8	001-083	July 1	Clear of clouds, no plume, dust to west. Distant views of Mount St. Helens and Spirit Lake. Details of south side, upper south cone, lava dome, rampart, and steam vents. Lowther.
80S8	084-167	July 7	Clear, no plume. Distant view of volcano and Spirit Lake. Views of cone to northwest, north, northeast, east, southeast, and south; details of upper cone, inner and outer crater walls, lava dome, rampart, and lower flanks. Lowther, Krimmel.
80S8	168-180	July 13	Scattered clouds, summit partially obscured in clouds. Views to south, Spirit Lake, and blast area. Lowther, Post.
80S9	001-097	July 13	Scattered clouds to clear, minor ash and steam in crater. Details of lower flanks, inner and outer crater walls, lava dome, rampart, Spirit Lake, tree blowdown, debris avalanche, and Camp Baker. Lowther, Post.
80S9	098-252	July 24	Clear of clouds but dust blowing from Mount St. Helens. Distant views of debris avalanche, Spirit Lake, and Coldwater Creek. Details of crater pit, crater walls, upper cone, Spirit Lake, ash flow, portions of lower flanks, and of blast area. Lowther, Post.
80S9	253-287	Aug. 7 (1630-1700)	Clear of clouds; dust, ash, and steam partially obscure crater. Distant views of Mount St. Helens and Spirit Lake. Details of outer crater walls, partially obscured views into crater. Krimmel.
80S9	288-308	Aug. 7 (1800-1830)	Scattered clouds, plume to approximately 4,600 m altitude. Distant views of volcano and plume. Details of plume looking east and north. Krimmel.
80S10	001-061	Aug. 19	Clear. Distant views of Mount St. Helens and Spirit Lake from north. Views of cone from all sides. Details of inner and outer crater walls and lava dome. Krimmel.
80S10	062-093	Sept. 3	Scattered clouds, crater obscured by steam and ash. Distant views looking south. Details of outer upper cone. Krimmel.
80S10	094-153	Sept. 9	Clear. View of cone from all sides, Spirit Lake. Details of lava dome and inner crater wall. Krimmel.
80S10	154-172	Oct. 4	Clear of clouds. Crater and areas to north obscured in dust and steam from Mount St. Helens. A few views of cone to east and north. Details of small portions of devastated area west of Spirit Lake. Krimmel.
80S10	173-203	Oct. 17	Clear of clouds. Crater obscured by dust and steam. Details of cone looking south, pumice flow from recent eruptions, and devastated area west of Spirit Lake. Krimmel.

[1]Stewart Lowther, Department of Geology, University of Puget Sound, Tacoma, Wash.

generally fix mounted in aircraft. Film processing is specialized, and color film and processing are extremely expensive. Cameras using 127-mm (5-in.) and 178-mm (7-in.) film are sometimes used, but such cameras and film are not as available as those with the larger format and provide lower quality photographs.

Various light aircraft have been used; we prefer fixed-wing single-engine aircraft because they are readily available and cheaper than helicopters or multi-engine aircraft. Generally, aircraft with a high wing have the best visibility and convenience for hand-held camera operation. High-quality photography requires camera ports or windows that open, as aircraft windows usually have distorting curves, many are tinted, and few are free of scratches. The 35-mm and 120-film cameras are almost always hand held. The large-format cameras are usually mounted to the aircraft; mounting often requires airframe modifications such as camera ports, mounting brackets, and vacuum and electrical power. An advantage of these installations is that one or more cameras can be remotely operated by the pilot or observer, but such operation requires a dedicated aircraft.

The USGS Glaciology Project has been taking large-format oblique aerial photographs of glaciers in North America since 1964. Glacier photography necessarily includes coverage of some surrounding terrain, and many photographs document volcanoes as well as glaciers. In addition to the glacier photography, observations of geothermal areas near snow- or ice-covered areas on Mount Baker have routinely been made. A series of missions to cover Mount St. Helens volcanic activity was begun on March 24, 1980, to observe and document any significant response of Mount St. Helens to the increased seismic activity in the vicinity.

The large-format negatives were taken using World War II-vintage K–17 241-mm cameras, one with a 305-mm-focal-length Pacific Optical lens, the other updated with a 305-mm Symar lens. The film used was Kodak Double-X Aerographic 2405 panchromatic black-and-white. The original black-and-white negatives are at EROS Data Center, Sioux Falls, S. Dak.; copy negatives are available at EROS Data Center and USGS Glaciology Project Office, Tacoma, Wash. Print copies can be purchased from EROS Data Center, Sioux Falls, S. Dak., 57198. Proof prints can be viewed at USGS offices in Tacoma and Vancouver, Wash.

Table 4 itemizes the black-and-white large-format Mount St. Helens oblique aerial photography missions flown March–October 1980. Prior to March 1980, photography missions were flown with the primary objective of glacier documentation. Many of the pre-March photographs are of interest for comparative purposes, although they were taken less systematically than those beginning in March. The earlier photographs can be viewed at the USGS, Tacoma, Wash.

Figures 17 through 34 are examples of the March-October oblique aerial photography. The photographs for March 24, 1980, show no evident surficial deformation. By March 30, the bulge on the north side is obvious from the photographs. Frames from March 30 until May 17 show the progression of bulge deformation and other changes of the upper cone. Photographs taken on May 17 show no major surficial changes that could have been considered precursors of the catastrophic eruption that occurred 20 hr later. The May 18 missions, which provided documentation of the major eruption, proved the importance of a quality standby system for oblique aerial photography. The missions after May 18 record results of that eruption and changes related to subsequent eruptions. The oblique photography missions continued on a sporadic basis through 1980.

Figure 17.—March 24, view of upper cone, looking west-southwest. Although seismic activity began under Mount St. Helens on March 20, this overflight showed no unusual features except numerous tracks of earthquake-triggered snow avalanches. No evidence of fracturing of summit area was detected during careful visual observations on the afternoon of March 24. On March 25 the first cracks were noted by Bud Kimball, Tacoma, Wash. (oral commun., 1980). Photograph by David Frank. This mission is not listed on table 4 because the photographs are on 57-mm film, on file with David Frank, USGS, Seattle, Wash.

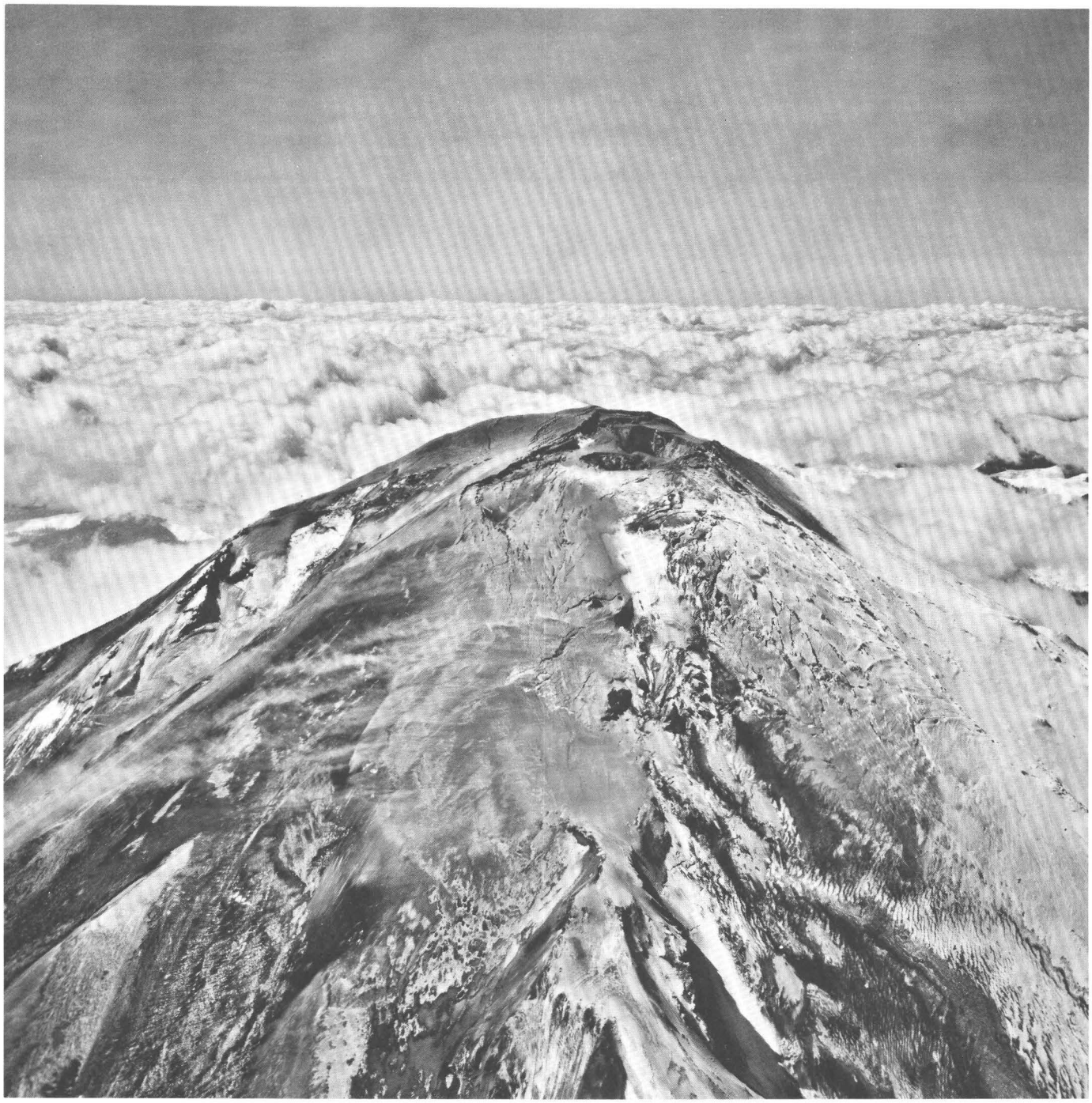

Figure 18.—March 30, view of upper cone, looking southwest. Three days after the first eruption. Compare with figure 17; fractured right side of cone came to be known as the bulge. Two craters are visible near summit; snow is overlain by a layer of dark ash. 80S1-083.

Figure 19.—March 30, looking north-northeast, Mount Rainier in distance. Distribution of dark ash resulted from wind control of plume drift. Left portion of cone is free of ash, right portion largely covered. Snowstorms later covered these ash layers, which in turn were covered by new ash; the result was many alternating layers of snow and ash. 80S1–071.

Figure 20.—April 25, looking west-southwest. The bulge is a prominent and rapidly changing feature. Fresh snow covered higher portions of Mount St. Helens; lower slopes are ash covered. 80S2–122.

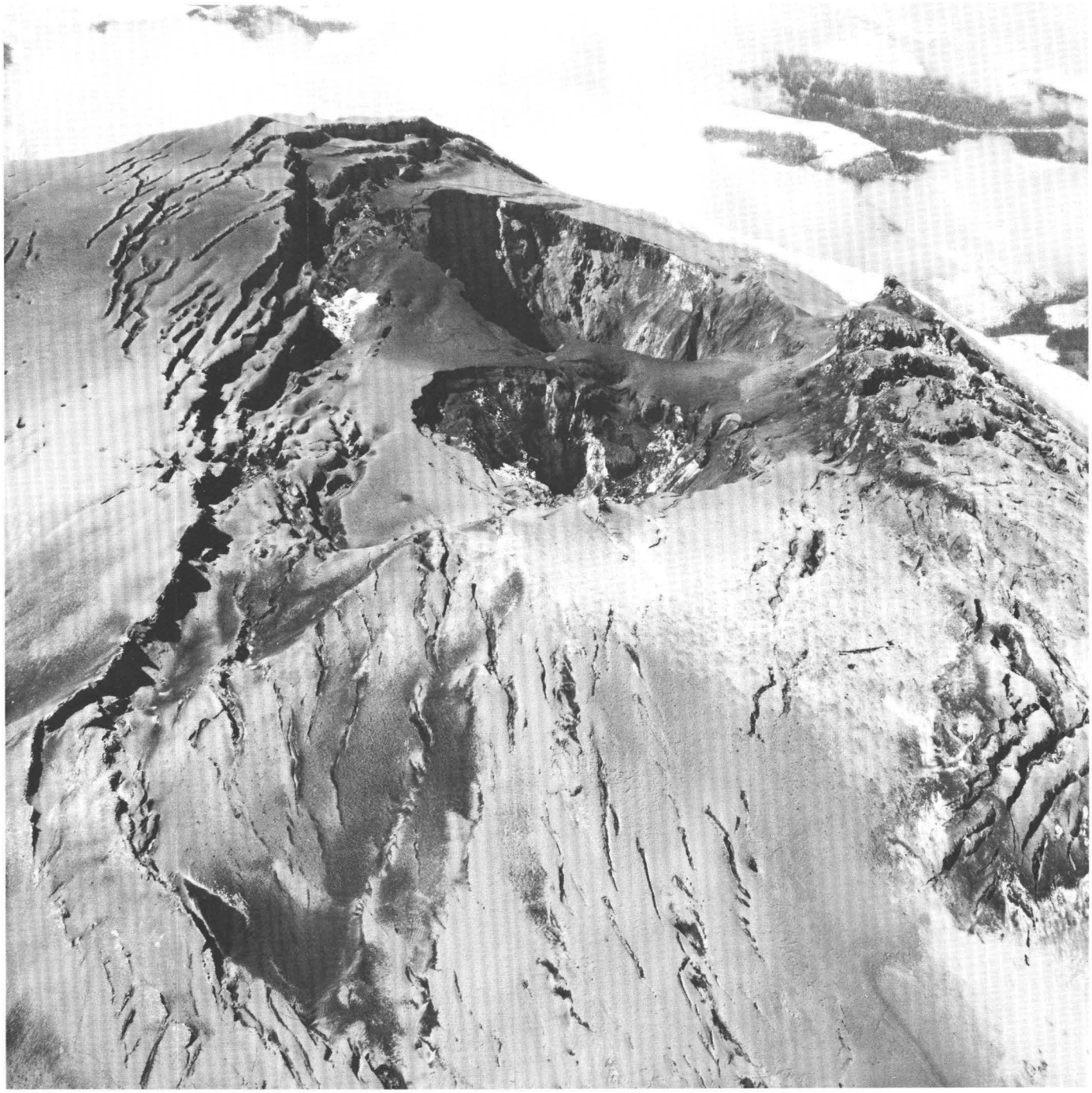

Figure 21.—March 30, looking west. Summit of Mount St. Helens after several small explosive eruptions. The smaller of the two pit craters was formed first on March 27. Subsequent eruptions opened the farther crater; the two craters later merged. 80S1–111.

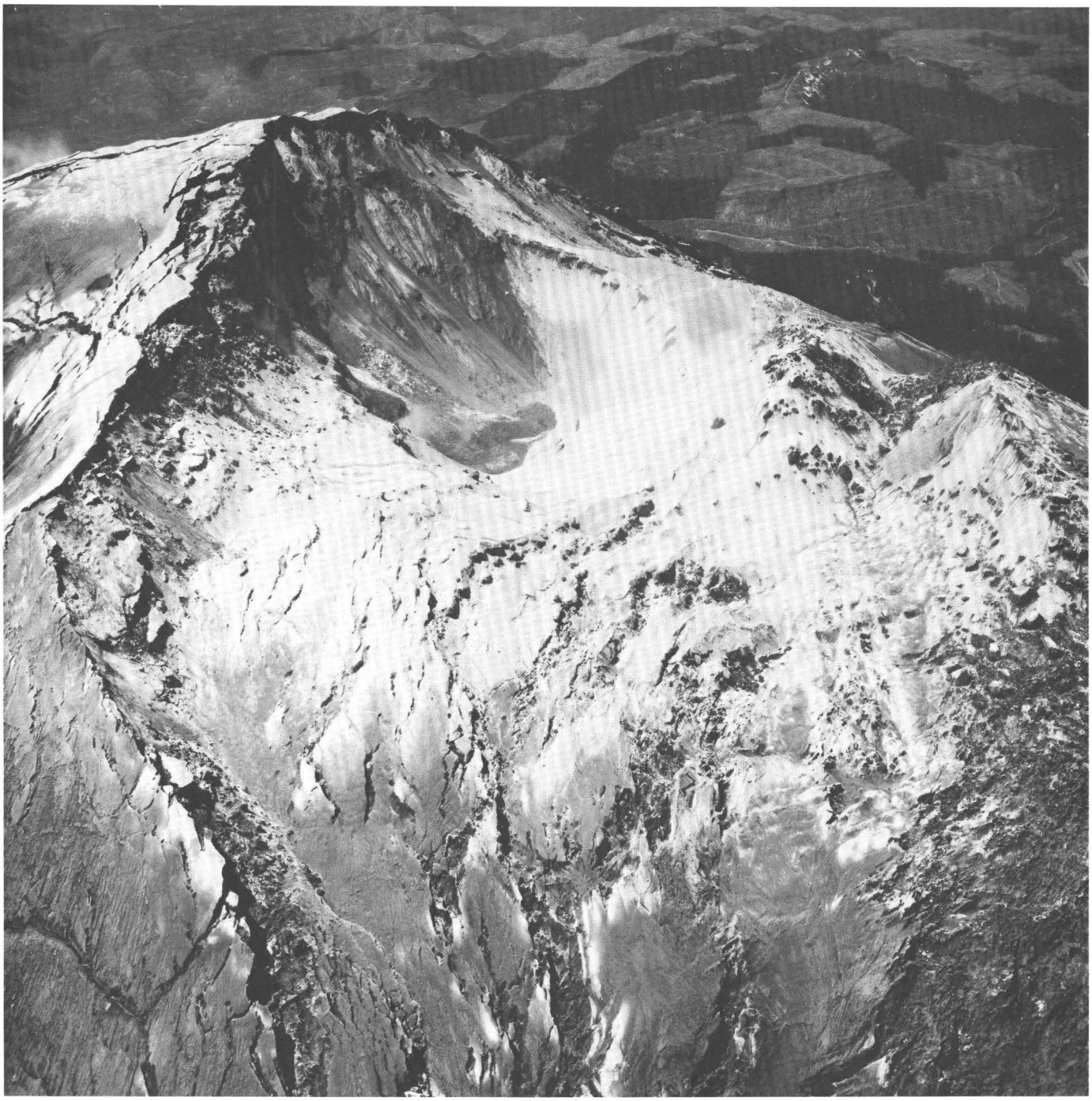

Figure 22.—May 17, looking west. Compare with figure 21. The crater has been much enlarged; as the bulge (at extreme right) has expanded, fracturing has become more extreme. Crater area has dropped relative to summit. 80S3-070.

Figure 23.—May 18, looking northeast. Catastrophic eruption began at 0832 PDT. Photo taken at approximately noon. The day had dawned clear, and clouds in this scene may be eruption related. Vapor rises from vent and from lakes, rivers, melted snow and ice, and from hot deposits of debris avalanche and pyroclastic flows. Ash billows from vent and from pulverized material collapsing into crater; smoke originates from forest fires ignited by initial eruptive blasts and from later pyroclastic flows. Lightning was occurring every few seconds. No air turbulence was felt on windward side of mountain. 80S3–132.

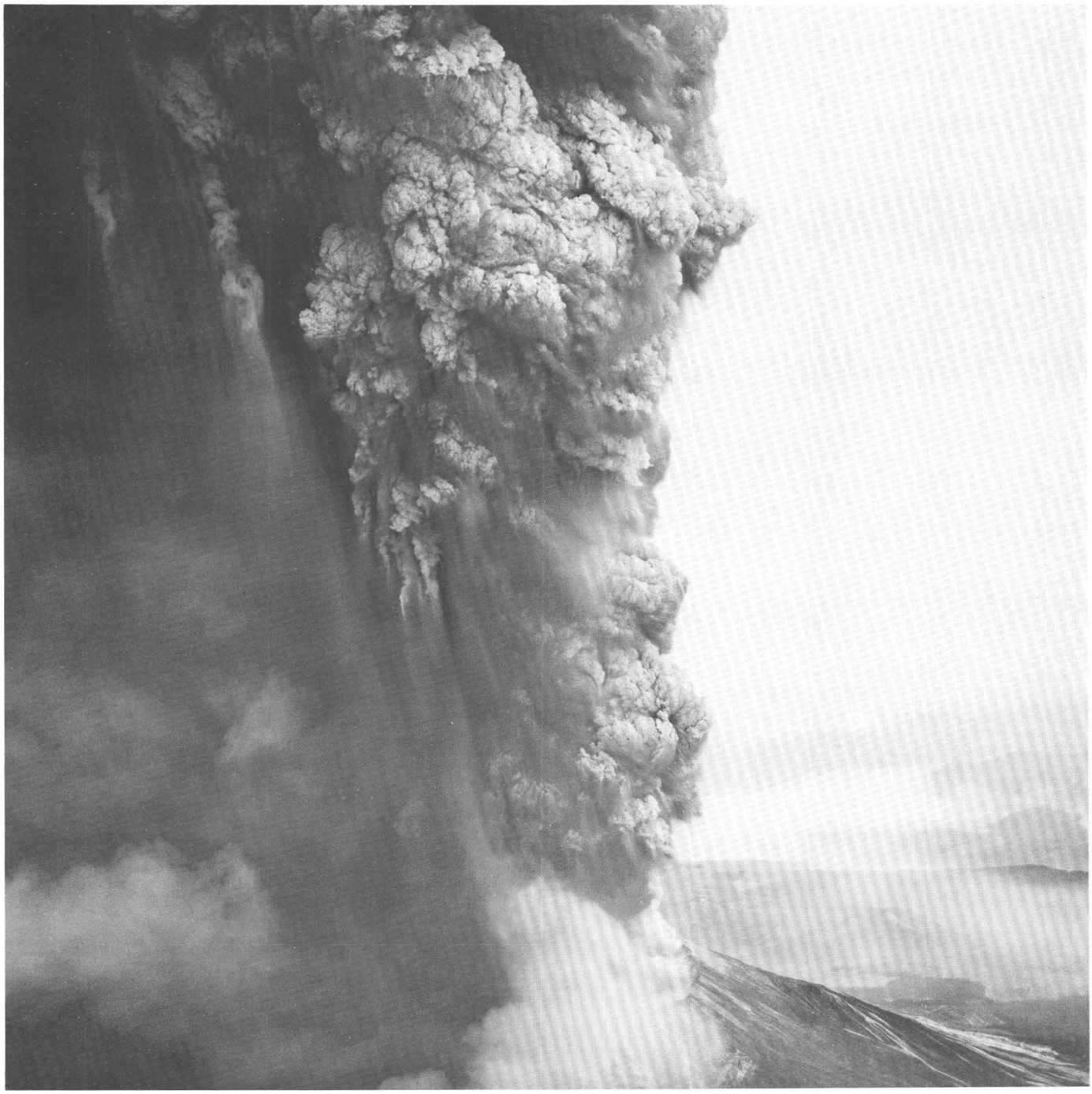

Figure 24.—May 18, looking southeast, showing detail of sharply defined windward edge of plume. 80S3–182.

Figure 25.—May 18, looking east, about 1900 PDT, when eruption plume had diminished considerably. Debris avalanche from north side of Mount St. Helens floods valley of North Fork Toutle River. Below the debris avalanche Toutle River is flooding. Much of the scene is obscured by dust and moisture clouds rising from immediately north of volcano. 80S3–277.

Figure 26.—June 30, looking south-southeast. A portion of the devastated area characterized by very little surviving vegetation, with most trees uprooted or broken off; a blanket of ash in many places; valleys partly filled by debris-avalanche material; lakes formed where debris avalanche has dammed tributary valleys. 80S7-009.

Figure 27.—July 13. Lava dome within the crater. Figure 28 is a similar view shortly after next eruption. 80S9-059.

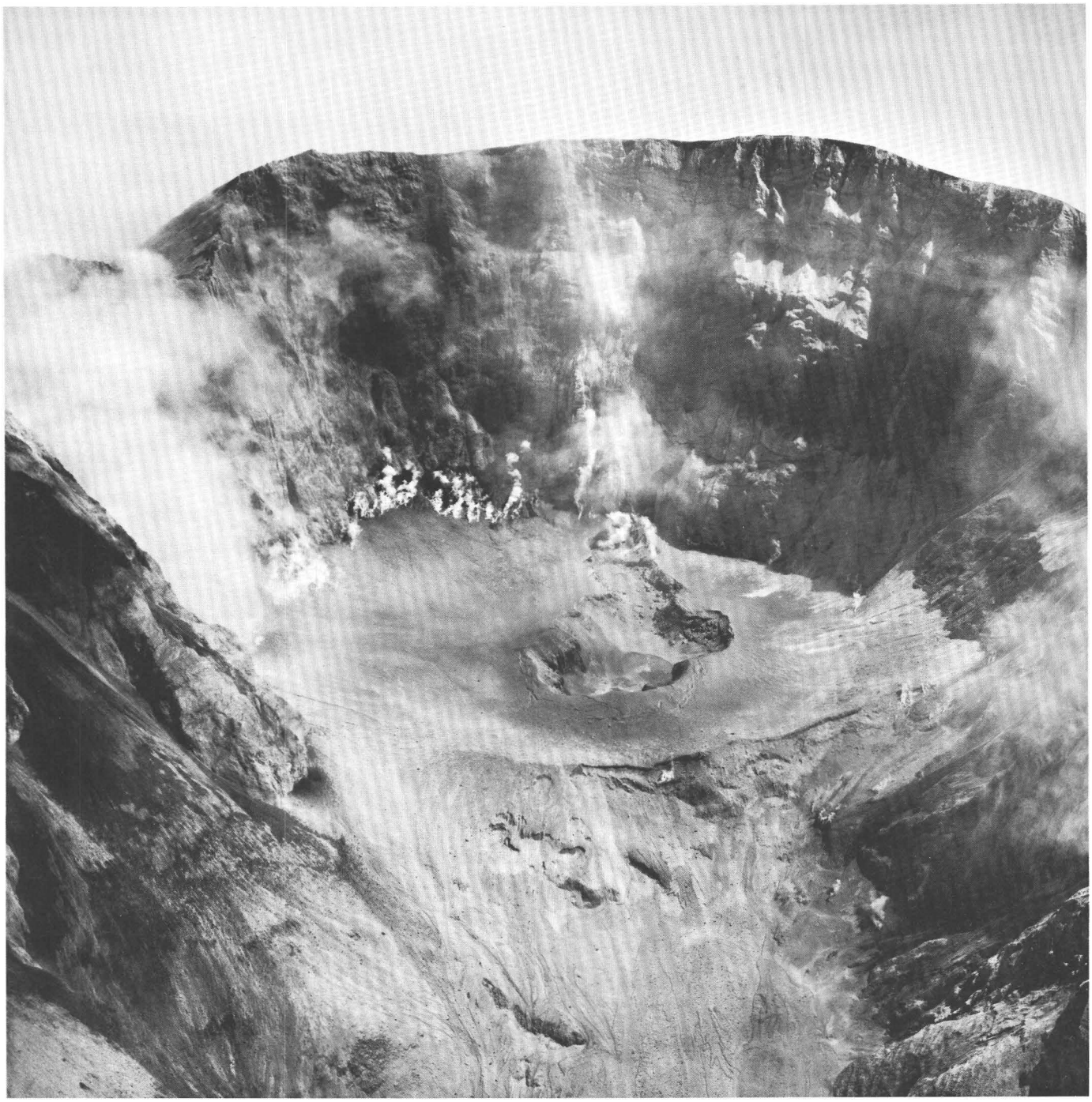

Figure 28.—July 24. Pit left after explosive eruption of July 22. Pyroclastic flows overrode low crater rim in foreground and moved downslope (north) toward Spirit Lake. 80S9-122.

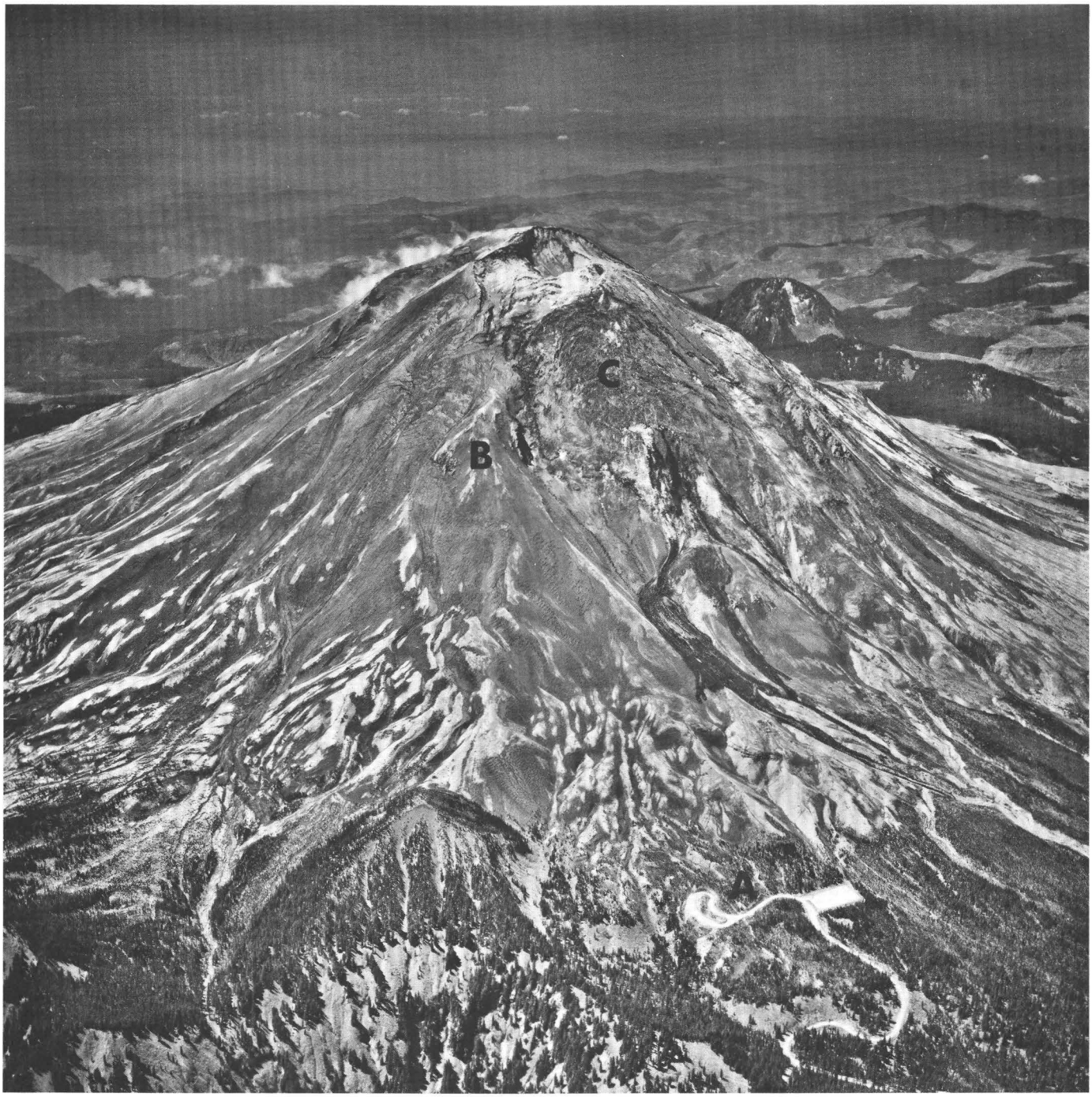

Figure 29.—May 17. Mount St. Helens the day before the catastrophic eruption, looking southwest. Features visible include road to Timberline viewpoint and parking area (A), Dogs Head (B), and the severely fractured, bulging, ash-covered Forsyth Glacier (C). An ice avalanche, darkened with volcanic debris, which originated from the bulging, oversteepened part of Forsyth Glacier, forms dark tracks below the bulge. 80S3–055.

Figure 30.—September 9. Compare with figure 29. Dogs Head (B) and part of the Forsyth Glacier remain. The road and Timberline viewing and parking area (A) were buried by air-fall ash and blast deposits and can only be discerned by careful scrutiny. 80S10–106.

Figure 31.—May 17, looking south directly toward the bulge, Loowit Glacier (A), and Goat Rocks (B). Numerous rock avalanches from Goat Rocks were triggered by earthquakes. 80S3-056.

Figure 32.—September 9. Compare with figure 31. Remaining lower part of Forsyth Glacier in left center. Loowit Glacier is completely gone. Many pyroclastic-flow deposit lobes can be seen in foreground. Windblown dust obscured some surface details. 80S10–113.

Figure 33.—May 4, looking southeast with Goat Rocks in left center and Dogs Head on left ridgeline. 80S2–215.

Figure 34.—August 19. Compare with figure 33. Note total devastation of vegetation on near side of cone. 80S10-005.

THE 1980 ERUPTIONS OF MOUNT ST. HELENS, WASHINGTON

SUMMARY OF EYEWITNESS ACCOUNTS OF THE MAY 18 ERUPTION

By J. G. ROSENBAUM *and* RICHARD B. WAITT, JR.

ABSTRACT

Many individuals who were in the vicinity of Mount St. Helens on May 18 were interviewed to gain information on phenomena associated with the eruption. The observed phenomena include an earthquake, a massive avalanche of the volcano's north flank, a directed blast, development of the vertical eruption, a mudflow in the South Fork Toutle River valley, and the fall of early eruptive products. The eyewitness accounts, although somewhat subjective, provide information about the sequence of events, descriptions of the directed blast (including velocity, temperature, and a preceding pressure change), and the timing and nature of early air-fall material. These observations supplement a variety of subsequent scientific investigations.

INTRODUCTION

On May 18, 1980, a large number of people at many locations in the vicinity of Mount St. Helens witnessed the awesome eruption of the volcano (fig. 35). Over the following months, many of these individuals were interviewed. In presenting summaries of geologically pertinent observations from these interviews we have attempted to retain the descriptive words and phrases used by the eyewitnesses. In like manner we have retained the measurement units used by the witnessess, converting them to the metric system in our discussion.

Locations of the various eyewitnesses are shown in figure 35 and described in table 5. For brevity, testimony by one or more witnesses at a specific location is referenced in the text only by site number. The site numbers consist of a distance and a direction relative to the preeruption summit of Mount St. Helens. For example, site 17NE is located approximately 17 km northeast of the old summit.

The eyewitnesses observed a wide variety of phenomena associated with the eruption, including an earthquake, a massive landslide, various aspects of a directed blast (such as its movement, temperature, and the material deposited), noises, winds, lightning, and the nature of air-fall material. Observations of the various eruptive events and their products are retold here in approximate chronological order.

Although eyewitness accounts provide a unique source of information about the eruption, they are subjective. Two individuals recalling the same phenomena may differ markedly in their perceptions as well as their descriptions. In particular, unless otherwise stated, all quantitative data (such as time intervals and distances) specified in these accounts are estimates of the witnesses and are often based on observations made under extremely stressful conditions.

EARTHQUAKE, LANDSLIDE, AND INITIATION OF ERUPTION

ACCOUNTS

At 0832 PDT, May 18, 1980, several witnesses felt a shallow earthquake that emanated from Mount St. Helens (Endo and others, this volume). A "solid jar" and noticeable ground motion lasting for 3–5 s were noted (12Wa) at about this time. Others who reportedly felt the quake include members of a tree-planting crew on the north side of Marble Mountain (8SE) and individuals to the north (23N, 29N) and northwest (17NW). Significantly, one observer felt the shock and then saw the north side of Mount St. Helens begin to move (12Wb). This sequence is consistent with a report of avalanching into the summit crater (presumably triggered by the earthquake) prior to failure of the north flank (0).

The massive failure of the bulging north side of

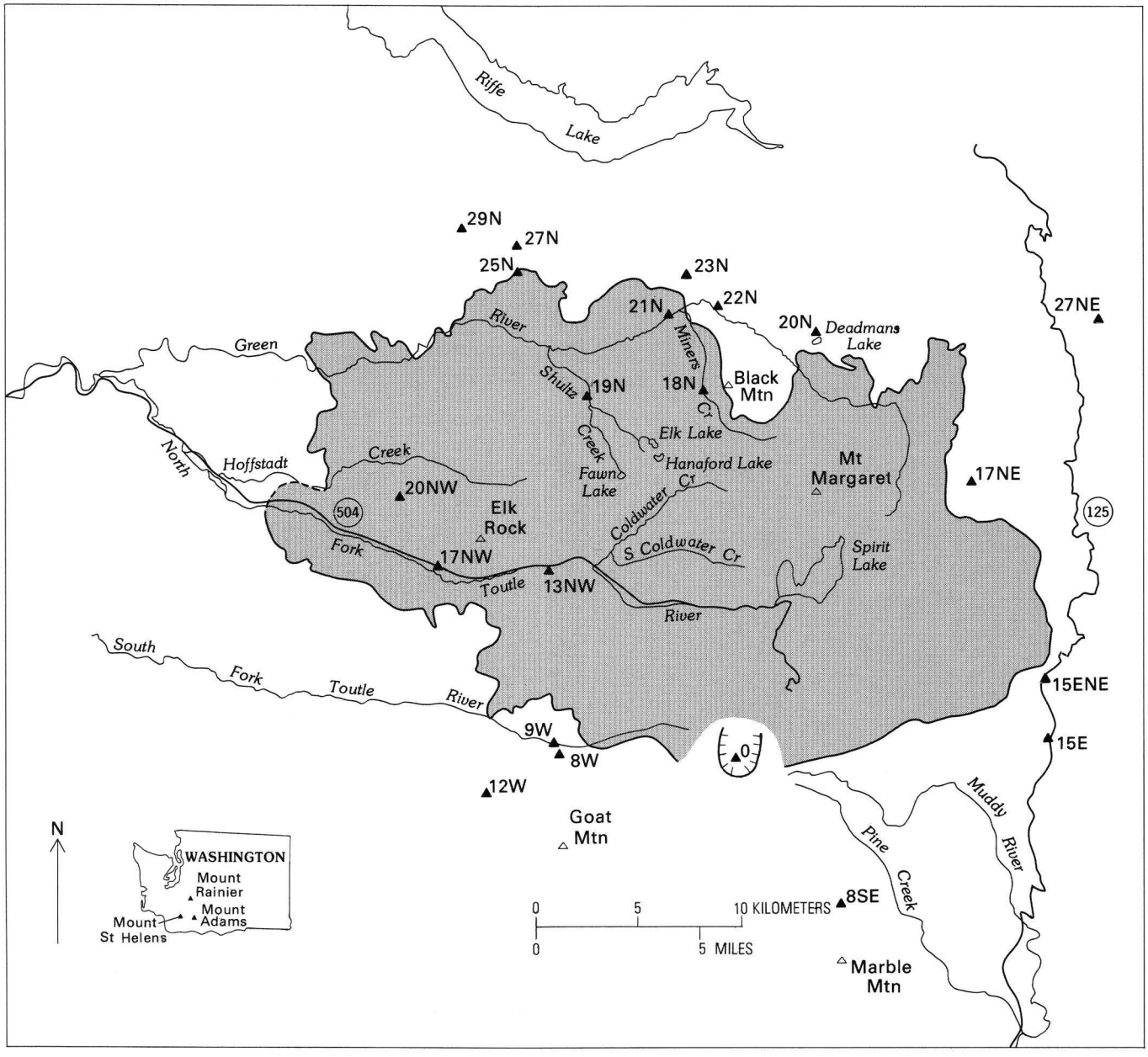

Figure 35.—Map showing location of eyewitnesses at time of the May 18 eruption (triangles). Shaded region, area of devastation in which the forest was destroyed by the directed blast. Hachured area, post-May 18 crater rim.

Mount St. Helens was viewed from a variety of locations. None of those viewing the start of the avalanche were able to observe its progress for more than a few tens of seconds because of topographic obstructions and rapid development of the eruption cloud. Fortunately, the initial events were recorded by

Table 5.—Locations of eyewitnesses to the May 18 eruption

Site No. (fig. 35)	Location at the time of eruption	No. in party	No. at interview	Names of those interviewed	Remarks
0	In a small aircraft directly over Mount St. Helens.	2	2	K. and D. Stoffel-----	This account was previously published (Stoffel, 1980).
8SE	North of Marble Mountain--------	2	2	K. Anderson, K. Kilpatrick.	
15E	Near road 125, east of Mount St. Helens.	2	2	P. and C. Hickson-----	Took photographs of initial stages of the eruption.
15ENE	---do----------	5	2	L. McCulley, J. Findley.	The witnesses drove to the locality after the start of the eruption.
12Wa	On high ridge, south of South Fork Toutle River.	2	2	T. and M. Kearny------	Took photographs of initial stages of the eruption.
12Wb	---do----------	2	1	F. Valenzuela---------	Do.
9W	On north side of South Fork Toutle River.	3	3	J. and A. Sullivan, M. Dahl.	
8W	On south side of South Fork Toutle River.	1	1	D. Crockett----------	Took video tape of part of his experience.
13NW	On south side of North Fork Toutle River.	2	1	C. McNerney----------	Drove down the North Fork Toutle valley outrunning the blast cloud.
17NW	At a roadblock on Highway 504 on north side of North Fork Toutle River.	2	2	G. and K. Baker-------	Do.
17NEa	On ridge top with a good view of Mount St. Helens.	1	1	K. Ronholm----------	Took photos of initial stages of the eruption.
17NEb	---do----------	2	2	W. and L. Johnson.	
17NEc	---do----------	5	4	G. Rosenquist, J. and L. Harvey, W. Dilly.	Took photos of the initial stages of the eruption.
20NW	On north side of ridge, south of Hoffstadt Creek.	4	1	J. Scymanky----------	Four persons at this locality were severely burned when overrun by the blast cloud. Three subsequently died.
19N	On west side of Shultz Creek, about 3 km south of the Green River.	3	3	D. and L. Davis, A. Brooks.	Overrun by the blast cloud.
18N	Adjacent to Miners Creek--------	3	1	E. Smith----------	Do.
21Na	On north bank of Green River----	4	2	B. Nelson, S. Ruff	Two persons were killed by falling timber knocked down by the blast cloud.
21Nb	---do----------	2	2	D. Balch, B. Thomas---	One witness was injured by falling timber; the other was burned when overrun by the blast cloud.
20N	Near Deadman's Lake----------	2	1	B. Cole.	
22N	On north side of Green River----	4	2	M. and L. Moore.	
23N	On ridge, 1.5 km north of the Green River.	5	1	D. LaPlaunt----------	Took one photo of blast cloud as it topped ridge north of Coldwater Creek.
25N	3 km north of the Green River	2	2	G. and K. Palmer.	
29N	---do----------	6	1	A. Gould.	
27NE	On ridge 2 km east of Highway 504.	2	1	V. Hodgson----------	Took photos of initial stages of the eruption.
[1]30N	Near northeast end of Riffe Lake	?[2]	1	S. Rylee----------	Exact location unknown.
[1]40NW	On the South Fork Toutle River, 2.5-3 km above its confluence with the North Fork.	2	2	V. Dergan, R. Reitan.	
[1]50Ea	3,600-m level on south side of Mount Adams.	12	10	J. Christensen (group leader).	Took photos of initial stages of the eruption.
[1]50Eb	2,500-2,800-m level on northwest ridge of Mount Adams.	4	1	D. Hanks.	
[1]50Ec	At Horseshoe Lake, 11 km northnorthwest of Mount Adams.	23	1	I. Guild.	
[1]75N	3,200-m level on Mount Rainier	5	1	J. Downing.	
[1]40W	Commercial airliner at an elevation of 10,700 m.	?[2]	1	J. Mathes.	
[1]100SE	Private aircraft over the Columbia River at an elevation of 2,900 m.	4	1	G. Treat.	

[1]Site not shown on figure 1.
[2]Query, exact number not known.

photographs from several locations (0, 12W, 15E, 17NE, 27NE). Two of the following accounts (17NEc, 15E) are based largely on these photographs rather than on visual observations.

0.—Within about 15 s after the start of avalanching into the summit crater "everything north of a line drawn east-west across the northern side of the summit crater began to move as one gigantic mass. * * * The entire mass began to ripple and churn up, without moving laterally. Then the entire north side of the summit began sliding to the north along a deep-seated slide plane * * * a huge explosion blasted out of the detachment plane. We neither felt nor heard a thing, even though we were just east of the summit at the time. * * * the southern portion of the summit crater began to crumble and slide to the north just after the initial explosion. From our view point, the initial cloud appeared to mushroom laterally to the north and plunge down. Within seconds, the cloud had mushroomed enough to obscure our view" (Stoffel, 1980).

17NEc.—One observer watching the mountain through binoculars saw the north side start to get "fuzzy, like there was dust being thrown down the side." Several seconds later the north face began to slide. The lower part of the north slope seemed to slide away more quickly than the upper. The first dark-colored cloud appeared near the middle of the north slope in an area vacated by the slide, and a light-colored cloud formed near the summit. A short time later, a very black cloud emerged from the summit area. The upper part of the north flank moved downward and the flank eruption seemed to explode through the moving material. The flank eruption grew rapidly, especially to the north.

15E.—"As the avalanche reached the halfway point on the mountain, the summit eruption began with a dense black cloud followed by lighter gray material. A second eruption halfway down the slope occurred moments later * * *." At this time the avalanche appeared to consist of upper and lower parts. The flank eruption was between the two. Seconds later the upper slide overrode the flank eruption and material was hurled far downslope onto the lower slide. About 45 s after the landslide began, the eruptive centers merged and the rapidly expanding cloud overtook the avalanche.

17NEa.—The "bulge was moving * * * the whole north side was sliding down." The first cloud appeared to form at the bottom of a "cirque-like" wall from which the bulge had moved. Within about 20 s the landslide was out of view behind a ridge. At this time, there were two distinct clouds which seemed to be emanating from separate vents; an extremely dark one rising vertically from the summit, and a lighter one from the north flank.

12Wa.—Goat Rocks (a volcanic dome at the 2,000-m level on the north flank) slid down to the north. Two eruption clouds formed, one from the summit and the other from the north side. The cloud from the north flank grew very quickly and discrete objects could be seen being hurled to the north.

DISCUSSION

The above accounts agree remarkably well and reveal the following sequence. The earthquake apparently preceded, and therefore probably caused, the catastrophic failure of the volcano's bulging north flank. The initial landslide followed the quake within seconds and initially consisted of at least two large slump blocks. Moments later, eruptive activity began near the middle of the north flank above the lower slump block, and near the summit. The upper slump block was blown apart as it descended across the rapidly growing flank eruption.

DIRECTED BLAST

ACCOUNTS

DISTANT OBSERVATIONS

50Ea.—Climbers on Mount Adams saw material moving to the north less than 1 min after the beginning of the eruption. One of the climbers reported seeing what seemed to be a shock wave, similar to that associated with a nuclear explosion, traveling to the north 30 s or less after the start of the eruption.

75N.—Climbers on Mount Rainier observed two distinct "flows," which began very shortly after the eruption started. These "flows" were described as clouds 1,000–2,000 ft thick that appeared to hug the ground. The heads of the "flows" disappeared into

valleys and reappeared as they "hopped" over ridges. The earlier flow traveled to the west, perhaps down the North Fork Toutle River, and was followed almost immediately by a "flow" that seemed to travel to the east.

OBSERVATIONS SOUTH, EAST, AND WEST OF DEVASTED AREA

15E.—About 45 s after it began, the avalanche was hidden by the developing eruption cloud. For a short time, a steep, smooth front of the eruption cloud could be seen rushing down the north slope of the volcano. In contrast, as the cloud spread eastward the front became billowy rather than smooth. The base of the cloud seemed to turn under and no basal avalanche was visible. There was no sign of a shock wave; trees were not knocked down ahead of the cloud, but disappeared under it.

17NEa.—A dark cloud grew vertically from the summit. A lighter cloud, which seemed to come from the area vacated by the landslide, grew more or less spherically except that a large "arm" shot out to the north in the direction of the avalanche. The spherical cloud seemed to approach from the mountain—not as part of the northward arm—and reached the ridge closest to the mountain 25–30 s after the start of the landslide. When the cloud hit the ridge, it rose and boiled upwards.

17NEb.—Shortly after the vertical eruption began, a large horizontal blast occurred. Just before the top of the mountain became obscured, the south side of the summit crumbled into the hole formed by the landslide. As the cloud grew, what appeared to be a shock wave similar to that associated with a nuclear explosion moved ahead of the cloud. About 1½ min after the start of the landslide and perhaps 45 s after the start of the blast, a noise like a clap of thunder accompanied some sort of pressure change. The initial noise was followed by a continuous rumbling "like a freight train."

17NEc.—A rumbling noise began within 7–8 s of the start of the landslide. One member of the group sensed a pressure decrease at about the same time. A "shock wave," which looked like heat waves, formed ahead of the blast cloud.

12Wa.—Spherical black clouds seemed to rise simultaneously from the summit and from the north flank. The cloud boiling out of the north side was larger than that from the summit and grew very quickly. After perhaps ½ min, discrete objects could be seen being hurled to the north. A barely audible rumbling was the only noise accompanying the eruption.

12Wb.—A very short time after the start of the landslide, a black jet developed at the top of the moving bulge. A light-gray, ground-hugging cloud moved downslope to the north. The west edge was about 45 m thick. This initial part of the directed blast was not particularly dense: "You could look into it but not through it."

13NW.—Following the collapse of the north side and the appearance of a black and white jet, a white ring, like campfire smoke, came down as an apron around the mountain. This foglike ring descended very quickly and expanded out from the mountain. A black cloud, which seemed to rise near the summit, followed and caught up with the ring near timberline. The leading wall of the black cloud could be seen through a white haze as it climbed over a ridge. A warm wind began to blow from the mountain. It increased in intensity to 30–40 knots, causing trees to bend and some branches to break.

About 2 min after the beginning of the eruption, the witnesses began driving west at about 70–75 mi/hr. At this speed, they did not seem to get any farther from the cloud. The wind blowing into the car through an open sun roof was warm enough to give the impression that the car heater was on. At State Highway 504 they increased their speed to about 85 mi/hr and began outdistancing the cloud. About 2.5 mi farther west on State Highway 504 they stopped and could not see the black cloud. After a short time the cloud reappeared, moving downvalley at about 45 mi/hr. The white mist still preceded the dark cloud by about ½ mi. The base of the black cloud looked "like avalanches of black chalk dust—first, one part of the black cloud would shoot out in front, then another, then another, like waves lapping up on a beach." Pulling back onto the highway they outran the cloud at about 65 mi/hr.

17NW.—A short time after the landslide, the view toward the mountain was replaced by a "big black

inky waterfall." This "waterfall" appeared to hit a ridge a few miles up valley within 15–30 s. At this time the witnesses began driving west on State Highway 504 at about 100 mi/hr. After 3–4 min the black cloud had almost reached them. The cloud front was shell shaped with the leading edge of the cloud 100 yd to either side and 50 yd behind. The material in the cloud was "coming down with much authority," then bubbling or bouncing back up. One witness compared the cloud to boiling oil with huge bubbles 6 or more feet in diameter. They continued driving at speeds between 80 and 105 mi/hr and about 5 min later began pulling away from the cloud.

9W.—Soon after the start of the eruption, a rock prominence high on the north flank exploded down toward Spirit Lake. As a big, black cloud started rolling over the hills, the witnesses jumped into their truck and began driving west at 75–80 mi/hr. After they had traveled about 4 mi, a dark-gray cauliflower cloud billowed above the ridge to the northwest ahead of them. They realized that something had moved down the North Fork Toutle River valley faster than they were able to drive parallel to it down the South Fork Toutle River valley.

27NE.—Following the landslide, two clouds, one from the summit and the other from the north flank, grew rapidly. About 25 s later, the cloud on the north began to billow near the base of the north side. After 45 s, the cloud seemed to be spreading laterally, with a tremendous amount of material coming from low on the north side and perhaps rising from the Spirit Lake area. A rumbling noise, which lasted only a few seconds, began 1¼–1½ min after the start of the eruption.

OBSERVATIONS NORTH OF DEVASTATED AREA

22N.—A noise similar to, but which "didn't sound quite right" for, a propeller-driven aircraft occurred for 10–20 s before a rapid pressure change, which caused ears to pop numerous times over a period of about 10 s. One person also felt as if she was being squeezed gently over her entire body. A short time later, an immense ash cloud approached that seemed to consist of a lower vertical wall and upper overhanging part.

20N.—A pressure change which caused ears to pop 10–15 times over an interval of ½–1 min was followed a half minute or so later by a rumbling which sounded very much like a jet plane. At this time the eruption cloud could be seen in the direction of Mount St. Helens. Two or three minutes later, as the upper part of the eruption cloud passed overhead, a wind, like the updraft around a large forest fire, began blowing toward the mountain.

25N.—The whole north side of the mountain seemed to explode out over Spirit Lake 5–10 s after a couple of small puffs of steam came from the summit. Almost simultaneously there was a noise like a distant cannon. A loud roaring noise—"like a train going by"—began 30–45 s after the first puffs of steam. The eruption cloud seemed to spread horizontally and then later rose vertically. As the cloud moved northward, it could be seen as it passed each ridge and seemed to follow the slope down into the next valley. The cloud reached the ridge north of Coldwater Creek about 1½ min after the initial puffs of steam were observed. About 5 min after the beginning of the eruption, a "wave front" moved southward across Riffe Lake. Then a 2- to 3-s, 50-mi/hr gust of wind from the north hit the wall of ash and "stood it up," slowing it greatly.

29N.—Following some white steam and a small black cloud from the summit, a much larger cloud rose from the north flank. At this time, a large piece of the north flank seemed to be airborne. Ten to fifteen seconds after the earthquake, light-colored material appeared over the high country around Mount Margaret. A gentle rumbling was heard about this time. An instant later, a huge dark wall appeared over the Mount Margaret area. Within seconds it had covered the area around Fawn, Hanaford, and Elk Lakes, and in another 10–15 s reached Elk Rock. "When it hit that point it seemed to split—you could see a wall of ash going down the North Fork of the Toutle." The other branch moved more northerly and there seemed to be standing green timber in between. At first timber was knocked down far ahead (estimated 2–3 mi) of the ash wall. The ground where the trees had been knocked down was no longer green. A wall of greenery "a mile high" could be seen in the air ahead of the wall of ash. The ash cloud overtook the green material before it reached Black Mountain, and trees were no longer flattened ahead of the ash. As the wall of ash moved downslope toward the Green River, it was preceded by a surflike wave of ash.

When the wall reached the Green River, it seemed to be stopped, as if the river was a firebreak. The cloud seemed to be "stood up" by something, then curled over so that the upper part preceded a lower vertical wall to the north. At about the same time a wind began blowing toward the mountain at 40–50 mi/hr.

23N.—About 20 s after the earthquake there was a loud roar and possibly a second quake. At this time a small plume of ash coming from the mountain began to grow so rapidly that within 5 or 6 s the mountain was completely obscured. Shortly after this, some ash appeared at some point to the west and then at some point near the headwaters of the Green River to the east of Mount Margaret. About 20 s after the roaring noise began, the front of the blast cloud appeared atop the ridge north of Coldwater Creek, and was described as follows: "All of a sudden the whole thing seemed to come up all in one big line and just loom right up in front of us." One photo taken at this time shows the cloud front to be no more than a few thousand feet high. Before the blast cloud appeared, the region around the mountain was visible, although the mountain itself was obscured. The cloud moved toward the witnesses at high speed, and seemed to follow topography—rolling over everything like a track on a caterpillar tractor. After driving several miles to the north, the witnesses noted "at least 80 mi/hr winds" were blowing off Riffe Lake to the south. The wind seemed to stand the blast cloud straight up.

30N.—Five to seven minutes after a rumbling noise, part of the eruption cloud passed high overhead. At about this time, a sudden 40-knot wind blew toward the mountain lasting about 10 s and was followed by an 80- to 90-knot wind that blew away from the mountain. The second gust was sufficiently strong to knock down one of the witnesses.

OBSERVATIONS WITHIN DEVASTATED AREA

19N.—A photo taken shortly after the eruption was first noticed shows the eruption cloud above and in the area of Mount St. Helens, viewed over the ridge north of Coldwater Creek. Seconds after the blast cloud crossed this ridge, "I looked east toward Hanaford Lake and Fawn Lake and that area—it looked like that whole mountain range had just exploded." As the blast cloud approached, "it looked like a boiling mass of rock—and just as high as you could see." Trees were picked up and thrown into the air at the leading edge of the cloud. The cloud seemed to follow the topography. As the blue-black cloud approached, there was a rumbling noise. No wind preceded the cloud's arrival.

As soon as the blast cloud enveloped the area, it became totally dark and got very hot. One witness received burns on the right side of both legs a little above the ankles. Although they did not blister, these burns were quite deep and not entirely healed at the time of the interview (3 mo after the eruption). A doctor said that the burns were similar to microwave burns. This person also received burns on the upper back of the thighs and another witness was burned along the forearms. Why the burns occurred in these places is not clear. In addition, the heat deformed the grill of the truck the witnesses were in, and a styrofoam cooler in the truck bed was melted.

For a short time after the blast cloud arrived, "chunks" of material could be heard hitting the truck. At this time the right side of the truck, which was toward the volcano, received extensive damage, including breaking of the vent window, stripping of the chrome trim and outside rear view mirror, and severe sandblasting of the paint. Shortly after the blast cloud arrived, the inside of the truck's windshield was found to be so cool and wet that the witnesses felt certain that the material deposited outside must have contained ice. In a short time it became lighter for a few seconds, then became totally dark again.

18N.—An external-frame tent which had been tipped on its side to dry was suddenly blown over by several gusts of wind. This was immediately followed by noises like three rifle shots in the distance and then by an apparent pressure change which seemed to force the witnesses to the ground. A black cloud shot overhead 10–15 s after the noises. "Golf-ball-sized" and smaller pieces of rock dropped from this cloud (some of these were collected and are a gray dacite). The cloud moved some distance to the north and then pulled back to the south (so that blue sky appeared overhead) in a span of about 5 s. Although the cloud pulled back, it did not completely disappear from sight. The cloud reapproached with a "roaring noise." As it passed overhead, a cedar tree began to fall and within seconds "there were no trees left." Seconds later it was totally dark and ash was falling so heavily that visibility, with a flashlight, was no more than a

foot. Although thousands of trees fell, the witnesses did not hear them, nor did they feel a blast or wind at that time: "whatever happened, it happened over our head." The first material to fall "was cold and was like mud," and may have contained some ice. The particles seemed to be somewhat larger than sand sized and appeared to fall vertically. A minute or two after the trees blew down, it became uncomfortably hot, as if a forest fire was nearby. The heat did not last long.

21Nb.—One of the witnesses may have sensed a pressure change; however, the other did not recall such a change. Nevertheless, for some reason they simultaneously sensed something unusual. One of the witnesses looked to the west (or southwest) and observed a "red column" extending to some height. He quickly "dove" out of the tent and rolled under a previously downed tree. As soon as he got under the tree "something hit—I could just hear this big rumble. I was just instantly buried." Trees came down on either side of the log he was under. His leg or hip was broken at this time. The other witness, in the open when the blast cloud arrived, was knocked to the ground immediately. He quickly reached forward and felt several logs which he used to drag himself more or less upright. The first material to hit him was "mud and ice. There were chunks hitting me in the back and melting." He was very wet after being hit with this material. After about 3 s, it got extremely hot. He became suddenly dry and was then burned on his hands, scalp, and several other places. The witness who was buried by downed trees and the initial blast material was not burned and perceived the heat only as being "real warm." Although it stayed very warm (estimated 130°F) for quite some time the intense heat which caused the burns was short lived. Material, which seemed to be "dirt clods," fell for about 7 min. During this time visibility ranged from 0 to 1 ft. This material quit falling quite suddenly. "Then it was almost sunny." At this time the deposit was 3–4 in. deep. Several minutes passed before ash began falling again.

21Na.—A very strong wind, which blew flames from the campfire flat along the ground and held braids of hair out horizontally, preceded the blast cloud by about 10–15 s. The witnesses were able to move about in the wind with little trouble, and no trees were toppled by it. No noise was associated with the approach of the cloud, and no concussion or loud noise was noted prior to the cloud's arrival. When the cloud arrived, it became totally black and all of the trees seemed to come down at once. The witnesses were instantaneously buried in a combination of timber and "ash" and probably fell into a hole left by the root ball of a blown-over tree. They could talk to each other but could see nothing. After perhaps 10 s, it got very hot. At this time they could hear their hair "start to sizzle" as it was singed. One witness, who is a baker, estimated the heat to be like an 300°F oven. "Pitch boiled out of trees" and remained hot enough to cause minor burns several minutes later. The sky cleared suddenly after several minutes and remained clear for a few more minutes. Then a dense ash fall began again.

20NW.—The witness and two companions were felling timber with chainsaws. Mount St. Helens was hidden by a ridge and the three men neither heard nor felt anything unusual until they were alerted to the eruption by a fourth man. About 10 s later, "a horrible crashing, crunching, grinding sound" came through the trees from the east. Suddenly it became totally dark: "I could see absolutely nothing." It immediately got very hot, and almost impossible to breathe. While the men were gasping for air, the inside of their mouths and their throats were burned. The witness was knocked down although he does not recall being hit by rocks or other projectiles. He arose with his back to searing, painful heat that lasted about 2 min. At about this time visibility began to return. All trees had been knocked down, and everything was covered with about a foot of drab gray ash. None of the men's clothing had been burned, but their bodies had been burned extensively. Three of the men subsequently died. Heavy ash fall resumed after about 20 min.

DISCUSSION

With few exceptions, the eyewitness accounts agree that: (1) close to the mountain no loud concussive noise was associated with the directed blast; (2) no shock wave preceded the blast cloud; (3) the blast cloud expanded horizontally, especially to the north, much faster than it rose vertically; (4) the velocity of this horitontal movement was great; and (5) the blast involved a brief period of intense heat that followed the blast front by a short time.

Although loud noises due to the eruption were heard hundreds of kilometers away, the blast seems to have been surprisingly quiet in the vicinity of Mount St. Helens. A similar phenomenon was reported for the climactic eruption of Krakatoa in 1883, which was heard 5,000 km away but not on neighboring islands (Symons, 1888). Close to Mount St. Helens, a variety of noises was associated with the early stages of the eruption. The most commonly described noise was a rumbling or roaring sound, which was variously described as from lasting only a few seconds and being barely audible to being a continuous loud roar. The source of this noise is not totally clear. One group, located approximately 17 km from the mountain (17NEc), thought that this sound began less than 10 s after the beginning of the landslide. Another estimate from the same locality (17NEb) places the onset of noises about 45 s after the start of the blast. The first estimate does not seem reasonable, because if the noise originated at the mountain, its onset would have been well before the beginning of the landslide. The second estimate seems more reasonable if the rumbling was generated by the onset of vigorous venting (that is, by the blast itself). Some rumbling noises may have been due to the landslides and debris avalanche. Also, the roaring may in part be due to the felling of thousands of trees by the blast, although most observers did not connect the two. Only one person's graphic description—"a horrible crashing, crunching, grinding sound"—seems to fit the destruction of a forest. In fact, the lack of reported noises associated with trees falling is striking.

Although three individuals reported seeing what appeared to be a shock wave preceding the blast cloud, no witness reported feeling one. The phenomenon described as a shock wave may have been something entirely different, perhaps similar to the white mist that led the blast cloud down the North Fork Toutle River valley (13NW). Several individuals sensed a pressure change. To some this was a rather vague feeling, while others experienced very definite sensations such as ear popping, being squeezed all over, or being pushed to the ground. This rather mild baric phenomenon certainly caused no damage.

As the blast cloud expanded, one might expect it to have displaced the air ahead of it, causing a strong wind away from Mount St. Helens. Surprisingly, only a few observers reported such a wind. One report (13NW) describes a warm 50–60 km/hr wind down the North Fork Toutle River valley. This wind was strong enough to break some branches, but not to fell trees. Two other accounts (18N, 21Na) report a wind preceding the blast cloud by 10–15 s in the Green River valley. This wind was strong enough to blow braids of hair out horizontally and knock over a propped-up tent, but it did no damage.

The absence of a shock wave or hurricane wind preceding the blast cloud is consistent with the fact that very few witnesses were able to observe trees being knocked down. Those who witnessed the cloud's advance from the east, the northeast, the North Fork Toutle River valley, and most localities to the north, did not see any damage done. Even some of those within the blow-down zone could not see trees fall (20NW, 21Na, b). The people within the blow-down zone reported that the trees fell suddenly at the moment of the cloud's arrival, and that it became completely dark at the same instant. Another report (19N), confirmed that the trees fell at the cloud's leading edge, although in this case the trees were seen thrown into the air. Of those within the blow-down zone, only one witness, located in the valley of Miners Creek (18N), saw trees fall and noted that the entire forest had been flattened before he was enveloped in total darkness. This seems to be the result of his being in a steep-sided valley and apparently having the blast cloud move overhead, hitting the upper parts of trees while momentarily permitting light from the north.

Only one account is not easily reconcilable with all destruction occurring at, or after, the arrival of the blast cloud (29N). This report indicates that, at least in some localities, the forest was destroyed a substantial distance ahead of the blast cloud. In the absence of a shock wave or preceding high wind, it is difficult to explain what mechanism might have caused destruction in advance of the cloud.

Photographs from the east, northeast, and west show the top of the blast cloud to be quite low (12Wa, 15E, 17NEa, c). From Mount Rainier, the head of the blast was seen disappearing into valleys and reappearing as it topped ridges (75N), and just north of the Green River, witnesses watched the cloud pass over each ridge and follow the slope into the next valley (25N). Impressive testimony to the ground-hugging nature of the blast cloud is provided by those north of the Green River who did not see its approach until it suddenly topped the ridge north of Coldwater Creek (23N, 29N). These witnesses looked over the top of the blast cloud to the vicinity of

Mount St. Helens while the cloud traveled 13 km to the north. The northward progress of the cloud from the top of this ridge down to the Green River was witnessed by a number of people. All of these felt that the cloud closely followed topography. However, in at least one case, the blast cloud traveled some distance above ground level (18N).

All eyewitness accounts agree that the blast cloud moved at a high velocity. Although the information in these accounts is highly subjective, it is possible to use it to make some crude estimates of the cloud's speed. Two reports, one from a location roughly 22 km north (23N) and the other about 27 km north-northeast (29N) of the north flank of Mount St. Helens, allow a rough calculation. The first describes a rumbling noise approximately 20 s prior to the cloud's topping the ridge north of Coldwater Creek; the latter a rumbling noise only a few seconds before the cloud reached this location. Both observers could first see the cloud after it had traveled approximately 13 km. It would take a sound from the vicinity of Mount St. Helens about 66 s to reach the first location and 81 s to reach the second. Therefore, if the roaring began at the time the blast began, the time for the cloud to travel 13 km can be estimated as:

$$66\text{ s} + 20\text{ s (estimated)} \approx 86\text{ s}$$
$$81\text{ s} + \text{a few seconds} \approx 85\text{ s}$$

Rounding this to 1½ min because of the approximate nature of the data yields an average velocity of 140–150 m/s (310–335 mi/hr) for the 13 km.

This high velocity applies to the "northward arm" of the blast (17NEa). In other directions the blast moved much more slowly. In particular, testimony from those who drove away from the blast cloud down the North Fork Toutle River valley (13NW, 17NW) indicates that the cloud's velocity may have been as low as 20 m/s and certainly was no higher than 45 m/s in that part of the valley west of Elk Rock.

Although material at and near the leading edge of the blast cloud flattened trees and damaged vehicles, movement of high-velocity material did not last very long. In two cases, individuals who had apparently been knocked down by the arrival of the blast cloud were able to regain their feet quickly (20NW, 21Nb).

The majority of those hit by the blast reported that the first material in it was cold and that a short time elapsed before it became hot (18N, 21Na,b). Several of these people suggested that this cold material contained ice. The difference between the blast's arrival and that of the heat was estimated to be 3 s by one individual who was directly exposed (21Nb). Other estimates were somewhat longer (18N, 21Na). Only one individual reported the simultaneous arrival of the blast and heat with no evidence of preceding cold material (20NW). The interviewees found the duration and intensity of the thermal event extremely difficult to judge. Most thought that the intense heat lasted a few minutes or less. This short duration explains why those who were completely unprotected received severe burns (20NW, 21Nb), whereas those who were somewhat protected by a vehicle or fallen timber escaped with few ill effects from the heat.

As the blast cloud reached the limits of its destruction, a number of observers to the north witnessed a rather sudden slowing of its movement. Many descriptions refer to strong winds towards the mountain, to the cloud front being "stood up," and to the cloud's curling over so that the upper part preceded a lower vertical wall to the north. These descriptions are extremely similar to the following description of the 1951 eruption of Mount Lamington, Papua, New Guinea (Taylor, 1951): "The black cloud whirling and billowing like an oil fire could be seen advancing * * *. The summit of the cloud appeared to curl over like a wave about to break on shore, but when its front was less than a mile away a brisk breeze sprang up and the cloud rolled back again."

SUBSEQUENT PHENOMENA

ACCOUNTS

DEVELOPMENT OF THE VERTICAL COLUMN

Most of those in the immediate vicinity of Mount St. Helens lost sight of the mountain very shortly after onset of the eruption. Hence, for the most part, they were unable to observe the development of the vertical column. Cool winds blowing toward the mountain were noted at many locations minutes after the beginning of the eruption, during or soon after the development of the vertical column (8W, 12Wb, 20N, 23N, 25N, 29N, 30N, 50Ea, 50Eb).

15E.—It was impossible to tell precisely when the vertical eruption began. However, it could be determined that no major vertical eruption took place for several minutes after the initial eruptive events, and

that a well-developed column was present within about 10 min.

40W.—The pilot of a commercial airliner, located about 25 mi west-southwest of Mount St. Helens at an altitude of about 35,000 ft, spotted the eruption at about 0838. The enormous energy of the eruption sent the ash column from about 25,000 ft to the plane's altitude in about 2 min. In another 2 min it had risen to 60,000 ft. The column then spread into a mushroom-shaped top reaching a diameter of about 35 mi in about 4 min. The column below the mushroom top was about 15 mi in diameter. A thistlelike spike projected above the top of the mushroom cloud. The top of the mushroom expanded so rapidly that it soon passed over the airliner. A short time later, the airline pilot heard another pilot flying on the east side of the mountain complain over the radio of being pelted by rocks, presumably falling from the mushroom cloud.

75N.—The column grew rapidly and assumed a classic mushroom shape in about 3–5 min. The mushroom shape continued to develop for about 15 min; then the top of the cloud began to drift to the east.

100SE.—When the eruption was first noted, the mountain was obscured, and a vertical tube of ash could be seen disappearing into a layer of haze about 1,000 ft above the summit. The witness' watch read 0835 at this time. A few minutes later the column began to grow, reaching a diameter of about 10 mi in 5 min.

ELECTRICAL PHENOMENA

Lightning and other electrical phenomena associated with the eruption were so spectacular that many witnesses mentioned them. Many witnessed displays of "ordinary lightning" impressive only in the size and frequency of bolts. To some the lightning appeared to be mostly from cloud to cloud (8SE). A heavy concentration of vertical lightning at altitudes of 25,000–30,000 ft was entirely within the vertical eruptive column (40W). Others noted many cloud-to-ground strikes (9W, 15E), some of which started forest fires (12Wb) and one of which struck an individual (20N). Beneath any part of the eruptive cloud, radios became useless because of static (8SE, 12Wa, 27N). On Mount Adams, climbers noted that the air became electrically charged as the ash cloud moved overhead, and one climber received an electrical discharge upon raising his ice axe (50Ea).

Some observers witnessed unusual forms of lightning. Some of the lightning (9W, 15ENE, 17NEa) appeared red. 25N: It wasn't normal lightning—"first a white dot appeared in the cloud, and then a bolt would shoot out from it." 100SE: The lightning was in ball form "streaking toward the ground, connected neither with the cloud nor with the ground. It was like a group of balls all going in the same direction, but going much too fast to have been projectiles." 29N: After the cloud passed overhead, lots of lightning started 600–800 ft in the air and formed "big balls, big as a pickup and just started rolling across the ground and bouncing."

MUDFLOW ON THE SOUTH FORK TOUTLE RIVER

8W.—Less than 10 min after the beginning of the eruption, a huge mass of water, mud, and trees crashed down a small tributary within the South Fork Toutle River valley. It snapped off trees and "exploded" when it hit lows, bursting as much as 60 ft when it hit obstacles. A similar flow then swept across the road about 100 yd to the north, moving trees, rocks, and stumps. A few minutes later a substantial but much smaller flow, containing numerous trees and other debris, was still moving down the valley. About 8 min after the first flood, the witness crossed the flow path by wading through material like "warm concrete" and a flow of very muddy, cool water. The river returned to and stayed within its deep channel until about 1400, when there occurred a second smaller flood deep enough to spill out of the channel.

40NW.—Sometime after 0900, the South Fork Toutle River began rising and quickly rose 2 or 3 ft. The river was slightly muddy and carried numerous logs. About 2–3 min after the first logs moved downstream, a railroad trestle moving at about 25 mi/hr appeared about ½ mi upstream with an enormous log jam behind it. Trees were being snapped off about 30 ft beyond the original streambanks. As the trestle went by, large logs behind it rolled up the bank. The mass of thick mud and logs pushed the witnesses and their car off the bank and into the river. They were swept along for about 5 min at about 25–30 mi/hr in very thick, warm (70°–80°F) mud. The witnesses

jumped from log to log toward shore where the flow was moving more slowly, and waded the last 40 yd in warm mud over 1½ ft deep. The mud continued to rise slowly for a short time. After perhaps 15–30 min the mud and logs stopped moving.

AIR-FALL MATERIAL

8SE.—Although a dark cloud passed overhead several minutes after the start of the eruption and remained overhead for 10–15 min, the area received no ash.

12Wb.—About 30 min after the start of the eruption, ash began to fall at a point somewhere between the initial observation point and Goat Mountain (southwest of the volcano; fig. 35). The ash fall lasted about 10 min.

8W.—About 15 min after the start of the eruption, a dark cloud descended from the mountain and sand-sized ash began raining down vertically. The witness sensed pressure pulses on his face and in his ears that seemed to correspond to periods of more intense ash fall. He experienced difficulty in breathing during the heavy ash fall and clearly attributed this difficulty to a lack of air, not to clogging of his nose and mouth with ash.

15ENE.—At roughly 0900, chunks of ice as much as 1 or 1½ in. in diameter began to fall. The ice fell for 2 or 3 min and was followed by "ice-cold mudballs" as much as 3½ in. across, which splattered when they landed. About 45 min after the eruption started, "B-B-like" ash began to fall. Warm pumice as much as 1½ in. in long dimension soon joined the ash fall. The witnesses drove south on road 125 and quickly left the ash fall.

15E.—Mud, which one of the witnesses (a geologist) recognized as accretionary lapilli, began to fall at about 0915. About an hour later (1015), the falling material included pumice.

20NW.—About 20 min after the arrival of the first cloud, it began to get dark again and quickly became "pitch black" as ash fell heavily. Forty-five minutes later it began to get light, but a dense vertical rain of dust-sized gray ash continued, gradually decreased, and finally stopped after about 4 hr.

19N.—A few minutes after the blast and a brief period of light, the ash fall was so dense that the truck's headlights produced only a dull diffuse glow. Even with the lights on the witnesses could not see the truck's hood. Breathing was difficult due to a "talcum powderlike" ash. By 0900 the witnesses were able to follow the edge of the road by using a flashlight held within 6 in. of the ground. "Pretty good sized" particles continued to fall with enough horizontal velocity that the witnesses were able to maintain some sense of direction from the angle at which these particles fell. It began to get light a little after 1000, and by 1020 visibility was roughly 30 ft.

21Na.—After the blast and a few minutes of clear sky, hot ash began to fall. Again it became totally dark. This ash seemed to fall vertically. It was "like someone pouring a bag of it over your head." This extremely heavy ash fall lasted about 15 min. The ash fall was so intense that the witnesses had to use their fingers to dig the ash out of their mouths. They put their shirts over their heads in an effort to keep the ash out of their mouths and noses. After 15–20 min "stuff started coming out of the sky." They could hear this material hitting trees. One witness was hit on the head by something large enough to raise a lump. During the heavy ash fall, they became cold, sleepy, and nauseous, but did not suffer from headaches. After an hour and a half visibility began to return.

21Nb.—After a period of clearing following the blast, powdery ash fell heavily for about ½ hr and at a lesser but significant rate for another half hour. The witnesses experienced difficulty in breathing in that their mouths and noses became clogged and they had to repeatedly spit out ash. The intensity of the ash fall varied somewhat so that visibility ranged from essentially zero to about 20 yd. The witnesses sat with their backs to the southwest and the ash seemed to be hitting them from that direction, although the horizontal velocity was not great.

18N.—Fifteen or twenty seconds after the blast cloud moved overhead, ash was falling so intensely that, even with a flashlight, visibility was no more than 1 ft. The first material to fall "was cold and was like mud" and seemed to fall vertically. During the heavy ash fall, the witness experienced feelings of peacefulness and serenity and had to make a conscious effort to stay awake. After 45 min to 1 hr, the

ash fall had diminished so that he could see the ground with the aid of a flashlight. Hours later ash in the area ranged from 6 in. to knee deep in drifts.

22N.—Eight to ten minutes after the witnesses first observed the eruption cloud, ash began falling in small clumps "like snowflakes." The ash fall increased so that within minutes the darkness was similar to that in a cave. The intense ash fall continued for a period of ½ to 1 hr. Although the ash made noise while falling, it felt dry, and when examined afterwards it felt like talc. Within hours after the ash fell it was about 2 in. deep. The next morning it had compacted to 1½ in. at the same locality.

20N.—The first material to fall was sand-sized ash, which felt moist and was not warm. As the ash fall intensified, it became extremely dark and, based on the noises that the ash made as it fell through the trees, the particle size increased. These larger particles fell for about 45 min and then stopped quite quickly. Ash continued to fall until about 1000, when it got light very quickly: "It was just like you opened your eyes." The depth of ash was about 1 in. Ash collected by the witnesses from a pickup truck 2½ mi to the northwest was examined by one of the authors and consisted entirely of ash with numerous accretionary lapilli.

25N.—Before the ash fall began, the witnesses drove to site 27N where they remained for the duration of the ash fall. As the eruption cloud moved overhead, "pea-sized ash" started to fall. This material was damp, and fell with a substantial northward component of motion. After 15 s, material that seemed to contain rocks pelted the car for 20–30 s; then fine ash fell vertically. The ash fall became very dense so that it was like a "giant sifter was over you." Except for a 3-s period of light after about 20 min, the complete darkness remained until 1100.

27N.—The first material to fall was a little muddy rain. This was followed by 20–40 "pings" of solid particles hitting the vehicle during a 30-s span. It then became totally dark as ash began to fall heavily. This continued for about 2 hr with a 10-min interval of very limited visibility occurring after about 40 min.

29N.—The witness was driving to the north when warm mudballs began to fall. These balls would flatten out but not spatter; "When they hit the windshield of the pickup, they'd be about the size of a golfball." He drove into dense falls of these mudballs four or five times. After a short time the mudballs began to be replaced by dry ash.

23N.—The witness drove north to Riffe Lake (about 4 mi) before any material began to fall. The first material consisted of mudballs "the size of 50-cent pieces," which splattered all over the car and covered the windshield. They were quite wet and "felt a little warm." The mudballs began falling roughly 15 min after the start of the eruption and fell for 2 or 3 min. As the mudballs tapered off they were replaced by dry ash.

17NEa.—The witness had driven 2 or 3 mi to the northeast. Seven or eight minutes after the eruption's start, rocks began falling from the part of the cloud that had passed overhead. He collected two "golfball-sized" rocks (determined by one of the authors to be dacite) from the fall. The rock fall continued for roughly 30 s and was then replaced by material that splattered on the windshield. As he drove, this material was replaced by "mud drops," which would flatten but not splatter. The maximum diameter of a mudball observed after flattening was about ¾ in. Gradually the mud fall abated and the ash fall became heavier. The ash was finer than sand. For a short time he encountered a second fall of mud drops, similar to but heavier than the first. This was quickly replaced by intense ash fall. Soon the ash fall became so intense that he could no longer see to drive. The ash fall eventually abated very gradually.

17NEb.—The witnesses left their original observation site roughly 2 min after the landslide began and had driven about 5 mi when the upper part of the cloud passed over them. The first material to fall was rock. Individual pieces ranged up to ½ in. in diameter, but most were pea sized. These rocks put small dents in the car's roof. The rocks were followed by large clods, 5–6 in. in diameter, that would "explode" upon impact. The clods were replaced after a few minutes by a warm mudfall, that gradually decreased over 15–20 min and was replaced by dry vertically falling ash. It was several hours before the ash fall abated.

27NE.—After leaving his vantage point, the

witness drove south to USFS road 125. Fairly dry pellets began falling about the time he turned north onto USFS road 125. These did not stick to his vehicle. A short time later ash began falling. The ash seemed to be associated with a good deal more water in that it stuck to the windshield and could not be removed by the wipers. Wet ash had to be scraped repeatedly from the windshield for about half an hour, after which the ash became drier.

50Ea.—At roughly 0900, the front of the eruption cloud passed overhead, and shortly thereafter ash began to fall. Mixed with the ash were charred "wood, cones, and some branches up to 12–16 inches long." Also noted in the falling material were a few pieces of pumice. The ash fall lasted about 30 min and left a deposit ¼–⅜ in. thick.

50Eb.—About 0900, the eruption cloud enveloped the area. The first material to fall consisted of B-B-sized pellets. About 5 min later branches and evergreen cones began falling. The branches were as much as 16 in. long and ¾ in. in diameter and so numerous that at any one time nearly 100 were in the field of view. These items were singed and hot when they landed. About 10 min after the ash fall began, the B-B-like pellets were replaced by larger disc-shaped pieces up to ¾ in. in diameter. Branches and ash continued to fall for about 80 min; then the ash fall ceased. By 1045 it was clear at 8,000 ft and above. However, below 5,500 ft ash continued to fall until after 1600.

50Ec.—At about 0850, chunks of light-gray pumice began falling, making a pinging noise in the trees. Most of the pumice was the size of pea gravel, but occasional pieces reached ¾ in. in diameter. The pumice fall lasted about 5 min. At 0900 the sky grew very dark and B-B-sized pellets began falling. The pellets splattered on impact. Coarse sand-sized ash, finer than the first B-B-sized material, continued to fall while the witness drove to Randle.

75N.—At 0915 (by the witness' watch), "twigs from evergreen trees coated with ash" began to fall. These twigs were as much as ¾ or 1 in. in length and were charred. The start of the ash fall was very gradual, but when the group reached their camp about 1 hr after the start of the eruption, a layer of fine ash coated the tent. The ash was finer than sand but caused a gritty sound on one's teeth. The ash fall remained quite light so that it was barely visible in the air. However, it did accumulate slowly on the ground so that several hours later, it had attained a thickness of 3/16–¼ in.

DISCUSSION

Several minutes elapsed between the initial eruptive events and the development of a vertical eruptive column. However, once the column began to develop it apparently grew very quickly, rising from about 7.5 to 18 km in roughly 4 min, and then mushrooming at about that altitude to a diameter of 55 km in another 4 min (40W). The column maintained its mushroom-shaped top for about 15 min, after which the top was blown in an easterly direction by high-altitude winds (75N). The rapid growth of the column and mushroom-shaped top and the rather short existence of the top may indicate that the early vertical eruption was most energetic during the first few minutes.

Mudflows, at least in the South Fork Toutle River valley, began very shortly after the eruption. Only about 10 min elapsed between the start of the eruption and the maximum flood down the South Fork Toutle, 10 km west of the mountain. In this part of the valley, the flood moved extremely fast, bursting into the air as it hit obstructions (8W). Further down valley, near the confluence of the North Fork and South Fork Toutle River, the mudflow had slowed considerably but still moved at a velocity perhaps as great as 40 km/hr (40NW).

High horizontal velocities were not associated with airborne material beyond the area devastated by the directed blast, nor with material that fell at points within that area, except for a short time immediately after the blast cloud arrival. At many localities, coarse lithic fragments preceded or accompanied the first minute or so of ash fall. Much of the early material was damp or wet and fell as large mudballs that may have been aggregates of accretionary lapilli. In general, the particle size and moisture content decreased with time.

Little evidence exists for the presence of large quantities of magmatic gases. When asked about odors, many eyewitnesses said only that they thought that they smelled "sulfur" during and after the dense ash fall and compared this odor to that of a match. Although several individuals experienced trouble with breathing, most attributed this difficulty to having

their mouths and noses clogged with ash. Two individuals (8W, 20NW) attributed breathing difficulties to a lack of oxygen. Two other descriptions might be interpreted to indicate a lack of oxygen or exposure to a noxious gas: one of the individuals mentioned being cold, nauseous, and sleepy (21Na); the other reported sleepiness accompanied by a feeling of serenity (18N). However, these symptoms may be the individuals' reactions to shock.

The material that fell on and near Mount Adams (50E) and on Mount Rainier (75N) was probably carried to great altitude by the vertical column and then by high-altitude winds to the northeast. Wind direction from Mount St. Helens on May 18 was not directly toward either Mount Adams or Mount Rainier. The short duration of the ash fall at Mount Adams might be explained if only the edge of the "mushroom top" passed over the area. The remnants of evergreen trees that fell on Mount Adams and Mount Rainier were certainly from the forest destroyed by the directed blast. Somehow these fragments became incorporated in the early stages of the vertical eruption and were carried to great heights and distances.

The early stages of the vertical eruption also contained pumice, which was the first material to fall at one locality (50Ec), and which was also noted on Mount Adams (50Ea). Closer to the mountain, both groups to the east of Mount St. Helens (15E, 15ENE) also observed falling pumice. The widespread presence of pumice in the air-fall material suggests that the eruption was magmatic at a very early stage.

REFERENCES CITED

Stoffel, K. L., 1980, The May 18, 1980 eruption of Mount St. Helens, A view from the top: Washington State Department of Natural Resources Information Circular No. 71, p. 9–11.

Symons, G. J., ed., 1888, The eruption of Krakatoa and subsequent phenomena: Report of the Krakatoa Committee of the Royal Society, London, 494 p.

Taylor, G. A., 1958, The 1951 eruption of Mount Lamington, Papua: Bureau of Mineral Resources (Australia) Bulletin 38, 100 p.

THE 1980 ERUPTIONS OF MOUNT ST. HELENS, WASHINGTON

TIME SCALE FOR THE FIRST MOMENTS OF THE MAY 18 ERUPTION

By BARRY VOIGHT

ABSTRACT

A sequence of photographs taken at irregular intervals by Gary Rosenquist documents a complex succession of events at the beginning of the catastrophic May 18 eruption of Mount St. Helens. Calculations of the time intervals between individual photographs and absolute times for these photographs were made in order to enhance their value to scientific studies of the events of the May 18 eruption. Time intervals were derived by comparing a dynamic model to the motion of ice avalanches as displayed by the photographic sequence. That analysis yielded an average interval between frames of about 1.8 ± 0.2 s (seconds), and a cumulative time of roughly 32–40 s for the sequence. Next, times were referenced to an earthquake at 0832:11.4 PDT, which initiated a catastrophic rockslide. Rockslide motion apparently commenced at about 0832:21 PDT. About 700 m of slip, which took place in about 26 s, then occurred before the first frame of the Rosenquist sequence that shows displacement was taken, at approximately 0832:47 PDT. Uncertainties include the time interval after the earthquake and before the slide, and assumed ice-avalanche dynamic parameters, but the data are relatively well constrained; blast-front destruction of seismic station SOS at 0833:29.5 PDT provides an upper bound, and consideration of frictionless ice-avalanche motion provides a lower bound.

INTRODUCTION

The photographs taken by Gary Rosenquist clearly document a complex succession of events that occurred during the first minutes of the May 18 eruption. Initiated by earthquake shocks, the north slope of Mount St. Helens (figs. 36, 37, 38) began to slide northward (slide I) along a newly formed fracture system, and was accompanied by ice avalanches on the northeast margin (figs. 36, 37*C*; Voight and others, this volume). The summit area collapsed and followed in a second block, termed slide II. Meanwhile, ash-rich eruption plumes developed both from the summit and from the 600-m-high scarp of slide I. The scarp eruptions expanded to form a large, laterally directed blast that devastated the landscape in a large sector north of the volcano (Christiansen and Peterson, this volume; pl. 1).

The evolution of each of these events can be followed in detail in the photographs, so that they are of enormous scientific value. However, because the film was advanced by manual manipulation of a wind lever, irregular time intervals separate the individual photographs. This report presents a first-approximation analysis of the timing of the Rosenquist photographs, in order to provide a basis for studies of dynamic evolution of events, including calculation of velocities, that occurred during the first few minutes of the May 18 eruption, and also to provide a better understanding of such events.

Comparable analyses, used by Moore and Albee (this volume), have been carried out by S. D. Malone of the University of Washington, using a different approach that involves several data sources. Malone

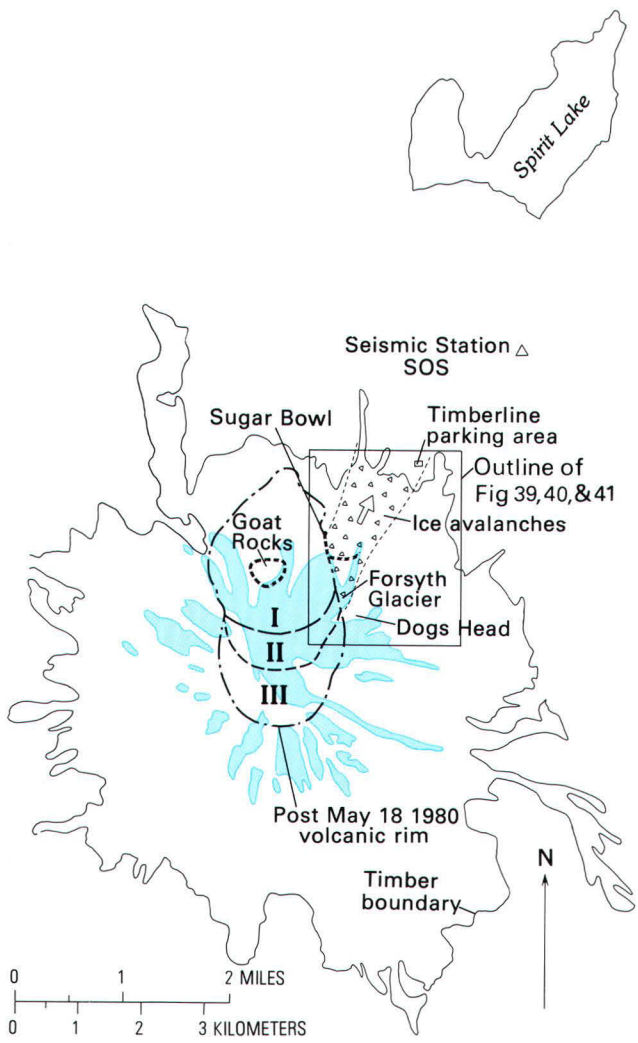

Figure 36.—Index map of Mount St. Helens showing area of rockslide-avalanches and Forsyth ice avalanches in relation to Gary Rosenquist's observation site near Bear Meadow. Glaciers indicated by screen pattern. Outline of figures 39, 40, and 41 shown.

generously exchanged information with me, and his comments on an earlier draft resulted in important improvements in this paper. We plan to compare our independent studies in further detail in the future, in order to provide a second-approximation analysis. This analysis was made possible by the generosity of Gary Rosenquist and Linda Harvey, who made available the complete photograph sequence.

Figure 37.—Sketches of Mount St. Helens based on Rosenquist photographs. A, sketch from frame b, just before May 18 eruption, showing spot elevations, approximate elevation contours (blue), and geographic names; B, outline of rockslides I and II boundaries on frame b; and C, sketch of frame d showing rockslide boundaries and Forsyth ice avalanches. Movement of slide II indicated by downward shift in the position of top of slide I scarp from frames b to d.

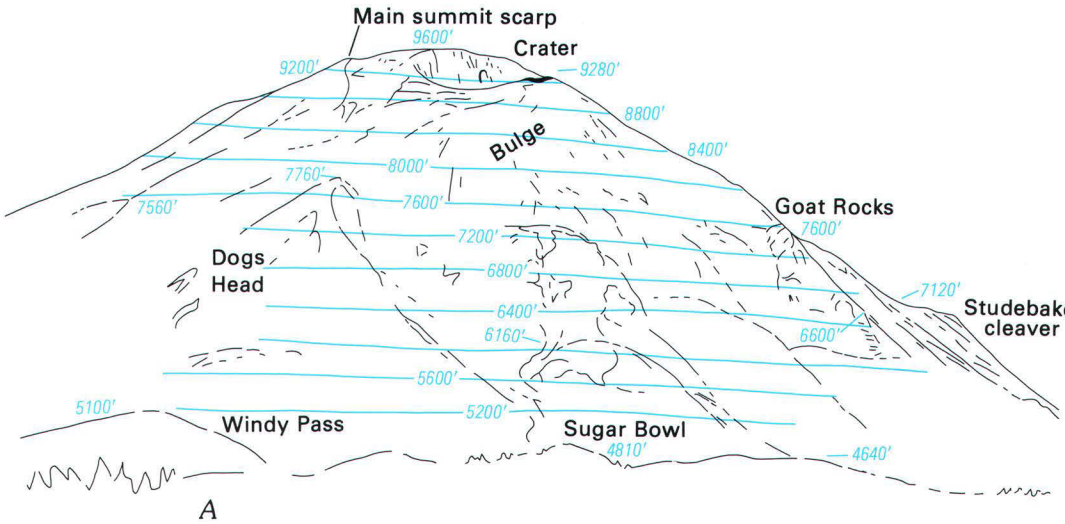
Main summit scarp
9600′
Crater
9200′
9280′
8800′
Bulge
8400′
8000′
7760′
7560′
7600′
Goat Rocks
7600′
7200′
Dogs
Head
6800′
7120′
Studebaker
cleaver
6400′
6160′
6600′
5600′
5100′
5200′
Windy Pass
Sugar Bowl
4810′
4640′
A

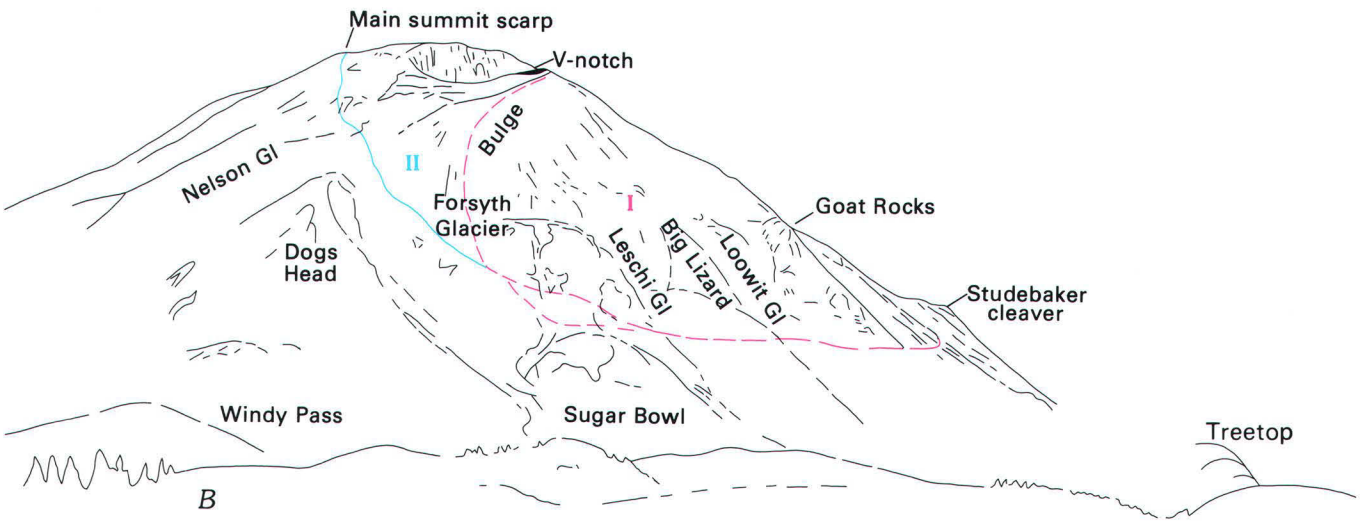
Main summit scarp
V-notch
Bulge
Nelson Gl
II
Forsyth
Glacier
I
Goat Rocks
Dogs
Head
Leschi Gl
Big Lizard
Loowit Gl
Studebaker
cleaver
Windy Pass
Sugar Bowl
Treetop
B

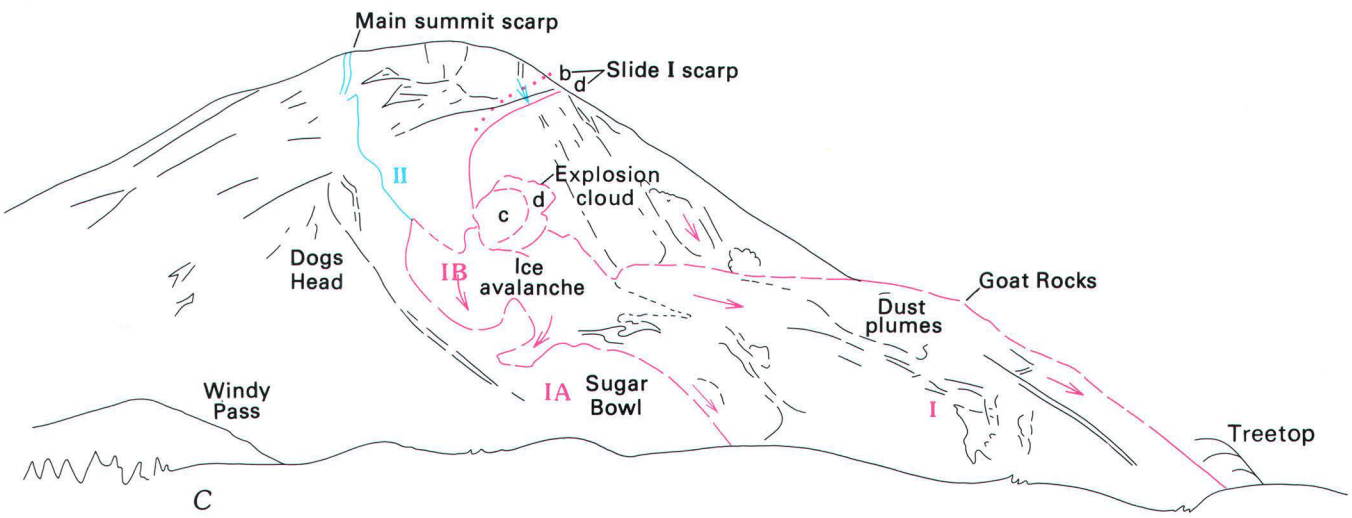
Main summit scarp
b
d
Slide I scarp
II
Explosion
cloud
d
c
Dogs
Head
IB
Ice
avalanche
Goat Rocks
Dust
plumes
Windy
Pass
IA
Sugar
Bowl
I
Treetop
C

A

B

Figure 38.—Slide and eruption sequence at Mount St. Helens. Copyrighted photographs by Gary Rosenquist, 1980, published with permission. Approximate time intervals indicated by $C_{.15}$ scale. See figure 37 for geographic names, elevations, and identification of ice avalanche and slide blocks. A, frame b. Time about 0827 PDT, roughly 5 min before the eruption. B, frame c. Time (t_C) approximately 0832:47 PDT. Slide I has been displaced 700 m from position in frame b; instantaneous velocity at that time about

C

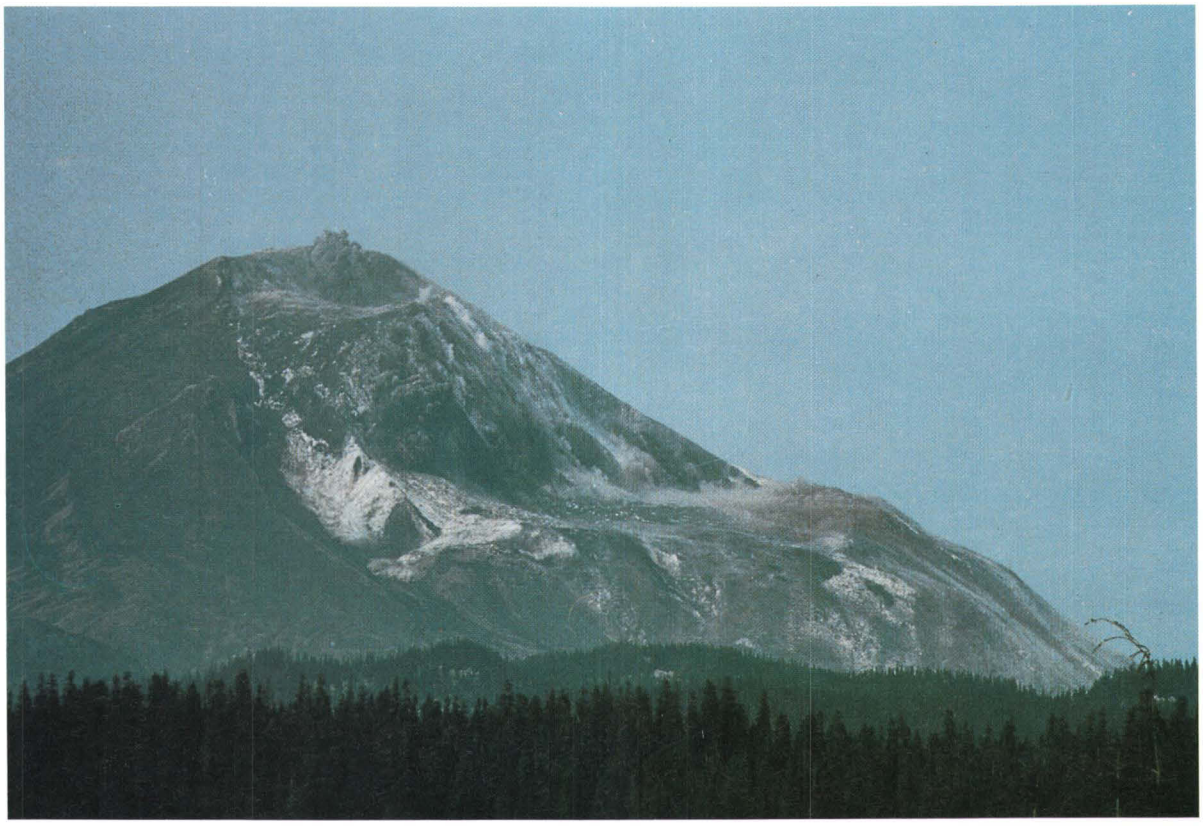

D

50 m/s. Slide II has been displaced 100 m, and slide I scarp is 600 m high. Ice avalanches IA and IB in motion. Blurred image reflects camera movement. C, frame d. Time, t_c + 0.8 s. Further movement indicated for slides I and II and ice avalanches IA and IB. Red-brown dust plumes trail Goat Rocks. Growth indicated for summit plume and explosion clouds from slide I scarp. D, frame f. Time, t_c + 2.4 s. Further development of slides I and II and eruption clouds. Summit plume rises behind main summit (slide II)

E

F

scarp. Ice avalanches IA and IB fully developed; ice avalanche II comprises several small lobes in early stage of development. E, frame i. Time, t_c + 6.3 s. Most of slide I beyond zone of depletion. Mixed juvenile and steam explosions hide slide I scarp, and sagging of slide II pronounced. Projectiles rise from summit plume. Ice avalanches IA and IB have coalesced, with the IA front over spur below Dogs Head. Further development of ice avalanche II. F, frame l. Time, t_c + 10.0 s. Summit plume exhibits growth, and blast

G

H

cloud fills zone of depletion behind slide I. Further development of slide blocks and ice avalanches. G, frame n. Time, t_c + 13.0 s. Pronounced vertical and lateral expansion of summit plume. Laterally directed blast develops behind slide I, with blast-cloud front moving over Sugar Bowl. Ice avalanche IA at head of ravine above Timberline parking area; and ice avalanche II coalesced into single lobe. H, frame o. Time, t_c + 16.7 s. Continued evolution of summit plume and blast cloud. Ice avalanche IA beyond limit

I

J

of visibility. Piecemeal collapse of the crown of the slide II scarp (amphitheater rim). I, frame r. Time, t_c + 24.1 s. Projectile trails encompass blast clouds; predominant lateral expansion of summit clouds. Ice avalanche II passes over spur below Dogs Head. J, frame u. Time, t_c + 31.8 s. Further development of blast clouds with projectile swarms. Expansion of summit cloud, and retrogressive collapse of amphitheater rim.

THE PHOTOGRAPHS

On the morning of May 18, 1980, Gary Rosenquist was camped near Bear Meadow, northeast of Mount St. Helens, about 17.5 km from the summit (fig. 36). Others in the group included Linda and Joel Harvey and William Dilly. Dilly described hearing "rumbles" on the morning of May 18, and reported the occurrence of a small billow of white steam near the summit. At that time Rosenquist mounted his camera on a tripod and took one photograph of the mountain. The camera was left on the tripod, while Dilly watched the mountain through binoculars. As he watched, the north slope west of Dogs Head (fig. 37) became "fuzzy, like there was dust being thrown down the side," and began to move. Dilly shouted that the "mountain was going," and within a few seconds Rosenquist began taking photographs in rapid succession.

The Rosenquist photographs (fig. 38) are classified alphabetically. Frame *a* is a photograph at dawn, and *b* is the photograph taken just a few minutes before the May 18 rockslide. Frame *c* is the first of the sequence showing displacement; the last of the sequence is *w*. Twenty-one frames display the movement record, and two show the initial conditions; ten of the frames are included in this report (fig. 38). The complete sequence can be obtained from G. Rosenquist, P.O. Box 66173, Seattle, Wash. 98166.

Figure 39.—Area of northeastern part of Mount St. Helens in vicinity of Sugar Bowl and Dogs Head. May 12 ice-avalanche deposits form brown tongues north and northeast from Sugar Bowl. Position of avalanche fronts were mapped on prints of the Rosenquist photographs, and transferred by eye directly onto this image. Figure 40 is produced from this image. Photograph by U.S. Forest Service (FO 42 8005 10).

DEVELOPMENT OF THE TIME SCALE

The time scale for the photographs was derived in two steps. First, the time intervals were established for successive photographs. Next, an absolute time estimate (t_C) was given for frame *c*, the first frame that records displacement. Absolute times for each frame were then approximated by adding successive time intervals to t_C.

TIME INTERVALS

Establishment of time intervals can be accomplished by at least two methods: (1) attempted replication of action by the photographer, as timed with a stopwatch, or (2) measurement of particle displacement between successive photographs, coupled to an adequate dynamic model of particle motion. The first method could give a time-interval scale useful for rough approximations of dynamic change. However, because of the relatively large number of photographs and the interval irregularity, the second method was considered more appropriate for this study.

This study was influenced by several additional considerations. For example, one of the principal purposes for establishing a time scale was to permit study of the dynamic evolution of the catastrophic rockslide-debris avalanche. Direct use of data from the rockslide-avalanche for interval time-scale determination was therefore deliberately avoided. A

geologic event or series of events depicted throughout the photographic sequence was, nevertheless, required to establish motion from frame to frame. Finally, a reasonably reliable dynamic model of motion-time relations was required.

These requirements were satisfied by analysis of three ice avalanches from the Forsyth Glacier, referred to as Forsyth ice avalanches IA, IB, and II. The three ice avalanches originated in the sector of the glacier between Sugar Bowl and Dogs Head on the northeast shoulder of Mount St. Helens (figs. 37*C*, 39). Ice avalanches IA and IB were in motion by the time frame *c* was taken. The front of IA can be followed through frame *o* to the ravine above the Timberline parking area (fig. 40*A*), where it passes out of sight. Avalanche IB can be followed as a distinct unit to frame *j*; it then merges with IA (fig. 40A). Ice avalanche II began somewhat later, and its evolution can be followed in the photographic sequence to the last frame, *w*, when it, too, passes from sight (fig. 40*B*). Average slope angles for the avalanche routes are 18.0° for IA, 23.5° for IB, and 22.0° for II (figs. 41, 42). The route for avalanche II flattens to about 18° in its lower part.

The boundary of each avalanche, on each frame, was mapped from 12.6×20.2-cm prints of excellent quality, and transferred by eye to a May 17, 1980, aerial-photographic base (fig. 39). Taken the day before the May 18 eruption, this base photograph contains various details in texture and color (such as the May 12 ice-avalanche deposit below Sugar Bowl) that permitted mapping of relatively high accuracy. Horizontal travel distances were scaled from the photograph, and actual travel distances were computed using slope angles from topographic profiles. Photographic distortion is a possible source of error, but is considered small relative to other factors.

It was assumed that the displacement of each avalanche front could be simulated, to a first approximation, by an Amonton-Coulomb (linear basal friction)

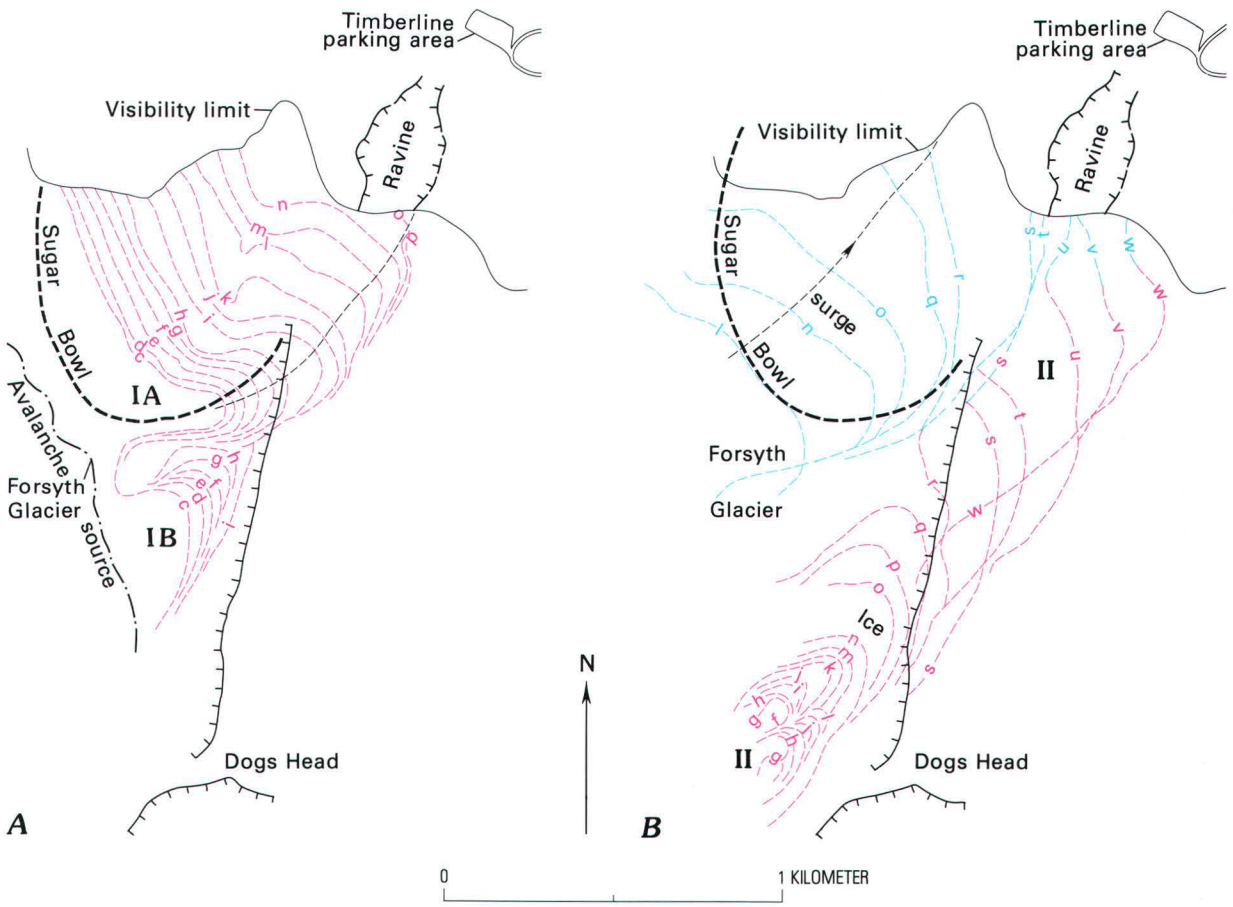

Figure 40.—Map of Forsyth Glacier ice-avalanche fronts as seen on Rosenquist photographs. Letters identify frames. A, ice avalanches IA, IB; B, ice avalanche II and blast cloud.

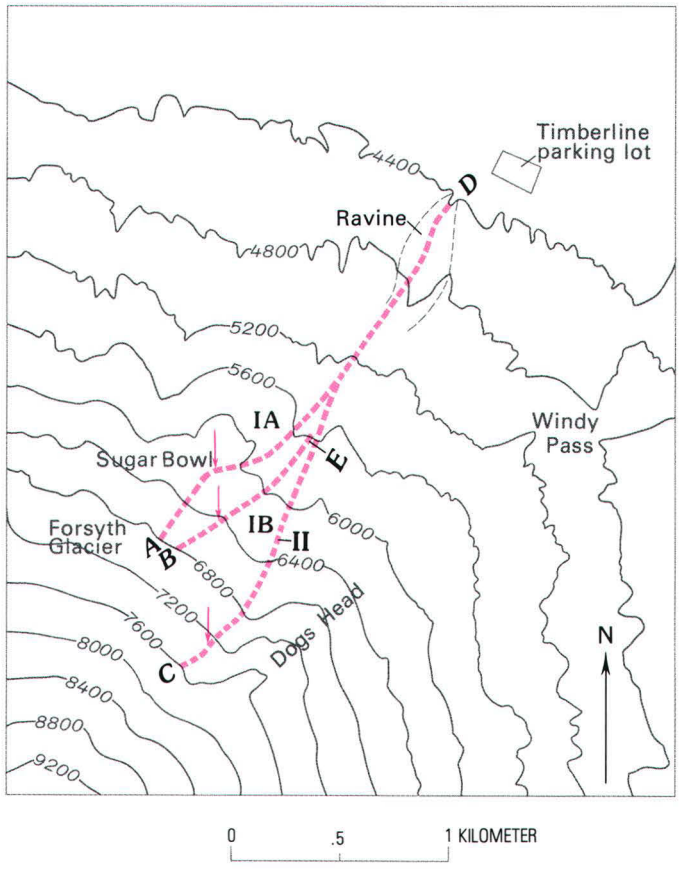

Figure 41.—Northeastern part of Mount St. Helens. Approximate track of ice-avalanche lobes indicated by red lines. Points of avalanche origin indicated by arrows. Topographic profiles A-D, B-E, C-D are shown in figure 42. Base map August 15, 1979 (Moore and Albee, this volume).

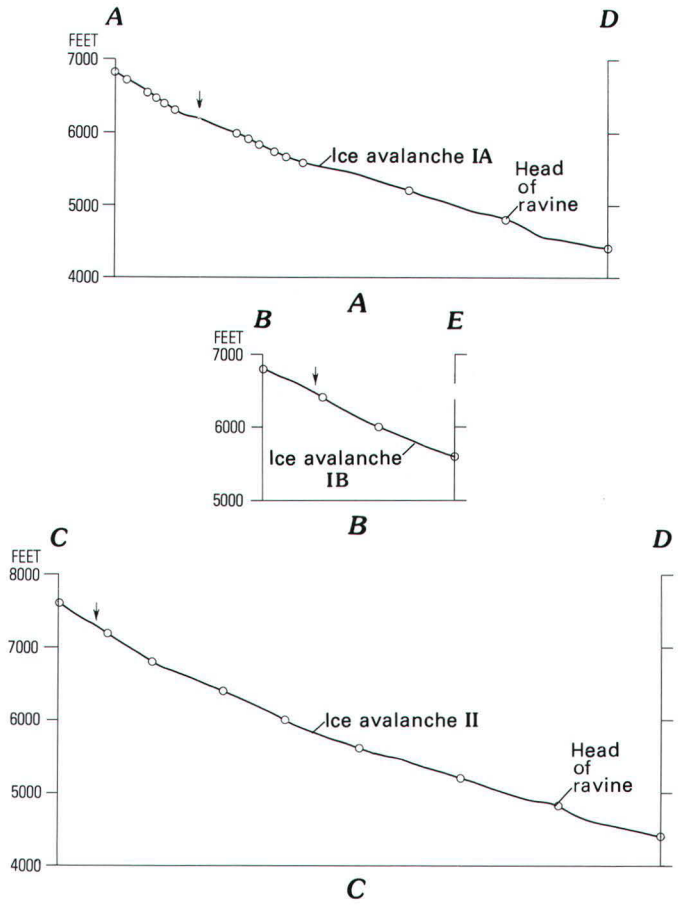

Figure 42.—Topographic profiles along ice-avalanche paths. Arrows indicate points of avalanche origin. A, A-D; B, B-E; C, C-D.

idealization. Air resistance was neglected, and uniform (average) slopes were used. Existing knowledge of ice avalanches is limited, compared to information available for snow avalanches (Mellor, 1968, 1978), but frictional models of ice movement have been used by other authors (Haefeli, 1965; Mellor, 1978; Slingerland and Voight, 1979, table 4), and similar models have been widely used for rock avalanches (Pariseau and Voight, 1979). Nevertheless, this use of frictional models has been mainly a convenience; a simple friction model can be useful, but is probably only an approximation of movement for an avalanche in rapid motion. Consideration of velocity-dependent boundary shear, for example, could lead to future time-scale adjustments, and the matter is presently under investigation.

The displacement-friction model was used in this study to calculate elapsed times, t; the relationship is $t=(2s/a)^{1/2}$, where s is travel distance based on the avalanche maps, and avalanche acceleration $a=g$ (sin i-μcos i); g is gravitational acceleration, i is slope angle, and μ is apparent friction coefficient for ice.

Some constraints on ice-avalanche friction coefficients are known. According to the friction-acceleration equation just presented, for example, no motion could occur on an 18° slope for $\mu > 0.3$; because rapid ice-avalanche motion, in fact, occurred on 18° slopes, a close but lesser value of $\mu = 0.25$ was originally assumed as a reasonable approximation to maximum friction and, hence, to upper bound time intervals. Upper bound time intervals are discussed further in the section on "Implications of destruction of seismic station SOS on the time scale." Absolute lower bound times were given by hypothetically frictionless motion ($\mu = 0$).

Furthermore, the driving force for the three avalanches was a function of sin i, which varies between 0.31 and 0.40 for assumed average slopes between

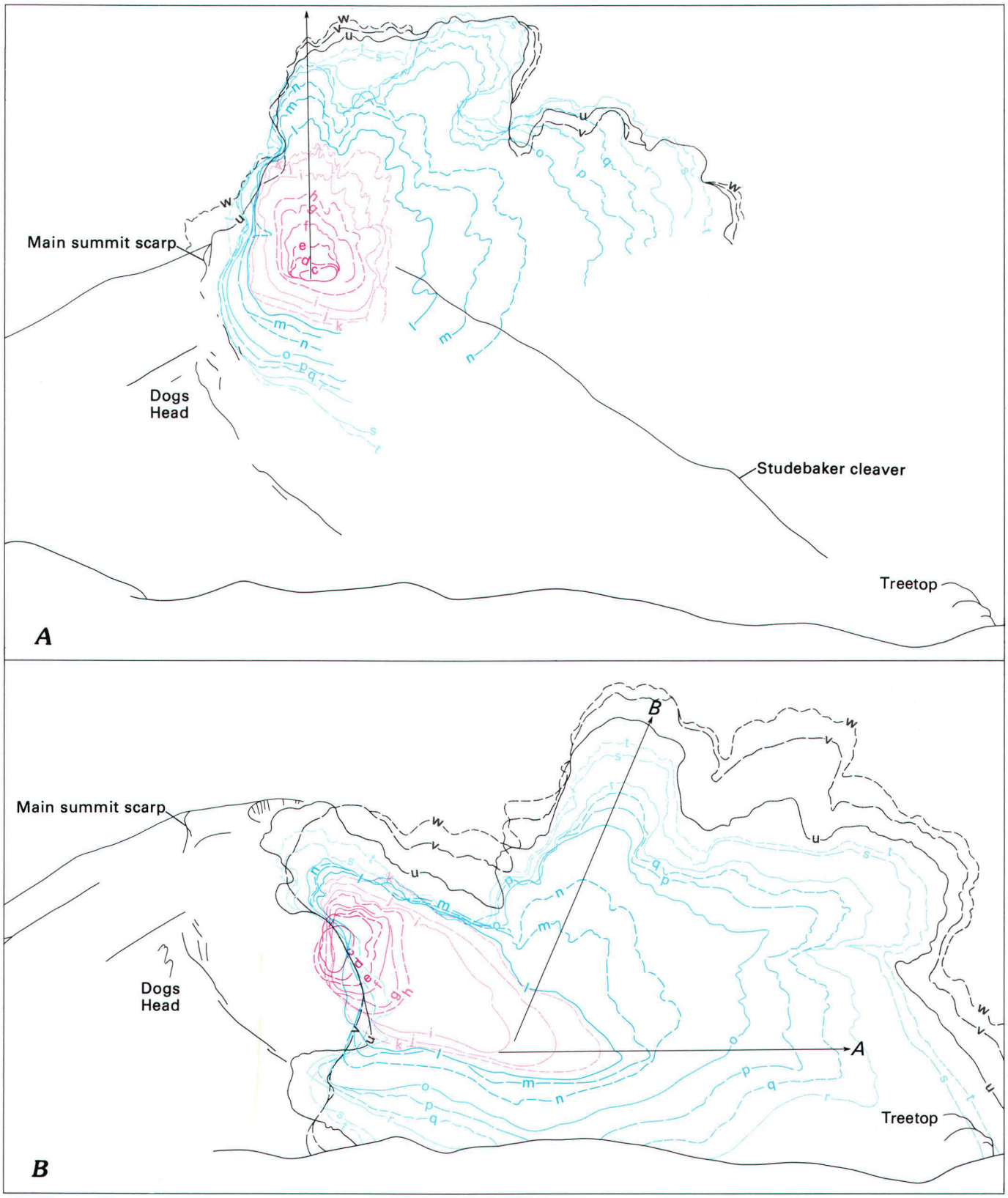
Main summit scarp
Dogs Head
Studebaker cleaver
Treetop
A
B
Main summit scarp
Dogs Head
Treetop
B
A
B

18.0° and 23.5°. If apparent friction coefficients were identical, the avalanches would have moved predictably different distances on different slopes for a given time interval. This fact makes possible the estimation of friction coefficients by comparing, for several avalanches on different slopes, the calculated time intervals for the different distances traveled during the same frame interval. Calculated time intervals for distances traveled were compared for avalanches IA and IB on frame sequences *c-d* to *g-h*; intervals were compared for avalanches IA and II on sequences *h-l* to *m-n*. Time differences were found to be least for $\mu = 0.15$–0.20. These values were, therefore, used as first-approximation estimates of apparent friction coefficients for the ice avalanches.

Average calculated time intervals for the three ice avalanches are given to one decimal point in table 6. For frame interval *n-o* and later, data are based exclusively on avalanche II. The convention C_μ is used as a shorthand designation for the time scales, and the subscript refers to the appropriate friction coefficient. The data suggest that the complete sequence of photographs was taken during a cumulative time of no less than 28.2 s and no more than 48.7 s. These are regarded as rather extreme values, and an intermediate better estimate is considered to be about 36 s, based on the $C_{.15}$ time scale that corresponds to the 0.15 friction coefficient. The average interval between frames is somewhat less than 2 s.

Table 6.—Time scale for Rosenquist photograph sequence of the May 18 eruption of Mount St. Helens

[First approximation. μ, apparent friction coefficient for ice]

Frame interval	Time interval (seconds) μ=0.00 (C_0)	μ=0.15 ($C_{.15}$)	μ=0.20 ($C_{.20}$)	μ=0.25 ($C_{.25}$)	Cumulative time (seconds) μ=0.15 ($C_{.15}$)
c-d	0.6	0.8	0.9	1.1	0.8
d-e	.6	.8	.9	1.1	1.6
e-f	.6	.8	.9	1.1	2.4
f-g	.7	.9	1.0	1.2	3.3
g-h	.7	.9	1.0	1.2	4.2
h-i	1.5	2.1	2.5	3.3	6.3
i-j	.9	1.2	1.4	1.8	7.5
j-k	.8	1.1	1.3	1.7	8.6
k-l	1.1	1.4	1.7	2.1	10.0
l-m	1.2	1.6	1.8	2.3	11.6
m-n	1.1	1.4	1.7	2.1	13.0
n-o	2.9	3.7	4.1	4.7	16.7
o-p	1.9	2.4	2.8	3.1	19.1
p-q	2.0	2.5	2.9	3.2	21.6
q-r	2.0	2.5	2.8	3.2	24.1
r-s	2.6	3.4	3.8	4.3	27.5
s-t	1.1	1.3	1.5	1.7	28.8
t-u	2.4	3.0	3.4	3.8	31.8
u-v	1.9	2.4	2.7	3.1	34.2
v-w	1.6	2.0	2.2	2.6	36.2
c-w	28.2	36.2	41.3	48.7	36.2

ABSOLUTE TIMES

The magnitude-5+ earthquake at 0832:11.4 PDT presumably started minor rock and ice falls from the south crater wall, as observed and described by Stoffel and Stoffel (1980). Following an interval of a few seconds, a major fracture propagated rapidly along the apex of the bulge north of the summit crater. North of this fracture, the rock mass "rippled and churned," apparently in place, for an interval of several additional seconds. The north face then slid down in a gigantic rockslide, as indicated by the Stoffel and Rosenquist photograph sequences (Voight and others, this volume, fig. 201; fig. 38). Each of the two time intervals mentioned above has been estimated at 5–10 s by Dorothy and Keith Stoffel (oral commun., November 1980). Noting the slowness with which slide movements begin from a static condition, the onset of rock sliding is arbitrarily taken as 0832:21 PDT. An error of several seconds could easily be associated with the estimated delay time, and an adjustment of this estimate may eventually be necessary.

Next, the time interval between the rockslide initiation and Rosenquist frame *c* was estimated from a dynamic model for rockslide motion. If friction is constant, acceleration (a^*) of the slide mass can be

Figure 43.—Sketches of Mount St. Helens based on Rosenquist photographs showing growth of eruption clouds. Letters identify sequential frames. Growth rates vary spatially and with time, but relative spacing roughly indicates relative time intervals between frames (compare with fig. 40). Measurement lines for A and B indicate eruption cloud data used in figures 46 and 45. A, vertical eruption plume from summit grows while plume source sinks due to rockslide movement (slide II). B, bulbous explosion clouds grow along scarp exposed by rockslide movement (slide I). Blast cloud moves out over Sugar Bowl and toward observer, in direction of seismic station SOS.

calculated as a function of displacement (x) from

$$a^* = \frac{T(x) - \mu^*[N(x)]}{m},$$

where μ^* is the apparent coefficient of rockslide friction, m is slide mass, and $T(x)$ and $N(x)$ are average shear- and normal-force components on the slide surface. Displacements and velocities were determined as a function of time, assuming various values for rockslide friction coefficient and using standard equations of motion (fig. 47). These theoretical results were compared to data on rockslide movement as determined from the Rosenquist photographs.

Measurement on the Rosenquist photographs indicates that the distance traveled by slide I by the time frame c was taken was about 700 m. With zero rockslide friction, a minimum time of 21.4 s was required to produce this displacement. But displacements and velocities for the rockslide after frame c was taken, plotted as a function of time using the ice-avalanche-based time scales (fig. 47), suggest that $\mu^* \cong 0.1$ for the rockslide. These data suggest that approximately 26 s elapsed between slide initiation and frame c. Therefore, for frame c, $t_C \cong$ 0832:47 PDT, acknowledging an uncertainty of a few seconds. Estimated absolute times for each frame can now be determined by adding the cumulative times to t_C (table 6).

IMPLICATIONS OF DESTRUCTION OF SEISMIC STATION SOS ON THE TIME SCALE

Telemetered seismic station SOS, at lat 46°14′38″ N., long 122°08′36″ W. (NE¼SE¼ sec. 23) between Spirit Lake and Mount St. Helens, was destroyed at 0833:29.5 PDT (S. D. Malone, oral commun., December 1980). Its destruction 78.1 s after the earthquake is interpreted by many to be the result of the passage of the blast front. This event can be used to place a maximum elapsed-time constraint on the time scale and the time interval between the earthquake and the rockslide, and then to make estimates of blast-cloud velocities.

An approximate minimum elapsed time of 33 s between the earthquake and Rosenquist frame c can be concluded by the allowance of only 7 s (approximately a lower bound) for the earthquake-to-rockslide initiation interval described by Stoffel and Stoffel (1980) and the acceptance of 26 s as the time required for slide I to move to the position shown in frame c. The position of the laterally directed blast cloud in the Rosenquist photographs in relation to the landscape indicates that the seismic station was not destroyed before frame w. A reasonable upper bound for the Rosenquist photographic sequence cumulative time from frame c to w is therefore 78–33 = 45 s. If the interval between earthquake and rockslide is 10 s, 78–36 = 42 s is the sum of the photographic-sequence time and the time required for the blast cloud to reach station SOS from its position on frame w. This 42-s value very nearly matches the cumulative time for the photographic sequence for the $C_{.20}$ scale, by itself. Thus, if 10 s is a reasonable time interval between the earthquake and the rockslide, and some time is allowed for travel of the blast from the frame w position to station SOS, then the cumulative time for the photographic sequence is likely less than 40 s.

A maximum time interval between the earthquake and slide initiation can be estimated by the following two arguments:

1. If an estimated time of 26 s is accepted for rockslide movement to frame c, and an absolute lower bound (zero ice-avalanche friction C_0) cumulative time of 28 s is assumed for the

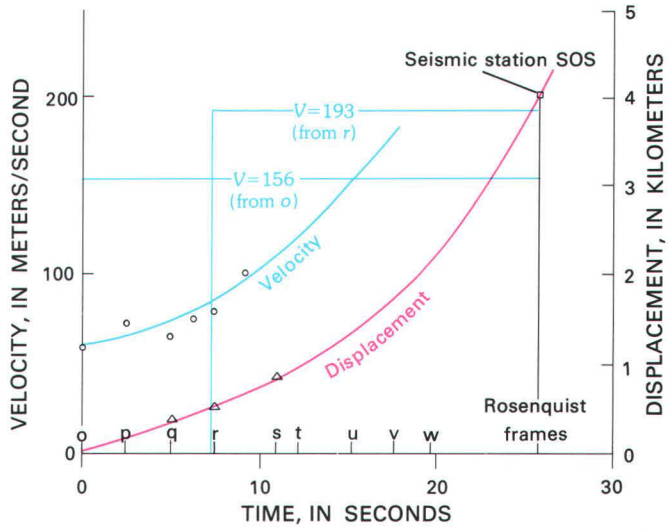

Figure 44.—Displacement and velocity plotted versus time, for time interval between frame o and destruction of seismic station SOS. Triangle, displacement data point based on direct measurement; circle, velocity data point based on displacement measurement and time calculated from Rosenquist photographs. $C_{.15}$ time scale.

Rosenquist sequence, 78–54 = 24 s remains to be divided between the earthquake-to-slide-initiation interval and the time required for the blast cloud to travel from its position in frame *w* to station SOS.

2. The minimum time interval between frames *c* and *o* is 12.7 s by the zero ice-avalanche friction time scale. Blast-cloud travel distance from frame *o* position to station SOS is about 4 km. An average blast-cloud velocity of 200 m/s is regarded to be a reasonable upper bound. Travel from the position in frame *o* to station SOS required no less than 20 s for an assumed upper bound average horizontal velocity of 200 m/s. Movement of slide I to its position in frame *c* required 26 s. The sum of these three values gives 58.7, leaving a maximum of 19.4 s for the interval between the earthquake and the landslide.

These data tend to confirm the Stoffels' estimate of a maximum of 20 s, based on their eyewitness observations.

The blast front is assumed to have destroyed station SOS. The blast cloud developed from the detachment surface behind the initial massive rockslide (slide I, figs. 38, 43; 202*C*), and moved forward to the

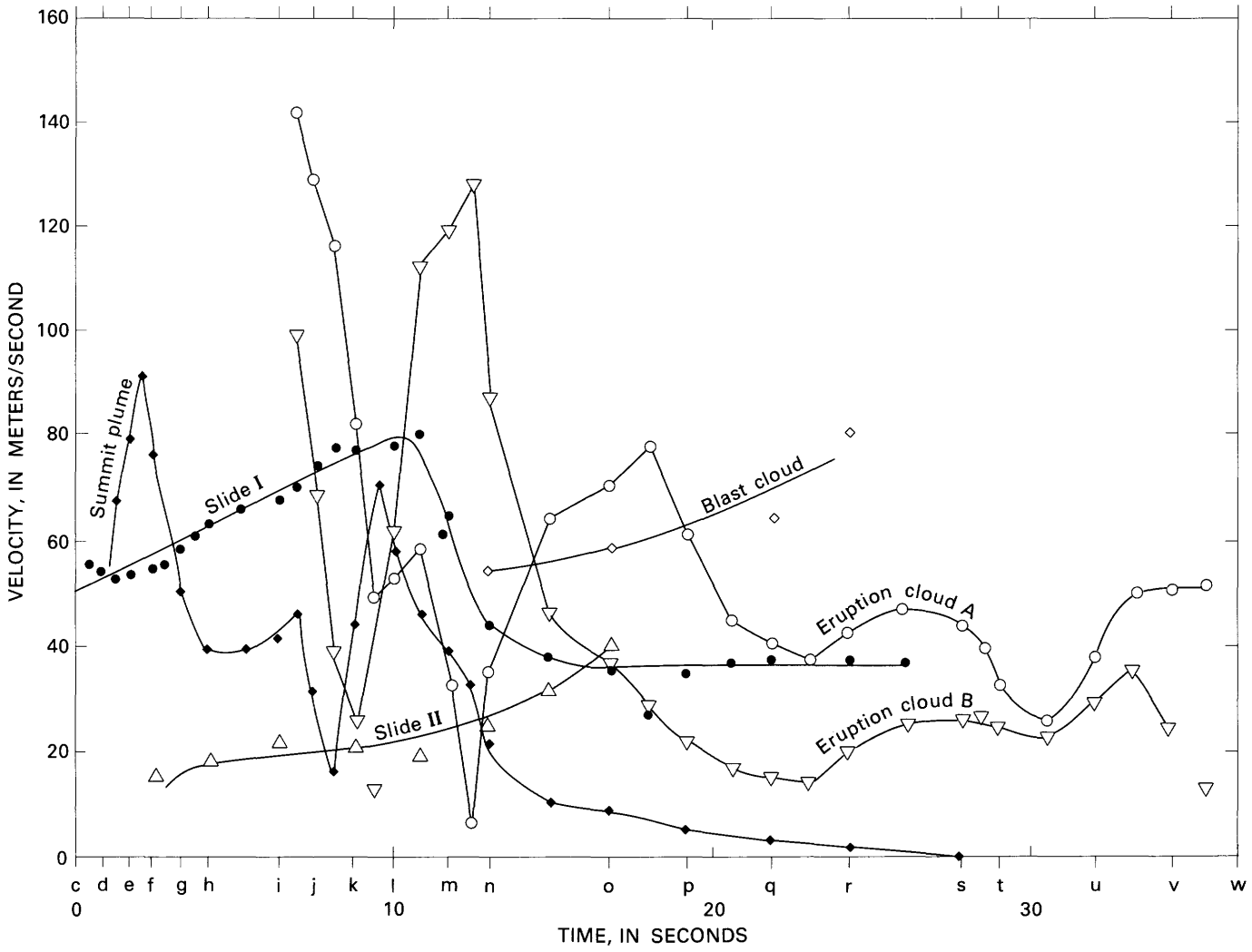

Figure 45.—Velocity of displacement of various slide and eruption phenomena plotted versus elapsed time from t_C, where t_C is time of first Rosenquist posteruption photograph. Time scale $C_{.15}$. Shown are Forsyth ice avalanches (IA, IB, and II in red), the rockslide-avalanche (slides I, II), the northeast-moving blast cloud front near Sugar Bowl, eruption clouds from rockslide scarp (A, B), and eruption plume from the summit. Data for slide I are averages from numerous points, data for slide II are from a single point.

north over slower moving slide debris and to the northeast over Sugar Bowl. After the time of frame *l*, the blast cloud passed beyond the limits of the slide-detachment surface (fig. 38). Over Sugar Bowl, the blast-cloud margin can be viewed until frame *r* (fig. 40*B*).

Using the $C_{.15}$ time scale and $t_C = 0832{:}47$ PDT, the blast cloud passed station SOS about 25.8 s after its position on frame *o* over Sugar Bowl. The horizontal distance is almost 4 km, so the blast's average horizontal velocity was 156 m/s (fig. 44; slope-parallel velocities are generally about 5 percent higher).

By frame *r* (figs. 40*B*, 44), the blast cloud had

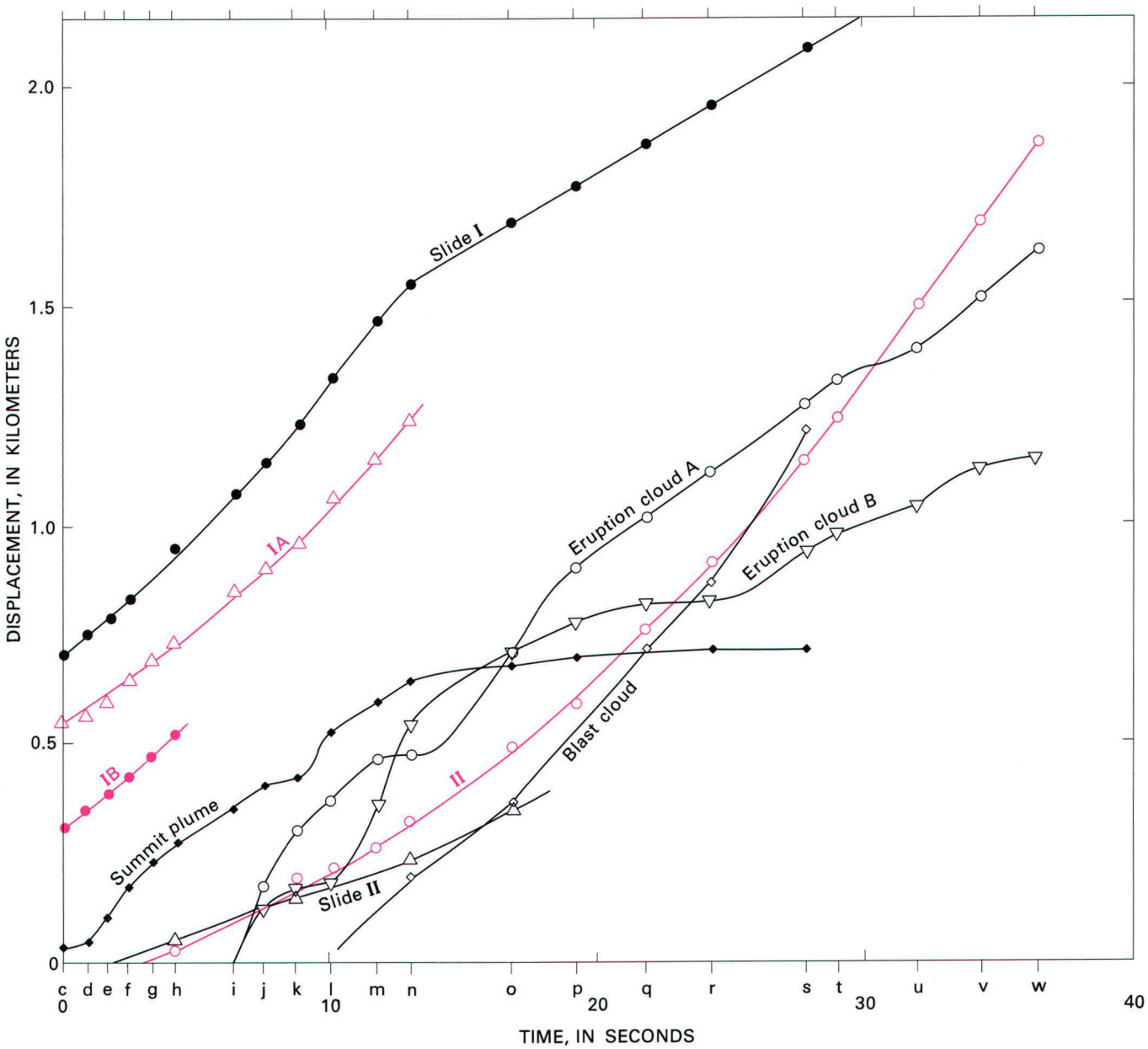

Figure 46.—Displacement of various slide and eruption phenomena plotted from first Rosenquist posteruption photograph. Time scale $C_{.15}$. Shown are Forsyth ice avalanches (IA, IB, and II in red), the rockslide avalanche (slides I, II), the northeast-moving blast cloud front near Sugar Bowl, eruption clouds from rockslide scarp (A, B) and eruption plume from the summit. Data for slide I are averages from numerous points, data for slide II are from a single point.

moved somewhat farther; the time interval from its position in frame *r* to station SOS is about 18.4 s, so the average horizontal velocity for 3.55 km travel from the position in frame *r* to SOS is about 193 m/s. These average horizontal velocity values may be compared to calculated instantaneous velocities of about 50–100 m/s for the blast cloud at the Sugar Bowl position (fig. 44, 45); the instantaneous velocity noticeably increased with displacement. The average blast-cloud velocities from Sugar Bowl to SOS are much higher than instantaneous velocities at the Sugar Bowl position.[1] Acceleration of the blast cloud as it passed over Sugar Bowl suggests that an instantaneous velocity higher than 200 m/s at SOS was possible.

These calculations were carried out using the premise that the blast-cloud front destroyed station SOS. An alternative view is that destruction was due to strong winds in front of the moving blast cloud,

[1]Orientations of felled trees near the SOS site suggest that blast cloud travel distances, as calculated from Sugar Bowl to SOS, are upper bounds. Calculated average velocities are thus also upper bounds.

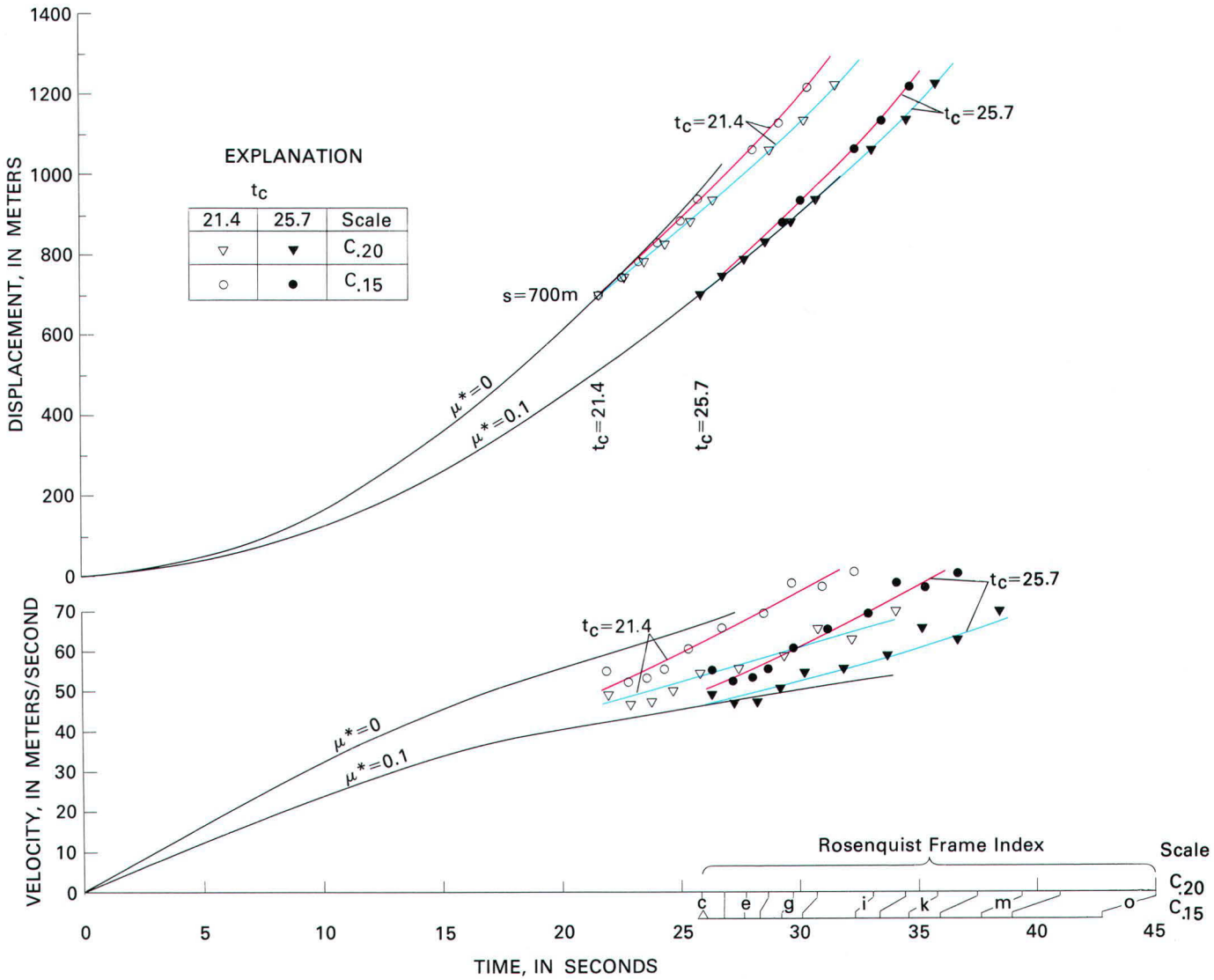

Figure 47.— Displacement and velocity versus elapsed time from onset of slide I motion. Theoretical curves for slide I assume kinetic frictional coefficients of 0 and 0.1. Data points from displacement measurements on Rosenquist photographs (see fig. 202) shown for two time scales, $C_{.15}$ and $C_{.20}$, and plotted with respect to two values of t_c, 21.4 and 25.7 s. Displacement of slide I at frame c taken as 700 m. The data reasonably fit the theoretical curve for 0.1 friction coefficient; the $C_{.20}$ scale seems preferable for frames indicated.

rather than to the blast cloud itself. This precursory wind could reduce the required blast-travel distance associated with loss of station SOS; for example, if the precursor wind were 200 m in front of the blast, the average blast velocity would have been about 6 percent less.

CONCLUSIONS

Methods discussed in this report permit the calculation of estimated times of events that fit dynamic models for the ice avalanches and slide I, and are consistent with both eyewitness observation and seismic events. A first-approximation timetable is as follows, starting with the reference earthquake at 0832:11.4 PDT.

1. For the interval between the earthquake and the rockslide, a range of values is estimated as 7–20 s, based on calculations and eyewitness reports. A reasonable estimate of 10 s after the earthquake gives 0832:21 PDT as the time of onset of slide I motion.

2. By the time of frame *c* (t_C), slide I had traveled about 700 m. A dynamic model of slide I indicates that no less than 21 s was required for this displacement. A value of 26 s is suggested by comparison of velocity and displacement data to theoretical curves, resulting in a time of about 0832:47 PDT for t_C.

3. Velocity data for slide I suggest that use of the $C_{.20}$ scale is preferable to the $C_{.15}$ scale until about frame *l*, inasmuch as the $C_{.15}$ scale predicts increases in velocity in excess of the frictionless rockslide idealization. On the other hand, the $C_{.20}$ cumulative time (41 s) for the entire photographic sequence is large with respect to the interval of time bounded by destruction of seismic station SOS. A cumulative time of 40 s for the photographic sequence is probably too high, whereas a time of 32 s, which was obtained using the $C_{.20}$ scale for frames *c* to *l* and the C_0 (frictionless) scale for frames *m* to *w*, is likely too low. The $C_{.15}$ scale provides a reasonable cumulative time estimate of 36 s. This value is probably accurate to within 4 s, or within 13 percent of the actual value.

4. The average time interval between frames is thus 1.8 ± 0.2 s. Individual intervals between frames for the $C_{.15}$ scale vary from 0.8 to 3.7 s. These intervals are at present considered slightly low for frames *c* to *l* and too high for the remaining frames.

Other eyewitness photographs can be fixed in time by correlation with the time scale based on the Rosenquist photographs. One method of correlating is by matching various slide or eruption-cloud positions, such as the height of the summit plume above the crater. Data that can be used for this purpose are shown in figures 46, 45, and 43.

Although further adjustments are anticipated, this time scale is considered to be sufficiently accurate to permit dynamic analyses of various eruption phenomena (see figs. 47, 44). For example, the data suggest velocities of 50–70 m/s for slide I, 50–100 m/s for the blast cloud at Sugar Bowl, and 90 m/s (peak velocity) for the summit plume.

REFERENCES CITED

Haefeli, R., 1965, Note sur la classification, le mécanisme et le contrôle des avalanches de glace et des crues glaciaires extraordinaires: International Union of Geodesy and Geophysics and International Association of Scientific Hydrology, International Symposium on Scientific Aspects of Snow and Ice Avalanches, Davos, Switzerland, 1965, Publication 69, p. 316–325.

Mellor, Malcolm, 1968, Avalanches, *in* Cold regions science and engineering—Pt. 3, Engineering, Section A3, Snow technology: U.S. Army Materiel Command Cold Regions Research and Engineering Laboratory, Hanover, N.H., 215 p.

_____1978, Dynamics of snow avalanches, *in* Voight, Barry, ed., Rockslides and avalanches, 1, Natural phenomena: Amsterdam, Elsevier, p. 753–792.

Pariseau, W. G., and Voight, Barry, 1979, Rockslides and avalanches—basic principles, and perspectives in the realm of civil and mining operations, *in* Voight, Barry, ed., Rockslides and avalanches, 2, Engineering sites: Amsterdam, Elsevier, p. 1–92.

Slingerland, R. L., and Voight, Barry, 1979, Occurrences, properties, and predictive models of landslide-generated water waves, *in* Voight, Barry, ed., Rockslides and avalanches, 2, Engineering sites: Amsterdam, Elsevier, p. 317–397.

Stoffel, D. B., and Stoffel, K. L., 1980, Mt. St. Helens seen close up on May 18: Geotimes, v. 15, no. 10, p. 16–17.

GEOPHYSICAL MONITORING

GEOPHYSICAL MONITORING

Geophysical monitoring techniques have provided the primary basis, at Mount St. Helens and other intensively instrumented volcanoes such as Kilauea in Hawaii, Etna in Italy, and Asama in Japan, for attempting relatively short-term forecasts or predictions of eruptive activity. Although the geologic record of past eruptive activity is especially useful in assessing frequency, style, and probable consequences of future eruptions, geophysical techniques for monitoring seismicity, ground deformation, gas compositions, thermal features, gravity and magnetic changes, and so on commonly provide the first definite signs that an inactive volcano will erupt in the near future.

At Mount St. Helens in 1980, the abrupt increase in earthquake activity at shallow depth beneath the volcano, beginning on March 20, was recognized within a few hours as indicating possible impending eruptive activity. Geophysical monitoring was especially important in April and early May, when continued relatively mild steam-blast eruptions provided little evidence that a catastrophic event was approaching. Both the sustained high level of seismic activity and of ground deformation on the north-flank bulge indicated that the volcano could be building toward some major event. Ground deformation was monitored both by geodesy and by photogrammetry.

After May 18, patterns of seismicity and ground deformation changed markedly, but these indicators continued to provide key information on the readiness of the volcano to erupt and the size and depth of the underlying magma body. Electronic-tilt, microgravity, and magnetic measurements recorded small but significant changes around Mount St. Helens at various times during the 1980 eruptive activity; while offering less clear predictive information, they provided valuable constraints on the geometry of the magma body beneath the volcano.

Before May 18, the volume of gas emissions was small, apparently because the magma body was too deep or too well sealed for gases to reach the surface. By early June the SO_2 emissions had reached much higher levels, probably reflecting rise to shallow depth of the magma body that erupted explosively on June 12 and shortly afterwards formed the first 1980 lava dome. Beginning in early July, CO_2 and H_2 were also monitored repeatedly, and variations in abundances and ratios of these gases provided possible advance indications of several eruptions.

Like the gas studies, aerial infrared thermal monitoring provided only limited indication of the major changes in the volcanic edifice prior to May 18, other than those associated with the summit crater. After May 18, thermal monitoring provided information about temperature distributions in relatively inaccessible slopes of the volcano, in the crater, and on the lava domes. Direct measurements of temperatures in erupted deposits provided a remarkable data set for the 1980 eruptive products that helps to constrain emplacement mechanisms for the debris avalanche, directed blast, and pumiceous pyroclastic flows of May 18 and subsequent eruptions.

Monitoring of eruptions by aviation radar yielded estimates of heights and density of ash-rich eruption columns above and downwind of the volcano. Visual observations of the volcano were supplemented beginning in late July by a closed-circuit video surveillance system installed on a vantage point 9 km north of the vent.

SEISMIC STUDIES

Continuous monitoring of earthquakes has been especially useful for anticipating volcanic activity and interpreting volcanic processes. Patterns of earthquake hypocenters can give indications of shifting locations and depths of activity within a volcano, and analysis of numbers and magnitudes of earthquakes provides information on rates of energy release. Most eruptions are preceded by notable increases in earthquake frequency, magnitude, and energy release beneath the volcano.

The earthquake swarm at Mount St. Helens preceding the May 18 eruption provided a remarkable opportunity to characterize precursory seismic phenomena associated with andesitic-dacitic volcanism (Endo and others). Daily earthquake counts gradually increased for 5 days prior to the first major earthquake on March 20, which was of magnitude 4.2 and located only a few kilometers beneath the volcano. The number of earthquakes peaked on March 27, concurrently with the first hydrothermal eruption. A gradual decrease in earthquake counts through April and early May was accompanied by an increasing number of larger magnitude events; as a result, the rate of energy release remained high and nearly constant. Most of these earthquakes were confined to a small volume, less than 2.5 km deep, beneath the growing bulge on the north flank of the volcano. The May 18 eruption was triggered by a magnitude-5+ earthquake, slightly larger than any previously recorded at Mount St. Helens, but no specific precursory seismicity has been recognized for the May 18 eruption, other than the entire earthquake sequence that started in late March.

After May 18, earthquakes beneath the volcano decreased in number and magnitude, occurred at depths as great as 20 km, and were widely distributed along zones extending tens of kilometers northwest and southeast of the volcano (Weaver and others). Complex earthquake sequences in the crater area, including periods of harmonic tremor, accompanied magmatic eruptions after May 18 and were helpful in forecasting some eruptive activity a few hours in advance, as discussed later in this volume (Malone and others).

THE 1980 ERUPTIONS OF MOUNT ST. HELENS, WASHINGTON

LOCATIONS, MAGNITUDES, AND STATISTICS OF THE MARCH 20–MAY 18 EARTHQUAKE SEQUENCE

By ELLIOT T. ENDO, STEPHEN D. MALONE[1], LINDA L. NOSON[1], *and* CRAIG S. WEAVER

ABSTRACT

The earthquake swarm at Mount St. Helens preceding the May 18 cataclysmic lateral blast provided an excellent opportunity to characterize precursory seismic phenomena associated with andesitic-dacitic volcanism. Major features of the swarm included a gradual increase in seismicity starting in mid-March, a magnitude-4.2 earthquake on March 20, a significant increase in the number of earthquakes on March 25, a saturated record until March 27, a gradual decrease in the daily number of earthquakes after March 27, and, on the morning of May 18, a magnitude-5.1 earthquake preceding the blast.

Of over 10,000 earthquakes recorded by an online computer system between March 20 and May 18, seven hundred were selected for preliminary hypocenter location. Epicenter locations were restricted to a 3-km-diameter region approximately coincident with a surface area of intense deformation. Hypocenter depths calculated during a preliminary test of a recently developed crustal model, which was based on explosion data, show the earthquakes were confined to a small volume less than 2.5 km deep beneath the north flank of Mount St. Helens.

From March 20 to May 18 more than 2,400 earthquakes with local magnitudes greater than 2.4 were recorded by the Mount St. Helens seismic network. Magnitude-frequency relations suggest two distinct classes of shocks. One class produced a *b*-value of 0.6, consistent with tectonic-type earthquakes. Another group, referred to as low-frequency earthquakes, produced a *b*-value of 2.8, consistent with volcanic swarms observed elsewhere.

Preliminary total seismic-energy-release calculations indicate a lower limit of 1.8×10^{20} ergs for the entire swarm up to May 18. Daily seismic-energy release prior to March 27 was low compared to daily energy release after March 27.

INTRODUCTION

At 1547 PST on March 20 a magnitude-4.2 earthquake beneath Mount St. Helens marked the first strong quake of an earthquake swarm that preceded the lateral blast and cataclysmic eruption of May 18. The swarm, unprecedented for Cascade Range volcanoes since the development of short-period, high-gain seismic telemetry systems, provided an excellent opportunity to characterize an earthquake swarm associated with orogenic-belt volcanism.

A combination of fortunate circumstances made possible a joint University of Washington and USGS effort to deploy both portable and telemetry seismic stations in the Mount St. Helens area. In Seattle, at the University of Washington, a recently installed online computer became the primary seismic data-acquisition system. From March 20 to May 18 approximately 10,000 earthquakes were digitized in real time and recorded on magnetic tape.

This report presents the hypocenter locations of a subset of the earthquakes recorded. In an expanded data set, earthquake magnitudes, counts, and seismic-energy release are also discussed. A short section on historical seismicity is included.

[1]University of Washington, Seattle, Wash. 98195.

ACKNOWLEDGMENTS

Our special thanks to the graduate students and electronic technicians who installed critical instruments under difficult conditions. We thank the Newport Observatory in eastern Washington for providing a list of reported magnitudes for our magnitude study.

DATA AND ANALYSIS

The data analyzed for this paper come from several sources. One of those sources is the detailed reanalysis of some data that could not be examined as carefully during the crush of events in the early stages of Mount St. Helens activity. For this reason, the results presented here supplement and in places supersede those reported by Malone and others (this volume), which describe the data collection network and the results of preliminary analysis.

The hypocenter data presented here were collected by the combined telemetry and portable recording network. This network was frequently reconfigured as the earthquake sequence progressed (fig. 59). (See Malone and others, this volume, for network description.) During the first few days of the sequence only a regional-station network was available, and thus hypocenters could not be accurately determined. As additional stations were added, the network improved, increasing the accuracy of solutions for earthquakes later in the sequence.

The seismograms for the earthquakes used in this study have been read from plots made from digital data at a scale of about 1 cm/s. Because of the large number of events and the time-consuming task of reading the seismograms, we have restricted the present hypocenter analysis to only those events larger than magnitude 3.2. We hope that in the future we can, with the adoption of more efficient computer-assisted timing routines, process a significant portion of the more than 10,000 earthquakes recorded.

At present, shallow-crustal-structure studies of the region around Mount St. Helens are not complete. Hence earthquake hypocenter locations were calculated first using an earth structure model originally determined to locate earthquakes in the central Puget Sound basin (Crosson, 1972). Although these earthquake locations are considered to be preliminary, we believe that the epicenters will change little compared to the change in computed focal depths. Because the accuracy of an earthquake location largely relies on the station distribution, number of stations operating, earthquake magnitude, and quality of first arrival data, our discussion on earthquake locations is divided into time periods corresponding to changes in the seismic network surrounding Mount St. Helens.

For study of the earthquake time sequence, we used magnitudes and energy-release data from particular stations that were recorded on visual drum recorders (Helicorders). Data from stations SHW (Mount St. Helens), located only 3.5 km from the summit, and CPW (Capitol Peak), located 110 km to the northwest, were used for analyzing the change in earthquake occurrence as well as the rate of seismic-energy release. Magnitudes were calculated from seismograms recorded by a standard Wood-Anderson torsion seismograph located in Seattle, 165 km to the north of the mountain. These magnitudes, as well as those reported by the Newport Observatory (457 km northeast of Mount St. Helens), were used to produce a new coda-duration magnitude scale appropriate for the earthquakes at Mount St. Helens.

EARTHQUAKE CLASSIFICATION

During the course of the 1980 swarm, obvious differences in earthquake signatures were observed on seismic records. In addition to earthquakes with impulsive P- and S-phases, earthquakes with emergent P-phases and indistinguishable S-phases were noticed early during the swarm. These earthquakes are similar to two types of earthquakes described by Minakami (1970, 1974) for earthquakes associated with volcanoes in Japan; with modification, we use a similar classification to describe the earthquake types observed at Mount St. Helens.

HIGH-FREQUENCY OR A-TYPE EARTHQUAKES

In Minakami's classification, A-type earthquakes occur at depths of 1–20 km beneath the volcano. Estimated depths can be inferred by the motions recorded on seismograms. Minakami's sample seismograms show impulsive P- and S-phases and a wide range of frequency components, somewhat similar to those of shallow tectonic earthquakes. However, the

use of a central Puget Sound basin crustal model for hypocenter locations limited A-type earthquake depths to less than 10 km. Although these earthquake seismogram signatures were similar to A-type earthquakes in Japan, sufficient evidence to make a distinction between volcanic and tectonic earthquakes does not exist here, especially as Weaver and others (this volume) showed that Mount St. Helens lies in an offset of a major northwest-striking, right-lateral strike-slip fault. Without refining the shallow crustal model used for the Mount St. Helens area and further studying the earthquake source mechanisms, we find it inappropriate to use Minakami's A-type classification for Mount St. Helens earthquakes. Instead we refer to all such earthquakes as high-frequency events.

LOW-FREQUENCY OR B-TYPE EARTHQUAKES

Unlike A-type earthquakes, B-type earthquakes are limited to shallow depths within or close under the edifice of a volcano. For Japanese volcanoes, magnitudes are small; seismic records are dominated by signals with frequencies that range from 1 to 5 Hz. A primary classification criterion is a shallow hypocenter depth inferred from the records by the absence of a clear S-phase. At Asama volcano in Japan, the frequency of occurrence of B-type earthquakes is found to increase before explosive eruptions.

B-type events were observed prior to the March 27 eruption of Mount St. Helens, and after March 27, B-type earthquakes of large magnitude became dominant on seismic records. In spite of similarities in earthquake signature, B-type earthquakes at Mount St. Helens differed from Minakami's classification in two notable ways: at Mount St. Helens, magnitudes were as high as 4.0, and hypocenter depths approached 2–3 km. Although a revision of the crustal model used for hypocenter location is expected to change maximum depths allowed in calculation of hypocenter, it is not expected to reduce all B-type hypocenters depths to less than 1 km, as Minakami's system would require.

At a distance of 110 km, the Mount St. Helens B-type earthquakes showed extended codas with 2–4 second period phases (fig. 48). As with Minakami's events, their S-phases could not be clearly identified.

Even though Minakami (1970) discusses characteristics of B-type earthquakes in detail, their source mechanics are not well known. Considering what is presently known about earthquake sources, it may be inappropriate to classify earthquakes on the basis of hypocenter location and appearance of seismic records. Therefore, for the purpose of discussions, we will refer to all B-type events as merely low frequency earthquakes.

ERUPTION EVENTS

Eruption events are seismic events that correlate with discrete ash eruptions. The initial seismic phases are emergent, followed by phases that rapidly attenuate with distance from the volcano. Eruption or explosion earthquakes are discussed in detail in Minakami (1970, 1974).

HARMONIC TREMORS

Harmonic tremor is identified as a nearly continuous train of vibrations on a seismic record (Shimozuru and others, 1966; Shimozuru, 1971; Minakami, 1970). A variation of harmonic tremors includes amplitude modulations recorded as a series of sporadic bursts of noise. Kubotera (1974) described in detail the characteristics of four types of harmonic tremors. Harmonic tremors were observed on Mount St. Helens seismic records prior to May 18; however, it was not until later eruptive phases that harmonic tremor became an important predictor.

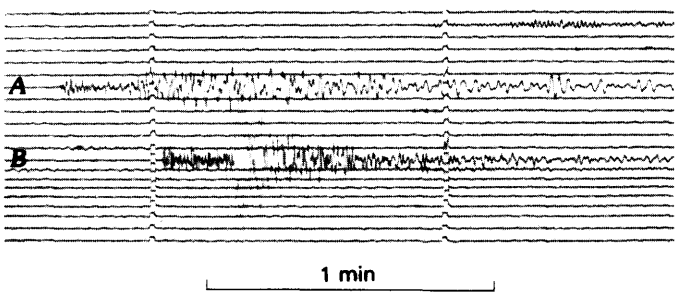

Figure 48.—An example from the Capitol Peak Helicorder record showing two types of earthquakes. First event, typical low-frequency earthquake (A) with a magnitude of 3.4 from Newport Observatory. Second event, typical high-frequency or tectonic-like earthquake (B) with a magnitude of 3.4 from Newport Observatory. Interval between time marks, 1 min.

HISTORICAL WORK

Little seismic work was done at Mount St. Helens before 1980. We are not aware of any record of earthquakes preceding or accompanying the eruptions early in the last century. A catalog of felt earthquakes in Washington (Rasmussen, 1967) lists a number of earthquakes in the early 1900's at Cougar, 18 km southwest of the peak, but there is no way of knowing whether these shocks were related to the volcano.

A microearthquake survey of Mount St. Helens and several other Cascade volcanoes was conducted in 1970 by Unger and Mills (1973). Two types of earthquakes were detected near the peak: one they interpreted to be similar to volcanic B-type earthquakes described by Minakami (1970), and the others they interpreted as more typically tectonic in character. The tectonic earthquakes were located just to the southwest and northeast of the peak at moderate depths of a few kilometers, while the volcanic earthquakes were located high on the cone itself at shallow depths. While Mount St. Helens had a higher earthquake rate than other Cascade volcanoes surveyed, Unger and Mills did not interpret their data to indicate that the mountain was showing signs of volcanic activity.

Additional seismic studies were undertaken at Mount St. Helens in the early 1970's (Weaver and Malone, 1976, 1979). Several field experiments were undertaken to isolate low-frequency, B-type earthquakes. Arrays of portable seismic stations placed around and high up on the mountain revealed the mountain's glaciers as the sources of the low-frequency "earthquakes." These, in reality, were not volcanic earthquakes but vibrations produced as the glaciers slid in jerky movements down the rather steep sides of the mountain. The low-frequency emergent character of these events was due to a propagation effect resulting in attenuation of high frequencies. The recordings of true volcanic earthquakes during the past year reaffirms this glacial interpretation of the earlier observations.

MAGNITUDES

THE MAGNITUDE PROBLEM

The lack of complete seismic records (in particular Wood-Anderson torsion seismograph records) of earthquakes from Mount St. Helens between March 20 and May 18 presented difficulties in generating a data set of earthquakes with uniform magnitudes. An additional problem detected early in the earthquake swarm was an inconsistency between Wood-Anderson magnitudes and coda-duration magnitudes. This inconsistency was determined by the University of Washington using a coda-duration magnitude scale developed for western Washington (Crosson, 1972). Coda-duration magnitudes were found to be several tenths to a full magnitude unit greater than Wood-Anderson magnitudes. This problem was confirmed by coda duration versus Newport magnitude plots developed with a list of Wood-Anderson magnitudes from the Newport Observatory and coda-duration magnitudes from the University of Washington film records. These plots indicated inflated coda-duration magnitudes and reflected incorrect use for volcanic earthquakes of the coda duration-magnitude relation originally developed for the earthquakes in the central Puget Sound basin. Other problems pointed out by these plots were a wide range in coda lengths for specific magnitudes and an absence of earthquakes assigned magnitudes between 4.0 and 4.5 (fig. 49).

In September-October 1980 we conducted a coda duration-magnitude study to fill gaps in the Wood-Anderson magnitudes reported by both the University of Washington and the Newport Observatory. As a first step in this study, station corrections were determined for Newport Observatory and University of Washington Wood-Anderson magnitudes. A comparison of amplitude magnitudes from these two sources resulted in a maximum difference of 0.3 magnitude unit, a reasonable figure considering the differences in distance, azimuth, and geologic structure between these two seismograph stations and Mount St. Helens.

With the corrected Wood-Anderson amplitude magnitudes, we then developed new coda duration-magnitude relations for Mount St. Helens earthquakes. Of the 2,385 earthquakes, with preliminary magnitudes 2.4 or greater, approximately 10–15 percent lacked amplitude information and were subsequently assigned coda-duration magnitudes. All events were assumed to have occurred beneath the edifice of Mount St. Helens. (This assumption is consistent with preliminary hypocenter locations.) Characteristic earthquake signatures of Mount St. Helens earthquakes permitted confident culling of

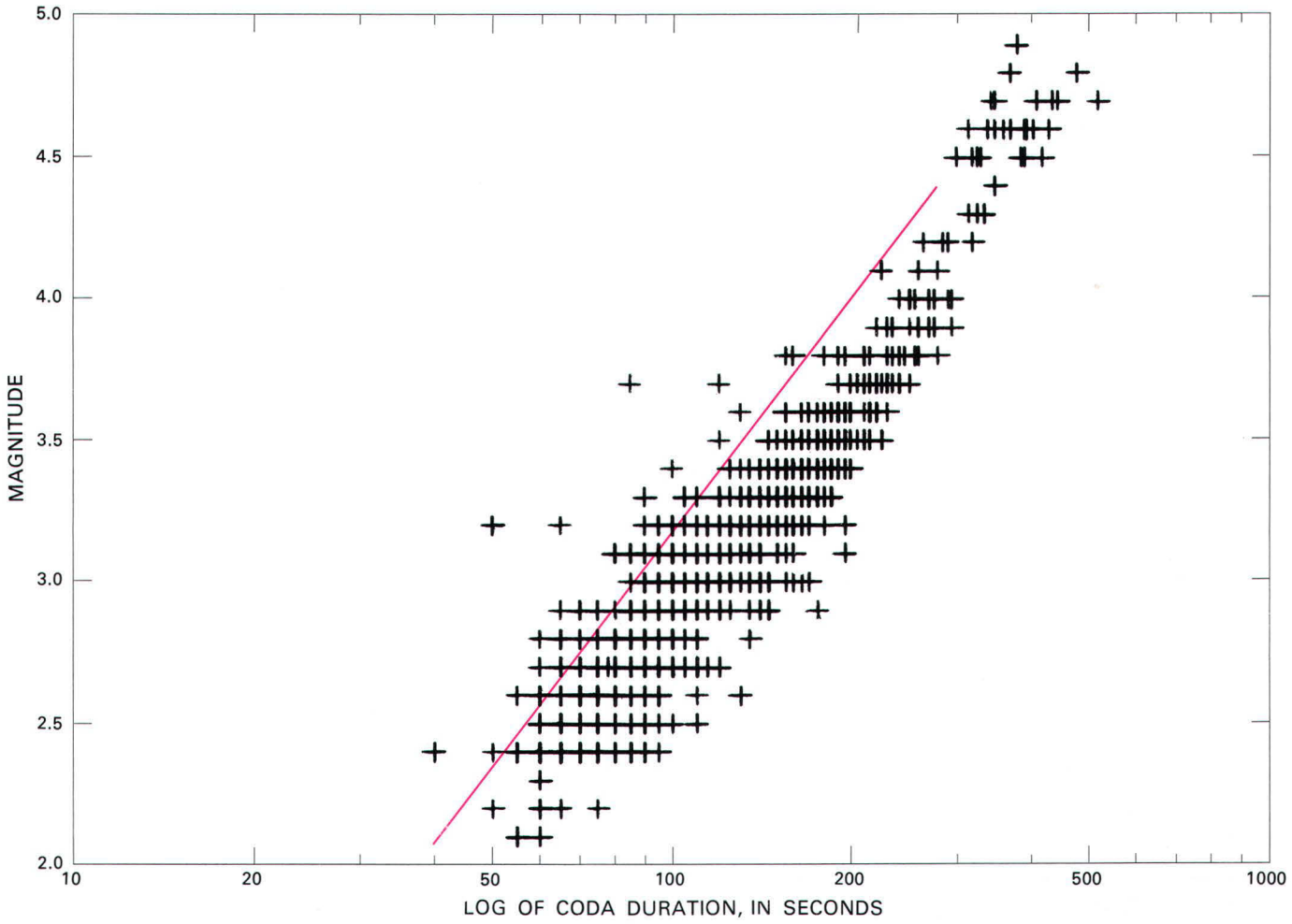

Figure 49.—Coda duration (using a film average) versus magnitude (from Newport Observatory) of Mount St. Helens earthquakes. Coda duration-magnitude relation (red line) developed by Crosson (1972) based on central Puget Sound basin results in larger, incorrect magnitude for earthquakes that fall to right of red line and smaller, incorrect magnitudes for events to left.

non-Mount St. Helens earthquakes from the data set. Coda-duration magnitudes also provided cross check on amplitude magnitudes.

CODA-DURATION MAGNITUDES

Our coda-duration studies, which used CPW (Capitol Peak) Helicorder records, showed significant differences for earthquakes of identical Wood-Anderson magnitudes. For these studies, events were subjectively classified as high- or low-frequency earthquakes. Duration measurements at CPW for two Mount St. Helens earthquakes of magnitude 3.4 (as measured by Newport) showed a 50–55 s greater coda duration for a low-frequency event than for a high-frequency event of comparable magnitude as measured by Newport (fig. 48). Duration was measured from the onset of the P-phase to a point where the amplitude of the coda drops down to background noise level for more than 10 s. Other events with identical magnitudes as measured at Newport showed similar discrepancies, resulting in the development of the previously described separate coda duration-magnitude relations for high- and low-frequency earthquakes (figs. 50, 51).

No short-period, high-gain seismograph station produced continuous records throughout the 2-mo period preceding the Mount St. Helens eruption on May 18. Thus, CPW (Capitol Peak), LVP (Lake View Peak), and COW (Cowlitz) Helicorder records were used to develop independent low- and high-frequency

coda duration-magnitude relations for each station. In the absence of amplitude-magnitude data, the available coda information was used, assigning earthquakes the average of CPW, LVP, and COW coda-duration magnitudes. High- and low-frequency coda duration-magnitude relations were also determined for average coda (as defined by Crosson, 1972) measured during routine processing of film records from western Washington stations. Significant scatter was noted in the average coda read from these film records. Events were assigned film average coda-duration magnitude only as a final measure; the coda study resulted in eight independent coda duration-magnitude relations: four high-frequency and four low-frequency relations for CPW, LVP, COW, and Develocorder-film coda. The study used 404 high-frequency earthquakes and 1,599 low-frequency events. Approximately 385 earthquakes were not classified. These events occurred during late March when Helicorder records were not available for CPW.

EARTHQUAKE COUNTS AND LOCATIONS

JANUARY 1975–MARCH 1980

Prior to the onset of the earthquake swarm on March 20, few events had been located near Mount St. Helens. From 1975 to early 1980, 44 events were successfully located within 35 km of the volcano

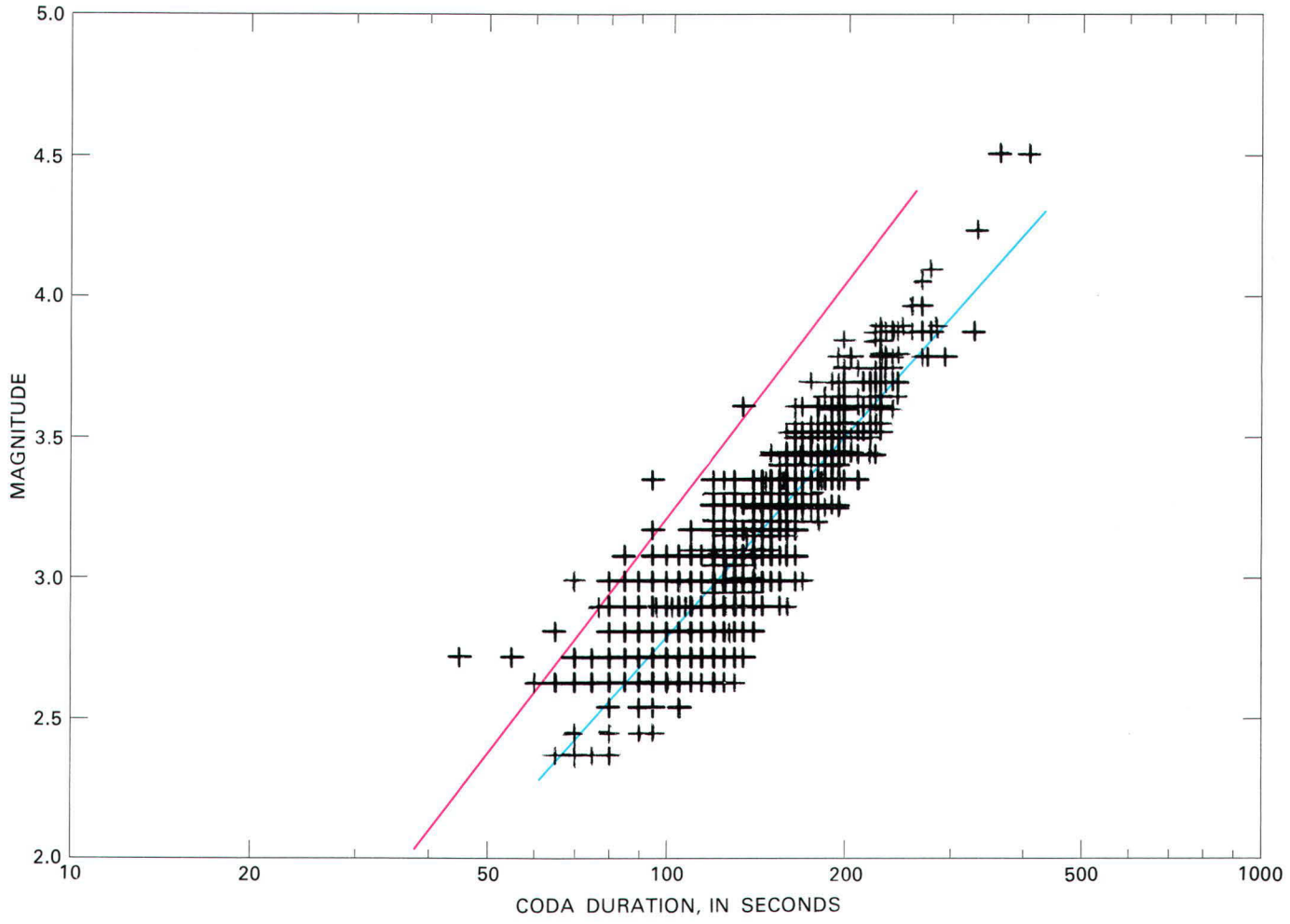

Figure 50.—Coda duration versus average amplitude magnitude of low-frequency Mount St. Helens earthquakes, using CPW Helicorder data. Red line, Crosson's (1972) central Puget Sound basin coda duration-magnitude relation; blue line, new coda duration-magnitude relation.

(fig. 52). An acceptable earthquake for plotting location met the following criteria: it was recorded on five or more stations, it had a preliminary coda-duration magnitude greater than 1.4, and SHW was one of the stations with data used for the location. The selection criteria, nevertheless, did not compensate for the poor distribution and small number of seismic stations existing in western Washington during this time. However, pre-March seismicity simply did not indicate a potential major eruption.

MARCH 16–MAY 18, 1980

Counts of earthquakes (fig. 53*A*) that occurred as early as March 16 showed a small increase in the number of earthquakes local to Mount St. Helens (detected on SHW, the only short-period high-gain seismic station located within 50 km of Mount St. Helens). Considering the possibility of loggers blasting for road contruction, however, this could have been considered normal. From several small events per day, the daily count went up to 13/day on March 16. On March 17, 18, and 19 the daily count was up to 34/day. Any doubts of the reality of increased seismicity were abruptly removed by a magnitude-4.2 earthquake located approximately 4 km beneath Mount St. Helens on March 20. This event was followed by a moderate number of low-magnitude, tectonic-like earthquakes. By March 23, Sunday morning, it was clear that the earthquake rate was not consistent with an aftershock sequence: rather than a decline in the number of events per hour (fig. 53*B*) detected by SHW, there had been

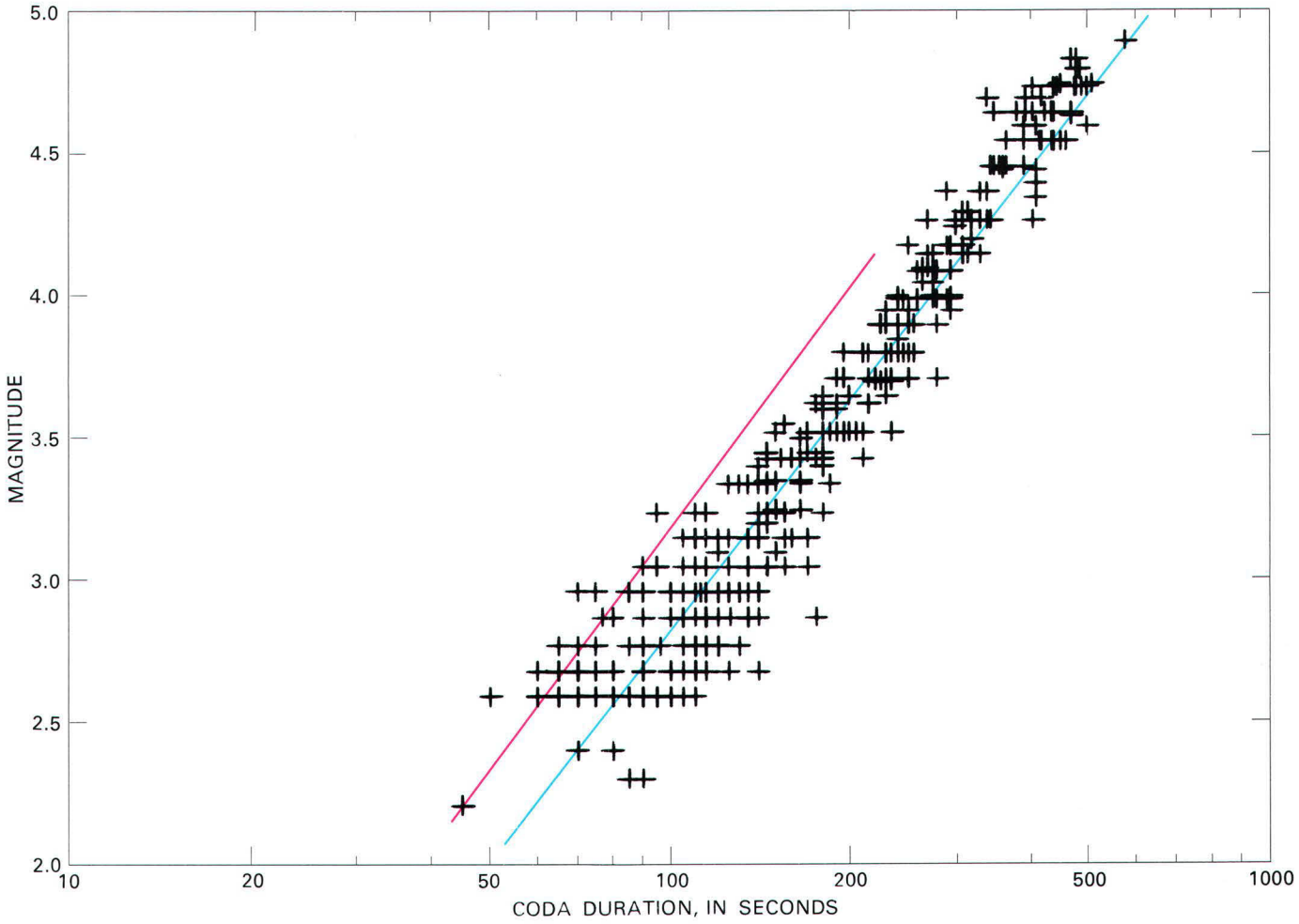

Figure 51.—Coda duration versus average amplitude magnitude for high-frequency Mount St. Helens earthquakes using CPW Helicorder data. Red line, Crosson's (1972) coda duration-magnitude relation; blue line, new coda duration-magnitude relation.

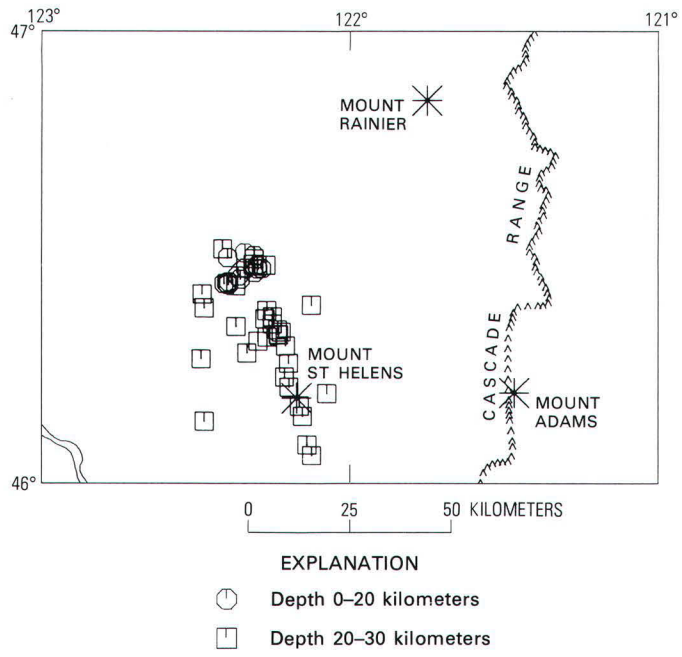

Figure 52.—Epicenter plot of earthquakes from 1975 to March 1980, within a 40 × 100-km area around Mount St. Helens. Most earthquakes were less than coda-duration magnitude 2.0.

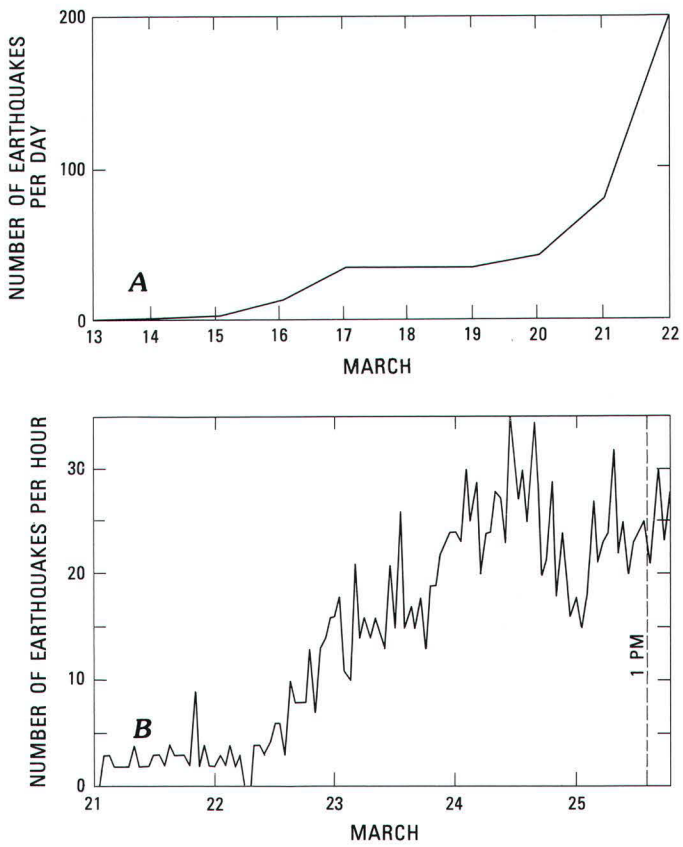

Figure 53.—Counts of earthquakes from SHW records in universal time. A, Daily counts from March 13 to 21, 1980. Most events were of insufficient magnitude to be detected by next nearest seismic station, 50 km from the volcano. B, Hourly counts from March 21 to midday on March 25, at which time individual events could no longer be recognized on Helicorder records.

an increase from several earthquakes per hour to an average of over 15/hr. With the exception of a few events, most earthquakes were small in magnitude (less than 2.0). Fewer than 2 percent of the detected events were being recorded on three or more stations of the western Washington regional seismic network.

By March 24, the hourly count exceeded 20/hr, and corresponding with the increased rate of occurrence was an increase in the average event magnitude. On Monday, March 24, a second earthquake exceeding magnitude 4.0 was located at shallow depth beneath the mountain. At approximately noon on March 25, a large number of events saturated the record of the SHW drum recorder. This increased seismicity coincided with a 10-fold increase in average background noise levels of the high-gain channels of the portable seismograph systems.

From March 20 to 1100 PST on March 25, there had been 10 earthquakes of magnitude 2.6 or greater. In contrast, 174 earthquakes with magnitudes greater than 2.6 were recorded in the 2 days preceding the first ash eruption on March 27. Earthquake counts after March 27 are presented in figure 54, along with seismic-energy release data confirming an increase in larger magnitude events.

EARTHQUAKE ENERGY

At this point in the analysis of swarm data from Mount St. Helens, an appropriate magnitude-energy relation has not been determined. Arbitrarily, Richter's relationship for local magnitudes was used (Richter, 1958).

$$\log E = 9.9 + 1.9M - 0.02M^2,$$

where M is local magnitude and E is energy in ergs.

The results presented in figure 54 indicate only relative temporal changes, and should not be regarded as absolute figures for seismic-energy release. In spite of the high earthquake counts leading up to March 27, the daily seismic-energy release was lower during this period than on all days after March 30. A

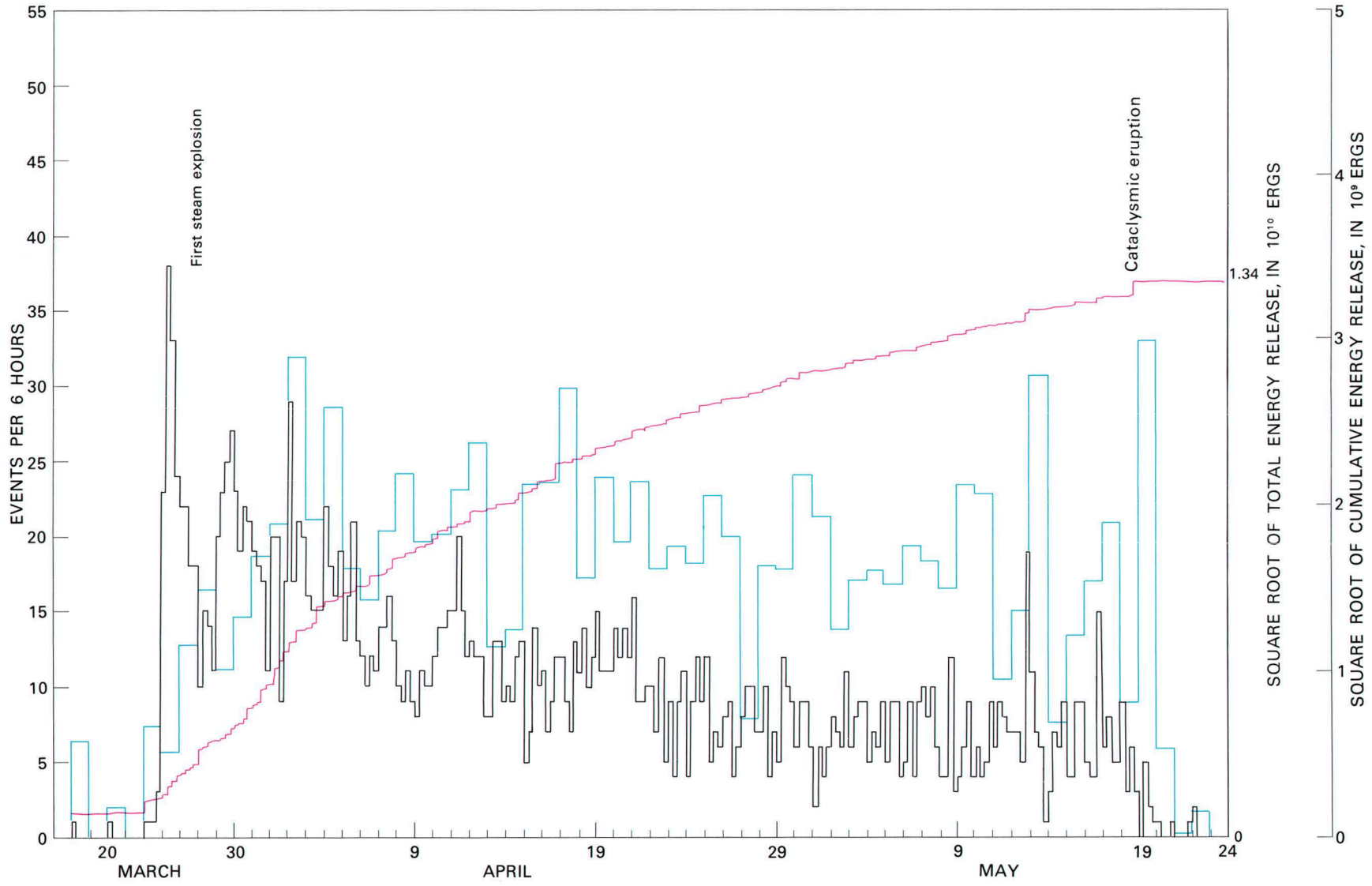

Figure 54.—Counts of earthquakes larger than magnitude 2.5 (black line), daily earthquake energy release (blue line), and square root of cumulative energy release (red line) from March 20 to May 24, 1980, UTC. The plot emphasizes significant increase in large-magnitude earthquakes after first eruption on March 27, as indicated by increase of energy release. Square root of total energy release, as of May 24, was 1.34×10^{10} ergs.

significant increase in daily energy release occurred after the first eruptive phase on March 27. After March 30 the daily energy release appeared to remain the same, reflecting the dual parameters of gradual decrease in total number of earthquakes per day and sustained number of larger magnitude earthquakes per day. Preliminary total seismic-energy-release calculations indicate a lower limit of 1.8×10^{20} ergs for the entire swarm up to May 18.

A cumulative square root of energy release plot (Gorshkov and Dubik, 1970; Tokarev, 1963, 1967, 1971) (fig. 54) shows a gradual decrease after a substantial increase in early April. No obvious changes are shown in the days just prior to the May 18 eruption. The shapes of temporal distributions for earthquake counts and energy release are similar to these on a plot presented by Gorshkov (1959) for the eruption of Bezymianny volcano in Kamchatka.

SPATIAL DISTRIBUTION OF HYPOCENTERS

Approximately 700 earthquakes were selected for analysis for the period March 20 to May 18. Initially, selected larger magnitude earthquakes were being located on a daily basis. By the first week of April, a magnitude-3.2 cutoff was required to reduce the daily analysis effort to a reasonable load. In spite of the larger magnitudes, arrivals frequently were emergent, further complicating the analysis effort. No distinction has been made between earthquake types for hypocenter plotting (figs. 55, 56, 57).

MARCH 20–26

From March 20 to March 26, 74 events were located. Selection of epicenters plotted in figure 55 was made based on the 3.2 magnitude cutoff and small location errors. This map shows 49 scattered epicenters on the north flank of Mount St. Helens. The scatter is believed to be primarily a result of poor seismic-station distribution.

MARCH 27–MAY 18

Utilizing identical selection criteria, 436 events were selected for plotting (from a total of 621 located during this later time period). Their epicenters form a tight 3-km diameter cluster approximately coincident with what was a region of intense surface deformation (fig. 56; Christiansen, 1980).

When a revised velocity structure is used for hypocenter calculations, a significant change is expected in earthquake focal depths. Because a new velocity model may well be developed, the cross-section hypocenter plot presented in figure 57 should be considered preliminary. In this plot, earthquake foci extend from less than 1 km to 6 km beneath the north flank of Mount St. Helens. (A small number of low-magnitude events that were located at depths approaching 10 km are not plotted.) Preliminary tests of a new crustal model based on recent refraction studies using explosion data, however, suggest that the average hypocenter depth was less than indicated here (fig. 57). Rather, it suggests that all were confined to a small volume at less than 2.5 km depth. Note that in the cross-section view showing a northwest-southeast depth profile, the earthquakes lie in an elliptical region beneath what was a region of intense surface deformation. These earthquakes probably represent rock fracturing due to magmatic pressures from below. As magma moved up into the region below the volcano, it displaced material above it, both upward and outward. The strong deformation appearing as a surface bulge and the earthquakes below it were expressions of this movement.

MAGNITUDE-FREQUENCY DISTRIBUTION

Richter (1958) noted a simple magnitude-frequency distribution for worldwide earthquakes. This distribution is

$$\log N = A - bM$$

where N is the number of shocks of magnitude M or greater. Values of b from 0.6 to 1.5 are commonly identified with tectonic seismicity and higher values with that of volcanic regions (Minakami, 1974).

A preliminary magnitude-frequency plot of Mount St. Helens earthquakes could not be interpreted because irregularities in the plot precluded estimation of a b-value. Subsequent and separate plots of magnitude-frequency distributions for low- and high-frequency earthquakes produced surprisingly regular

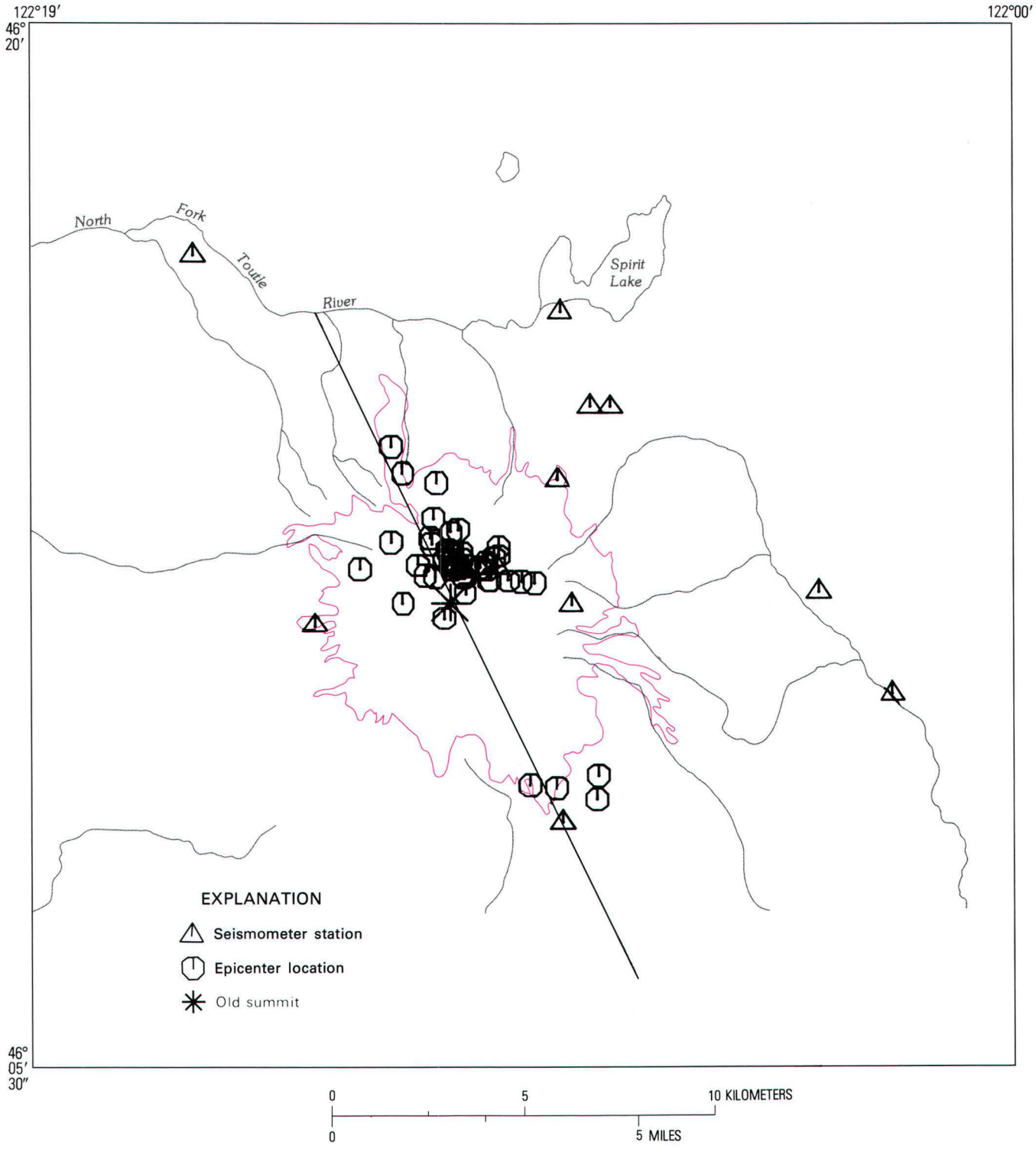

Figure 55.—Epicenters of earthquakes occurring from March 20 to 26, 1980. Red line, 4,000-ft topographic contour and approximate timberline. Scatter in epicenter locations is a result of poor seismic station coverage early in the earthquake sequence. Triangles, seismometer stations; northwest-southeast line is the projection plane for figure 57.

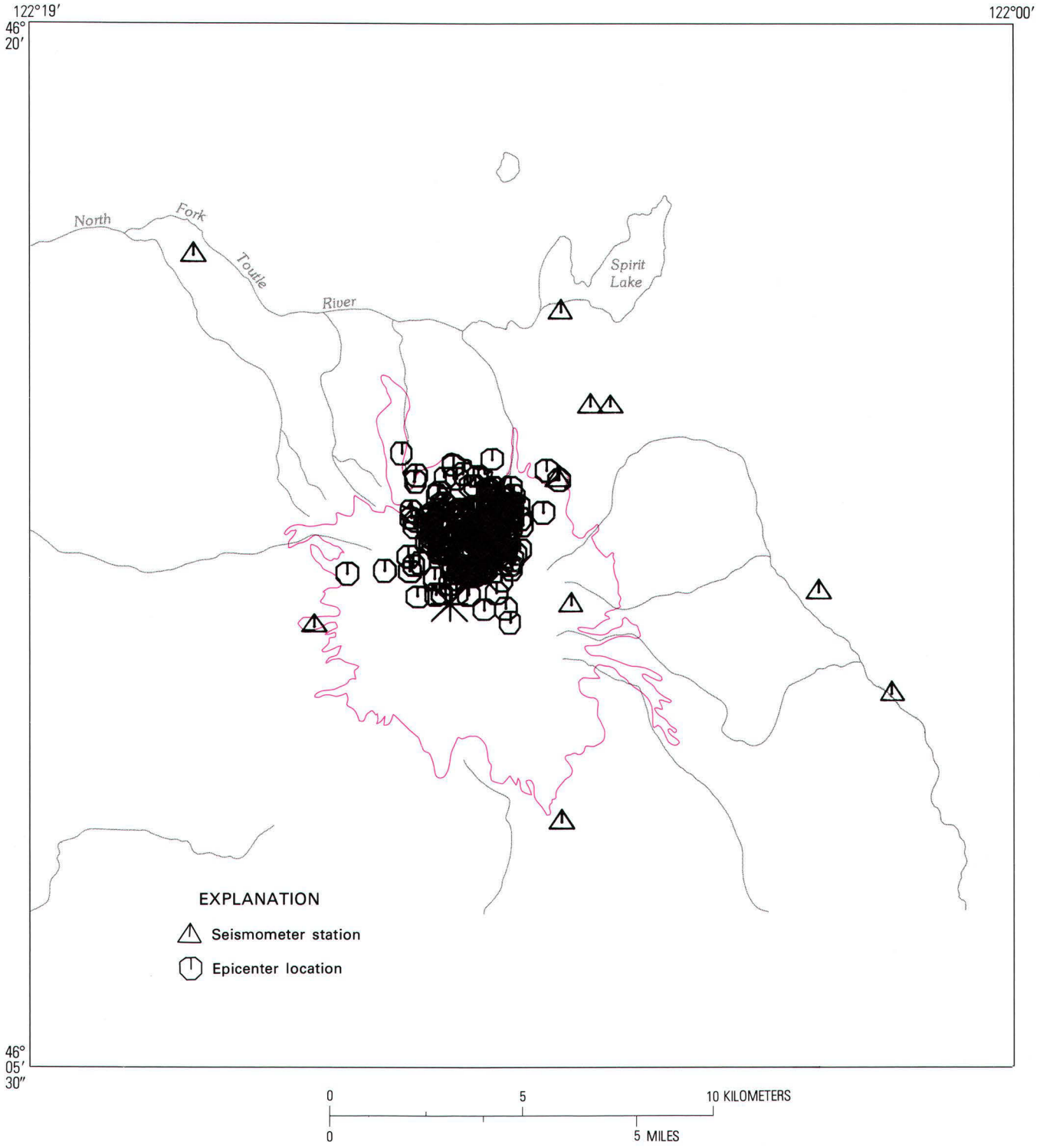

Figure 56.—Epicenters of earthquakes occurring from March 27 to May 18. Improved station distribution during this period resulted in better locations, approximately coincident with region of intense surface deformation prior to May 18. Red line, 4,000-ft topographic contour and approximate timberline.

plots with *b*-values that could be interpreted (fig. 58). A *b*-value of 2.8 for low-frequency earthquakes appears to be consistent with reported values for volcanic earthquakes (Shimozuru, 1971). The 0.6 value determined for high-frequency events agrees with values reported for tectonic earthquake sequences (Utsu, 1971). Mogi's experimental works (Mogi, 1962a, 1962b; 1963) suggest the *b*-value as an indicator of mechanical structure within the source region of earthquakes, provided that the earthquakes are a result of fracture or fracture-like phenomena. The effect of applied-stress conditions was also studied by Mogi. Mogi interpreted a high *b*-value to be caused by extreme heterogeneity in structure and high stress concentration. In contrast, low *b*-values, such as our 0.6 figure, indicate moderate heterogeneity and a uniform stress field.

SUMMARY OF IMPORTANT SEISMIC EVENTS

The major seismic events at Mount St. Helens were:

1. A gradual increase in daily earthquake counts from March 15 to March 20, 1980.
2. The first magnitude-4.2 earthquake, located at shallow depth beneath Mount St. Helens, 1547 PST on March 20.
3. An increase in hourly counts primarily of low-magnitude tectonic-like earthquakes starting March 21.
4. Numerous earthquakes saturating the SHW seismograph record at approximately noon on March 25.
5. Earthquake counts peak on March 27, the day of the first observed eruption activity.
6. Gradual decrease in earthquake counts after March 27, accompanied by an increasing number of larger magnitude earthquakes.
7. Swarm following first eruption, dominated by shallow large-magnitude events with emergent P-phases and lacking clear S-phases. High-frequency components of seismic signals consistently attenuated at more distant seismic stations.
8. Largest magnitude earthquake, 5.1, occurring on May 18 at 0832 PDT; preliminary location lat 46°12′55″ N., long 122°11′72″ W., and hypocenter depth 1.5 km.

The earthquake parameters presented thus far represent preliminary results of analysis of a subset of

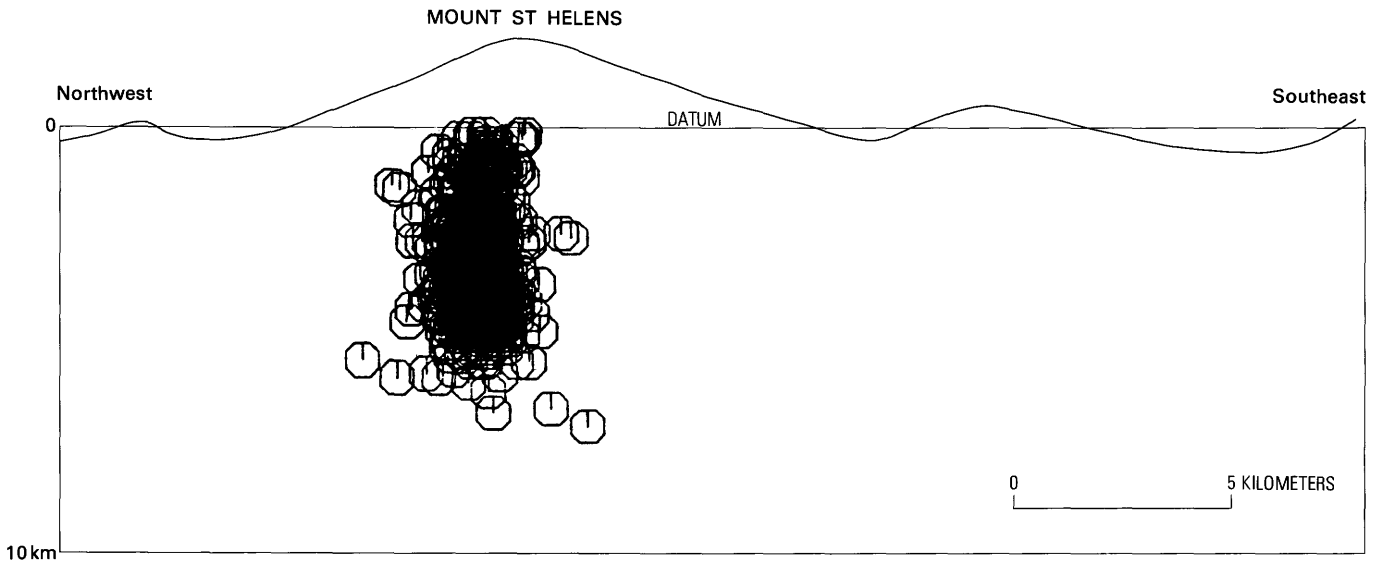

Figure 57.—A cross-section view, from the southwest, of earthquake hypocenters. Hypocenters form an ellipsoidal pattern directly beneath region of major deformation. Tests of crustal model derived from refraction studies indicate earthquakes were generally restricted to a zone less than 2.5 km deep. Datum is average elevation of the seismic stations (approximately 3,000 ft).

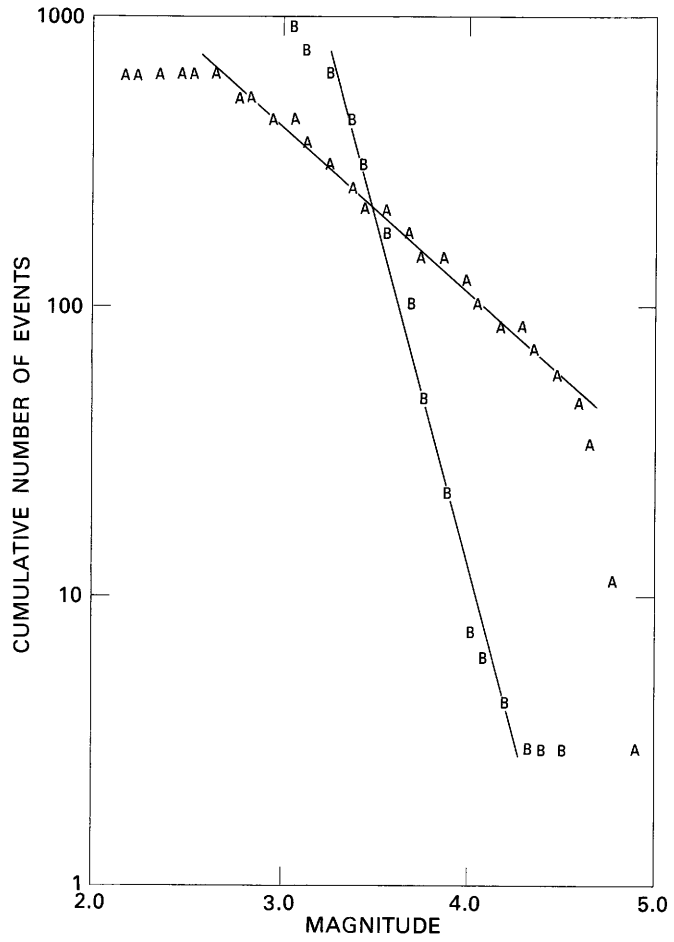

Figure 58.—Frequency-magnitude relations for high-frequency (A) and low-frequency (B) earthquakes. Regression lines fit to selected portions of the data produce b-values of 2.77 and 0.6 for low- and high-frequency events, respectively. The correlation coefficients (r^2) are 98.8 for low-frequency earthquakes and 99.8 for high-frequency earthquakes. Errors in classifying earthquakes are suggested by scatter on the low-frequency plot at magnitudes 4.3 and greater.

the Mount St. Helens seismic data. Numerous investigators, particularly in Japan and Russia, have documented earthquake swarm activity associated with volcanism, and similarities in seismic swarms preceding major eruptions have been noted in available literature. A detailed comparison between earthquake swarm characteristics cannot be made, however, until analysis is completed and data presented in a form that makes direct comparisons feasible. We hope that rather than developing only simple empirical seismic/volcanism relationships, a thorough analysis of the Mount St. Helens seismic data will provide a better understanding of the physics of volcanic activity and magma transport.

REFERENCES CITED

Christiansen, R. L., 1980, Eruption of Mount St. Helens—Volcanology: Nature, v. 285, p. 531–533.

Crosson, R. S., 1972, Small earthquakes, structure, and tectonics of the Puget Sound region: Seismological Society of America Bulletin, v. 62, p. 1133–1171.

Gorshkov, G. S., 1959, Gigantic eruption of the Bezymianny Volcano: Bulletin of Volcanology, v. 20, p. 77–112.

Gorshkov, G. S., and Dubik, Y. M., 1970, Gigantic directed blast at Shiveluch volcano (Kamchatka): Bulletin of Volcanology, v. 34, p. 261–288.

Kubotera, A., 1974, Volcanic tremors at Aso volcano, *in* Civetta, L., Gasparini, P., Luongo, G., and Rapolla, A., eds., Physical Volcanology: Amsterdam, Elsevier p. 29–48.

Minakami, T., 1974, Seismology of volcanoes in Japan, *in* Civetta, L., Gasparini, P., Luongo, G., and Rapolla, A., eds., Physical Volcanology: Amsterdam, Elsevier, p. 1–27.

Minakami, T., Utibori, S., Hiraga, S., Miyazaki, T., Gyoda, N., and Utsunomiya, T., 1970, Seismometrical studies of volcano Asama, pt 1: Earthquake Researh Institute Bulletin, Tokyo University, v. 48, p. 235–301.

Mogi, K., 1962a, Study of elastic shock caused by the fracture of heterogenous materials and its relations to earthquake phenomena: Earthquake Research Institute Bulletin, Tokyo University, v. 40, p. 125–173.

_____1962b, Magnitude-frequency relation for elastic shock accompanying fractures of various materials and some related problems in earthquakes: Earthquake Research Institute Bulletin, Tokyo University, v. 40, p. 831–853.

_____1963, The fracture of a semi-infinite body caused by an inner stress origin and its relation to the earthquake phenomena: Earthquake Research Institute Bulletin, Tokyo University, v. 41, p. 596–614.

Rasmussen, N., 1967, Washington State earthquakes 1840–1965: Seismological Society of America Bulletin, v. 67, p. 463–476.

Richter, C. F., 1958, Elementary Seismology: San Francisco, W. H. Freeman and Co., p. 768.

Shimozuru, D., Kamo, K., and Kinoshita, W. T., 1966, Volcanic tremor of Kilauea volcano, Hawaii, during July-December, 1963: Earthquake Research Institute Bulletin, Tokyo University, v. 44, p. 1093–1133.

Shimozuru, D., 1971, Seismological approach to the prediction of volcanic eruptions, *in* The Surveillance and Prediction of Volcanic Activity: Paris, France, United Nations Educational, Scientific, and Cultural Organization, p. 19–45.

Tokarev, P. I., 1963, On a possibility of forecasting of Bezymianny volcano eruptions according to seismic data: Bulletin of Volcanology, v. 26, p. 379–386.

_____1967, The gigantic eruption of the Sheveluch volcano on November 12, 1964, and its forerunners: Earth Physics, no. 9, p. 11–22.

_____1971, Forecasting volcanic eruptions from seismic data: Bulletin of Volcanology, v. 35, p. 243–250.

Unger, J. D., and Mills, K. F., 1973, Microearthquakes near Mt. St. Helens, Washington: Geological Society of America, v. 60, p. 1065–1068.

Utsu, T., 1971, Aftershock and earthquake statistics (III): Japan, Journal of the Faculty of Science, Hokkaido University, ser. 7, Geophysics, v. 3, p. 379–411.

Weaver, C. S., and Malone, S. D., 1976, Mount St. Helens seismic events: volcanic earthquakes or glacial noises?: Geophysical Letters, v.3, p. 197–200.

_____1979, Seismic evidence for discrete glacier motion at the rock-ice interface: Journal of Glaciology, v. 23, p. 171–184.

THE 1980 ERUPTIONS OF MOUNT ST. HELENS, WASHINGTON

POST-MAY 18 SEISMICITY: VOLCANIC AND TECTONIC IMPLICATIONS

By CRAIG S. WEAVER, WENDY C. GRANT, STEPHEN D. MALONE[1], *and* ELLIOT T. ENDO

ABSTRACT

Seismicity following the May 18, 1980, eruption of Mount St. Helens has had a markedly different spatial distribution than that occurring before the eruption. Whereas before the May 18 eruption the earthquakes were clustered in a small volume in the shallow crust, after the eruption they occurred beneath the volcano to depths of 20 km, and within 2 weeks earthquakes were occurring in two distinct zones, one north and one south of the volcano. The zone north of Mount St. Helens is 35 km long, and the largest earthquake since the eruption (M_L = 4.2) was located in this zone. Focal mechanisms are right-lateral strike-slip, with north-south fault planes. The second zone is south-southeast of the cone and is 20 km long. Focal mechanisms show right-lateral strike-slip faulting with fault planes striking N. 25° W.

Under Mount St. Helens, seismicity defined a northeast-striking fault located 1 km northwest of the lava dome that was emplaced after June 12. Earthquake fault-plane solutions beneath the mountain showed strike-slip and thrust faulting. Mount St. Helens is in a horizontal compressional tectonic environment, and by adopting the model for plate motions suggested by Rogers (1979), there is good agreement between the compressional axis predicted by plate tectonics and that determined from the fault-plane solutions.

INTRODUCTION

Marked changes in the seismicity in the Mount St. Helens region occurred after the May 18, 1980, eruption. The seismic sequence that started on March 20 (and produced a combined total seismic energy equivalent to a minimum of a magnitude-6.0 earthquake) was confined to a small volume in the shallow crust directly beneath the north side of the volcano (Endo and others, this volume). In marked contrast, earthquakes after the May 18 eruption occurred beneath the volcano at depths down to 20 km, and within several weeks following that eruption, earthquakes were occurring at distances 35 km north and 20 km south of Mount St. Helens.

The dramatic change in the seismicity following the May 18 eruption thus forms a natural break point in any discussion of earthquakes at Mount St. Helens. An analysis of the seismicity data, with the exception of the 10 days immediately following the May 18 eruption, is virtually complete through August 31. Consequently, the post-May 18 data allow a more detailed discussion of the tectonic and volcanic implications of the seismicity than is appropriate for the pre-May 18 earthquakes. One important result of the analysis in this report is to clearly establish that Mount St. Helens is situated in a zone of horizontal compressional stress, consistent with existing plate-tectonic models (Riddihough and Hyndman, 1976; Riddihough, 1977; Rogers, 1979).

Compressional stress dominates the post-May 18 seismicity with the deeper (>5 km) earthquakes having thrust and strike-slip focal mechanisms. An understanding of the regional stresses surrounding the mountain lays a foundation for the specialized geological and geophysical studies of the volcano.

[1]Geophysics Program AK-50, University of Washington, Seattle, WA 98195.

ACKNOWLEDGMENTS

H. M. Iyer made numerous helpful suggestions for this report. The effort Bruce Julian made to clarify several sections is gratefully acknowledged. John Coakley and Jim Ramey worked long hours in difficult field conditions on the seismic network around Mount St. Helens.

SEISMIC DATA AND ANALYSIS

The seismic network used for the collection of the data consisted of a mixture of permanent telemetered stations and some temporary stations. The permanent network was completed on July 2 and, with the exception of occasional station failure, has not been changed since. Six temporary stations were utilized for varying lengths of time between May 28 and July 10, when all portable stations were removed. At three sites occupied by portable recorders prior to May 18, operation resumed when conditions allowed entry to the area (Stations APE, SFT, and CDF; fig. 59). The instrument at MUD was buried by a mudflow, but was retrieved, cleaned, and reinstalled on higher terrain at MDR, 1.5 km north of the original site. A station, MIC, was installed above Miners Creek to improve focal depth resolution for a swarm of earthquakes northwest of Spirit Lake, and another station, SCB, was operated for 8 days on Smith Creek Butte in an attempt to find an additional permanent station site east of Mount St. Helens. Stations operating after May 18 are as follows:

[Present, as of Dec. 31, 1980]

Station	Lat N.	Long W.	Elevation (km)	Date	
	Deg Min S	Deg Min S		On	Off
JUN	46 08 48	122 09 11	1.05	March 25	- Present
COW	46 29 28	122 00 44	.31	March 27	- Present
MTM	46 01 32	122 12 42	1.12	March 29	- Present
ELK	46 18 20	122 20 27	1.27	May 23	- Present
SBL	46 20 25	122 02 20	1.67	June 20	- Present
CDF	46 06 58	122 02 51	.78	March 30	- May 19
				May 28	- Present
APE	46 05 58	122 12 27	.58	March 21	- May 20
				May 28	- July 10
LVP	46 04 06	122 24 30	1.17	April 2	- Present
SFT	46 12 42	122 21 23	.78	March 29	- May 19
				May 28	- July 10
MIC	46 22 37	122 12 46	.97	May 30	- June 10
MDR	46 12 01	122 03 57	.76	May 29	- June 30
MUD	46 10 36	122 02 27	.49	March 24	- May 18
SCB	46 12 30	122 03 14	1.12	July 2	- July 10
EDM	46 11 50	122 09 00	1.61	June 30	- Present
SHW	46 11 33	122 14 12	1.42	Oct. 25, 1972	-Present

Data from the permanent network stations are recorded digitally at the University of Washington on a Digital Equipment Corporation PDP-11/34 (DEC 11/34) computer system. For events in May, selected seismograms were recorded visibly and P-arrivals read by hand. Events in June, July, and August were analyzed from digital data using an interactive picking and location routine and a graphics display terminal. Coda lengths for small events (magnitudes less than about 2.0) were measured using the interactive routine; for larger magnitude events and all May events, they were measured using Develocorder film records. Timing of the portable station data was done by manually reading analog playouts of digitized events.

The seismic events were located with a modified version of the computer program HYPO79 (W. H. K. Lee, unpub. program, 1979) on the University of Washington's DEC 11/70 computer system. A layered crustal model based on preliminary refraction studies was used in the location program. The seismic velocities in the upper 8 km of the crust, 4.8, 5.0, 6.0 and 6.4 km/s, were determined using traveltime data from blasts at a strip mine 80 km northwest of Mount St. Helens. The velocities of lower crustal layers were taken from the Puget Sound velocity model determined by Crosson (1976), which he derived from inversion studies of western Washington earthquakes. The velocity model for the upper layers, down to 10 km, is similar to that found in a detailed refraction experiment in the Mount Hood, Oreg., area (Kohler and others, 1981).

In all, a total of 558 earthquakes was located in the Mount St. Helens area in this study. To date, 110 earthquakes have been located that occurred in May following the eruption, 144 in June, 185 in July, and 119 in August. The results for May reflect a preliminary analysis of the data and do not include all events for this period. Most of the larger magnitude earthquakes have been located for May, although there may still be some earthquakes undetected in the records containing extensive harmonic tremor sequences (Malone and others, this volume); these will be located when the data from more distant stations are analyzed. Some of the smaller events in May were chosen to give a representative sample of the earthquake swarms that followed the May 18 and May 25 eruptions. The data set for June, July, and August is complete and only minor modifications are anticipated.

MAGNITUDES

Magnitudes for the earthquakes after May 18 have been calculated using the coda-duration-magnitude scale developed for western Washington (Crosson, 1972). In many cases, the events occurring after May 18 are spatially removed from the cone and are not volcanic earthquakes. For purposes of consistency, the same coda-duration-magnitude scale is used in comparing past and current activity.

The largest earthquake after May 18 was magnitude 4.2, and was part of a swarm of earthquakes north of the volcano. Since June 1, only four earthquakes greater than magnitude 3.0 have occurred, and none was located beneath the volcano. The distribution of magnitudes is shown in figure 60*A*: the discrete and uneven nature of the data for small magnitudes is a result of not locating all the small events, and a result of measuring coda durations to the nearest second.

The slope of the magnitude-frequency plot (fig. 60*B*) for the entire data set is 0.67 ± 0.01. A standard regression analysis was performed on earthquakes between magnitudes 1.2 and 3.6. Whereas the total data set contains earthquakes both from beneath the volcano and from the surrounding region, the data were not separated according to location for this analysis. The larger ($M_{coda} > 3$) earthquakes in this period beneath Mount St. Helens were all below 5 km, at depths comparable to depths of the larger events for the entire region. Furthermore, the event waveforms are characteristic of tectonic earthquakes. Low-frequency volcanic earthquakes that occurred on July 22 prior to the eruption on that day are all

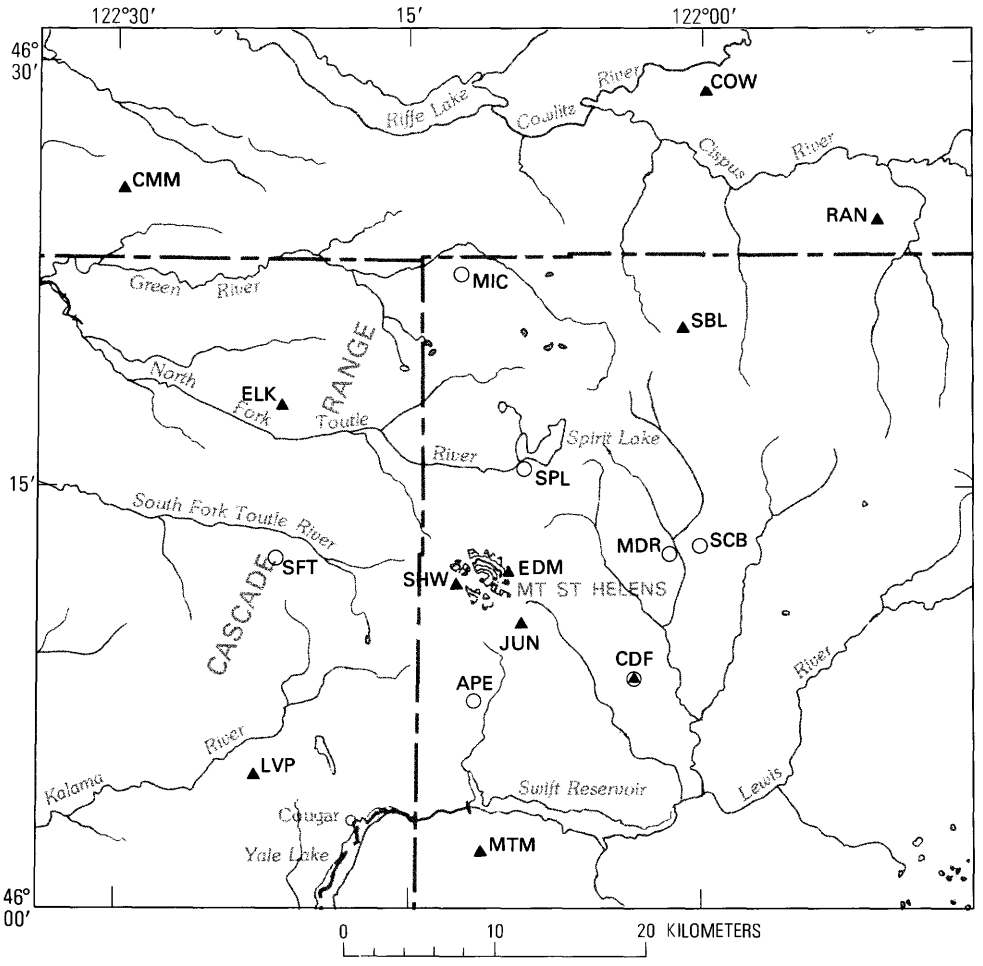

Figure 59.—Map showing all seismic stations in the Mount St. Helens network, with station codes. Triangles, telemetered stations; circles, portable tape-recorder stations; solid symbols, stations still operating.

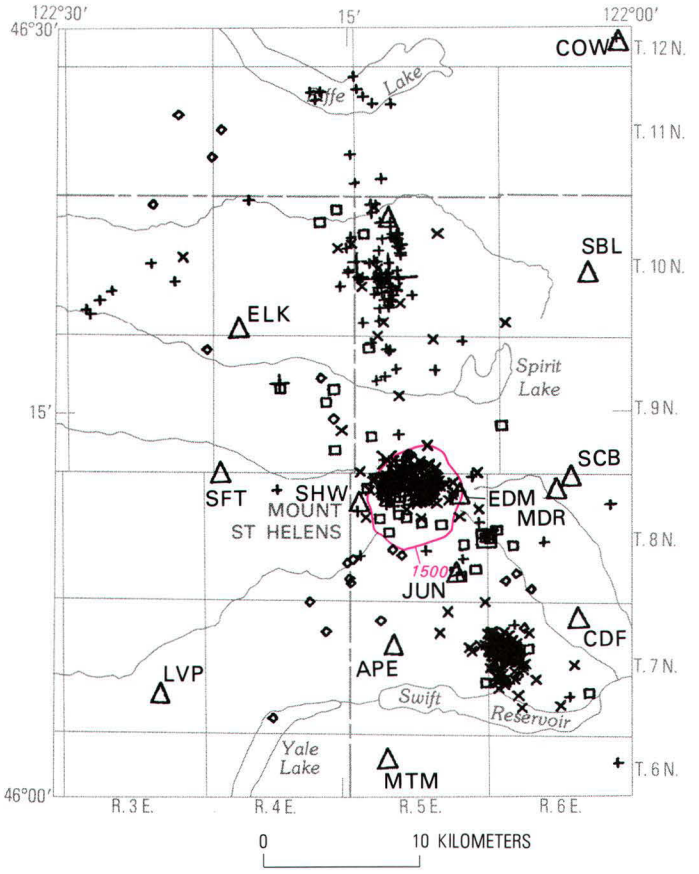

Figure 61.—Composite seismicity pattern from May 18 to August 31. Triangles, seismic stations. Symbol size indicates magnitude: small symbols, events with magnitudes less than 2.8; large symbols, events with magnitudes greater than 2.8. Depth indicated as follows: +, 0–5 km; x, 5–10 km; square, 10–15 km; diamond, greater than 15 km. Red line, posteruption 1,500-m topographic contour on the mountain.

In June, seismicity began to define a regional pattern (fig. 62*B*). North of Mount St. Helens, additional earthquakes were located on a north-northwest striking zone. Depths of these earthquakes remained shallow, above 15 km. The largest magnitude events in this zone were less than 3.0. Beneath Mount St. Helens, most of the earthquakes occurred in a swarm associated with the June 12 eruption. Their magnitudes were all less than 2.5, and their depths were shallower than 15 km, with most clustered between 5 and 8 km. South of Mount St. Helens, scattered seismicity covered a broad zone approximately 8 km wide. Focal depths in this zone were less than 20 km, and magnitudes were all less than 2.0. A fourth zone of deeper events may exist southwest of the cone. This zone is nearly coincident with earthquakes observed during a special study of Mount St. Helens in 1973 (Weaver and Malone, 1976), although these earlier events were shallower than 5 km.

Earthquakes at Marble Mountain, south of Mount St. Helens, and the sequence of events associated with the July 22 eruption dominated the seismicity in July (fig. 62*C*). At Marble Mountain, four earthquakes had magnitudes greater than 3.0, and earthquake depths were generally less than 15 km. Along the northern zone, activity remained shallow and all magnitudes were less than 3.0.

Small events with magnitudes less than 2.2 characterized the seismicity in August (fig. 62*D*). Events were clustered near Marble Mountain to the south and directly beneath Mount St. Helens. The latter events were almost exclusively associated with the eruption on August 7.

SEISMICITY BENEATH THE CRATER

Earthquakes and harmonic tremor have been both important and fairly reliable predictors of impending volcanic eruptions at Mount St. Helens since May 18. For real-time predictions, the most useful seismic data are event counts, signal character, and preliminary event locations. These data as they pertain to predicting eruptions are discussed in a companion report (Malone and others, this volume). In this section, the locations of the earthquakes during the eruptive sequences of May 25, June 12, July 22, and August 7 are discussed from the perspective of their relation to the seismicity preceding May 18 and to the location of the lava dome that appeared following the June 12 eruption.

Seismicity following the May 18 and May 25 eruptions remained distributed in the same area as the pre–May 18 activity. However, the character of the events, their magnitudes, and their depths were, with a few exceptions, markedly different than before the May 18 eruption. After onset of the eruption on May 18 the largest magnitude earthquakes directly beneath the mountain were a 3.8 event on May 18 at 1852 UTC and a magnitude-3.7 event on May 19 at 0718 UTC (approximately 16 hr after the onset of the eruption). No events with magnitudes greater than 3.0 occurred beneath the cone after May 21. The depths ranged from about 5 km to 20 km, and the event waveforms were generally of tectonic type. The

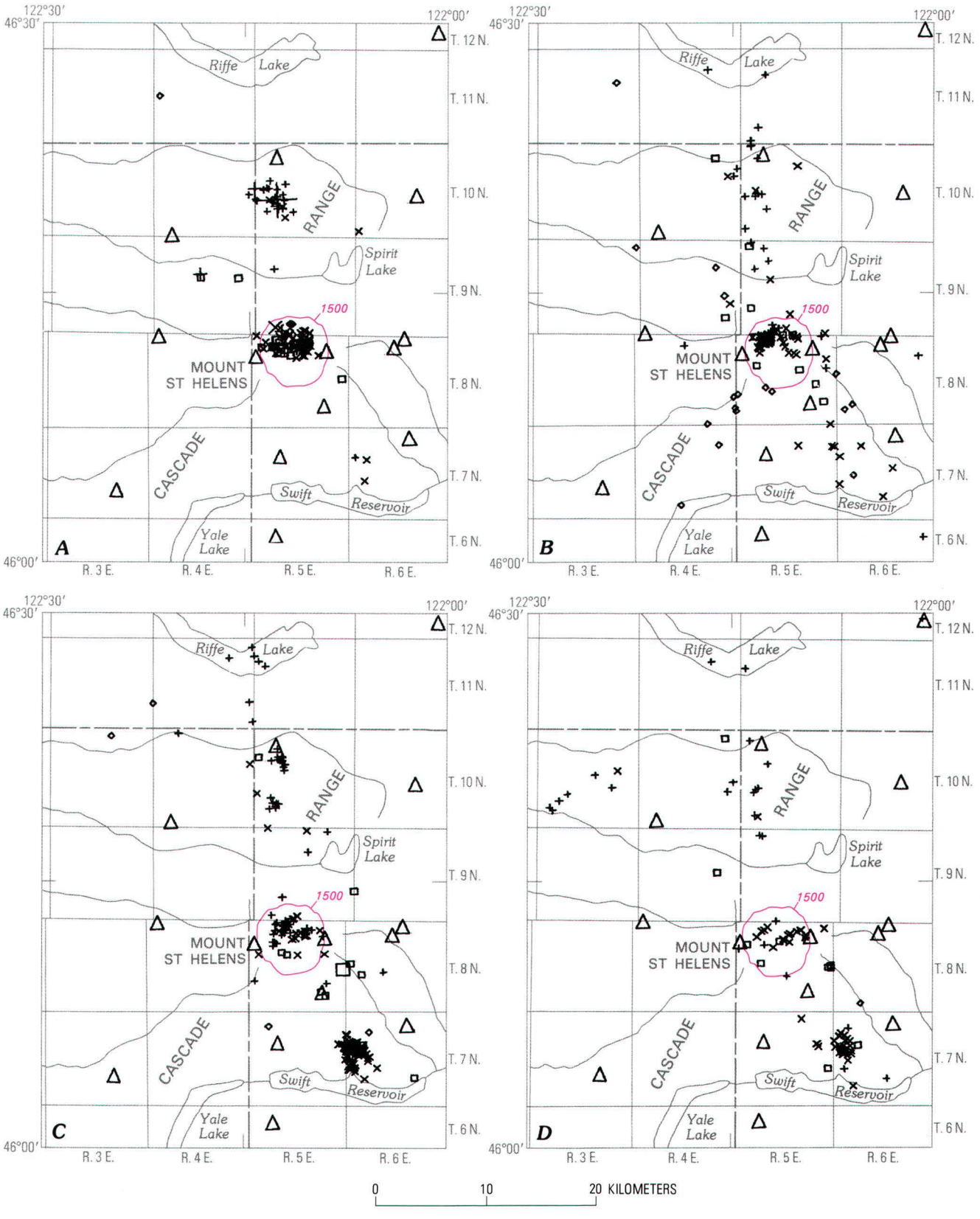
122°30′
122°00′
46°30′
46°00′
T. 12 N.
T. 11 N.
T. 10 N.
T. 9 N.
T. 8 N.
T. 7 N.
T. 6 N.
R. 3 E.
R. 4 E.
R. 5 E.
R. 6 E.
Riffe Lake
RANGE
Spirit Lake
1500
MOUNT ST HELENS
CASCADE
Swift Reservoir
Yale Lake
A
B
C
D
0
10
20 KILOMETERS

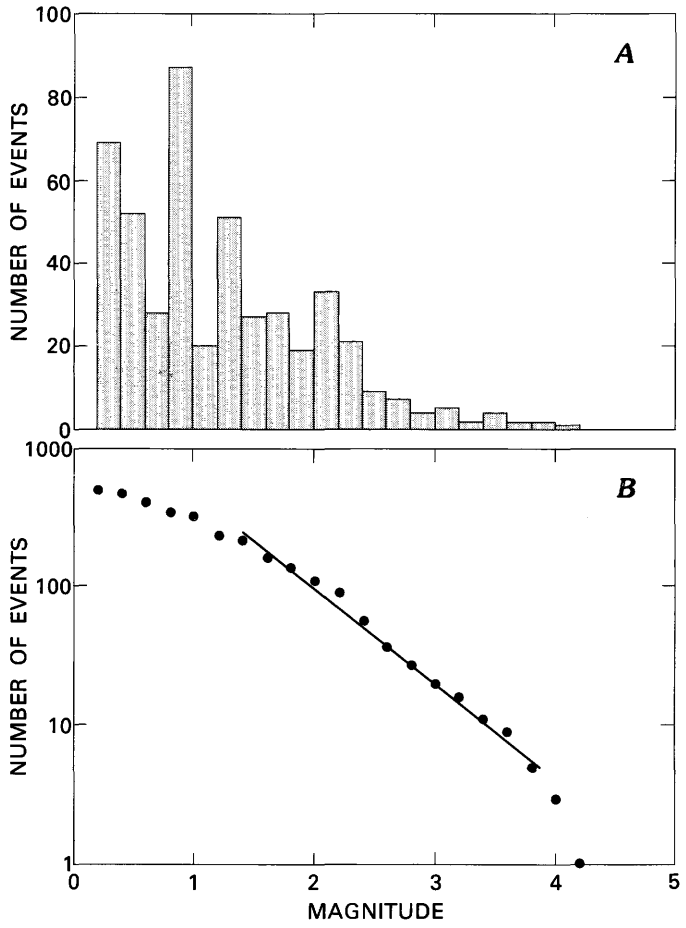

Figure 60.—Frequency of events versus magnitude plots for the time interval May 18–August 31. Total number of events with magnitudes greater than 0.0 is 477. A, number of events, grouped by 0.2 magnitude units, versus magnitude. B, log of cumulative number of events versus magnitude. The slope of the least-squares-fit line gives a b-value of 0.67 ± 0.01.

smaller than magnitude 1.2 and are not included in the analysis. The value of 0.67 may be compared with the values of 0.60 and 2.80 determined by Endo and others (this volume) for the high- and low-frequency volcanic events prior to May 18. The similarity between the post-May 18 value, based primarily on events not from under the cone, and the value based on high-frequency volcanic events beneath the volcano that preceded the May 18 eruption may indicate that the high-frequency volcanic earthquakes should be considered tectonic in nature. The slope of the cumulative frequency magnitude distribution plot for the earthquakes around Mount St. Helens is lower than that calculated for crustal earthquakes in the Puget Sound region (Crosson, 1972); this may indicate a regional variation of the *b*-value in western Washington, because both studies used the same coda-duration-magnitude relation. One possibility is that the stress drops of tectonic earthquakes in the Mount St. Helens area are higher than for earthquakes of the same magnitude in Puget Sound.

EARTHQUAKE LOCATIONS

The composite seismicity pattern for the post-May 18 period is strikingly different from that seen during the 2-mo period preceding the May 18 eruption. While earthquakes were concentrated in a small shallow crustal volume before May 18, earthquakes after May 18 are much more widely distributed (fig. 61). In addition to earthquakes directly beneath the mountain, two distinct zones of seismicity, one north and one south of the mountain, are evident (fig. 61). The north zone extends from the vicinity of Spirit Lake to Riffe Lake in the Cowlitz valley, a distance of 35 km. South of Mount St. Helens, the active zone strikes southeast 20 km, with a major cluster of events near Marble Mountain, immediately north of Swift Reservoir (fig. 61).

Changes in the seismicity became apparent on May 18, approximately 10 hr after the onset of the eruption. Earthquakes as deep as 20 km (fig. 62*A*) were located beneath the tight cluster of pre–May 18 earthquakes. The waveforms of these deep events resembled tectonic, rather than volcanic, earthquakes.

Throughout the remainder of May, earthquake activity continued beneath the new crater on Mount St. Helens. Included in this activity was an earthquake swarm that followed the May 25 eruption. The largest event in this swarm was of magnitude 2.3, and all events were less than 15 km in depth. A magnitude-2.8 earthquake on May 21 was the first earthquake noticed north of Mount St. Helens, but events may have been missed on May 18 during the periods of intense harmonic tremor. Several other events in the magnitude range 1.5–2.5 occurred during the 3 days after May 21 before a magnitude 3.8 event on May 24 (fig. 62*A*). This earthquake was followed on May 28 by a magnitude 4.2 in the same zone, the largest posteruption earthquake to date. The May activity north of Mount St. Helens was considered to be an earthquake swarm, because the magnitude difference between the two largest events was only 0.3. Earthquakes in this northern zone were shallow (< 15 km).

distribution of the deep earthquakes suggests that they may lie on a common structure lying to the northwest, beneath the west side of the crater (fig. 63*A*). A few low-frequency volcanic earthquakes with magnitudes less than 2.0 and depths less than 5 km were located between May 19 and May 25.

Following the June 12 eruption, a lava dome emerged within the crater. The deep earthquakes that accompanied this eruption were located northwest of the dome, in an area on the edge of the concentrated pre-May 18 activity. The locations were characteristic of an earthquake swarm, clustered in a tight volume about 1 km in radius and 3 km in vertical extent centered near a depth of 7 km. These events, all with magnitudes less than 2.8, were shallower than the deep zone suggested in figure 63*A*. Only scattered seismicity was evident beneath the east side of the crater, and shallow events in the upper 5 km of the crust were almost totally absent (fig. 63*B*).

The July eruption was preceded by a sequence of shallow, low-frequency volcanic earthquakes (Malone and others, this volume). These events again occurred northwest of the dome at depths less than 3 km. These events were above the deep events recorded on May 18 and 19 and also directly above the swarm of June 12 (compare figs. 63*A*, *B*, *C*). The magnitudes for these shallow events were less than 2.4. While activity in July was generally concentrated northwest of the dome, a few more events were located beneath the east side of the crater in July than in June.

Few earthquakes followed the August 7 eruption, and with only three exceptions, all events beneath the cone were deeper than 5 km. While few in number, the earthquakes in August defined two northeast-striking linear zones. The zone northwest of the dome had been apparent earlier, but the zone southeast of the dome had not been defined by the earlier seismicity.

Figure 62.—Cumulative seismicity patterns, by month, for the Mount St. Helens area. Triangles, seismic stations. Symbol size indicates magnitude: small symbols, events with magnitudes less than 2.8; large symbols, events with magnitudes greater than 2.8. Depth indicated as follows: +, 0–5 km; x, 5–10 km; square, 10–15 km; diamond, greater than 15 km. Red line, posteruption 1,500-m topographic contour on the mountain. A, May 19 to 31; B, June 1 to 30; C, July 1 to 31; D, August 1 to 31.

FOCAL MECHANISMS

Earthquake focal mechanisms have been calculated for all earthquakes located after June 1 with magnitudes greater than 2.4. In addition, 10 single-event mechanisms have been calculated for the June 12 posteruption swarm. Further, selected events in May have been studied, including the larger events north of Mount St. Helens (figs. 61, 62*A*) and some of the deep earthquakes beneath the cone that followed the two May eruptions. Data for earthquakes beneath Mount St. Helens are more complete for the June 12 eruptions because several stations that failed during the May 18 eruption, and which had not been restarted by May 25, were operating by June 12. Because uncertainties in earth structure lead to uncertainties in the takeoff angles for seismic waves leaving the earthquake focus, earthquakes along both the north and south zones were analyzed with both a linear velocity model using the computer program LOQUAKE (R. S. Crosson, unpub. program, 1980) and the layered model using the computer program HYPO79. All takeoff angles calculated using a linear velocity model are continuous functions of epicentral distance, while for a layered model, the calculated angles are discontinuous step functions for refracted arrivals. In the case of pure strike-slip faulting, either model yields the same theoretical solution.

Fault-plane solutions for the north and south zones are shown schematically in figure 64, and for the area around the crater in figure 63. Representative detailed mechanisms and first motion observations are given in figure 65. Nearly pure strike-slip faulting dominates all mechanisms away from the cone of Mount St. Helens. In the north zone, the mechanism for the May 28 magnitude-4.2 event is purely strike slip with nearly north-south and east-west fault planes (fig. 65*G*). With the good azimuthal distribution of observations (fig. 65) giving well-constrained fault-plane directions and the general north-south alinement of epicenters (figs. 61, 62), the preferred fault plane for these events strikes north-south, and the motion is right lateral, strike slip.

South of Mount St. Helens, near Marble Mountain, the larger events all have nearly pure strike-slip faulting (fig. 65*J*, *K*). The preferred fault plane strikes N. 25° W. with the general strike of the epicenters again justifying this selection. As with the events to the north, azimuthal control is excellent, and allows

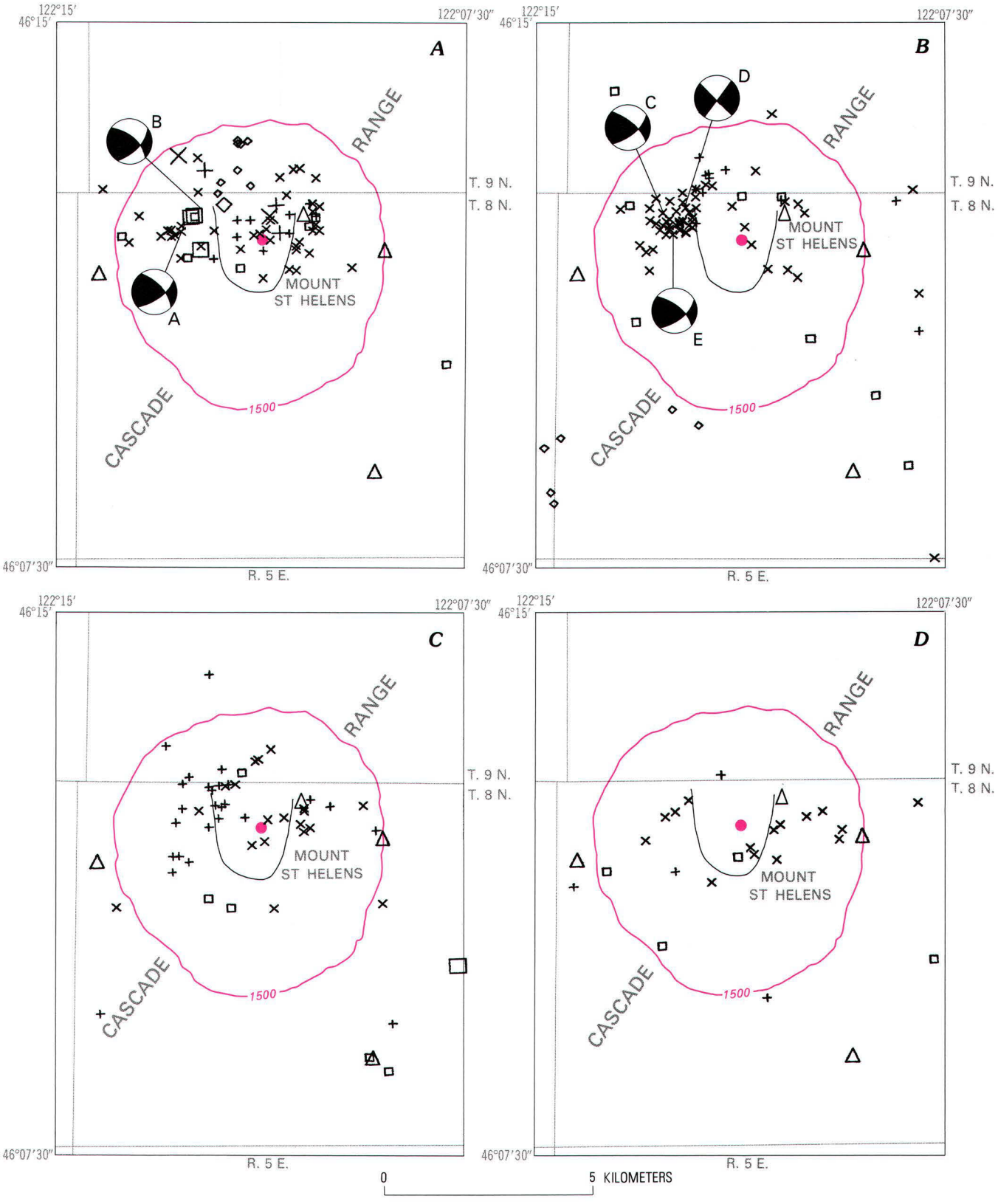
A
B
C
D
E
RANGE
CASCADE
MOUNT
ST HELENS
1500
122°15′
122°07′30″
46°15′
46°07′30″
T. 9 N.
T. 8 N.
R. 5 E.
0
5 KILOMETERS

the mechanism for the larger magnitude events to be constrained to ±5 degrees. Furthermore, for these mechanisms the high angles of incidence result in well-determined dips of the fault planes. There is little room for alternate mechanisms.

Directly beneath Mount St. Helens, the fault-plane solutions show components of both strike-slip and thrust faulting. Following the May 18 eruption, earthquakes occurred at depths down to 20 km. These deep events were divided into three groups: depths less than 10 km, 10–14 km, and greater than 14 km. To date, focal mechanisms have been obtained only for events in the middle category. One single-event solution and a composite focal mechanism using four events show significant thrusting along northeast- or northwest-striking fault planes (figs. 63, 65*A*, *B*). Fault planes for the composite mechanism (fig. 65*B*) were drawn on the basis of the polarity reversals at stations ELK and LVP. For this group of four events, both dilatations and compressions were recorded at these two stations, while all other stations used in the mechanism recorded the same polarity for all events. All of these mechanisms suffer from not having usable data from stations SHW and, often, JUN located on the cone. When the final processing is done for May, the addition of readings for more distant stations in eastern Washington will probably help improve these solutions.

As noted above, earthquakes immediately following the June 12 eruption are outside of the epicentral area of the pre-May 18 seismicity. The fault-plane solutions for these events show a mixture of strike-slip and thrust faulting (figs. 64, 65*C*, *D*, *E*). The fault planes strike generally northwest or northeast. The ones striking northeast nearly concur with the northeast-striking seismic zone outlined earlier (fig. 63*B*, *C*, *D*). No mechanisms have yet been calculated for the events under the southeast side of the cone. Generally, because of the steep angles of departure, the June 12–13 mechanisms are well constrained.

Focal mechanisms A–D in figure 65 all have steeply dipping fault planes that strike northeast. The strike of the inferred fault planes nearly matches the strike of the deep seismicity in May (depths to 20 km), and the earthquakes between 5 and 10 km following the May 25, June 12, July 22, and August 7 eruptions (fig. 63). It is reasonable to postulate that these hypocenters define a nearly vertical fault. The relations between this proposed fault, the eruptive processes,

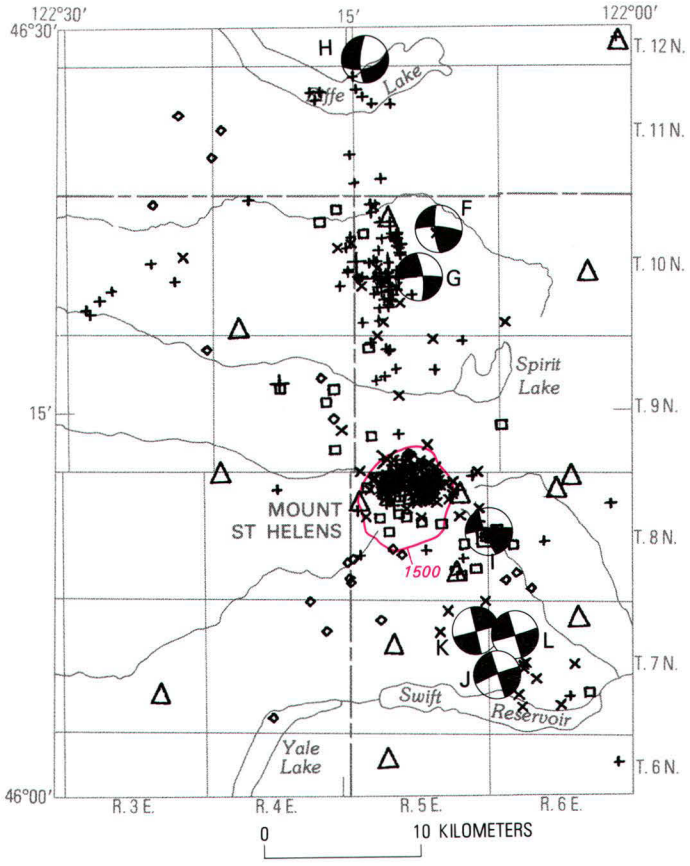

Figure 64.—Cumulative seismicity and focal-mechanism diagrams for some of the events between May 18 and August 31. Focal mechanisms are upper hemisphere plots, with darkened quadrants indicating compression, white quadrants indicating dilatations. Mechanisms are keyed, by letter, to detailed mechanisms plotted in figure 65. Red line, posteruption, 1,500-m topographic contour on the mountain.

Figure 63.—Cumulative seismicity patterns under Mount St. Helens. Triangles, seismic stations. Symbol size indicates magnitude: small symbols, events with magnitudes less than 2.8; large symbols, events with magnitudes greater than 2.8. Depth indicated as follows: +, 0–5 km; x, 5–10 km; square, 10–15 km; diamond, greater than 15 km. Red line, posteruption 1,500-m topographic contour on the mountain. The location of the lava dome is shown as a red circle. Enlargements of focal-mechanism diagrams, keyed by letter, seen in A and B are shown on figure 65. A, May 18 to May 31; B, June 1 to June 30; C, July 1 to July 31; D, August 1 to August 31. Focal mechanisms are upper hemisphere plots, with darkened quadrants indicating dilatations. Mechanisms are keyed by letter to detailed mechanisms plotted in figure 65.

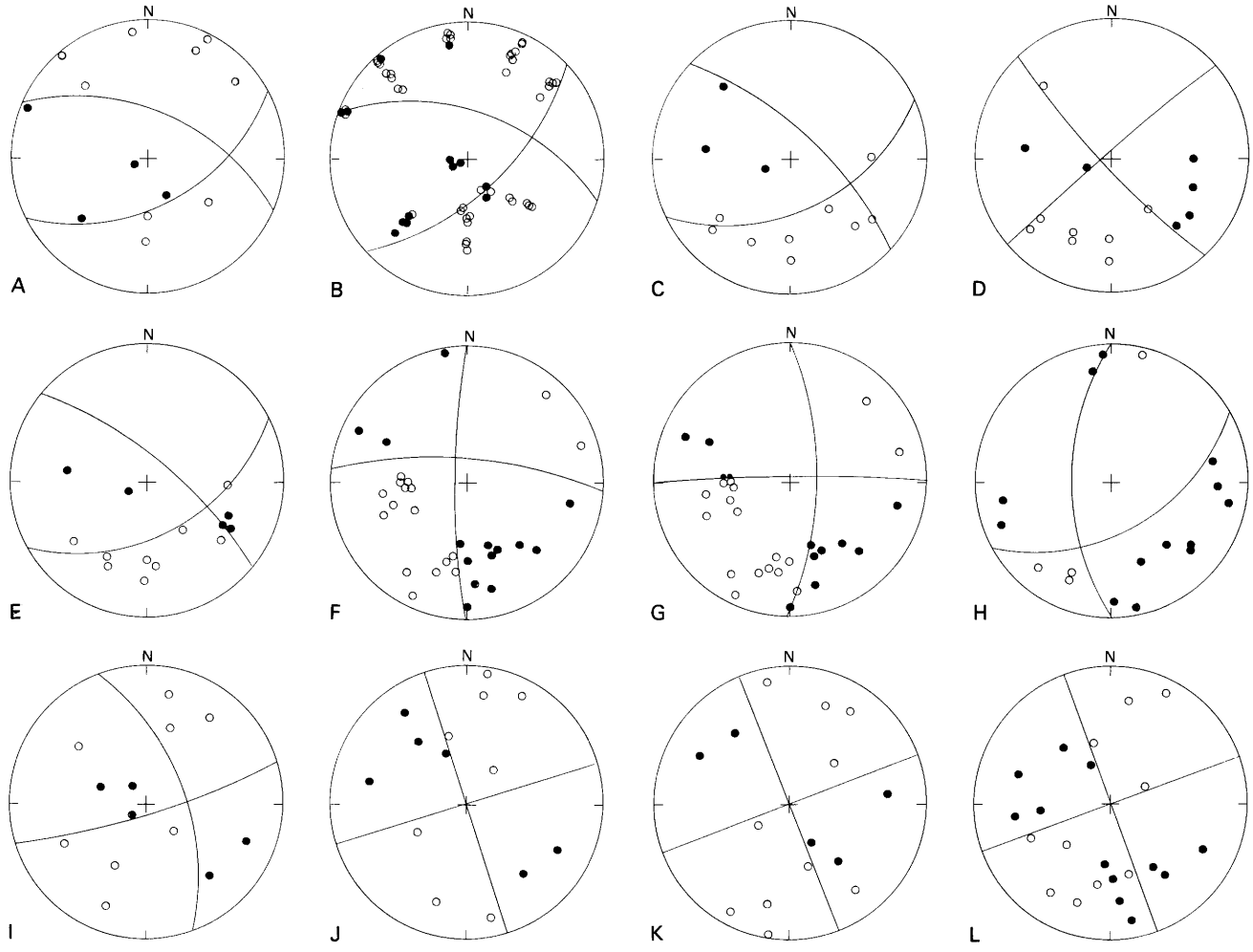

Figure 65.—Focal mechanism diagrams and first-motion data. Locations of focal mechanisms are shown in figures 63 and 64. The diagrams are upper hemisphere plots; solid circles, compressions; open circles, dilatations. Mechanism B is a composite solution discussed in text, all other solutions are single-event solutions.

the lava dome, and the preeruption seismicity will require a detailed examination, which is outside the scope of this report.

A second observation regarding the seismicity beneath the crater concerns the second zone of earthquakes defined by the August activity (fig. 63*D*). If the earthquakes in this zone lie on a single fault, then it appears that the pre-May 18 seismicity may well have been a fault-bounded process. The majority of earthquakes before May 18 had hypocenters immediately northwest of this alinement of earthquakes (compare fig. 55 with fig. 63*D*). This hypothesis will be tested when final processing is completed on the pre-May 18 data.

Compression (P) and tension (T) axes that were calculated for each focal mechanism are plotted in figure 66. Axes for events directly beneath the mountain are distinguished from the regional events because the magnitudes of earthquakes beneath the crater used in this study were much smaller; this difference in magnitude, in fact, might help identify any consistent difference between the two classes of events. In addition to the axes from the events plotted in figure 65, P- and T-axes were added from another 12 mechanisms of earthquakes under the cone. The results (fig. 66) show that the T-axes, with the exception of three events, cluster tightly in azimuth between N. 45° W. and N. 90° W. The P-axes show more variation in azimuth, but are generally alined to the northeast. While some of the swarm events beneath the mountain have nearly vertical T-axes, the P-axes for these events fall in the same azimuthal range as those for earthquakes both north and south of the mountain.

DISCUSSION

The two zones of earthquakes defined north and south of the mountain represent a crustal response to the release of seismic energy at Mount St. Helens. Comparing the historically located events in these two zones (fig. 52) with those located since May 18 reveals a dramatic increase in seismicity. While the magnitude threshold for detection has been lowered by the increased number of seismic stations, the sequence of magnitude-3 and greater events in both zones is unprecedented when compared with instrumentally located earthquakes prior to March 1980. It seems unlikely that this increase in activity would have taken place without the eruption of Mount St. Helens.

The fault-plane solutions (figs. 63, 64) show that the Mount St. Helens region is dominated by horizontal compressional stress. The directions of the P-axes vary from north-south to N. 65° E.; the average azimuth is about N. 30° E. This range of P-axes is consistent with those from larger magnitude earthquakes in western Washington (Crosson and Frank, 1975; Crosson and Lin, 1975; Yelin and Crosson, 1979), at Mount Hood (Weaver and others, 1981), and in eastern Washington (Malone and others, 1975). Compression is expected in this region, as the Pacific Northwest is in a zone of convergence between the Juan de Fuca and the North American plates (Riddihough and Hyndman, 1976; Riddihough, 1977). From a study of relative plate motions, Riddihough (1977) has determined an angle of convergence between the two plates of N. 50° E. In a recent re-survey of a geodimeter network in the Puget Sound Basin, Savage and others (1981) found that the axis of greatest contraction was oriented N. 71° E. ± 6°. These authors interpreted this direction as in fair agreement with Riddihough's findings.

Nevertheless, earthquake focal mechanisms in the Northwest give compression axes oriented more north-south than those predicted by Riddihough or measured in the deformation network. Savage and others (1981) gave a lucid discussion of a model proposed by Rogers (1979) that seeks to explain the more north-south orientation of the compression axes determined from fault-plane solutions. Rogers (1979) has modified a model of the subduction process proposed by Fitch (1972) in which oblique subduction is decomposed into a thrust component on the subduction boundary and a nearly vertical strike-slip component near the volcanic arc. Noting the lack of thrust events at the subduction zone, he proposed that the thrust component of subduction is accommodated aseismically, leaving only the strike-slip shear component. In the Vancouver Island area where Rogers was attempting to explain the north-south orientation of the compression axis for the 1946 magnitude-7.1 earthquake, the plate boundary strikes approximately N. 45° W. Resolving the plate shear into principal components gives a north-south compression and an east-west extension.

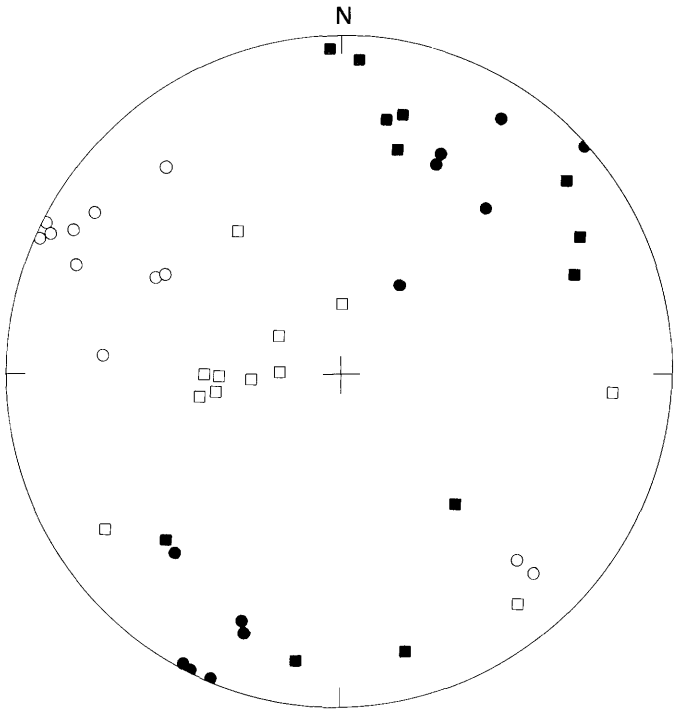

Figure 66.—Compression (P) and tension (T) axes inferred from all focal mechanisms. Solid symbols, P-axes; open symbols, T-axes; squares, axes determined for events beneath the volcano; circles, events both north and south of Mount St. Helens.

The plate boundary offshore of the Mount St. Helens area (fig. 67) is oriented about N. 15° W. Following Rogers' (1979) subduction component assumption, resolving the plate shear into components gives an approximate compressional direction of N. 30° W., or good agreement with the P-axis direction determined from the focal mechanisms at Mount St. Helens. The nearly vertical nature of the fault planes (figs. 63, 64) is also consistent with Rogers' model.

The consistency of the P-axes at Mount St. Helens contrasts with data from Lassen Peak, where the T-axes are alined with the regional east-west exten-

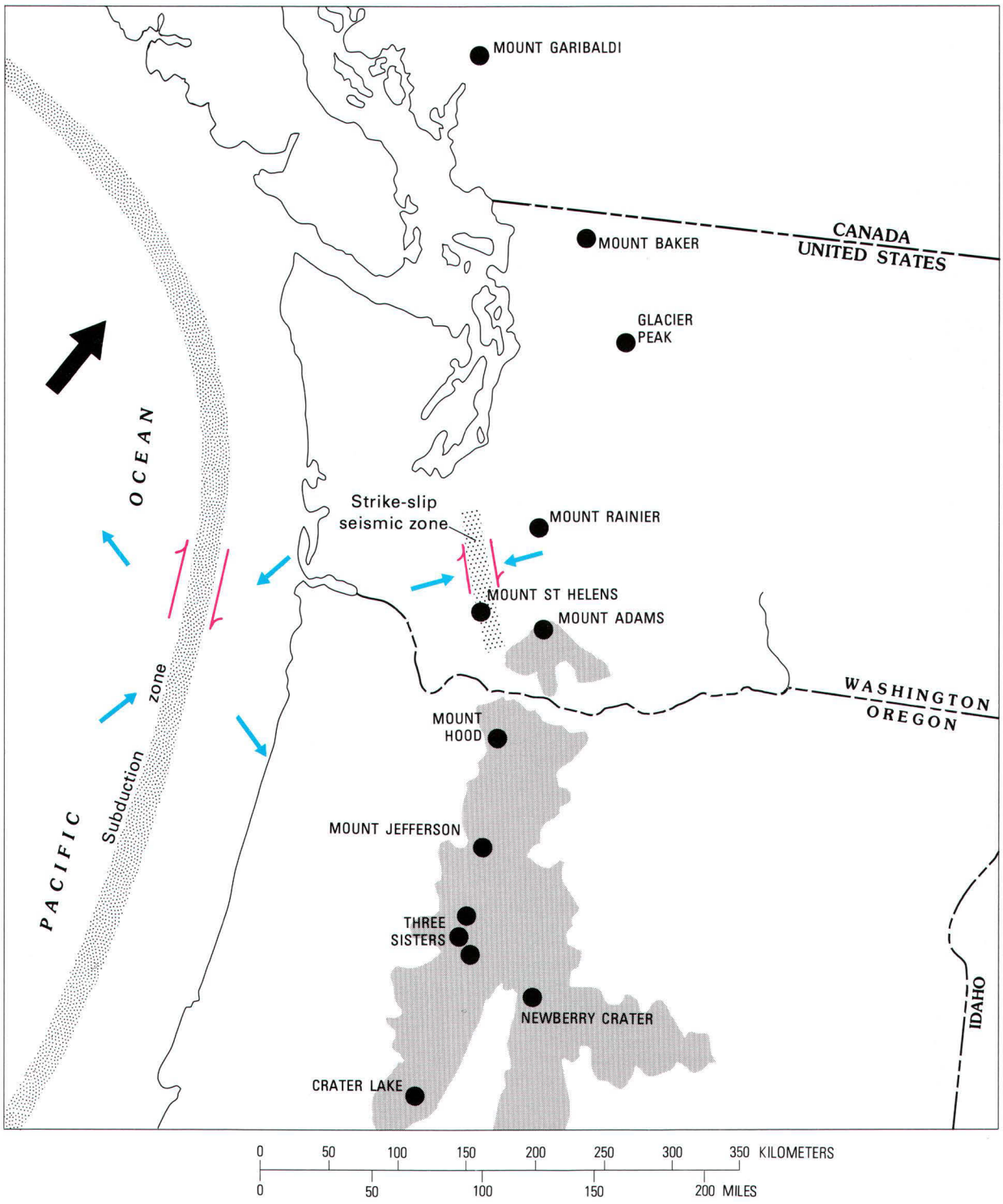

Figure 67.—Regional tectonic model showing horizontal compressional regime at Mount St. Helens. Solid circles, Cascade Range volcanoes; shaded area, approximate extent of Quaternary volcanism where more extensive than solid circles. Large arrow indicates motion of Juan de Fuca plate relative to North American plate (Riddihough, 1977). Red arrows along subduction zone indicate direction of relative movement along plate boundary. Blue arrows show inferred stress resolved into an extensional component (arrows point out) and a compressional component (arrows point in) along the subduction zone, and dominant compressional stress direction observed in the Washington Cascade Range along the strike-slip seismic zone.

sion (Klein, 1979). The difference in the behavior of the stresses at these two volcanoes reflects the changes from a compressional environment in the northern Cascade Range to an extensional environment in the southern Cascade Range.

It is worth speculating on the transition between these two regimes. Nakamura (1977) has classified volcanic belts based on whether compression or extension is the dominant horizontal stress acting. The Cascades north of Mount St. Helens fit Nakamura's compressional category. The Oregon Cascades, with chains of cinder cones alined north-south and major mapped normal faults (McBirney, 1978; Lawrence, 1976) fit Nakamura's extensional class with the tension axis east-west (similar to Lassen Peak). East-southeast of Mount St. Helens, the Indian Heaven basalt field and the extensive basalts near Mount Adams (fig. 67) are features expected in extensional environments. Mount St. Helens may, then, lie near an important transition in the Cascade Range, where the stress regime changes from compression to extension.

REFERENCES CITED

Crosson, R. S., 1972, Small earthquakes, structure, and tectonics of the Puget Sound region: Seismological Society of America Bulletin, v. 62, p. 1133–1171.

Crosson, R. S., 1976, Crustal structure modeling of earthquake data, 2, Velocity structure of the Puget Sound region, Washington: Journal of Geophysical Research, v. 81, p. 3047–3054.

Crosson, R. S., and Frank, D., 1975, The Mt. Rainier earthquake of July 18, 1973, and its tectonic significance: Seismological Society of America Bulletin, v. 65, p. 393–401.

Crosson, R. S., and Lin, J. W., 1975, A note on the Mt. Rainier earthquake of April 20, 1974: Seismological Society of America Bulletin, v. 65, p. 549–552.

Fitch, T. J., 1972, Plate convergence, transcurrent faults, and internal deformation adjacent to southeast Asia and the western Pacific: Journal of Geophysical Research, v. 77, p. 4432–4460.

Klein, F. W., 1979, Earthquakes in Lassen Volcanic National Park, California: Seismological Society of America Bulletin, v. 69, p. 867–875.

Kohler, W. M., Healy, J. H., and Wegener, S. S., 1981, Upper crustal structure of the Mount Hood, Oregon region as revealed by time-term analysis: Journal of Geophysical Research, v. 86 (in press).

Lawrence, R. D., 1976, Strike-slip faulting terminates the Basin and Range province in Oregon: Geological Society of America Bulletin, v. 87, p. 846–850.

McBirney, A. R., 1978, Volcanic evolution of the Cascade Range: Annual Review of Earth and Planetary Science, v. 6, p. 437–456.

Malone, S. D., Rothe, G. H., and Smith, S. W., 1975, Details of microearthquake swarms in the Columbia Basin, Washington: Seismological Society of America Bulletin, v. 65, p. 855–864.

Nakamura, K., 1977, Volcanos as possible indicators of tectonic stress orientation—principle and proposal: Journal of Volcanology and Geothermal Research, v. 2, p. 1–16.

Riddihough, R. P., 1977, A model for recent plate interactions off Canada's west coast: Canadian Journal of Earth Sciences, v. 14, p. 384–396.

Riddihough, R. P., and Hyndman, R. D., 1976, Canada's active western margin—the case for subduction: Geoscience Canada, v. 3, p. 269–278.

Rogers, G. C., 1979, Earthquake fault plane solutions near Vancouver Island: Canadian Journal of Earth Sciences, v. 16, p. 523–531.

Savage, J. C., Lisowski, M., and Prescott, W. H., 1981, Geodetic strain measurements in Washington: Journal of Geophysical Research, v. 86 (in press).

Weaver, C. S., and Malone, S. D., 1976, Mount St. Helens seismic events—volcanic earthquakes or glacial noises?: Geophysical Letters, v. 3, p. 197–200.

Weaver, C. S., Green, S. M., and Iyer, H. M., 1981, Seismicity of Mount Hood and structure as determined from teleseismic P-wave delay studies: Journal of Geophysical Research, v. 86 (in press).

Yelin, T. S. and Crosson, R. S., 1979, A significant sequence of earthquakes in South Puget Sound [abs]: Earthquake Notes, v. 50, no. 4, p. 61.

DEFORMATION STUDIES

Previous studies of deformation accompanying volcanic activity have yielded significant results mainly at basaltic volcanoes such as Kilauea in Hawaii, where eruptions have occurred frequently. There, slow inflation or swelling of the volcanic edifice has preceded activity as magma rises and accumulates within a reservoir a few kilometers beneath the summit, and more abrupt deflation commonly accompanies eruption of lava. Few deformation studies have previously been made on composite stratovolcanoes, both because relatively infrequent eruptions at any volcano have impeded collection of representative data, and because their explosive nature hampers measurements during activity. Accordingly, Mount St. Helens in 1980 has presented an exceptional opportunity to obtain deformation data of types rarely attempted previously. A few baseline distance measurements had been made by D. A. Swanson in 1972 at Mount St. Helens, but these had not been repeated before the beginning of the 1980 activity. Changes on the cone were monitored in 1980 by electronic-distance and theodolite-angle measurements, photogrammetry and topographic mapping, microgravity measurements, and by continuously recording electronic tiltmeters and magnetometers.

Deformation measurements were begun in early April, in an attempt to determine the significance of the fracturing and bulging visible at the summit and upper north slope of the volcano, but poor weather and frequent steam explosions limited these efforts to microgravity readings and several types of tilt measurements on the lower slopes; these showed relatively small, inconclusive, and partly inconsistent changes (Dvorak and others; Jachens and others).

In mid-April, analysis of the first posteruption vertical aerial phototographs documented startlingly large deformation of the bulge area (Moore and Albee; Jordan and Kieffer). About the same time, geodetic measurements to newly established targets high on the north flank showed that deformation was continuing at high rates (Lipman, Moore, and others). The photogrammetric results demonstrated that the upper north slope had moved outward more than 100 m and upward slightly, and the geodetic measurements documented continued lateral displacements of as much as 2.5 m/day. Despite this extraordinary local deformation, no significant changes were measured on the east, south, or west slopes. These deformation measurements, along with continued high levels of seismic energy release, provided compelling evidence in April and early May that the volcano could be nearing a major event, despite the seemingly mild nature of the intermittent phreatic activity. Concern focused on the probability of landsliding of the north flank, and attempts were made to design a monitoring procedure to obtain advance warning. Even in hindsight, however, no changes in deformation rates preceding the failure on May 18 have been identified. Probably the north slope was not at that time sufficiently destabilized to fail gravitationally without a trigger, which finally was provided on May 18 by the large earthquake at 0832 PDT.

A notably different style of deformation has characterized Mount St. Helens since the catastrophic May 18 eruption: the entire cone has shown only small changes that are radially oriented with respect to the crater area (Swanson and others). The rates of geodetic change seemingly slowed during the year, and little analytically significant change was observed on the main cone during the last few months of 1980. Geodetic and electronic-tilt data have shown a general pattern of slow deflation, interrupted by brief small inflationary episodes preceding and accompanying the major pyroclastic eruptions on June 12, July 22, and August 7. Within the crater, larger and more complex deformation was seemingly related to dome growth: the north side of the inner crater (the rampart) moved northward at rates of as much as several centimeters per day. Transient magnetic anomalies, recorded during the May 18, May 25, and June 12 eruptions, are thought to reflect elastic strain release related to the eruptions (Johnston and others).

THE 1980 ERUPTIONS OF MOUNT ST. HELENS, WASHINGTON

TOPOGRAPHIC AND STRUCTURAL CHANGES, MARCH–JULY 1980—PHOTOGRAMMETRIC DATA

By JAMES G. MOORE *and* WILLIAM C. ALBEE

ABSTRACT

Six new topographic maps (1:24,000, 80-ft contour interval) were made by photogrammetric methods from aerial photographs taken before and during the 1980 volcanic activity at Mount St. Helens. They show the early development of the summit explosion crater (March 27, 1980) centered within a subsiding and northward-expanding graben initially about 1.5 km long (east-west) and 0.4 km wide. North of the graben, a bulge about 1.8 km in diameter formed and its surface began migrating north at 1.5–2 m/day. By May 12, the high point of the bulge was 150 m above preexisting topography. This apparent uplift resulted both from horizontal movement on the 30° north slope of the mountain and from an absolute uplift of the south- central part of the bulge. By May 18 the net volume increase of the mountain produced by the graben-bulge system was 0.11 km^3, which was presumably the volume of a shallow-level dacite cryptodome intruded beneath the north side of the 16th–17th century summit dome.

On May 18 a giant landslide and explosions removed 2.7 km^3 from the mountain. Chance photographs of landslide failure and resulting explosions could be compared to the topographic maps by use of computer-generated models of the maps as they would appear from the camera station. This method permitted estimation of the topography of the upper landslide surface, and consequently of the shape of the first two slide blocks. The northern block, which moved first, coincided with the area of the bulge and included the 19th century Goat Rocks dome. This block dropped down and moved north, producing a steep headwall scarp 700 m high inclined north about 65°–70°. The chief source of the most massive explosions that fed the pyroclastic surge was from this scarp, which apparently intersected, exposed, and depressurized the cryptodome and its associated hydrothermal system in the second block. This second block contained the graben and included most of the cryptodome and the summit dome. Continued landsliding and explosions destroyed the second block and migrated south 800 m to the south edge of the new amphitheater crater, exposing the main volcanic conduit 1 km deeper than before landsliding.

ACKNOWLEDGMENTS

R. V. Lugn aided in the original photogrammetric measurements of bulge growth. M. J. Davis and R. D. Garrett made the topographic maps from aerial photographs by photogrammetric methods. B. S. Bennett aided in the preparation of computer-generated map models. Paul and Carol Hickson provided their unpublished photographs for analysis. C. A. Hopson provided data from his previous mapping of Mount St. Helens. S. D. Malone made available his analysis of the timing of the Rosenquist photographs. The help of these individuals is gratefully acknowledged.

INTRODUCTION

Aerial photographs taken April 12, 1980, and delivered a few days later were first compared with the published 1958 contour sheet (based on 1952 photographs) and important topographic differences were noted. To eliminate the possibility that glacial changes had modified the surface during the intervening 28 yr, a new topographic map was hastily pre-

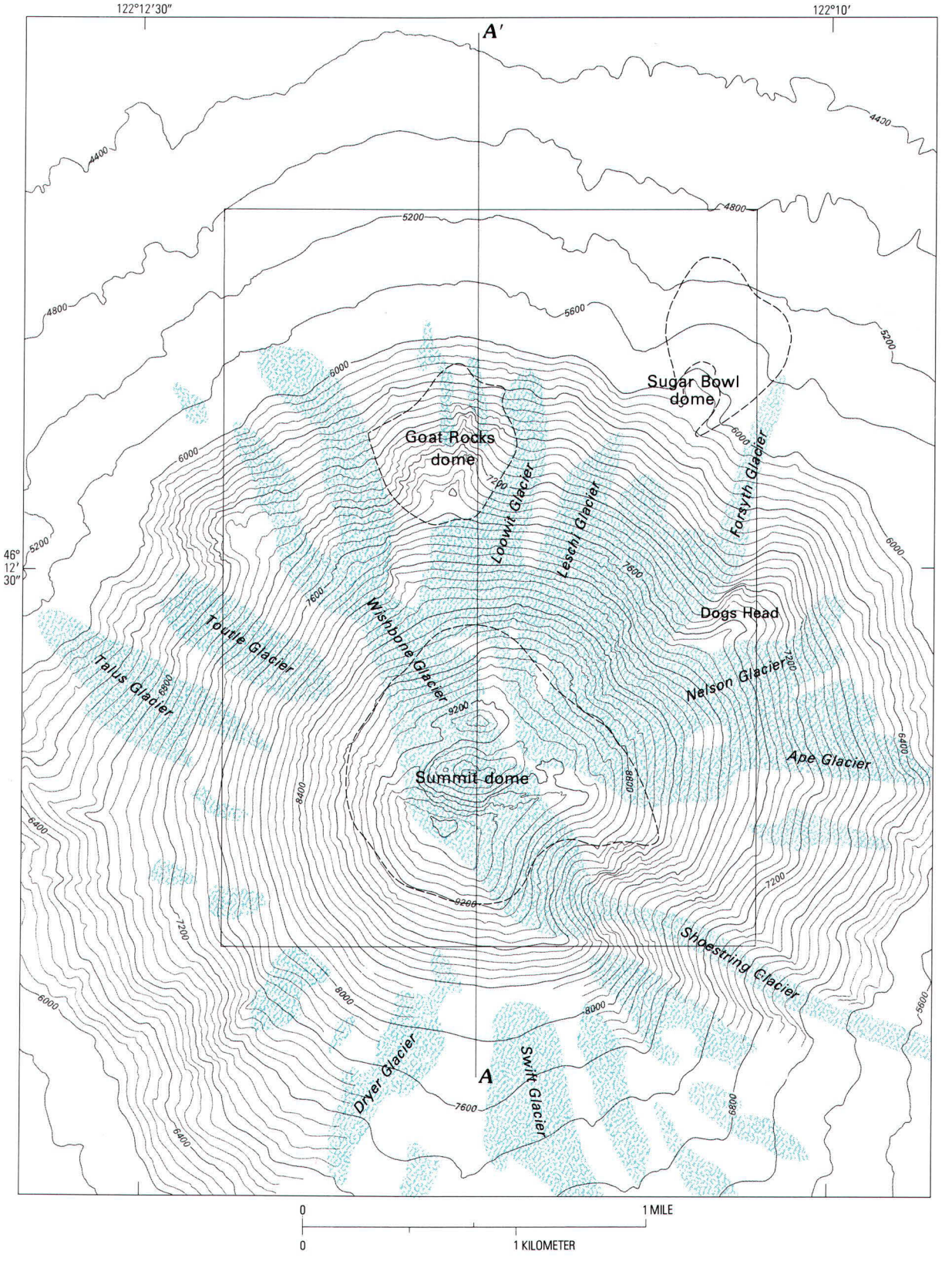

Figure 68.—Topographic map of Mount St. Helens from aerial photography of April 12, 1980. Ice fields and glaciers (blue); dashed lines indicate limits of dacitic domes modified from C. A. Hopson (written commun., 1980). Outline of inset maps (figs. 70 and 72) is shown; section line refers to figs. 73 and 76.

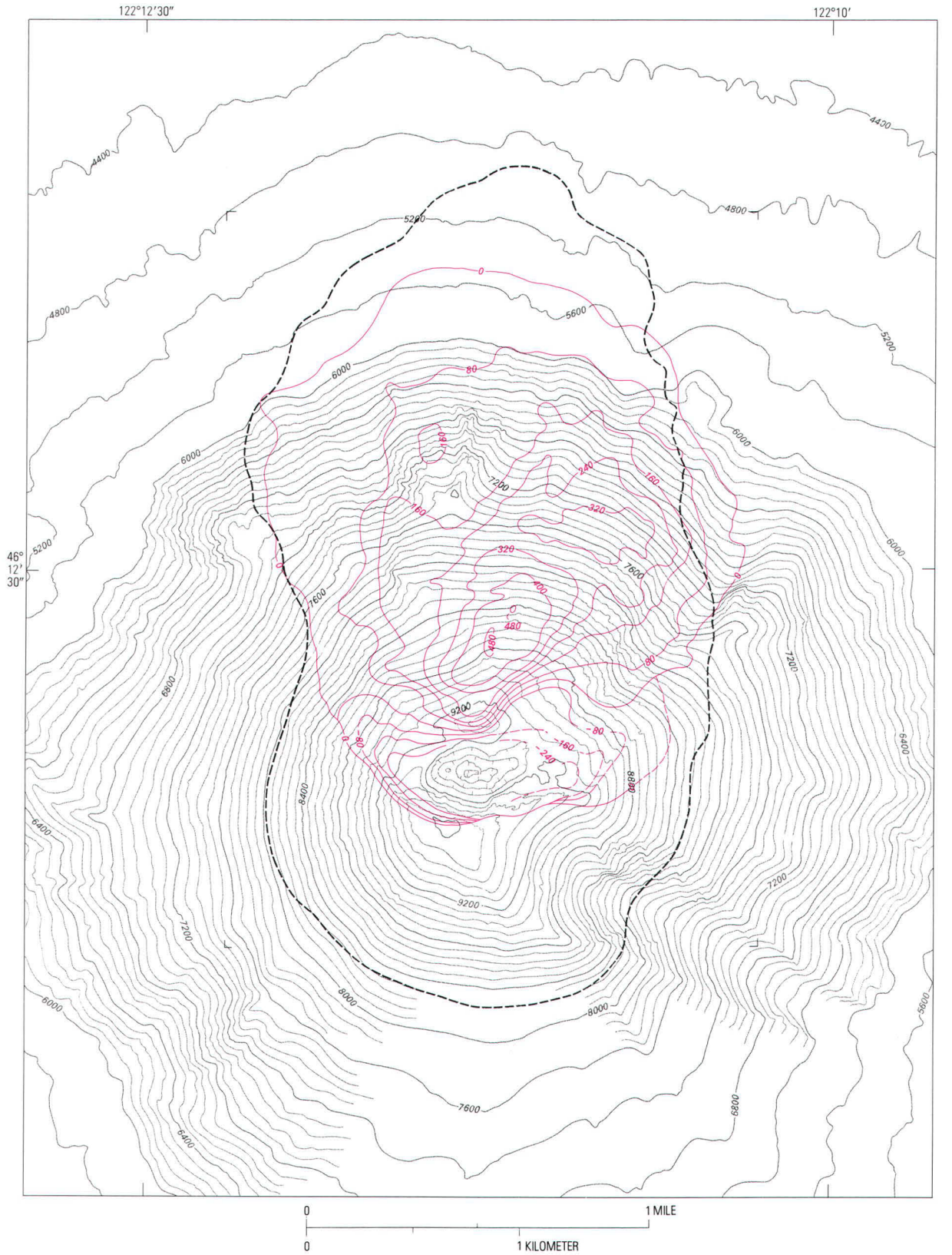

Figure 69.—Map of April 12, 1980, showing elevation changes (red), in feet, between August 15, 1979, and May 12, 1980. Bold dashed line, May 18 crater rim.

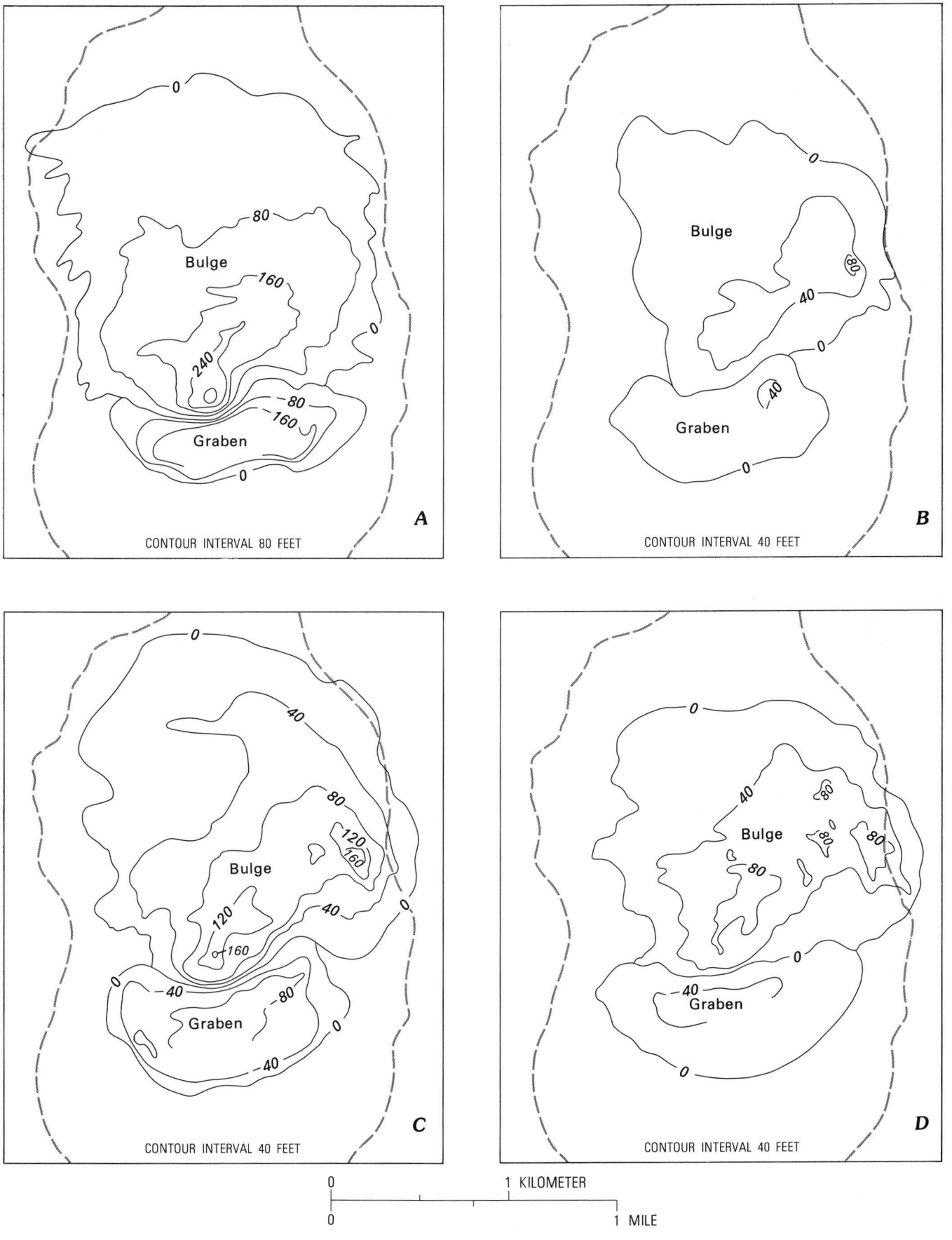
0
80
Bulge
160
240
0
80
160
Graben
0
A
CONTOUR INTERVAL 80 FEET
0
Bulge
80
40
0
40
Graben
0
B
CONTOUR INTERVAL 40 FEET
0
40
80
120
160
Bulge
120
160
40
0
0
40
80
Graben
0
40
C
CONTOUR INTERVAL 40 FEET
0
40
80
Bulge
80
80
80
0
40
Graben
0
D
CONTOUR INTERVAL 40 FEET
0
1 KILOMETER
0
1 MILE

pared from photography of the previous summer (August 15, 1979). This preeruption map was then compared with a map based on the April 12 photography which clearly outlined the growth of a summit graben and bulge on the north side of the volcano (figs. 68, 69, 70). The photogrammetric data described here, in conjunction with ground geodetic measurements (Lipman, Moore, and Swanson, this volume), were of prime importance in understanding the processes acting within the volcano and in assessing the hazard due to oversteepening of the north slope. In retrospect, the photogrammetric data set was acquired at low risk, and consequently should be an important element in monitoring future activity of potentially explosive volcanoes of similar type.

A total of six contour maps (scale 1:24,000, contour interval, 80 ft) were prepared from aerial photographs (August 1979, and April 7, April 12, May 1, May 12, and July 1, 1980) as they became available to the USGS. These maps utilized English units to facilitate rapid comparison with existing maps as well as with measurements made in the field and from aircraft. Most of the maps include the volcanic cone above the 4,400-ft contour, but incomplete photographic coverage, varied camera systems and elevations, and presence of volcanic fume and atmospheric clouds affected map quality. The maps are controlled by a geodetic net averaged from ground control established in 1952, the same as used for the published Mount St. Helens, 1958, 15-min quadrangle map. Although absolute elevation errors as large as 20 ft may be present, the relative errors between maps of the series are believed to be less than 5 ft.

ACTIVITY PRIOR TO MAY 18

A swarm of relatively shallow earthquakes began March 20, 1980, beneath the north flank of the mountain, 1–2 km north of the summit. The first in a series of phreatic eruptions began in the early afternoon of March 27 and excavated a small summit crater in the center of a new 1.5-km-long graben alined east-west (Williams, 1980, p. 72). A second crater formed to the west by March 29, and by April 7 the two craters had merged to produce an elongate crater. After April 7, the volume of the crater increased slowly to a maximum of about 9×10^6 m^3 by May 12 (fig. 71). The phreatic explosions that began on March 27 were probably initiated by pressure release due to thinning and fracturing of cover rocks and ice within the graben.

Small lakes and ponds were in the phreatic crater prior to May 18 and are visible in all of the aerial photographs of mapping quality. Commonly the lakes were frozen and contained floating blocks of ice but were recognizable by their horizontal surfaces. These lakes were fed by melt-water streams flowing down the crater walls from the base of melting glaciers, as well as from ice talus melted by steam vents on the crater floor. Lake water was blown out during phreatic explosions but quickly accumulated again between eruptions.

The map of April 7, when compared with that of August 1979, showed that dramatic changes had occurred (fig. 70*A*). A prominent bulge about 1.8 km

Figure 70.—Elevation change, in feet, between consecutive topographic maps; see figure 68 for location. A, August 15, 1979 to April 7, 1980. B, April 7 to April 12. C, April 12 to May 1. D, May 1 to May 12. Dashed line, edge of May 18 crater.

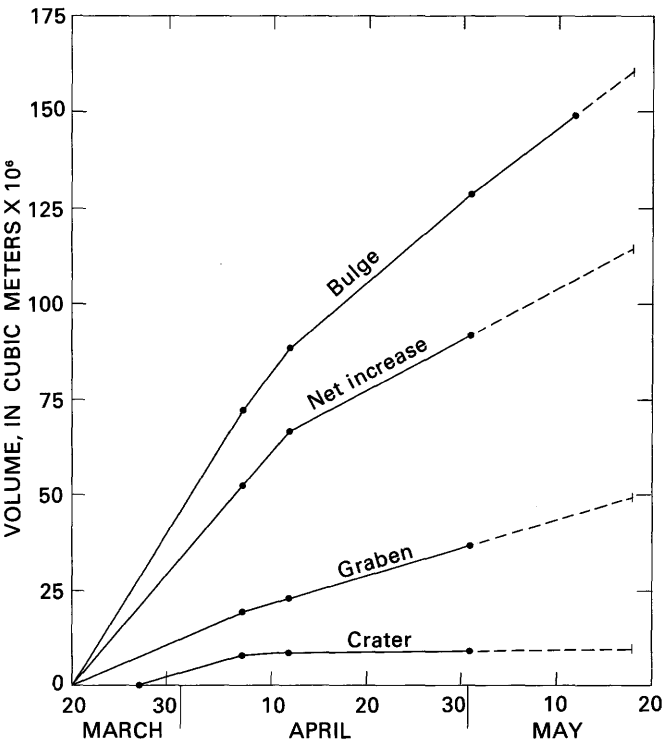

Figure 71.—Volume changes of Mount St. Helens, March 20 to May 18, 1980. Dashed lines are estimates (where features are not discernible on photos due to cloud cover).

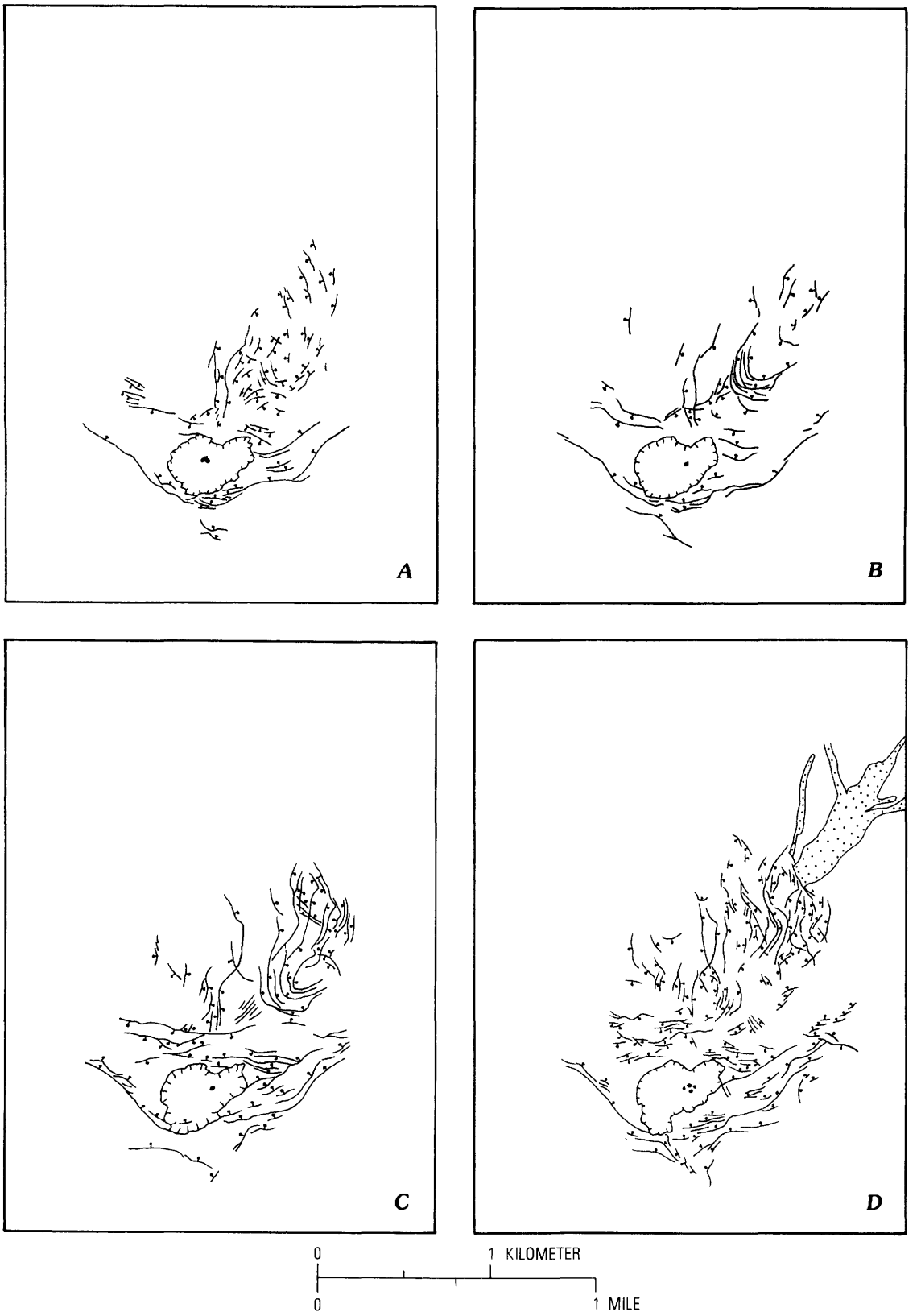

Figure 72.—Faults and fractures on north flank of Mount St. Helens; see figure 68 for location. Bar and ball on downthrown side of fault. A, April 7; B, April 12; C, May 1; and D, May 12, 1980. Dotted area is avalanche of May 12, 1980; black dots in crater are small lakes.

in diameter had developed immediately north of the graben. The long axis of the bulge crest was oriented northeast-southwest, oblique to that of the elongate crater and the graben. The apparent vertical displacement of both graben downward and bulge upward grew until the climactic eruption of May 18. The volume increase of the graben was about one-quarter that of the bulge (fig. 71) so that the net volume of the volcano increased. By April 7 the net increase in volume relative to August 1979 was 52×10^6 m^3, and by May 18, an estimated 114×10^6 m^3; the average rate of volume increase from April 12 to May 12 was 1.3×10^6 m^3/day. Contours of apparent elevation changes between maps (fig. 70) indicate that the north-south width of the graben grew from 360 m (from August 1979–April 7, 1980) to 600 m (May 1–12, 1980). The zero contour (boundary between downdrop of graben and uplift of bulge) migrated north at an average rate during this period of 8.6 m/day.

The initial area of greatest uplift of the bulge occurred in the south-central part adjacent to the northern boundary of the graben (figs. 70*A* and *B*). Projection of growth-rate curves backward in time suggests that the bulge may have begun growing no earlier than the beginning of seismic activity on March 20 (fig. 71); however, its early growth may have been more rapid than measured later, and it may have begun slightly before March 27, 1980, when growth was first apparent. The region of greatest uplift enlarged as the bulge developed, and the primary uplift moved north in concert with the expanding graben. In addition, a secondary mound developed 1 km to the northeast in the upper part of the combined Forsyth and Leschi Glaciers (figs. 70*B–D*). This secondary mound is believed to have been caused by very accelerated movement of ice due to oversteepening of the mountain, because on May 12 the lower part of it failed, producing the largest pre-May 18 avalanche, composed largely of ice (fig. 72*D*), and on May 18 large ice avalanches came from this region (figs. 74*B* and 75*B*). Further evidence that the northeastern mound was only surficial and not caused by a localized intrusion is the fact that it overlapped and lay partly northeast of the rim of the amphitheater produced by the landslide and explosions of May 18 (fig. 69).

The evolving pattern of faults and fractures was well established by April 7 (fig. 72*A*), with the largest fault marking the south side of the graben. This fault retained its position though other nearly parallel faults, also downthrown on the north, developed south of it (fig. 72*B*). However, north of the explosion crater, east-west fractures formed a widening band as the boundary of the graben migrated northward (fig. 72*C* and *D*). Also a zone of faults and fractures in ice and snow enlarged to the northeast as the combined Leschi and Forsyth Glaciers responded to bulge oversteepening before avalanching on May 12 (fig. 72*D*).

The increase in elevation of points within the bulge above the preexisting surface is the net effect of both absolute uplift and northerly horizontal movement. The rate of horizontal motion within the bulge was rather constant at 1.5–2.0 m/day as determined by geodetic measurements (Lipman, Moore, and Swanson, this volume). This rate is verified by the mapped displacement of Goat Rocks (the only readily recognizable mapped point), which moved 64 m in a N. 32° W. direction from April 7 to May 12, a rate of 1.8 m/day. Assuming a horizontal rate of 2 m/day and a slope of 30°, the amount of apparent vertical uplift should average about 2 tan $30° = 1.2$ m/day. Assuming uplift began March 20, 1980, the rate of apparent vertical uplift of the bulge at the point of greatest displacement at successive intervals was 5.6 m/day (fig. 70*A*), 4.3 m/day (fig. 70*B*), 2.6 m/day (fig. 70*C*), and 2.7 m/day (fig. 70*D*). Hence the high point of the bulge was generally rising above the mountain slope more than twice as fast as would have been expected from strictly horizontal motion. Roughly the upper half of the bulge was that part which underwent some absolute vertical uplift. No geodetic targets could be maintained in this part of the bulge because of its unstable character.

The behavior of the bulge and graben suggests that uplift of the south edge of the bulge resulted from growth and expansion of a shallow intrusion of magma (cryptodome) beneath the summit and north flank. The volume of the cryptodome attained 0.11 km^3 by May 18, equivalent to a sphere with a diameter of about 600 m. The top of the cryptodome apparently migrated north as it reached higher levels causing early uplift of a peak north of the graben. This area later subsided as a second peak further north became elevated (fig. 73). As the dome rose, it stretched and shouldered aside the area north of the summit, producing the graben, and it oversteepened the north flank, causing it to move north under the influence of gravity at a rate of 1.5–2 m/day (Lipman, Moore, and Swanson, this volume). The inferred

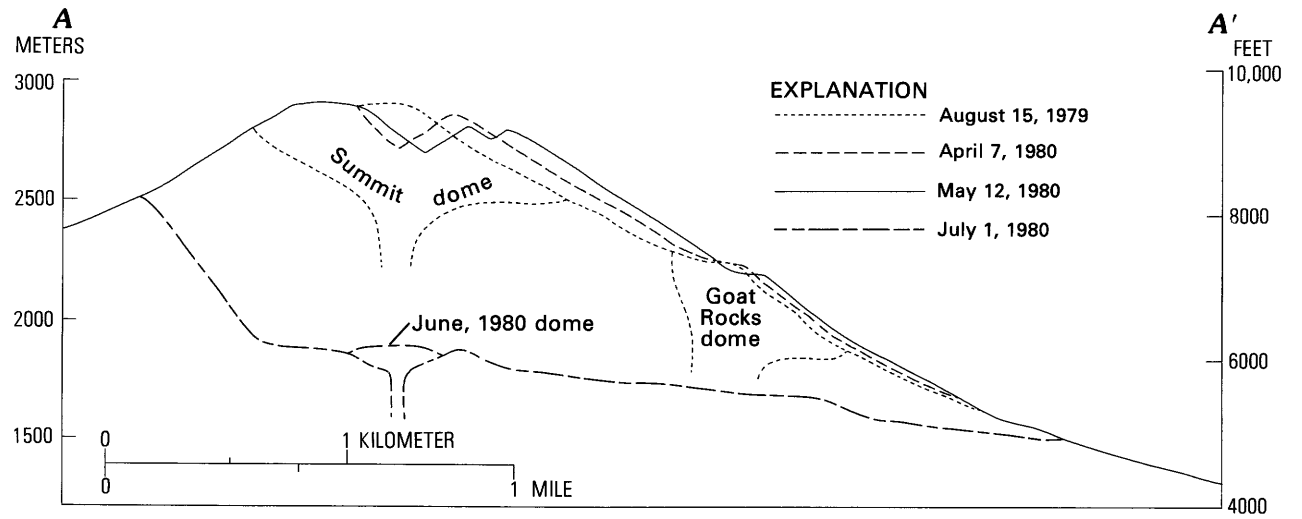

Figure 73.—South-north profiles of Mount St. Helens, August 1979 to July 1980. Scale slightly reduced from figure 68.

presence of a shallow dacitic cryptodome was later supported by the fact that fragments of fresh, originally hot dacite derived from it comprise a large proportion of the directed-blast deposits (Hoblitt and others; Moore and Sisson; Waitt, this volume). The cryptodome was apparently intruded beneath the large (1.2 km diameter), 16th–17th century dacite summit dome (fig. 68), which was funnel shaped and probably filled an earlier summit crater (C. A. Hopson, written commun., 1980). After stretching and splitting the summit dome, producing the graben, the cryptodome expanded northward beneath the summit dome, uplifting its north edge and producing the bulge.

EVENTS OF MAY 18

A significant photographic record was obtained by several observers from the ground and from the air during the early failure of the landslide. The photographs taken by Keith and Dorothy Stoffel from the air (Williams, 1980), by Gary Rosenquist from near Bear Meadow, 17 km northeast of the summit (Williams, 1980), and by Paul and Carol Hickson (written commun., 1980) from 15 km east of the summit are outstanding.

An analysis of the Rosenquist and Hickson photographs is aided by comparison with computer-generated perspective models (Dynamic Graphics, Inc., 1978) of preeruption and posteruption digitized maps as viewed from the camera stations (figs. 74*A* and *C* and 75*A* and *C*). This new technique permits

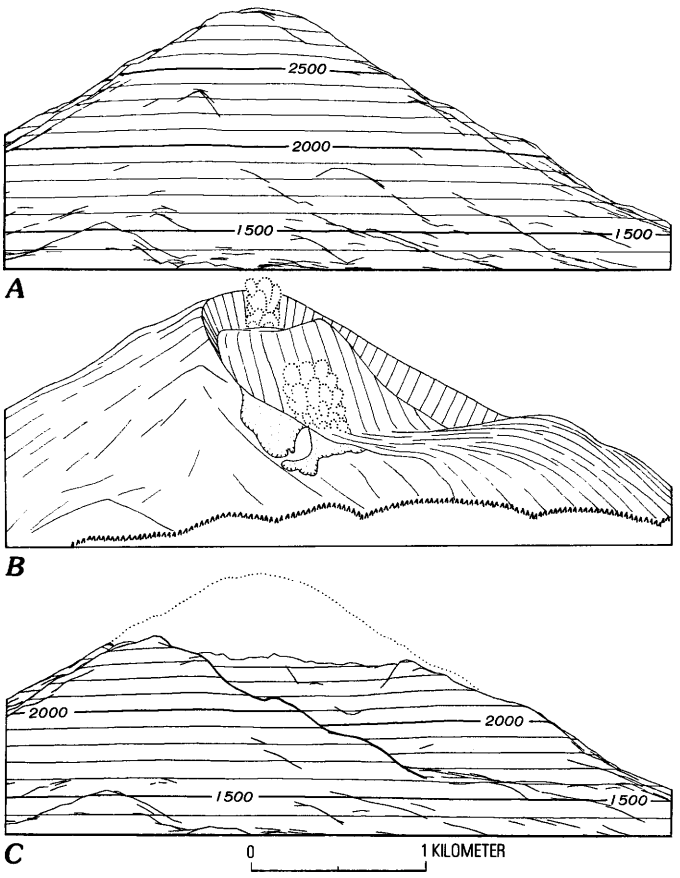

Figure 74.—Perspective views on various dates of Mount St. Helens from Bear Meadow, 17 km to the northeast. A, Computer-generated model showing topography, August 15, 1979. Contours in meters. B, Sketch from photograph by Gary Rosenquist at about 0832:35, May 18, 1980. Ice and snow avalanches shown by light-dotted pattern. C, Computer-generated model showing topography, July 1, 1980. Preeruption profile shown by dotted line.

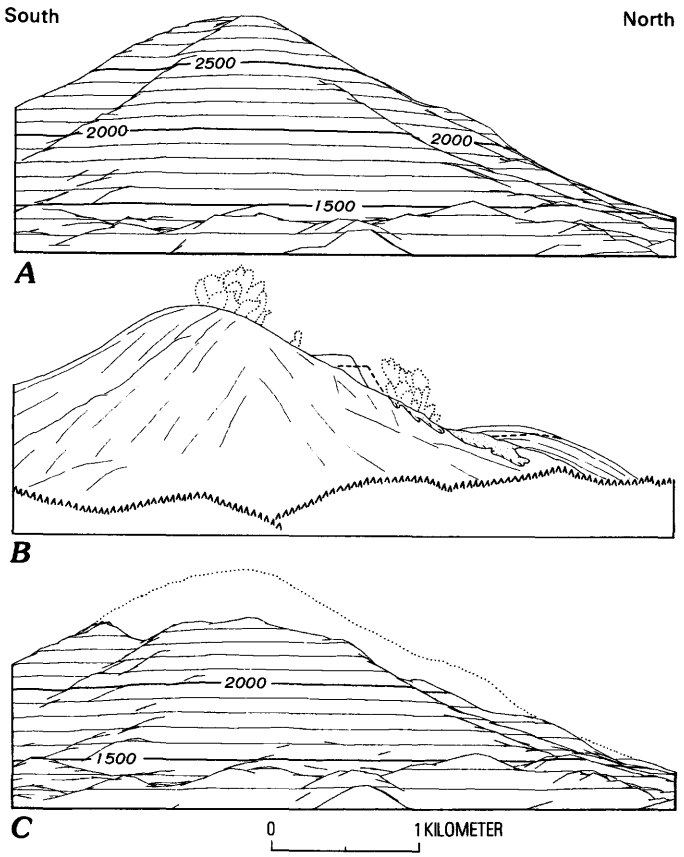

Figure 75.—Perspective views of Mount St. Helens from 15 km to the east. A, computer-generated model showing topography, August 15, 1979. Contours in meters. B, Sketch from photograph by Paul and Carol Hickson at about 0832:39, May 18, 1980. Dashed line, profile of landslide block in photograph 4 s later. Ice and snow avalanches shown by light-dotted pattern. C, Computer-generated model showing topography, July 1, 1980. Pre-eruption profile shown by dotted line. Scale is approximate.

reliable estimation of the elevation and position of features visible in the photographs.

The Stoffels, flying over the crater area in a light plane, witnessed several small ice-falls within the crater apparently triggered by the magnitude −5+ earthquake at 0832:11 PDT. About 15 s later they observed the north side of the summit crater begin moving north as a massive landslide. This landslide developed as two giant blocks (fig. 76; and Voight, this volume), here referred to as the bulge block (northern) and the graben block (southern), because they correspond to the regions of uplift and downdrop as defined in figure 70*D*. The headwall scarp of the bulge block developed slightly north of the north peak, and that of the graben block was about coincident with the main fault south of the crater (fig. 76).

The bulge block began dropping 8–10 s before the graben block, so that by the time the first Rosenquist photograph was taken 15–20 s after landsliding began (fig. 11-9*B*), the graben block had descended about 200 m and the bulge block, 650 m. (This timing of the Rosenquist photographs, slightly different from that of Voight (this volume), is based on an analysis by S. D. Malone, written commun., 1980.) At this time the headwall scarp between the blocks was 600 m high inclined 65°–70° to the north. The initial explosions began at this time near the base of the high headwall scarp of the bulge block at an elevation of about 2,200 m. By about 0832:43 PDT (fig. 76*C*) the graben block had descended a total of about 550 m, and the bulge block, 1,100 m, so that the headwall scarp between them was about 700 m high and its base was at an elevation of about 1,750 m. During this time vertical explosions began ripping out of the area of the old phreatic crater in the center of the graben block while those from the high headwall between the blocks intensified, involving the entire scarp. Subsequently these two explosion loci at the top and exposed north side of the graben block merged into a gigantic explosion buttressed on the south (fig. 76*C*). This eruption fed the north-directed blast that devastated the area to the north and deposited about 0.19 km^3 of ash and blocks, about half of which was hot, relatively dense dacite apparently derived from the cryptodome (Moore and Sisson, this volume).

Comparison of the pattern of surface deformation (figs. 70, 73) and the location of the 700-m-high landslide scarp between the graben block and the bulge block suggests that this scarp followed closely the north side of the cryptodome and possibly intersected a part of it (fig. 76). Removal of the bulge block by landsliding effectively exposed and depressurized the cryptodome and its surrounding hydrothermal system of superheated water. The water flashed to steam, and the dacite exsolved magmatic gases, producing the giant explosion.

The sequence of events that followed the downward movement of the graben block was obscured by eruption clouds that enveloped the mountain. Eventually, more of the central part of the mountain south of the graben block failed along successively more southern faults (or by piecemeal crumbling), and the fragments joined the landslide until much of the amphitheater crater was formed, and the main

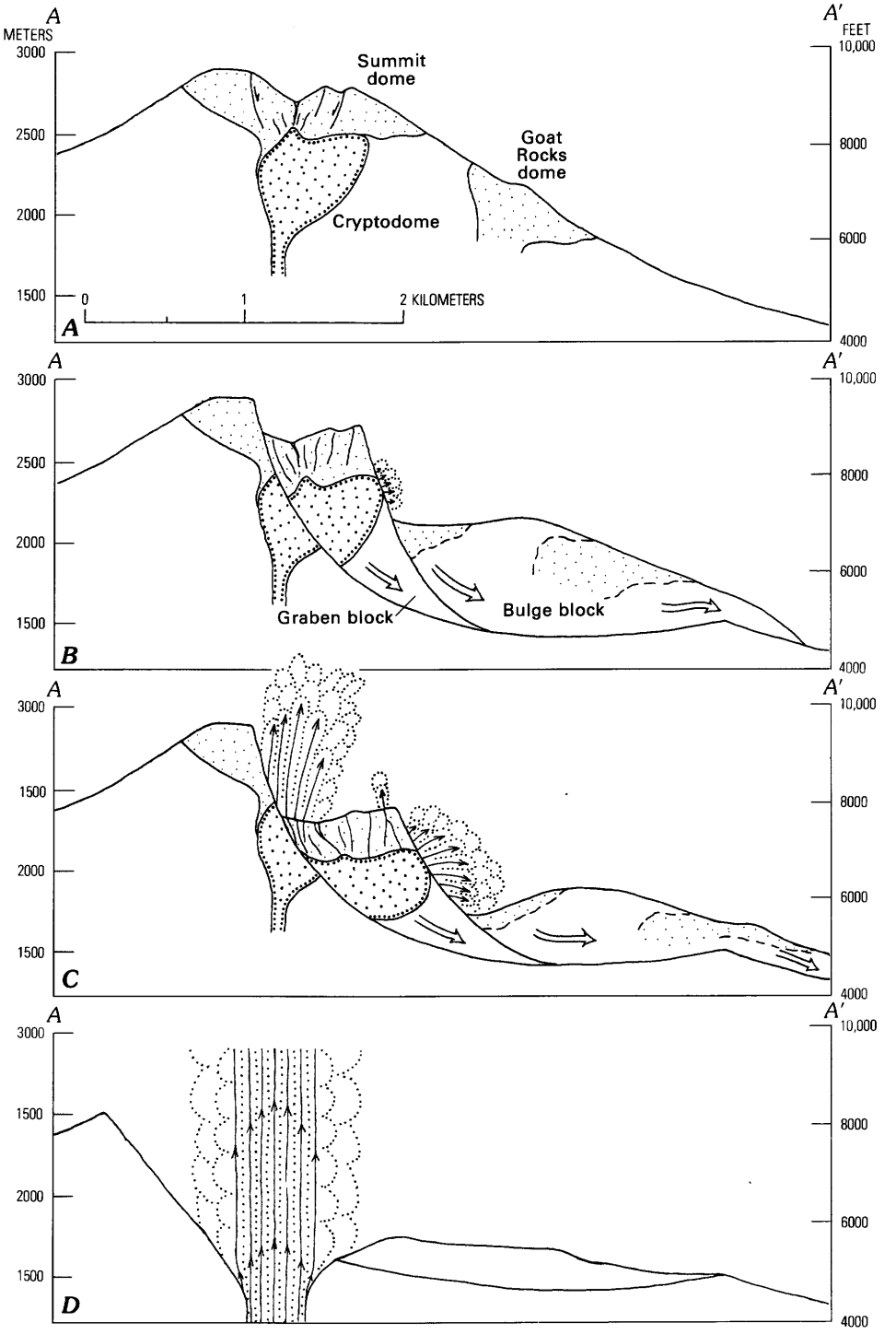

Figure 76.—Changes in profile of Mount St. Helens during morning of May 18, 1980, along line A-A' (see fig. 68). A, Before eruption, showing intrusion of cryptodome (heavy dotted pattern) beneath 16th–17th century summit dome (light-dotted pattern at summit). B, About 20 s after landsliding began showing development of bulge and graben landslide blocks; explosions have begun on headwall of bulge block where cryptodome is exposed in graben block. C, About 30 s after landsliding began, showing massive explosions from side and top of fractured graben block. D, After landsliding has exposed the main volcanic conduit from which a vertical eruption column rises to more than 20 km.

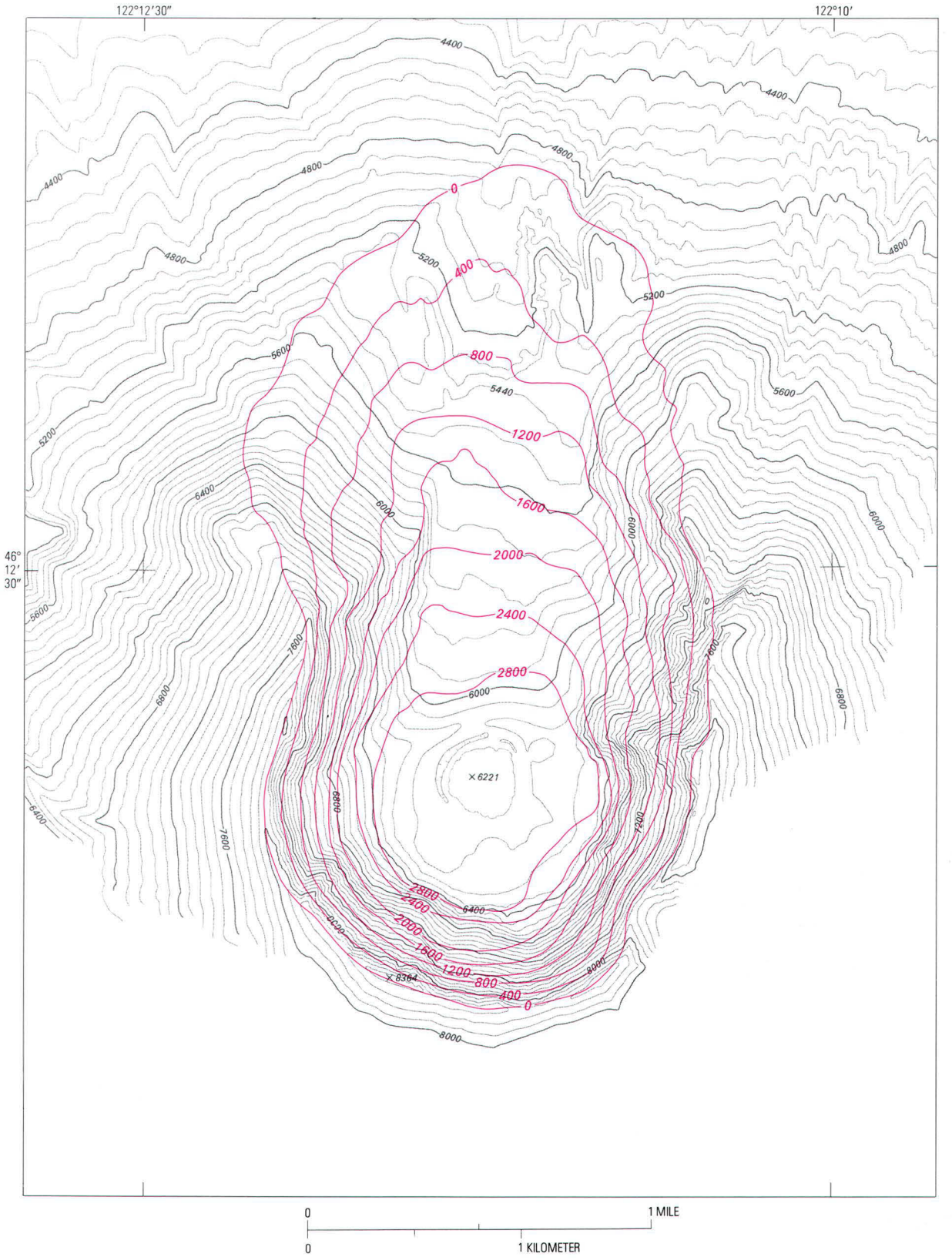

Figure 77.—Topographic map of July 1, 1980, showing elevation changes, in feet, between August 15, 1979, and July 1, 1980, and their relation to the topography after the May 18 eruption.

volcanic conduit was exposed more than 1 km deeper than prior to landsliding. The 25-km-high vertical eruption column which then developed was produced by magmatic explosions generated by reduction of confining pressure on the volcanic conduit as a result of the removal of this extraordinary amount of cover rock (fig. 76*D*).

AFTER MAY 18

The map generated from July 1 aerial photography (fig. 77) indicates that, with the new amphitheater-shaped crater, the height of the mountain was reduced from 2,950 m (9,677 ft) to 2,549 m (8,364 ft). Comparison of contours between the maps of August 15, 1979, and July 1, 1980, indicates that the volume of rock and ice of the volcano above the 4,800-ft contour was 2.62 km^3 less than in 1979. However, because the mountain had increased in volume 0.11 km^3 from 1979 to May 18, 1980, a total of 2.73 km^3 was removed on May 18, most of which was deposited in the landslide-debris avalanche.

The new amphitheater-shaped crater is nearly precisely the width of the mapped bulge but extends 0.5 km north of the previous northern bulge limit. The crater is 2 km wide and 3.9 km long and extends in a northerly direction. The northern limit of the crater is well defined, because the 4,400- and 4,800-ft contours are virtually unmodified (figs. 68 and 77). Despite the fact that about 2.5 km^3 of landslide rubble passed over this region, little erosion or deposition took place. This fact places a northern limit on the slip surface bounding the base of the landslide mass. The position of the base of the slip surface (fig. 76) can be estimated from its northern extent, from the height and angle of the headwall scarps as determined from the Rosenquist photographs (fig. 74*B*), and from the nature of movement of the graben block as seen in the Hicksons' photographs (fig. 75*B*). (Compare figs. 6 and 9.) The loft imparted on the landslide mass as it left the amphitheater may have been what prevented significant erosion or deposition until deposition began 2 km to the north.

Subsequent to May 18, moderate explosive eruptions and small ash flows occurred on May 25, June 12, July 22, August 7, and October 16–18. The June, August, and October events produced small dacitic domes all with volumes of less than a few million cubic meters (Moore and others, this volume). The location of the primary vent as defined by the location of the post-May 18 domes (figs. 73 and 77) lies directly below the center of the pre-May 18 phreatic crater.

REFERENCES CITED

Dynamic Graphics, Inc., 1978, User Manual for the Surface Display Library: Berkeley, Calif., Software Development Group, Dynamic Graphics, Inc., 2150 Shattock Avenue, pages unknown.

Williams, Chuck, 1980, Mount St. Helens, a changing landscape: Portland, Oregon, Graphic Arts Center Publishing Company, 128 p.

TOPOGRAPHIC CHANGES AT MOUNT ST. HELENS: LARGE-SCALE PHOTOGRAMMETRY AND DIGITAL TERRAIN MODELS

By RAYMOND JORDAN *and* HUGH H. KIEFFER

ABSTRACT

A topographic map of Mount St. Helens was made from aerial photographs of August 5, 1972; scale is 1:10,000, contour interval 10 m. Additional contours on the same map show topographic changes as of four dates in April and May 1980, before the major eruption of May 18. Corresponding digital terrain models have also been prepared; these have been used to quantitatively determine topographic changes and to create terrain-difference models for the time from March to mid-May. The increase in net volume of the mountain in the spring of 1980 prior to May 18, because of changes of the bulge and graben areas, is estimated as 0.116 km^3. Digital terrain models were processed to produce shaded-relief images of the topography of the summit and north flank of the volcano. By subtracting a digital terrain model of one date from that of another date, terrain-difference models were obtained and were used to calculate volume change. The entire map, too large to be included here, is available as a separate publication (Jordan and Kieffer, 1981).

ACKNOWLEDGMENTS

We would like to acknowledge the outstanding cooperation of the people who contributed to this work. We thank Jim Walker, Washington State Department of Transportation, who supplied us with complete sets of aerial photos taken by that department; Bob Fox, U.S. Forest Service, Portland, Oreg., who supplied the 1972 photographs and control; and Hugh Thomas and Ray Sabala for their assistance in preparing this unusual map for publication. We especially appreciate Kay Edwards' efforts in production of the digital terrain models and processing of the digital data.

DISCUSSION

After the initial 1980 eruption and apparent topographic changes of Mount St. Helens, detailed topographic mapping was needed to determine where changes had occurred, and the rate and magnitude of those changes. For mapping of the preeruption volcano, we used U.S. Forest Service photography at a scale of 1:60,000 obtained on August 5, 1972 (F70 53059 172, frames 45 and 46). Because no surveyed control points on the ground were available at the time of map compilation, we used photogrammetrically derived control for establishing a stereomodel of frames 45 and 46. The absolute accuracy of the mapping was therefore less than desirable, but accuracy was adequate because we were looking for relative changes.

We then established a stereomodel from frames 45 and 46, using our computer-operated AP/C analytical stereoplotter and six photogrammetrically derived initial control points. The residual error of the adjustment (about 1 m) was well within our requirements. The stereoplotter was then used to derive a much higher density of secondary control points.

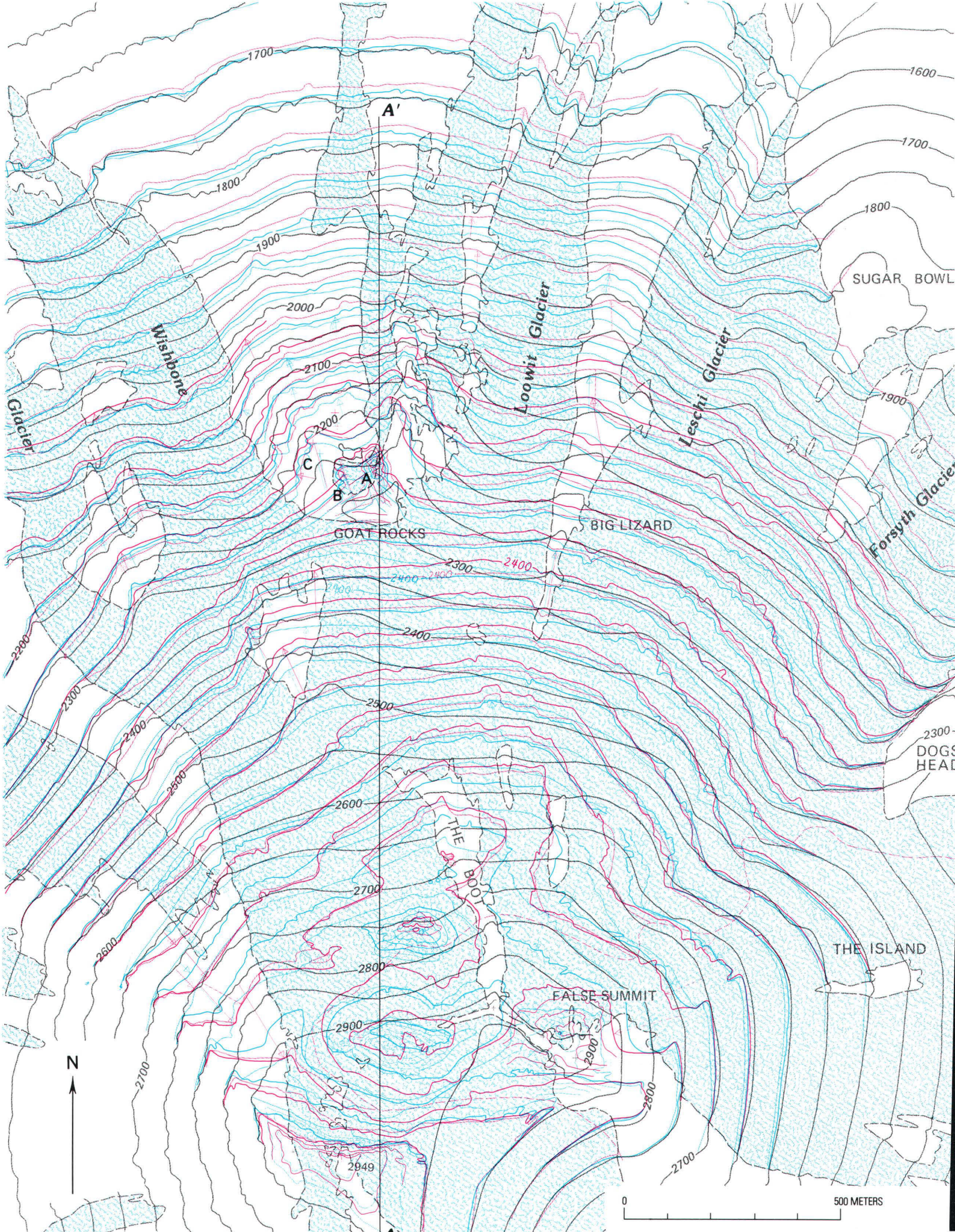
A'
1700
1600
1800
1700
1900
1800
2000
2100
2200
1900
C
A
B
2300
2400
2400
2400
2200
2300
2400
2500
2600
2700
2600
2800
2900
2900
2800
2700
2949
Wishbone Glacier
Loowit Glacier
Leschi Glacier
Forsyth Glacier
SUGAR BOWL
GOAT ROCKS
BIG LIZARD
DOGS HEAD
THE BOOT
FALSE SUMMIT
THE ISLAND
N
0
500 METERS

These points were used later for control and orientation of photographs at a scale of 1:40,000, taken on several occasions between the initial eruption and May 18.

Many problems were encountered in the selection of the initial control points. No good "hard" features on the ground, such as road intersections, occur in the area mapped. Also, since the 1972 photography, some obvious changes on the mountain flanks had occurred, such as extensive clear-cutting of trees. Where possible, control points on bedrock were chosen, but because many more points were needed, we chose others at the most distinctive contacts visible between snow and rock. This latter procedure yielded uncertain results because of both the variable positions of the margins of the snowfields over almost 8 yr and the rapid melting of the snow in some areas during the eruptive phase. Another unusual problem was caused by fallen ash after an eruption. Locally, the ash made snow-covered areas darker than exposed rock—actually creating a complete tone reversal from other photographs. Moreover, in some of the pictures, clouds, ash plumes, and haze partly or totally obscured ground features. With these problems in mind, we used the largest possible number of control points in establishing the post-March 27 stereomodels. The computer adjustment and residual errors indicated points with serious problems, and these points were excluded from the final adjustments.

Because digital output was desired, another stereomodel was established on our AS11-AM analytical stereoplotter from 1972 frames 45 and 46. From this model, we compiled a preeruption map at a scale of 1:10,000 with a contour interval of 10 m. This plotting system automatically digitized the contours during compilation at a collection interval of 200 μm (micrometers) at the scale of the photographs. Because we considered the extent of bare rock at the time the photographs were taken critical for our purposes, our map shows more extensive snowfields than the 1958 15-minute Mount St. Helens topographic quadrangle map. We also digitized the location of snow-covered areas so that we could assign different weight to the digital data for rock and snow areas.

The next step was to determine the areas that had changed topographically between 1972 and the major blast on May 18. On the latest available photography at an appropriate scale before May 18, taken at 1100 PDT on May 16 (EG & G roll 3214, frames 49 and 50), the lower part of the volcano was obscured by cloud cover. Photographs on May 12 showed all of the volcano except for a small part of the summit area obscured by a plume. Using both sets of photographs, we compiled topographic data at 1:10,000 scale with a contour interval of 50 m. This mapping was compared to the preeruption map derived from the stereomodel and, within the limits of measurement accuracy and repeatability, the areas of change were delineated, and the topography in these areas was contoured at 10-m intervals. Mappable changes had occurred only at the summit and on a bulge on the north flank; the greatest displacement in the bulge by May 16 was approximately 80 m laterally.

Next, we determined incremental changes between March and mid-May. The State of Washington Department of Transportation had obtained aerial photographs over the mountain every 3 days, weather permitting, beginning in early April 1980. The following photographs were used to produce new contour lines that show the incremental changes in the topography:

Photography	*Date*	*Days since previous flight*
Flight 4, photographs 22 and 23	April 11	--
Flight 11, photographs 53 and 54	May 1	19
Flight 13, photographs 62 and 63	May 12	11
EG&G 3214, photographs 49 and 50	May 16	4

Figure 78.—Summit and north flank of Mount St. Helens showing changes in topography between April 11 and May 16, 1980; contours for April 11 shown in blue; May 1, light blue; May 12, light red; May 16, red. Contour interval 50 m, locally supplemented by 10-m contours. Scale 1:10,000 (approximately 6 in. to the mile). Topography shown in gray compiled from photography of August 5, 1972; contour interval 10 m. Local high and low points are shown by small colored crosses; colored crosses with tails show direction and amount of horizontal displacement of identifiable ground features from their original positions. Colored vectors indicate direction and amount of horizontal displacement of specific points on contour lines (dashed where only connecting two contours of the same value). That part of summit area obscured by plume on May 12 photographs (dashed light-red line) was mapped using May 16 photographs. Cross section A-A' shown in figure 82.

This new contouring was then composited with the preeruption map, showing the changes and rates of change (fig. 78). Approximate vectors were drawn on the map connecting identifiable points on the preeruption contour lines with corresponding points on the new contours. To minimize clutter, only a few of the 10-m contour lines are shown on the composite map, although all the contour lines were useful to help determine changes.

During map compilation, several features on the volcano were noted that might warrant further analysis with a stereoplotter; these included fractures, ice

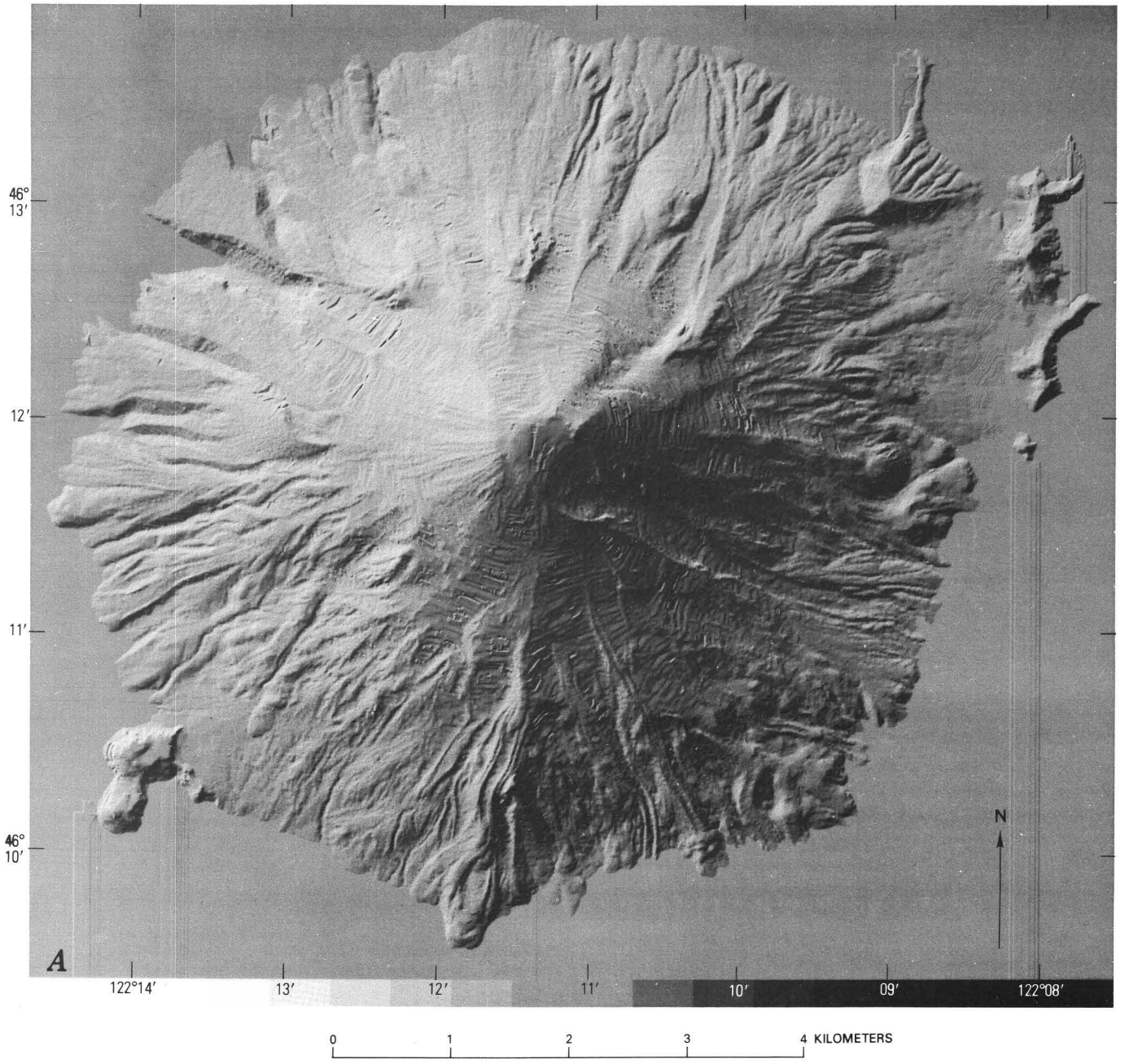

Figure 79.—Computer-generated shaded-relief images of filtered digital terrain models of volcano. Data were filtered by averaging pixel values over 3×3 areas. Increased uncertainty of contour location within snowfields appears as terraces (in southeast) and crevasses (in northwest). A, model from photographs of August 5, 1972; B, model from photographs of May 12 and 16, 1980. Small discontinuity just south of Dogs Head is an artifact of the join between May 12 and May 16 digital terrain models.

and snow thicknesses where cracks in the glaciers reveal bedrock below, changes in texture of rock and ice on the bulge, and differences in snow condition and runoff.

In order to produce a digital terrain model, the three-dimensional coordinates digitized during map compilation were transferred by magnetic tape to the U.S. Geological Survey Flagstaff Image Processing Facility. Raster images of the contour lines were made with a resolution of 5 m per pixel (picture element). The resulting raster image of contour lines, approximately 2,000 pixels square, was filled in by broadening individual contour lines until they met, and generating an intermediate contour level at their intersection. This process was repeated until no picture elements were unassigned, thus generating a full elevation array on the digital terrain model.

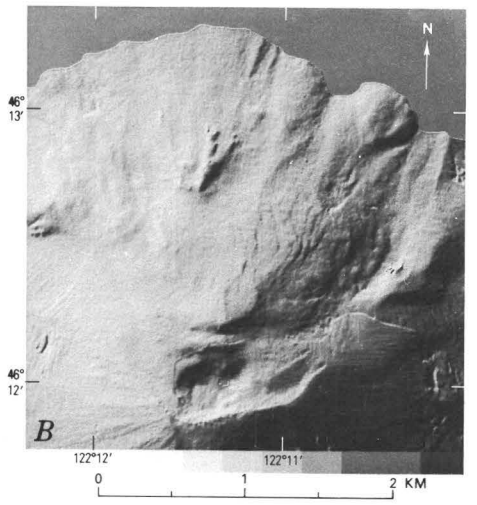

This procedure differs from conventional topographic mapping in that no hand-editing of any kind is done to the position of the contour lines. In areas where the positional uncertainty exceeds the contour interval, contour lines may actually cross. This problem is particularly noticeable within large snowfields that have no identifiable surface features. The digital terrain model can be cosmetically improved by use of a 3×3 pixel (15 m square) low-pass filter that replaces each pixel with the average of nine pixels in the original array. This process has no effect in areas of uniform slope; it tends to subdue the topography slightly in areas of rapid slope changes, and it is particularly effective in removing the slope reversals due to erroneous contour crossing. The preeruption digital terrain model, filtered in this manner, was processed to produced a shaded-relief image of the topography (fig. 79).

As mentioned previously, during the last few days before May 18, suitable photography could rarely be obtained without the presence of some atmospheric obscuration. In order to construct as complete a digital model as possible for a late date prior to May 18, the digital terrain data for May 16 were used to fill in the region obscured on May 12; the resulting composite is called the May 12/16 model.

The changes in elevation and thus changes in volume could be automatically determined by simply subtracting the digital terrain model for one date from that of another. From these terrain-difference models, a map was produced to show the changes from pre-1980 to May 12/16 (fig. 80). The total volume change can be computed directly by summing over all the elements of the elevation-difference array. This automatic processing of elevation data renders obvious the major topographic variations: the large apparent upward motion of the surface of the upper Forsyth Glacier, subsidence of the large graben across the summit area of the mountain, and the northwest displacement and small vertical change in the Goat Rocks area. Topographic change between pre-1980 and April 11 and from April 11 to May 12/16 are shown in figures 81*A* and *B*, respectively. The bulging of the north side of the mountain and the graben formation at the summit can be seen in both images. Over the second period, the response of the Forsyth Glacier to initial oversteepening can be seen as a relative increase in elevation (actually, largely lateral motion of a sloping surface) of the lower part of the glacier.

The general unreliability of control points on the upper parts of Mount St. Helens resulted in apparent elevation changes of several meters in areas that surveying indicated to be stable in April and May (Lipman, Moore, and Swanson, this volume). In order to correct for these errors in the photogrammetric models, the apparent elevation changes were determined along a line surrounding the area of definite topographic change (fig. 80). The mean and standard deviation of the differences between digital terrain models for this line of about 1,500 points are:

1972 to April 11, 1980: $+1.2 \pm 11.2$ m,
1972 to May 12/16: $+1.3 \pm 7.9$ m.

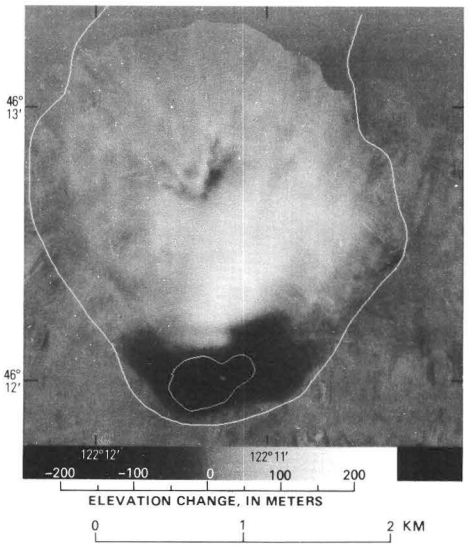

Figure 80.—Computer-generated elevation-difference image showing total elevation changes, in meters, from 1972 to May 12/16, 1980. Elevation change along outer line was assumed to be negligible for purposes of computing volumes from digital terrain models. Inner line indicates approximate boundary of summit crater.

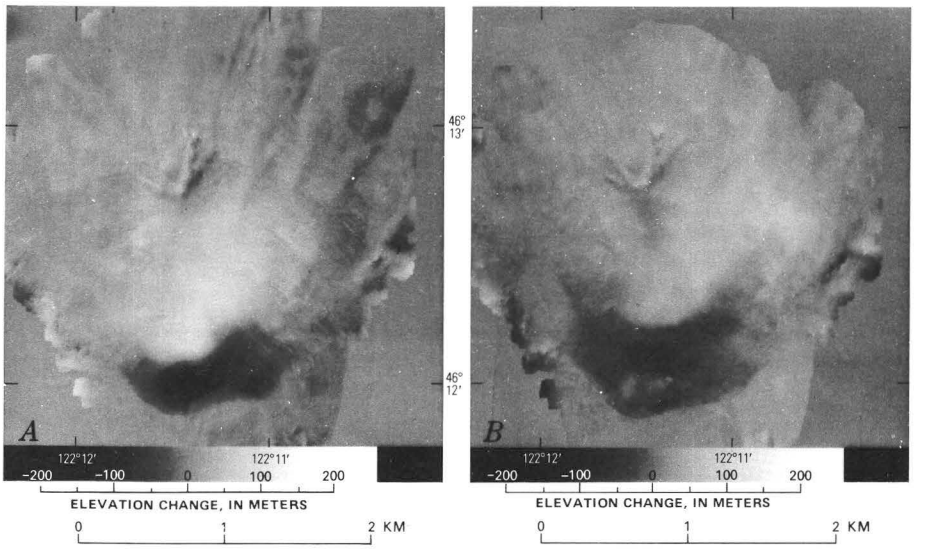

Figure 81.—Computer-generated elevation-difference images produced by subtraction of digital terrain models. A, April 11, 1980, minus August 5, 1972. Shows development of north peak 1. B, May 12/16 minus April 11, 1980. Development of north peak 2 during this period is shown as a second area of elevation increase north of the graben.

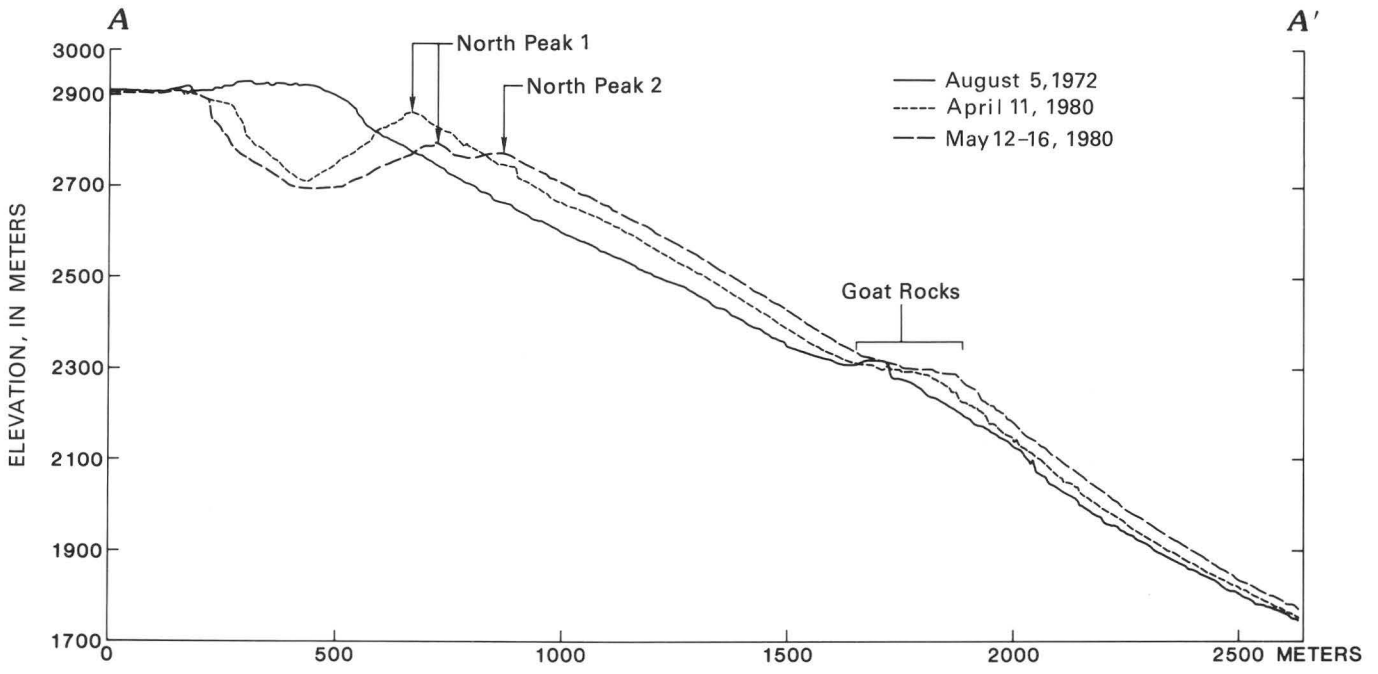

Figure 82.—Cross section A-A' showing change in topography from 1972 to May 12/16, 1980. Line section shown in figure 78. Topography was produced from digital terrain models. Profiles are to scale.

For volume calculations these mean values were subtracted from the terrain-difference models. The total change in volume of Mount St. Helens from before the eruption to May 12/16, 1980, is estimated as 0.116 km^3; this includes the change in volume of snow and ice (if no correction were made corresponding to the apparent elevation change for the line around the bulge, the computed volume change is 0.124 km^3). From 1972 to April 11, 1980, net volume of the volcano increased by 0.055 km^3, with areas of elevation increase accounting for 0.092 km^3 and areas of subsidence and crater formation accounting for 0.037 km^3 (of which, the volume decrease within the crater area as outlined in fig. 80 was 0.017 km^3). From April 11 to May 12/16, 1980, the corresponding change was a net increase of 0.061 km^3 (upward +0.077 km^3, downward -0.015 km^3, of which the crater was -0.006 km^3). A refined measure of changes in bedrock volume relative to 1972 is possible by determination of elevation changes of rock areas only, with interpolation across the snowfields.

Profiles along a north-south line through the center of the area of change (fig. 82) show the progressive enlargement of the crater, the development of north peaks 1 and 2, and the essentially horizontal displacement of Goat Rocks.

One shortcoming of both a topographic map and a digital terrain model in quantifying the changes at Mount St. Helens is their inability to distinguish between lateral and vertical motion in areas of uniform slope. To determine unambiguously the actual surface displacement, the three-dimensional positions of individual features were determined during compilation of each of the maps. These positions can then be subtracted, yielding a three-dimensional displacement vector over the time between successive aerial photographs. Extreme changes in surface contrast due to the eruptions, ash fall, snowfall, and sublimation seriously limited the number of points for which reliable three-dimensional positions could be determined on the different photographs. Three recognizable points in the Goat Rocks area (see table 7) were displaced 52.8, 60.0, and 61.0 m toward N. 20° W. at an average, nearly steady rate of 1.87 m/day (April 11 to May 12). The average elevation change of these points was subsidence of 3.1 m during this same period.

Table 7.—Displacement (in meters) of identifiable points in the Goat Rocks area relative to their positions on April 11, 1980

[Points A, B, and C are shown on fig. 78]

	Displacement			
Point	East	North	Vertical	Net
	May 1, 1980			
A	-9.5	3.0	-3.1	9.9
B	-13.9	24.8	-0.6	28.4
C	-16.7	34.0	-3.3	37.9
	May 16, 1980			
A	-20.6	48.7	-4.3	52.8
B	-15.1	59.1	-0.8	61.0
C	-19.9	56.6	-4.3	60.0

REFERENCE CITED

Jordan, Raymond, and Kieffer, H. H., 1982, Topographic map of Mount St. Helens, Washington, showing changes between April 11 and May 16, 1980: U.S. Geological Survey Miscellaneous Investigations Series I-1411, scale 1:10,000.

THE 1980 ERUPTIONS OF MOUNT ST. HELENS, WASHINGTON

BULGING OF THE NORTH FLANK BEFORE THE MAY 18 ERUPTION—GEODETIC DATA

By PETER W. LIPMAN, JAMES G. MOORE, *and* DONALD A. SWANSON

ABSTRACT

Geodetic measurements of ground deformation on the relatively inaccessible upper slopes of Mount St. Helens were begun in mid-April 1980 to evaluate deformation of bedrock after increased crevassing of glaciers had become visually obvious. Every 1–3 days, weather permitting, horizontal and vertical angles were measured by theodolite to as many as 19 unmanned, fixed targets; slope distances were measured by electronic laser instruments. The combined readings permitted calculation of displacement vectors for each target. Results from April 23 through May 18 indicated startlingly rapid movement of the north flank at remarkably constant rates. Targets within an elliptical bulge, approximately 1.5 by 2.0 km in area, showed subhorizontal northerly movements of 1.5–2.5 m/day. The last measurements were made by David Johnston only 90 min before the May 18 eruption. Boundaries of the bulge were relatively abrupt, as indicated by decreases in displacement rates by two orders of magnitude within distances of 0.5 km away from the bulge, and coincided closely with northern margins of the crater resulting from the May 18 explosion. Nearly continuous movement within the bulge was documented by measurements at 15-min intervals over one 8-hr period, without clear correlation with major earthquakes. The subhorizontal nature of displacements, despite slopes averaging 25°–35° within the area of the bulge, was interpreted early as indicating intrusion of magma. The resultant oversteepening of slopes within the area of the bulge was recognized as posing a major hazard to the north flank from gravitational failure and landsliding. These results contributed to assessments by USGS personnel in late April and early May that Mount St. Helens remained highly dangerous despite the seemingly mild small-scale phreatic eruptions that were then the most conspicuous activity.

INTRODUCTION

Topographic and structural changes were evident at the summit of Mount St. Helens as early as March 27, when phreatic eruptive activity began. In addition to development of a new crater, the summit area was bisected by an east-trending fracture system, 2 km long, that defined an irregular graben. The area north of the graben appeared to be bulging outward and possibly upward. At first, the obscuring effects of heavy and continuing snow cover, interlayered with ash deposits from the phreatic eruptions, made it uncertain whether the graben and associated fractures involved the bedrock edifice or mainly reflected melting and increased movement on the summit ice cap. Frequent eruptions and poor weather also precluded direct ground examination of these features in early April, and initial attempts to obtain quantitative data on deformation related to the volcanic activity were accordingly confined to tilt measurements on the lower flanks and beyond the base of the volcano.

By mid-April, the bulge had become ominous, and there was increasing concern for stability of the north flank of the volcano. Aided by the temporary cessation of eruptive activity and with arrival of the required equipment, we then established a network

for ground deformation measurements on the cone (fig. 83). Within a few days, these measurements yielded clear evidence of large-scale northwesterly movements of the bulge area, at rates of as much as 2.5 m/day. Concurrently, the first detailed photogrammetric measurements revealed that the bulge had moved upward and outward as much as 100 m between August 1979 (the last preeruption vertical photography) and April 12, 1980 (Moore and Albee, this volume). The geodetic data, which provide details of deformation rates, and the photogrammetric results, which better define the overall geometry of the deformation, are complementary.

The growth of the bulge was inferred to record emplacement of magma into the volcanic edifice, and emplacement of a lava dome was anticipated because several other domes had been emplaced asymmetrically on the north half of the volcano in the last few thousand years (Mullineaux and Crandell, this volume). In late April and early May, results from the geodetic and photogrammetric studies confirmed that gravitational failure and landsliding of the bulge area were likely, and we hoped that changes in deformation rates could be observed as indications of imminent failure. Unfortunately, no such changes took place. Nevertheless, these studies helped convince State and Federal officials to maintain closure of the north side of the volcano to public access (Miller and others, this volume).

ACKNOWLEDGMENTS

We thank Ronald Gordon, Arnold Okamura, and Norman Banks for much assistance in constructing geodetic targets, making measurements, and reducing

Figure 83.—Theodolite station at Timberline Viewpoint, at 1700 PDT, May 1, 1980. The afternoon low sun angle enhances visibility of the bulge on the upper Forsyth Glacier area. Named features, indicated by X, are sites of geodetic reflector targets. Dashed line indicates approximate limits of deformed area and of rock subsequently removed during the May 18 debris avalanche and lateral volcanic blast.

the data. Helicopter pilot Lon Stickney (Aerocopters, Inc.) provided skillful service and accurate observations of activity. John Estrem and Dave Reneau, of the National Center for Earthquake Research, installed the dry-tilt stations, made many of the tilt measurements, and helped arrange loan of other surveying equipment. Dan Johnston and John Faustini, students at the University of Puget Sound, helped find the benchmark at Smith Creek Butte beneath 2 m of snow—the proverbial needle in a haystack. Al Eggers (University of Puget Sound) directed installation of initial spirit-level tilt stations, freely shared information, and was a cheerful companion during the March and April foul weather. The last measurements prior to the May 18 eruption were made by David Johnston, our close friend and a superb scientist.

INITIAL TILT OBSERVATIONS

In late March and early April, when we were prevented from doing geodetic work on the upper cone, several types of measurements were undertaken to measure tilt on the lower flanks and around the base of the volcano. In addition to deployment of three continuously recording platform tiltmeters (Dvorak and others, this volume), the ice-covered surface of Spirit Lake was utilized as a large liquid tiltmeter, and two spirit-level triangles were established on the north slope of the volcano at the parking lots for the Timberline and Spirit Lake campgrounds. The changes observed by these methods were mostly small, however, and partly inconsistent.

The tilt measurements on Spirit Lake were useful, because they permitted early evaluation of the size of the magmatic system developing within Mount St. Helens and because they could be made during poor weather. The observational procedure was simple. Cheap wooden yardsticks were nailed to stable objects (such as tree stumps or dock piers) around the lake shore at six sites where open water was present. Water levels at these sites were read in rapid succession, typically within about 20 min, and differences calculated. The ice cover over most of the lake damped wave oscillations, and values could typically be read to 1/16 of an inch (about 2 mm). Because the east and west arms of Spirit Lake are nearly radial to the volcano and as much as 3 km long, changes could be observed to within about 1 part in 500,000, equivalent to a tilt of within 2 μrad (microradians). No significant tilts were observed, however, indicating that no deformation related to the Mount St. Helens activity extended out this far; accordingly, by comparison with deformation geometry observed at other volcanoes (Kinoshita and others, 1974), the source of deformation at Mount St. Helens was either small or shallow. After mid-April, the observations were complicated by melting of the ice cover on the lake, and could only be made infrequently when the air was calm.

Two spirit-level tilt stations (Kinoshita and others, 1974) were also established on the northeast flank of the mountain in late March and early April, with the assistance of John Estrem and Dave Reneau, at sites of earlier temporary stations installed by Al Eggers (University of Puget Sound). A Zeiss Ni-1 level and Kern rods and stayers were used for the measurements. One station, in the parking lot of the Spirit Lake campground, was occupied only once and was to be reoccupied if the lake surface or the other spirit-level station showed a large cumulative tilt. The second station, in the parking lot of the Timberline campground, was occupied seven times between March 30 and April 30, and showed a generally consistent tilt of about 2 μrad/day, down to the northeast away from the volcano. Early in April, the significance of the spirit-level tilt results at Timberline was obscured by discrepancies with an adjacent platform tiltmeter (which turned out to have electronic problems); interpretations were further confused by large, short-term changes in tilt. By the end of the month the significance of this tilt was clear and was believed to reflect marginal deformation related to growth of the bulge.

The short-term changes in tilt were initially manifested in poor instrument closures during early attempts to measure the spirit-level tilt station at Timberline. Such poor closures were at first feared related to bad reading conditions (cold temperatures, high winds, snow, and sleet), unstable setups, or instrumental problems; but rapidly repeated observations and reversed directions of sighting convinced us of real deformation. We then began to monitor a 40-m line every minute or less for several hours at a time; significant changes were noted within periods of a few minutes. A triangle with short (14 m) legs was then established to minimize reading errors, and tilts in both inflationary and deflationary senses of as much as 50 μrad/hr were measured. Tilt vectors

consistently pointed either from or toward the Goat Rocks area, not the summit crater. On April 10, the bulls-eye bubble, used for crude leveling of the instrument, even moved off center as we watched it, and during the following 3.75 hr, two periods of inflation and one of deflation were recorded (fig. 84).

Most felt earthquakes had no obvious effect on the tilt pattern, but one earthquake on April 10 correlated with a change from inflation to deflation. During some of the monitoring experiments, inflation occurred before phreatic eruptions, and deflation during them, but this was not a consistent pattern.

West and others (1981) observed similar periods of large, rapid, complex tilts during the phreatic eruptive activity of La Soufriere on Guadaloupe in 1976. These workers ascribed the tilts to rapid pressurization by "phreatic fluids" transported by hydraulic fracturing and to flow through porous media. Such may have been the case at Mount St. Helens, too, although the consistent orientation of short-term tilt vectors toward or away from the center of the growing bulge suggests that the tilts could have been recording episodic movement of the intruding magma beneath the bulge.

GEODIMETER AND THEODOLITE MEASUREMENTS

By mid-April, the various types of tilt measurements taken low on the volcanic edifice seemed to be indicating only small and rather inconsistent long-term patterns of deformation. Yet the bulge high on the north slope was appearing increasingly visually ominous (fig. 83), adding to concerns about the gravitational instability of this area. Accordingly, a logis-

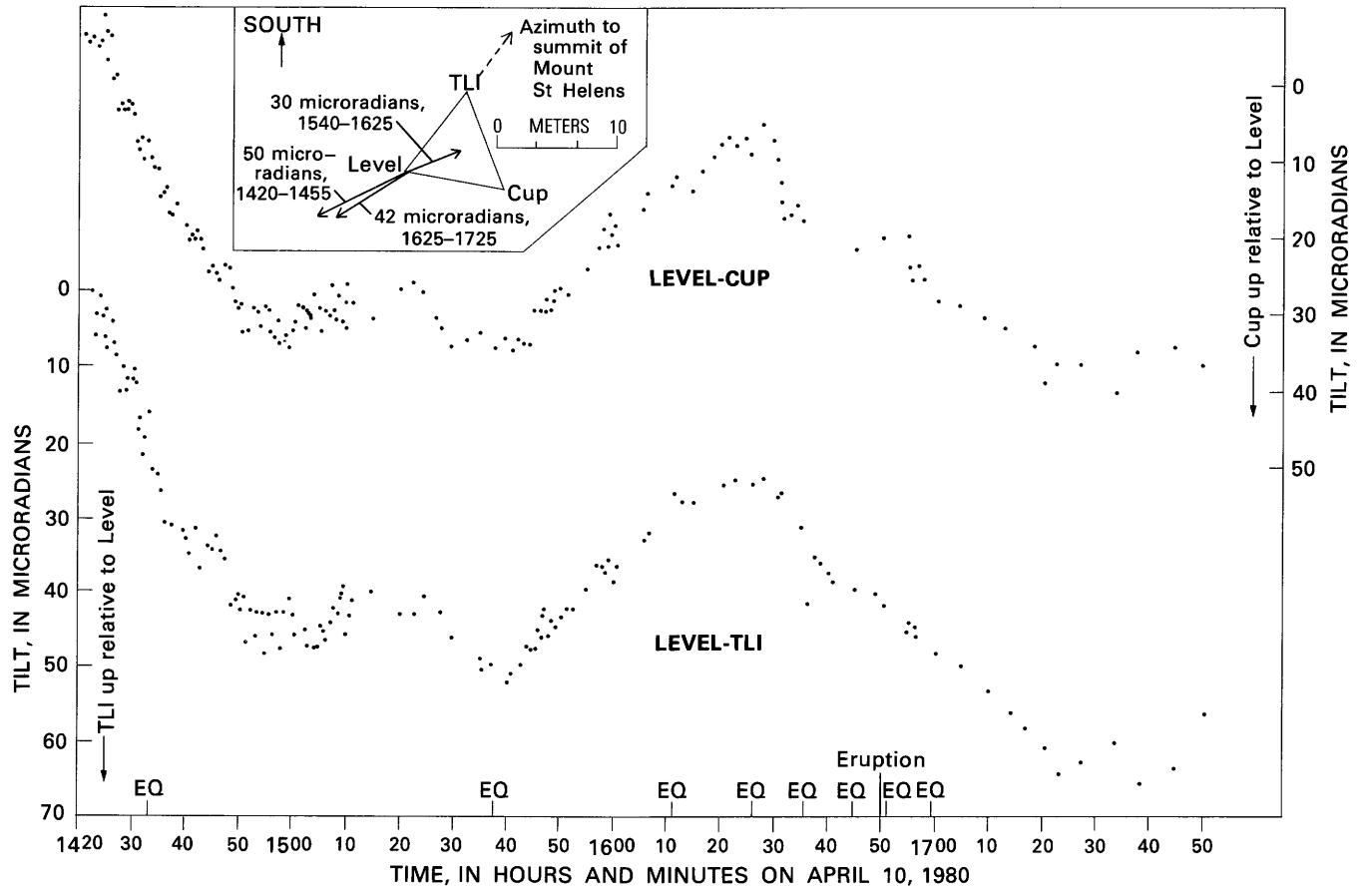

Figure 84.—Tilt at parking lot of Timberline campground, from 1420–1750 PST, April 10, 1980. Tilt vectors (insert) derived from changes in elevations of points named **TL1** *and* **Cup** *relative to* **Level**. *Note that the direction of tilt changed dramatically at about 1540 and 1625. EQ marks times when earthquakes were felt at the tilt site. A phreatic eruption occurred at 1650.*

tically more difficult effort was begun on April 20 to measure ground deformation by geodetic methods at points higher on the cone, within the areas of visible glacier crevassing and probable ground cracking.

METHOD OF GEODETIC MEASUREMENT

Our techniques in measuring ground deformation were based largely on experience at the Hawaiian Volcano Observatory with Kilauea and Mauna Loa Volcanoes. There, horizontal distances are measured by sighting to manned reflector targets with electronic distance-measuring equipment (AGA Geodimeter Model 8), and vertical changes are monitored by spirit leveling (Kinoshita and others, 1974). Modification of the Hawaiian approach was required at Mount St. Helens, because most of the desirable survey points were accessible only by helicopter, were frequently obscured by adverse weather, and were exposed to hazards from volcanic eruptions and from snow and rock avalanches triggered by the continuing seismic activity. In addition, the steep slopes of Mount St. Helens and the extensive snow cover prevented, without major effort and danger, establishing vertical control by leveling.

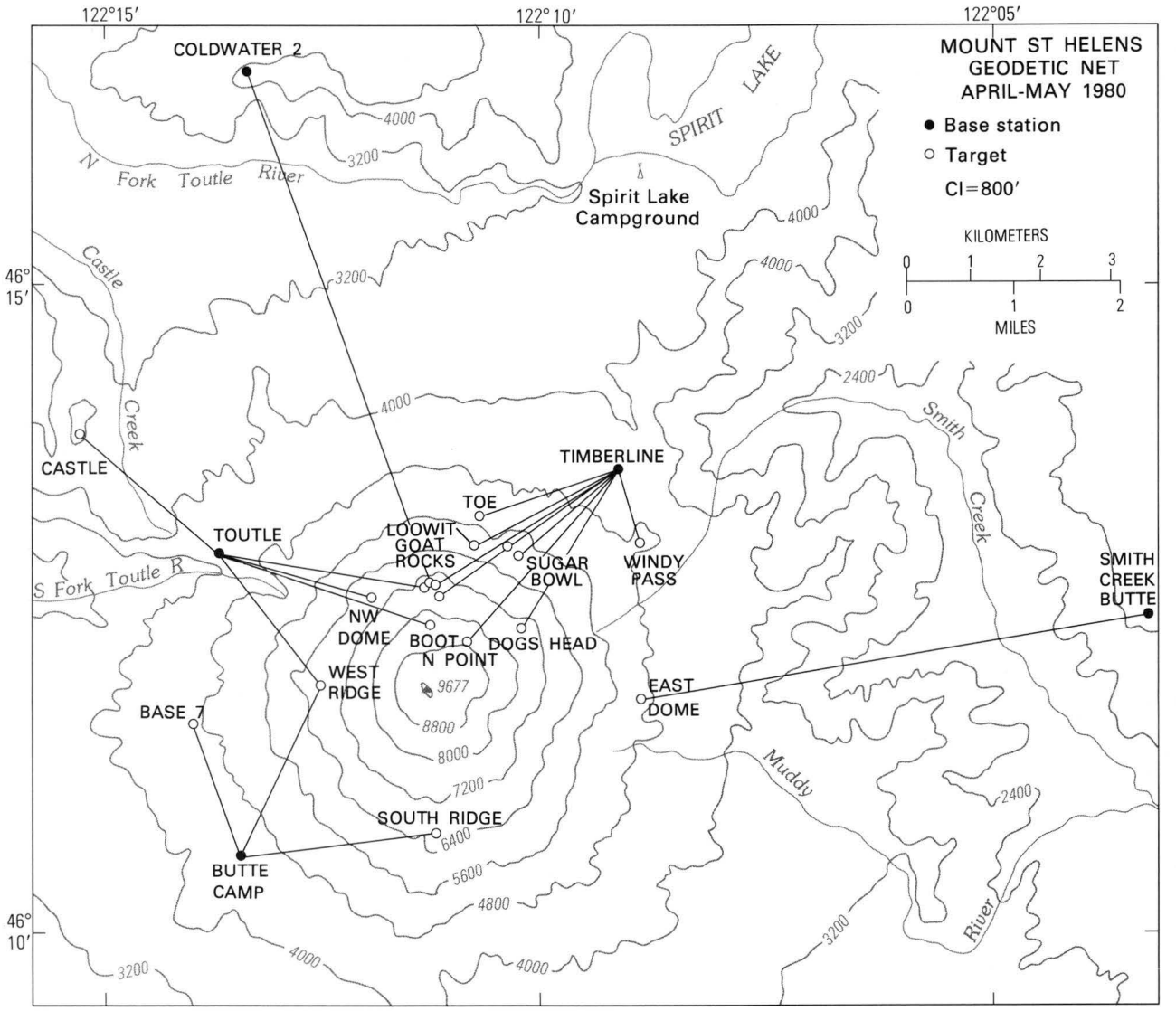

Figure 85.—Locations of stations used for measuring surface displacements at Mount St. Helens; horizontal and vertical angles and slope distances were measured from instrument stations low on the flanks to targets higher on the volcano. Contours in feet.

Accordingly, we began a program of measurements by theodolite (Wild T-2, old style) and Geodimeter, using unmanned permanently installed targets high on the volcano and three instrument stations at relatively low and stable locations (fig. 85). One instrument station, Timberline, was accessible by road and thus could be occupied without helicopter support whenever weather conditions permitted observations. The horizontal and vertical angles from theodolite observations, combined with a slope-distance measurement by Geodimeter, yielded the unique location in space of the target relative to a single base station; repeated measurements permitted determination of 3-dimensional displacements. At the distances involved, about 2–4 km, the slope distances obtained are believed accurate to within ±10 mm; the uncertainties in the theodolite measurements, ±5–10 s of arc, are about an order of magnitude greater.

The unmanned targets consisted of steel sign posts, on which were bolted wooden cross boards (the theodolite target) to which were attached inexpensive plastic highway reflectors 8 cm in diameter (target for the Geodimeter laser). These unmanned targets (fig. 86) had several advantages: (1) Because they were inexpensive and constructed from readily available materials, they could be established in large numbers, and loss due to eruptive activity or avalanches was tolerable. (2) They could be measured any time a brief break in the weather permitted visibility. (3) Exposure of personnel to hazards on steep slopes of the volcanic cone was limited to relatively brief periods during installation and maintenance.

Figure 86.—Establishing an unmanned target (Sugar Bowl East; fig. 85) on April 23. The steel post was driven into ash (or wedged in rock) and guyed for stability. The wooden crossboard was painted fluorescent orange to enhance visibility as a theodolite target, and the attached cluster of plastic highway reflectors served as the Geodimeter target. This target was destroyed by a rock and ice avalanche on May 12.

In addition, our borrowed Geodimeter equipment simply did not come with enough conventional corner-cube prisms to establish more than a few standard reflector stations at a time. The major disadvantages of the unmanned Geodimeter targets were: (1) The maximum range for distance measurements utilizing the plastic reflectors was 3.5–4.0 km under good weather conditions, somewhat less during times of windy conditions or partial obscuration by fume, ash, or humidity. (2) Errors owing to poorly known atmospheric density were somewhat greater, because temperature and pressure were measured at only one end of the shot line. For the relatively short distances involved and the large changes commonly observed, however, this turned out to be a relatively minor problem.

The geometry of the geodetic net (fig. 85) was based on an attempt, within the 3–4 km constraints on distance for the plastic reflectors and the fall-off in precision of the theodolite measurements with increasing distance, to provide widespread general coverage of the volcano and also to make maximum use of the one instrument station at Timberline accessible by road. Also, the obvious deformation of the volcano was on its north side. As the nature of motions within the bulge became evident, more targets were added to document rates of movement there. The interpretation of displacements of targets on the volcano was based on an assumption that the instrument stations remained effectively stable. Stability was evaluated for each instrument station by Geodimeter shots to targets off the volcano or low on its flanks (Windy Pass, Castle, and Base 7; fig. 85); at no time were any significant changes in distance observed. For that matter, no target on the west, south, or east side of the volcano (West Ridge, South Ridge, East Dome, and Dogs Head), away from the area of the bulge, showed analytically significant changes. Some instability, however, was indicated for Timberline by the dry-tilt measurements in the nearby parking lot during April, but these were apparently small compared to displacements of the bulge.

Additional targets were established at three sites (Goat Rocks, Sugar Bowl, and Dogs Head), both to evaluate the reliability of the previously untested target design, especially their stability in high wind conditions, and to provide some redundancy in case of damage by avalanches or rock falls. Bedrock locations were limited or unsatisfactory at several sites because of heavy snowpack, and two of the supplemental targets were anchored in snowbanks (Dogs Head and Goat Rocks). At Goat Rocks, where the bedrock site (Goat Rock) was in an area of abundant ground cracking and was very exposed to rockfall, the supplemental target (Goat Snow) yielded consistent angles and distances (figs. 87, 88) throughout the observation period. If anything, Goat Snow showed smaller fluctuations—especially in slope distance—than the bedrock target. The supplemental snowbank station at Dogs Head was removed after about 10 days, both because of a lack of detectable movement at either Dogs Head target and because results from the Goat Rocks targets indicated no stability problems with the target installations. The paired targets at Sugar Bowl, although indicating only small changes in slope distances (fig. 87), tracked together until Sugar East was destroyed by a rock and ice slide on May 12. The dual targets at Goat Rocks were important in confirming, on the first remeasurement only 3 days after installation, the significance of the large observed changes in deformation. Almost certainly, such changes would have initially been attributed to reading errors, had it not been possible to duplicate the results on separate targets.

GEOMETRY OF DEFORMATION

The general pattern of ground deformation was relatively simple: within the elliptical area of the bulge, about 1.5 by 2 km, that subsequently was removed by landslides and explosions on May 18, all stations indicated large subhorizontal displacements, as much as 2.5 m/day in northerly directions. Rates based on measurement intervals of a few days were remarkably uniform, although fragmentary data indicate sizeable variations in rates over periods of a day or less, as do tilt data (fig. 84). Outside the area of the bulge, little or no significant ground deformation was detected.

The most precise measurements are for changes in slope distance, determined by Geodimeter (fig. 87). Although the rates of change are variable among targets, both as a function of position relative to the bulge and of the component of the total displacement, the rate of change for each target was nearly constant during the period of observations. In early May the Goat Rock target showed slight deviations from the

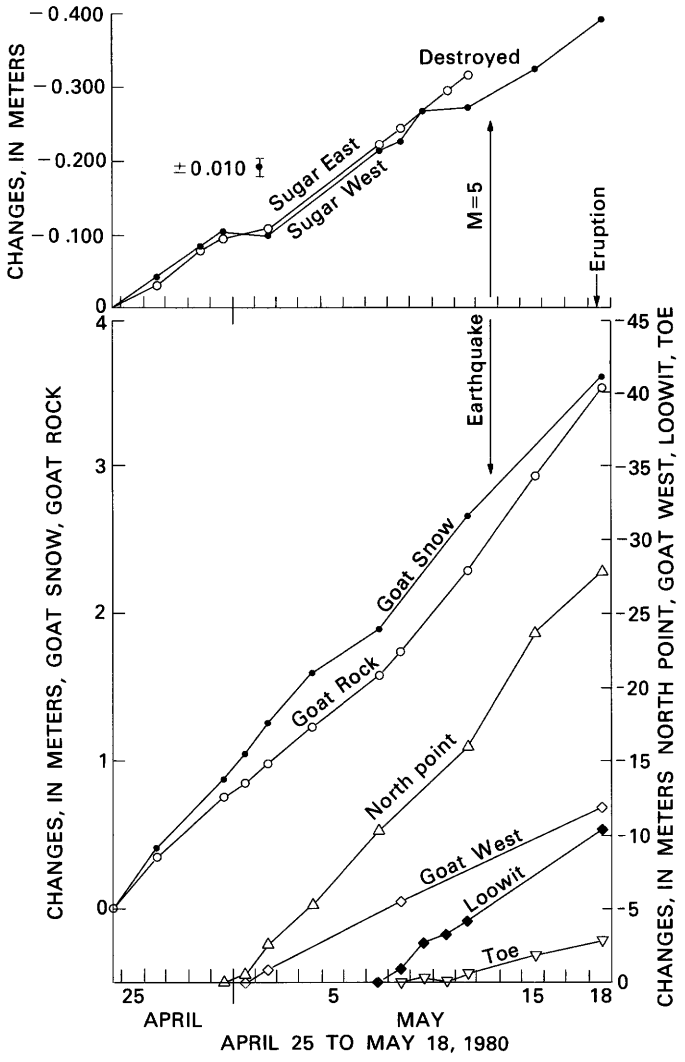

Figure 87.—Changes in slope distances, measured by Geodimeter from Timberline and Toutle instrument stations. Goat West target was measured from Toutle; all others were measured from Timberline.

trend defined by the adjacent Goat Snow target, apparently reflecting minor differential movement because of intense ground cracking observed between these two nearby targets. Only the North Point target showed marked nonlinear behavior: while the average rate of contraction of the North Point–Timberline line in early May was 1.4–1.5 m/day, it contracted at a rate of 2.6 m/day for the interval May 11–14. This interval encompasses the time of a magnitude-5 earthquake on May 12 that triggered a major ice and rock slide on the north slope, and both the Geodimeter data for North Point and theodolite data for several other north slope targets (fig. 88) show discontinuities in rates of motion for the time interval encompassing this event. Other than during this time interval, the trends defined by the horizontal angle measurements (fig. 88) are even more linear than the slope-distance data.

By combining distance changes determined by Geodimeter and changes in horizontal angles determined by theodolite, horizontal displacement vectors could be constructed graphically (fig. 89). Rarely could all targets be measured on a single day because of limitations of weather and helicopter support, but because of the relatively constant rates of deformation shown by each target, the rates of change vary only slightly. Accordingly, the displacement vectors plotted for early May on figure 89 would not be significantly different if plotted for other dates. The largest displacements, about 2 m/day, were high on the bulge (North Point and Boot) and along its center (Loowit). Lower on the bulge, the vectors show a broad fan pattern radiating outward toward margins of the deforming area. The amount of deformation

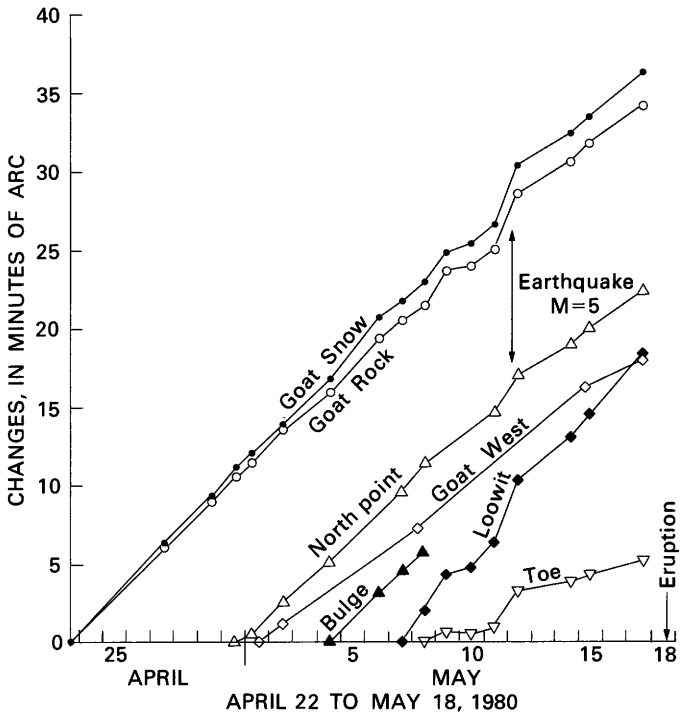

Figure 88.—Changes in horizontal angles, measured by theodolite from Timberline and Toutle instrument stations. Goat West and Bulge targets were measured from Toutle; all others were measured from Timberline.

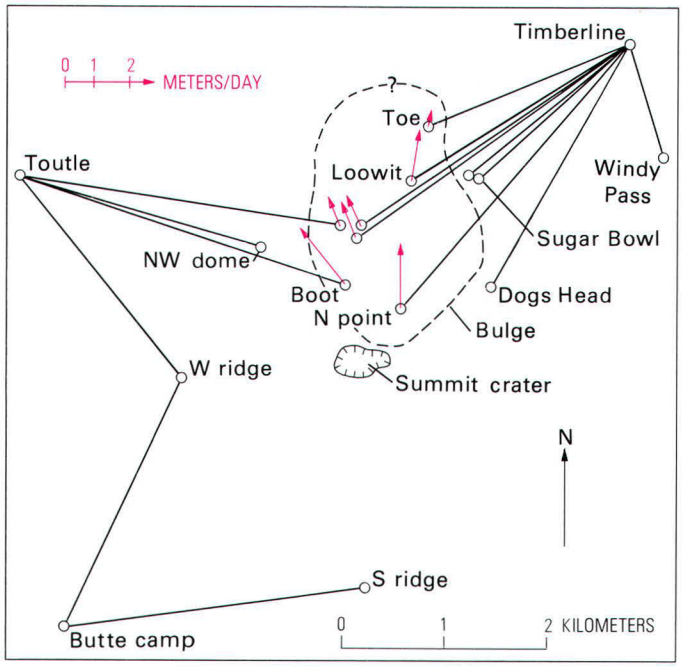

Figure 89.—Map showing typical daily displacement vectors in the area of the bulge on the north flank of Mount St. Helens before May 18. Target stations without vector arrows showed no displacement or had values too small to plot.

decreases relatively abruptly at margins of the bulge, from meters per day at Loowit and Boot, to a few millimeters per day within about 500 m laterally toward Sugar Bowl on the east and Northwest Dome on the west.

Vertical displacements were extremely small for all targets compared to horizontal changes; only at Goat Rock and North Point were changes in vertical angles consistently greater than measuring uncertainty. The vertical angles were measured by theodolite and recorded as zenith angles, a standard surveying practice in which (neglecting any change in slope distance) an increased angle reflects downward displacement of the target. For Goat Rock, where the line of measurement is almost perpendicular to the displacement vector (fig. 89) and the change in slope distance is accordingly small, a plot of the horizontal and vertical angular relations approximates the true displacement vector in vertical section (fig. 90*A*). The net displacement is northward at a low inclination of about 3°. The rate of downward movement may have been slightly greater after May 11 than before. In 20 days, the target moved subhorizontally northward about 28 m and downward only about 1.5 m. Because the topographic slope in the Goat Rocks area is about 30°, the net effect of such displacements was to further steepen the already steep terrain.

In contrast, at the North Point target the zenith angle decreased regularly, but the effects of large changes in the slope distance (28 m in 18 days) must be considered. A plot of these displacements in the plane of the shot line (fig. 90*B*) shows that the changes in vertical angle at the North Point target were largely related to changes in slope distance. When these effects are removed, the average displacement vector plunges gently northwards, as at Goat Rock. During the first days of observations, from April 20 through May 7, the North Point target increased slightly in elevation; then from May 7 through May 17 it subsided. In their photogrammetric analysis of areas of uplift and subsidence on the north side of Mount St. Helens, Moore and Albee (this volume) noted that the boundary between subsidence associated with the summit graben and uplift associated with the bulge swept gradually northward in April and May. The change in polarity of vertical changes at North Point on about May 7 appears to record passage of this boundary.

Outside the area of the bulge, movements were mostly too small to measure. At Sugar Bowl, just beyond the photogrammetrically measured margin of the bulge and on the rim of the May 18 crater, slope distances shortened regularly by about 15 mm/day (fig. 87), but any angular changes were entirely within measuring uncertainties. The Northwest Dome target, on the opposite side of the bulge, moved outward at an even smaller rate—about 3 mm/day. No other targets beyond the area of the bulge, including Dogs Head, East Dome, South Ridge, and West Ridge, showed detectable motion. Especially notable are results for a 7.6-km Geodimeter line from Smith Creek Butte to East Dome (fig. 85), established by D. A. Swanson in 1972. When first reoccupied on April 10, 1980, the net change in 8 yr was a contraction of only 16 mm (with atmospheric corrections made at both endpoints), well within the measuring uncertainty for a line of this length. Further reoccupation on April 25 also showed no significant change (+15 mm), and even when reoccupied after the May 18 event, the observed change was only −18 mm. Clearly, except for the bulge, Mount St. Helens was geodetically stable during this period.

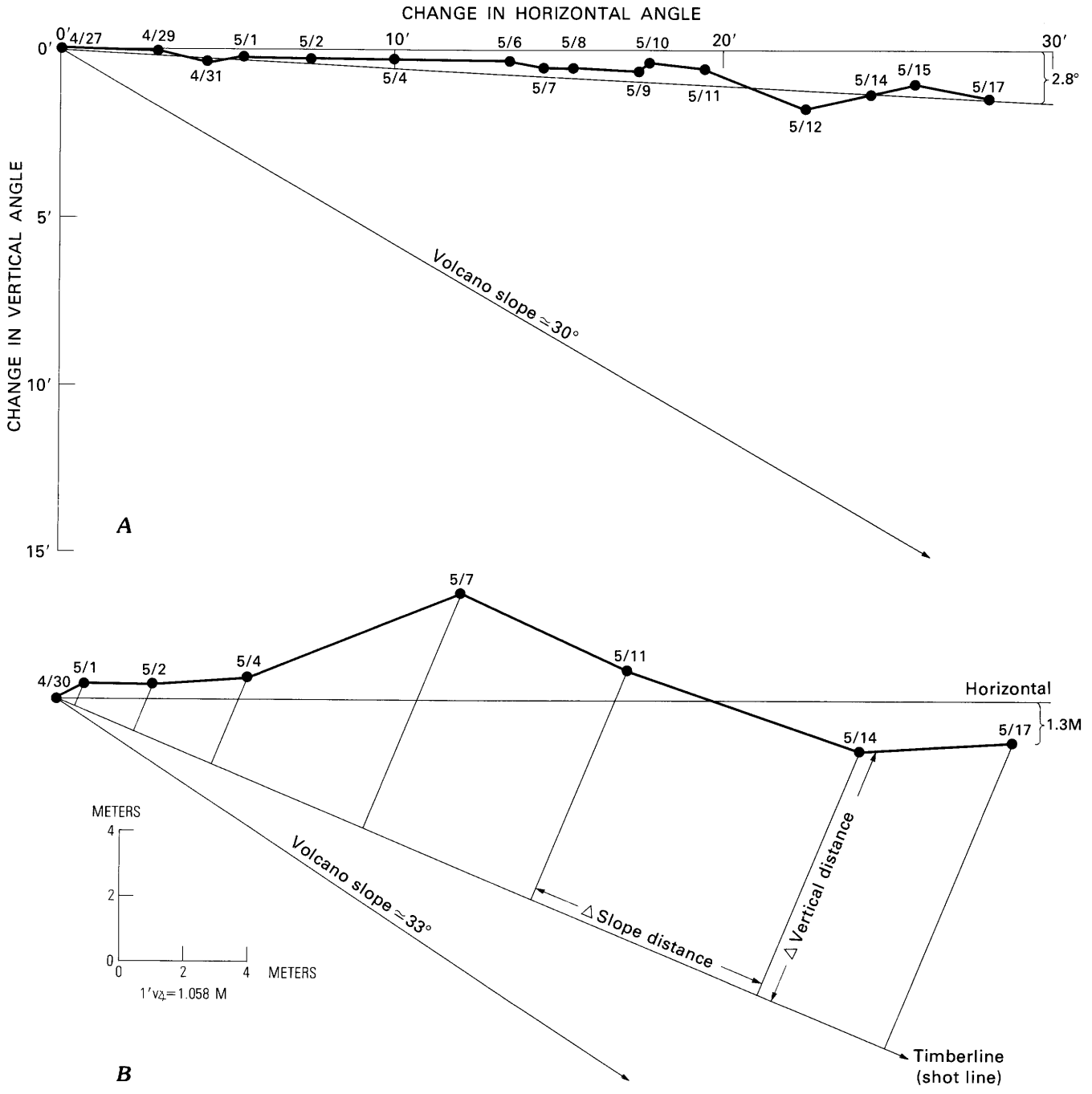

Figure 90.—Vertical changes at Goat Rock and North Point: A, Plot of changes in vertical versus horizontal angles for Goat Rock target. Average local slope of the volcano is about 30°, much steeper than the displacement vector. B, Plot of vertical angle versus slope distance for North Point target. For each measurement interval, the change in slope distance is scaled along the shot line, and the change in vertical angle is converted into a length (1 min vertical angle = 1.058 m for the 3.65 km line) and plotted perpendicularly to the shot line.

We also attempted to determine whether deformation of the bulge occurred by creep at relatively steady rates or by abrupt movements associated with the larger earthquakes, which were occurring at rates of 20–40 magnitude 3+ and 3–10 magnitude 4+ per day. Accordingly, we established an 8-km-long line from the Coldwater 2 observation station to a glass prism at Goat Saddle (fig. 85). This line was oriented

within a few degrees of the azimuth of the displacement vector for the other Goat Rocks stations, as measured in late April and early May (fig. 89) and accordingly was ideally situated to measure the maximum shortening in slope distance. On May 4 we measured this line several times per hour for an 8-hr period (fig. 91*A*); during this interval, six earthquakes occurred with magnitudes greater than 3.5, two of them greater than 4.0. The line shortened at a nearly constant rate, with few or no inflections that correlated with any of the recorded earthquakes, but the shortening was at a rate of only about 0.37 m/day, about 25 percent of the average displacement of 1.4–1.6 m/day measured for the Goat Rocks area in late April and early May. Clearly, we sampled a period of anomalously slow movement, demonstrating that significant fluctuations in rates of deformation were not being detected by our routine measurements at intervals of 1–3 days (fig. 87). Also, because our measuring interval on May 4 did not include the largest earthquakes occurring at this time (magnitudes as great as 4.8), it remains very possible that abrupt deformations associated with maximum bursts of seismic energy accounted for part of the cumulative total displacement. Such an interpretation is also supported by the discontinuities, already described, in rates of movement associated with several targets during the period encompassing the magnitude-5 earthquake and associated rock and ice slide on May 12.

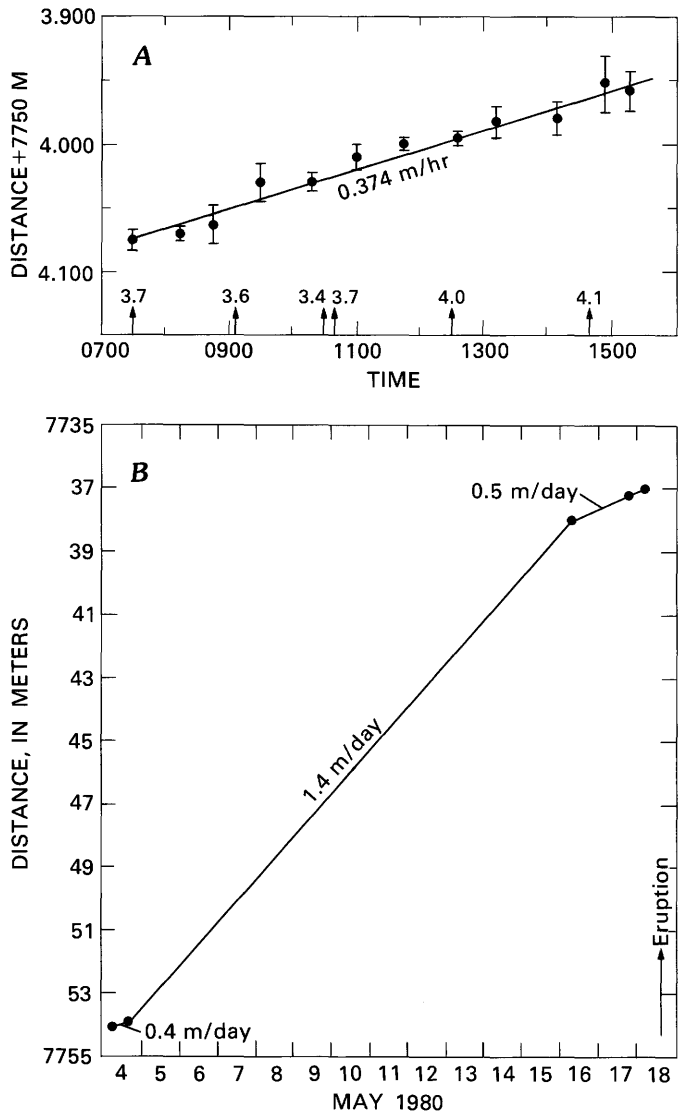

Figure 91.—Changes in slope distance between Coldwater 2 and Goat Saddle (located between Goat West and Goat Rock). Measurements on May 4 were made with a Model 8 Geodimeter; subsequent measurements were with a K&E Ranger. A, Changes on May 4. Error bars indicate spread among the three separate frequencies measured by the Geodimeter. Arrows indicate times of earthquakes under Mount St. Helens with magnitudes greater than 3.5. B, Changes from May 4 to May 18.

From May 5 to May 16 further attempts to measure the Goat Saddle target from Coldwater 2 were stymied by poor weather. The next successful remeasurement, on May 16, indicated an average rate of shortening over the interval since May 4 of 1.4 m/day (fig. 91*B*), similar to rates observed for Goat Rock, Goat Snow, and Goat West targets during this general period. However, further measurements from Coldwater 2 to Goat Saddle on May 17 and early on May 18 indicate that the deformation rate had again slowed, to about 0.5 m/day. Three key measurements showing this slow rate, each taken about half an hour apart, were radioed in by David Johnston on the morning of May 18, the last at 0653 PDT—only an hour and a half before the catastrophic failure of the north slope and the beginning of the eruption.

DISCUSSION

The rates of deformation measured geodetically during growth of the bulge on the north flank of Mount St. Helens, as much as 2.5 m/day, are the largest that we know of over a sustained period on an active volcano. In contrast, on Kilauea Volcano in Hawaii, where many of the definitive geodetic studies

of volcanically related ground deformation have been made, rates of extension and uplift during inflation premonitory to eruptive events are typically only a few millimeters per day.

The closest analog to the growth of the bulge and associated events on Mount St. Helens with which we are familar is the rapid uplift at the base of Usu Volcano in Japan, just prior to the emplacement of the Showa Shinzan dacite lava dome in 1944–1945 (Ishikawa, 1950; Minikami and others, 1951). There, an elliptical area about 1 by 1.5 km across began to rise in April 1944, in conjunction with intense seismicity and intermittent phreatic eruptions. Rates of uplift were as much as 30 cm/day, and by September 1945, previously flat lying rice fields had been uplifted as much as 150 m, forming what the local geologists called a "roof mountain" (Minikami and others, 1951). In November 1944, viscous dacitic lava reached the surface near the center of the uplifted area and accumulated as a typical lava dome more than 100 m high before activity ceased in 1945.

Although the rates of deformation associated with growth of the bulge on Mount St. Helens are well established for late April and early May, the history of the bulge in late March and early April is less certain. If the remarkably constant geodetically determined rates of deformation are extrapolated back to the beginning of eruptive activity and the first observed ground cracking at the summit area on March 27, they cannot account for the size of the bulge as measured photogrammetrically for the period August 1979 (the last preeruption photography) to early April (Moore and Albee, this volume, fig. 71). Accordingly, either the rate of growth of the bulge was more rapid during the initial stages of volcanic activity than when later measured geodetically, or alternatively, some deformation proceeded unrecognized prior to March 27 or even aseismically prior to March 20. We favor the first alternative, which would correlate maximum rates of deformation to the period of maximum seismic release of energy in late March.

Whatever the details of bulge growth, by the end of April the scale of deformation associated with growth of the bulge clearly indicated that magma was moving upward into the volcanic edifice. In particular, the subhorizontal motions of most targets and slight upward movement of the North Point target demonstrated that the bulging could not simply be reflecting gravitational slumping of the north flank. Most probably, a body of dacite magma was emplaced into the edifice in late March, with slower upward and outward growth in April and early May. Emplacement of a new lava dome was anticipated in the vicinity of the bulge, by analogy both with events at Showa Shinzan in Japan in 1944–45 and with prior activity of Mount St. Helens. In the past few thousand years, at least four dacitic domes had been emplaced on Mount St. Helens, at the summit and on the north side of the volcano; none are known to have formed on the south side (Crandell and Mullineaux, 1978, Hoblitt and others, 1980).

The purposes of our monitoring activities were to determine the rates of deformation and to anticipate effects of any oversteepening on the north flank of the volcano. We realized that gravitational failure could occur as a secondary consequence of the intrusion event. These results thus contributed to hazard assessments in late April and early May that Mount St. Helens remained highly dangerous, despite the seemingly mild small-scale phreatic eruptions that were then the most conspicuous activity. As a result, the north flank of the volcano was kept closed to general public access (Miller and others, this volume), despite heavy public pressure for access. Meanwhile in our geodetic studies, we hoped to see some acceleration in rates of deformation, prior to catastrophic failure; such progressive increases in deformation rates have been documented in the transition from slow creep to failure in landslide environments (D. J. Varnes, written commun., 1980). No such transition occurred on the north flank of Mount St. Helens within the period of our observations; possibly the anticipated change in deformation rate occurred in late March at the time of onset of major seismicity. Alternatively, the landslide model may not have been applicable to the slope failure at Mount St. Helens, because the deformation was primarily intrusion-driven, rather than gravitational, and was associated with high seismic-energy release. Clearly, the flank was not yet ready to slide by itself. Instead, it required a triggering event to start to fail. The magnitude-5+ earthquake provided such a trigger.

Finally, the ground deformation data described in this report provide an important framework for interpreting the events of May 18. No significant increases in rates of deformation preceded or caused the failure of the north flank and the subsequent eruptive events on the morning of May 18. Both analysis of the seismic data and eyewitness accounts strongly suggest

that the failure of the north flank was triggered by the magnitude-5+ earthquake at 0832, a seismic event slightly larger than but otherwise similar to many preceding earthquakes. By May 18 the growth of the bulge had simply so oversteepened the north flank that it was ripe for failure. Also, the variations in deformation rates over periods of a few hours to a few days, documented by the measurements from Coldwater 2 to Goat Saddle, along with the trend toward fewer but larger earthquakes (Endo and others, this volume), suggest that in mid-May larger stresses were accumulating between seismic events. In any case, the lateral eruption accompanying and following the earthquake-induced failure of the north flank on the morning of May 18 is reasonably interpreted as primarily driven by phreato-magmatic explosions of hot water-saturated rocks within the volcano, when the lithostatic confining pressure was abruptly released by slope failure.

Such a gravitational-failure mechanism may well have been significant at other well-known (but mostly poorly documented) lateral volcanic blasts, such as Bandai-san in Japan (Sekiya and Kikuchi, 1889) and Bezymianny and Shiveluch in Kamchatka (Gorshkov, 1959; Gorshkov and Dubik, 1970). The accounts of events at Bandai-san and Shiveluch are too fragmentary to interpret, but at Bezymianny photographic evidence demonstrates that deformation similar to that on Mount St. Helens occurred prior to the paroxysmal explosion in March 1956. At Bezymianny the old dome that constituted the central mass of the volcano was uplifted about 100 m, the summit crater was widened by 230 m, and the adjacent flank of the volcano increased in steepness from about 30° to 35° (Gorshkov, 1959, p. 83). The mechanism of laterally directed blasts from a central-vent volcano, which formerly seemed enigmatic to us, is readily understandable if related to phreato-magmatic explosions triggered by gravitational failure of a deforming flank of a volcano. Accordingly, the difference between the 1980 events at Mount St. Helens and the 1944–45 activity of Showa Shinzan would be that the magma body at Showa Shinzan was emplaced in relatively flat terrain at the base of Usu Volcano, whereas the dacite at Mount St. Helens could deform the already steep north flank of the volcano, probably weakened by repeated prior emplacement of lava domes on that side.

REFERENCES CITED

Crandell, D. R., and Mullineaux, D. R., 1978, Potential hazards from future eruptions of Mount St. Helens Volcano, Washington: U.S. Geological Survey Bulletin 1383–C, 26 p.

Gorshkov, G. S., 1959, Gigantic eruption of the volcano Bezymianny: Bulletin Volcanologique, v. 20, p. 77–112.

Gorshkov, G. S., and Dubik, Y. M., 1970, Gigantic direct blast at Shiveluch Volcano (Kamchatka): Bulletin Volcanologique, v. 34, p. 261–288.

Hoblitt, R. P., Crandell, D. R., and Mullineaux, D. R., 1980, Mount St. Helens eruptive behavior during the past 1,500 years: Geology, v. 8, p. 555–559.

Ishikawa, T., 1950, New eruption of Usu Volcano, Hokkaido, Japan, during 1943–1945: Journal Fac. Science Hokkaido University, v. 7, p. 237–260.

Kinoshita, W. T., Swanson, D. A., and Jackson, D. B., 1974, The measurement of crustal deformation related to volcanic activity at Kilauea Volcano, Hawaii, *in* Civetta, L., Gasparini, P., Luongo, G., and Rapolla, A., eds., Physical volcanology: Amsterdam, Elsevier, p. 87–115.

Minikami, T., Ishikawa, T., and Yagi, K., 1951, The 1944 eruptions of Volcano Usu in Hokkaido, Japan: Bulletin Volcanologique, v. 11, p. 45–157.

Sekiya, S. and Kikuchi, Y., 1889, The eruption of Bandai-san: Journal of College of Science, Tokyo Imperial University, v. 3, p. 91–172.

West, F., Heiken, G., Homuth, E., Peterson, R., Crowe, B., and Wohletz, K., 1981, Tilts associated with volcanic activity, Guadaloupe, F.W.I., Fall, 1976: Journal of Volcanology and Geothermal Research, in press.

THE 1980 ERUPTIONS OF MOUNT ST. HELENS, WASHINGTON

GEODETIC MONITORING AFTER THE MAY 18 ERUPTION

By D. A. SWANSON, P. W. LIPMAN, J. G. MOORE, C. C. HELIKER, *and* K. M. YAMASHITA

ABSTRACT

Geodetic monitoring of Mount St. Helens, which was resumed shortly after the May 18 eruption, has proved to be useful in defining deformation of this volcano related to magmatic processes. Deformation was rather small as a result of the May 18 eruption. The volcano probably subsided between 20 and 70 cm between mid-June and late November, mostly in late June and early July and perhaps as an after effect of the May 18 event. Distances from one side of the mountain to the other shortened a total of 20–25 cm throughout the summer and fall. Periods of expansion that lasted several days to 3 weeks preceded most magmatic eruptions and major periods of gas discharge. The rampart, an accumulation of tephra immediately north of the vent, moved northward several tens of centimeters between eruptions and accelerated before the July and October eruptions. Preeruption expansion of the cone, faster movement of the rampart, and formation of new radial cracks on the crater floor may be premonitory either to magmatic eruption or to major gas discharge. A northwest-trending structural element weakly affects the pattern of deformation, particularly deformation related to contraction of the cone, and may relate to a throughgoing fault zone beneath or within the cone. Swelling of the volcano is approximately radial; it represents the combined effects of a shallow pressure source, which affects the rampart only and may be related to increased volatile pressure high in the conduit system, and a deeper pressure source, which affects the entire cone and may be related to movement of magma into or within a holding reservoir.

INTRODUCTION

Geodetic monitoring of Mount St. Helens resumed shortly after the May 18 eruption and was continued through 1980. The purpose of the monitoring is to define how the cone responds to magmatic processes such as intrusion, vesiculation, and eruption. Such response, on both a short-term (days) and a long-term (months) basis, provides constraints on the nature of these processes and may lead to the recognition of premonitory deformation before eruptions.

Monitoring of ground deformation has proved useful in evaluating "readiness to erupt" in areas of basaltic volcanism, such as Kilauea and Mauna Loa (Kinoshita and others, 1974), Mount Etna (Wadge, 1976), and Krafla, Iceland (Tryggvason, 1978). Geodetic monitoring of stratovolcanoes of more silicic composition is less common, and the significance of such monitoring is uncertain.

Surveying of Mount St. Helens after May 18 began as an experiment to see if the volcano does deform and, if so, how valuable this deformation might be in understanding magmatic processes. Results to date show small repetitive deformations, many of which can be correlated to observed preeruptive and erup-

tive behavior. Some of the deformations that are not strictly radial to the volcano may partly be influenced by a northwest-trending tectonic grain beneath or within the cone.

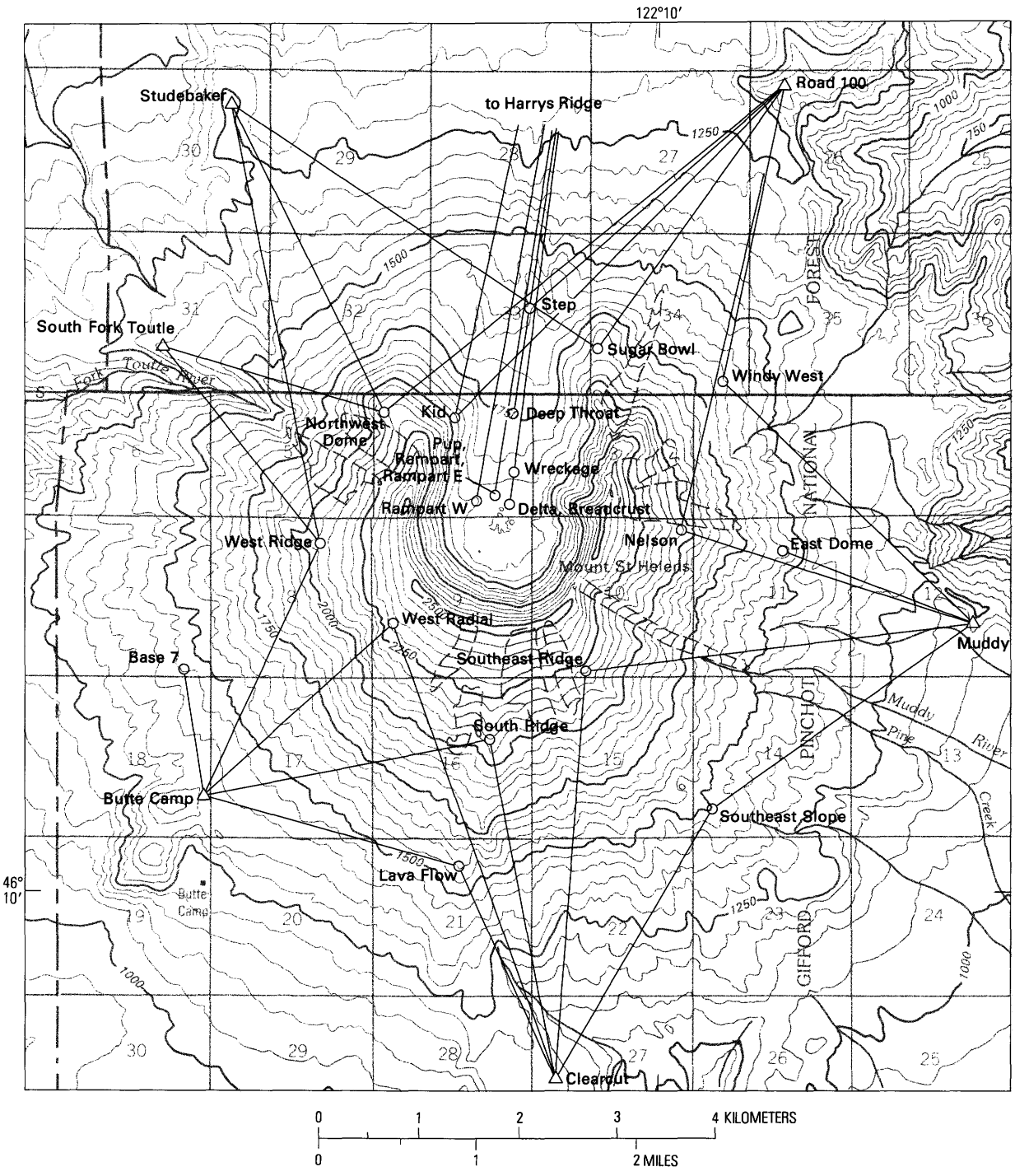

Figure 92.—Geodetic network used to monitor deformation of Mount St. Helens after the May 18, 1980 eruption. Triangle, instrument station; circle, target.

ACKNOWLEDGMENTS

We thank helicopter pilots Bob Edwards, Warren Fortier, Bob Sisk, and especially Michael Holtsclaw and Michael Montgomery, for support and advice. Dave Sawyer and Tom Sisson ably assisted with geodetic surveying. Many USGS personnel from Vancouver and elsewhere also assisted with the geodetic-monitoring activities.

NETWORK AND METHODS

All targets in the geodetic network established in April and May (Lipman, Moore, and Swanson, this volume) were destroyed on May 18, except for Castle and South Ridge, both of which were severely damaged, and Base 7, which survived intact. Benchmarks remained at South Fork Toutle, Butte Camp, East Dome, and Smith Creek Butte, although the South Fork Toutle mark was not found until after a new station had been installed. The electronic distance-measuring equipment used to monitor growth of the bulge (Lipman, Moore, and Swanson, this volume) was destroyed at Coldwater 2 during the May 18 eruption.

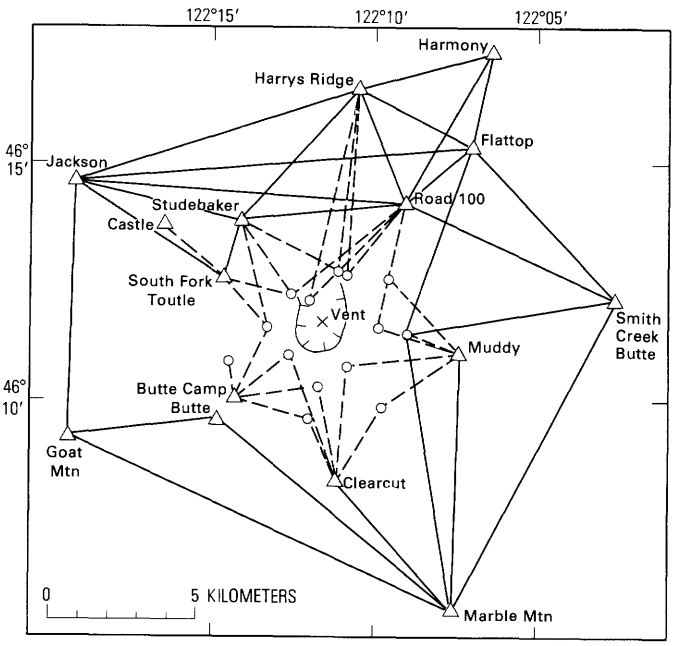

Figure 93.—Trilateration network at Mount St. Helens. Dashed lines measured frequently (see fig. 92); solid lines infrequently. Triangle, instrument station; circle, target.

Reestablishment of the network (fig. 92) began on May 24 with angle measurements from Butte Camp. Measurements of slope distance began from Butte Camp on May 29, South Fork Toutle on June 4, Clearcut on June 7, Muddy and Road 100 on June 18, and Harrys Ridge on June 29. The network evolved during this time as stations were added, instrumentation was changed, and techniques were improved. Instrument stations routinely used to monitor the volcano are tied to points farther from the cone by a trilateration network (fig. 93). This "outer" network, established during late June and July, will be reoccupied should major deformation of the cone occur. Access to all stations is by helicopter.

Angles and slope distances were measured with a Wild T-2 theodolite (old style) and a Hewlett Packard 3808A distance meter through most of June, until a new style T-2 theodolite and a longer range distance meter, a K&E Rangemaster III, became available.

Inexpensive, unmanned targets, similar to those used before May 18 (Lipman, Moore, and Swanson, this volume), were installed initially. Plastic highway reflectors, so effective before May 18, proved to be unsuitable, because they rapidly became sandblasted by windblown ash and lost their reflectance; consequently, each bank of plastic reflectors was replaced by one standard corner-cube glass prism. Even these prisms became sandblasted at vulnerable sites, but they nonetheless proved to be far superior to the plastic reflectors. Glass prisms installed within the crater became etched by hydrogen fluoride in the volcanic gas and had to be replaced periodically. Condensation of water on reflecting surfaces of the prisms has repeatedly caused problems because of weakened signal strength. Attempts to seal the prisms and housings have been successful only occasionally.

As fall approached, the need to "winterize" targets and instrument stations became imperative. In a cooperative venture, personnel of the USGS and of the Pacific Power and Light Company, whose concern was about effects of future eruptions on its hydroelectric reservoirs, installed heavy steel instrument and target towers at most survey stations (fig. 94). These

towers are embedded in concrete and are designed to withstand winds of 240 km/hr; they stand 3–3.5 m above ground level, about the anticipated maximum thickness of the snowpack. Instruments are bolted directly to the flat top of the instrument tower; a catwalk halfway up the tower can be used when snow depth is low. The target tower has a long neck to which prisms are bolted. Because these towers are stable, the quality of measurements has improved noticeably in heavy winds. How well the towers will survive avalanches remains untested at this time (November 1980). One 360-kg tower, which was not cemented in place but was weighted with several tens of kilograms of rocks, was swept from the crest of the the rampart more than 300 m downslope by an ash flow on October 16 or 17 (fig. 95). Many target towers have had thick coatings of snow and rime ice that had to be removed before measurements could be made.

The geodetic network has been occupied about once every week or 10 days; completion of the network requires about 6 hr under favorable weather conditions. Measurements of slope distance from Harrys Ridge to the mountain have been taken more often, about once every 2–3 days, because they are sensitive indicators of deformation of the volcano. Vertical and horizontal angles have been measured less frequently because of their imprecision compared to measurements of slope distance, and because of instability of the tripod owing to strong winds that commonly buffet exposed instrument stations. Poor weather has been a continuing problem, and many attempts to take measurements have been aborted by clouds or winds. An important result of the attempts at geodetic observations has been an opportunity to monitor the volcano visually and photographically, on a nearly daily basis.

Raw measurements of slope distance have been ad-

Figure 94.—Steel towers used in geodetic monitoring of Mount St. Helens. A, instrument tower at Harrys Ridge; B, reflector tower "Delta" on rampart.

justed for atmospheric index of refraction by using meteorologic data at the instrument station only, to minimize helicopter expense and hazardous time spent on the volcano. Thus the reported slope distances are nominal, not true ones. Meaningful comparison of measurements to the same target at two different times is contingent on the assumption that the index of refraction varies regularly along the light path, and so atmospheric measurements (chiefly of temperature) at any one point adequately define the variation. This assumption is invalid, but the errors introduced are within acceptable limits. Attempts to evaluate errors resulting from poor meteorologic control have been made periodically by measuring temperature and pressure at both endpoints and by comparing the corrected distances with those based on one endpoint reading only. These comparisons show that errors of as much as 2 cm in an 8-km distance (2.5 parts in 10^6) have resulted from using only one endpoint set of readings, although more common errors are about 1 cm per 8-km distance (1.25 parts in 10^6). The extent to which errors may change as weather conditions vary with the seasons is being investigated.

DEFORMATION RESULTING FROM THE MAY 18 ERUPTION

The volcano deformed little as a result of the May 18 eruption, except for the remarkable destruction of the bulge (Moore and Albee, this volume). The South Ridge target may have moved 10–20 cm southward between May 17 and 24, on the basis of horizontal-angle measurements from Butte Camp. However, the posteruption position of the South Ridge target had to be adjusted because its vertical pole was bent about 60° southward by the blast; errors in reestablishing this position were probably large and may account for all the apparent change. Similarly, possible errors in reestablishing the damaged Castle target cast doubt on the validity of an apparent 36-cm extension of a line between Castle and South Fork Toutle. The slope distance from Butte Camp to Base 7 did not change appreciably. A 7.6-km distance from Smith Creek Butte (east of the volcano) to East Dome shortened 18 mm between April 25 and June 17, which is close to or within measurement error.

These scanty data suggest that the rest of the volcano responded only slightly, if at all, to removal of the bulge and to formation of the crater and amphitheater.

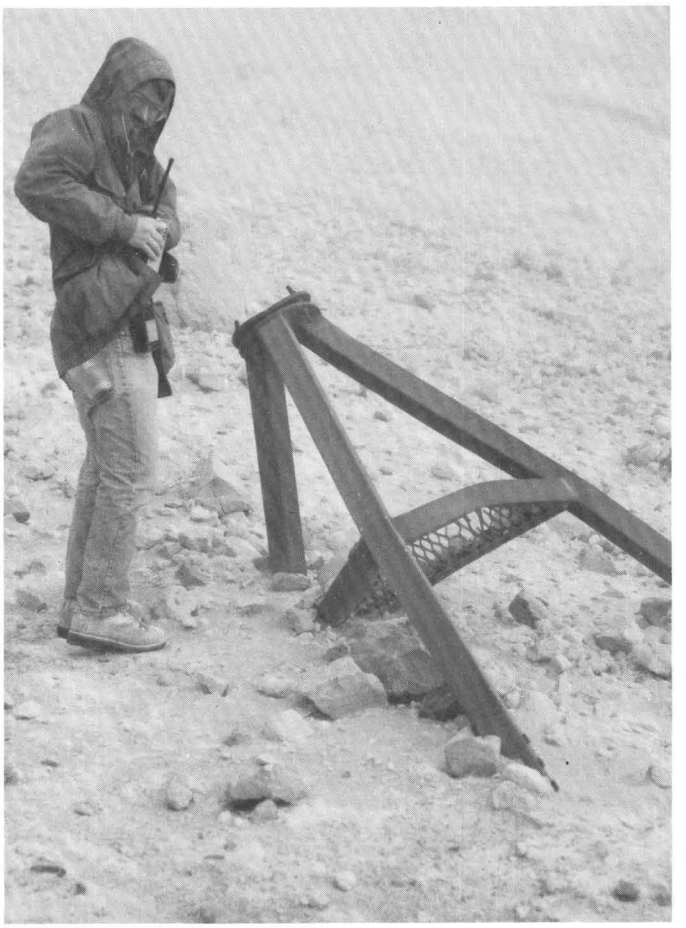

Figure 95.—Delta tower shown in figure 94B moved more than 300 m downslope from rampart and partly buried by pyroclastic flow on October 16 or 17. Neck on tower was sheared off. A prism has been attached to leg of damaged tower, and slope distance from Harrys Ridge is routinely measured to this station, named Wreckage.

NET DEFORMATION DURING SUMMER AND FALL

CHANGES IN ELEVATION

Changes in elevation of targets relative to instrument stations were too small to resolve accurately by the rather crude vertical-angle measurements. Nonetheless, these measurements show a general pattern of net relative subsidence of the cone (fig. 96). The data suggest that the cone subsided most rapidly during June and early July and became relatively stable

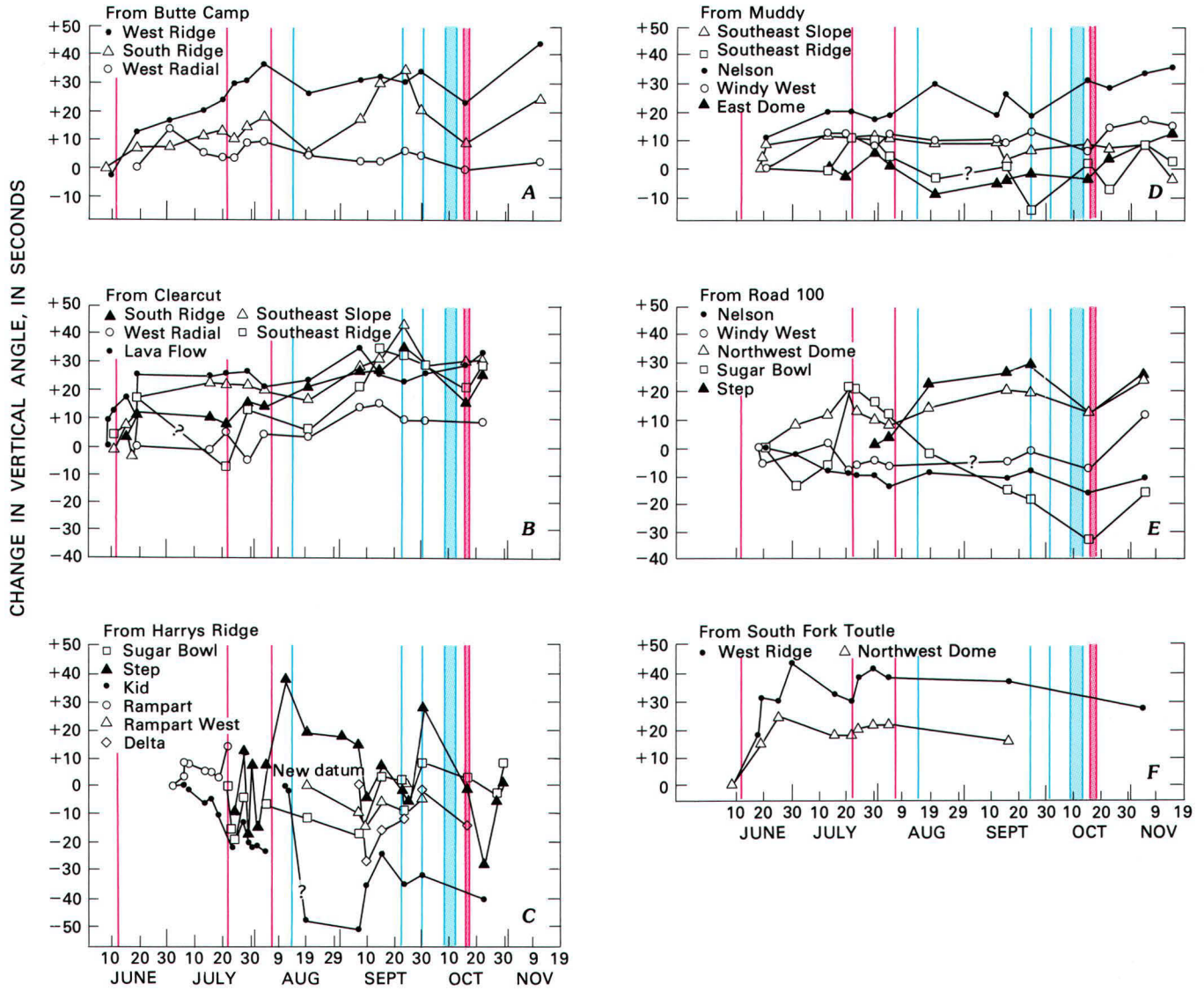

Figure 96.—Change in vertical angles from instrument stations to targets on Mount St. Helens, June–November 1980. Angles are from zenith, and so positive changes correspond to subsidence of target relative to instrument. Vertical lines denote magmatic eruption (red) or vigorous gas discharge (blue). Light-blue area, periodic gas discharge; red area, intermittent magmatic eruptions. Data shown are from the following instrument stations: A, Butte Camp; B, Clearcut; C, Harrys Ridge; D, Muddy; E, Road 100; F, South Fork Toutle.

thereafter. Perhaps the early subsidence denotes the final adjustments related to the May 18 events; later eruptions of small volumes of magma affected the volcano little.

The south flank of the volcano apparently subsided a few tens of centimeters in late August and September, as shown by vertical-angle measurements to South Ridge, Southeast Ridge, and Southeast Slope from Butte Camp and Clearcut. This episode corresponds to a prolonged period of horizontal expansion without eruption.

Vertical-angle measurements from Road 100 indicate relative uplift of several targets, contrary to data from other instrument stations. We interpret this to reflect actual subsidence of the Road 100 station, which is located on a thick directed-blast deposit (Hoblitt and others; Moore and Sisson; Waitt; all this volume) that settled as it cooled, and as smoldering logs buried within the deposit collapsed.

A change in vertical angle does not necessarily indicate a change in elevation until the effect of slope distance is evaluated. As an extreme, a large decrease

in slope distance could result in apparent uplift but actual subsidence, as occurred at several targets before May 18 (fig. 89). However, the small changes in slope distance since May 18 have a negligible effect on changes in vertical angle, and so measured angles approximate elevation changes after considering observation error. Such error is hard to assess for these data, but it is probably rather large owing to meteorologic uncertainties and to often indistinct targets. We believe that an estimate of ±8–10 s is realistic, and many of the angle measurements show net changes greater than this. For small changes in slope distance, the maximum amount of subsidence is given approximately by $D \sin V$, where D is the initial slope distance and V is the change in vertical angle, provided that this change is small. From this relation, amounts of maximum subsidence for points on Mount St. Helens are about 20–70 cm; the actual subsidence is probably slightly less.

CHANGES IN SLOPE DISTANCE

Most measured slope distances on the volcano lengthened several centimeters between June and November (fig. 97). The overall precision of these measurements is probably ±1–2 cm. The lengthening, together with vertical-angle measurements, indicates net contraction of the cone relative to the instrument stations. Vectors of horizontal displacement, calculated from changes in slope distance assuming stability of instrument sites, indicate several centimeters of movement (maximum of 15 cm, except for the poorly constrained vector of Southeast Slope) and show the overall pattern of contraction (fig. 97). Strictly, these vectors should be corrected for changes in elevation of target relative to instrument site, but such corrections are negligible for the small observed changes. Changes in horizontal angles are too small to constrain the vectors.

The pattern of displacement vectors shows both elements of radial symmetry and important departures from such symmetry. Directions of movement of South Ridge and Nelson, which depart from a radial pattern, together with movements of other targets (except for Kid), are consistent with contraction of a northwest-trending structure influencing the radially contracting cone. Northwest-trending faults, probably right lateral, are being recognized widely in the Cascade Range and adjacent Columbia Plateaus province (Lawrence, 1976; Beeson and others, 1975; Anderson, 1978; Bentley and others, 1980), and locations of earthquakes suggest that Mount St. Helens sits astride one such fault zone (Weaver and others, 1980; this volume). Patterns of expansion of the cone are generally more nearly radial than are patterns of contraction; this difference in pattern suggests that increased magmatic pressure dominates over regional stresses at such times.

In summary, net deformation of the cone from June to November consists of subsidence of about 20–70 cm and horizontal contraction of about 20–25 cm, twice the radial displacement of any one target. From November through December, changes on the cone were very small, mostly within measurement error.

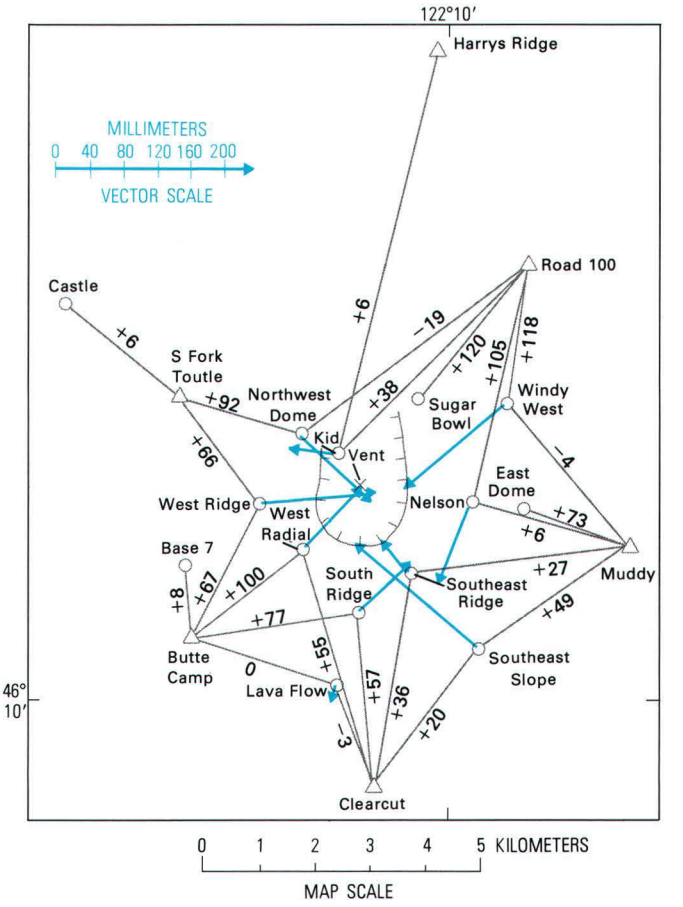

Figure 97.—Net change, in millimeters, of slope distances (shown as values on black network lines), between June 19 and November 13. Displacement vectors (blue) derived relative to instrument stations (triangles), assumed to be stable. Change from Harrys Ridge to Kid is for period July 1 to November 13.

EPISODIC DEFORMATION RELATED TO MAGMATIC ACTIVITY

The net deformation of the volcano results from a sequence of episodic contractions ("deflation") and expansions ("inflation"), most of which are directly correlated with eruptive or noneruptive activity. Before September 3, longer periods of contraction were punctuated by short periods of expansion immediately followed by a Plinian-type eruption (fig. 98). This pattern changed slightly in early September when a 3-wk period of slow expansion began, and finally ended on September 24 when several large pulses of degassing took place from vents along the margin of the dome. After that, the volcano contracted slightly until mid-November, including the time immediately preceding the October eruption, then expanded until early December. The episodic deformation commonly shows both radial and northwest elements, although swelling is generally more nearly radial than is contraction.

Because of the relative inaccuracy and infrequency of vertical-angle measurements, elevation changes are difficult to correlate with the episodic "horizontal" deformation. The September period of expansion may have been accompanied by subsidence of south-flank targets South Ridge, Southeast Ridge, and Southeast Slope and north-flank targets Sugar Bowl and Kid (fig. 96); Step target may have been uplifted during this same period. The large degassing events on September 24 ended these trends.

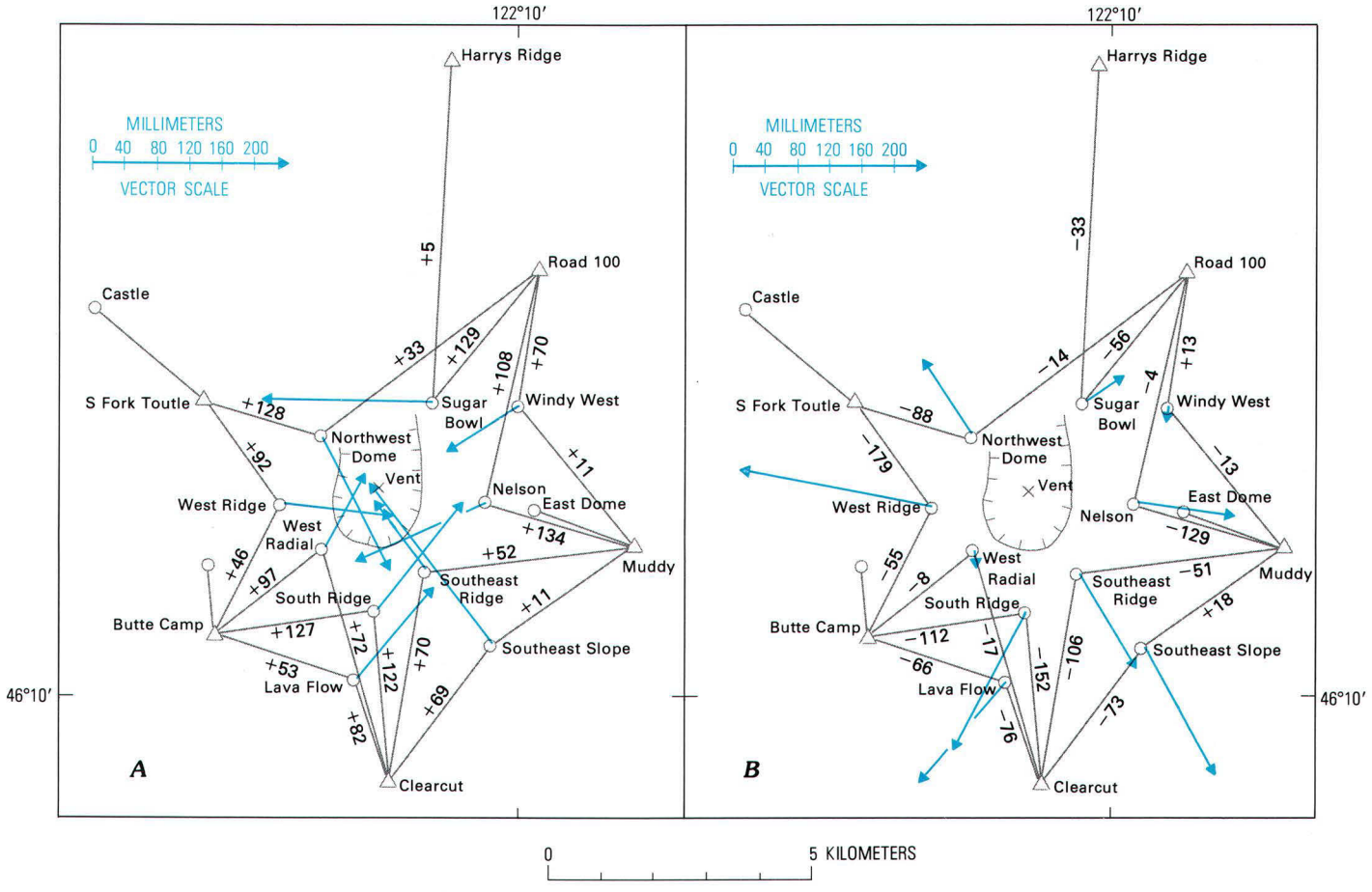

Figure 98.—Cumulative change, in millimeters, in slope distances (shown as values on black network lines) during periods of contraction and expansion. Displacement vectors (blue) of targets (circles) were derived relative to instrument stations (triangles), assumed to be stable. A, periods of contraction: June 18 to July 13–15, July 20–21 to August 4, August 8–9 to September 3; B, periods of expansion, immediately preceding or bracketing magmatic eruptions or vigorous gas release: June 8–18, July 13–15 to July 20–21, August 4 to 8–9, September 3–24, 1980.

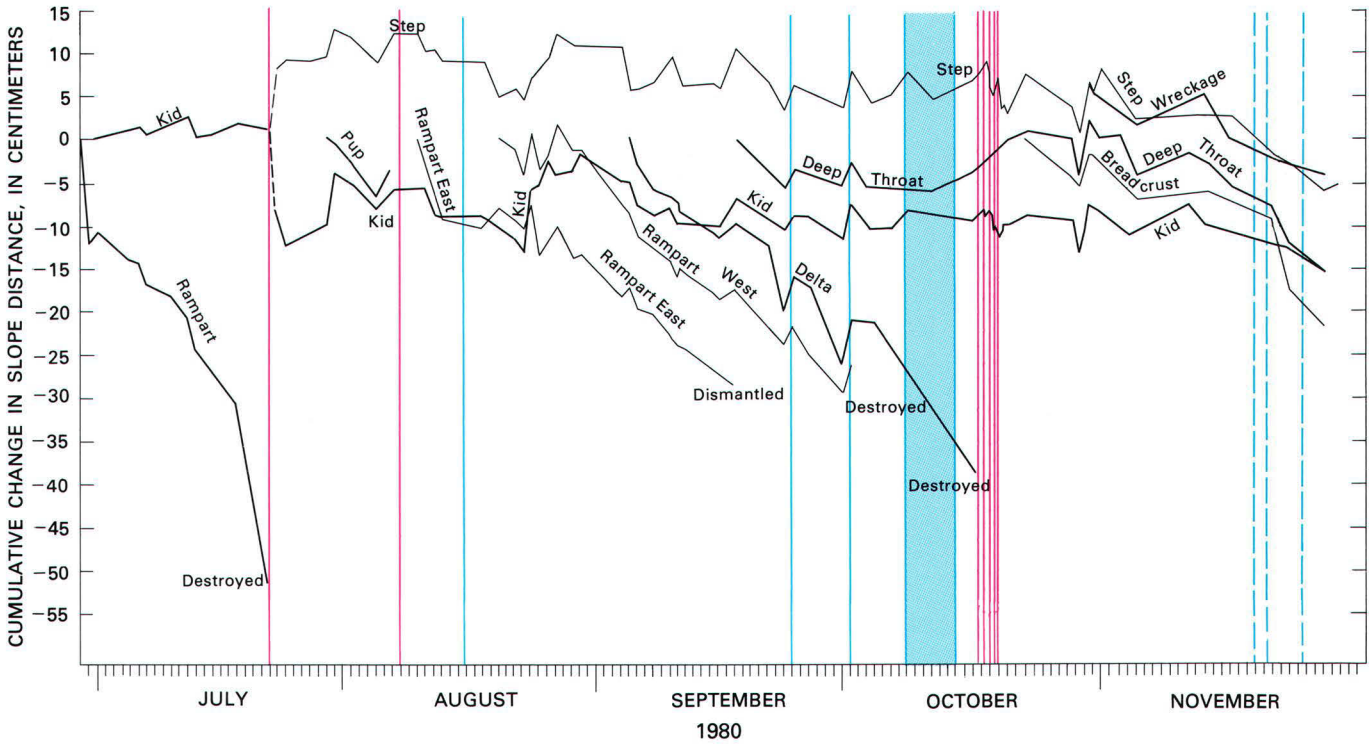

Figure 99.—Cumulative change in slope distances during summer and fall between Harrys Ridge and targets in crater and on north flank of Mount St. Helens. For purposes of computing extensional strain, approximate distances from Harrys Ridge are: Step, 6,348 m; Deep Throat, 7,507 m; Kid, 7,527 m; Rampart, 8,237 m; Pup, 8,294 m; Delta, 8,378 m; Rampart East, 8,393 m; Rampart West, 8,408 m; Breadcrust, 8,417 m. Dashed data line (black) indicates reestablishment of a damaged station. Blue lines, gas discharges; blue area, periodic gas discharge; red lines, magmatic eruptions. Dashed blue line, new fumarole.

MOVEMENT OF THE RAMPART

Shortening of slope distances between Harrys Ridge and the crest of the rampart, notably in the weeks before the July and October eruptions (fig. 99), suggests northward displacement of the rampart. Shortening also preceded the August eruption, although the last period of measurement (August 4–6) showed an extension of about 3 cm, possibly within measurement error. The rate of shortening was rather consistent, about 1 cm/day before the July eruption and somewhat less afterward (figs. 99, 100). The rate accelerated before the July and October eruptions to as much as 5 cm/day. Net shortening between Harrys Ridge and the rampart is at least 135 cm (fig. 100), assuming that the movement is irreversible; this assumption is untestable, because each eruption has destroyed the rampart target.

Such striking displacement affected neither the amphitheater floor (Deep Throat) nor walls (Kid, Sugar Bowl). A plot showing changes in slope distance to the rampart relative to Kid, a stable point compared to other targets (fig. 100), shows a pattern similar to but slightly smoother than that shown in figure 99. The smoother pattern probably reflects elimination of much of the error caused by atmospheric uncertainty, which is far more serious for the long distance between the Harrys Ridge station and Kid than for the rather short distance between Kid and the rampart.

Early suggestions that local movement of the rampart was related to slumping or cooling of the tephra seem disproved by a similar pattern of movement following the August eruption at three locations on the rampart, which are far apart and in areas of different slope and topography. Moreover, vertical angles show no clear evidence of subsidence and in fact suggest either slight net uplift or no change (fig. 96).

The rate of shortening of slope distances to the rampart (Delta and Rampart West) accelerated before major episodes of vigorous gas release on September 24 and October 1. These events, from vents just off

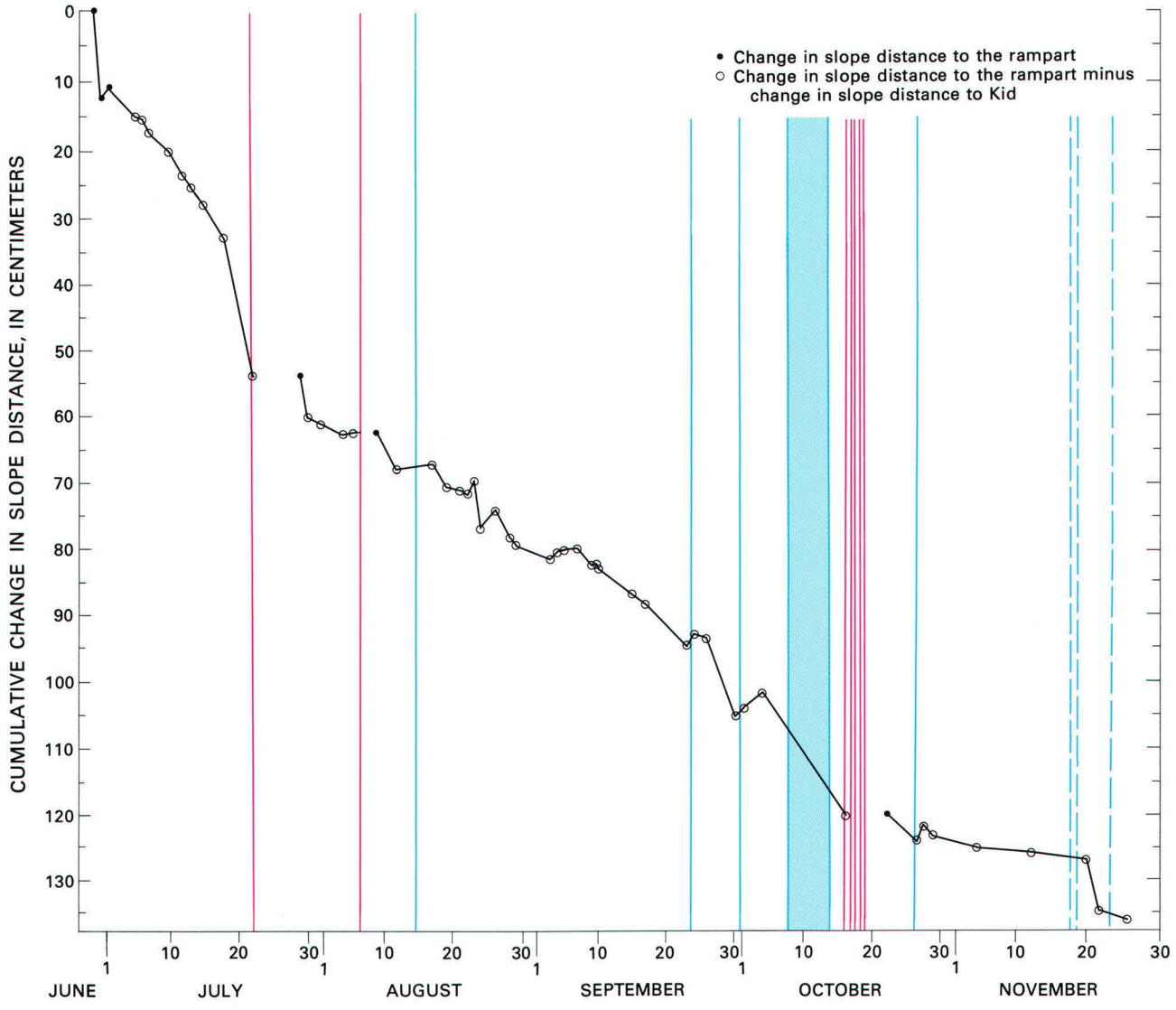

Figure 100.—Cumulative change in slope distance from Harrys Ridge to rampart stations minus change from Harrys Ridge to Kid (shown as circles). This plot minimizes error caused by poorly known atmospheric conditions between Harrys Ridge and Kid and shows a gradually diminishing rate of shortening from June 29 to November 26. Dots indicate that a slope distance was measured only to the rampart. No change is assumed during periods of eruption, when targets on rampart were destroyed and new targets were established (July, August, and October; see fig. 99). Between August and October eruptions, when there was more than one target on rampart, Rampart East was plotted until September 17 and Delta thereafter. Blue lines, gas discharges; blue area, periodic gas discharge; red lines, magmatic eruptions. Dashed blue line, new fumarole.

the east side of the August dome, were accompanied or immediately followed by extension of all distances measured from Harrys Ridge (fig. 99), indicating detumescence of the volcano. Another degassing event, late on October 27, correlates in time with accelerated expansion of the cone (fig. 99), although the rampart station moved less than did the north-flank stations (figs. 99, 100). This expansion was quickly canceled by abrupt detumescence between October 28 and 29, a time during which no vigorous degassing was reported.

Radial cracks on the crater floor south of and on the rampart became apparent in mid-September. The cracks radiated from the explosion crater at the vent. Repeated measurements of the width of four of the cracks showed continued widening until the October

eruption (fig. 101). The rate of widening generally increased during periods in which new radial cracks formed; these periods also correlate with increased rates of northward movement of the rampart (figs. 99, 100). The total width of cracking can account for only a small amount of the movement of the rampart, probably less than 15 percent, even if all crack widening were directed northward. Many radial cracks that formed after the October eruption continued to widen until early December. Complex cracking and faulting of the crater floor accompanied emplacement of the two lobes of the dome in late December.

Correlation between movement of the rampart and development of cracks is probably not fortuitous. We believe that both are related to changing magmatic pressure in a narrow, subvertical conduit beneath the crater. The pressure changes are so small and shallow that they affect only the crater itself. Larger and probably deeper changes in pressure affect the entire cone and cause episodic expansions and contractions recorded by the geodetic network. The two pressure sources are at times independent, and the systematic movement of the rampart indicates the shallower of the two is more consistent. Perhaps the two pressure sources are actually part of one reservoir system—the shallower source reflecting changes, usually increases, in volatile pressure in the upper part of a degassing magma body; the deeper source reflecting ingress and egress of magma itself in the lower part of the reservoir. Accelerated rate of shallow-level expansion before magmatic eruptions and episodes of vigorous gas discharge, as recorded by measurements from Harrys Ridge to the rampart, may reflect rapidly increased volatile pressure owing to magma mixing, convective overturn, or other processes within the reservoir system.

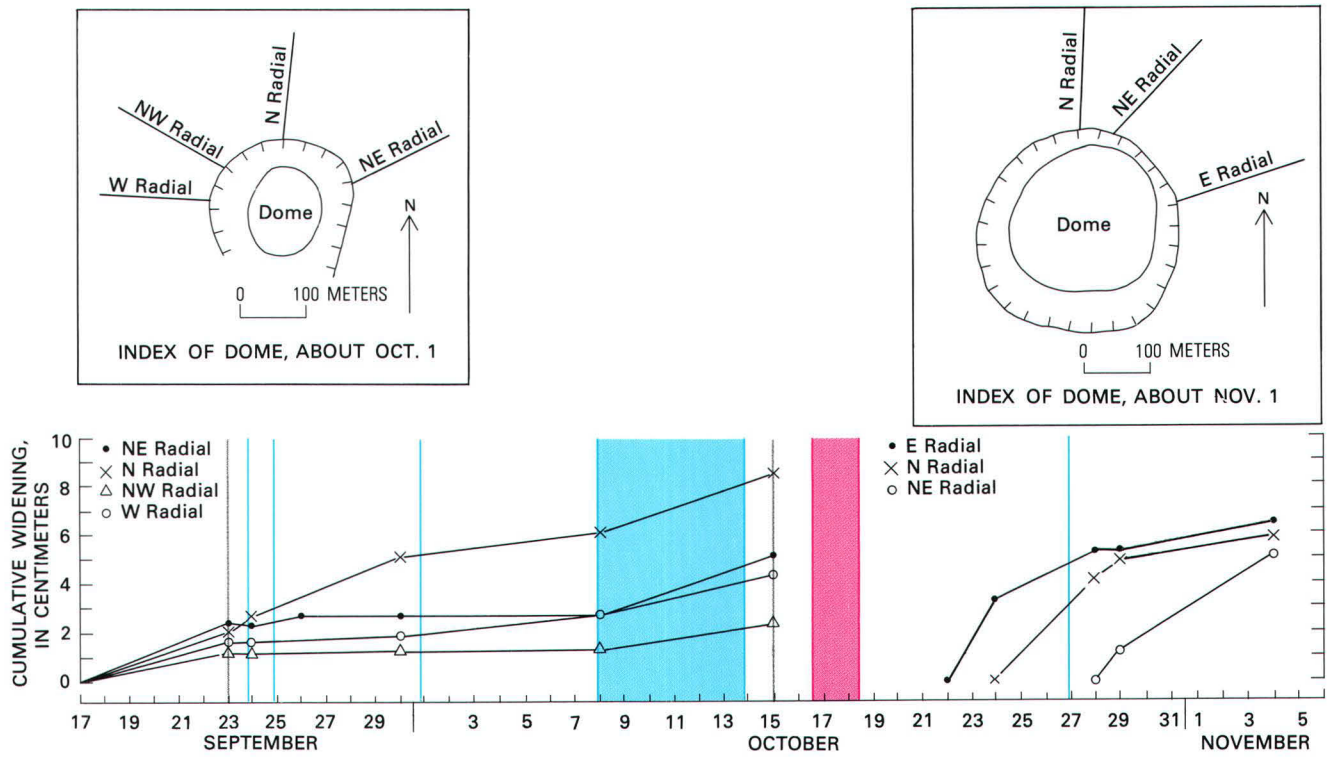

Figure 101.—Plot of widening of selected radial cracks measured on rampart and crater floor, September 17 to November 5. Cracks were first measured on September 17, and subsequent measurements refer to this datum. Inset index maps are diagrammatic; scale approximate; hachured line, rim of inner crater; lines representing cracks indicate direction only, not length. Cracks measured from September 17 to October 15 were destroyed by subsequent eruption, and different cracks appeared thereafter. Blue lines, gas discharges; blue area, periodic gas discharge; red lines, magmatic eruptions. Gray vertical lines indicate dates when additional radial cracks were first observed.

CONCLUSIONS

1. Deformation of the outer flanks of Mount St. Helens was rather small as a result of the May 18 eruption, except for destruction of the bulge.

2. The volcano experienced net subsidence, probably between 20 and 70 cm, and horizontal contraction of 20–25 cm since mid-June. Most of the subsidence took place in late June and early July, whereas horizontal contraction accumulated episodically throughout the summer and fall.

3. Long periods of contraction of the cone were punctuated by shorter periods of expansion of the entire cone, which lasted several days to 3 weeks. No expansion preceded the October eruption.

4. The rampart moved northward between eruptions and accelerated before the July and October eruptions.

5. Preeruption expansion of the cone, accelerated movement of the rampart, and formation of new radial cracks on the crater floor may be premonitory either to magmatic eruption or to major gas discharge.

6. A northwest-trending structural element weakly affects the deformation pattern, particularly that related to contraction of the cone, and may relate to a throughgoing fault zone. Patterns of expansion are generally more nearly radial than are patterns of contraction.

7. Two pressure sources, which perhaps represent the upper and lower parts of a magma reservoir system, can be interpreted from the geodetic data.

REFERENCES CITED

Anderson, J. L., 1978, The stratigraphy and structure of the Columbia River basalt in the Clakamas River drainage: Portland State University, M.S. Thesis, 136 p.

Beeson, M. H., Johnson, A. G., and Moran, M. R., 1975, Portland environmental geology-fault identification: Portland State University, 107 p.

Bentley, R. D., Anderson, J. L., and Farooqui, S. M., 1980, Wrench tectonics in the Yakima Ridges of the Columbia Plateau: Geological Society of America Abstracts with Programs, v. 12, no. 6, p. 267.

Kinoshita, W. T., Swanson, D. A., and Jackson, D. B., 1974, The measurement of crustal deformation related to volcanic activity at Kilauea Volcano, Hawaii, *in* Civetta, L., Gasparini, P., Luongo, G., and Rapolla, A., eds., Physical volcanology: Amsterdam, Elsevier, p. 87–115.

Lawrence, R. D., 1976, Strike-slip faulting terminates the Basin and Range province in Oregon: Geological Society of America Bulletin, v. 87, p. 846–850.

Tryggvason, E., 1978, Distance measurements in 1977 in the Krafla-Myvatn area and observed ground movements: Nordic Volcanological Institute Report 78-10, 47 p.

Wadge, G., 1976, The deformation of Mount Etna, 1971–1974: Journal of Volcanology and Geothermal Research, v. 1, p. 237–263.

Weaver, C. S., Malone, S. D., Endo, E. T., and Noson, L. J., 1980, Seismicity pattern of the Mount Saint Helens eruptive sequence: EOS,(American Geophysical Union Transactions), v. 61, no. 46, p. 1133.

THE 1980 ERUPTIONS OF MOUNT ST. HELENS, WASHINGTON

SUMMARY OF ELECTRONIC TILT STUDIES AT MOUNT ST. HELENS

By JOHN DVORAK, ARNOLD OKAMURA, CARL MORTENSEN, *and* M.J.S. JOHNSTON

ABSTRACT

During April and early May 1980, a network of five electronic tiltmeters was installed around Mount St. Helens, at radial distances ranging from 3 to 15 km from the center of the volcano. Each instrument telemetered two perpendicular components of tilt in approximately 10-min intervals to a monitoring station 70 km to the southwest, in Vancouver, Wash.

From the beginning of their operation, two of the three tiltmeters that were within 6 km of the volcano continued to indicate a general inflation or uplift of the region surrounding the volcano. The end of this general inflationary trend roughly coincided with the appearance of the first lava dome in mid-June 1980. The third tiltmeter within 6 km of the summit recorded an apparent deflationary trend that was probably related to formation of an east-west summit graben, whereas the two tiltmeters more than 6 km away recorded only very minor tilt changes. From mid-June to early October, data from the tiltmeters closest to the volcano showed a possible very slight subsidence of the region surrounding Mount St. Helens.

No obvious tilt changes immediately preceded any of the major eruptions of Mount St. Helens that occurred between April and September 1980. At the onset of eruptive activity on May 18, a tiltmeter 6 km south-southwest of the volcano indicated an abrupt inflationary change in tilt of roughly 4 μrad (microradians); possible short-term, transient tilt changes of as much as 2 μrad occurred during the time when the highest amplitude of harmonic tremor was recorded during this eruption.

Only during one post-May 18 eruption has a definite change in tilt been measured during eruptive activity at Mount St. Helens. A tiltmeter 6 km south-southwest of the center of the volcano recorded a deflationary change of 2 μrad, corresponding to the beginning of eruptive activity on May 25. Through September, no tilt changes larger than 0.5 μrad have corresponded to any other eruptive activity of Mount St. Helens.

INTRODUCTION

The precise measurement of surface deformation around active volcanoes gives an indication of unseen long-term changes taking place beneath the surface that, in part, are related to subsurface movement of magma. Following the initiation of eruptive activity at Mount St. Helens in March, a network of electronic tiltmeters was installed to monitor possible ground deformation.

The first instruments were installed during the latter half of April, within 1 mo of the beginning of earthquake activity (Malone and others, this volume) and phreatic activity (Christiansen and Peterson, this volume). Five Kinemetrics biaxial tiltmeters were installed at radial distances ranging from 3 to 15 km from the center of the volcano prior to the large eruption of May 18 (fig. 102). These are platform-type instruments that measure horizontal tilt about two perpendicular axes over a horizontal base length of approximately 200 mm. They were secured with expansion bolts to cast-concrete baseplates that were firmly cemented to rock outcrops.

The two tiltmeters north and east of Mount St. Helens were destroyed at the beginning of the May 18 eruption. These instruments were later replaced by two borehole tiltmeters installed west and south of the volcano, out of the area devastated by the May 18 eruption and in locations probably safe from future minor pyroclastic flows or mudflows. The borehole

tiltmeters were also biaxial Kinemetrics instruments that measure tilt changes about two perpendicular axes over a vertical base length of approximately 1 m. They were installed in cylindrical steel clamps that were packed firmly into boreholes with fine silica sand (Mortensen and others, 1977). These tiltmeters have been emplaced on the lower, gentler slopes surrounding the volcano to increase the chance of continued operation throughout the winter.

Perpendicular components of tilt were telemetered from each site in approximately 10-min intervals to a monitoring station 70 km to the southwest in Vancouver, Wash., where they were digitally recorded on paper tape. Each instrument is capable of measuring short-term tilt changes as small as 0.1 μrad; however, owing to drift of the electronic components and to the short base of these instruments, long-term tilt trends cannot be confidently determined to this accuracy. To partly reduce the diurnal contribution to the background noise, the three most southerly instruments were placed inside lava tubes to achieve a more stable thermal environment.

ACKNOWLEDGMENTS

We express our appreciation for the cooperation and assistance given to us by the staffs of the USGS Mount St. Helens project office in Vancouver, and of the USGS Hawaiian Volcano Observatory. The maintenance of field equipment by Ken Honma, Bruce Furukawa, and Eugene Iwatsubo led to the success of this study. We also thank Alan Rohay for loaning us equipment, and Don Swanson and Dan Dzurisin, whose discussions contributed to the study.

LONG-TERM TRENDS IN TILT

The tilt vectors estimated by fitting linear trends to the tilt data received between May 6 and May 18 are shown in figure 102. The Ape Cave South station did not operate until May 9. During this 2-week period, both the Timberline and Ape Cave North tiltmeters indicated continual inflation at a rate of 1–1.5 μrad per day, recorded at radial distances of 4–6 km from the center of the volcano. The apparent deflation indicated by the station on East Dome was probably the result of the formation of the east-west summit graben (Moore and Albee, this volume). Data from the more distant Ape Cave station suggested a possible slight deflation of the far-field region surrounding the volcano.

The long-term trends in the tilt data are displayed in figure 103 as time plots for three stations. Figure 103 shows the daily averages of the tilt data beginning May 1 and continuing through October 1, determined

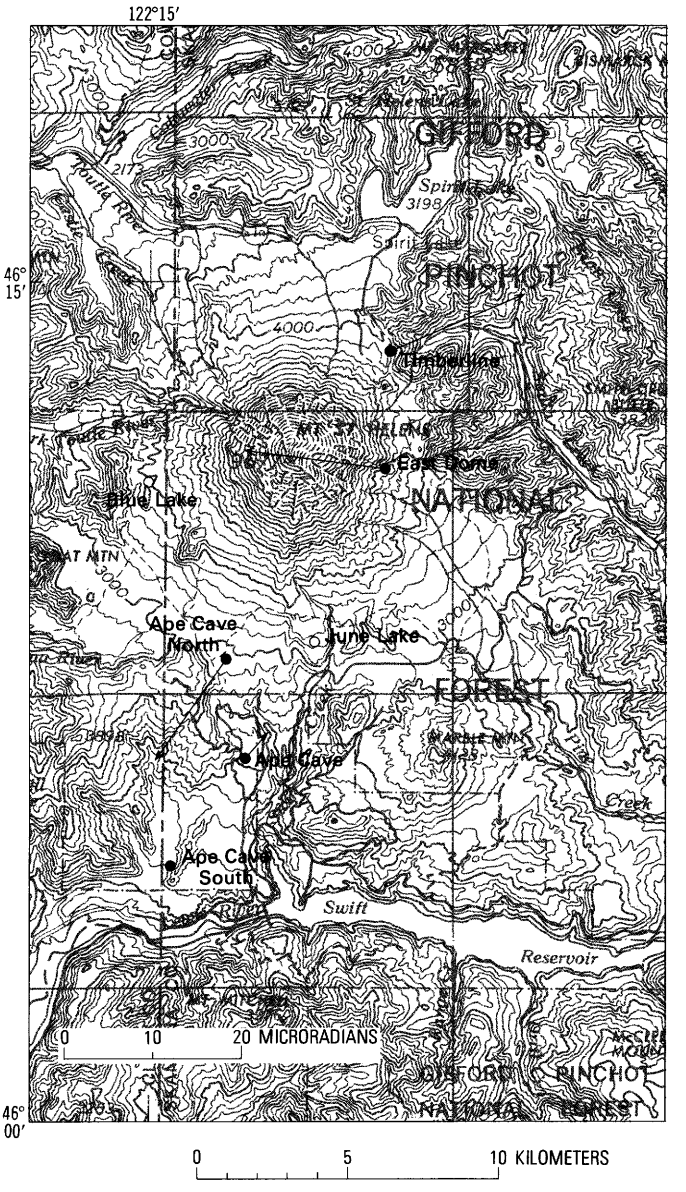

Figure 102.—Locations of electronic tiltmeters around Mount St. Helens. Those indicated by solid circles are platform instruments, installed before May 18; the two open circles indicate borehole instruments, installed after May 18. Tilt vectors indicate approximate tilt direction and magnitude determined at each site from May 6 to May 18.

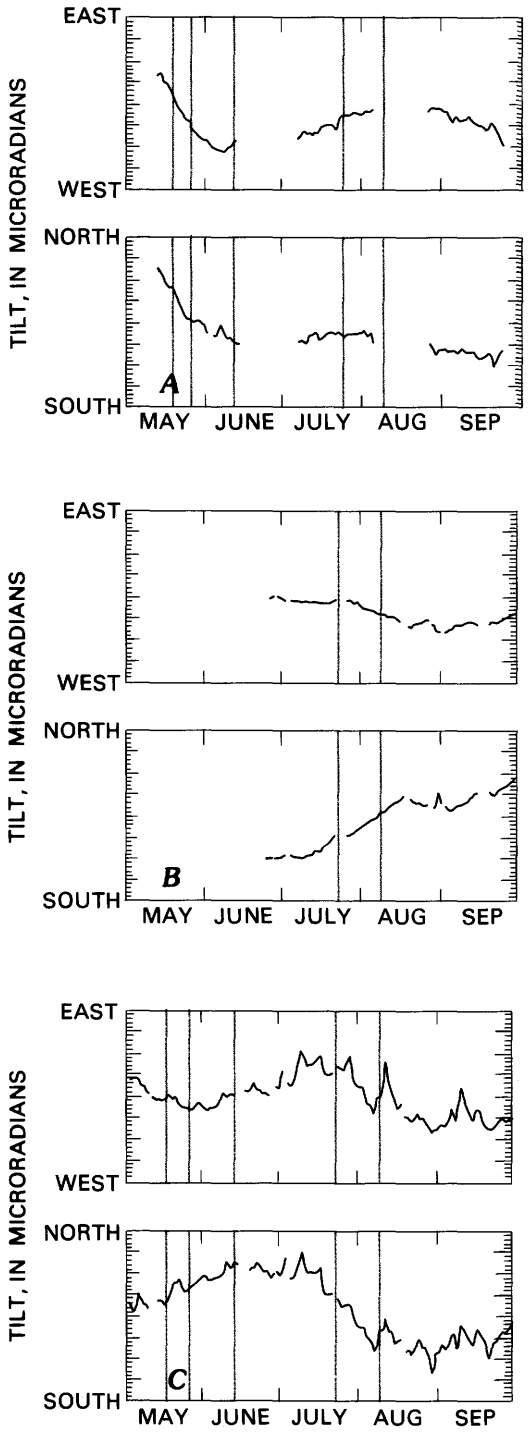

Figure 103.—Daily averages of tilt (in two directions) at each of three stations near Mount St. Helens. A downward tilt to east or north is defined as positive. Vertical lines indicate major eruptive activity. Gaps in the data indicate times when no usable data were collected. A, data from Ape Cave North station; B, from June Lake station; C, from Ape Cave station.

by averaging all of the data received during 6-hr intervals, thus minimizing diurnal variations.

Baseline values were lost at the Ape Cave North station during two long time gaps, in mid-June and mid-August, because of electronic difficulties and physical problems, such as rock falls and rock cracking at the site. Data recorded at the nearby June Lake station suggest that only small tilt changes occurred during these intervals.

No long-term changes in tilt are directly associated with major eruptive activity, including the large May 18 eruption. The overall tilt pattern indicated by data from the Ape Cave North station (fig. 103*A*) is an almost constant inflation rate beginning at the time the tiltmeter became operational and continuing until mid-June. The measured tilt change at this station was 30 μrad recorded between May 6 and June 13. Data for the initial 9-day adjustment period for this tiltmeter is not shown in figure 103*A*. By mid-June, the tilt change apparently was reduced. Data recorded by the June Lake station tiltmeter (fig. 103*B*) suggest a possible slight deflation or subsidence between June and October 1. The change in the tilt pattern from an inflationary trend to a constant or slightly deflationary trend occurred approximately at the same time as the appearance of the first lava dome, shortly after the June 12 eruption. The measured amount of deflation recorded by the June Lake tiltmeter (fig. 103*B*) suggests a net deflation of as much as 20 μrad, which occurred between mid-June and early October. However, Ape Cave North station data do not indicate a deflation larger than 5–10 μrad, a deflationary change in tilt that is considerably less than the inflationary change measured between late April and mid-June.

The more distant tiltmeter, at Ape Cave station, recorded a much more erratic tilt pattern than was recorded by the other instruments, and long-term variations (fig. 103C) as large as 30 μrad occurred for several months. However, this long-term variation is questionable, because these changes could not be corroborated by other tiltmeters installed at similar distances from the volcano.

MAY 18 ERUPTION

Two tiltmeter stations, Timberline and East Dome, were destroyed by the blast of May 18. The remaining three tiltmeters continued to transmit data throughout this eruption, and these data (received from the two

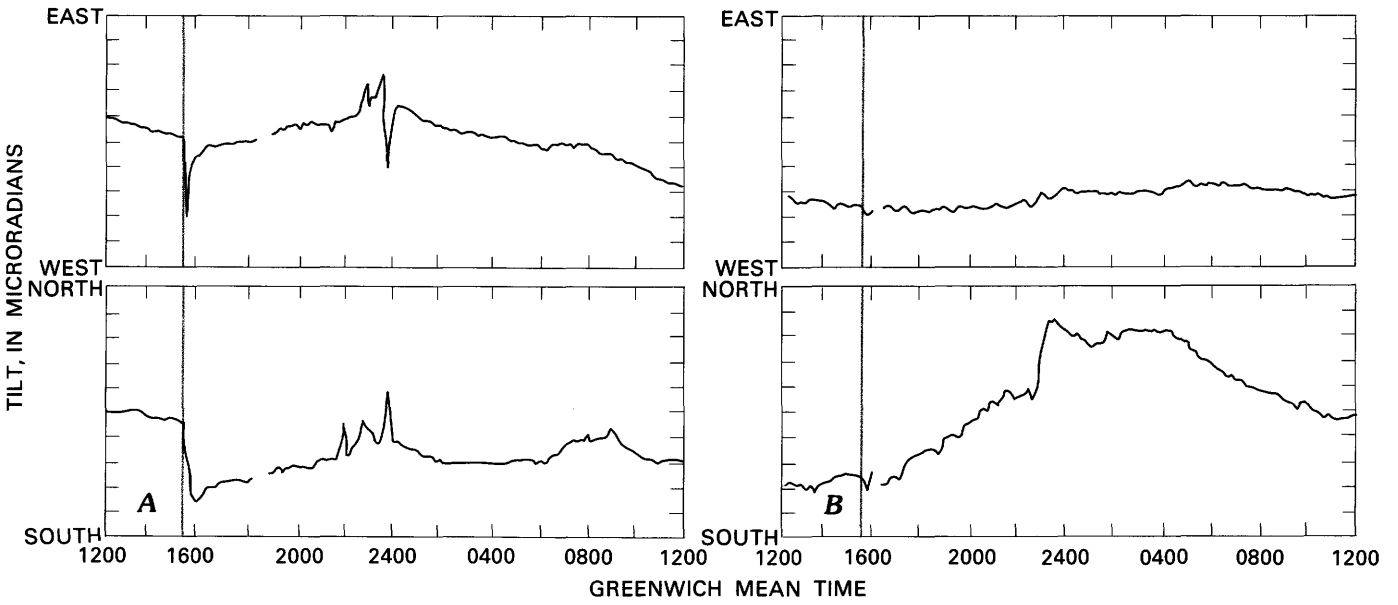

Figure 104.—Twenty-four-hour tilt data that span the May 18 eruption. A downward tilt to east or north is defined as positive. Data were taken at approximately 10-min intervals; diurnal variations have not been removed. Vertical line indicates 0832 PDT, time of earthquake that initiated eruptive activity. A, data from Ape Cave North station; B, data from Ape Cave station.

nearest stations) are shown in figure 104. These data were received in approximately 10-min intervals, and they are shown beginning from 1200 GMT on May 18—that is, 3.5 hr before the onset of eruptive activity.

The closer station, Ape Cave North, recorded a sudden inflationary tilt change of about 4 μrad, which coincided with the beginning of eruptive activity; at the same time, the more distant station, Ape Cave, did not record any abrupt change in tilt larger

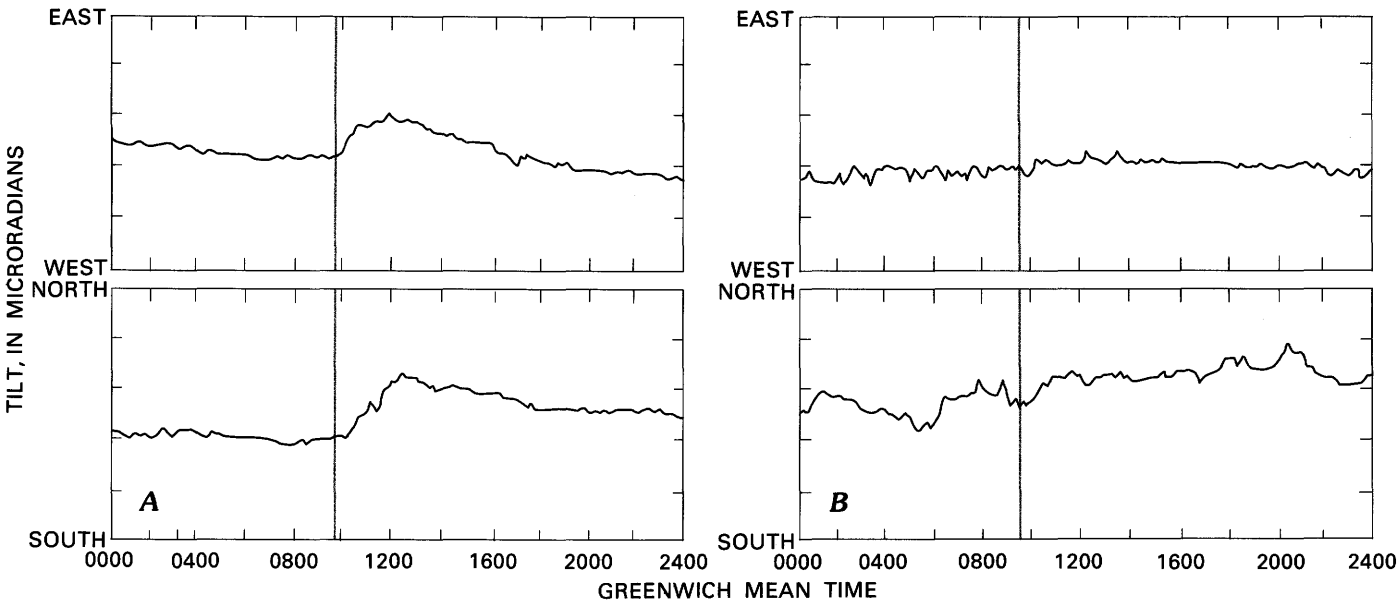

Figure 105.—Twenty-four-hour tilt data that span the May 25 eruption. A downward tilt to east or north is defined as positive. Vertical lines indicate onset of major eruptive activity as indicated by seismic data. A, data from Ape Cave North station; B, data from Ape Cave station.

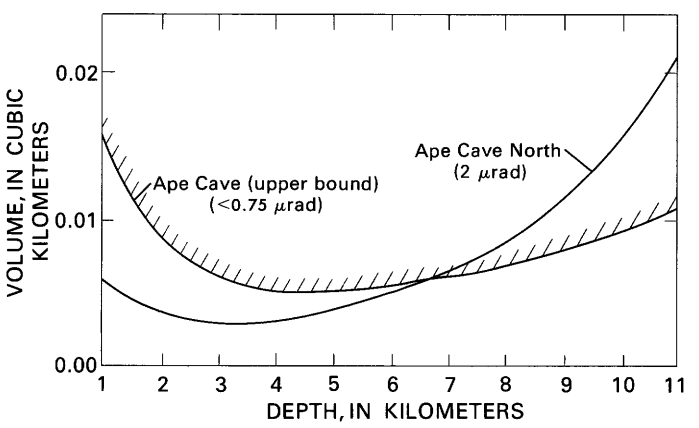

Figure 106.—Plot of theoretical volume of material transported during May 25 eruption. Calculation based on tilt data shown in fig. 105, assuming a point source in an elastic half-space. The family of possible solutions must lie on the solid line (determined from tilt data from Ape Cave North) below the hachured line (upper bound, determined from tilt data from Ape Cave).

than 1 μrad. Between 2200 and 2400 GMT, when the highest amplitude of harmonic tremor was being recorded (Malone and others, this volume), short-term, transient deflationary tilt changes of a few microradians were recorded by both instruments.

No obvious precursory tilt changes preceded the large eruption of May 18. A more complete picture of the tilt changes that occurred during this eruption, and possibly of short-term changes that may have preceded the eruption, may be revealed when the diurnal variation has been removed from these data.

POST-MAY 18 ERUPTIONS

A series of eruptive plumes and dome extrusions occurred at Mount St. Helens during the months after the large eruption on May 18. The timing and style of this eruptive activity are discussed by Christiansen and Peterson (this volume). Of the four major eruptive sequences that occurred between late May and September 1980, definite tilt changes accompanied only the May 25 eruption.

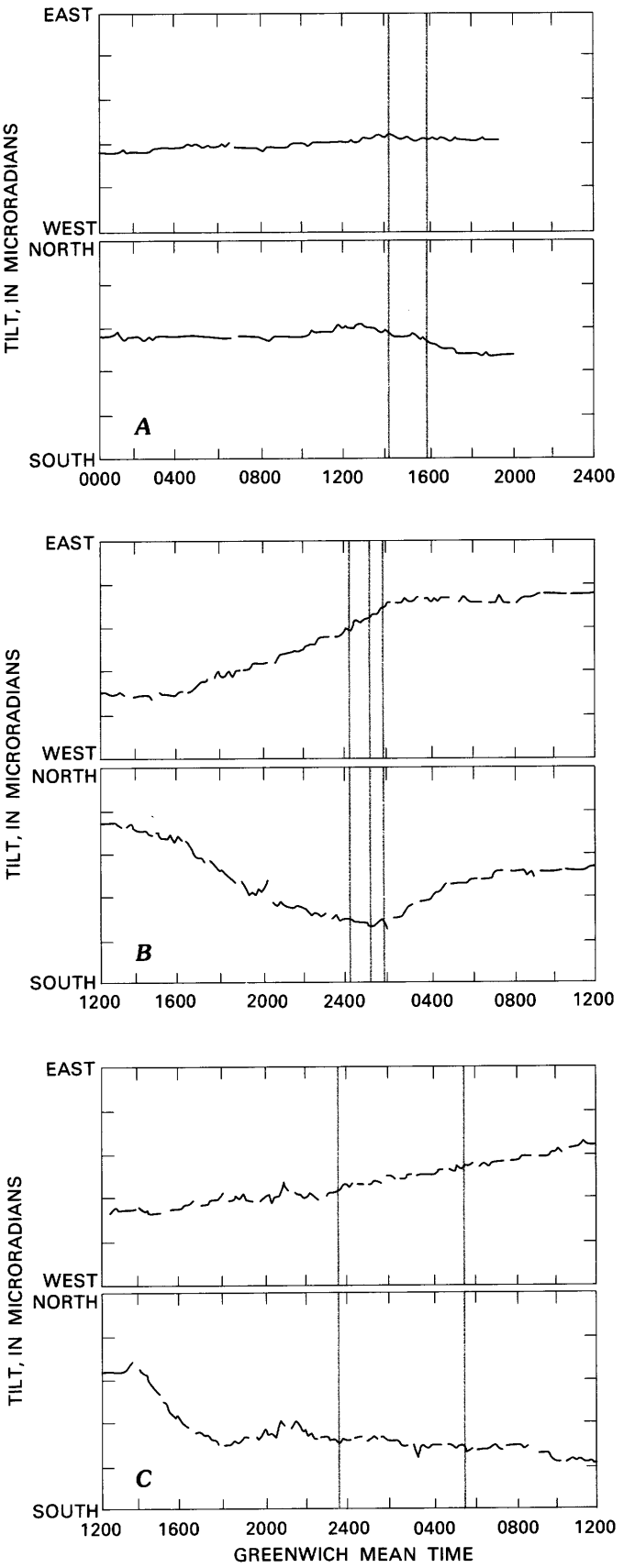

Figure 107.—Twenty-four-hour tilt data recorded at Ape Cave North station that span the eruptions of June 12, July 22, and August 7. A downward tilt to east or north is defined as positive. Vertical lines indicate onset of major eruptive activity as indicated by seismic data. A, June 12; B, July 22-23; C, August 7-8, 1980.

Tilt data received in approximately 10-min intervals during the 24 hr spanning the May 25 eruption are shown in figure 105. An abrupt deflationary change in tilt that coincided with the beginning of the major eruptive phase was recorded at the Ape Cave North station (fig. 105*A*). A similar though much smaller deflationary change in tilt may also have been simultaneously recorded by the Ape Cave station (fig. 105*B*); however, the magnitude of this change is not convincingly above the noise level of this station, which is about 0.75 μrad. A maximum value of 0.75 μrad tilt change is indicated by the record shown in figure 105*B*.

The tilt change recorded on May 25 at the Ape Cave North station and the maximum value estimated for the change at the more distant Ape Cave station allow the rough estimation of the maximum depth of the source giving rise to these possible tilt changes (fig. 106). Assuming a small spherical or point source in an elastic half-space, the volume change of the volcano as a function of depth may be computed from the observed and the bounded values of changes in tilt. Assuming that this point source is directly below the center of the volcano, a tilt change of 2 μrad at the distance of the Ape Cave North tiltmeter would result in a volume transported from various depths to the surface as indicated by the solid curve. An upper bound on the change in tilt recorded by the Ape Cave tiltmeter of 0.75 μrad requires all possible volume changes to lie below the hachured line in figure 106. The intersection of these two curves indicates that the maximum source depth for this eruption, based on this model, is less than 7 km.

None of the eruptions later in the summer at Mount St. Helens produced immediate tilt changes larger than 0.5 μrad at the Ape Cave North station (fig. 107) or at other stations (fig. 102).

SUMMARY

Electronic tiltmeters are well suited to measure rapid, small changes in tilt that accompany eruptive activity of short duration; however, these instruments do not allow dependable determination of long-term tilt changes of small magnitude because of drift of the electronic components, the short base of the sensor, and the site installation.

At Mount St. Helens, the electronic tiltmeter network has met with modest success; changes associated with eruptions produced small changes in tilt. These instruments recorded the gradual inflation of the region surrounding the volcano, which continued until the appearance of the first lava dome in mid-June. Since then, additional tiltmeters, together with those that survived the May 18 eruption, have indicated no net change or at most a very minor deflation or subsidence of the region immediately surrounding the volcano from mid-June to early October. Rapid changes in tilt of a few microradians were recorded at the onset of activity during the May 18 and May 25 eruptions. No immediate tilt changes larger than 0.5 μrad accompanied surface activity during subsequent major eruptions of Mount St. Helens, which occurred on June 12, July 22, and August 7.

REFERENCE CITED

Mortensen, C. E., Iwatsubo, E. Y., Johnston, M. J. S., Myren, G. D., Keller, V. G., and Murray, T. L., 1977, U.S. Geological Survey tiltmeter networks, operation and maintenance: U.S. Geological Survey Open-File Report 77-655, 39 p.

TEMPORAL GRAVITY VARIATIONS AT MOUNT ST. HELENS, MARCH-MAY 1980

By ROBERT C. JACHENS, D. RANDALL SPYDELL, G. STEPHEN PITTS[1], DANIEL DZURISIN, *and* CARTER W. ROBERTS

ABSTRACT

A sequence of gravity measurements began on Mount St. Helens on March 29, 1980, 9 days after the onset of seismic activity beneath the mountain and 2 days after the initial eruption from the summit region. A network of seven stations on the north and east flanks of the volcano was established between March 29 and April 2, and parts of the network were remeasured five times between April 4 and May 9. Three stations (Timberline, Windy Pass, and East Dome) were within 2–3 km of the bulge that formed on the north flank before the catastrophic eruption of May 18. Gravity values were tied to a remote station in the North Fork Toutle River valley about 17 km from the summit and taken repeatedly at each station along closed loops using three gravimeters. Uncertainties associated with the measurements averaged about 10 μGal (1 standard error).

Interpretation of the gravity data led to the conclusion that the growth of the bulge was the only significant event detectable through these techniques. Gravity at Timberline remained virtually constant during the period March 29–May 9. Gravity at Windy Pass and East Dome increased by approximately 30 μGal between April 2 and 7, then decreased by 30–50 μGal between April 7 and May 9. The gravity data from the three stations, with the effects associated with the volcanic processes and redistribution of snow and ground water eliminated, show only small total changes (<20 μGal) and maximum fluctuations of only 30 μGal. Calculations based on topographic maps show that the growth of the north-flank bulge should have caused gravity to decrease almost uniformly with a rate of 1.0 μGal/day at Timberline and Windy Pass and a rate of 0.5 μGal/day at East Dome, which would account for only part of the decrease and does not account for the measured increase. Based on the relationship between gravity change and elevation change (about -2 μGal/cm), the gravity data imply net elevation changes of less than 10 cm at all three stations.

From the relative constancy of the data indicating small elevation changes and using the estimated volume increase of the bulge to account for most of the fluctuations, it is reasonably certain that the source region of the magma that intruded the north flank was deeper than 7 km and probably was deeper than 10 km, and could not have been nearer the surface without detection by precision gravity measurements.

INTRODUCTION

Precise gravity measurements are a rapid and inexpensive means for monitoring deformation and mass movement associated with volcanic activity. Assuming that the effects of solid-earth tides, ocean tides, and mass movements in the atmosphere have been taken into account, gravity measured at a point fixed to the Earth's surface will vary with time in response to vertical displacement of the observation point and to variations of mass distributions near the observation point. Temporal gravity changes associated with volcanic activity typically range from a few microGals to a few hundred microGals ($1\ \mu\text{Gal} = 1 \times 10^{-6}$ cm/s^2) and generally display a good correlation with elevation changes.

Recent advances in the design of gravimeters and refinements in observational techniques permit gravity differences between widely spaced points to be

[1]School of Oceanography, Oregon State University, Corvallis, Oreg. 97331.

measured with uncertainties of 10 μGal or less. These instruments and techniques have been used successfully to study volcanic events in Hawaii, Iceland, and Japan. When volcanic activity began at Mount St. Helens in March 1980, a program of repeated gravity measurements was set up in order to study the deformation and mass movements associated with this activity.

DATA COLLECTION AND REDUCTION

On March 29, 1980, 2 days after the initial eruption from the summit of Mount St. Helens and 9 days after the onset of seismic activity beneath the mountain, a network of high-precision gravity stations was established on the north side of the volcano (fig. 108). The network consisted of a reference station in the North Fork Toutle River valley about 17 km northwest of the summit, two stations in the same valley directly north of the mountain, a station just south of Spirit Lake, and a station in the Timberline parking area. The following day two new stations (Windy Pass and East Dome) on the northeast and east flanks of the volcano were added to the network.

Measurements were made every day for 5 days (March 29–April 2) and then repeated for part of the network on April 4, 7, 10, and 17, and May 9. After the first 4 days of measurement, the observed temporal gravity variations appeared very small throughout the network, and the three stations farthest from the summit (Spirit Lake and two stations immediately to the west) were abandoned in order to concentrate effort at the three stations closest to the summit. The

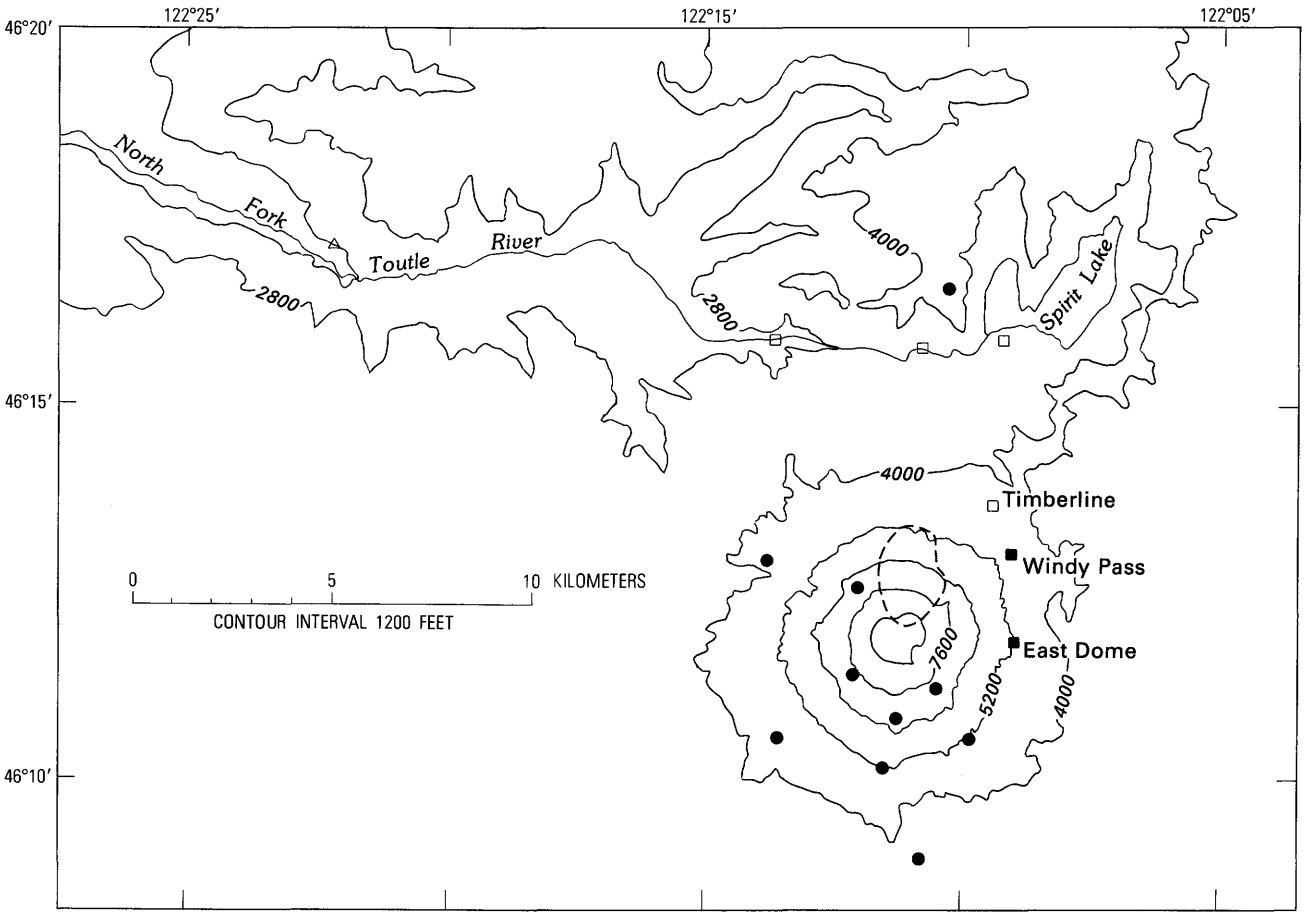

Figure 108.—Precision gravity stations on Mount St. Helens: open triangle, reference station for all pre-May 18 surveys; open squares, pre-May 18 stations buried during May 18 eruption; solid squares, pre-May 18 stations recovered following the May 18 eruption and included in post-May 18 network; solid dots, stations established after May 18. Dashed line, general outline of bulge that developed on north flank prior to May 18 eruption.

catastrophic eruption of May 18, 1980, effectively ended this phase of the study by burying five of the stations, including the reference station, which is now beneath an estimated 30–60 m of debris. Following this eruption, one of the two former instrument sites at East Dome was recovered, but severely disrupted local terrain prevented recovery of the second instrument site at East Dome and the one at Windy Pass. New instrument sites were established at these stations and made part of a new network (fig. 108) whose reference station is located in Vancouver, Wash.

Gravity measurements, tied to the reference station, were taken repeatedly at each station using LaCoste and Romberg gravimeters equipped with electronic readout. In a typical survey every network station was measured with three gravimeters during two complete loops through the network per day with the reference station remeasured every 2–4 hr. Earth-tide effects were removed according to the formulation of Longman (1959), with a compliance factor of 1.160; a linear or parabolic function of time was used to approximate daily gravimeter drift. Calibrations of all gravimeters are based on measurements taken over the USGS's Mount Hamilton calibration range (Barnes and others, 1969).

For each survey, the use of three gravimeters over two closed loops of the network generally yielded 12 one-way measurements of gravity difference between the reference station and the network stations. The measurements at each station were averaged to obtain one observed gravity data point per day. Uncertainties associated with these data average about ± 10 μGal (1 computed standard error). Because the uncertainty limits were computed from the data, they include contributions from errors in gravimeter calibration, tide correction, and drift removal, as well as uncertainties in gravimeter readings caused by high-frequency ground motion from numerous local earthquakes.

The variation of gravity at four stations for the period March 29–May 9, 1980, is shown in figure 109. During this interval, gravity at Timberline remained virtually constant within the limits of uncertainty. The data for March 30 and April 1 at Windy Pass and East Dome are highly uncertain because they are based on a single loop made with only one gravimeter. Starting on April 2 the measured gravity at both Windy Pass and East Dome increased until April 7 and then decreased during the remainder of the observation period. At Windy Pass the increase amounted to 25 μGal and the decrease to 56 μGal, while at East Dome a 31 μGal increase was followed by a 34 μGal decrease.

Apparent short-term phenomena also were seen during some surveys. While measuring at East Dome, two of the authors (Dzurisin and Roberts) watched the level bubbles on two gravimeters move in a manner that suggested a short-term tilt event (down to the east followed by down to the west) of roughly 100 μrad magnitude. A summit eruption occurred during the event. During another measurement at East Dome, Pitts noted an apparent short-term gravity change that accompanied a series of strong local earthquakes. However, because the apparent change (about 30 μGal over a 40-min period) was seen on only one gravimeter (only one gravimeter was being read at the time), it was not possible to determine whether this represented a real gravity change or simply rapid gravimeter drift caused by the shaking.

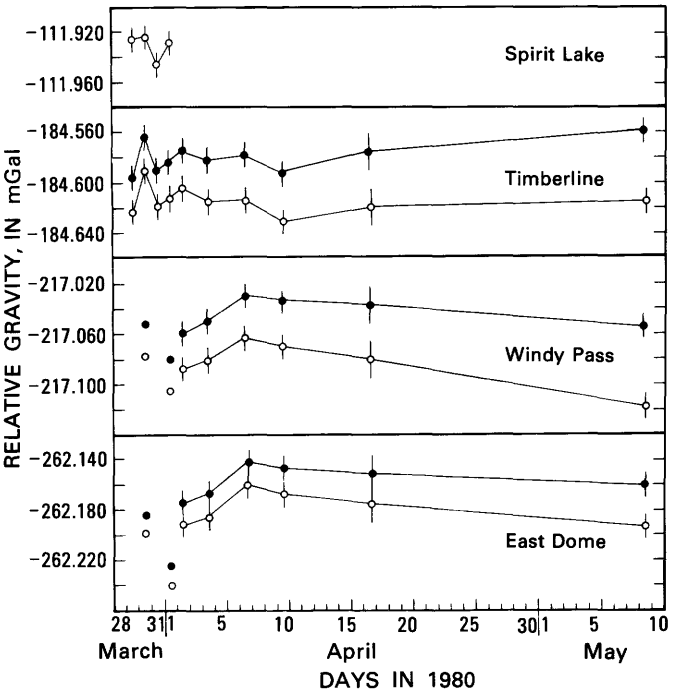

Figure 109.—Temporal variations of gravity at four stations of the pre-May 18 gravity network; open circles, observed gravity data; solid circles, gravity data corrected for the effects of the north-flank bulge. Error bars represent ±1 standard error. Error bars for April 17 data are larger than others because battery failures caused this survey to be terminated before two loops could be completed. Data for March 30 and April 1 at Windy Pass and East Dome are highly uncertain because they are based on a single loop made with only one gravimeter.

INTERPRETATION OF THE GRAVITY DATA

Recent studies of temporal gravity variations during volcanic activity at other volcanoes have shown that changes in the gravity field generally reflect changes of elevation (Jachens and Eaton, 1980; Dzurisin and others, 1980; Johnsen and others, 1980; Torge and Kanngieser, 1980). Most gravity changes and elevation changes at specific observation points followed an approximate Bouguer relationship of -2 μGal/cm, a relationship that is compatible with deformation resulting from simple inflow and outflow of magma from a subsurface reservoir. Before interpreting the Mount St. Helens results shown in figure 109 in terms of a Bouguer relationship, however, the effects of large, nonlocal deformation and of snow and ground-water distributions must be considered.

Examination of topographic maps of Mount St. Helens constructed by photogrammetric techniques from aerial photographs taken on August 15, 1979, April 7 and 12, 1980, and May 1 and 12, 1980, revealed that the summit region and part of the north flank of the volcano were deforming rapidly during the period covered by the gravity observations (Moore and Albee, this volume). The deformation had two main components. The largest consisted of northward and possibly upward displacement of a large area (approximately 1.5×2.5 km) on the north flank, accompanied by subsidence in a graben near the summit. The rapid displacement of the north flank later was confirmed and more precisely defined by ground-based geodetic measurements (Lipman, Moore, and Swanson, this volume). This deformation has been interpreted as resulting from the emplacement of magma high within the volcano's edifice (Moore and Albee, this volume; Lipman, Moore, and Swanson, this volume). The second component consisted of the formation of two summit craters that eventually coalesced into one. These craters were formed by explosive eruptions in the summit region. A preliminary estimate by Moore and Albee suggested that the volume of the mountain showed a net increase of 0.11 km^3 between August 15, 1979, and May 12, 1980, despite the formation of the craters.

The redistribution of mass within and below Mount St. Helens implied by the deformation studies must have affected the gravity field over the mountain. Because mass was being added at an elevation higher than the gravity stations during the observation period, the effect should have been to decrease gravity. The magnitudes of the gravity changes at Timberline, Windy Pass, and East Dome that accompanied the bulging of the north flank were estimated by direct calculation from the successive topographic maps. For the region below the 8,800-ft contour where deformation was relatively simple, the gravity effect of the bulge alone was calculated. The position and magnitude of the bulge at various times were determined by measuring differences between the topographic map of August 15, 1979, and those of 1980. The growth of the bulge is shown in figure 70 (Moore and Albee, this volume). For the region above the 8,800-ft contour where the pattern of deformation was complex, the gravity effect of the entire mountain top was computed from each of the five topographic maps and the calculated gravity changes determined by comparing the computed values corresponding to various different times. A constant density ($\rho = 2.3$ g/cm^3) was assumed for all calculations.

These calculations indicate that between April 7 and May 12, 1980, deformation high on the mountain should have caused the gravity to decrease almost uniformly with a rate of 1.0 μGal/day at Timberline and Windy Pass and a rate of 0.5 μGal/day at East Dome. The calculated rates probably represent minimum estimates, because of difficulty in identifying areas of low-amplitude deformation from topographic maps with 80-ft contours and because some material removed from the summit crater was ice with a density substantially lower than the assumed density of 2.3 g/cm^3.

The observed gravity data were corrected for the effects of known mass movement by using the calculated deformation rates and extrapolating backward in time to the start of the gravity surveys (fig. 109). Changes in these corrected data between the beginning and end of the observation periods at the three stations are slightly positive, with a maximum of about 20 μGal seen at Timberline. Considering the uncertainties associated with the gravity data and the additional uncertainties associated with the estimation of the gravity effect of the north-flank bulge, the total gravity changes measured at Windy Pass and East Dome can be almost fully explained by the growth of the north-flank bulge.

Another process that affected the gravity field during the measurements was the redistribution of mass by melting of snow and movement of ground water. No direct information is available on water-table fluctuations in the vicinity of any of the gravity stations. The snow pack, however, did vary with location and time. No snow was present at the reference station at any time during the surveys, and wind prevented any significant accumulation of snow on East Dome. The Windy Pass station also was kept clear of snow by wind, but an estimated 0.3–0.6 m of snow was present on nearby slopes during April. A snow pack at least 1.5 m thick was present at Timberline until mid-April. By May 9, snow was almost completely gone at all stations. Because the initial snow pack was thickest at Timberline and the slope of the land surface near Timberline was gentler than that near the other stations, the gravity change due to snow and ground-water redistribution probably was largest at Timberline. If, during the melting process, the total snow mass above ground at Timberline moved into the ground, the gravity increase would have amounted to 7–8 μGal. The gravity increase could have been slightly larger if the ground water beneath the station was supplemented by contributions from melting snow higher on the mountain. Thus, inclusion of the effects of snow and ground-water variations probably would decrease the total gravity changes at Windy Pass and East Dome by a few μGals and reduce the increase at Timberline to about 10–15 μGal.

Therefore, after eliminating the estimated effects of growth of the north-flank bulge and of snow and ground-water variations, the total calculated gravity changes at the three stations are small (< 20 μGal) and probably are not significant in light of uncertainties associated with both the gravity data and the estimates of the perturbing influences. Such small changes are surprising because they imply, according to the Bouguer relationship between gravity change and elevation change (-2 μGal/cm), that any net vertical displacements of the three stations over the observation interval were less than 10 cm, even though only 2–3 km away, more than 100 m of horizontal displacement took place during the same period (Lipman, Moore, and Swanson, this volume). The implications of the absence of measurable vertical displacement at the three gravity stations will be examined in the next section.

DISCUSSION AND CONCLUSIONS

Studies of deformation patterns on active volcanoes in Hawaii (Fiske and Kinoshita, 1969), Japan (Mogi, 1958; Yokoyama, 1974) and Iceland (Johnsen and others, 1980) have revealed the existence of shallow magma reservoirs beneath the volcanoes. Calculations based on models of localized sources of variable pressure at depths of 2–3 km generally show good agreement with the observed deformation patterns, although in the case of Sakurazima Volcano (Mogi, 1958) a source depth of 10 km seemed to fit the observed data best. In contrast, at Mount St. Helens the most pronounced deformation prior to May 18 seemed to be associated with emplacement of magma (probably with a density similar to that of the surrounding material) at a depth of less than 1 km beneath the mountain's north flank (Moore and Albee, this volume). Because, as indicated by the photogrammetric observations and geodetic measurements, the localized deformation probably did not extend as far as the gravity stations, the gravity observations cannot contribute much new information about it. However, the gravity measurements can help set limits on the location of the deeper source region that supplied magma to the shallow intrusion.

Deformation associated with the transfer of magma from a reservoir beneath Mount St. Helens to the region beneath the north flank was considered by computing the vertical displacements at the gravity stations that would have been caused by a localized volume decrease at various depths beneath the mountain. The localized volume decrease could be due to partial emptying of either a small isolated magma reservoir or a localized region of a large reservoir. The vertical displacements were estimated from the formula of Walsh (1975),

$$h = \frac{\Delta V}{\pi}(1-\nu)\frac{c}{(r^2+c^2)^{3/2}} \qquad (1)$$

where h represents the vertical displacement at the surface due to a volume change in a small region buried in a homogeneous, isotropic, elastic half-space. In this formula ΔV is the volume change, ν is Poisson's ratio, c is the depth to the source, and r is the horizontal distance from the observation point to the point directly above the source. For these calculations, the source was placed directly beneath the

former summit of the volcano, a position that is suggested by the positions of the lava domes that have formed following the May 18 eruption (Moore and others, this volume) and by the distribution of seismicity beneath the mountain both before and after the May 18 eruption (Endo and others, this volume). Displacing the source 1 km northward, in better agreement with the seismicity distribution, causes only slight increases in the calculated displacements at Windy Pass and Timberline. The magnitude of the volume decrease at depth was assumed equal to 0.13 km^3, and a Poisson's ratio of 0.25 was used. The assumed volume decrease at depth is 0.01 km^3 larger than the net volume increase of the mountain estimated by Moore and Albee because their estimate includes a -0.01 km^3 contribution from the formation of the summit crater, a contribution that would not reflect the volume change at depth.

The calculated changes of elevation at the gravity stations for various source depths from 1–20 km are given in table 8. These displacements have been adjusted according to the growth history of the bulge (Moore and Albee, this volume) and represent only those that should have occurred during the intervals covered by the gravity observations. Comparing the results in this table with the inferred net elevation changes of less than 10 cm at all three stations suggests that the source region, depleted during the growth of the bulge, should lie deeper than 7 km and probably deeper than 10 km.

Table 8.—Subsidence, relative to the base station, calculated using various magma source depths

[Station Timberline: based on data collected March 29–May 9, 1980; stations Windy Pass and East Dome: based on data collected April 2–May 9]

Hypothesized source depth (km)	Subsidence (cm)*		
	Timberline	Windy Pass	East Dome
1	33	35	64
2	50	52	83
3	52	51	73
5	39	36	43
7	26	23	26
10	14	12	13
15	6	5	5
20	3	3	3

*A refined estimate of the net volume change of the mountain (Moore and Albee, this volume) suggests that all displacements in this table should be decreased by approximately 8 percent.

A deep source region would not be in conflict with the results from geodimeter measurements taken between East Dome station and Smith Creek Butte, 8 km to the east, and by the interpretation of heat-flow measurements made near Mount St. Helens. The geodimeter measurements, first made in 1973 and repeated during the period leading up to May 18, showed no change in the distance between the two sites that was larger than the estimated uncertainty of ±2.5 cm (Lipman, Moore, and Swanson, this volume). Depletion of a source at 7 km or shallower should have caused a change in this distance of more than 3 cm, greater than the limit of the uncertainty. Additional support for a deep source comes from heat-flow data, which have been interpreted to indicate that no large, shallow magma chamber exists beneath Mount St. Helens above about 10 km (Blackwell and others, 1980).

The gravity results do not completely rule out the possibility of a magma reservoir at shallow depth beneath Mount St. Helens. The absence of measurable vertical displacements could be the result of uplift (associated with the north-flank bulge) that almost cancelled subsidence (associated with depletion of a deeper reservoir) at all three stations. This seems unlikely, however, because the ground-based geodetic measurements indicated that displacements on the lower parts of the bulge (at elevations roughly comparable to the station elevations) were predominantly horizontal with a slight downward component (Lipman, Moore, and Swanson, this volume). Alternatively, a shallow reservoir could have supplied some of the magma to the north-flank intrusion provided that the shallow reservoir, in turn, was resupplied from a source at greater depth. Finally, the magma could have come from a shallow reservoir of large areal extent rather than the localized reservoir assumed for the calculations. However, the heat-flow results (Blackwell and others, 1980) argue against this possibility.

POST-MAY 18 STUDIES

A new network of gravity stations was established on and around Mount St. Helens following the catastrophic eruption of May 18 (fig. 108). Gravity at some stations was measured during surveys on June 12–18, and remeasured at the expanded network during surveys on July 28–August 1 and Septem-

ber 14–17. Most stations of the new network are at geodimeter-instrument or reflector sites. The reference station is at Pearson Air Park, Vancouver, Wash., which is, in turn, tied to a station at Rocky Butte in Portland, Oreg., and to the U.S. National Gravity Base Net (Schwimmer and Rice, 1969).

Most of the gravity changes measured so far are smaller than 15 μGal and show no consistent pattern. Large changes (40–60 μGal) have been measured at two stations high on the south and southeast flank of the volcano but various tests of data consistency indicate that these changes probably reflect local site instability or inaccurate readings rather than actual gravity changes in this region. We plan to resurvey this network at 1–3-mo intervals in order to monitor any future deformation of the volcano and to better define the location of the source region.

REFERENCES CITED

Barnes, D. F., Oliver, H. W., and Robbins, S. L., 1969, Standardization of gravimeter calibrations in the U.S. Geological Survey: American Geophysical Union Transactions, v. 50, p. 526–527.

Blackwell, D. D., Steele, J. L., Schuster, E. J., and Korosec, M., 1980, The regional geothermal setting of the Mount St. Helens Volcano [abs.]: American Geophysical Union Transactions, v. 61, p. 1134.

Dzurisin, D., Anderson, L. A., Eaton, G. P., Koyanagi, R. Y., Lipman, P. W., Lockwood, J. P., Okamura, R. T., Puniwai, G. S., Sako, M. K., and Yamashita, K. E., 1980, Geophysical observations of Kilauea volcano, Hawaii, 2, Constraints on the magma supply during November 1975 -September 1977: Journal of Volcanology and Geothermal Research, v. 7, p. 241–269.

Fiske, R. S., and Kinoshita, W. T., 1969, Inflation of Kilauea volcano prior to its 1967–1968 eruption: Science, v. 165, p. 341–349.

Jachens, R. C., and Eaton, G. P., 1980, Geophysical observations of Kilauea volcano, Hawaii, 1, Temporal gravity variations related to the 29 November 1975, M=7.2 earthquake and associated summit collapse: Journal of Volcanology and Geothermal Research, v. 7, p. 225–240.

Johnsen, G. V., Bjornsson, A., and Sigurdsson, S., 1980, Gravity and elevation changes caused by magma movement beneath the Krafla caldera, northeast Iceland: Journal of Geophysics, v. 47, p. 132–140.

Longman, I. M., 1959, Formulas for the tidal acceleration of gravity: Journal of Geophysical Research, v. 64, p. 2351–2355.

Mogi, K., 1958, Relations of eruptions of various volcanoes and the deformation of the ground surfaces around them: Earthquake Research Institute Journal, Tokyo University, v. 39, p. 99–134.

Schwimmer, P. M. and Rice, D. A., 1969, U.S. National Gravity Base Net: American Geophysical Union Transactions, v. 50, p. 527.

Torge, W., and Kanngieser, E., 1980, Gravity and height variations during the present rifting episode in northern Iceland: Journal of Geophysics, v. 47, p. 125–131.

Walsh, J. B., 1975, An analysis of local changes in gravity due to deformation: Pure and Applied Geophysics, v. 113, p. 97–106.

Yokoyama, I., 1974, Crustal deformations associated with volcanic activities: Tectonophysics, v. 23, p. 349–360.

THE 1980 ERUPTIONS OF MOUNT ST. HELENS, WASHINGTON

VOLCANOMAGNETIC OBSERVATIONS DURING ERUPTIONS, MAY-AUGUST 1980

By M. J. S. JOHNSTON, R. J. MUELLER, *and* JOHN DVORAK

ABSTRACT

Three recording magnetometers of 0.25 nT (nanotesla) sensitivity were installed on Mount St. Helens 10 days before its catastrophic May 18 eruption. Two units were lost in this eruption. The third, located about 5 km to the west of the main crater, continued to operate through two subsequent eruptions at a recorded rate of once every 10 min. By referencing these data to other synchronized data at Victoria, Canada, and from a recording magnetometer array in California, magnetic field transients exceeding 10 nT can be identified at the times of three major eruptions. Precursive activity may have occurred prior to the May 25 and June 12 eruptions. No precursive transients are apparent in the data in the few hours before the May 18 eruption, but a positive offset of 9 ± 2 nT occurred during this eruption. This offset is more easily explained by elastic strain release than as a result of the removal of 2.5 km^3 of magnetic material during the May 18 eruption.

INTRODUCTION

The increase in seismic and volcanic activity from March–August 1980, offered the first opportunity in the continental United States for a definitive determination of rapid magnetic changes associated with volcanic activity. Transient magnetic anomalies have been observed on a number of volcanoes throughout the world, but many details remain unclear. The best studies have been made on Oshima volcano in Japan (Rikitake, 1951), Ruapehu and Ngaurahoe volcanoes in New Zealand (Johnston and Stacey, 1969a, 1969b), Kilauea volcano in Hawaii (Davis and others, 1979) and La Soufrière volcano in the Caribbean (Pozzi and others, 1979).

Three proton magnetometers, each with a 0.25 nT (nanotesla) sensitivity, were installed on Mount St. Helens on May 8 at sites on the northeast (SHN), east (SHE), and west (SHW) sides of the mountain (fig. 110). The instruments sampled synchronously once every 10 min and data were recorded with on-site digital printers.

Unfortunately, two of the magnetometers, at stations SHN and SHE, were lost in the May 18 eruption. As indicated in figure 110, both sites were covered by ash and mudflows. The magnetometers (and records up to the time of the site destruction) may have survived intact due to the solid and sealed construction of the instrument case, but neither unit has yet been found.

The amplitudes and spatial scales of magnetic effects of volcanic origin are difficult to ascertain with the records from only the one magnetometer at SHW during the May 18, and subsequent large eruptions on May 25 and June 12. Some discrimination against broad-scale magnetospheric disturbances is possible by referencing to the nearest synchronized magnetometers at the Victoria Geomagnetic Observatory (VIC) or to the most northern USGS proton magnetometer stations BLM and MTH (fig. 110) near San Francisco. The measurement precision that can be ob-

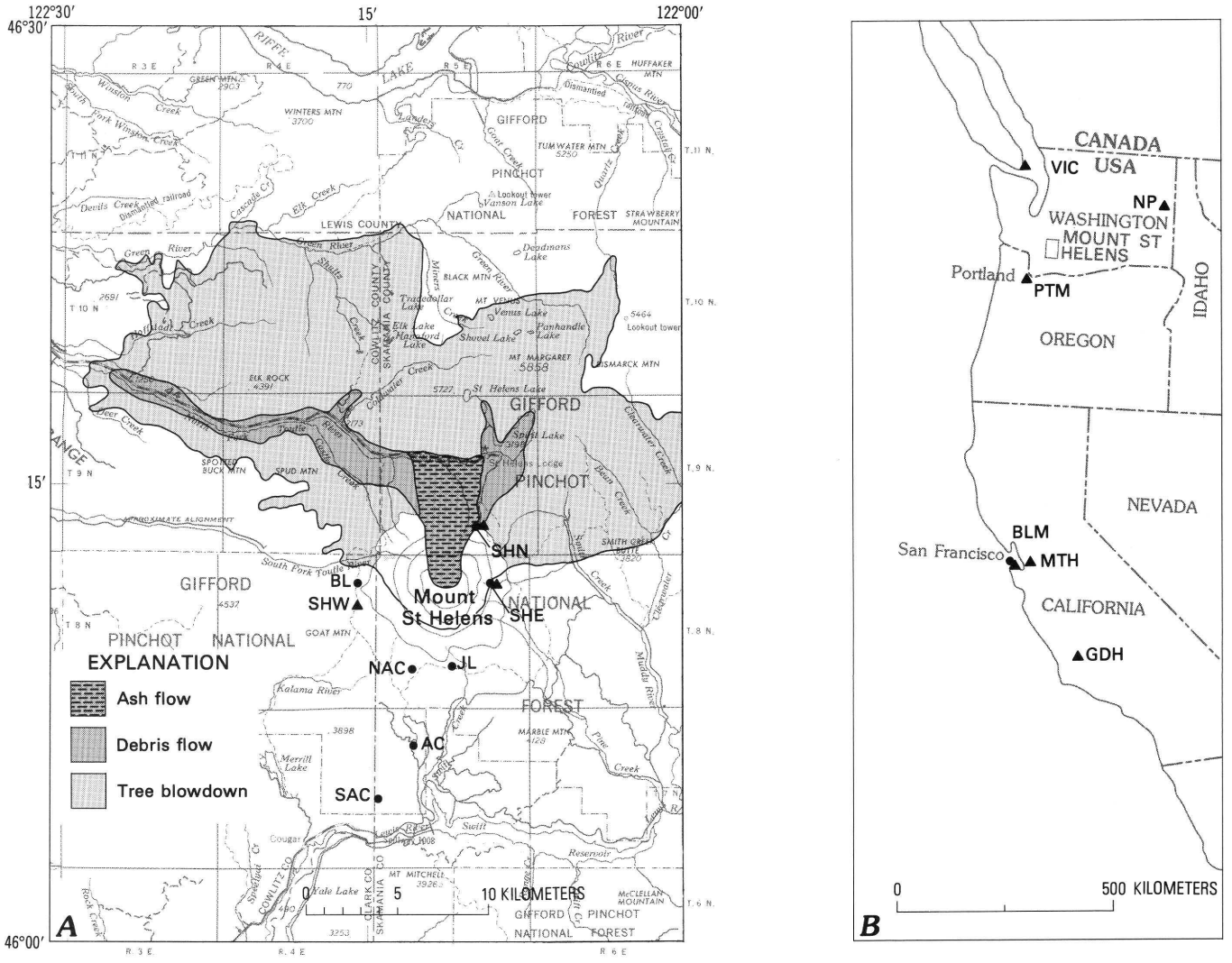

Figure 110.—Locations of proton magnetometer and tiltmeter stations discussed in this report. A, Proton magnetometer stations installed on Mount St. Helens prior to May 18 eruption (triangles) and recording tiltmeter stations installed before and after eruption (solid dots). B, Large-scale map shows locations of permanent recording magnetometer stations (triangles) in Canada, Washington, Oregon, and California used in this study.

tained for the VIC-SHW station pair is about 5 nT for hourly means. For the BLM-SHW station pair it is about 8 nT.

By a remarkable coincidence, a recording proton magnetometer was operated at the Portland airport by Carson Geoscience Co. for a few hours before and after the May 18 eruption. Because the airport is only 80 km from the volcano, the measurement precision for determination of changes during the eruption is less than 2 nT.

The purpose of this report is to present the magnetic observations at SHW during three magmatic eruptions from Mount St. Helens and to discuss the implications that these data have for physical processes that occur during an eruption sequence of this scale.

MAGNETIC OBSERVATIONS

Figure 111 shows comparative difference plots using similar 280-km baselines and time spans for stations VIC and SHW and a station pair in California, BLM and GDH. The VIC-SHW difference should show any volcanomagnetic effects generated by eruptions of Mount St. Helens whereas the BLM-GDH difference

should not. Although BLM and GDH are at a slightly lower geomagnetic latitude than VIC and SHW, these data indicate a measurement resolution (standard deviation of hourly means) for a 280-km station separation of 4.2 nT. The standard deviation of hour averages during times when the mountain was not erupting was 4.8 nT for the VIC-SHW difference and 8.2 nT for the BLM-SHW difference.

The occurrence times of the three major eruptions on May 18 at 0832 PDT (1532 UTC), on May 25 at 0232 PDT (0932 UTC), and on June 12 at 2110 PDT (June 13 at 0410 UTC) are also shown in figure 111. Many minor eruptions occurred also during this period. However, the total energy release for the three major events, particularly the one on May 18, dominates the record of energy release for any of the other eruptions. If volcano-related effects occurred, therefore, they should be most clear for these three events.

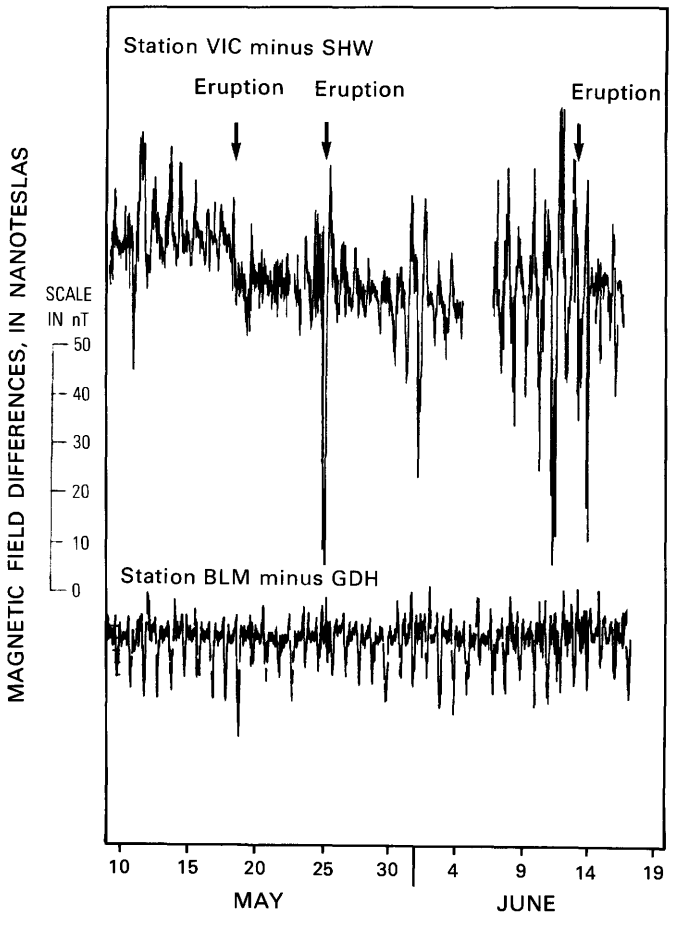

Figure 111.—Comparative plots for the same 280-km baseline of magnetic-field differences between stations VIC and SHW and stations BLM and GDH. Occurrence times (in UTC) of major eruptions on May 18, May 25, and June 12 are indicated by arrows.

The main features of the data are as follows:

1. Generally greater variability in the VIC-SHW record, particularly at times of the May 25 and June 12 eruptions.
2. An increase in magnetic field at SHW during the May 18 eruption of 9 ± 2 nT as indicated by the decreased daily means of the VIC-SHW difference. We note that because the ambient field at VIC is greater than that at SHW, an increase at SHW will decrease the difference (VIC-SHW).
3. Transient variations apparently associated with the May 25 and June 12 eruptions exceeding 50 nT. These are comparable with, and have time scales similar to, records from eruptions of New Zealand volcanoes (Johnston and Stacey, 1969a, 1969b).

Of particular interest is the question of whether magnetic changes preceded these eruptions, as apparently happened for eruptions from New Zealand volcanoes. Figure 112 shows the individual 10-min differences, together with their standard deviations, between SHW and the station PTM magnetometer operated by Carson Geoscience Co. at the Portland airport on the morning of the May 18 eruption. It is evident that no short-term precursor occurred up to the point 2 min before this eruption at 1532 UTC. Because the eruption was probably triggered by landsliding of the volcano's bulging north face, this result is perhaps not surprising.

The first indications of positive field offset are apparent right after the beginning of the eruption (fig. 112). Superimposed on this offset are cyclic variations having amplitudes of about 5 nT. Because these variations are evident also in the total-field record at PTM but with different amplitude, they probably resulted from shock-wave perturbation of the ionosphere.

During the May 25 and June 12 events, the records are less clear because we have no reference magnetometer at the Portland airport to reduce normal geomagnetic disturbances below the 2-nT level. Figure 113*A* shows 2 days of individual 10-min differences between station VIC and SHW around the time of the May 25 eruption. Some indication of disturbed magnetic field at SHW is evident for several hours before the eruption. The most dominant feature of the record, however, is the amplitude of the field fluctuations that occurred after the eruption.

These exceeded 50 nT in amplitude and probably resulted in part from eruptive shock-wave effects on the ionosphere, as large perturbations are evident in the total-intensity records at VIC and the Newport Geomagnetic Observatory (NP) in western Washington. However, similar perturbations are not apparent in the total-field records on the 28 recording magnetometers in California from 800–1,600 km to the south.

After about 12 hr, the field returned approximately to its preeruptive value and no net offset is apparent above the measurement error. Because the energy dissipated by this eruption was from two to four orders of magnitude less than that for the May 18 eruption and was of different form, an offset of comparable amplitude should not be expected.

An expanded time scale around the time of the June 12 eruption is shown in figure 113*B*. Pronounced disturbance is apparent in this record near the time of this eruption. Even larger disturbances (> 50 nT) occurred during the few days prior to the eruption (fig. 111).

The total-intensity record from station BLM (fig. 114) shows no large perturbations at the times of each eruption, but some minor variations are apparent on May 25 and perhaps also in early May and early June. The shock wave from the relatively small May 25 eruption would appear therefore to have been more efficient at producing an ionospheric perturbation than that from the other eruptions. The May 25 perturbation is apparent in records of other recording magnetometers located out to at least 1,000 km from the mountain.

DISCUSSION

We have made some general investigations of the possible physical mechanisms that might have contributed to these records. Thermal-diffusion effects can be ruled out because the process is too slow. Magnetogasdynamic (MGD) effects certainly occurred within the eruption clouds. For gas velocities of as much as 100 m/s and using reasonable estimates of pressure, density, and charge density of hot ionized air, resulting magnetic and electric field perturbations in excess of 300 nT and 2000 V/m, respectively, could have occurred within the cloud (Shercliffe, 1965). Lightning was observed both within the eruption cloud and from the cloud to ground. However, there are two reasons why these effects are an unlikely explanation for the main features of the magnetic record. Firstly, the MGD effects from a turbulent gas cell within the eruption cloud would fall off at least as the inverse square of distance or more probably, as the inverse cube of distance. To be observable at distances in excess of 5 km, the source fields would need to be at least several orders of magnitude larger than the values calculated. Secondly, these MGD effects would be apparent as high-frequency transients (> 1 Hz) and would cause random scatter in the data. Inspection of figure 112 indicates that, during the eruption period, sequential 10-min samples differ only slightly, and many do not deviate from the preceding sample by more than one standard deviation (2 nT).

Four possible causal mechanisms remain: removal of magnetic material, electric currents, stress-

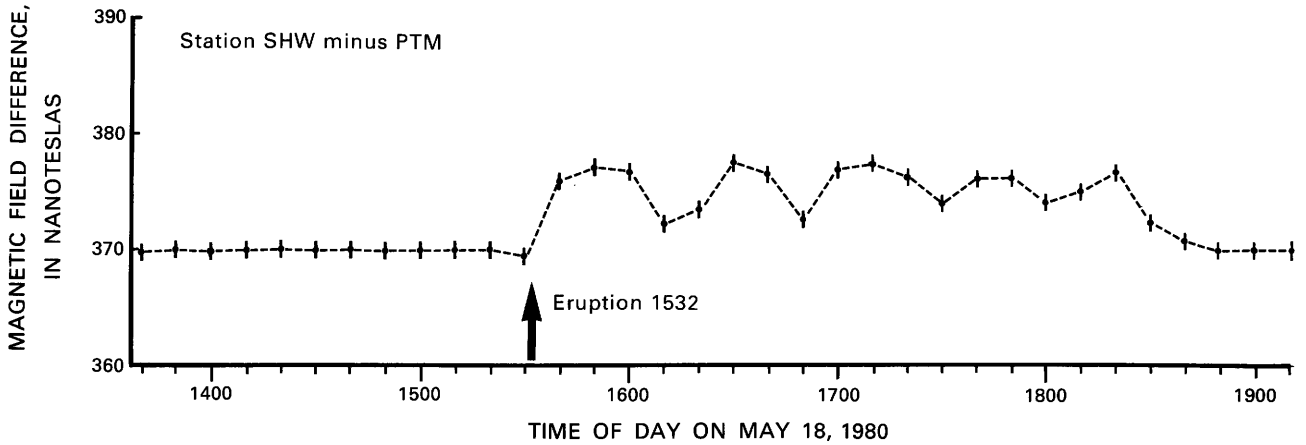

Figure 112.—Magnetic-field differences between stations SHW and PTM recorded at 10-min intervals for several hours preceding and following catastrophic May 18 eruption (arrow) at 0832 PDT (1532 UTC). Time scale is in UTC.

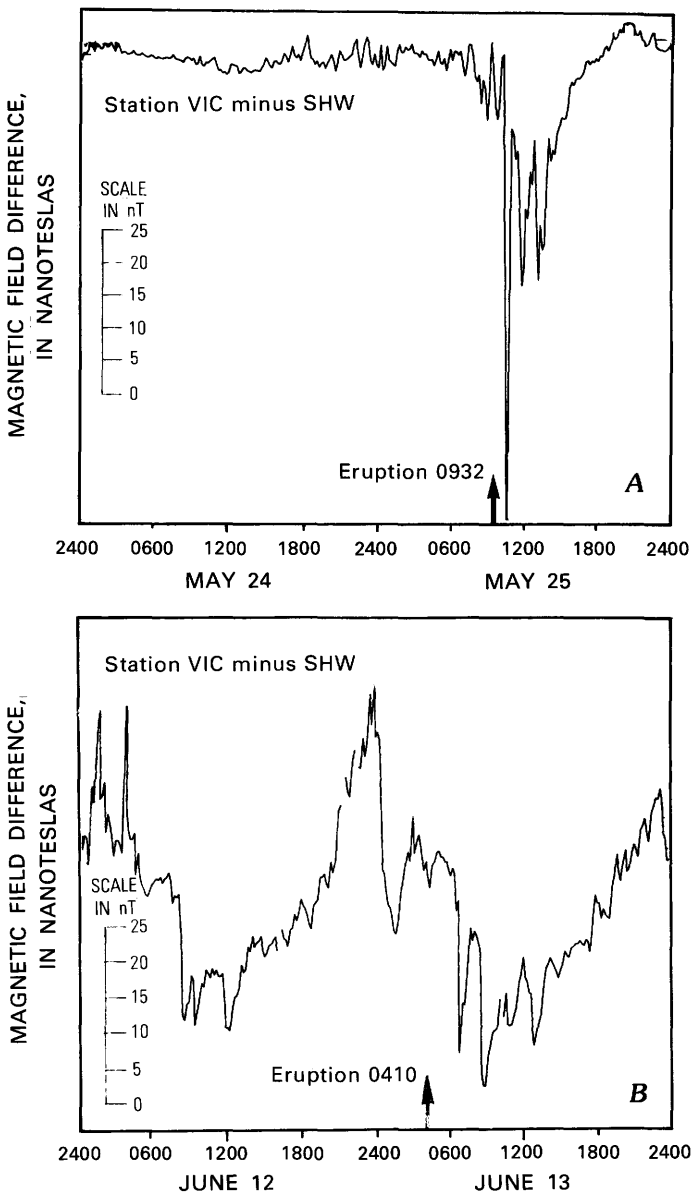

Figure 113.—Magnetic-field differences between stations SHW and VIC recorded at 10-min intervals. A, data for 2 days around the time of the May 25 eruption (arrow) at 0232 PDT (0932 UTC); B, data for 2 days around the time of the June 12 eruption (arrow) at 2110 PDT (0410 UTC on June 13). Time scale is in UTC.

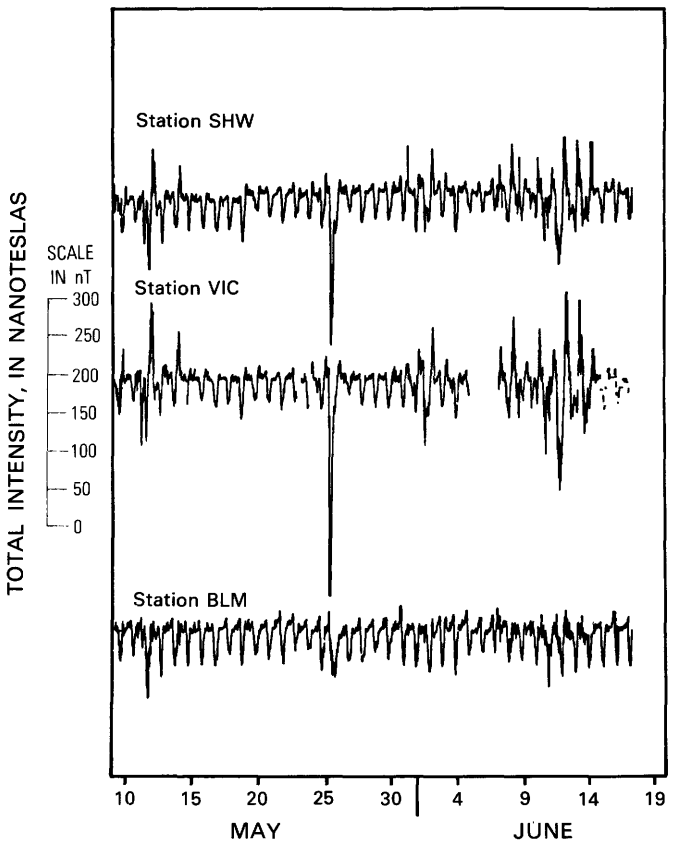

Figure 114.—Total-intensity plots from Mount St. Helens (SHW), Victoria (VIC), and Black Mountain (BLM) during May and June 1980. Time scale is in UTC.

magnetic or piezomagnetic effects and interaction between the eruptive shock wave and the Earth's ionosphere. The first process can only be relevant for the May 18 eruption when 2.5 km^3 of material was removed from the mountain (Moore and Albee, this volume) and for which a clear offset was observed.

Assuming all of this material was cool enough to have a normal magnetization of 0.5 ampere/m (as indicated by our later surface samples of this material), a simple spherical model of the removed material indicates that an anomaly of 8 nT could have been generated by the May 18 eruption. However, the offset expected at SHW as a result of the removal of material is negative, whereas the offset observed was positive. Because the regional magnetic anomaly at Mount St. Helens (U.S. Geological Survey, unpub. mapping, 1975) can be fitted most easily with a distribution of normally magnetized material, appealing to the occurrence of reverse magnetization in the removed material is unreasonable. The only real option for a mass-removal explanation is to appeal to an unknown, complex magnetization distribution whose interaction was such that the field at SHW changed in a positive sense when mass was removed during the formation of the new crater.

Given the observed magnetic data, we find it hard to propose a realistic physical source of substantial electric currents within the volcano. The offset

following May 18 could not have been caused by electrical currents, but some of the rapid transients may have been. Good physical models that identify the form and likely amplitudes of electric current systems during volcanic eruptions have yet to be developed. So, although electric current systems may have been generated, we cannot estimate their importance.

Because the stress state of the mountain changed during these eruptions, piezomagnetic effects should have occurred. The magnitudes of the effects expected can easily be calculated from various models (Stacey and others, 1965), provided reasonable assumptions can be made regarding change in stress state and magnetization. An anomaly with the correct amplitude and sense can be generated by a piezomagnetic model of the volcano in which we have either a spherical or a cylindrical (Yukutake and Tachinaka, 1967) pressure source of about 1 km in diameter. In order to get the correct magnitude and to not violate the surface observations of tilt and displacement, it is necessary that the source extend to at least 5 km. At this depth the pressure release at the time of the May 18 eruption would be of the order of 1 kbar.

Interaction between the eruptive shock waves and the ionosphere can be easily demonstrated by the total-intensity records at PTM, VIC, NP, and stations in California. It does seem that the effects were different for the different eruptions and were quite significant out to distances of a few hundred kilometers from Mount St. Helens. Figure 114 shows the extremely disturbed field at VIC following the May 25 eruption and also the disturbance preceding and following the June 12 event. Data for NP in eastern Washington (fig. 110) show similar disturbances after the May 25 and June 12 events. Curiously, no really significant disturbance occurred at the time of the May 18 eruption.

The total-intensity records that were taken almost continuously at the Portland airport (PTM), which is at a distance of 80 km from Mount St. Helens, by Carson Geoscience Co. show no disturbance until about 13 min after the eruption initiation. This would be quite consistent with the time required for an eruption shock wave, traveling at about 250 m/s, to reach the E-region of the ionosphere. The maximum initial disturbance from the shock wave would be about 20 nT. This would rapidly become lost within the normal diurnal or S_Q variation which occurred at most western stations about 1000 local time. At a propagation velocity of several hundred meters per second, the time of arrival of a propagating wave at most western magnetometers is just at the onset time of the S_Q variations.

CONCLUSIONS

Magnetic transients occurred at the times of three major eruptions from Mount St. Helens. Some precursive activity may have occurred prior to the May 25 and June 12 eruptions, but no activity is apparent in the few hours before the catastrophic May 18 eruption. This would be consistent with the prevailing view that the eruption was landslide triggered. The 10-day record prior to this eruption may be too short to identify any longer term precursors, if they occurred.

An offset of 9 ± 2 nT occurred during the first 12 hr following the May 18 eruption. This is most easily explained as the result of a release of stress during the eruption. To explain the offset by mass removal requires a complex magnetization distribution that somehow reverses the sign of the expected field anomaly when 2.5 km^3 of material is removed from the volcano. Reverse magnetization of the removed material is not consistent with a regional magnetic anomaly map.

The shock waves from the eruptions produced ionospheric perturbations, apparently of different form for different eruptions. These perturbations were apparent in magnetic records at points out to several hundred kilometers from Mount St. Helens. The amplitudes of these perturbations are about 20 nT at Portland for the May 18 eruption; at greater distances from the mountain these are correspondingly smaller and cannot be uniquely separated from the onset of the S_Q variation.

ACKNOWLEDGMENTS

We thank Vince Keller for help with the installation, Dr. L. Law and Dr. Don Auld for magnetic data from Victoria Geomagnetic Observatory, and Carson Geoscience Co. for data recorded at the Portland airport on May 18, 1980.

REFERENCES CITED

Davis, P. M., Hastie, L. M., and Stacey, F. D., 1974, Stresses within an active volcano—with particular reference to Kilauea: Tectonophysics, v. 22, p. 355–362.

Davis, P. M., Stacey, F. D., Zablocki, C. J., and Olsen, J. V., 1979, Improved signal discrimination in tectonomagnetism—discovery of a volcanomagnetic effect at Kilauea, Hawaii: Physics of the Earth and Planetary Interiors, v. 19, p. 331–336.

Johnston, M. J. S., and Stacey, F. D., 1969a, Volcano-magnetic effect observed on Mt. Ruapehu, New Zealand: Journal of Geophysical Research, v. 75, p. 6541–6544.

_____1969b, Transient magnetic anomalies accompanying volcanic eruptions in New Zealand: Nature, v. 224, p. 1289–1291.

Pozzi, J. P., Le Mouel, J. L., Rossignol, J. C., and Zlotnicki, J., 1979, Magnetic observations made on La Soufrière volcano (Guadeloupe) during the 1976–1977 crisis: Journal of Volcanology and Geothermal Research, v. 5, p. 217–237.

Rikitake, T., 1951, Changes in magnetic dip that accompanied the activities of volcano Mihara: Tokyo University Earthquake Research Institute Bulletin, v. 19, p. 499–502.

Shercliffe, J. A., 1965, A textbook of magnetohydrodynamics: London, Pergamon Press, 265 p.

Stacey, F. D., Barr, K. G., and Robson, G. R., 1965, The volcano-magnetic effect: Pure and Applied Geophysics, v. 62, p. 96–104.

Yukutake, T., and Tachinaka, H., 1967, Geomagnetic variations associated with stress change within a semi-infinite elastic earth caused by a cylindrical force source: Tokyo University Earthquake Research Institute Bulletin, v. 45, p. 785–796.

GAS STUDIES

Until recently, volcanic gases have been frustratingly difficult to study quantitatively or to use for monitoring of activity. Major gas vents on volcanoes are often too inaccessible or dangerous to approach for ground sampling, and gas samples from smaller vents commonly contain so much intermixed atmospheric air and water vapor of meteoric origin that concentrations of probable magmatic components such as sulfur, carbon, and hydrogen have been difficult to determine. Furthermore, many components of volcanic gases are unstable and tend to react to form new compounds; falling temperature and pressure, even during the collection process, complicate identification of equilibrium volcanic assemblages.

In the last few years, much progress has been made using airborne and ground remote-sensing techniques for measuring volcanic gases. A correlation spectrometer (COSPEC), originally designed to monitor industrial pollutants, has been successfully used for remote monitoring of volcanic SO_2 emission at several volcanoes, especially by Richard Stoiber and associates of Dartmouth College. A recording hydrogen probe, which is essentially a small fuel cell that generates electricity in proportion to the amount of hydrogen available to combine with air, has been operated at Kilauea Volcano in Hawaii since 1973 by Motoaki Sato of the USGS. Finally, an airborne technique to measure CO_2 in volcanic gas plumes, developed by Sato and David Harris, was successfully used for the first time at Mount St. Helens in 1980.

These ground and airborne techniques, while still partly experimental, have already produced data on compositions and rates of volcanic gas emissions from Mount St. Helens. Before May 18, emissions of SO_2 were low, near limits of COSPEC detectability, despite seismic and geodetic evidence for a shallow cryptodome within the volcano; either the cryptodome was too well sealed for abundant gases to escape or hydrothermal fluids absorbed most available sulfur gases during this period (Casadevall and others). Sulfur:chloride ratios in ash leachates, which provide an indirect method of monitoring gas emission, indicated a gradual increase during this period, although no abrupt changes occurred before the May 18 eruption (Nehring and Johnston). SO_2 plume emissions increased by an order of magnitude after May 18, as shown by airborne COSPEC measurements, and increased markedly again in early June, prior to the June 12 eruption. These increases probably reflect decreasing depth and less effective sealing of the dacitic magma body. After the June 12 eruption, SO_2 levels remained at high levels but decreased overall during the rest of the year.

Airborne monitoring of CO_2 in the plume, begun in early July, documented a total flux greater than that of SO_2 and a similar general pattern of overall decreased emission later in 1980 (Harris, Sato, and others). Pyroclastic magmatic eruptions on July 22, August 7, and October 16–18 appear to have been preceded by several days of significantly decreased CO_2 emissions, a pattern that may help anticipate future explosive eruptions. The total amounts of both CO_2 and SO_2 released to the atmosphere in 1980 exceed by several times amounts of these gases that could have been derived from the volumes of magma erupted during the monitoring period. Much of the gas appears to have emanated from unerupted magma within the volcano.

Hydrogen concentration in the ground at a site on the south flank of Mount St. Helens, relative to the

local atmospheric concentration, has varied complexly since measurements began in July (Sato and McGee). Smooth diurnal variations are probably related to daily reversals of orographic winds. Irregular short-period increases are tentatively interpreted as reflecting seismically triggered emission of magmatic H_2. Changes in average daily concentrations are thought to reflect mainly varying concentrations in the atmosphere from the gas plume; some such changes may have preceded by several days the magmatic eruptions in August and October, as well as several prominent gas-emission events and episodes of volcanic tremor.

Although these remote techniques have thus had some success in relating gas abundances to volcanic activity, direct sampling of fumaroles remains the best way to inventory the range of gas species and to sample for isotopic analyses. Analyses of fumarole samples from the crater indicate that sulfur is released from the magma mainly as H_2S and oxidizes to SO_2 as it cools in the plume (Casadevall and Greenland). High concentration of air and water vapor in fumaroles from the flowage deposits confirms that entrainment and heating of nonmagmatic gases contribute to the mobility of pyroclastic flows. Study of encrustations at fumaroles indicates that sublimate mineralogy reflects fumarole temperature and subsequent cooling and hydration history (Keith and others). Isotopic analyses of carbon, oxygen, and hydrogen from fumarolic gases and thermal waters show large deviations from surficial meteoric and organic compositions (Barnes and others; Evans and others). These data demonstrate major volatile contributions from high-temperature environments, probably in part directly from the magma and in part from interactions between ground water and heated rocks.

THE 1980 ERUPTIONS OF MOUNT ST. HELENS, WASHINGTON

SO_2 EMISSION RATES AT MOUNT ST. HELENS FROM MARCH 29 THROUGH DECEMBER, 1980

By THOMAS J. CASADEVALL, DAVID A. JOHNSTON, DAVID M. HARRIS, WILLIAM I. ROSE, JR.,[1] LAWRENCE L. MALINCONICO,[2] RICHARD E. STOIBER,[2] THEODORE J. BORNHORST,[1] STANLEY N. WILLIAMS,[2] LAUREL WOODRUFF,[3] *and* JOHN M. THOMPSON

ABSTRACT

Emission rates of SO_2 were determined by ground-based and airborne correlation spectrometry beginning March 29. SO_2 emission rates of 0–40 t/day (metric tons per day) were measured in the period of phreatic eruptions from March 29 to May 14. From May 25 to June 3, the emission rate of SO_2 was 130–260 t/day, but the rate increased abruptly to 1,000 t/day on June 6 and remained at about this level (range 500–3,400) through December. In general, from July to December, the emissions during times of nonexplosive eruptive activity accounted for the majority of the total gas released. The magma body required to account for this emission is at least 0.3 km^3 in volume. A slight but consistent decrease in average daily SO_2 flux occurred from July through December. This decrease correlates with similar CO_2 changes (Harris, Sato, and others, this volume). Further interpretations of the gas data await more observational experience, data on other gases, and continued comparison with other measurements made at the volcano.

INTRODUCTION

Since the resumption of volcanic activity at Mount St. Helens in late March 1980, study of gas emissions has been an integral part of the USGS monitoring program. The goal of the gas-studies program is to characterize the chemistry and daily flux of the major gaseous emissions of Mount St. Helens, to provide information about the degassing of the subsurface magma body, and, eventually, to provide advance warning of volcanic eruptions. A basic requirement for monitoring studies is that samples be collected or measurements be made as regularly as possible, so that comparisons can be made with other monitoring techniques such as deformation, seismicity, and field observations of activity. Only by such routine measurements can we hope to interpret the variety of changes observed in the data.

Field and laboratory studies of gases from fumaroles in the crater and in the plume emanating from the crater indicate that H_2O, CO_2, CO, SO_2, H_2S, and HCl are the major constituents of the volcanic-gas emissions (Casadevall and Greenland, this volume; Evans and others, this volume). SO_2 is the major sulfur gas detected in the plume, and H_2S makes up about 10–20 percent of the total sulfur gas in the plume during times of nonexplosive gas emissions (Hobbs and others, 1981).

Measurements of SO_2 emission rates have been made at other active volcanoes since 1972 (Stoiber and Jepsen, 1973; Okita and Shimozuru, 1975; Haulet and others, 1977; Malinconico, 1979). At Mount Etna, Malinconico (1979) observed large increases in the rate of SO_2 emission before each of two Strom-

[1]Michigan Technological University, Houghton, Mich. 49931.
[2]Dartmouth College, Hanover, N. H. 03755.
[3]University of Wisconsin, Madison, Wis. 53706.

bolian eruptions in 1977. An earlier study of gas emissions at Asama volcano, Japan, showed that the emissions of sulfur gases increased prior to explosive eruptive activity (Noguchi and Kamiya, 1963). These studies suggest that increases in SO_2 emission rates may precede eruptive activity at other volcanoes.

Using available instrumentation, SO_2 and CO_2 have been measured within the plume at Mount St. Helens during times of nonexplosive activity. This report describes the technique used in making the SO_2 measurements, the results for several periods of observation, and the preliminary interpretation of the data and its applicability to forecasting eruptive activity.

ACKNOWLEDGMENTS

We acknowledge the skill and patience of the pilots and mechanics of Willamette Air Taxi Service of Hillsboro, Oreg., who supplied the monitoring aircraft used for plume studies. Barringer Research Ltd., of Toronto, Ontario, provided excellent service and technical advice; we particularly thank Millan Millan for determining the importance of the interference of CS_2 in the SO_2 absorption spectra. We also acknowledge Lisa McBroome, Mike Doukas, and Jim Wells, who assisted with some of the measurements reported here. Rose and Bornhorst acknowledge the support of Michigan Technological University and the National Science Foundation. The investigators from Dartmouth College, Malinconico, Stoiber, and Williams, acknowledge partial funding for this project from U.S. National Aeronautics and Space Administration Cooperative Agreement 5-22 and National Science Foundation Grant EAR 8020796. We are grateful for the cooperation of the staff of the Gifford Pinchot National Forest, Vancouver, Wash.

SOURCE OF EMISSIONS

Prior to March 27, 1980, only two sources of thermal activity and possible gas emission were known on Mount St. Helens. An area of weak fumarolic activity (temperature 88°C) occurred at The Boot at 2,740 m elevation on the north flank (Phillips, 1941). A second thermal area (temperature 89°C) was at approximately 2,740 m elevation on the southwest flank of the volcano (Friedman and Frank, 1977). Neither area showed signs of unusual gas emissions, fumarolic encrustations, or elevated temperature prior to their destruction on May 18. David Johnston sampled gases from The Boot on May 17, but these samples were lost with him on May 18.

The first phreatic eruption of March 27 produced a small crater at the summit of Mount St. Helens. This crater was the only significant source of gas emissions prior to the eruption of May 18. The crater had no visible plume during most of the time from March 27 to May 18. When the plume was present, its color varied from gray or black, when its ash content was high, to white, when it was ash free and composed largely of steam. Eruptions of these plumes usually lasted from a few tens of seconds to as long as several hours. From April 22 to May 7, the volcano produced no eruption plumes.

A blue flame, first observed in the crater by Johnston during the night of March 29, was reported by other aerial observers through early April. Despite Johnston's persistent attempts, the chemistry of the flame was never positively identified. However, the presence of the flame is evidence that degassing was indeed taking place in the crater even in the so-called quiet times between phreatic eruptions.

Since the eruption of May 18, the principal source of gas emissions has been from fumaroles within the crater (Casadevall and Greenland, this volume). Since June 15, fumaroles on the successive domes and around their margins have been the principal source of gas emissions. Gas emissions from the crater during nonexplosive (nonpyroclastic) eruptive activity typically form whitish puffs that rise from the crater floor at velocities of several meters per second to several tens of meters per second, and rise above the crater rim at an altitude of 2,600 m. The direction of plume movement and the shape and rate of dispersion of the plume downwind are strongly dependent on the direction and velocity of the wind. At low wind speeds (less than 5 knots) the plume tends to be thicker and wider than during high wind speeds (more than 15 knots). The plumes typically carry no ash but contain aerosols of H_2SO_4 in addition to steam and other gases (Woods and Chuan, 1980). In September 1980, temperatures in plumes 3–5 km downwind of the volcano were measured at $15° \pm 1°C$, approximately that of the ambient air adjacent to the plume. Explosive activity, such as occurred on May 18, May 25, June 12, July 22, August 7, and October 16–18, produced opaque erup-

tion plumes high in ash content (Rowley and others, this volume) that penetrated the tropopause, at 12–14 km elevation, for periods of time ranging from minutes to hours (Harris, Rose, and others, this volume). During these explosive eruptions, tephra and gases were injected directly into the stratosphere (Inn and others, 1980).

METHODS AND UNCERTAINTIES

The emissions of SO_2 from Mount St. Helens have been measured using a correlation spectrometer (COSPEC), which was designed for use in pollution studies (Millan and others, 1976), and which has been successfully applied to volcanic-gas studies (Stoiber and Jepsen, 1973; Okita and Shimozuru, 1975; Malinconico, 1979). Correlation spectrometry is a remote-sensing method that uses solar ultraviolet light scattered by the Earth's atmosphere as a source. The spectrally tuned instrument measures the amount of ultraviolet absorption by SO_2 present along the optical path through the plume, in units of concentration-pathlength (ppm-m) at 1 atm (atmosphere). Calibration is performed by use of an internal standard consisting of a fused-quartz gas cell with a known concentration-pathlength of SO_2.

At Mount St. Helens, most measurements have been made from a low-wing, twin-engine aircraft aided by U.S. Federal Aviation Administration (FAA) radar for precise location determination. Prior to May 18, some measurements were also made from the ground or from a helicopter. The customary procedure for measuring SO_2 was to make from three to six traverses below the plume, at right angles to the plume trajectory, in order to determine the concentration-pathlength of SO_2 within a cross section of the plume (fig. 115). The product of the concentration-pathlength, the plume velocity, and the plume width is the SO_2 emission rate, normally reported as metric tons per day. The time required for measurements is 1–2 hr each day. On July 6, we began to measure CO_2 as well as SO_2 emission rates during the same flights (Harris, Sato, and others, this volume). From March 29 to late July, measurements were attempted every 2–3 days, whenever weather conditions permitted.

Excellent flying conditions in August made possible almost daily measurements of the plume. Daily measurements give noticeably better resolution and allow more confidence in recognizing and interpreting trends and anomalies in the data.

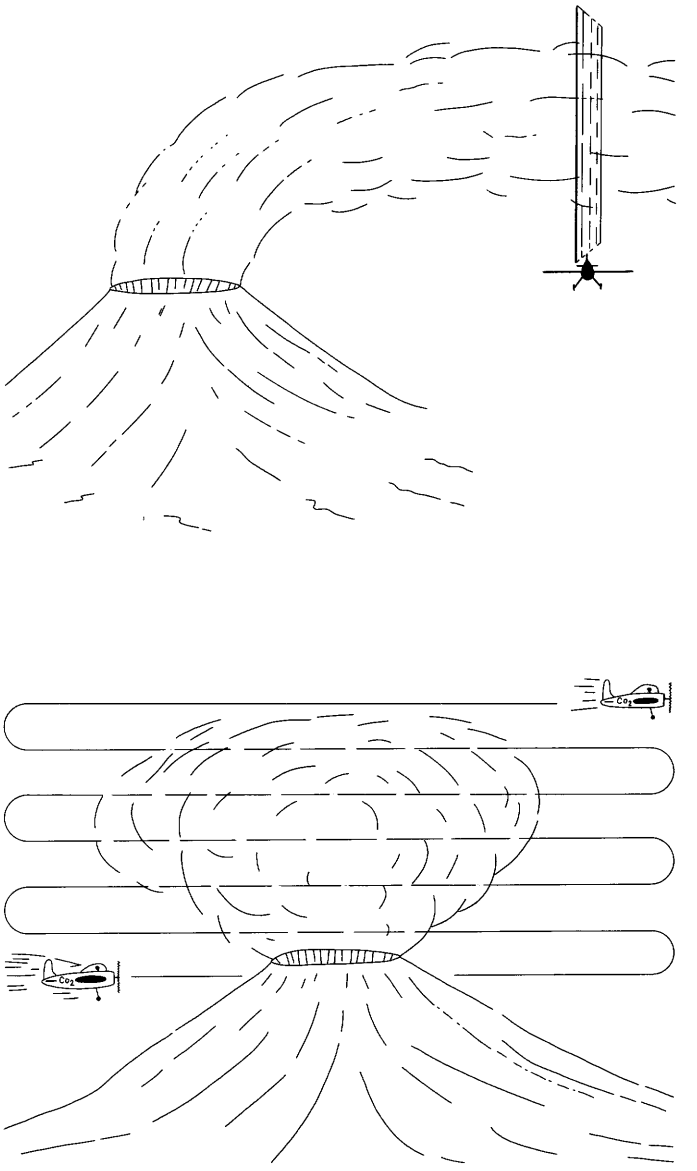

Figure 115.—Diagrams showing flight patterns used while making airborne measurements of gas emissions from Mount St. Helens. A, To measure SO_2, aircraft flies below plume with vertically aimed correlation spectrometer (COSPEC). B, To measure CO_2, aircraft flies under, through, and above plume to obtain a concentration profile of a plume cross section.

The emission rate of SO_2 reported each day incorporates uncertainties due to instrumental factors and variations due to natural causes. These include:

1. Real variation in gas emissions. Field observations have indicated the pulsating nature of gas emissions. Also, explosions of short duration (tens to

hundreds of seconds), low in ash, release greater than average amounts of gas to the atmosphere.

2. Variation in plume velocity.
3. Changes in conditions of cloud cover obscuring part of the plume.
4. Opacity of the plume due to incorporation of ash, either eruptive or windblown.

Uncertainties in the SO_2 flux arise from several instrumental factors:

5. Uncertainty in the instrument calibration (± 5 percent).
6. Variation in aircraft speed (± 2 percent).
7. Uncertainty in data processing (± 5 percent).
8. Uncertainity in the measurement of plume velocity. This factor usually is the chief variable that influences the precision of our measurements. Before August, the plume velocity (m/s) was obtained from weather data available from the U.S. National Oceanic and Atmospheric Administration office at the Portland, Oreg., airport. After August 2, the wind speeds were determined by comparing aircraft air speed with aircraft ground speed for flight paths parallel to the plume in two directions. Ground speeds were obtained from FAA radar measurements. Precision of the plume-velocity measurements in good weather conditions is probably ± 10 percent on days of strong winds and only ± 50 percent on days of light winds.

The effect of several of these uncertainties and variations (1, 2, 6, 7, 8) on the reported SO_2 emission rate can be minimized by averaging the results of several traverses each day.

RESULTS

MARCH 29–MAY 14

SO_2 emissions were measured by monitoring the light-colored, transparent part of eruption plumes, as well as the sky above the crater during times when no plume was visible. Measurements were made from low-wing aircraft, helicopter, the edge of the crater, and the ground at Timberline viewpoint, 4 km northeast of the summit. From March 29 to April 12, emission rates of as much as several metric tons per day of SO_2 were measured during times of no visible eruptive activity. Rates of as much as 30 t/day were measured during intervals of ash and steam eruption (Stoiber and others, 1980). For the 5 weeks of volcanic activity after April 12, the maximum flux of SO_2 during times of steam and ash eruption was less than 40 t/day (fig. 116). Due to the low emission rates, the uncertainty in each of these measurements is approximately equal to the determined flux. More precise measurements obtained from phreatic eruptions on May 14 provide a more accurate average of approximately 15 ± 5 t/day.

MAY 25–JULY 5

After the cataclysmic eruption of May 18, measurements were resumed on May 25. An eruption on May 25 generated a 14-km-high eruption column. The SO_2 flux was measured at 2,500 t/day during the waning stages of this eruption, after the eruption column had dropped to about 6 km in height. From May 26 to July 6, measurements were attempted every 2 to 3 days (fig. 116), as weather permitted. From May 26 to June 3, SO_2 production ranged from 130 to 260 t/day. The next measurements, made on June 6, indicated an abrupt increase in SO_2 emission to 1,000 t/day. On June 4, inflation of the mountain ceased, as indicated by a continuously recording tiltmeter at Ape Cave North station (6 km southwest of the summit); subsequently in 1980 this instrument recorded only slight slow deflation (Dvorak and others, this volume). A third eruption occurred on June 12, and a lava dome was first observed on June 15; yet neither of these events was directly preceded or followed by significant changes in the rate of SO_2 emissions. From June 6 to June 22, SO_2 emissions ranged from 950 to 1,300 t/day during times of nonexplosive gas emission. On June 9, during a minor steam explosion lasting about 15 min, two traverses were made, and an average emission rate of 3,700 t/day was measured. On traverses made immediately prior to this small explosion, an average rate of SO_2 emission of 600 t/day was measured. Due to poor weather conditions, no successful measurements were made from June 23 to July 4. On July 5, measurements showed an increase in SO_2 emission rates to 2,600 t/day.

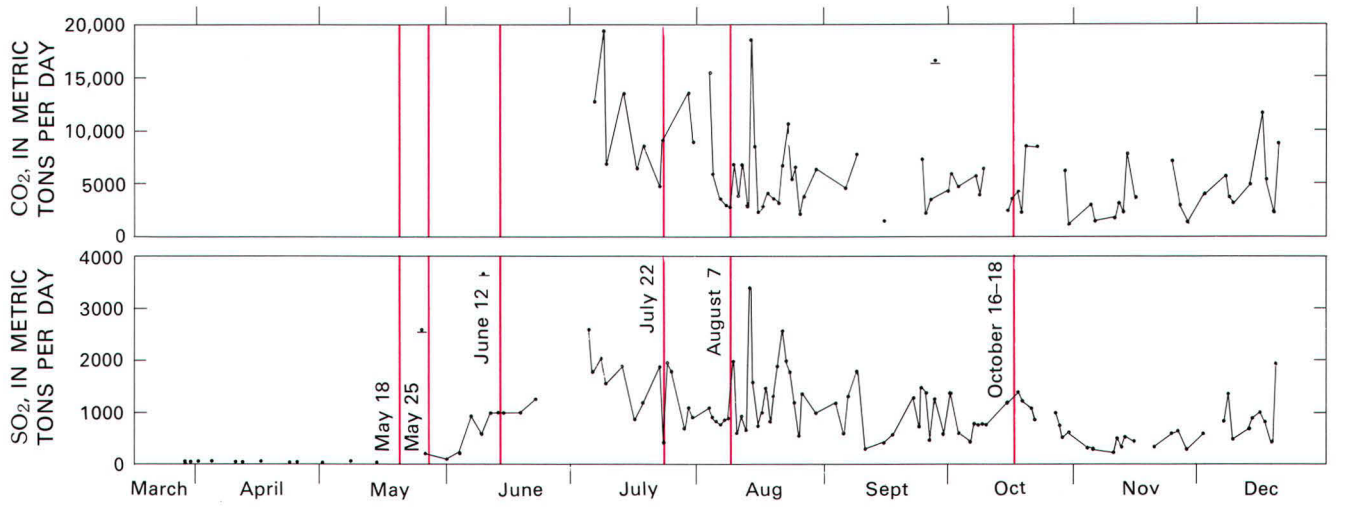

Figure 116.—Variation of SO_2 and CO_2 (in metric tons per day) with time, from March 29 through December, 1980. Underlined dots indicate measurements made during explosive activity. Red vertical lines indicate major eruptive events. CO_2 data from Harris, Sato, and others, this volume.

JULY 6 THROUGH DECEMBER

On July 6, routine simultaneous monitoring of SO_2 and CO_2 was begun (fig. 116). SO_2 emission rates decreased from July 6 to 16 (2,600–880 t/day) then increased from July 18 to 22 (1,200–1,900 t/day), prior to the eruption of July 22. Following the eruption, the SO_2 emission rates were highly variable and ranged from 800 to 2,000 t/day, but after July 28 they remained at 900 ± 200 t/day until August 7. For the balance of the month of August, SO_2 emissions averaged 1,300 t/day and ranged from 530 to 3,400 t/day. From late August through September, emission rates ranged from 430 to 1,800 t/day and averaged approximately 1,000 t/day. In the 2 weeks prior to the eruptions of October 16–18, SO_2 emissions averaged 700 t/day, a significant decrease from the 1,000 t/day average for late August through September. During and for a few days following the October 16–18 eruptions, SO_2 rates increased to an average of 1,100 t/day (table 9). The average rates of SO_2 emission steadily declined from a maximum in July of 1,500 t/day, to a minimum average rate for November of 400 t/day. The average emission rate for December was 890 t/day, possibly indicating increased SO_2 emissions related to the eruptive activity in late December. The averages for each month are (t/day): July, 1,500 ± 570; August, 1,300 ± 680; September, 950 ± 500; October 880 ± 300; November, 400 ± 150; December, 890 ± 600.

DISCUSSION

Interpretations of SO_2 emission data depend critically on the emission rates of gases in addition to SO_2, especially H_2S. Silicic magmas should emit significant H_2S, especially when the emissions are relatively high in water (Ohmoto and Rye, 1979; Gerlach, 1980). Indeed, high-temperature fumaroles in the Mount St. Helens crater have yielded gases dominated by H_2S (Casadevall and Greenland, this volume). Airborne measurements of the plume have recorded levels of H_2S generally 10–30 percent those of SO_2; however, during the major eruption of May 18, and for 1 week following, the H_2S levels were as much as ten times higher than SO_2 (Hobbs and others, 1981). Casadevall and Greenland (this volume) suggested that most of the H_2S emitted at high temperatures is rapidly oxidized to SO_2 in the hot cracks on or near the dome. This oxidation is probably inhibited at times of intense activity because atmospheric admixture is less efficient.

We interpret the very low emission rates of SO_2 prior to the eruption of May 18 as indicating that little sulfur gas was being released from the new Mount St.

Table 9.—SO_2 emission rates at Mount St. Helens from March 29 to December 19, 1980

[>, more than]

Date	SO_2 (t/day)	Date	SO_2 (t/day)
March 29-Apr. 4	[1]3-10	Aug. 25	530
Apr. 10	30±20	26	1,400
16	0	29	1,000
23	10±10	Sept. 3	1,200
25	10±8	5	600
May 1	10±8	6	1,300
8	48±40	8	1,800
14	15±5	10	300
25	[2]2,600	15	430
26	200	17	600
31	130	22	1,300
June 3	260	23	720
6	1,000	24	1,500
9	[3]600	25	1,400
11	1,000	26	480
13	[4]1,000	27	1,300
14	1,000	29	620
18	1,000	30	590
22	1,300	Oct. 1	1,400
July 5	2,600	3	600
6	1,800	6	470
8	2,200	7	800
9	1,600	8	760
13	1,900	9	800
16	880	10	760
18	1,200	15	1,200
22	[5]1,900	18	1,400
23	800	19	1,200
24	2,000	21	1,100
25	1,800	22	840
July 28	700	Oct. 27	1,000
29	1,100	28	700
30	900	29	500
Aug. 3	1,100	30	600
4	930	Nov. 4	330
5	850	5	270
6	780	10	230
7	[6]870	11	480
8	900	12	340
9	2,000	13	520
10	590	15	410
11	940	20	350
12	650	24	560
13	3,400	26	630
14	1,600	28	260
15	760	Dec. 1	570
16	1,000	6	830
17	1,460	7	1,350
18	800	8	470
19	1,300	12	660
20	1,900	13	870
21	2,600	15	970
22	2,000	16	830
23	1,800	18	400
24	1,200	19	1,950

[1]Range for 4 days of measurements.
[2]Late stage of May 25 eruption.
[3]3,700 during minor steam eruption.
[4]One traverse due to rain.
[5]Six hours before eruption.
[6]Two hours before eruption.

Helens magma. The SO_2 emissions may have been derived directly from a magma or from reactions of water with previously formed sulfur in the hydrothermal system above the magma body. The absence of juvenile material in ejecta from eruptions prior to May 18 supports the hypothesis that the new magma was probably too deep or its shell too impermeable to allow liberal release of sulfur gas from the melt. Alternatively, the active hydrothermal system may have absorbed any sulfur gas released from the melt, thereby preventing its escape into the atmosphere. Another uncertainty in the data is the role of H_2S during this period. H_2S in the plume varied from 10 to 50 percent of the total sulfur gases released prior to May 18 (Hobbs and others, 1981). The lower temperature of the gaseous emissions may have greatly inhibited its oxidation to SO_2.

Following the major eruption of May 18, the SO_2 emission rate during nonexplosive eruptive activity remained at a low level of 200 ± 50 t/day from May 26 to June 3, and then increased to 1,000 ± 300 t/day from June 6 through early July. This increase coincided with the end of a period of inflation that had continued from May 14 to June 4, and it is interpreted to indicate upward movement of a shallow magma body beneath Mount St. Helens. The fivefold increase in the rate of SO_2 emissions suggests that between June 3 and 6, the magma body moved close enough to the surface to permit increased loss of sulfur gas from the melt (fig. 117). On June 15, following the eruption of June 12, a dome was observed in the crater and remained intact until the eruption of July 22. During that time, the SO_2 emissions ranged from 880 to 2,600 t/day and averaged about 1,500 t/day. This example shows how interpretations of the gas-emission data can be constrained by other data. We do not feel

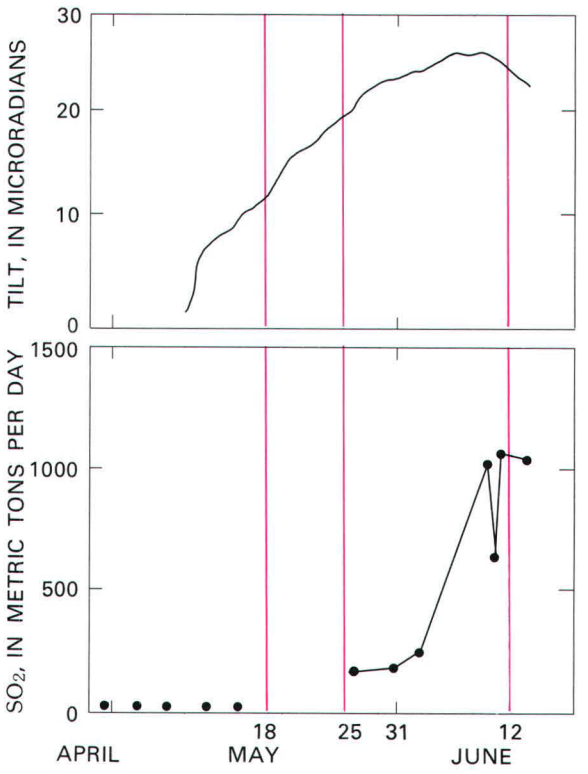

Figure 117.—SO_2 emissions compared with the change in east-west tilt as recorded at Ape Cave North station, 6 km southwest of the summit of Mount St. Helens, between April 29 and June 28, 1980. Red lines indicate eruptions on May 18, May 25, and June 12. Numerical increase in microradians indicates tilt downward to west.

nearly as confident in interpreting changes in gas emissions that do not correlate with other geophysical measurements or geological observations.

Our data document sustained high emission rates of both SO_2 and CO_2 since early July. The logical source for the SO_2 and most of the CO_2 is the shallow magma body (Harris, Sato, and others, this volume). If we assume that the SO_2 detected in the plume represents 90 percent of the total sulfur lost from the melt, and the other 10 percent is H_2S, we may calculate a minimum volume of sulfur lost from the melt to the atmosphere during periods of nonexplosive emissions. The total $SO_2 + H_2S$ emissions from May 25 through December is equivalent to about 220,000 t of SO_2 or 110,000 t of sulfur. This amount of sulfur, if it comes from a shallow dacite magma body containing less than 500 ppm sulfur (Melson and others, 1980), must come from a dense magma body of at least 0.3 km^3 volume. This volume is much larger than the total volume of all new magma erupted since May 18 (0.05 km^3, Lipman, Norton, and others, this volume, table 68). Although the May 18 eruption probably released a larger tonnage of sulfur than all of the explosive emissions since, this amount is difficult to calculate. The measurements indicate that a significant change in style of SO_2 release occurred in early June. Before this time, the main gas emissions were at low levels between relatively brief explosive events that released large amounts of sulfur (May 18, May 25, June 9). In contrast, since early June, the bulk of the SO_2 was released as nonexplosive emissions between eruptions. The sulfur released by the 0.05 km^3 of magma erupted since May 18 could be, at most, about 50,000 t of SO_2, significantly less than the total of 220,000 t emitted since May 18. This difference in amount suggests that a significant volume of magma is close enough to the surface to outgas. Such lava may remain in the volcanic edifice as intrusive masses or may eventually erupt.

Concepts that should be continually evaluated in the interpretation of short-term (daily and weekly) trends in the gas emissions are:

Intrusion of new magma to a shallow level.—When this occurs, an increase in the emissions may take place. SO_2 emission rates are known to increase before activity at Mount Etna (Malinconico, 1979). This explanation may account for the increased SO_2 emissions in early June, and for the increases before the July 22 eruption.

Changes in the permeability of the solidifying shell of the magma body.—Periods of sealing of the magma body may precede some eruptions because gas pressures are not released. Decreases in emissions of SO_2 and CO_2 before eruptions may indicate this sealing. The occurrence of large, gas-rich puffs from the crater of the volcano before and after eruptions may indicate transitions between well-sealed and poorly sealed states of the intrusive body. Local deformations in the crater area may correlate with sealing (Swanson and others, this volume).

Changes in the emission rates of other components.—By measuring SO_2 and CO_2, we study only part of the total gases emitted. H_2S should be measured more frequently. The amounts of H_2O, the major component of the emissions, should also be routinely measured. These new measurements will help our interpretations significantly.

We also need to develop concepts that explain longer term changes in gas emissions, such as the consistent monthly decreases in both CO_2 and SO_2 from July through December. For example, how do we distinguish between hypotheses that imply depletion of

the shallow magma body and those that imply a better sealed body? The first type of hypothesis implies a quiet future, the second does not.

REFERENCES CITED

Friedman, J. D., and Frank, David, 1977, Heat discharge from Mount St. Helens, Washington, Part 3 *of* Thermal surveillance of active volcanoes using the Landsat-1 data collection system: U.S. Geological Survey Open-File Report 77-541, 30 p.

Gerlach, T. M., 1980, Chemical characteristics of the volcanic gases from Nyiragongo lava lake and the generation of CH_4-rich fluid inclusions in alkaline rocks: Journal of Volcanology and Geothermal Research, v. 8, no. 2-4, p. 177-190.

Haulet, R., Zettwoog, P., and Sabroux, J. C., 1977, Sulphur dioxide discharge from Mount Etna: Nature, v. 268, no. 5622, p. 715-717.

Hobbs, P. V., Radke, L. F., Eltgroth, M. W., and Hegg, D. A., 1981, Airborne studies of the emissions from the volcanic eruptions of Mt. St. Helens: Science, in press.

Inn, E. C. Y., Vedder, J. F., Condon, E. P., and O'Hara, D., 1980, Gaseous constituents in the eruption plumes of Mount St. Helens at stratospheric altitudes: EOS, v. 61, no. 46, p. 1154.

Malinconico, L. L., Jr., 1979, Fluctuations in SO_2 emission during recent eruptions of Etna: Nature, v. 278, no. 5699, p. 43-45.

Melson, W. G., Hopson, C. A., and Kienle, C. F., 1980, Petrology of tephra from the 1980 eruption of Mount St. Helens: Geological Society of America Abstracts with Programs, v. 12, no. 7, p. 482.

Millan, M. M., Gallant, A. J., and Turner, H. E., 1976, The application of correlation spectroscopy to the study of dispersion from tall stacks: Atmospheric Environment, v. 10, p. 499-511.

Noguchi, Kimio, and Kamiya, Hiroshi, 1963, Prediction of volcanic eruption by measuring the chemical composition and amounts of gases: Bulletin Volcanologique, v. 26, p. 367-378.

Ohmoto, Hiroshi, and Rye, R. O., 1979, Isotopes of sulfur and carbon, *in* Barnes, H. L., ed., Geochemistry of hydrothermal ore deposits (2d ed.): New York, Wiley-Interscience, p. 509-567.

Okita, Toshiichi, and Shimozuru, D., 1975, Remote sensing measurements of mass flow of sulfur dioxide gas from volcanoes: Volcanological Society of Japan Bulletin, v. 19, 2d ser., no. 3, p. 151-157 [in Japanese; includes English summary].

Phillips, K. N., 1941, Fumaroles of Mount St. Helens and Mount Adams: Mazama, v. 23, no. 10, p. 37-42.

Stoiber, R. E., and Jepsen, Anders, 1973, Sulfur dioxide contributions to the atmosphere by volcanoes: Science, v. 182, no. 4112, p. 577-578.

Stoiber, R. E., Williams, S. N., and Malinconico, L. L., 1980, Mount St. Helens, Washington, 1980 volcanic eruption—Magmatic gas component during the first l6 days: Science, v. 208, no. 4449, p. 1258-1259.

Woods, D. C., and Chuan, R. L., 1980, Characterization of stratospheric aerosols in eruption plumes from Mt. St. Helens: EOS, v. 61, no. 46, p. 1153.

THE 1980 ERUPTIONS OF MOUNT ST. HELENS, WASHINGTON

EMISSION RATES OF CO_2 FROM PLUME MEASUREMENTS

By DAVID M. HARRIS, MOTOAKI SATO, THOMAS J. CASADEVALL, WILLIAM I. ROSE, JR.[1], *and* THEODORE J. BORNHORST[1]

ABSTRACT

Most of the CO_2 that emanated from Mount St. Helens became part of the gas plume as it moved away from the volcano. An airborne technique was developed for continuous sampling and infrared analysis for CO_2 in the plume. The CO_2-emission rates were determined by measuring the area, the horizontal velocity, and the CO_2 concentration anomaly in vertical cross sections of the plume. CO_2-emission rates were measured 55 times from July 6 to October 29, 1980. The precision of individual CO_2-emission rates is estimated to be ±10–40 percent. The emission rate varied from 2,100 t/day (metric tons per day; 2.1×10^9 g/day) to about 22,000 t/day (2.2×10^{10} g/day). Degassing of dacitic liquid is the most likely source of excess CO_2 in the gas plume. The total amount of CO_2 released to the atmosphere by volcanic activity during noneruptive periods at Mount St. Helens from the beginning of July 1980 to the end of October is about 910,000 t (9.1×10^{11} g). The contribution of CO_2 to the atmosphere exceeded that of SO_2. The monthly mean emission rate of CO_2 decreased significantly from 11,500 t/day (July 1980) to 5,300 t/day (October 1980). Significant changes in the emission rate of CO_2 may have occurred as a result of migration of CO_2 from deeper magma, intrusion of magma at a shallow level, change in the permeability of the vent, and change in the rate of crystallization of magmatic liquid. It is not possible at the present time to establish the actual cause or causes for changes in the CO_2-emission rate. Three Plinian eruptions (July 22, August 7, and October 16–18) of dacitic magma were preceded by significant decreases of CO_2-emission rates. The decreases, which occurred several days before eruptions, were useful for anticipating the August 7 and October 16–18 eruptions.

[1]Michigan Technological University, Houghton, Mich. 49930

INTRODUCTION

The resumption of volcanic activity at Mount St. Helens in March 1980, and potential hazards from eruptions, prompted studies of the gaseous emissions and their discharge rates. The objectives of these studies are to provide information about the degassing of the subsurface magma body and to provide advance warning of volcanic eruptions. This report describes an airborne method for determination of the CO_2-emission rate and the results obtained at Mount St. Helens from July 6 to November 1, 1980.

ACKNOWLEDGMENTS

We would like to acknowledge our appreciation to certain people who have shared with us their previous experience and who have contributed their efforts to this study. These people include: A. T. Anderson and R. R. Braham (University of Chicago); R. D. Cadle and Walter Komhyr (National Center for Atmospheric Research, Boulder, Colo.); Michael Doukas, Lisa McBroome, and Gary Olhoeft (U.S. Geological Survey); W. G. Melson (Smithsonian Institution, Washington, D.C.); James Wells (Dartmouth College, Hanover, N.H.); and L. G. Woodruff (University of Wisconsin, Madison, Wisc.). We also acknowledge our appreciation to the pilots (Milo

Moys, Mark Fry, Scott Henry, and Dave Switzer) of Willamette Air Taxi, Inc., Hillsboro, Oreg., and our appreciation for radar observations provided by the U.S. Federal Aviation Administration (Seattle, Wash.). We thank the staff of Gifford Pinchot National Forest for their cooperation. We are especially grateful to the staff of the U.S. Geological Survey in Vancouver, Wash., for their enthusiastic support.

DETERMINATION OF CO_2-EMISSION RATES

Most of the CO_2 that emanated from the volcano moved away in the gas plume. Hence, the CO_2-emission rate could be determined by measuring the area, the horizontal velocity, and the CO_2 concentration anomaly in a vertical cross section of the plume. Because the plume consisted of volcanic gases greatly diluted by atmospheric air, and because both contain CO_2, only the "excess" CO_2 concentration (that amount above the concentration normally found in the atmosphere) can be attributed to the volcanic source. CO_2-emission rates reported herein refer to the excess CO_2 present in the plume.

PROCEDURE FOR MEASURING EXCESS CO_2 IN THE PLUME

The airborne method for determination of excess CO_2 in the plume utilized continuous airborne sampling and infrared analysis for CO_2 during flights through the plume. An air-sampling tube was attached to the fuselage of a twin-engine, propeller-driven aircraft. The sample inlet (open to the front) was placed in a position such that contamination from aircraft engine exhaust was avoided. Because of the speed of the aircraft (72 m/s), the air sample flowed continuously through the gas cell (5.64 L) of an infrared spectrophotometer (Miran 1A, Foxboro Analytics, Inc., Foxboro, Mass.) at a rate of 0.4 L/s. The gas in the cell was completely replaced about every 15 s. The variations in spectral transmission through the gas over a 6.75-m path length were continuously recorded at the 4.26 μm absorption band for CO_2 while the aircraft flew into and across the plume (that is, at right angles to the plume trajectory) at some constant altitude (± 10 m) and the constant airspeed of 72 ± 2 m/s. The transmission was constant for air from outside the plume, but it decreased within the plume due to increased absorption caused by elevated amounts of CO_2 (fig. 118). After a step increase or decrease of CO_2 concentration in ambient air along a flight path, about 15 s are required for the gas in the instrument to attain the new composition. For an aircraft speed about 72 m/s and the overall response time about 15 s, the distance traveled before attainment of the full analytical response is about 1.1 km. The slow response time causes the measured shape of the plume cross section to be distorted and limits the spatial resolution of CO_2-concentration variations. The apparent width of the plume, as defined by the width of the measured CO_2-concentration anomaly, should exceed the actual width of the plume by as much as 2.2 km. Step changes of CO_2 concentration should appear as gradual changes over a 1.1-km distance. The distortions of the apparent plume width and the concentration profiles do not affect the integral (along the flight path) of the excess CO_2 concentration, provided the actual plume width exceeds 1.1 km.

Because the response of the instrument to changes in the mass of CO_2 per unit volume can be determined by calibrations, the excess CO_2 concentration in the

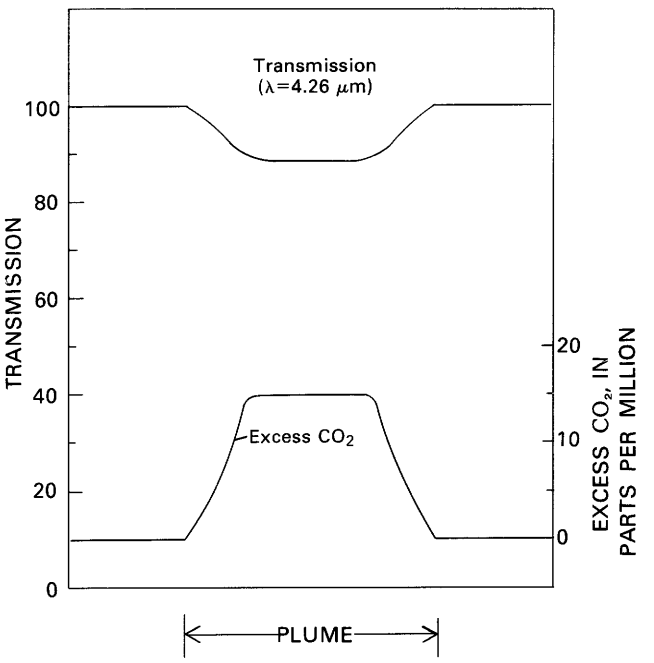

Figure 118. —Decrease of transmission at the 4.26-μm absorption band for CO_2 during flight through the plume at an altitude of 2,500 m.

plume can be calculated directly from the transmission measurements. Because pressure and temperature vary with altitude, and the total mass of CO_2 per unit volume can be calculated from the ideal gas law for a given composition of air, it is possible to calibrate the instrument response by varying altitude in air outside the plume and measuring the changes in transmission. We have assumed a CO_2 concentration of 330 ppm by volume in atmospheric air outside the plume, and have used the National Advisory Committee for Aeronautics formulas (Haltiner and Martin, 1957, p. 52) for pressure and temperature in the standard atmosphere (fig. 119). The logarithm of the transmission ratio varies inversely with the mass of CO_2 per unit volume. The excess CO_2 concentrations along flight paths through the plume have been calculated from the transmission measurements and include corrections for pressure and temperature.

Measurements along each flight path yield a line profile of the excess CO_2 concentrations in the plume at a particular altitude. A sequence of flight paths (often as many as eight) at various altitudes gives a sequence of CO_2-concentration profiles through an entire cross section of the plume. The results are used to construct a graph (for example, fig. 120) that shows the spatial dependence of excess CO_2 in a vertical cross section through the plume. As discussed above, the apparent plume cross section is as much as 2.2 km wider than the actual plume and the concentration gradients in the actual plume are greater than shown in figure 120. The CO_2-concentration anomaly is integrated (graphically) to obtain the product (ppm·m^2) of the mean CO_2 concentration (ppm) and the plume area (m^2).

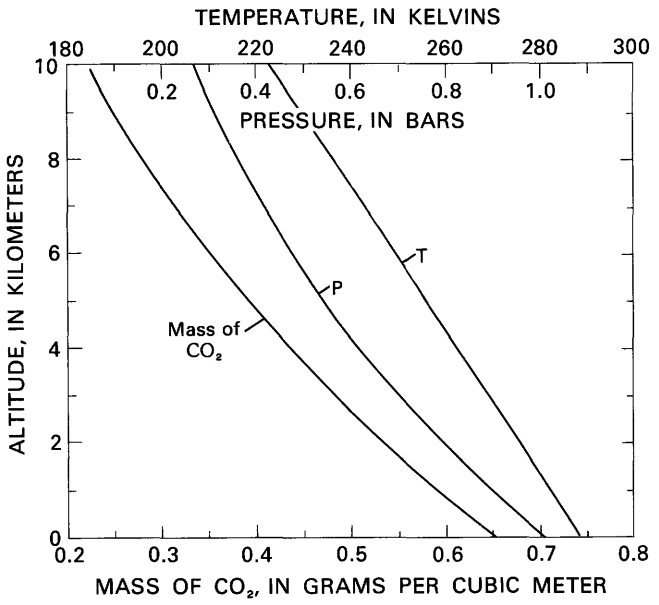

Figure 119.—Pressure, temperature, and mass of CO_2 per unit volume in the atmosphere. Pressure (P) and temperature (T) were calculated from National Advisory Committee for Aeronautics formulas for the standard atmosphere (Haltiner and Martin, 1957, p. 52). Mass of CO_2 per unit volume of air was calculated from the ideal gas law for 330 ppm CO_2 and pressures and temperatures used in formulas for the standard atmosphere.

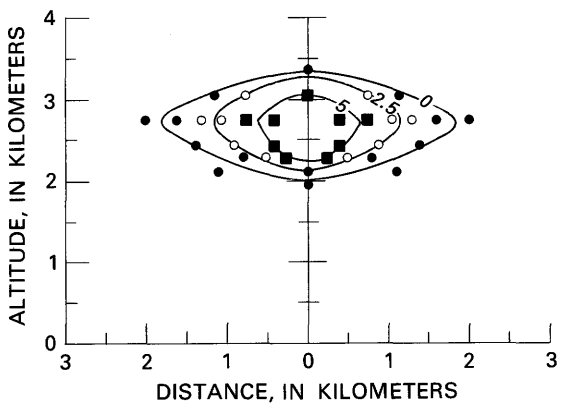

Figure 120.—Spatial distribution of excess CO_2 concentration in a cross section of plume on July 9, 1980. Solid circles, 0 ppm; open circles, 2.5 ppm; solid squares, 5 ppm CO_2 by volume in excess of the CO_2 concentration in the atmosphere distant from plume. The 0, 2.5, and 5 ppm contours are shown as solid lines.

MEASUREMENT OF THE WIND SPEED

The average horizontal velocity of the plume at the altitude and position of the CO_2-concentration anomaly must be known in order to calculate an emission rate for CO_2. Emission rates obtained through August 2 are based upon official National Weather Service forecasts of the winds aloft at altitudes appropriate for the plumes. Emission rates obtained after August 2 are more accurate because the wind speeds were actually determined from differences in the aircraft's true ground speeds for two flight paths parallel to the plume direction and in opposite directions, both flown at a constant air-speed.

True ground speeds were obtained by the pilot from Federal Aviation Administration radar measurements and (or) calculated from airborne radio navigation position measurements and elapsed time. Errors due to short-term fluctuations of the wind speed were reduced by flying in each direction for about 8 min, but changes in the average wind speed during the 2-hr measurement period may be significant.

CALCULATION OF THE CO_2-EMISSION RATE

The CO_2-emission rate is obtained from the product of the spatially averaged CO_2-concentration anomaly ($ppm \cdot m^2$), the wind speed (m/s), and the density of CO_2 (g/m^3) at the pressure and temperature estimated for the mean altitude of the plume. Although the emission rates are reported in units of 10^9 g/day (10^3 t/day), each value represents about 2 hr of measurements.

ACCURACY AND PRECISION OF CO_2-EMISSION RATES

The accuracy and precision of individual measurements of the CO_2-emission rates are limited by the following sources of error:

1. The concentration of CO_2 in atmospheric air outside the plume is probably different from the assumed value of 330 ppm (volume). The CO_2 concentrations in air samples collected outside the plume in the vicinity of Mount St. Helens on October 22, 27, and 30, 1980, were determined by gas chromatography to be 351, 335, and 348 ppm, respectively (R. D. Cadle, written commun., 1980). Because the errors in emission rates are proportional to the errors in the assumed concentration of 330 ppm CO_2 in atmospheric air, the results determined in this study may be too small by 1–6 percent.

2. The CO_2 concentrations may be in error due to instrument calibration and (or) reading errors. Excess CO_2 concentrations determined in this study may be compared with those determined by R. D. Cadle, who collected gas samples in the plume at the same time our continuous measurements were made. On October 22, a flight through the plume at an altitude of 2,530 m gave a peak excess CO_2 concentration of 9 ppm in the plume, whereas Cadle's result for a bulk sample, based on the difference of two analytical results, was 11 ppm. Similar measurements on October 30 showed values of 2 ppm excess CO_2 for our technique and 2–3 ppm excess CO_2 by Cadle's methods. Results obtained by the two methods on October 27 showed large discrepancies, which might be due to an analytical error in the background value (335 ppm) for CO_2 in atmospheric air outside the plume on that day. Two measurements of CO_2 concentrations in atmospheric air on October 22 and 30 gave values of 351 and 348 ppm, respectively. If 350 ppm CO_2 is assumed for the atmospheric air on October 27, then the excess CO_2 concentrations obtained by the two methods are in much better agreement.

3. Graphical integration of the CO_2-concentration profile is subject to error and requires careful judgment and experience in order to obtain the best precision. Each plume cross section requires reading 100–200 points from the continuous chart recording of the infrared transmission, although only about 30 measurements of the apparent plume widths at various excess-CO_2 concentrations are shown in figure 120. The errors made at this stage are estimated to be about ± 10 percent.

4. The actual wind speed is probably known to about ± 25 percent for speeds between 10 and 20 knots, and to ± 10 percent for speeds larger than 20 knots. At wind speeds of 3–5 knots, which are uncommon, the uncertainty is about ± 40 percent.

5. The actual flight speeds and altitudes may be incorrect by ± 5 percent.

The overall precision of the individual emission rates is estimated to range from ± 10 to ± 40 percent of the amount. Because the precision is so poor, it is necessary to obtain redundancy in order to demonstrate trends or changes in emission rates. Errors in the wind speed contribute large errors to individual measurements, but, because the errors should be random, the mean values of the emission rates have smaller errors.

RESULTS

The CO_2-emission rate was measured 34 times during the 55-day period from July 6 to August 29, 1980, and 20 times during the 44-day period from September 17 to October 29, 1980. The intervals between measurements averaged 1.6 and 2.2 days for the two periods, respectively. During these two periods, the plume was being sampled about 5 percent of the time.

The emission rates of CO_2 are plotted chronologically in figure 121. The emission rates of SO_2 (Casadevall and others, this volume) and the CO_2:SO_2 mass ratio are shown for comparison.

Table 10 lists the monthly variations of emission rates of CO_2 and SO_2. During each month, the CO_2-emission rate varied over a large range. From July to October, the monthly mean CO_2-emission rate *decreased* by a factor of two. However, from September 15 to October 9 there was a gradual *increase* in the CO_2-emission rate from 2,100 t/day to 5,400 t/day, except for a much larger rate (17,000 t/day) on September 27. Between October 9 and the October 16 eruption, the rate decreased to about 3,500 t/day.

Table 11 shows that the CO_2-emission rate decreased before the July 22, August 7, and October 16–18 Plinian eruptions. The preeruption decreases in the CO_2-emission rates are sufficiently large to be beyond the estimated errors of individual measurements. Because several measurements were taken in each time span, there is redundancy within each sequence of measurements.

The total amount of CO_2 emitted by Mount St. Helens from the beginning of July through the end of October is estimated to be about 910,000 t (9.1×10^{11} g). The relative amounts of magmatic and nonmagmatic CO_2 in this total are not known, but possible sources of the CO_2 will be considered.

DISCUSSION

The origin of CO_2 in the plume is not known at the present time. The geologic environment of the magma body within the active crater suggests two sources of CO_2 to be considered: (1) heating of ground water containing dissolved CO_2 and HCO_3^-, and (2) degassing of CO_2 from silicate liquids of dacitic composition.

The amount of ground water that circulates near the magma body in a given period of time is not known. However, if we assume that all of the excess CO_2 in the plume owes its origin to the heating of ground water and release of the dissolved CO_2 near the magma body, then we can estimate the rate at which water would have to be supplied. For a CO_2-emission

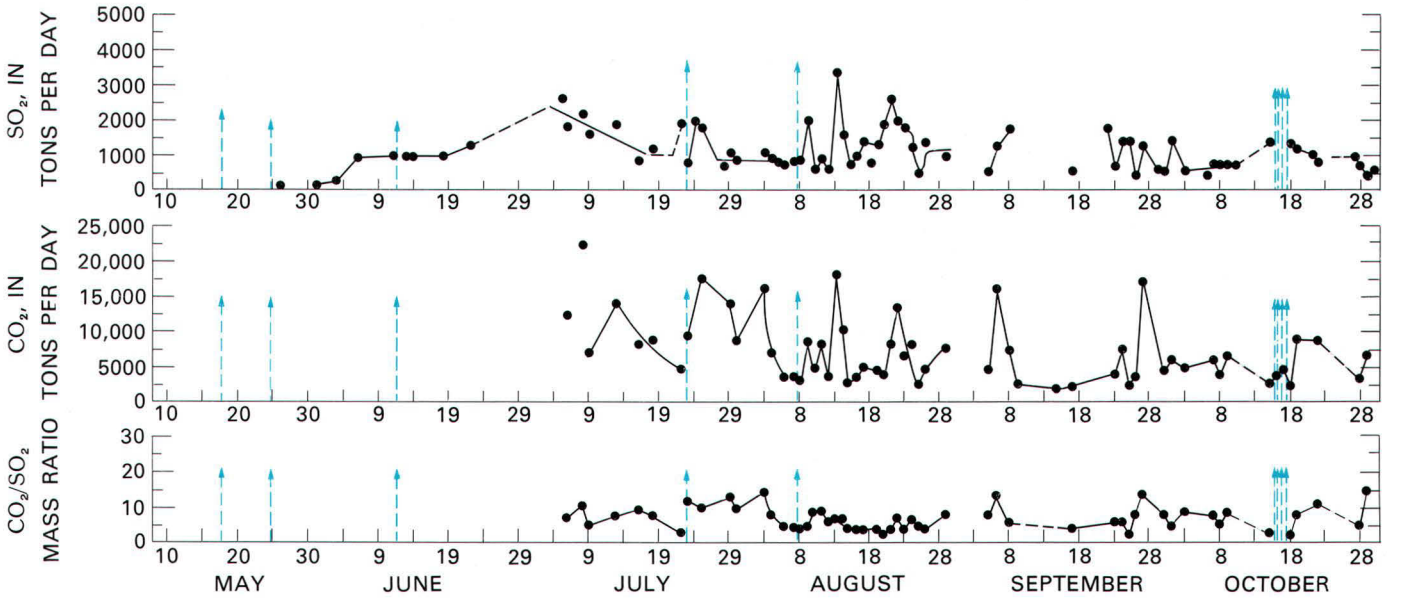

Figure 121.—Chronological variations in CO_2- and SO_2-emission rates and the CO_2/SO_2 mass ratio. The SO_2-emission rates are from Casadevall and others (this volume). Blue lines with arrows represent Plinian eruptions of dacitic magma. Dashed lines represent extrapolations.

Table 10.—Monthly variations of CO_2- and SO_2-emission rates, June to October 1980

[Leaders (---) indicate no data; SO_2 data from Casadevall and others, this volume]

	June	July	August	September	October
			CO_2		
Number of measurements---	0	11	23	12	11
Monthly mean (t/day)-----	---	11,500	7,100	6,000	5,300
Minimum----------	---	4,800	2,500	1,500	2,400
Maximum----------	---	22,000	16,000	17,000	8,900
			SO_2		
Number of measurements---	8	14	25	15	16
Monthly mean (t/day)-----	900	1,500	1,300	950	880
Minimum----------	260	700	530	430	470
Maximum----------	1,300	2,200	3,400	1,800	1,400
$\frac{\text{Monthly mean } CO_2}{\text{Monthly mean } SO_2}$	---	7.7	5.5	6.3	6.0

Table 11.—Changes in mean CO_2-emission rates before eruptions

[Number in parentheses is number of measurements in the mean]

Number of days before eruption	CO_2 emission rate (t/day)			
	July 22	August 7	October 16	Average
9 to 16--------	14,000 (4)	13,700 (5)	5,400 (4)	11,000
3 to 8---------	8,600 (2)	10,600 (3)	5,200 (2)	8,100
Less than 2----	4,800 (1)	3,700 (2)	3,200 (2)	3,900

rate of 10,000 t/day and assumed concentrations of 100–500 ppm (by weight) CO_2 dissolved in the ground water (see for instance, Davis and DeWiest, 1966, p. 106), the flow rate of water toward the magma body would have to be about 0.02–0.1 km^3 H_2O/day ($0.24–1.2 \times 10^9$ g H_2O/s). The volume of water required each day is equivalent to a layer with an area of 400 km^2 and a thickness of 5–25 cm. The required flow appears to be much too large for ground water to be the dominant source for the CO_2 emissions. Isotopic data also suggest that both the carbon and water in fumarolic gases are not meteoric (Evans and others, this volume).

Another possible source for the CO_2 is the degassing of the dacitic magma. The gas occluded in vesicles of pumice erupted in June 1980 includes CO_2 as an abundant species (Gary Olhoeft, oral commun., 1980). Also, CO_2 is an abundant component of the fumarole gases sampled at the crater in September 1980 (Casadevall and Greenland, this volume). The minimum amount of silicate liquid required to explain the CO_2 gas emissions could be estimated if the initial (preintrusion) CO_2 concentration of the liquid were known. Unfortunately, the initial CO_2 concentration of the liquid has not yet been determined. However, in order to consider the dacitic magma as a source for the CO_2, we might assume that the liquid phase of the dacite contained 0.13 weight percent CO_2 before degassing. (CO_2 was determined to be 0.13 weight percent in melt inclusions in olivine crystals in a subduction zone basalt studied by Harris, 1979.) Complete degassing of 0.77×10^{12} g of dacitic liquid per day could supply 10,000 t/day CO_2. The volume of completely degassed liquid required would be about 3×10^5 m^3/day.

For the period July through October 1980, a 0.26 km^3 volume of dacitic liquid would be required to supply the 910,000 t (9.1×10^{11} g) of CO_2 emitted over this period of time. This amount is about five times the total volume (0.053 km^3 of magma; Lipman and others, this volume) of dacite, including air-fall ash, pyroclastic flows, and dome, erupted during the May 25, June 12, July 22, August 7, and October 16–18 eruptions. If intrusion and degassing of magma released more than 0.13 weight percent CO_2 from the dacitic liquid (possibly due to initial vapor saturation of CO_2 at a confining pressure of 5 kbar or more), then the volume of intruded liquid that is required would be less than 0.26 km^3.

Emission rates of CO_2 may change as a result of migration of CO_2 from deeper magma, intrusion of magma at a shallow level, change in the permeability of the vent, and change in the rate of crystallization of liquid. It is not possible at the present time to establish the actual cause or causes for observed changes in the CO_2-emission rate.

The results in figure 121 show that the CO_2- and SO_2-emission rates often show similar changes. However, the emission rates of the two gases appear to have varied independently at certain times (especially on July 9, July 22, August 4 to 7, October 15, and October 18). The CO_2/SO_2 ratio was not constant but varied over a large range. Although the correlation

coefficient for the CO_2- and SO_2-emission rates is 0.57, the emission rates of the two gases were not correlated in a simple way.

Each of the three eruptions (July 22, August 7, and October 16–18) of dacitic magma during the time interval of this study was preceded by a significant decrease of the CO_2-emission rate. The decreases occurred several days before each eruption. Because the large decrease of the CO_2-emission rate from July 14 to July 22 was followed by an eruption and the pattern was repeated (August 3–6), the August 7 eruption was anticipated. Finally, the much lower emission rate of CO_2 on October 15, as compared to the September 15 to October 9 trend of increasing CO_2-emission rate, suggested that an eruption might be imminent; several Plinian columns were erupted from October 16 to 18.

Forecasting of volcanic eruptions by geochemical techniques may be possible, but a quantitative understanding of the behavior of volatile elements during magmatic processes is required in order to make better forecasts. For example, on August 20, on the basis of changes of the CO_2- and SO_2-emission rates, another eruption was anticipated to occur between August 20 and August 23, but no eruption occurred. Because the principal propellant in the explosive eruptions at Mount St. Helens is probably H_2O vapor, its role in the mechanisms of eruption and degassing of magma should be thoroughly investigated.

CONCLUSIONS

1. Degassing of dacitic liquid is the most likely source of excess CO_2 in the gas plume.

2. The total amount of CO_2 released to the atmosphere by volcanic activity at Mount St. Helens during noneruptive periods from the beginning of July to the end of October is about 910,000 t (9.1×10^{11} g). Since the CO_2:SO_2 mass ratio of the emissions is greater than unity, the contribution of CO_2 to the atmosphere exceeded that of SO_2.

3. The monthly mean emission rate of CO_2 has decreased significantly from 11,500 t/day (July 1980) to 5,300 t/day (October 1980).

4. Three Plinian eruptions of dacitic magma (July 22, August 7, and October 16–18, 1980) were preceded by significant decreases of CO_2-emission rates up to several days before the eruptions. These changes may be useful for anticipating eruptions.

REFERENCES CITED

Davis, S. N., and DeWiest, R. J. M., 1966, Hydrogeology: New York, John Wiley, 463 p.

Haltiner, G. J., and Martin, F. L., 1957, Dynamical and physical meteorology: New York, McGraw Hill, 470 p.

Harris, D. M., 1979, Pre-eruption variations of H_2O, S, and Cl in a subduction zone basalt: IAVCEI Abstracts and Timetable, International Union of Geodesy and Geophysics, 7th General Assembly, Canberra, Australia, Dec. 1979.

THE 1980 ERUPTIONS OF MOUNT ST. HELENS, WASHINGTON

CONTINUOUS MONITORING OF HYDROGEN ON THE SOUTH FLANK OF MOUNT ST. HELENS

By MOTOAKI SATO *and* KENNETH A. MCGEE

ABSTRACT

Differences in the H_2 (hydrogen) concentration between atmospheric air and in the ground at a depth of 50 cm have been monitored with an electrochemical sensor at the 2,100-m level on the south flank of Mount St. Helens since June 20, 1980. Sensor output and reference voltages were radio telemetered to Vancouver, Wash., and recorded about every 4 minutes.

Three types of changes in the H_2 sensor signal were recognized through November 1, 1980. (1) Smooth diurnal variations in which ground H_2 concentrations are smallest relative to the atmosphere in the morning (0800–1000 PDT) and largest in the evening (1900–2100). These variations are probably caused by daily reversal of orographic winds. (2) Irregular short-period increases in the ground H_2 concentration that follow shallow local seismic events by a few tens of hours. These increases are probably caused by magmatic emission of H_2 through the flank of the volcano. (3) Changes in the daily average of the relative ground H_2 concentration, which first abruptly decreases below the atmospheric H_2 value and then increases within tens of hours. The changes are probably caused by a rapid degassing of H_2 in the crater, which increases the H_2 concentration in the air relative to the ground until the slower ground emissions catch up. Such changes preceded the August 7 and the October 16–18 eruptions by several days, and also may have preceded or coincided with prominent gas emissions and volcanic tremor. No such change was observed before the July 22 eruption.

These observations suggest the important influence of atmospheric H_2 derived from the crater plume on the patterns of the H_2 sensor signal in nonfumarolic ground. Separate monitoring of H_2 in the ground and in ambient air in comparison with an isolated reference gas, and monitoring at several more sites around the crater to eliminate regional wind effects will be necessary for better results.

INTRODUCTION

Hydrogen is present in most magmatic gases (White and Waring, 1963). Because it is a light, mobile gas, H_2 is probably one of the best geochemical communicators that hidden magma sends to the surface. The high oxygen fugacities of extrusive rocks, compared to intrusive rocks formed at depth, suggest that hydrogen readily escapes from magma at shallow levels in the crust (Sato, 1972, 1978). Monitoring of H_2 emission, therefore, may provide information on the activity of magma within a volcano. Acquisition of data on diverse volcanoes is an initial step for developing techniques that may eventually permit eruption predictions. We began continuous monitoring of hydrogen in a fumarole at Kilauea Volcano, Hawaii, in 1973. Since then, we have extended fumarole H_2 monitoring to Mauna Loa (Hawaii), Mount Baker (Washington), Krafla (Iceland), and Vulcano (Italy) in cooperation with other scientists. The resumption of volcanic activity in March 1980 prompted us to start the hydrogen monitoring experiment on Mount St. Helens.

Because monitoring instruments could not be placed in the primary fumaroles in the post-May 18 crater due to eruption hazards, we chose a site for H_2 monitoring on a blocky, ridge-forming lava flow, about 400–500 yr old, at the 6,900-ft (2,100-m) level on the south flank of the volcano (fig. 122). Preliminary

measurements indicated that H_2 passed through the porous lava flow from the volcano's interior. Monitoring was begun on June 20, 1980.

ACKNOWLEDGMENTS

We gratefully acknowledge the help of: Thomas J. Casadevall for coordinating the geochemical research efforts, David M. Harris for assisting in preparing pertinent data files, and Bruce Furukawa for assisting in maintaining the monitoring-telemetry system. We also thank the University of Washington/USGS seismic team for the use of Mount St. Helens computer seismic file.

METHOD OF MONITORING H_2

The difference in H_2 concentration between the ambient atmosphere and gas about 50 cm deep in loose pyroclastic material, interstitial to blocks of the lava flow, was monitored continuously by an electrochemical sensor. The sensor (fig. 123) is essentially a small fuel cell that generates an electric current in proportion to the amount of H_2 available for electrochemical oxidation by O_2 in air. The cell consists of an acidified and platinized perfluorosulfonic acid membrane (electrolyte for H^+ ion), perforated foils of $Pd_{70}Au_{30}$ alloy (current collectors), $Au_{80}Pt_{20}$ alloy and tantalum wires (conductors), and Teflon body and tubing. The platinized electrolyte membrane was obtained from a commercial hydrogen generator. General principles of H_2/O_2 fuel cells based on ion-exchange membranes have been described by Vielstich (1970, p. 191–200).

When the inside of the sensor is filled with atmospheric reference air and a load resistor is connected to the conducting wires, H_2 in the gas to be tested is converted to H^+ ions, moves through the membrane, and combines with O_2 in the air to produce H_2O. An electric current is generated from the interior current collector to the exterior current collector through the load resistor, resulting in a voltage drop across the load resistor. The voltage drop is the sensor output. The current (and hence the output voltage) is linearly proportional to the difference in H_2 concentration between the external gas and the internal reference air when the load resistance is sufficiently low. A higher load resistance produces a higher voltage output, but it makes the sensor response nonlinear and slower. For a few hundred parts per million (ppm) H_2, a load resistance of as much as 100 kilo-ohms can be used without degrading the linearity. The sensor installed on the south flank of Mount St. Helens, which is connected to a 100 kilo-ohm resistor, has a sensitivity of about 7.5 mV (millivolts) per 100 volume ppm H_2 at 1 atmosphere total pressure and responds to 90 percent of the final value for a step change in H_2 concentration in about 1 min. The slow response time was not detrimental for this study.

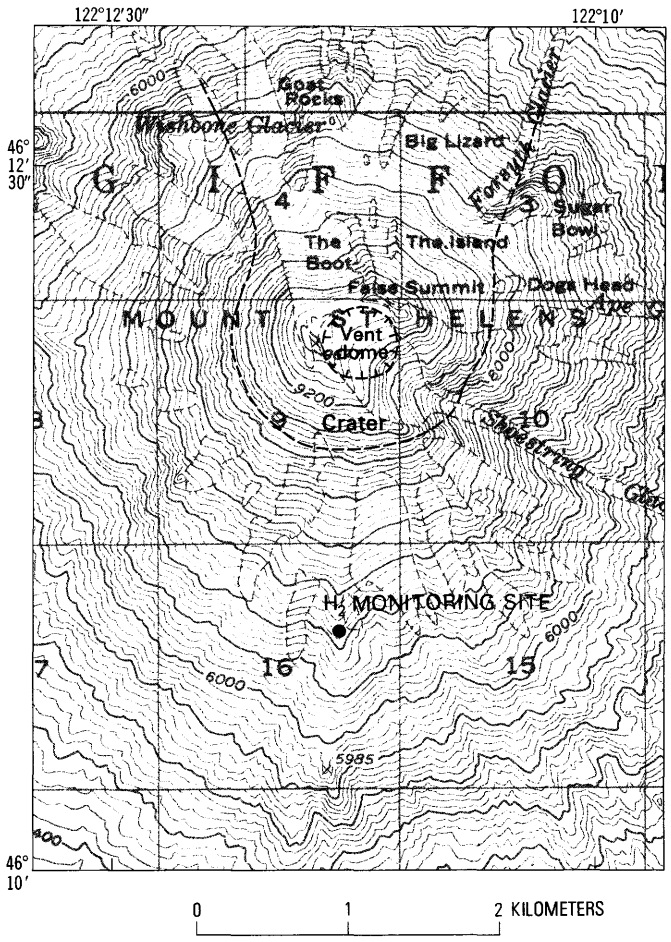

Figure 122.—Location of the H_2 monitoring site on the south flank of Mount St. Helens.

Because O_2 is consumed and H_2O is produced on the interior surface of the electrolyte membrane as the result of the electrode reaction, air must be circulated inside the cell to supply O_2 and remove the H_2O film. Atmospheric air, scrubbed of sulfur gases by being passed through a column of soda lime, is circulated through the sensor by a small diaphragm pump

(fig. 124). The sensor-output wires go through the air-intake tube to the pump box, where they are connected to a four-conductor cable (two conductors for the pump power supply). The cable is connected to an electronics board and radio transmitter, housed in an airtight box.

The electronics board functions as a signal multiplexer, voltage-to-frequency (V/F) converter, and radio switch. The board used for this study is similar to earlier versions (McGee, and Sato, 1979; McGee 1979), except that it does not utilize a clock; instead, it switches a four-channel multiplexer input when the V/F converter produces a fixed number of pulses. The radio transmitter is switched on only every fourth cycle of the multiplexer to conserve the battery (the average power requirement is less than 1 watt). The multiplexer scans through 0- and +10-mV reference voltages and through unattenuated and attenuated (by a factor of eight) sensor voltage outputs. The V/F converter is biased to match one of the conventional seismic audio channels and is trimmed to deviate from the center frequency by 100 Hz (hertz) for 10-mV signal input.

A five-element Yagi antenna is used to transmit the modulated VHF radio signals (about 200 mW, or milliwatt) directly to Vancouver, Wash., 68 km to the southwest, where the signals are received, discriminated, and converted back to time-multiplexed dc voltages. A dot-printing strip-chart recorder marks four separate traces of the voltage signals on pressure-sensitive paper, as shown in figure 125. The traces of the reference voltages are used to detect changes in the voltage span, noisy radio conditions, and malfunctioning of the telemetry system.

The sensor output is bipolar, and the output voltage can change depending on at which side of the electrolytic membrane the H_2 concentration is higher. Because the sensor null, which represents equal concentrations of H_2, was found to be offset by 6.2 mV in the field installation, the unattenuated sensor signal is less than 6.2 mV when the H_2 concentration in the

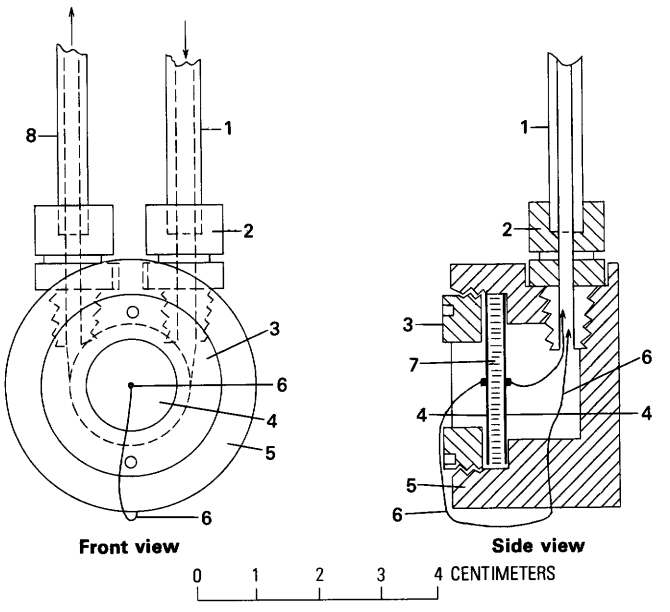

Figure 123.—Diagram of the H_2 sensor used at Mount St. Helens: 1, air-intake Teflon tube; 2, commercial Teflon tubing connector; 3, threaded Teflon nut; 4, perforated $Au_{30}Pd_{70}$ foils; 5, Teflon sensor body; 6, $Au_{80}Pt_{20}$ alloy wires; 7, acidified, platinized perfluorosulfonic acid membrane; and 8, air-exhaust Teflon tube.

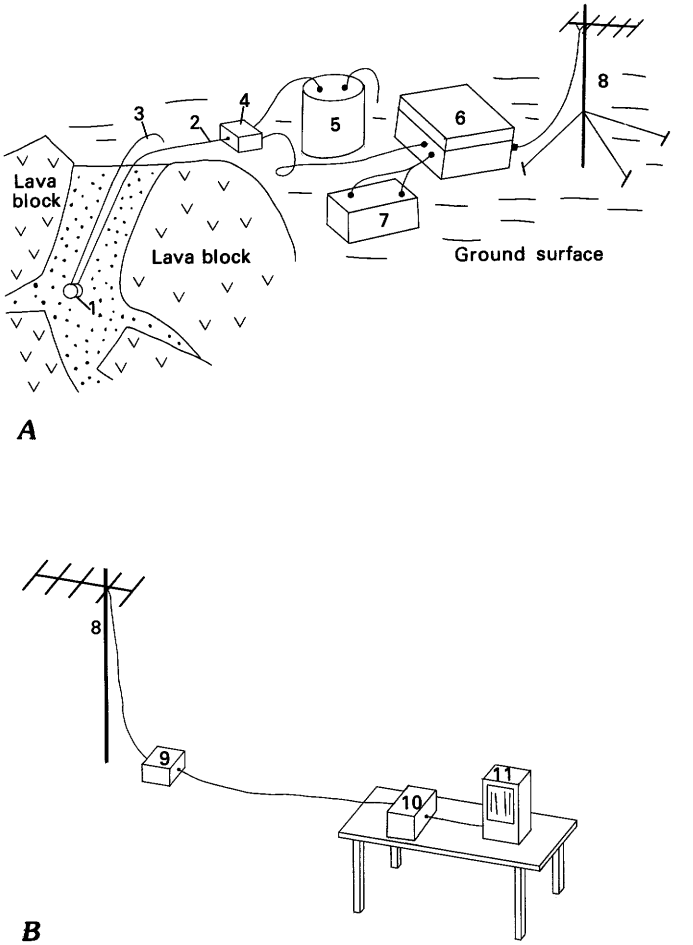

Figure 124.—Schematic arrangement of the H_2 monitoring and radio-telemetry systems. A, monitoring station. 1, sensor; 2, air-intake tube; 3, air-exhaust tube; 4, pump box; 5, soda-lime scrubber; 6, electronics and radio-transmitter box; 7, battery; 8, Yagi antenna. B, receiving station. 8, Yagi antenna; 9, radio receiver; 10, frequency-to-voltage converter; and 11, dot-printing strip-chart recorder.

ground is higher than that in the atmospheric air, and vice versa.

For most monitoring purposes, the pattern of changes is more important than the actual concentration of H_2, provided that sensitivity remains constant. To estimate magnitudes of the changes, however, the recorded voltage can be converted to relative H_2 concentration from the calibrated sensor sensitivity (7.5 mV/100 volume ppm H_2 at 1 atmosphere total pressure). The output of the sensor probably depends on the population density of H_2 molecules (g/cm^3) rather than the H_2 concentration (ppm) relative to other gas phases, although this has not been verified experimentally. Because the barometric pressure at the monitoring site is only about 0.78 atmosphere, the calculated H_2 concentrations are probably about 20 percent low.

Slow changes can be studied more easily if the H_2 signals are averaged for 24-hr periods and plotted chronologically. Because of the large number of

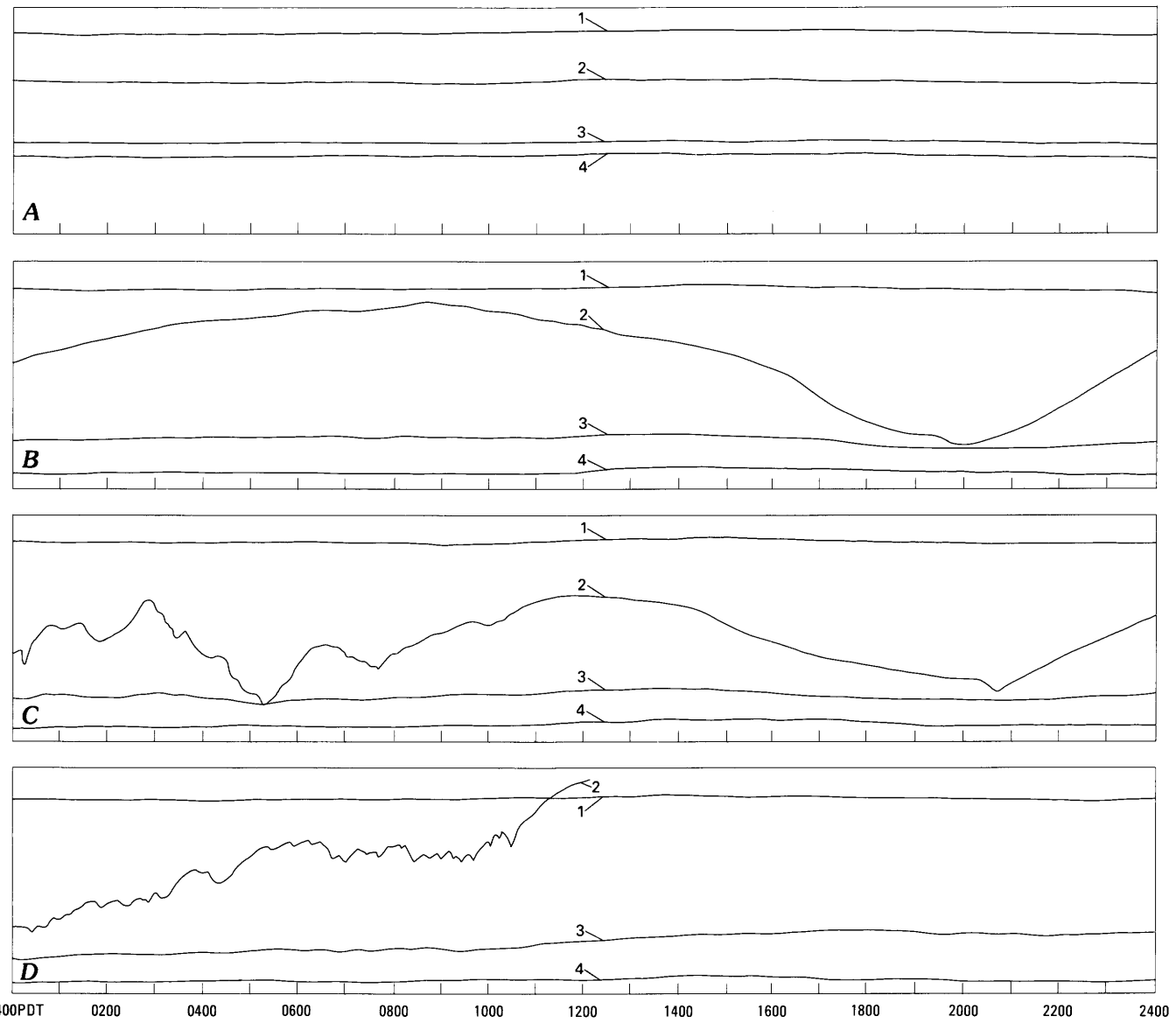

Figure 125.—Recorded traces of H_2 emissions and reference voltages for selected dates in 1980 showing: 1, +10-mV reference voltage; 2, H_2-sensor output voltage in the unattenuated scale; 3, H_2 sensor voltage in the attenuated scale; and 4, 0-mV reference voltage. When the H_2 concentration in the ground increases relative to that in the atmosphere, the sensor voltage decreases. A, September 27; B, July 28; C, July 27; D, August 3.

measurements (more than 360/day), we have used a graphic-area integration method, whereby the area on the recorder chart between a sensor signal and 0-mV reference traces from midnight to midnight is subtracted from that for the sensor null (the area on the recorder chart between 6.2 mV and 0 mV). The difference is converted to the average H_2 concentration by using the 1-atmosphere sensitivity.

RESULTS AND DISCUSSION

Significantly, we observed distinct changes in the relative H_2 concentration at the monitoring site, even though it is 1.2 km from the nearest fumaroles in the May 18 crater. Previously, at other volcanoes, H_2 was monitored only in fumaroles, and thus choices of monitoring sites were restricted. The possibility that more diverse locations and methods may be used for H_2 monitoring is encouraging.

Relative H_2 concentration was measured and recorded about 360 times a day from June 20 through November 1, except for five gaps totaling 21 days, caused by battery failure and relocation of the recording facilities. From September 25 to October 8, the H_2 sensor was accidentally suspended in air because the loose pyroclastic material around the sensor had fallen deeper into the crevices between lava blocks, probably due to seasonal melting of ice underneath. The data are uneventful and stable for this period, as shown in figure 125*A* for September 27. This accidental blank test in the field shows that the sensor-telemetry system is not affected by ambient temperature variations (probably more than 10°C) or other environmental factors that changed during that time, and that there is a voltage offset of 6.2 mV for the sensor null point.

We recognize three patterns of changes in relative H_2 concentrations for the other recording periods: (1) smooth diurnal variations; (2) irregular increases in ground H_2 concentration; and (3) slower, nonperiodic changes in the daily average concentrations.

SMOOTH DIURNAL VARIATIONS IN RELATIVE H_2 CONCENTRATION

A pattern of smooth diurnal variations is recognizable during the periods July 14–August 12, and September 4–17. At other times, either the magnitudes of the changes are small, or they are masked by larger irregular changes, described later. An example of the smooth diurnal variations (recorded on July 28) is shown in figure 125*B*. Typically, the relative ground H_2 concentration decreased in the morning (0800–1000 PDT) and increased in the evening (1900–2100 PDT). These variations amount to several tens of volume parts per million H_2 within a day, when this pattern is pronounced. Often the relative ground H_2 concentration becomes negative during the morning; that is, there is more H_2 in the atmosphere than in the ground.

Possible causes for these diurnal variations include changes in ambient atmospheric temperature, earth tides, and orographic winds. Changes in ambient temperature alone are probably not the cause. The timing for minimum and maximum values of the relative H_2 concentration does not coincide with that for the ambient temperature. Earth tides might produce periodic changes in the H_2 emission but cannot account for the near constancy of the timing. Furthermore, the higher H_2 concentration in the atmosphere than in the ground in the morning is difficult to explain by this mechanism.

Most likely, daily reversals of the vertical air currents at the volcano, which descend in the morning and ascend in the evening (orographic winds), could alternately retard and facilitate mixing of H_2 from the crater plume into the ambient atmosphere. If wind blows H_2 from the plume down in the morning, H_2 could be more concentrated in the atmospheric air (used for sensor reference) than in the ground during this period. The orographic winds are subject to weather conditions. Calm, clear weather would be conducive to strong orographic currents, and cloudy, rainy, or windy weather would retard them. We intend to investigate further the effect of local weather on the intensity of the observed diurnal variations.

IRREGULAR INCREASES IN GROUND H_2 CONCENTRATION

Irregular short-period increases in ground H_2 concentration are recognizable by nonperiodic, irregularly shaped trends on the recorder chart, and also by initial change toward a higher relative ground H_2 concentration. These changes may be superimposed on the smooth diurnal variations; an example is shown in figure 125*C* (July 27). The magnitudes of these

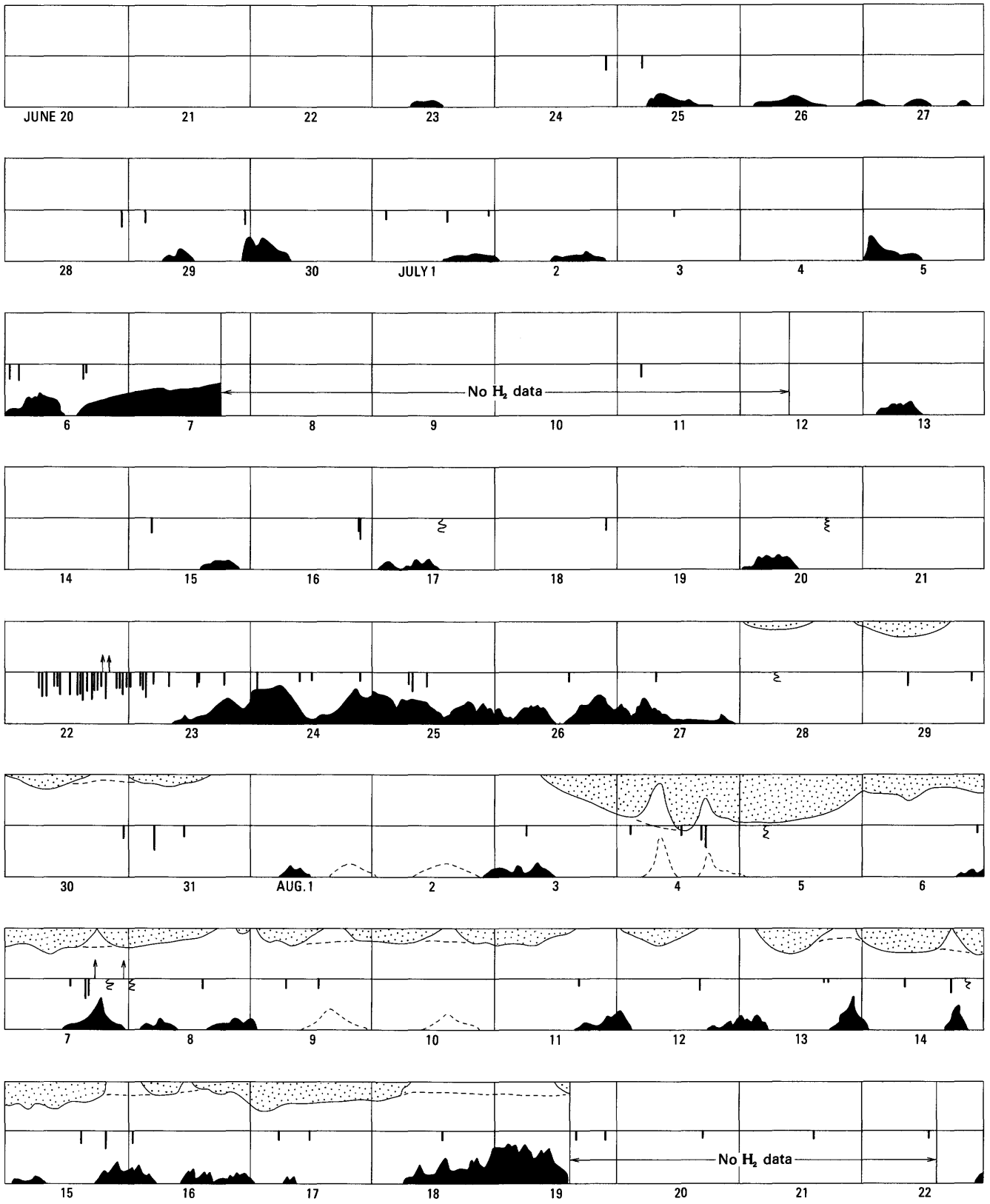

Figure 126.—Correlation chart showing H_2 emission, eruptions, and seismic events from June 20 to November 2, 1980. Black areas, irregular ground H_2 emission (dashed lines, inferred); patterned areas, minimum H_2 in the air, presumably from the crater plume (dashed lines, inferred); upward arrows, Plinian eruptions (width indicates duration); bars above center horizontal lines, steam puffs; sinuous lines below center horizontal lines, seismic events

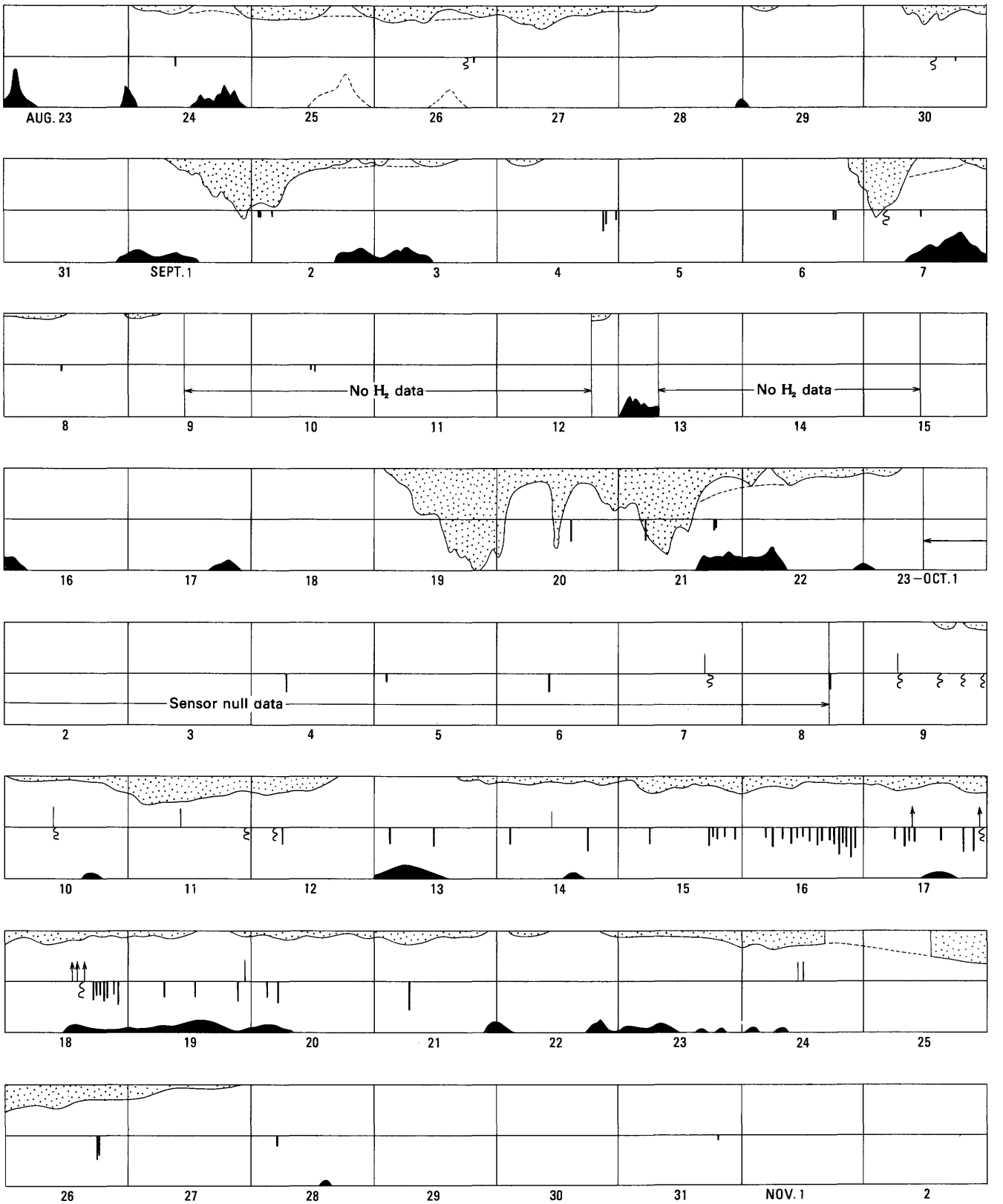

classified as tremor; bars below center horizontal lines, seismic events classified as short-period seismicity (bar length proportional to magnitude). Seismic and eruption data courtesy of University of Washington/USGS seismic computer file.

changes amount to as much as 135 volume ppm. The duration of each increase, or burst, is variable, but generally is less than a day. Such bursts followed the July 22, August 7, and October 16–18 eruptions, but they also occurred at other times in June, early July and in mid-September (fig. 126). The shapes and relative magnitudes of the areas shown in figure 126 closely reproduce the recorded data, except for somewhat arbitrary subtraction of the inferred diurnal variation. On some days, it was impossible to determine whether diurnal changes occurred. Such uncertainties were so pronounced during August 13–19 that we place no confidence in the interpretation for this period; the irregular H_2 events are shown in dotted lines (fig. 126) for other times of uncertainty about diurnal variations.

At least some of these irregular increases in relative ground H_2 concentration appear directly related to volcanic activity. As noted earlier, the frequency of the burstlike changes in H_2 concentration increased markedly following the three major eruptions (fig. 126). Because H_2 is buoyant and mobile, it could not remain underground for prolonged periods or enter the ground from the atmosphere. The irregular shapes of the traces of the changes suggest a dynamic process. For these reasons, we believe that the irregular increases in ground H_2 concentration result from bursts of H_2 through fractures and pores from within the volcano.

To examine further the relation of H_2 emissions to other volcanic activity, we tried to correlate the H_2 bursts with major seismic events, but there were too many seismic events with which to correlate. Next, we compared only shallow seismic events (less than about 1 km) under Mount St. Helens, eruptions, and significant degassing events (fig. 126).

Specific seismic events do not correlate uniquely with H_2 bursts (fig. 126), but generally similar trends in frequency and magnitude suggest that the H_2 increases may be caused by the same volcanic events that caused the seismicity. The ground H_2 emissions observed at the monitoring site also generally tend to lag behind seismic events by a few hours to several tens of hours. Perhaps the lag represents the time required for H_2 pulses to travel through the fractures and pores of the volcanic material from the source. H_2 may also be created by the reaction of ground water with heated rocks, but such H_2 need not rise in bursts or correlate with magmatic activities. In the absence of strong reasons to support a meteoric-water origin, we favor a magmatic origin for the bursts of ground H_2 emission.

CHANGES IN DAILY AVERAGE H_2 CONCENTRATION

In addition to the above patterns, slower, nonperiodic changes in relative H_2 concentrations are evident in 24-hour averages of the H_2 concentrations; these averages eliminate the effects of diurnal variations and the short-period bursts (fig. 127). An abrupt decrease and then increase in the daily average concentrations of ground H_2 occured prior to two eruptions (fig. 127); during August 3–5 (eruption on Aug. 7) and October 9–13 (eruption on Oct. 16–18). Similar changes in average H_2 concentration took place during August 31–September 3, September 18–20, and October 22–28; no eruption followed these changes, but episodes of volcanic tremor and degassing events occurred at about the same times. Conspicuously, no H_2 anomaly correlates with the July 22 eruption.

These abrupt decreases in the daily average H_2 concentration, followed by abrupt increases, may thus correlate generally with volcanic activity manifested by eruptions, vigorous gas emissions, and (or) volcanic tremor.

A clue to understanding the causes of these changes is that the H_2 concentration in the atmosphere becomes greater than that in the ground (negative H_2 concentration in fig. 127). The concentration of H_2 in the atmosphere due to the emission through the ground is presumably small, because H_2 would diffuse much faster in free air than in the ground, and surface winds would resupply air from outside areas. The main source for atmospheric H_2, in excess of the ground concentration, is likely the plume from the crater. H_2 probably diffuses rapidly from the plume to the atmosphere, perhaps within minutes of emission. The H_2 emission through the ground, in contrast, may lag behind the plume emission by hours to several tens of hours, as discussed earlier. Therefore, after a major emission of H_2 from within the volcano, the H_2 concentration in the atmosphere may become higher than that in the ground at first; then the ground H_2 concentration could match, or exceed (if the degassing duration were short), that of the atmosphere a day or so later. This hypothesis can explain the observed changes in average relative H_2 concentration.

ATMOSPHERIC H_2 FROM THE CRATER PLUME

From the preceding discussion, the H_2 concentration in the atmosphere at the monitoring site is clearly variable, and the magnitude of the variation is comparable to, or larger than, that of the ground emissions. Unfortunately, absolute concentrations of H_2 in neither the atmospheric air nor the ground can be determined; only the difference was measured. Nevertheless, we can estimate the minimum concentrations for both by assuming that changes caused by

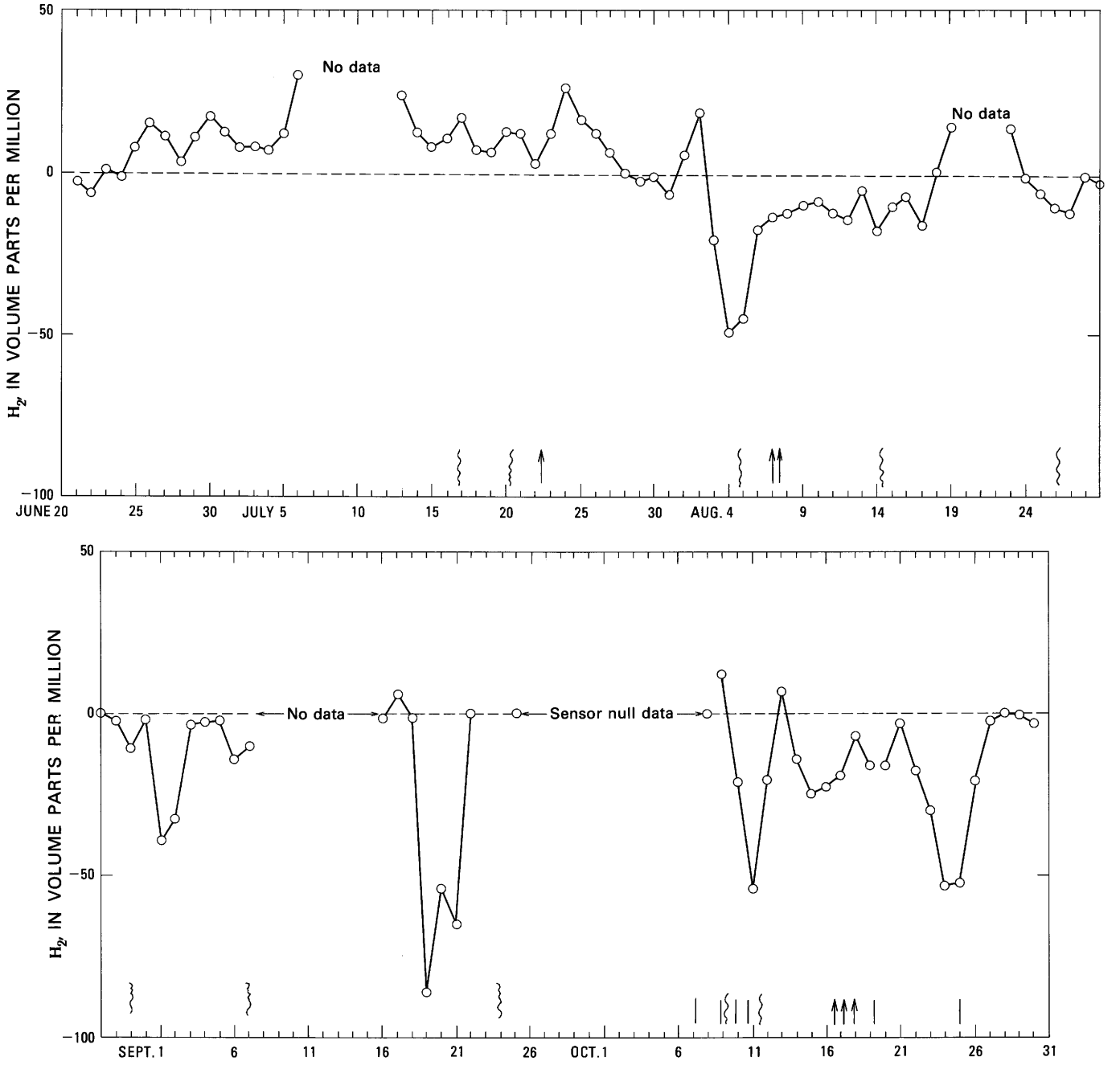

Figure 127.—Daily average of H_2 concentration in the ground relative to the ambient air at the H_2 monitoring site. Negative values mean that the H_2 concentration is higher in the ambient air than in the ground. Arrows, Plinian eruptions; bars, degassing events; sinuous lines, volcanic tremor (University of Washington/USGS seismic computer file).

the plume are slower and smoother, and the sensor signal initially increases (fig. 125*D*), whereas changes of H_2 emission from the ground are more irregular and brief, and the sensor signal initially decreases. Estimates of the amount of change in H_2 concentration due to emission through the ground have been discussed earlier. The minimum concentration of H_2 in the ambient air is obtained from the departure of the sensor signal from the null voltage (6.2 mV) toward larger values, that is, higher atmospheric H_2 concentration. Such minimum plume contributions of H_2 to the atmosphere are shown graphically in figure 126. When the ground H_2 emission increases temporarily, the H_2 levels in the ambient air can be inferred by adding the amount ascribable to the ground H_2 emission. Such inferred H_2 levels in the atmosphere are shown with dashed lines in figure 126. Increases in the atmospheric H_2, sometimes as much as 180 volume ppm (Aug. 4), may be premonitory to eruptions, vigorous degassing, and volcanic tremor, except for the period preceding July 27 when no such increases are recognizable.

The contribution to the atmosphere of H_2 at the monitoring station by the plume is undoubtedly subject to the local winds. The orographic wind descending in the morning would bring the plume down and contribute H_2 to the ambient air (at least 50 ppm H_2 at 1000 PDT on July 30), producing the diurnal variations in the H_2 sensor signal. When regional winds blow the plume away from the south side of the volcano, the atmospheric H_2 would not increase at the sensor site. Southerly winds that prevailed before July 22 may have prevented an increase in the atmospheric H_2 on the south side of the volcano before the July 22 eruption.

Although H_2 oxidizes only slowly at temperatures below several hundred degrees Celsius, and thus would tend to remain in the atmosphere, we did not anticipate that H_2 would be contributed to the ambient air from the plume in magnitudes comparable to those in the ground, because of the high buoyancy of H_2. The observed results are contrary to this preconception and point strongly to the value of monitoring H_2 in the ambient atmosphere near the crater, if direct monitoring in primary fumaroles or vents is not feasible. In the future, we plan to modify our monitoring procedure at Mount St. Helens to permit independent monitoring of H_2 in the atmosphere and in the ground relative to an isolated reference gas to separate plume effect from emissions through the ground. Several locations spread around the crater rim should be monitored, as was done by Noguchi and Kamiya (1963) for sulfur and chlorine at Mount Asama, to eliminate the regional wind effects. The recorded H_2 concentrations from these stations should be added and averaged for 24-hr periods to alleviate the effects of both orographic and regional winds.

CONCLUSIONS

The results of monitoring of H_2 at a nonfumarole site on the south flank of Mount St. Helens indicate the following:

1. H_2 is emitted from the volcanic system through the flank of the volcano as well as through the central vents.
2. The emission of H_2 through the ground at the monitoring site lags behind the emission from the central vent by tens of hours.
3. Some correlations of nonperiodic H_2 emissions with magmatic activities manifested by eruptions, vigorous degassing, and (or) volcanic tremor suggest a magmatic origin of the H_2 rather than origin by rock-meteoric water interactions.
4. Orographic winds cause smooth diurnal variations in the H_2 sensor signal by blowing the plume H_2 down in the morning and up in the evening.
5. The H_2 emitted from the central vent may increase a few days before an eruption.
6. Monitoring of absolute concentrations of H_2 both in the ground and in the ambient air at three or four sites around the volcano is necessary for more informative H_2 monitoring.

REFERENCES CITED

McGee, K. A., 1979, An analog data telemetry system for remote monitoring applications, Version II: U.S. Geological Survey Open-File Report 79-946, 11 p.

McGee, K. A., and Sato, Motoaki, 1979, An analog telemetry system for remote monitoring applications, Version I: U.S. Geological Survey Open-File Report 79-276, 11 p.

Noguchi, Kimio, and Kamiya, Hiroshi, 1963, Prediction of volcanic eruption by measuring the chemical composition and amounts of gases: Bulletin Volcanologique, v. 26, p. 367-378.

Sato, Motoaki, 1972, Intrinsic oxygen fugacities of iron-bearing oxide and silicate minerals under low total pressure: Geological Society of America Memoir 135, p. 289-307.

_____1978, Oxygen fugacity of basaltic magmas and the role of gas-forming elements: Geophysical Research Letters, v. 5, no. 6, p. 447-449.

Vielstich, Wolf, 1970, Fuel cells [English translation by D. J. G. Ives]: London, Wiley Interscience, 501 p.

White, D. E., and Waring, G. A., 1963, Volcanic emanations, *in* Chapter K, Data of geochemistry (6th ed.): U.S. Geological Survey Professional Paper 440-K, p. K1-K27.

THE CHEMISTRY OF GASES EMANATING FROM MOUNT ST. HELENS, MAY-SEPTEMBER 1980

By THOMAS J. CASADEVALL *and* L. PAUL GREENLAND

ABSTRACT

Gas samples collected from fumaroles within the crater, from the plume emanating from the crater, and from rootless fumaroles on the pyroclastic flows, debris avalanche, and the blast deposit contain the following gases in addition to air: H_2O, CO_2, CO, SO_2, H_2S, COS, CS_2, and CH_4. Gas samples from rootless fumaroles on the flowage deposits are dominantly air with trace amounts of sulfur and carbon gases. Samples from the crater fumaroles contained CO_2 to CO volume ratios of 147 ± 10 (eight samples). Samples from a high-temperature (828°C) fumarole contained H_2S as the only sulfur gas; samples from low-temperature (less than 150°C) fumaroles contained both SO_2 and H_2S. From the ratio of CO_2 to CO, the oxygen fugacity of the Mount St. Helens magma was calculated to be $\log f_{O_2} = -13.3 \pm 0.1$ at 828°C. The high concentration of air in the fumaroles in the flowage deposits suggests that entrainment and heating of air and water during eruption of the pyroclastic deposits may enhance the mobility of pyroclastic flows. The abundance of H_2S in the high-temperature fumarole samples, together with calculated oxygen fugacity, suggests that sulfur is released from the melt as H_2S. The abundance of H_2S is low relative to SO_2 in the plume, which means that oxidation of H_2S to SO_2 occurs rapidly upon introduction of H_2S into the atmosphere.

INTRODUCTION

Gases emanating from Mount St. Helens after the May 18 eruption until September were studied to identify the major kinds of gaseous emissions and to evaluate their importance in the volcanic process. Fumaroles within the crater were presumed to have a direct connection to magmatic heat and gas. Rootless fumaroles in the flowage deposits (debris avalanche, blast deposits, and pyroclastic flows) derive their heat and gas from the flowage deposits themselves and are no longer directly connected to the magma (Keith and others, this volume). Before September, the crater could not be entered to directly sample the fumarole emissions, so remote monitoring techniques were used to measure SO_2 (Casadevall and others, this volume) and CO_2 (Harris, Sato, and others, this volume) in the plume. Airborne measurements of gases in the plume can be related directly to measurements of gases from fumaroles within the crater.

ACKNOWLEDGMENTS

We acknowledge the assistance of N. G. Banks (USGS) and Terry Leighley (Sandia Laboratory), who helped collect the gas samples. We especially dedicate this effort to our colleague David Johnston, whose death on May 18 deprived us of a scientist with valuable experience in the study of volcanic gases from other Cascade Range and Alaskan volcanoes.

METHODS OF STUDY

Twenty-eight gas collections were made from fumaroles in the crater, from the plume emanating from the crater, and from rootless fumaroles on flowage deposits during the 4 mo after the eruption of May 18. Gas samples were collected in Pyrex glass bottles with Teflon stopcocks. Sample bottles were either evacuated before sampling at fumaroles to allow capture of gas from the vent, or samples were pumped through nonevacuated bottles having two stopcocks. At most low-temperature (less than 150°C) fumaroles, samples were collected through a Teflon tube inserted in the opening of the fumarole. When a sampling tube was not used, evacuated sample bottles were opened directly in the stream of gas emanating from the fumarole. For the high-temperature gas collections of September 25, a 1-m-long, 2-cm-diameter titanium tube was inserted into a fumarole along a crack and allowed to heat for 5 min. The temperature at the bottom of the tube was 828°C; the temperature of gas at the top of the tube was 397°C. When the titanium tube was removed from the crack, it had developed a thin layer or crust of metallic luster.

Samples were analyzed at the USGS Hawaiian Volcano Observatory 1 to 2 weeks after collection. Each sample was analyzed by four gas chromatographic techniques. A thermal-conductivity detector and a Chromosorb 107 column were used to determine air ($N_2 + O_2 + Ar$), CH_4, CO_2, H_2S, and SO_2 at concentrations greater than 0.01 percent. A flame photometric detector and a Chromosil 310 column were used to determine SO_2, H_2S, CS_2, and COS at concentrations of 5–100 ppm. A flame ionization detector and molecular sieve 5A column were used to determine CH_4 and CO (after conversion of CO to CH_4 using a nickel catalyst) at concentrations greater than 5 ppm. C_2 hydrocarbons were sought (but not detected, less than 5 ppm) by a flame ionization detector and a Porosil C/OPN column.

CO_2, CO, CH_4, SO_2, H_2S, CS_2, and COS were detected in the gas samples. H_2 and helium were not determined. Water was observed in all samples, although gas analyses are reported on a water-free basis. Samples were collected by Casadevall, Greenland, and N. G. Banks. Carbon isotope analyses were performed by L. D. White.

RESULTS

SAMPLES FROM ROOTLESS FUMAROLES

Seven gas-sample collections were made from rootless fumaroles on the blast deposit and debris avalanche of May 18, and the pyroclastic flow of June 12 (table 12). Except for samples collected on July 1 from the June 12 pyroclastic flow, all samples are dominantly air. No analyses were made for halide gases, although HF was qualitatively detected (by odor) in fumaroles of the June 12 flow. There were small to large amounts of CO_2 compared to ambient air (0.03 percent volume per volume) in emissions from all rootless vents, and values range from 0.07 to 59.6 volume percent. CO was detected in samples from the blast deposit and from the pyroclastic flow, and values range from 4 to 30 ppmv (parts per million by volume).

SO_2, H_2S, and CS_2 were detected in gases from the rootless fumaroles. From the vents in the June 12 pyroclastic flow, sulfur gases ranged from less than 0.02 to 0.32 percent SO_2 and as much as 0.27 percent H_2S. The sample (TC–7) from the high-temperature (184°C) fumarole contained more H_2S than SO_2, whereas the low-temperature (97°C) fumarole sample (TC–6) was dominated by SO_2. Also, deposits of native sulfur were observed more commonly on the pyroclastic flow of June 12 than on the other pyroclastic flows. CS_2 was detected in one sample (TC–4) from the blast deposit.

The air, as well as the carbon and sulfur gases in these rootless vents, may have several possible sources: (1) air engulfed by the ash or debris during emplacement; (2) outgassing of juvenile material within the deposits; (3) outgassing of older rock material, due to decarbonation and sulfidation reactions when heated by juvenile material; and (4) combustion of entrained organic debris. Air and water are the major components of the gases evolving from these deposits, which suggests that they were incorporated during emplacement. Heating and expansion of the air and water may have contributed to the mobility of the debris avalanche and pyroclastic flows.

Sulfur gases do not seem to have been abundant in emissions from the rootless fumaroles. CO_2 was an

Table 12.—Analyses of gas samples

[ppmv, parts per million by volume; >, greater than; < less than; leaders (----), not measured or calculated; concentrations are volume per volume; source: P, plume from dome, C, low-temperature (less than 150°C) cracks in rampart; HC, incandescent crack in rampart; PF, fumarole in June 12 pyroclastic flow below amphitheater; P-A, plume sampled from aircraft. L, not detected, less than 5 ppm; +, present but less than 5 ppm; ND, not determined]

Sample	Date	Source	$Ar+O_2+N_2$ (percent)	CO_2 (percent)	CO (ppmv)	CH_4 (ppmv)	SO_2 (ppmv)	H_2S (ppmv)	[1]CO_2/CO	[2]CO_2/SO_2	[3]SO_2/H_2S	Temperature (°C)
					Crater samples							
NB-1	8/16/80	P-A	99.9	0.093	L	+	+	L	---	---	---	---
NB-2	8/24/80	P-A	100	.050	L	+	8.0	L	---	---	---	---
NB-3	8/28/80	P-A	99.9	.054	L	+	7.0	+	---	---	---	---
NB-4	8/29/80	P-A	99.9	.079	L	+	+	L	---	---	---	---
PG-1	9/01/80	C	99.9	.11	5	+	82	8	156	6.4	10	<150
PG-2	9/01/80	C	100	.074	+	+	49	8	---	5.8	6	<150
PG-3	9/03/80	C	96.3	3.56	224	+	1,440	77	158	16.6	18.7	<150
PG-4	9/03/80	P	100	.054	+	+	30	10	---	---	---	---
PG-5	9/03/80	C	98.7	1.31	88	+	11	+	145	>1,000	---	<150
PG-6	9/03/80	C	99.8	.17	9.6	+	78	7	144	12.0	11	<150
PG-7	9/03/80	C	100	.055	L	+	350	29	---	---	---	<150
PG-8	9/03/80	C	100	.058	L	+	58	8	---	---	---	<150
PG-9	9/05/80	P	99.9	.075	+	+	10	6	---	---	---	---
PG-10	9/07/80	C	99.3	.70	48	+	10	+	140	>700	---	<150
PG-11	9/07/80	P	100	.048	L	+	40	L	---	---	---	---
PG-12	9/08/80	P	99.9	.13	7.8	+	36	+	---	---	---	---
[4]TC-1	9/25/80	HC	83.8	15.9	1,080	+	<50	2,300	147	---	---	828
[4]TC-2	9/25/80	HC	85.1	14.7	950	+	<50	1,800	154	---	---	828
[4]TC-3	9/25/80	HC	68.1	31.4	2,440	31	<50	2,300	128	---	---	828
					Rootless fumarole samples							
[5]TC-4	5/28/80	Blast	99.8	0.11	19	+	400	L	41	1.9	---	141
TC-5	5/28/80	Blast	99.9	.081	30	+	L	L	16.3	---	---	141
NB-5	6/14/80	PF	99.5	.17	ND	ND	3,200	<200	---	---	---	---
TC-6	7/01/80	PF	40.2	59.6	5	38	1,400	<200	---	---	---	97
TC-7	7/01/80	PF	61.1	38.7	4	12	<200	2,700	---	---	---	184
TC-8	6/15/80	PF	99.2	.78	ND	ND	<200	<200	---	---	---	135
TC-9	6/15/80	Debris	99.9	.07	ND	ND	<200	<200	---	---	---	<180

[1] CO_2 - 320 ppm/CO (volume ratio).
[2] CO_2 - 320 ppm/SO_2 (mass ratio).
[3] SO_2/H_2S (volume ratio).
[4] COS detected (less than 100 ppm).
[5] CS_2 detected (less than 5 ppm).

abundant constituent of several samples. The $\delta^{13}C$ values of CO_2 in samples collected from the June 12 pyroclastic flow range from −9 to −10 per mil (PDB standard) and are depleted by several per mil relative to either magmatic or atmospheric CO_2 ($\delta^{13}C \cong -7$ per mil). This depletion suggests some contamination from organic material. The possibility of contamination by modern organic debris seems unlikely, because of the lack of vegetation in this area since May 18, and considering that the area is covered by pyroclastic flows of May 18, May 25, and June 12. Some of the CO_2 may have been derived by heating of carbonate or carbonaceous material in wall rocks at depth below the volcanic edifice.

PLUME SAMPLES

Ten samples of gas were collected either from aircraft flying through the plume, or directly in the plume from the rampart adjacent to the dome (table 12). All samples contained more than 99.9 volume-percent air ($Ar+O_2+N_2$). CO_2 levels ranged from 400 to 1,300 ppm, indicating enrichment of CO_2 in the plume by as much as three times the levels in air. As much as 7 ppm CO was measured in a plume sample from over the August dome. SO_2 levels ranged from less than 5 to 40 ppm. H_2S concentrations ranged from less than 5 to 10 ppm. The mass ratios of CO_2 to SO_2 in plume samples range from 8 to 52 and are higher than those detected by airborne remote

monitoring, which range from 2 to 16 (Casadevall and others, this volume; Harris, Sato, and others, this volume). Because of the high levels of air in the samples and the inherent problems of sampling a plume (contamination by aircraft exhaust, for example), it is difficult to interpret the significance of the plume sample values.

CRATER SAMPLES

By September 1, 1980, we could enter the crater to sample fumaroles. Within the crater were three types of fumaroles: (1) those on the surface and at the margin of the active dome; (2) those in cracks on the tephra rampart adjacent to the dome; and (3) those along the intersection of the crater wall and the floor. Fumarole types 1 and 3 were not accessible during our studies. The tephra rampart surrounding the August 7 dome covered the remains of the June 15 dome, which was partially destroyed by the eruption of July 22. The second dome appeared in the crater following the eruption of August 7.

Eleven samples were collected from fumaroles on the tephra rampart in the crater, eight from low-temperature (less than 150°C) fumaroles in the tephra rampart, and three from a high-temperature (828°C) fumarole in an incandescent crack in the rampart (table 12). The samples from the low-temperature fumarole (PG-1, -2, -3, -5, -6, and -10) contained more than 96 percent air in addition to CO_2, CO, SO_2, H_2S, and CH_4. The volume ratios of CO_2 to CO range from 140 to 158. CH_4 content was similar to that of ambient air.

The high-temperature gas samples TC-1, -2, and -3 were collected on September 25, 1980, from a fumarole along a N. 35° E.-trending fracture in the tephra rampart adjacent to the August 7 dome. Incandescent solid rock, probably of the June 15 dome, was visible in the crack and had a maximum temperature of 838°C measured at a depth of 1 m. The gases were probably derived from the still-cooling June dome. The radial fracture extended to the northeast for approximately 100 m and was 10 to 50 cm wide. The crack extended down into the dome from 30 cm to more than 1 m, depending on the amount of ash and blocks in the crack.

The high-temperature gas samples contain 68 to 85 volume percent air in addition to CO_2, CO, CH_4, SO_2, H_2S, and COS. Of note is the ratio of CO_2 to CO, which ranges from 128 to 154 and is virtually identical to the ratio of these gases in the low-temperature crater fumaroles. In the high-temperature collections, H_2S is the dominant sulfur gas, in contrast to the low-temperature fumarole samples, where the volume ratio of SO_2 to H_2S ranges from 6 to 18.

DISCUSSION

Despite the large amounts of air in these collections, useful information can be obtained from the ratios of CO_2 to CO. There is a strong correlation ($r=0.99$) between CO_2 and CO in samples from fumaroles within the crater (fig. 128). (CO_2:CO $=147\pm10$; eight samples). The ratios for high-temperature samples are statistically the same as those for low-temperature samples, which suggests that the ratio of CO_2 to CO has not been affected by cooling of the gases. If we assume that this volume ratio represents the proportion of CO_2 to CO as released from the magma, we may calculate the oxygen fugacity in the magma by equilibrium constants calculated from Robie and others (1978) and by:

$$CO+\tfrac{1}{2}O_2=CO_2 \qquad (1)$$

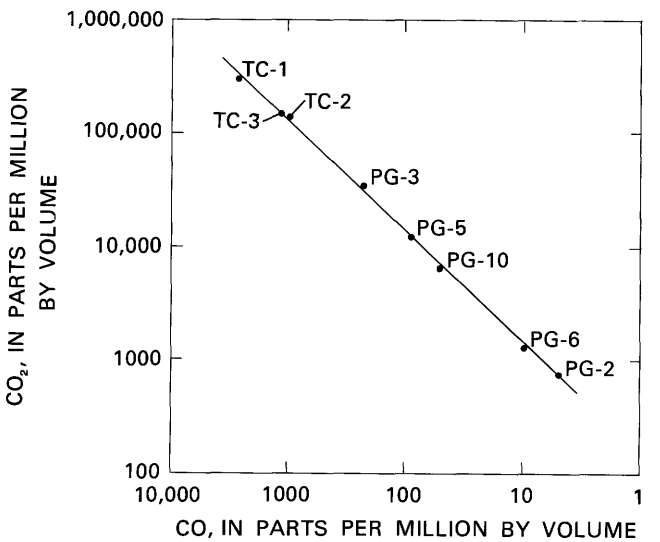

Figure 128.—Concentrations of CO_2 versus CO for gas samples collected within the Mount St. Helens crater during September 1980. Concentrations are in log units, actual values are in table 12. Three samples were collected at temperatures of 828°C and five samples were collected at temperatures of less than 150°C.

The conditions of oxygen fugacity during degassing (log $f_{O_2} = -13.3 \pm 0.1$ at 1,100K) are slightly more oxidizing than the quartz-fayalite-magnetite buffer (fig. 129). The oxygen fugacity calculated for Mount St. Helens dacite magma is plotted (fig. 129) relative to the equal concentration boundary of $SO_2 = H_2S$. This boundary has been calculated from equation 2 at $P_{fluid} = P_{H_2O} = 0.5$ and 1 kb and $X_{H_2O} = 1$

$$H_2S + 3/2O_2 = SO_2 + H_2O. \quad (2)$$

At 1 kb total pressure and the oxygen fugacity of the Mount St. Helens magma, we can expect H_2S to be the dominant sulfur gas (H_2S:SO_2 = 100) released from the melt. This conclusion is supported by the gas analyses (table 12), which show that H_2S is the dominant sulfur gas in the high-temperature fumaroles. The position of the SO_2:H_2S equal-concentration boundary is affected by the fluid pressure (P_f) and the mole fraction of water in the volatile phase of the melt (Ohmoto and Rye, 1979). A decrease in the total pressure, such as might be due to decompression of magma during ascent, or a decrease in the mole fraction of water, such as might be due to large increases in the concentration of CO_2, will shift the $SO_2 = H_2S$ boundary to lower values of f_{O_2}. Therefore, during certain periods of activity, SO_2 could be an abundant gas of sulfur derived directly from the melt.

Study of the gas data suggests the following thermochemical process of evolution of sulfur gases at Mount St. Helens. H_2S is the dominant gas of sulfur released from the melt (H_2S:SO_2 = 100). SO_2 is the dominant sulfur gas measured in the plume, as well as in low-temperature fumaroles in the crater. The absence of large amounts of H_2S in the plume suggests that most, if not all, H_2S is efficiently oxidized to SO_2 prior to its incorporation in the plume. We suggest that this oxidation occurs shortly after H_2S is liberated from the magma, probably in the high-temperature cracks in and adjacent to the dome. Continued oxidation of SO_2 to SO_4^{2-} may occur at ambient air temperatures after reaction of SO_2 with steam, ground fog (clouds), ground water, or rain, to form sulfurous acid:

$$SO_2 + H_2O = H_2SO_3$$

Atmospheric oxidation of sulfurous acid may then produce sulfuric acid:

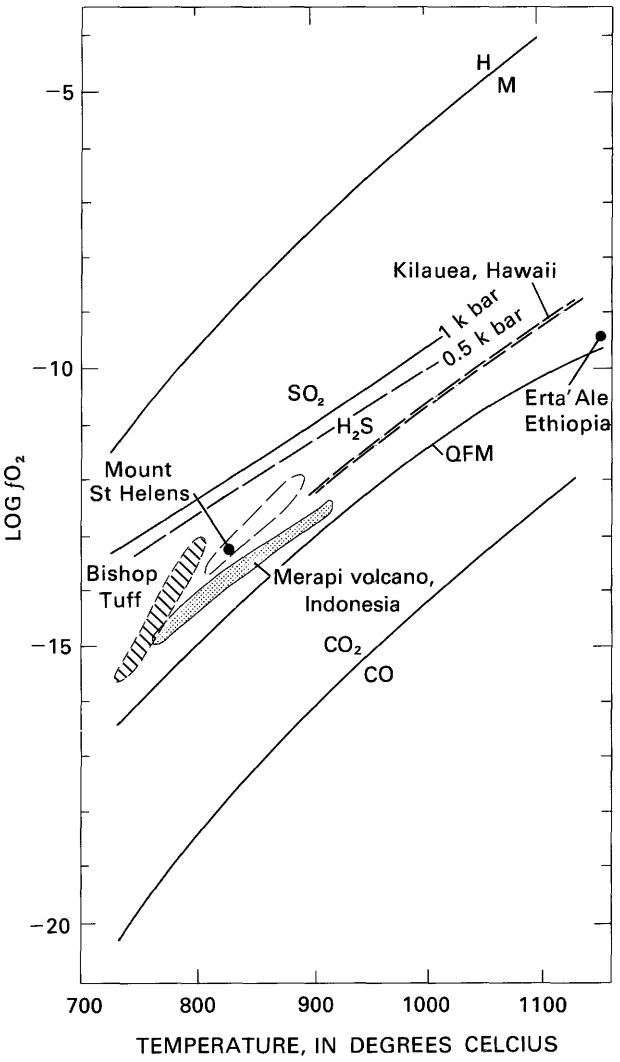

Figure 129.—Log f_{O_2} versus temperature diagram for selected volcanic systems. Mount St. Helens oxygen fugacity calculated from ratio of CO_2 to CO. Hematite-magnetite (H/M) buffer and quartz-fayalite-magnetite (QFM) buffers shown for reference; CO_2/CO equal-concentration boundary calculated from thermodynamic data in Robie and others (1978); SO_2/H_2S equal-concentration boundary summarized from Ohmoto and Rye (1979) at the condition of $P_{H_2O} \cong 0.5$ kbar and 1 kbar, and $X_{H_2O} \cong 1.0$. f_{O_2} versus temperature conditions for the Pleistocene Bishop Tuff, California, from Hildreth (1979); Erta'Ale volcano, Ethiopia, data from Gerlach (1980); Kilauea volcano, Hawaii, data from Sato and Wright (1966); Merapi volcano, Indonesia, data from LeGuern and Gerlach (1979).

$$H_2SO_3 + \tfrac{1}{2}\, O_2 = H_2SO_4$$

The volume ratio of SO_2 to H_2S in low-temperature fumarole gas ranges from 6 to 18 (mass ratio 11 to 34). Since early June, SO_2 has typically accounted

for as much as 90 percent of the total sulfur gas of the plume during nonexplosive degassing, and H_2S constitutes the balance of the sulfur gas (Hobbs and others, 1981). Also, a significant, but as yet unmeasured, portion of the sulfur gas released from the melt is converted to sulfurous acid droplets or aerosols that ultimately can form sulfuric acid aerosols (Woods and Chuan, 1980) and encrustations of various sulfate minerals found in the crater (Keith and others, this volume). Thus, not all of the sulfur gas released by the melt enters the plume, where it can be measured by airborne monitoring techniques now in use (Casadevall and others, this volume).

CONCLUSIONS

The mass ratio of CO_2 to SO_2 in samples collected in early September from the low-temperature fumaroles in the crater range from 5.8 to 16.6. During this period, the mass ratio of CO_2 to SO_2 in the plume was about 6.0 ± 1.0 (Casadevall and others, this volume; Harris, Sato, and others, this volume). The similarity between the CO_2:SO_2 ratios of fumarole gases and airborne measurements in the plume suggests that the ratio of the gases measured by airborne methods does indeed give information about the gases released directly from the crater fumaroles. Oxidation of sulfur gases appears to be the principal change that occurs to the sulfur-carbon gases on release from the melt.

The data presented here show that our gas-monitoring methods are indeed giving indications of the activity of volatile constituents in the Mount St. Helens volcanic system. Future geochemical experiments will help to clarify the role that volatile constituents play in driving explosive volcanic eruptions.

REFERENCES CITED

Gerlach, T. M., 1980, Investigation of volcanic gas analyses and magma outgassing from Erta'Ale Lava Lake, Afar, Ethiopia: Journal of Volcanology and Geothermal Research, v. 7, p. 415–441.

Hildreth, E. W., 1979, The Bishop Tuff—Evidence for the origin of compositional zonation in silicic magma chambers: Geological Society of America Special Paper 180, p. 43–75.

Hobbs, P. V., Radke, L. F., Eltgroth, M. W., and Hegg, D. A., 1981, Airborne studies of the emissions from the volcanic eruptions of Mt. St. Helens: Science, in press.

LeGuern, F., and Gerlach, T. M., 1980, High temperature gases from Merapi volcano, Indonesia—Application of a new technique for field gas measurements [abs.]: American Geophysical Union, Pacific Northwest meeting, Bend, Oreg., Sept. 1979, EOS, v. 61, no. 6, p. 67.

Ohmoto, Hiroshi, and Rye, R. O., 1979, Isotopes of sulfur and carbon, in Barnes, H. L., ed., Geochemistry of hydrothermal ore deposits [2d ed.]: New York, Wiley-Interscience, p. 509–567.

Robie, R. A., Hemingway, B. S., and Fisher, J. R., 1978, Thermodynamic properties of minerals and related substances at 298.15 K and 1 bar (105 pascals) pressure and at higher temperatures: U.S. Geological Survey Bulletin 1452, 456 p.

Sato, Motoaki, and Wright, T. L., 1966, Oxygen fugacities directly measured in magmatic gases: Science, v. 153, no. 3740, p. 1103–1105.

Woods, D. C. and Chuan, R. L., 1980, Characterization of stratospheric aerosols in eruption plumes from Mt. St. Helens [abs.]: EOS, v. 61, no. 46, p. 1153.

THE 1980 ERUPTIONS OF MOUNT ST. HELENS, WASHINGTON

ANALYSES OF GAS SAMPLES FROM THE SUMMIT CRATER

By WILLIAM C. EVANS, NORMAN G. BANKS, *and* LLOYD D. WHITE

ABSTRACT

Gas samples collected from the plume consisted mainly of atmospheric air; H_2, SO_2, and volcanic CO_2 were at detectable levels. Gas emitted from crater fumaroles contained H_2O, CO_2, H_2, H_2S, SO_2, CO, HCl, HF, and some air. Concentrations of H_2O, H_2, CO_2, and CO would have been at chemical equilibrium at temperatures between 525°C and 650°C. $\delta^{13}C$ values of -10.4 per mil to -10.8 per mil (PDB) indicate that the CO_2 may have originated in the mantle. The fumarolic water differs in δD value (-33 per mil SMOW) and $\delta^{18}O$ value (+5.94 per mil SMOW) from locally derived meteoric water (about -90 per mil in D and -12 per mil in ^{18}O), indicating a deep component in the fumarolic gas.

INTRODUCTION

The gas plume rising from the August lava dome in the central crater persisted downwind for tens of kilometers but varied greatly in appearance from day to day. At times (as on August 20), it was almost transparent, and the south wall of the crater was clearly visible when viewed through the plume from the north. At other times (as on August 23), visibility through the plume was less than a few meters. We sampled the plume during both types of conditions, but the vents producing the plume were not accessible for direct sampling.

After the October 16–18 eruptions destroyed the August dome, an even larger dome formed in the same area (Moore and others, this volume). Many small fumaroles and cracks, radiating out from the October dome, discharged gas from the crater floor. The cracks were about 10–60 cm wide and tens of meters long. Samples were collected from a small fumarole 25 m northeast of the dome margin, from a nearby crack, and from a large fumarole next to the northwest margin of the dome. At a depth of 30 cm, the crack was hotter than 400°C (mercury thermometer), and hot enough to exceed the softening point of the Pyrex sampling tube (approximately 565°C). Measured temperatures of several small fumaroles were all approximately 93°C. Conspicuous mineral encrustations were deposited around the fumaroles (Keith and others, this volume). In contrast to the cooler fumaroles, no visible condensate formed above the cracks. Although collected at different times, the geologic setting of these fumarole and crack samples was similar to that of the samples collected and analyzed by Casadevall and Greenland (this volume).

SAMPLE COLLECTION

Most plume samples were collected from the edge of the tephra rampart adjacent to the inner crater and dome by reaching into the plume as it drifted upward and then opening a ground glass stopcock on an evacuated 2-L glass bulb. We also collected a few samples by helicopter, hovering in the plume 30–40 m above the August dome.

In October, a small fumarole and a crack were sampled by inserting to a depth of about 40 cm a 1.5-m length of 6-mm O.D. Pyrex tubing with a right-angle bend into the orifice. This was connected

to a glass U-tube immersed in a dry ice-ethanol slush. A stainless steel valve was connected to the U-tube, followed by a tee that accommodated both a 150-cc evacuated glass sample tube and a 50-cc plastic syringe with a three-way valve. The syringe was used to evacuate the tee and to pull a known volume of gas through the cold trap. This arrangement allowed only cold dry gas to contact the stainless steel valve. The internal volume of the collecting apparatus was 80 cc. About 450 cc of dry gas was pulled through the cold trap before opening the stopcock of the sample tube. A milky condensate, which formed in the glass tube just upstream from the cold trap while both the small fumarole and the crack were being sampled, was transferred to the cold trap after sampling was complete.

The ground immediately surrounding the large fumaroles was unstable, preventing close approach. We sampled one large fumarole from a distance of 10–12 m through 0.25-in. O.D. aluminum tubing (one end of which had been weighted and thrown down into the fumarole). No attempt was made to separate water vapor by freezing during collection. The lack of any visible condensate in the glass sample tube indicated that most of the water vapor condensed in the aluminum tubing.

METHODS OF ANALYSIS

The samples in glass tubes were analyzed by gas chromatography, using Porapak Q and Linde Molecular Sieve 5A for all gases except SO_2. Concentrations of SO_2 were determined using a Teflon column packed with polyphenyl ether and phosphoric acid on Chrom T (Stevens and others, 1971). Samples were generally analyzed within 2 weeks of collection. Plume samples were reanalyzed after 10 days to check for loss of SO_2 over time.

The CO_2-equilibration method of Cohn and Urey (1938) and the uranium technique of Bigeleisen and others (1952) were used in the analysis for oxygen and deuterium isotopes. Isotopic ratios of ^{18}O:^{16}O, D:H, and ^{13}C:^{12}C were determined on a modified Nier double-collecting, 6-in., 60°-sector mass spectrometer (McKinney and others, 1950).

Water from the cold trap was filtered through a 0.45-μm Millipore filter and analyzed for anions by ion chromatography. Na^+, K^+, Ca^{+2}, Mg^{+2}, Al^{+3}, and Fe^{+3} were analyzed by atomic-absorption spectrophotometry; H^+ and NH_4^+ were analyzed by specific-ion electrodes.

PLUME ANALYSES

All the plume samples are compositionally similar, within analytical uncertainties, to ambient air except for higher concentrations of H_2, CO_2, and SO_2 (table 13). SO_2, at the low concentrations present, may be lost by adsorption or reaction in the sample tube; repeat analyses after 10 days showed no change in SO_2 concentrations, but some SO_2 might have been lost prior to the initial analysis. The calculated temperatures at which samples would be saturated with water vapor (table 13) indicate that the two samples collected when visibility in the plume was only a few meters would be water saturated at low temperatures (20°C and 12°C). Although plume temperatures were not measured during sampling, they were uncomfortably hot, and would have been well above the water-saturation temperature; therefore water droplets might not have been responsible for the opacity of the plume. Clear, cold air was continuously mixing with margins of the optically dense plume, causing dilution that may have been responsible for the low water contents in the samples.

FUMAROLE ANALYSES

The O_2, N_2, and Ar levels in samples from the small fumarole and crack resulted mainly from air contamination, although some N_2 and Ar may have come from other sources. Air and air-saturated rainwater may have circulated into the porous ash of the crater floor and entered the fumarole below the sampling point. The problem of air contamination in fumaroles has been widely discussed (for example, Giggenbach and LeGuern, 1976).

Water vapor was the most abundant constituent in these fumaroles. Knowing the volume of dry gas pulled through the cold trap and the amount of water frozen out, we calculated the percent of water vapor in the gas. Because only one trap remained unbroken after reaching the fumarole area, it was used to sample both the small fumarole and the crack. Thus, the value for these samples is the average for both sites. A total of 3.0 mL (0.17 moles) of water was recovered from the cold trap after 1.3 L (0.043 moles) of

Table 13.—Plume and fumarole analyses of gas from Mount St. Helens from August to November 1980

[Gas compositions are exclusive of H_2O, HCl, and HF; na, not analyzed; leaders (---) indicate no analysis possible]

Date	Aug. 16	Aug. 16	Aug. 20	Aug. 23	Aug. 23	Aug. 24	Nov. 4	Nov. 4	Nov. 4	Nov. 4	(2)
Sample No.	CQ145NB80	CQ144NB80	CQ171NB80	CQ172NB80A	CQ172NB80B	CQ173NB80	CQ243IB80	CQ244IB80	CQ246IB80	CQ247IB80	
Sample type	Plume, dense, low visibility	Plume, dense, low visibility	Plume, transparent[1]	Plume, dense, blue, visibility ±3 m	Plume, dense, blue, visibility ±3 m	Plume, semi-transparent[1]	Small fumarole at 93°C	Crack >400°C	Large fumarole	Large fumarole	Ambient air
					Composition in volume percent						
He	<0.005	na	<0.005	<0.005	<0.005	<0.005	<0.005	<0.005	<0.005	<0.005	<0.005
H_2	.007	na	.005	.006	<.005	<.005	10.8	8.61	.79	1.74	<.005
Ar	.92	na	.94	.93	.94	.94	.12	<.02	.89	.82	.93
O_2	21.1	na	21.0	21.0	20.9	21.0	2.72	.03	19.4	18.1	21.0
N_2	78.5	na	78.2	78.3	78.4	78.5	11.7	1.64	73.4	68.4	78.3
CH_4	<.001	<0.001	<.001	<.001	<.001	<.001	<.0002	<.0002	<.002	<.002	<.0002
CO_2	.112	.0834	.0657	.0811	.0407	.0438	70.5	86.6	5.74	11.1	.0324
C_2H_6	<.01	<.01	<.01	<.01	<.01	<.01	<.01	<.01	<.01	<.01	<.01
CO	na	na	na	na	na	na	.49	.57	.03	.07	na
H_2S	<.0005	<.0005	<.0005	<.0005	<.0005	<.0005	2.16	2.09	.12	.21	<.0005
SO_2	.0028	.0015	.0017	.0006	.0002	.0005	.49	.84	.19	.40	<.0002
Total[3]	100.6	---	100.2	100.3	100.3	100.5	99.0	100.4	100.6	100.8	100.3
					Gas properties						
CO_2/H_2 (by volume)	[4]11	---	[4]6.7	[4]8.1	---	---	6.5	10	7.3	6.4	---
CO_2/SO_2 (by volume)	[4]29	[4]34	[4]20	[4]81	[4]42	[4]23	144	103	30	28	---
H_2O (percent by volume in original gas)	na	na	.72	2.3	1.4	.46	[5]>80	[5]>80	na	na	na
Temperature(°C) of saturation with H_2O	---	---	2	20	12	-4	---	---	---	---	---
$\delta C_{13}O$ of CO_2 (per mil PDB)	-10.7	-9.5	-9.1	-10.7	-8.4	-8.8	-10.7	-10.5	-10.4	-10.8	-7.5
δD (per mil SMOW)[6]	na	na	na	na	na	na	[5]-33.0	[5]-33.0	na	na	na
δO_{18} (per mil SMOW)[6]	na	na	na	na	na	na	[5]+5.94	[5]+5.94	na	na	na

[1]Sampled from helicopter.

[2]Average of several analyses, to be used for comparison.

[3]Analytical error is ±1 percent.

[4]CO_2 corrected for ambient air.

[5]Average value for both samples CQ243IB89 and CQ244IB80 combined (see discussion in text).

[6]SMOW, Standard Mean Ocean Water.

dry gas at 0.78 atm and 15°C had been pulled through the trap. Therefore, at least 80 percent of the fumarole gas was water vapor. However, as much as 2.0 mL of water condensed in the first part of the apparatus and could not be transferred to the cold trap. Recalculating for this lost water indicates that, at most, 87 percent of the fumarole gas was water vapor.

After water vapor, CO_2 is the next most abundant constituent in the fumarole samples (table 13). Near-surface reactions could produce all other observed constituents of these gases, but the CO_2 is probably derived from the magma at depth, as suggested by depletion in ^{13}C by about -10.5 per mil relative to the widely used PDB standard (Craig, 1953). Although some CO_2 may be from shallow breakdown of organic material that is generally depleted in ^{13}C by at least -20 per mil (Craig, 1953), the value of -10.5 per mil is close to values proposed for mantle carbon of -4.7 per mil to -8.0 per mil (Barnes and others, 1978).

Because we were unable to sample far down into the large fumarole, samples from this site are mostly air (table 13). Otherwise, these samples are similar to those from the other fumaroles, except that relative abundances of H_2S and SO_2 are reversed.

DISCUSSION

Amounts of H_2S and SO_2 in volcanic gases can be controlled by the reaction

$$H_2S + 2H_2O \rightleftharpoons SO_2 + 3H_2 \qquad (1)$$

with higher temperatures favoring higher SO_2:H_2S ratios (Ellis, 1957). This reaction requires that an increase in SO_2 relative to H_2S be accompanied by a threefold increase in H_2. The CO_2:H_2 ratios for the large fumarole and small fumaroles are in the same range, however, indicating that the different amounts of H_2S and SO_2 at these two sites cannot be due only to different subsurface temperatures. Alternatively, H_2S could have been oxidized to S, SO_2, or SO_3 prior to filling the sample tube, as ample atmospheric O_2 was present. Oxidation of H_2S is favored by the compositions of the plume samples collected from the August dome, which contained no detectable H_2S, although SO_2 was present, and the CO_2:SO_2 ratios were similar to that of the large fumarole sample.

Equation 1 shows that once some H_2S has been produced by reaction of sulfide minerals with water, SO_2 and H_2 can form. Oxidation of ferrous iron is another source for H_2 (Clarke, 1916). H_2 can react with CO_2 to form CO, H_2O, and CH_4. Two possible reactions are:

$$CO_2 + H_2 \rightleftharpoons CO + H_2O \quad (2)$$

$$CH_4 + H_2O \rightleftharpoons CO + 3H_2 \quad (3)$$

By substituting concentration values from table 13 and equilibrium constants for equation 2 at elevated temperatures (Darken and Gurry, 1953), apparent equilibration temperatures for reaction 2 are 525°C for the small fumarole and 560°C for the crack. These temperatures become 625°C and 650°C, respectively, if the water vapor content were 87 percent. Similar calculations, using equilibrium constants for equation 3 at these temperatures, show that with measured values of H_2O, CO, and H_2 from table 13, very little CH_4 would exist at equilibrium. We cannot make these calculations for the large fumarole because we do not know the H_2O content.

The filtrate analysis shows that the fumaroles contained considerable gaseous HF and HCl (table 14). These gases probably result from the following reaction (Ellis, 1957):

$$H_2O + 2\,NaX + SiO_2 \rightleftharpoons Na_2SiO_3 + 2HX \quad (4)$$

where X is either F^- or Cl^-. The small amount of SO_4^{-2} in the filtrate may have originally been SO_3 or a salt of some minor cation. Some of the encrustations that lined the throats of these fumaroles (Keith and others, this volume) may have entered the sampling tube.

Table 14.—Analysis of fluid from cold trap

[Analysis of 3.0 mL of fluid at pH 0.8]

Constituent	Content found in sample	
	µmoles	µg
H^+	475	480
Na^+	10.0	230
K^+	1.0	39
Mg^{+2}	1.5	36
Ca^{+2}	5.4	216
NH_4^+ as N	<2	<30
Al^{+3}	16.7	450
[1]Fe^{+3}	1.4	78
[2]F^-	123	2,340
Cl^-	583	20,700
[3]SO_4^{-2}	13.8	1,320

[1]Total iron in solution as Fe^{+3}.
[2]Mostly in HF at this pH.
[3]Mostly in HSO_4 at this pH.

A light-yellow to white precipitate that formed during our sampling of the small fumarole and crack is mostly elemental sulfur, as shown by energy-dispersive and diffraction X-ray analyses (T. Keith, written commun., 1980). This sulfur may have been a gas in the fumarole, or it may have formed in the collection tube by the reaction (Giggenbach, 1975):

$$2H_2S + SO_2 \rightleftharpoons 3S + 2H_2O \quad (5)$$

The precipitate weighed 7.4 mg and, neglecting the small amount of ash present, represents 230 µmoles of S. The amount of SO_2 and H_2S collected through the cold trap equals the total moles of gas collected (0.043) times the fraction of SO_2 and H_2S contained in the gas (2.8 percent—the average of the small fumarole and crack samples). This represents 1,200 µmoles of sulfur. Therefore, a maximum of 20 percent of the sulfur entering the collection tube as H_2S and SO_2 could have reacted to form elemental sulfur.

The D and ^{18}O values for the water collected in the cold trap are -33 per mil and +5.9 per mil, respectively, relative to SMOW (Craig, 1961). Barnes and others (this volume) showed that the stable isotopic composition of meteoric water in the Mount St. Helens area is much lighter, about -90 per mil in D and -12.6

per mil in ^{18}O. The fumarolic water may also have been isotopically fractionated during collecting due to condensation upstream from the cold trap. Condensation would preferentially remove the heavier isotopes (D and ^{18}O) from the gas phase, making the water reaching the cold trap lighter than the water in the fumarole. Therefore, the actual isotopic composition of the water in the fumarole may be shifted even further from meteoric water than these values indicate. These values suggest that the fumaroles have a significant component of metamorphic water, as well as some meteoric water that has reacted at depth with igneous rocks at high temperatures. Incorporation of a brine such as discharges from the spring at Pigeon Springs, about 30 km southeast of Mount St. Helens (found to have 22,000 mg/L Cl^-, -45 per mil in D, and -4.29 per mil in ^{18}O; Barnes and others, this volume), could be responsible for some of the HCl and the unusual isotopic composition of the fumarole water.

REFERENCES CITED

Barnes, Ivan, Irwin, W. P., and White, D. E., 1978, Global distribution of carbon dioxide discharges, and major zones of seismicity: U.S. Geological Survey Water Resources Investigation 78-79, Open-File Report, 12 p.

Bigeleisen, Jacob, Perlman, M. L., and Prosser, H. C., 1952, Conversion of hydrogenic materials to hydrogen for isotope analysis: Analytical Chemistry, v. 24, p. 1356-1357.

Clarke, F. W., 1916, The data of geochemistry: U.S. Geological Survey Bulletin 616, 821 p.

Cohn, Mildred, and Urey, H. C., 1938, Oxygen exchange reactions of organic compounds and water: American Chemical Society Journal, v. 60, p. 679.

Craig, Harmon, 1953, The geochemistry of the stable carbon isotopes: Geochimica et Cosmochimica Acta, v. 3, p. 53-92.

_____1961, Isotopic variations in meteoric waters: Science, v. 133, p. 1702-1703.

Darken, L. S., and Gurry, R. W., 1953, Physical chemistry of metals: York, Pennsylvania, McGraw-Hill, 535 p.

Ellis, A. J., 1957, Chemical equilibrium in magmatic gases: American Journal of Science, v. 255, p. 416-431.

Giggenbach, W. F., 1975, A simple method for the collection and analysis of volcanic gas samples: Bulletin Volcanologique, v. 39, p. 132-145.

Giggenbach, W. F., and LeGuern, Francois, 1976, The chemistry of magmatic gases from Erta'Ale, Ethiopia: Geochimica et Cosmochimica Acta, v. 40, p. 25-30.

McKinney, C. R., McCrea, J. M., Epstein, Samuel, Allen, H. A., and Urey, H. C., 1950, Improvements in mass spectrometers for the measurement of small differences in isotopic abundance ratios: Review of Scientific Instruments, p. 724-730.

Stevens, R. K., Mulik, J. D., O'Keefe, A. E., and Krost, K. J., 1971, Gas chromatography of reactive sulfur gases in air at the part-per-billion level: Analytical Chemistry, 43, p. 827-831.

PROPERTIES OF GASES AND WATERS OF DEEP ORIGIN NEAR MOUNT ST. HELENS

By I. BARNES, D. A. JOHNSTON, W. C. EVANS, T. S. PRESSER, R. H. MARINER, *and* L. D. WHITE

ABSTRACT

Fluids discharging from depth in the Mount St. Helens area include a metamorphic brine, as represented by Pigeon Springs water discharging from metavolcanic rocks to the west, CO_2 from the mantle as represented by the CO_2 well field at Klickitat, and CO_2 from the breakdown of organic matter as represented by the gases from springs north and south of Mount St. Helens and in a pond in the April 1980 crater.

INTRODUCTION

Carbon dioxide (CO_2) is a major gas component in some explosive eruptions (Johnston, 1980; Barnes and McCoy, 1979), in some hot springs (White and others, 1973; Mariner and others, 1975; Mariner and others, 1980), and in discharges from cold volcanic sources (Johnston, 1978, p. 78) and throughout the world in seismically active areas (Irwin and Barnes, 1980; Barnes and others, 1978).

As a guide to the interpretations of the $\delta^{13}C$ compositions referred to the well-known PDB standard, $\delta^{13}C$ values in the range $+3$ to -3 per mil are typical of marine carbonates (Craig, 1953) and values of -20 per mil and more depleted are typical of organic matter (Craig, 1953). Mantle-derived $\delta^{13}C$ lies in the range -5 to -8 per mil (Pineau and others, 1976; Moore and others, 1977). Meteoric water has isotopic compositions given by the equation (Craig, 1961)

$$\delta D = 8\delta^{18}O + 10$$

where δD and $\delta^{18}O$ are the deuterium and oxygen compositions in per mil relative to SMOW (standard mean ocean water).

Methods used for analyses of the waters are summarized by Presser and Barnes (1974). Gas samples were collected in evacuated glass sample tubes with high vacuum stopcocks and were analyzed with a gas chromatograph. Strontium carbonate samples were precipitated in the field and the CO_2 subsequently evolved by treatment with H_3PO_4. All bicarbonate titrations were done in the field except for the water sample from the pre-May 18 crater, which was titrated in the laboratory. Isotope analyses were made by L. D. White in the laboratory of J. R. O'Neil.

FIELD RELATIONS

Soda Spring, Mount St. Helens, and Government Mineral Springs lie on a line (fig. 130) that extends south-southeast to Mount Hood. Water was collected on April 23, 1980, from a pond 15 m in diameter that occupied the bottom of the summit crater of Mount St. Helens. Gas escaping through the pond raised the surface as much as 15 cm about 2 m from the shore of the pond, and there was a strong odor of hydrogen sulfide (H_2S) in the crater.

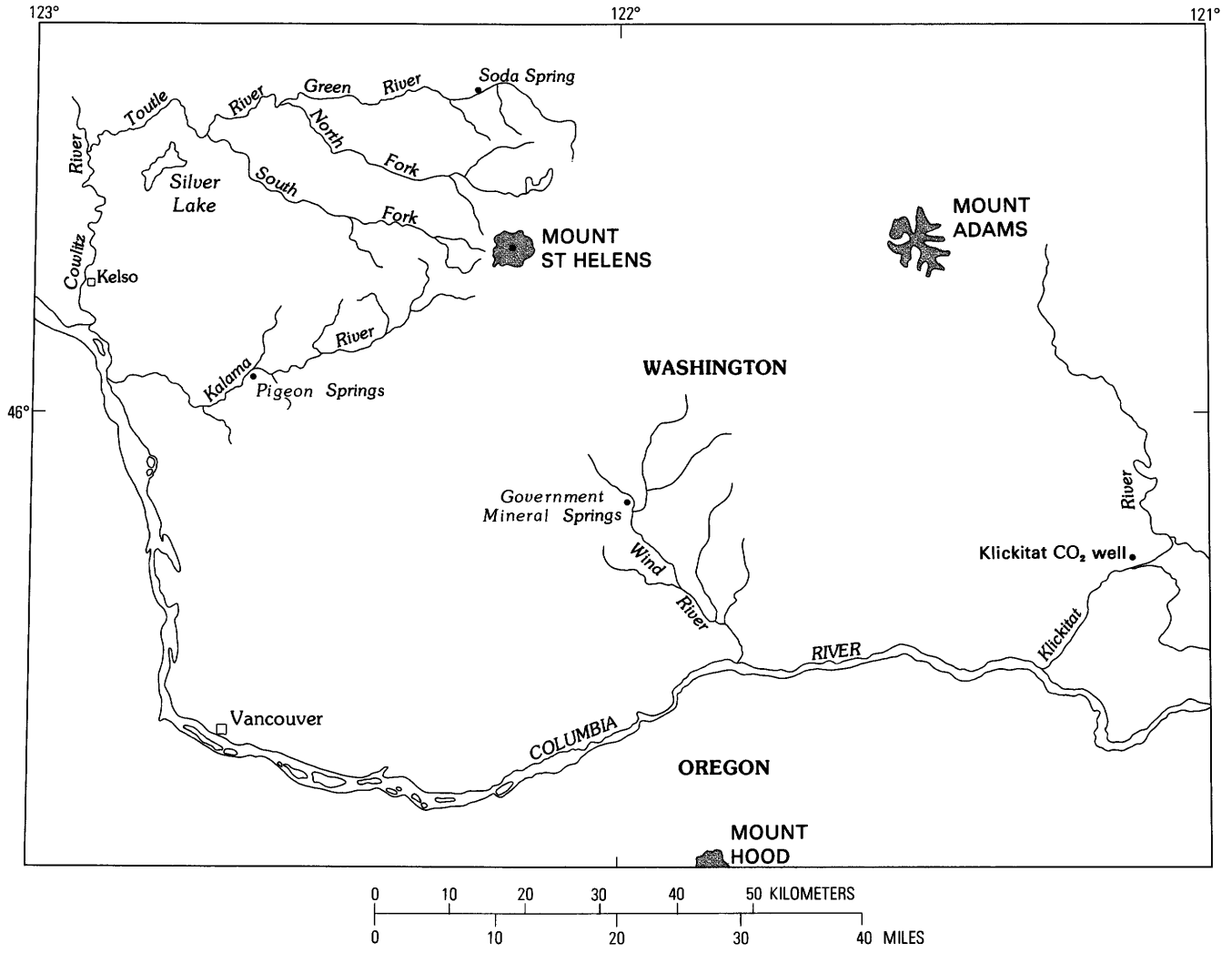

Figure 130.—Location of five deep-water sample sites, where water was collected for chemical and isotopic analyses and gases were collected for chemical analyses.

The sampled well at the Klickitat CO_2 field, east of Government Mineral Springs, discharges irregularly, erupting CO_2 and gas-laden water for 3 min at half-hour intervals. Pigeon Springs is to the west of Government Mineral Springs (fig. 130) and southwest of Mount St. Helens; the altered volcanic country rock consists of quartz, chlorite, calcite, and albite, as indicated by optical and X-ray study.

DISCUSSION

The isotopic compositions of the CO_2-rich waters at Government Mineral Springs, Soda Spring, the Klickitat CO_2 well, and water from the pond in the Mount St. Helens crater are all in the range of meteoric water (table 15; fig. 131). None of them show the shift in ^{18}O expected from water that has reacted with or exchanged isotopically with volcanic rocks (Craig, 1963). The water at Klickitat is relatively depleted in both ^{18}O and D, because it is farther from the ocean along the path of air masses yielding precipitation.

The isotopic compositions of the CO_2 being discharged show two sources. For the CO_2 at Klickitat, $\delta^{13}C$ is -5.38 to -6.10 per mil, a value characteristic of CO_2 from the mantle. The other CO_2 discharges are more depleted in ^{13}C, especially that from the crater pond (-19.53 per mil), probably due to decomposition of organic (woody) material incorporated in older subsurface volcanic rocks. From the pH and HCO_3^- values, the calculated CO_2 pressure that

Table 15.—Results of chemical and isotopic analyses of waters near Mount St. Helens, Wash.

[Chemical analyses by T. S. Presser, isotopic analyses by L. D. White (carbon, oxygen and deuterium) and Mark Heubner ($^{34}SO_4$). Concentrations in mg/L, isotopic compositions in per mil, D and 180 referred to SMOW, ^{13}C to PDB, and ^{34}S to CDM. Leaders (---), not determined]

Name	Klickitat CO_2 Well	Government Mineral Springs	Pond in Mount St. Helens crater	Soda Spring	Pigeon Springs
Location	NW1/4 sec. 24, T. 4 N., R. 13 E., Klickitat County	SW1/4 sec. 30, T. 5 N., R. 7 E., Skamania County	SE1/4 sec. 4, T. 8 N., R. 5 E., Skamania County	NE1/4 sec. 2, T. 10 N., R. 4 E., Cowlitz County	NE1/4, sec. 36, T. 7 N., R. 1 E., Cowlitz County
Sample No.	CQ29IB80	CQ30IB80	CQ79DJ80	CQ31IB80	CQ32IB80
T^0C	23	6	17	10	8
pH	5.89	5.97	5.97	6.58	8.34
Specific conductance (mmhos)	1.36	3.65	.47	7.0	47.6
H_2S	<1	<1	<1	<1	<1
NH_4 (N)	<.1	1.0	.35	6.3	2.9
Na	64.	420.	17.	1,350.	6,100.
K	10.	9.0	4.8	79.	6.9
Mg	100.	75.	15.	93.	5.5
Ca	120.	260.	41.	220.	7,100.
HCO_3	1,070.	1,230.	52.	2,715.	18.
SO_4	2.	120.	36.	2.	280.
Cl	4.2	550.	97.	1,250.	22,000.
F	.34	.12	.60	.42	<.5
SiO_2	140.	64.	37.	94.	9.2
B	<1.	15.	<1.	28.	3.0
U	<.0008	.0017	---	<.0008	<.0032
Hg	<.0001	<.0001	---	.0001	<.001
Al	.003	---	---	<.001	.001
$\delta^{18}O$	-15.90	-11.12	-12.57	-11.38	-4.29
δD	-111.4	-82.3	-89.8	-84.1	-43.4
$\delta^{13}CO_2$ gas	-5.38	-13.95	---	-13.10	---
$\delta C^{18}O_2$ gas	+27.44	+31.36	---	+31.79	---
$\delta^{13}C$ $SrCO_3$	-6.10	-14.35	-19.53	7.97	---
$\delta^{34}SO_4$	---	---	+9.5	---	---

would be in equilibrium with the dissolved CO_2 is 0.05 atm, more than two orders of magnitude higher than the CO_2 pressure in air.

In contrast to the CO_2-rich meteoric waters at the above locations, nitrogen-rich nonmeteoric water discharges from Pigeon Springs. Neither the ^{18}O nor the D concentrations at Pigeon Springs resemble those of local meteoric water, nor do the isotopic compositions plot on the meteoric water line (fig. 131). Pigeon Springs water resembles metamorphic waters of nonmeteoric origin (White and others, 1973). In contrast to the complex chemistry of most metamorphic waters, Pigeon Springs water also resembles seawater that has reacted with rocks to lose Na and gain Ca, and its Cl concentration (22,000 mg/L) is similar to that of modern seawater (19,000 mg/L Cl). The negative δD of Pigeon Springs water is at variance with this interpretation, however. All known silica-alumina hydrates are depleted in D relative to water they are in equilibrium with (Friedman and O'Neil, 1977, fig. 40), and if seawater of 0 per mil deuterium reacted to form chlorite, positive δD values would result.

Although the origin of the saline water of Pigeon Springs is unclear, its relations to the minerals of the altered volcanic rock are known. The reaction states of Pigeon Springs water with respect to possible coexisting minerals were calculated (table 17) by computer (Kharaka and Barnes, 1973). The calculated states are from the equation

$$\Delta G_R = RT \ln(Q/K)$$

where ΔG_R is the free-energy difference between the equilibrium state and the actual state, and

R is the gas constant,
T is the temperature (absolute),
Q is the reaction quotient, and
K is the equilibrium constant.

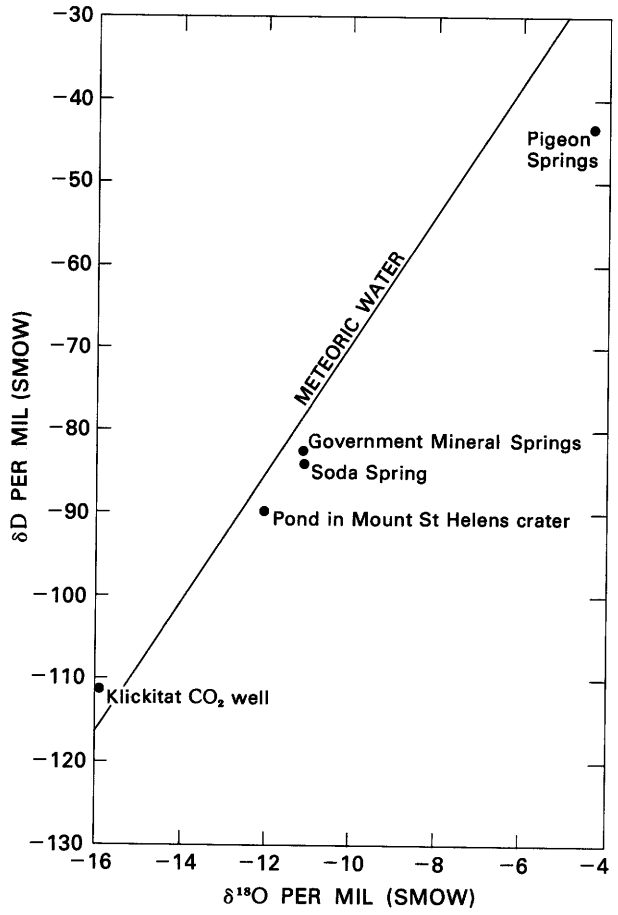

Figure 131.—Isotopic compositions of deep-origin water samples and their relation to meteoric water.

The states of reaction and the mineral composition of the altered volcanic rock at Pigeon Springs are compatible. The water is supersaturated with respect to the quartz, chlorite, albite, and calcite that constitute the altered volcanic rock and thus could be the metamorphic fluid existing when the present minerals of the rock formed. Although the water is supersaturated with respect to many clays, they cannot precipitate because the water is supersaturated with respect to the minerals now in the rock, and hence a free-energy barrier exists to clay-forming reactions. Thus, the minerals found and the water described can coexist indefinitely with no further reaction possible. If, however, the brine is removed and fresh (meteoric) water enters the rock, the calcite-low albite pair will be incompatible and will react to form laumontite (Barnes and others, 1978).

Table 16.—Chemical compositions of gases, in volume percent

Name-	Klickitat CO_2 Well	Government Mineral Springs	Soda Spring	Pigeon Springs
He----	<0.02	<0.02	<0.02	<0.02
H_2----	<.01	<.01	<.01	<.01
Ar----	.02	<.02	.02	.14
O_2----	.22	.03	.17	.55
N_2----	.83	.60	1.10	99.44
CH_4----	.11	<.002	.12	<.005
CO_2----	99.03	99.25	98.70	.06
C_2H_6---	<.01	<.01	<.01	<.05
Total-	100.10	99.88	100.11	100.19

REFERENCES

Barnes, Ivan, Downes, C. J., and Hulston, J. R., 1978, Warm Springs, South Island, New Zealand, and their potentials to yield laumontite: American Journal of Science, v. 278, p. 1412–1427.

Barnes, Ivan, Irwin, W. P., and White, D. E., 1978, Global distribution of carbon dioxide discharges and major zones of seismicity: U.S. Geological Survey Water Resources Investigations 78–39, 12 p.

Barnes, Ivan, and McCoy, G. A., 1979, Possible role of mantle derived CO_2 in causing two "phreatic" explosions in Alaska: Geology, v. 7, p. 434–435.

Craig, Harmon, 1953, The geochemistry of the stable carbon isotopes: Geochimica et Cosmochimica Acta, v. 3, p. 53–92.

_____1961, Isotopic variations in meteoric waters: Science, v. 133, p. 1702–1703.

_____1963, The isotopic geochemistry of water and carbon in geothermal areas, *in* Tongiorgi, E., ed., Nuclear Geology on Geothermal Areas: Pisa, Consiglio nazionale ricerche, 284 p.

Friedman, I., and O'Neil, J. R. 1977, Compilation of stable isotope fractionation factors of geochemical interest, *in* Data of geochemistry (6th edition): U.S. Geological Survey Professional Paper 440-KK, 12 p.

Irwin, W. P., and Barnes, Ivan, 1980, Tectonic relations of carbon dioxide discharges and earthquakes: Journal of Geophysical Research, v. 85, p. 3115–3121.

Johnston, D. A., 1978, Volatiles, magma mixing, and the mechanism of eruption of Augustine Volcano, Alaska: University of Washington, Ph. D. dissertation, 177 p.

_____1980, Volcanic contribution of chlorine to the stratosphere—More significant to ozone than previously estimated?: Science, v. 209, p. 491–493.

Kharaka, Y. K., and Barnes, Ivan, 1973, SOLMNEQ: Solution-mineral equilibrium calculations: U.S. Geological Survey Computer Contribution, 81 p.

Mariner, R. H., Presser, T. S., Rapp, J. B., and Willey, L. M., 1975, The minor and trace elements, gas, and isotope compositions of the principal thermal springs of Nevada and Oregon: U.S. Geological Survey Open-File Report, 27 p.

Table 17.—States of reaction of Pigeon Springs water with respect to selected minerals

[States are (+), super saturation; (-), unsaturation; and ΔG_R values are in kilocalories]

Mineral	ΔG_R	Q/K	Mineral	ΔG_R	Q/K
Adularia--------	0.96	$5.6x10^{0}$	Gypsum----------	-0.22	$6.7x10^{-1}$
Low albite------	1.32	$1.1x10^{1}$	Halloysite----------	-2.6	$8.8x10^{-3}$
High albite-----	-.20	$7.0x10^{-1}$	Illite----------	2.2	$5.7x10^{1}$
Analcime--------	-1.35	$8.9x10^{-2}$	Kaolinite----------	2.4	$6.8x10^{1}$
Andalusite------	.10	$1.2x10^{0}$	Kyanite----------	.0	$1.0x10^{0}$
Anhydrite-------	-.69	$2.9x10^{-1}$	Laumontite----------	6.6	$1.3x10^{5}$
Anorthite-------	-1.8	$3.8x10^{-2}$	Leucite----------	-6.0	$2.1x10^{-5}$
Aragonite-------	.96	$5.6x10^{0}$	Magnesite----------	-3.3	$2.9x10^{-3}$
Boehmite--------	-.69	$2.9x10^{-1}$	Microcline----------	.96	$5.6x10^{0}$
Brucite---------	-7.1	$3.1x10^{-6}$	Monticellite--------	-10.9	$3.6x10^{-9}$
Calcite---------	1.0	$6.0x10^{0}$	Ca montmorillonite--	3.2	$3.4x10^{2}$
Chalcedony------	.07	$1.1x10^{0}$	K montmorillonite---	2.3	$6.9x10^{1}$
Chlorite--------	13.3	$2.3x10^{1}$	Mg montmorillonite--	2.7	$1.2x10^{2}$
Chrysotile------	-6.0	$2.3x10^{-5}$	Na montmorillonite--	3.3	$3.7x10^{2}$
Clinoenstatite--	-4.5	$3.1x10^{-4}$	Muscovite----------	11.7	$1.3x10^{9}$
Corundum--------	-2.0	$2.6x10^{-2}$	Nepheline----------	-3.9	$1.0x10^{-3}$
Dickite---------	1.1	$7.2x10^{0}$	Quartz----------	.69	$3.4x10^{0}$
Diopside--------	-1.2	$1.1x10^{-1}$	Talc----------	2.5	$8.6x10^{1}$
Dolomite--------	-1.4	$7.6x10^{-2}$	Wairakite----------	-1.4	$7.3x10^{-2}$
Forsterite------	-13.2	$5.0x10^{-11}$	Wollastonite--------	-2.9	$5.4x10^{-3}$
Gibbsite--------	-1.4	$7.8x10^{-2}$			

Mariner, R. H., Swanson, J. R., Orris, G. J., Presser, T. S., and Evans, W. C., 1980, Chemical and isotopic data for water from thermal springs and wells of Oregon: U.S. Geological Survey Open-File Report, 13 p.

Moore, J. G., Bachelder, J. M., and Cunningham, C. G., 1977, CO_2-filled vesicles in mid-ocean basalt: Journal of Volcanology and Geothermal Research, v. 2, p. 309–327.

Pineau, P., Javoy, M., and Bottinga, Y., 1976, $^{13}C/^{12}C$ ratios of rocks and inclusions in popping rocks of the mid-Atlantic Ridge and their bearing on the problem of isotopic composition of deep seated carbon: Earth and Planetary Sciences Letters, v. 29, p. 413–421.

Presser, T. S., and Barnes, Ivan, 1974, Special techniques for determining chemical properties of geothermal water: U.S. Geological Survey Water Resources Investigations 22–74, 11 p.

White, D. E., Barnes, Ivan, and O'Neil, J. R., 1973, Thermal and mineral waters of non-meteoric origin, California Coast Ranges: Geological Society of America Bulletin, v. 84, p. 547–560.

FUMAROLE ENCRUSTATIONS: OCCURRENCE, MINERALOGY, AND CHEMISTRY

By TERRY E. C. KEITH, THOMAS J. CASADEVALL, *and* DAVID A. JOHNSTON

ABSTRACT

Fumaroles associated with the 1980 eruptive activity of Mount St. Helens occur (1) within the crater, where heat and fluids may be derived directly from magma and from crustal rocks in contact with the rising magma, and (2) as rootless fumaroles in the flowage deposits, where heat and fluids are derived locally from within the deposits. Much of the encrustation material was deposited at temperatures less than 250°C as noncrystalline yellowish films on ash particles and rock fragments and as encrustations around fumarole vents. Encrustations are mostly red, orange, yellow, and white. They begin to crystallize during cooling and dehydration immediately after deposition. Common mineral phases are sulfur, gypsum, halotrichite, and hematite. Less common phases are sal ammoniac, thenardite, glauberite, anhydrite, melanterite, alunite, and halite. Numerous unstable and poorly crystalline phases in process of dehydration and crystallization are under study. The major chemical components making up the fumarole deposits are Cl, F, H_2O, SO_4, Fe, Al, Ca, Na, K, and S.

INTRODUCTION

A fumarole is a vent that emits only gases and vapor. Encrustations are the colorful yellow, orange, red, and white deposits that generally surround fumaroles. Sublimate, a term often used for these encrustations, refers specifically to a solid phase deposited directly from a gaseous state without going through a liquid phase; the term is applicable to most encrustations, but not all.

Our study of fumaroles at Mount St. Helens focuses on the occurrence and distribution of different kinds of fumaroles and the chemistry and mineralogy of the encrustations. Reactions and products of hydrothermal alteration associated with the 1980 activity (Dethier and others, this volume) are not considered here.

ACKNOWLEDGMENTS

Field studies were by T. E. C. Keith and T. J. Casadevall, and by D. A. Johnston, who collected the first deposits from the summit crater on April 23 and analyzed the leachates. Identifications of mineral phases and chemical analyses were made by T. E. C. Keith, N. L. Nehring, T. S. Presser, D. P. Dethier, and D. R. Pevear.

METHODS

Temperatures of fumaroles were measured at the hottest accessible place in each vent. Gas and encrustation samples were collected simultaneously at several sites (see Casadevall and Greenland, this volume). The encrustation samples were sealed in plastic bags in the field until ready for laboratory

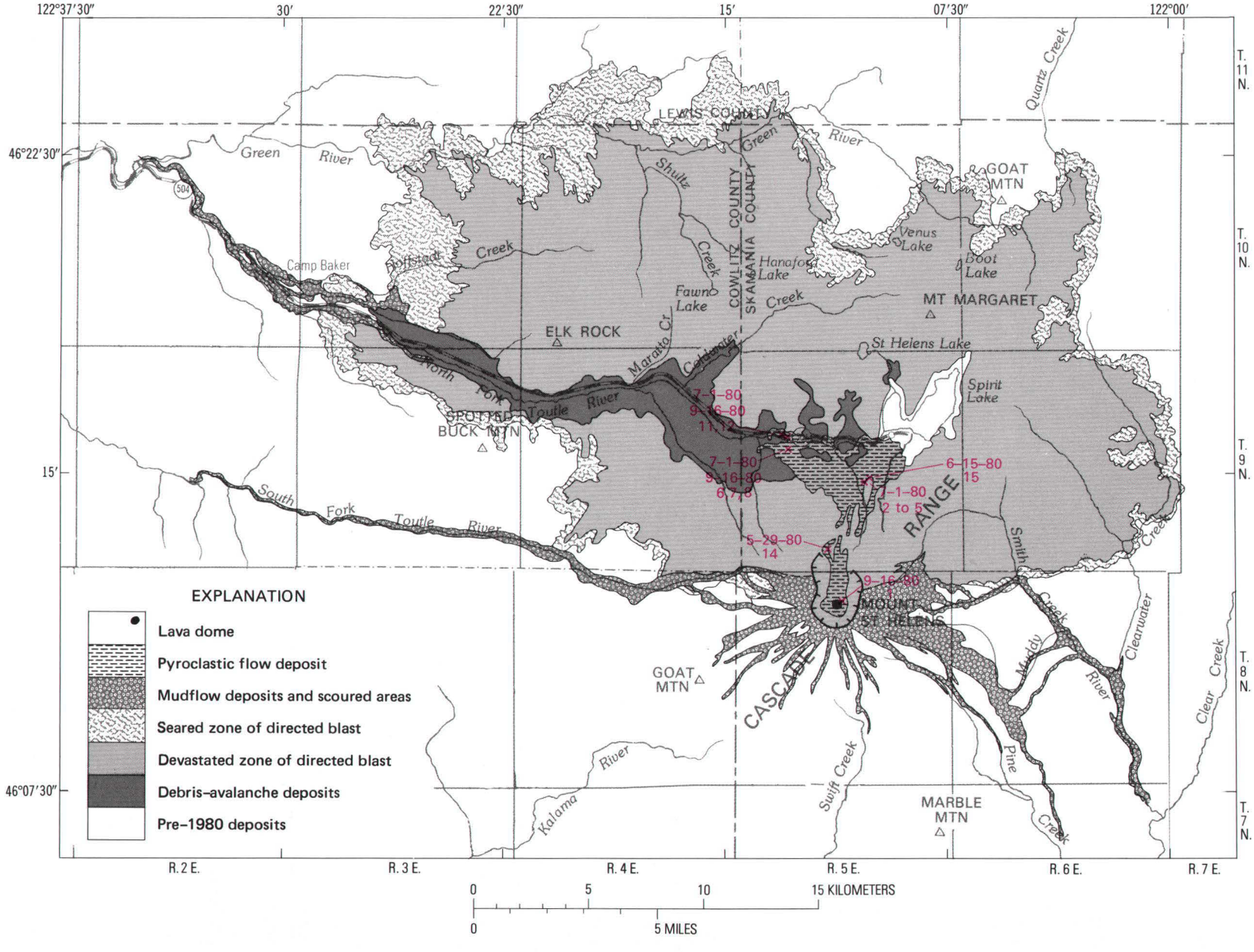

Figure 132.—Locations and numbers of sampled fumaroles. Sample numbers in this report consist of the date each sample was taken (month-day-year) followed by the fumarole number.

study by X-ray diffraction (XRD) and scanning electron microscope (SEM). An energy dispersive X-ray analyzing system (EDAX) was used on the SEM to determine qualitatively most of the chemical components (most cations, Cl, and S) of the encrustation phases. Some soluble phases may have dissolved in water which condensed in the plastic bags. The hydration states of aluminum chloride, aluminum sulfate (± iron), calcium sulfate, and iron chloride probably changed somewhat during study. The color of some encrustations has changed from pale green (ferrous iron), to yellow, to orange, and finally to pale brownish red, indicating that iron in these hydrated phases oxidized after collection. Not all crystalline phases have yet been identified; however, the common morphologies and mineral phases have been determined by SEM and XRD.

FUMAROLES AT MOUNT ST. HELENS

Fumaroles at Mount St. Helens occur (1) within the crater, (2) on flowage deposits of the May 18 eruption and on more recent pyroclastic deposits, and (3) on

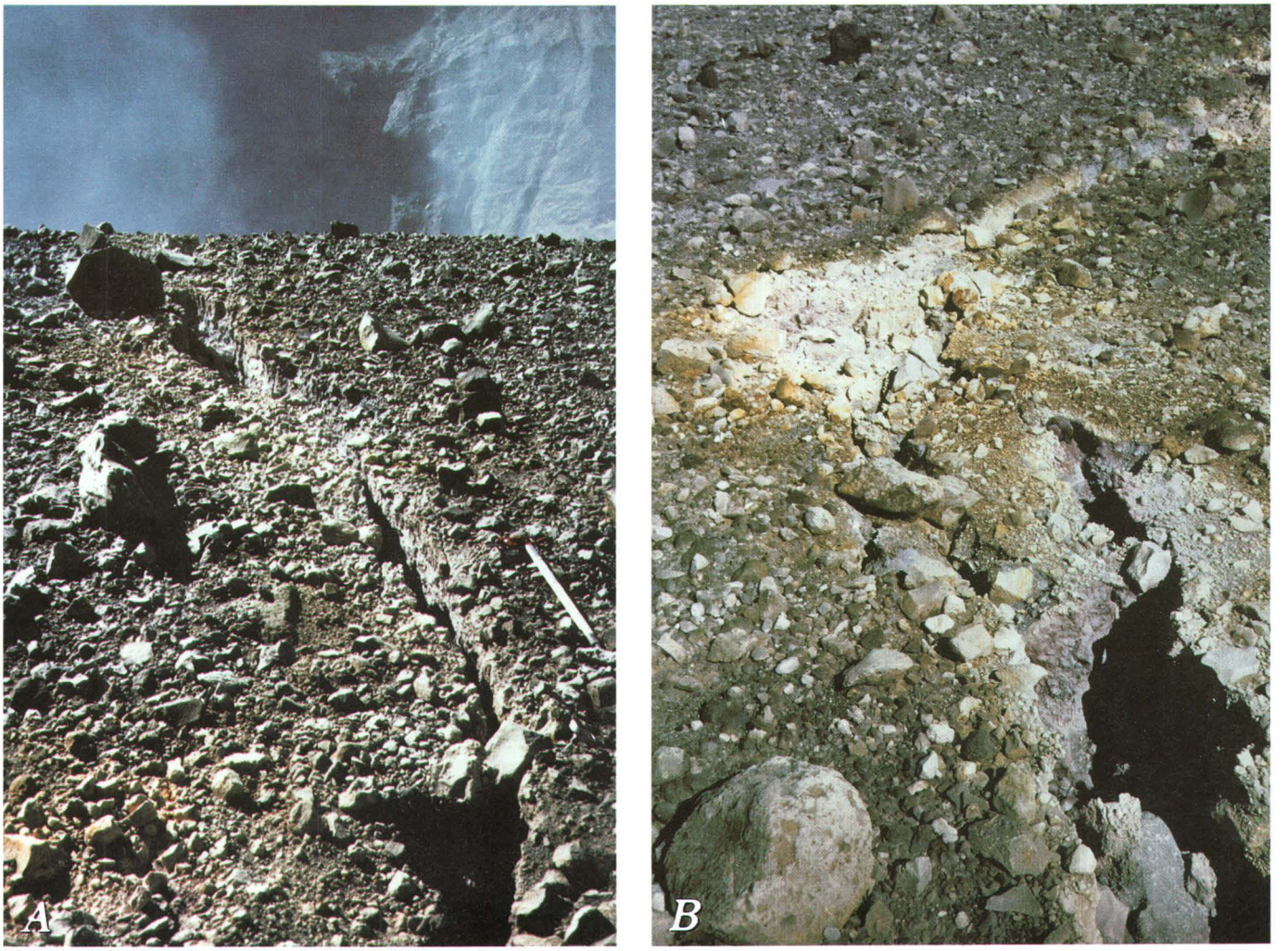

Figure 133.—Radial fracture in the tephra blanket in the crater on September 16, 1980; the rock in and adjacent to the fracture is light-pink oxidized dacite; the yellow encrustations form an outer zone beyond the oxidized dacite. Temperature measured at a depth of 1 m in the fracture was 200°C. A, South-southwest view of fracture toward center of crater. Ice axe at right is about 1 m long. B, Same fracture showing yellow encrustations outward from crack.

the May 18 blast deposit (fig. 132). The fumaroles within the crater may be connected directly with a magmatic source of gas and heat. Fumaroles on the flowage deposits and on the blast deposit are termed "rootless" because they are not connected directly to a magmatic source of heat or gas.

Prior to 1980, Mount St. Helens exhibited little thermal activity. Phillips (1941) reported weak fumarolic activity (T = 88°C) at The Boot, at 2,740 m elevation on the north flank. A second thermal area at approximately 2,740 m elevation on the southwestern flank of the volcano (T = 89°C) was reported by Friedman and Frank (1977). Both thermal areas were destroyed on May 18.

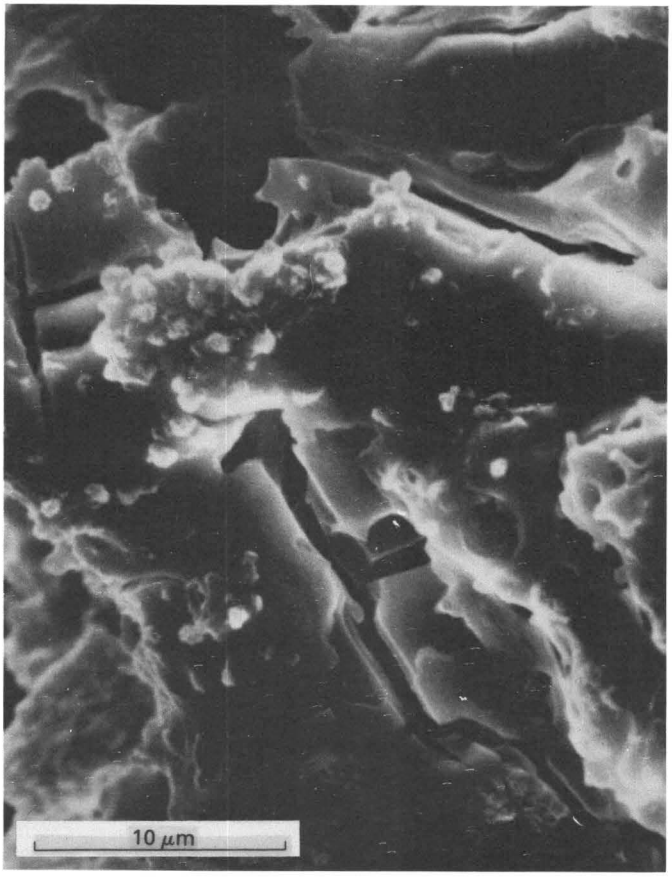

Figure 134.—SEM photograph of yellow noncrystalline encrustation material from the radial crack of the tephra blanket in the crater (sample MSH 9-16-80-1). The material consists of Al, Cl, Ca, Fe, S, and water. Dehydration cracks and incipient crystallization develop as cooling begins.

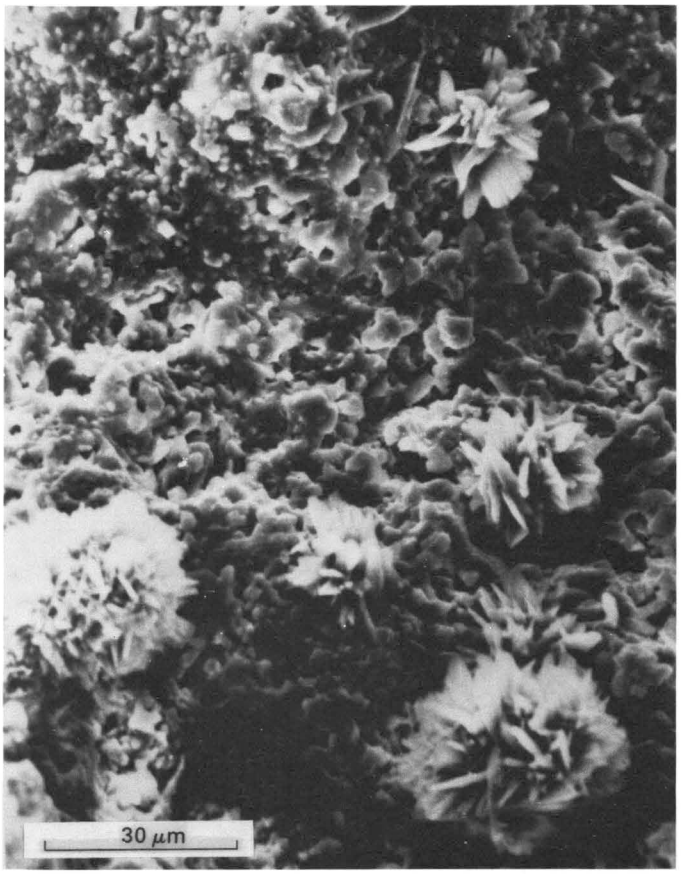

Figure 135.—SEM photograph of hemispheres of bladed crystals (S, Ca, Al, Fe hydrate) on poorly crystalline, partly dehydrated crust similar to that shown in figure 134, from encrustations along a radial crack in the tephra blanket in the crater (sample MSH 9-16-80-1).

FUMAROLES WITHIN THE CRATER

Within the crater, fumaroles occur (1) on the surface and at margins of successive dacite domes, (2) in cracks of the tephra blanket adjacent to the dome (fig. 133), and (3) along the intersection of the crater wall and the floor. Types 1 and 3 were not accessible during our sampling. Fumaroles of type 2 were studied on September 16 and 25 during visits into the crater.

The first dome, initially observed on June 15, was partially destroyed on July 22 (Moore and others, this volume). A second dome appeared in the crater following the eruption of August 7; a tephra blanket surrounded this dome and covered remnants of the June dome. Cracks in the tephra blanket, first observed on

September 8, radiated northeast, north, and northwest from the dome. The cracks were as much as 50 cm wide, and many opened appreciably between visits on September 16 and 25. Incandescent rock, probably of the June dome, was locally visible in the cracks, and temperatures in them ranged from less than 200° to 838°C. Gases responsible for the deposition of encrustations were also probably derived from the June dome.

In the hottest (northeast) fracture, the crack walls contained no encrustation coatings but had apparently been slightly oxidized to a reddish, friable rubble. Yellow encrustation material was abundant on the surface a few centimeters outward from the cracks (fig. 133). This material is noncrystalline and is composed of Al, Cl, Fe, Ca, S, and H_2O. Dehydration cracks developed (fig. 134), and blades of a crystalline material (Cl, Al, Fe, S, Ca, + water) began to form (fig. 135), finally resulting in a fuzzy bladed coating (fig. 136). Native sulfur was rarely observed as crystals on the ground surface adjacent to major cracks.

Deposition of a sublimate film from fumaroles within the crater began at temperatures below about 250°C. Rapid cooling of the almost colorless vapor produced a pale-yellowish-brown stain on crack walls. The stain did not obscure the textures of ash or rubble in the crack (fig. 133*A*). This stain material is soluble in water, has a high Cl^{-1} content (N. L. Nehring, written commun., 1980), and appreciable Fe^{+3}, F^{-1}, SO_4^{-2}, and Al (T. S. Presser, written commun., 1980).

Volcanic ash collected by David Johnston from the

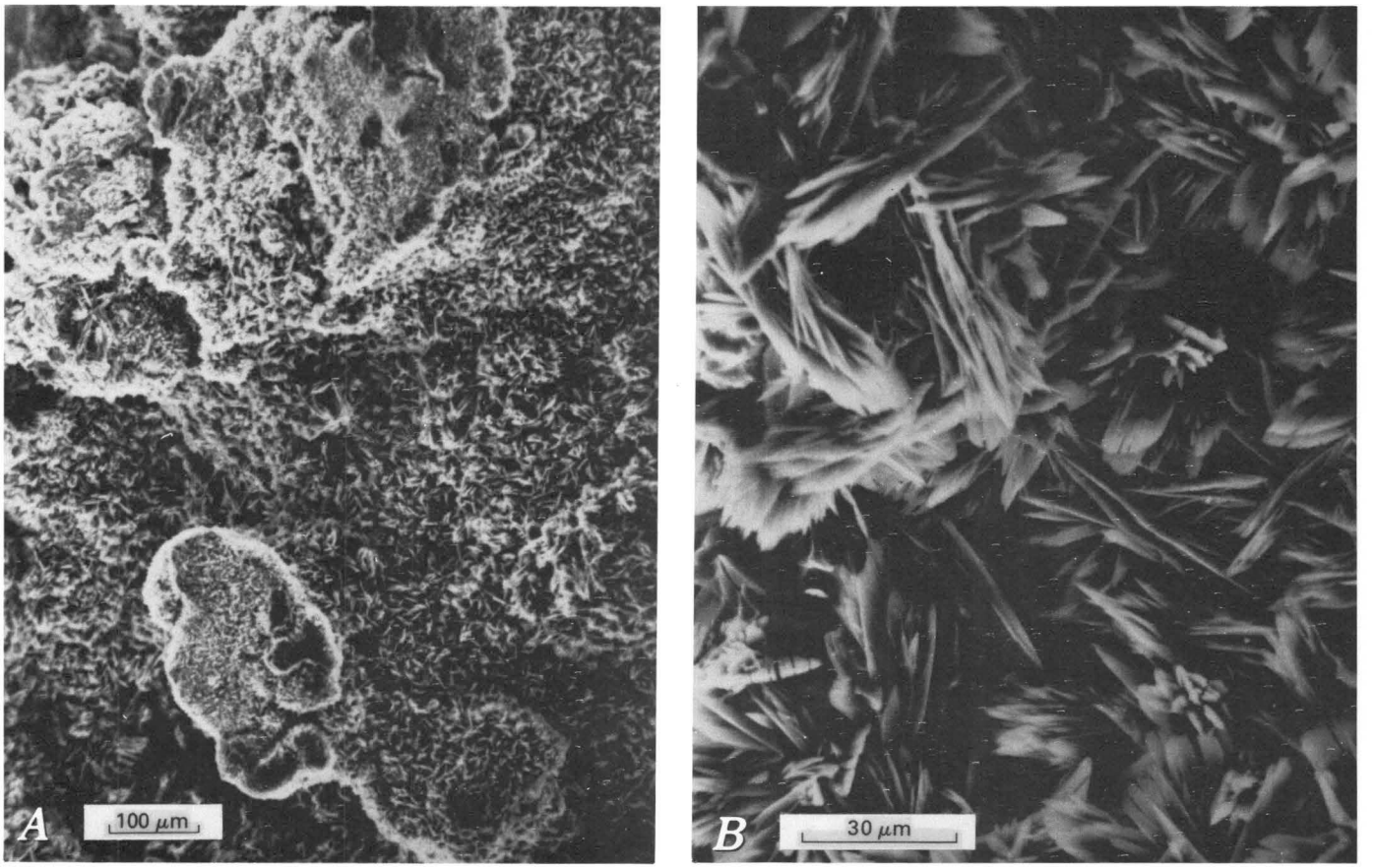

Figure 136.—SEM photographs of dark-yellow bladed crystals that make up the "fuzzy" botryoidal crust (Cl, Al, hydrate) along radial fractures in the crater. These crystals developed from the noncrystalline and poorly crystalline material shown in figures 134 and 135 (sample MSH 9-16-80-1F2). A, overall view showing botryoidal nature of blade groups; B, detail of one group showing well-developed blade texture.

summit crater on April 23, 1980, was coated with similar yellowish film. Field analysis of the leachate of this film material showed appreciable Cl^{-1} and SO_4^{-2}. SEM study showed only ash particles, but EDAX analyses of the particle surfaces showed high Fe and Cl content, which must have been in some material forming very thin coatings on the ash particles. Scarce gypsum crystals had formed on the surface of one rock associated with the yellow deposit.

ROOTLESS FUMAROLES

Locations of rootless fumaroles on the flowage deposits were controlled by features such as preeruption surface drainage, contrasting permeability of flowage deposits, and posteruption fractures produced by cooling or by settling of flowage deposits. Most rootless fumaroles that were active more than a few days were associated with pyroclastic flows that extended from north of the crater to Spirit Lake or with the debris-avalanche deposits in the North Fork Toutle River east of the mouth of Coldwater Creek (fig. 132).

Organic material (tree trunks, branches, and needles) is common in the flowage deposits of May 18. Where the deposits were hot, this material was distilled to varied products with sweet, turpentinelike odors. These distillates mostly escaped from individual small fumaroles or rows of fumaroles, and the ash overlying the organic material was discolored or coated by brownish-red material. When temperatures were high enough, the trees smoldered or burned. As temperatures decreased, fumaroles over buried trees became fertile places for growth of fungi, algae, and, eventually, new plants.

Figure 137.—Fumarole deposit of sulfur and gypsum on the June 12, 1980, pyroclastic flow (now covered by later pyroclastic flows). Temperature of the fumarole on July 1, 1980, was 97°C.

PYROCLASTIC FLOWS

Each pyroclastic flow had associated fumarolic activity. Temperatures were as high as ~850°C in these flows (Banks and Hoblitt, this volume), but fumarolic encrustations do not appear to have formed until the near-surface zone (less than 1-m depth) cooled to about 250°C or less. Of the pyroclastic flows examined (5/18, 5/25, 6/12, 7/22, 8/7), only the flow of June 12 contained solfataric fumaroles (fig. 137), distributed evenly over its surface at roughly 1- to 1.5-m spacing. These solfataras developed within a day of emplacement of the flow and persisted for several weeks before sulfur deposition declined. Gases from these fumaroles consist mostly of air and steam (Casadevall and Greenland, this volume).

Encrustations at fumaroles on pyroclastic flows are

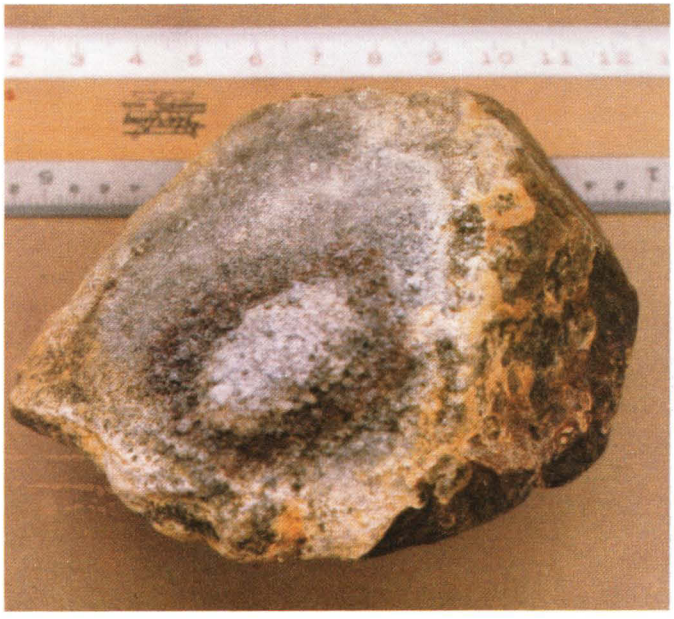

Figure 138.—Sample MSH 5-29-80-14 of dacite cobble from fumarole with temperature of 141° when sample was collected on debris avalanche. Dark-red iron hydroxide was deposited first at high temperature. Yellow encrustations, consisting mostly of calcium sulfate in various hydration stages, were deposited in the cooler zone away from the orifice. Scale at top is in centimeters. Table 18 gives trace-element analyses of this sample.

typically crusted with nearly white deposits, tinted with reddish iron oxides or hydroxides. Most contain an assemblage of gypsum and (or) anhydrite, iron oxide (hematite) or iron hydroxide, and native sulfur. Low-temperature fumaroles on the pyroclastic flows are yellow, as they are coated with native sulfur (fig. 137).

Iron leached from mafic material in dacitic ash is precipitated as an orange to red coating on the material through which the vapor passes. The red iron-rich coatings are deposited at high temperatures, usually during the initial stages of fumarolic activity (fig. 138). Metallic trace elements are also present in the dark-red coating from sample MSH 5-29-80-14 (T = 141°C; table 18). At high temperatures this reddish material is hematite; at lower temperatures it is amorphous iron hydroxide (fig. 139). Yellow encrustations (table 18) deposited over the dark-red material contain much lower concentrations of metallic trace elements, especially Ag, B, Ba, Cu, Zn, Zr, and Ga. Fumaroles 11 and 12, near the west edge of the May 18 pyroclastic flow, also exhibit this type of deposit. Anhydrite needles partly coated with anhedral blobs of alunite (probably natroalunite, fig. 140) form a later white deposit on iron oxide associated with fumarole 12 (now buried).

BLAST DEPOSIT

Rootless fumaroles in the blast deposit generally had temperatures below 150°C and were most common within a few kilometers of the crater, where the blast deposit is thickest. Feeble steaming at such fumaroles generally lasted only a few days to a few weeks, probably because the blast deposit was thin and cooled rapidly.

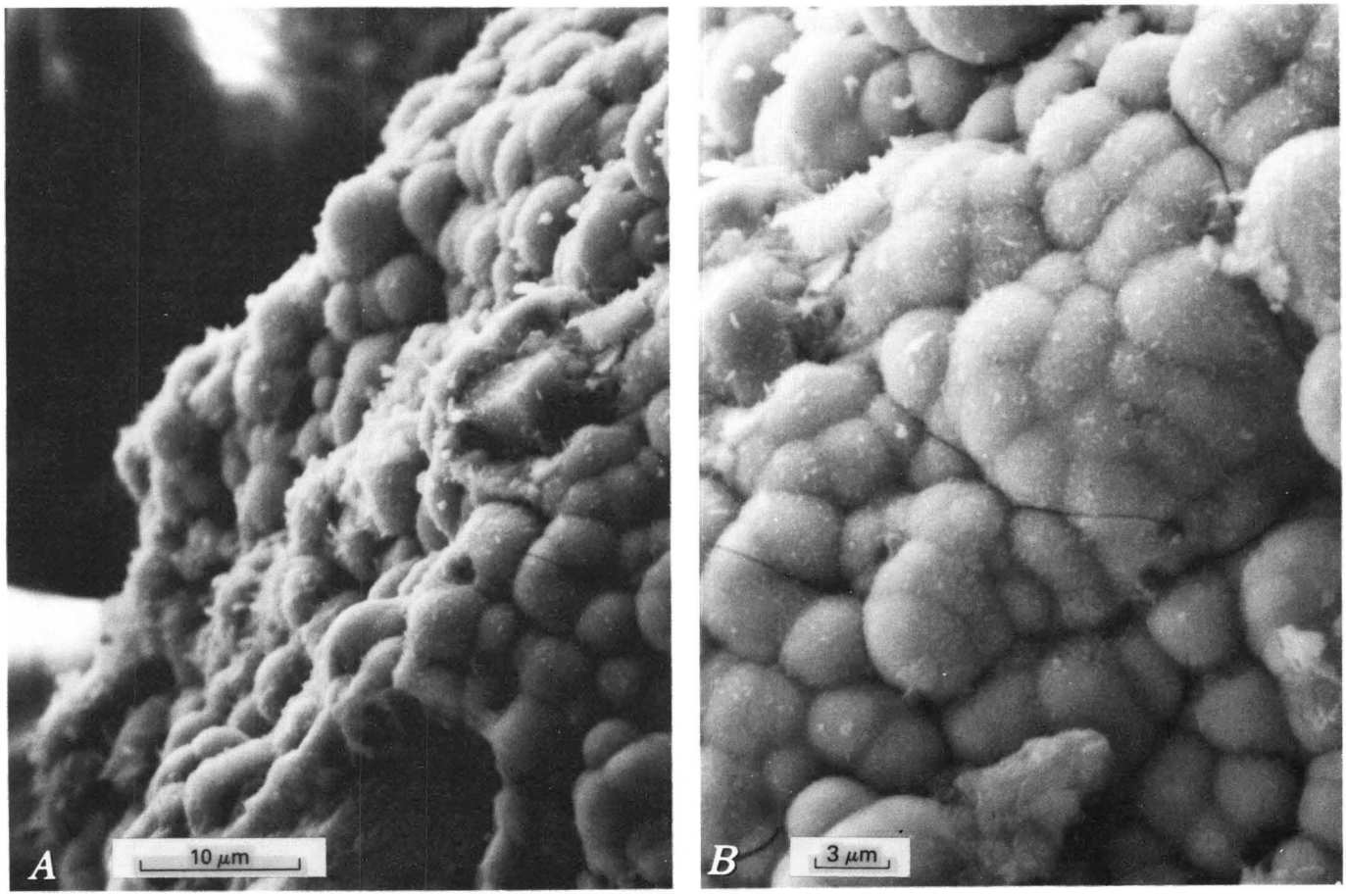

Figure 139.—SEM photographs of botryoidal iron hydroxide coating on ash particles (in this photograph a pyroxene grain). The thin, brick-red deposits on the dacitic pumice fragments of the pyroclastic flows consist largely of this material. Sample MSH 6-15-80-15C. A, iron hydroxide partly broken away from a pyroxene crystal; B, high magnification of same material to show texture.

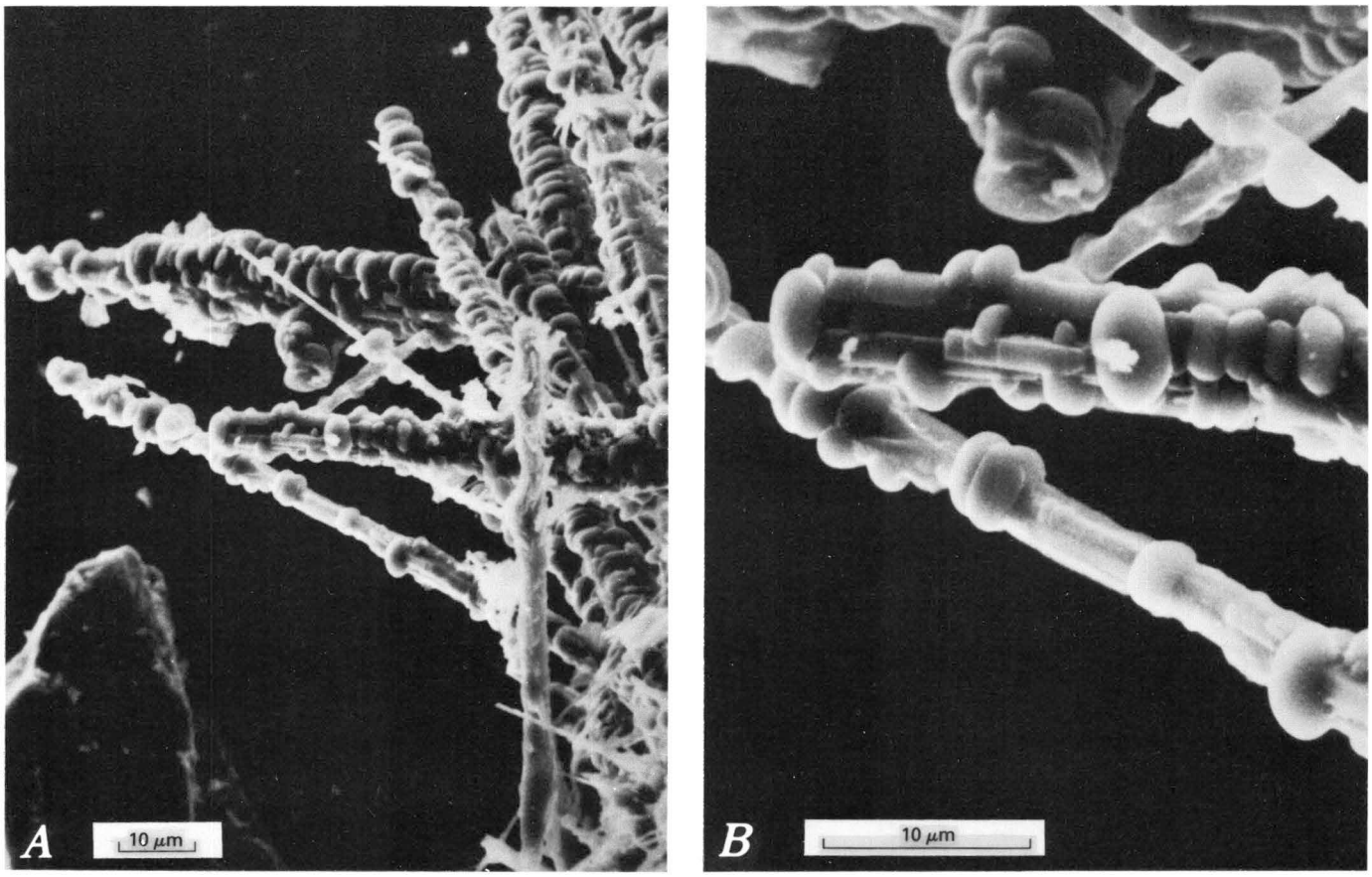

Figure 140.—SEM photographs of anhydrite needles with later deposits of alunite (identified by XRD). This material crystallized as wispy, white crystals on a thin, red hematite-iron hydroxide deposit around fumarole 12 in the pyroclastic flow (sample MSH 7-1-80-12D).

DEBRIS AVALANCHE

The debris avalanche is composed of material from the pre-May 18 edifice of Mount St. Helens mixed with sparse gray dacite from the 1980 cryptodome (Voight and others, this volume). These blocks of gray dacite showed little alteration or vesiculation, suggesting that they were not the major source of the volatiles responsible for the encrustations around the rootless fumaroles on the debris avalanche. Fumaroles on the debris avalanche had maximum measured temperatures of 125° to 150°C and cooled with time (fig. 141).

Fumarole 6, from the debris avalanche (fig. 141), was sampled on July 1, 1980, when the maximum temperature was 94°C. The encrustations consisted of an orange to yellow-orange deposit in the hottest area, grading outward to a greenish colloform deposit, surrounded by a zone of abundant white, gelatinous colloform material. A dark-gray outer zone resulted simply from water wetting the light-gray dacite ash. When the same fumarole was resampled on September 16, 1980, the maximum temperature was 69°C, and almost all orange and yellow color was gone (fig. 141*B*). The configuration of the fumarole was the same, however, and the encrustations consisted almost entirely of white colloform gypsum. The outer limit was still dark gray because of moisture. The yellow to orange material is mostly poorly crystalline and consists of S and Al with or without Cl, Fe, and Ca (fig. 142). As dehydration cracks develop in the material, hydrous calcium sulfate (containing much more water than gypsum) crystallizes (fig. 143). If dehydration continues, the

Table 18.—Semiquantitative spectrographic analysis of sample MSH 5-29-80-14, from fumarole in debris flow on northwest flank of Mount St. Helens

[Maximum measured temperature was 141°C. Figure 135 shows different colors of encrustations analyzed. Analyst: Chris Heropoulos]

Element	Yellow material	Red material
Data in weight percent		
Si	2	10
Al	.7	3
Na	1	1.5
K	.3	.5
P	.1	.3
Fe	3	5
Mg	.5	.5
Ca	3	3
Ti	.1	.15
Data in parts per million		
Mn	700	700
Ag	1	1.5
As	<2	2
B	50	200
Ba	30	100
Be	<.7	<.7
Bi	<.2	<.2
Cd	<.3	<.3
Co	7	10
Cr	15	15
Cu	50	200
La	150	100
Mo	<2	<2
Nb	<10	<10
Ni	10	7
Pb	<7	10
Pd	<1	<1
Pt	<5	<5
Sb	<1	<1
Sc	10	7
Sn	<2	<2
Sr	200	200
Te	<1	<1
U	<150	<150
V	150	200
W	<10	<10
Y	100	100
Zn	30	100
Zr	10	50
Ce	100	100
Ga	7	20
Ge	<7	<7
Hf	<50	<50
Ih	<1.5	<1.5
Li	<100	<100
Re	<7	<7
Ta	<50	<50
Th	<150	<150
Tl	<2	<1
Yb	7	7
Pr	<20	<20
Nd	<20	<20
Sm	<50	<50
Eu	<1	<1
Gd	<5	<5
Tb	<100	<100
Dy	<20	<20
Ho	<5	<5
Er	<30	<30
Tm	<2	<2
Lu	<15	<15
Hg	<1	<1
Se	<5	<5

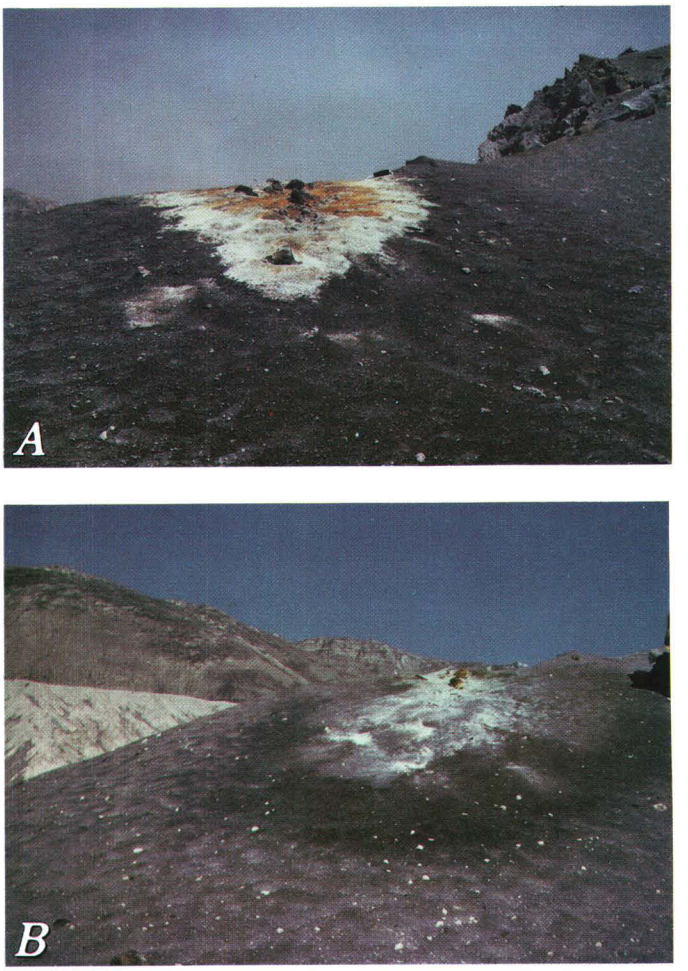

Figure 141.—Orange-yellow encrustations deposited from fumarole 6 in the debris flow. A, Appearance on July 1, 1980, was conspicuously zoned; temperature was 94°C. Yellow area was about 3 m across. B, By September 16 the yellow coloration had nearly disappeared, the temperature had cooled to 69°C, and the white encrustations had crystallized to gypsum.

stable product seems to be gypsum (fig. 144). Other phases that ultimately crystallize as the system cools are halotrichite (fig. 145) and hydrated aluminum sulfate. Native sulfur crystallizes on some deposits of this type as cooling continues, but little sulfur is present in fumarole deposits on the debris avalanche. The yellowish deposits consist largely of gypsum covered with a thin yellow coating, which seems to be noncrystalline and composed of iron and chloride with or without sulfate.

DISCUSSION

Fumaroles at Mount St. Helens apparently evolve in a predictable chemical and mineralogical pattern. For fumaroles with temperatures below about 250°C, most encrustations are white to yellowish orange and are first deposited as thin, noncrystalline deposits on rock fragments. Continued deposition results in a deposit of amorphous, often gelatinous material, typically colloform in appearance. With decreasing

temperature and time, these deposits begin to crystallize and dehydrate through a series of unstable phases. Some phases are water soluble and easily leached by rain or surface drainage. The most stable phases that remain are gypsum, anhydrite, sulfur, hematite, and iron hydroxides. All minerals identified from Mount St. Helens fumaroles to date (table 19) have been found previously as fumarole encrustations. (See Stoiber and Rose, 1974, for an excellent review.) The principal anions identified are Cl^{-1} and SO_4^{-2}, and the principal cations are Fe^{+2}, Fe^{+3}, Al^{+3}, Na^{+}, Ca^{+2}, and K^{+}; minor constituents are not yet known. Sulfur is the only element found in the native state. Nearly all phases are hydrous, but the extent of hydration is still under study.

Table 19.—Minerals identified from fumarole encrustations at Mount St. Helens

Mineral	Chemistry	Fumarole location[1]	Temp. (°C)	Analysts[2]
Sulfur-------	S----------	C,D,P----	<115	All.
Gypsum-------	$CaSO_4 \cdot 2H_2O$----------	C,D,B,P--	Variable	All.
Anhydrite----	$CaSO_4$----------	P--------	<117	TK.
Thenardite---	Na_2SO_4----------	P--------	82-100	DP,DD.
Melanterite--	$FeSO_4 \cdot 7H_2O$----------	P--------	≤260	DP,DD.
Glauberite---	$Na_2Ca(SO_4)_2$---------	P--------	<260	DP,DD.
Natroalunite	$(Na,K)Al_3(SO_4)_2(OH)_6$	P--------	<117	TK,DP,DD.
Hematite-----	Fe_2O_3----------	D,P------	193, ≤260	TK,DP,DD.
Fe hydroxides	----------	D,B------	Variable	TC,TK.
Halotrichite	$FeAl_2(SO_4)_4 \cdot 22H_2O$---	B--------	141	TK.
Unnamed (ASTM 23-128)	$CaSO_4 \cdot 15H_2O$---------	B--------	141	TK.
Halite-------	NaCl----------	P--------	≤260	DP,DD.
Sal ammoniac	NH_4Cl----------	P--------	96, 178	TK.

[1] C, crater; D, debris flow; B, blast deposit; P, pyroclastic flows.

[2] TK = Terry Keith; TC = Tom Casadevall; DD = David Dethier; DP = David Pevear.

Figure 142.—SEM photograph of botryoidal, noncrystalline hydrate of S, Al, Cl, and Fe showing concentric dehydration cracks (sample MSH 7-1-80-8B). This material forms abundant yellow encrustations around fumaroles in the debris avalanche.

Most encrustations are deposited from fumaroles with temperatures below 250°C. In general, fumaroles on the debris avalanche were initially cooler (less than 100°C) than those on the pyroclastic flows and in the crater. This difference in temperature is reflected in the mineralogy of the encrustations: those from the pyroclastic flows tend to have hematite; native sulfur and gypsum occur in both types of fumaroles; the higher temperature encrustations typically contain abundant chlorides and sulfates of Ca, Fe, and Al; and the hottest fumaroles adjacent to the dome entirely lack encrustations. These data support the observations of Stoiber and Rose (1974, p. 513), who found that encrustations deposited at high temperatures are generally less abundant than those deposited at lower temperatures.

Most fumarolic encrustations at Mount St. Helens are yellow to orangish yellow. Commonly, these are described by field observers as sulfur, but the color is generally due to hydrated chlorides and sulfates of Fe and Al. Only rarely did sulfur occur with a mineral other than gypsum. For example, fumarole 7, in the debris avalanche, had cooled to the point where it no longer deposited chloride-bearing minerals, and

sulfur was apparently deposited over the earlier chloride assemblage. In the hotter fumaroles in the crater area and on the pyroclastic flows, encrustations are commonly buff to white with patches of iron-rich reddish-brown material.

Studies of burning refuse piles at coal mines demonstrate that mineral assemblages reminiscent of volcanic sublimates can be produced by heating fine-grained sedimentary rocks (Dunrud and Osterwald, 1980; Finkleman, 1978). Many elements (alkaline earths, halides, sulfur, metals) are easily leached from fine-grained sediments and volcanic rocks by hydrothermal solutions with neutral or slightly acidic pH (Ellis and Mahon, 1967). Thus, many requisite components of fumarolic encrustations on the debris-avalanche deposits may be derived by heating the older rock of Mount St. Helens in a water-rich environment. Much rock was already heated and partly altered in the pre-May 18 hydrothermal system, and water from streams, marshes, and lakes could become an effective hydrothermal fluid capable of leaching cations and anions from rocks of the debris avalanche. Fumarolic encrustations could form following cooling of this fluid upon reaching the ground surface.

White and Waring (1963) pointed out the problems of determining which components of fumarolic encrustations were precipitated from vapor and which were derived from acid attack on surrounding rock particles. Our studies are continuing on this problem.

Figure 143.—SEM photograph of a bladed crystal of hydrous calcium sulfate containing minor amounts of Fe and Al forming from botryoidal yellow noncrystalline material shown in figure 142 (sample MSH 7-1-80-6B).

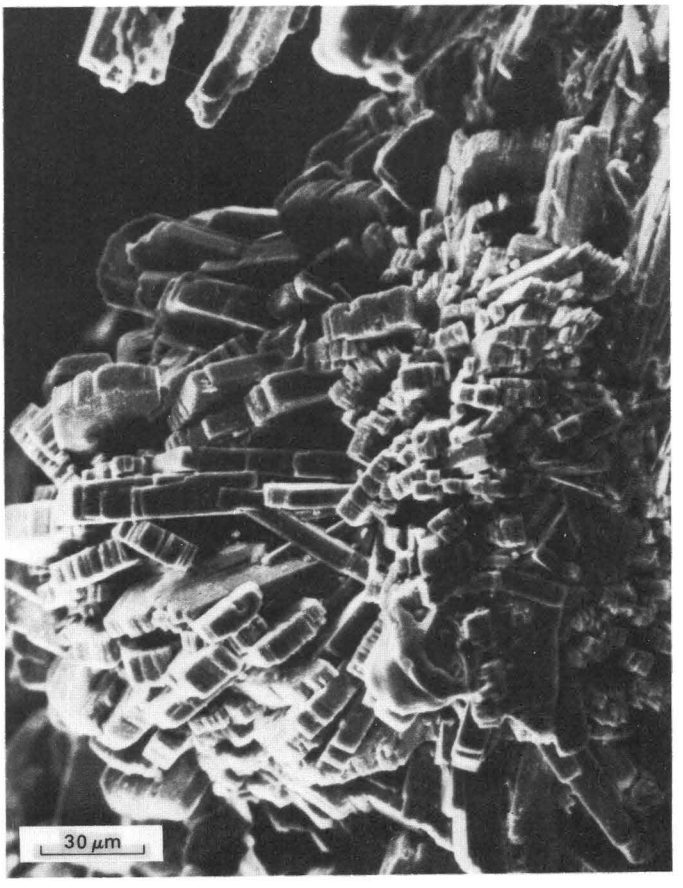

Figure 144.—SEM photograph of a group of gypsum crystals (sample MSH 7-1-80-8B). Clear to pale-yellow crystal groups of this type form on the darker yellow material shown in figure 142.

REFERENCES CITED

Dunrud, C. R., and Osterwald, F. W., 1980, Effects of coal mining subsidence in the Sheridan, Wyoming, area: U.S. Geological Survey Professional Paper 1164, 49 p.

Ellis, A. J., and Mahon, W. A. J., 1967, Natural hydrothermal systems and experimental hot water/rock interactions: Geochimica et Cosmochimica Acta, v. 28, p. 1323–1357.

Finkleman, R. B., 1978, Release of trace elements from a burning bituminous culm bank: U.S. Geological Survey Open-File Report 78–864, 37 p.

Friedman, J. D., and Frank, David, 1977, Thermal surveillance of active volcanoes using the Landsat-1 data collection system, Part 3, Heat discharge from Mount St. Helens, Washington: U.S. Geological Survey Open-File Report 77–541, 30 p.

Phillips, K. N., 1941, Fumaroles of Mount St. Helens and Mount Adams: Mazama, v. 23, no. 12, p. 37–42.

Stoiber, R. E., and Rose, W. I., Jr., 1974, Fumarole incrustations at active Central American volcanoes: Geochimica et Cosmochimica Acta, v. 38, p. 495–516.

White, D. E., and Waring, G. A., 1963, Volcanic emanations, *in* Data of geochemistry (6th ed.): U.S. Geological Survey Professional Paper 440–K, p. K1–K27.

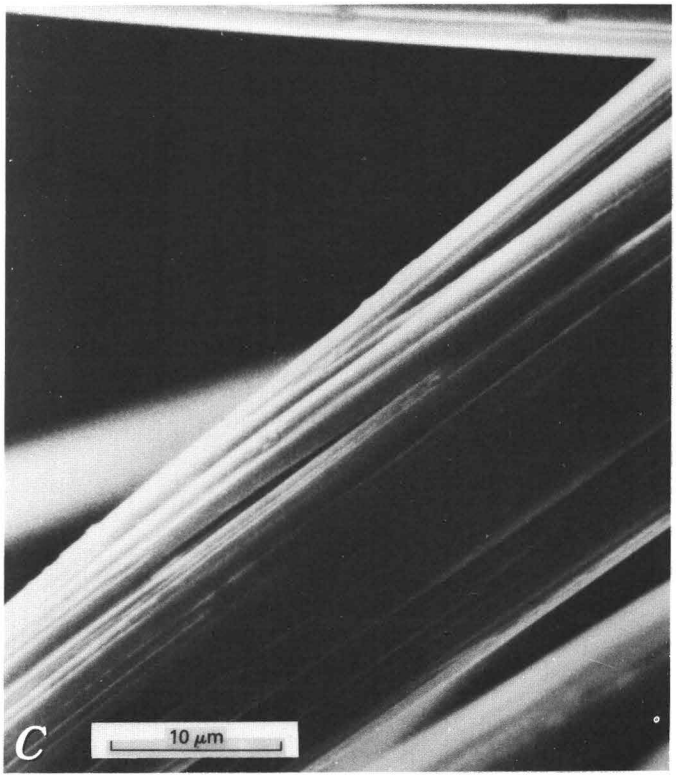

Figure 145.—SEM photographs of clear, fibrous bundles of halotrichite ($FeAl_2(SO_4)_4 \cdot 22H_2O$) crystals, which crystallize on white colloform hydrous calcium sulfate encrustations (sample MSH 7-1-80-6A). A, radiating crystal groups and some bent crystals; B, more detail of needles showing fresh, unleached appearance. C, Greater magnification shows that needles actually consist of fibrous bundles.

USE OF ASH LEACHATES TO MONITOR GAS EMISSIONS

By NANCY L. NEHRING *and* DAVID A. JOHNSTON

ABSTRACT

The S:Cl ratio of volcanic gases at Mount St. Helens was monitored, beginning on March 28, by leaching ash samples in water and analyzing the leachate for SO_4 and Cl. The ratio gradually increased from March 28 to May 18; leachate samples from ash of the major eruptions after May 18 yielded erratic results. The major components of the leached material were $CaSO_4$ and NaCl, probably produced by rapid reaction between acid volcanic gas and ash; leachable trace elements were probably derived from both the gas and the ash.

INTRODUCTION

A promising technique for monitoring volcanic activity is measurement of changes in gas composition. A 30-fold increase in S:Cl ratios preceded a major eruption at Mount Asama, Japan, by 2–3 weeks (Noguchi and Kamiya, 1963). Fuego Volcano, Guatemala, has shown as much as a five-fold increase in S:Cl before major eruptions, the magnitude of change in S:Cl correlating with eruption size (Rose, 1977). At Kilauea Volcano, Hawaii, Cl:F ratios and He and H_2 concentrations have changed prior to eruptions (Naughton, Finlayson, and Lewis, 1975; Naughton, Lewis, Thomas, and Finlayson, 1975; M. Sato, oral commun., 1980). Increases in H_2 content have also been correlated with eruptions at Hekla, Iceland (M. Sato, oral commun., 1980).

Frequent eruptions of ash and the danger of ice and rock avalanches prevented direct sampling of gas vents inside the crater at Mount St. Helens from the onset of activity on March 27 through May 18. Placement of remote sensing equipment, such as that used by Noguchi and Kamiya (1963) or the H_2 sensor of Sato (Sato and McGee, this volume), would not have been effective on the crater rim because of variable winds and rapid enlargement of the crater. Moreover, ash eruptions would have destroyed equipment placed in or near the crater. Sampling of gases was thus limited to the eruption plumes, where gases are highly diluted by air, and to ash, which scavenges some of the more reactive gases. Because the plumes were small during eruptions prior to May 18, a gas-monitoring program was established based on leaching of ash for scavenged gases.

Magmatic gases that are unstable in the atmosphere (such as SO_2, H_2S, and HCl) will react to form stable compounds. Of the magmatic sulfur gases, SO_2 is especially unstable; it rapidly forms an aerosol of liquid H_2SO_4 droplets (half time of approximately 4 min (Dana and others, 1975)). Such H_2SO_4 droplets have been observed in volcanic gas plumes (Cradle and others, 1971). H_2SO_4, a very efficient desiccant, absorbs water vapor and other acid components from the plume. The aerosol becomes adsorbed on ash particles, and the acids form salt crusts by leaching ions from the ash (Taylor and Stoiber, 1973; Rose, 1977). Scanning electron micrographs show salt encrustations on fresh ash (Rose and others, 1973).

METHODS AND RESULTS

Ash samples were leached with distilled water and the leachate was analyzed for Cl (chloride), F, SO_4, and pH (table 20). Because it was not known how long before a major eruption the Cl:S ratios might increase, and because large changes were expected, SO_4 and Cl were analyzed in the field to obtain rapid results. Therefore, fast portable methods were chosen.

Usually, 20 g of ash was stirred with 50 mL of triply distilled water for 1 hr. Less than 20 g of ash was available for some March and April 1980 eruptions, so ash and water concentrations were adjusted. The ash was allowed to settle briefly and the pH measured to ±0.1 pH unit using a portable meter. The sample was filtered with Whatman 50 paper, then with 5 micron cellulose acetate paper if the filtrate was still cloudy. The sample was analyzed for SO_4 by the turbidometric method. The Spectrokit Reagent System for SO_4 and Spectronic Mini 20 spectrophotometer were used. The mercurimetric method was used for Cl determination (Brown and others, 1970). Fluoride values were determined using a specific ion electrode.

Table 20.—Analyses of SO_4, Cl, F, and pH, Mount St. Helens ash, March 28 to August 7, 1980

[Analyses by N. Nehring, D. Johnston, and H. Glicken; n.d., no data]

Sample No.	Date erupted	Date collected	Collector	Locality; description	Weight ash (g)	Water used (mL)	pH	Cl (mg/L)	F (mg/L)	SO_4 (mg/L)	S:Cl (molar)
DSH2	March 28	March 29	R. B. Waitt	NE1/4SE1/4 sec. 35, T. 8 N., R. 6 E.; from leaves.	14.46	70	5.7	10	1.1	5	0.18
DSH4	March 30	March 31	--do	NW1/4SW1/4 sec. 29, T. 7 N., R. 6 E.; Swift Reservoir from leaves; washed with acetone before received.	10.30	50	5.4	10	2.1	5	.18
DSH13	April 4	April 4	--do	NE1/4NW1/4 sec. 13, T. 9 N., R. 4 E.; on Highway 504, air fall.	4.82	30	6.5	60	1	48	.30
SH9	April 11	April 11	R. Moore	NE1/4NW1/4 sec. 9, T. 8 N., R. 5 E.; Summit.	19.08	50	4.4	330	2.5	180	.20
Station 10	April 16	April 16	A. M. Sarna-Wojcicki	NE1/4NW1/4 sec. 9, T. 8 N., R. 5 E.; Summit.	20.85	50	5.0	100	1.8	115	.42
42380-2	April 23	April 23	D. A. Johnston	SE1/4 sec. 4, T. 8 N., R. 5 E.; west side summit, wet.	19.90	50	5.4	15	.9	20	.49
43080-4	April 30	April 30	--do	Crater rim	20	50	3.9	115	n.d.	230	.74
RBW80-40	May 18	May 19	R. B. Waitt	Sec. 18, T. 12 N., R. 3 E.; Mossyrock; burnt wood smell.	19.52	50	6.7	330	1.2	700	.78
RBW80-41	May 18	May 19	--do	Sec. 2, T. 12 N., R. 4 E.; Morton; burnt wood smell.	19.48	50	6.3	335	1.4	1000	1.10
RBW80-42	May 18	May 19	--do	Sec. 8, T. 12 N., R. 7 E.; Randle; burnt wood smell.	19.49	50	6.5	340	1.3	860	.93
RBW80-43	May 18	May 19	--do	Sec. 15, T. 12 N., R. 8 E.; burnt wood smell.	19.50	50	6.6	310	1.4	800	.95
RBW80-45	May 18	May 19	--do	Sec. 23, T. 12 N., R. 5 E.; 1 mi northeast of Davison Lake, burnt wood smell.	19.48	50	6.5	375	1.2	600	.59
Wood 1	May 18	May 20	S. Wood	Moscow, Idaho, Federal Building	18.42	50	5.6	150	2.2	300	.74
Mt. Adams	May 18	May 18	R. L. Christiansen	Mt. Adams, burnt wood smell	21.81	50	5.6	230	1.3	800	1.28
DZ220.20	May 18	May 20	D. Dzurisin	20 mi north of Yakima, oven dried	20.20	50	n.d.	115	n.d.	240	.77
518	May 18	May 18	T. Newcombe	Near Starbuck, Wash.	17.21	50	6.1	170	n.d.	410	.89
RBW80-77A	May 18	May 23	R. B. Waitt	Sec. 30, T. 11 N., R. 8 E.; Road 123 and Smooth Rock Creek, wet.	20.41	50	7.2	255	1.5	960	1.39
RBW80-77B	May 18	May 23	--do	Sec. 30, T. 11 N., R. 8 E.; Road 123 and Smooth Rock Creek, damp pumice.	17.70	50	7.2	6	1.2	20	1.23
RBW80-77C	May 18	May 23	--do	Sec. 30, T. 11 N., R. 8 E.; Road 123 and Smooth Rock Creek, damp.	18.16	50	7.7	8	1.2	10	.46
RBW80-77D	May 18	May 23	--do	Sec. 30, T. 11 N., R. 8 E.; Road 123 and Smooth Rock Creek, wet.	18.26	50	8.2	10	1	18	.66
RBW80-132D	May 25	May 30	--do	Sec. 9, T. 9 N., R. 5 E.; 2 mi west of Spirit Lake, damp pumice ground to 1/8 in. in lab.	17.94	50	7.5	12	n.d.	10	.31
525	May 25	May 25	T. J. Casadevall	Vancouver, Wash	11.15	25	5.8	120	n.d.	125	.38
RBW80-165	June 12	June 12	R. B. Waitt	--do	21.22	50	4.2	275	n.d.	100	.13
612	June 12	June 12	T. J. Casadevall	--do	8.32	25	4.7	140	n.d.	48	.13
615	June 12	June 15	--do	3600 ft, warm	20	50	6.1	25	n.d.	60	.89
620	June 12	June 12	--do	3960 ft, warm	20.14	50	7.5	5	n.d.	16	1.18
MPD12	July 22	August 8	M. Doukas	Toppenish	21.56	50	5.5	25	n.d.	100	1.48
MPD2C	August 7	August 8	--do	Mossyrock	21.03	50	5.0	65	n.d.	40	.23

Table 21.—Elemental composition of selected ash leachates

[The following elements were not detected above the detection limits reported in parentheses (ng/g): Zr (10), Be (1), Rb (15), As (100), Se (25), Bi (5), Cd (0.5), Sb (100), Co (2.5), Cr (1), Pb (20). Cation analyses by J. Buchard and D. Vivit]

Sample No.--	DSH2	St 10	42380-2	RBW80-42	RBW80-45
			µg/g ash		
SO_4	2.4	27	5.0	220	150
Cl	4.9	24	3.8	87	96
F	.53	.43	.23	.33	.31
Si	6.3	.74	1.6	1.4	1.2
Na	2.5	9.4	3.8	51	54
K	1.0	2.6	1.3	8.7	9.0
Ca	2.3	10	1.4	74	75
Mg	.73	3.4	.48	9.0	9.5
			ng/g ash		
Li	50	25	25	97	160
B	19	50	38	190	210
Hg	1.0	.5	.5	8.7	1.7
Mn	17	230	30	1400	1500
Al	870	110	14	2.5	4.4
Cu	7.3	20	1.8	1.7	2.0
Zn	29	16	8.8	4.4	6.2
Sr	9.7	60	700	460	360
Ti	47	3.0	3.0	22	23
Fe	777	10	10	10	10
Ba	12	19	220	41	51
Ni	2.0	2.9	1.8	3.6	4.1
Mo	1.5	1.0	1.0	1.2	3.6
V	2.5	1.5	1.5	4.1	3.1
Tl	2.0	1.0	1.0	12	6.9

Fluoride showed essentially no variation from March through June, and so analysis for fluoride was eventually discontinued.

A few samples were also analyzed for cations using a Spectrospan III A DC argon plasma spectrophotometer (table 21). The values are tentative because a rigorous determination of cross interferences has not been completed.

DISCUSSION

CHANGES IN SULFUR AND CHLORIDE

The S:Cl ratio increased steadily during the numerous small ash eruptions from March 28 to May 18 (fig. 146). From May 18 on, only ash from the major eruptions (May 18, May 25, June 12, July 22, and August 7) was analyzed. These later samples showed no consistent pattern. This contrasts with data for Fuego Volcano, Guatemala, where S:Cl ratios correlate with intensity of eruption (Rose, 1977).

Amounts of leachable SO_4 and Cl on the ash varied greatly even for products of a single eruption, although sulfate concentrations remained approximately 2 times that of chloride, prior to May 18 (also noted by Rose (1977) for Fuego Volcano). Variation of S:Cl was greater after May 18, as shown by the May 18 and June 12 samples. Samples of the ash erupted on June 12, collected in Vancouver, Wash. (S:Cl = 0.13), are distinctly different from samples collected on the flanks of Mount St. Helens (S:Cl = 1.18 and 0.89). The analytical procedures cannot account for the large spread in the data. The variations are possibly due to changes in gas composition during eruption, meteorologic conditions, or variations in chemical and physical processes of the eruption.

Data presented by Rose (1977) and Noguchi and Kamiya (1963) showed a significant increase in S:Cl before a major eruption and a significant decrease after a major eruption (or series of eruptions). Although a gradual increase occurred before the May 18 eruption, it was smaller than expected, probably because magma had already risen in the volcano and was emitting magmatic gases before the earliest sampled ash eruptions. Likewise, no significant decrease has been seen in S:Cl between May 18 and August 7. The patterns of gas ratios observed elsewhere suggest that more eruptions are possible until the S:Cl ratio decreases.

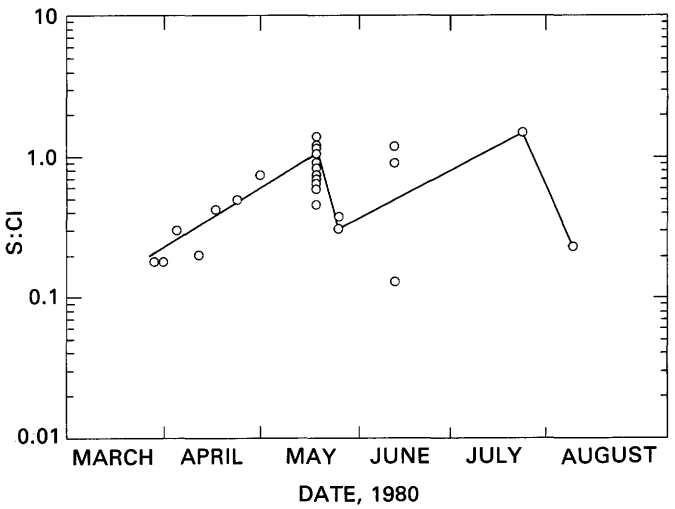

Figure 146.—Change in S:Cl through time.

CHEMICAL COMPOSITION OF THE LEACHABLE MATERIAL

The high anion content and near-neutral pH of the leachates suggest that the acidic gases reacted with the ash to produce neutral compounds. Selected samples were analyzed to determine cation concentrations (table 21). The anions probably were derived from acid aerosols and the cations from attack of the acid on the ash. Correlations between Ca and SO_4 and between Na and Cl are poor for the early eruptions but are evident for the May 18 samples. The major leachable components were apparently $CaSO_4$ and NaCl. Potassium and magnesium were sometimes present, particularly in the early leachates.

Numerous trace elements were also found in the leachates. Elements such as boron and mercury were probably present in the gas phase and deposited on the ash. Others were probably leached from the ash along with sodium and calcium.

CONCLUSIONS

A gradual increase in the S:Cl ratio was observed from March 28 to before the May 18 eruption. No sharp changes were observed that could have predicted the eruption. This ratio has varied erratically since the eruption on May 18 and has not shown a significant decrease comparable to that seen at Fuego Volcano, Guatemala. If the Fuego gas-ratio patterns are applicable to Mount St. Helens, further eruptions could be expected.

REFERENCES CITED

Brown, Eugene, Skougstad, M. W., and Fisherman, M. J., 1970, Methods for collection and analysis of water samples for dissolved minerals and gases: Techniques of Water Resources Investigations of the U.S. Geological Survey, Book 5, Chapter A1, p. 71–73.

Cradle, R. D., Wartburg, A. F., and Grahek, F. E., 1971, The proportion of sulfate to sulfur dioxide in Kilauea Volcano fume: Geochimica et Cosmochimica Acta, v. 35, p. 503–507.

Dana, M. T., Hales, J. M., and Wolf, M. A., 1975, Rain scavenging of SO_2 and sulfate from power plant plumes: Journal of Geophysical Research, v. 80, p. 4229–4129.

Naughton, J. J., Finlayson, J. B., and Lewis, V. A., 1975, Some results from recent chemical studies at Kilauea Volcano, Hawaii: Bulletin Volcanologique, v. 39, p. 64–69.

Naughton, J. J., Lewis, V. A., Thomas, D. M., and Finlayson, J. B., 1975, Fume compositions found at various stages of activity at Kilauea Volcano, Hawaii: Journal of Geophysical Research, v. 80, p. 2963–2966.

Noguchi, Kimio, and Kamiya, Hiroshi, 1963, Prediction of volcanic eruption by measuring the chemical composition and amounts of gases: Bulletin Volcanologique, v. 26, p. 367–378.

Rose, W. I., Jr., 1977, Scavenging of volcanic aerosol by ash—Atmospheric and volcanologic implications: Geology, v. 5, p. 621–624.

Rose, W. I., Jr., Bonis, S., Stoiber, R. E., Keller, M., and Bickford, T., 1973, Studies of volcanic ash from two recent Central American eruptions: Bulletin Volcanologique, v. 37, p. 338–364.

Taylor, P. S., and Stoiber, R. E., 1973, Soluble material on ash from Central American volcanoes: Geological Society of American Bulletin, v. 84, p. 1031–1042.

Thomas, D. M., and Naughton, J. J., 1978, Changes in fumarolic gas compositions as precursors to volcanic eruptions: Geological Society of America Abstracts with Program, v. 10, no. 7, p.504.

THERMAL STUDIES

Two main types of volcanic thermal studies were carried out at Mount St. Helens during 1980. Thermal surveillance of large areas, commonly by airborne infrared techniques, was used to monitor changes in thermal expression of internal structural and magmatic features. In addition, measurements were made directly in new volcanic deposits to determine their emplacement temperatures and thermal properties. Eruption and emplacement temperatures were also estimated from effects on vegetation and on man-made materials.

Thermal infrared monitoring prior to May 18 generally showed only small changes, except in the area of the crater that initially formed on March 27 (Kieffer and others). Of two previously known thermal areas, one on the southwest side of the cone remained unchanged until May 18. The other historic thermal area, within the deforming area of the bulge on the upper north flank, showed small but gradually increasing heat emission before May 18.

Infrared images from late May through August show thermal anomalies associated with the new crater and vent areas, pyroclastic deposits north of the crater and locally on upper slopes of the cone, and with the successive lava domes that emerged in June and August (Friedman, Frank, and Kieffer). En-echelon northwest-trending fractures within the crater and on its walls, evident on thermal images, may represent local expression of regional structural trends, also expressed seismically, that probably are related to plate subduction and are important structural controls of Cascade volcanoes.

Direct measurements by thermocouple indicate that emplacement temperatures of the May 18 debris avalanche ranged from about 70° to 100°C; those of the directed blast ranged from about 100° to 300°C and varied with azimuth from the crater (Banks and Hoblitt). Emplacement temperatures of the main pumiceous pyroclastic flows erupted from May 18 to October 16–18 were about 300°–730°C, and near-vent deposits were emplaced at about 750°–850°C. In general, the later deposits had higher initial temperatures. Except near the vent, temperatures in individual pyroclastic-flow lobes did not decrease substantially along the flow path, and deposits of the directed blast also had similar temperatures over

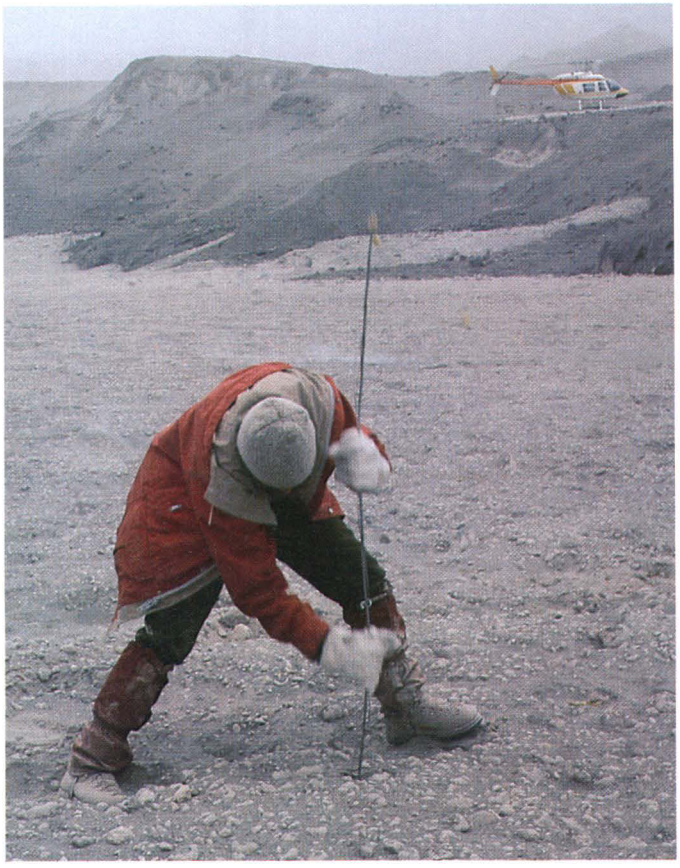

distances as far as 20 km from the vent. Measurements of pyroclastic-flow deposits indicate that after initial rapid cooling of several hundred degrees by adiabatic expansion and incorporation of air during eruption and development of flowage, the main body of a flow incorporated too little air along the subsequent flow path to cool markedly.

Eruption temperatures of the directed blast, estimated by effects on plastic objects and wood within the devastated zone, are similar to those directly measured. Temperature effects on wood are azimuthally variable, and correlate with the amount of juvenile gray dacite in the blast deposit. Effects on plastics indicate only a few minutes of peak temperatures, and the thermal effects decrease markedly near margins of the blast area. Needles of fir trees from the seared zone around margins of the blast area show cuticular melting patterns that, when compared with experimentally heated needles, suggest temperatures of 50° to 200°C in the seared zone (Winner and Casadevall).

THE 1980 ERUPTIONS OF MOUNT ST. HELENS, WASHINGTON

THERMAL INFRARED SURVEYS AT MOUNT ST. HELENS—OBSERVATIONS PRIOR TO THE ERUPTION OF MAY 18

By HUGH H. KIEFFER, DAVID FRANK, *and* JULES D. FRIEDMAN

ABSTRACT

Thermal infrared observations by the USGS were begun on March 30, 3 days after the first 1980 Mount St. Helens eruption. The objectives of these observations were both hazards prediction, in terms of identifying locations of enhanced heat flow that might possibly precede a flank eruption or landslide and debris avalanche, and quantitative measurements of the thermal changes associated with the sequence of eruptive events.

Aircraft-based instruments used included: film-recording uncalibrated scanners, moderate- and very high resolution video-recording systems, handheld imaging systems and radiometers, and calibrated digitally recording scanners. March 30 observations showed anomalous heat in the summit crater, locally along the southern bounding fault of the newly developed summit graben, in two large fractures in a region of historic thermal emission on the upper north slope that later became the bulge, and at the other historic thermal area high on the southwest slope. Although there were many visual reports of hot spots (based largely on melting of newly fallen snow), no areas of unusual heat emission were found by infrared observation, except near the summit.

During an early April eruption, a majority of the hot blocks ejected cooled within a few minutes; these were apparently heated surficially by steam condensation in the few seconds of upward trajectory, rather than by residence in a hot interior region.

In the area of the bulge, infrared anomalies increased in abundance from early April until just prior to the May 18 eruption, when the upper part of the bulge appeared to be perforated by heat leaks of a few to 100 m lateral extent. All these areas of excess thermal emission were removed by the May 18 eruption. During periods between eruptions, excess thermal radiation from the summit of Mount St. Helens on May 16 was approximately 3 MW (megawatts). The traces of the first two May 18 landslide failure surfaces were through clusters of thermal anomalies.

PRE-1980 INFRARED SURVEYS AND THE HISTORICAL THERMAL AREAS OF MOUNT ST. HELENS

Mount St. Helens was known to be an active volcano (Crandell and Mullineaux, 1978) and had two active thermal areas prior to 1980. Both thermal areas were discussed in mid-20th century geologic reports by Lawrence (1939, p. 54) and Phillips (1941, p. 37–39). Various earlier reports of visual observations referred to by Majors (1980, p. 42–44) indicate that the thermal areas were active at least as far back as 1910–17, and perhaps since the time of the last eruptions in the mid-19th century. Both thermal areas were detected by early airborne infrared observations, although individual surveys rarely recorded both areas simultaneously. Moxham (1970) reported only one area north of the summit in a 1966 survey, although the second area southwest of the summit faintly appears in his published infrared image. Five aerial infrared line-scan surveys, utilizing the 8–14 μm spectral region, flown between April 3, 1971, and December 13, 1975, confirmed the persistence and delimited the boundaries of the two thermal areas on the upper slopes of Mount St. Helens, designated historic thermal areas A and B (Friedman and Frank, 1978; fig. 147*A*, *B*). Site A, at 2,740 m elevation along the east side of Wishbone Glacier at The Boot on the north slope, consisted of about 200 m^2 of warm

ground, elongated along an axis striking north-northwest within the summit dome dacite and in alinement with the Goat Rocks dacite dome (fig. 148). Site B comprised a cluster of five sharply defined linear zones striking generally southwest, about 650 m^2 in area, between 2,650 and 2,750 m elevation on the southwest slope. Ground reconnaissance at site B in 1972 revealed that the thermal area was associated with a dark-red alteration zone along the contact of the summit dacite dome with older andesite lava flows.

A temperature-sensor array emplaced at site B recorded (via LANDSAT) temperature measurements between July 20, 1973, and April 18, 1974, of ambient air, thermal and nonthermal ground surfaces, and unconsolidated material at 15- and 50-cm depths (Preble and others, 1977). These temperature observations provided the basis for estimating the differential radiant exitance at site B at about 84 W/m^2, equivalent to the Fourier conductive flux in the upper 15 cm of the ground. The differential geothermal flux at this site, using the method of Sekioka and Yuhara (1974) based on the heat balance of the ground surface, and considering evaporation, diffusion, conduction, and radiation contributions to heat exchange with the atmosphere, was considerably greater, about 375 W/m^2 (Friedman and Frank, 1978). Friedman and Frank estimated the total heat discharge at Mount St. Helens in 1973 to be $0.1–0.3 \times 10^6$ W.

ACKNOWLEDGMENTS

The assistance of the following individuals and organizations contributed significantly to this work: Bruce Crowe, Los Alamos Scientific Laboratory, U.S. Department of Energy; David Hawley and William Ginsberg, EG&G Corp.; Charles Rosenfeld, Oregon State University and Oregon Army National Guard; Lt. Comdr. Jack Jordon and other personnel of At-

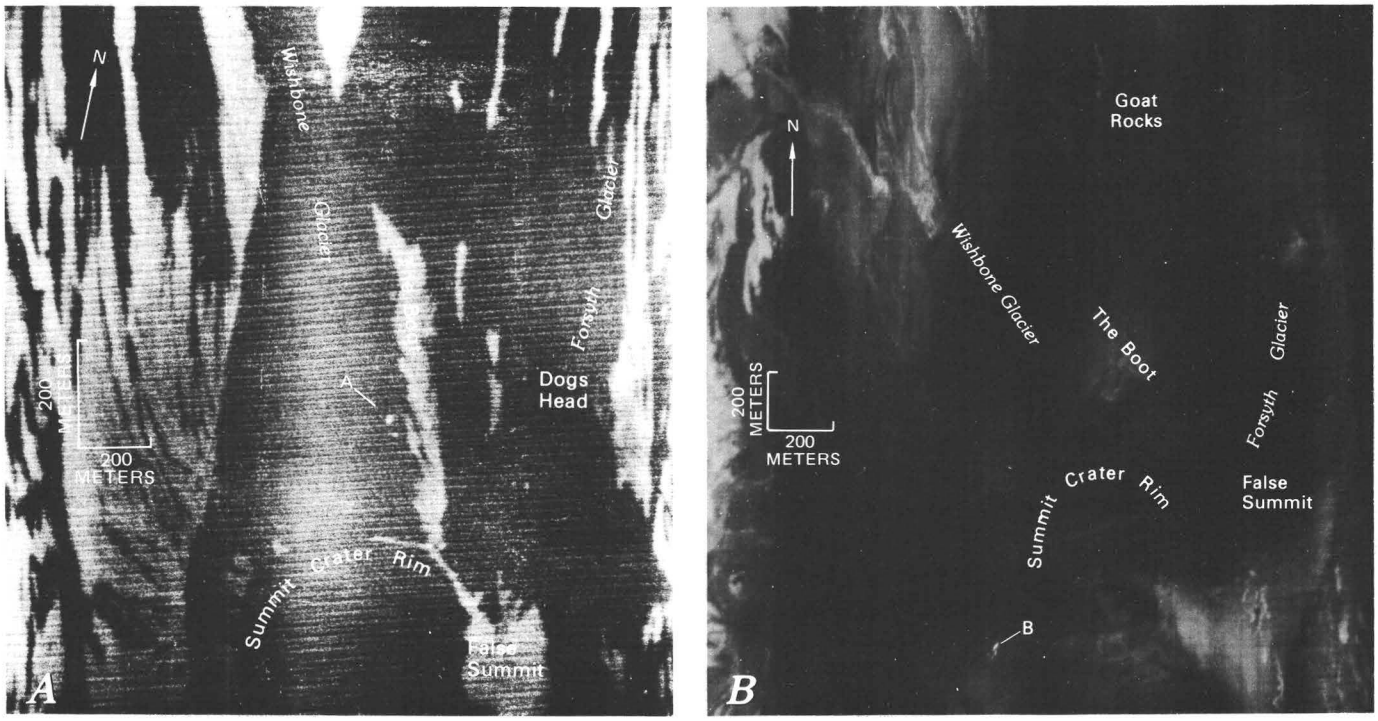

Figure 147.—Thermal infrared images of Mount St. Helens obtained prior to 1980 eruption sequence, showing the two historic thermal areas. Images produced by U.S. Forest Service for the USGS. A, Image of August 7, 1971, showing thermal area A, a small area of weak fumarolic activity at The Boot, on north flank at 2,740 m (9,000 ft) elevation. On this late-summer morning, instruments were set to depict two levels of background heat emission—glaciers and few remaining snow patches as cold, and snow-free ground as warm. B, Image of April 26, 1973, showing thermal area B on southwest flank at an elevation of 2,650–2,750 m (8,700–9,000 ft). The thermal features have a distinctive downslope linear trend. More snow was present at this time than in August 1971, with the result that thermal area A was covered by snow and does not appear in this image.

tack Squadron 128, Whidbey Island Naval Air Station, Wash., U.S. Navy; Gary Shelton and Dale Becker, U.S. Environmental Protection Agency; Capt. John McAdams and crew, Electronics Proving Ground, Fort Huachuca, Ariz., U.S. Army; Dale Gable and John Warren, Boise Interagency Fire Center, and John Voth and Jim Elm, formerly of the Northern Forest Fire Laboratory, Missoula, U.S. Forest Service; Kay Edwards, USGS, Flagstaff; and Red Darringer, Telatemp Corp. Special credit and thanks are due the personnel of the Headquarters and Emergency Coordination Center, Gifford Pinchot National Forest, U.S. Forest Service.

OBJECTIVES OF THE 1980 INFRARED SURVEYS

The two major objectives of thermal infrared observations of Mount St. Helens were: (1) monitoring for thermal changes indicative of a change in the volcanic hazard, and (2) documenting the thermal evolution of the eruption sequence for later analysis. Observation techniques and equipment that allow rapid assessment of location and magnitude of volcanogenic thermal activity are needed for the first objective. Rapid availability of data is less important for the second objective, but quantitative measurements are highly desirable. One immediate objective of these surveys was to check reports of sightings of so-called hot spots. These reports were of areas commonly free of snow, places where liquid water had been observed on rocks, or where small clouds were seen. A possible flank eruption, or exceptional subsurface heating of the glaciers, would have constituted a potential hazard; the direction of eruption or failure might be determined by early detection of increased heat flow.

METHODS AND INSTRUMENTS

The thermal infrared observations of Mount St. Helens utilized a wide variety of instruments and several organizations (table 22). The methods and instruments are briefly described here in order of sophistication, cost, and time required to process data. Unless otherwise noted, the instruments are sensitive in the 8–14 μm band and thus respond only to thermal emission, not reflected sunlight. All uncalibrated systems have an adjustable offset and gain.

Handheld radiometers have a single field of view of

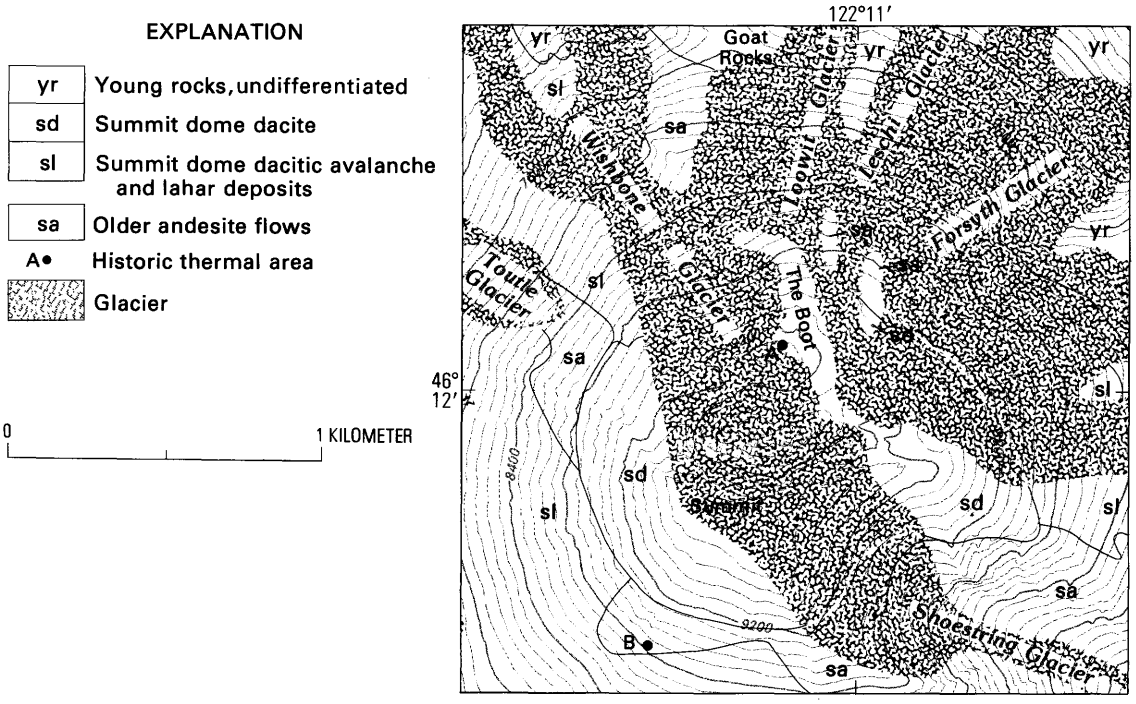

Figure 148—Location of historic thermal areas A and B in relation to topography, glaciers, and major geologic units. Geology modified from C. A. Hopson.

Table 22.—Log of thermal infrared observations of Mount St. Helens

[All instruments are sensitive in the 8-14 μm band unless noted otherwise. The more common thermal infrared scanners were developed for nongeologic applications and have no flux calibration; some have automatic gain control or AC coupling that attempts to maintain a uniform scene contrast. Such uncalibrated thermal imagery is useful for detection of the initiation, expansion, or cessation of thermal activity, but cannot quantitatively determine changes of the intensity of thermal activity. DF, David Frank; JF, J. D. Friedman; DG, Dale Gable (USFS); HK, Hugh Kieffer; DM, C. D. Miller; U-MT, University of Montana, Barnes PRT-5 radiometer and AGA Thermovision 750 imaging system; NK, not known]

Year	Month	Day	Time	Organization	Flight lines	Comments
1966	Sept.	4	Predawn	USGS----	5	Thermal site A obvious; thermal site B marginally visible.
1971	Apr.	3	2040-2102	USFS, JF, DF.	4	Thermal site B obvious; thermal site A not apparent.
1971	Aug.	7	0448-0459	--do----	2	Thermal site B warm; thermal site A not apparent.
1972	Apr.	18	2340-2355	--do----	3	Thermal site B barely discernible.
1973	Apr.	26	0412-0459	--do----	4	Thermal site B obvious.
1975	Dec.	13	NK	OANG----	1	Two spots at thermal site A.
1980	Mar.	27	NK	--do----	1	Hot area in bottom of first crater.
	Mar.	30	0515	OANG----	NK	
	Mar.	30	1630-1700	--do----	NK	
	Mar.	30	2243-2258	Army----	6	
	Mar.	30	To Apr. 4	U-MT----	Ground	Ground observations from 9 km north.
	Apr.	3	1500-1630	USN-HK--	Circled	General survey, recorded eruption, tape erased.
	Apr.	4	0630-0800	USGS-HK	H-P	
	Apr.	7	1303-1421	EG&G----	18	
	Apr.	9	0620-0730	USGS-HK	H-P	Cloudy above 2,800 m.
	Apr.	10	1136-1224	EG&G----	9	Partly cloudy.
	Apr.	10	1342-1406	EPA-----	4	
	Apr.	10	2100-2200	FLIR----	NK	
	Apr.	11	0510-0527	EPA-----	3	Just after eruption.
	Apr.	11	0540-0717	USGS-HK	H-P	
	Apr.	16	1921	OANG----	NK	
	Apr.	21	1945	--do----	NK	
	Apr.	22	NK	--do----	NK	Low pass over crater.
	Apr.	30	NK	--do----	H-R	Temperature peaks from 12° to 37°C.
	May	2	0430-0630	USN-DF--	Continuous	Clouds below 1,800 m. Hot spots within the bulge.
	May	16	0345-0537	EG&G----	18	Complete coverage. Many hot spots near top of bulge.
	May	16	NK	USGS-DM	H-R	31°C in the bulge.
	May	17	0447	OANG----	NK	
	May	18	0551	--do----	NK	
	May	19	NK	NASA----	NK	U2 aircraft. Cloudy, no significant data obtained.
	May	20	NK	OANG----	NK	North Fork Toutle River debris avalanche.
	May	20	1300-1400	USN-DF--	Continuous	Cloudy.
	May	20	1516-1720	USFS-HK	H-R	West flank, South and North Forks Toutle River debris flows.
	May	24	1000-1200	USFS-DG	H-V	
	May	30	0500-0600	USN-DF--	Continuous	Cloud tops at 1,700 m. Crater, ash flows, Mount Margaret ponded blast deposit.
	May	30	1000-1200	USFS-DG	H-V	Interior of crater.
	May	30	1500-1600	USFS-DG	H-V	Low clouds. Ash 15°C warmer than dirty ice.
	May	31	1680	USGS-DF	H-R	Mount Margaret ponded blast deposit.
	May	31	1100	USFS-DG	H-V	Low clouds. Warmest ash near summit.
	May	31	1700-1830	FLIR----	H-V	Amphitheater, ash deposit on northwest flank.
	June	3	0640-0930	--do----	H-V	
	June	7	0510-0700	--do--	H-V	
	June	12	0430-0500	USN-HK--	Continuous	Cloudy.
	June	13	1600-1630	USN-DF--	--do--	Cloudy. New dome seen on radar.
	June	19	0415-0445	--do----	------	Dome, ash flow, southeast shore of Spirit Lake.
	June	19	0500-0600	FLIR----	H-V	
	Aug.	11	0900-1207	USGS-JF	NK	Test flight.
	Aug.	12	0343-0607	--do----	10	Grid survey. Lava dome, pyroclastic flow deposits. May 18 blast deposits.
	Aug.	13	0423-0607	--do----	10	Grid survey. Lava dome, pyroclastic flow deposits. May 18 blast deposits. Survey on same grid as Aug. 12.

Table 22.—Log of thermal infrared observations of Mount St. Helens—Continued

Year	Month	Day	Time	Organi-zation	Flight lines	Comments
1980	Aug.	13	1817-1951	--do----	10	Do.
	Aug.	13	2023-2162	--do----	10	Do.
	Aug.	19	1300-1440	EG&G----	9	Do.
	Aug.	19	1500-1700	USGS-DF	H-R	Pyroclastic flows and ash surfaces in amphitheater as high as 37°C.
	Aug.	20	0330-0621	EG&G----	16	Survey on same grid as Aug. 12-13.
	Aug.	21	0900-1100	USGS-DF	H-R	Ash in crater adjacent to dome as high as 33°C.

DESCRIPTION OF INSTRUMENTS

EG&G, Daedalus DS-1260 calibrated, digital-recording scanner, Hg-Cd-Te and In-Sb (3-5 μm) detectors.
EPA, Daedalus DS-1260 calibrated digital-recording scanner, Hg-Cd-Te at 2 gains.
FLIR, FLIR, Inc., video-recording imaging, uncalibrated.
USGS, 1966 Recon IX scanner, uncalibrated, film-recording; 1980, RS-14A scanner, calibrated, analog recording.
USFS, 1971 Recon XI scanner, uncalibrated, with Polaroid recording; 1972-73 Texas Instruments RS-7 scanner; 1980 Inframetrics video-recording, imaging, calibrated relative temperature.
USN, Hughes TRAM video-recording imaging, uncalibrated.
Army, AAS-24 film-recording scanner, uncalibrated.
OANG, AAS-24 film-recording scanner, uncalibrated, data courtesy of Charles Rosenfeld, OANG.
H-P, Helicopter, ProbEye Thermal Imager Survey, 3-5 μm, uncalibrated.
H-R, Helicopter, Telatemp calibrated radiometer measurements.
H-V, Helicopter, Video-recording thermal imager.

typically 2½° width, a sensitivity of a fraction of a degree Celsius, and an absolute calibration of about 1°C or better, and show a meter display of the brightness temperature.

The handheld, nonrecording thermal imaging system used (Hughes ProbEye) is sensitive in the 3–5 μm band, where reflected solar energy can be comparable to ambient thermal emission. This device provides an approximately 5° × 10° red image at natural angular scale, with brightness proportional to radiance, that can be viewed with one eye while the other eye views the external scene. Although the Hughes ProbEye system is completely uncalibrated, a sensitive survey was possible, as confirmed by ability to thermally discern trees in still air before sunrise where only small temperature variations exist. Because this instrument is sensitive in the 3–5 μm band, surveys for internal heating were less sensitive on the east side of Mount St. Helens, where sunshine was present before the area could be reached by helicopter. Commonly, though, the instrument could be used to look deep into the dark part of crevasses.

The video-recording, thermal imaging systems used have a field of view of approximately 15° × 20° and provide a thermal image at standard video rates that can be viewed on a television monitor during observation, as well as recorded. Thermal resolution is from 0.2° to 5°C, depending on gain setting. One brand (Inframetrics) allows some determination of temperature differences, but not absolute temperature.

The film-recording aerial infrared scanners scan a line extending approximately 45° from each side of vertical, directly below the aircraft; the successive lines are offset by the aircraft's forward motion. Spatial resolution is typically approximately 2.5 milliradians. The detected thermal signal is recorded on film; no data are immediately available except an oscilloscope display of the response across the scan lines (used to set the recording levels). The 3–5 and 8–14 μm bands are recorded simultaneously by some scanners. The film is processed after the flight to produce a graphic image.

The calibrated aerial infrared scanners operate and have a scan pattern similar to the film-recording systems; the major difference is the presence of two blackbody references that are sensed at the ends of each line scan. The response to the scene and the

blackbodies is recorded on magnetic tape. Graphic output of basic response, calibrated radiance, or brightness temperature is produced by successive steps of computer processing; production of prints typically takes days to weeks after the flight.

The infrared imaging system used in surveys by the U.S. Navy (Hughes TRAM, a military infrared tracking system) has high spatial and temperature resolution, but is AC coupled and uncalibrated, so that absolute temperatures and temperature differences cannot be recorded. The thermal image is recorded at video rates but in a format that requires special playback equipment.

The optimal time for thermal infrared surveys for low-level heat flow is just before dawn, when ambient temperatures are at the diurnal minimum and the local variations due to topography and albedo variations are moderated. The variation (one sigma) of thermal radiance with location at Mount St. Helens near midday was about 40 W/m^2, versus 10 W/m^2 just before dawn, so that predawn surveys are four times more sensitive to internal heat flow. The obvious disadvantages of nighttime operations are increased navigation requirements, the inadvisability of low-altitude flights, and the absence of simultaneous visual observations. Using fixed-wing aircraft, predawn thermal observations were made when possible. Thermal observations using helicopters were made as early in the morning as safe practice allowed.

Although processes not measured by a thermal infrared survey dominate the heat flow in an active volcano, such surveys are very sensitive to those changes in heat flow that become expressed as radiation. The basic detectivity of the calibrated surveys was 0.4 W/m^2, or a 0.1°C change of temperature. Airborne thermal infrared surveys allow large areas to be measured with uniform sensitivity.

In this study, only the simplest quantitative assessments of heat flow have been made; the excess emitted radiation has been computed by determining the 8–14 μm radiation level for a rectangular perimeter outside the area of obvious volcanic heat flow, which was then used as the natural level to be subtracted from the heated areas. No attempt has been made to correct for emissivity less than unity or atmospheric attenuation; these corrections should be minor. Inclusion of the large factors necessary to account for convection, advection, and latent heat in an estimate of total heat flow has not been attempted in this study. Friedman and Frank (1980) thoroughly discussed the determination of these effects at Mount Baker.

THERMAL IMAGES

The 1980 thermal images shown in this report were processed at the U.S. Geological Survey, Flagstaff, Ariz., image processing facility. The cylindrical distortion inherent in scanner systems has not been removed from the thermal images in this report. The viewing angle, a, varies from vertical (0°) at the center line to about 45° at both edges of the flight path, so that the horizontal crosstrack distance represented by each measurement is

$$\frac{HF}{\cos^2 a},$$

where H is the altitude difference between the aircraft and the ground being viewed, and F is the instantaneous field of view of the scanner, in radians. The horizontal downtrack distance represented by each measurement is V/S, where V is the aircraft velocity and S is the line-scan rate. The downtrack length sensed in a measurement is HF; the line-scan rate is normally adjusted to make these two comparable. For steep terrain, an additional factor is required to determine the local surface area along slope:

$$\frac{\cos a}{\cos (a-b) \cos c},$$

where b is the crosstrack slope component measured toward the aircraft and c is the slope component parallel to the aircraft path. All thermal images in this report are presented with temperature increasing from black to white.

THERMAL OBSERVATIONS FROM MARCH TO MAY 18

MARCH 24

Aerial photographs taken on March 24, 4 days after the beginning of the earthquake swarm, indicated that both historically active thermal areas ap-

Figure 149.—Oblique aerial photographs of summit area, March 24, 1980, showing historic thermal areas. Distance from False Summit to summit about 600 m. Photographs by David Frank. A, Viewed from north, thermal area A, near The Boot, is covered by snow, but its location corresponds to shallow dimple in snow surface. B, Viewed from the southwest, thermal area B appears as a cluster of snow-free patches of ground.

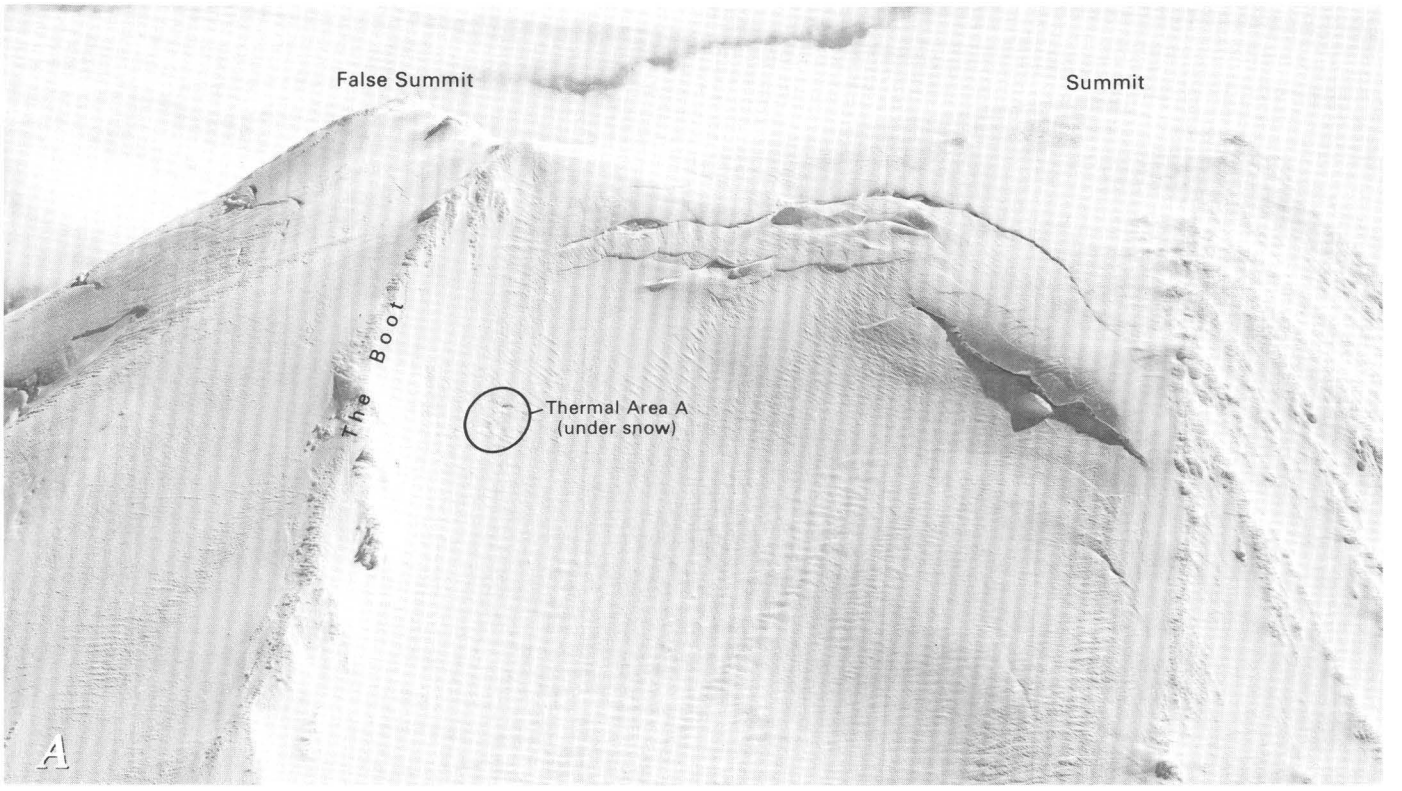
False Summit
Summit
The Boot
Thermal Area A
(under snow)
A

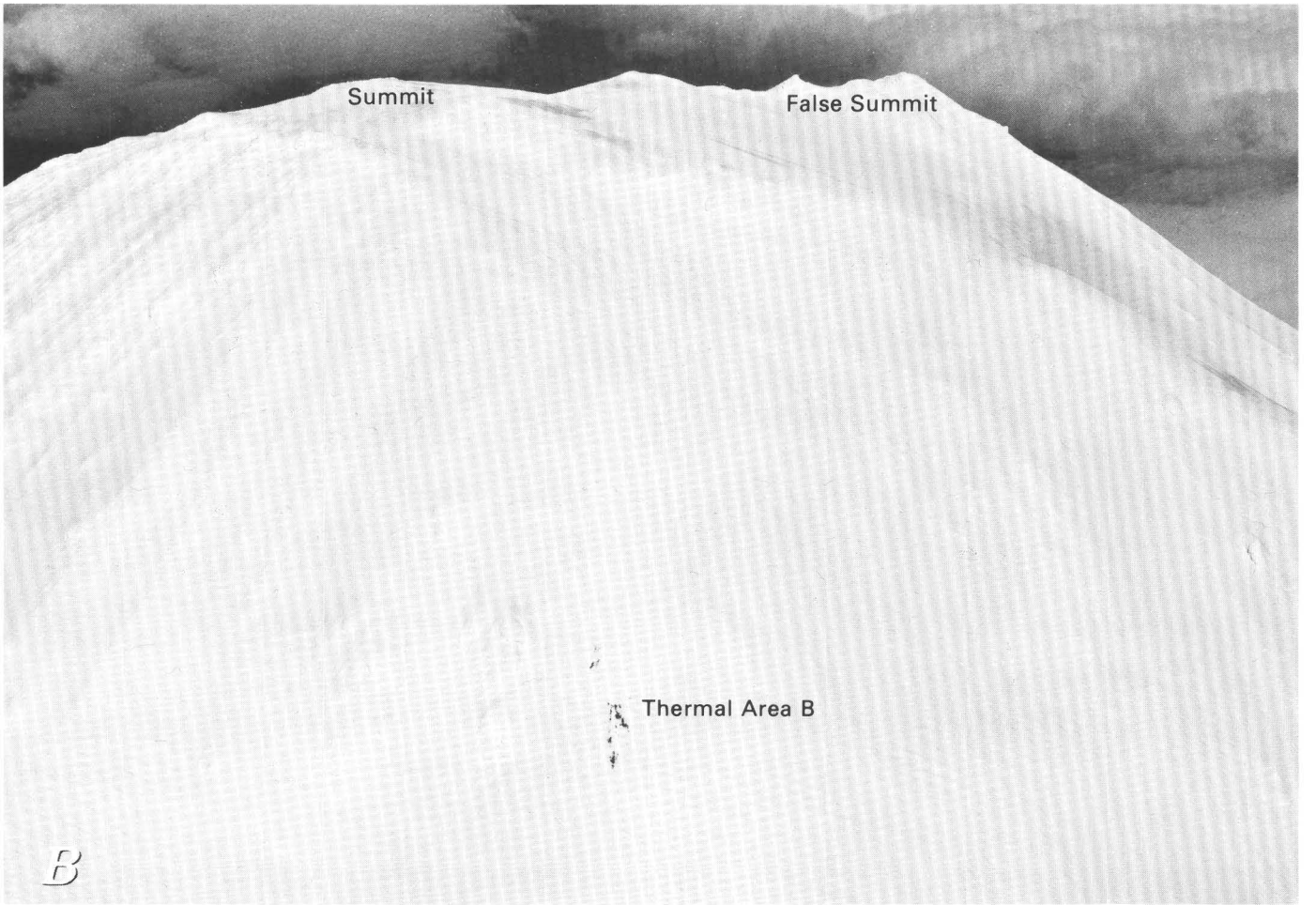
Summit
False Summit
Thermal Area B
B

peared normal for this season. The Boot area was snow covered, and the southwest area was partially snowfree (fig. 149).

MARCH 27

Following the first eruption, photographic observations on March 27 showed that The Boot area was heavily fractured (fig. 150). One fracture crossed through, or very near, thermal area A.

The first thermal infrared observations of the 1980 eruptive sequence were obtained by OANG (Oregon Army National Guard) on the afternoon of March 27 (Rosenfeld, 1980, fig. 1). (A list of observation times and instruments is in table 22.) Identification of low-level geothermal flow is particularly difficult with afternoon observations, because of masking by radiation from solar-heated ground. The only nonsolar thermal feature identified in the uncalibrated thermal image available was within the single 70-m-diameter crater present at that time. The heated area was approximately 25 m in diameter and had two small, higher temperature areas along its northeast side.

MARCH 30

Six flight lines of thermal infrared observations were obtained by the U.S. Army for the USGS on March 30 between 2243 and 2258. Five low-altitude passes covered all flanks of Mount St. Helens, and one pass was directly over the summit graben. The alternating layers of ash and snow, and the many recent snowslides yielded a rich and complex thermal image (fig. 151). However, the only thermal features clearly of nonsolar origin are (1) those within and immediately adjacent to the two new pit craters, (2) two spots along the fault bounding the graben on the south, where the fault scarp bends northeastward near the original False Summit (loc. C, fig. 151*A* and 153), and (3) within north-trending fractures immediately north of the septum between the two craters then present (locs. A and D, fig. 151*A*). These north-trending fractures formed between March 24 and March 27, probably on March 25, when the earthquake swarm peaked; they cross The Boot at an acute angle (fig. 152). The infrared anomaly is strongest near historic thermal area A on the west side

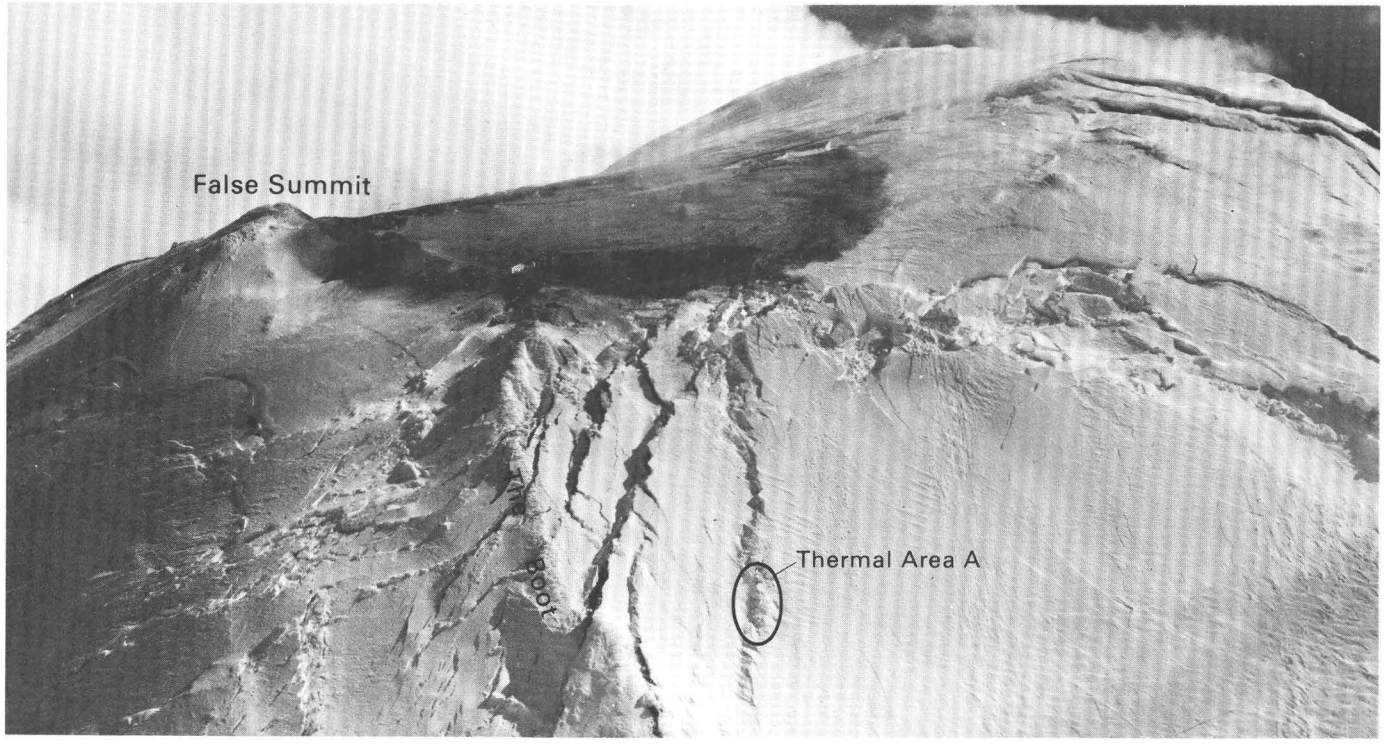

Figure 150.—Oblique aerial photograph of summit of Mount St. Helens, looking south, March 27, 1980. Location of thermal area A indicated. Note that the new fractures cross ice and rock areas with no apparent change of style, indicating the fractures are deep seated. Photograph by David Frank.

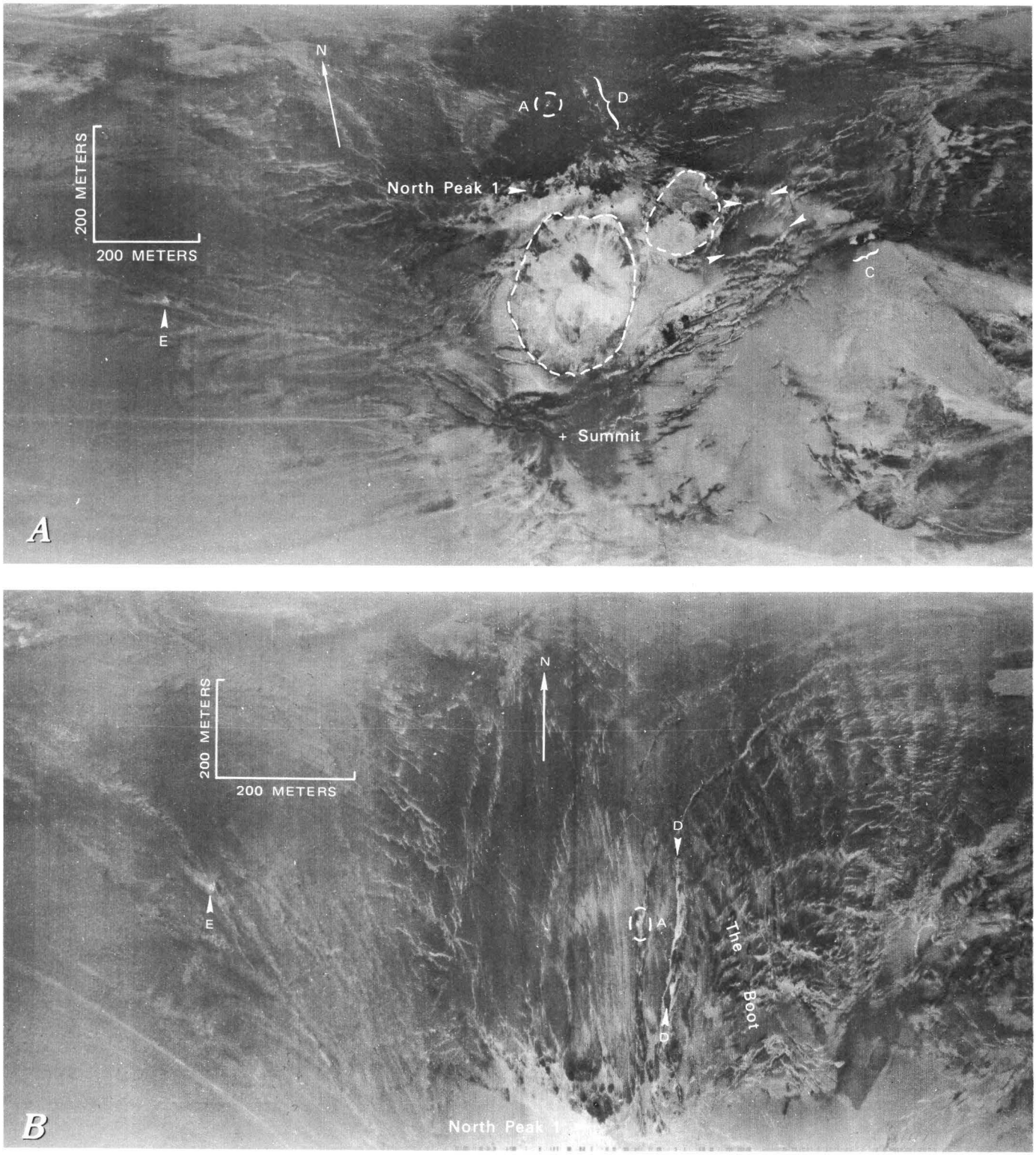

Figure 151.—Thermal infrared images of summit area obtained by U.S. Army at approximately 2300 on March 30, 1980. Thermal feature E is a topographic prominence and may result from solar heating. There are large-scale distortions in these images. A, Scan obtained on a low-altitude pass directly over crater. Some apparent cooling (dark areas) north and south of crater is an artifact of scanner automatic gain control. Anomalous areas are visible 150 m north of north peak 1 (locs. A, D) and in southernmost fracture east of main crater (loc. C). (See fig. 152 for oblique view of sites A, D, and E.) Outline of two craters is shown by dashed line. Two pairs of unlabeled arrows indicate warm fractures also shown in figure 153. B, View of upper north flank showing heating within major fractures near The Boot (fracture D and fracture through area A). In this image observations near The Boot were approximately perpendicular to the local surface.

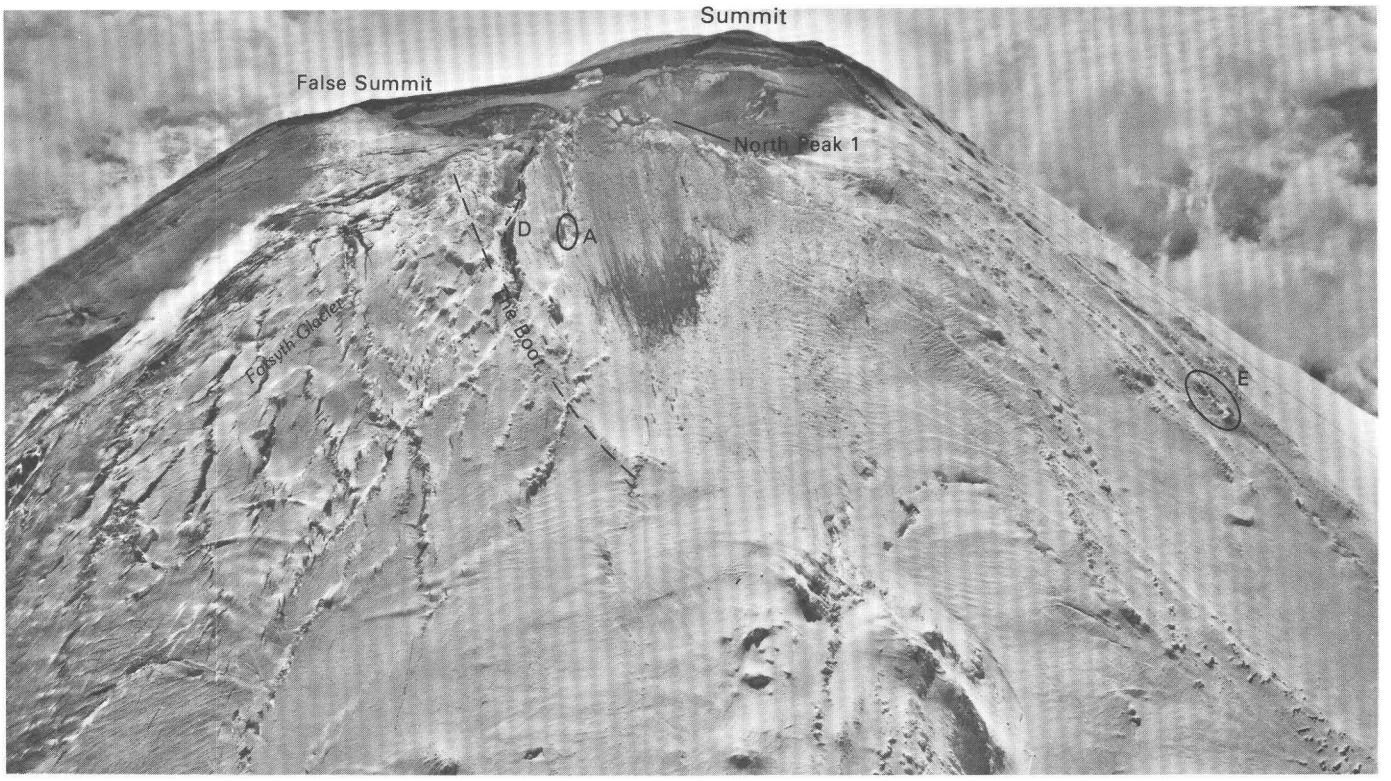

Figure 152.—Oblique aerial photograph of summit area, looking south, March 30. Crater on the left was the first to form. Features which showed enhanced thermal emission at 2300 (see fig. 151) are indicated by A, D, and E. Subsidence of graben (between summit and north peak 1) and False Summit can be seen by comparison with figure 150. Photograph by Austin Post.

of The Boot. These fracture-related thermal features were more readily seen from the north at small angles (5°–30°) from the local surface normal (fig. 151*B*) than in observations made directly over the summit graben (55°–60° from the local surface normal, fig. 151*A*). Several other features of moderate to high thermal contrast were observed in this survey, but they are not unequivocally related to anomalous ground heat; some correspond to topographic prominences and probably were due to solar heating. A single warm feature at the west end of the fault bounding the summit graben on the south (loc. E, fig. 151*A*) and some warm features seen within the Forsyth Glacier (fig. 151*B*) may result from geothermal heating. No thermal infrared anomalies were found on the east, south, or west flanks of Mount St. Helens, although historic thermal area B was within a small triangular area not covered by this survey.

The feature indicated as location C in figure 151*A* is exceptional; it is the only definite occurrence of volcanogenic heating along this major structural feature, the fault bounding the summit graben on the south, away from the crater proper. Although the thermal infrared anomalies on the upper bulge persisted until May 18, this eastern thermal feature was not observed on April 10 or 11, or at any later date.[1]

APRIL 3

The first U.S. Navy infrared observation flight was made on April 3 at about 1500 PST. A general survey of the flanks of Mount St. Helens revealed no obvious hot areas, although the survey should not be considered definitive because it was the first use of this high-resolution equipment by USGS personnel, and it occurred in midafternoon, the poorest time of day for discrimination of volcanogenic heat flow. A moderate eruption was observed during this flight. Hot blocks, 10 cm to 1 m in size, arced out of the rising

[1]In this study we were unable to examine all of the thermal data collected by various organizations. Future examination of all available data may extend the periods during which various thermal features were observed.

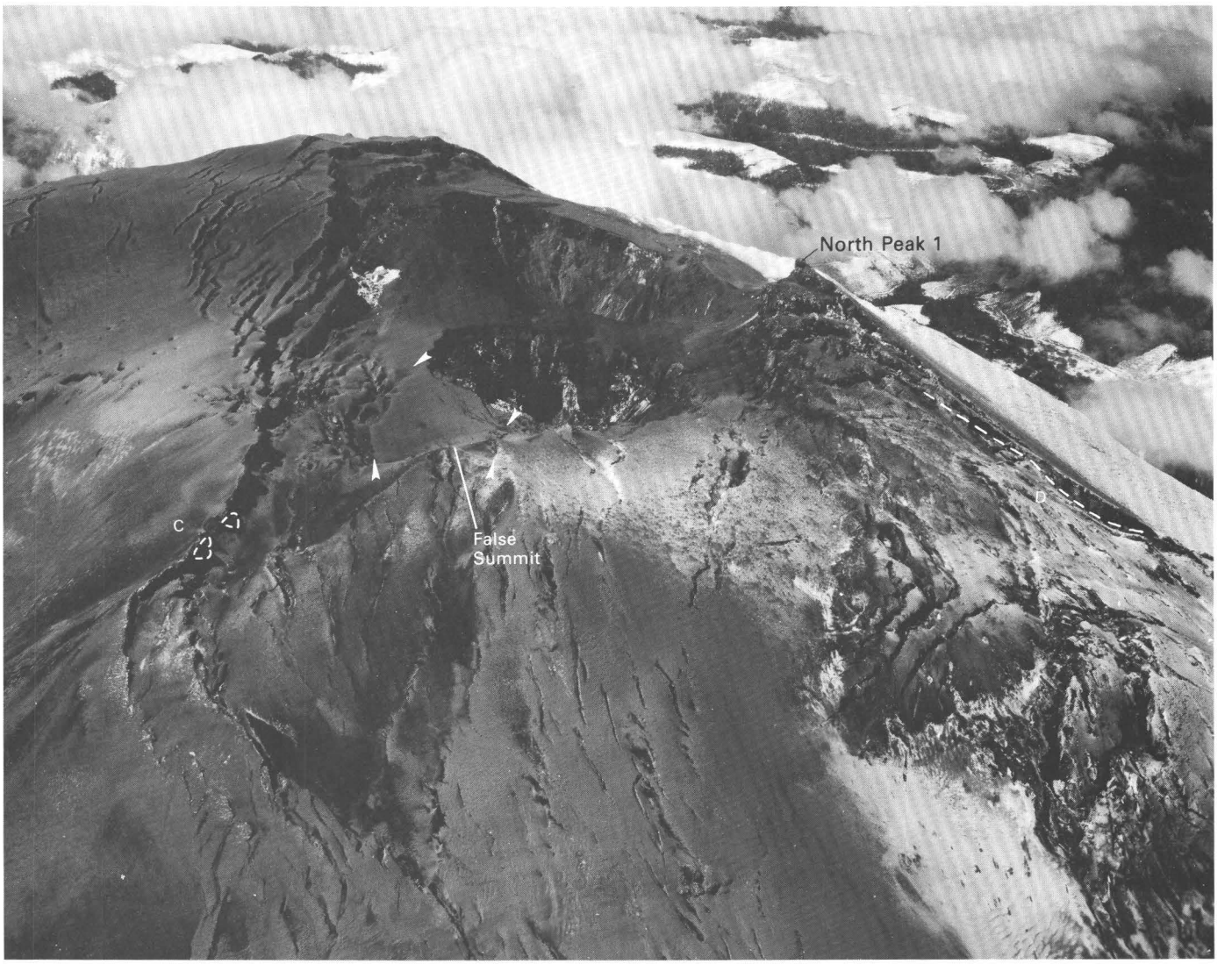

Figure 153.—Oblique aerial photograph of summit area, March 30, showing location of infrared anomalies (loc. C) seen that evening on east extension of southern graben-fault (see fig. 151A). The two pairs of arrows and dashed line (loc. D) indicate warm fractures also shown in figure 151 A. Photograph by Austin Post.

plume and splashed into cold surficial ash and snow. The exterior of the plume itself was highly variable in temperature but not as hot as the blocks. An apparently hot horizontal streak was observed on the mountain near the top of the Shoestring Glacier on the last circuit of the mountain. The precise location of the feature is not known; however, it was in an area that was facing away from the sun. It may have been an internally heated crevasse, but it was never seen again. Unfortunately, the video recording of this flight was erased before it could be reexamined by geologists.

Particular attention was given to the area immediately above the Timberline parking lot, which was frequently occupied by scientific teams. No unusual thermal features were seen upslope between the parking lot and an elevation of 2,500 m.

APRIL 4

The first helicopter-based thermal survey was conducted at dawn (0630–0800 PST) on April 4 using a handheld thermal imaging system (Hughes ProbEye). On that date, there had been several reports of hot

spots in the area of Goat Rocks, in the incised canyon below Loowit Glacier, which is east of Goat Rocks, and along the sides of upper Shoestring Glacier. A fairly complete survey of the slope above treeline from azimuth 200° clockwise to 010° (measured from the center of Mount St. Helens), including thorough surveys of Goat Rocks and the canyon below Loowit Glacier, revealed no unusual heat except near the north summit above 2,700 m elevation. A sensitive survey of the northeast and southeast quadrants of the cone could not be made due to the presence of fog until after these areas were heated by sunlight. A thin orographic cap cloud prevented viewing the south side of the summit.

During an eruption beginning at 0703, hot, newly fallen rocks were visible along the west shoulder of the crater. A nearly horizontal platform north of the inner crater was covered with recent ash and was uniformly warm. On the next pass, approximately 15 min later, many or most of the rocks on the west shoulder had cooled and were thermally indistinct. This rapid cooling suggests that they were cool rather than hot bedrock when incorporated in the eruption column and were surficially heated by steam condensation during ejection.

APRIL 7–11

A second helicopter survey on April 9 was limited to elevations below about 1,800 m and in the northwest quadrant. No thermal infrared anomalies were seen.

Airborne calibrated, thermal infrared scanner surveys were conducted near midday on April 7 and 10 and before dawn on April 11. The midday surveys showed temperatures appreciably above ambient only within the summit crater (much of this data has not yet been examined in detail). The thermal areas observed in the predawn survey on April 11 probably existed throughout the period of April 7–11 but did not have adequate contrast to be distinct from the midday solar heating.

Three flight lines of observations were obtained before dawn on April 11. Two of these were at aircraft elevations of 5,100 m and had an instantaneous field of view of 5.3 m at the summit of Mount St. Helens. At this low spatial resolution, topographic features and the major fractures could be discerned, but there was no evidence of extensive volcanogenic heating outside of the summit crater. A 15-min eruption had just ceased, and a mildly warm plume was recorded trailing off to the southwest. A flight line was made at 3,400 m aircraft altitude (0.9-m resolution at the summit) at 0527 (fig. 154). This low-altitude flight line covered only a 1-km-wide path across the summit area; outside of the summit graben, a single infrared anomaly corresponding to thermal area A was seen just north of north peak 1. The thermal image shows that the maximum temperature was in the easternmost of several vents active in early April. The temperatures appear to be proportional to the thickness of ash accumulation; the higher temperatures are at two local vents within the crater and along steep chutes that probably had ash slides during or immediately after the eruption. There was no appreciable heating of the uppermost northern part of the crater's interior wall; however, the level terrain immediately above the north wall showed both generalized heating and an abundant population of small blocks or warm pits from the eruption.

The average surface temperature of the summit of Mount St. Helens during this observation was -9°C; the apparent temperature through the residual plume was approximately -6°C. Only areas near the crater exceeded 0°C (fig. 154). The maximum temperature observed was approximately 50°C, well above the calibration level of the infrared scanner (21°C). About 10 percent of the area within the crater exceeded 14°C.

A helicopter-based infrared survey was conducted on April 11 in exceptionally fine weather. There had been a moderate eruption from about 0430 to 0445, and intermittent eruptions occurred throughout the survey, which was from 0540 to 0717. Infrared anomalies were found at the following locations: in fractures in the saddle above Goat Rocks, a single hole near the middle of the upper Wishbone Glacier, in fissures immediately west and north of the north peak 1, at many locations within the crater, and associated with blocky ejecta during and following eruptions. The following locations were scanned but no infrared anomaly was found: the northern and southern fractures that extend west from the boundaries of the summit graben; the northern and southern fractures extending east to northeast along the summit graben; the fracture extending northeast over the False Summit area; and the upper 250 m of the Shoestring Glacier. Ash from previous eruptions was drifting across the summit and was being trapped by fractures. This ash, which reaccumulated at the am-

bient air temperature, would insulate and could have masked appreciable heat flow in these fractures.

Eruption clouds did not appear hot. During an eruption, except for the initial venting and relatively dense fingers of ash that burst out of the column, the column appeared to be heated primarily by solar radiation; the shadowed west side of the plume appeared cool (at least thermal emission was minor compared to reflected solar radiation in the 3–5 μm band). The warmest locations were the tips of bursting fingers and at the base of the eruption column. By the time the initial velocity was lost (approximately 3 s), the exterior ash in the eruption cloud was cooler than the bright steam cloud. These results agree with those reported from remote ground observations (St. Lawrence and others, 1980).

The temperature was variable within the crater. The hottest locations were ash deposits exposed by slumping of their upper parts; stable ash surfaces cooled quickly. During this survey, the vents commonly were relatively cold immediately after an eruption, as they refilled with water and floating ice debris. The lower talus slopes surrounding the vents were relatively hot.

Peak local temperatures measured from a helicopter with a handheld radiometer on April 30 ranged from 12° to 24°C within the crater (data courtesy of Charles Rosenfeld and the OANG).

MAY 2

High-resolution thermal observations were made of Mount St. Helens before dawn on May 2 by the U.S. Navy. This survey provided our first clear evidence of increased heat flow from localities within the bulge, other than those associated with The Boot. Infrared anomalies strong enough to be interpreted as representing geothermally heated ground occurred in the following areas (figs. 155, 156): (1) At the bottom and extending part way up the north and south walls

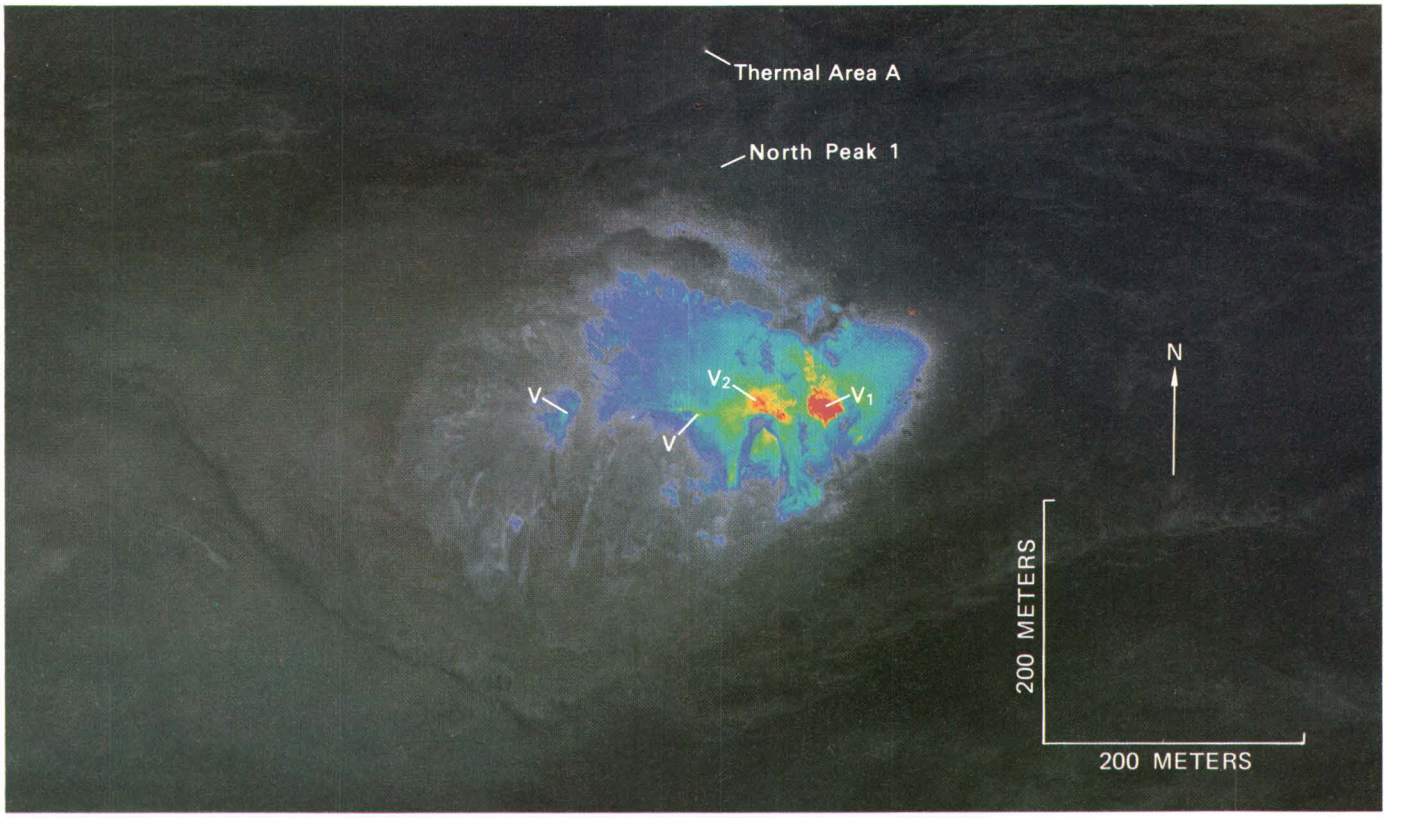

Figure 154.—Thermal-infrared image of summit area, April 11 at 0527; image obtained by U.S. Environmental Protection Agency. In this false-color image, black is coolest (−19°C), light gray is 1°C, blue is 3.5°C, and red is 41°C or greater. The warmest are at bottom of crater; eastern vents were active on this day. A 15-min eruption from vent 1 (V1) and perhaps vent 2 (V2) had ended at about 0500 and another eruption began 16 min after this image was obtained. Vents inactive during this eruption shown by V.

Figure 155.—Oblique aerial photograph of summit area, looking southwest, May 1; thermal features observed for the first time before dawn the next day are indicated as F and G (fig. 156). Thermal feature G may be extreme south end of linear thermal feature D (fig. 151A), which disappeared as a continuous linear thermal feature by April 11. There was strong thermal emission from the southeast part of the crater May 2. Photograph by D. R. Hirst.

of the crater. The thermal pattern within the crater was north-south, perpendicular to the trend of the graben. Warm vapor emission from the crater was observed both instrumentally and visually. (2) A weak anomaly on the south slope of the north peak 2. Vapor emission was observed instrumentally from this area. (3) A strong anomaly on the north slope of north peak 2, corresponding to the infrared anomaly observed on April 11 near The Boot thermal area. (4) A cluster of at least four strong anomalies in the heavily fractured region of the upper Forsyth Glacier. (5) A weak anomaly with a linear pattern trending downslope, coinciding with historic thermal area B on the upper southwest flank of Mount St. Helens. Particular attention was paid to the Goat Rocks area, and no unusual features were observed.

The thermal pattern in the middle of the bulge (loc. F, figs. 155, 156) coincides with the scarps formed by normal faults on the north slope. These faults resulted from slumping in and beneath the upper Forsyth Glacier. Slumping probably occurred in response to earthquake-generated ground shaking and to over-steepening by the outward movement of the bulge. A daytime radiometric temperature measurement from

a helicopter on May 16 was 31°C for an area approximately 2 m across within the bulge anomaly, while nearby solar-heated ground surfaces ranged from 5° to 22°C (C. D. Miller, oral commun., 1980).

On May 2, The Boot thermal area produced the strongest infrared anomaly (loc. A, figs. 155, 156) outside of the crater and graben. The Boot thermal area also produced the highest radiometric temperature measurement on April 30, 37°C, in comparison with nearby background ice and rock temperatures of about -1°C (data courtesy of Charles Rosenfeld and the OANG).

The infrared anomaly on the north-bounding fault of the graben (G, fig. 156) occurred on the south slope of north peak 2; this area had a radiometric temperature of 29°C on April 30.

Figure 156.—Anomalous thermal features A, F, and G on north flank of the volcano, May 2; data obtained by U.S. Navy. Features shown are on The Boot (A), on the north bounding fault of summit graben at southeast slope of north peak 2 (G), and on highly fractured lower east part of the bulge (F). Crater and fracture pattern from May 1 photographs.

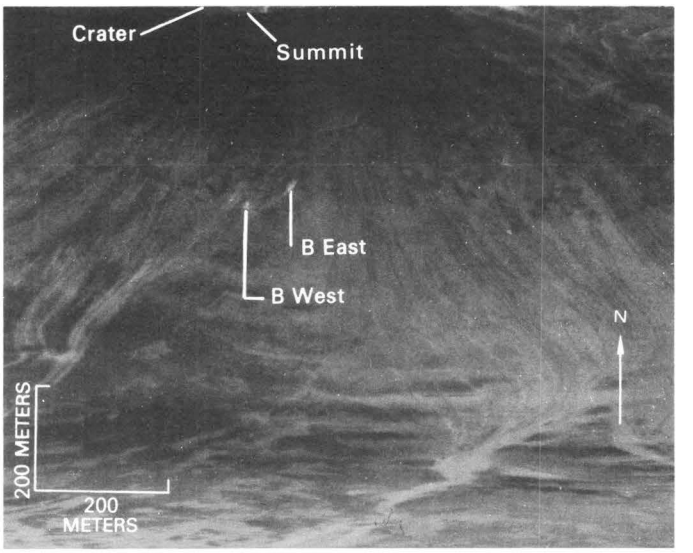

Figure 157.—Thermal-infrared image of historic thermal area B on May 16 at 0508. Image obtained by EG&G. Note that thermal area B has changed very little or not at all, while anomalous thermal activity on the north slope has increased significantly. The east and west features are listed separately in table 23.

MAY 16

Extensive digitally recorded, calibrated airborne infrared observations were made before dawn on Friday, May 16, but processing of these data was not carried out until the following Monday. Nine east-west flight lines were flown at each of 750 and 1,500 m above the summit. Both sets of observations cover the entire mountain above tree line. Strong thermal anomalies were observed in the southeast quadrant of the crater, on the steep slope of the graben just outside the southeast boundary of the crater, through an orifice near the top of Shoestring Glacier, and near the summit of north peak 2. Weaker anomalies were present in the west half of the summit crater and the graben wall just south of the crater, at many locations in the fractures near the north peaks, and at the base of the southeast flank of north peak 1 where it joins the nearly level graben floor. Several small thermal features were present in fractures through the upper part of Forsyth Glacier within the bulge. The historic southwest thermal area B appeared relatively unchanged from pre-1980 observations (fig. 157).

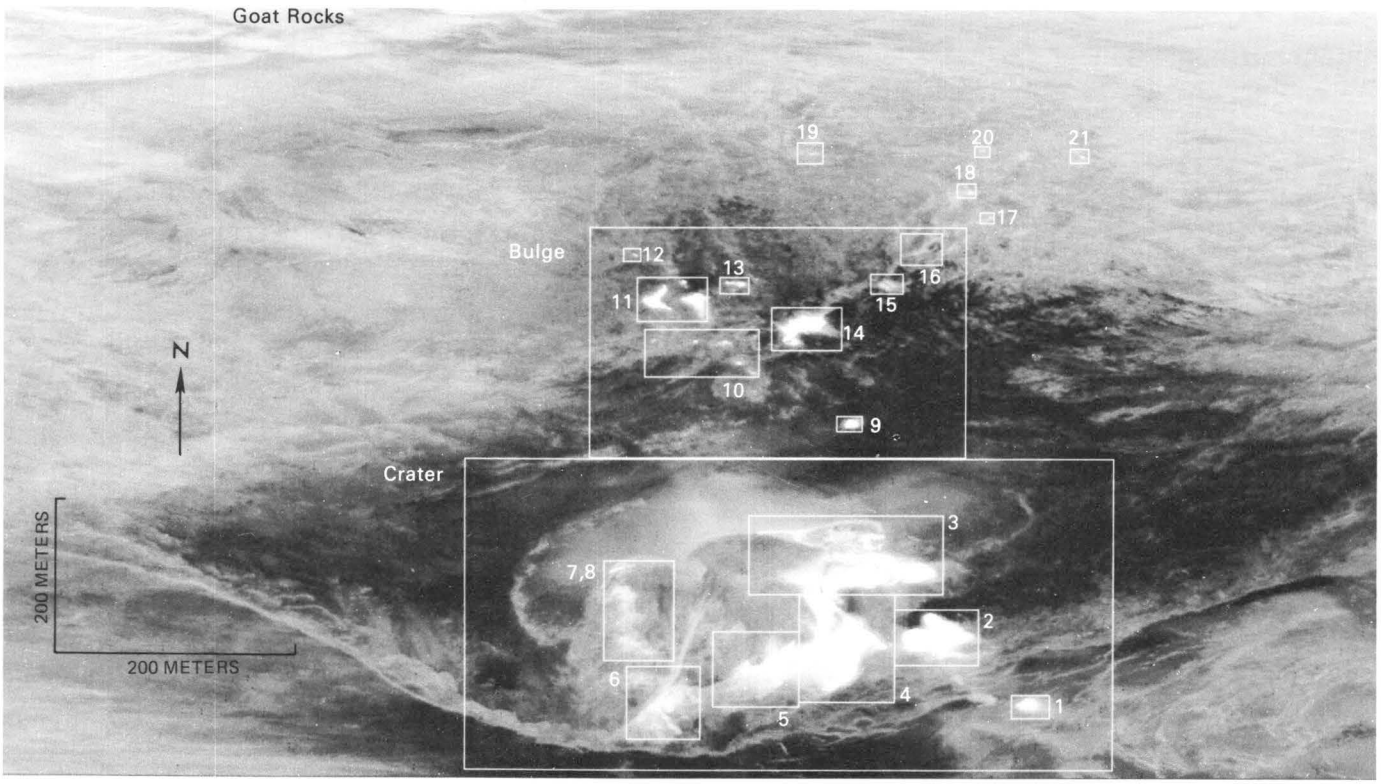

Figure 158—Thermal-infrared image of crater at 0503 on May 16; image obtained by EG&G. Individual areas analyzed for heat emission are indicated by small numbered rectangles; crater and bulge areas by larger rectangles. (See table 23 for analyses.) Ground temperatures range with altitude from −13° to −8°C in this image.

Areas of volcanogenic heat flow are identified in figure 158. Additional computer processing was done to increase the detail in the warmest areas and to remove most of the normal temperature variation associated with differences in altitude and slope (fig. 159). The number and spacing of the thermal features is suggestive of extensive near-surface heating. In particular, thermal area 14 (fig. 158), which corresponded to an area of recent slope failure, shows no evidence of an open fumarolic pathway to the surface, based on examination of aerial photographs at scale 1:2,500 taken 5 hr after the thermal survey. Nevertheless, most of the surface exposed by the slope failure was hot; an area of approximately 35 × 65 m was emitting approximately 57 KW (kilowatts) of excess radiation.

If there were no transport of heat by fluids moving up into a heated region, its apparent excess heat flow could be converted to an estimated subsurface temperature gradient. Making the conservative assumption that the excess radiance observed constitutes all of the excess heat flow, and using a nominal thermal conductivity of $1 Wm^{-1}K^{-1}$ (watts per meter kelvin), the thermal gradient for area 14 would be approximately 10 K/m; thus, a temperature of 400°C would be at a depth of only 40 m. Intense hydrothermal circulation probably supplied heat to this surface area, or, less likely, magma was extremely close to the surface.

Most of the thermal features identified in the May 16 predawn infrared survey have been located on high-resolution vertical photography obtained approximately 5 hr later (fig. 160). At the hottest locations, where temperatures were above 12°C, pits having no visible bottom were found. Steam plumes can be seen in the May 16 photography at thermal areas 2, 4, and 11. Vertical photography on May 12 shows the orifice at the top of the Shoestring Glacier to be steaming; it was open and steaming as early as May 7, according to visual observations.

The infrared surveys on May 16 recorded a much smaller area of anomalous heat discharge from the lower bulge area (loc. 18, fig. 158; loc. F, fig. 156), but greatly increased heat emission in the upper part

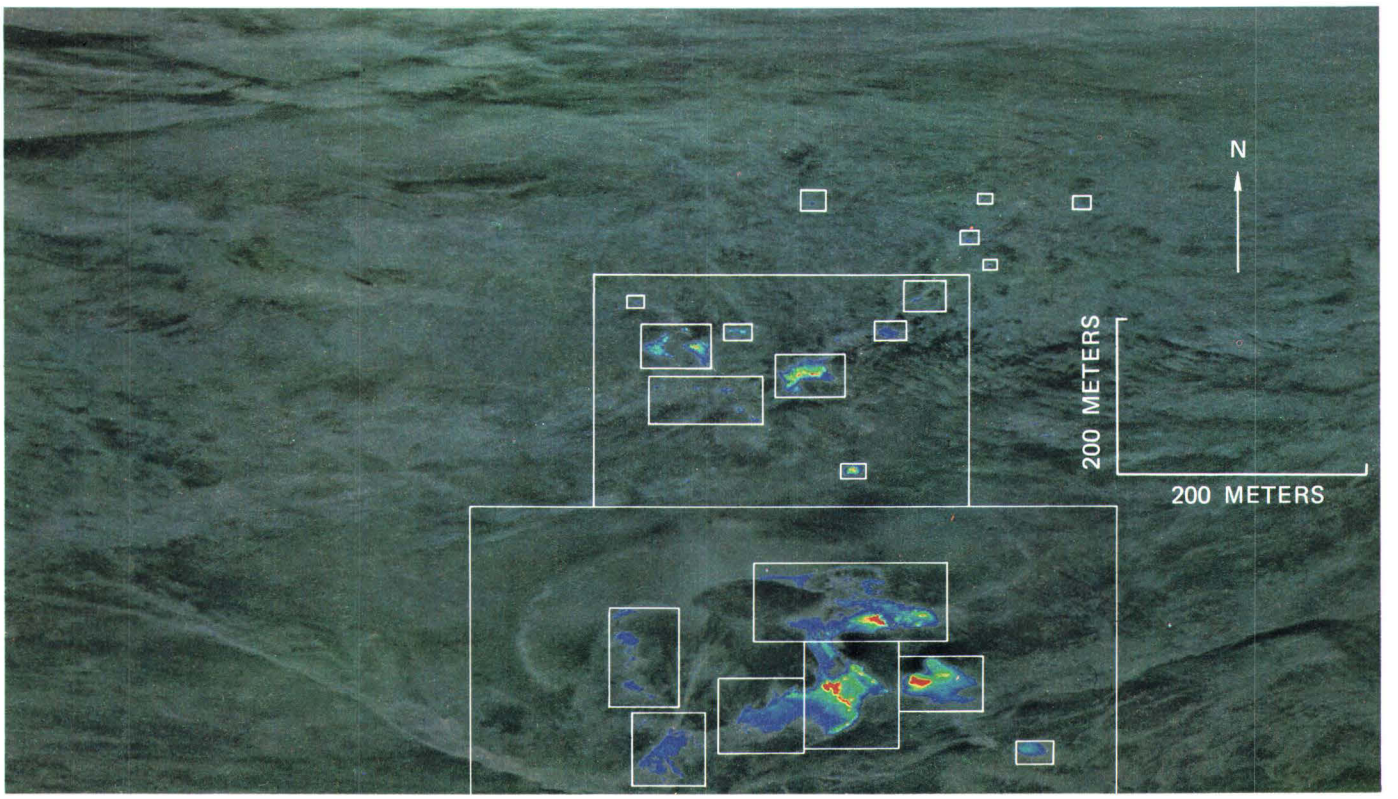

Figure 159.—False-color thermal-infrared image of crater, May 16 0503; image obtained by EG&G. General decrease in ambient ground temperature with increasing altitude has been removed by subtracting the array resulting from application of a quasi-Gaussian 65x65 pixel (approximately 150x130 m) low-pass filter to all areas below −6.8°C. The areas more than 1.5°C above their surroundings are color coded from blue to red (coolest to warmest).

of the bulge near The Boot and north peaks 1 and 2, compared to observations of May 2. One possible explanation is that as bulging progressed on the north slope, crack opening from tension-related slumping in and beneath the Forsyth Glacier changed to crack closing from compression-related bulging.

Two more infrared surveys were obtained before the major eruption of May 18 (Rosenfeld, 1980). These predawn observations by the OANG show thermal patterns similar to those on May 16, and also the development of two small thermal features in the upper Wishbone Glacier at approximately the location of the thermal anomaly seen from helicopter on April 11. There was apparently no major change in the pattern of thermal emission from Mount St. Helens during the last 50 hr prior to the major eruption that would have signaled its immediate occurrence.

Summing the excess radiant energy of each of the infrared anomalies identified in figure 158, and using the terrain immediately surrounding each anomaly as the natural radiation level, yields a total emitted excess radiant power from the summit of Mount St. Helens of approximately 1 MW (table 23). This procedure ignores the large areas only slightly above ambient temperature. A more inclusive procedure is to consider the crater and upper bulge areas as two larger regions, adapting background temperatures for each based on locations away from volcanic thermal sources. Using the two larger regions outlined in figure 158, with background temperatures of -10.76° and -11.17°C for the crater and bulge, respectively, the excess radiation is 2.3 and 0.34 MW, respectively, in these areas. All of the above calculations ignore the opacity of the atmosphere and presume graybody emission. Thus, a reasonable estimate of the excess radiant exitance from the summit area of Mount St. Helens on May 16 is 3 MW. The total geothermal heat flow is an unknown factor, probably large, greater than the excess radiance, as convective fumarolic flux, subglacial melting, and advective heat loss were likely major processes. The total power for these

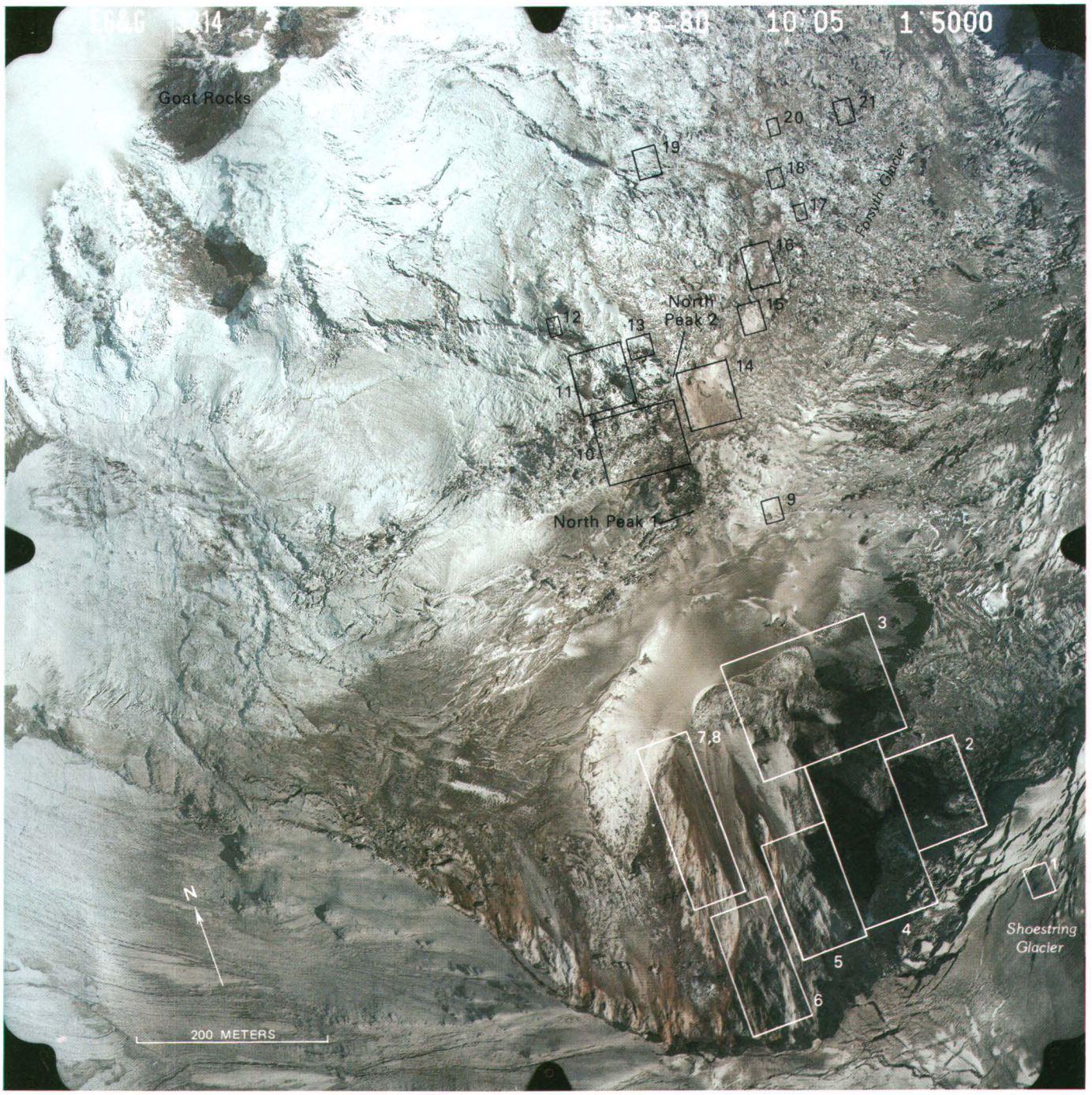

Figure 160.—Vertical photograph of summit crater and north flank, obtained at 1005 on May 16; photograph by EG&G. The regions of anomalous infrared emission are outlined by small rectangles (figs. 158, 159, and table 23). Anomalous areas on figures 158 and 159 were located on this photograph using a zoom-transfer scope; areas 17 through 20 are not reliably located because of the absence of features which could be positively identified in both images. Areas 1 through 4 and 11 were steaming on May 16. Areas 1, 2, 3, 10, 12, and 13 contain pits whose bottoms could not be seen. Areas 2 and 4 through 8 occur in rock below a steep ice cliff. An east- to northeast-facing cliff along areas 14 to 19 contains brown to pink-brown material that probably represents alteration along a preexisting fracture system; patches of similar material just to west of areas 20 and 21 may be the thermal sources for these areas. Western warm feature in area 11 probably corresponds to historic thermal area A (fig. 147). Slip surface of initial landslide on May 18 passes through areas 10, 11, and 14. The trace of the first and second failure surfaces is based on photographs 16 BK and 19 BK by Keith and Dorothy Stoffel. The lip formed by the second failure receded rapidly in the few seconds covered by the last two Stoffel photographs, which followed 19 BK (Stoffel and Stoffel, 1980).

Table 23.—Excess thermal radiation from Mount St. Helens, May 16, 1980

Location (fig. 158)	Background temperature (°C)	Maximum temperature[1] (°C)	Viewing angle degrees from vertical	Power[2] (KW)
1	-10.7	-4.4	37	13.2
2	-11.1	>13.3	30	131.0
3	-10.8	>13.3	23	240.0
4	-11.4	>13.3	30	290.0
5	-10.7	4.4	32	80.0
6	-10.8	-7.0	37	34.0
7, 8	-10.6	7.7	27	13.4
9	-11.9	7.9	6	9.1
10	-11.3	5.5	2	8.5
11	-11.2	7.8	7	26.0
12	-11.3	-8.1	12	.5
13	-11.4	2.6	9	3.2
14	-11.6	10.1	5	57.0
15	-11.7	-8.4	9	4.1
16	-10.9	-9.4	12	.7
17	-10.3	-8.6	16	.3
18	-10.4	-6.4	19	1.1
19	-10.5	-8.9	23	1.1
20	-10.3	-8.4	23	.4
21	-10.1	-7.1	23	.6
Total----------				910.0
Crater area	-10.8	>13.3	25	2,340.0
Bulge area	-11.2	10.1	3	338.0
Total----------				2,678.0
B[3] east	-10.6	-8.2	15	3.6
B[3] west	-10.5	-8.7	12	2.0
Total----------				5.6

[1]Maximum temperature listed is the highest recorded for the whole sample area of about 5 m^2. Much higher temperatures of smaller extent must have occurred within each area.

[2]Local slopes in the rugged terrain around the thermal features have not been accounted for individually. Several areas, notably 12 and 17-21, were oriented well away from the aircraft, and their values are seriously underestimated. An accurate calculation of local surface areas would increase the calculated radiated power of all areas by an average of about 15 percent.

[3]Thermal area B, fig. 157.

quiescent periods is two to three orders of magnitude smaller than that during even the minor eruptions. When geothermal fluids reach the surface, thermal radiation is often only a minor fraction of the power loss; the thermal energy released by steam exiting an orifice at 0.85 bar and condensing is 1.15 MJ/m^3 (megajoules per cubic meter), whereas the excess radiation of an orifice at the associated saturation temperature (95.5°C), relative to a background of -10°C, is 775 W/m^2. Thus, a steam-flow rate of only 0.00067 m/s could provide enough power to generate radiation corresponding to the maximum possible steam-heat temperatures. Most of the heat escaping from Mount St. Helens between eruptions was through a hydrothermal system: escape of steam to the atmosphere, and subglacial melting.

In the eruption of Mount St. Helens on May 18, all the areas known to ever have had excess thermal emission were removed.

STRUCTURAL CONTROL OF HEAT EMISSION

Convective heat discharge from volcanoes usually occurs in localized areas of high permeability, particularly faults, fractures, or brecciated zones. Thus, the pattern of thermal anomalies can provide clues to the nature of structures within the volcanic edifice.

Figure 161 shows infrared anomalies recorded on May 16. Figure 162 is a cross section through the upper cone of Mount St. Helens and shows the locations of the anomalies projected onto the plane of the section. By combining the thermal pattern with what is known of the pre-1980 geology (C. A. Hopson, un-

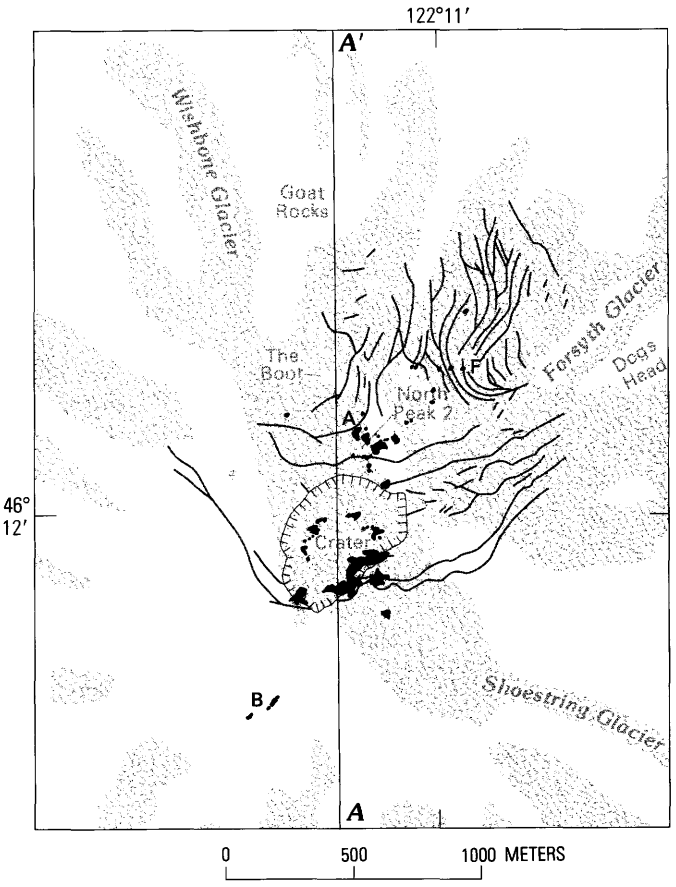

Figure 161.—Anomalous thermal features in and near summit crater recorded by EG&G on May 16 and by OANG on May 18. Thermal features shown are in crater, at The Boot (A), on southwest flank (B), and in central area of bulging north flank (F). All features except A and B were newly developed between March and early May 1980. Crater and fracture pattern from May 1 photographs. Section A-A′ shown in figure 162.

pub. mapping) and the sequence of eruptive activity and observed ground breakage, the structures within the upper cone can be inferred.

This analysis suggests that the pre-1980 thermal areas on the southwest slope (B) and The Boot (A) occurred along inward-dipping brecciated zones associated with the lower margin of the old summit dome. Ground shaking from the late-March earthquake swarm, explosive phreatic eruptions in March and April, and perhaps magmatic pressure, cracked the summit dome in half and shattered the northern part of the dome and underlying cone. The resulting increased permeability through the northern slope allowed greater heat discharge at The Boot. By early May, increased heat emission developed in areas downslope from The Boot (F, fig. 161). The cluster of heat emission on The Boot just north of north peak 2 (including historic thermal area A) coincided with the top of the initial landslide scarp of May 18. The locations of the most intense thermal emission on May 16 were along and adjacent to the slip surface for the second slide of the May 18 slope failures.

SUMMARY OF THERMAL EMISSION

1. The historic southwest thermal area (B) remained unchanged during the eruptive sequence. Its connective pathway to the heat source probably had a time constant greater than 60 days.

2. The area of the historic thermal anomaly at The Boot (A) was involved in the initial structural failure of the summit and showed increasing thermal activity throughout the pre-May 18 eruptive sequence.

3. New areas of thermal emission were initially confined to the crater, and, for a short time, one loca-

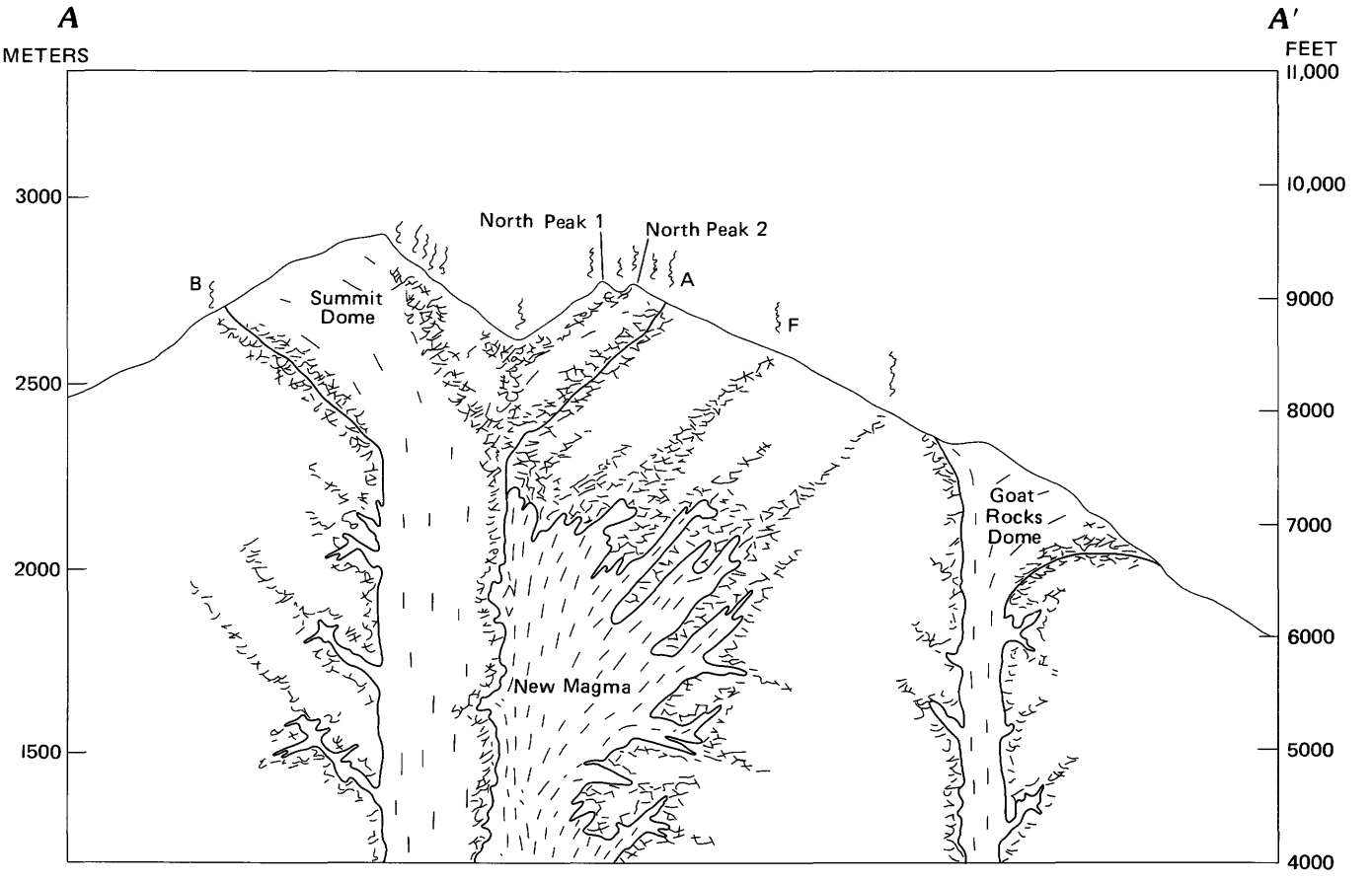

Figure 162.—Schematic north-south cross section A-A' through summit just prior to May 18 eruption, showing inferred brecciated zones (cross-hatching). Those zones marginal to summit dome localized heat emission through the pre-1980 thermal areas on The Boot (A) and southwest slope (B). New eruptive activity in 1980 was centered over the north part of the summit dome where newly developed brecciated zones controlled the location of hydrothermal emission, and perhaps new magma. There is no evidence for a conductive pathway between new magma and either area B or the Goat Rocks dome. Areas of anomalous thermal emission such as feature F (figs. 158 and 159) are shown by short vertical squiggles. One possible geometry of a new magma body is shown schematically as a set of northward-directed dike and cone sheets; the plane of one such dike is projected onto the section.

tion on the eastern part of the fault bounding the summit graben on the south.

4. Heat emission from bedrock locations near the top of the bulge, once established, showed continuous activity. Thermal areas within glaciers were more variable with time.

5. The only new thermal feature south of the summit graben (Shoestring Glacier orifice) was first recorded only 11 days before the May 18 eruption.

6. The two clusters of thermal infrared anomalies mapped on May 16 occurred on surfaces of failure of the May 18 landslides.

7. Mixing with ambient air rapidly cooled the visible exterior of eruptive columns.

CONCLUSIONS CONCERNING THERMAL INFRARED OBSERVATIONS FOR VOLCANIC MONITORING

1. Predawn airborne thermal infrared observations using current technology allow sensitive surveys for new volcanogenic features. Such surveys can cover all of the area of likely activity for one volcano in one flight mission.

2. Determining a baseline thermal emission pattern prior to eruption is extremely valuable.

3. Daytime (midday to evening) observations are of considerably less utility than predawn observations, particularly where steep terrain and large albedo changes are involved. Geothermal features that can be unambigiously identified by daytime thermal infrared observations will commonly be distinctive visually.

4. A portable thermal imaging system is of great utility, particularly for evaluating reports of hot spots based on visual observations. An aircraft-based video recording system is the most useful for hazard analysis, as thermal observations can be reexamined carefully and compared to conventional photography. Predawn, calibrated scanner surveys are preferred for detection of small changes and for monitoring large areas. Nonrecording thermal imaging systems have the convenience of great portability, but their use is exhausting under the adverse conditions likely to be encountered in volcanic monitoring (for example, cold helicopters in high winds over irregular terrain, one eye viewing red equals warm, and reversed contrast in the other eye, which views white equals bright), which aggravates the problem of accurate location of geothermal features. Fixed-wing aircraft are more stable but commonly do not allow window removal (thermally sensitive systems must either be externally mounted or be used through open windows). Instruments of low angular resolution have an additional disadvantage of not being able to make extensive predawn thermal surveys, as close-to-terrain flights in the dark are hazardous.

5. The current time for production of calibrated thermal images is too long to provide information for civil authorities during hazardous volcanic activity. In the near future, uncalibrated, film- or video-recording thermal-imaging systems are likely to be most suitable for hazard assessment, whereas calibrated, digitally recorded observations will provide the basis for determining long-term variations.

REFERENCES CITED

Crandell, D. R., and Mullineaux, D. R., 1978, Potential hazards from future eruptions of Mount St. Helens Volcano, Washington: U.S. Geological Survey Bulletin 1383-C, 26 p.

Friedman, J. D., and Frank, David, 1978, Thermal surveillance of active volcanoes using the LANDSAT-1 data collection system, Part 3—Heat discharge from Mount St. Helens, Washington: U.S. Geological Survey Open-File Report 77-541, 30 p.

———1980, Infrared surveys, radiant flux, and total heat discharge at Mount Baker volcano, Washington, between 1970 and 1975: U.S. Geological Survey Professional Paper 1022-D, 33 p.

Lawrence, D. B., 1939, Continuing research on the flora of Mount St. Helens: Mazama, v. 21, no. 12, p. 49–54.

Majors, H. M., 1980, Mount St. Helens series: Northwest Discovery, v. 1, no. 1, p. 4–51.

Moxham, R. M., 1970, Thermal features at volcanoes in the Cascade Range, as observed by aerial infrared surveys: Bulletin Volcanologique, v. 34, no. 1, p. 77–106.

Phillips, K. N., 1941, Fumaroles of Mount St. Helens and Mount Adams: Mazama, v. 23, no. 12, p. 37–42.

Preble, D. M., Friedman, J. D., and Frank, David, 1977, Surveillance of active volcanoes using the LANDSAT-1 data collection system, Part 5—Electronic thermal sensor and data collection platform technology: U.S. Geological Survey Open-File Report 77-87, 64 p.

Rosenfeld, C. L., 1980, Observations on the Mount St. Helens eruption: American Scientist, v. 68, no. 5, p. 494–509.

Sekioka, Mitsuru, and Yuhara, Kozo, 1974, Heat flux estimation in geothermal areas based on the heat balance of the ground surface: Journal of Geophysical Research, v. 79, no. 14, p. 2053–2058.

St. Lawrence, William, Qamar, Anthony, Moore, Johnnie, and Kendrick, George, 1980, A comparison of thermal observations of Mount St. Helens before and during the first week of the initial 1980 eruption: Science, v. 209, no. 4464, p. 1526–1527.

Stoffel, D. B., and Stoffel, K. L., 1980, Mount St. Helens seen close up on May 18: Geotimes, v. 25, no 10, p. 16–17.

THE 1980 ERUPTIONS OF MOUNT ST. HELENS, WASHINGTON

THERMAL INFRARED SURVEYS OF THE MAY 18 CRATER, SUBSEQUENT LAVA DOMES, AND ASSOCIATED VOLCANIC DEPOSITS

By JULES D. FRIEDMAN, DAVID FRANK, HUGH H. KIEFFER, *and* DON L. SAWATZKY

ABSTRACT

Qualitative infrared images in the 8- to 11.5- and 8- to 14-μm (micrometer) spectral region were obtained over Mount St. Helens by forward-looking and vertical-mount aerial scanning systems on May 31, June 3, 6–8, and 19, and July 15, 1980. Quantitative or calibrated images were obtained on August 11–13, 19, and 20. Night and predawn infrared images, obtained during times of diurnal surface-temperature minima, depict the spatial pattern of high thermal emission associated with the crater and vent area on June 7 and 8. Following the eruption of June 12, the emergence of a dacite dome was confirmed by radar images on June 13, and subsequently on June 15 by visual observation. The infrared images of June 19 show a concentric and annular distribution of thermal emission associated with the emergent dome. On June 19 the emergent dome, the rampart, and a southeast-striking fracture controlling alinement of fumaroles within the crater floor area were studied in detail, using three different scanning systems. A large circular area also appears in the images of June 19 southeast of the dacite dome; it is about equal in size to the dome and is outlined by a ring of fumaroles. Infrared images of July 15 show the annular and radial fracture pattern of the dome prior to its destruction on July 22. An en-echelon set of northwest-striking fractures in the crater and amphitheater region are also clear on the July 15 image. These fractures appear related to the location of the first and subsequent lava domes and at least two of three smaller hot spots. The calibrated surveys of August 13–17 give the temperature of the partly cooled rind of the August dome and the day-night temperature differences of an array of pyroclastic-flow deposits, as well as the temperature of Spirit Lake, several secondary phreatic fumaroles, and surrounding terrain.

INTRODUCTION

Infrared surveys at Mount St. Helens from the early 1970's through the cataclysmic eruption of May 18, 1980, are described in Kieffer and others (this volume); in that report, the evolution of points of convective thermal emission, initially at the contacts of the summit dome dacite with older geologic

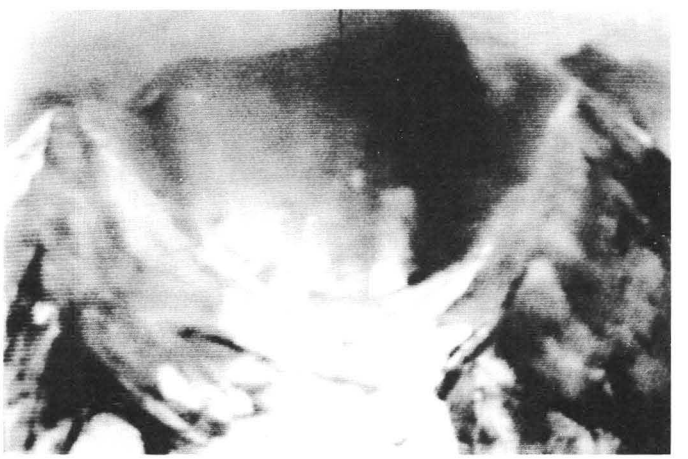

Figure 163.—FLIR oblique thermographic image of crater, looking south into amphitheater, May 31, 1980, mission time 1700–1830 PDT; 8–11.5 μm spectral region. Shows thermal emission (white = hot) associated with pyroclastic deposits and fumarolic emission. No evidence of dome.

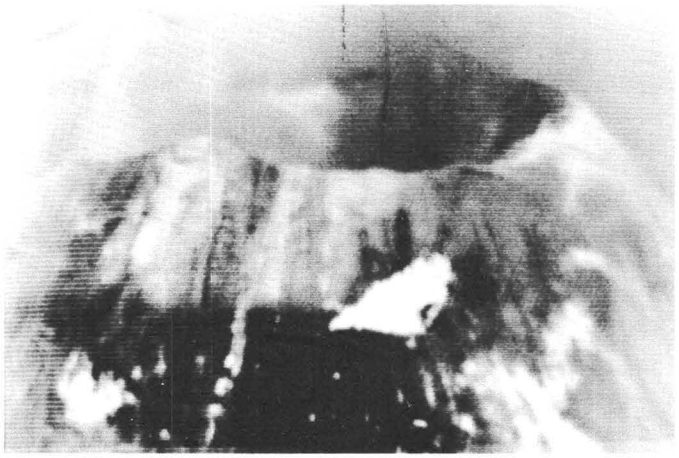

Figure 164.—FLIR oblique thermographic image, looking east at outer west rim, May 31, 1980, 1700–1830 PDT; 8–11.5 μm spectral region. Warm and hot areas (white) on outer slope may be pumice-fall deposits.

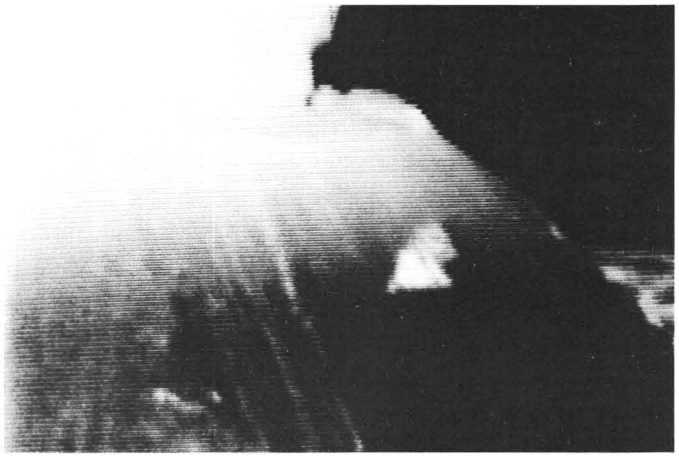

Figure 165.—FLIR oblique thermographic image, looking east, June 3, 1980, 0643–0930 PDT; 8–11.5 μm spectral region. Shows persistent warm or hot triangular area on west slope and warm vapor column from crater.

Table 24.—Temperature calibration for RS–14A scanner, 8–14 μm channel, August 13, 1948–1951 PDT

[Flight line 9A north; hot blackbody image brightness = 179; V = 4.491 = 52.6°C; cold blackbody image brightness = 86; V = 1.825 = 5.2°C; refers to fig. 173*D*]

Radiometric temperature °C	Image brightness units	Color
<5.7	0–87	Blue.
5.7– 9.8	88–95	Blue/cyan.
9.8–13.9	96–103	Cyan.
13.9–18.0	104–111	Cyan/green.
18.0–22.0	112–119	Green.
22.0–25.6	120–126	Green/yellow.
25.6–29.2	127–133	
29.2–32.7	134–140	
32.7–36.3	141–147	Yellow.
36.3–39.9	148–154	
39.9–43.5	155–161	Orange.
43.5–47.0	162–168	
47.0–55.7	169–185	
55.7–90.9+	186–255	Red.

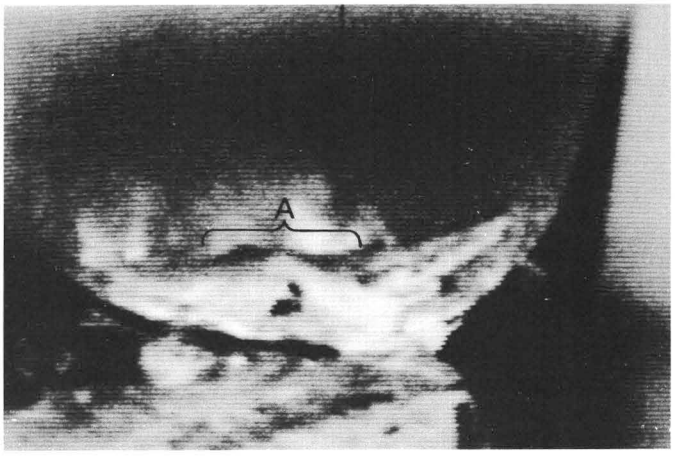

Figure 166.—FLIR oblique thermographic image, looking south from 4.8 km distance, June 7, 1980, 0510–0711 PDT. Shows crater-area thermal emission and first incidence of low, relatively cool topographic feature on crater floor (A), which may mark rise of June dome to near-surface or preemergent position.

materials, is traced through time, culminating in the complex thermal-emission pattern at the volcano's summit crater and upper margin of the Forsyth bulge on May 18. After the cataclysmic eruption, primary thermal emission patterns were controlled by structures within the newly formed amphitheater, and secondary thermal emission was associated with volcanic deposits and phreatic fumaroles within the devastated area, mostly between the volcanic edifice and Spirit Lake.

The purpose of aerial infrared surveys of the Mount St. Helens volcanic area during the June–August 1980 period was to provide two-dimensional

Table 25.—Temperature calibration for RS-14A scanner, 8-14 μm channel, August 13, 1941-1943 PDT

[Flight line 9 south; hot blackbody image brightness = 200; V = 4.491 = 52.6°C; cold blackbody image brightness = 11; V = 1.825 = 5.2°C; refers to fig. 173C]

Radiometric temperature °C	Image brightness units	Color
<6.0	0-14	Blue.
6.0-11.2	15-35	Blue/cyan.
11.2-16.5	36-56	Cyan.
16.5-21.7	57-77	Cyan/green.
21.7-27.2	78-99	Green.
27.2-31.7	100-116	Green/yellow.
31.7-36.2	117-134	
36.2-40.7	135-153	
40.7-45.0	154-170	Yellow.
45.0-49.2	171-187	
49.2-53.5	188-204	Orange.
53.5-57.7	205-221	
57.7-62.0	222-238	
62.0-66.2+	239-255	Red.

Table 26.—Temperature calibration for RS-14A scanner, 8-14 μm channel, August 13, 0530 PDT

[Flight line 9 south]

Radiometric temperature °C	Image brightness units	Color	Radiometric temperature °C	Image brightness units	Color
Figure 173B			Figure 173A		
<3.3	0- 62	Blue.	<14.6	0- 89	Blue.
3.3- 6.2	63- 69	Blue/cyan.	14.6-16.7	90- 94	
6.2- 9.2	70- 76	Cyan.	16.7-18.8	95- 99	Blue/cyan.
9.2-12.1	77- 83	Cyan/green.	18.8-20.9	100-104	
12.1-14.6	84- 89	Green.	20.9-22.6	105-108	Cyan.
14.6-19.3	90-100	Green/yellow.	22.6-24.7	109-113	
19.3-23.9	101-111		24.7-26.8	114-118	Cyan/green.
23.9-28.5	112-122	Yellow.	26.8-28.9	119-123	
28.5-33.1	123-133		28.9-30.6	124-127	Green.
33.1-37.7	134-144	Orange.	30.6-32.7	128-132	
37.7-42.4	145-155		32.7-34.8	133-137	Green/yellow.
42.4-84.4+	156-255	Red.	34.8-36.9	138-142	
			36.9-38.6	143-146	Yellow.
			38.6-40.7	147-151	
			40.7-42.8	152-156	Orange.
			42.8-44.9	157-161	
			44.9-84.4+	162-255	Red.

thermal data on structural control of heat emission in the areas of active volcanic processes, and to monitor the volcano for evidence of increased heat flow or increased volcanic activity at any new locations, especially on its flanks. Many of the features observed during this period were still relatively inaccessible to field investigation at least part of the time, and ground temperatures around the crater rim and dome surfaces were not well known at the time of the surveys. The images obtained show structure patterns that can be correlated with fracture systems in the crater-floor area and around margins of the June dome and August dome. The calibrated images obtained in August also provide direct information on radiometric surface temperatures and differential radiant exitance from various surfaces. Night and predawn infrared images, obtained during times of diurnal surface temperature minima, were used for these objectives.

ACKNOWLEDGMENTS

We gratefully acknowledge the work of R. Kipfinger, M. Steward, I. Friedman, and M. Veatch in successfully carrying out the USGS Queenair aircraft mission to obtain infrared data over Mount St. Helens between August 11 and 13, 1980. C. Nelms and S. Simpson helped convert high-density analog data tapes to digital form, prepared shade prints and histogram analyses, and prepared color-coded positive transparencies of the calibrated images using an image-processing laboratory of the USGS, Denver, Colo. To these USGS scientists, technicians, and pilots we owe our thanks as we also do to C. Rosenfeld of Oregon State University and J. Casey of FLIR Systems, Inc., Lake Oswego, Oreg., who provided thermograms and infrared images published in this report.

HELICOPTER-BASED THERMAL OBSERVATIONS AFTER MAY 18

Helicopter-based observations using a Hughes ProbEye video-recording system were made May 20, 24, 30, and 31, and also through June with a forward-looking infrared scanner (FLIR).[1] On May 20 thick haze severely hampered measurements, and only the west and northwest azimuths were accessible. Small fires and hot spots within debris flows were located. At 1600 PDT May 20, the pyroclastic deposits on the

[1]FLIR thermographic images published with permission of FLIR Systems, Inc., Lake Oswego, Oreg.

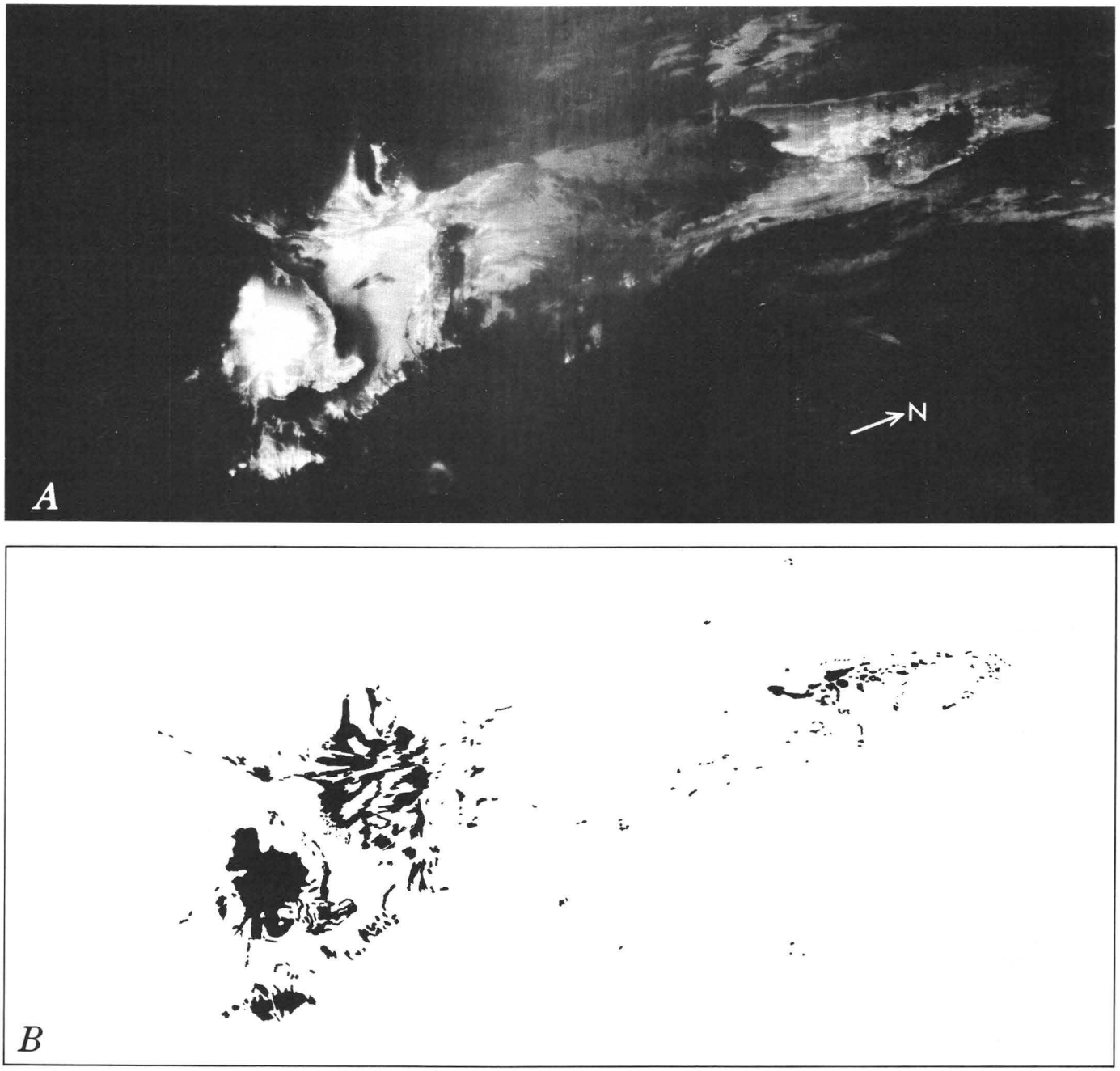

Figure 167.—Vertical thermal image of crater floor. Area where dome emerged on about June 12 appears warmer than on earlier images (fig. 166). AAS-24A scanner thermal image from Oregon Army National Guard. June 8, 1980, 2128 PDT; 8–14 μm region. Hottest areas appear white on A and black on B.

west and northwest flanks of Mount St. Helens had about 8° to 10°C variation.

The May 24 observations, made largely below thick clouds, covered the east and north sides of Mount St. Helens. Small fires were abundant northeast of the mountain. No primary heat sources were found on the flanks, although many secondary heat sources were active in the debris-avalanche deposits southwest of Spirit Lake.

On May 30 the pyroclastic deposits within gullies on the upper flanks (above 1,830 m) typically were 6°C warmer than the ridges covered by thin ash. The maximum thermal contrast observed on the flanks was 15°C (ignoring the general cooling at higher

Figure 168.—FLIR oblique thermographic image, looking south from a distance of 13 km. June 19, 1980, 0500–0600 PDT. Vertical exaggeration results from incorrect aspect ratio of image. Strong thermal emission from crater area, including dome (arrow) that by this time was 65 m in height above crater floor. Area to southeast (left and rear of dome) appears warm to hot. Warm pyroclastic-flow deposits in area of ramp are prominent.

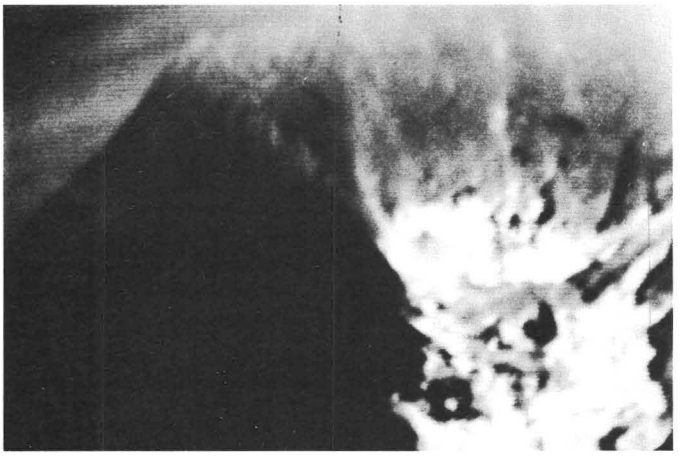

Figure 169.—FLIR oblique thermographic image, looking south from a distance of 4.8 km. June 19, 1980, 0500–0600 PDT; 8–14 μm spectral region. Vertical exaggeration results from incorrect aspect ratio of image. Dome is distinct from a circular warm area to the southeast within the crater. Rampart just north of dome remains cool. Closer position of scanner (relative to figure 168) provided increased resolution of dome.

elevations). Thermal layering was apparent in cliffs of the May 18 ash deposit exposed near the crater floor. Temperature contrasts were as much as 40°C, although the most active locations were obscured by

Table 27.—Differential radiant exitance in W/m² for three color-coded temperature levels at Mount St. Helens, August 13, 1948–1951 PDT

[Refers to figure 173*D*]

Color code for fig. 173D	°C	K	$W d\lambda_1$ (W/m^2)	$W d\lambda_1 - W d\lambda_2$ ($279K=0.437 \times 10^2$ W/m^2)	W/m^2
Yellow----	32.7-36.3	306-310	5.116×10^2	4.643×10^2	464
Orange----	39.9-43.5	313-317	5.600×10^2	5.127×10^2	513
Red-------	55.7-91.4	329-365	8.242×10^2	7.769×10^2	777
Incandescent (proper point).	525	798	$4.321.10^3$	4.274×10^3	4,274
Lava------	850	1,123	2.967×10^4	2.962×10^4	29,620

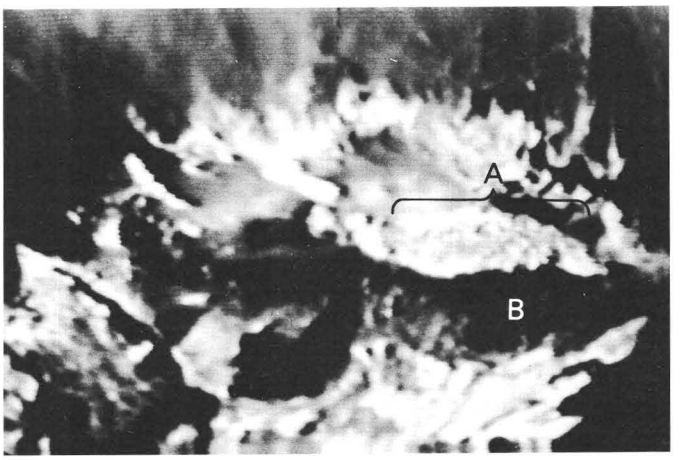

Figure 170.—FLIR oblique thermographic image, looking south from a distance of 1.6 km. June 19, 1980, 0500–0600 PDT. Vertical exaggeration results from incorrect aspect ratio of image. Good depiction of thermal structure of crater and dome (A). Rampart (B, dark) across middle ground remains cool. Southeast-trending thermal lineaments (fumarole alinements) appear east (left) of dome. Note thermal variations on dome surface.

steam. The thermal activity was most intense in the northwest sector of the crater floor.

On May 31 a warm, thick pyroclastic deposit was evident low on the northeast flank near Windy Pass. The warmest ash deposits outside the crater, however, were near the crater rim, immediately northeast of the Shoestring Glacier saddle.

INFRARED IMAGES OF JUNE DOME AND ASSOCIATED DEPOSITS

The thermal emissions associated with the June dome, the volcanic edifice, and related deposits are depicted in uncalibrated oblique and vertical

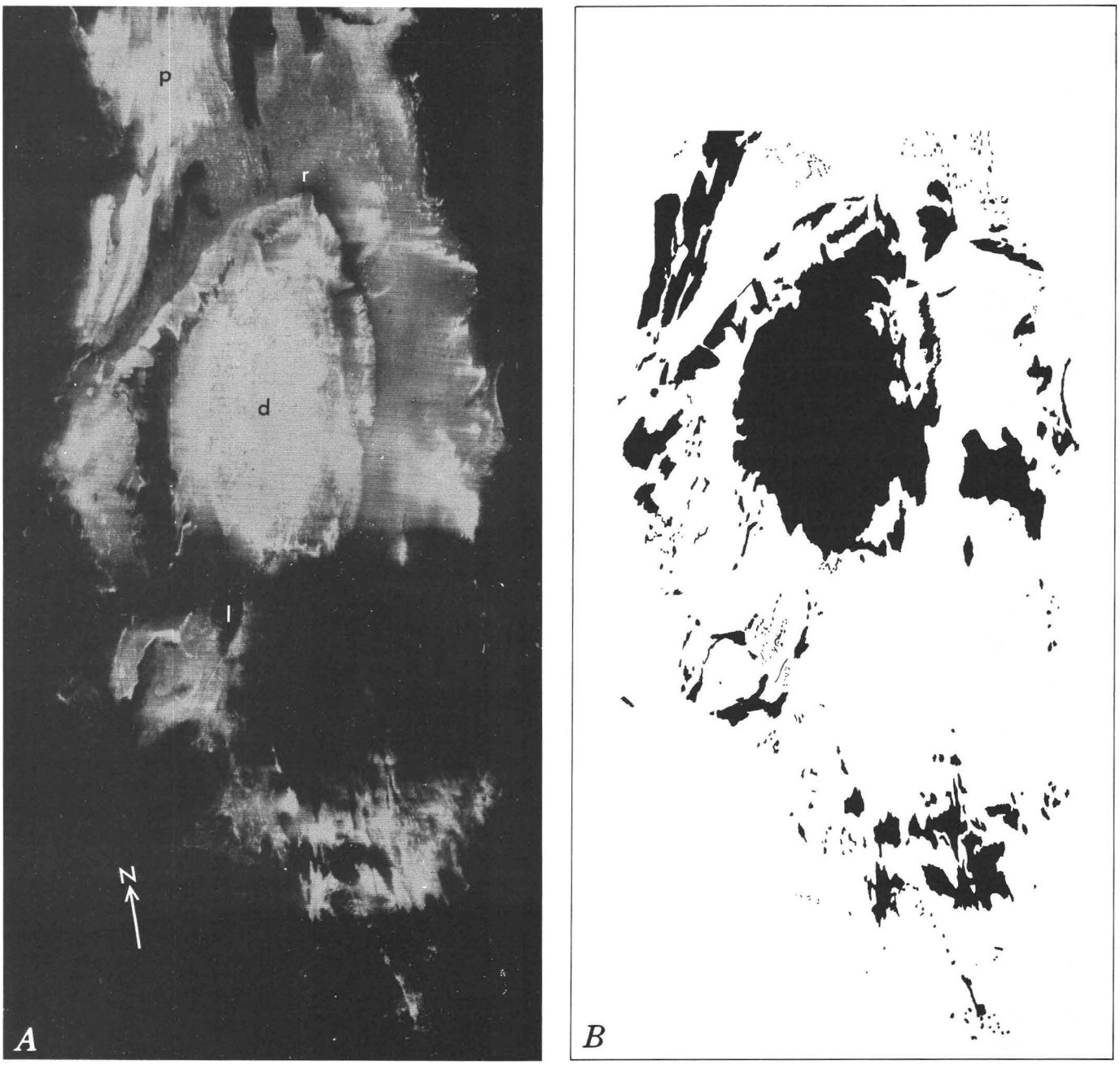

Figure 171.—Thermal details of emergent dome (d), cool tephra rampart (r), and warm surfaces of pyroclastic deposits (p) on ramp extending northward out of amphitheater toward Spirit Lake. Within crater area, alined fumaroles demarcate southeast-striking fractures, one of which passes beneath a small lake (l, dark = cool) on crater floor. Dark area (cool) southeast of dome, between dome and inner walls of amphitheater and about equal in area to dome, is outlined by a ring of fumarolic emission. Hottest areas appear white on A and black on B. AAS-24A scanner vertical thermal image from Oregon Army National Guard. June 19, 1980, 1000 PDT.

images made between May 31 and July 15, 1980 (figs. 163–172). These images depict locations of hot pyroclastic deposits, warm ground within the crater, and the evolution of the June dome. A triangular patch of ash high on the northwest flank that was first observed on May 20 remained thermally distinct through June 3 (figs. 164, 165).

The emergence of the June dome can be dated within limits by the infrared images. On May 31 no thermal expression of a near-surface dome is evident

(fig. 163). In contrast, by June 7 a low and relatively cool topographic feature is apparent on the crater floor (fig. 166), possibly indicating the rise of the June dome close to the surface. Other images show hot areas on the crater floor where the dome subsequently appeared (fig. 167). Following the eruption of June 12, a radar image (not figured) showed an emergent dome on June 13 (1415 PDT), providing a a basis for estimating the rate of dome growth and its energy yield (Friedman, Olhoeft, and others, this volume). Other images obtained in late June and early July show thermal emission from the dome and the still-warm June 12 pyroclastic-flow deposits (figs. 168–171).

The best thermal image obtained between the eruption of June 12 and July 22 (fig. 172) depicts structures of the crater floor and amphitheater. Radial and concentric fractures are well developed on the June dome, and en-echelon fractures east of the dome appear related to the location of the dome and at least one smaller hot spot farther northeast. Individual fractures strike northwest, but the en-echelon set trends north-northeast and includes an alined fracture on the dome surface.

INFRARED IMAGES OF THE AUGUST DOME AND PYROCLASTIC-FLOW DEPOSITS

Calibrated infrared images of the dome that emerged on August 7, obtained by the USGS on August 11–14, were color coded by computer processing (fig. 173). A linear temperature scale between 0°C and 50°C provides calibration (tables 24–26) and relates color coding to integrated radiometric temperature increments. An approximately trimodal temperature distribution separates ambient terrain (< 5° to 17°C) from pyroclastic flow deposits (18° to 32°C) and thermal features of the amphitheater (32°

Figure 172.—Thermal emission from crater floor and amphitheater. Dome fracture pattern (1) is radial and concentric or annular, giving spiderweb appearance. En echelon fractures (2) east of dome appear related to location of dome and a smaller hot spot northeast of dome. Individual fractures strike northwest, but en-echelon set trends north-northwest. A fracture in dome surface (3) appears alined with the southernmost northwest-striking fracture. Another smaller hot spot or vent appears to be controlled by this alinement. Inset shows, in more detail, spiderweb and annular fracture patterns of dome. AAS-24A scanner vertical thermal image from Oregon Army National Guard. July 15, 1980, 2030 PDT.

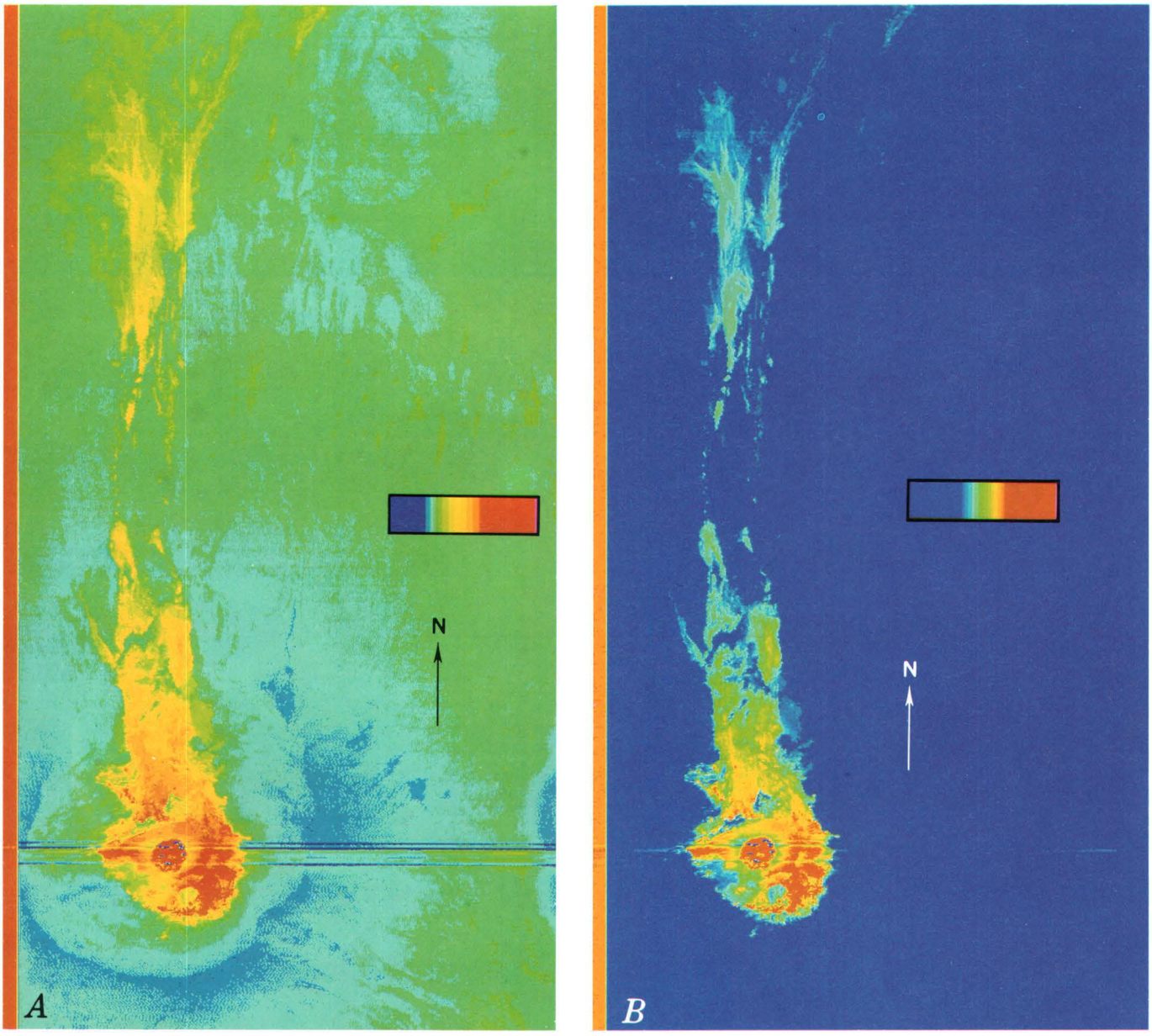

Figure 173.—Vertical thermal images of Mount St. Helens. RS-14A scanner; 8–14 μm region; 4,572 m flight altitude. U.S. Geological Survey calibrated color-coded images processed by computer; 3 mrad (milliradian) spatial resolution. Vertical stripe on side of image indicates color-coded temperature of upper blackbody of RS–14A scanner. A, August 13, 0530 PDT. Color-coded image showing thermal details of figure 173B, based on finer color coding of hotter regions. B,

to >90°C). The August dome has the highest temperatures, although its carapace had cooled significantly since its emplacement. A concentric pattern in the August dome may delineate growth ridges or annular fractures, as in the June dome. East-southeast of the August dome is a "hot spot," perhaps the same as that appearing on the image of July 15 (fig. 172). Northwest-striking alined hot spots delineate two of the three fractures seen prominently on July 15 (fig. 172). The middle northwest-striking fracture of the July 15 image (fig. 172) is obscured on the image of August 13 (fig. 173*D*) by the cold pattern (dark blue) caused by a vapor plume or cloud in the southeast quadrant of the amphitheater.

Surfaces of the pyroclastic-flow deposits have temperatures slightly higher than their surroundings,

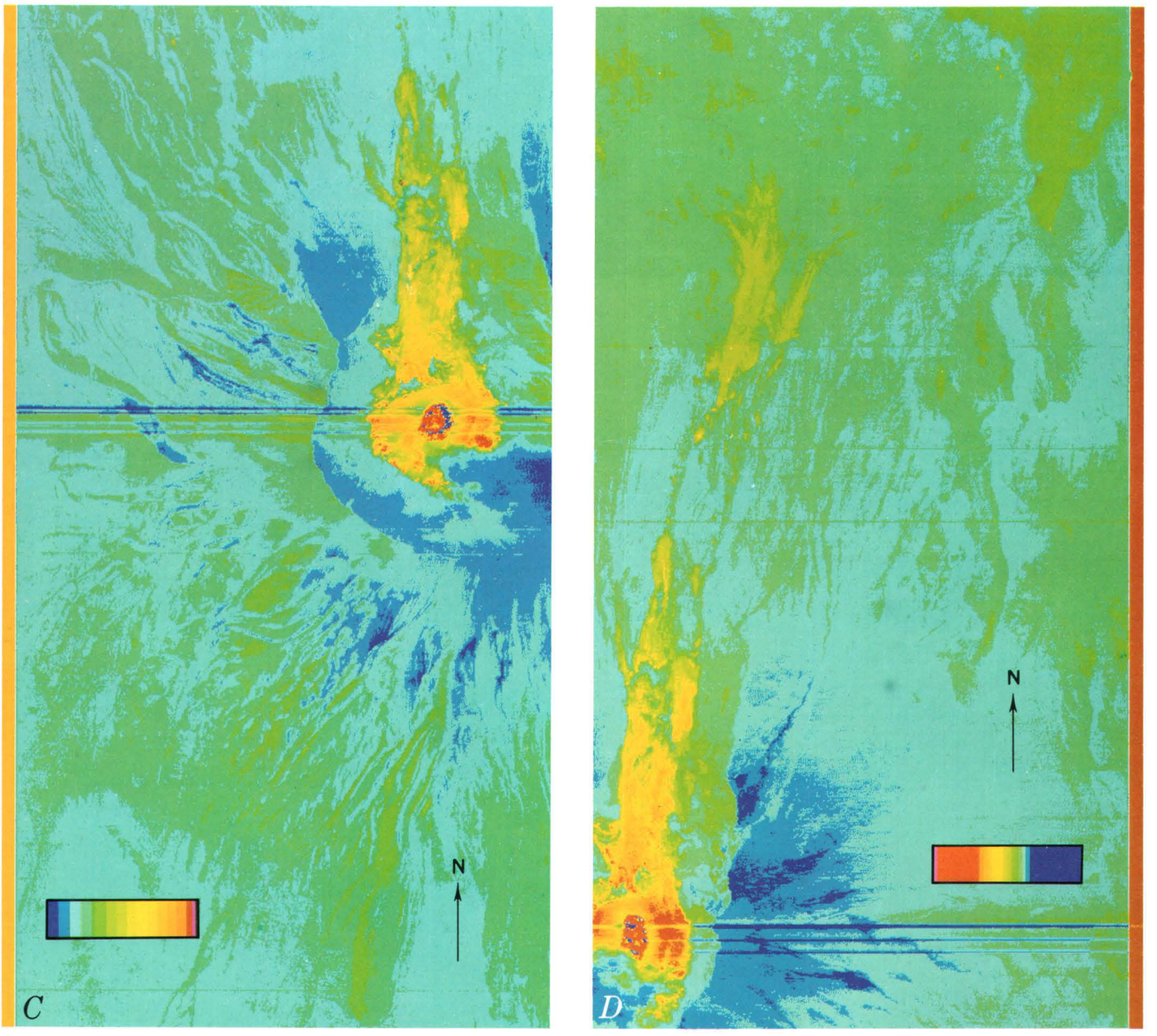

August 13, 0530 PDT, showing crater, dome, amphitheater, and pyroclastic-flow deposits. C, August 13, 1941-1943 PDT, showing crater, amphitheater, and pyroclastic-flow deposits. D, August 13, 1948–1951 PDT, showing crater, amphitheater, and pyroclastic-flow deposits.

both in the late evening and also in the early morning, attesting to continuing heat loss from the cores of these flows.

The August dome (figs. 174, 175*C*) appears as a hot core in the crater. A roughly concentric pattern of heat emission also occurs along the inner wall of the crater, but expands into a particularly extensive area across the southeast part of the crater floor. The more intense pattern represents areas of fumarolic activity or the hot dome surface. The less intense, diffuse background pattern represents pyroclastic deposits that fill the crater and extend down the north flank of the volcano. Individual thermal lineaments are associated with a 15–m-wide dike on the south wall (fig. 174) and with ground fractures. Most of the fractures occur in new pyroclastic deposits, perhaps from settling, but one northwest lineament on the west crater wall is probably related to a major structural

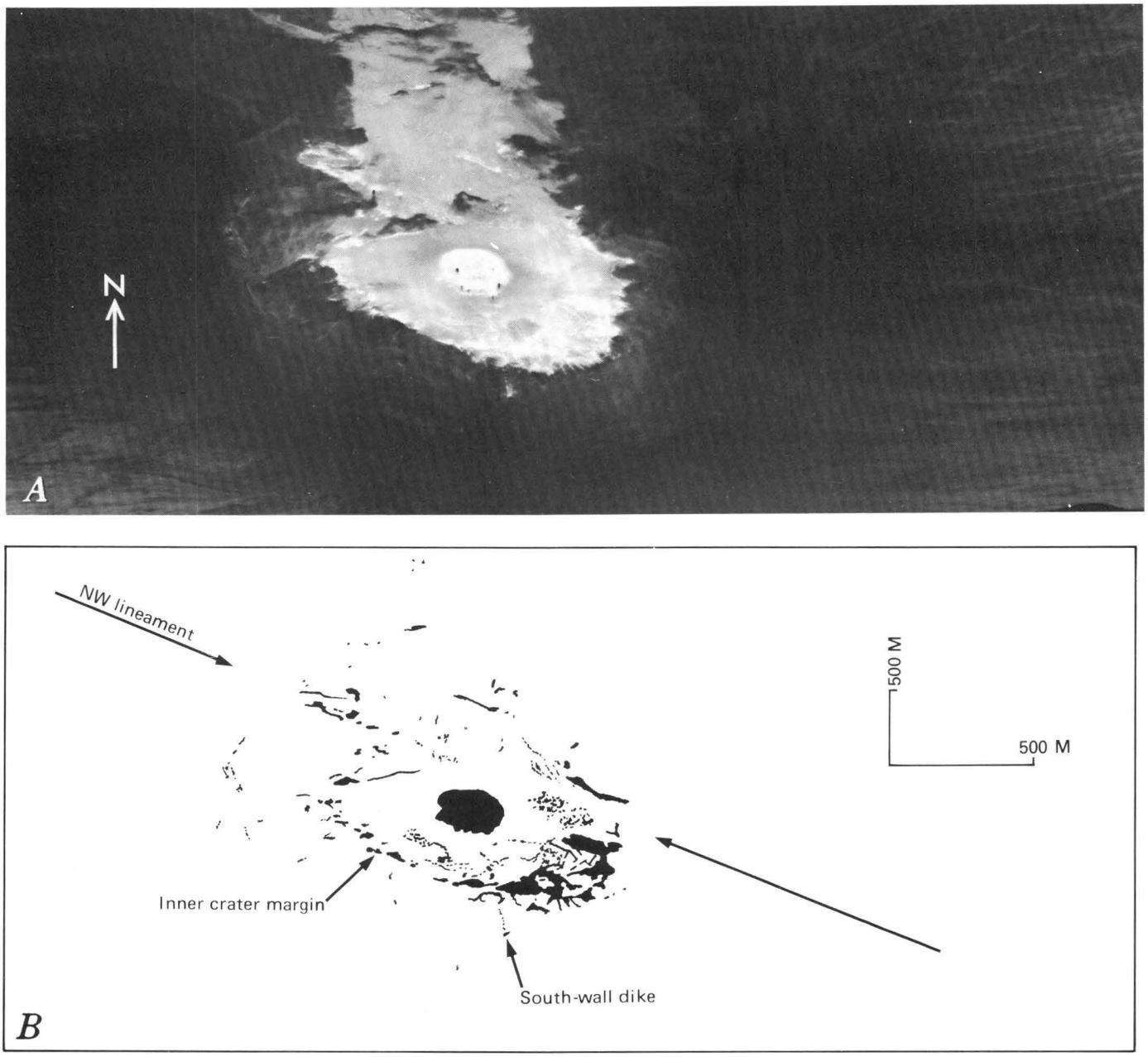

Figure 174.—Daedalus multispectral vertical scanner image, from EG&G. August 20, 1980, 0330 PDT; 8–14 μm region. Hottest areas appear white on A and black on B.

trend cutting across the core of the volcano (Weaver and others, this volume). The orientation of the dome and the southeast thermal cluster also suggest northwest-trending structural control of heat emission.

HEAT FLOW

Differential radiant exitance ($Wd\lambda_1$–$Wd\lambda_2$, a measure of the change in power radiated per unit

area, relative to that of a standard surface) can be estimated for moderate to high heat flows from figure 173, using a two-point differential radiant exitance model (Birnie, 1973; Friedman and Frank, 1980). The blackbody radiation from warm or hot surfaces in relation to a cool reference surface (5.7°C) on August 13, 1980, was calculated from radiometric surface temperatures (table 27, fig. 176*A* and *B*). The crater floor and inner ramp, for example, average about 464 W/m^2; fumarolic areas about 513 W/m^2, and the carapace of the August dome about 777 W/m^2. The differential radiant exitance from incandescent cracks ranges between 4×10^3 and 3×10^4 W/m^2 (table 27).

From the surface temperatures derived from the RS–14A images (fig. 173), we can next estimate the total heat flow in the crater area by application of a two-point differential geothermal-flux model (Sekioka and Yuhara, 1974). Although the Sekioka and Yuhara model requires analysis of micrometeorological factors not readily available for the present study, the corrections would be small. From analogous investigations (Friedman and Frank, 1980, p. 30), we can infer that between eruptions, the radiant heat loss is typically between 4 and 10 percent of the total volcanic heat flux (the examples used are Mount Baker, 1975; Surtsey, Iceland, 1966; Alae lava lake, Hawaii, about 1964).

From our infrared data of August 13, 1980, the differential radiant flux for the August dome averaged 777 W/m^2 (or greater from incandescent cracks) and 464 W/m^2 for the crater floor area (and greater for areas of fumaroles (table 27)). Integrating these differential radiant flux estimates over the August dome area of 23,000 m^2 and crater floor area of 785,000 m^2 (fig. 175*C*) yields a flux estimate of 18+ MW for the August dome and 354 MW for the crater floor area, exclusive of the dome. Using the estimated partition of radiant flux energy, the total flux from the volcano on August 13 was $0.4–1.0 \times 10^4$ MW.

From the heat content, volumetric growth rate and density of the June dome, Friedman, Olhoeft, and others (this volume) estimated a rate of thermal energy yield of between 2.9 and 3.7×10^4 MW for the active stage of dome growth. Our present radiant-flux and energy partition estimates suggest that on August 13 the total heat flow was 10–35 percent of that during the active June phase of dome growth.

STRUCTURAL IMPLICATIONS

The concentric and radial fracture pattern, inferred from the infrared images around the June dome and to a lesser extent the August dome (fig. 175), is compatible with geologic models of fracture systems around vertically elongate magma chambers. Dome fracture patterns can be used to infer the geometry of the extrusive. Cylindrical magma chambers that contain intermediate-composition magmas have many structural features in common with dacite plugs and domes. Koide and Bhattacharji (1975) found that radial and concentric extension fractures develop in plan around vertically elongate magma bodies as a response to stress when magma pressure exceeds lithostatic confining pressure. Under these conditions, stress contours (in section) near the apex of the magma column can be expected to be arcuate, with one of the maximum shear directions dipping toward the axis of the magma column. We infer that under the tephra and breccia of the crater floor is a vestigial fracture pattern, which we can observe in the infrared images. Emplacement of the June dome was accompanied by development of a concentric and radial fracture system, which also controlled the development of a breccia zone around the dome, hence the concentric development of fumaroles on the crater floor.

Thus, northwest-striking fractures, marked by alined fumaroles, have controlled, within a central volcano, the location of the main eruptive center and several secondary hot spots. The en-echelon pattern of these fractures (that is, the northwesterly strike of individual fractures and the nearly north-south trend of the set) expresses at Mount St. Helens an inferred structural control of Cascade Range volcanoes along northwest-striking en-echelon structures whose distribution is north-south, parallel to the plate margin (Weaver and others, this volume).

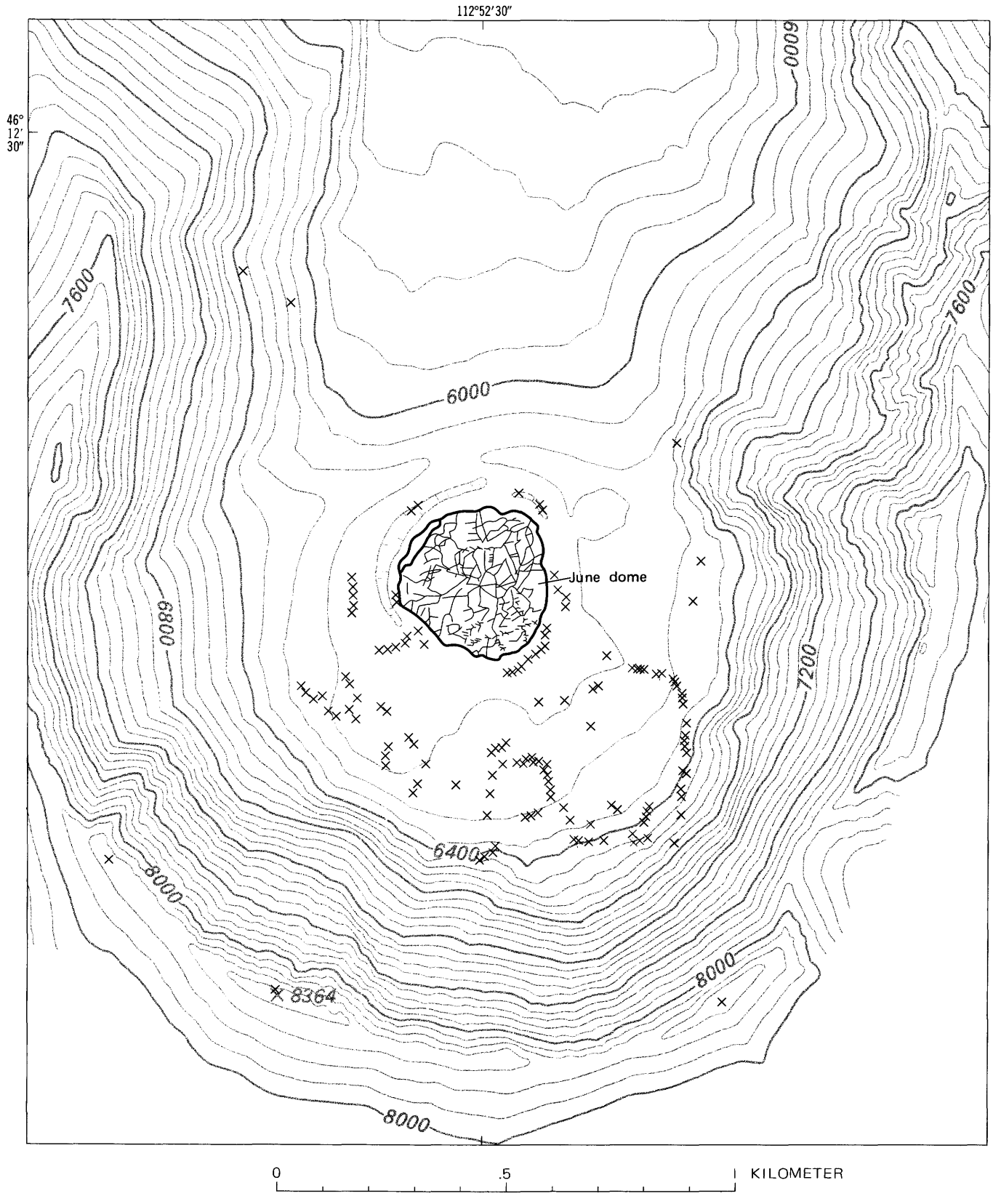

Figure 175.—Sketch maps of crater and sites of fumarole emission (x). Base from USGS advance print, 1:24,000, based on June–July 1980 photography. A, Following June 12 eruption, based on vertical aerial photography of July 1. B, Following July 22 eruption, based on vertical aerial photography of July 31. Hachures indicate steep slopes of elongate

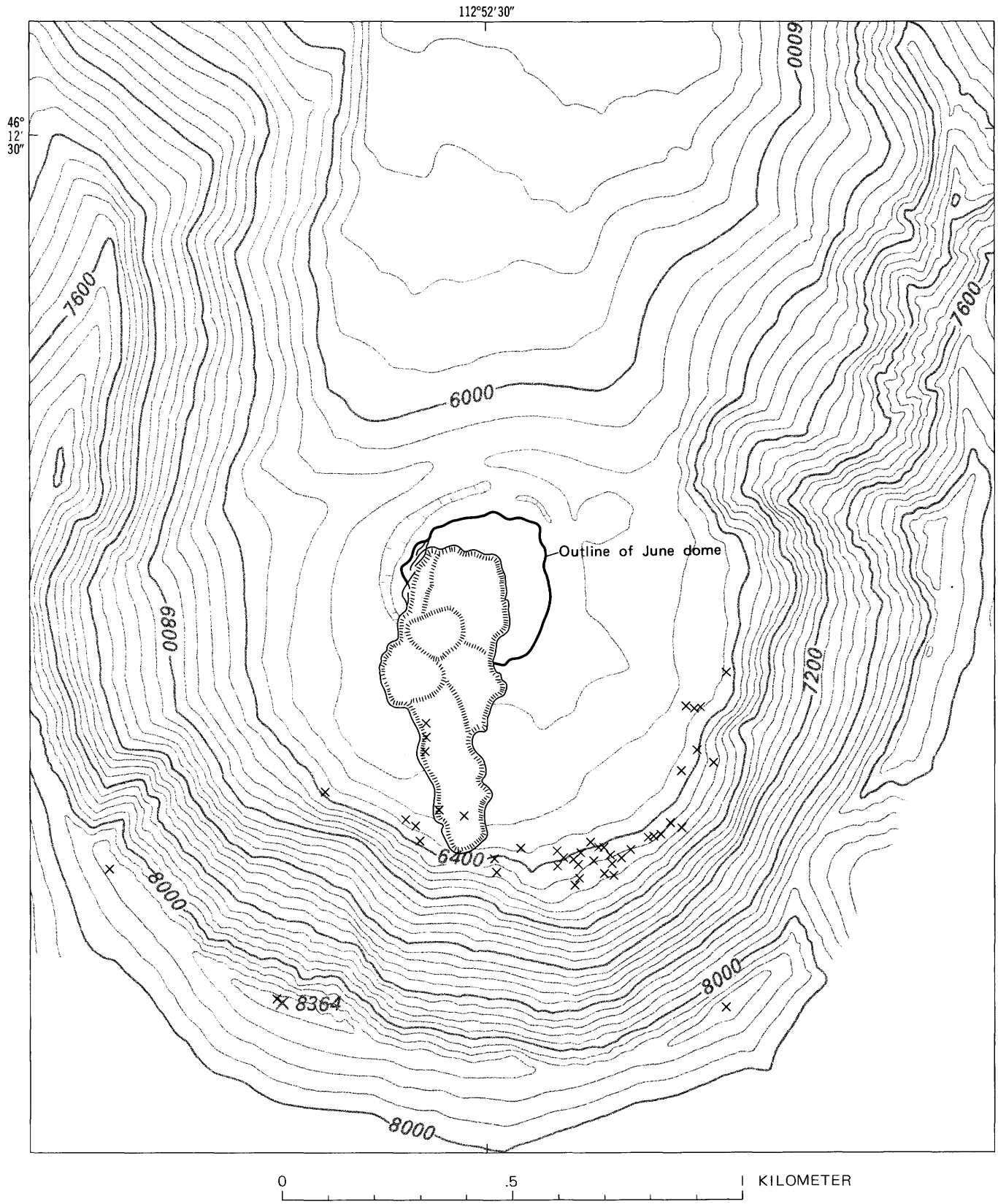

inner crater formed on July 22. C, Following August 7 eruption, based on vertical aerial photography of August 20. Pattern indicates steep slopes on walls of inner crater.

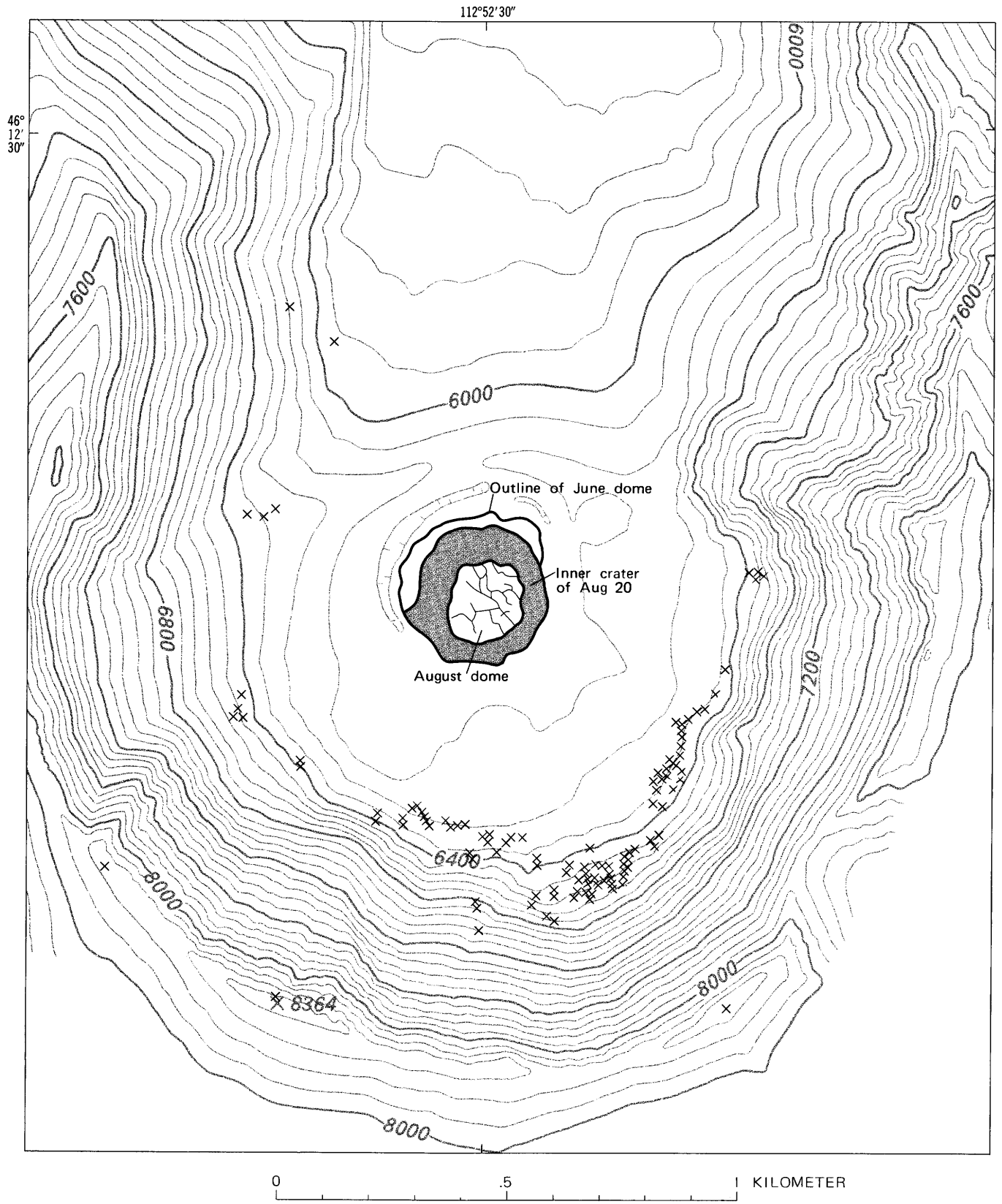

Figure 175.—Sketch maps of crater and sites of fumarole emission—Continued

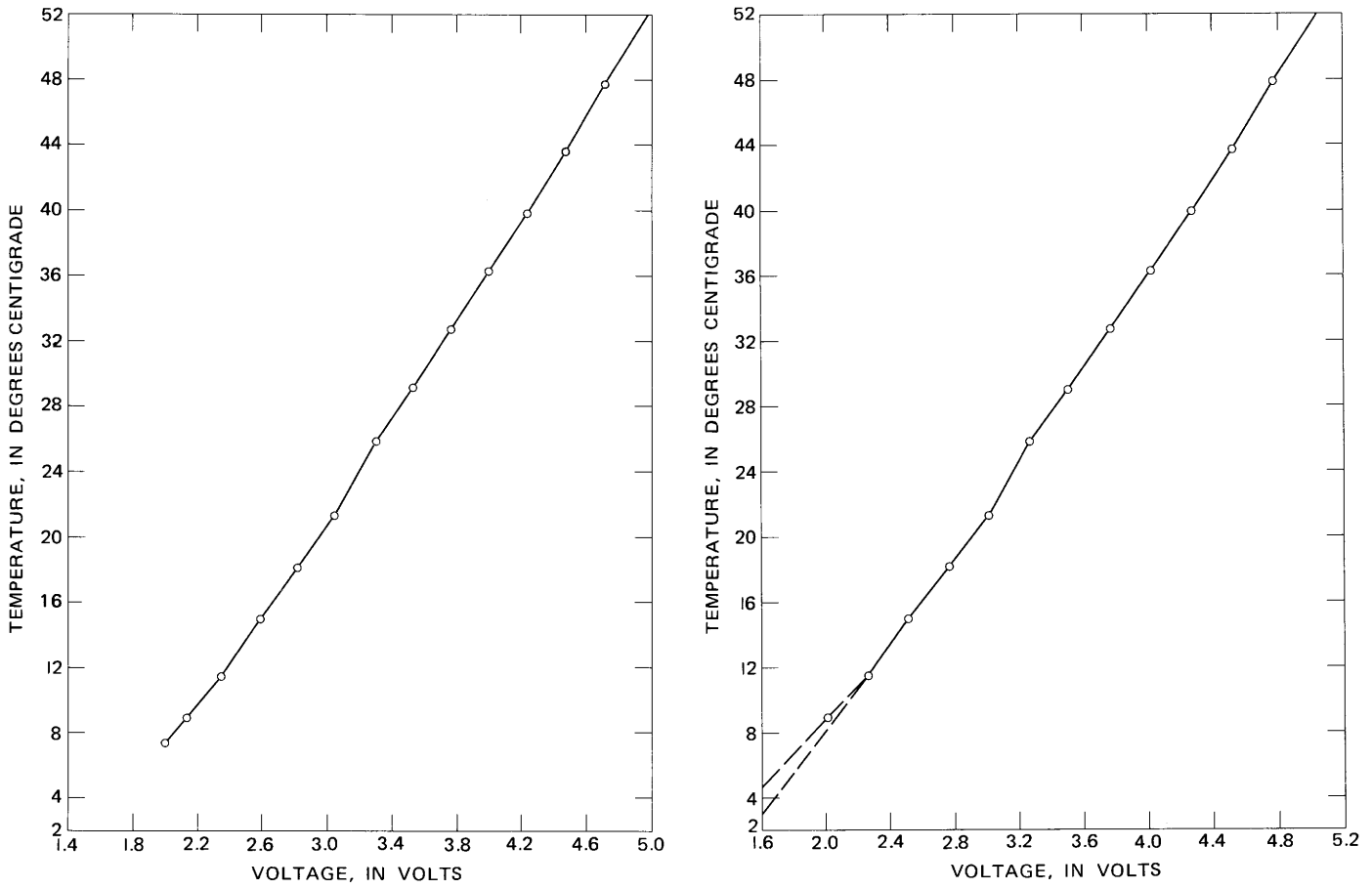

Figure 176.—Voltage versus temperature for calibrated images of USGS RS-14A scanner. A, blackbody 1; B, blackbody 2.

REFERENCES CITED

Birnie, R. W., 1973, Infrared radiation thermometry of Guatemalan volcanoes: Bulletin Volcanologique, v. 37, no. 1, p. 1–36.

Friedman, J. D., and Frank, David, 1980, Infrared surveys, radiant flux, and total heat discharge at Mount Baker volcano, Washington, between 1970 and 1975: U.S. Geological Survey Professional Paper 1022-D, 33 pages.

Koide, H., and Bhattacharji, S., 1975, Formation of fractures around magmatic intrusions and their role in ore localization: Economic Geology, v. 70, no. 4, p. 781–799.

Sekioka, Mitsuru, and Yuhara, Kozo, 1974, Heat flux estimation in geothermal areas based on the heat balance of the ground surface: Journal of Geophysical Research, v. 79, no. 14, p. 2053–2058.

Yeats, R. S., and Rosenfeld, C. L., 1980, NW- and NE-trending fracture system at Mount St. Helens volcano, Washington [abs.]: American Geophysical Union, P.N.A.G.U. 1980 meeting, Victoria, B. C., Program with abstracts.

THE 1980 ERUPTIONS OF MOUNT ST. HELENS, WASHINGTON

SUMMARY OF TEMPERATURE STUDIES OF 1980 DEPOSITS

By NORMAN G. BANKS *and* RICHARD P. HOBLITT

ABSTRACT

Temperatures were measured in deposits of the May 18 debris avalanche and directed blast and in the pyroclastic-flow deposits of the May 18, May 25, June 12, July 22, August 7, and October 17 eruptions. The measurements were supplemented by studies of the heat effects on tree remnants and plastics exposed to the May 18 directed blast and on wood included in the resulting deposit. Efforts are underway to mathematically recover the emplacement temperatures of deposits that cooled before they were measured, and techniques are being developed to measure temperatures in moving and newly deposited pyroclastic flows.

Emplacement temperatures of the debris avalanche ranged from about 70° to 100°C, and those of the directed blast ranged from about 100° to 300°C and varied with azimuth from the volcano. Emplacement temperatures of the pyroclastic-flow deposits ranged from about 300° to 730°C, near-vent deposits were emplaced at about 750°–850°C, and, in general, the more recent eruptions have emplaced deposits at higher temperatures than did the earlier eruptions.

The temperatures in the pyroclastic-flow deposits did not substantially decrease along the path of flow, and deposits of the directed blast behaved similarly along flow paths as far as 20 km from the vent. The data suggest that, after initial rapid cooling of several hundred degrees by adiabatic expansion and incorporation of air during eruption and development of flowage, the main body of both the directed blast and the pumiceous pyroclastic flows incorporated little cool air along the flow path except at the front where mixing, turbulence, and deposition occurred.

INTRODUCTION

Temperature studies of the eruptive products of Mount St. Helens were begun 2 days after the paroxysmal eruption of May 18. We summarize here direct temperature measurements on deposits of the directed blast and debris avalanche of May 18 and on the pyroclastic-flow deposits of May 18, May 25, June 12, July 22, August 7, and October 17. We also present preliminary information on the thermal effects of the directed blast of May 18 on plastics, trees, and blast-buried wood. Three studies are in progress: (1) analyses that should yield quantitative estimates of the temperatures experienced by the trees and buried wood; (2) efforts to mathematically recover emplacement temperatures at localities where delays resulting from poor weather, inappropriate equipment, access problems, the immense area requiring examination, and considerations of safety precluded the obtainment of isothermal profiles; and (3) development of new techniques of measuring temperatures, such as aerially emplaced, radio-controlled, thermocouple probes, and the use of temperature-sensitive paints to determine temperatures in ash clouds.

The cooling history data currently being collected are expected to provide in-place thermal parameters of pyroclastic-flow deposits and to be useful to other studies such as petrology (welding, devitrification, vapor-phase transport), magnetic properties, and other physical parameters of pyroclastic flow deposits.

ACKNOWLEDGMENTS

This study could not have been performed without the skillful, courageous efforts of helicopter pilots Mike Holtsclaw, Lon Stickney, Michael Montgomery, and Robert Brown.

We were assisted in the field and laboratory principally by Terry Leighley, James Vallance, Bruce Furukawa, C. D. Miller, Joseph Rosenbaum, Paul Greenland, Dallas Jackson, Michael Doukas, Peter Rowley, Edward Graeber, and Herman Hoffschneider. Mark Davis and Edward Graeber of Sandia Laboratories provided the temperature data on the plastics that were recovered by themselves and by U.S. Geological Survey personnel. This report is dedicated to D. A. Johnston, our friend and colleague who lost his life while studying Mount St. Helens. Our science will suffer from his loss.

PREVIOUS WORK

Few temperatures have been measured in pyroclastic-flow deposits of stratovolcanoes, owing to inaccessibility, long repose times, considerations of safety, and lack of appropriate equipment. The most comprehensive studies are those of Allen and Zies (1923), Zies (1924, 1929), Griggs (1918), Sayre and Hagelbarger (1919), Kozu (1934), Kienle and Swanson (1980), and Johnston (1978), and some addtional data are found in Gorshkov and Dubik (1970) and Gorshkov (1959). Temperatures of pyroclastic deposits also have been inferred from optical properties of ash flows, from the thermal effects on articles incorporated by or in the path of pyroclastic flows, and from theoretical and laboratory studies (Perret, 1937; Macdonald and Alcaraz, 1956; Cotton, 1952, p. 200; Van Bemmelen, 1949, p. 192; Taylor, 1958; Mimura and others, 1975; Maury and others, 1973; Aramaki and Akimoto, 1957; Hoblitt and Kellogg, 1979; Gilbert, 1938; Day and Allen, 1925; Smith and others, 1958; Smith, 1963). Such studies suggest that the emplacement temperatures of pyroclastic flows of intermediate and acid composition range from nearly 1000°C to less than 500°C. Smith (1963) attributed this wide temperature range to cooling of ejecta in a vertical eruption column rather than to profound differences in magma temperatures; cooling during development of directly emitted flows also may play a part.

METHODS

DIRECT MEASUREMENTS

Temperatures were measured with chromel-alumel and Pt-Pt10%Rh (platinum/platinum-10 percent rhodium) thermocouples and direct-reading, electronically compensated (cold junction), digital voltmeters. Although meters and thermocouples were not calibrated with standards of known melting temperature (except ice), temperatures measured on the same thermocouple with as many as five meters invariably agreed within 1°–2°C of the same value, as did temperatures from several adjacent thermocouples (of two types) implanted to the same depth.

Several configurations of thermocouples were used. Most commonly, we used individual metal-sheathed thermocouples (1.5-mm diameter and as much as 10 m long, or 6-mm diameter and as much as 3 m long), strings of metal-sheathed thermocouples (1–3 m long for rapid profiling), and strings of Teflon-insulated thermocouples (to monitor cooling histories). When possible, the sheathed thermocouples were inserted directly into the deposits. For less penetrable deposits and for deeper measurements, the thermocouples were inserted into standard 1/2-in. i.d. (inside diameter) plumbing pipe that had been implanted and allowed to thermally equilibrate (4–5 hr). Profiles obtained in pipes 5 hr to 16 days after implantation were identical to those obtained by direct insertion of thermocouples at the same site. Thermocouples inserted stepwise into a deposit or a pipe reached thermal equilibrium within 5–10 min.

We considered that emplacement temperatures were obtained when a segment of a temperature pro-

file was isothermal. Thus, whenever possible, we obtained temperature profiles in preference to single measurements. Additionally, the profiles will allow mathematical determination of the thermal properties of deposits and of emplacement temperatures at those sites where we were unable to obtain isothermal segments.

As the study evolved, we developed and adhered (to the extent that conditions allowed) to the following strategy. Measurements were first made at the distal, middle, and proximal parts of a flow deposit; then measurements were made across the axis of the flow path at these and additional localities. A similar strategy, along three evenly spaced radial traverses outward from the vent, maximizes efficiency in measuring temperatures on deposits of directed blasts.

THERMAL EFFECTS ON PLASTICS

The thermal effects on eight vehicles and one piece of heavy equipment were examined to provide information about temperatures within the directed blast. Significant thermal effects were found only in plastics, apparently because of the short duration of the thermal pulse, the low thermal diffusivities of the plastic, and the low temperature required to soften and decompose polymer plastics. Plastics from vehicle turn signal lights, tail lights, and instrument panels were used to standardize the data at all sites. Comparative samples were obtained from vehicles of the same type and year of manufacture as those in the devastated area, and the standard materials were exposed (Davis and others, 1980) to various thermal cycles in a forced-air oven or in silicone oil. The two media were used to bound the natural case—ash-laden air of unknown humidity, velocity, and content of juvenile gases.

Davis visually compared the standards with the matching artifacts to yield the best estimates of the time-temperature history of the samples (Hoblitt and others, 1980; Davis and others, 1980). Several criteria were used: temperatures required to initiate flowage or decomposition, depth of penetration of the thermal effects, flowage characteristics, foaming characteristics, bubble size, and bubble distribution. Because of unknowns such as the time of exposure and the heat-transfer coefficients of the pyroclastic cloud, it is difficult to quantify the uncertainty in the temperature estimates.

THERMAL EFFECTS ON TREES AND BURIED WOOD

To supplement the data from the plastics and the direct temperature measurements of the deposits of the directed blast, we examined the thermal effects on trees that were still standing in the devastated zone and on the wood included in the blast deposits. Data were taken at about 60 sites along eight radial traverses centered on Mount St. Helens. At each site, 50–200 trees (usually within an area of 10^4–10^5 m^2) and wood buried in the deposit were empirically ranked according to the example in table 28. The ranking procedure was standardized by examining only those tree parts that were 1–5 cm in diameter and 30–100 cm above the ground. The buried wood came from the center of the deposit. Samples of buried wood, trees, and blast deposit that were collected at each site are presently being analyzed more quantitatively.

SUMMARY OF TEMPERATURE STUDIES

The eruptive history and resultant stratigraphy of the Mount St. Helens eruptions of 1980 appear in detail elsewhere in this volume. However, for ease of reference, the map distribution and an outline of the major events are presented in figure 177 and table 29, respectively.

DEBRIS AVALANCHE OF MAY 18

Temperatures of 68°–98°C were measured at five localities on the debris avalanche along the North Fork Toutle River and at one locality north of Spirit Lake (fig. 178*A*; table 30) between 10 and 12 days after emplacement. At each locality, four or five measurements were made at depths of 1–1.5 m. A thermal profile was measured at only one locality; however, the thermal gradient was steep, between 0.5

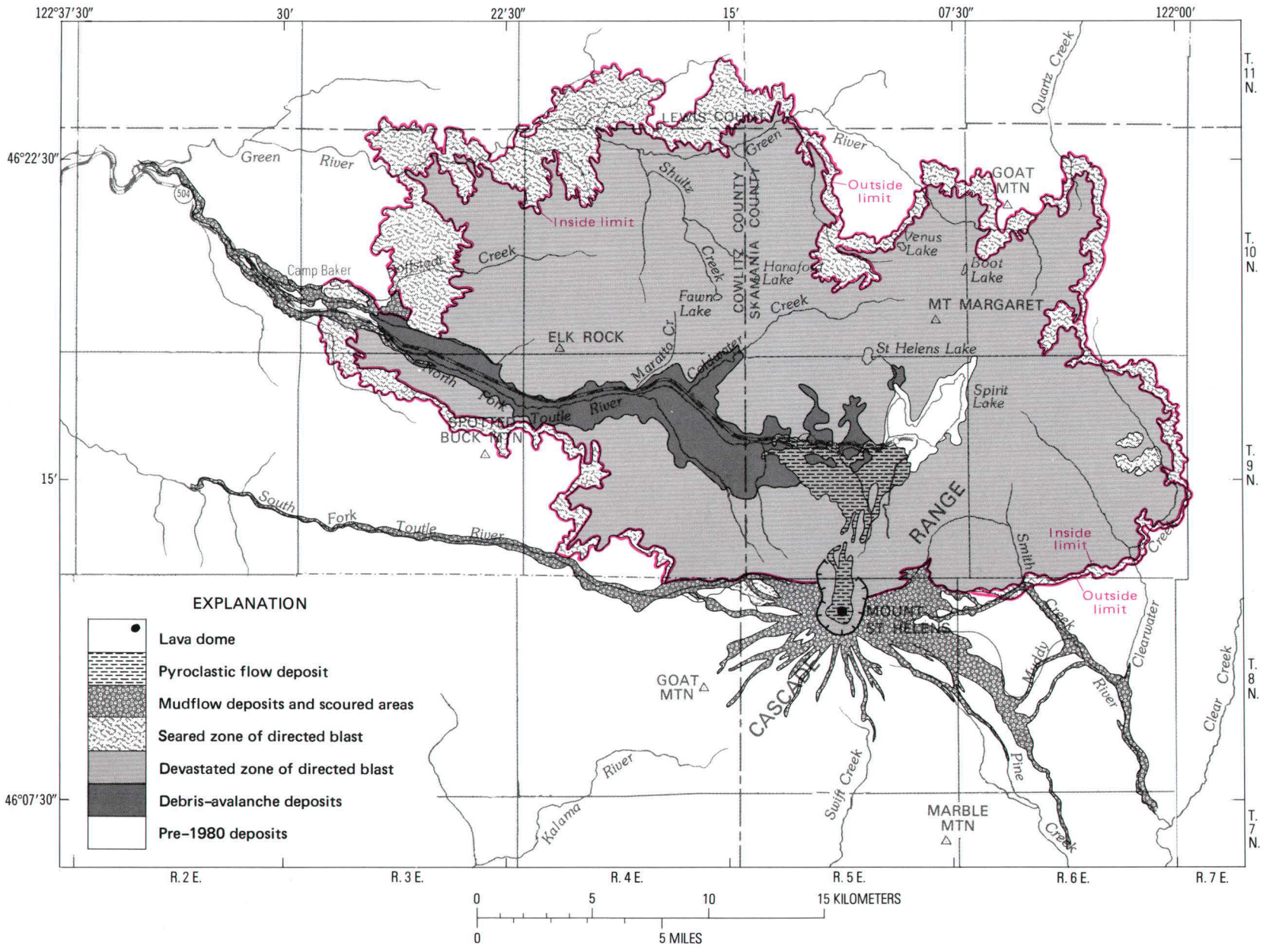

Figure 177.—Generalized sketch map of the products of the May 18 eruption, Mount St. Helens, Wash. Modified from plate 1.

Table 28.—Criteria for ranking of thermal effects on tree remnants and on wood buried by the directed blast of May 18, 1980 and an example of the data obtained from trees examined at a single locality

[Colors from rock chart of Goddard and others (1948)]

Thermal effects on trees					Thermal effects on trees at one locality	
Visible effects	No. of trees	Fraction of population	Scorch rank	Fractional scorch rank[1]	Visible effects	Thermal rank
Green needles-------	0	0	0	0	Green needles------------------	0
Needles singed------	0	0	1	0	Wood flexible------------------	1
Bark heat-checked[2]--	0	0	2	0	Wood brittle-------------------	2
Wood heat-checked[2]--	0	0	3	0	Slight smell of distillation, not discolored----------------	3
Spotty wood tanning-	0	0	4	0	Smell of distillation, not discolored-------------------	4
Wood tanning[3]: 60°	0	0	5	0	Strong smell of distillation, brittle, surface discolored, no streak---------------------	5
120°	0	0	6	0	As above, hard, yellowish brown streak 10*YR*6/2---------	6
180°	0	0	7	0	As above, hard, pale-olive-gray streak-------------------	7
240°	0	0	8	0	Brownish wood, hard, moderate-yellowish-brown streak 10*YR*5/2----------------------	8
300°	0	0	9	0	As above, hard, light-olive streak 5*Y*6/1------------------	9
360°	0	0	10	0	As above, hard, medium-olive-gray streak 5*Y*5/1------------	10
Spotty wood charring	0	0	11	0	Brown wood, hard, light-gray streak *N*7---------------------	11
Wood charring[3]: 60°	0	0	12	0	Dark-brown wood, soft, brownish-red streak 5*YR*5/1------------	12
120°	2	0.11	13	0.13	Chocolate-brown wood, dark-yellowish-brown streak 10*YR*4/2----------------------	13
180°	7	0.04	14	0.56	Chocolate-brown wood, moderately yellowish brown streak 10*YR*4/4----------------	14
240°	18	0.10	15	1.50	Brownish-black charcoal, dark-yellowish-brown streak 10*YR*3/4----------------------	15
300°	39	0.22	16	3.50	Black vitreous charcoal, dusky brown streak 5*YR*3/2----------	16
360°	111	0.63	17	10.71	As above, very dusky red streak 10*R*2/2----------------	17
Totals---	177	1.0		16.4	Observed rank------------	16

[1]Fractional scorch rank=(fraction of population)x(scorch rank).
[2]Heat-induced cracks.
[3]Angular circumference affected.

and 1.4 m, and was isothermal below 1.4 m. Thus, the temperatures obtained at the four other localities in the Toutle River probably represent temperatures near those of emplacement. Temperatures were measured at five other localities (9°–33°C) by Barry Voight between May 30, and June 3 (written commun., 1980); however, all were measured in pits less than 0.5 m deep.

The debris-avalanche deposits consist dominantly of old rocks that composed the north flank of the mountain, and the low temperatures measured agree with the low percentage of juvenile material present. The fractured old rock probably was heated by steam or water derived from the hydrothermal system associated with the cryptodome.

The measured temperatures decrease away from

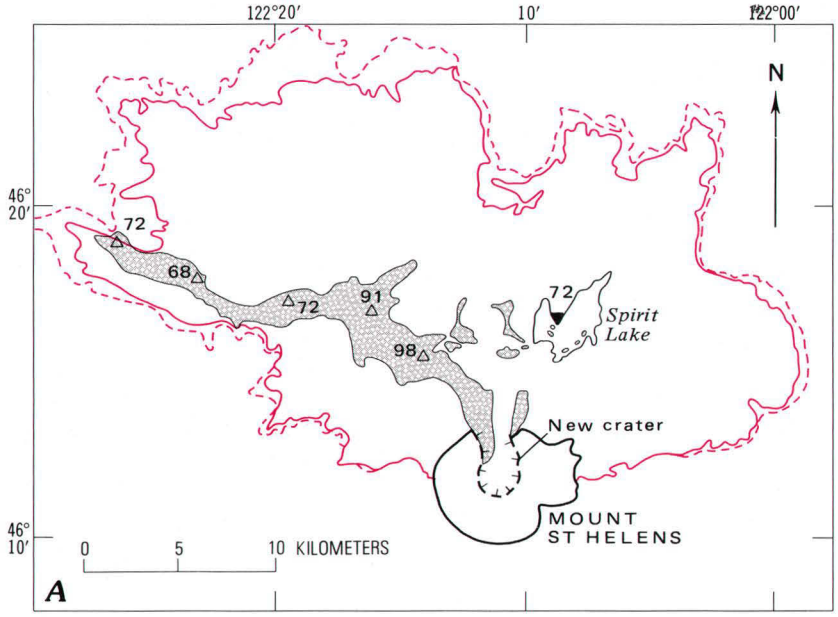
122°20′
10′
122°00′
N
46° 20′
46° 10′
72
68
72
91
98
72
Spirit Lake
New crater
MOUNT ST HELENS
0 5 10 KILOMETERS
A

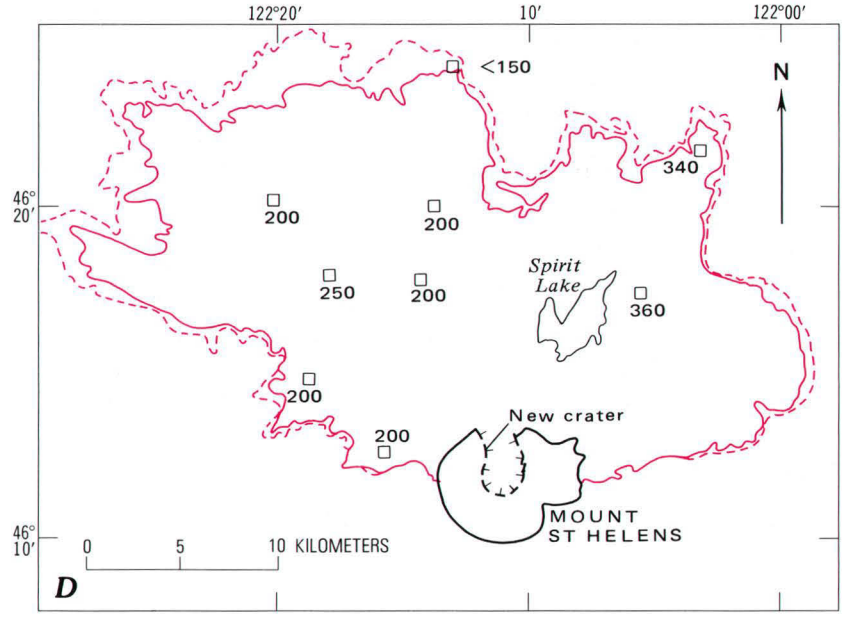
122°20′
10′
122°00′
N
46° 20′
46° 10′
<150
340
200
200
250
200
Spirit Lake
360
200
200
New crater
MOUNT ST HELENS
0 5 10 KILOMETERS
D

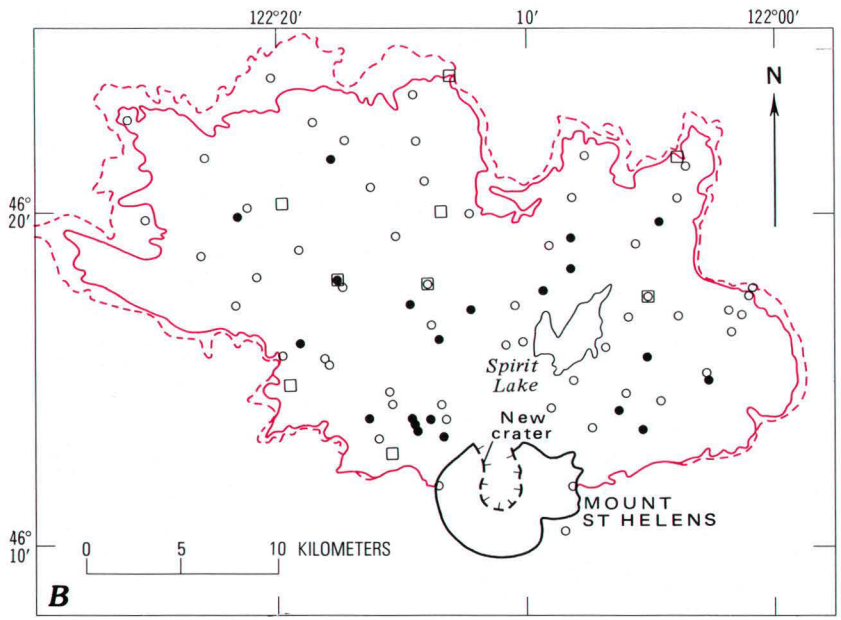
122°20′
10′
122°00′
N
46° 20′
46° 10′
Spirit Lake
New crater
MOUNT ST HELENS
0 5 10 KILOMETERS
B

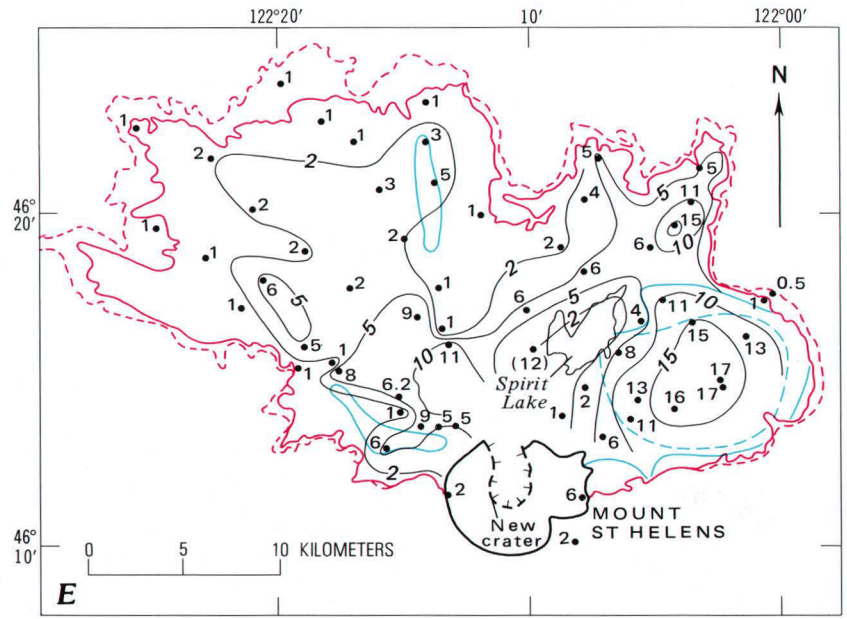
122°20′
10′
122°00′
N
46° 20′
46° 10′
(12)
Spirit Lake
New crater
MOUNT ST HELENS
0 5 10 KILOMETERS
E

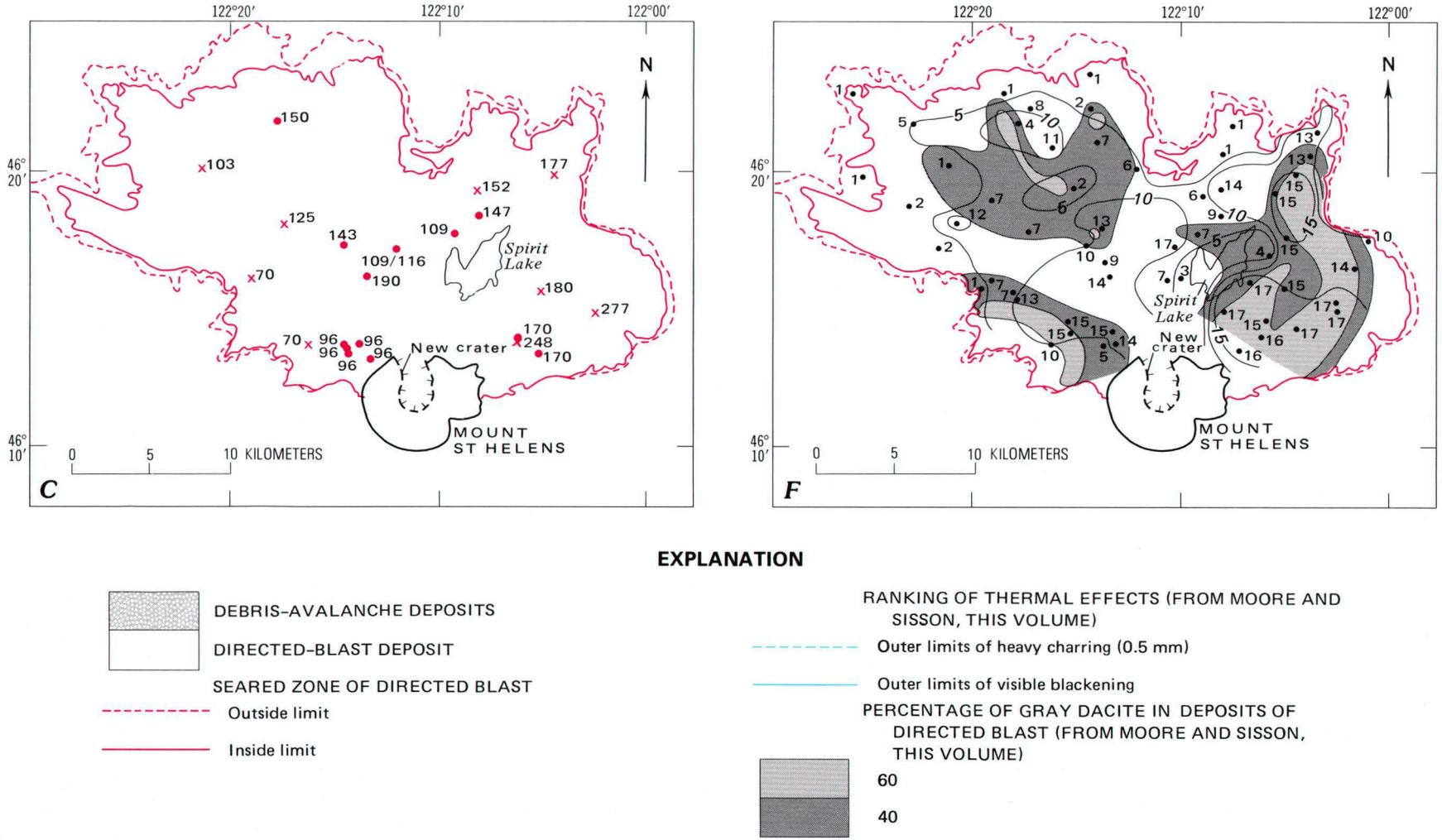

Figure 178.—Temperature data for deposits of the debris avalanche and the directed blast of May 18. A, Temperatures (°C) directly measured on the debris-avalanche deposit. Open triangles, North Fork Toutle River lobe; solid inverted triangle, Spirit Lake lobe. B, Localities at which temperature information was obtained on deposits of the directed blast. Open circles, localities at which wood and charcoal samples were obtained; solid circles, localities at which temperatures were directly measured; open squares, localities at which samples of plastics were obtained. C, Temperatures (°C) directly measured on deposits of directed blast. Temperature pairs separated with a slash mark indicate that two distinct temperature units were present in temperature profile. Red circles, probable emplacement temperatures; red x, minimum temperatures (temperatures that were probably below the true emplacement temperatures). D, Temperatures (°C) of the directed blast estimated by studying thermal effects on plastics. E, Qualitative ranking of thermal effects on tree remnants in devastated area; contour lines indicate scorch rank (table 28); zero is unscorched. Solid circle, sample locality; (12) indicates thermal effect from ash cloud related to pumiceous pyroclastic flows rather than the directed blast. F, Qualitative ranking of thermal effects on wood included in deposits of directed blast; solid circle, sample locality; contour lines indicate thermal rank (table 28); zero is no thermal effect.

Table 29.—Generalized chronology of deposit-forming events, Mount St. Helens, Wash., 1980
[PDT, Pacific Daylight time]

Date	Time (PDT)	Type of deposit
Oct. 17	2116	Pumiceous pyroclastic flow.
Oct. 17	0935	Do.
Aug. 7	1623	Do.
July 22	1900	Do.
July 22	1830	Do.
June 12	1905-2400	Do.
May 25	0232	Do.
May 18-25	----	Minor eruptions, mudflows.
May 18	~1217(?)-~1730	Pumiceous pyroclastic flows; at least six events.
May 18	~0835-2400	Mudflows.
May 18	~0833-~0845	Directed blast.
May 18	0832-~0842	Debris avalanche.
March 27-May 18	----	Phreatic eruptions, mudflows.

the summit along the North Fork Toutle River lobe (fig. 179), suggesting that progressively deeper (hotter) levels of the mountain fed the debris-avalanche, or, less likely, that there was downflow incorporation of air, water, and debris from the river bed. The temperature obtained by Barry Voight (written commun., 1980) for the flow lobe north of Spirit Lake plots well below the curve for the North Fork Toutle lobe (inverted triangle, fig. 179). This low temperature could be attributed to the shallow depth of the measurement (0.5 m), to cooling due to incorporation of Spirit Lake water, or to different sources for the two lobes of the debris flow.

DIRECTED BLAST OF MAY 18, 1980

Temperatures ranging from about 70° to 277°C were measured at 21 localities in deposits of the directed blast (table 30, fig. 178*B-C*). All but one of these localities were on ponded deposits in topographic lows. Temperature profiles were measured at one or more sites at 17 of these localities; single measurements were made at four other localities.

Isothermal profiles, indicative of emplacement temperatures, were obtained in ponded deposits in six drainages (Studebaker Creek, North Fork Toutle River below Coldwater Ridge, three flow units in South Coldwater Creek, west Shultz Creek, creek near Lang Mine, west arm of Spirit Lake; for location of drainages, see pl. 1 and fig. 177). Comparisons of near-isothermal profiles and single measurements with isothermal profiles from adjacent or nearby sites suggest that temperatures near those of emplacement were obtained at six other localities (one more in Studebaker Creek, two in Castle Creek, south fork of Castle Creek, Jackson Creek, Smith Creek; figs. 177, 178), representing four additional drainages.

Two features of the data are notable: (1) emplacement temperatures change little or even increase along individual flow paths between 4 and 20 km from the vent (fig. 180*A,C-F*), and (2) emplacement temperatures vary with azimuth from the mountain (fig. 180*B*). Deposits in the eastern sector of the devastated area were emplaced at higher temperatures than were those in the northern sector, which in turn were hotter than deposits in the western sector (fig. 178*C*; compare figs. 180*C-F*).

Field and temperature evidence suggests that more than one flow unit constituted the ponded deposits of the directed blast in several drainages. An emplacement temperature of 143°C was obtained from the lower part of South Coldwater Creek, whereas at an upstream locality, temperatures of 116° and 109°C were obtained for a lower unit and an upper unit, respectively (fig. 178*C*). Similarly in Smith Creek, the upper temperature profile at one locality is isothermal at 170°C with hotter strata beneath (>248°C; fig. 178*C*).

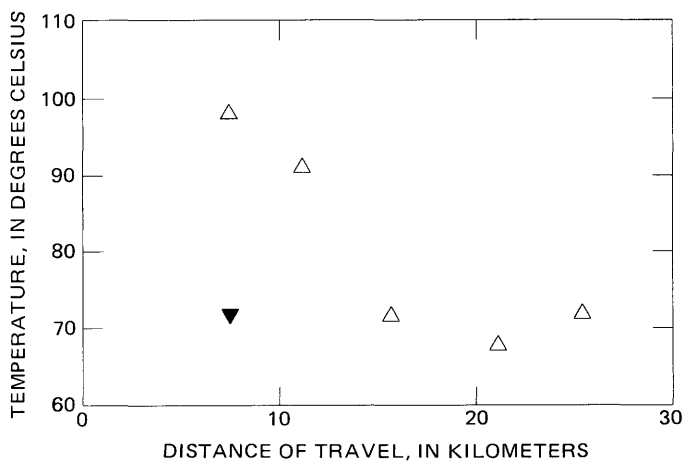

Figure 179.—Measured temperature versus distance of travel of the debris avalanche of May 18. Open triangle, North Fork Toutle River lobe; solid inverted triangle, Spirit Lake lobe.

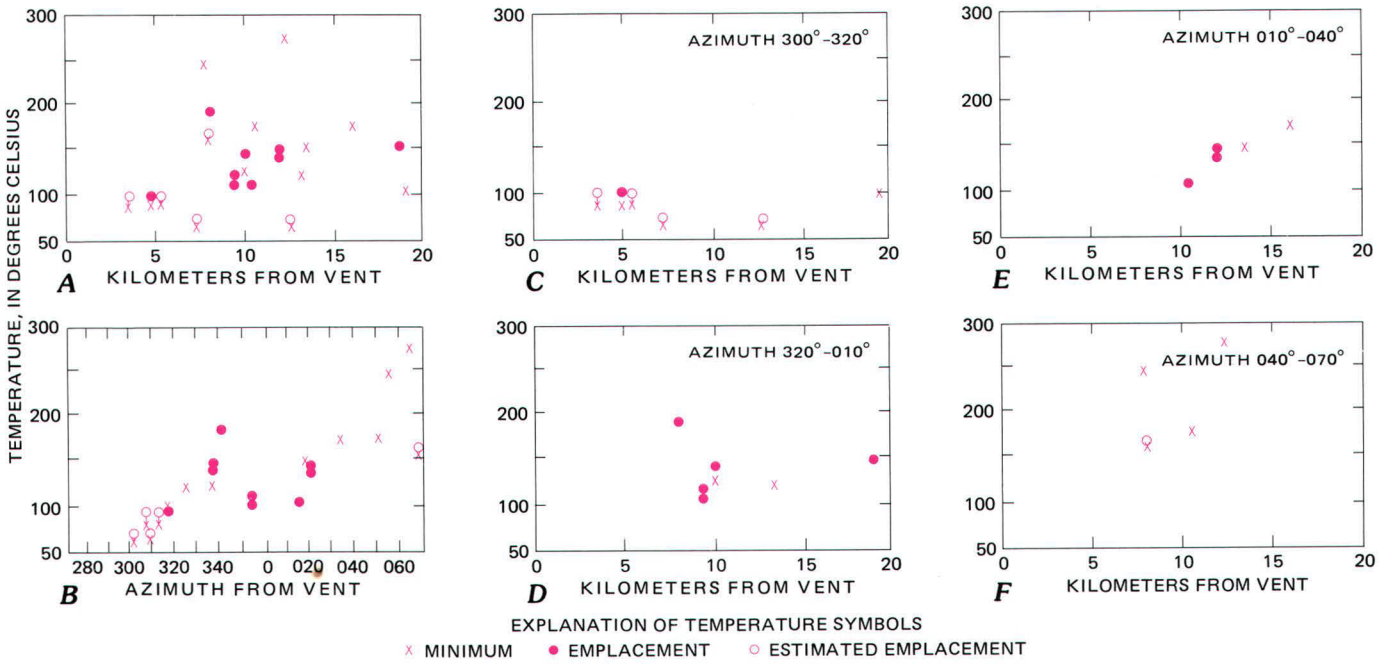

Figure 180.—Temperatures of deposits of directed blast of May 18, versus distance and azimuth of measurement locality from the vent.

Temperatures estimated for the directed blast from study of the plastics (fig. 178*D*; Hoblitt and others, 1980; Davis and others, 1980) are similar in pattern to that of the emplacement temperatures. The estimates are somewhat higher than the emplacement temperatures, however, and temperatures of clasts imbedded in the plastics appear to have been 100°C above the overall temperature experienced by the plastic. Plastics on the downflow side of vehicles and in "protected" sites behind seats and under papers and clothes were generally unaffected.

The shape and size of the bubbles and the depth of bubble nucleation indicate that the temperature peak passed within 1–10 min at all localities, and that the temperature dropped rapidly below 150°C. This short period of peak temperature is consistent with eyewitness reports, with the survival of paints, color film, cans of beer, polystyrene insulation, and, in the northern and western sectors of the devastated area, with the lack of charring of newsprint (charring temperature of about 250°C). Taylor (1958) also suggested a short peak period from studies of plastics exposed to the pyroclastic flow of Mount Lamington in 1951.

The qualitative ranking of the thermal effects on tree remnants (fig. 178*E*) and buried wood (fig. 178*F*) also indicates that the eastern sector experienced the highest temperatures in the devastated area. In addition, these data indicate that thermal effects on the trees and buried wood decreased markedly near the margins of the blast zone (compare fig. 180 with figs. 181 and 182). The thermal effects on the trees and buried wood correlate generally with the percentage of juvenile gray dacite in the blast deposit (fig. 178*F*; Moore and Sisson, this volume).

PYROCLASTIC-FLOW DEPOSITS OF MAY 18

Emplacement and near-emplacement temperatures ranged from 418° to 297°C in the pyroclastic-flow deposits of May 18 (table 30). Temperatures were measured at 13 localities between 1.8 and 9 km from the vent. Attempts to obtain emplacement temperatures nearer to the vent than 1.8 km were frustrated because deposits were thin and spotty and had cooled appreciably before they were visited and because conditions were unsafe on the rampart around the vent until after the June 12 eruption.

Isothermal segments (297°, 326°, 342°, and 367°C, fig. 183*A*, table 30) were measured at four localities, and nearly isothermal segments were measured close to the vent (418°C; fig. 183*A*) and 1.5 km north of the main flowage deposits in deposits from the ash cloud

Table 30.—Summary of emplacement and minimum temperatures of deposits, Mount St. Helens, Wash., May 18–October 17, 1980

[Times are PDT; temp, temperature; C, Celsius; km, kilometer; hr, hour; min, minute; m, meter]

Deposit	Description of deposits[1]	Range of temp[2] (°C)	Distance from vent (km)	Summary of measurement
		Deposits of debris avalanche		
May 18 0832 PDT	Deposits as much as 120 m thick; heterogeneous rock mass composed of N. flank of volcano; emplaced dry, speeds in excess of 200 km/hr; 2.5 km^3.	68-98	7.4-25.2	Six localities, isothermal profile (98°C) at one locality, several single temps to 1.5 m at other localities.
		Deposits of directed blast		
May 18	Explosive eruption, 4-unit stratigraphy; 30->60 percent gray dacite of cryptodome; local ponded deposits to >10 m thick; speeds in excess of 200-400 km/hr, 550 km^2 area, 0.18 km^3.	M70-M277	3.7-19.3	Several sites at 21 localities, some with two or three flow units; several single temps to 1.5-m depth at four localities, 23 temp profiles, 11 isothermal for at least one flow unit; little or no down-flow variation of temp; azimuthal variation in temp.
		Pumiceous pyroclastic flows--flowage deposits of ash, pumice lapilli and blocks		
May 18	Deposits mostly north of the vent; thicken downflow, 0-0.3 m at 0.3-2 km from vent, 1-m thick deposits and a few 1- to 5-m thick ponded deposits at 2-4 km from vent, as much as 30+ m thick 4-8 km from vent; fine-grained ash-cloud deposit 8-20 km NNE. of volcano; 0.15 km^3.	M96-M418	1.8-9.5	Fourteen localities, 13 north of vent, one on east flank of volcano; temp profiles at six localities, six isothermal or nearly isothermal; single temps to 1.5-m depth at six localities, two in the same area but separated stratigraphically by 30 m of deposit suggested an isothermal section for a seventh location; little across-flow and down-flow variaton of temp.
May 25	Rootless and <3 m thick; negligible volume.	M155-M156	2.7-4.4	Temperature profiles through the deposits at two localities; curves already parabolic when measured 6 days after the eruption.
June 12	Flows generally 1-5 m thick, ponded at base of stairsteps and in phreatic pits in May 18 deposits; 0.04 km^3.	361-602	4.4-7.4	Seven localities; 13 temp profiles; 12 isothermal or near isothermal; some profiles suggested presence of two to three flow units (totaling four units); older units hotter (about 370°, 450°, 490°, 600°C); little down-flow variation in temp.
July 22	Flows <1-2 m thick; two events, 1830 and 1900; 0.02 km^3.	640-705U M508-270L	3.4-6.9	Seven localities; several isothermal profiles at three localities, 35 min to 22 hr after emplacement; several profiles measured at four other localities during next 25 days; lower (1830-hr) flow unit (L) emplaced at lower temps than upper (1900-hr) flow unit (U); little down-flow variation of temp.
Aug. 7	Flows <1-2 m thick; one event observed at 1623; negligible volume.	640-828	0.2-4.4	Three localities, several profiles with one or more isothermal or near-isothermal at each locality; high temp in near-vent ejecta; little down-flow variation in temp in flowage deposit.
Oct. 17	Flows <1-2 m thick; two events, 0935 and 2116; negligible volume.	M567-M849U 465L	0.0-4.3	Four localities; several profiles at two; single and partial profiles at two; 0935-hr unit (L) emplaced at lower temperature than upper 2116-hr flow (U); high temp in near-vent ejecta; little down-flow variation in temp in flowage deposits.

[1]Volumes cited are from oral communications with R. W. Decker, R. J. Janda, J. G. Moore, P. D. Rowley, R. B. Waitt, Jr. Velocities from R. W. Decker.

[2]M, minimum temperature; U, upper flow unit; L, lower flow unit.

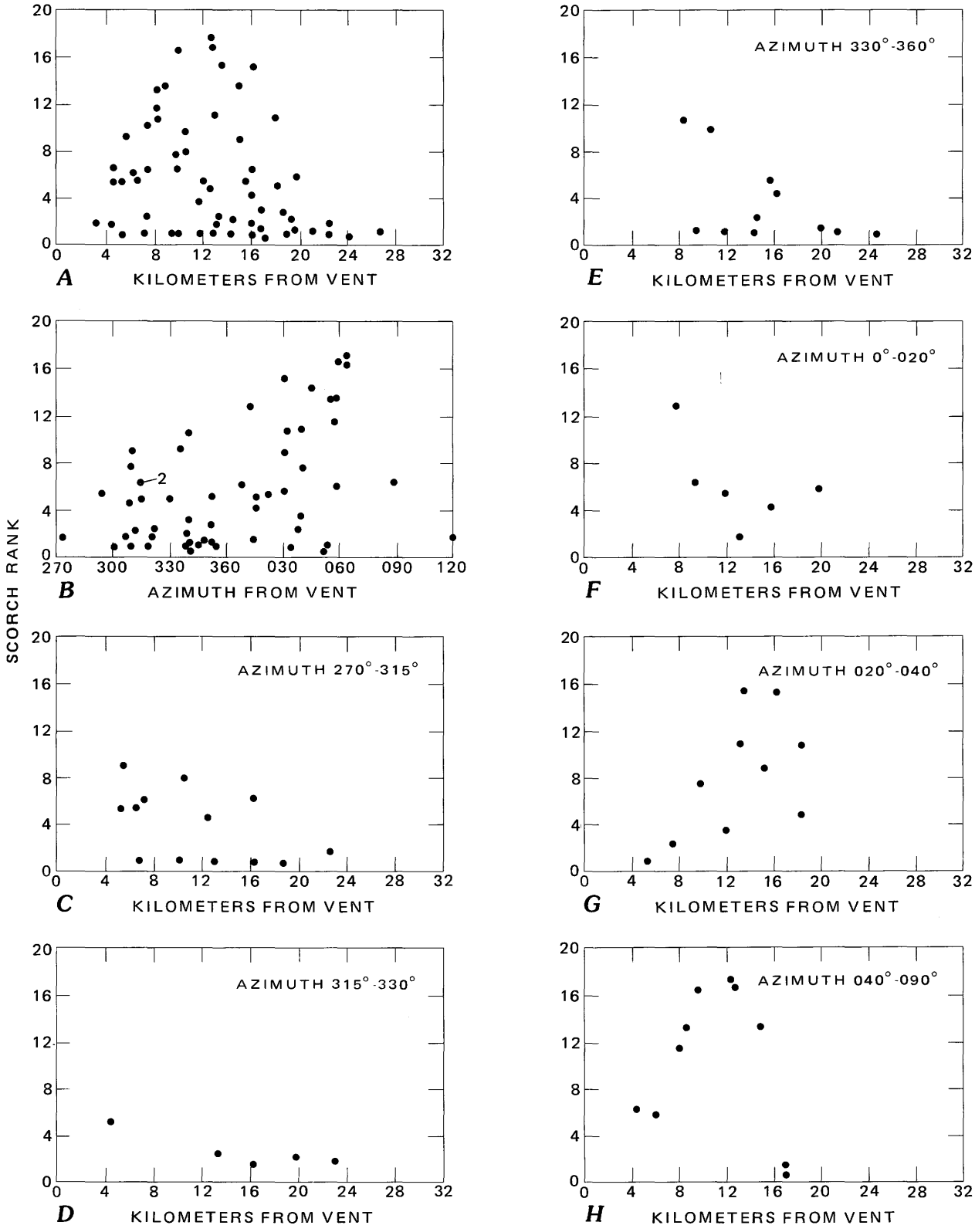

Figure 181.—Rank of thermal effects on tree remnants (scorch rank of table 28) in area devastated on May 18, versus distance and azimuth of locality from vent. The number 2 in B indicates two data points at same locality.

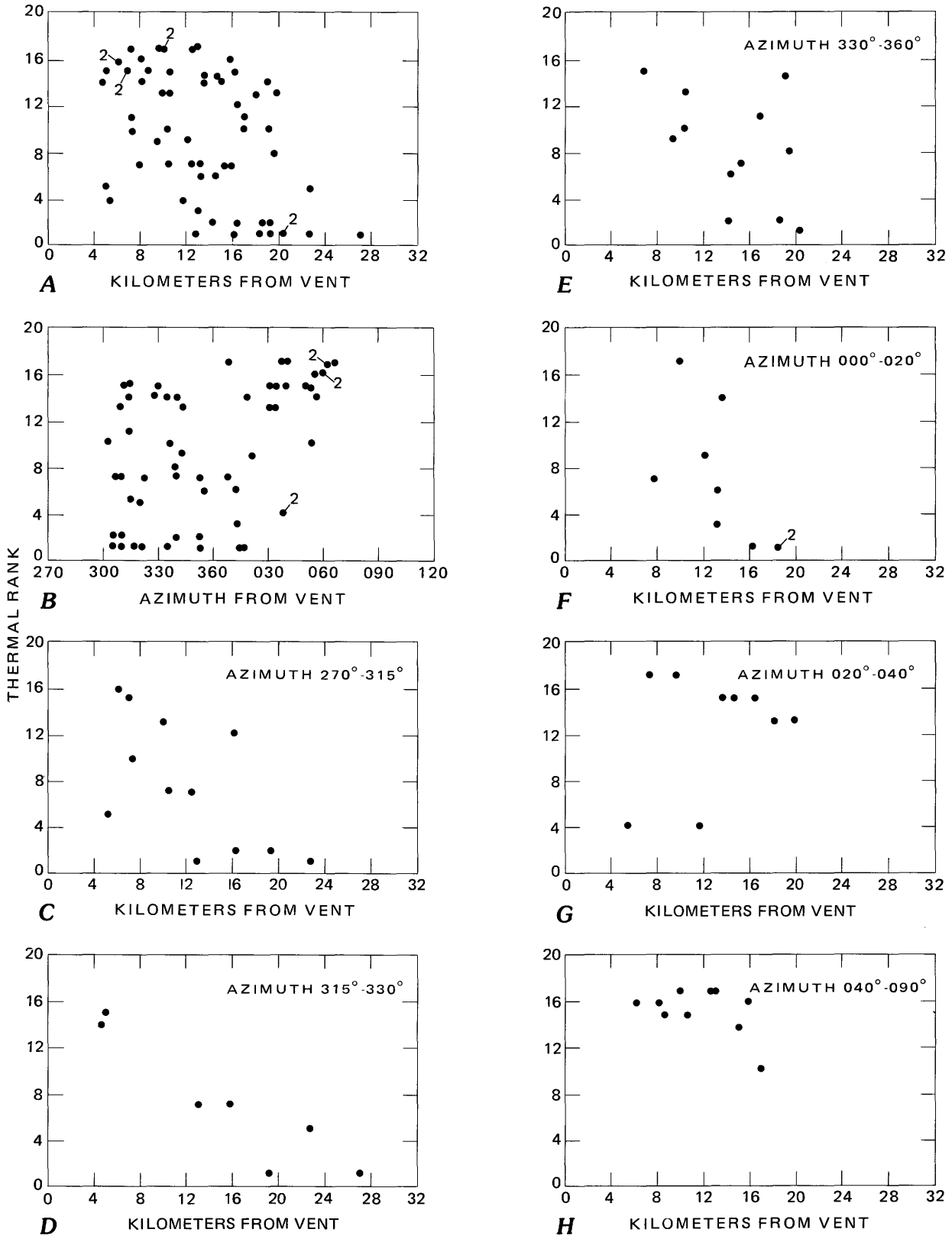

Figure 182.—Rank of thermal effects on wood (thermal rank of table 28) included in deposits of directed blast of May 18, versus distance and azimuth from vent. The number 2 in A and B, indicates two data points at same locality.

that accompanied the pumiceous pyroclastic flows (159°C; fig. 183*A*). Two of the single temperature measurements yielded the same value (307°C, fig. 183*A*), although obtained at sites separated horizontally by 850 m and stratigraphically by at least seven flow units that had an aggregate thickness of 30 m. Thus, they are probably emplacement temperatures. Other single measurements gave temperatures of 217°, 297°, 288°, 270°, and 305°C at depths of 1–1.5 m.

The low temperature (217°C; fig. 183*A*) was obtained at 1.5-m depth in surge deposits of unknown thickness that locally mantle the flowage deposits. The surge deposits were produced when phreatic explosions over the former bed of the North Fork Toutle River excavated debris pits in the pyroclastic-flow deposits. Consequently, this temperature is not representative of the underlying flowage deposits. Similarly, a temperature of 96°C obtained at a depth of 1 m 4 days after the eruption (east of the mountain and not shown on fig. 183 or in table 30) is thought not to be an emplacement temperature. This value equals the boiling point of water at the site.

Emplacement temperatures vary little across the direction of flowage of the deposits (fig. 183*A*), and although the measurement taken nearest to the vent was somewhat greater than the others, temperatures did not drop significantly between 1.8 and 7 km from the vent (fig. 184*A*). On the other hand, the temperature measured in the deposit from the ash cloud (159°C) was significantly lower than that in the flowage deposits (fig. 184*A*).

PYROCLASTIC-FLOW DEPOSITS OF MAY 25

Two areally restricted pyroclastic-flow deposits resulted from the eruption of May 25. The main deposit terminated at 3,900 ft elevation, below what is informally called the stairsteps (fig. 183*B*). A smaller deposit was emplaced on top of deposits of May 18 on the Forsyth Glacier between about 6,000 and 5,000 ft elevation. Because of poor weather, these deposits were not discovered (by another field party) until 2 days after the eruption, and temperature measurements were not made until 6 days after emplacement. Temperature profiles, measured near the distal ends of both lobes where the deposits were thickest (as much as 3 m), were parabolic; thus, emplacement temperatures were not obtained. The maximum temperatures on the two profiles were 156° and 155°C (fig. 183*B*; table 30).

PYROCLASTIC-FLOW DEPOSITS OF JUNE 12

The June 12 deposits consist of pumice blocks of tan, banded, and gray dacite in an ash matrix. Measurements 15 hr after the eruption indicate that emplacement temperatures generally were higher than those of the previous two eruptions: 361°–389°C for late flow lobes and 450°–602°C for the early flow lobes (fig. 183*C*; table 30).

At two localities, measurements suggested that the matrix was emplaced at a lower temperature than some of the pumice blocks and that insufficient time had elapsed prior to measurement to permit equilibration. Profiles obtained near the terminus of the eastern lobe had 1.9-m-long isothermal (490°C) segments. At the same site, a single measurement of 521°C was obtained at a depth of 1.5 m where the probe encountered an obstruction. Similar results were obtained from a thick deposit at the terminus of the main lobe (fig. 183*C*) where four, 3-m-long adjacent profiles had 490°C isothermal segments, and a single temperature of 528°C was measured against an obstruction at a depth of 3 m.

Within 2 days of the eruption, one or more profiles to 3-m depth at five localities had isothermal segments, and two deeper profiles (to 7 m) were established 55 days after the eruption. At three of these localities, the profiles exhibited abrupt temperature changes with depth, suggesting the presence of two or more flow units that had different emplacement temperatures. For example, the surface unit nearest the vent had an isothermal segment at 389°C, whereas an underlying unit yielded a minimum value of 420°C. Temperature pairs deduced at the other localities are separated by a slash mark on figure 183*C*; the higher temperatures are from the stratigraphically lower units and suggest that at least four units comprise the deposits (361°–389°, 450°, 490°, and about 600°C).

PYROCLASTIC-FLOW DEPOSITS OF JULY 22

Two units, recognizable by color, compose the flowage deposits of July 22 (table 29). The first unit

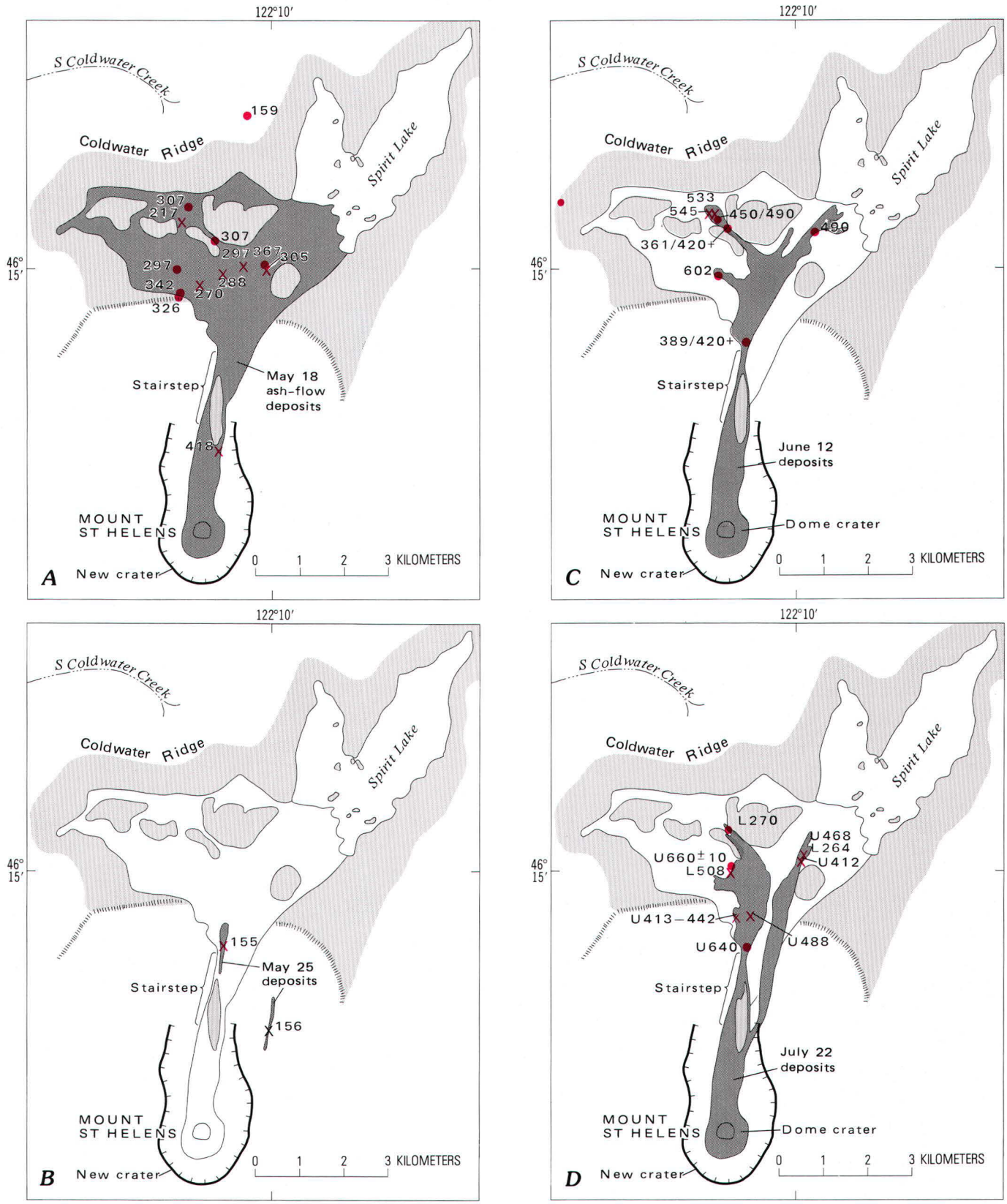

Figure 183.—Sketch maps and temperature data of deposits of the pyroclastic flows in 1980. A, May 18; B, May 25; C, June 12; D, July 22; E, August 7; F, October 17.

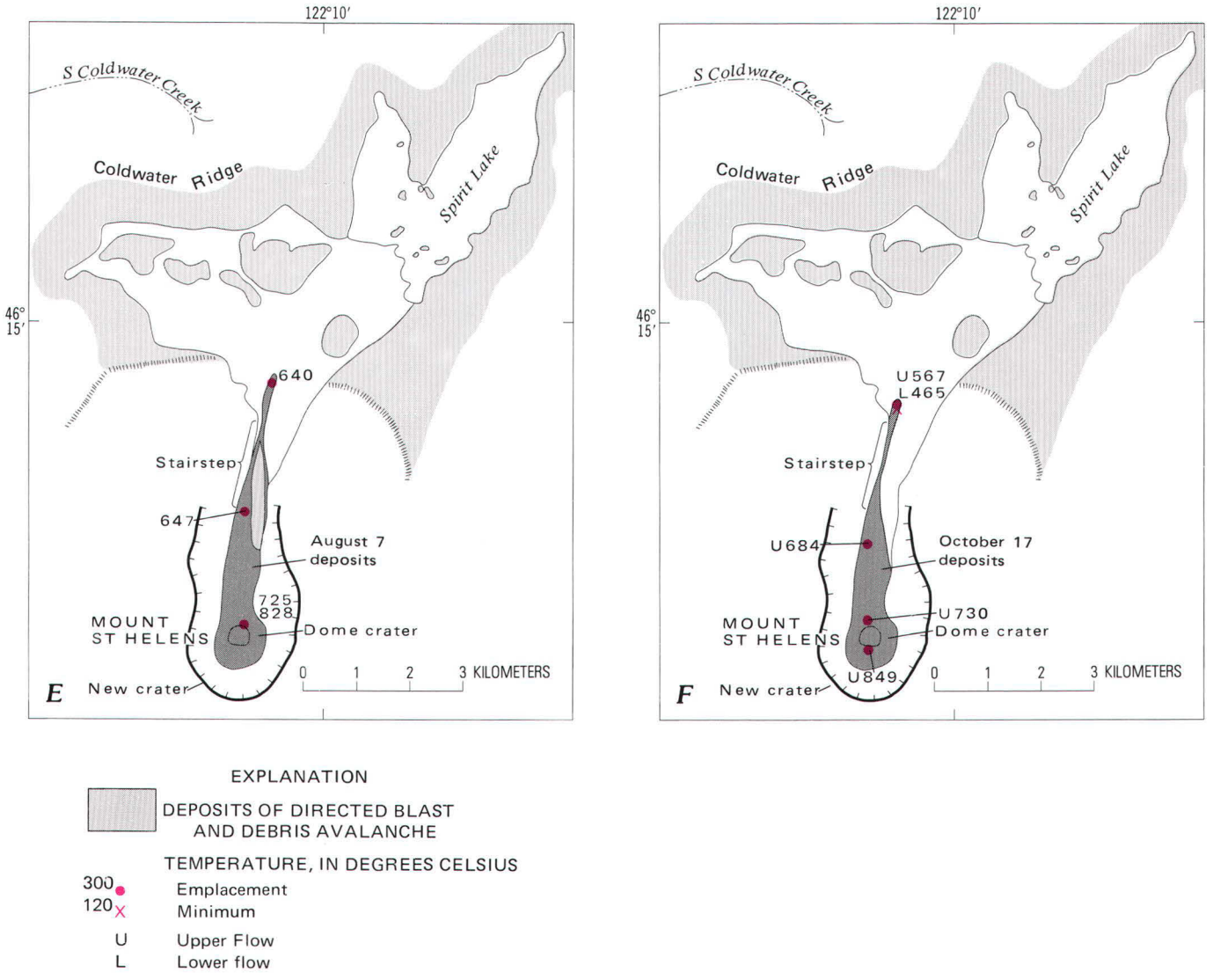

erupted was light tan, and the second (emplaced 30 min later) was light salmon-pink. A single temperature measurement was made on the distal portion of the second unit about 35 minutes after emplacement (658°C at 10 cm). Eighteen hours later, the highest temperature on a profile at the same site was 588°C at 30 cm, indicating that substantial cooling had occurred. However, at three sites about 50 m away, the same unit yielded isothermal profile segments at 660°C (fig. 183*D*), and at a locality 1.5 km nearer the vent, several other profiles yielded isothermal segments at 640°C. Similar to deposits of June 12, the profiles had temperature irregularities (to 705°C) that suggested thermal equilibration between the ash matrix and some of the larger pumice blocks had not yet occurred.

Profiles measured in the tan unit lacked isothermal segments; the maximum temperatures of these profiles were much less than those of the upper unit; 270°C (at 16 hr, distal end), 508°C (at 18 hr, same locality at which 660°C was measured in the upper unit), and 442°C (at 4 days, same locality at which 640°C was measured in the upper unit).

A final interesting temperature for the July 22 eruption is suggested by the complete removal of plastic and the softening of glass in a fiberglas survey stake in the path of the salmon-colored flow. A temperature of about 800°C for a minute was required to produce these effects on the stake (Mark Davis, oral commun., 1980). This temperature exceeds by 150°C the average emplacement temperature of the flow (and by 95°C the highest clast-related temperature

in the deposit), a relationship similar to that noted earlier between emplacement temperatures of the May 18 blast deposits and estimated temperatures of the plastics exposed to the directed blast.

PYROCLASTIC-FLOW DEPOSITS OF AUGUST 7

Isothermal and nearly isothermal segments of 645° ± 5°C were obtained in profiles at two localities (several sites each) on the flowage deposits of August 7 (figs. 183*E*; table 30). The profiles were measured within 20 hr of emplacement. Slightly higher temperatures were measured in medial and lateral levees han in the centers of the deposits presumably because the thicker levees had lost less heat by convection and radiation. Overall, the August deposits appeared to cool faster than the deposits of earlier eruptions, possibly because a comparatively higher clast-to-matrix ratio allowed faster convective cooling.

In August, temperature profiles were measured for the first time on the ejecta rampart around the vent. Measurements as deep as 2.7 m at seven sites on the rampart were completed by August 13. The temperatures ranged from 725° to 828°C, indicating that much cooling of the material in the basal avalanche occurred during formation of the flow between the vent and the first locality downslope (figs. 183*E* and 184*D*). Thereafter, however, this material cooled little or not at all along the rest of the flow path (fig. 184*D*).

Attempts to drive pipes deeper than 2.7 m at about 20 other sites on the rampart were futile. Penetration usually ceased rather uniformly at about 1–1.5 m, except in the thickest, coarsest, and lowest temperature deposits on the eastern part of the rampart (2–2.7 m penetration). The high temperatures and the nearly uniform depth of impenetrability suggest that the near-vent facies of the August 7 deposits might be welded to some degree. An incipiently welded unit was observed in an older (June 12 or July 22) near-vent unit exposed on the north side of the vent rampart. However, temperatures of welding of the older unit are unknown.

PYROCLASTIC-FLOW DEPOSITS OF OCTOBER 17

Two main flowage units were erupted on October 17 (table 29). Five profiles, measured near the distal end of the first unit (0935 PDT) within 5 hr of the eruption, suggest an emplacement temperature of 465°C (fig. 183*F*; table 30). Because of hazardous conditions nearer the vent, no other measurements were made on these deposits prior to their burial by deposits of the 2116 eruption.

Four profiles measured in distal deposits of the 2116 eruption, 14 hr after emplacement, had nearly isothermal segments of 567°C, a temperature considerably higher than that obtained at the same place in the terminal deposits of the earlier unit (fig. 183*F*). Shallow profiles and single-temperature measurements were obtained at two other localities upflow in the 2116 unit (fig. 183*F*), and several single temperatures were obtained on the ejecta rampart south of the dome (highest = 849°C, 10 cm depth). Because of poor penetration of the thermocouples and because the thin flows cooled slightly during the span of the measurements (13–41 hr after emplacement), somewhat less is known about the emplacement temperatures of the October 17 deposits than earlier deposits. However, the data define a pattern similar to the data of August (compare fig. 184*D* and 184*E*): a substantial decrease between the vent-facies material and the flowage deposits only a few hundred meters downslope, and a less substantial decrease in the next 4 km of flowage.

SUMMARY AND DISCUSSION

Vent-facies deposits of the August and October eruptions were emplaced at about 100°–150°C below magmatic temperature (950°C; Melson and others, 1980). This initial cooling probably was due to adiabatic expansion of the eruptive cloud and to mixing with air during eruption. Emplacement temperatures decreased by at least another 150°–200°C within the first several hundred meters of travel of the flows, and presumably this additional cooling resulted from incorporation of air and additional adiabatic expansion during development of flowage. However, the emplacement temperatures of the deposits were approximately uniform over the rest of the flow path, despite a 700-m drop in elevation and an additional 2–4 km of travel.

Like the deposits of August and October, uniform and nearly uniform emplacement temperatures along flow paths characterize the deposits of May 18, June 12, and July 22. The near-uniformity of emplacement

temperatures along flow paths of the directed blast is even more striking (as far as 20 km from the vent), and the direct measurements are supported by data from the the plastics, trees, and included wood. This recurring trend of isothermal emplacement temperatures along substantial distances of the flow paths requires that most of the ejecta cooled during eruption and early stages of both the directed blast and the pumiceous pyroclastic flows, and that little cool air was incorporated by the flows along most of the flow path. In essence, our data are a direct confirmation of the observations of Smith (1963) that the ash-flow mechanism must be extremely heat conservative to explain welding in ash flows at distances of tens of

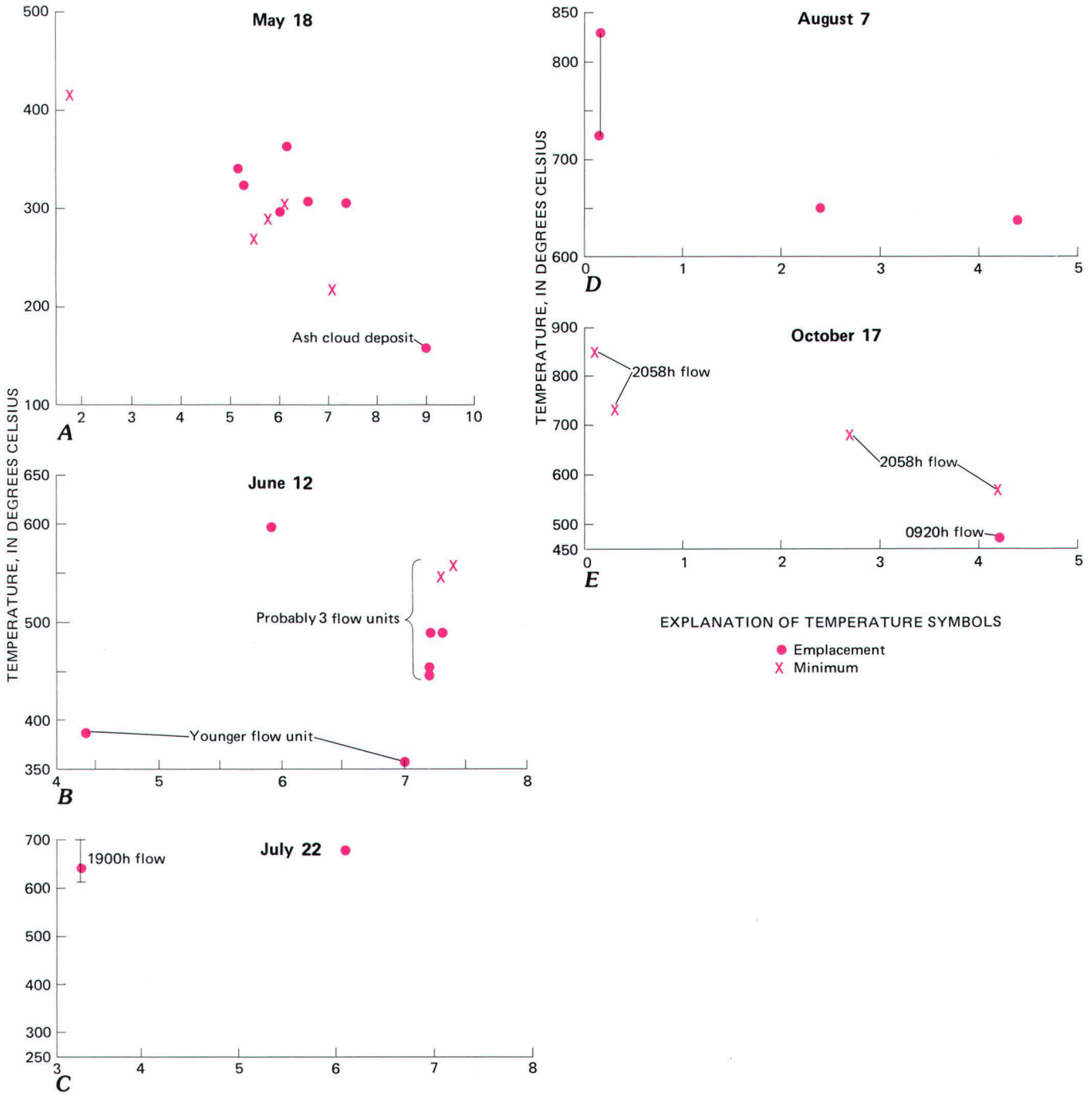

Figure 184.—Temperature versus distance from vent of pyroclastic-flow deposits emplaced during a 5-mo period in 1980.

kilometers from the vent.

Long distances of travel and the impressive, turbulent ash clouds shown in the literature and observed along the flow paths of the directed blast and the May, July, August, and October pumiceous pyroclastic flows indicate the presence of a significant gas phase along the entire path of flow. At some of the deposits, soon after their emplacement when they still were degassing strongly, the emitted gas was neither objectionable nor toxic and seemed to be almost entirely hot atmospheric air (Casadevall and Greenland, this volume).

The air probably was entrapped turbulently at the flow fronts (see also Wilson, 1980; Wilson and Head, this volume). However, had much of the material in the turbulent flow front been incorporated into the basal avalanche, it seems likely that gradual downflow cooling of the basal avalanche would occur, in conflict with the temperature data. On the other hand, if the material that was cooled by interaction with air was immediately deposited and overrun by the basal avalanche, and part of the fines contributed directly to the ash cloud, no cooling of the overriding avalanche would occur. In addition, the air that had been heated while it interacted with the flow front, could be incorporated in the following mass without significantly cooling it. This air would help both to maintain fluidization of the avalanche and to feed the elutriation cloud. Furthermore, the heated air escaping from the deposit would lubricate the sole of the overriding basal avalanche.

We believe that material at the leading edge of the flow cools and is deposited during turbulent mixing with air, whereas the overriding avalanche remains at a relatively constant and presumably higher temperature than the emplacement temperature of the deposit. No data are available that demonstrate that the flow front is the major site of deposition of the basal avalanche, but if the thermal data from the plastics truly reflect the temperature within the active flows, then temperatures of emplacement were less than those within the flows.

REFERENCES CITED

Allen, E. T., and Zies, E. G., 1923, A chemical study of the fumaroles of the Katmai Region: Contributed Technical Papers of the National Geographic Society, Katmai Series, no. 2, p. 75–155.

Aramaki, S., and Akimoto, S., 1957, Temperature estimation of pyroclastic deposits by natural remanent magnetism: American Journal of Science, v. 255, p. 619–627.

Cotton, C. A., 1952, Volcanoes as landscape forms: London, John Wiley, 416 p.

Day, A. L., and Allen, E. T., 1925, Volcanic activity and hot springs of Lassen Peak: Carnegie Institution of Washington Publication 360, p. 50–51.

Davis, M. J., Graber, E. J., Harrah, L. A., and Hayes, D. B., 1980, Temperature estimates of May 18 eruption of Mount St. Helens made from observations of material response [abs.]: EOS, v. 61, p. 1136.

Gilbert, C. M., 1938, Welded tuff in eastern California: Geological Society of America Bulletin, v. 49, p. 1829–1862.

Goddard, E. N., chm., and others, 1948, Rock-color chart: National Research Council (reprinted by Geological Society of America, 1951, 1970), 6 p.

Gorshkov, G. S., 1959, Gigantic eruption of Bezymianny Volcano: Bulletin Volcanologique, v. 20, p. 77–109.

Gorshkov, G. S., and Dubik, Y. M., 1970, Gigantic directed blast at Shiveluch Volcano, Kamchatka: Bulletin Volcanologique, v. 34, p. 261–288.

Griggs, R. F., 1918, Are the Ten Thousand smokes real volcanoes?: Ohio Journal of Science, v. 19, no. 2, p. 97–116.

Hoblitt, R. P., and Kellogg, K. S., 1979, Emplacement temperatures of unsorted and unstratified deposits of volcanic rock debris as determined by paleomagnetic techniques: Geological Society of America Bulletin, pt. 1, v. 90, p. 633–642.

Hoblitt, R. P., Banks, N. G., Ryan, M. P., Rosenbaum, J. G., and Davis, M. J., 1980, Emplacement temperatures of Mt. St. Helens eruptive products: Geological Society of America Abstracts with Programs, v. 12, no. 7, p. 447.

Johnston, D. A., 1978, Volatiles, magma mixing, and the mechanism of eruption of Augustine Volcano, Alaska: University of Washington Ph. D. thesis, 177 p.

Kienle, Juergen, and Swanson, S. E., 1980, Volcanic hazards from future eruptions of Augustine volcano, Alaska: Fairbanks, Geophysical Institute, University of Alaska report UAG R-275, 122 p.

Kozu, S., 1934, The great activity of Komagatake in 1929: Tchermaks Mineralogische and Petrographische Mitteilungen, p. 133–174.

Macdonald, G. A., and Alcaraz, Arturo, 1956, Nuées ardentes of the 1948–1953 eruption of Hibok-Hibok: Bulletin Volcanologique, v. 18, p. 169–178.

Maury, R., Arai, F., Mimura, K., Hayatsu, K., and Kobayashi, K., 1973, Estimation des températures de mise en place de brèches pyroclastiques du Japon d'aprés l'étude de leur bois carbonisés: Comptes Rendus Hebdomadaires des Séances de l'Académie des Sciences, v. 277, ser. D, p. 1621–1624.

Melson, W. G., Hopson, C. A., and Kienle, C. F, 1980, Petrology of the tephra from the 1980 eruption of Mount St. Helens: Geological Society of America Abstracts with Programs, v. 12, no. 7, p. 482.

Mimura, Koji, Kobayashi, K., and Maury, R. C., 1975, A carbonized wood and associated "fossil smoke" in the Kurofuji pyroclastic flow: Volcanological Society of Japan, Bulletin, v. 20, 2d ser., no. 2, p. 79–86.

Perret, F. A., 1937, The eruption of Mt. Pelee 1929–1932: Carnegie Institution of Washington Publication 458, 126 p.

Sayre, J. D., and Hagelbarger, P. R., 1919, A study of the temperatures in the Valley of Ten Thousand Smokes: Ohio Journal of Science, v. 19, p. 249–278.

Smith, R. L., 1963, Ash-flow problems—a synthesis based on field and laboratory studies [abs.]: Bulletin Volcanologique, v. 25, p. 109–110.

Smith, R. L., Friedman, Irving, and Long, W. D., 1958, Welded tuffs, Experimental I [abs.]: American Geophysical Union Transactions, v. 39, no. 3, p. 532–533.

Taylor, G. A., 1958, The 1951 eruption of Mount Lamington, Papua: Commonwealth of Australia, Department of National Development, Bureau of Mineral Resources, Geology and Geophysics, Bulletin 38, 99 p.

Van Bemmelen, R. W., 1949, Geology of Indonesia, volume 1: The Hague Government Printing Office.

Wilson, C. J. N., 1980, The role of fluidization in the emplacement of pyroclastic flows—An experimental approach: Journal of Volcanology and Geothermal Research, v. 8, p. 231–249.

Zies, E. G., 1924, Hot springs of the Valley of Ten Thousand Smokes: Journal of Geology, v. 32, p. 303–310.

_____1929, The fumarolic incrustation and their bearing on ore deposition: National Geographic Society Technical Paper, v. 1, no. 4, 61 p.

FIR LEAVES AS THERMOMETERS DURING THE MAY 18 ERUPTION

By WILLIAM E. WINNER[1] *and* THOMAS J. CASADEVALL

ABSTRACT

Fir leaves (needles) were heated at 20°C, 100°C, and 250°C for 2 min, and the melting patterns of cuticular waxes were observed with a scanning electron microscope. These patterns were compared with the cuticular appearance of leaves from two sites in the zone of seared, brown trees at the margin of the blast zone from the May 18 eruption of Mount St. Helens. We conclude that the maximum air temperatures at these sites were about 50°C and 250°C. The appearance of the cuticular waxes of leaves from sites in the seared zone may be used to infer the maximum temperatures at the margin of the blast zone and to determine if heat could have been the cause of death of needles on trees that remained standing after the eruption.

INTRODUCTION

The May 18 eruption of Mount St. Helens devastated many hectares of forest with heat, pressure, gases, and ash of the laterally directed blast. Because instruments for monitoring air temperature, barometric pressure, and gas concentrations were lost during the eruption, few data were available for analyzing the thermal and gas characteristics of the eruption cloud that swept downslope from the crater. In addition, because leaf death can result from either exposure to volcanic SO_2 (Winner and Mooney, 1981) or heat, the cause of death to leaves that remained on trees standing at the perimeter of the blast zone after the eruption was unknown.

Aerial photographs taken 1–2 hr after the start of the May 18 eruption show a discolored zone along the western perimeter of the blast area. In the following weeks the foliage in this zone became brown as it died (fig. 185). This suggests that damage to the leaves was due to a rapid thermal pulse, associated with the early directed blast of the May 18 eruption, and evidence from eyewitnesses suggests that the pulse lasted only a few minutes. The later phase of the eruption responsible for the pumiceous pyroclastic flows, which began shortly after noon, had little additional effect on the vegetation at the perimeter of the blast area. Figure 186 shows the contrast between zones of healthy foliage, seared foliage, and downed trees along the valley of Green River.

We have found that the cuticular waxes of heated fir (*Abies* sp.) leaves (needles) melt in patterns which are temperature specific, providing the time of exposure is the same. One purpose of this report is to show how the appearance of cuticles provides a record of the maximum air temperature to which a leaf has been exposed. In addition, we have analyzed the cuticles of leaves gathered from two sites near Mount St. Helens. These leaf samples demonstrate the potential for using cuticular features to estimate maximum temperatures at sites throughout margins of the blast zone. The estimated temperatures are high enough to indicate that heat alone could have killed leaves in the blast zone. Fir leaves from three additional sites are being studied.

[1]Department of Biological Sciences, Stanford University, Stanford, Calif. 94305.

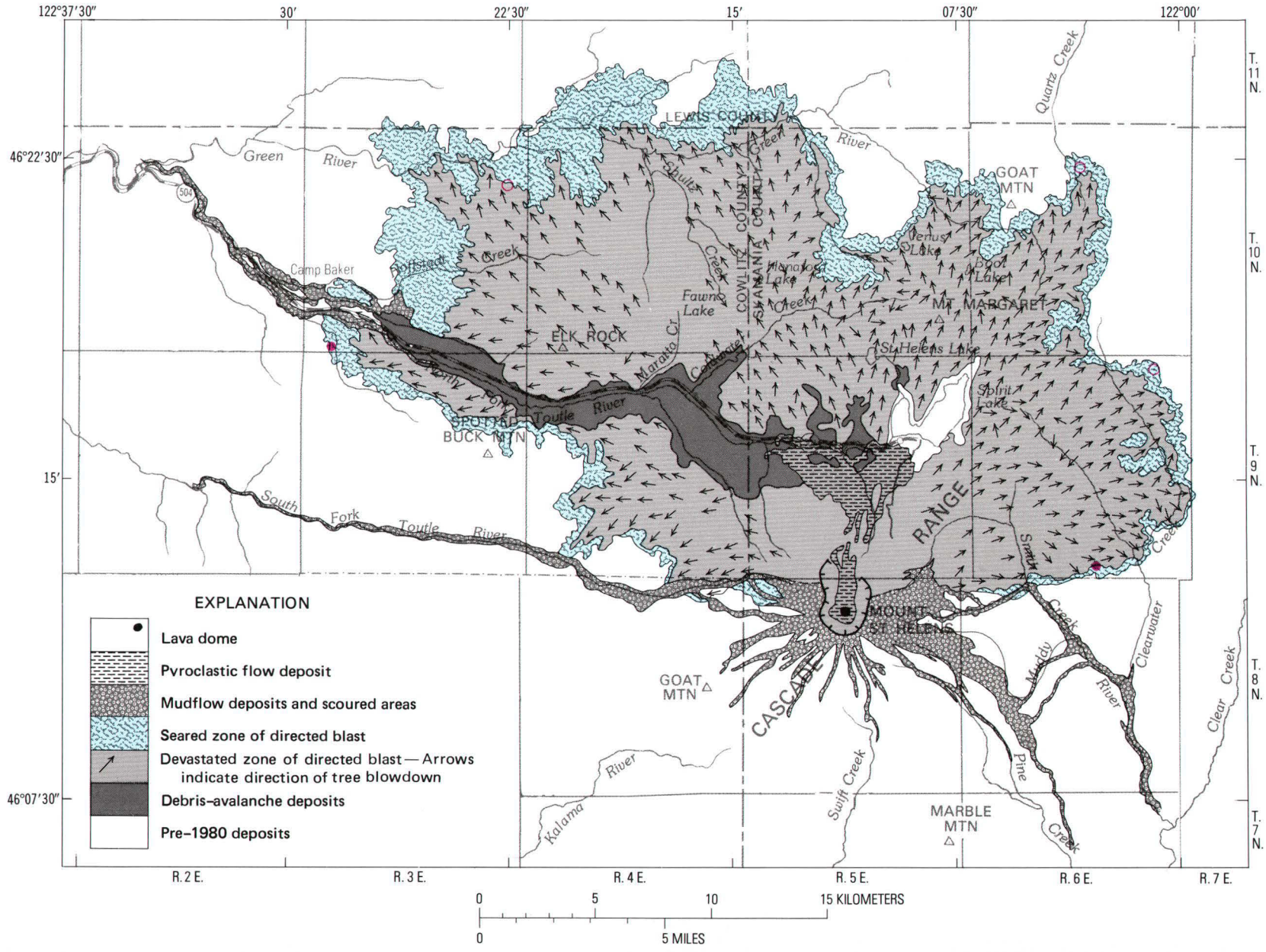

Figure 185.—Location map showing seared zone produced by the May 18 eruption. Samples from sites 1 and 2 (solid circles) are discussed in this report; fir leaves collected from additional sites (open circles) are currently under study.

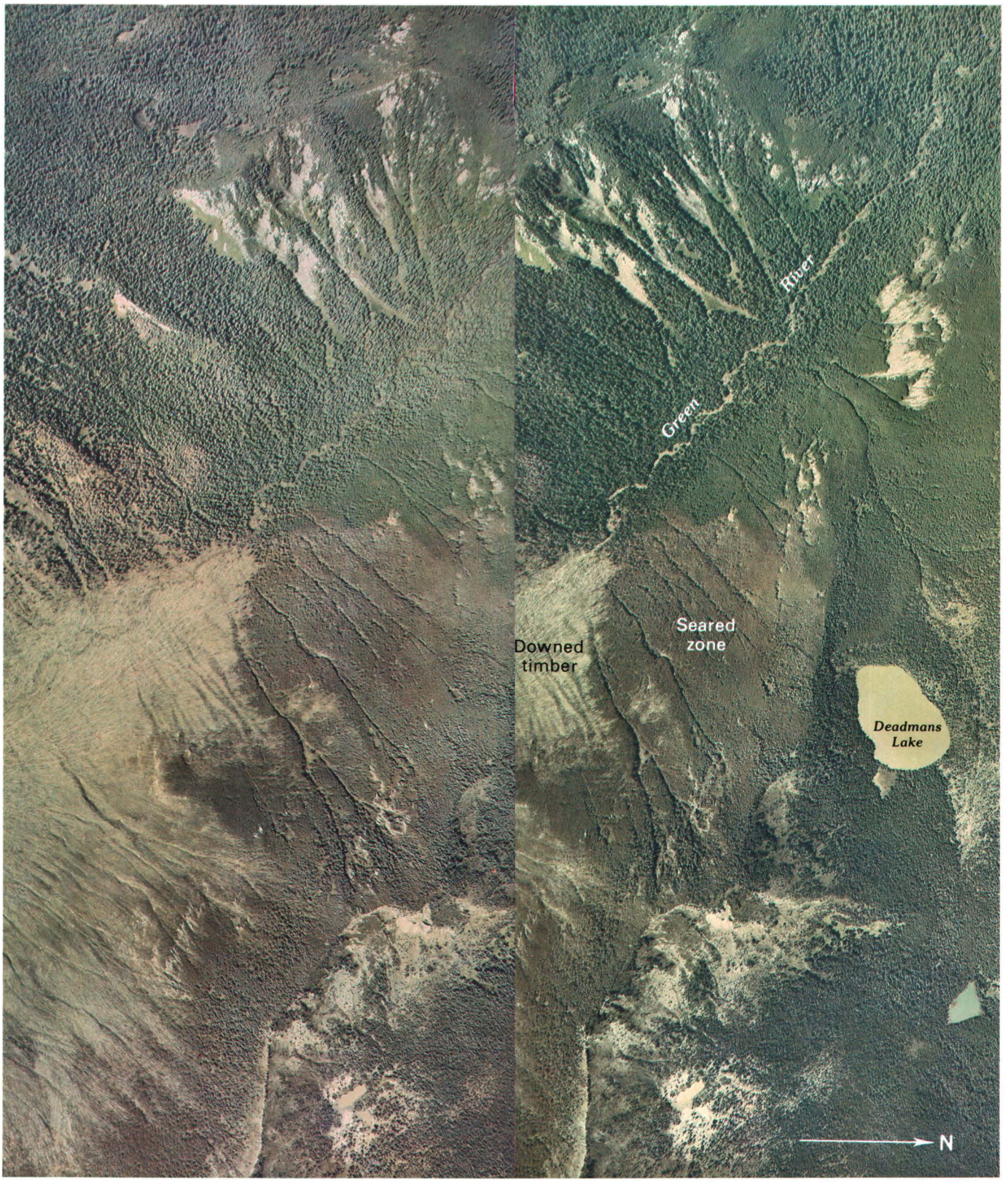

Figure 186.—Stereophotographs taken on June 19, 1980, showing seared zone along the valley of Green River, 20 km north of the volcano. Note sharp contrast between areas of healthy foliage (green) and seared zone (brown). To the south, note the pattern of downed timber. Photographs from U.S. Forest Service (USDA 180–104 and 180–105).

MATERIAL AND METHODS

Mature fir branchlets (probably *Abies amabilis* [Dougl.] Forbes; all taxonomy follows Hitchcock and Cronquist, 1973) killed on May 18 were collected from two sites from the seared zone at the perimeter of the blast area. Site 1, near Smith Creek Butte at 960 m elevation, is 8 km east of the volcano (fig. 185). The site was covered with 6–8 cm of blast material overlain by lumps of pumice as large as 5 cm in diameter. Trees at the site were not physically damaged except for their leaves, which had changed from green to brown. Site 2, near Camp Baker at 530 m elevation, is 21 km west-northwest of the volcano. Less than 5 mm of fine gray ash covered the ground at this site. The demarcation between healthy trees and those with dead leaves was abrupt at most localities (see fig. 186). Randomly picked leaves were prepared for the scanning electron microscope (SEM) by air drying, wiping with wetted tissue to remove volcanic ash, and mounting on aluminum stubs with silver-conducting paint. The mounted leaves were coated with carbon in a vacuum. Images were taken with an AMR (Bedford, Mass.) model 1000 SEM operating at 20 kV.

In addition, branchlets picked from a 2-m-tall Grand fir (*Abies grandis* [Dougl.] Forbes) purchased from a nursery in a stage of seasonal development comparable to those in the seared zone, were placed in one of three ovens preset at 20°C, 100°C, and 250°C, respectively. The heat treatments lasted 2 min, which is our best estimate of the duration of peak temperatures from the eruption, based on eyewitness observations (Rosenbaum and Waitt, this volume). Leaves picked from the branchlets following the heat treatments were mounted for the SEM in the manner previously described.

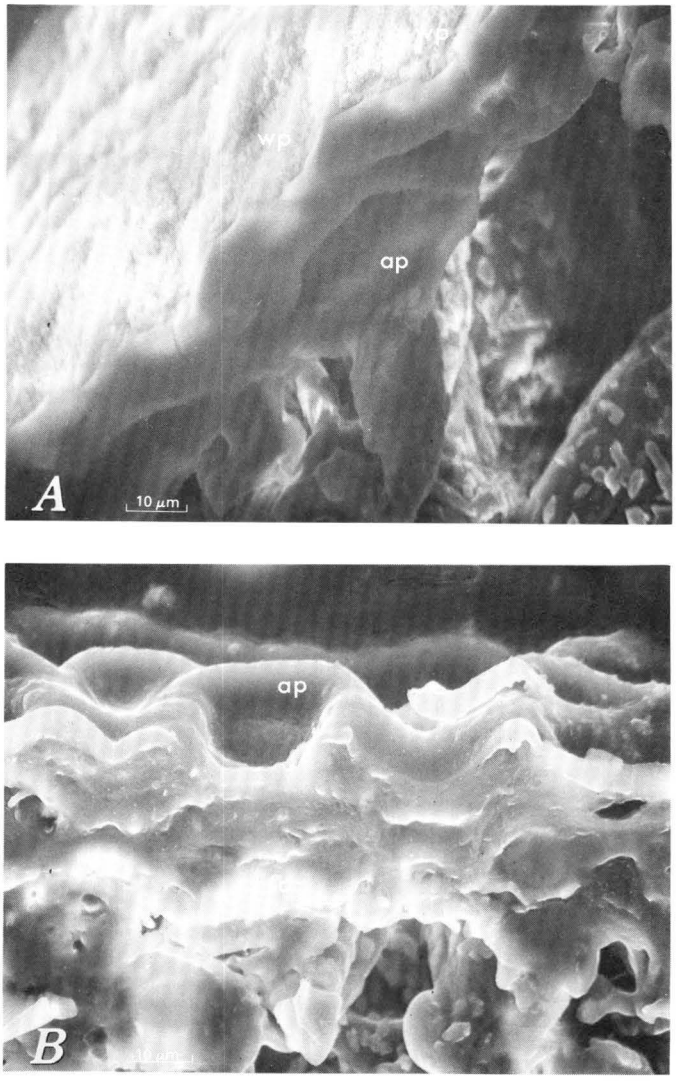

Figure 187.—Cross sections of stomata on leaves of Grand fir after heat treatments. A, heated to 20°C; B, 250°C. Wax plug (wp) *in antechamber pore* (ap) *rose into the substomatal cavity* (sc) *following the 250°C heat treatment.*

RESULTS AND DISCUSSION

Fir leaves have a waxy cuticle, which prevents water loss from the leaf. The bottom (abaxial) leaf surface has stomata that allow the transpiration of gases such as CO_2 and H_2O between the leaf and air. At each of the elevated oven temperatures, the cuticle wax was melted, particularly the wax plugging stomatal pores. The degree of cuticular deformation provided a record of the maximum temperature to which the leaf was exposed.

Figure 187*A* shows the appearance of a Grand fir stomata, in longitudinal cross section. A prominent feature of the stomata is a wax-plugged antechamber. The leaves of the Sitka spruce (*Picea sitchensis*), a conifer studied more thoroughly than the fir, have stomatal structures (Jeffree and others, 1971) similar to those we observed. Wax plugs in antechambers of Sitka spruce leaves are composed of tubules that are about 150 mm in diameter and 1 mm long. The plugs are thought to increase stomatal resistance to H_2O from about 6 to 18 s/mm, thereby acting to conserve water. These waxy plugs in fir leaves are assumed to have a similar function.

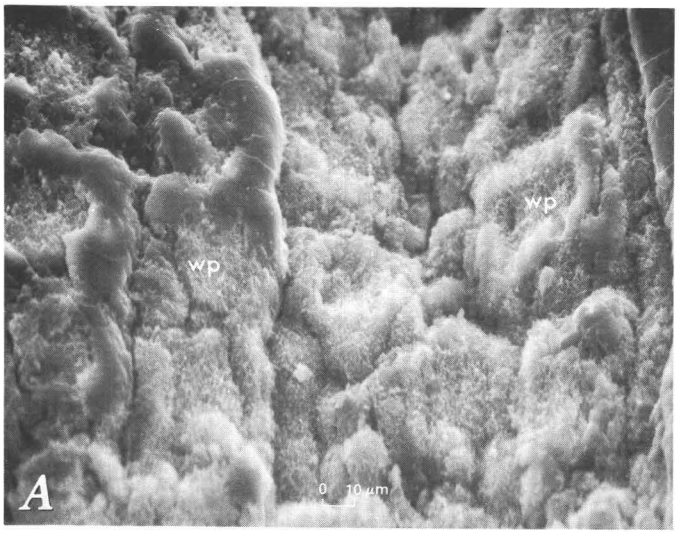

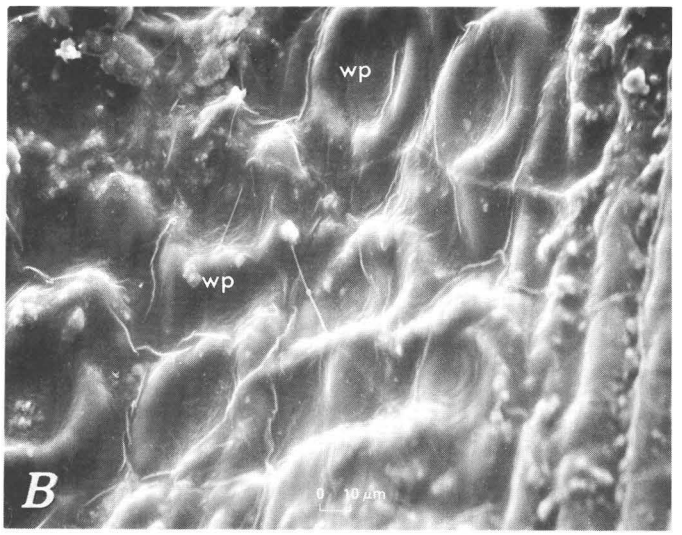

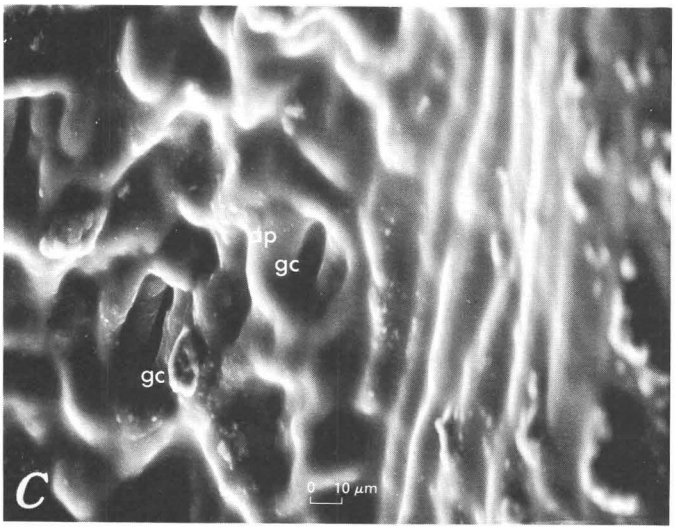

Figure 188.—Whole mount of lower leaf surface of Grand fir after heat treatments. A, heated to 20°C; B, 100°C; C, 250°C. As temperature increased, the wax plug (wp) in the stomatal antechamber pore (ap) melted. Guard cells (gc) are exposed after 250°C treatment (C).

Heating a Grand fir leaf to 250°C for 2 min melted the cuticular wax, and the wax plug in the stomatal antechamber rose into the space above the guard cells (fig. 187*B*), probably by capillary action. In addition, the porous wax tubes of the cuticle disappeared following the heat treatment, and the tips of some leaves were blackened.

The melting of cuticle is also apparent on abaxial surfaces of heat-treated Grand fir leaves. Leaves treated at 20°C have wax-filled antechamber pores (fig. 188*A*). Following heating for 2 min at 100°C, the waxes had melted and filled the stomatal antechamber (fig. 188*B*). Following the 250°C treatment, the waxes had melted and apparently risen into the substomatal cavity, revealing outlines of the guard cells (fig. 188*C*).

Leaves from site 1 showed little cuticle melting, and most antechambers had wax plugs which appeared unaffected by heat (fig. 189*A*). However, the rims of the antechamber pores and the crests of the ribs running longitudinally down the leaf had a glazed appearance (fig. 189*A*), similar to leaves oven heated at 50°C (figure not presented). The lethal temperature for fir leaves in mid-summer is 48°C (Larcher, 1975), although lower temperatures might have been lethal to trees on Mount St. Helens in May. Thus, evidence from the cuticular waxes of both oven- and volcano-heated leaves, as well as information about the lethal summer temperature of fir leaves, suggests that the highest temperature sustained for as long as 2 min at site 1 was about 50°C.

The wax on cuticles of leaves from site 2 was melted and appeared to have risen into the stomatal antechambers (fig. 189*B*). Waxes in some antechamber pores melted and rose into sub-stomatal cavities, revealing outlines of the guard cells. In other cases, remnants of antechamber wax plugs remained in the pores. None of the leaves from site 2 had blackened tips. The melting pattern of the cuticle and absence of charring suggest that the highest temperature sustained for as long as 2 min at site 2 was slightly less than 250°C.

The appearance of the cuticle of leaves from sites 1 and 2 indicates that heat at both locations during the

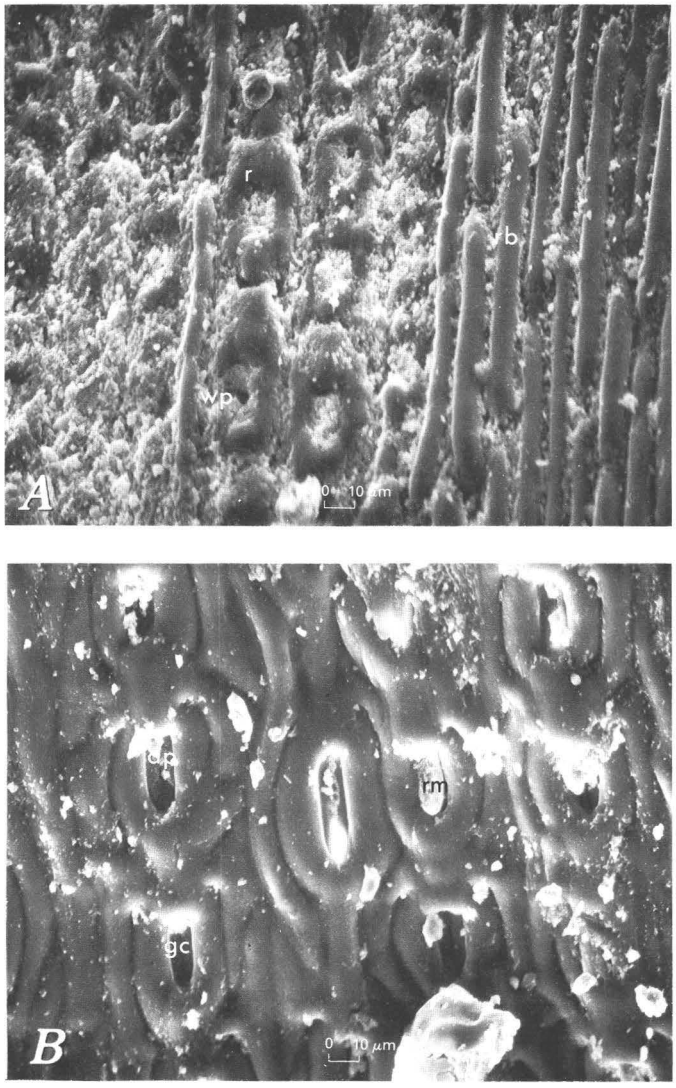

Figure 189.—Lower surfaces of dead fir leaves from sites 1 and 2 in the seared zone (see fig. 185). Wax plug (wp) *in stomatal antechamber pore* (ap) *seems intact in leaf from site 1 (A), but only wax plug remnants* (rm) *remain on leaf from site 2 (B). Cuticle of rim* (r) *of antechamber pore and ribbing* (rb) *appears glazed in leaf from site 1 (A), and outlines of guard cells* (gc) *are apparent in some stomata on leaf from site 2 (B).*

eruption was greater than 50°C, hot enough to result in leaf death. However, volcanic SO_2 or droplets of H_2SO_4 may also have played a role in causing leaf death. Site 1 was closer to the volcanic crater, was higher in elevation, and was subjected to temperatures nearly 200°C cooler than site 2. Although hot ejecta were deposited on site 1, this site was at the southern margin of the eruption cloud and it is inferred from this study that the air temperatures remained relatively cool. Site 2 was 2,400 m lower in elevation than the crater and 21 km away, but it was in one main path of the directed blast. The higher air temperatures at site 2 may have resulted from heated air, which was trapped and carried between hot ash particles that were falling and flowing downhill. Analyses of leaves from additional sites (fig. 185) may provide further insight into the temperature patterns in the seared zone of the blast area. These estimates would be of geological interest and could reveal patterns of heat dispersion from the eruption of May 18, 1980.

REFERENCES CITED

Hitchcock, C. L., and Cronquist, A., 1973, Flora of the Pacific Northwest: Seattle, University of Washington Press, 730 p.

Jeffree, C. E., Johnson, R. P. C., and Jarvis, P. G., 1971, Epicuticular wax in the stomatal antechamber of Sitka spruce and its effects on the diffusion of water vapour and carbon dioxide: Planta, v. 98, p. 1–10.

Larcher, W., 1975, Physiological plant ecology: New York, Springer Verlag, 252 p.

Nielson, R. E., Ludlow, M. M., and Jarvis, P. G., 1972, Photosynthesis in Sitka Spruce (*Picea sitchensis* [Bong.] Carr.), II—Response to temperature: Journal of Applied Ecology, v. 9, p. 721–745.

Winner, W. E., and Mooney, H. A., 1981, Responses of Hawaiian plants to volcanic SO_2—Stomatal behavior and foliar injury: Science, in press.

REMOTE MONITORING

An obvious need existed to monitor features of eruptive activity as continuously as possible. At first this was accomplished by frequent overflights of the volcano and by manned ground observation posts, methods that worked reasonably well but were often hampered by poor radio communications and by adverse weather. Other useful monitoring techniques included observations of ash eruptions by aviation- and weather-radar systems and monitoring of the crater area with a closed-circuit video system.

Radar observations were possible because of nearby Federal Aviation Administration installations at Seattle and near Spokane, Wash., and the National Weather Service system at Portland, Oreg. Explosive eruptions could be monitored because concentrations of ash particles are detectable by radar; moreover, observations could be made at night and in overcast weather when conventional observations were difficult. Radar measurements were especially useful in determining existence, height, and duration of an eruptive column, and direction and rates of ash-cloud movement (Harris, Rose, and others). Radar observations also permit estimation of the mass in an ash cloud and potential ash fall over specified areas; estimates for the May 18 ash fall, however, are somewhat high relative to fallout measured on the ground.

The video-surveillance system, consisting of a remotely controlled camera on a ridge about 9 km north of Mount St. Helens, a microwave repeater west of the volcano, and viewing and recording equipment in the Emergency Control Center in Vancouver, became operational in mid-July. The system was used to evaluate fluctuations in gas emission, avalanche frequency, local wind conditions, and blowing ash in potential work areas, and to assess eruptive events. It was cost effective and reasonably reliable, and it reduced residence time of personnel in high-risk areas (Miller and Hoblitt).

THE 1980 ERUPTIONS OF MOUNT ST. HELENS, WASHINGTON

RADAR OBSERVATIONS OF ASH ERUPTIONS

By DAVID M. HARRIS, WILLIAM I. ROSE, JR.[1], ROBERT ROE[2], *and* MARTIN R. THOMPSON[3]

ABSTRACT

Radar systems located at Portland, Oreg., Seattle, Wash., and near Spokane, Wash., have been used extensively for observations of ash clouds from explosive volcanic eruptions at Mount St. Helens during 1980. Eruption clouds are composed of silicate particles and are therefore detectable by radar. Radar observations can be made at night and in overcast weather when conventional observations of eruptions are difficult.

Radar observations show that the May 18, 1980, eruption lasted about 9 hr and had a column height of at least 14 km relative to sea level for most of the period. During the eruption, there were four periods of increased column height, which correlated with the appearance of individual, dense ash clouds shown on the radar plan position indicator (PPI) screen. The examples of radar observations described here demonstrate the potential of radar for measuring the heights of eruption columns, determining the duration of eruptions, and determining the direction and rates of ash cloud movements downwind from the volcano. If the particle size distribution within an ash cloud is known or can be estimated, then radar observations may, in principle, provide the additional data required to estimate the mass of ash suspended in the cloud and potential ash-fall amounts over specified areas.

INTRODUCTION

Public safety could be enhanced if the locations, times, and amounts of potential ash fall could be accurately predicted during an eruption. The need for a rapid, remote-sensing method and a sound scientific basis for inferring the amount of volcanic ash that is in the atmosphere downwind from a volcano is obvious. The purpose of this paper is to illustrate the theory and application of radar to volcanic-ash clouds. Our understanding of ash-fall processes and our abilities to forecast ash fall may increase as a result of radar observations of ash clouds.

The use of radar to observe ash eruptions and to track ash clouds away from their sources is a new and significant area for volcanological research. Johnston (1978) cited radar measurements made in Alaska during eruptions of Augustine volcano in January 1976. Radar measurements of eruption column heights over Augustine were made at the National Weather Service (NWS) office in King Salmon, Alaska, and at Sparrevohn Air Force Base, apparently the first radar observations of airborne volcanic ash in the United States. In March 1980, David Johnston advised the NWS in Portland and Seattle that weather surveillance radar might be used to observe the growth, width, tops, and movement of major eruption clouds from Mount St. Helens. Two of the authors (Rose and Harris) also made requests for radar observations of ash clouds and eruption column heights without knowledge of Johnston's earlier discussions with NWS personnel, all of which led to the joint effort by the NWS and USGS reported here.

[1]Department of Geology, Michigan Technological University, Houghton, Mich. 49930.
[2]U.S. National Weather Service, 5420 N.E. Marine Drive, Portland, Oreg. 97218.
[3]U.S. National Weather Service, 3101 Auburn Way S., Auburn, Wash. 98002.

ACKNOWLEDGMENTS

This study has benefited substantially from discussions with R. C. Srivastava (Department of Geophysical Sciences, University of Chicago) and with M. D. Krohn (USGS, Reston, Va.). We are grateful for the enthusiasm and interest of the National Weather Service (Portland, Oreg., and Auburn, Wash.) and the Federal Aviation Administration (Auburn, Wash.) in recording the volcanic activity at Mount St. Helens.

DETECTION OF VOLCANIC ASH BY RADAR

The minimum concentration of volcanic ash required for detection by radar is a function of the physical parameters of the particular radar system, the size distribution and concentrations of particles in the ash cloud, and the distance between the radar source and the cloud.

THE RADAR EQUATION FOR DISTRIBUTED TARGETS

Volcanic-ash clouds are similar to thunderstorms as radar targets. Ash clouds and thunderstorms cause backscatter of some of the energy that is incident on their constituent ash particles or raindrops. Particle fallout from ash clouds may involve the growth of ash particles by coalescence of smaller ones, a physical process that is also important in rainfall. Also, thunderstorms and ash clouds are large compared to the volume occupied by one pulse of the radar. Thus, the theory governing radar reflections from meteorological targets (such as thunderstorms) may be applied to radar reflections from ash clouds.

The development of theory governing radar reflections from randomly distributed targets (such as thunderstorms) was summarized by Probert-Jones (1962). He found errors in previous theoretical radar equations, produced a mathematically correct version, and showed that radar observations agreed with the new equation within the limits of experimental error.

Probert-Jones's (1962) expression for the received power (P_r) from a target composed of randomly distributed particles is

$$P_r = \frac{\pi^3}{16 \ln 2} \frac{P_o h}{\lambda^2} \frac{G^2 \theta \phi}{R^2} \left| \frac{\epsilon - 1}{\epsilon + 2} \right|^2 \Sigma r^6 , \qquad (1)$$

where P_r = received power
P_o = peak transmitted power
h = radar pulse length in space (distance)
G = actual gain of antenna
θ = horizontal beam width to the -3 dB level for one-way transmission
ϕ = vertical beam width to the -3 dB level for one-way transmission
ϵ = dielectric constant of spherical particles
λ = wavelength
R = range
r = radius of spherical particles.

The summation, Σr^6, is taken over all the particles of various sizes in a unit volume of target space. Equation 1 above is valid when the target completely fills the beam as defined by θ, ϕ, and h at a particular range R. The actual gain, G, is the antenna gain along the beam axis relative to an isotropic radiator. The gain is related to the beam widths by

$$G = \frac{\pi^2 k^2}{\theta \phi} , \qquad (2)$$

where k is a factor that corrects for the nonuniformity of illumination of the antenna (Probert-Jones, 1962); k is approximately unity for antennas of circular cross section.

Equation 1 includes four variables in addition to those specific to a particular radar system. The terms P_o, h, λ, G, θ, and ϕ are radar-system parameters and are constant for a particular radar system. The term, $|(\epsilon - 1)/(\epsilon + 2)|^2$, depends upon the dielectric constant (ϵ) of the particles. The term, Σr^6, depends upon the size distribution and number density of the particles in the target. The term, $1/R^2$, depends upon the distance (range) between the radar system and the target. The term for received power, P_r, is a function of all of the above. Therefore, for a particular radar system, the variables in the radar equation are Σr^6, $1/R^2$, ϵ, and P_r. A solution can be obtained if three of the variables are known.

REFLECTIVITY OF ASH CLOUDS

REFLECTIVITY

The reflectivity of a radar target is a function of the abundance of particles and their scattering cross sections within the target. The reflectivity, η, is the summation of the backscatter cross sections of the particles per unit volume averaged over the radar pulse volume (Atlas, 1964). For solid spherical particles which obey Rayleigh scattering, the reflectivity is equal to:

$$\eta = \frac{2^6 \pi^5}{\lambda^4} \cdot \left| \frac{\epsilon - 1}{\epsilon + 2} \right|^2 \cdot \Sigma r^6 \qquad (3)$$

The reflectivity, η, does not appear explicitly in equation 1, but the dependence of the reflectivity upon the particle-size distribution, number density, and dielectric constant and wavelength are evident by comparing equations 1 and 3. The dielectric constant, ϵ, is that of the void-free silicate glass and (or) crystals.

REFLECTIVITY FACTOR

The reflectivity factor, Z, is a parameter of the radar target; it is equal to $\Sigma(2r)^6$, the summation of the sixth-power of the particle diameter for all of the particles in a unit volume of target space. The conventional units for Z are mm^6/m^3 (Atlas, 1964).

EFFECTS OF PARTICLE SHAPE ON REFLECTIVITY

In the case of volcanic-ash clouds, it is necessary to consider what effects, if any, the presence of voids and the occurrence of nonspherical particle shapes will have on the reflectivity. It has been shown (for instance, Atlas, 1964) that in relation to hail, enlarging an ice particle and filling voids in the particle with air changes the density, diameter, and dielectric factor in such a way that the particle's contribution to the reflectivity is unchanged. This argument also applies, by analogy, to vesicular silicate glass.

Studies of backscatter for nonspherical particles (see review in Atlas, 1964) show that the reflectivity varies as the particle shapes become more distorted from that of a sphere, as the refractive index increases, and as the orientations of the particles within a population become less random. Preferred orientation of aspherical particles may increase or decrease the reflectivity, depending upon how the long axes of the particles are alined relative to the direction of polarization of the radar wave. For a population of angular glass shards of various shapes and probably no preferred orientation within an ash cloud, the increase or decrease in reflectivity is probably small. Because the largest ash particles tend to be equant (Rose and Hoffman, 1980 and 1981) and because these make the largest contribution to the total reflectivity, failure to make corrections for the angular shapes of glass shards in the smaller size ranges probably is not significant.

RADAR TARGET PARAMETERS FOR ASH AND RAIN

Radar target parameters calculated for an ash cloud that was sampled by a research aircraft (Rose and others, 1980) are compared in table 31 with analogous parameters for warm orographic rain and thundershowers. The comparisons are helpful in determining whether such an ash cloud should be detectable by radar. Radar target parameters for the ash cloud are most similar to those for warm orographic rain even though their reflectivities differ by an order of magnitude. However, because the reflectivity factor depends on the sixth power of the particle diameter and on the number density of particles, the reflectivity factor for the ash cloud would increase nearly an order of magnitude (by a factor of 8) if the particle diameters were increased from 0.15 to 0.22 mm. Furthermore, the greater refractive index factor, $|K|^2 = |(\epsilon - 1)/(\epsilon + 2)|^2$, for the ash particles as compared to the raindrops (0.36 versus 0.197) enhances the detectability of an ash target by nearly a factor of 2, relative to a rain target with identical particle size distribution and number density. Radar detection of volcanic ash would be further enhanced if there were either a larger number of density particles or larger particle diameters in the ash cloud compared to those shown in table 31.

Table 31.—Comparison of radar target parameters for orographic rain, thundershowers, and volcanic ash

[Ash-fall parameters from Rose and others (1980) and from this study; orographic rain parameters from Blanchard (1953); thundershower parameters from Jones (1956) and Atlas and Chmela (1957)]

Radar target parameters	Ash fall (Fuego volcano, Guatemala)	Warm orographic rain[2] (Hawaii)	Thundershowers (Illinois)		
			Light	Moderate	Heavy
Ash-fall or rainfall intensity (mm/hr)---------	Light	0.02	0.016	6	21
Particle concentration or liquid water content (g/m^3)----------	0.04	0.05	0.0009	0.3	1.0
Particle diameter (mm)----------	0.15	0.22	1.2	1.4	1.7
Number density (per m^3)--------	8.7×10^3	3.6×10^4	1.0	210	390
Reflectivity factor (mm^6/m^3)--------	0.1	2.0	5.0	3.4×10^3	1.4×10^4
Refractive index factor, K^2----	0.36	0.197	0.197	0.197	0.197

Also, for a given concentration and size distribution of silicate particles in a target, the reflectivity of an ash cloud varies inversely with the fourth power of the radar wavelength used. Therefore, the wavelength is an important consideration when evaluating the suitability of a particular radar system for observations of volcanic ash. On the basis of these comparisons, we can expect that detection of volcanic ash for the conditions shown in table 31 would be similar to radar detection of orographic rain, particularly because of similarities of particle diameter and particle concentrations.

DESCRIPTION OF RADAR SYSTEMS

The eruption of Mount St. Helens on May 18, 1980, was observed on three radar systems. Ash clouds were tracked on Federal Aviation Administration (FAA) radar systems located at Seattle and near Spokane, Wash. In addition, the NWS radar system at Portland, Oreg., was used to measure the height of the eruption column directly above Mount St. Helens. Although the locations and specifications for all three radar systems are given in table 32, only data obtained from the Portland and Seattle radar systems were used for quantitative calculations in this paper; data from Spokane were used only for qualitative tracking of the ash cloud.

The radar systems at Portland (NWS) and Seattle (FAA) differ greatly in peak transmitting power, vertical beam width, and wavelength. The 6.2° vertical beam width of the Seattle radar precludes its use for measurement of vertical dimensions of ash clouds, but the Portland radar is ideal for this purpose. The greater peak power of the Seattle radar as compared to that of the Portland radar does not result in a large advantage for the system because of the attenuating effects of the longer wavelength, shorter pulse length, and larger vertical beam width, all of which reduce the power received from a given target. Both systems have the capability for operation in contour-logging mode. In this mode, the power received from a target is measured, corrected for the $1/R^2$ range attenuation, and compared to particular reference levels. Then the selected levels are displayed on the radar's plan position indicator (PPI) and range height indicator (RHI) screens. This mode contrasts with ordinary operation in which the PPI and RHI screens display the images of the detected targets without regard to signal strength.

Attenuation of the radar beam by intervening rainfall was not a major problem because clear weather prevailed for the May 18, July 22, August 7, and October 16–18 eruptions. However, we can evaluate the significance of attenuation by rainfall for radar observations of ash clouds. Atlas (1964) reviewed observations and theory on attenuation of radar signals by snow and rain. The amount of attenuation depends on

Table 32.—Specifications of radar systems

[NWS, National Weather Service; FAA, Federal Aviation Administration; kW, kilowatts; dBm, decibels below milliwatts; W, watts]

Nearest city-------	Portland, Oreg.	Seattle, Wash.	Spokane, Wash.
Agency----------	NWS	FAA	FAA
Lat N.----------	45°36'	47°34'	47°34'
Long W.----------	122°36'	122°25'	117°05'
Radar parameters:			
Peak transmitted power (kW)----------	230	5,000	5,000
Horizontal beam width (degrees)----------	1.65	1.35	1.3
Vertical beam width (degrees).----------	1.65	6.2	22
Pulse Length:			
(time,)s)----------	3	2	6
(distance, km)---------	0.9	0.6	1.8
Wavelength (cm)----------	5	23	23
Sensitivity:			
(dBm)----------	103	111	111
(W)----------	5×10^{-14}	8×10^{-15}	8×10^{-15}
Pulse rate (per s)-------	259	360	Not known.
Maximum range (km)-------	400	400	400

the wavelength, raindrop size distribution and concentration, and path length through rainfall. For the radar system wavelength at Portland (5 cm), attenuation by rain is more important than for those operating at longer wavelengths (for example, 23 cm at Seattle). The rainfall attenuation coefficient per unit rainfall rate (mm/hr) for one-way transmission at a wavelength of 5 cm is about 0.003 (dB/km)/(mm/hr) (Wexler and Atlas, 1963). For example, the amount of attenuation expected from a 2-mm/hr rainfall rate and a 100-km pathlength is about 0.6 dB, or about a 15 percent reduction of power. Attenuation by rainfall would be a possible source of error in Portland radar observations of Mount St. Helens when rain is present along the path.

MEASUREMENTS OF ASH-CLOUD DIMENSIONS

An important question is whether radar observations can be used to measure ash-cloud dimensions. A thorough discussion of radar measurements of storm dimensions is given in Atlas (1964). The horizontal dimensions of radar-detected ash clouds from the May 18 eruption exceeded the horizontal beam width of the Seattle radar. The maximum reflectivity of typical ash clouds (at a constant range) downwind from Mount St. Helens on May 18 corresponded to a level 2 in the contour-logging mode (reflectivity equivalent to that due to stratiform rainfall intensities of 2.5–12.5 mm/hr). However, within the eruption column over the volcano, the maximum reflectivity observed corresponded to a level 4 (reflectivities equivalent to those due to stratiform rainfall intensities of 25–50 mm/hr). The observed ranges in reflectivity in eruption columns and ash clouds from Mount St. Helens are less than those of severe storms, and therefore, accurate measurements of ash-cloud dimensions are possible. False echoes (spurious reflections) caused by radiation from the side lobes of the antenna beam, which could have indicated erroneous column heights, have not been detected. Furthermore, our observations of eruption columns show that the reflectivity decreases rapidly near the radar-detectable tops. Column heights were measured with the Portland radar and have been corrected for curvature of the Earth and for beam width; the latter correction involved subtraction of one-half beam width. The degree of correspondence between the visible boundary of an ash cloud and its boundary as detected by radar is not known.

RADAR OBSERVATIONS OF THE MAY 18 ERUPTION

ASH EMISSION AT MOUNT ST. HELENS

The May 18 eruption began at 0832 PDT, and the Plinian eruption column which resulted was observed on radar. The height of the eruption column (directly above Mount St. Helens) was measured at the Portland NWS office from 0900 to 2200 PDT (fig. 190). The height of the eruption column exceeded 14 km (relative to sea level) for most of the eruption, 9 hr, and the maximum reflectivity level observed for the column varied from 2 to 4 during the eruption. Periods of increased column height generally correlated with increased reflectivity, especially between 0840 and 0900 PDT, and from 1030 to 1230, 1330 to 1400, and 1600 to 1700 PDT.

Particle-size studies of the May 18 ash indicate a multimodal distribution, with size peaks at 90, 25, and 10 μm (Rose and Hoffman, 1980, 1981; Sarna-Wojcicki, Shipley, and others, this volume). Terminal velocities would have been too slow for the fine particles to have settled individually, and they probably fell as composite particles of about 90 μm in diameter, possibly enhancing the radar reflectivity of the ash cloud. Sulfate coatings on ash particles (Rose, 1977; Rose and others, 1980; Nehring and Johnston, this volume) probably were too minor during the May 18 eruption to have significantly influenced the radar reflectivity.

TRACKING OF ASH CLOUDS

At hourly intervals on May 18, Martin Thompson traced the radar images of ash clouds as displayed on the radar PPI screens of the Seattle and Spokane radar systems. (These radar systems are operated remotely by the FAA Seattle Air Route Traffic Control Center in Auburn, Wash.) Thompson's tracings are composites from the two radar systems and are shown in figure 191. The horizontal boundaries of the ash plume, as seen in National Oceanic and Atmos-

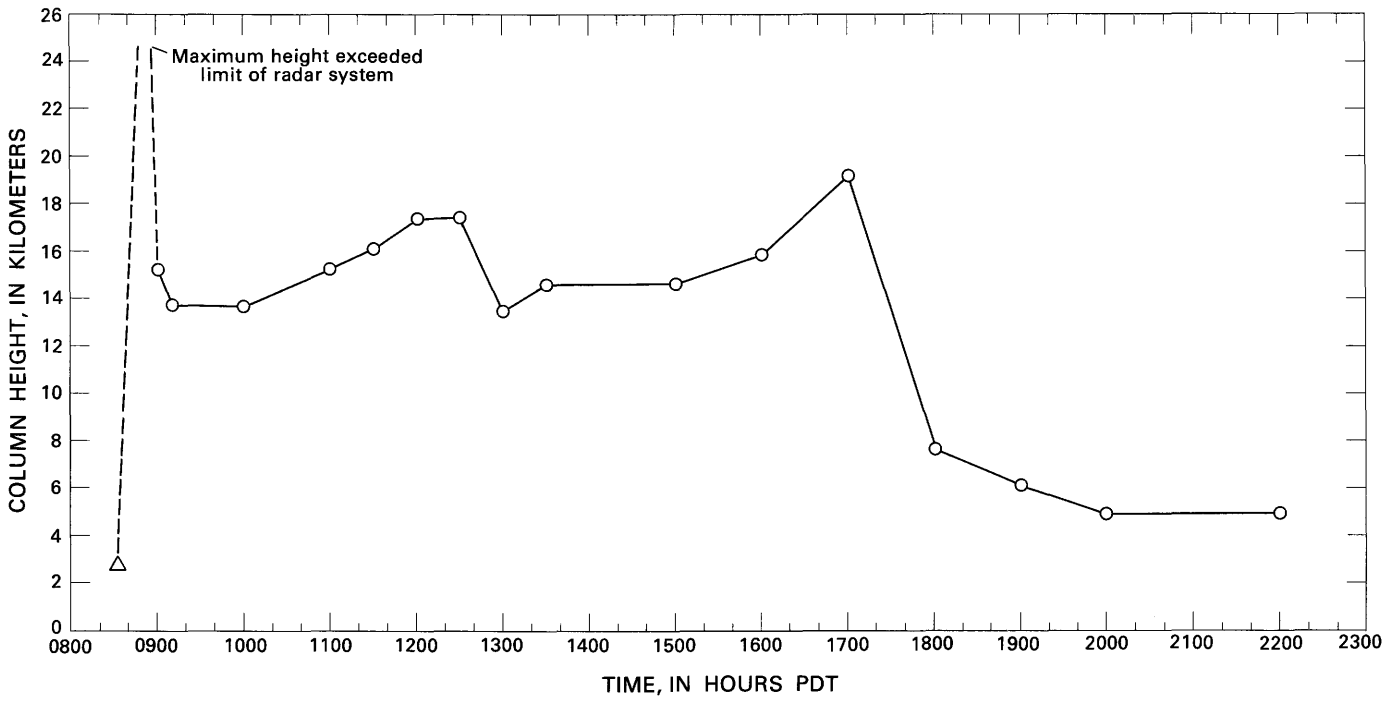

Figure 190.—Heights of the May 18 Plinian eruption column near Mount St. Helens, as determined by Portland radar. Heights are relative to sea level. Base value (triangle) is plotted at time eruption began and at approximate altitude of vent; it is followed by an unmeasurable value (connected approximately by a dashed line).

pheric Administration (NOAA) satellite images, are also shown. The satellite images reveal the overall shape of the entire cloud and of the high-altitude ash trajectory, whereas radar pulses penetrate the ash clouds and are partly reflected by particles within the dense cores of ash clouds. The radar-detectable ash clouds were mostly within the broad plume shown on satellite images.

The radar images in figure 191 show details of the shape of the denser portions of the eruption cloud at hourly intervals. Several of the images show more than one discrete ash cloud (for example, images from 1340 and 1440 PDT). Successive appearances of these discrete ash clouds near the volcano correlate with increases in column height and, we believe, reflect increases in the eruption rate (for example, fig. 190 and table 33). The times of increased column height (eruption rate) (beginning at approximately 0845, 1015, 1245, and 1600 PDT) are interpolated from figure 191 to the nearest quarter hour because we do not have a continuous record of ash-cloud sizes and column heights. The data are sufficient, however, to demonstrate that the column height and therefore the eruption rate varied substantially during the 9-hr eruption.

DIMENSIONS OF THE INITIAL ASH CLOUD

The plan area of the initial ash cloud, as detected by radar, appeared largely unchanged from 0940 to 1040 PDT; however, the plan area increased from 1040 to 1140 PDT as the ash cloud moved farther from Mount St. Helens volcano and began to be tracked on the Spokane radar system. The initial ash cloud contained much of the ash erupted in the Plinian column at Mount St. Helens from about 0832 to 0900 PDT on May 18. The portion of the cloud from which level-1 radar echoes could be detected on the Seattle radar, as measured at 1040 PDT, had a plan area of 4,900 km^2. The range between Seattle and the center of the cloud was about 190 km. At the ash-cloud location, the vertical beam width (from the Seattle radar) would have been about 20 km and the horizontal beam width would have been about 4.6 km. The ash-cloud thickness is not known, but is estimated to have been about 12 km. Thus, the ash cloud may only have intersected about 60 percent of the radar pulse volume. However, correcting for this is not justified because the ash-cloud thickness and variation of reflectivity as a function of height within

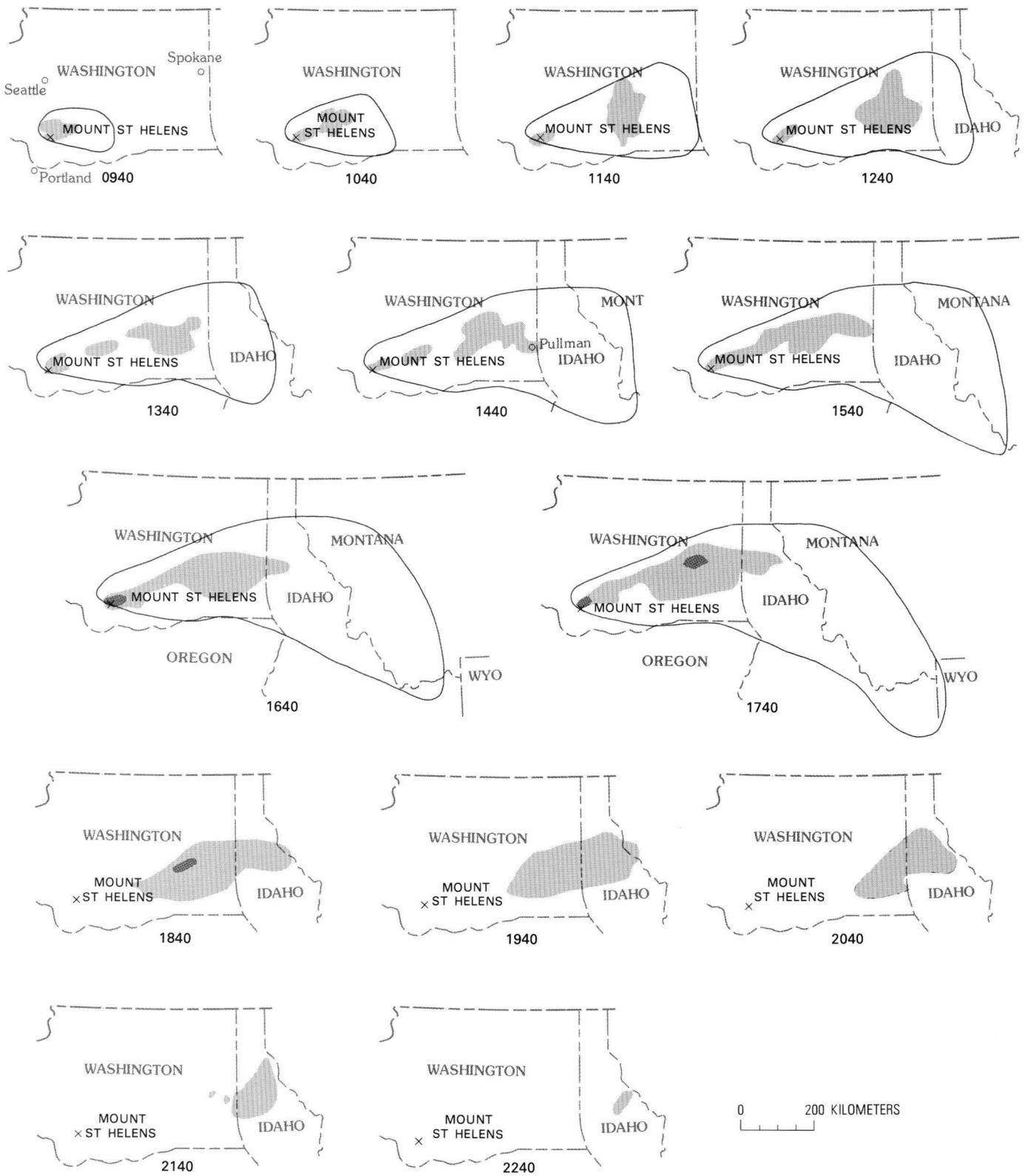

Figure 191.—Shape and structure of the May 18 eruption cloud from Mount St. Helens (X), as depicted by Seattle and Spokane radar systems and NOAA weather satellite. The solid line outlines the whole ash cloud, as seen in the satellite images. Hourly tracings of radar reflections of level 1 are shown as light patterned areas; level-2 reflections are shown as dark patterned areas. Time is shown in PDT.

Table 33.—Estimates of magma eruption rates on May 18 using radar measurements of Plinian column heights

[Calculations based upon the formulae, $H = 8.2 \times Q^{0.25}$, and $\dot{Q} = \sigma \dot{V} s (\theta - \theta_A) F$, of Wilson and others (1978), where H = measured column height above vent, Q = steady-state release of thermal energy, σ = density of dacite (2500 kg/m^3), s = specific heat of dacite (1.1×10^{-3} joules/kg.deg), θ = magmatic temperature of dacite (1200 K), θ_A = air temperature (300 K), and F = 0.9 (an efficiency factor)]

Time of measurement (PDT)	Column height above vent, H (km)	Eruption rate of dense dacite, $\dot{V}$ (10^3 m^3/s)
≈0845	22	23.0
0915	12	2.0
0938	12	2.0
1100	13	2.8
1158	15	5.0
1255	11	1.5
1330	13	2.8
1500	13	2.8
1605	14	3.8
1705	17	8.3
1800	5	0.06

the ash cloud were not measured. The estimated volume of the radar-detectable ash cloud is 5.9×10^4 km^3.

METHOD FOR ESTIMATING POTENTIAL ASH FALL

THE FIRST ASH CLOUD FROM THE MAY 18 ERUPTION

The volume of airborne volcanic ash, and therefore the potential ash fall, depends on the plan area, the vertical thickness, and the mean particle concentration of the ash cloud. The most reliable radar data for estimates of ash volume are likely to be those obtained before substantial amounts of particle coalescence and ash fall occurred, because the particle-size distributions within clouds during ash fall are not known. If a substantial amount of particle coalescence has not occurred, then the particle size distribution within an ash cloud may be approximated by the size distribution of air-fall ash for the eruption. These considerations suggested that the 1040 PDT image (Seattle radar) of the first ash cloud was the best one for which a crude estimate of potential ash fall might be made.

REFLECTIVITY FACTOR INFERRED FROM RADAR OBSERVATIONS

The minimum value of the reflectivity factor (Z) required for detection of the ash cloud was determined from the radar equation 1, the antenna gain equation 2, the range ($R = 190$ km) to the center of the ash cloud, and the parameters for the Seattle radar system (table 32). We assumed that the power received (P_r) from the radar-detected ash cloud was equal to the detection limit (8×10^{-15} W) of the radar system. The dielectric constant (ϵ) of the silicate particles (mostly dacitic glass) from Mount St. Helens was assumed to be 5.5 for the wavelength (23 cm) of the Seattle radar. Campbell and Ulrichs (1969) measured the dielectric constant of obsidian from Newberry caldera, Oregon, and obtained a value of 5.5 for a wavelength of 8.6 cm. The minimum value of the reflectivity factor for the ash cloud is 8.5 mm^6/m^3. The minimum reflectivity factor inferred for the May 18 ash cloud (0832–0900 PDT) exceeds those shown in table 31 for warm orographic rain and light thundershowers.

PARTICLE CONCENTRATION INFERRED FROM REFLECTIVITY FACTOR

The silicate-particle concentration of the ash cloud can be inferred from the reflectivity factor ($Z = \Sigma (2r)^6$), if the size distribution of particles in the ash cloud is known.

PARTICLE-SIZE-DISTRIBUTION MODEL

The silicate-particle concentration in the cloud can be estimated for a particle-size-distribution model that approximates the measured size distribution of the May 18 air-fall ash in eastern Washington. We modeled the particle-size distribution in the ash cloud by assuming that 25 percent (by weight) of the ash particles were spheres of diameter 150 μm, 50 percent were spheres of diameter 100 μm, and 25 percent were spheres of diameter 30 μm.

REFLECTIVITY FACTOR PER UNIT MASS OF ASH

The reflectivity factors per unit mass of ash (for each particle size) are 2.57 mm^6/g (150 μm), 0.764 mm^6/g

(100 μm), and 2.06×10^{-2} mm⁶/g (30 μm). The weighted value of the reflectivity factor per unit mass for the model size distribution is 1.0 mm⁶/g. The relative contributions of the three ash sizes to the total reflectivity factor are 62.4 percent, 37.1 percent, and 0.5 percent, respectively.

PARTICLE CONCENTRATION IN THE ASH CLOUD

The inferred concentration of silicate particles in the ash cloud, using the observed reflectivity factor and the particle-size-distribution model, is 8.5 mm⁶/m³/ 1.0 mm⁶/g = 8.5 g/m³. This represents the concentration of ash in the first ash cloud downwind from Mount St. Helens, 1.5–2 hr after it was erupted.

POTENTIAL ASH-FALL MASS AND VOLUME

The potential ash-fall mass can be calculated from the volume (5.9×10^4 km³) of, and the concentration of silicate particles (8.5 g/m³) in, the radar-detected part of the ash cloud. The calculated mass of ash is 5.0×10^{14} g. Similarly, the potential ash-fall volume is about 0.20 km³, for a particle density of 2.5 g/cm³. These estimates represent the mass and volume of ash remaining in the first ash cloud downwind from Mount St. Helens, 1.5–2 hr after it was erupted.

ESTIMATES OF POTENTIAL ASH FALL

In theory, the potential ash fall from the radar-detected part of the ash cloud can be estimated. The ash cloud, as detected by radar, was about 70 km wide and it traveled in an east-northeasterly direction at about 135 km/hr. The minimum potential ash-fall area (km²) and mean amount of ash (mm) could be estimated if either the duration of ash fall from the cloud or the ash-fall intensity (mm/hr) is known. The ash-fall intensity is the more important of the two parameters because it might be used, along with the quantities inferred from radar, to forecast the duration and the mean ash-fall amounts over the potential ash-fall area. Table 34 illustrates one procedure that might be used to estimate, in retrospect, the ash-fall intensity from the radar-detectable part of the initial ash cloud downwind from Mount St. Helens. The calculated ash-fall intensity is 13 mm/hr and it represents our best estimate for the peak ash-fall rate sustained for a period of about 30 min. Also, we have estimated the minimum potential ash-fall areas and amounts (table 35). These data suggest, in retrospect, that for any reasonable duration of ash fall, the impact from the first ash cloud of the May 18 eruption ought to have been great.

Table 34.—Ash-fall intensity estimated from physical characteristics inferred for the initial ash cloud of the May 18 eruption

Particle diameter[1] (μm)	Mass fraction of ash in cloud[1]	Concentration of ash in cloud[2] (g/cm³)	Total mass of particles in ash cloud[3] (g)	Calculated terminal velocity[4] (cm/s)	Calculated ash-fall intensity[5] (mm/hr)
150	0.25	2.1×10^{-6}	1.25×10^{14}	70	5.3
100	0.50	4.3×10^{-6}	2.5×10^{14}	48	7.4
30	0.25	2.1×10^{-6}	1.25×10^{14}	5	.4
Totals---	1.00	8.5×10^{-6}	5.0×10^{14}		13.1

[1]From particle size-distribution model described in text.

[2]Minimum concentration inferred from radar observations and particle size-distribution model.

[3]Calculated from volume (5.9×10^4 km³) of radar-detectable ash cloud and ash concentration shown in column 3.

[4]Calculated by Rose and Hoffman (1981).

[5]The ash-fall intensity (mm/hr) = (10 mm/cm) x (3.6×10^3 s/hr) x (concentration of ash in cloud, g/cm³) x (terminal velocity of particles, cm/s) x (density of uncompacted air-fall ash, g/cm³). A density of 1.0 g/cm³ was assumed for the uncompacted air-fall ash.

The prospects for making useful ash-fall forecasts from radar and field observations appear good. However, such forecasting capability will require additional detailed radar observations of ash clouds, measurements of ash-fall intensities, studies of ash-fall mechanisms in eruption clouds, and comparison of radar observations with the actual distribution, times, and amounts of ash fall.

ONSET OF ASH FALL IN EASTERN WASHINGTON

Ash fall began at Tampico, Wash. (about 30 km west-southwest of Yakima), at about 1000 PDT. According to Seattle radar observations, the leading edge of the first ash cloud reached Yakima at about 0950 PDT and the trailing edge remained until after 1100. The same ash cloud, as tracked on the Spokane radar, reached Pullman, Wash., at about 1400 PDT (fig. 191), at which time ash fall began there (Hooper and others, 1980). Thus, ash fell for more than 4 hr from the first ash cloud as it moved from Tampico to Pullman.

Table 35.—Potential ash-fall amounts estimated from radar observations

[Data based on the following assumptions: potential ash-fall volume = 0.20 km^3; potential ash-fall mass = 5.0×10^{14} g; ash cloud width = 70 km; horizontal speed of ash cloud = 135 km/hr; uncompacted density of air-fall ash = 1.0 g/cm^3; complete dissipation of ash cloud, and constant ash-fall intensity. Results have been rounded]

Assumed duration of ash fall (hr)	Minimum potential ash-fall area (km^2)	Estimated mean ash fall	
		(mm)	(g/cm^2)
1	10,000	50	5.0
2	20,000	25	2.5
5	50,000	10	1.0
10	100,000	5	0.5
20	200,000	2.5	0.25

According to photographs of eastern Washington on May 18, the ash cloud obscured the sky for periods of up to several hours prior to onset of ash fall at ground level. The duration of the obscured sky may be the time required for the fine-grained ash to fall to the ground from heights of 5–20 km in the atmosphere. It seems likely that the secondary maximum of ash-fallout thickness around Ritzville, Wash. (Sarna-Wojcicki and others, this volume), may be due to the rapid eastward transport of fine-grained (and slowly falling) ash from the first (and possibly later) eruptive pulses.

ESTIMATES OF MAGMA ERUPTION RATE

The maximum height to which Plinian eruption columns rise is a sensitive indicator of the magma eruption rate (Wilson and others, 1978). Measured column heights from the Portland radar and calculated magma eruption rates for the May 18 eruption are shown in table 33. They show that magma eruption rates during the early part of the eruption (about 0845–0900 PDT) were an order of magnitude higher than during most of the remainder of the 9-hr eruption. The total magma volume, which is suggested by these rates, can be estimated by considering the duration of the eruption. From the data in table 33, a total volume of about 0.15 km^3 of dense dacite is suggested. This estimate assumes high efficiency of heat transfer to the atmospheric air entrained by the rising Plinian column, an efficiency which is not achieved in the case of pyroclastic flows. It also assumes that no interaction of ground water with magma occurred. Both of these assumptions are probably incorrect and will result in underestimation of the true magma volume. (See also Wilson and others, 1978.)

Such calculations illustrate that an "order of magnitude" volume estimate can be obtained from column-height measurements if the duration of the eruption is also known. Using radar data for later eruptions (for example, from table 36), we calculated dense-magma volumes of 0.002, 0.003, 0.003, 0.001, and 0.001 km^3 for the eruptions of May 25, June 12, July 22, August 7, and October 16–18, 1980, respectively. These calculations illustrate the much smaller magnitudes of these later eruptions of Mount St. Helens, as compared to the May 18 eruption.

CONCLUSIONS

Radar observations show that the Plinian eruption of Mount St. Helens on May 18 lasted for about 9 hr. The maximum height of the Plinian eruption column (> 24 km above sea level) was attained several minutes after the eruption began (0832 PDT); however, by 0900 PDT the column height immediately over the vent was only about 16 km and continued to decrease. After 0900 PDT, the height of the eruption column exceeded 14 km for an additional $8\frac{1}{2}$ hr. During the 9-hr eruption there were four periods of relatively increased height and reflectivity of the Plinian column, which probably resulted from increased rates of ash emission. Radar observations of discrete ash clouds downwind from the volcano also suggest that the eruption had four distinct relative maxima in the rate of ash emission.

Table 36.—Maximum heights of Plinian eruption columns at Mount St. Helens

Date (1980)	Maximum column heights of successive pulses (km)	Duration of ash emission with column height >12 km (relative to sea level)
May 18	>24, 17.3, 14.6, 19.2	About 9 hr.
May 25	12.2	<30 min.
June 12	15.2, 10.7, 9.8, 10.7	About 30 min.
July 22	13.7, 14.5, 8.7	25 min.
Aug. 7	13.4, 10.0, 6.1, 7.6, 6.1, 5.2.	2 to 5 min.
Oct. 16	12.8	<5 min.
Oct. 17	14.3, 13.7	Do.
Oct. 18	5.2, 7.9, 6.1	0 s.

A mean particle concentration of 8.5 g/m^3 is inferred for the first ash cloud downwind from Mount St. Helens, about 1.5–2 hr after the 0832–0900 Plinian eruption. The mass of silicate particles in the cloud (5×10^{14} g) was estimated using the total ash-cloud volume (5.9×10^4 km^3) and the particle concentration. The potential ash-fall volume calculated for the radar-detected portion of the ash cloud is 0.20 km^3.

Radar observations of Plinian eruptions at Mount St. Helens subsequent to the May 18 eruption show that the later ones were of shorter duration and erupted much smaller volumes of ash as compared to the May 18 eruption.

REFERENCES CITED

Atlas, D., 1964, Advances in radar meteorology, *in* Landsberg, H. E., and Van Mieghem, J., eds., Advances in geophysics, volume 10: New York, Academic Press, p. 317–479.

Atlas, D., and Chmela, A. C., 1957, Physical-synoptic variations of drop-size parameters: American Meteorological Society Weather Radar Conference, 6th, Boston, Proceedings, v. 4, p. 21–29.

Blanchard, D. C., 1953, Raindrop size distribution in Hawaiian rains: Journal of Meteorology, v. 10, p. 457–473.

Campbell, M. J., and Ulrichs, J., 1969, Electrical properties of rocks and their significance for lunar radar observations: Journal of Geophysical Research, v. 74, p. 5867–5881.

Hooper, P. R., Herrick, I. W., Laskowski, E. R., and Knowles, C. R., 1980, Composition of the Mount St. Helens ashfall in the Moscow—Pullman area on 18 May 1980: Science, v. 209, p. 1125–1126.

Johnston, D. A., 1978, Volatiles, magma mixing, and the mechanism of eruption of Augustine volcano, Alaska: University of Washington, Seattle, Ph. D. thesis, 177 p.

Jones, D. M. A., 1956, Rainfall drop-size distribution and radar reflectivity: Illinois State Water Survey, Meteorology Laboratory Research Report no. 6, 20 p.

Probert-Jones, J. R., 1962, The radar equation in meteorology: Quarterly Journal of the Royal Meteorological Society, v. 88, p. 485–495.

Rose, W. I., Jr., 1977, Scavenging of volcanic aerosols by ash—atmospheric and volcanologic implications: Geology, v. 5, p. 621–624.

Rose, W. I., Jr., Chuan, R. L., Cadle, R. D., and Woods, D. C., 1980, Small particles in volcanic eruption clouds: American Journal of Science, v. 280, p. 671–696.

Rose, W. I., Jr., and Hoffman, M. F., 1980, Distal ashes of the May 18, 1980, eruption of Mount St. Helens [abs.]: Transactions of the American Geophysical Union, v. 61, p. 1137.

_____1981, The May 18 eruption of Mount St. Helens—the nature of the eruption, with an atmospheric perspective, *in* Deepak, A., ed., NASA Symposium on the Mount St. Helens eruption—Its atmospheric effects and potential climatic impact: Hampton, Va., Institute for Atmospheric Optics and Remote Sensing (IFAORS).

Wexler, R., and Atlas, D., 1963, Radar reflectivity and attenuation of rain: Journal of Applied Meteorology, v. 2, p. 276–280.

Wilson, L., Sparks, R. S. J., Huang, T. C., and Watkins, N. D., 1978, The control of volcanic column heights by eruption energetics and dynamics: Journal of Geophysical Research, v. 83, p. 1829–1836.

THE 1980 ERUPTIONS OF MOUNT ST. HELENS, WASHINGTON

VOLCANO MONITORING BY CLOSED-CIRCUIT TELEVISION

By C. DAN MILLER *and* RICHARD P. HOBLITT

ABSTRACT

Visual monitoring of Mount St. Helens volcano by closed-circuit television allows eruptive events to be observed as they occur and an immediate evaluation of potential hazards to be made. Use of the remotely controlled TV system also reduces risks to personnel during eruptions by eliminating the need for close-in observers on the north side of the volcano, and reduces the need for continuous observation from aircraft.

INTRODUCTION

Visual monitoring of Mount St. Helens volcano by closed-circuit television was started in July 1980. The TV system consists of a remotely controlled video camera (fig. 192) situated on a ridge 9 km north of Mount St. Helens (fig. 193), a microwave repeater station west of the volcano, and viewing and recording equipment (fig. 194) at the Emergency Coordination Center (ECC) in Vancouver, Wash. There, the picture is monitored during daylight hours by personnel of the U.S. Geological Survey and U.S. Forest Service. The TV surveillance system was installed to allow direct visual monitoring of the volcano by personnel in Vancouver, to reduce or eliminate hazards to ground observers during eruptions, and to reduce the need for, and thereby the cost of, continuous observation from aircraft. A system was selected, assembled, and installed near the volcano by July 15, and became fully operational on July 20.

Advantages of the TV surveillance system, in addition to those mentioned above, are as follows:

1. Eruptive events can be observed as they occur and their potential dangers can be immediately assessed.
2. The volcano can be examined any time during daylight hours except during periods of cloudy weather (at night, incandescent events can be observed).
3. The video system permits events at the volcano (for example, eruption plumes, avalanches) to be correlated with other monitoring data received by telemetry at the Emergency Coordination Center in Vancouver.
4. Weather conditions can be viewed each morning prior to planning the day's activities at and near the volcano.
5. The video signal can be recorded on magnetic tape to provide a record of events for subsequent scientific studies.

ACKNOWLEDGMENTS

We thank Guy F. Gunthorpe, Reynolds Electrical and Engineering Co., Inc., for providing descriptions and schematic layouts of video-system components.

Figure 192.—Video-camera installation on ridge 9 km north of Mount St. Helens. Camera is mounted on top of shelter that contains microwave telemetry equipment.

DESCRIPTION OF SYSTEM

The video and microwave systems were fabricated by Reynolds Electrical and Engineering Co., Inc. (REECO) and Sandia National Laboratories under authority given by the U.S. Department of Energy. The systems were installed at Mount St. Helens by REECO, Sandia Labs, USFS and USGS personnel. System layout and components are described at the end of this report.

The camera is located directly north of the volcano at a site that affords a clear view of the volcano, a view of the interior of the crater, and a 360° view of the surrounding area. The camera can pan 355°, can tilt over a wide vertical range, and has a zoom ratio of 10 to 1; and both focus and iris diaphragm can be adjusted. These functions can all be controlled from the monitor console (fig. 194) in Vancouver. Power is supplied by batteries that are recharged by propane thermoelectric generators. The system can be turned on and off remotely each day and during poor weather conditions, to save electrical power.

USE OF THE SYSTEM

The video system provides a sharp, live color picture of the mountain and has proven to be a valuable monitoring tool for hazards response and in planning daily operations. During periods of good weather in July and August, the system was operated for as much as 13 hr/day. Electrical power is adequate for about 65 min of pan, tilt, and zoom functions per day, which permits viewers in Vancouver to investigate the state of the volcano each morning and look for changes that may have occurred overnight. During late summer and fall, 1980, the video-

surveillance system replaced one daily, early morning USFS observation flight and, during periods of poor or marginal weather, some other flights as well.

The system is used regularly to examine fluctuations in gas emission, avalanche frequency, local wind conditions, blowing ash in potential work areas, and eruptive events. The system is also useful for briefing scientists and public officials without visiting the volcano.

When combined with seismic, tilt, and other real-time monitoring data telemetered into Vancouver, the video system allows USFS and USGS personnel at ECC to make accurate and rapid assessments of the state of the volcano and associated hazards.

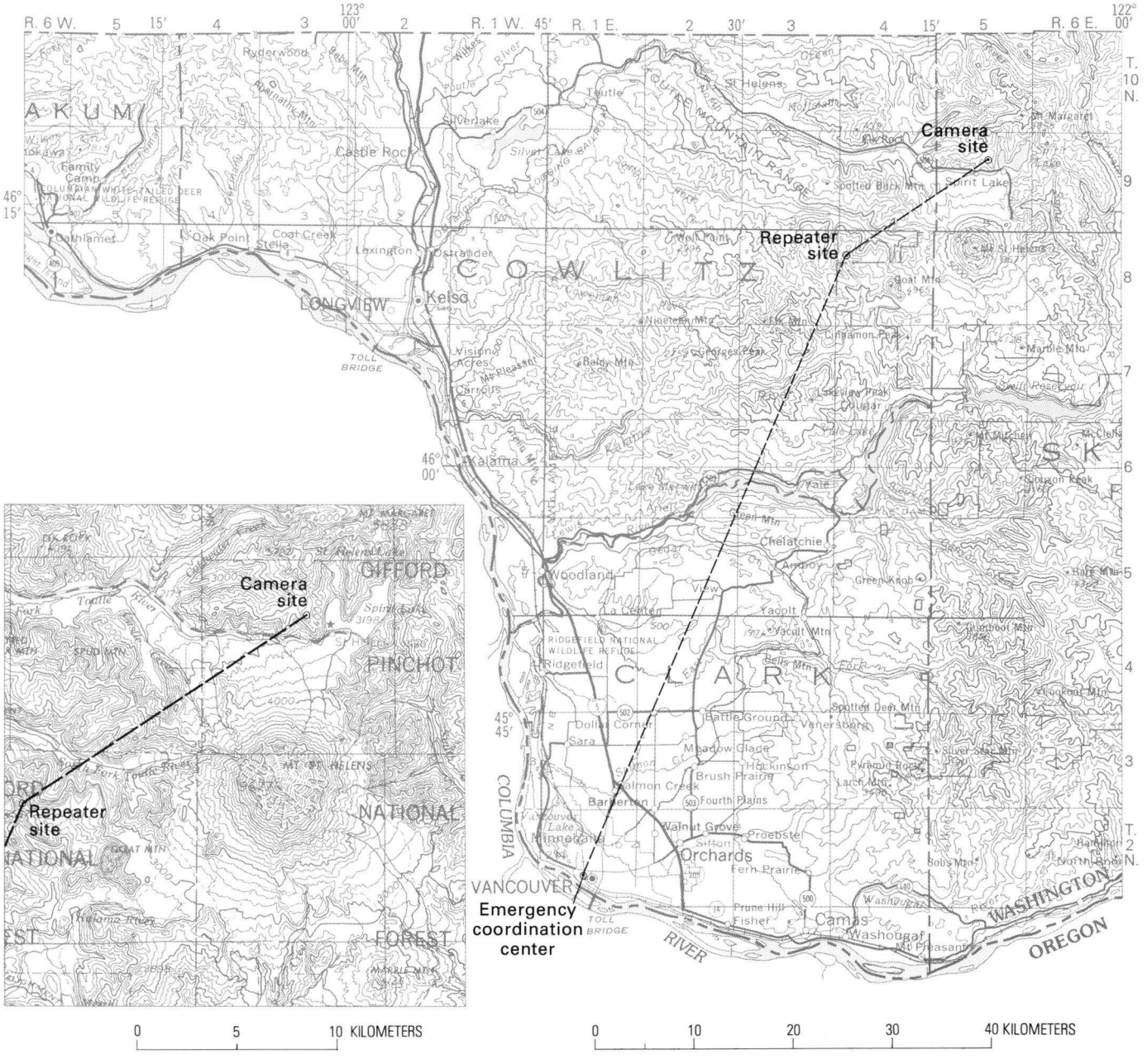

Figure 193.—Locations of camera and repeater sites near Mount St. Helens and Emergency Coordination Center (with video monitor) in Vancouver, Wash. Solid line shows microwave beam path.

CONCLUSIONS

Installation of a similar surveillance system should be considered at the outset of eruptive activity at other volcanoes. The video-surveillance system at Mount St. Helens has proven to be useful, efficient, and reasonably reliable, and it may save lives by reducing exposure to risk in hazardous areas.

DESCRIPTION AND SCHEMATIC LAYOUT OF COMPONENTS OF VIDEO SURVEILLANCE SYSTEM

The camera station (fig. 195) uses a Sony Model 1610 NTSC color camera equipped with a motorized Angenieux zoom lens. This lens provides a zoom ratio of 10 to 1 over a focal length of 15 to 150 mm. The camera was designed for electronic news gathering applications and, therefore, was enclosed in a fiberglass NEMA-12 cabinet for protection from the elements. The camera, lens, and housing are mounted to a Pelco pan and tilt unit. The pan and tilt unit was mounted on a utility trailer to increase the height and stability of the camera and the stability of the microwave antenna, and to provide environmental protection for the batteries and the control equipment. The trailer is cribbed and anchored to provide stability. Color video information is fed from the camera via coaxial cable to a Teledyne Video Microwave Transmitter Model TR 1806-TV. This transmitter provides a nominal 10 watts of RF at 1846 MHz. A 2-ft Andrews Parabolic antenna is connected to the transmitter via 1/2-in. foam Heliax cable.

Figure 194.—Video-monitor and control console in the Emergency Coordination Center in Vancouver.

The control system at the camera station provides two on/off functions and pan/tilt and lens function over a separate VHF radio receiver. A small portable radio was used for the receiver. Two on/off functions were provided so that the entire system could be remotely activated and the power drain from the pan and tilt unit and its associated control system could be remotely deactivated. Battery capacity is thereby conserved, which allows smaller battery capacity as well as better recovery during the times when the system is off. The on/off functions use Motorola Quick Call devices that operate on a two-tone simultaneous basis. A Motorola digital remote-control system is used to control the pan and tilt and provides the lens functions of zoom, iris, and focus.

Power at the camera station is provided by two 8D 12 volt batteries. The batteries are float charged by the use of two Teledyne Telan Model 2T4 thermoelectric generators. Original design allowed a 20-day supply of propane in four bottles so that a changeover of two bottles could occur every 10 to 15 days. A total loss of the propane supply for a period of 5 days can be sustained by the batteries, but at the end of this period the batteries should be replaced because recovery could not be accomplished by means available at the camera station.

The repeater station (fig. 196) consists of a Farinon SS2000W microwave receiver and a Teledyne TR 1806-TV transmitter. The RF signal at 1846 MHz is received via a 2-ft Andrews Parabolic antenna and passed to the receiver via 1/2-in. Heliax cable. The video information is transferred via coaxial cable to the transmitter. The transmitter provides 10 watts of RF at 1715.5 MHz through 1/2-in. Heliax cable to a 4-ft Andrews Parabolic antenna. The antennas are

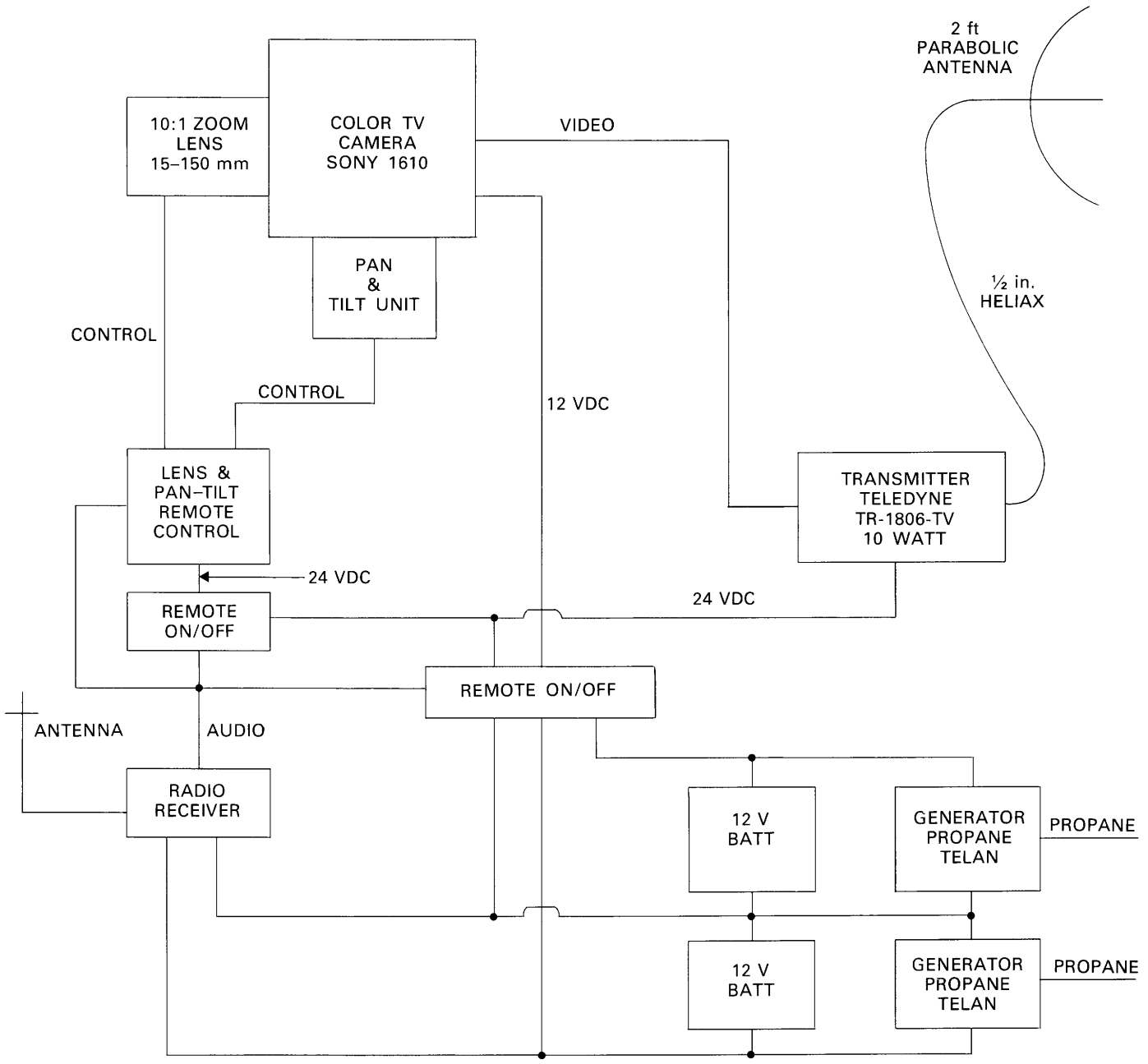

Figure 195.—Schematic layout of camera-station components of the video-surveillance system.

mounted on a pipe structure attached to a utility trailer. This trailer serves as an environmental housing for the transmitter and receiver, and provides a stable platform for the antenna pipe. The trailer is cribbed and anchored to provide stability. The same Motorola Quick Call two-tone simultaneous system is used to control the on/off function. A portable radio was used to receive the function commands.

The power system of the repeater station is identical to the camera station.

The receiver in Vancouver (fig. 197) is in a weatherproof box on the roof of an apartment building. A 10-ft section of Rohn tower has been temporarily installed to hold a 6-ft Andrews Parabolic antenna. Power for the receiver, as well as a Dynair distribution amplifier, is taken from the building. A 75-ohm

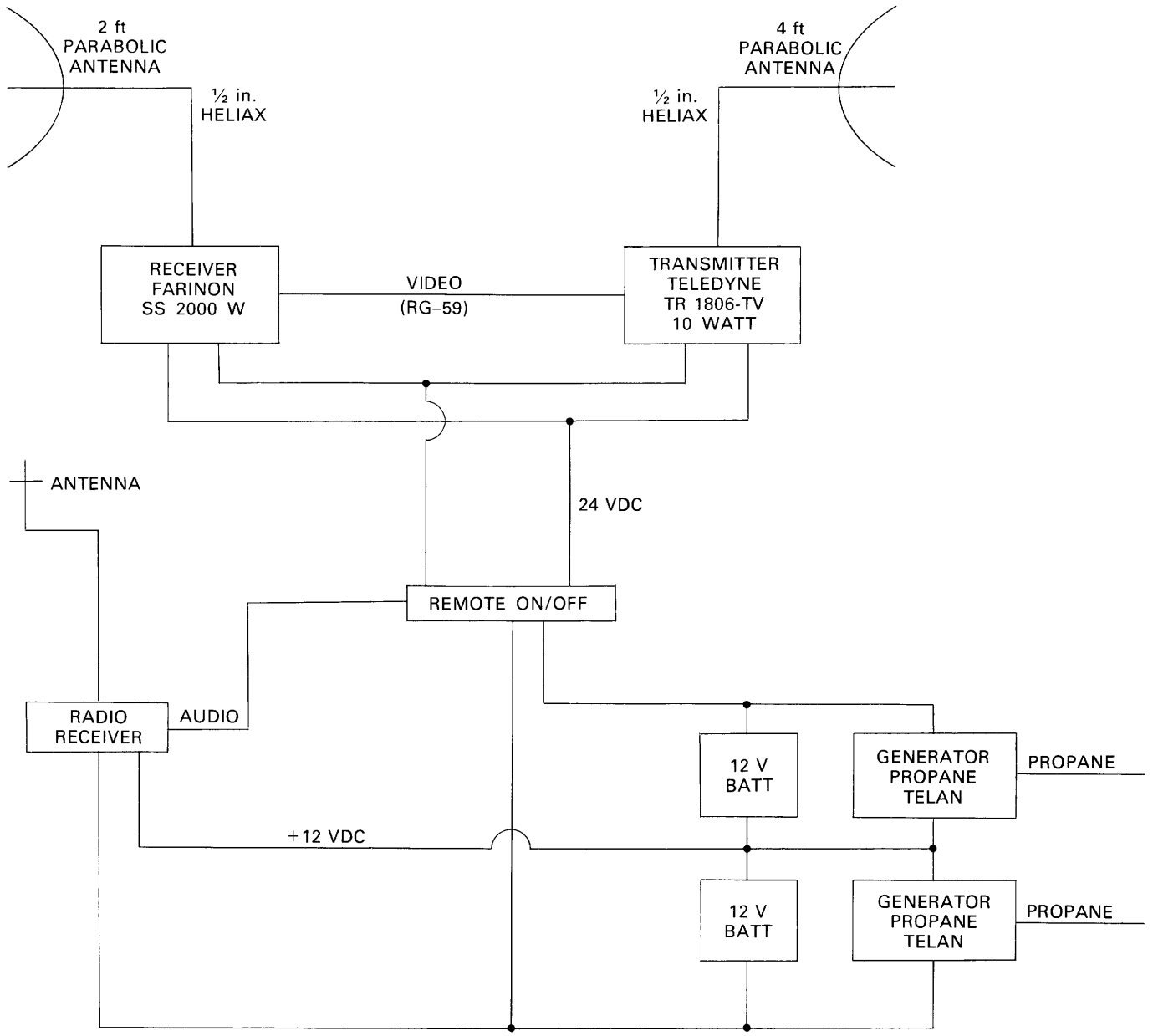

Figure 196.—Schematic layout of repeater-station components of the video-surveillance system.

coaxial cable (RG-59) is routed from the roof of this building to the ECC via power and telephone poles.

The signal from this coaxial cable is processed through a Dynair Clamp amplifier that provides two outputs. The first output is routed to a general room monitor for display of the picture. The second output is routed through a patch panel to either or both of the Panasonic NV-9200 video-tape recorders and thence to a 13-in. Sony Color Monitor. In this way, the 13-in. monitor can be used for viewing while recording and while playing back tapes. The remote control encoders for the pan/tilt and lens functions and the on/off function are located in the same cabinet with the video-tape recorders.

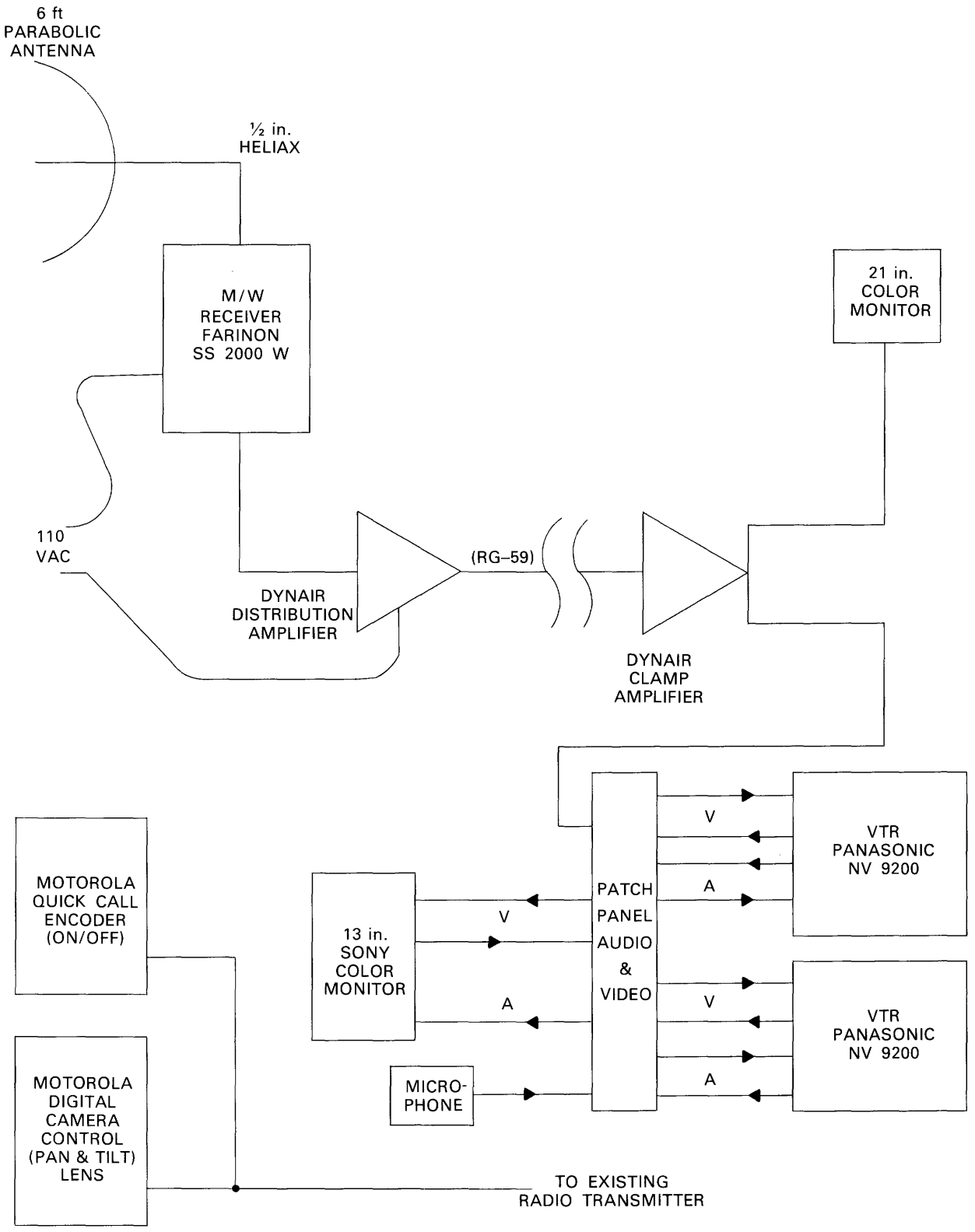

Figure 197.—Schematic layout of receiver and control components of the video-surveillance system.

VOLCANIC DEPOSITS

VOLCANIC DEPOSITS

The 1980 eruptions at Mount St. Helens presented exceptional opportunities to correlate observations of volcanic events with physical features of the resulting deposits. Most geologic studies examine deposits that formed in the past by events and processes that must be inferred from features of the deposits. In many paleovolcanic deposits it is difficult or impossible to infer such important elements as: timing of events, nature of emplacement processes, emplacement temperatures of deposits, composition of associated gas phases, and magmatic chemistry of deposits that rapidly oxidize, hydrate, and otherwise alter. Some studies of these and other aspects of andesitic-dacitic volcanism are already complete at Mount St. Helens.

The major near-source deposits and effects of the 1980 eruptions are shown on a geologic map (scale 1:50,000, in pocket), compiled from reconnaissance mapping and field observations by many USGS scientists, supplemented by interpretation of vertical aerial photographs (Lipman). Major units included on the map and discussed in this chapter are: deposits of the debris avalanche of May 18, deposits of the immediately following directed blast, mudflow deposits generated by rapid melting of snow and ice, pumiceous pyroclastic flows that formed later on May 18 and during subsequent magmatic eruptions, and lava domes in the crater. Also shown on the map are major zones of devastation on May 18, including areas of mudflow scouring on upper parts of the volcanic cone and zones of tree removal, tree blowdown, and tree searing within the blast area. Relatively thin air-fall deposits cover the entire map area but are not shown separately.

The debris-avalanche deposits derived from landsliding of the north flank on May 18 represent the largest historic gravitational slide known, having a volume of 2.5–3 km^3 and extending about 25 km from the source area. The hummocky-surfaced chaotic debris filled about 60 km^2 of the North Fork Toutle River valley to an average depth of 45 m, and raised the level of Spirit Lake 60 m. Seven map units are distinguished within the avalanche deposits and can be correlated in part with successive slide movements recorded by photographs. Transitory seismic stresses apparently initiated sliding, and additional mechanisms such as liquefaction were necessary to sustain their movement. These deposits are described in one paper (Voight and others), which combines under a single title the following aspects: review of the conditions of failure, description of the deposits, data on physical properties, and a summary of possible analogs at other volcanoes. For each other type of deposit, various aspects are considered separately in several reports.

Analysis of the dynamics, effects, and deposits of the directed blast that occurred at the beginning of the eruption on May 18 has added significantly to understanding of this devastating type of volcanic event. The directed blast produced a complex assemblage of deposits that vary laterally and vertically. Analysis of the blast dynamics indicate that about 24 megatons of energy were released over a period of several minutes. The Mount St. Helens blast was triggered by landslide-induced depressurization of a cryptodome within the volcano, which caused explosive expansion of steam and other magmatic gases.

Destructive mud and debris flows developed within minutes of the beginning of the May 18 eruption, as hot pyroclastic debris melted snow and ice on upper slopes of the cone; these flows developed most vigorously on the east and west flanks amd and locally reached velocities of as much as 45 m/s. The largest mudflow developed later on May 18 from water-saturated debris-avalanche deposits in the upper North Fork Toutle River; it extended more than 120 km into the Cowlitz and Columbia River Valleys.

Pumiceous pyroclastic flows of mafic dacite occurred during the six major 1980 eruptions (May 18, May 25, June 12, July 22, August 7, October 16–18), along with eruption of large vertical ash columns. The resulting pyroclastic-flow deposits provided excellent opportunities to study primary depositional features, measure thermal and rheological properties, and monitor compositional changes in a differentiated magmatic system. Advance warning of later eruptions allowed observers to witness and photograph pyroclastic flows in motion. In general, the time between successive pyroclastic eruptions increased, and eruptive volumes, vesicularity, and degree of chemical differentiation decreased during 1980.

Lava domes grew within the central crater after three explosive eruptions (June 12, August 7, and October 16–18), and two additional dome lobes emerged from flanks of the October dome in late December. In the successive eruptions, the proportion of magma

erupted as viscous lava domes rather than as pyroclastic fragments increased progressively; no pyroclastic deposits were observed in December. Physical-property measurements show that dome lavas had largely degassed prior to extrusion.

Air-fall deposits were laid down during every explosive magmatic event, as well as during the early steam-blast eruptions from March 27 to May 18. The pre-May 18 ash was of small volume and consisted entirely of lithic and crystal fragments derived from preexisting rocks within the volcano. Air-fall ash erupted on May 18 formed visible deposits at least as far as 1,500 km to the east, and is as much as 20 cm thick within 10 km of the the volcano. Volumes of the post-May 18 air-fall deposits progressively decreased. Compositions of air-fall ash became richer in glass shards and silica content with increasing distance from the source, as relatively dense lithic fragments and mafic phenocrysts preferentially fell out.

The 1980 eruptions also offered opportunities to sample diverse magmatic products of andesitic-dacitic volcanism, erupted at known times, prior to surficial alteration. Many petrologic studies are still in progress, but available data on major-element chemistry already document small but significant compositional variations in erupted magmatic materials, which became generally more mafic as volumes decreased with time. Compositionally diverse banded pumices indicate mixing of different magmas before or during eruptions and suggest the presence of more mafic melts within the magma chamber than have thus far been erupted. The volume of magma erupted in 1980 was about 0.24 km^3, a volume smaller than that of several previous explosive eruptions of Mount St. Helens, a few of which represented magmatic volumes of as much as a cubic kilometer.

THE 1980 ERUPTIONS OF MOUNT ST. HELENS, WASHINGTON

CATASTROPHIC ROCKSLIDE AVALANCHE OF MAY 18

By BARRY VOIGHT, HARRY GLICKEN, R. J. JANDA, *and* P. M. DOUGLASS

ABSTRACT

Following 2 mo of intense slope movement associated with magmatic intrusion and seismicity, and a trigger earthquake at 0832 PDT on May 18, a 2.3-km^3 rockslide detached from the north slope of Mount St. Helens. Within 26 s, the first of a retrogressive series of blocks had moved 700 m—velocity of the first slide block was about 50 m/s and increasing—and a second block had moved 100 m. Meanwhile, steam and magmatic explosions had begun due to pressure release behind the slide scarp, and the slide became engulfed in the resulting blast cloud. The slide masses evolved into an enormous, pulsing hot avalanche, and within about 10 min avalanche lobes had traveled as far as 8 km northward and 22 km westward. About 60 km^2 of the North Fork Toutle River valley system was choked with 2.8 km^3 of hummocky-surfaced, poorly sorted debris to an average depth of 45 m, and the level of Spirit Lake was catastrophically raised 60 m. Seven map units have been recognized within the avalanche deposit, and the geologic details of these units permit their correlation with the succession of slide movements shown on eyewitness photographs. Transitory seismic stresses were necessary for detachment of the slide masses; additional, continued strength-loss mechanisms such as liquefaction were necessary to sustain movement of the avalanche.

INTRODUCTION

On May 18, 1980, at 0832 PDT, collapse of the bulging sector of the north slope of Mount St. Helens created one of the most dramatic mass-movement events of historic time (fig. 198) and precipitated a devastating volcanic eruption.

This report summarizes our work on the slope failure and on the distribution, composition, and physical properties of the resulting deposits. The report is based on field observations in April and May prior to the slope failure, further observations from May 18 throughout the summer, and supplementary laboratory studies and interpretation of photographs and maps.

ACKNOWLEDGMENTS

The assistance, advice, and criticism of numerous colleagues has been important to our efforts. In particular, we would like to thank U.S. Geological Survey (USGS) colleagues working on Mount St. Helens studies, and Fred Swanson, S. D. Malone, A. M. Johnson, and T. Ui. Keith and Dorothy Stoffel, Linda Harvey, and Gary Rosenquist generously provided photographic materials and gave permission to include them in this report. We are grateful to C. A. Hopson, who provided guidance and samples that aided the identification of key rock units. Laboratory work was carried out by the geotechnical laboratory staff of the USGS at Denver under the supervision of R. W. Nichols. Logistical assistance was provided by Charles Hosler, J. Markman, and L. Stickney.

TERMINOLOGY

Major catastrophic mass movements are typically complex, involving various combinations of slide and flow at different stages of development and within different parts of the moving mass (Varnes, 1978, p. 20–23; Voight, 1978, chap. 1–9). Barely perceptible movements of a rock mass can pass through a stage of accelerating creep into a rockslide—the rapid downward and outward displacement of a rock mass along one or several surfaces or relatively narrow zones. Disaggregation of the rock mass can then cause the movement to take on the character of a flow, which may itself change further because of change of water content or velocity.

The gigantic May 18 mass movement on the north slope of Mount St. Helens was complex, and it occurred approximately as indicated above; the term "rockslide-avalanche" (Mudge, 1965) seems appropriate for its description. Avalanche is a term many use to describe rapid rock-fragment flows associated with phreatic eruptions. Such flows have commonly been regarded as relatively "dry" (Sekiya and Kikuchi, 1889; Crandell, 1971, p. 9; Nakamura, 1978), inasmuch as steam, gas, and air, rather than liquid water, were considered to be the dominant pore fluids. A "lahar," on the other hand, is a rapid water-saturated flow of rock debris derived from a volcano

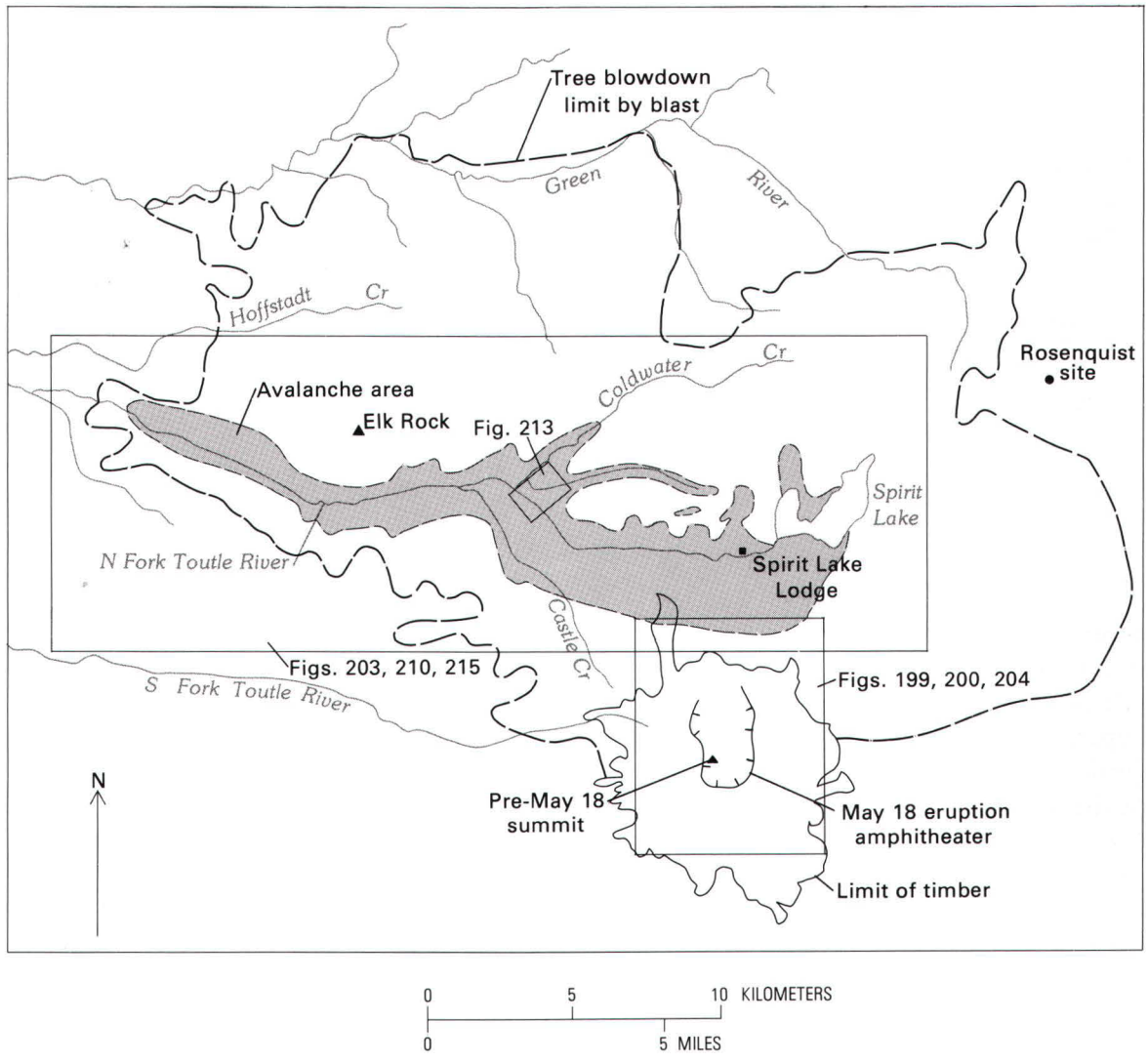

Figure 198.—Location map of avalanche study showing outline of figures 199, 200, 203, 204, 210, 213, 215 and Rosenquist observation site.

(Bemmelen, 1949; Crandell, 1971, p. 3; Neall, 1976, p. 2). Many lahars have originated in avalanches and became lahars only by incorporation or segregation of substantial amounts of liquid water (Crandell, 1971, p. 5, 9, 22, 35).

In this report, the rock-fragment flow deposit from Mount St. Helens is referred to as the "avalanche deposit" to emphasize the fact that the material was not completely saturated by liquid water when emplaced. The evidence suggests that during emplacement, the temperature of much of this material was near the boiling temperature of water and that steam formed a significant part of the pore fluid. The deposit includes small amounts of juvenile material that were emplaced at temperatures exceeding the Curie point, and some portions that remained water saturated during emplacement or that became saturated through condensation, pore fluid flow, or incorporation of surface water. Portions of the avalanche deposit are, therefore, transitional both to lahars and to pyroclastic flows; furthermore, lahars were later mobilized locally from the avalanche debris.

EVENTS OF MAY 18

A magnitude-4 earthquake on March 20 was followed by 2 mo of slope deformation, accompanying magmatic injection, intense seismicity, and phreatic eruptions, which set the stage for the events of May 18. These events began at 0832:11.4 PDT with an earthquake of magnitude 5+ (Endo and others, this volume). Geologists Keith and Dorothy Stoffel, while airborne over Mount St. Helens at an altitude of about 300 m above the north slope, observed minor falls of rock and ice debris into the summit crater, apparently directly triggered by this earthquake (Stoffel and Stoffel, 1980). New fractures then formed in the summit area, and within an interval of 5–10 s (Keith and Dorothy Stoffel, oral commun., Nov. 1980), a major and apparently new fracture system about 1½ km in length propagated across the north slope, approximately along the apex of the bulge that had developed during the preceding 2 mo (figs. 199, 200). The new fracture is the scarp of slide I as shown in figure 200. North of this fracture the mass then pulsed for several seconds under the influence of earthquake-generated surface waves of large amplitude; according to their observations, "The mass rippled and churned in situ * * *" (Stoffel and Stoffel, 1980), as if influenced by giant "standing waves" (Dorothy Stoffel, oral commun., Nov. 1980).

Within 7 to no more than 20 s after the initial earthquake (Voight, this volume; Keith and Dorothy Stoffel, oral commun., Nov. 1980), the north slope began to slide northward along the new fracture system. Termed "slide I," this slide represents the first of a succession of multiple, retrogressive slope failures. The detachment surface of slide I dipped northward at about 50°–60° but flattened with depth; in detail this detachment surface may have been compound, involving combinations of curved and planar elements.

Many details concerning slide evolution can be ascertained from remarkable photograph sequences of the Stoffels, Gary Rosenquist, and others. The Stoffel photographs indicate rapid slide movement, and show ash and steam issuing both from the main scarp at the 2,200-m (7,200-ft) contour and from the crown fractures (fig. 201). The steep unsupported scarp was metastable, and photographs document failure of a 100-m-wide slab along a portion of the crown (figs. 200, 201), which was superposed upon the head of slide I debris.

About 26 s after its detachment, slide I had moved nearly 700 m; its velocity was about 50 m/s and increasing, and the movement was taking on the character of a flow. The graben-crater area behind the slide I scarp had shifted downward 100 m as slide II (fig. 202*A*, *B*). The Rosenquist photograph sequence documents the sequence of events the next 32–40 s (Voight, this volume), and the motion of individual points can be followed through successive frames (fig. 202). The next 700 m required only 11 additional seconds; velocity was now 70–80 m/s. Lobes of avalanching ice from Forsyth Glacier were pouring over Sugar Bowl and the lower spur of Dogs Head (fig. 202), en route to the Timberline parking area (figs. 200, 201).

Explosions from exposed magma and hydrothermal chambers in the 600-m-high rear scarp of slide I (see figs. 201*B*, 202*A*) produced a devastating lateral blast that overran slide I (fig. 202*C*), mantled the avalanche debris, and to some extent mixed with it. Pressure reduction permitted flashing of steam in pore spaces and release of magmatic gas. At the same time, retrogressive failure continued behind the slide I scarp. The crown collapsed, including the remaining portion of the upper cone north of the summit graben wall

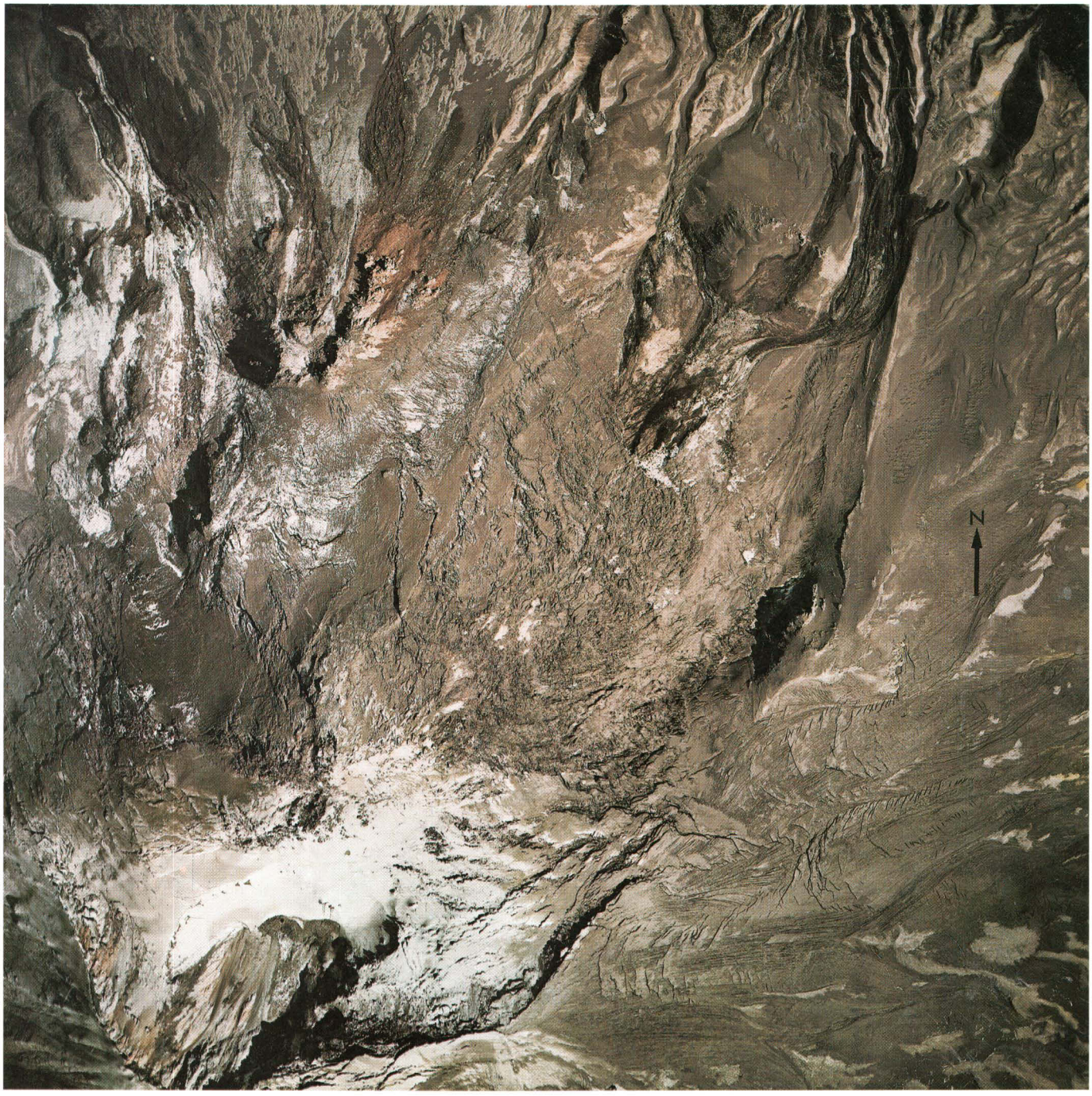

Figure 199.—Summit and north slope of Mount St. Helens on May 17. Geology of this area shown in figures 200 to 204. May 12 ice avalanche formed brown tongues north of Sugar Bowl. Photograph by U.S. Forest Service (FO 42 8005–10).

(see fig. 202*C*; fig. 38); this massive failure is termed "slide II." Its movement can be followed for several hundred meters on the Rosenquist photograph sequence, until the view becomes obscured by eruption clouds. The toe of slide II abutted against the heel of slide I, and to a certain extent the slides moved together as juxtaposed masses with, perhaps, a common basal movement zone (see Leighton, 1966; Varnes, 1978, fig. 2.30), but not necessarily with equal rates. In slide II, shear displacements appear to have been distributed over a broad zone, rather than on a single discrete fracture. The moving material of

slide II includes sources of erupting ash plumes and blast clouds, resulting in co-mingling of blast material with avalanche debris and providing additional energy for propulsion via expanding steam in void spaces.

Meanwhile, retrogressive failure continued behind the slide II scarp. Numerous relatively discrete, successive failures were probably involved, but the details are shrouded in explosion clouds. The movements are collectively referred to here as "slide III." Successive masses probably were partially superposed or partially juxtaposed with respect to earlier masses.

The cumulative effect of these multiple slope failures was the development of an enormous avalanche of fragmental debris that flowed downslope in pulses or waves. The flow of avalanche debris was strongly influenced by physiography and divided into several lobes (figs. 198, 203). One lobe traveled northward for about 7 km from the toe of the rupture surface; distal portions topped a 300- to 380-m ridge and reached South Coldwater Creek (fig. 198). Another lobe that rammed through Spirit Lake caused wave runup to 260 m above the original lake level and raised the lake level by about 60 m. For about 10 min, the main lobe funneled down the 1- to 2-km-wide North Fork Toutle River valley to a distance of about 22 km and formed a hummocky chaotic deposit (fig. 214).

A vertical eruption column developed following slide-induced pressure reduction. The combination of slide and eruption events resulted in formation of a horseshoe-shaped amphitheater about 2 × 4 km in size.

Lahars that were mobilized from avalanche debris by excess water (Janda and others, this volume) mantled avalanche materials and generated flooding down to the Cowlitz and Columbia Rivers.

PREFAILURE CONDITIONS

GEOLOGIC SETTING

The volcanic edifice consisted of two parts (figs. 204, 205), an older eruptive center characterized by a complex of dacitic domes (the "old Mount St. Helens" of Verhoogen (1937) or the "ancestral assemblage" of C. A. Hopson (written commun., 1980)), and a younger part consisting largely of dacitic domes and flows of pyroxene andesite and olivine basalt (Verhoogen, 1937). New exposures in the amphitheater show that extensively altered rocks of the older center made up a significant portion of the mountain to a height of 2,100 m (C. A. Hopson, written commun., 1980). The volcano rests on dissected Tertiary bedrock.

Shown in figure 204 are the outlines of the amphitheater, the pre-May 18 deformed area including the summit crater and graben system and the north slope "bulge," and the boundaries of the retrogressive movement sequence. Geologic map relations indicate that slide I is chiefly composed of andesite and basalt lava flows and unconsolidated breccias of the modern cone, a portion of the summit dacite dome, and in the west half, the Goat Rocks dacite dome and its avalanche apron. Slide II contains a capping wedge of summit dacite dome, lava flows and breccias of the modern cone, and at the base a sliver of the ancestral assemblage. Different proportions of the same units, and the altered root of the summit dome, are contained in slide III (figs. 204, 205). Juvenile dacite intruded in 1980 is presumed to be present in slides II and III. Slide boundaries indicated in figure 205 are schematic; probably they were somewhat influenced by layering within the modern cone and by morphology of the ancestral dome complex.

Evidence presented in the next section suggests that the deformed area in figure 204 began to develop soon after the magnitude-4 earthquake on March 20. Within 5 days, seismic activity had increased dramatically, and a steam eruption formed a crater on March 27 (Christiansen and Peterson, this volume). During this period, a remarkable series of changes had taken place at the volcano summit and on the upper north flank; an east-trending fracture system over a kilometer in length had formed across the summit, and another parallel fracture system bounded a block of the volcano's north flank (Christiansen and Peterson, this volume). The principal fractures of both systems dipped to the north at about 50° and formed a ridgetop depression (graben) between them (fig. 204). By the end of March, the southern fracture system could be followed downslope on the northwest for a vertical distance of roughly 500 m, and to a lesser distance on the northeast where it passed under Forsyth Glacier west of Dogs Head. This fracture system later formed the scarp of slide II.

Northward displacement of the volcano's north

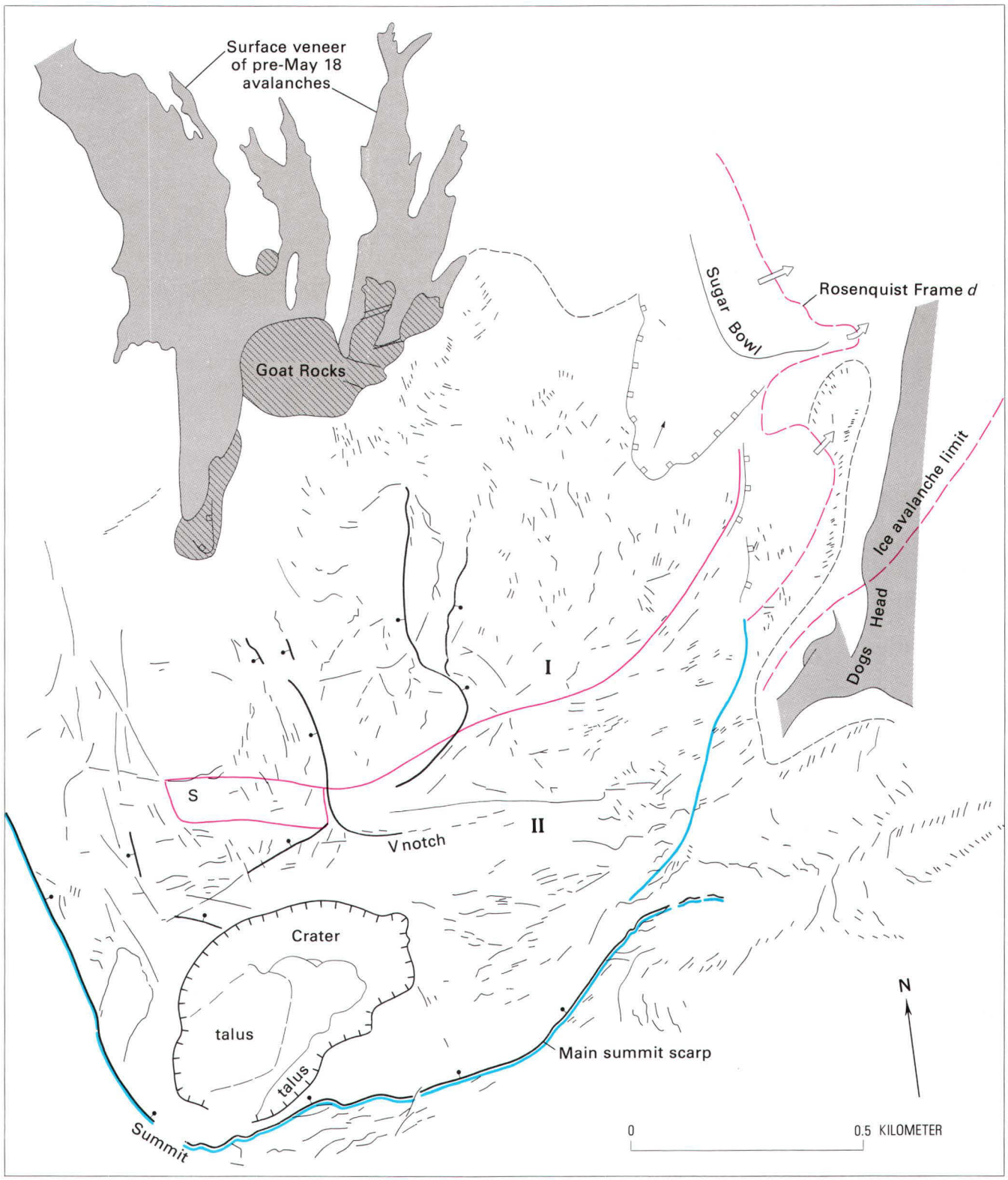

EXPLANATION

Rock outcrop

Pre-May 18 rock avalanche

Fracture

Extensional fault

Glacier margin

Avalanche scar

Crater rim

May 18 ice avalanche limit

East boundary of May 18 ice avalanche

Figure 200.—Deformational features of summit and north slope of Mount St. Helens on May 17 and boundaries of May 18 slides. See figure 199 for photograph of map area. Boundaries of May 18 slides I (red) and II (blue) are compared to structural conditions on May 17. Dashed red line, frontal position of May 18 ice avalanches derived from Forsyth Glacier. Retrogressive slab failure marked "S" follows slide I (see fig. 201B, C). Lined pattern shows prominent outcrops at Goat Rocks.

flank, which occurred in conjunction with development of the graben fracture system and continued into May, enlarged the conspicuous bulge formed in late March (fig. 206). Transverse and radial fracture systems, and extensional faults, developed to the point indicated in figures 199 and 200 for May 17, the day preceding slope collapse. Uphill-facing triangular-faceted patterns of fracture had characterized the front of the bulge in early April, but faulting evolved in a complex fashion. Downhill-facing arcuate scarps predominated along the apex of the bulge by May (fig. 206; D. J. Varnes, oral commun., 1981).

The volcano was largely saturated with water, probably due chiefly to melting snow and ice. Ponds commonly were observed in the summit crater (Christiansen and Peterson, this volume; Stoffel and Stoffel, 1980). The pre-May 18 summit eruptions were phreatic, which required high-elevation water tables, and on the morning of May 18, large wet areas glistened around Goat Rocks and Sugar Bowl (Stoffel and Stoffel, 1980).

DEFORMATION MEASUREMENTS

Ground-displacement surveys started on April 25 (Lipman and others, this volume) showed a kilometer-wide zone to be moving subhorizontally northward at relatively steady rates of 1.5–2.5 m/day. One target near the summit displayed a slight upward component; others showed small but significant downward components. The remainder of the volcano remained relatively unchanged.

Figure 201.—Views to west from aircraft of head of slide I dropping along steep-dipping detachment surface. A, Steam plumes rise from scarp and from depression north of summit crater. B, Further movement along slide I. Slab failure occurs at crown of scarp (see S in fig. 200). Dark explosion plume originates in slide scarp (shown in fig. 202A). C, Further movement of slide I. Deformation of summit area related to slide II movement. Explosion plume grows along slide I scarp. Copyrighted photographs by D. B. and K. L. Stoffel, 1980, published with permission.

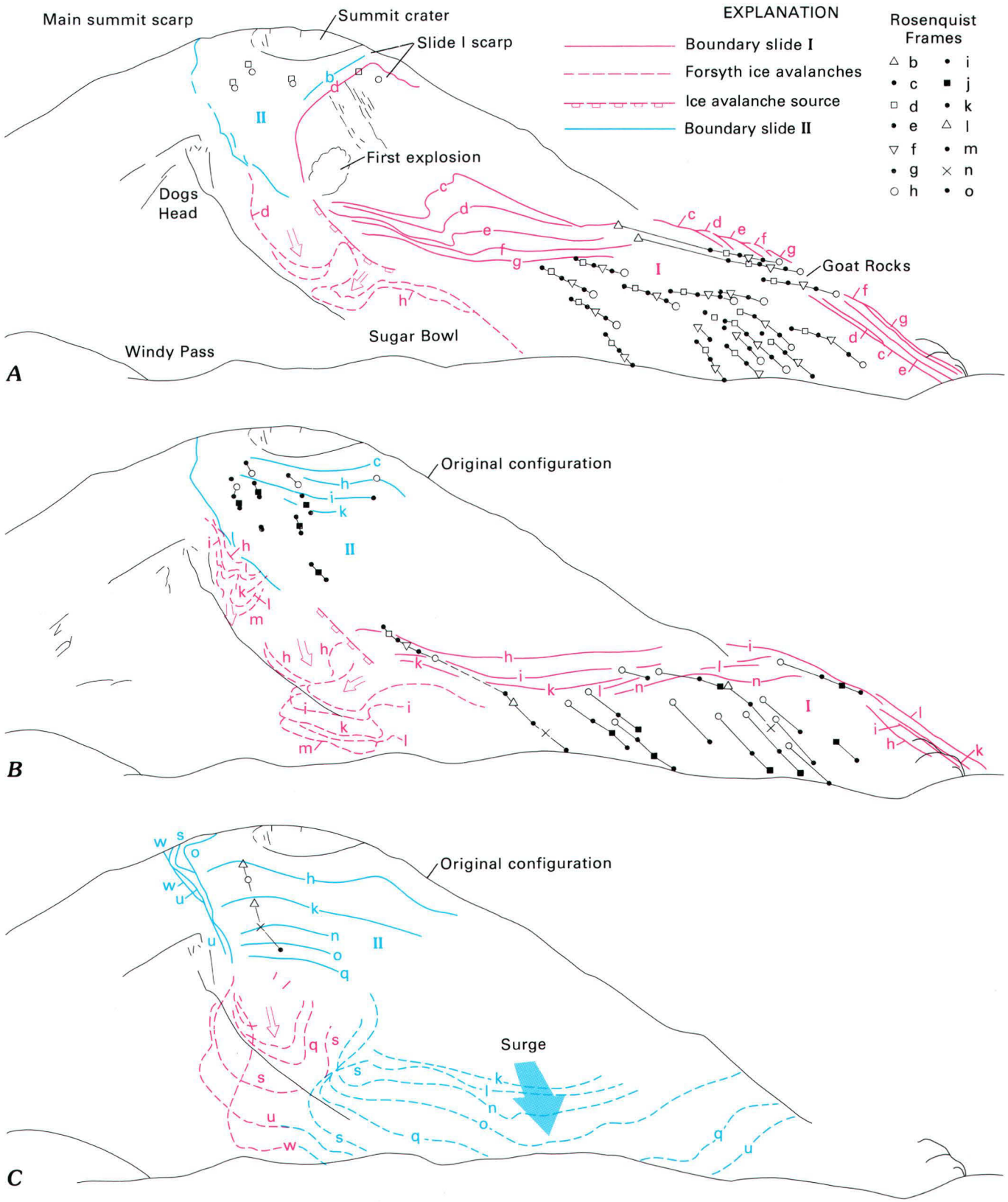
Main summit scarp
Summit crater
Slide I scarp
First explosion
Dogs Head
Goat Rocks
Sugar Bowl
Windy Pass
A
EXPLANATION
Boundary slide I
Forsyth ice avalanches
Ice avalanche source
Boundary slide II
Rosenquist Frames
Original configuration
B
Original configuration
Surge
C

Additional data on deformation of the volcano are provided by 1:24,000 contour maps produced from aerial photographs taken August 15, 1979, April 7 and 12, 1980, and May 1 and 12, 1980; a 1958 topographic map base was used for ground control (Moore and Albee, this volume).

Horizontal displacements can be closely approximated from the map data. Measurements based on a conspicuous, closed contour at Goat Rocks indicate for this area a cumulative displacement vector inclined northward at about 5° for August 15, 1979, to May 12, 1980 (fig. 207); these measurements suggest that the dominantly subhorizontal motion indicated by geodetic work extended over the full deformation period.

Horizontal displacement contours were generated from the topographic maps (fig. 208; see fig. 204 for boundary of deformed area). Significant horizontal movements for August 15, 1979, to April 7, 1980, involved most of the deformed area; movements were greatest north of the crater, and diminished northward and toward lateral margins. The pattern is only slightly skewed to the northeast. By contrast, movements for April 7 to May 12, 1980, are concentrated in the eastern two-thirds of the deformed area. Maximum movements occurred in a warped band that extended in a north-northeast direction from a point due north of the crater to the couloir between Sugar Bowl and Dogs Head. The surface of rupture for slide I developed approximately along this axis of most intense horizontal displacement (see figs. 208, 201, 200), and the slide-scarp explosions (fig. 38) were most strongly developed near the contour maximum.

The volume increase associated with the bulge to May 12 was by our measurement about 0.190 km^3, and the volume decrease associated with the summit graben and crater was 0.031 km^3. The volume lost by pre-May 18 lithic ash eruptions is only about 0.0004 km^3 (Sarna-Wojcicki and others, this volume). The resulting net volume increase is about 0.16 km^3, a somewhat greater value than the 0.11 km^3 suggested by Moore and Albee (this volume). The discrepancy perhaps reflects our use of a 1958 topographic map base for ground control. The volume increase is assumed to be due mainly to magma injection, but mass rock dilatation probably accounts for some part of it. Preeruption magma volume thus would be about 0.14 km^3, equivalent to a rectangular block of dimensions $1,000 \times 370 \times 370$ m.

Additional information on ground deformation, especially during the time interval preceding the systematic geodetic surveys in the field, was provided by the motion history of 18 points on sequential topographic contour maps prepared from aerial photography between August 15, 1979, and May 12, 1980 (fig. 207). Displacements were calculated for each point and displacement-time curves were constructed. These data indicate that for May 1 through May 12, the average velocity is 1.7 m/day, a value comparable to geodetic survey data (1.5–2 m/day; Lipman, Moore, and Swanson, this volume) for the overlapping period. But successively higher, average horizontal rates of movement are evident for earlier dates; namely, 2.4 m/day from April 12 to May 1, and 3.1 m/day from April 7 to 12.

Displacement data for each point and for each of the time intervals were then normalized by dividing by the corresponding displacement component derived for April 7 to May 12. Normalized displacements were then plotted versus elapsed time from April 7 (fig. 209), and a curve was drawn connecting mean values. Extrapolation of this curve to the pre-April 7 period suggests that, on average, "initial" movements occurred in the period March 25–31; linear extrapolation gives a lower bound "initial" value of March 19.

These projections correspond well with the onset of earthquake activity on March 20, intense seismic activity from March 25–29 (fig. 209; see Crosson and others, 1980; Endo and others, this volume), the first crater-forming phreatic eruption on March 27, and development of the east-trending summit fracture systems in the period March 25–27. Average horizontal rate of displacement derived for March 25 to April 7 was 4.7 m/day; the maximum rate was 9.7 m/day.

Figure 202.—Movement of the north slope of Mount St. Helens as indicated by the Rosenquist photographs (Voight, this volume). Frame b was taken about 5 min before the slide. Slide displacement is first shown by frame c; successive frames are indicated alphabetically. Approximate time intervals between frames are shown on figure 47 (Voight, this volume). A, Connected points indicate movement paths for natural objects identifiable on several frames. Small slide II movements shown at the crown of the slide I scarp. B, Further movement paths for slides I and II, and frontal positions of ice avalanches. C, Positions of the head of slide II are compared with fronts of the surge and of ice avalanches from Forsyth Glacier.

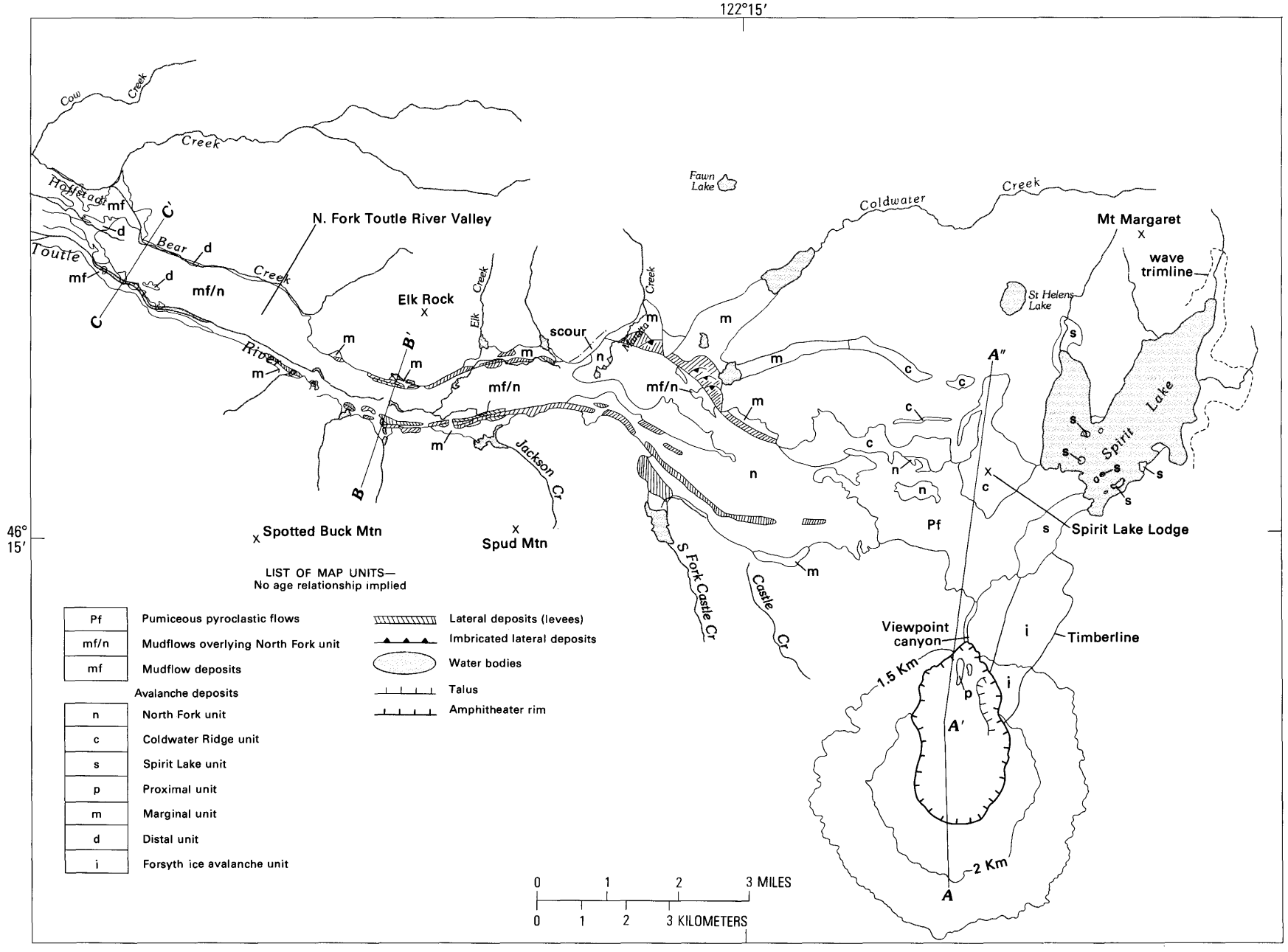

Figure 203.—Geologic map of Mount St. Helens avalanche deposit showing lines of cross sections.

According to these calculations, average movement rates thus systematically decreased with time, from initial rates that probably exceeded 5 m/day to final rates of about 1 m/day as measured for the last 5 days preceding slope collapse (Lipman, Moore, and Swanson, this volume). The relationship of displacement with time, which is approximately logarithmic, suggests deceleration of ground movements. Seismic data in figure 209 display a similar pattern, but the relation may be indirect. Magmatic activity probably is related to both ground movement and seismicity.

Compared to the conventional threefold partition of deformation exhibited in the laboratory in constant-load creep experiments, the field data are reminiscent of primary (decelerating) and secondary (approximately steady state) creep. There is no indication of tertiary (accelerating) deformations, which inevitably precede major slope collapse where such failures are not triggered directly. On the other hand, the Mount St. Helens deformation pattern is similar to that observed at the Chuquicamata pit slide (Voight and Kennedy, 1979, p. 610–620, fig. 14), where the slope deformed according to a regular pattern (approximately logarithmic) until that pattern was disrupted by external causes (blasting, earthquakes, excavation). Although quantitative deformation data are not available from the classic major earthquake-triggered rockslides, observational evidence makes clear that prefailure ground movements occurred (for example, Hadley, 1978, p. 177–178; Plafker and Ericksen, 1978, p. 284–285) and implies that the almost systematic patterns of prefailure deformation were abruptly altered by trigger earthquakes.

AVALANCHE DEPOSIT

The avalanche deposit consists of unconsolidated, poorly sorted volcaniclastic debris that buried about 60 km^2 of terrain to an average depth of 45 m (fig. 203). Its maximum thickness, 195 m, occurs north of the cone, 2.5 km west of the old Spirit Lake Lodge (figs. 210, 203). The deposit spans 25 km east to west (fig. 211); on average it exceeds 2 km in breadth (figs. 205, 212). A volume of 2.5 km^3 has been calculated from isopachs for the portion of the deposit shown in figure 210. The addition of avalanche material in Spirit Lake basin and the Coldwater Creek drainage system raises this estimate to about 2.8 km^3 for the entire deposit. The volume missing from the pre-May 18 cone is estimated to be 2.76 km^3; in addition to avalanche debris, some of this volume is included in pyroclastic flows, blast deposits, and tephra. The calculated in-place volume of the rockslide-avalanche mass in the cone is about 2.3 km^3. Measurements discussed in the "Physical Properties" section of this report suggest average bulk specific gravities for the avalanche deposit of 1.8 (dry) and 2.0 (moist); corresponding values for 2.3 km^3 of original cone material are about 2.2 (dry) and 2.4 (moist). Potential energy loss associated with drop in elevation for the avalanche mass is estimated as 7×10^{16} J.

Seven map units are recognized within the avalanche deposit. These are informally referred to as the North Fork, Coldwater Ridge, Spirit Lake, marginal, proximal, and distal units, and Forsyth ice avalanches, according to representative locations of their deposits (fig. 203; see pl. 1). Additional May 18 and younger deposits are mixed within and partially overlie the avalanche, and mantling lahar deposits on the surface of the avalanche deposit west of Castle Creek (Janda and others, this volume) cover increasing percentages of its surface area toward the west (fig. 203).

NORTH FORK UNIT

Comprising the bulk of the avalanche deposit, this unit extends throughout the valley of the North Fork Toutle River from under the pumice fan on the north volcano flank to within a kilometer of the western distal boundary (fig. 203). Its characteristic morphologic features are hummocks that protrude 6 to about 30 m above the mean elevation of the debris surface (fig. 214). Hummocks are as much as 170 m wide. Many are roughly conical or domical, but they more commonly have irregular morphology (fig. 213) and are bounded by normal faults or slumps. Many hummocks probably represent horsts that have originated through lateral spreading.

Closed depressions are common features (fig. 213). They are often roughly circular in plan and as much as 130 m across and 40 m deep. Some depressed areas may be complex grabens associated with lateral spreading. Glacier ice blocks are included in avalanche debris, and some depressions are due to melting of ice. However, most large depressions were present at noon on May 18, long before the surficial

Figure 204.—Simplified geologic map of pre-May 18 Mount St. Helens showing deformed area and May 18 slides I (red), II (blue), and III (black). Cross section A-A″ shown in figure 205. Geology modified from unpublished mapping of C. A. Hopson.

LIST OF MAP UNITS

i	Glaciers
d	Summit dacite dome
d	Goat Rocks and Sugar Bowl dacite domes
a	Pyroxene andesite lava flows
b	Basalt lava flows
g	Dacitic hot and cold avalanches, lahars, and talus, mainly from Summit dome
ggr	Dacitic hot and cold avalanches, lahars, and talus, from Goat Rocks dome
ga	Andesitic avalanches
u	Unconsolidated deposits; laharic, fluvial, avalanche, and glacial
do	Dacitic and andesitic domes
To	Tertiary bedrock
	Contact, dotted where concealed
	Extensional fault
	Mid-April crater
	Approximate deformed area boundary, pre-May 18
	Amphitheater boundary, May 18

ice blocks had melted; therefore, these depressions probably did not result from collapse of material into regions vacated by melting ice. Many appear to be approximately alined along the buried stream channel of the North Fork Toutle River, and these may represent collapse features over buried voids. Finally, ejecta deposits, fumarolic sublimates, and steeply plunging striae present on the rims of some deep, steep pits suggest that some depressions formed by high-velocity release of large volumes of steam.

Levees as much as 30 m high near lateral margins occur plastered against the valley walls or blocking the mouths of tributaries. Commonly they mark the contact between North Fork and marginal units, but often two (and occasionally three or four) parallel, well-defined levees are present within the North Fork unit, separated by V-shaped troughs. Levees near Coldwater Creek exhibit imbricate structures that reflect lateral compressive shove from pulses of the flowing avalanche (fig. 203).

The North Fork unit is typically 20–70 m (maximum 150 m) in thickness, but has no prominent flow front. The deposit is composed of multicolored heterolithologic breccia; some blocks within the avalanche breccia are monolithologic, and others are fragments of older heterolithologic breccia. The blocks, which vary in shape and size and range from less than 1 to 170 m across, evidently decrease in maximum size toward the distal end. Both fresh and altered rocks are present.

C. A. Hopson (written commun., 1980) provided instruction and samples that greatly aided the field identification of key rock units. Many clasts identified are dacite from the ancestral assemblage and from the summit dome. Goat Rocks material is present locally, and other blocks contain brecciated basalt, andesite, and associated scorias. Locally present are small (< 0.5 m diameter), prismatically jointed blocks of gray vesicular dacite that are thought to represent juvenile material injected into the cone between March 20 and May 18. Blocks of Tertiary bedrock as well as alluvium, colluvium, and old tephra occur locally; tree trunks, splintered wood, and other

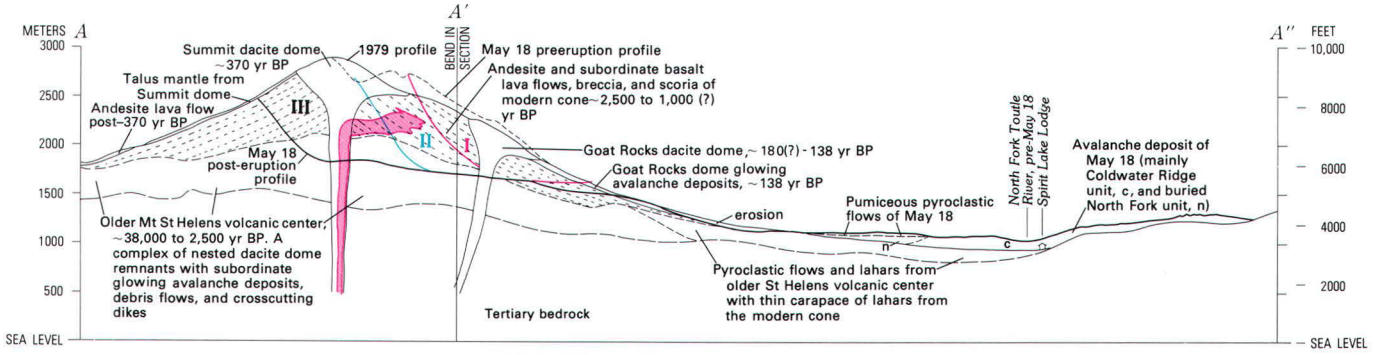

GEOLOGIC CROSS-SECTION A-A′-A″

Figure 205.—Cross section A-A″ showing August 1979 and May 18 preeruption profiles, and May 18 posteruption profile. Geology of cone from C. A. Hopson, based on unpublished pre-May 18 mapping and inspection of amphitheater. Slide boundaries I (red), II (blue), and III (black) are approximately located, but precise configuration at depth is uncertain. Dacite intrusion of March–May 1980 indicated by light-red pattern.

organic and manmade debris were sporadically incorporated in the deposit. Glacier ice slivers and blocks as much as 12 m across, now melted, were observed at the surface in canyon exposures or on hummock or canyon walls. Many blocks display fragile stratigraphic or structural features formed on or within the pre-May 18 cone, and their preservation in the avalanche debris is interpreted as the result of laminar "plug flow," a recognized characteristic of flowing debris (Johnson, 1970, p. 442). Many exposures

Figure 206.—Mount St. Helens from the northeast on May 1, showing bulge on north slope west of Dogs Head, south of Sugar Bowl, and north of main summit scarp. Goat Rocks on north slope contains pinnacle that shows as closed topographic contour on figure 208. Timberline parking area at lower right. Photograph by Austin Post (80-52-140).

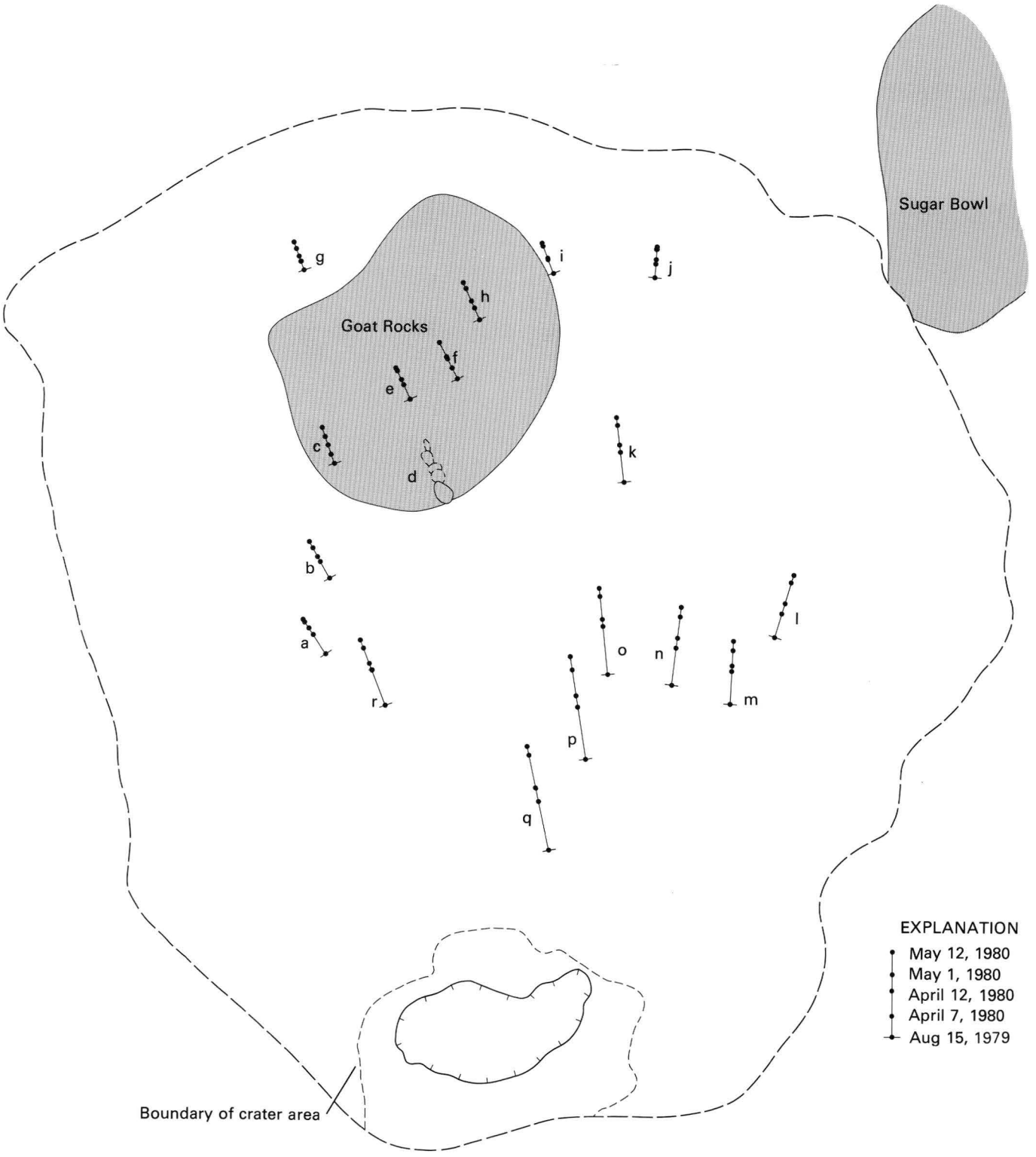

Figure 207.—Horizontal displacement vectors as indicated on topographic maps for August 15, 1979, to May 12, 1980. Vertical displacement components are small, as indicated by movement of a closed contour at Goat Rocks (d.) Boundary of deformed area as shown on figure 204.

reveal thoroughly sheared material, but no evidence of chaotic disruption was found to suggest the influence of turbulent motion.

In May and June 1980, shallow excavations in much of the deposit revealed warm, moist material. Temperature data provided in figure 215 indicate that much of the deposit approached 100°C at the time of emplacement. Probe measurements suggest a systematic temperature decrease downvalley, from 98°C at the base of the cone to 68°C at the distal end (Banks and Hoblitt, this volume). This decrease may reasonably reflect initial temperature differences in avalanche material. The hotter material probably originated from a deeper source within the thermal system of the pre-May 18 cone. Avalanche emplacement was so rapid that special cooling effects, or mixing with surface water, probably cannot explain the data.

COLDWATER RIDGE UNIT

Present only on and adjacent to the ridge between South Coldwater Creek and the North Fork Toutle River, this unit contains some irregularly shaped hummocks as well as terraces that range to 360 m high and 150 m across. Closed depressions are uncommon and steam pits are absent. Many deposits plastered against the southern slope of the ridge exhibit prominent shear planes dipping south, perhaps an indication of "fall-back" from positions at higher elevations. The deposit appears in the lower valley of South Coldwater Creek as isolated hummocks that protrude from the surface of a blast pyroclastic-flow deposit. Maximum thickness of the Coldwater Ridge unit is 195 m.

More than 90 percent of the unit consists of blocks as much as 100 m across of fresh (black) and altered (red) brecciated andesite, basalt, and associated scorias. The remainder consists of brecciated dacite, and locally derived Tertiary rocks, old tephra, and colluvium. The unit is locally mixed with but everywhere veneered by blast deposits, and is covered with thin pumice flows and ash-cloud deposits in the "runup" area north of the old Spirit Lake Lodge (fig. 203).

SPIRIT LAKE UNIT

This unit is exposed in a 2×0.6 km patch south of Spirit Lake, in an embayment at the head of the west

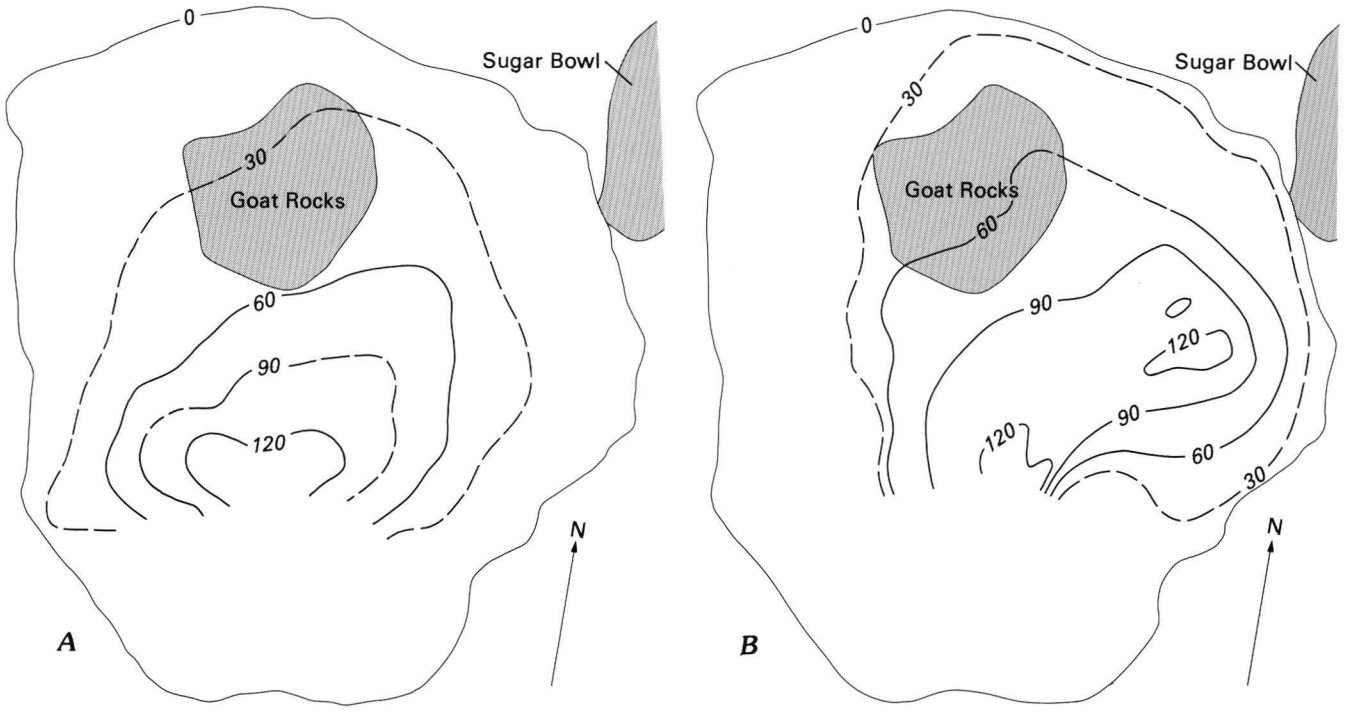

Figure 208.—Horizontal displacements as indicated by topographic maps for August 15, 1979, to May 12, 1980. Zero contour is deformed-area boundary shown in figure 204. Vertical displacement components are assumed negligible. A, Interval August 15, 1979, to April 7, 1980. Mass movements are inferred to have occurred in interval March 20 to April 7. B, Interval April 7 to May 12, 1980. Pattern is strongly skewed to east.

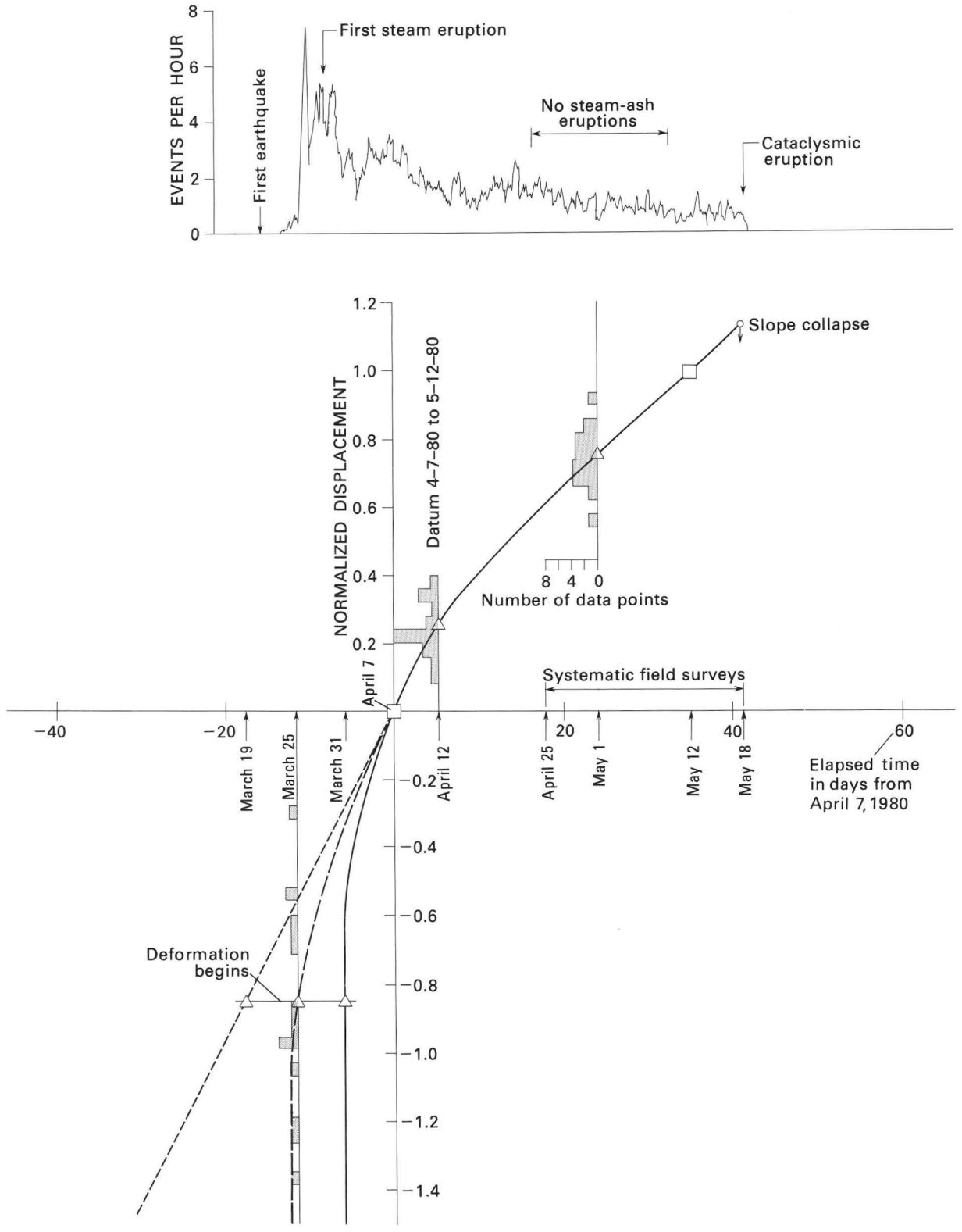

Figure 209.—Normalized displacements versus elapsed time from April 7, 1980. Displacement data normalized with respect to the interval April 7 to May 12; histograms indicate distribution of individual points, and triangle shows mean value. Curve connects mean values for April 7 to May 12. Extrapolation to the pre-April 7 period suggests that movements began in period March 19–31. Normalized displacement rate decreases as a function of time, and movement after mid-April is approximately steady state. Seismic events per hour plotted versus time for purposes of comparison (modified from Crosson and others, 1980).

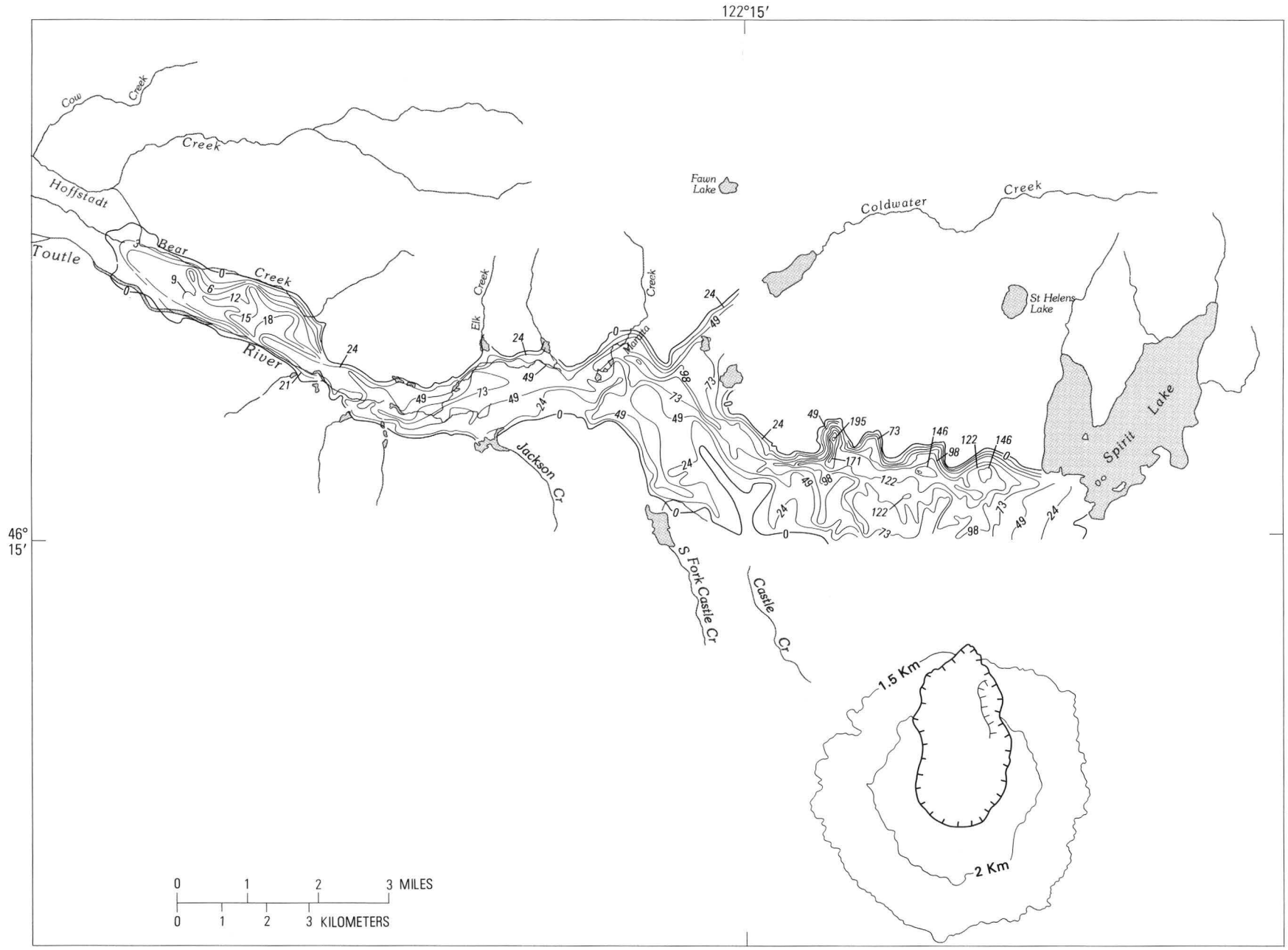

Figure 210.—Isopach map of portion of avalanche deposit. Contour interval is 24 m, except for portion of western area where contour interval is 3 m. Map is preliminary; zero contour imprecisely reconciled to geologic map.

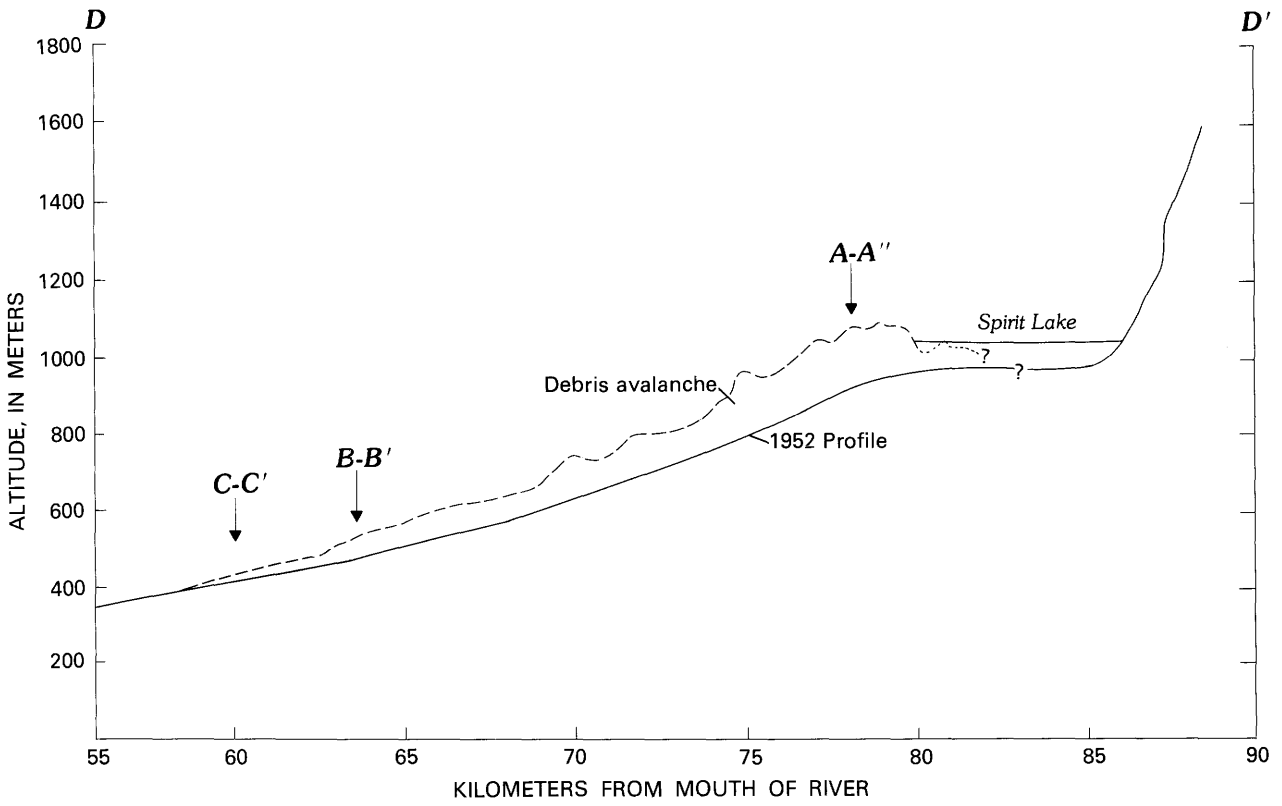

Figure 211.—Longitudinal topographic profile of North Fork Toutle River approximately along axis of debris avalanche comparing 1952 and post-May 18, 1980, data. Vertical exaggeration ×10.8. Location of cross-sectional profiles *A-A'-A", B-B', and C-C'.*

arm, and in a few islands and shoreline mounds. Maximum thickness of the deposit is about 100 m.

Blocks of breccia occur in roughly conical slump-bounded hummocks as much as 10 m high. Lithic types include altered ancestral and summit dacites; juvenile dacite; andesites, basalts, and associated scorias; wood debris; and locally derived Tertiary bedrock, tephra blocks, and colluvium.

High-velocity avalanche emplacement caused a huge sheet of water to surge along the shore, up re-entrants, and then upvalley beyond both arms of Spirit Lake, devastating the landscape to wave trimline (fig. 203). Runup exceeded 260 m, a value comparable to a catastrophic surge at Vaiont, Italy, and over three times the maximum height of Norwegian slide-generated waves (Slingerland and Voight, 1979, table 3). This water then swashed back and overrode portions of the avalanche mass. Spirit Lake was lifted about 60 m above its former level, but the return wave caused wash to higher elevations along the south shore and caused further lake oscillations for a period of time thereafter. This water action produced a variety of erosional modifications and fluviolacustrine deposits. Deep erosional channels were carved in the west arm deposits and hummock faces were oversteepened; slumps occurred at hummock walls and the slump masses were reworked by water; and trunk fragments of shattered trees as much as 20 m in length and finer wood debris lodged high on hummock tops and sides.

Stratigraphic relationships between avalanche debris and adjoining wave-influenced deposits are complex. Mudflow deposits interspersed in channels among hummocks contain a significant coarse fraction of wave scour-derived clasts of Tertiary bedrock from adjacent ridges; deltas containing similar material were produced along the shore of Spirit Lake.

PROXIMAL UNIT

The proximal unit comprises a few isolated hummocks veneered by post-May 18 deposits in the north part of the amphitheater. These are the only visible avalanche deposits that remain in the zone of depletion of the May 18 slide (see Varnes, 1978, fig. 2.1).

MARGINAL UNIT

The marginal unit backfills tributaries of the North Fork Toutle River and forms lobate deposits, which are truncated by debris levees of the North Fork unit (fig. 203). The lobes exhibit flow fronts as much as 5 m high. Thickness of the unit varies from 1 to about 100 m. The marginal unit consists primarily of an unsorted, unstratified mixture of clasts and splintered wood enclosed in a monochromatic dark-brown, poorly sorted muddy matrix. The deposit, which includes andesite, basalt, and associated scoria and

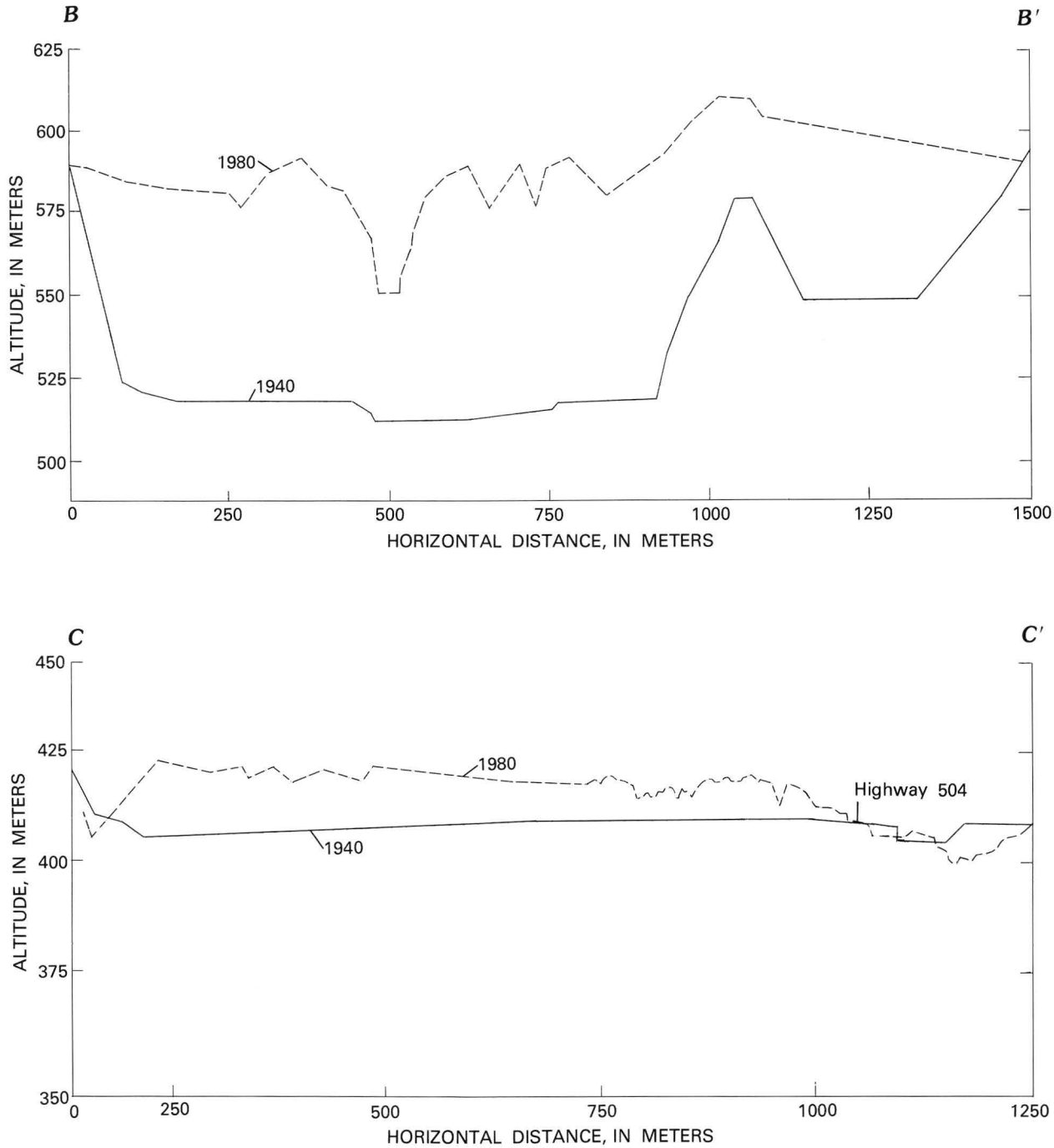

Figure 212.—Transverse topographic profiles crossing debris avalanche comparing 1940 and August 1980 data. Vertical exaggeration ×10.8. Survey data for 1940 courtesy of Weyerhauser Corporation. A, profile B–B' near Elk Rock; B, profile C-C' near western distal end.

dacite, is rich in colluvial material. The ratio of matrix to blocks of breccia is much higher than that in the North Fork unit.

The distribution of the marginal unit suggests that it was moved up and pushed in front of and to the side of the main mass of the flow, and that it came to rest while the North Fork unit was still in motion. The lobate, mudflowlike morphology, the occasional occurrence of "bubble" vesicles in fine matrix, and the relatively high ratio of matrix to blocks of breccia suggest that its flow behavior differed from that of the North Fork unit. This difference probably reflects the presence of significant quantities of liquid water. Bubbles have been reported elsewhere for lahars, mudflows, and water-deposited sediments (Bull, 1964, p. A31; Crandell, 1971, p. 6).

DISTAL UNIT

Mapped only at the west end of the debris-avalanche deposit, the distal unit consists of an accumulation of jumbled mounds of trees and wood debris, as much as 10 m high and 20 m wide, in a matrix of splintered wood, organic-rich soil, and perhaps 10–30 percent inorganic debris. Flow fronts are prominent and are as much as 8 m high. Locally, more fluid facies of the deposit that are not as rich in organic material slope down from the main mass of distal material and grade into mudflow deposits.

The contact between distal and North Fork units is generally gradational over 10–20 m, but it occasionally is sharp and dips 5°–10° to the west. The dip of the contact and the distribution of the deposits sug-

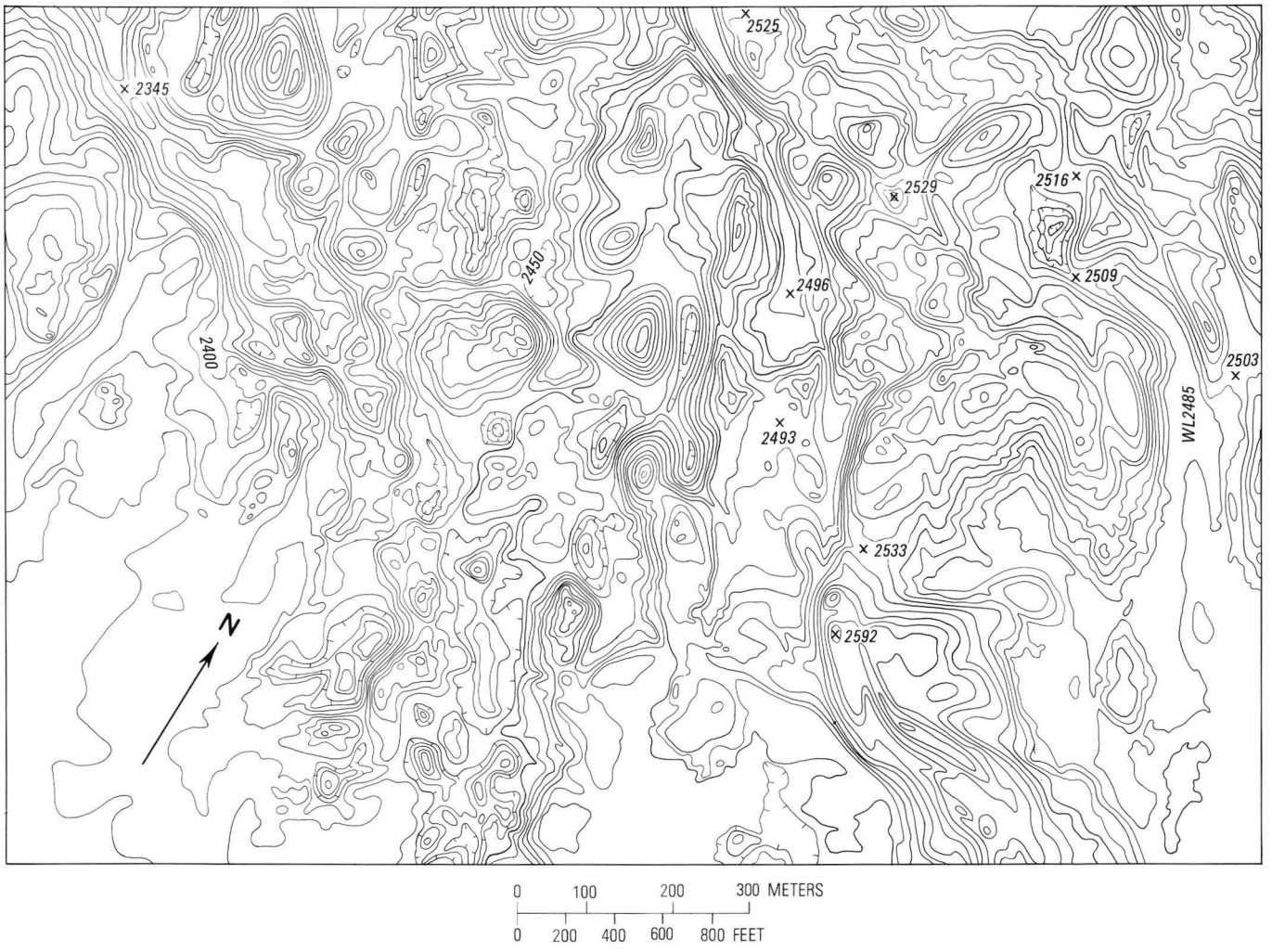

Figure 213.—Topographic map showing surface detail on debris avalanche in vicinity of Coldwater Creek. See figure 198 for location. Avalanche surface contains hummocks, depressions, and levees.

gest that the distal unit in the valley bottom consists largely of timber that was felled by the blast or avalanche front and was shoved along at the avalanche front.

FORSYTH ICE AVALANCHES

This map unit represents accumulations from three overlapping ice avalanche lobes that originated from

Figure 214.—View east along North Fork Toutle River at Elk Rock bend on June 30. Hummocky avalanche deposit of May 18 filled the valley to 45 m average depth. Photograph by R. M. Krimmel.

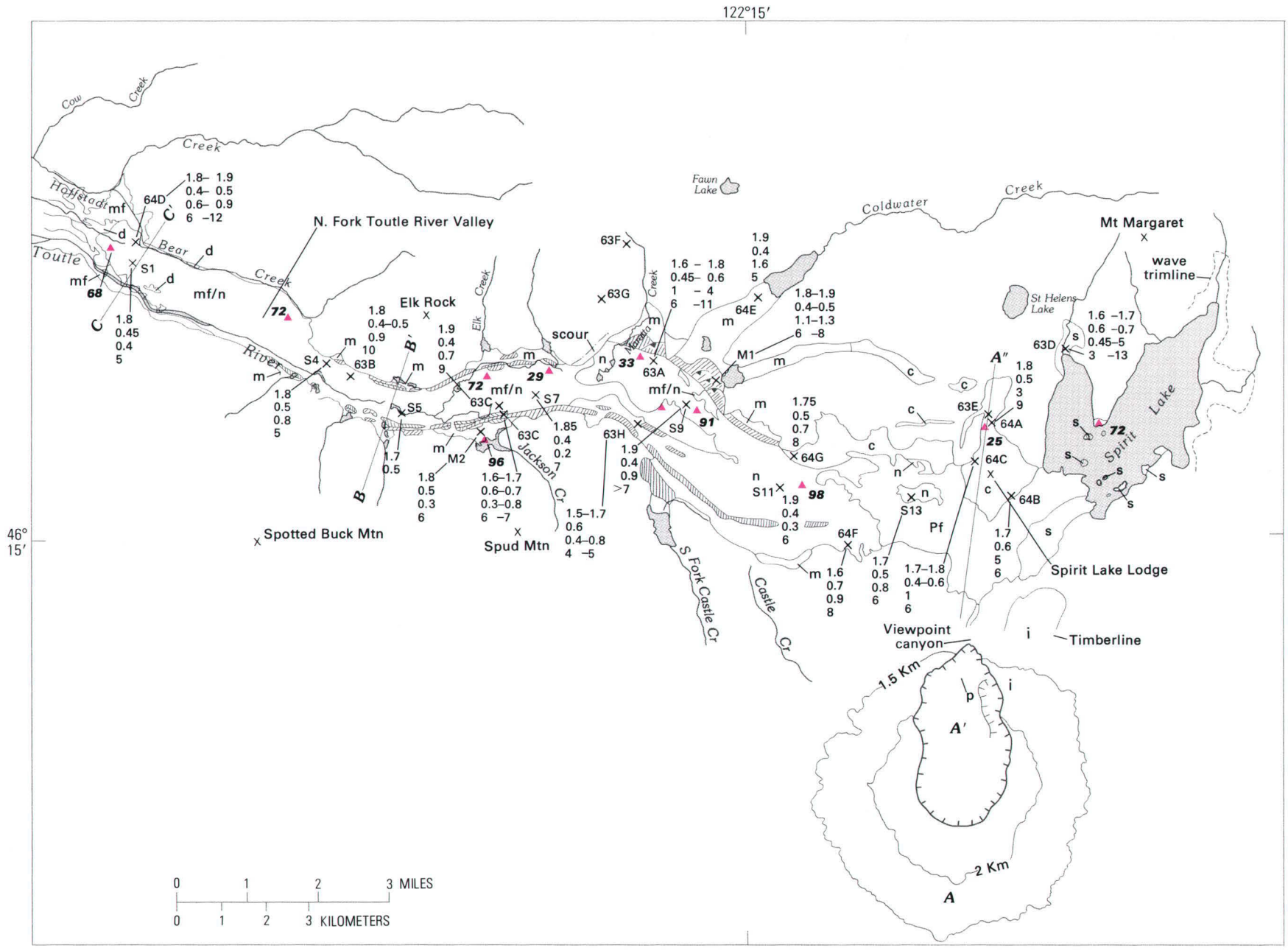

Figure 215.—Sketch map of avalanche deposit indicating sample localities and density and textural data. Data shown from top to bottom: dry bulk density (g/cm³), void ratio, and for some localities, median diameter (mm) and sorting coefficient. Temperatures in degrees Celsius, for shallow measurements, indicated by triangles. Avalanche units as shown in figure 203.

the Forsyth Glacier. The northern limit of visibility of the Forsyth ice avalanches in the Rosenquist photographs is south of the Timberline Campground (figs. 200, 203); the extent of ice-avalanche accumulation north of this boundary is therefore not known. Suspected ice avalanche deposits were observed along the valley 0.8 km northeast of Timberline Campground (P. W. Lipman, oral commun., January 1981). Mapping of successive ice-avalanche front positions (see figs. 200, 202) was used to develop a time scale (Voight, this volume) applicable to various eruptive and mass movement events displayed on eyewitness photographs.

AVALANCHE DEPOSIT UNITS IN RELATION TO SLIDE SEQUENCE

The Coldwater Ridge unit, which lacks significant proportions of either modern or ancestral dacite, is correlated with the eastern sector of slide I (fig. 204). We infer that the avalanche pulse representing slide I spread out along the base of the cone. The western sector was deflected by Coldwater Ridge to the west, but the remaining part ran up and partly overlapped a saddle in Coldwater Ridge, and deposited a breccia of andesite and basalt fragments.

The western sector of slide I, which contains dacite from Goat Rocks, occupied the North Fork Toutle River valley floor. Much of this material was then shoved by the succeeding avalanche pulse to the valley side and mixed with valley floor debris and stream water to form the marginal unit. Clasts of Goat Rocks dacite occur in the avalanche deposits south of the North Fork unit levee near Castle Creek, and in the marginal unit in Coldwater Creek.

The North Fork unit originated in hot, mobile, steam-rich avalanche pulses from slides II and III. Hummocks of ancestral material that are found against plowed-up distal-unit mounds of woody debris conceivably represent the smeared-out toe of slide II. The apparently more mobile tip of the North Fork unit west of Elk Rock could represent, almost in its entirety, slide II material. North Fork deposits rich in summit dome clasts, which are found east of Jackson Creek, are regarded as avalanche pulses from slide III. Mobility was largely provided by the hot lower zone of fluid-saturated ancestral dacite and modern cone material.

Similarly, the Spirit Lake unit was hot when emplaced. Because it contains much altered dacite along with andesite and basalt, the unit is interpreted to represent northeast-deflected portions of avalanche pulses from slides II and III.

In slides II and III, pressure reduction likely permitted flashing of steam within the pore spaces and caused forcible, directed volumetric expansion, increase in void ratio, and profound loss of strength. At the same time, the unsaturated surface zone rich in summit dome blocks (fig. 205) was capable of faulting. Transverse and longitudinal extension (lateral spreading) occurred in the transition from slides to avalanche pulses and resulted in intersecting systems of horsts and grabens. Intersecting horsts produced hummocks and intersecting grabens produced depressions, both features evolving from a relatively early stage in slope movement. The various morphologies underwent continued changes through jostling and differential volume changes, and the moving North Fork unit was sporadically punctured by fumaroles that released accumulated steam.

Although these hypotheses are based on clast counts at many localities, they are regarded as preliminary. Detailed mapping of the deposit is planned, using improved topographic maps (see fig. 213). Detailed studies of the amphitheater by C. A. Hopson (written commun., 1980) may reveal additional, recognizable "marker" lithologies and improve interpretations.

PHYSICAL PROPERTIES

The avalanche deposit is huge and the material is widely graded—from particles of clay-size to blocks several thousand cubic meters in volume. Representative sampling is thus not feasible. The reader should bear this in mind when reviewing test results summarized in tables and discussed herein, and should furthermore be careful to distinguish between the properties of the existing avalanche deposit and those assumed for moving avalanche debris. Some physical-property data on mudflows and pyroclastic flows are tabulated for comparison with avalanche properties.

TEXTURE

Grain-size distribution studies were made on 19 samples of about 15-kg weight from diverse localities on the avalanche deposit (fig. 215). Samples were col-

lected within a meter of the avalanche outcrop surface, but the effective sampling depth was greater because of hummocks and incised channel exposures. The question of vertical gradation in texture at individual localities has not been systematically evaluated.

The texture at each locality is summarized by table 37; clay-size fractions of the samples from the avalanche deposit range from 1 to 7 percent, silt-size fractions from 5 to 21 percent, and sand-size fractions from 31 to 69 percent. Average values are 4, 11, and 42 percent for clay, silt, and sand, respectively; the remaining 43 percent comprises the >2-mm fraction of gravel and organic debris. Sorting coefficients of these samples range from 2.9 to 13.0, and the average value is 7.1. Coefficients of uniformity (Terzaghi and Peck, 1967) range from 13 to 300, and the average value is about 150. These coefficients mainly reflect gradation of the matrix rather than the deposit as a whole, inasmuch as the fraction of boulders and enormous blocks is inadequately represented. Median diameters range from 0.27 to 4.7 mm, and the average value is 1.9 mm. However, most samples have median diameters between 0.6 and 1.2 mm, and much of the variation in grain-size distribution reflects the influence of one or a few large clasts. Cumulative curves prepared from the particle-size distribution data are given in figure 216.

Spatial variations in the texture of the avalanche matrix exhibit little systematic change. In the North Fork unit, sorting and uniformity coefficients maintain similar average values from near the source to the distal end, a distance of about 20 km (fig. 215). This is not unusual for fragmental flow deposits; for example, the only downvalley change in texture noted for the Holocene Osceola Mudflow at Mount Rainier was an apparent decrease in maximum stone size in the basal zone (Crandell, 1971, p. 28); sorting coefficients were about the same for a distance of over 100 km (fig. 217). Sorting values similar to the North Fork unit are found in Coldwater Ridge material (table 37; geologic units of samples are listed in table 38). On the other hand, two of five cumulative curves demonstrably influenced by cobble-size clasts represent Coldwater Ridge unit, which suggests the possibility of greater proportions of large clasts. Cumulative curves from the Spirit Lake unit and the marginal unit also appear somewhat unusual by contrast with North Fork material (fig. 216); indeed, two Spirit Lake samples encompass the entire range of sorting and uniformity coefficients found for the avalanche deposit. Preliminary data are sparse but suggest that cumulative curves possibly could provide a quantitative means to discriminate between map units.

Table 37.—Particle-size distribution data from avalanche and associated deposits

[Values not in parentheses: >sand, >2 mm; sand, 0.0625–2 mm; silt, 0.004–0.0625 mm; clay, <0.004 mm. Values in parentheses: >sand, >4.76 mm; sand, 0.075–4.76 mm; silt, 0.005–0.075 mm; clay, <0.005 mm. A.S.T.M. (American Society for Testing and Materials) classification]

Sample No.	Particle-size classification				Median diameter (mm)	Gradation	
	>sand (percent)	sand (percent)	silt (percent)	clay (percent)		Uniformity coefficient	Sorting coefficient
Avalanche deposits							
6-3A-2	46(31)	35(49)	14(15)	5(5)	1.0	150	7.4
6-3A-3	59(47)	31(42)	8(9)	2(2)	3.6	110	11.0
6-3A-4	55(42)	34(47)	7(7)	4(4)	2.7	110	6.2
6-3B-2	42(33)	39(47)	13(13)	6(7)	.87	160	9.5
6-3C-1	40(31)	40(48)	13(14)	7(7)	.70	170	9.2
6-3C-3	27(19)	45(51)	21(22)	7(8)	.27	74	6.7
6-3C-4	40(26)	45(57)	11(13)	4(4)	.80	67	6.2
6-3D-1	20(12)	69(75)	8(10)	3(3)	.45	13	2.9
6-3D-2	56(50)	35(40)	8(8)	1(2)	4.6	300	13.0
6-3H-1	36(21)	50(63)	13(14)	1(2)	.83	33	4.8
6-3H-2	22(13)	59(66)	16(18)	3(3)	.40	22	3.9
6-4A-1	57(46)	36(47)	5(5)	2(2)	3.3	77	8.6
6-4B-1	60(50)	32(41)	6(7)	2(2)	4.7	110	6.4
6-4C-1	46(34)	42(53)	8(9)	4(4)	1.2	75	6.4
6-4D-1	39(33)	40(45)	15(15	6(7)	.63	180	12.0
6-4D-2	43(28)	40(54)	13(14)	4(4)	.90	122	6.3
6-4E-1	47(33)	43(56)	9(10)	1(1)	1.6	47	5.0
6-4F-1	42(34)	45(51)	11(13)	2(2)	.88	48	7.7
6-4G-1	39(29)	41(49)	17(18)	3(4)	.72	100	8.2
Mudflow							
6-3A-1	14(11)	60(61)	20(21)	6(7)	0.26	46	4.0
6-3C-2	78(63)	15(30)	5(4)	2(3)	9.2	107	4.1
Blast deposit							
6-3F-1A	10(5)	49(51)	31(33)	10(11)	0.10	41	3.9
6-3F-1B	2(1)	60(57)	32(35)	6(7)	.10	16	2.4
6-3F-1C	0(0)	27(23)	59(61)	14(16)	.026	13	2.9
6-3G-1A 6-3G-1B	2(0)	54(53)	35(38)	9(9)	.081	21	3.0
6-4E-2	1(0)	34(31)	54(56)	11(13)	.040	16	2.8
Ash flow							
6-3E-1	0(0)	41(37)	51(53)	8(10)	0.045	13	3.0

Textures similar to the avalanche deposit were reported by Mullineaux and Crandell (1962, p. 859–864) for Holocene lahars in the Toutle River valley. Sorting coefficients for lahars near Silver Lake, about 50 km downvalley from Mount St. Helens, range from 4.9 to 10.2. A deposit near Spirit Lake Lodge, interpreted as a lahar, has a sorting coefficient of 9.2 and a median diameter of 2.0 mm (fig. 217). This deposit contains breadcrust bombs, which were hot when emplaced, and both charred and uncharred wood fragments; the matrix was at first very hot, but was not sufficiently hot to char wood by the time of deposition in the North Fork Toutle River valley. The evidence does not exclude emplacement of the deposit near Spirit Lake Lodge as

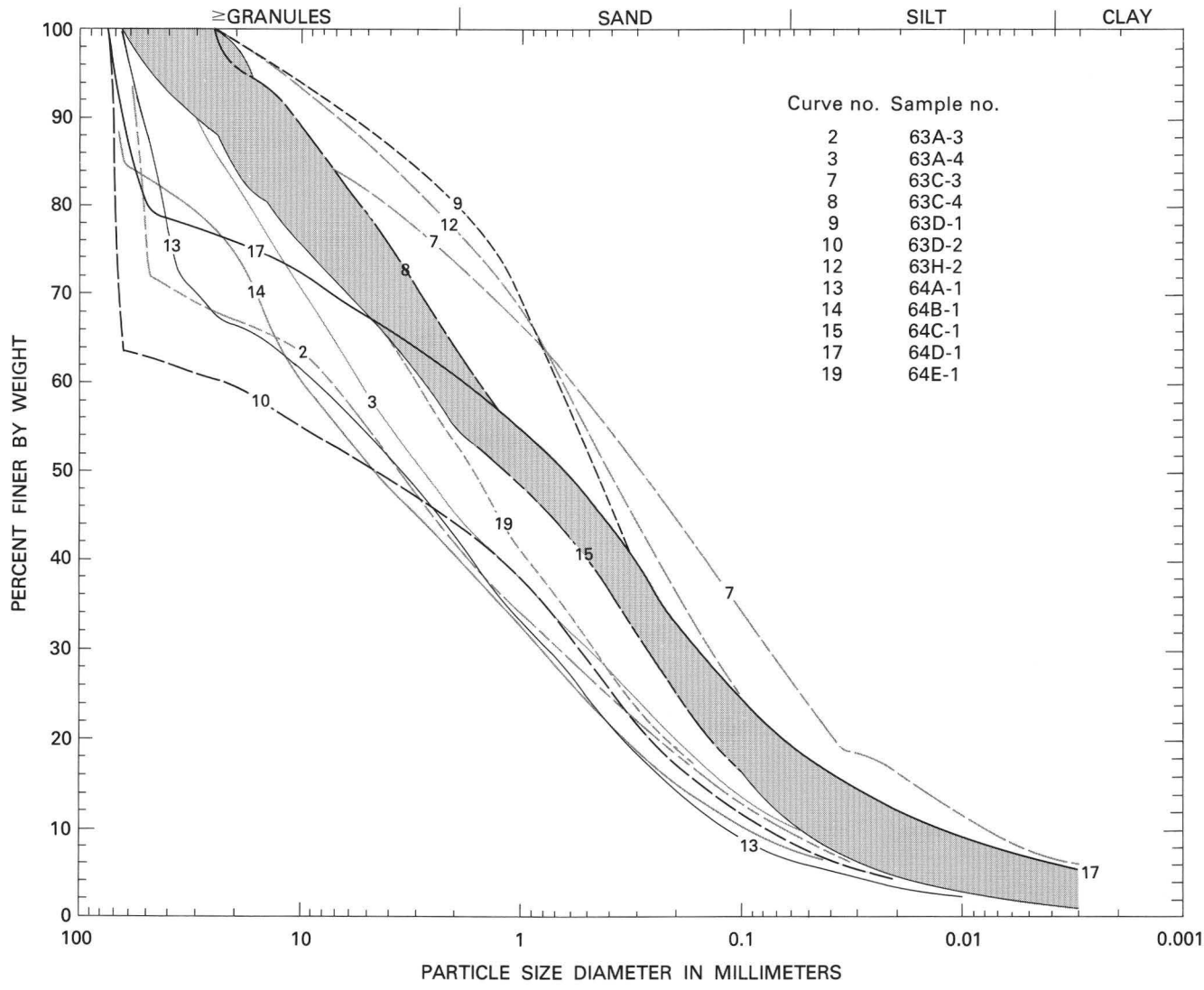

Figure 216. Cumulative curves of particle-size distribution data of the May 18 avalanche and associated deposit at Mount St. Helens. Curves for eight localities shown contained within shaded area. Localities shown on figure 215.

a hot avalanche rather than as a lahar mobilized by water.

Lahars from Mount Rainier discussed in Crandell's (1971) comprehensive summary exhibit a range of sorting coefficients from 3.4 to 17. It is not feasible to achieve true representative sampling of such deposits, and probably all the calculated sorting coefficients are minimum values. The Paradise lahar, which originated as a moist debris avalanche and which later was transformed into a lahar, has sorting coefficients of 8–14 and median diameters of 0.2–13 mm near the region of supposed transition; farther downvalley, where interpreted movement was that of a lahar and where better sorting might be expected, the sorting coefficient is about 16 and the median diameter is 1.4–4 mm (Crandell, 1963; 1971). Finally, we compare data from two samples of 1963 avalanche deposits from Little Tahoma Peak (fig. 217; see Crandell and Fahnestock, 1965; Fahnestock, 1978; Crandell, 1971). Sorting coefficients are 6–7; both values are minimums because of abundant large clasts excluded from the sample.

SPECIFIC GRAVITY AND DENSITY

Specific gravity of solids (grain density, table 38) of the fine-grained fraction ranges from 2.62 to 2.78 and averages about 2.70. Larger clasts commonly have lower specific gravity, in inverse relation to their porosity.

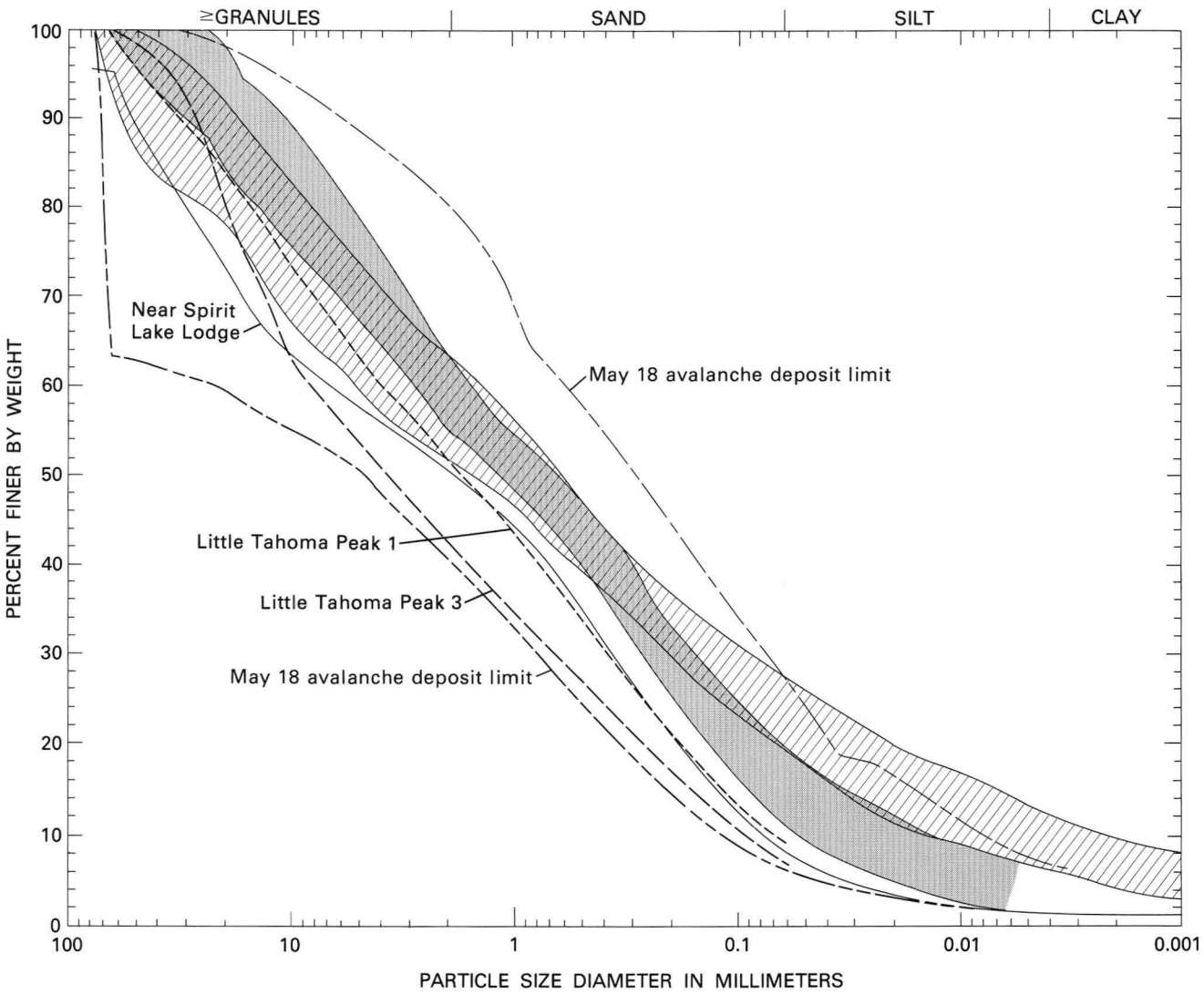

Figure 217. Cumulative curves of particle-size distribution comparing the May 18 avalanche deposit at Mount St. Helens with older deposits at Mount St. Helens and Mount Rainier. Data for May 18 avalanche indicated by limit lines and shaded patterns (see fig. 216). Other data include a recent lahar deposit near the old Spirit Lake Lodge (Mullineaux and Crandell, 1962), and Osceola Mudflow (cross hatched) and Little Tahoma Peak avalanche deposits from Mount Rainier (Crandell, 1971, figs. 4 and 11).

Dry-bulk densities were variously determined by nuclear densitometer (Campbell MC-1) and conventional sand cone, along with laboratory determination of moisture content. Dry-bulk densities range widely, from 1.54 to 2.01 g/cm³. This range reflects to some extent late-depositional or postdepositional disturbances sustained by portions of the deposit. "Disturbed" material in hummock crests, fault- or slump-influenced boundary zones, and sheared or slumped levee walls have an average dry-bulk density near 1.68 g/cm³. For relatively "undisturbed" zones, both methods indicate an average dry-bulk density of about 1.80 g/cm³. Dry-bulk density of two altered blocks of ancestral breccia measured in the field by sand cone is 1.94–2.01 (samples S-11A-1, S-11B-1 in table 38).

POROSITY AND WATER CONTENT

Water content (w), given by weight of water divided by weight of dry solids and expressed as a percent, ranges from 5.0 to 14.0 percent; the average value is 8.7 percent. Total (moist) bulk density may be calculated from table 38 by the product of $(1+w)$ and dry bulk density. For "undisturbed" material, an

Table 38.—In-place geotechnical properties

[Avalanche deposit: NF, North Fork; NFl, North Fork levee; SL, Spirit Lake; CR, Coldwater Ridge; M, marginal; ---, no data. Data in parentheses in dry bulk density column measured by sand cone method]

Sample No.	Geologic unit	Disturbance	Density: Dry bulk (g/cm^3)	Density: Grain (g/cm^3)	Water content (percent)	Void ratio	Porosity	Saturation (percent)
			Avalanche deposit					
6-3A-2----	NF	(1)	1.83	2.68	12.1	0.45	0.31	71
6-3A-3----	NF	(1)	1.63	2.69	9.7	.63	.38	41
6-3A-4----	NF	(1)	1.66	2.71	6.3	.60	.37	28
6-3B-1----	NF	(1)	1.76	---	11.4	.51	.34	59
6-3B-2----	NF	---	1.84	2.70	10.4	.44	.31	63
6-3B-2----	NF	---	(1.83)	---	10.4	.45	.31	61
6-3C-1----	NF	---	1.92	2.73	8.2	.38	.28	57
6-3C-3----	NF1	(1)	1.69	2.71	10.1	.57	.36	47
6-3C-4----	NF1	(1)	1.59	2.73	9.7	.67	.40	38
6-3D-1----	SL	---	1.69	2.72	7.9	.57	.36	37
6-3D-2----	SL	(1)	1.58	2.78	5.4	.68	.40	21
6-3H-1----	NF	(1)	1.54	2.76	8.3	.72	.42	31
6-3H-2----	NF	(1)	1.67	2.62	14.0	.59	.37	63
6-4A-1----	CR	---	1.76	2.67	5.8	.51	.34	30
6-4B-1----	CR	---	1.70	2.67	8.7	.56	.36	41
6-4C-1----	CR	---	1.66	2.76	5.0	.60	.37	22
6-4C-3----	CR	---	1.84	---	6.0	.44	.31	36
6-4D-1----	NF	---	1.88	2.68	5.9	.41	.29	38
6-4D-2----	NF	---	1.79	2.71	11.7	.48	.32	65
6-4E-1----	M	(1)	1.94	2.73	5.4	.37	.27	39
6-4F-1----	NF	(1)	1.56	2.63	9.6	.70	.41	36
6-4G-1----	CR	(1)	1.75	2.71	9.5	.51	.34	49
S-1A-1(2)---	NF	---	(1.83)	---	---	.45	.31	---
S-4A-1(2)---	NF	---	(1.79)	---	6.0	.48	.32	33
S-5A-1(2)---	NF	---	(1.72)	---	---	.54	.35	---
S-7A-1(2)---	NF	---	(1.85)	---	7.9	.43	.30	39
S-9A-1(2)---	NF	---	(1.91)	---	---	.43	.28	---
S-11A-1(2)--	(3)	---	(1.94)	---	---	.37	.27	---
S-11-B-1(2)-	---(3)	---	(2.01)	---	---	.32	.24	---
S-13A-1(2)--	NF	---	(1.73)	---	---	.53	.35	---
M-1-1-----	M	---	(1.88)	---	---	.41	.29	---
M-1B-1----	M	---	(1.75)	---	---	.51	.34	---
M-2-1-----	M	---	(1.80)	---	---	.47	.32	---

[1]In-place material disturbed by faulting or slumping.
[2]Density data for samples provided by R. L. Schuster and T. L. Youd.
[3]Discrete blocks of ancestral breccia included in avalanche deposit.

average value of total bulk density is thus about 1.96 g/cm^3. Porosity was calculated from dry-bulk density and grain density (table 38); grain density was arbitrarily taken as 2.65 g/cm^3 for this purpose. Porosities range from 0.27 to 0.42; corresponding void ratios are 0.37–0.72. An average porosity value for "undisturbed" material is about 0.32, and the void ratio is 0.47. Saturation for samples collected June 3 and 4 ranges from 21 to 71 percent, and the average is 44 percent.

PERMEABILITY

Constant-head permeability measurements were conducted on laboratory samples on which void ratios had been measured (table 39). Samples were screened through a No. 4 (4.75 mm) sieve and poured in a loose state into the permeameter; some samples were mechanically agitated and others were jostled by flowing water. Permeability rates (table 39) range from 1.8×10^{-4} to 2.9×10^{-2} cm/s, and the associated range of void ratio is 0.65–0.80. Average permeability rate for mechanically agitated samples is 8.6×10^{-3} cm/s, and average void ratio is 0.73; for water-jostled samples, corresponding values are 7.3×10^{-3} cm/s and 0.72. These permeability values provide probable upper bounds for the in-place avalanche because of differences in void ratio between laboratory and in-place material.

STRENGTH

Direct shear tests were conducted in the laboratory on representative split-screened portions of a number of moist field samples. Various test procedures were used. For the data reported here (fig. 218), samples were screened through a No. 4 (4.75 mm) sieve and poured loose into the direct shear frame of 6.4 cm diameter. Normal load was applied, the specimen was consolidated, and shearing accomplished at a displacement rate of 0.048 mm/min. The specimen was then cycled to additional displacements, sheared again to provide a measure of residual resistance, or consolidated under additional normal load and then sheared. These test procedures were repeated as

Table 39.—Laboratory permeability measurements on samples from avalanche and associated deposits

[Avalanche deposit: NF, North Fork; SL, Spirit Lake; CR, Coldwater Ridge; M, marginal; Mf, mudflow. Void ratios correspond approximately to condition of samples during permeability tests]

Sample No.	Geologic unit	Run 1[1]: Rate of permeability (cm/s)	Run 1[1]: Void ratio	Run 2[2]: Rate of permeability (cm/s)	Run 2[2]: Void ratio
6-3A-4---	NF	4.5×10^{-3}	0.72	1.5×10^{-2}	0.74
6-3B-2---	NF	1.4×10^{-3}	.73	6.64×10^{-3}	.71
6-3C-1---	NF	7.2×10^{-3}	.84	4.6×10^{-4}	.64
6-3D-1---	SL	2.9×10^{-2}	.80	8.6×10^{-3}	.79
6-4A-1---	CR	2.7×10^{-2}	.70	8.8×10^{-3}	.76
6-4B-1---	CR	6.4×10^{-4}	.58	1.1×10^{-2}	.72
6-4C-1---	CR	5.2×10^{-3}	.79	8.8×10^{-3}	.96
6-4D-1---	NF	2.6×10^{-3}	.77	2.4×10^{-4}	.54
6-4E-1---	M	1.8×10^{-4}	.65	7.3×10^{-3}	.66
6-3A-1---	Nf	3.4×10^{-3}	.75	3.1×10^{-4}	.65
6-3C-2---	Mf	8.3×10^{-3}	.74	2.9×10^{-4}	.66
6-3F-1A--	Blast	1.4×10^{-3}	.84	7.8×10^{-5}	.72
6-3F-1B--	Blast	8.4×10^{-4}	.74	2.8×10^{-4}	.81
6-3G-1---	Blast	6.4×10^{-4}	.71	5.3×10^{-5}	.65
6-3E-1---	Ashflow	1.0×10^{-4}	1.19	1.2×10^{-4}	1.19

[1]Sample mechanically compacted by dropping weights and lateral agitation for 30 min.
[2]Different sample of same identification number poured loose into permeameter. Water flowing into permeameter caused sample to settle.

desired until a suitable, normal load range was evaluated. Normal pressures were thus varied within the range 3.5 to 28 bars. Postconsolidation void ratios for the data of figure 218 vary within the range 0.80 to 1.31, and the lower ratio values correspond to higher normal pressures. These void ratios are not directly comparable to reported field values (table 38), because only the < 4.75-mm fraction is used in laboratory tests.

Most curves of shear load versus horizontal displacement (fig. 218) show little development of peak strength. The curves display characteristics of loose specimens of particulate material. Shearing produced some volume change, and the final volume typically is slightly greater than the preshear value. Changes in void ratio for individual samples vary from 0.10 to 0.32; most of these changes are due to increase of normal pressure. Only one specimen (at the maximum 28-bar normal pressure) displays a pronounced peak in shear load versus displacement, an indication of relatively dense material.

Linear Coulomb plots drawn through the origin indicate friction angles of about 40°–43°. Equivalent friction coefficients (tangents of friction angle) are 0.84–0.93. Some decreases in resistance, however, are noted for pronounced displacements, implying for the ultimate condition a decrease in friction angle of a few degrees.

These preliminary laboratory results indicate to a reasonable approximation the frictional strength of avalanche debris in its present condition. These values also provide lower bound strength estimates for fragmental deposits in the north slope of Mount St. Helens in its pre-May 18 deteriorated condition.

ANALOGS

Hummocky volcaniclastic deposits similar to the Mount St. Helens debris avalanche deposit are recognized around other volcanoes of the Pacific rim. Three of these deposits were emplaced during historic time in eruptions remarkably similar to the May 18 event at Mount St. Helens.

The July 15, 1888, eruption of Bandai-san volcano in Japan began after a week of earthquakes that were felt by residents. Lateral explosions occurred at 0745, and within minutes a relatively dry debris avalanche of 1.2 km³ had inundated an area of 70 km² (Sekiya and Kikuchi, 1889, p. 106, 148). The summit and northern flank of the mountain were replaced by a horseshoe-shaped amphitheater, and thousands of conical, domical, and pyramidal mounds as much as tens of meters across stood out from the avalanche surface. The debris was nonjuvenile and consisted of

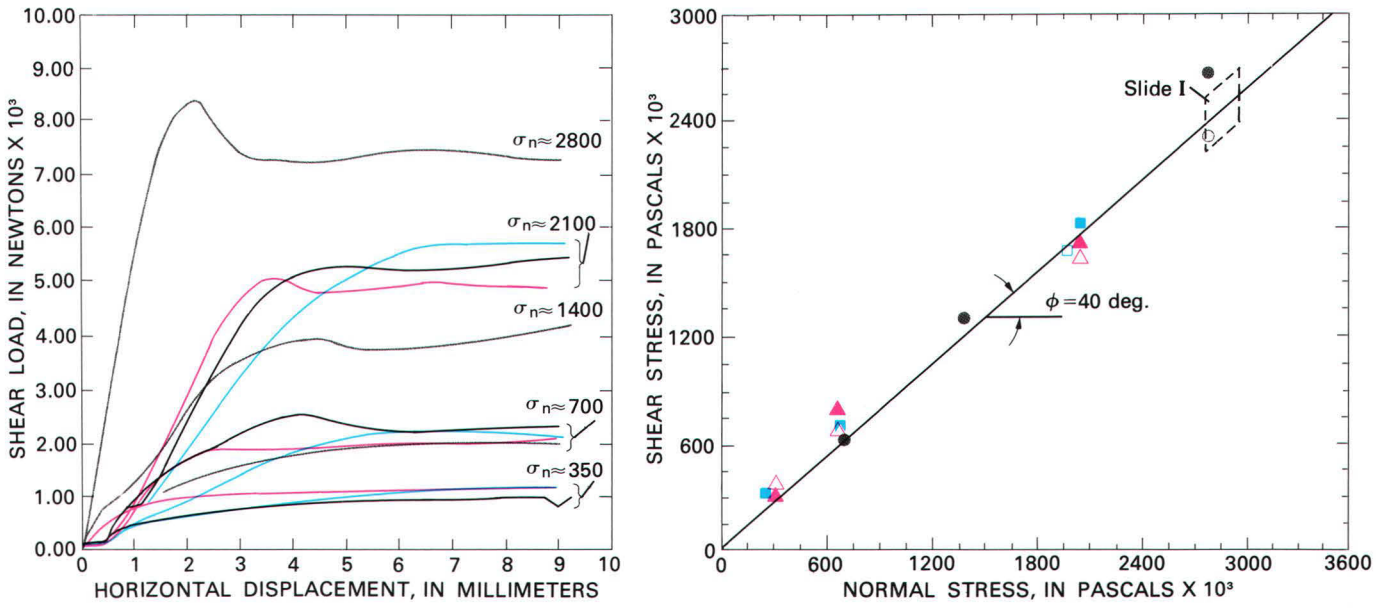

Figure 218.—Direct shear test results on samples from May 18 deposit at Mount St. Helens. Solid symbols indicate first run and open symbols indicate recycled run for following samples: triangle, 63C3; square, 63A4; and circles, 63C1.

angular blocks as much as 10 m in diameter in a matrix of finer debris. Photographs and descriptions (Sekiya and Kikuchi, 1889; Nakamura, 1978) suggest profound similarity to the Mount St. Helens debris avalanche.

A comparable deposit resulted from the paroxysmal eruption of Bezymianny volcano in Kamchatka, which followed 6 mo during which earthquakes were felt and eruptions and visible deformation of the mountain occurred. On March 30, 1956, a "rather strong" earthquake apparently triggered a gas-impregnated "agglomerate flow" and lateral blast that felled large trees to a distance of 25 km (Gorshkov, 1959). Nonjuvenile material from a new 1.5×2.0-km horseshoe-shaped amphitheater was the source of much of the "chaotic mixture" in the 1.8-km^3 agglomerate flow, but a substantial quantity of juvenile material was included in the deposit. Photographs by Gorshkov (1959, pls. 26, 32) show that the flow had an irregular surface and thousands of secondary fumaroles and associated phreatic pits.

The Sheveluch eruption in Kamchatka on November 12, 1964, occurred after 11 mo of preliminary earthquakes (Gorshkov and Dubik, 1969, 1970). A large earthquake occurred "in close connection" with lateral blasts and mass movements that resulted in excavation of a 1.5×3.0-km horseshoe-shaped amphitheater (Gorshkov and Dubik, 1970, p. 266). Photographs and descriptions indicate that much of the "deposits of the directed blast" were akin to the Mount St. Helens 1980 debris avalanche. The Sheveluch deposits occurred in a digital lobe that exceeded 1.5 km^3 in volume and blanketed an area of 98 km^2 to a distance of 10 km from the crater. The deposit was composed almost entirely of nonjuvenile material, including glacial ice, large blocks of breccia with recognizable volcanic structures preserved, and semilithified blocks of pumice (tephra?) deposits. The surface of the debris was covered with "thousands of large and small hills" (Piip and Markhinin, 1965, fig. 3; Gorshkov and Dubik, 1969, figs. 10–13; 1970, p. 276).

The lower Holocene deposit, Greenwater lahar, an informal unit (Crandell, 1971, p. 18–23), that extends at least 45 km downvalley from Mount Rainier has a surface covered by "scores" of mounds consisting primarily of fresh and altered blocks of andesitic breccia. Although there is no clearly defined scar on the volcano, Crandell (1971) ascribed the origin of the deposit to rockfalls and rockslides from a portion of the northeast side of Mount Rainier that was, as a consequence, "largely destroyed." A temporal correlation exists between lithic tephra layer "*S*" and the Greenwater lahar; Crandell (1971, p. 22) stated that "the explosion that created the pyroclastic deposit could have also triggered the rockslides that caused the lahar." A likely counterpart at Mount Rainier is the Paradise lahar, also an informal unit, which contains hummocky ground in some places and is thought to have originated in an avalanche on the south side of the volcano (Crandell, 1963, 1971, p. 33–26).

Prehistoric hummocky volcaniclastic deposits that lack well-defined source regions are found around other stratovolcanoes. In the South Pacific, such deposits have been recognized adjacent to Galounggoung and Raung volcanoes, Indonesia (Escher, 1925, Neumann van Padang, 1939) and at the foot of Ruapehu and Egmont volcanoes in New Zealand (Grange, 1931). In Japan, similar prehistoric deposits are next to Asama volcano (Aramaki, 1963, p. 290–292), Bandai-san volcano (Nakamura, 1978), Chokai and Gassan volcanoes (Tadahide Ui, Kobe University, Japan, oral commun., July 1980), Shikaribetsu volcano (Ando and Yamagishi, 1975), Usu volcano (Oba, 1966), Yatsuga-dake volcano (Mason and Foster, 1956), and Komaga-take volcano (Ishikawa and Yokoyama, 1962).

The many hummocky deposits interpreted to be analogous to the debris avalanche at Mount St. Helens are suggestive of materials that were incompletely saturated by liquid water during emplacement. Deposit morphology indicates enormous mobility, but the surficial portions were apparently capable of deforming by faulting rather than by uniform flow. The hummocky topography may in many cases imply unroofing and incorporation within avalanches of hydrothermal systems that existed within fragmental volcanoes. Much of the volcano material could have been initially saturated, but at a temperature higher than the boiling point of water at the existing atmospheric conditions. Pressure release by detachment and thinning of an avalanche created widespread boiling of liquid pore water. The development of the avalanche created asymmetry in explosions from the hydrothermal or magmatic-hydrothermal system, which in turn formed a directed blast.

REFERENCES CITED

Ando, S., and Yamagishi, H., 1975, Hill topography on the Nuée Ardente deposits of Shikaribetsu volcano, Hokkaido: Volcanological Society of Japan Bulletin, 2d ser., v. 20, p. 31–36.

Aramaki, S., 1963, Geology of Asama volcano: Tokyo University Faculty of Science Journal, v. 14, pt. 2, p. 229–443.

Bemmelen, R. W. van, 1949, General geology of Indonesia and adjacent archipelagoes, *in* The geology of Indonesia: The Hague, Government Printing Office, 732 p.

Bull, W. B., 1964, Alluvial fans and near-surface subsidence in western Fresno County, California: U.S. Geological Survey Professional Paper 437–A, 71 p.

Crandell, D. R., 1963, Paradise debris flow at Mount Rainier, Washington, *in* Short papers in geology and hydrology: U.S. Geological Survey Professional Paper 475–B, p. B135–B139.

_____1971, Postglacial lahars from Mount Rainier volcano, Washington: U.S. Geological Survey Professional Paper 677, 75 p.

Crandell, D. R., and Fahnestock, R. K., 1965, Rockfalls and avalanches from Little Tahoma Peak on Mount Rainier, Washington: U.S. Geological Survey Bulletin 1221–A, 30 p.

Crosson, R. S., Endo, E. T., Malone, S. D., Noson, L. J., Weaver, C. ., 1980, Eruption of Mount St. Helens—Seismology: Nature, v. 285, no. 5766, p. 529–531, July 19.

Escher, B. G., 1925, L'Eboulement prehistorique de Tasikmalaja et le volcan Galounggoung: Leidsche Geologische Mededeelingen, Deel 1, Aflevering 1, v. 1, p. 8–21.

Fahnestock, R. K., 1978, Little Tahoma Peak rockfalls and avalanches, Mount Rainier, Washington, *in* Voight, B., ed., Rockslides and avalanches, 1, Natural phenomena: Amsterdam, Elsevier, p. 181–196.

Gorshkov, G. S., 1959, Gigantic eruption of the volcano Bezymianny: Bulletin Volcanologique, ser. 2, v. 20, p. 77–109.

Gorshkov, G. S., and Dubik, Y. M., 1969, Directed explosion in Sheveluch volcano: Vulkany Isverzheniya, Moscow, Nauka Press, p. 3–38.

_____1970, Gigantic directed blast at Sheveluch volcano (Kamchatka): Bulletin Volcanologique, v. 34, p. 261–268.

Grange, L. I., 1931, Conical mounds on Egmont and Ruapehu volcanoes: New Zealand Bulletin of Science and Technology, v. 12, p. 376–384.

Hadley, J. B., 1978, Madison Canyon rockslide, Montana, *in* Voight, B., ed., Rockslides and avalanches, 1, Natural phenomena: Amsterdam, Elsevier, p. 167–180.

Ishikawa, I., and Yokoyama, I., 1962, Komaga-take volcano, *in* Guidebook for excursions: International Symposium on Volcanology, p. 35–42.

Johnson, A. M., 1970, Physical processes in geology: San Francisco, Freeman, Cooper and Co., 577 p.

Leighton, F. B., 1966, Landslides and hillside development, *in* Engineering geology in southern California: Association of Engineering Geologists Special Publication, p. 149–207.

Mason, A. C., and Foster, H. L., 1956, Extruded mudflow hills of Nirasaki, Japan: Journal of Geology, v. 64, p. 74–83.

Mudge, M. R., 1965, Rockfall-avalanche and rockslide-avalanche deposits at Sawtooth Ridge, Montana: Geological Society of America Bulletin, v. 76, no. 9, p. 1003–1014.

Mullineaux, D. R., and Crandell, D. R., 1962, Recent lahars from Mount St. Helens, Washington: Geological Society of America Bulletin, v. 73, no. 7, p. 855–869.

Nakamura, Y., 1978, Geology and petrology of Bandai and Nekoma volcanoes: Tohoku University Science Reports, ser. 3, v. 14, no. 1, p. 67–119.

Neall, V. E., 1976, Lahars—global occurrence and annotated bibliography: Wellington, New Zealand, Victoria University, Geology Department, Pub. 5, 18 p.

Neumann van Padang, 1939, Uber die vielen tausend Hugel im westlichen Vorlande des Raoeng-Vulkans (Ost Java): De Ingenieur in Nederl.-Indie Jg. 6, no. 4, sect. 4, p. 35–41.

Oba, Y., 1966, Geology and petrology of Usu Volcano: Hokkaido University Faculty of Science Journal, ser. 4, v. 13, no. 2, p. 185–236.

Piip, B. I., and Markhinin, E. K., 1965, Gigantic eruption of Sheveluch volcano on 12 November 1964: Byull. Vulk. Sta., v. 39, p. 28–34.

Plafker, G., and Ericksen, G. E., 1978, Nevados Huascaran avalanches, Peru, *in* Voight, B., ed., Rockslides and avalanches—1, Natural phenomena: Amsterdam, Elsevier, p. 277–314.

Sekiya, S., and Kikuchi, Y., 1889, The eruption of Bandai-san: Imperial University of Japan, College of Science Journal, v. 3, pt. 2, p. 91–172.

Slingerland, R. L., and Voight, B., 1979, Occurrences, properties, and predictive models of landslide-generated water waves, *in* Voight, B., ed., Rockslides and avalanches, 2, Engineering sites: Amsterdam, Elsevier, p. 317–397.

Stoffel, D. B., and Stoffel, K. L., 1980, Mt. St. Helens seen close up on May 18: Geotimes, v. 25, p. 16–17.

Terzaghi, K., and Peck, R. B., 1967, Soil mechanics in engineering practice [2d ed.]: New York, John Wiley, 566 p. [1st ed., 1948].

Varnes, D. J., 1978, Slope movement types and processes, *in* Shuster, R. L., and Krizek, R. J., eds., Landslides, analysis, and control: National Research Council, Transportation Research Board Special Report 176, p. 11–33.

Verhoogen, Jean, 1937, Mount St. Helens, a recent Cascade volcano: University of California, Department of Geological Sciences Bulletin, v. 24, no. 9, p. 263–309.

Voight, B., ed., 1978, Rockslides and avalanches—1, Natural phenomena: Amsterdam, Elsevier, 833 p.

Voight, B., and Kennedy, B., 1979, Slope failure of 1967–1969, Chuquicamata mine, Chile, *in* Voight, B., ed., Rockslides and avalanches—2, Engineering sites: Amsterdam, Elsevier, p. 595–632.

DIRECTED-BLAST DEPOSITS

The directed volcanic blast that devastated an area of nearly 600 km² northwest, north, and northeast of Mount St. Helens within a few minutes on May 18 is probably the most remarkable aspect of the 1980 eruptions. Similar catastrophic laterally directed explosions have occurred at a few other volcanoes in historic time, notably Bandai-san in Japan in 1888, and Bezymianny and Shiveluch in Kamchatka in 1956 and 1964, but the eruptive mechanism that causes a volcano to vent laterally rather than vertically has not previously been as well observed.

The May 18 directed blast was generated by massive explosions that occurred when an enormous landslide on the north flank released the confining pressure on a shallow dacite cryptodome and its associated hydrothermal system. Propelled by expanding gases and gravity, the mixture of gas, rock, and ice moved off the volcano as a catastrophic, hot, ground-hugging, turbulent pyroclastic cloud at velocities of as much as 300 m/s. Within a few minutes, the directed blast had extended about 25 km and carried off or knocked down all trees in its path. Photographs show that the explosion cloud remained low, extending to only a few kilometers above ground level; then, as forward motion diminished, convecting ash clouds began to billow up. Analysis of the fluid dynamics of the blast, as representing supersonic expansion of a multiphase mixture (vapor-solid-liquid) from a high-pressure reservoir, accounts for many features of the blast deposits and associated devastation (Kieffer). The total energy released over the first few minutes is calculated as about 24 megatons.

The deposit emplaced directly by the high-velocity blast cloud varies in thickness from about a meter near the volcano to only about a centimeter near margins of the affected area. A distinctive general feature is the relatively limited maximum thickness of the deposit even in areas of rugged topography, except for local blast-related pyroclastic flows that moved downslope and ponded in valleys. About half the blast deposit consists of fresh, originally hot, gray dacite derived from the exploded cryptodome; the remainder is chiefly mixed lithic fragments from the former north flank of the volcano and entrained soil and organic material. The blast deposit shows crude normal grading in most places, but textural discontinuites and local stratification generally permit recognition of at least four subunits: (1) basal coarse deposit, (2) finer grained middle unit characterized by textural features similar to pyroclastic-surge deposits, (3) secondary blast-related pyroclastic flows, and (4) an upper blast-related airfall unit containing abundant accretionary lapilli.

Nomenclature applied to the blast and associated deposits has been controversial. Depositional mechanisms active during the blast produced complex deposits, some of which are similar to previously described pyroclastic-flow, pyroclastic-surge, and pyroclastic-fall materials. In the following reports, some authors have emphasized the distinctiveness of the laterally directed eruption and associated deposits, referring to the event as a volcanic blast (Kieffer) that produced blast deposits (Hoblitt and others); others have interpreted the character of the event as dominantly a pyroclastic surge (Moore and Sisson) or a pyroclastic density flow (Waitt). For the present volume as a whole, the terms *directed blast* and *directed-blast deposit* have been used to refer to the initial laterally directed eruptive event and its deposits. Terminology also differs for subunits of the directed-blast deposits, for which generalized correlations are indicated as follows:

Hoblitt and others	*Moore and Sisson*	*Waitt*
Directed blast	Pyroclastic surge	Pyroclastic density flow
Accretionary-lapilli unit	Air-fall unit	Sandy silt facies (A3)
Blast pyroclastic-flow unit	Secondary pyroclastic-flows	Not discussed
Pyroclastic-surge unit	Fine upper unit	Fine sand facies (A2b)
Massive unit	Fine upper unit	Coarse sand facies (A2a)
Basal unit	Coarse basal unit	Basal gravel facies (A1)

THE 1980 ERUPTIONS OF MOUNT ST. HELENS, WASHINGTON

FLUID DYNAMICS OF THE MAY 18 BLAST AT MOUNT ST. HELENS

By SUSAN WERNER KIEFFER

ABSTRACT

The lateral blast that was the first phase of the May 18 eruption of Mount St. Helens devastated an area of about 500 km² north of the volcano. Preliminary mapping of the direction of fall of the trees in the devastated area shows that two major, irregularly shaped zones can be defined: (1) an inner zone, termed the "direct blast zone," in which the flow of the blast was approximately radial from the volcano and was relatively undeflected, in plan view, even by large topographic features, and (2) an outer zone, termed the "channelized blast zone," in which the flow followed or was deflected, in plan view, by the local topographic features. Streamlines of the flow were thus not simple radii from the source. The blast was a supersonic expansion of a multiphase (vapor-solid-liquid) mixture from a reservoir at a pressure much greater than that of the atmosphere into which it expanded. The model for the flow presented here explains the existence of the two blast zones, characteristics of the transition between the devastated area and surrounding undamaged forest, and many of the eyewitness and instrumental observations of the blast. The model can easily be scaled with pressure, temperature, and dimensional ratios, but plausible initial conditions used here for illustration are: a reservoir pressure of 12.5 MPa (megapascals) (125 bars), a temperature of 600K (327°C), and a solid-to-vapor mass ratio of 25.

The eruption is assumed to have been triggered by the landslide failure of the north slope, with the resulting formation of a nearly vertical face (the vent) through which the blast emanated. The discharge developed as rarefaction (expansion) waves propagated into the reservoir and as the gases in the hydrothermal and (or) magmatic system inside of the mountain expanded. Unsteady flow developed into steady flow, having an initial (choked) velocity equal to the speed of sound of the moving reservoir fluid, about 100 m/s (meters per second).

As the material discharged from the vent at sonic velocity, it expanded supersonically in all directions. Because of the high pressure of the reservoir fluid relative to that of the surrounding atmosphere, the flow expanded more than 90° laterally (96°), both east and west of the approximate northerly direction of the normal to the plane of the vent. Rarefaction waves emanating from the corners of the vent reflected from the boundary between the flow and the atmosphere, and became compression waves that coalesced into weak peripheral shocks subparallel to the flow boundary. These weak shocks joined to form a strong Mach disk shock about 11 km from the vent. The reflection of the rarefaction waves into compression waves resulted in a northerly deflection of the margins of the flow away from the initial east and west directions. This deflection saved the lives of some observers initially in line with the flow, for example, those in the South Fork Toutle River and parts of the North Fork Toutle River drainages.

As the flow diverged from the vent, the velocity increased and the pressure decreased rapidly; within about 6 km of the vent, the flow was overpressured relative to the atmosphere, but beyond this zone, the flow became strongly underpressured. A Mach disk shock formed at about 11 km in response to the zone of underpressure within the flow, and the flow velocities dropped from supersonic on the upstream side of the shock to subsonic on the downstream side. The boundaries between the direct and channelized blast zones probably correspond to the positions of the peripheral and Mach disk shocks. The solid particles entrained in the blast were a heat source for the expanding vapor, so that temperatures dropped only by about 20 percent from the vent to

the limits of the blast zone. At the limits of the blast zone, the density of the flow had dropped below the density of the (dusty) atmosphere, so the blast cloud simply lifted from the ground and ramped upward into the atmosphere, leaving only a thin transition zone between the devastated area and the surrounding undamaged forests.

Although the flow, on the average, traveled at a velocity less than the speed of sound in air, so that strong atmospheric shocks were not generated near the volcano, the white clouds photographed on the periphery of the blast may have been condensation clouds formed in zones of negative pressure that followed passage of weak local atmospheric shocks. Sounds generated within the blast by the destruction of the forest, and mixing and transport of boulders, trees, and glacial ice blocks, were not heard by eyewitnesses for two reasons: first, sounds were focused downstream into cones of narrow solid angle (about 20°–30°) by the supersonic flow, and eyewitnesses outside of these cones would not have heard sounds; second, sound was attenuated more than 10,000 times as rapidly as in clear air by absorption of energy by the particles in the blast.

About half of the mass of the blast was discharged through the vent in 10 to 20 s (seconds) at the initial velocity of 100 m/s; the remainder followed at decreasing velocities. Because of this range of initial velocities, as well as spreading of the blast cloud due to basal friction, the duration of the blast increased with distance from the vent. The maximum mass flux, during temporary steady flow at the vent, would have been 0.6×10^4 g/s/cm^2 (grams per second per square centimeter), and the thermal flux would have been 2.5 MW/cm^2 (megawatts per square centimeter). The total thermal energy released was 24 Mt (megatons), of which 7 Mt was released during propagation of the blast through the devastated area, and 17 Mt during penecontemporaneous condensation of the steam and cooling of the condensed water and entrained solids.

INTRODUCTION

The first phase of the May 18 eruption was the lateral blast that devastated the conifer forests in a sector covering 500 km^2 north of the volcano. The onset of the blast at 0832 PDT was widely recorded on barometers and seismometers, and gave instrumental amplitude variations comparable to those caused by detonation of nuclear devices in the 1–10 Mt range (Reed, 1980).

Usage of the word "blast" can be traced back nearly 1,000 yr (Oxford English dictionary, 1971). For centuries its meaning was "a blowing or strong gust of wind," for example, as used by Chaucer in 1338, "Reed that boweth down with every blast." The usage implied an event of considerable force and duration, for example, Dana in 1840, "Broken by the blast of a hurricane." In the mid-1700's the word "blast" came into usage to mean "a blowing up by gunpowder or other explosive," and with the advent of the atomic era, the word came to denote an event that was almost instantaneous. In this report, I show that, in its original context, the word "blast" is an appropriate description of the events of the morning of May 18.

OBSERVATIONS OF THE BLAST AND ITS EFFECTS TO BE ADDRESSED BY THE MODEL

The eruption began through a vent centered between about 1,900 and 2,500 m (6,300 and 8,000 ft altitude) about 1 km north of the old summit of the mountain (for example, see Moore and Albee, fig. 76). Eyewitness descriptions and photographs of the blast show that it was a roiling, turbulent gray cloud (Rosenbaum and Waitt, this volume). A preceding wind was reported in only a few places, and several eyewitnesses reported a wind blowing toward the volcano. In the photographs taken by Gary Rosenquist (fig. 38), a low cloud of dust appears in front of the advancing blast, indicating sufficient wind to entrain particles. Many witnesses heard no sound as the blast approached, except for dull rumbling probably associated with visible lightning flashes or with the landslide. Sequences of photographs show that the top of the blast appeared to travel faster than the bottom, and it therefore developed a towering or oversteepened appearance. Lenticular white clouds emanating from the edges were photographed from a number of positions around the edge of the advancing blast front.

A minimum velocity of 100 to 110 m/s, an average over the first 6.1 km in a northeast direction, has been deduced by Malone and others (1980). This velocity presumably is the velocity of the basal layer of the blast, which destroyed ground-based instruments. Keith and Dorothy Stoffel (oral commun., 1980), who were above the volcano in an airplane at the onset of the blast, estimated a similar velocity for the first laterally ejected material.

Barometric records from 30 stations in the Pacific Northwest show a systematic trend of peak-to-peak amplitude displacement with distance and orientation from the volcano (Reed, 1980). The record from Toledo, Wash., 54 km northwest of the volcano, shows a sharp rise of the pressure above ambient, followed by a drop to a comparable negative pressure, a slow recovery lasting for 13 min, and then another period of positive overpressure lasting 1 hr.

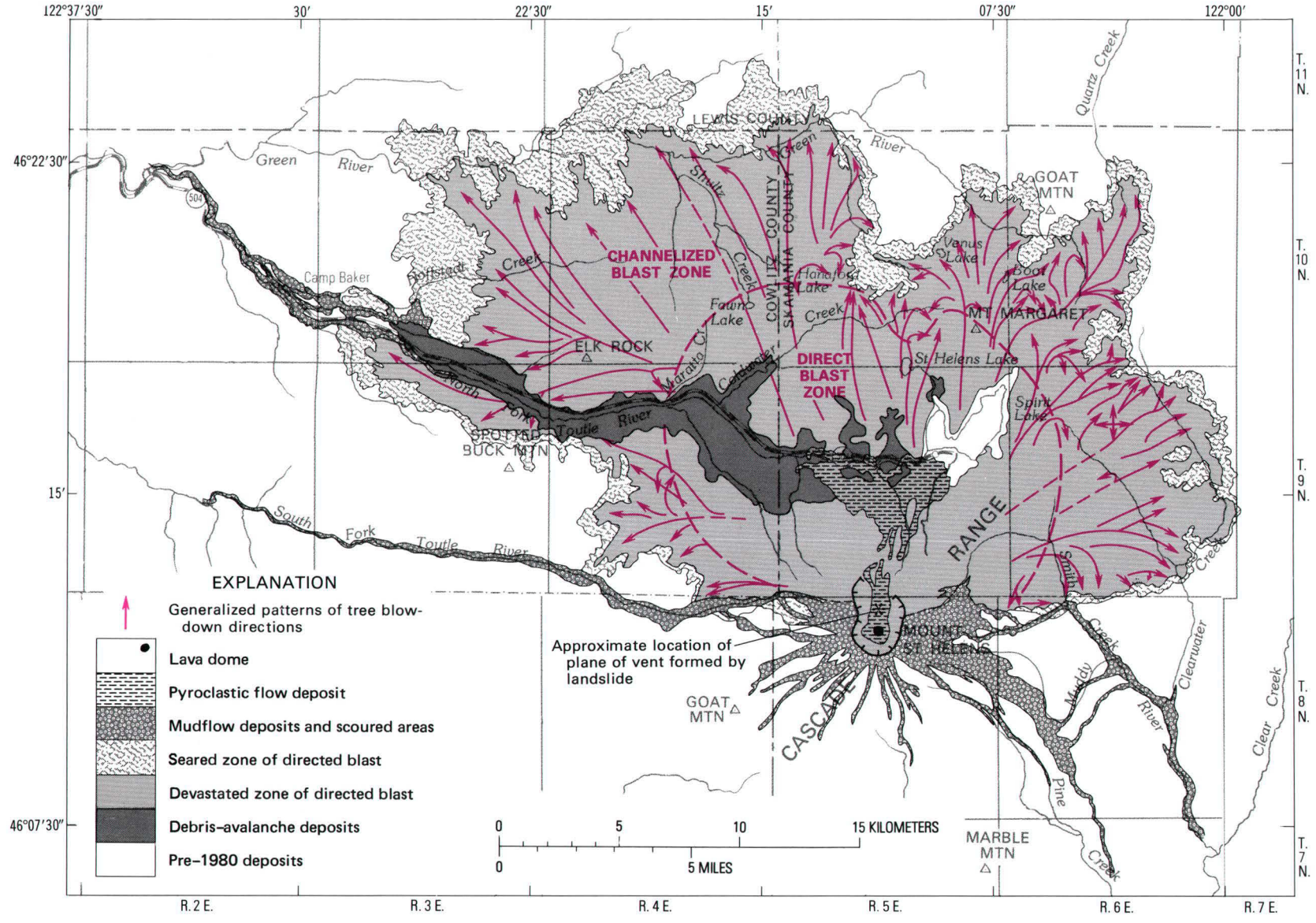

Figure 219.—Schematic map of devastated area and generalized directions of streamlines of the blast flow, as indicated by directions of alinement of fallen trees. Streamline arrows are dashed where information is lacking. Devastated area is divided into two zones (dashed line), the inner direct blast zone and the outer channelized blast zone. Note that near new vent (approximate location indicated by X), margin of blast zone lies south of vent in spite of the fact that flow emerged to north; however, at a distance of 10 to 20 km, margins have been deflected to northeast and northwest. Note also that singed zone is narrow compared to devastated area, and is wider where blast approached rising terrain (as in the northwest) and narrower where the blast approached falling terrain (as in the east) at its outer limits.

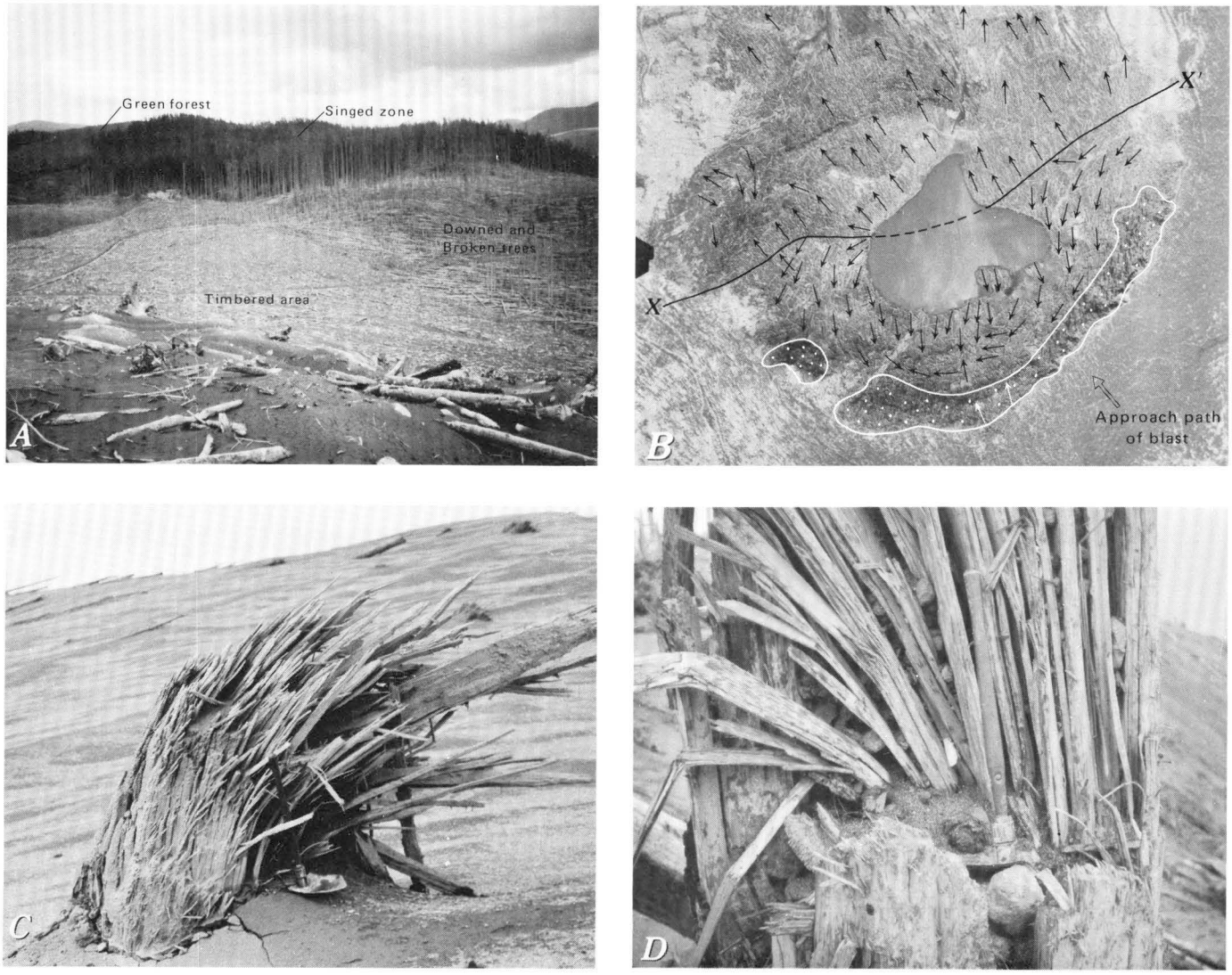

Figure 220.—Views of the devastated area and damaged tree stumps. A, Margin of the devastated area in the Green River drainage near the intersection with Shultz Creek. View north. Note transition from devastated area in foreground through a narrow singed zone into undamaged forest in background. B, Fawn Lake, a small cirque lake about 0.5 km in diameter. Trees in northwest half of the basin, above line X–X', show direct blowdown. Trees in southeast half of the basin below line X–X', show reverse blowdown; this is particularly easy to see on small island in southeast part of lake. Note that, in detail, blowdown pattern is complex; some partial trees are still upright on cirque wall, as indicated by two enclosed areas with dots, and some zones intermediate between direct and reverse blowdown occur (near line X–X'). C, Splintered stump on ridge between North Fork Toutle River and South Coldwater Creek, abraded on upstream side and deformed by blast after breakage and loss of top part of the tree. D, Lithic fragments and scoriaceous gray dacite driven into upstream side of a splintered stump on ridge east of Studebaker Creek.

The strongest peak-to-peak amplitudes extrapolate linearly to approximately 2×10^4 Pa (pascals) (0.2 bar) at 1 km from the summit and to $(5–8) \times 10^3$ Pa (0.05–0.08 bar) at 5 km.

The devastated area (the area in which trees have been uprooted, displaced, or knocked down) is a sector of about 500 km² generally extending to the north of an imaginary east-west line through the new vent (fig. 219). However, high on the mountain, the southern boundary of the devastated sector actually bends south of this east-west line. This southern boundary sweeps northward east and west from the volcano, and trends about 30° north of due east and west at 10 to 20 km from the mountain. The northern

boundary of the devastated area is irregular, but has two pronounced lobes extending to the northwest (25 km) and northeast (22 km). It is surrounded by a zone, referred to as the "singed zone," in which trees are still standing but have singed needles and limbs.

Preliminary mapping of the direction of fall of the trees in the devastated area by the author (see the summary of this work on pl. 1) shows two major, irregularly shaped zones (fig. 219): (1) an inner zone, termed the "direct blast zone," in which the blast flow was approximately radial from the volcano and was relatively undeflected, in plan view, by even large topographic features, and (2) an outer zone, termed the "channelized blast zone," in which the flow followed or was deflected, in plan view, by local topographic features. Streamlines of the flow were thus not simple radii from the source.

The transitions between the devastated area of downed trees, the zone of singed trees, and the surrounding forest of standing green trees have a number of remarkable characteristics that are explained by the blast-flow model that follows. The transition distance from the area of uniformly downed trees in the devastated area to standing trees in the singed zone is usually on the order of one tree length (fig. 220*A*). The singed zone is narrow compared to the dimensions of the devastated area; it ranges in width from a few meters to 4 km. Commonly, the zone is wider on ridges and slopes facing toward Mount St. Helens than on slopes facing away (figs. 219, 220*A*).

In vertical cross section, the local topography had a pronounced effect on the blast flow. Within the direct blast zone, as the flow crossed terrain that dropped in elevation (for example, crossed from a ridge to a valley or from the top of a cirque wall to a lake below), parts of the flow reversed direction, and reverse tree blowdown patterns were formed. A spectacular example occurs at Fawn Lake (fig. 220*B*). These tree reversals are less common in the channelized blast zone.

Ground reconnaissance studies conducted by the author in May 1980, and detailed studies by Moore and Sisson (this volume), showed a complex variety of tree destruction mechanisms. Field observations indicated that the devastation was not produced by an airshock alone, but by a complex multiphase flow of finite duration. Some of the evidence for this conclusion is that splinters remaining after tree breakage were deformed away from the center of the volcano by a flow that was sustained after the trees fell over (fig. 220*C*), root balls on fallen trees are deformed away from the source of the blast, and rocks and splintered wood are deeply driven into previously splintered trunks (fig. 220*D*) and into deformed root balls.

The total blast deposit is approximately 0.25×10^{15} g (Moore and Albee, this volume) and consists of at least three components: lithic fragments derived from the older volcanic edifice; a scoriaceous gray dacite; and organic material and soils entrained as the eruption progressed. The volatile components in the blast probably came from both the dacite and surrounding hydrothermal water. The material in the blast was, therefore, a complex multiphase vapor-liquid-solid mixture.

ASSUMPTIONS USED IN THE MODEL OF BLAST DYNAMICS

In order to model the fluid dynamics of the blast, both the reservoir geometry and the thermodynamic conditions must be greatly simplified from the complex pressure, temperature, and material composition conditions that probably existed in the volcano. The reservoir was certainly heterogeneous in composition, containing the gray dacite, parts of the mountain's hydrothermal system, and cold rock and glacial ice; however, much of the initial compositional and thermal heterogeneity was erased in the early stages of flow of the blast by turbulent mixing of the components. Disregarding the problem of phreatic, magmatic, or phreatomagmatic mechanisms, the process is here modeled in terms of an eruption from a reservoir initially at a uniform pressure, temperature, and density, and having a specified mass ratio of solid to vapor phases (m) (fig. 221*A*).

The reservoir is assumed to have been a disk-shaped volume of the north side of the mountain just large enough to contain the mass (0.25×10^{15} g) ejected by the blast, 0.2 km^3 at an average preeruption density of 1.3 g/cm^3 (Moore and Sisson, this volume), or 0.12 km^3 at a preeruption density of 2.0 g/cm^3. The reservoir is assumed to have had a frontal surface area of 0.25 km^2 (that is, the plane called here the "vent" is assumed to have been a rectangle 1 km in east-west dimension and 0.25 km in height) and, therefore, to have been 0.5 km deep.

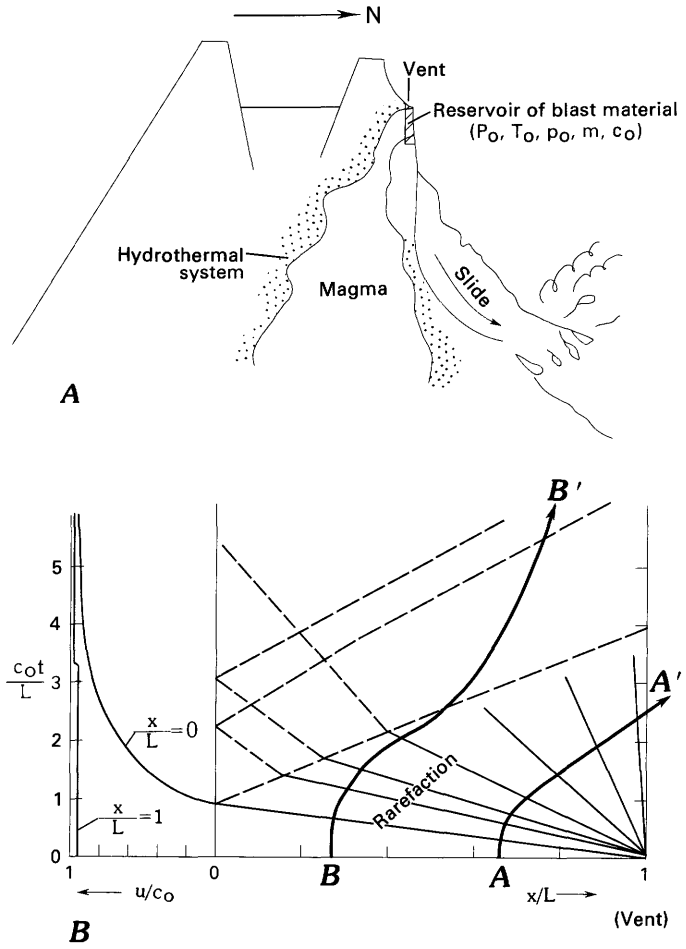

Figure 221.—Sketches of volcano and reservoir before the blast and development of reservoir discharge. A, Schematic cross section of volcano and reservoir conditions before the blast, as assumed in model for blast dynamics. Uniform reservoir conditions are assumed: P_o, initial pressure; T_o, initial temperature; ρ_o, initial density; m, mass ratio of solid to vapor components; c_o, initial sound speed. The eruption emanated through the vent created by the landslide down the north flank. It is assumed that magma underlay and partially intruded the disk-shaped area (reservoir) from which the blast material originated. The magmatic heat probably created a hydrothermal system in the reservoir of blast material. B, Space-time diagram showing development of discharge from reservoir. The multiphase rarefaction fan originated at vent, x/L=1, and propagated into reservoir, reflecting from back of reservoir (x/L=0), which is assumed to be at constant pressure. Distance is normalized to reservoir depth, and time is normalized by ratio of sound speed, c_o, to reservoir depth, L. Shown on the left is a graph of velocity of the blast (normalized to reservoir sound speed) versus time (normalized by the ratio of sound speed to reservoir depth). Curve labeled x/L=1 shows velocity of very shallow material; curve labeled x/L=0 shows velocity of very deep material. Illustration is schematic, modified from Shapiro (1953, 1954).

The blast is modeled as flow from a one-dimensional reservoir. The initial pressure, P_o, is taken as a plausible mean pressure between the top and the bottom of the reservoir (overpressures within the magma chamber are unknown at this time, but, as is shown later, pressures higher than a mean hydrostatic pressure are not required to explain the blast phenomenon). The initial temperature, T_o, is here taken to be the saturation temperature of pure H_2O at the initial pressure P_o, but it may also be considered to be an averaged temperature intermediate between the dacite at its solidus temperature, warm hydrothermal water, and cold rocks and glacial ice. The reservoir composition is specified simply by a mass ratio of solid to vapor phases, m, even though the material in the blast likely came from both a dacitic magma intrusion and from a surrounding hydrothermal system, and, therefore, had rather large variations in solid-vapor ratio as well as in initial temperature.

The equation of state of the material that expanded from the reservoir is modeled by considering the material to be a multiphase fluid consisting of two thermally interacting components: a vapor phase and an entrained solid phase. For this model, the vapor phase is taken to be steam; but because the flow characteristics are dominated by the abundance of the entrained solid phase, it would make only slight changes in the results if this phase were assumed to be another vapor, such as CO_2. The density of the entrained solid phase is assumed to be 2.0 g/cm^3.

Upon adiabatic expansion, the thermal history of a multiphase mixture can lie between two extremes: the first, in which the vapor and solid phases do not interact thermally, and the second, in which the particles and vapor are at all times in thermal equilibrium. Because of the large amount of fine-grained material in the blast deposit (Moore and Sisson, this volume; Hoblitt and others, this volume), transfer of heat between the two phases was important during the blast flow and thus the second extreme is assumed here. The solid and vapor components are assumed to flow together (homogeneous flow). Transfer of mass between the solid and gas phases (for example, due to degassing of pyroclastic particles or to condensation of the steam on the solids as the flow expanded) is ignored because the scoriaceous nature of the dacite suggests that degassing from the magmatic component was restricted, and because temperatures throughout most of the area devastated by the blast were greater than the condensation temperature of

water (about 92°C at 2,100 m elevation).

For an adiabatic, quasi-isentropic expansion, the mixture of vapor and solid particles described above can be modeled as a thermally equilibrated pseudogas and can be characterized by equations of state of the form of the perfect gas laws (Wallis, 1969):

$$PV = R_b T \tag{1a}$$

$$PV^{\gamma_b} = \text{constant}. \tag{1b}$$

$$c_{ob} = (\gamma_b R_b T)^{\frac{1}{2}} \tag{2}$$

In these equations, P is the pressure, V is the volume, γ_b is the isentropic exponent, R_b is the gas constant of the blast mixture, T is the temperature in Kelvin, and c_{ob} is the sound speed of the blast mixture in the reservoir. γ_b and R_b are appropriately modified from the values of the pure vapor phase to account for the effect of the entrained solids in the mixture:

$$\gamma_b = \frac{C_{P_g} + mC_s}{C_{V_g} + mC_s} \tag{3a}$$

$$R_b = \frac{R_g}{(1+m)} \tag{3b}$$

where C_P and C_V are, respectively, the specific heats at constant pressure and volume; the subscripts g and s denote the gas and solid phases, and m is the mass ratio of solid to vapor components. Notice that because of the dominant effect of m in the above equations, the molecular nature of the vapor phase is generally less important in determining the thermodynamic properties than the mass abundance of the solid phase.

Although the blast-flow model can easily be scaled (for constant γ_b, the results scale linearly with dimensional and pressure ratios, and as the square root of temperature ratios), the model is presented here for a single set of plausible initial conditions at Mount St. Helens. It is assumed that 10 percent of the volume that flowed into the blast was initially filled with liquid water that vaporized during the eruption; this assumption gives $m = 25$. For this value of m, $\gamma_b = 1.04$, and $R_b = 17.8 \times 10^4$ ergs/°C/mole. The initial source pressure is assumed to have been 12.5 MPa (125 bars), appropriate to 0.65 km of overburden, and the initial temperature is assumed to have been 600K (327°C), the saturation temperature of pure H_20 at 12.5 MPa. The initial density of such a mixture at 12.5 MPa pressure would have been 1.0 g/cm^3. Atmospheric pressure is taken as 8.7×10^4 Pa (0.87 bar).

INITIATION OF THE ERUPTION, AND THE DEVELOPMENT AND DURATION OF DISCHARGE

The Mount St. Helens blast was initiated by the removal of the overburden contained in the landslide, an event that resulted in the sudden exposure of volatile material in a reservoir at high pressure to much lower pressure. The removal of the overburden is considered instantaneous for purposes of modeling reservoir discharge. The geometry, simplified as discussed above, is shown in figure 221*A*, and the events that followed the overburden removal are shown in figure 221*B*, a space (x)-time (t) diagram of wave and particle motions. The initial conditions for the model are that the reservoir contained a fluid, initially at rest, with the thermodynamic properties discussed above, bounded by a rigid wall 500 m behind the vent. At time $t = 0$, the pressure at the plane of the vent was instantaneously reduced to that of the atmosphere.

The rarefaction (decompression) that propagated into the reservoir was complex, and consisted of at least three parts: a precursor rarefaction that reduced the pressure to that of saturation of the material; a vaporization wave, across which the vapor phase nucleated and grew and some acceleration may have occurred; and a multiphase expansion wave that accelerated the mixture of vapor and solid material from the vent. Further discussion of this series of waves is given in Appendix 1, "Precursor, vaporization, and multiphase expansion waves"; to simplify the model, the multiphase expansion wave is assumed to have accomplished the major part of the acceleration of the blast material, and it is referred to as "the"rarefaction wave.

A rarefaction wave travels into a fluid at the speed of sound of the fluid, 105 m/s for the assumed multiphase reservoir fluid at Mount St. Helens. The wave was initially a discontinuity as it began at the vent at $t = 0$, but, because the speed of sound in the fluid decreases with decreasing pressure as the fluid expands, the wave spread out with time (as represented by the rarefaction fan on the x-t diagram of

fig. 221*B*). The particles in the reservoir accelerated as they crossed the rarefaction wave, reaching sonic velocity, $u = c$ (where u is the particle velocity and c is the local sound speed) as they crossed the vertical part of the rarefaction fan at the exit of the reservoir (the vent). This local sonic velocity is 103 m/s for the assumed reservoir conditions. At the vent, the pressure was still above ambient; further expansion to lower pressure could not take place inside the reservoir and had to occur outside of the vent, a process discussed in the section on "Steady state expansion from the vent."

The head of the rarefaction wave reflected from the bounding surface of the reservoir, with the boundary condition that the particle velocity, u, on this surface must have remained zero. The reflected wave traveled back through the reservoir to the vent, arriving at a time, D (after initiation of the eruption), that is slightly less than $2\,L/c_{ob}$ (where L is the depth of the reservoir and c_{ob} is the sound speed of the material at rest in the reservoir). D is 10 s for the model. Particles, such as AA′ in fig. 221*B*, that escaped the reservoir before interacting with this wave exited with the maximum (sonic) velocity; particles, such as BB′, that were caught by the reflected wave, had slower velocities. In principle, some material never left the vent because of the boundary condition $u = 0$. However, material originating a length of ℓ/L from the closed end of the reservoir would have expanded to ℓ'/L, given by

$$\frac{\ell'}{L} = \frac{V'}{V}\left(\frac{\ell}{L}\right)$$

where V and V' are the specific volumes in the reservoir and at atmospheric pressure, respectively. Because the final expansions were so large (V'/V is about 10^3), ℓ'/L is greater than 1 for all $(\ell/L) > 10^{-3}$, that is, most of the material ultimately left the vent, though with ever-decreasing velocities. In fact, about two-thirds of the material left the vent before the arrival of the reflected wave. It is reasonable, therefore, to define the "duration of the blast at the vent" as $(1\text{–}2) \times D$, or as 10–20 s. The duration is certainly dependent on the assumed reservoir geometry; for example, an extreme case would be a long, small-diameter reservoir, but this shape is not realistic because the vent created by the landslide scarp was nearly 1 km in diameter, and the total mass in the blast deposit therefore requires a disk-like shape.

The reservoir was at such high pressure compared to the ambient atmospheric pressure that the flow choked at the vent and exited at the choked or sonic-flow velocity (Shapiro, 1953–54). For unsteady flow, the choked velocity is

$$u^*_{us} = \frac{2}{\gamma_b + 1} c_{ob} \tag{4}$$

where c_{ob} is the speed of sound of the mixture at rest in the reservoir; the subscript us refers to unsteady flow conditions, and the superscript asterisk denotes sonic flow conditions. c_{ob} is given by

$$c_{ob} = (\gamma_b R_b T)^{1/2}. \tag{5}$$

For the mixture postulated, c_{ob} is 105 m/s, and the unsteady-flow choked velocity is 103 m/s. Passage of the transient rarefaction waves allowed steady flow to develop, and the sonic or choked velocity to increase to the steady-state value of

$$u^*_s = \left(\frac{2}{\gamma_b + 1}\right)^{1/2} c_{ob} \tag{6}$$

which is 104 m/s. Under steady-flow conditions, the pressure at the vent would have decreased to $P^* = 0.60 P_o$ (7.5 MPa, or 75 bars), the temperature to $T^* = 0.98 T_o$ (588 K (315°C)), and the density to $\rho^* = 0.61 \rho_o$ (0.61 g/cm^3). The mass flux, controlled at the vent by choking, was

$$\dot{m}^* = \rho^* u^* A^*, \tag{7}$$

where ρ^*, u^*, and A^* are, respectively, the density, velocity, and area at sonic conditions at the vent. For the calculated ρ^* and u^*, the mass flux per unit area was 0.6×10^4 g/s/cm^2. With an average temperature 325K above ambient, a specific heat, C_P, of 0.84×10^7 ergs/g/K for the solid phase and 4.2×10^7 ergs/g/K for the steam, and a latent heat of vaporization of the steam, L, of 2.2×10^{10} ergs/g, the thermal-energy flux or power per unit area was

$$\dot{E}^* = \dot{m}^*(C_P \nabla T + L). \tag{8}$$

For the model conditions, $\dot{E}^*$ was 2.5×10^{13} ergs/s/cm^2 or 2.5 MW/cm^2. (For comparison, the power per unit area developed by the Advanced Saturn 5 Stage 1 motors that launched the Apollo astronauts to the moon was about 1 MW/cm^2.) The horizontal thrust was $\sim 3.3 \times 10^{12}$ Newtons.

THE MODEL FOR STEADY-STATE EXPANSION FROM THE VENT

Material discharged from the vent into the atmosphere at sonic velocity would have expanded supersonically in all directions. In the vertical direction, the expansion would have been complicated by gravitational accelerations and by the ground surface. In lateral directions, the expansion could have occurred relatively unimpeded. The model presented in this section represents the flow in a lateral plane through the blast cloud.

In the absence of gravity, friction, phase changes, and addition or loss of mass from a flowing fluid, the steady-state equations of motion for an expanding fluid are (Thompson, 1972):

$$\nabla \mathbf{x}(\rho \mathbf{u}) = 0 \qquad \text{(continuity)} \quad (9)$$

$$\nabla \mathbf{x}\, \mathbf{u} = 0 \qquad \text{(irrotationality)} \quad (10)$$

$$\nabla\left(\frac{u^2}{2}\right) + \frac{1}{\rho}\nabla P = 0 \qquad \text{(momentum)} \quad (11)$$

In these equations, ρ is the density, $\mathbf{u}$ is the vector velocity, P is the pressure, ∇ is the spatial differential operator. These equations, supplemented by the equation of state of the fluid and boundary conditions, define the steady-state condition of the flow everywhere. However, they are not analytically solvable because they are nonlinear. The method of characteristics was used for solution because it explicitly defines waves within the flow.

A detail of the expansion of the flow around a corner of the vent, for example, the east corner (fig. 222*A*), illustrates some of the phenomena of supersonic flow that the model suggests occurred during the blast. Streamlines of the flow are shown as heavy lines A′B′ and AB. The characteristics of the flow are shown as thin black lines, radiating from the corner of the vent; they are labelled by the Mach numbers of the flow, M, as it crosses the characteristics. Physically, the characteristics of the flow can be thought of as small sound waves, in this case, expansion waves, across which the fluid diverges and accelerates (the Mach number increases) and the pressure decreases. The fluid expanded around the corner of the vent because its pressure was much larger than the atmospheric pressure. The angle of expansion was determined by the ratio of fluid pressure to atmospheric pressure, the Mach number of the flow, and the thermodynamic properties of the fluid (the angle of expansion is the Prandtl-Meyer angle, well known in aerodynamic studies). The deflection of the flow at any point on a streamline depended on the extent of passage through the rarefaction wave. Particles that originated close to the walls of the reservoir (for example, a particle on streamline AB in fig. 222*A*) were more rapidly accelerated to their final velocities than those closer to the center of the vent (for example, a particle on streamline A′B′) which had to travel farther through the rarefaction fan. On figure 222*A* small arrows (d, e, f, g) show the degree of turning of particles through the rarefaction fan. These arrows might be thought of as the direction in which individual trees knocked down by the flow now point. Note that they do not point directly away from the origin of the flow at the vent. For example, tangent CC′ on streamline A′B′ does not point to the place where streamline A′B′ left the vent. In particular, where the divergence exceeds 90°, a linear extrapolation of the directions of tree fall back to the vent would give an apparent flow origin in front of the vent. This fact illustrates that even close to the vent in the direct blast zone, streamlines of the flow are not simple radii from the source.

The actual flow from the vent was more complex than this simple example of corner flow because rarefaction waves from opposite sides of the vent intersected in a complex way, creating complex regions of intersecting expansion waves and regions of reflected compression waves that built into shock waves. The flow at Mount St. Helens depended on reservoir conditions and material properties that are unknown at this time, so that quantitative solutions are difficult to obtain, but general features of such expansive flows are illustrated schematically in figure 222*B*. Most data for the flow regimes come from development of propulsive engines (JANNAF, 1975), which are different in scale and material properties from the Mount St. Helens blast. These data and theories, nevertheless, are a valuable base for studying the process that may have occurred in the blast at Mount St. Helens.

Qualitatively, the following phenomena shown in figure 222*B* can occur in expansive flows. A rarefaction wave, initially identical to that discussed above, emanates from each side of a vent (corners x and x′ in fig. 222*B*). The flow pattern is "simple" (in the fluid-

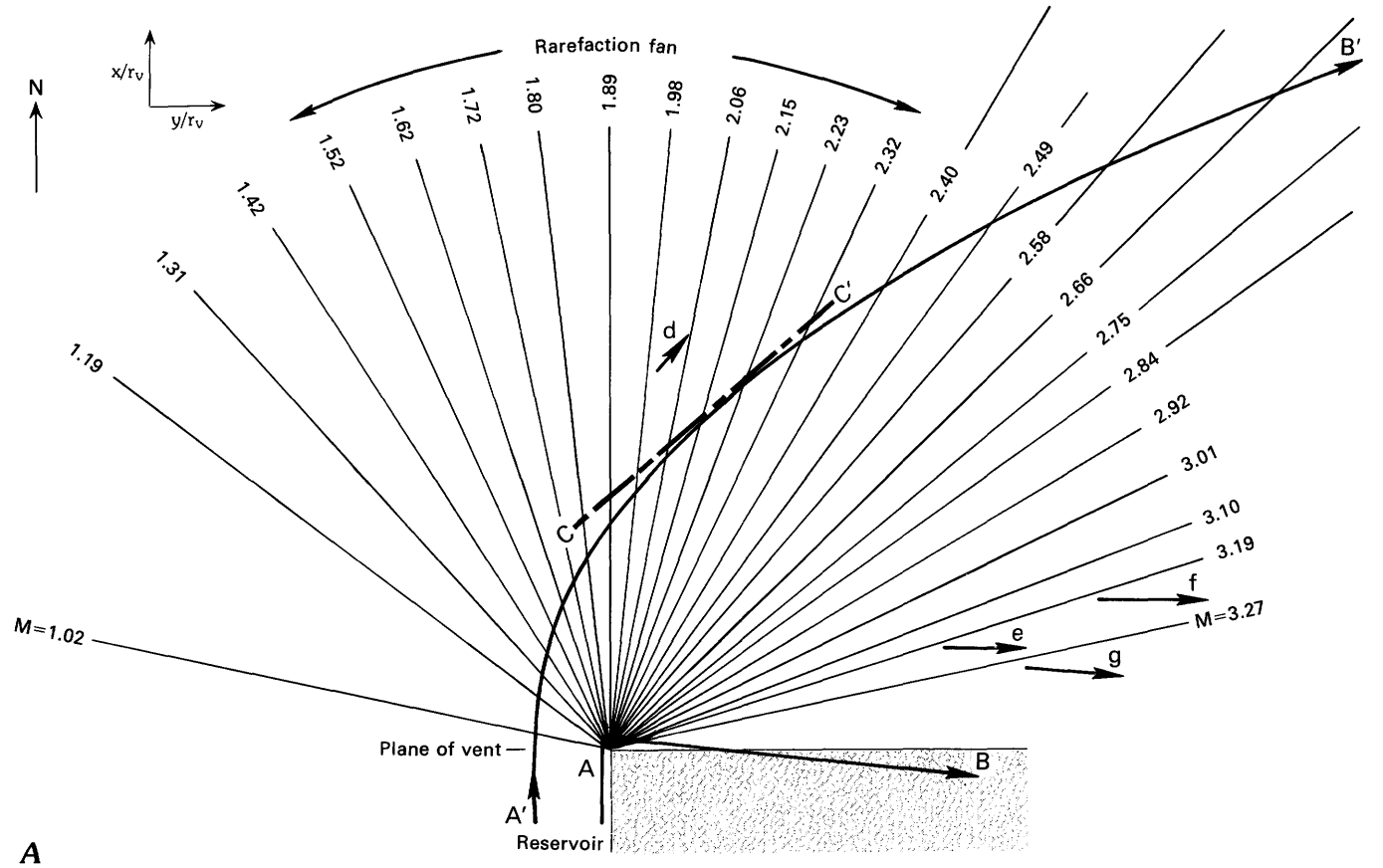

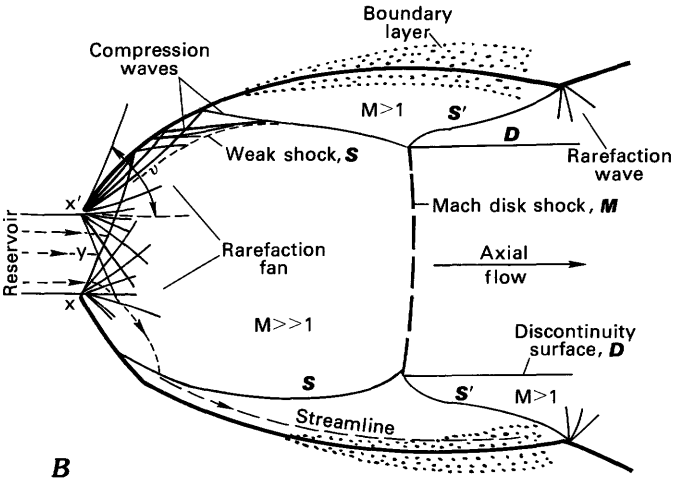

Figure 222.—Diagrams of supersonic flow patterns. A, Supersonic flow around a corner. Map view of flow pattern from east corner of vent. Coordinates x and y, normalized to vent radius, r_e, are parallel and perpendicular to flow, respectively. Characteristics of flow are thin lines that radiate from corner of vent. They are labeled by the Mach number, M, of the flow as it crosses the characteristics. AB and A'B' are streamlines of flow; CC' is a tangent to A'B'. The small arrows d, e, f, g represent calculated local directions of flow, as would be recorded in directions of tree blowdown. B, Schematic flow field of underexpanded supersonic flow after leaving a (nearly) straight nozzle (from JANNAF, 1975). Flow leaves nozzle through vent at plane xx'. It is initially deflected through the Prandtl-Meyer angle, v, by rarefaction waves (the rarefaction fan) emanating from corners of nozzle. The flow is simple (in the fluid dynamics sense of the word) until the rarefaction waves intersect, which first happens at y. Rarefaction waves reflect from flow boundary, shown as a heavy line, as compression waves that coalesce into the weak intercepting shocks, S and S'. These are connected across the flow by the Mach disk shock, M. The flow pattern repeats downstream of the Mach disk shock. Discontinuity surfaces, D, can develop, separating axial flow from the deflected flow near the boundary layer. The boundary layer of the flow with the ambient atmosphere (shown as the stippled region) increases in width downstream. Supersonic (M > 1 or M >> 1) and subsonic (M < 1) regions of flow are shown. Dashed lines are streamlines of the flow.

dynamics sense of the word) near the vent, and the flow is initially deflected through the Prandtl-Meyer angle, ν. As the expansion waves from opposite corners of the vent intersect (at y), the flow becomes "nonsimple" and differs from the simple flow shown in figure 222*A*. The pressure decreases as the flow passes through these simple and nonsimple rarefaction waves. It is equal to atmospheric pressure at the flow boundary but can fall considerably below atmospheric pressure near the axis of the flow.

When the rarefaction waves reach the boundaries of the flow, they are reflected as compression waves and coalesce into weak shocks, referred to as intercepting shocks because they intercept and terminate the initial rarefaction waves. The intercepting shocks consist of two parts, an incident and a reflected shock (S and S′ in fig. 222*B*), connected by a Mach disk shock, in front of which the flow is supersonic ($M>>1$) and behind which the flow is subsonic ($M<1$). Downstream from the Mach disk shock, subsonic and supersonic regions of flow subparallel to the boundary are separated by discontinuity surfaces (*D*, fig. 222*B*). The pressure in front of the Mach disk shock is very low because the flow overexpands through the nonsimple region of the rarefaction waves. Consequently, there is a pressure gradient acting from the flow boundary, which is at atmospheric pressure, toward the underpressured core; this pressure gradient causes the flow boundary to curve inward away from the initial Prandtl-Meyer angle, as shown in figure 222*B*. A boundary layer that increases in thickness downstream develops because of interaction of the flow with the atmosphere.

The flow model for the boundary and reservoir conditions assumed above for Mount St. Helens is shown in figure 223. The phenomena described above are visible. The solution interior to the region bounded by shocks was obtained by hand calculations using the method of characteristics. The minimum pressure in this region was calculated from the numerical solution and checked from the method of Pack (1948). The location of the Mach disk shock was estimated by scaling from methods described in JANNAF (1975). The contour of the boundary of the flow was estimated from the methods described in JANNAF (1975). The position of the intercepting shock is entirely schematic, based on (1) the assumption that it was nearly tangential to the boundary near the vent because the angle of incidence of the characteristics onto the boundary equals their angle of reflection, and (2) connection to the Mach disk edges. Although numerical uncertainties could, in principle, be assigned to a model such as this, they are meaningless in view of the uncertainties in physical principles we still face in interpretation of the blast fluid dynamics.

In the model conditions assumed for the Mount St. Helens blast, the rarefaction waves that emanated from both sides of the vent deflected the flow through an initial angle of 96°. The reflection of the expansion waves from opposing boundaries deflected the flow from its initial angle of 96° to an angle of about 60° at $x/d \sim 10$. The fluid exited the vent at the sonic velocity of 104 m/s. At Mach 2.23 (near the vent) the flow was moving at a velocity of 225 m/s; at Mach 3.41, just in front of the inferred Mach shock disk, the velocity was 325 m/s.

Within the diverging flow, the pressure dropped rapidly away from the vent. At the boundary of the flow, the pressure was reduced to the local atmospheric pressure. The pressure contours (fig. 223) show that the pressure dropped below ambient outside of a zone about six vent diameters distance. This zone of negative pressure is shown as stippled in figure 223. The calculated pressure drop is to about one-half of ambient, but absolute pressure values are not very significant because of the effect of hydrostatic pressure, ignored here, on different parts of the flow. However, the existence of a low-pressure region within the flow is significant. This low-pressure core formed because the compression waves could not be reflected back into the flow quickly enough to prevent overexpansion.

As the pressure within the flow decreased, the density likewise decreased rapidly. Temperatures, however, were rather uniform across the flow because of the buffering effect of the entrained solid phases that acted as a heat source for the expanding vapor. At the limits of the blast zone, the temperature only dropped to 80 percent of the initial value. The heat supplied to the vapor by the solids augmented the density decrease caused by the extreme volumetric expansion.

In response to the formation of the low-pressure core, the intercepting shocks would have connected across the flow to have formed a Mach disk shock. Across this shock, the pressure increased from the subatmospheric values toward atmospheric pressure, and the flow decelerated from supersonic to subsonic velocities. Based on scaling relations given in JANNAF (1975), the Mach disk is shown in figure 223 at a distance $x/d \sim 11$ and having a diameter $s/d = 8$. The pressure, density, and velocity changes across

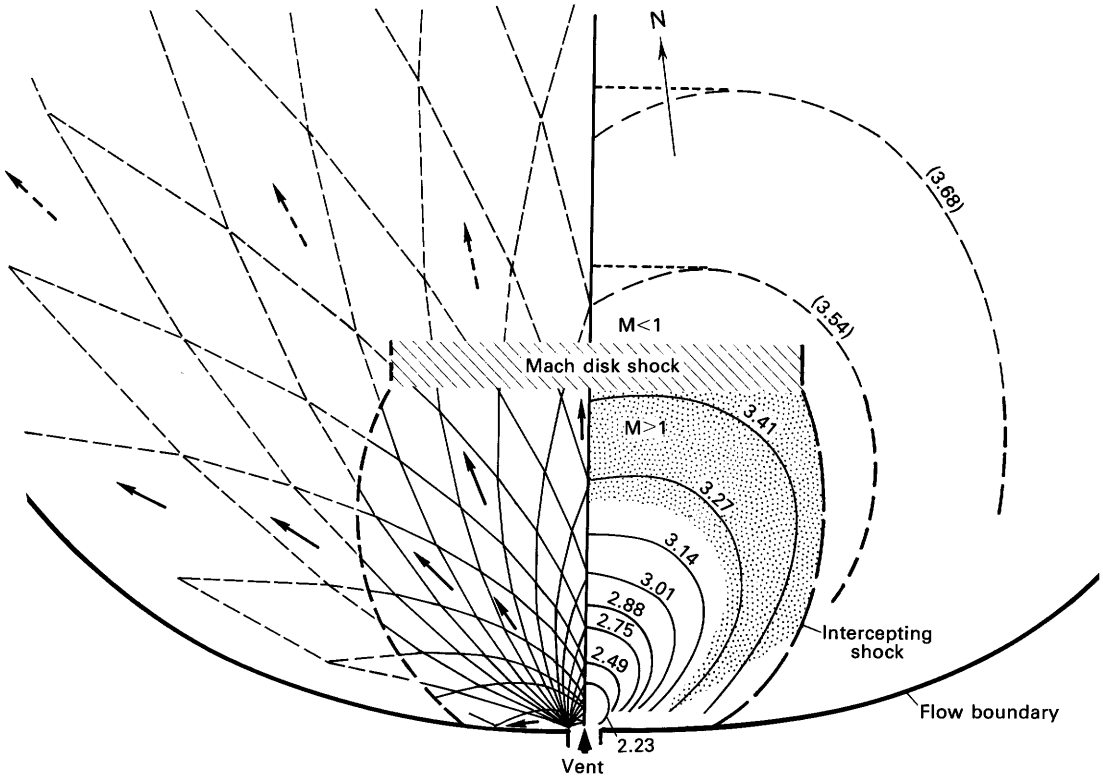

Figure 223.—Map of flow field according to model of blast dynamics. To ease numerical computation problems, the exit Mach number of the flow is assumed to have been 1.02 instead of the sonic Mach number, 1.00. All length dimensions, x and y, are normalized to vent diameter. The model is symmetric about axis of vent, so it is split into two halves here for conciseness. On left, the characteristics are shown as thin lines radiating from corner of vent. Boundary of flow is assumed to have been at constant pressure, 8.7×10^4 Pa (0.87 bar). The peripheral intercepting shock formed by reflection of the expansion waves from this boundary is shown as dashed line. Note how reflection of expansion waves deflects boundary of flow away from its original expansion angle of 96°. Flow directions are shown by representative arrows, solid within zone where model is strictly valid, dashed in zone where model is extrapolated across shock waves. On right, contours of constant Mach number M and, therefore, constant pressure (P/P_o), temperature (T/T_o), and density (ρ/ρ_o) are shown. Velocities are given implicitly by the Mach numbers. Each contour is labeled by the value of the Mach number, M. From the innermost contour outward, values of M, P/P_o, T/T_o, and ρ/ρ_o are given. In the supersonic region, these values are respectively (2.23, 0.087, 0.91, 0.095); (2.49, 0.047, 0.89, 0.053); (2.75, 0.025, 0.87, 0.029); (2.88, 0.018, 0.86, 0.021); (3.01, 0.013, 0.85, 0.016); (3.14, 0.009, 0.83, 0.011). Extrapolated into the subsonic region, where in fact, M is less than 1, these values are: (3.27, 0.006, 0.82, 0.007); (3.41, 0.004, 0.81, 0.006); (3.54, 0.003, 0.80, 0.004); and (3.68, 0.002, 0.785, 0.002). The approximate location of the Mach disk shock is shown; it separates the inner region of supersonic flow, for which the model is valid, from the outer subsonic zone in which no solution has been obtained. Model is extended into this region where the contours are shown as long dashed lines and Mach numbers are shown in parentheses. Downward curvature of outer contours near axis of flow is probably an artifact of the grid size used in the numerical solution, and the likely contour shape is shown by short dashed lines.

the shocks cannot be calculated at this time, because the numerical model is only valid inside at the shock waves. Under the assumption that the shocks were not too strong, the model has been extrapolated across them (as shown in fig. 223) to obtain estimates of density and temperature, estimates that are necessary for prediction of the range of the flow.

A number of effects not considered in this simplified analysis must be kept in mind in applying this model to Mount St. Helens. Friction would have de-

creased the supersonic flow velocities toward sonic conditions (that is, toward about 100 m/s); changing topography would have increased and decreased velocities as the flow progressed. Thus, as the flow initially expanded and dropped about 1 km in elevation toward the North Fork Toutle River, the effects of friction and gravity would have opposed each other. After crossing the North Fork Toutle River, the flow rose again into relatively high country, and the effects of friction and gravity would both have slowed the flow. The effects of mass addition to, and loss from, the flow were assumed here to have been compensatory, as large debris fell out and trees and soil were entrained; in detail, this assumption cannot be correct because of the differing sizes, temperatures, and densities of the materials. Because of these considerations, I believe that the model velocities are high upper limits on actual flow velocities.

INFERENCES AND APPLICATIONS OF THE MODEL TO THE BLAST AT MOUNT ST. HELENS

The model can be applied directly to the Mount St. Helens blast with the choice of a vent width, position, and orientation. Examination of the photographs taken by eyewitnesses suggests a vent width of about 1 km (the actual width probably was somewhat less at the onset of the blast and somewhat greater by the end of it), and a position centered at 8,000 ft (2,500 m) elevation. The normal to the plane of the vent is assumed to have been 5° east of north. The model, superposed on the map of figure 219, is shown in figure 224.

BLAST VELOCITIES

The initial velocity of the blast is assumed to have been initially the sonic velocity of the multiphase mixture, about 100 m/s. The velocity increased toward an upper limit of 325 m/s due to lateral expansion. A simple model for the effect of the blast on the near-field atmosphere is given as Appendix 2. Because 325 m/s is probably a high upper limit to flow velocities, due to the effects discussed in the last section, the velocity of the blast apparently did not, on the average, exceed the speed of sound in the surrounding atmosphere (about 330 m/s). Thus, a strong atmospheric shock wave was not generated. However, velocity variations in the flow due to turbulence could have caused velocities in parts of the blast to be very close to or even to exceed the sound speed of air. These parts of the blast would generate significant velocity and pressure perturbations in the atmosphere locally, and, in places, may have generated local atmospheric shocks. The white lenticular clouds on the periphery of the blast and, particularly, in reentrants in the advancing blast front (as pointed out by H. H. Kieffer, oral commun., 1981), may have indicated the formation and dissipation of such local compressions and shocks. The reentrants would be regions of transient high pressure as atmospheric compression waves generated by lobes of the blast intersected head-on or obliquely in the air surrounded by the lobes. It is well known from bomb detonations that temporary condensation clouds can form in the zone of negative pressure that follows the passage of atmospheric shocks (Young, 1965). This phenomenon occurs because subcooling of a saturated atmosphere in the negatively pressured air causes temporary condensation of the atmospheric moisture. Condensation clouds of this origin were photographed at volcanic eruptions at Ngauruhoe in New Zealand (Nairn, 1976).

As the material of the flow expanded from the vent, it was deflected through an angle somewhat greater than 90° (96°) around the edges of the vent due to the high pressure of the reservoir, compared to that of the surrounding atmosphere. This large initial deflection accounts for the felled trees in regions behind or south of the vent. As the flow progressed away from the vent, the south margin veered toward the northwest and northeast because the initial expansion waves were reflected from the constant pressure boundary of the flow, that is, the atmosphere pressed in on the flow, keeping it from overexpanding. The survival of eyewitnesses at whom the flow was initially directed (for example, in parts of the North Fork and South Fork Toutle River drainages) is solely due to these internal wave reflections.

PRESSURES, TEMPERATURES, AND DENSITIES

Near the volcano (within about 6 km), the pressure in the flow was above ambient pressure, but beyond

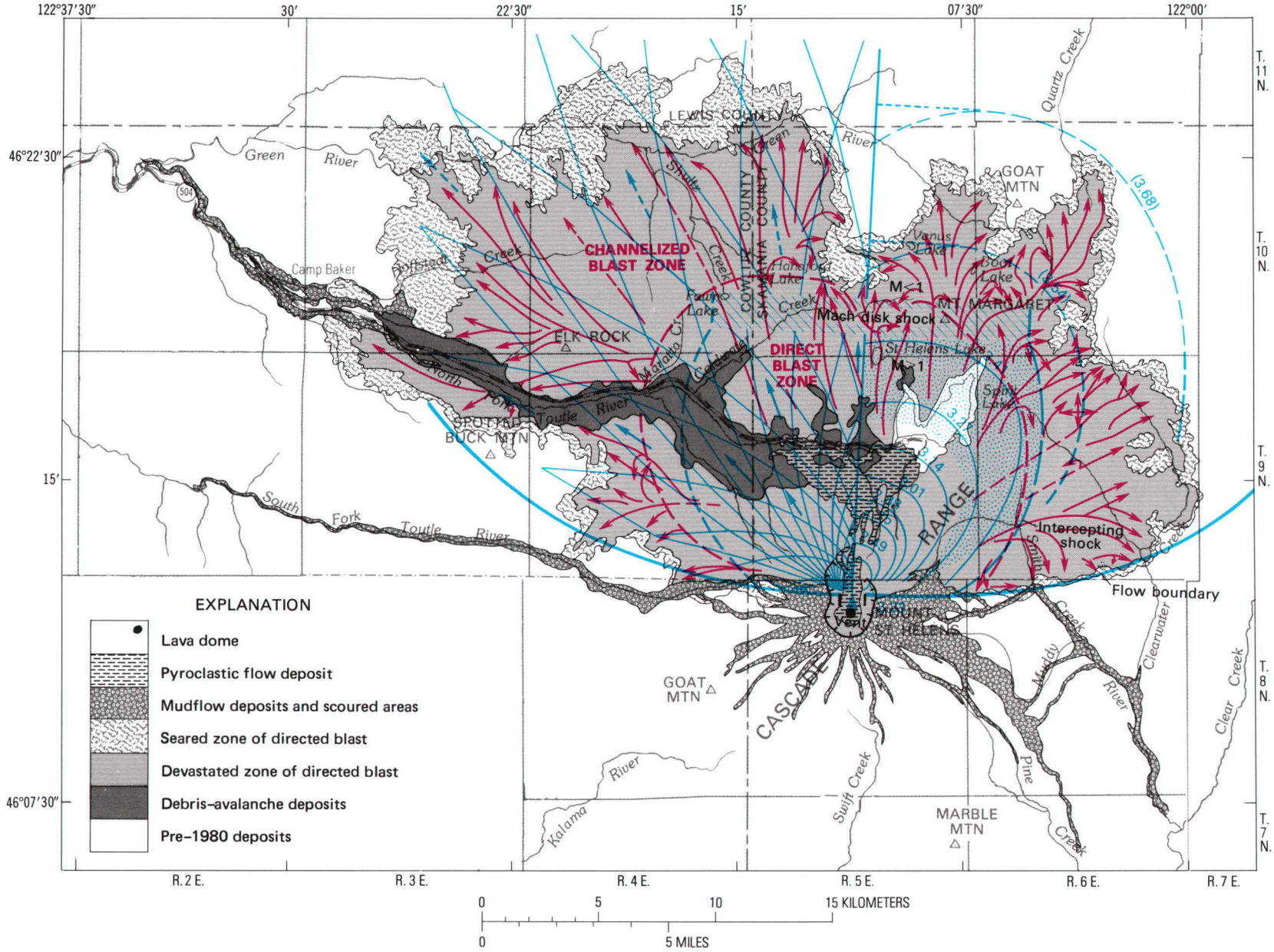

Figure 224.—The blast model shown in figure 223 superposed on map of devastated area (fig. 219). For this superposition, vent diameter used was 1 km, vent was placed at the 8,000-ft contour north of old summit of mountain and was oriented 5° east of due north.

this distance, to about 11 km, the pressure dropped below ambient because the overexpansion created a stable low-pressure core within the blast flow. The existence of this low-pressure zone may explain why vehicle windows in some parts of the devastated area exploded (Bea Johnston, University of Washington, oral commun., 1980) rather than imploded.

If there had been no admixture of cold organic or rock debris as the flow advanced outward from the volcano, the temperature of the flow would have remained relatively high, owing to the buffering of the gas temperature by the heat content of the included solids; the temperature would have dropped only 20 percent, from the initial temperature of 600K (327°C) to 480K (207°C) at the singed zone. These calculated temperatures agree remarkably with temperatures deduced by Davis and Graeber (1980) from material degradation within the devastated area.

The density distribution in the flow, shown in figure 224, suggests the mechanism by which the range of the flow was determined, a mechanism that explains the observed pecularities of the transition zones discussed in the section on "Observations of the blast and its effects to be addressed by the model." Consider first the likely density of the atmosphere in the vicinity of the mountain as the quasisteady flow modeled here became established. This flow regime followed the landslide and the unsteady flow front, and overrode its own basal shear layer; field evidence and theoretical considerations suggest that the part of the flow modeled here as steady flow outdistanced the slide and the unsteady front. In fact, it is conceivable that late stages of the flow overtook early stages, because deeper material tapped later was presumably hotter and, therefore, would expand with higher velocities. In spite of the fact that the atmosphere would have been heated by passage of the initial pressure wave in it (Appendix 2) and, therefore, would have had a density decrease of a few percent, dust ladening due to the landslide and the early stages of unsteady flow would have caused a substantial density increase. The most energetic part of the blast would either have been following the blast's dusty precursors or approaching an atmosphere with an enhanced density: an atmosphere having a density between its normal value (for example, to the west, the direction from which the prevailing winds came) and a value increased by a factor of two, three, or even five (for example, to the east, where the winds might have carried dust, or where previously erupted blast material had arrived) is plausible. As the flow expanded into this atmosphere, the density of the flow continually decreased until the density became less than that of the atmosphere (or flow) in front of it. The flow therefore simply lifted from the ground and ramped upward into the atmosphere, thus being "stood up" in the words of eyewitnesses (Rosenbaum and Waitt, this volume). Because it lifted nearly vertically, rather than dispersing laterally, the width of the transition zones and the sharpness of the boundaries depended on the topography. At areas where the topography dropped away under the rising blast cloud, the transition zones are narrow and sharply demarked, whereas where the topography rose subparallel to the rising blast, the zones were wider and less clearly defined. The close agreement of the contour where the density of the flow was two times atmospheric density ($M = 3.68$ contour) with the actual boundary of the devastated area (fig. 224) suggests that hazard zones for such flows may ultimately be predictable. Limiting factors for predictive accuracy will be knowledge of reservoir conditions and of processes at the boundary of the flow atmosphere.

DIRECT AND CHANNELIZED BLAST ZONES

Reflection of the expansion waves from the flow boundaries into compressive waves that ultimately coalesced into the intercepting shocks probably produced a Mach disk shock about 11 km north of the vent. The flow on the upstream side of this disk would have been supersonic, and the flow on the downstream side, subsonic. It is proposed here that the boundary between the direct blast zone and the channelized blast zone in the region north of the vent marks the position of the Mach disk shock, and that possibly the boundaries on the east and west represent the positions of the much weaker intercepting shocks (fig. 224). This inference is based not only on the coincidence of the model shock boundaries and the map boundary between the direct and channelized blast zones, but also on the fact that supersonic flows are not deflected by the topography in the same way as subsonic flows and, therefore, should leave different patterns of downed trees in relation to

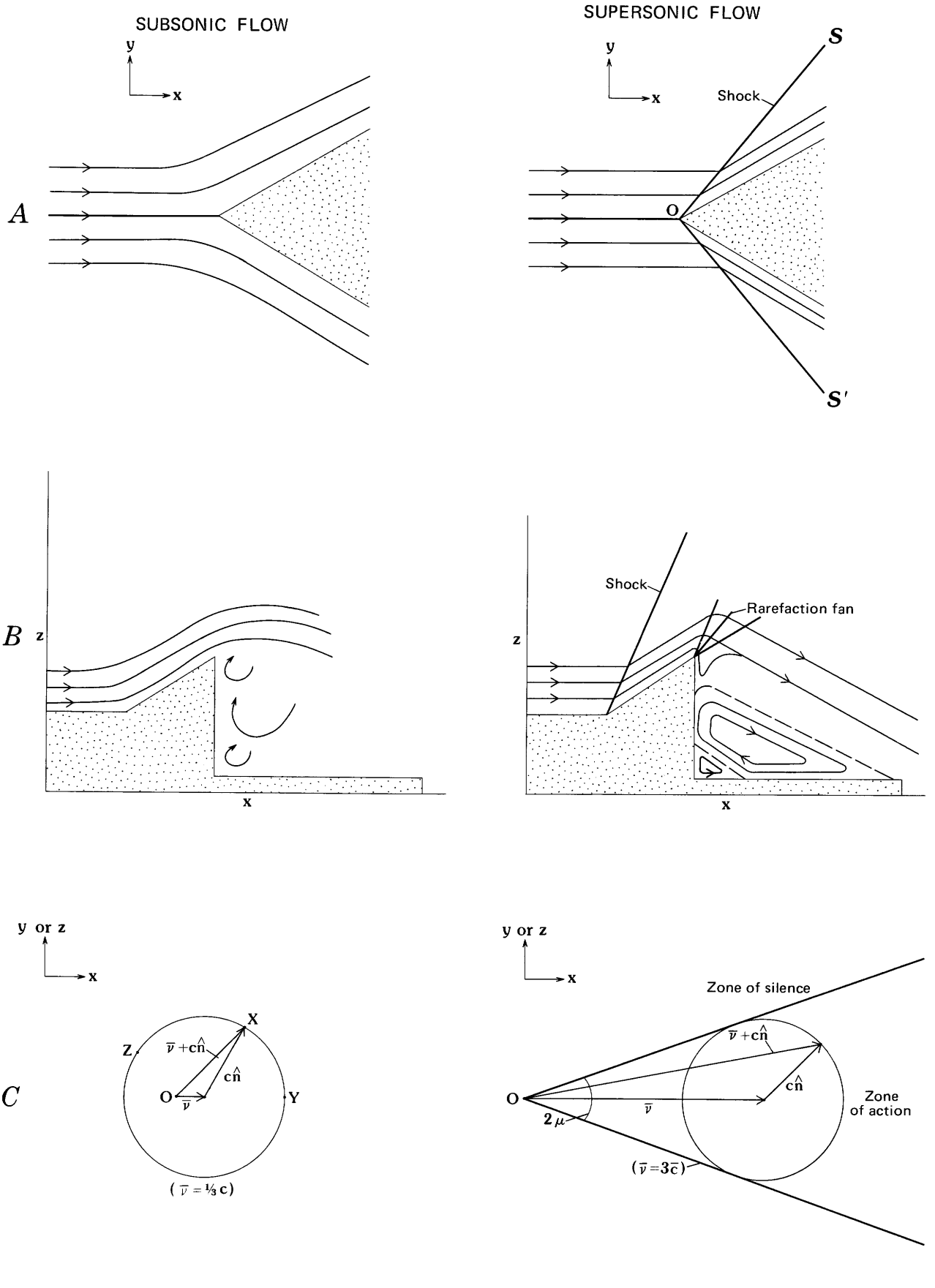
SUBSONIC FLOW
y
x
A
SUPERSONIC FLOW
y
x
Shock
S
O
S′
B
z
x
Shock
Rarefaction fan
z
x
y or z
x
C
X
Z
$\bar{v}+c\hat{n}$
$c\hat{n}$
O
$\bar{v}$
Y
$(\bar{v}=\frac{1}{3}c)$
y or z
x
Zone of silence
$\bar{v}+c\hat{n}$
$c\hat{n}$
O
$\bar{v}$
2μ
Zone of action
$(\bar{v}=3\bar{c})$

topographic features, patterns that are consistent with the proposed boundaries.

Compare first the lateral deflection of supersonic and subsonic streamlines by topographic features, such as valleys. As shown in figure 225*A*, subsonic flow is diverted smoothly around obstacles because signals of the obstacle's presence are propagated upstream into the flow. However, supersonic flow is diverted around obstacles through shock waves that are oriented downstream from the flow, because signals of the obstacle cannot propagate upstream. Because of the time and distance needed for temporal or spatial disturbances to propagate into supersonic flow, it tends to be less affected by complex terrain than subsonic flow. Thus, the generally radial nature of the streamlines, in spite of large topographic features within the direct blast zone, is consistent with supersonic flow, and the more topographically controlled shape of the streamlines within the channelized blast zone is consistent with subsonic flow.

Although in map view a supersonic flow may be relatively unaffected by the topography, a vertical cross section shows more influence of topography because the basal boundary-layer is strongly affected. Supersonic and subsonic boundary layer flow is shown schematically in figure 225*B*. The felled-tree reversals that occur at places like Fawn Lake (fig. 220*B*), although not qualitatively inconsistent with subsonic flow, are compatible with supersonic boundary-layer behavior. As such tree-reversal patterns are predominant in the direct blast zone and are less common in the channelized blast zone, the patterns are consistent with the concept of transition from supersonic to subsonic flow across the Mach disk shock at the boundary between the two zones.

ACOUSTIC PROPERTIES OF THE BLAST

Within the expanding blast flow, a forest was being uprooted and destroyed, soils were being ripped from the ground, and boulders, trees, and glacial ice blocks were being mixed and transported kilometers from their source; yet, the blast approached eyewitnesses with amazing silence. There were two causes of this silence: first, supersonic focusing of sounds in a downstream direction, and second, strong attenuation of sound by the multiphase particulate cloud. Consider the propagation of sound within supersonic and subsonic flow, as illustrated in figure 225*C*. In

Figure 225.—Comparison of subsonic and supersonic flows. A, Schematic map view of subsonic and supersonic flow past a wedge-shaped obstacle, such as the toe of Harrys Ridge west of Spirit Lake. In subsonic flow, the disturbance of the obstacle is propagated upstream so that flow is deflected smoothly around obstacle. In supersonic flow, the disturbance cannot be propagated upstream and is confined to zone of action discussed in the text; therefore, the flow is deflected discontinuously upon reaching the shocks SO and S'O. Because of these differences, in map view, supersonic flow may appear less responsive to variations in terrain. B, Vertical cross section of subsonic and supersonic boundary-layer flow from a level area on left, up a hill, and over a vertical wall; an example is the approach of the blast to and over the Fawn Lake cirque (fig. 220B). Subsonic flow of a fluid over this geometry shows smooth transition in flow direction up the slope and usually results in separation of the streamlines from boundary and formation of eddies. Supersonic flow over same geometry differs in having a shock at base of slope, an expansion fan emanating from top of wall, and one or even two eddies in lee of wall. Dashed lines, flow separation layers. This flow pattern could explain tree blowdown pattern at Fawn Lake. Subsonic flow sketch modified from Batchelor, 1967; supersonic sketch modified from Kayser and Danberg, 1974. C, Diagram showing the spreading of sound waves in subsonic and supersonic flow (modified from Landau and Lifshitz, 1959). The subsonic case is illustrated for a flow velocity, v, equal to 1/3 of the sound speed, c; the supersonic case, for $v = 3c$. In each case, a sound pulse is emitted when the fluid is at 0. In a unit time, the fluid travels a distance shown by the vector $\mathbf{v}$, *and the sound pulse travels a distance* $\mathbf{v} + c\mathbf{n}$, *where* $\mathbf{n}$ *is the unit normal in any direction. All possible values of* $\mathbf{v} + c\mathbf{n}$ *are obtained by placing one end of the vector* $\mathbf{v}$ *at 0, and drawing a sphere (circle) of radius c centered at the other end. The vectors from 0 to points on the sphere give the possible magnitudes and directions of the sound waves. If* $v < c$, *then the* $\mathbf{v} + c\mathbf{n}$ *can have any direction in space relative to the source of the sound, as points X, Y and Z illustrate. If* $v > c$, *the vector* $\mathbf{v} + c\mathbf{n}$ *can only lie within a cone of solid angle* 2μ. *Thus, a disturbance starting from any point in a supersonic flow is focused forward.*

subsonic flow, sound pulses generated within the flow (for example, at O) travel downstream faster than the flow itself advances and, therefore, will eventually reach all external points, such as X, Y or Z. However, in supersonic flow, sound pulses propagate downstream only within a cone, called the Mach cone, whose angle is given by

$$\mu = \sin^{-1}\left(\frac{1}{M}\right). \tag{12}$$

M is the Mach number of the flow, the ratio of the flow velocity to the local sound speed. Von Karman (1947) called the region inside the Mach cone the "zone of action" and the region outside of it, the "zone of silence." Assuming Mach numbers of 2 to 3 (fig. 224), the above equation shows that sound should have been strongly focused within $\pm 20°$ to $\pm 30°$ of the local direction of streamlines. Thus, observers not on or close to streamlines would have been in the zone of silence.

Even observers in line with the flow, or embedded in it, would have heard little because of the strong attenuation of the dense particulate cloud. For reference, in clear air, sound is attenuated by viscous dissipation and irreversible heat flow as the pressure oscillations of the sound waves propagate. The attenuation (fraction of energy lost per unit distance traversed) is (Morse and Ingard, 1968):

$$2\alpha \cong \left(\eta + \frac{4}{3}\mu\right)\frac{k^2}{\rho c}\left[1 + \frac{K}{C_P}\frac{\gamma - 1}{\eta + \frac{4}{3}\mu}\right] \tag{13}$$

where η is the coefficient of bulk viscosity, μ is the coefficient of viscosity, k is the wave number, ρ is the density, c is the sound speed, K is the thermal conductivity, C_P is the specific heat at constant pressure, and γ is the isentropic exponent of air, and α is the attenuation coefficient. At a typical acoustic frequency of 1,000 cps (cycles per second), the attenuation coefficient α for clear air is approximately 3×10^{-7}/cm (Morse and Ingard, 1968). Therefore, sound is attenuated to 1/e of its strength (where e is the base of natural logarithms, 2.72) in a distance of roughly 10 km. If the air is filled with a cloud of small particles, acoustic energy is both scattered and absorbed by the particles. Although both processes contribute to the attenuation (as well as others not considered here), absorption was the more important factor in the blast at Mount St. Helens.

The attenuation coefficient for absorption by the cloud is (Morse and Ingard, 1968)

$$2\alpha = N\Sigma_a \tag{14}$$

where N is the number of scattering particles per unit volume, and Σ_a is the absorption cross section per scatterer, given by

$$\Sigma_a \cong 2\pi a^2\left(\gamma - 1\right)kd_h + \frac{4}{3}\pi a^2\left(\gamma_\rho'\right)kd_v \tag{15}$$

where a is the particle radius, γ is the isentropic exponent of the gas phase, k is the wave number, γ_ρ' is a density ratio [$\gamma_\rho' = (3\rho_e - 3\rho)/(2\rho_e + \rho)$, where ρ_e is the density of the entrained particles, and ρ is the air density], and d_h and d_v are, respectively, thermal and viscous boundary layer thicknesses:

$$d_v = 2\mu/\rho\omega \tag{16}$$

$$d_h = 2K/\rho\omega C_P \tag{17}$$

where μ, K, and C_P were defined above, and ω is the angular frequency of the acoustic wave.

Consider the attenuation in the distal edges of the blast where some eyewitnesses survived. Assume, from figure 224, that the density of the blast in these regions was about 10 times atmospheric density. Assume, also, that the particles were 0.01 cm radius. These assumptions require about 1,000 particles/cm^3. Then, using typical values of the parameters, $\gamma = 1.4$, $k = 0.19$/cm, $\gamma_\rho' = 3/2$, the absorption cross section per scattering particle was

$$\Sigma_a = 1.5 \times 10^{-6}\text{cm}^2, \tag{18}$$

and the attenuation coefficient of the blast in this region was

$$\alpha = N\Sigma_a \sim 0.7 \times 10^{-3}/\text{cm}. \tag{19}$$

Additional attenuation would have arisen from particulate scattering, and from absorption and scattering by turbulent cells within the flow. Thus, sound intensity would have decreased to 1/e of its intensity in less than 10 m, an attenuation more than 10,000 times that of clear air.

DURATION, FLUX, AND ENERGY OF THE BLAST

Duration of the blast cannot be inferred from steady-state flow considerations, and, although the above steady-flow model may well explain spatial observations, it cannot be used to infer temporal relations. The blast duration may have been quite different at different places within the devastated area. Unsteady flow considerations suggest a duration of 10–20 s at the vent.

The mass flux per unit area during steady flow implied by the model is 0.6×10^4 g/s/cm^2 or, for a vent area of 0.25×10^{10} cm^2, the mass flux was 0.15×10^{14} g/s. These values may be maximum fluxes. The thermal-energy flux per unit area was 2.5 MW/cm^2, or the thermal flux was 0.63×10^{10} MW for the assumed vent area. The total mass in the blast (0.25×10^{15} g) would have been discharged through the vent in 17 s of steady flow. The brevity of this time implies that much of the flow was unsteady and that accurate models of the blast based on unsteady flow must be developed.

From the measured mass ejected and the assumed initial temperature of 600K, the total thermal energy released upon cooling to ambient temperature (273K) was 10^{24} ergs or 24 Mt, of which 7 Mt was released during the propagation of the blast through the devastated area, and 17 Mt during penecontemporaneous condensation of the steam and cooling of the condensed water and entrained solids.

REFERENCES CITED

Barclay, F. J., Ledwedge, T. J., and Cornfield, G. C., 1969, Some experiments on sonic velocity in the phase one-component mixtures and some thoughts on the nature of two-phase critical flow: Institute of Mechanical Engineering, Proceedings, v. 184, p. 185–194.

Batchelor, G. K., 1967, An introduction to fluid dynamics: London, Cambridge University Press, 615 p.

Davis, M. J., and Graeber, E. J., 1980, Temperature estimates of May 18 eruption of Mount St. Helens made from observations of material response [abs.]: EOS, v. 61, no. 46, p. 1136.

JANNAF [Joint Army, Navy, NASA, Air Force], 1975, JANNAF handbook of rocket exhaust plume technology: Chemical Propulsion Information Agency Publication 263, Chap. 2 [237 p.].

Kayser, L. D., and Danberg, J. E., 1974, Experimental study of separation from the base of a cone at supersonic speeds: American Institute of Aeronautics and Astronautics Journal, v. 12, no. 11, p. 1607–1609.

Kieffer, S. W., 1977, Sound speed in liquid-gas mixtures—water-air and water-steam: JGR—Journal of Geophysical Research, v. 82, no. 20, p. 2895–2904.

Landau, L. D., and Lifshitz, E. M., 1959, Fluid mechanics: Oxford, Pergamon Press, 536 p.

Malone, S. D., Weaver, Craig, and Endo, Elliot, 1981, Seismic details of the May 18, 1980 cataclysmic eruption of Mount St. Helens [abs.]: EOS, v. 62, no. 6, p. 62.

Morse, P. M., and Ingard, K. U., 1968, Theoretical acoustics: New York, McGraw Hill, 927 p.

Nairn, I. A., 1976, Atmospheric shock waves and condensation clouds from Ngauruhoe explosive eruptions: Nature, v. 259, no. 5540, p. 190–192.

Pack, D. C., 1948, On the formation of shockwaves in supersonic gas jets: Journal of Mechanics and Applied Mathematics, Section B, v. 1, p. 1–17.

Reed, J. W., 1980, Air pressure waves from Mt. St. Helens eruptions: EOS, v. 61, no. 46, p. 1136.

Shapiro, A. H., 1953–54, The dynamics and thermodynamics of compressible fluid flow: New York, Ronald Press Co., 2 v., 1185 p.

Thompson, P. A., 1972, Compressible fluid dynamics: New York, McGraw-Hill, 665 p.

Von Karman, Theodore, 1947, Supersonic aerodynamics—principles and applications: Journal of Aeronautical Sciences, v. 14, no. 7, p. 373.

Wallis, G. B., 1969, One-dimensional two-phase flow: New York, McGraw-Hill, 408 p.

Young, G. A., 1965, The physics of the base surge: U.S. Naval Ordnance Laboratory, Silver Spring, Md., report NOLR 64-103, 294 p.

APPENDIX 1

PRECURSOR, VAPORIZATION, AND MULTIPHASE EXPANSION WAVES

The discussion of the initiation of the eruption has ignored a number of details that are important in explaining observed phenomena at the beginning of the blast. For example, the discharge did not begin immediately at the appearance of the landslide scarp. Nearly 20 s elapsed between the time of the first appearance of an exposed scarp and the first appearance of the puffs of dust and steam that heralded the blast (Moore and Albee, this volume; Malone and others, 1981; Voight, this volume). This delay could have indicated that the material immediately adjacent to the exposed scarp did not contain volatile components

and that tapping of a deeper reservoir may have been necessary (with the delay due to the migration of the volatiles through the overlying drier material). However, even if the reservoir were immediately adjacent to the exposed scarp, a delay in discharge is to be expected, due to the time required for a series of finite-amplitude expansion waves to establish the blast flow. The complex expansion process that actually occurred can be simplified conceptually by dividing it into three separate processes that are initially necessary for establishment of the flow. First, a precursor rarefaction wave must reduce the pressure of the system locally to the pressure of the saturation curve; second, a vaporization wave must accomplish the transformation from liquid water to steam (or nucleation and growth of a vapor phase from other dissolved gases or a magma if the gases are abundant); and third, a multiphase expansion wave must accelerate the vapor and particles together out of the vent. This multiphase expansion wave would actually spread further into two components, a frozen expansion wave of the vapor phase alone (the solid particles temporarily immobile because of inertial effects), and an equilibrium wave in which the particles move with the expanding gases. The effects of these two waves were visible in the March and April phreatic eruptions, in which the eruption was frequently heralded by puffs of clear white steam (accelerated by the frozen expansion), followed by the development of the ash-laden plume (accelerated by the equilibrium wave).

Few data are available on the speed of such finite amplitude rarefaction waves in such complex mixtures. The precursor rarefaction wave is assumed to have moved into a water-saturated hydrothermal system or into an undersaturated magma, and, therefore, is assumed to have had a speed of about 1 km/s. The velocity of a finite amplitude vaporization wave, even in pure H_2O at 12.5 MPa, is not known, but it is reasonable to assume that it is about 50 m/s, about half of the equilibrium sound speed of small-amplitude sound waves at that pressure (Kieffer, 1977; Barclay and others, 1969). The velocity of the equilibrium multiphase expansion wave was calculated in the text (equation 5), and was shown to have been about 100 m/s.

The flow would not become established until this series of transient waves had passed into the reservoir and been reflected back at least once (Shapiro, 1953–54). The development of the discharge would be controlled by the slowest process, that of the nucleation and formation of the vapor phase. For expected vaporization-wave velocities of 50 m/s and reservoir depth of about 500 m, a time on the order of 10 s from the exposure of the scarp to the development of the flow is not unreasonable, just due to the transient dynamic processes necessary to establish the flow.

APPENDIX 2

SIMPLIFIED MODEL FOR THE EFFECT OF THE BLAST ON THE NEAR-FIELD ATMOSPHERE

Available estimates of pressure, temperature, and wind velocity in the atmosphere in front of the approaching blast provide constraints on the blast dynamics. A more detailed model than the one presented here, particularly of the near-field to far-field acoustic propagation, has been reported by Reed (1980).

Consider the initial phase of the Mount St. Helens eruption to have had two stages: (1) the slip and subsequent motion of the landslide toward the North Fork Toutle River drainage; and (2) at a later time, t_o, (about 20 seconds), the eruption of the blast, having an initial velocity, v_o, of about 100 m/s, (equation 6) and expansion to about 300 m/s (fig. 224). In order to calculate the effect of the motion of the landslide and the blast on the atmosphere, consider both the slide and the blast to be rigid bodies (an approximation justified in the early stages of the eruption by the fact that the impedances (ρc) of the slide [$(\rho c)_{\text{slide}} \sim 10^5$] and of the blast [$(\rho c)_{\text{blast}} \sim 10^4$] are much greater than of those of air [$(\rho c)_{\text{air}} \sim 3 \times 10^3$)]). Assume that the motion of the landslide can be described by

$$s = \left(\frac{1}{2} g \sin \bar{\theta} - \frac{1}{2} \mu g \cos \bar{\theta} \right) t^2, \qquad \bar{\theta} = 11^\circ \quad \text{(A1)}$$

where s is the distance traveled, g is the gravitational acceleration, $\bar{\theta}$ is the average angle of the slope across which it moved, $\mu = 0.12$ is the coefficient of friction, and t is the time after the initiation of motion. The

velocity of the slide is given by

$$v = (g \sin \bar{\theta} - \mu g \cos \bar{\theta})t^2, \qquad \bar{\theta} = 11° \quad \text{(A2)}$$

and is assumed to have been a maximum when the slide arrived at the North Fork Toutle River drainage, 4.95 km from its point of origin. From equation A1, the time of arrival of the slide at the North Fork Toutle River would have been 114 s after inception of motion, and from equation A2, the velocity at this time would have been 87 m/s. Compression waves were propagated from the landslide into the atmosphere from the instant of its first motion; ultimately, they would have coalesced to give an atmospheric shock. It can be calculated (Thompson 1972, p. 401) that in a uniform atmosphere, the shock would have formed at a distance s^* given by

$$s^* = \frac{c_o^2}{(\gamma+1)A} \quad \text{(A3)}$$

at a time t^* given by

$$t^* = \frac{c_o}{(\gamma+1)A}, \quad \text{(A4)}$$

where A is related to the acceleration by

$$A = \left(\frac{1}{2} g \sin \bar{\theta} - \frac{1}{2} \mu\, g \cos \bar{\theta}\right). \quad \text{(A5)}$$

For $\bar{\theta}$ taken as 11° (the average slope across which the slide traveled from 6,400 ft to 3,200 ft elevation), the shock would have formed 123 km from the origin, and 367 s after the beginning of the slide.

By analogy to the pressure built up in front of an airplane wing, the pressure P_o in front of the moving wedge of debris was

$$\frac{P_o}{P_\infty} = \left[1 + \frac{(\gamma-1)v^2}{2c_{air}^2}\right]^{\frac{\gamma}{\gamma-1}}, \quad \text{(A6)}$$

where γ is the adiabatic exponent of air, and c_{air} is the speed of sound in air, 335 m/s. The far-field atmospheric pressure, P_∞, is taken as 8.7×10^4 Pa (0.87 bar). Thus, the pressure was 0.910×10^5 Pa (0.91 bar) at the North Fork Toutle River drainage, corresponding to an overpressure of 4.0×10^3 Pa (0.040 bar). As a first approximation, assume that the pressure decay was proportional to $1/r^3$ (that is, due to spherical divergence alone), and assume that the overpressure was produced inside of the radius $r_o = 5$ km from the summit. Then, at the nearest barograph at Toledo, Wash., 54 km from the summit, or about 50 km from the source of the overpressure, the overpressure would have been about 3 Pa (3.0×10^{-5} bar), and at Seattle, 150 km from the mountain, the overpressure would have been only about 0.1 Pa (0.1×10^{-5} bar). The overpressure due to the landslide would barely be detectable on the Toledo barograph and would not have been audible in Seattle (15 Pa (1.5×10^{-4} bar) is considered the minimum overpressure for audible detection). A higher coefficient of friction and(or) stronger attenuation, both likely, would have rendered the atmospheric perturbation due to the landslide undetectable, and I conclude that the landslide was not the cause of the Toledo (or any other far-field) barograph deflection or audible noise.

The blast started about 20 s later than the landslide (Moore and Albee, this volume; Malone and others, 1981; Voight, this volume) and had an initial vent velocity of about 100 m/s and a calculated maximun areal expansion of 325 m/s. I assume that the shock audible at distances greater than 54 km (Toledo) was produced as the highest velocities were obtained (that is, that shocks produced at lower velocities were inaudible, were overtaken by the stronger shock, or both). I further assume that the acceleration to the highest velocities was produced over the same distances as given by the steady-state solution (figs. 223 and 224). The acceleration is then given by

$$a = \frac{dv}{dt} = \frac{dv}{dx}\frac{dx}{dt}. \quad \text{(A7)}$$

Assuming that at least locally,

$$x = \frac{1}{2} a t^2 \quad \text{(A8)}$$

then, equations A3 and A4 can be applied to give the distance and time of shock formation, with the coefficient $A = \frac{1}{2}a$. From the steady-state solution, the acceleration from $M^* = 2.79$ to $M^* = 3.09$ (from 290 m/s to 321 m/s) occurred over 6,080 m, giving an acceleration of 155 cm/s² and a coefficient $A = 78$ cm/s². The

shock would then form 60 km from the region of acceleration, which was 12 km from the old summit; that is, the shock would have formed about 72 km from the old summit. This distance for shock formation satisfies observational constraints that the shock formed somewhere between Toledo (54 km) and Seattle (150 km). From equation A6, the pressure in front of the blast as it reached 325 m/s would have been 1.6×10^5 Pa (1.6 bars), corresponding to a peak-to-peak barograph deflection of 1.54×10^3 Pa (0.015 bar), about twice that inferred from Reed's (1980) data, at Toledo, 54 km from the old summit. These values should be considered in satisfactory agreement in view of (1) the use of a one-dimensional equation to calculate the distance of shock formation; (2) the assumption of a homogeneous atmosphere; (3) the assumption of a $1/r^3$ divergence; and (4) the fact that 325 m/s is an upper limit on actual velocities. A more detailed treatment treating actual propagation paths for the compressive waves has been given by Reed (1980).

Temperature changes induced in the atmosphere by the blast front would have been quite mild. Within the first few kilometers, where the blast cloud was sufficiently more dense than the atmosphere to have acted as a rigid wedge, temperature changes were approximately given by

$$T_{\text{transient}} - T_{\text{atmosphere}} = \frac{V^2}{2C_P}, \tag{A9}$$

where T is the temperature, V is the wedge velocity, and C_P is the specific heat of air, about 10^7 ergs/g/K. For velocities of about 200 m/s close to the mountain, the temperature change would have been about 20°C, perhaps sufficient to cause index of refraction changes and, thus, the observable atmospheric disturbance ahead of the blast reported by some eyewitnesses (Rosenbaum and Waitt, this volume). As the density of the blast decreased, it was less capable of causing high pressure, temperature, and velocity perturbations in the atmosphere and, therefore, even though increasing in speed itself, did not generate significant atmospheric temperature effects.

These calculations, although based on greatly simplified assumptions, show that the model conditions for the blast dynamics are at least consistent with the observational data available.

THE 1980 ERUPTIONS OF MOUNT ST. HELENS, WASHINGTON

ORIGIN AND STRATIGRAPHY OF THE DEPOSIT PRODUCED BY THE MAY 18 DIRECTED BLAST

By RICHARD P. HOBLITT, C. DAN MILLER, *and* JAMES W. VALLANCE

ABSTRACT

On May 18, 1980, a catastrophic directed blast from Mount St. Helens devastated a broad area northwest, north, and northeast of the volcano. The deposit formed by the blast thins overall, from more than 1 m near the source to less than 1 cm near the margin of the devastated area. At any given distance from the volcano, it is thinner on valley sides and thicker in topographic lows than on ridge crests. The blast deposit includes the following five main units (from bottom to top): (1) The basal unit is friable, massive, and at some places normally graded; it consists of blocks, lapilli, and ash in which abundant shredded wood and preexisting soil are concentrated near the base. This unit is the coarsest part of the blast-deposit sequence. (2) On ridge crests between about 8 and 15 km north of the volcano, the basal unit is overlain by a massive unit that consists of lapilli in an ash matrix. (3) The massive unit is overlain by a layer of lapilli and ash that has sand-wave or plane-parallel bedding; it is referred to as the pyroclastic-surge unit. This unit forms irregular hummocks and transverse dunes between about 9 and 22 km northwest of the volcano. (4) A nonstratified pyroclastic-flow unit of lapilli and ash, which was derived from the directed-blast cloud, forms fill deposits in topographically low areas. (5) The topmost unit is a normally graded, coarse to fine ash that is rich in accretionary lapilli.

At least half of the clasts in the blast deposit are prismatically jointed, gray microvesicular dacite whose mean maximum size decreases exponentially with distance from the volcano. These clasts clearly are a juvenile component of the blast deposit derived from the cryptodome that formed in the volcano during March, April, and May.

The overall normally graded nature of the blast deposit and the progressive decrease in size of juvenile clasts away from the source suggest gravity settling within and deposition from a single, rapidly moving, inflated cloud containing blocks, lapilli, and ash. Following passage of the flow front and deposition of the basal, massive, and surge units, the trailing lower velocity, lower density portion of the cloud began to deflate and thus increased its density. The deflating cloud settled into topographic lows where the particles eventually became sufficiently concentrated for pyroclastic flows to form. Once the coarse-grained fraction was mostly settled and kinetic energy was largely spent, the remaining gas phase cooled to the point that water vapor began to condense. The ash particles still in suspension in the dilute upper parts of the blast cloud adhered to moisture droplets and formed accretionary lapilli.

The blast deposit has three principal characteristics that appear to be diagnostic of origin by directed blast: (1) the deposit is relatively thin and has a wide distribution that is insensitive to topography, (2) the basal unit has characteristics that are different from those of deposits that originated by pyroclastic fall, pyroclastic flow, and pyroclastic surge, and (3) the similar areal extent of stratigraphic units with diverse characteristics and evidence that they were emplaced in rapid succession show that the units were produced by a single event; their collective characteristics indicate that they could have been formed only by a cloud of volcanic-rock debris moving laterally across a broad sector at high speed.

INTRODUCTION

On the morning of May 18, 1980, an extremely destructive and poorly understood volcanic phenomenon—a laterally directed explosion—occurred at Mount St. Helens, Wash. This event was observed and, in some cases, photographed by witnesses at many points around the volcano (Rosenbaum and Waitt, this volume); consequently, it may well be the best documented event of its kind. Gorshkov (1963) has termed such an explosion a "directed blast." We adopt Gorshkov's "directed blast" here as a convenient term for an event that produced a variety of deposit types. Collectively, these deposits cannot be attributed to any single known depositional process. Strata displaying features normally attributed to pyroclastic fall, flow, and surge are present. In addition, one unit has features that cannot be readily explained by any previously described process.

Directed blasts typically devastate large areas (10^2–10^3 km^2) and kill essentially all above-ground life within these areas (Lacroix, 1904; Gorshkov, 1959). Because of its great destructive potential, the directed-blast phenomenon must be considered in volcanic-hazards assessments of potentially explosive volcanoes.

The best guide to the future activity of a dormant volcano is the record of its past behavior. Few

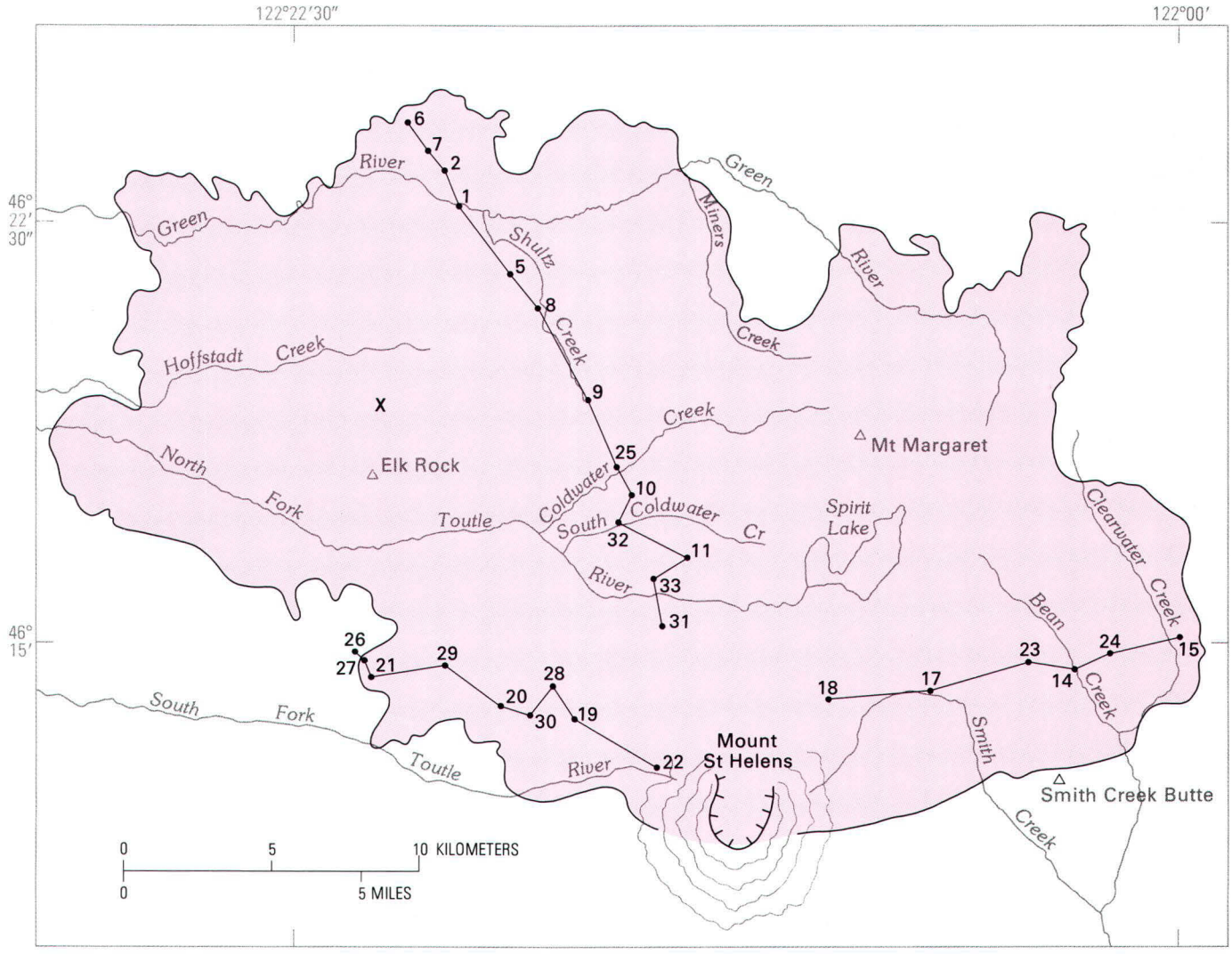

Figure 226.—Area covered by deposit of directed blast (in red; from Moore and Sisson, this volume) showing west, northwest, and east sample traverses and study sites. **X**, *location of section shown in figure 227. Drainages shown are pre-May 18.*

Figure 227.—Blast-deposit section showing four units: a, *basal;* b, *surge;* c, *pyroclastic flow; and* d, *accretionary lapilli. Location shown on figure 226.*

volcanoes have an adequate record of historic eruptive activity, and so it is necessary to rely on the record preserved in the products of prehistoric eruptions. The value of such a depositional record, however, is no better than our ability to interpret it correctly. The eruption of May 18 provided us with the opportunity to examine a deposit that was unequivocally the product of a directed blast and that was fresh, unvegetated, and accessible.[1] Accordingly, we began a study whose main purpose was to determine the stratigraphy and other characteristics of the deposit so that deposits of similar origin might be more readily recognized elsewhere in the geologic record. This paper presents our initial data, criteria for recognizing deposits from directed blasts, and inferences concerning the processes that produced the blast deposit at Mount St. Helens.

The area devastated by the directed blast, about 600 km² (fig. 226), is blanketed with an unconsolidated stratified deposit composed of several recognizable units. Throughout this area, trees have been blown over or topped or scorched.

The blast deposit was studied in detail at sites along three traverses radial to the volcano (fig. 226). To examine deposits emplaced in similar depositional environments, we selected sites on relatively flat surfaces on or near successive ridgetops or valley bottoms. Most sites are on roads in areas from which trees have been removed either by the blast or by logging operations prior to the eruption. At each site, at least one vertical-walled trench was dug through the entire deposit; the trench alinement was normal to any dune ridges evident on the surface. We then examined individual units within the blast deposit and sampled each one for laboratory grain-size analysis. At each site, a suite of the largest clasts of a distinctive gray dacite was also collected. In addition, the blast deposit was examined at many other sites not along the three principal traverses.

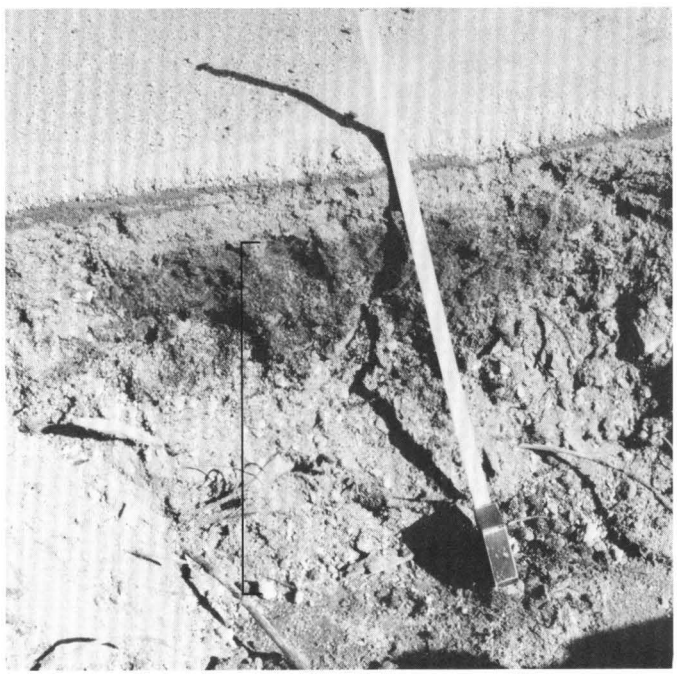

Figure 228.—Blast-deposit section showing well-developed basal unit (bracket) at location 30 on west traverse (fig. 226). Note wood-rich, nonstratified nature of deposit. Centimeter tape shown for scale.

[1]Study of these deposits during a period of intermittent eruptions in the summer and fall of 1980 was made possible by the use of helicopters in conjunction with volcano-monitoring and radio-communication systems. Thus, we had access to otherwise inaccessible areas and were immediately warned of the need to evacuate hazardous areas.

ACKNOWLEDGMENTS

We wish to thank the U.S. Forest Service (USFS) staff at Gifford Pinchot National Forest for providing personnel, equipment, and logistic support to the U.S. Geological Survey during our investigation. Fieldwork near the volcano was much safer because of USFS communications equipment and aerial surveillance. We thank David Gibney and other USFS observers for their vigilance. We extend special thanks to the University of Washington/USGS seismic research group for their continuous monitoring of Mount St. Helens seismicity and for their prompt advisories of seismic events. We thank Janis Markman for conscientious performance of her duties as helicopter dispatcher. Able assistance in the field and photographic skills were provided by Terry Leighley. Investigations near the volcano after May 18 could not have been accomplished without helicopter support. We are especially grateful to pilots Michael Montgomery, Michael Holtsclaw, Bob Edwards, David Kaplan, and Warren Fortier for their skills, cooperation, and enthusiasm. We dedicate this report to our friend and colleague David Johnston.

BLAST DEPOSIT

Photographs of the May 18 event show that failure of the north slope of Mount St. Helens generated a massive debris avalanche (Voight, this volume). A horizontally directed blast cloud appeared a few seconds after the avalanche started and overrode the avalanche before it reached the ridge crest north of North Fork Toutle River valley. Stratigraphic relations of the resulting avalanche and blast deposits confirm this sequence and, in addition, indicate that the directed blast persisted after deposition of the avalanche debris. The stratigraphic relation between the two deposits varies laterally and is locally complex. Nonetheless, the deposits produced by the two processes generally can be differentiated with confidence. In this paper, "blast deposit" refers only to the sequence of strata deposited by the directed-blast cloud.

DISTRIBUTION

The directed blast devastated a rugged mountainous area and blanketed all but the steepest slopes with unconsolidated debris. The blast deposit forms a thin layer that has a wide areal extent (about 600 km^2) in spite of multiple transverse topographic barriers, some of which are higher than 600 m. Only the Mount Margaret region—the most massive topographic feature in the devastated area—had an appreciable effect on the extent (fig. 226). The blast deposit thins with increasing distance from the source, and, at any given distance from the volcano, is thinner on slopes and thicker in topographic lows than it is on ridge crests. With the exception of the uppermost, finest grained unit, the blast deposit terminates at the outer edge of the devastated zone.

Prior to May 18, much of the affected area was covered with a mature conifer forest that was composed predominantly of Douglas fir, true fir, hemlock, and cedar. Trees 1 m in diameter were abundant, and others with trunks as much as 2 m in diameter were not uncommon. Clearcut logging had produced a patchwork of logged and forested areas that was interconnected by a labyrinth of logging roads.

The blast cloud killed nearly every tree and most other living things in its path. Three damage zones are recognizable (pl. 1): (1) a zone nearest the mountain in which trees are absent, though some stumps remain; (2) a zone in which trees are topped, broken off near the base, or uprooted (this zone includes nearly all of the devastated area); and (3) a zone between downed trees and apparently unaffected forest in which the trees are scorched and many are dead, but still standing.

STRATIGRAPHIC UNITS

Five main units are recognized in the blast deposit, though all five were not seen in the same stratigraphic section; generally, only three or four units (fig. 227) are present at any one location. The stratigraphic units of the blast deposit are described sequentially, beginning with the lowest unit.

THE BASAL UNIT

The basal unit (fig. 228) consists of friable grain-supported rock debris that encloses abundant organic matter. Near the volcano the debris is composed primarily of blocks, lapilli, and coarse ash; near the blast margin it is composed mostly of coarse ash and few lapilli.

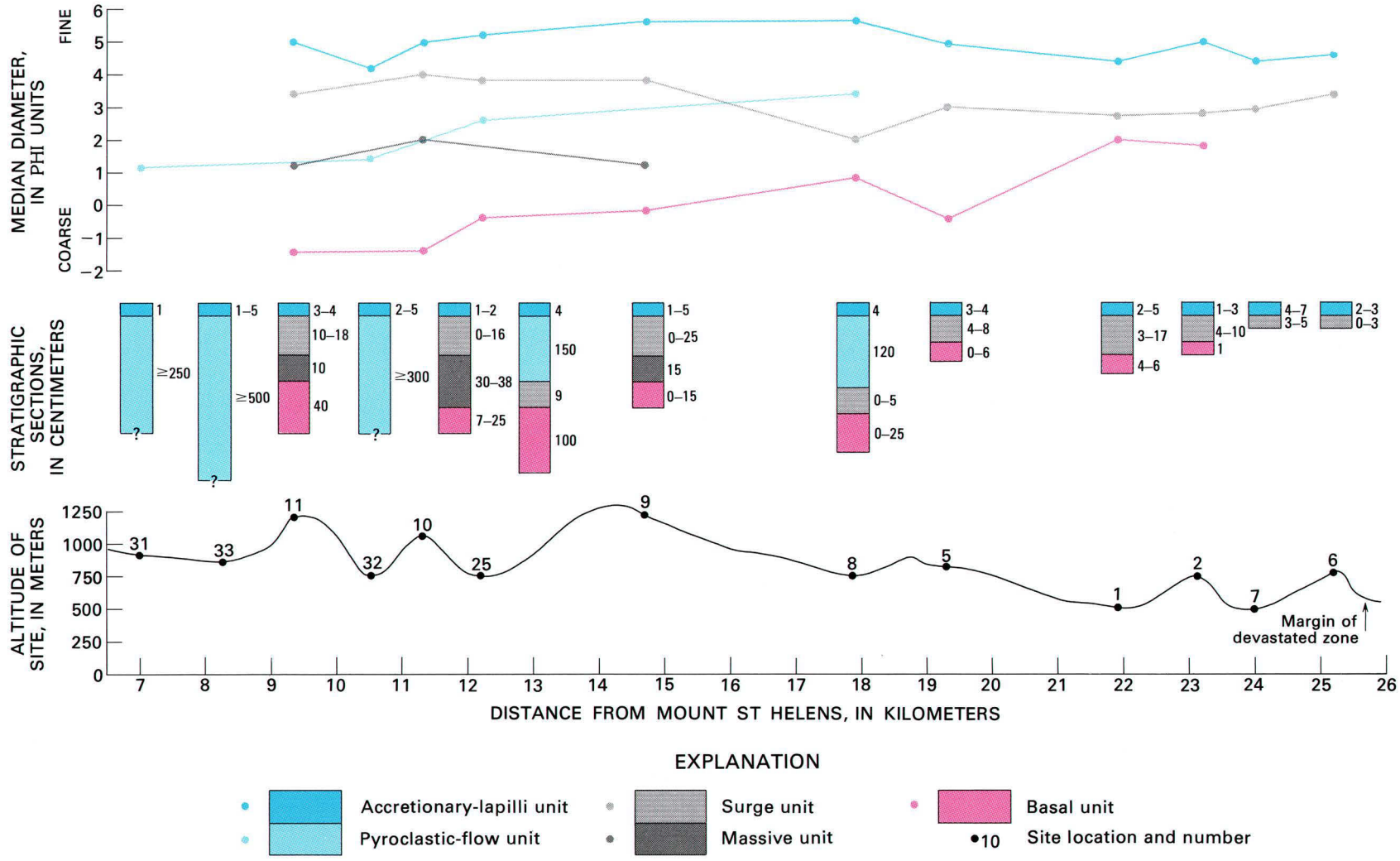

Figure 229.—Stratigraphic sections of blast deposit, median grain size of sampled units, and location of sites (dots) on generalized topographic profile along northwest traverse (fig. 226). Distance is measured from former summit of Mount St. Helens. Stratigraphic sections are diagrammatic; thicknesses of units (in centimeters), are shown to right of sections.

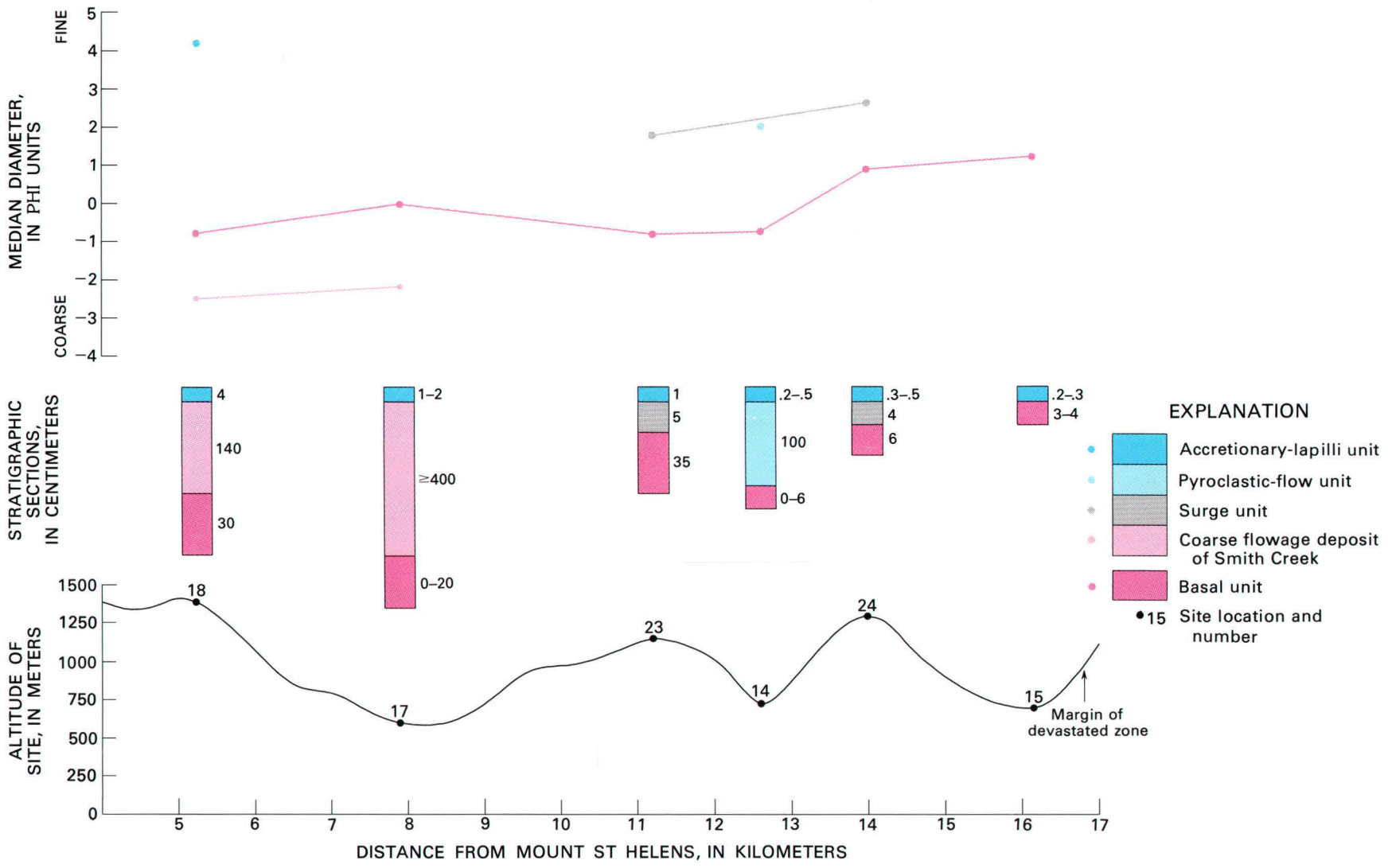

Figure 230.—Stratigraphic sections of blast deposit, median grain size of sampled units, and location of sites (dots) on generalized topographic profile along east traverse (fig. 226). Distance is measured from former summit of Mount St. Helens. Stratigraphic sections are diagrammatic; thicknesses of units (in centimeters) are shown to right of sections.

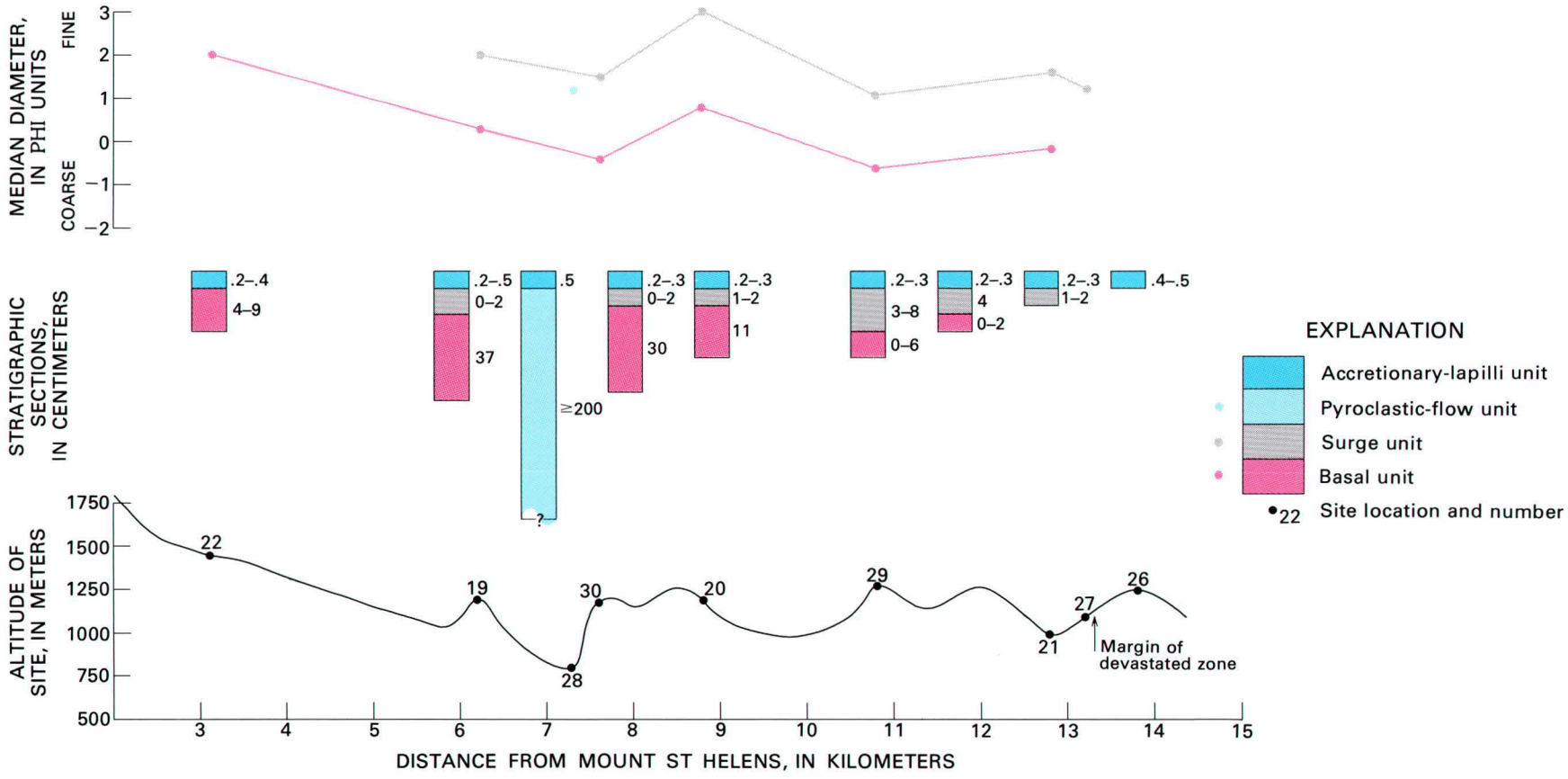

Figure 231.—Stratigraphic sections of blast deposit, median grain size of sampled units, and location of sites (dots) on generalized topographic profile along west traverse (fig. 226). Distance is measured from former summit of Mount St. Helens. Stratigraphic sections are diagrammatic; thicknesses of units (in centimeters) are shown to right of sections.

The unit is devoid of internal structures and is mostly ungraded, though faint normal grading is discernible at some sites. It is the coarsest unit (figs. 229 to 232), except at two sites along the east traverse (fig. 230; sites 17, 18). The median diameter of the basal unit shows an overall, but not consistent, decrease with increasing distance from the volcano along the northwest and east traverses (figs. 229, 230); along the west traverse it remains nearly constant beyond the flank of the volcano (fig. 231). The unit includes abundant void space and is friable because of the relatively low proportion of small particles.

On a graph (fig. 233) of sorting (deviation)[2] against median diameter[3], the basal unit plots in the transition zone between fields of pyroclastic-flow and air-fall deposits (Walker, 1971). These plot positions are near those (fig. 233) of the prehistoric Sugar Bowl blast deposit that Crandell and Mullineaux (1978) concluded was a directed-blast deposit on the basis of extent, lenticular character, anomalous grain-size distribution, and enclosed soil and charred wood.

The thickness of the basal unit varies with distance from the volcano and with local environment of deposition. On open, unobstructed surfaces the unit may be relatively thin or absent, even though it is relatively thick in nearby depressions and in the lee of

[2]Deviation ($\sigma\phi$) = Half the distance in ϕ between the points at which the cumulative curve crosses the 84 and 16 weight-percent levels (Inman, 1952).

[3]Median diameter (Mdϕ) = The ϕ value at which the cumulative curve crosses the 50 weight-percent level (Inman, 1952).

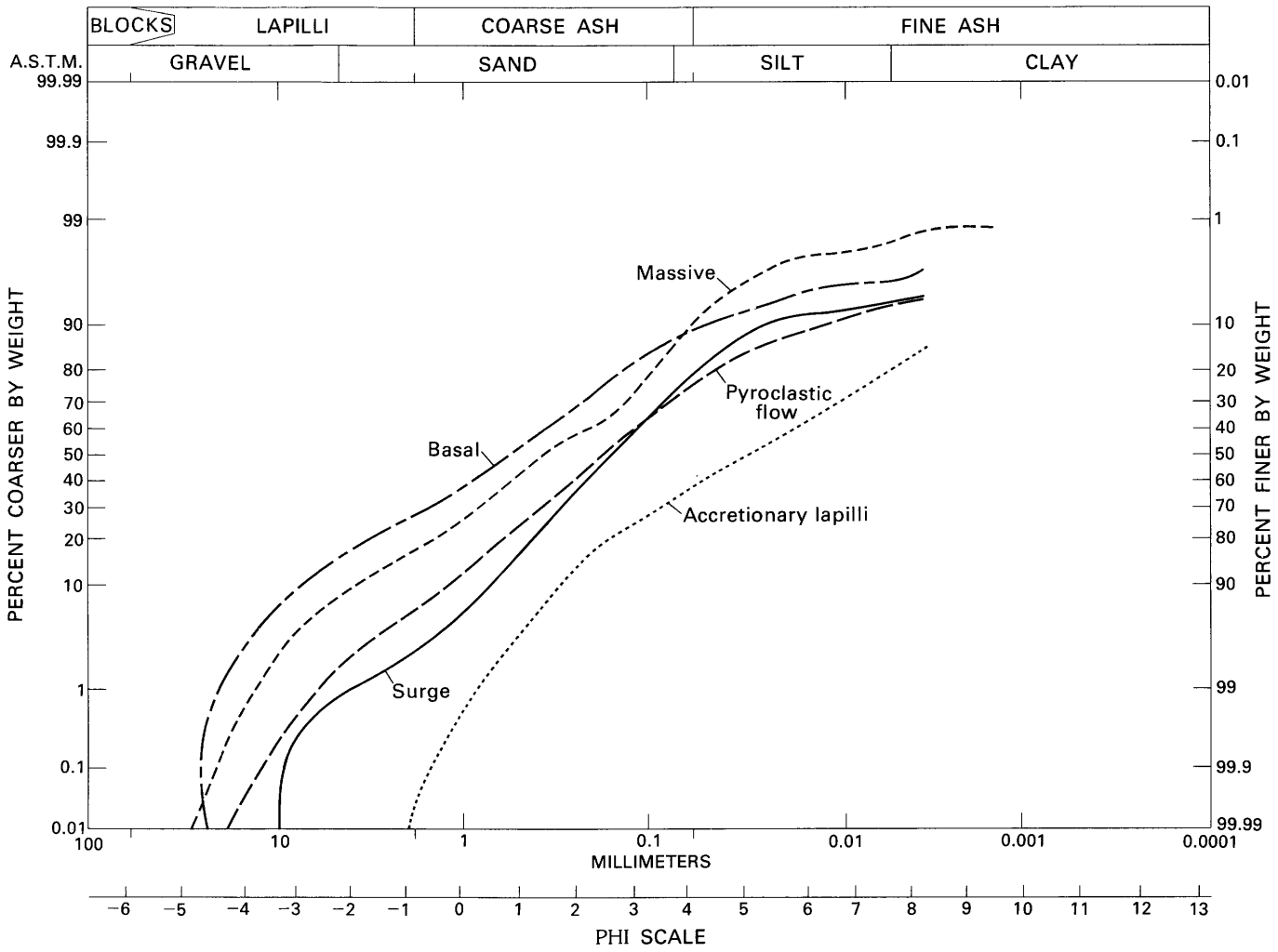

Figure 232.—Particle-size distribution curves for units of directed-blast deposit exposed at location shown on figure 227. Sample of massive unit (not present at this location) was collected 6.5 km to the east at locality 9 (fig. 226). Particle-size distribution curves for each unit plotted are similar to those for most other localities.

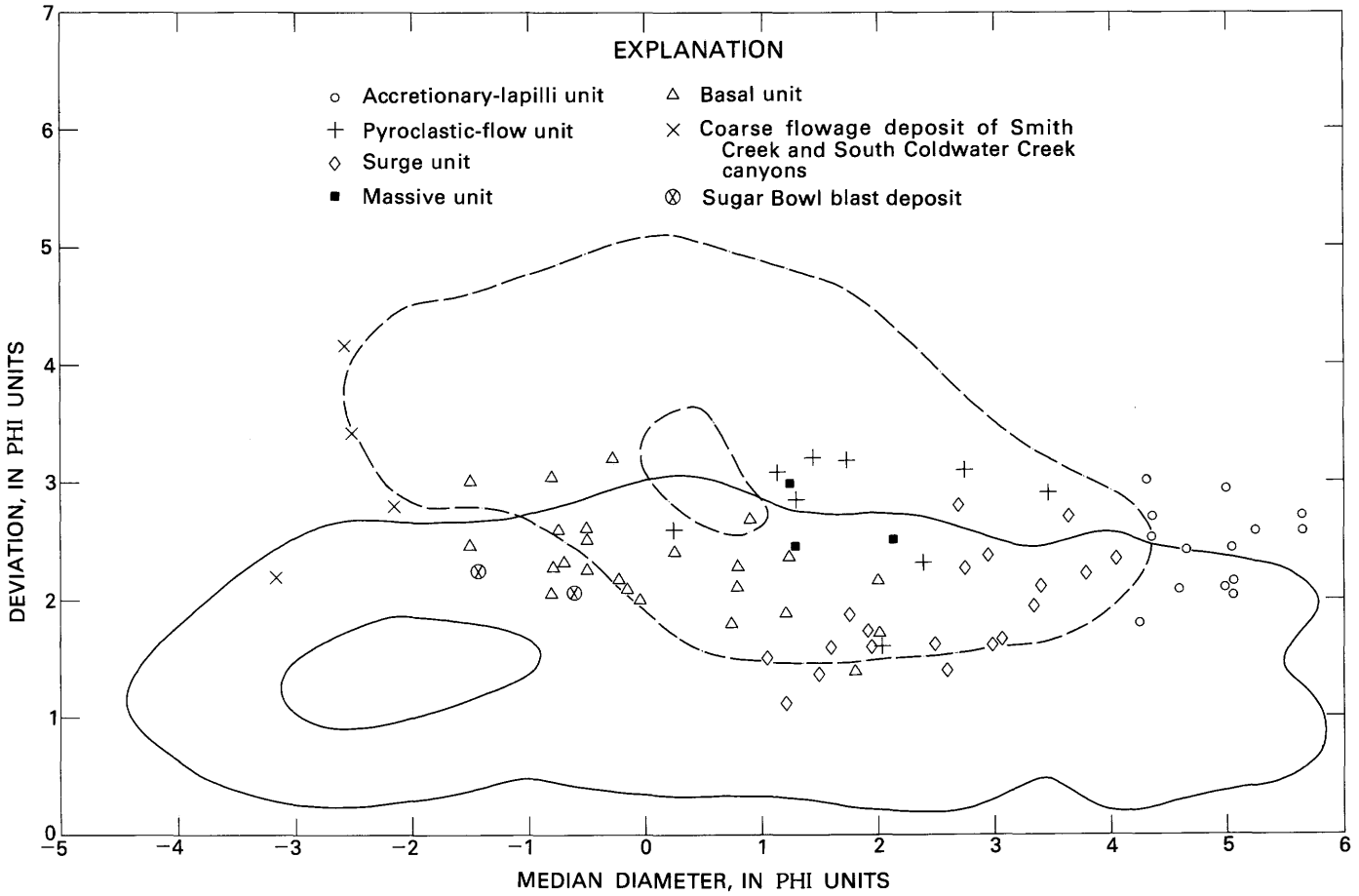

Figure 233.—Plot of median diameter versus deviation for the May 18 and the Sugar Bowl directed-blast deposits. Outlined areas are pyroclastic-flow (dashed lines) and pyroclastic-fall (solid lines) fields of Walker (1971). Inner contours enclose areas of greatest density of Walker's plot data. Some plot points are from sites not along any of the three sample traverses.

obstructions. On a larger scale, however, the thickness is insensitive to topography; depths on valley floors and adjacent ridges are similar. Observed thicknesses range from about 1 m to less than a centimeter. The unit thins with increasing distance from the volcano (figs. 229 to 231) and cannot unequivocally be identified near the blast margin on the northwest and west traverses.

Although the basal unit is heterolithologic, 50 percent or more of the megascopically identifiable clasts consist of a distinctive gray dacite. As a result, the unit as a whole is generally gray. In places, abundant masses of locally derived yellow-brown soil and rock fragments have been incorporated into the base of the unit. Conifer needles, bark, moss, logs, pieces of limb, and other wood fragments are also typically abundant. Many of the logs are devoid of bark and branches and are splintered at their ends (fig. 234). Most of the organic matter is uncharred, though discoloration and surface charring are evident locally along the western and eastern traverses. The contact with the overlying unit is gradational at most places but is sharp locally.

THE MASSIVE UNIT

The massive unit (fig. 235) consists primarily of a cohesive mixture of blocks and lapilli that is supported in a matrix of coarse ash. Like the basal unit, it lacks internal structures and may show crude normal grading. At a given site, its median diameter is less than that of the basal unit but is greater than those of the overlying units (fig. 229). The massive unit contains a higher proportion of fine grains than the basal unit does (fig. 232) and, thus, lacks the abundant voids that are typical of the basal unit. Megascopically, the

Figure 234.—Typical splintered log eroded from blast deposit in South Coldwater Creek canyon.

massive unit resembles the pyroclastic-flow unit (discussed later).

Where identified, the thickness of the massive unit varies between about 10 and 40 cm. It is the least extensive of the major units in the blast deposit and has been identified only on ridges between 9 and 15 km north of the mountain (fig. 229). The massive unit is distinguished from the pyroclastic-flow unit by its restriction to ridgetops and by its stratigraphic relation to the overlying surge unit, which is below the pyroclastic-flow unit.

The distinctive gray dacite is the most abundant rock type in the massive unit, but, in contrast to the basal unit, organic matter is rare.

Coarse-grained, flat-topped flowage deposits that consist dominantly of blocks and lapilli are locally exposed at the heads of South Coldwater Creek and Smith Creek canyons. The stratigraphic relationship of these deposits to the other units is uncertain in South Coldwater Creek canyon, but in Smith Creek canyon, they occur in the same stratigraphic position as the massive unit (fig. 230). Thus, they may be a facies of the massive unit. However, these deposits have the largest median diameters of any of the units sampled (fig. 233) and therefore may constitute a separate unit. The coarse grain size and the evidence of flowage suggest that these deposits could be the products of a primary pyroclastic flow; that is, a basal avalanche that was cogenetic with the blast cloud.

THE PYROCLASTIC-SURGE UNIT

The pyroclastic-surge unit (fig. 236) is composed almost entirely of coarse to fine ash. It is stratified, though the stratification may be very faint, and has sand-wave (Wohletz and Sheridan, 1979) structures or plane-parallel bedding. Dune forms are present between about 9 and 22 km from the volcano along the northwest traverse. There is no consistent pattern of grading; the unit locally is normally or reversely graded or ungraded.

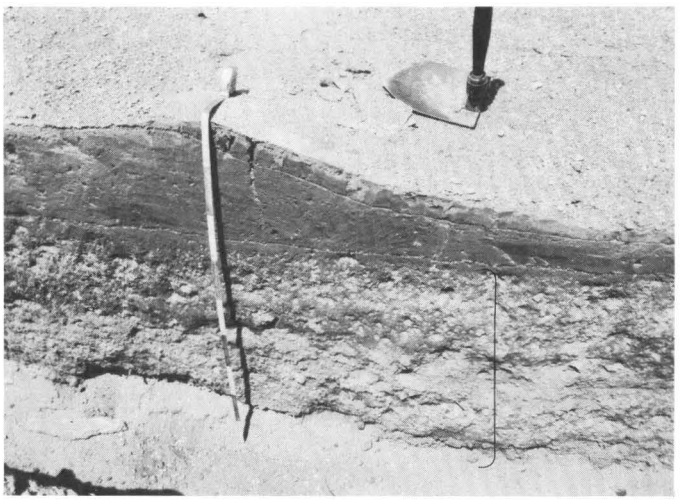

Figure 235.—Massive unit (delineated by bracket) exposed on ridgetop at locality 11, 9 km north of Mount St. Helens. Massive unit is overlain by surge and accretionary-lapilli units, which form a dune. Tape segments are 10 cm.

The surge unit typically has median-diameter values that are less than those of any unit other than the uppermost (accretionary lapilli) unit (figs. 229 to 232). The median-diameter values of the surge unit do not appear to be related to distance from the volcano, and, overall, the unit is better sorted than any other unit in the deposit (fig. 233).

The thickness of the surge unit ranges from less than a centimeter to about 40 cm. Because of the presence of dunes, the thickness of the unit varies widely at most sites (figs. 229 to 231). If a consistent relationship between thickness and distance from source is present, it is obscured by this local variability. The surge unit is apparently distributed over most, if not all, of the devastated area (figs. 229 to 231). The most abundant single rock type is the distinctive gray dacite. Organic matter is far less common than in the basal unit. Both the upper and lower contacts are generally gradational.

It is difficult to generalize about the nature of dunes formed by the surge unit because of the irregular terrain upon which the dunes were deposited. However, with increasing distance from the volcano along the northwest traverse (fig. 226), irregularly shaped hummocks that have a spacing of 1–3 m and amplitudes of as much as 30–40 cm grade into transverse dunes that have wavelengths of 1.5–3 m and amplitudes of 5–15 cm. The hummocky dune forms are found in those sections that contain the massive unit (fig. 229). Dune forms become indistinct or unrecognizable as the blast-zone margin is approached. Along the east and west traverses, dune forms are sparse and, where present, generally have low amplitudes (5 cm or less).

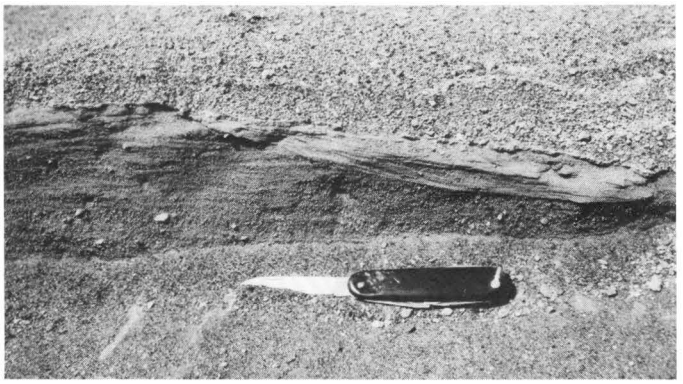

Figure 236.—Pyroclastic-surge unit exposed at locality 19 (fig. 226) on west traverse. Note dune crest and stratification.

THE BLAST PYROCLASTIC-FLOW UNIT

Pyroclastic-flow deposits that are derived from the directed-blast cloud form fill deposits in topographically low areas (fig. 237). These deposits are referred to here as the blast pyroclastic-flow unit to distinguish them from other pyroclastic-flow deposits formed on May 18 (Rowley and others, this volume). Megascopically, the blast pyroclastic-flow deposits

Figure 237.—Flat-topped blast pyroclastic-flow deposit in South Coldwater Creek canyon. Photograph taken in direction of flow.

resemble the massive unit. The blast pyroclastic flows are massive, and have median diameters that cover a wide range (fig. 233). The unit generally is as poorly sorted as the basal unit (fig. 233), although the upper few centimeters of some flow deposits are better sorted than their main portions. Valleys and other depressions that contain blast pyroclastic-flow deposits are isolated from one another by topographic barriers (pl. 1), and the volume of flowage material they contain decreases with increasing distance from the source. The maximum thickness of the blast pyroclastic-flow unit is at least 10 m.

At places where the base of the blast pyroclastic-flow unit is exposed, it is apparent that the flow scoured away part of or all the underlying blast units; in these exposures, the pyroclastic-flow unit can be seen to overlie either bedrock, the basal unit, or the surge unit. The stratigraphic position of the pyroclastic-flow unit was confirmed by tracing the surge and basal units from valley walls downslope to points at which they are overlapped by the flat-topped flowage deposits. The erosive power of the pyroclastic flows is also indicated by the presence of local bedrock clasts in the flowage deposits. The pyroclastic-flow deposits are everywhere overlain by the accretionary-lapilli unit.

At most exposures, we recognized only a single pyroclastic-flow deposit. At a few places, however, a thin layer of accretionary lapilli separates two flowage deposits of similar appearance. The time interval between the deposition of the two is unknown but probably was not more than a few minutes.

Locally, the flowage deposits are wood rich (fig. 238); some flows contain enormous log jams that resemble those deposited by water. However, the deposits in which the logs are embedded were hot and dry when first examined on May 20. In places, the paths followed by blast pyroclastic flows can be traced by the absence of logs in areas that are otherwise covered with them. The blast cloud felled the

Figure 238.—Valley-fill deposit in upper Smith Creek canyon, formed by a blast pyroclastic flow. Note abundant delimbed and debarked logs and wood fragments concentrated near the surface of the deposit.

trees prior to the formation of pyroclastic flows, as the alinements of logs in areas adjacent to the flow deposits bear no relation to pyroclastic-flow directions.

The distribution pattern of the flowage deposits and the flow directions inferred from the deposits indicate that flowage was analogous to water runoff. Debris moved down slopes and was channeled by the drainage system or was ponded in depressions. Thus, flows moved in directions dictated by the topography. In the valleys of Coldwater and South Coldwater Creeks for example, they moved southwest and west at right angles to the blast direction; in some other valleys, they even flowed south toward the volcano.

In cross section, the blast pyroclastic-flow deposits typically display subvertical openwork pipes of lapilli and coarse ash. These pipes extend to the surface of the deposit where they are surrounded by cones of fine ejecta winnowed from the pipes by escaping gases. The largest cones have diameters of several meters, but most are only a few tens of centimeters across. The pipes are crudely cylindrical and have lengths up to several meters; most have diameters between 1 and 10 cm. Some pipes contain spheroidal accretions of fine ash particles as much as 2 cm in diameter; they formed in the escaping gas column, as dry particles adhered to other particles that were moistened by condensing steam. These pipes and associated cones must have developed soon after the deposit was emplaced, because the cones are covered by the accretionary-lapilli layer and, in South Coldwater Creek canyon, by pumiceous ash-cloud deposits that were also erupted on May 18 (Rowley and others, this volume). When first observed on May 20, the pipes were no longer ejecting solid material. Nevertheless, vents at some large cones continued to emit steam for several weeks after emplacement. In many places, vents at the surface of the blast pyroclastic-flow deposits are stained with a black tarry organic substance derived from steam distillation of buried wood.

The measured emplacement temperatures of the blast pyroclastic-flow deposits (Banks and Hoblitt, this volume) were relatively low (70°–277°C). Most measured temperatures were less than 160°C; consequently, most wood in the deposits is uncharred or only slightly charred.

An interesting morphologic feature of the blast pyroclastic-flow unit was observed near the head of South Coldwater Creek canyon and in a reentrant in the north wall of upper North Fork Toutle River valley (fig. 226). At these sites, the sloping surface of the deposit is interrupted by 1- to 2-m high scarps; below each scarp the surface slope is roughly the same as that above it. In plan view, the scarps have a scalloped pattern, as if a series of "bites" had been taken out of the deposit. These features are not the products of erosion, because they were first observed before any significant erosion had taken place. Similar features were present in the pumiceous pyroclastic flows of June 12 when they were first observed on the day following emplacement, before any erosion had occurred. The most likely explanation for these features is that the flow came to rest in a metastable state; then, presumably a short time later, portions of the deposit remobilized and flowed away leaving scallop-shaped scarps. A clue to the cause of remobilization can be seen in the stratigraphy exposed in the scarps: the blast pyroclastic-flow deposit is overlain by ash-cloud deposits as much as 1 m thick that were derived from the pumiceous pyroclastic flows of May 18. Perhaps loading of the still-inflated, blast pyroclastic-flow deposits by the subsequent ash deposits triggered the failure.

THE ACCRETIONARY-LAPILLI UNIT

The uppermost unit consists primarily of normally graded coarse to fine ash (fig. 232) that commonly encloses abundant accretionary lapilli (figs. 239, 240). It is the finest grained unit in any given section (figs. 229 to 231, 233). In places, the upper few millimeters are horizontally bedded, and individual layers are locally separated by voids of irregular shape. Accretionary lapilli are present below this zone, but commonly decrease in abundance downward; however, their diameter increases with increasing depth. The thickness of the unit varies between 0 and 6 cm. Locally, the thickness varies around dunes and other topographic irregularities, which suggests that the ash was emplaced with a component of lateral motion. At one locality, the accretionary-lapilli layer was found inside a vehicle whose windows had been destroyed by the directed blast; this also suggests that lateral motion was a factor in the deposition of the unit. Along the three traverses, the thickness seems to show no consistent change with distance from the mountain (figs. 229 to 231), but the unit is thicker along the northwest

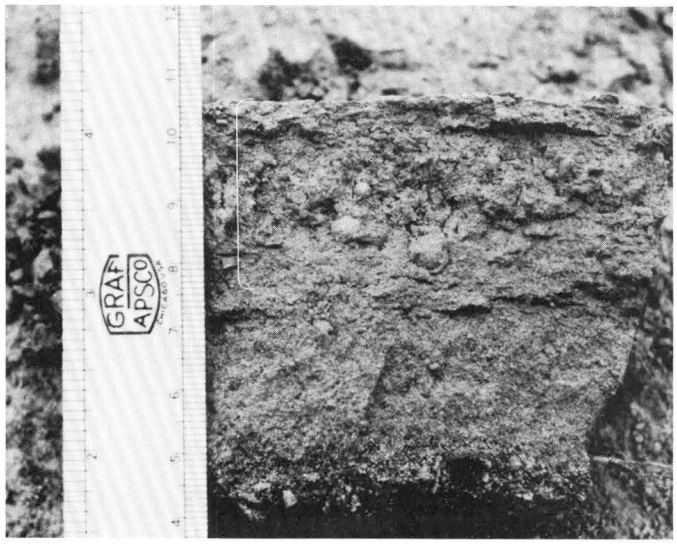

Figure 239.—Section through the directed-blast deposit at locality 1 (fig. 226) on the northwest traverse. Accretionary-lapilli unit shown by bracket.

traverse than it is along the east or west traverses. Because of this, uncontaminated samples were obtained at only a few sites along the east and west traverses. The accretionary-lapilli layer is the only unit that extends beyond the boundaries of the devastated area. The contact with the underlying surge or pyroclastic-flow unit is generally gradational.

JUVENILE GRAY DACITE

A distinctive gray, microvesicular to subpumiceous hypersthene-hornblende dacite is ubiquitous in all units of the blast deposit. Most clasts of the dacite that are larger than a few centimeters in diameter are prismatically or incipiently prismatically jointed. Clasts having some breadcrusted faces are common, but wholly breadcrusted clasts are rare. When examined 2 days after emplacement, dacite blocks were hot to the touch. The intermediate dimensions of the five largest clasts found at each site were measured and averaged. The mean maximum clast size decreases exponentially with distance from the volcano along each traverse (fig. 241); the rugged terrain traversed by the blast has no apparent affect on this relationship. The northwest traverse has larger juvenile clast sizes for any given distance than do the east and west traverses (fig. 241); this fact indicates that the area north of the volcano was the path of the greatest blast force.

The chemical composition of a representative sample of the distinctive dacite in the blast pyroclastic-flow deposit is indistinguishable from that of the air-fall pumice and the pumice of pyroclastic flows erupted on May 18 (table 40). The gray dacite clasts are clearly a juvenile component of the blast deposit. We conclude that these clasts were derived from an intrusive mass (a "cryptodome") within the cone, which was blown apart and incorporated into the directed-blast cloud.

Figure 240.—Handful of accretionary lapilli from directed-blast deposit at locality 32 (fig. 226).

The densities of 232 samples of juvenile dacite clasts that were collected along the three traverses (7–15 per site) range from 1.0 to 2.1; the density distribution (fig. 242) has a mean of 1.66, a central tendency between 1.6 and 1.8, and is negatively skewed. The density of the crust of one breadcrusted bomb was determined to be 1.74, whereas that of the interior was 1.22.

BLAST DEPOSIT SUMMARY

Summarized below are features of the distribution, stratigraphy, and other characteristics of the deposit that resulted from the directed blast.

DISTRIBUTION

1. Overall, the deposit forms a thin blanket that has a wide areal extent (about 600 km²) in spite of

multiple transverse topographic barriers, some of which are higher than 600 m.

2. Deposits formed by pyroclastic flows derived from the directed blast cloud are found in valleys and depressions that are topographically isolated from the volcano. Flow direction was controlled by topography: at some localities, blast-pyroclastic flows actually moved down valleys transverse to or even toward the volcano.
3. Overall, the deposit thins with increasing distance from the volcano. However, at any given distance from the volcano, the deposit is thinner on slopes and thicker in topographic lows than it is on ridge crests.

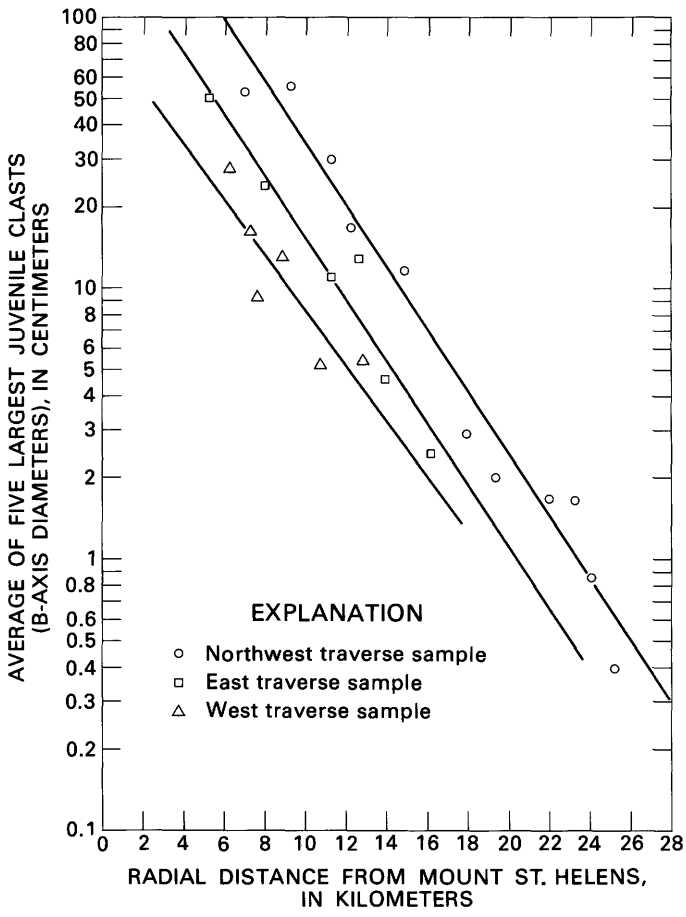

Figure 241.—Plot of the mean intermediate dimensions of the largest juvenile dacite clasts versus distance from Mount St. Helens along west, northwest, and east traverses. Note that the regression lines calculated for the three traverses are nearly parallel, and that the northwest traverse has the largest clast size for a given distance from the volcano.

STRATIGRAPHY AND OTHER CHARACTERISTICS

1. The deposit is composed of several stratigraphic units. One unit has field characteristics consistent with deposition by pyroclastic surge, another would be attributed to pyroclastic flow, and a third to pyroclastic fall.

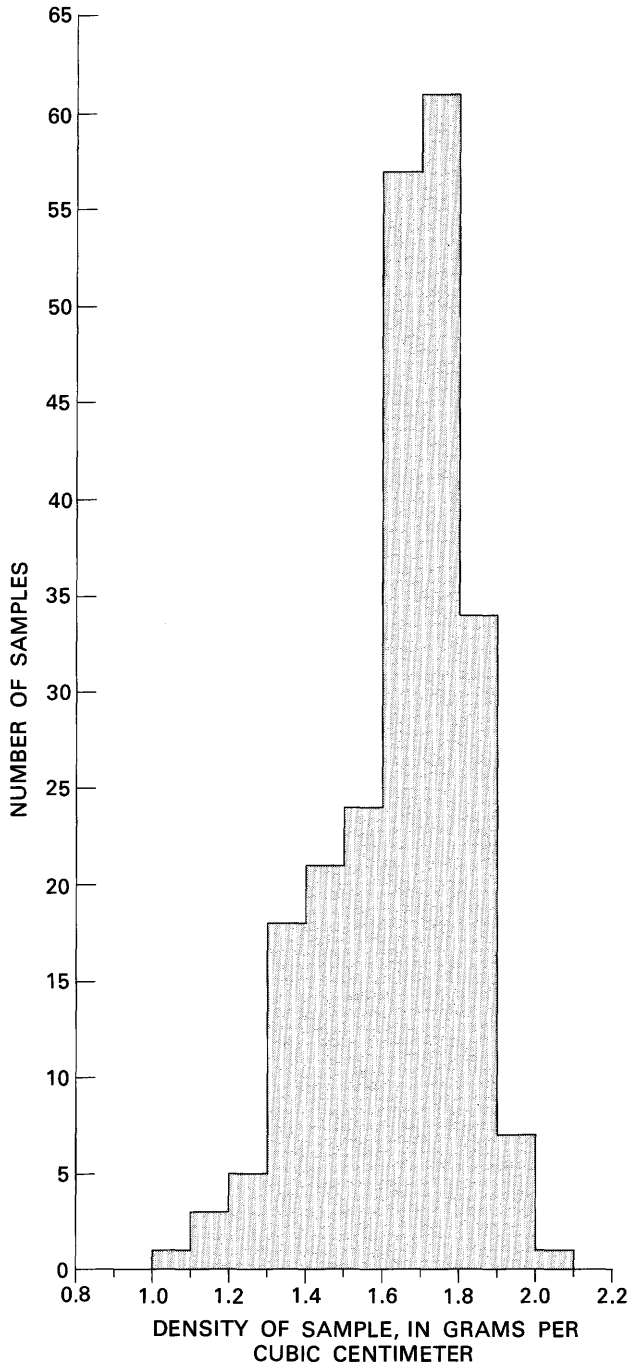

Figure 242.—Histogram of the densities of 232 samples of juvenile dacite from Mount St. Helens directed-blast deposit.

2. The basal unit has characteristics that collectively are atypical of pyroclastic flow, pyroclastic surge, or pyroclastic fall. It contains abundant shattered wood that is uncharred or slightly charred; it is grain supported, locally includes soil masses, and has a thickness that is controlled by local obstructions and by distance from the volcano, but not by major topographic features.
3. Inman parameters (Inman, 1952) of the various blast-deposit units (fig. 233) plot in or near an area of overlap between the fields for pyroclastic-fall and pyroclastic-flow deposits (Walker, 1971).
4. The sequence as a whole is normally graded.
5. All units are heterolithologic; the most abundant rock type is microvesicular to subpumiceous juvenile dacite.
6. Evidence from organic matter and from direct measurement indicates low to moderate temperatures of emplacement.

ORIGIN AND MECHANISM OF DIRECTED BLAST

Intrusion of dacite magma into the cone of Mount St. Helens was evidently responsible for the events that began at the volcano on March 20 and that culminated in the directed blast of May 18. As intrusion continued, the north side of the mountain was deformed into an increasingly unstable configuration (Lipman and others, this volume). Concurrently, the heat and magmatic gases undoubtedly contributed to, and perhaps were mainly responsible for, the hydrothermal system that was driving the phreatic eruptions that began on March 27. The accompanying seismic activity (Endo and others, this volume) is also attributable to the intrusion.

At 0832 PDT (Pacific Daylight time) on May 18, an earthquake of magnitude 5+ triggered the failure of the unstable northern portion of the mountain. The portion of the cone that failed consisted mainly of an assemblage of older intrusives and domes, and included Goat Rocks dome, the youngest dome on the mountain (Hoblitt and others, 1980). As is now apparent from exposures in the walls of the crater, much of the southern part of the mountain consists of thinly bedded lava flows; these flows may have buttressed the south flank and made it structurally more stable than the north flank. This buttress may account for the localization of the deformation on the north side. Photographs (Rosenquist, 1980) taken northeast of

Table 40.—Comparison of major-oxide and trace-element compositions of juvenile dacite from directed-blast deposit with pumiceous dacite from pyroclastic-flow and pyroclastic-fall deposits also erupted on May 18

[X-ray spectroscopy of major oxides by J. E. Taggart; trace elements by induction-coupled plasma technique by F. Lichte; a, juvenile dacite clast from blast pyroclastic flow of May 18; b, pumice block from pyroclastic-flow of May 18; c, air-fall pumice erupted on May 18]

	Major-oxide analyses (weight percent)		
	a	b	c
SiO_2	63.9	64.4	63.2
Al_2O_3	17.3	17.4	17.2
Fe_2O_3	4.40	4.30	4.43
MgO	1.84	1.81	1.91
CaO	4.90	4.86	4.92
Na_2O	4.68	4.68	4.59
K_2O	1.32	1.34	1.32
TiO_2	.58	.56	.57
P_2O_5	.11	.13	.13
MnO	.06	.06	.06
LOI[1]	.35	.34	.46
Total	99.44	99.88	98.79
	Trace-element analyses parts per million)		
Ba	294	298	290
Be	.8	.8	.8
Ce	28	21	25
Co	12	11	11
Cr	8	12	6
Cu	31	32	32
Ga	10	5	4
La	10	10	10
Li	24	23	23
Mn	570	565	566
Mo	<1	<1	<1
Ni	7	6	6
Pb	8	7	5
Sc	9	8	8
Sr	452	452	448
V	74	69	71
Y	9	8	8
Yb	1	1	1
Zn	59	58	60

[1]LOI, loss on ignition; 925°C for 45 min.

the mountain shortly after the north slope began to fail show that colossal slump blocks detached high on the north flank along crescentic fractures that dipped northward. The blast cloud emanated from the midst of the second of two northward-slumping masses visible in the photographs. The cloud consisted of a subhorizontal fountaining mass of debris and expanding gases. As the gases expanded through the disintegrating mass, they entrained various rock types into the blast cloud; this accounts for the heterolithologic nature of the resulting blast deposit.

The sudden decompression caused by the failure of the north slope allowed the volatiles in the cryptodome and in the hydrothermal system to expand rapidly and to generate the blast cloud. The relative volumes of expanding gases contributed by the cryptodome and by the hydrothermal system are uncertain. However, two lines of evidence suggest that the cryptodome may have been the dominant contributor. First, the juvenile dacite is ubiquitous in all units of the blast deposit and, in most places, accounts for about 50 percent of its recognizable clasts. This ubiquitous distribution is best explained by expansion of gas that emanated from within the cryptodome. If the gas emanated predominantly from areas external to the dome (that is, from the hydrothermal system), a more irregular distribution of juvenile clasts would be expected. Secondly, the dacite clasts display a wide range of densities and many clasts are breadcrusted. The most likely explanation for the observed density range (fig. 242) is that it reflects varying degrees of cooling of near-solidus cryptodome magma prior to its fragmentation; fragments from the margin of the intrusive would presumably be cooler, less prone to vesicle growth, and thus more dense than those from the interior. The presence of breadcrusted bombs of juvenile dacite in the blast deposit indicates that at least some of the vesiculation occurred during the explosion. Some vesiculation, however, may have occurred prior to disruption of the intrusive.

The above arguments support the possibility that the blast cloud formed when expanding juvenile gases caused the partly cooled cryptodome to explode as it was unloaded by failure of the north slope. In such a process, gas release would be sustained, perhaps over a period of minutes, as gases escaped from the cryptodome fragments at an ever decreasing rate.

Photographs and the accounts of witnesses indicate that the blast cloud was opaque, rapidly moving, and ground hugging, and had a leading edge that was no more than a few hundred meters thick. The few witnesses that survived within the devastated zone north of the volcano reported (Rosenbaum and Waitt, this volume) that the passage of high-velocity material did not last more than "a very short time" after they were engulfed by the cloud front. From this we conclude that the front portion of the cloud was the highest energy portion of the system and that the blast deposit is the product of the passage of a single cloud. Deposition commenced as the cloud front passed; because the basal unit is the coarsest unit of the sequence, the coarsest material evidently was carried at or near the cloud front and was deposited first.

The blast cloud clearly was very inflated (high void fraction): the resulting deposit covers an area of about 600 km^2, yet it is relatively thin. The grain size and sorting characteristics of the blast-deposit units (fig. 233) suggest that the blast debris was subjected to a sorting process that was transitional between that operative in pyroclastic flows and that operative in tephra fallout. The overall normally graded character of the deposit and the decrease in mean juvenile clast size with increasing distance from the source suggest deposition by settling from an inflated, turbulent cloud.

On the basis of the previous discussion, we propose that the blast cloud was a density flow composed of solids dispersed in a much greater volume of turbulent gases. In this model, particle size and concentration decrease upward and backward in the advancing cloud (fig. 243). Following passage of the flow front and deposition of the basal, massive, and surge units, the trailing lower velocity, lower density portion of the cloud begins to deflate and thus increases its density. The deflating cloud settles into topographic lows where the particles eventually become sufficiently concentrated for pyroclastic flows to form. Once the coarse-grained fraction is mostly settled and kinetic energy is largely spent, the remaining gas phase cools to the point that water begins to condense. The ash particles still in suspension in the dilute upper parts of the blast cloud adhere to the moisture droplets and form accretionary lapilli. Evidence cited earlier suggests that, at this time, the cloud still retains some lateral motion. Finally, lateral motion and condensation cease, and the finest particles settle out or drift away.

The model we have described is subject to change as more stratigraphic information becomes available. On the basis of our current stratigraphic

data, we are less confident of the applicability of the model to the near-blast area (within about 10 km of the volcano) than to the far-blast area. Within the near-blast area, we are uncertain whether (1) the blast cloud contained a "primary" pyroclastic flow that had a particle-concentration discontinuity at the flow-cloud interface or (2) the particle concentration varied smoothly with distance above the ground. Because of their coarse-grained character, the flowage deposits in South Coldwater Creek and Smith Creek canyons are at present the best candidates for a primary pyroclastic-flow unit, if any exists.

Our model has features in common with the current models of pyroclastic surge (Fisher, 1979; Wohletz and Sheridan, 1979). However, the characteristics of the blast deposit conform only in part to the characteristics expected on the basis of the pyroclastic-surge models. The most notable dissimilarity is the presence of the basal unit in the blast deposit. The texture and depositional "habit" of the basal unit are atypical of pyroclastic-fall, pyroclastic-flow, or pyroclastic-surge deposits. Either it is the product of a depositional process not included in the tripartite—pyroclastic fall, flow, and surge—classification of Sparks and others (1973), or it was deposited by a previously unrecognized, high-energy depositional regime of pyroclastic surges.

CRITERIA FOR RECOGNIZING DIRECTED-BLAST DEPOSITS

Some of the distinctive features of the Mount St. Helens directed-blast deposit that may be diagnostic of deposition from a directed-blast cloud are given below. Until the characteristics of other deposits known to have originated by directed blast have been determined, these recognition criteria must be considered provisional.

Distribution of deposits may be an important indicator of directed-blast deposition. Relatively thin deposits with a wide areal distribution that is not controlled by topography could be emplaced by either tephra fallout or directed blast. These two possibilities can be differentiated by evidence of rapid lateral motion that will be present only in directed-blast deposits.

The basal unit, probably the most distinctive part of the Mount St. Helens deposit, may be unique to directed-blast deposition. The plot of Inman (1952) parameters (fig. 233) shows that the basal unit has grain size and sorting characteristics that could be attributed to either pyroclastic flowage or tephra fallout. However, we believe that the basal unit can be differentiated from most pyroclastic-flow deposits; the basal unit is grain supported, contains abundant

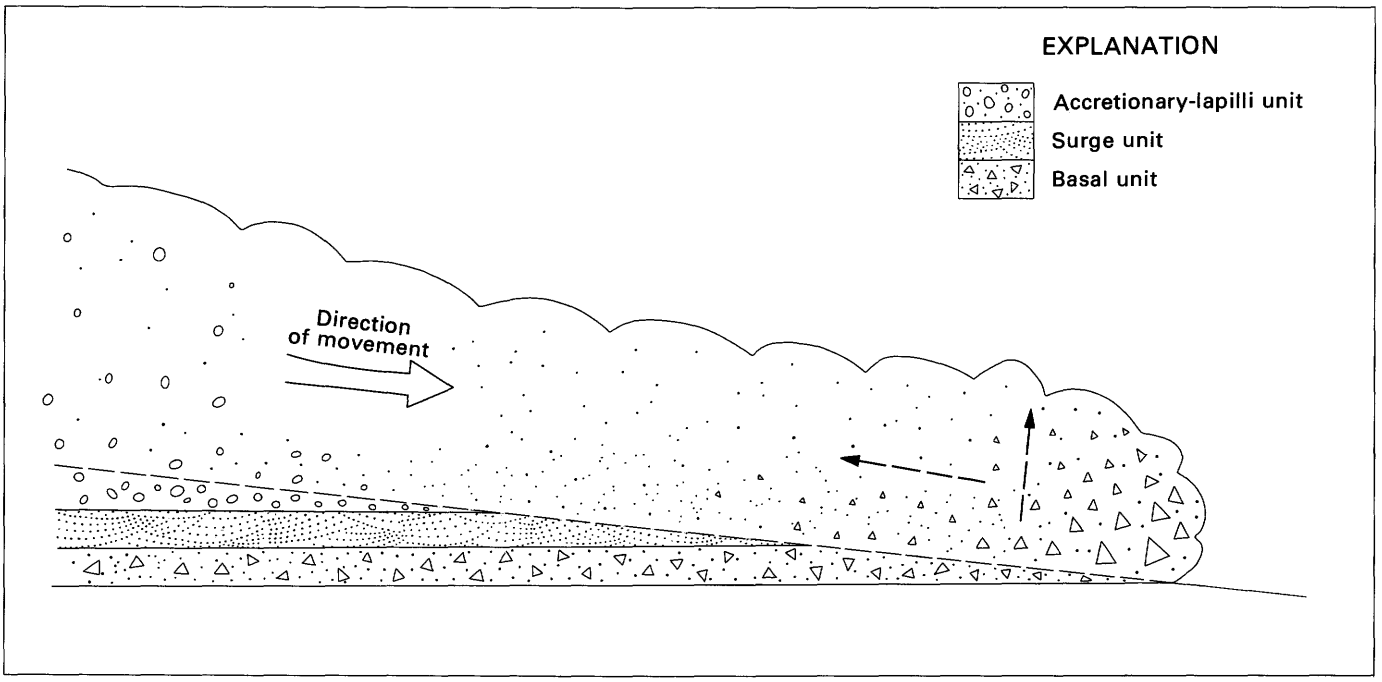

Figure 243.—Diagrammatic model showing deposition of basal, surge, and accretionary-lapilli units from blast cloud. Particle size and concentration decrease upward and backward (dashed arrows) in the cloud.

uncharred or only slightly charred wood, contains masses of soil stripped from the underlying surface, and has a distribution that is insensitive to topography. Evidence of rapid lateral transport (incorporated wood and soil, lee-side deposition near obstacles) serves to differentiate the basal unit from pyroclastic-fall deposits. The basal unit is massive and, therefore, considered by itself, is not likely to be attributed to a pyroclastic surge.

The similar areal extent of stratigraphic units with diverse characteristics and evidence that they were emplaced in rapid succession show that the units were produced by a single event; their collective characteristics indicate that they could have been formed only by a cloud of volcanic-rock debris moving laterally across a broad sector at high speed.

REFERENCES CITED

Crandell, D. R., and Mullineaux, D. R., 1978, Potential hazards from future eruptions of Mount St. Helens volcano, Washington: U.S. Geological Survey Bulletin 1383-C, 26 p.

Fisher, R. V., 1979, Models for pyroclastic surges and pyroclastic flows: Journal of Volcanological Geothermal Resources, v. 6, p. 305–318.

Gorshkov, G. S., 1959, Gigantic eruption of the Bezymianny volcano: Bulletin Volcanologique, ser. 2, v. 20, p. 77–109.

_____1963, Directed volcanic blasts: Bulletin Volcanologique, v. 26, p. 83–88.

Hoblitt, R. P., Crandell, D. R., and Mullineaux, D. R., 1980, Mount St. Helens eruptive behavior during the past 1,500 years: Geology, v. 8, p. 555–559.

Inman, D. L., 1952, Measures for describing the size distribution of sediments: Journal Sedimentary Petrology, v. 22, no. 3, p. 125–145.

LaCroix, A., 1904, La Montagne Pelée et ses éruptions [Mount Pelée and its eruptions]: Paris, Masson et Cie, 662 p.

Sparks, R. S. J., and Walker, G. P. L., 1973, The ground surge deposit—a third type of pyroclastic rock: Nature; Physical Science, v. 241, p. 62–64.

Taylor, G. A., 1958, The 1951 eruption of Mount Lamington: Australia Bureau of Mineral Resources Geology and Geophysics Bulletin 38, 117 p.

Walker, G. P. L., 1971, Grain-size characteristics of pyroclastic deposits: Journal of Geology, v. 79, p. 696–714.

Wohletz, K. H., and Sheridan, M. F., 1979, A model of pyroclastic surge: Geological Society of America Special Paper 180, p. 177–193.

THE 1980 ERUPTIONS OF MOUNT ST. HELENS, WASHINGTON

DEPOSITS AND EFFECTS OF THE MAY 18 PYROCLASTIC SURGE

By JAMES G. MOORE *and* THOMAS W. SISSON

ABSTRACT

The May 18 pyroclastic surge was generated by massive explosions that occurred when a giant landslide released the confining pressure on a shallow dacite cryptodome and its associated hydrothermal system. Explosions resulted from three processes: flashing of pore water to steam, exsolution of magmatic gases, and heating of steam, air, and other gases by contact with fragmenting hot rock. Similar pyroclastic surges, produced by directed explosions from volcanic systems that were depressurized by landslide movement, have apparently occurred during several other historic eruptions.

The surge affected an area of 600 km^2 largely north of the volcano, leveled trees as far as 28 km from the crater, and emplaced about 0.19 km^3 of surge and related air-fall deposits. Trees were strongly abraded and blackened in an inner zone where the temperature of the moving surge cloud was in excess of $350° \pm 50°C$. Near its outer limit the temperature of the surge cloud was 50°–200°C.

The surge deposits consist of two major units: coarse basal unit (volume of 0.09 km^3) and fine upper unit (0.07 km^3), which systematically become finer grained and better sorted away from the source. An overlying air-fall unit (0.03 km^3) containing accretionary lapilli is associated with the surge deposits. Each successive unit that was emitted is smaller in total volume but covers a larger area, and is thickest progressively farther north of the mountain. This fact and the stratigraphic relations suggest that the two units resulted from flow segregation that yielded a lower, relatively dense part and an upper low-concentration, gas-rich part. Thin cross-laminations in the fine upper deposit resulted from the interaction of the horizontally moving pyroclastic surge and billowing convective clouds rising from it. The overlying air-fall unit was deposited from ash carried to great heights by convective clouds rising from the moving surge, as well as from ash thrown up from the explosion source.

About half of the surge deposits are composed of fresh, originally hot dacite derived from the exposed cryptodome, and they account for about half the volume of the cryptodome (0.11 km^3); the remainder is presumably mixed with the debris avalanche. The high temperature of the surge cloud is largely attributed to the entrained fragments of hot dacite because areas of heavy tree charring correspond to areas having the highest proportion of fresh dacite deposits.

INTRODUCTION

The explosive eruption of May 18 was initiated by pressure release caused by the rapid failure and landsliding of the north side of the volcano. The landslide resulted from oversteepening of a growing bulge that was produced by intrusion of a shallow dacitic cryptodome during the previous 2 mo. Explosive eruptions were generated by flashing of superheated ground water as well as by release of magmatic gases when the dome system was intersected, exposed, and depressurized by rapid landslide movement.

Photographic sequences indicate that a few seconds after the abrupt beginning of landslide movement, an explosion locus developed on the steep headwall of the landslide (Moore and Albee, this volume). This locus quickly grew to produce a massive explosion cloud that expanded most rapidly to the north. Its initial velocity was about 250 m/s (Vortman, 1980), and it reached a distance of 50 km in 13 min, amounting to an average velocity of 64 m/s (Sarna-Wojcicki and others, 1980). This pyroclastic surge left a deposit thicker than 1 cm over an area of 550 km^2, where most trees were blown down or killed.

The term pyroclastic surge (Sparks, 1976) is used

herein as part of a general threefold classification of dispersal mechanisms for pyroclastic deposits: fall, flow, and surge (Sparks and Walker, 1973; Sheridan, 1979; Wright and others, 1980). Pyroclastic fall refers to the downfalling of pyroclastic material ejected into the air by explosive eruption, by gas streaming from a vent, or by convective clouds rising from a flow or surge. Pyroclastic flow and surge both involve the lateral movement of pyroclasts in ground-hugging density flows of generally hot fragmental material and gas that move in part under the influence of gravity. Surge and flow differ in that the surge is less dense with a lower concentration of fragmental material, is more turbulent, and is generally of higher velocity and more short lived. Transitions and interactions between falls, flows, and surges are common, and they complicate interpretation of the resulting deposits. In general, the surge deposits (relative to flow deposits) are thinner and better sorted, and they contain internally stratified layers that commonly are crossbedded. The pyroclastic surge deposits mantle the topography, although their thickness is not uniform, and show a general decrease in average grain size and average thickness, and an increase in degree of sorting, with increasing distance from the source. The aqueous analog of a pyroclastic flow is a mudflow, and that of a pyroclastic surge is a torrent or flood (Sparks and Walker, 1973).

Pyroclastic surges are attributed to phreatomagmatic explosions, plug explosions, directed blasts, and changes in venting characteristics during Plinian and Peléan eruptions (Sheridan, 1979). The May 18 directed blast that produced the pyroclastic surge resulted from explosions generated by rapid removal of cover rock at the headwall of a giant landslide, which had been rendered less stable by intrusion of a cryptodome (Moore and Albee, this volume). This mechanism, which could occur only on a relatively steep volcano, is well suited to produce a directed explosion, because it involves a subvertical landslide headwall scarp which buttressed the explosion on the south side. Other pyroclastic surges apparently related to landsliding have occurred in similar historic eruptions at Bandai-san, Japan, in 1888 (Sekiya and Kikuchi, 1889), Bezymianny, Kamchatka, in 1956 (Gorshkov, 1959), and perhaps Shiveluch, Kamchatka, in 1964 (Gorshkov and Dubik, 1970). Therefore, pyroclastic surges produced by explosions emanating from a region depressurized by landslide movement may be relatively common.

Samples were collected and measurements of the deposits and observations of the effects of the surge were made at 210 stations scattered over the affected area (figs. 244, 247). Stations are primarily on ridge crests and flat areas to minimize the secondary effects of the deposits sloughing off steep slopes and ponding in valleys. Maps developed from these data (figs. 245–255) are generally based on at least half of these stations; not all parameters were measured at all stations despite the fact that many stations were visited two or three times. A summary of the change in parameters of the surge deposits with distance from the explosion locus (taken as 1 km north of the pre-May 18 vent) is shown in figure 248. This plot was developed from the position of contours in figures 245–254 along a north-northwest line extending out from the explosion source (fig. 244).

ACKNOWLEDGMENTS

Rapid data collection from several hundred localities was made possible through the skillful flying of several helicopter pilots, chief of whom were Lon Stickney, Mike Holtsclaw, and Michael Montgomery. Discussions with our colleagues N. G. Banks, R. L. Christiansen, R. P. Hoblitt, P. W. Lipman, N. S. Macleod, C. D. Miller, A. M. Sarna-Wojcicki, D. A. Swanson, and R. B. Waitt, Jr., enhanced our perspective and improved the manuscript. We are grateful for their help.

TREE DAMAGE

The area affected by the pyroclastic surge included mixed forests of conifers, and at lower elevations, deciduous trees including alder. Areas clearcut by logging at various times are scattered over the region; within the affected area, old or virgin forests existed near Spirit Lake and in the high country farther north.

Within the boundary of tree blowdown (shown on all maps), most of the large trees were snapped off (generally near the base) or uprooted. Within an inner zone extending a few kilometers north of the vent, the large trees were not only knocked down but also blown away (pl. 1, tree-removal zone). However, this generalization must be qualified within the Spirit Lake basin, because water displaced by a debris

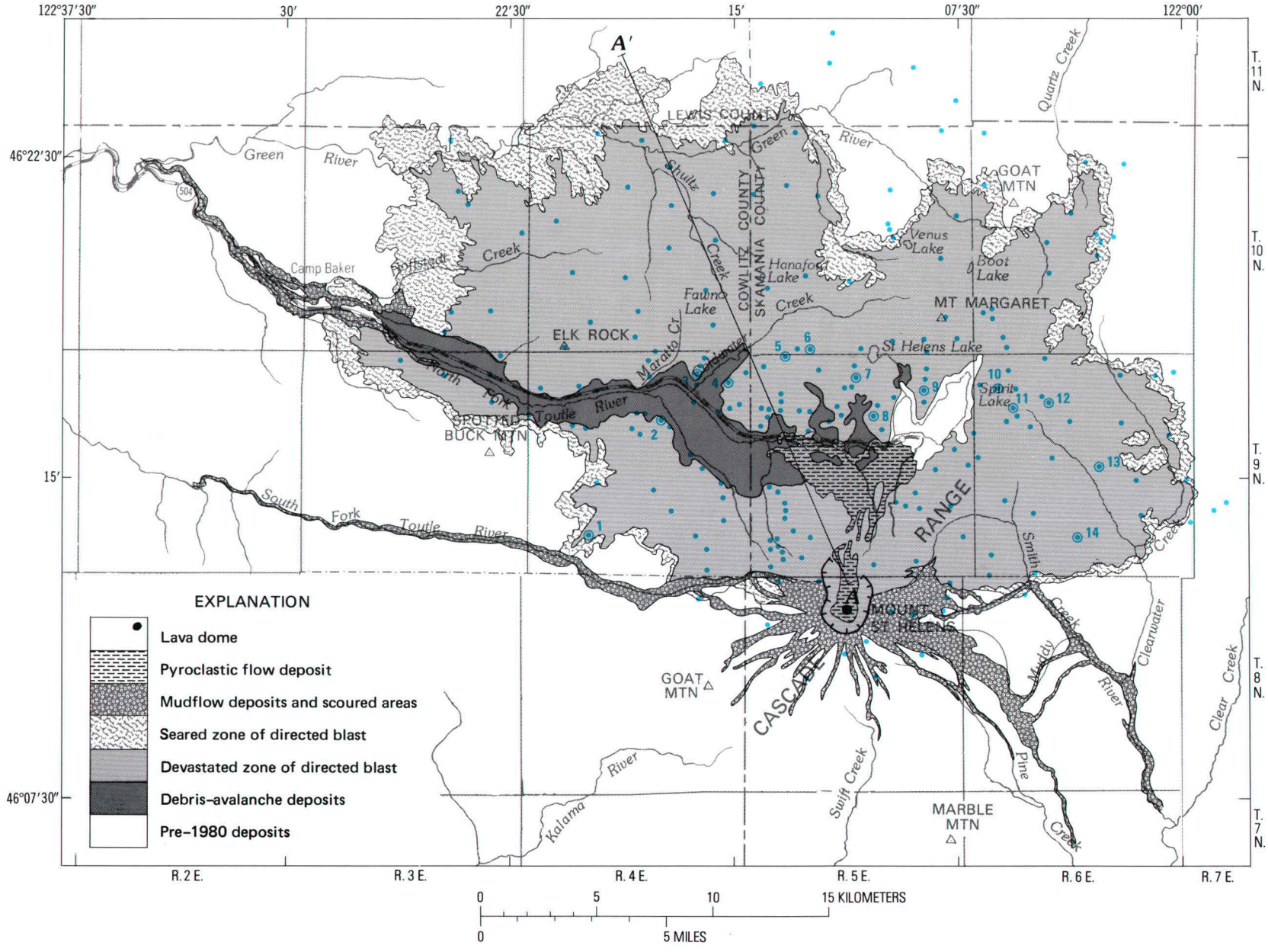

Figure 244.—Vicinity of Mount St. Helens showing location of points of measurement (solid circles), stratigraphic sections shown in figure 247 (open circles and numbers), and cross section A-A′. Geology modified from plate 1.

avalanche (Voight and others, this volume) also washed away trees more than 200 m above the existing lake level, many of which washed back into the lake and were left floating.

The downed trees are damaged and abraded about equally from bottom to top on the side that faced the volcano and, in addition, the roots facing the mountain are sandblasted. Hence the period of abrasion was sustained long enough to affect the tree trunks while they were standing and also the roots after the trees fell. For this reason such trees were avoided for abrasion measurements, because no part of them records the entire period of abrasion.

The maximum thickness of wood that was removed by abrasion from the blast side of trees was measured primarily on stumps and sawn sections of trees. The thickness of removed wood was determined by reconstructing the original contour of the tree based on the remaining outer surface as well as on the growth rings. Most abrasion measurements were made on stumps in clearcut areas and stumps from snapped-off trees. Far-field measurements (0.5- and 1-mm contours in fig. 245), however, could be made on standing small trees averaging 10 cm in diameter. All abrasion values are for wood only. Generally the bark (averaging 1–2 cm thick for large trees and 1 mm for small trees) was rapidly removed on the blast side. Half the bark (that is, bark within a circumferential angle of 180°) was removed from small trees at a radial distance of 14–20 km except at the southern margin of the area covered by the surge (fig. 245). Closer to the volcano, more than half the bark was removed.

Nearer the vent, abrasion of small trees is progressively less than abrasion of the stumps, because the small trees bent over horizontally in the surge. Consequently, small trees do not reflect total damage close to the volcano. In figure 245, only the 1- and 0.5-mm contours are based on small tree abrasion; other contours show stump abrasion. The extreme decrease in abrasion with distance from the explosion center (fig. 248) resulted from the simultaneous decrease in size, velocity, and number of the fragments carried by the surge.

In addition to being abraded, stumps and standing small trees are blackened by heat only on the side facing the vent area. The remaining sand-blasted wood is charred, yet in several places minor abrasion has in turn removed some of the charred wood. Heavy charring (fig. 246) produces a blackened layer on abraded trees as much as 0.5 mm thick; slight charring is generally less than 0.1 mm thick. The data clearly show that the hottest part of the surge was directed to the east-northeast. However, other relatively hot areas also extend northwest.

Because the surge duration is estimated at 2 min, wood was heated in simple furnace experiments for 2 min at different temperatures. These experiments produced charring at 350° ± 50°C that is equivalent to the heavy charring contoured in figure 246 and at 300° ± 50°C, equivalent to the slight charring. The outer limit of searing, where foliage is browned and killed, probably represents a cloud temperature of 50°–200°C (Winner and Casadevall, this volume).

Similarly, wood shreds within the blast deposit are charred in places and further define the temperature distribution within the surge. Heavily charred wood fragments, which are reduced to vitreous charcoal as much as 1 cm in thickness, are most commonly found buried in the deposits within the eastern, heavily charred tree zone (fig. 246).

STRATIGRAPHY AND STRUCTURE

In this study the pyroclastic surge deposits have been divided into two units: a coarse basal unit and a fine upper unit (fig. 247). In addition, an air-fall unit, representing ash ejected by the explosions that fed the surge and by convective clouds rising from the moving surge, has been investigated. A fourth unit, deposited by secondary, localized pyroclastic flows fed from downslope sloughing of the fine upper surge unit (Hoblitt and others, this volume) is not considered here. The thickest part of each of these first three units is progressively more distant from the source (fig. 248); the coarse basal unit is thickest about 6 km away; the fine upper unit, 12 km distant; and the air-fall unit, 15–20 km away. Each of the pyroclastic-surge units has distinct intergradational subfacies which successively dominate the strata in a uniform progression that depends on both distance and direction of surge flow.

The coarse basal unit covers an area of 140 km^2 and is restricted to about 14 km from the vent, with an irregular but relatively distinct areal limit. It is distributed north of the vent in a broad fan with several lobes controlled partly by topographic depressions (fig. 249). The coarse basal unit is the most voluminous (0.09 km^3) and consists principally of blocky

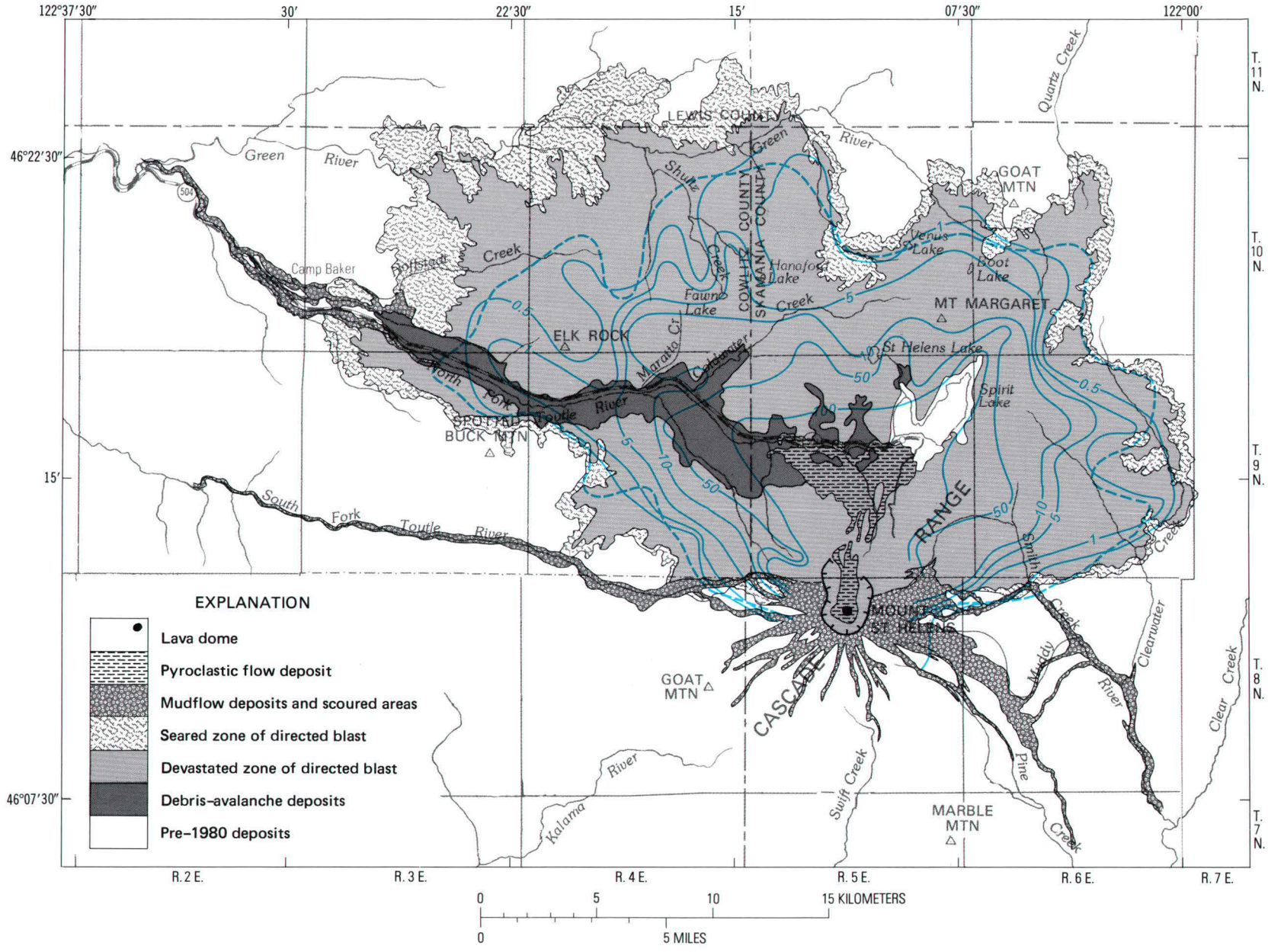

Figure 245.—Contours showing thickness of wood removed from side of trees and stumps facing volcano, in millimeters (blue). Dashed blue line is outer limit of area where more than one-half the circumference of small trees (180°) is debarked.

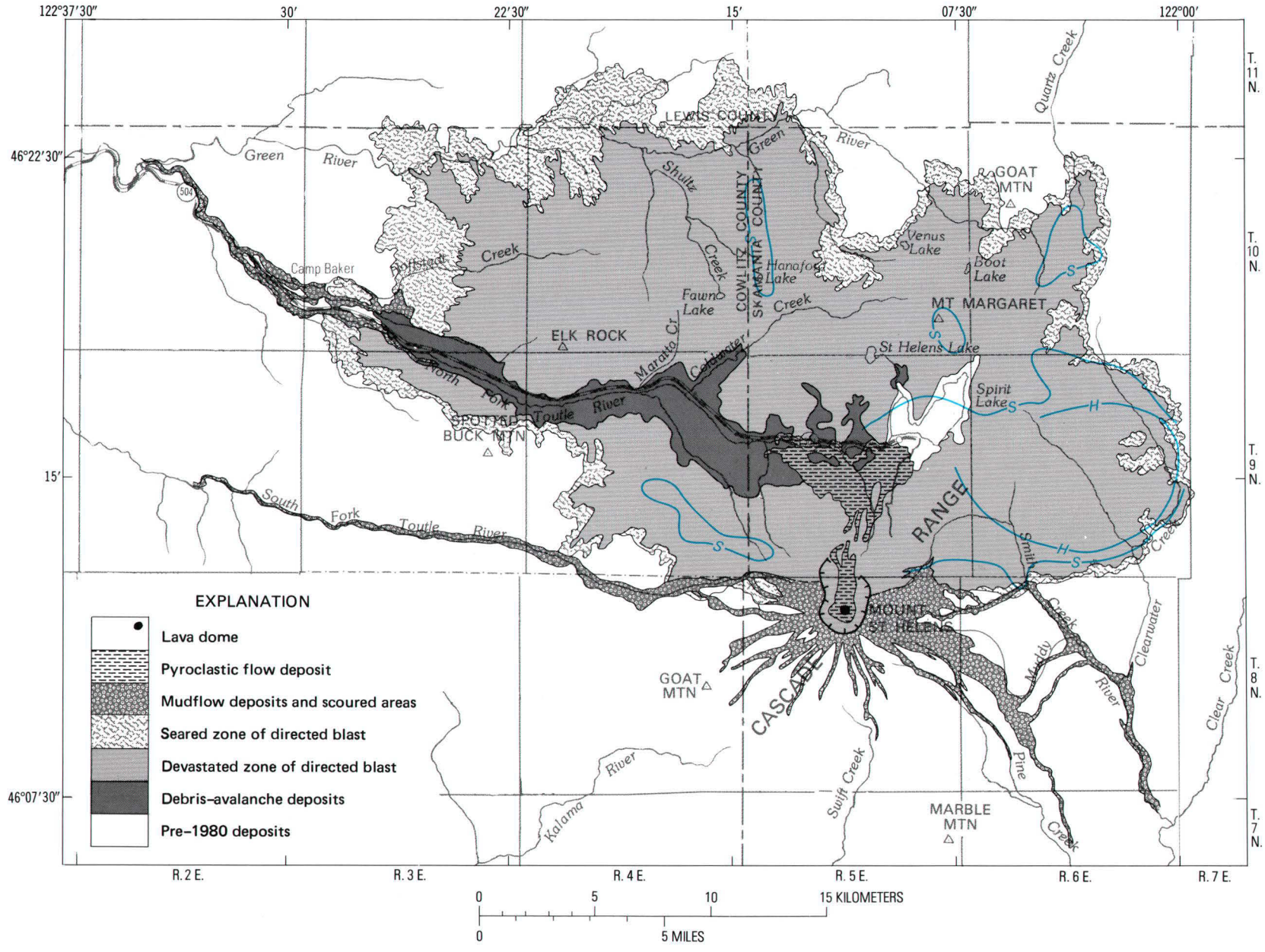

Figure 246.—Contours showing charring of small trees (blue): S, outer limit of visible blackening; H, outer limit of heavy charring (as thick as 0.5 mm). Assuming a heat duration of 2 min, furnace experiments suggest the S contour represents a surge temperature of 300° ± 50°C and the H contour represents a surge temperature of 350° ± 50°C.

material. The unit (fig. 247) consists of a thick, massive, or slightly normally graded, matrix- to clast-supported layer that grades upward to a finer grained clast-supported top with progressive depletion of sand- to silt-sized ash and large blocks. A poorly developed imbricate arrangement in which the larger elongate clasts dip toward the source is present in some places. Median grain size is generally larger than 1 mm, and the average of the three largest clasts at each locality is greater than 5 cm except for the east side where the grain size is finer (compare fig. 249 with fig. 250).

The fine upper unit generally does not grade into the coarse basal unit. The fine upper unit is better sorted and more thinly bedded, particularly in the upper part. It extends slightly beyond the limit of seared trees and covers about 600 km^2 (fig. 251) with an abrupt outer limit. Despite the fact that it covers an area four times as large as that of the coarse basal unit, it includes a smaller volume (0.07 km^3). The fine upper unit retained its mobility for a considerably longer period; it sloughed off steep slopes and ponded to considerable thickness in canyon bottoms and on the stagnant margins of the debris flow.

Where the fine upper unit is underlain by the coarse basal unit, its lower part commonly consists of a poorly bedded to massive, normally graded bed of ash and lapilli from less than 1 cm, to several centimeters, in thickness. This bed commonly grades upward into a thinly stratified or cross-stratified silt-sized ash several centimeters, or tens of centimeters, thick. The basal part of the graded layer, where traced upflow, is found in places to intergrade with the underlying top of the coarse unit by an increase in content of lapilli-sized fragments.

Stratification of the fine upper unit commonly consists of several superposed tabular cross sets that resemble migrating straight-crested dunes. Outward from the limit of the coarse basal unit, the thickness of the lower graded part of the fine upper unit decreases, bedding and cross-stratification become increasingly well developed, and bedforms change to transverse dunes with bifurcating and undulose crests. Dunes are generally not superposed; they are particularly well developed in the northwest sector having wavelengths averaging 1 m and amplitudes of as much as 6 cm. Fossil fumaroles a few centimeters in diameter and tens of centimeters long penetrate the unit in its proximal region and were fed from the underlying coarse unit and from large fragments of wood. In most places they terminate against the overlying air-fall unit.

Beyond the limits of the coarse basal unit, the fine upper unit generally rests directly on the scoured ground surface. Locally, in the areas between and marginal to the broad lobes of the coarse basal unit, the fine unit lies on discontinuous lenses of coarse ash, lapilli, and blocks. These lenses are of two types. Type 1 consists of coarse lapilli and blocks on the lee sides of preexisting minor topographic obstructions and stumps. These lenses are commonly overlain by a thick, poorly sorted, massive or graded facies of the

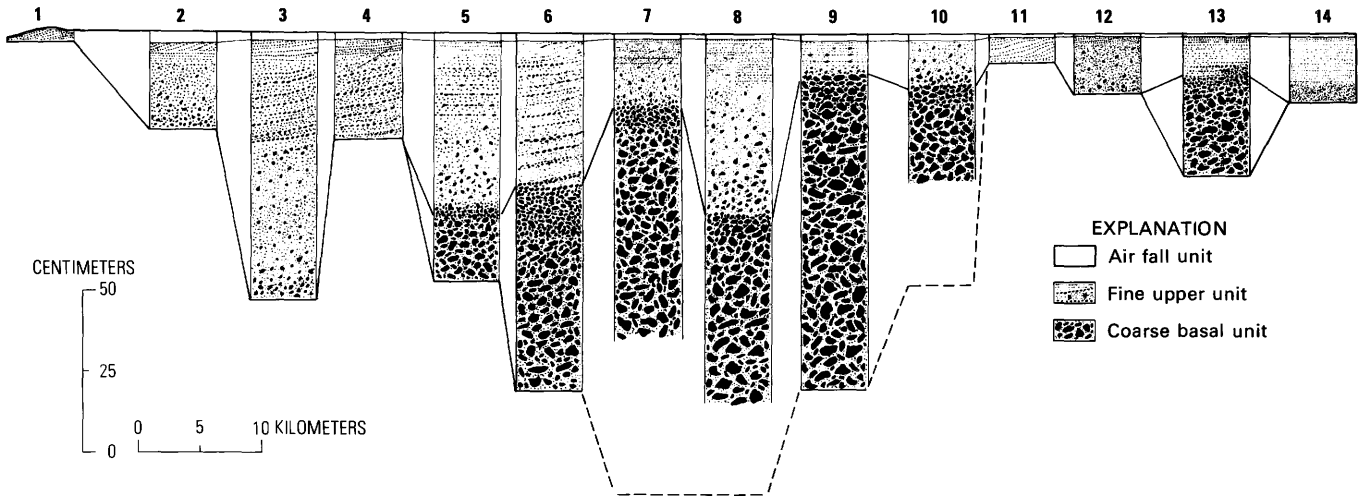

Figure 247.—Representative stratigraphic sections of pyroclastic-surge and related air-fall deposits. Localities shown in figure 244. Dashed line indicates estimated bottom.

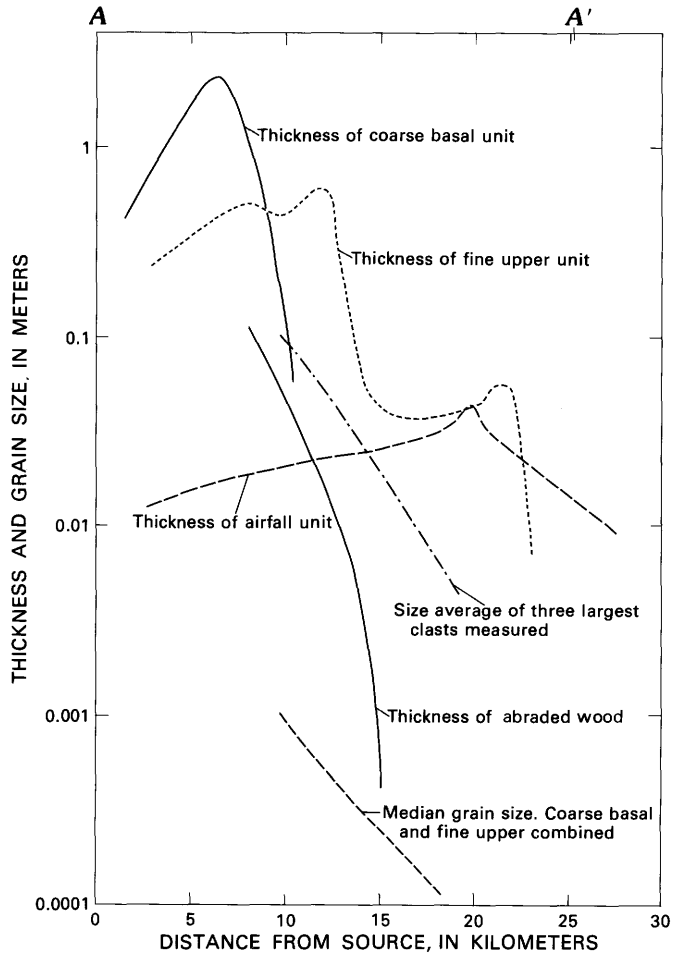

Figure 248.—Change in characteristics of the pyroclastic surge deposits as a function of distance from the source as measured on line A-A' (shown in fig. 244).

fine unit; they apparently result from deposition of large clasts behind obstructions due to lower flow velocities. Type 2 consists of both continuous and discontinuous dunes of lapilli and coarse ash. The dunes are commonly overlain by well-sorted, cross-bedded ash and lapilli that form secondary dunes on the lee side of the coarser dunes. The coarser dunes are not restricted to areas behind obstructions and may be a distal equivalent of the upper clast-supported part of the coarse basal unit.

Thick, structureless silt-sized ash layers of the upper unit containing widely spaced lapilli and blocks are located on the crests and lee sides of several bedrock ridges that are transverse to the surge flow direction. This distinctive facies of the fine upper unit may result from rapid deposition, with little sorting, in eddies and low-flow-velocity zones, along and behind the ridge crests.

The air-fall unit not only covers the region affected by the pyroclastic surge but extends to the north (fig. 252) and downwind to the northeast for a great distance. It is thickest, not adjacent to the surge source, but in a zone centered 15–20 km north, where it locally attains a thickness of greater than 6 cm. The deposit is a fine silt-sized ash with abundant accretionary lapilli, most of which are 2–4 mm in diameter. Larger, flattened accretionary lapilli 1–1.5 cm in diameter are present; these generally contain a rock-fragment core a few millimeters in size. These larger accretionary lapilli penetrated the ash layers 1–1.5 cm, producing small bedding sags. The locus of the maximum thickness of the deposit north of the vent area results from the rapid rise of ash-laden convective clouds from the entire surface of the moving pyroclastic surge (see Findley, 1981, p. 25). Condensing steam and water vapor in these rising clouds wet some of the ash, producing accretionary lapilli.

The air-fall unit includes about 0.016 km^3 of material within the mapped area (fig. 252). Because a significant proportion of the air-fall unit occurs in the total downwind fallout plume, however, the related dust cloud must have risen to great heights. If we assume that about one-half of the air-fall unit is present in the proximal region, its total volume is about 0.03 km^3 and the total volume of the three surge-related units is about 0.19 km^3.

LITHOLOGY AND SIZE

The pyroclastic surge deposits are unconsolidated and are composed of two general groups of rock types: old material and fresh gray dacite. The old material includes a heterogeneous assemblage of volcanic rocks from the volcano as well as material picked up by the moving surge. It includes fragments of andesitic lava flows, basaltic cinders and flows, dacitic dome rock, Tertiary volcanic rocks and sediments, old air-fall pumice, and shreds of wood and foliage. New air-fall pumice is present only in very minor amounts at the top of the fine upper unit and in the surge air-fall unit. Clearly the great bulk of the Plinian air-fall pumice and fallout from ash clouds associated with the pumiceous ash flows settled after the surge came to rest and after its associated fallout was deposited.

The fresh gray dacite is relatively dense (average

specific gravity about 1.8), has a subtle blue-gray cast, and has angular vesicles a few millimeters in size and fine-rounded vesicles about 10 μm in size in a glassy groundmass. Most fragments are angular, but some of the larger ones show an abraded breadcrust surface texture. All of the blocks larger than about 10 cm in diameter break along irregular, cooling-induced, radial fractures when struck with a hammer, demonstrating that the fragments were hot during transport and deposition.

In order to assess the amount of fresh dacite in the blast deposit, all the dacite was picked out of the coarser fractions of representative samples of the surge deposit and its weight compared with that of the entire sample (fig. 253). On the average, the fresh dacite constitutes about 50 percent by weight of the coarse fraction (and presumably all) of the deposit. However, the dacite is unequally distributed with the largest zone of concentration (> 60 percent) occurring to the east, approximately coincident with the hottest zone defined by both charring of standing trees (fig. 246) and charcoal in the deposit. Zones of particularly low dacite content occur directly north of the new amphitheater crater and down the course of the North Fork Toutle River. Here the dacite-rich pyroclastic surge apparently eroded and mixed with the moving dacite-poor debris avalanche over which it passed. The part of the surge that flowed east bypassed, and avoided mixing with, the cooler debris avalanche and consequently maintained a high enough temperature to char trees.

Size analyses were made on 94 samples collected to be representative of the coarse basal unit and the overlying fine upper unit collectively. Analyses of the proximal facies are no doubt biased toward the small size because of the difficulty of collecting large enough representative samples. The two parameters used to quantify size distribution are the median diameter Md_ϕ (the size at which the cumulative curve crosses the 50 weight percent level) and the deviation σ_ϕ (half the value in ϕ units between the points at which the curve crosses the 84 and 16 weight percent levels; see Walker, 1971). The median grain size decreases systematically outward from greater than 1 mm near the source to generally less than 0.25 mm at the pyroclastic-surge margin (fig. 254). The sorting of the deposit as measured by the deviation ranges from greater than 3 σ_ϕ near the source to less than 1.5 σ_ϕ at the margin (fig. 255). The size-sorting parameters of the deposit (fig. 256) clearly lie between the axes of the fields of the air-fall and ash-flow fields of Walker (1971, fig. 256).

Maximum clast size was measured by averaging the length of the intermediate axis of the three largest clasts. The maximum size exceeds 1 m in the proximal facies, and decreases to about 0.5 cm or less near the outer limits of the surge deposit (fig. 250).

DISCUSSION AND CONCLUSIONS

The massive explosions that generated the pyroclastic surge came from the headwall scarp of a huge landslide. The scarp was 700 m high, about 1 km wide, and inclined about 70° (Moore and Albee, this volume). Explosions began at the base of the scarp, but rapidly developed over much of the exposed slip surface as well as from the summit area of the volcano. During this initial phase this headwall scarp was itself moving down and north on a second, nearly parallel landslide fault about 600 m to the south; such action no doubt stressed and fractured the block exposed by the first slip surface permitting enlargement of the explosion source.

The geometry of deformation in the 2 mo prior to landslide failure on May 18 suggests that a large (0.11 km^3) cryptodome was emplaced at shallow depth in the region that was exposed in the initial landslide headwall. Explosions seem to have been generated by this sudden release of pressure (as much as 175 bars), caused by removal of preexisting rock material from the top and sides of the dome system. This permitted gases to expand explosively, to tear off pieces of material from the headwall, and consequently to involve a large mass of hot material in the eruptive processes.

Several features suggest that ground water was abundant in the mountain, that the cryptodome was surrounded by a hydrothermal system, and that much of the explosion was generated by flashing of this pore water to steam upon pressure release. Small lakes, ponds, streams, and steaming areas were common on the crater floor and the area adjacent to the crater prior to May 18. After May 18, water continued to drain from springs on the walls of the new amphitheater crater and to pond in lakes; these lakes finally dried up in early July. The repeated explosive activity from the summit crater prior to May 18 was apparently caused by steam explosions; no fresh magmatic material was erupted. Although nearly half

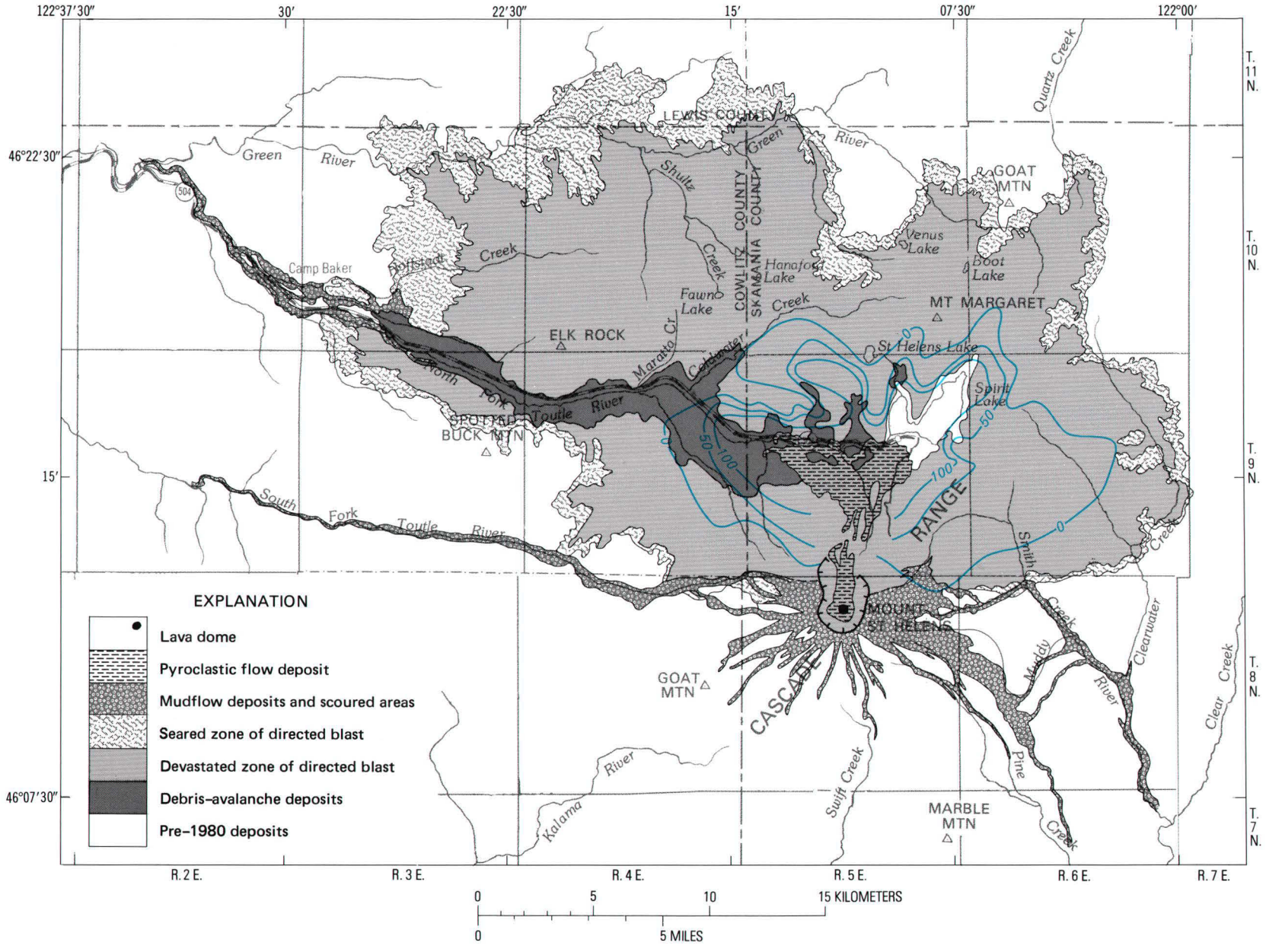

Figure 249.—Thickness of coarse basal unit of surge deposit in centimeters (blue).

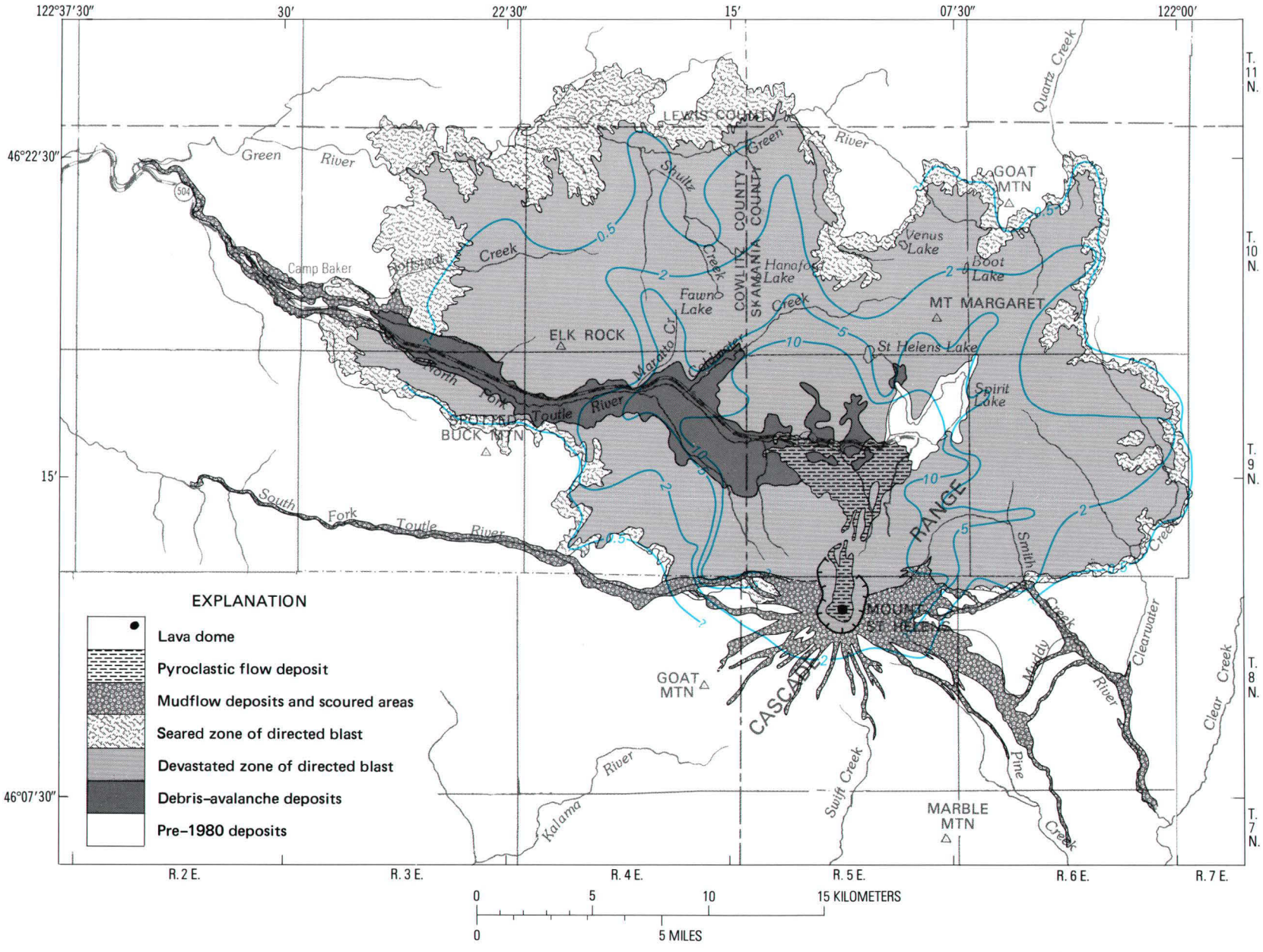

Figure 250.—Average diameter of the three largest clasts measured, in centimeters, within the surge deposit (blue).

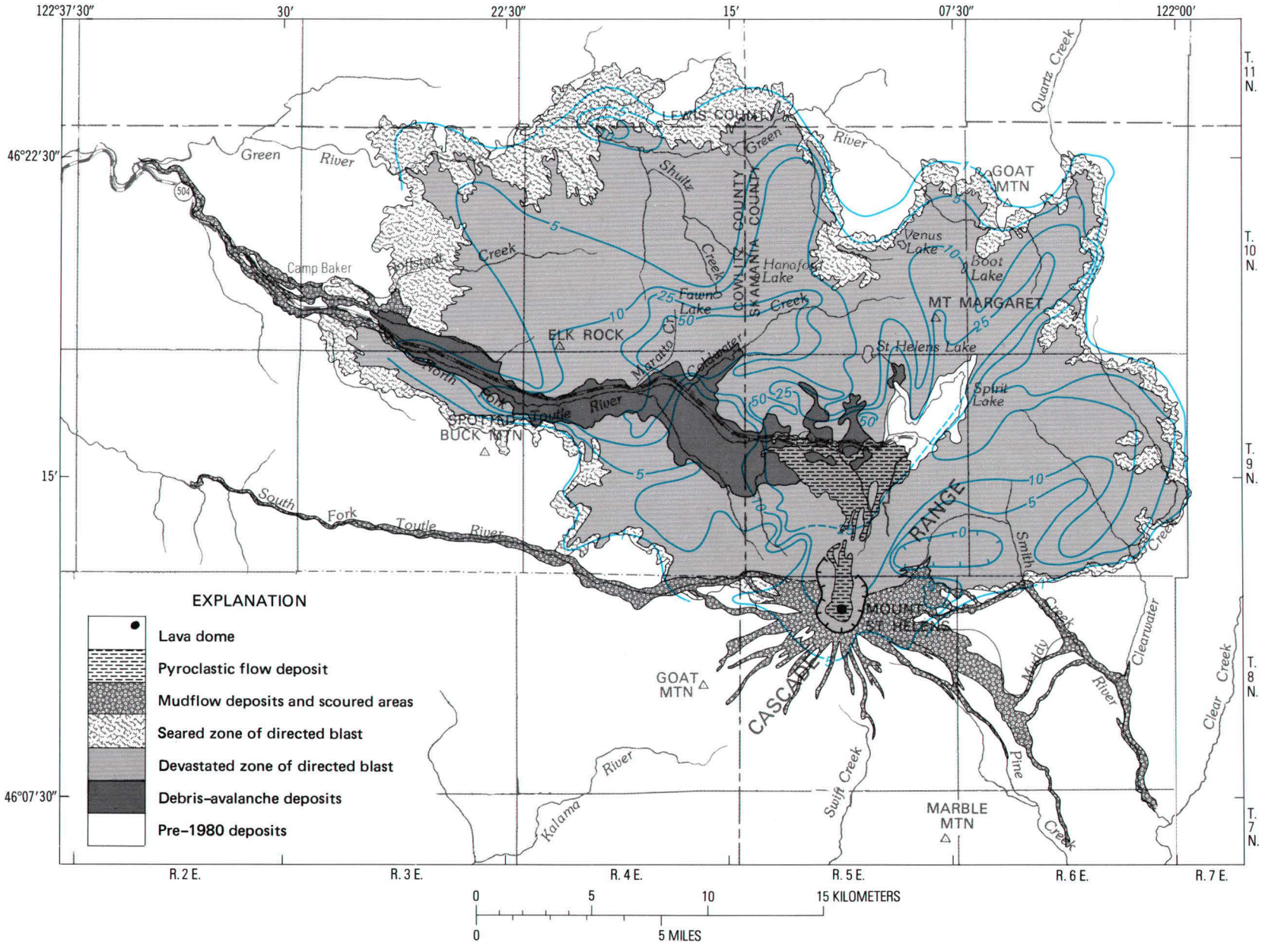

Figure 251.—Thickness of fine upper unit in centimeters (blue).

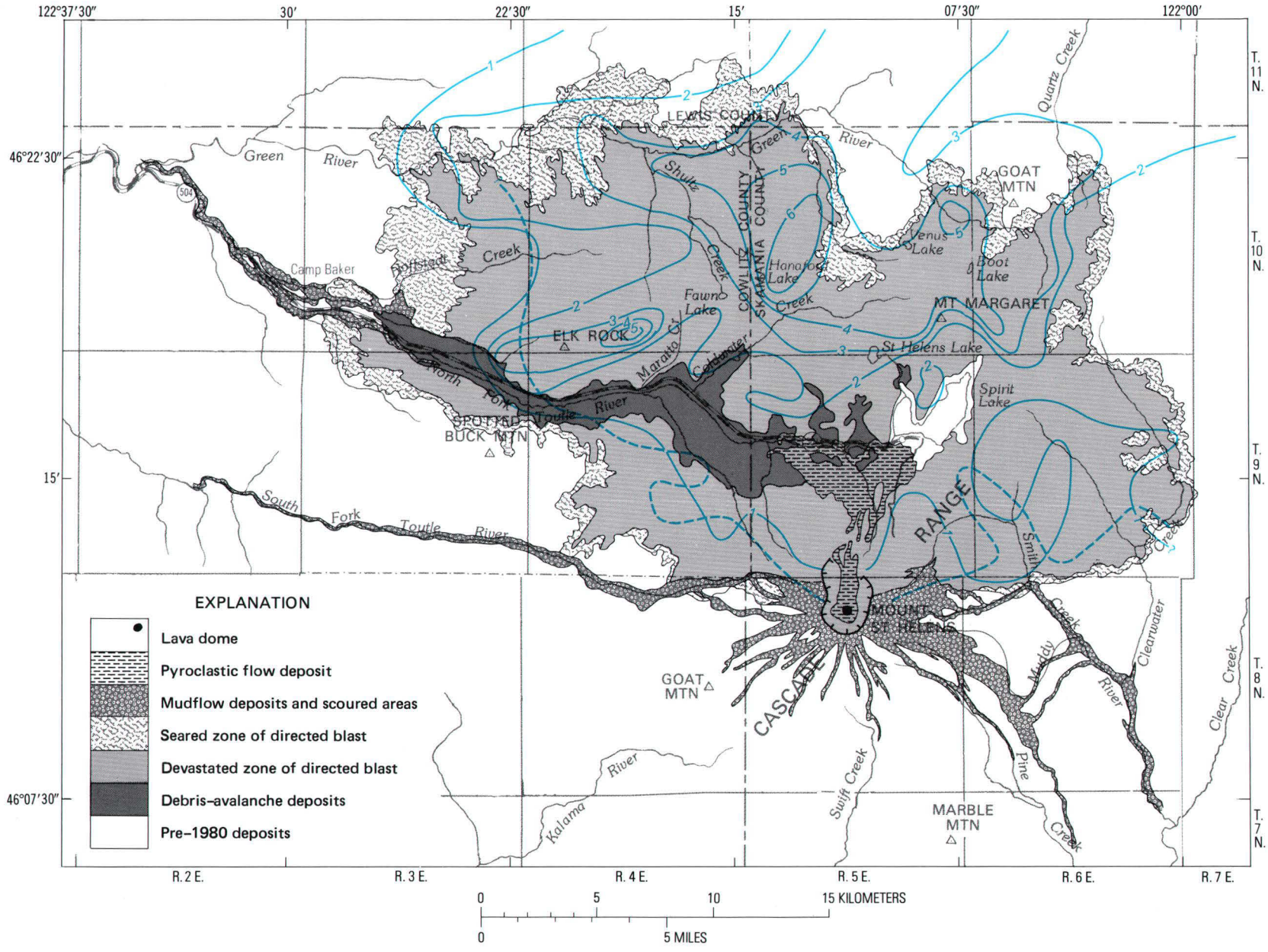

Figure 252.—Thickness of surge air-fall deposit in centimeters (blue). Dashed blue line, outer limit of accretionary lapilli.

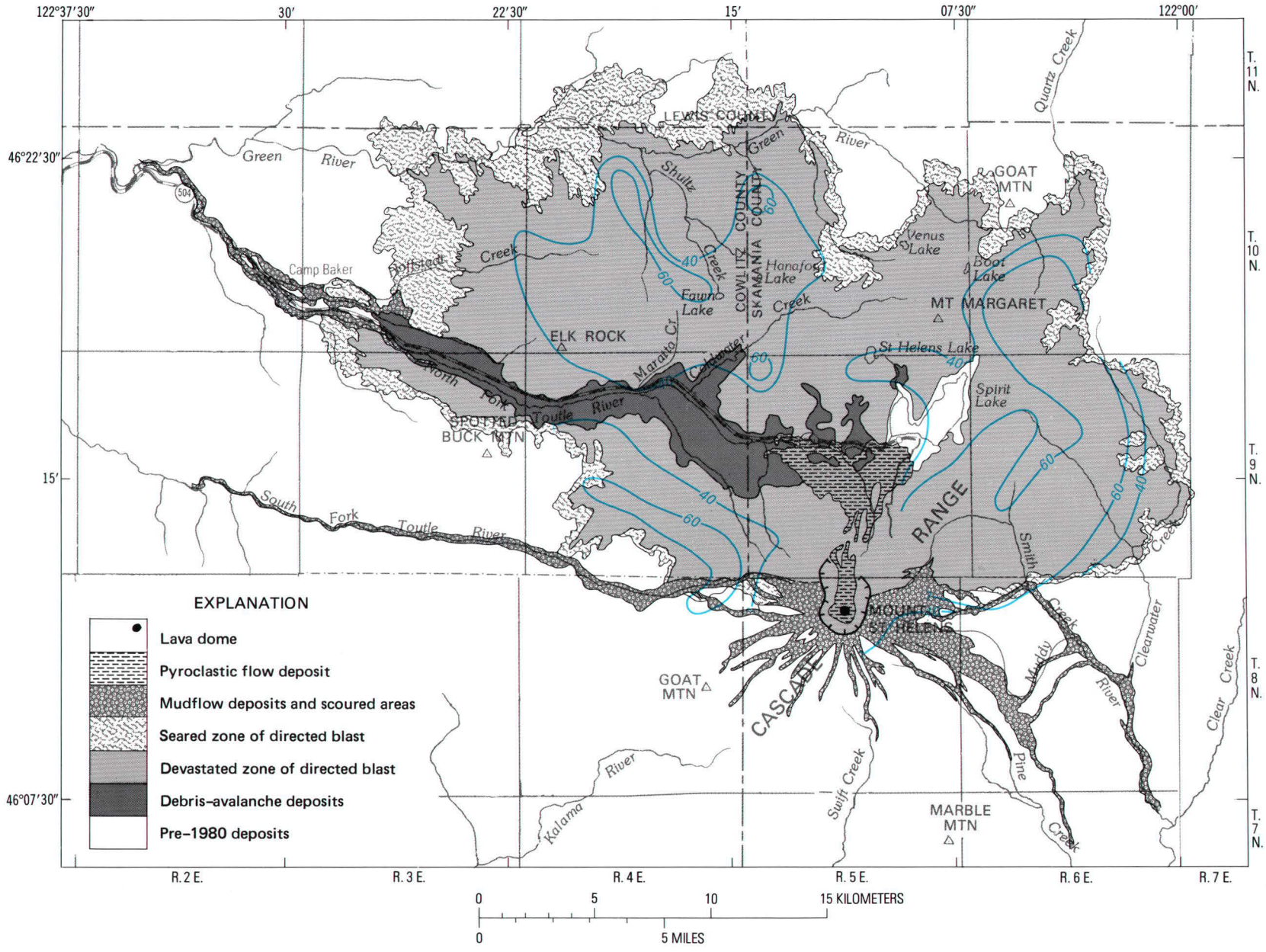

Figure 253.—Weight percent of fresh, gray dacite in composite samples of both basal and upper units of surge deposit (blue).

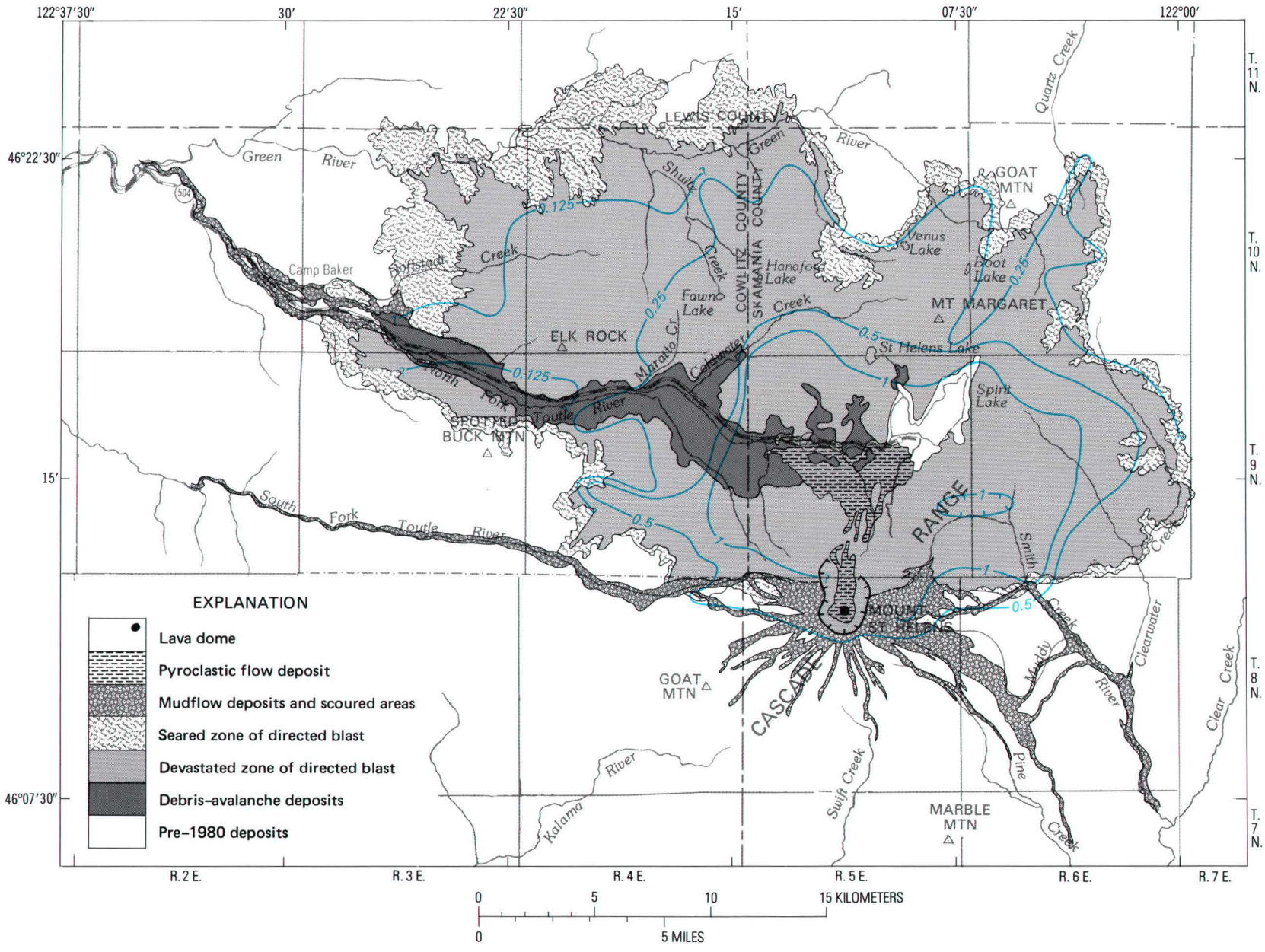

Figure 254.—Median grain size in millimeters of composite samples of both basal and upper units of surge deposit (blue).

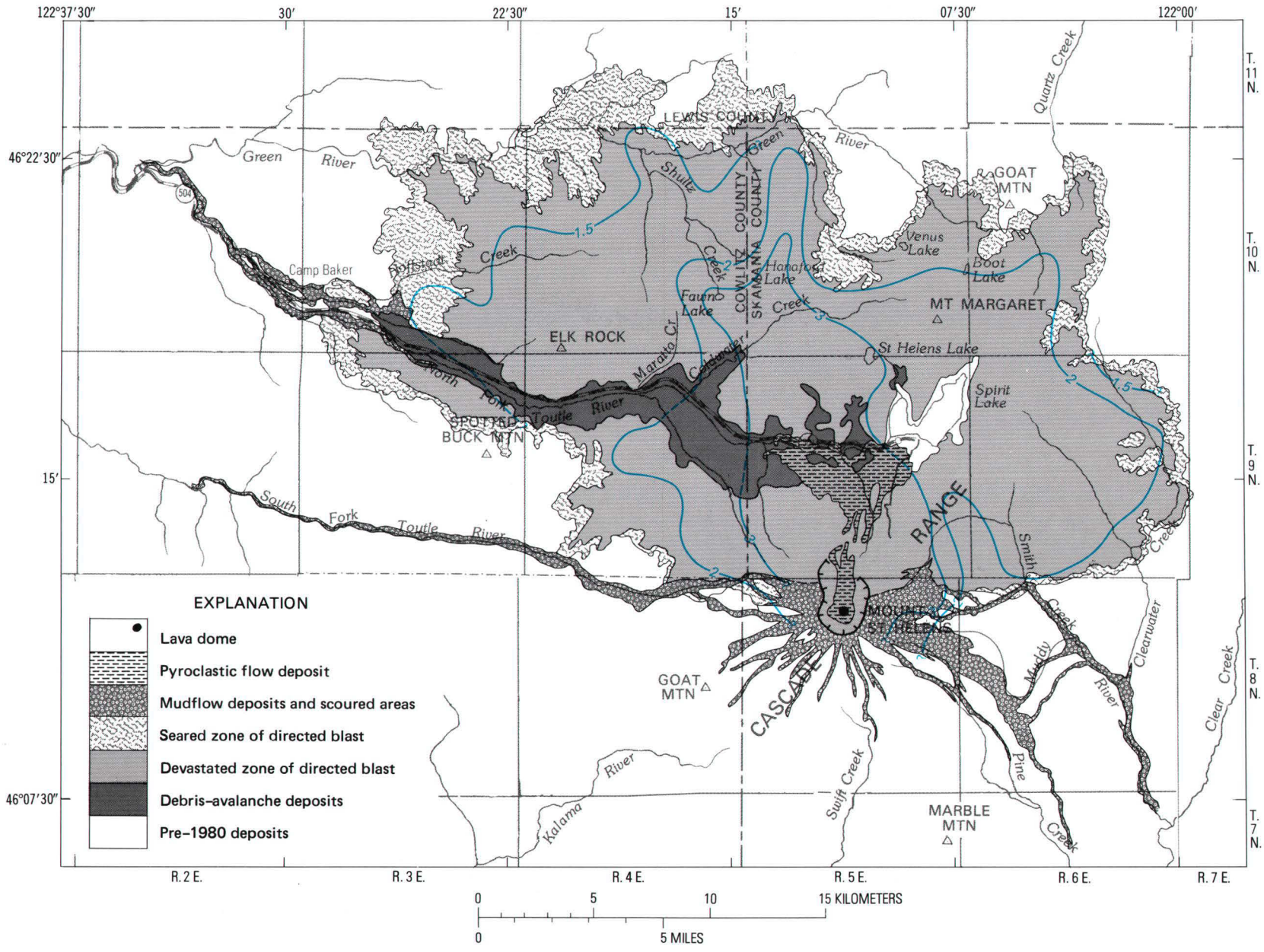

Figure 255.—Deviation (sorting) in σ_ϕ units of composite samples of both basal and upper units of surge deposit (blue).

of the pyroclastic-surge deposit is composed of fresh, hot dacite, it is relatively dense (specific gravity about 1.8), is generally microvesicular rather than pumiceous, and seems to have been too cool and viscous to have exsolved a large amount of magmatic gases explosively. The upper part of the surge deposit commonly contains fossil fumaroles, which are produced apparently by release of steam from a damp deposit. Abundant accretionary lapilli in the surge air-fall deposit attest to abundant water in the surge cloud (although much was no doubt mobilized from the hot surge flowing over moist and snow-covered ground).

The hot, fresh dacite constitutes about one-half

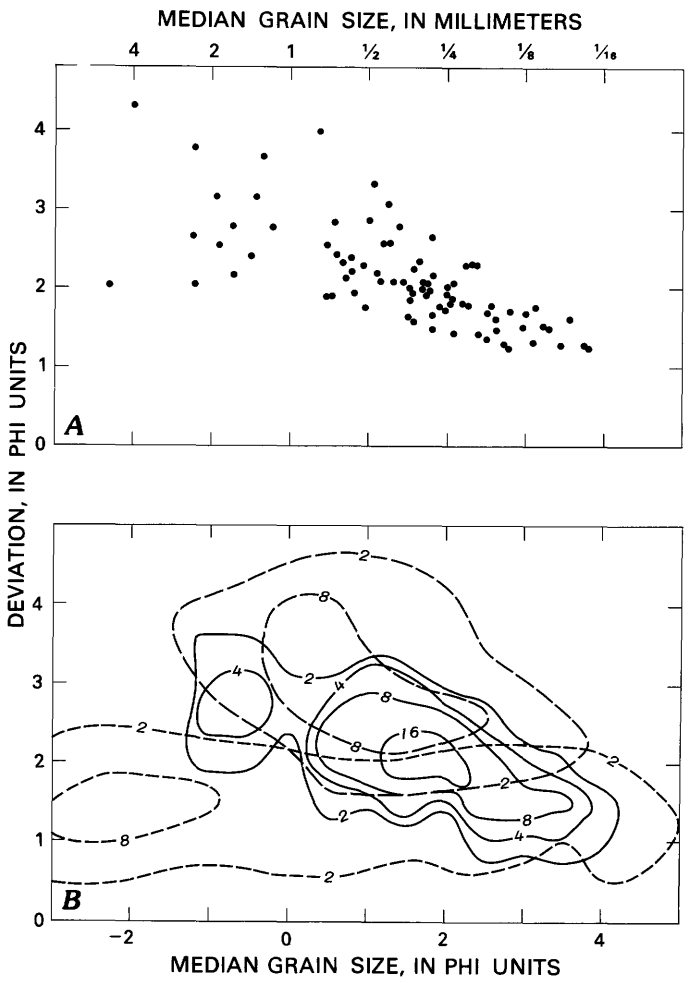

Figure 256.—Median grain size (Md_ϕ and mm) and deviation (σ_ϕ) of composite samples of basal and upper units of surge deposit. A, Measured samples. B, Contours of percent of samples within 1ϕ diameter circles. Solid lines, samples from A; dotted lines, air-fall deposits (from Walker, 1971); dashed lines, ash-flow deposits (from Walker, 1971).

of the pyroclastic-surge deposit or about 0.095 km³. Assuming that the surge deposit has a specific gravity on the ground of one-half that of the cryptodome (taken as 2.6), then the corrected volume of dense dacite in the surge deposit is 0.048 km³, and about one-half of the apparent volume of the cryptodome can be accounted for in the pyroclastic-surge deposit. The remainder probably was incorporated in the landslide. Because the temperature of the surge cloud where it charred trees (about 350°C) is clearly too high to have originated solely from steam explosions, the hot dacite must have contributed heat to the surge cloud. Apparently heat was transferred from the fragmented cryptodome to steam, entrained air, and other gases during explosion and transport. The correlation between areas of heavy charring of standing trees (fig. 246) and highest proportion of fresh dacite (fig. 253) supports this view.

The explosions feeding the pyroclastic surge appear to have originated from three processes: (1) flashing of pore water at elevated temperature to steam within a hydrothermal system surrounding the cryptodome resulting from landslide-induced reduction of pressure of as much as 175 bars, (2) limited exsolution of magmatic gases from the viscous and shattered dacitic cryptodome, and (3) further heating and expansion of steam, air, and magmatic gases by contact with the fragmenting cryptodome. The first process was probably dominant in the earliest phases of the eruption. The relative contributions of the three processes are not known, but the relatively dense character of the dacite fragments suggests that the second was least effective.

Photographs and eyewitness accounts (Rosenbaum and Waitt, this volume) indicate that the pyroclastic surge moved outward from the explosion source at high velocity as a ground-hugging cloud. The surge cloud moved off the mountain at more than 600 km/hr, but slowed to about 100 km/hr near its outer limits 25 km from the mountain. The steep-fronted head of the flow appeared to be less than 200 m high, but rapidly rising convective clouds billowed up from the moving surge and obscured features behind its leading edge. Eyewitnesses near the areal limit of the surge reported that when the cloud arrived, the temperature rapidly increased, and that the hot, ash-laden hurricane lasted less than 2 min (Rosenbaum and Waitt, this volume).

The fine upper unit apparently separated from the coarse basal unit during transport by a process of flow segregation. Despite the rather definite upper limit and areal extent of the coarse basal unit, in detail it tends to intergrade with the fine upper unit as distance decreases from the volcano. In addition, the fine upper unit covers a much larger area and is thickest farther from the source than the thickest deposit of the basal unit (fig. 248) despite its smaller total volume. These relations suggest that the upper unit separated from the basal unit during a single period of flow; the distribution would be difficult to explain by separate periods of flow originating from discrete, successive explosions at the source.

This flow segregation resulted from the more rapid settling of a lower, dense part enriched in coarse-grained material from an upper, low-concentration part enriched in gas and fine-grained material (see Fisher and others, 1980). The disconformity between the coarse basal and fine upper units results from shear produced by the greater velocity of the more mobile upper unit.

During flow, hot rock fragments heated and expanded entrained gas and air causing billowing and turbulent convective clouds to rise through the horizontally moving surge. These rising gases carried fine material upward, and further enriched the upper surge in fine material, later deposited as the fine upper unit. Thus, the interaction of the rising convective cells and the ground-hugging surge tended to sort entrained fragments that were locally deposited as the thinly cross-laminated upper part of the fine unit (fig. 247).

Photographs taken from Mount Adams 50 km east of Mount St. Helens, slightly before the pyroclastic surge reached its greatest extent (Findley, 1981, p. 24), show ash-laden convective clouds rising more than 6 km high. These clouds rising from the entire area covered by the moving surge (600 km^2) carried fine ash to great heights, which later fell as the air-fall unit. Accretionary lapilli were formed as airborne ash particles were moistened and accreted by condensing steam or water vapor.

REFERENCES CITED

Findley, R., 1981, St. Helens, Mountain with a death wish: National Geographic, v. 159, no. 1, p. 3–33.

Fisher, R. V., Smith, A. L., and Roobol, M. J., 1980, Destruction of St. Pierre, Martinique, by ash-cloud surges, May 8 and 20, 1902: Geology, v. 8, p. 472–476.

Gorshkov, G. S., 1959, Gigantic eruption of the Bezymianny Volcano: Bulletin Volcanologique, ser. 2, v. 20, p. 77–109.

Gorshkov, G. S., and Dubik, Y. M., 1970, Gigantic directed blast at Shiveluch volcano (Kamchatka): Bulletin Volcanologique, v. 244, p. 261–288.

Sarna-Wojcicki, A. M., Shipley, S., Waitt, R. B., Dzurisin, D., Hays, W. H., Davis, J. O., Wood, S. H., and Bateridge, T., 1980, Areal distribution, thickness, and volume of downwind ash from the May 18, 1980, eruption of Mount St. Helens: U.S. Geological Survey Open-File Report 80–1078, 11 p.

Sekiya, S., and Kikuchi, Y., 1889, The Eruption of Bandai-san: Journal of the College of Science, Imperial University, Japan, v. 3, part 2, p. 91–172.

Sheridan, M. F., 1979, Emplacement of pyroclastic flows—A review: Geological Society of America Special Paper 180, p. 125–136.

Sparks, R. S. J., 1976, Grain size variations in ignimbrites and implications for the transport of pyroclastic flows: Sedimentology, v. 23, p. 147–188.

Sparks, R. S. J., and Walker, G. P. L., 1973, The ground surge deposit—a third type of pyroclastic rock: Nature Physical Science, v. 241, no. 107, p. 62–64.

U.S. Geological Survey, 1980, Preliminary aerial photographic interpretive map showing features related to the May 18, 1980 eruption of Mount St. Helens, Washington: U.S. Geological Survey Open-File Report 80–925, scale 1:62,500.

Vortman, L. J., 1980, Deduced physical characteristics of the May 18, 1980, eruption [abs.]: EOS, American Geophysical Union, v. 61, p. 1135–1136.

Walker, G. P. L., 1971, Grain-size charcteristics of pyroclastic deposits: Journal of Geology, v. 79, no. 6, p. 696–714.

Wright, J. V., Smith, A. L., and Self, S., 1980, A working terminology of pyroclastic deposits: Journal of Volcanology and Geothermal Research, v. 8, p. 315–336.

THE 1980 ERUPTIONS OF MOUNT ST. HELENS, WASHINGTON

DEVASTATING PYROCLASTIC DENSITY FLOW AND ATTENDANT AIR FALL OF MAY 18—STRATIGRAPHY AND SEDIMENTOLOGY OF DEPOSITS

By RICHARD B. WAITT, JR.

ABSTRACT

Triggered by an earthquake at 0832 PDT on May 18, 1980, an enormous landslide abruptly relieved pressure on hot gas and fluids trapped within Mount St. Helens, which consequently exploded laterally through part of the landslide mass. The gas-and-rock mixture swept off the volcano as a catastrophic, hot, steep-fronted pyroclastic density flow that leveled timber in a 500-km² area north of the mountain. Within 15 km of the volcano on ridges as well as in valleys, the density flow deposited a layer of massive to indistinctly bedded, normally graded gravel (layer A1); trailing phases of the flow deposited normally graded bedded and laminated sand (layer A2), which carried beyond the limits of layer A1 and even beyond the downed-timber zone. Some of the fine material and scorched tree fragments from a cloud that convected off the density flow were drawn up by the initial central-eruptive column; they were distributed by air fall as a sandy silt (layer A3) characterized by pisolites (accretionary lapilli). The zones of maximum thickness of layers A1, A2, and A3 are progessively farther from the mountain. The material of layer A2 was transported laterally through the turbulent zone of the mountain flank; the material of layer A3 bypassed the mountain flank owing to its upward and outward trajectory.

Timber was downed and vehicles were overturned during an initial erosive phase that preceded the deposition of layers A1, A2, and A3. A wave of searing gas from the mountain followed the erosive interval and the accumulation of layer A1, accompanied and outlasted the accumulation of layer A2, and preceded the accumulation of layer A3. The widespread air-fall layer A3 accumulated between 15 min and 1 hr after the beginning of the eruption.

The pyroclastic density flow closely followed the topography as it passed over successive ridges and valleys, but was preferentially channeled by valleys, broad gaps through ridges, and other relatively low parts of the landscape. Deposits of the density flow at Mount St. Helens differ from the deposits of historic pyroclastic flows or surges but have some characteristics of each. The eruptive and emplacement processes at Mount St. Helens also differ from processes of pyroclastic flows and surges commonly deduced from ancient deposits. The density flow at Mount St. Helens owed nothing to classic processes of base surge or column collapse; it may reveal the emplacement process of widespread agglomerates around other modern and ancient volcanoes.

INTRODUCTION

Oversteepened by weeks of northward bulging, the north flank of Mount St. Helens failed as two catastrophic deep-seated landslides at 0832 PDT on May 18, 1980 (Moore and Albee; Rosenbaum and Waitt; Voight and others; all this volume). The sudden removal of a nearly 1-km thickness of overlying material caused entrapped gas to escape explosively over and through the landslides descending the mountain. A resultant hot pyroclastic density flow moved generally downslope by gravity. It moved at an average 200 km/hr outward as far as 25 km in the northwest through north-northeast sector, but to shorter distances east and west. It leveled and

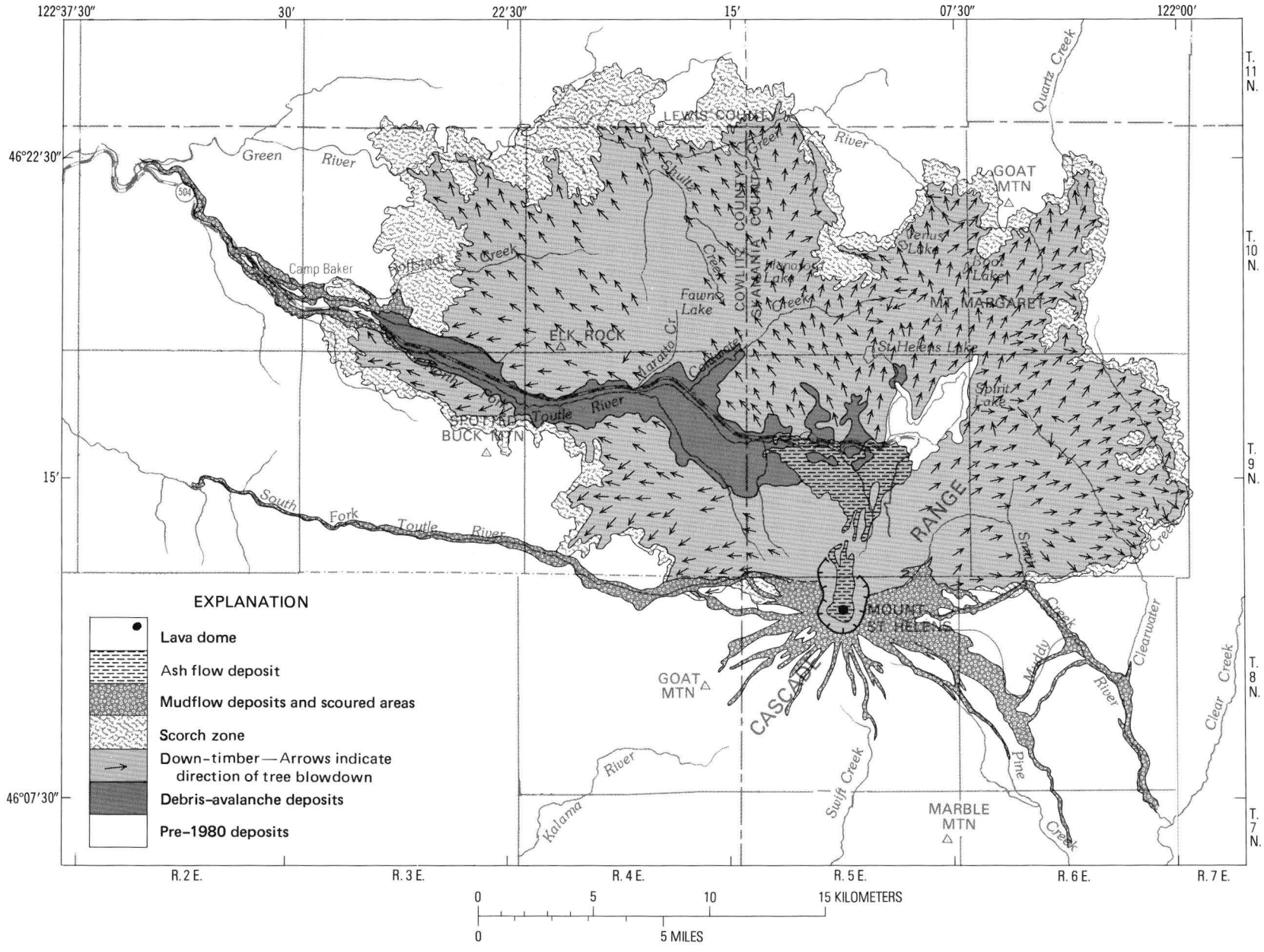

Figure 257.—Index map of Mount St. Helens area showing eruption features and the limits of down-timber and scorch zones. Geology modified from plate 1.

scorched timber (fig. 257), blanketed the area within 15 km of the volcano with a layer of hot lithic gravel, and covered most of the down-timber area with lithic sand.[1] An anvil-shaped cloud, part of the initial vertical column that shot up starting 4 min after the beginning of the density flow, blanketed not only the area of devastation but a vast area beyond with lithic sandy silt that fell partly as pisolites (accretionary lapilli). Of the air-fall and associated sequence deposited on May 18 (units A, B, C, and D of Waitt and Dzurisin, this volume), the deposits of the pyroclastic density flow and the attendant air fall constitute unit A.

The term "pyroclastic density flow" is applied herein to a phenomenon that broadly encompasses the realms of "pyroclastic flow" and "pyroclastic surge" as those terms have been differentiated in recent years. Excluded from discussion here, on the other hand, are the initial explosions high on the volcano that engendered the pyroclastic density flow. Thus the term "directed blast," which in this volume applies to the whole event—initial explosions, transformation into flow, and the flow—is inappropriate to my subject, the flow alone.

ACKNOWLEDGMENTS

This work has benefited by collaboration with colleagues in the U.S. Geological Survey. Some of the fieldwork in May and June was with Daniel Dzurisin. Judy A. Barker, Susan Shipley, and Michael P. Doukas assisted in the field in August and September. Discussions with J. G. Moore, N. S. MacLeod, R. P. Hoblitt, and C. D. Miller contributed to my understanding of various pyroclastic-flow and surge deposits. Vicki L. Hansen reduced much of the data from field notes to isopach maps and stratigraphic sections.

COMPOSITE STRATIGRAPHIC COLUMN

The pyroclastic density-flow deposit is divisible by grain size or texture into two or more units (fig. 258). Near the mountain a basal cobble or pebble gravel (layer A1) decimeters thick is overlain by a sand unit (layer A2) centimeters thick. Layer A2 is overlain by a sandy silt air-fall unit (layer A3) millimeters thick that is commonly characterized by pisolites 1–5 mm in diameter. All three layers are generally gray and contain abundant fragments of juvenile, vesicular gray dacite; they have the same stratigraphic succession everywhere they occur. Beyond about 13 km from the mountain, layer A2 forms the base of the section, and beyond the scorch zone layer A3 forms the entire unit (fig. 259). The boundary between layers A1 and A2 is very sharp in some areas but is gradational in most places, suggesting that layer A1 and the lower part of layer A2 are closely related in time and genesis.

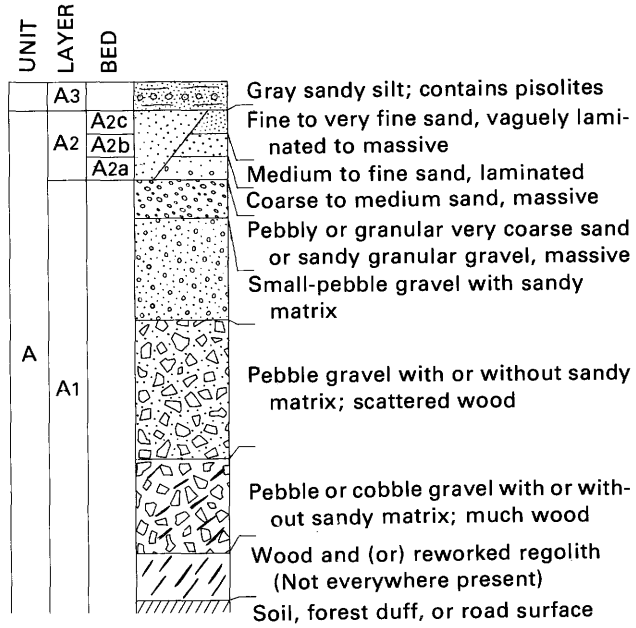

Figure 258.—Composite stratigraphic column of pyroclastic density flow and air-fall deposit (unit A). Sediment terms refer only to grain size and have no implications of rounding, sorting, or genesis.

[1]Although deposits discussed herein are to some degree pyroclastic in origin, they are also sediments. This and companion reports need a grain-size designation for each phi interval between silt and cobble size to apply commonly to various pyroclastic, water-laid, mudflow, and landslide deposits and to clastic deposits of uncertain origin. Pyroclastic size terms (ash, lapilli, blocks) are insufficiently divided for these purposes, whereas the Wentworth sediment-size terms (silt, sand, gravel) are sufficiently divided. The use of sediment-size terms for pyroclastic deposits may irritate some readers, but the terms are unambiguous and they avoid the need to invent a nonstandard ad hoc division of pyroclastic terms. Grain sizes were determined from field comparison to Wentworth size standards; clastic materials are classed by median size of particles (Folk, 1974, p. 24–29). "Gravel" thus designates only the median size of particles composing a unit and has no implications whatever of rounding, sorting, or genesis. Specific names like "small-pebble gravel," "very fine sand," "granular medium sand," or "sandy silt' are Folk's classification, which utilizes the standard Wentworth size designations.

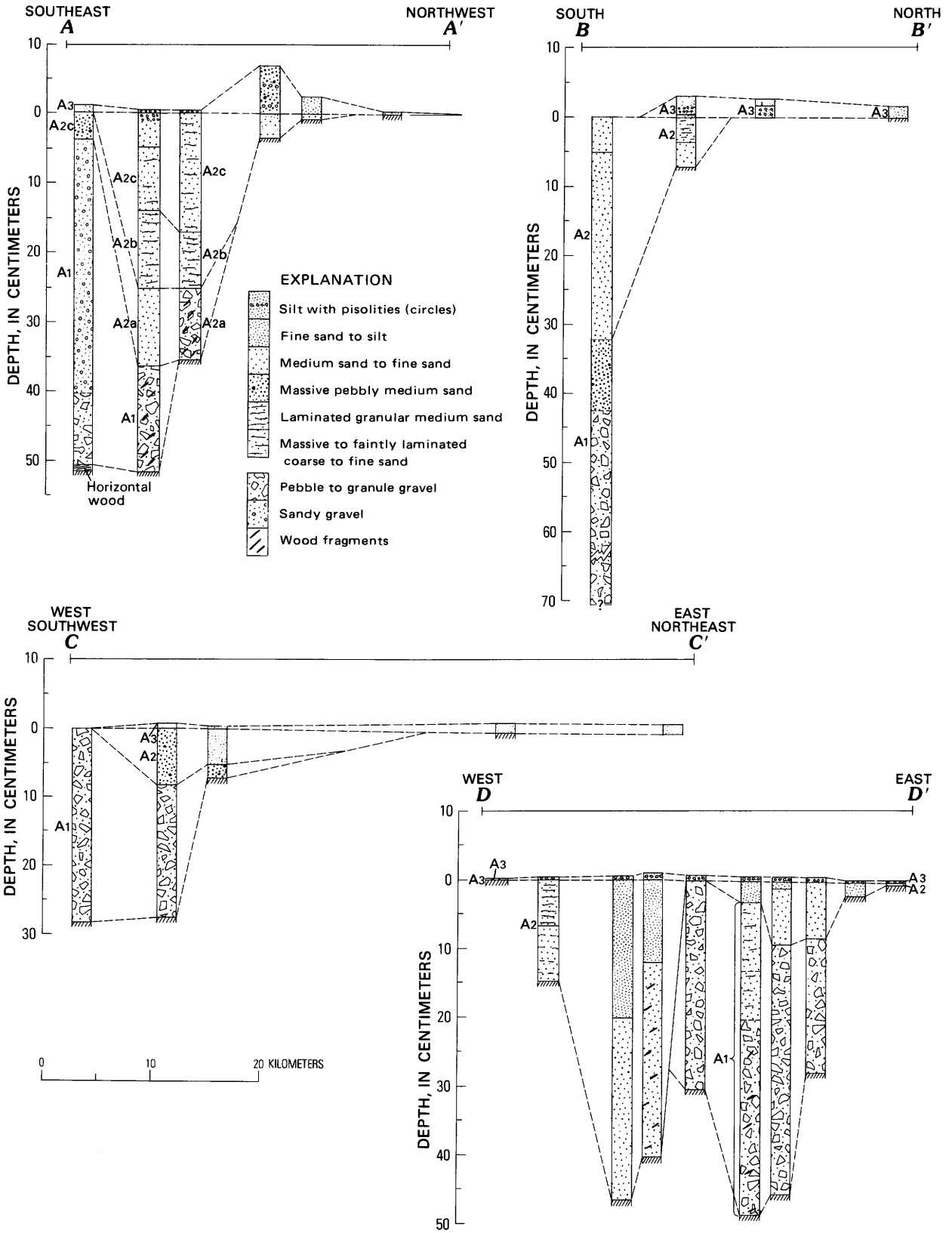
SOUTHEAST
A
NORTHWEST
A'
DEPTH, IN CENTIMETERS
A3
A2c
A2b
A2a
A1
Horizontal wood
EXPLANATION
Silt with pisolities (circles)
Fine sand to silt
Medium sand to fine sand
Massive pebbly medium sand
Laminated granular medium sand
Massive to faintly laminated coarse to fine sand
Pebble to granule gravel
Sandy gravel
Wood fragments
SOUTH
B
NORTH
B'
WEST
SOUTHWEST
C
EAST
NORTHEAST
C'
WEST
D
EAST
D'
0 10 20 KILOMETERS

The contact between layers A2 and A3 is sharp in most exposures but is gradational in some places where layer A2 is thickest. The generally sharp changes in grain size, texture, and color that define this contact indicate that layer A3 was formed by a different process and at a later time than layers A1 and A2.

BASAL GRAVEL FACIES (LAYER A1)

Within 8 km of the crater in the northwest-through-northeast sector, the basal layer of the pyroclastic density-flow deposit is a poorly sorted, weakly stratified to nonstratified gravel of angular clasts. Stratigraphic cross sections parallel and normal to the direction of emplacement illustrate the variability within layer A1 (fig. 259). Near the volcano the lower part of layer A1 is cobble or pebble gravel whose large angular clasts are juvenile light-gray dacite and locally derived dark volcanic rocks. Most large local clasts are in the basal 20 cm. Beyond 10 km from the volcano, layer A1 ranges from small-pebble to sandy granule gravel, whose clasts are also juvenile dacite and other angular volcanic rocks. On the east side of Spirit Lake, pumice fragments reworked from ancient set W (Mullineaux and others, 1975; Crandell and Mullineaux, 1978) are abundant. The light-gray to gray vesicular dacite clasts that constitute 10–50 percent of the deposit are fragments of an intrusive dome that exploded on May 18 to initiate the density flow (Moore and Albee, this volume; Moore and Sisson, this volume). The basal third of layer A1 commonly is rich in wood fragments. In some places where trees had been removed prior to May 18, the concentration of wood occurs above the base.

Layer A1 commonly grades upward from cobble to pebble gravel, from pebble to granule gravel, or from sandy gravel to granular sand. Because the top of this layer in places is gradational upward into sand, the contact between layer A1 and overlying layer A2 is arbitrary in places. On the northeast flank of the mountain, layer A1 is reversely graded, contrary to the general trend. The internal structure of layer A1 is massive to weakly stratified, but is obscure at the lateral margins of the deposit where a thin layer A1 consists entirely of massive granule gravel. In upper Smith Creek valley, where patterns of abrasion on standing flexible trees suggest that the density flow arrived from two directions at different times, layer A1 is thick and has the coarsest lithic fragments 40–60 cm above the base. At some sites 2–15 km north of the mountain, the sandy pebble gravel of layer A1 contains sand lenses.

The surface of layer A1 is undulatory. Where the deposit is a meter or less thick, relief may be 20 cm but generally is less. Where layer A1 is ponded meters deep in vales, surface relief may be more than half a meter over lateral distances of 5 m. Most of the surficial relief owes to drifting during emplacement. The deposit is thicker in the lee of stumps, downed logs, or other obstacles. But some of this surficial relief was caused by differential settling. Hours after emplacement unit A had many collapse pits, particularly where layer A1 had ponded. Some pits resulted from collapse into an openwork of downed logs and air entrained during emplacement. Above altitude 1,350 m, layer A1 accumulated on snow, which later melted to produce a "stagnant-ice" topography of kettles and hummocks with a relief of as much as 0.5 m.

Layer A1 was loose and hot for a few weeks after the eruption, but by September it had so cooled that only meter-thick sections remained warm. While hot, the very loose material nearly fluidized when disturbed, and had an odor of wood ash. By August, when the deposit had cooled and had been infiltrated by rainwater, the deposit was less fluid and the odor had disappeared. The deposit remained hot longest in the west-northwest and northeast sectors.

SAND FACIES (LAYER A2)

A sand facies 5–40 cm thick overlying the gravel facies (figs. 258, 259) is normally graded from granular coarse sand to fine sand, or from coarse or medium sand to very fine sand. In some areas the base of layer A2 is gradational with layer A1. Beyond the outer and lateral limits of layer A1, layer A2 forms the base of the density-flow deposit.

Figure 259.—Stratigraphic cross sections of pyroclastic density-flow and air-fall deposits at Mount St. Helens. See figure 261 for locations of sections. A-A', northwest radial; B-B', north radial; C-C', northeast radial; D-D', northwest-northeast arc 11 km from volcano.

STRATIGRAPHY

In many sections a lower, coarser massive bed A2a is overlain by a finer, vaguely to conspicuously laminated bed A2b (fig. 258 and cross section *A-A'*, fig. 259). The contact between the beds is generally sharp, suggesting that they were emplaced by somewhat different processes of sedimentation. The lower massive bed A2a commonly is gradational with the top of layer A1, suggesting that bed A2a was emplaced by the same general processes as layer A1. Immediately beyond the outer limit of layer A1, bed A2a forms the base of the density-flow deposit; farther out, bed A2a disappears and bed A2b forms the base. In some intermediate areas where A2a is missing, the boundary between layer A1 and bed A2b is very sharp.

The three-bed sequence is common but not universal. Where layer A2 is thick within the northwest-through-northeast sector, three beds constitute the normally graded layer A2: laminated medium sand (A2b), laminated fine sand (A2b), and massive very fine sand (A2c). The contacts between the beds as well as the basal and upper contacts of layer A2 are very sharp. Bed A2b locally comprises a fine sand bed sandwiched between two medium to coarse sand beds. In relatively distal areas where layer A2 forms the base of the deposit but where bed A2a is missing, the entire layer A2—beds A2b and A2c—is vaguely laminated. Although bed A2c is texturally transitional between bed A2b and layer A3, its upper contact with the darker colored layer A3 is generally sharp. In some areas where beds A2b and A2c are missing altogether, layer A3 sharply overlies granule gravel or coarse sand of layer A1 or bed A2a. Bed A2c did not accumulate toward the lateral margins of the flow in the east-northeast and west-northwest sectors.

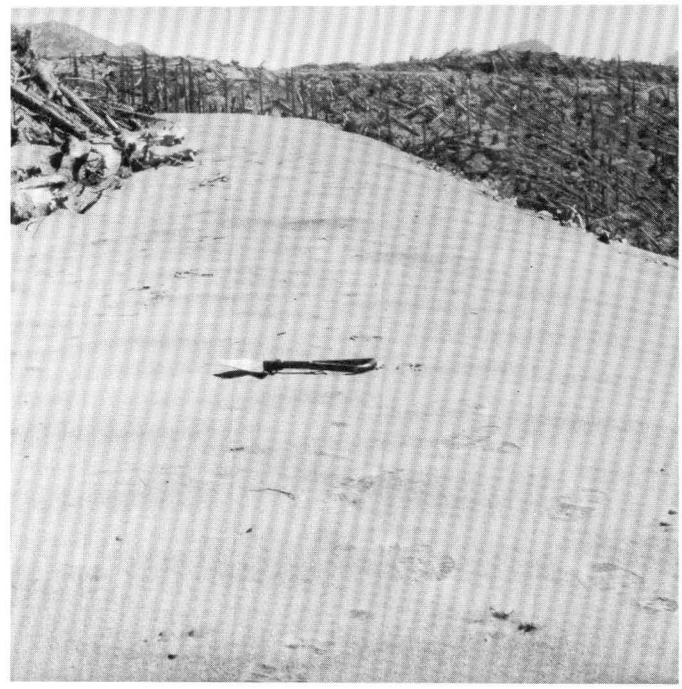

Figure 260.—Dunes or antidunes at surface of layer A2. View is roughly toward volcano from 11 km to the northwest.

LOCAL RELIEF AND SEDIMENTARY STRUCTURES

The surface of layer A2 is in many places quite wavy. The massive bed A2a where distinguished from layer A1 by a sharp contact may vary in thickness by as much as 20 cm, causing the wavy surface. The overlying laminated bed A2b forms ripples or dunes that embellish the broader relief at the surface of bed A2a. Some dunes are developed in bed A2a, embellished by bed A2b, and draped by bed A2c. Where bed A2c is missing, the nearly planar top of bed A2a is capped by bed A2b only at dune crests. Where only beds A2b and A2c are present, bed A2b forms the dune and trough topography, while bed A2c subdues the dunes, being thicker in troughs than on crests.

The laminated bed A2b, which is thickest in the northwest-through-northeast sector 10–20 km from the crater, shows plane laminae, dune-foreset laminae, and antidune-backset laminae. In some places the dune or antidune internal structure corresponds to surficial waves, most of whose crests are normal to the inferred direction of flow (fig. 260).

COMPOSITION AND ENTRAINED ORGANIC DEBRIS

In layer A2, as in A1, the juvenile gray dacite constitutes 10–50 percent of the clasts, and lithic fragments most of the rest. Along the lateral margin of the deposit just east of the volcano, layer A1 does not contain gray vesicular dacite; but farther out on this margin, in an area swept by an arm of the density flow from a more northern radial, layer A2 contains the gray dacite. Some areas in the north-through-

northeast sector contain white to light-brown pumice apparently reworked from thick deposits of ancient pumice layers (Crandell and Mullineaux, 1978; Mullineaux and Crandell, this volume).

Layer A2 generally contains less than 1 percent tree fragments, but toward the outer limit of downed timber it contains 2–5 percent broken limbs and twigs, stripped bark, and needles. Where layer A2 forms the base of the flow deposit and is divisible into beds A2a, A2b, and A2c, as near Elk Rock on the northwest and east of Spirit Lake on the northeast, bed A2a is rich in entrained wood—further evidence that bed A2a is closely related to layer A1. Where layer A2 forms the basal part of the flow deposit on the ridge north of the South Fork Toutle valley, the basal few centimeters is of soil and forest duff eroded and redeposited by the initial phase of the flow. At the edge of downed timber on the south side of the valley, this layer of reworked soil is overlain only by layer A3, and thus the zone of regolith erosion extends beyond the lateral margins of layer A2. Near the lateral margin of the flow east of the mountain, the basal redeposited regolith is absent. But the basal A1 and A2 layers there commonly contain as much as 10 percent wood fragments and needles; near the outer edge of downed timber layer A2 contains as much as 20 percent twigs and needles.

SANDY SILT FACIES (LAYER A3)

Capping the pyroclastic density-flow deposit in most places is massive dark-olive-gray[2] sandy silt (layer A3) generally less than 2 cm thick (figs. 258, 259). Layer A3 typically contains pisolites that are smaller than 5 mm, although some in proximal areas are as large as 1 cm. The pisolites consist of silt plastered over a core of similar silt or a sand-sized lithic or gray-dacite fragment; concentric structures indicate their accretionary origin.

Within 12 km north and northeast of the volcano, the pisolites are concentrated at the top of layer A3; beyond 30 km they are at the bottom. At 15–25 km north of the volcano, a pisolitic zone is both overlain and underlain by nonpisolitic silt (fig. 258). The color and texture of the silt seems not to change between the pisolitic and nonpisolitic zones in any area.

[2]Colors measured moist; designations from Munsell Soil Color Chart.

Variation in local thickness is much less in layer A3 than in layers A1 and A2 or even in the beds of layer A2. Where the surface of layer A2 is broadly wavy, layer A3 is nearly constant in thickness, although in some places layer A3 distinctly thins over each dune crest at the surface of bed A2b. These relations suggest that the material of layer A3 fell on lateral trajectories, but more nearly vertically than did the material of layers A1 and A2.

Within 20 km of the volcano in the northeast sector, white-pumice lapilli occur at and near the base of layer A3. Their subangular shapes might suggest that they were derived from older pumice deposits, which were thicker than 1 m on the northeast flank of the volcano (Crandell and Mullineaux, 1978, fig. 2). The density flow may have eroded some of these deposits from the volcano flank, and convection from the flow made them airborne. When part of this convecting cloud was drawn up by the developing central column a few minutes later, the pumice could have fallen with the earliest part of layer A3. Chemical analyses of the pumice, on the other hand, are more similar to those of juvenile May 18 pumice than to those of pumice from ancient tephras T, W, and Y (C. E. Meyer and M. J. Woodward, oral commun., 1980). Juvenile pumice like that of the subsequent central column air fall therefore may have been present in the trailing phase of the pyroclastic density flow. The restriction of this pumice to the Spirit Lake area suggests that a small amount of magma squirted out along the east margin of the moving landslide shortly after the beginning of the density flow but before the development of the central column.

Before it had become wet, layer A3 like layers A1 and A2 had the odor of wood ash. This odor was reported by eyewitnesses in the down-timber zone and characterized the freshly deposited layer A3 in distal areas like the Cowlitz River valley and Mount Adams.

AREAL THICKNESS VARIATIONS

The thickness of the pyroclastic density-flow and attendant air-fall deposit generally decreases outward (fig. 261), although local variation is large because of topography. The contours of figure 261, mostly drawn from thicknesses on slopes less than 5° on broad ridges, are thought to be representative. The deposit is thinner on steep slopes and thicker in vales.

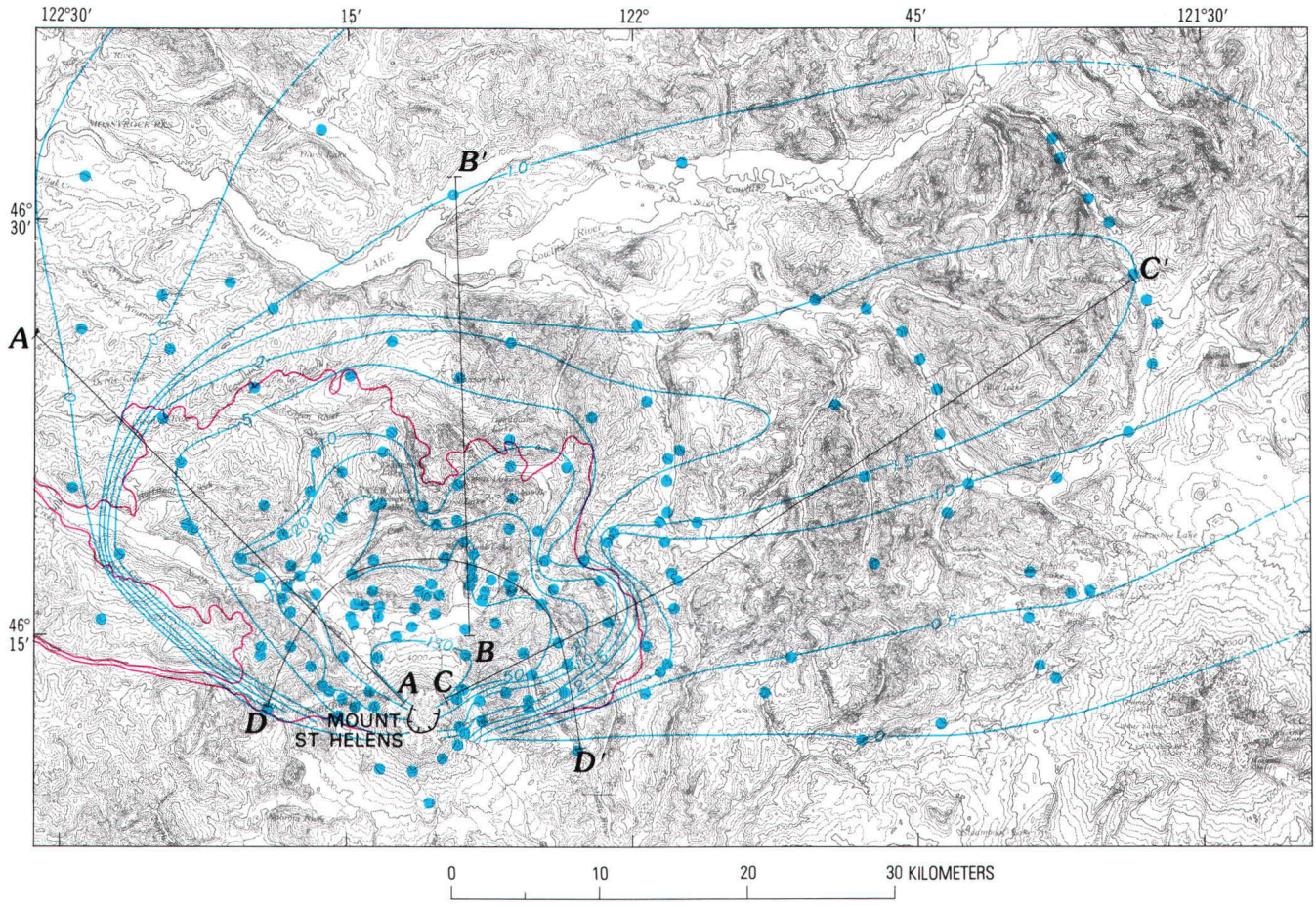

Figure 261.—Isopach map of May 18 pyroclastic density-flow and air-fall deposit (unit A), showing lines of cross sections A-A′ through D-D′ and outline of devastated area (in red). Solid circles, sample localities. Contour values in centimeters.

There has been little compaction since late May except in layer A3, which compacted 35 percent within a few days of May 18. In the Cowlitz River valley at Randle, layer A3 was 1.7 cm thick when measured dry 15 hr after it fell. It had compacted to 1.4 cm on May 22 after it had been wet from rain, and to 1.1 cm on May 26 when it had become saturated. The isopach maps are based on compacted thicknesses.

The deposit has four principal lobes following four topographic lows: upper Smith Creek valley on the east, Spirit Lake and upper Green River valley on the north-northeast, Maratta and Shultz Creek valleys on the north-northwest, and the North Fork Toutle River valley on the northwest (fig. 261). Around the high ridges north of Spirit Lake, the deposit bifurcates into two conspicuous lobes. The shape of these lobes mimics the configuration of the outer limits of the down-timber and scorch zones (fig. 257), showing that both the deposition of unit A and the downing of the timber were caused by a somewhat topographically channeled ground-hugging flow.

The zones of maximum thickness of layers A1, A2, and A3 are successively displaced outward from the volcano (figs. 262, 263, 264). Layer A1 is thickest just beyond the lower flanks of the volcano in the northeast-through-northwest sector; it thins out and disappears within 15 km northward, at shorter distances toward the lateral margins, and abruptly on the volcano flank (fig. 262). The thickness of layer A1 varies enormously with the underlying slope. Though it is a meter thick in level parts of broad ridges near the volcano, it may be only a centimeter thick on nearby steep slopes and meters deep in vales surrounded by these steep slopes. The material clearly was emplaced by a flow that was nondepositional on slopes steeper than 25°. The lobes of layer A1 (fig.

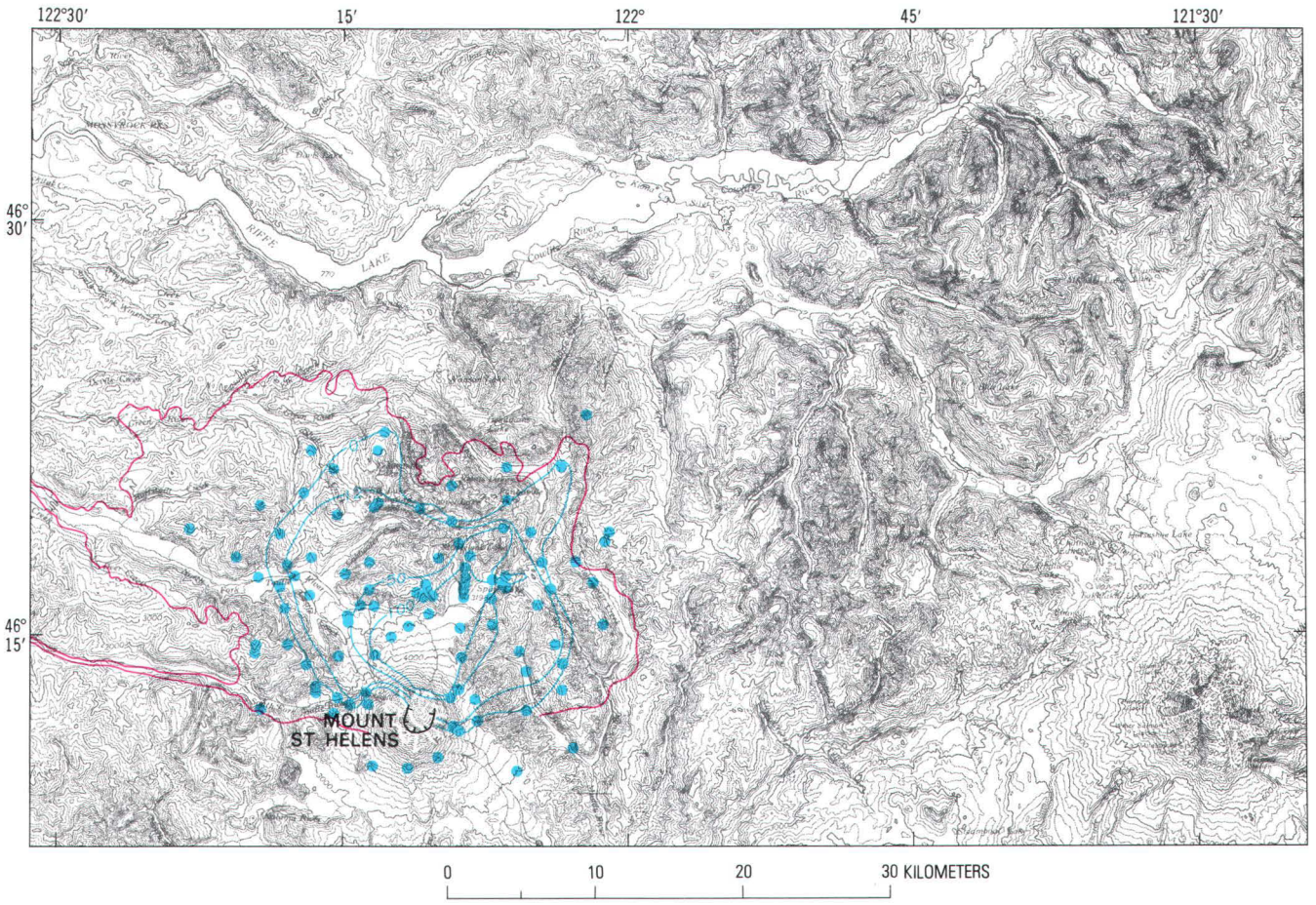

Figure 262.—Isopach map of gravel facies of May 18 pyroclastic density-flow deposit (layer A1), showing outline of devastated area (in red). Solid circles, sample localities. Contour values in centimeters.

262) in the general topographic lows correspond to the total-thickness lobes (fig. 261). The lobate zero isopach of layer A1 shows that the density flow channeled through ridgecrest sags and followed topographic lows northeastward along Spirit Lake and upper Green River valley, northwestward along the North Fork Toutle River valley and Maratta and Shultz Creek valleys, and eastward and southward down upper Smith Creek valley. The high ridges north of Spirit Lake blocked the flow, bifurcating layer A1 as well as the down-timber zone into lobes. This pattern reveals that layer A1 was emplaced as a ground-hugging flow moderately channeled by the principal topographic lows in distal areas, though it was relatively uninfluenced by proximal relief.

Layer A2, from its maximum thickness in an arc 11 km north of the volcano, tapers out 14 km farther north (fig. 263). It pinches out more abruptly toward the volcano, so thick sections of layer A1 low on the volcano flank are only thinly veneered by layer A2. The general thickness of layer A2 was influenced by major topographic features, as was that of layer A1. Layer A2 is relatively thick north of the North Fork Toutle River valley, along Spirit Lake and upper Green River valley, and along upper Smith Creek valley. The 20-cm contour, for example, is farther from the crater on the northwest where flow channeled down valleys than it is on the north where transverse ridges impeded flow. Layer A2 thins on slopes, but not nearly so much as does layer A1.

Layer A2 extends beyond the outer and marginal limits of layer A1 and even somewhat beyond the scorch zone. Layer A2 represents a phase of the pyroclastic density flow that was less competent than the phase responsible for layer A1. On the north the A2 phase trailed the A1 phase; beyond the lateral and outer margins of A1 it constituted the entire density flow. Layer A2 has a less lobate distribution than

does layer A1 (fig. 263), showing that the trailing phase of the density flow was less influenced by topography than was the A1 phase. Thus the A2 phase was less dense and not so strictly ground-hugging as the A1 phase.

Layer A3 is thickest about an arc from 16 km north to 7 km east of the volcano (fig. 264). It gradually thins for 50 km to the north and more than 150 km to the east-northeast, and it apparently constitutes part of the basal unit of the distal air-fall stratigraphy (Sarna-Wojcicki, Shipley, and others, this volume). Layer A3 has fairly uniform thickness over all but the steepest slopes. Vertical stumps within 20 km of the volcano are only meagerly veneered by A3 material, which is thicker toward no particular azimuth. Beyond 20 km in the north-through-east sector, however, the inclined branches on the near sides of standing conifers are more thickly plastered than are branches on the far sides. This distribution shows that the initial A3 material, which fell wet according to eyewitnesses, nonetheless fell along steep trajectories away from the volcano. Unlike the isopach maps of layers A1 and A2, the isopach map of layer A3 shows no influence of topography (fig. 264)—evidence that layer A3 was deposited as air fall, not from a density flow.

A thick zone of layer A3 trends east-northeast, the azimuth of the air fall from the central-eruptive column (figs. 358-362). This thickness trend in A3, however, extends from an area 20 km north of the volcano. A large volume of the layer A3 material carried downwind must have first been impelled northward from the volcano. Although all materials of unit A were distributed northward from the volcano, only the material of layer A3 was further distributed east-northeastward by winds aloft. This distribution shows that layer A3, which constitutes all of unit A beyond the outer limits of layer A2, was

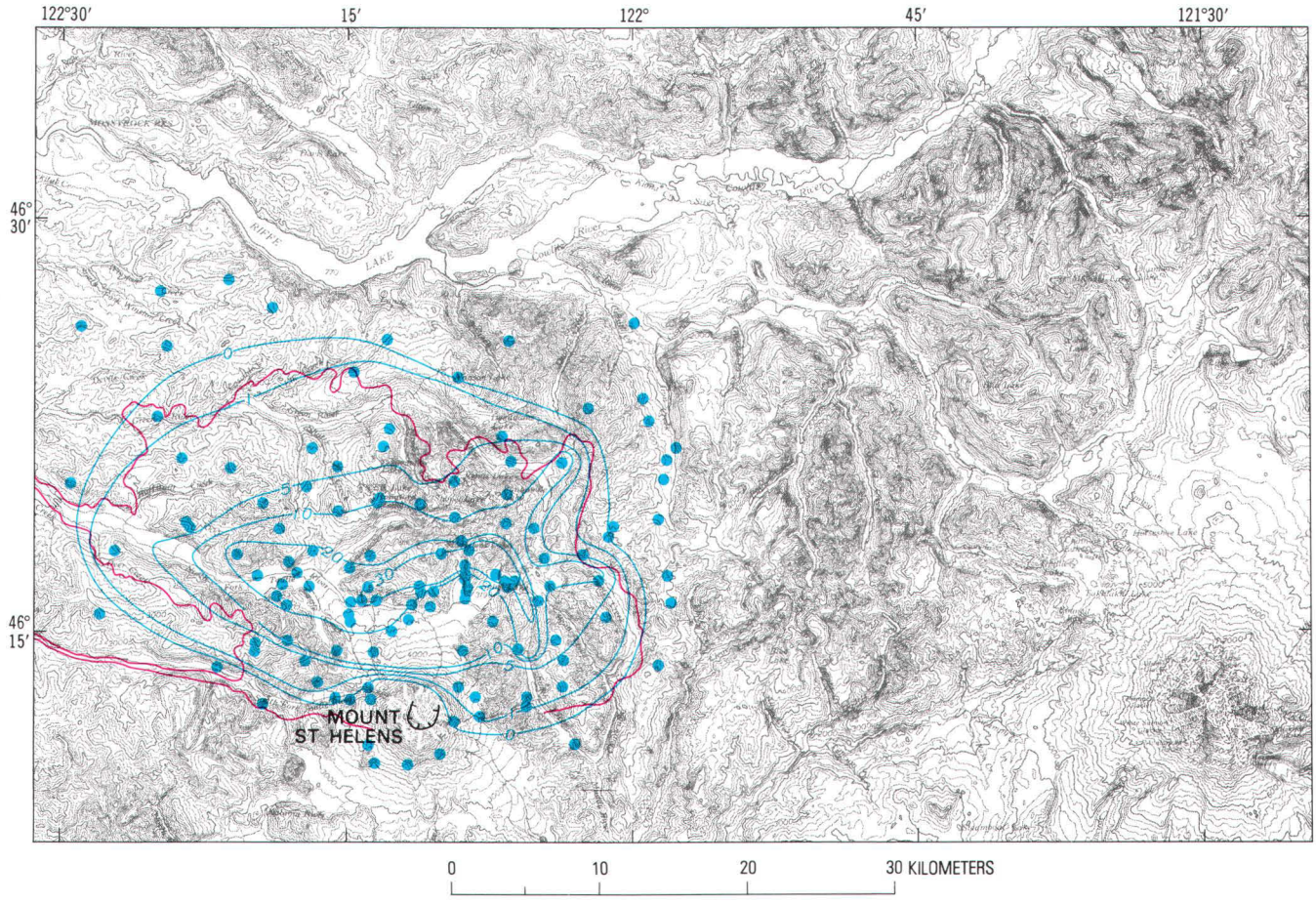

Figure 263.—Isopach map of sand facies of May 18 pyroclastic density-flow deposit (layer A2), showing outline of devastated area (in red). Solid circles, sample localities. Contour values in centimeters.

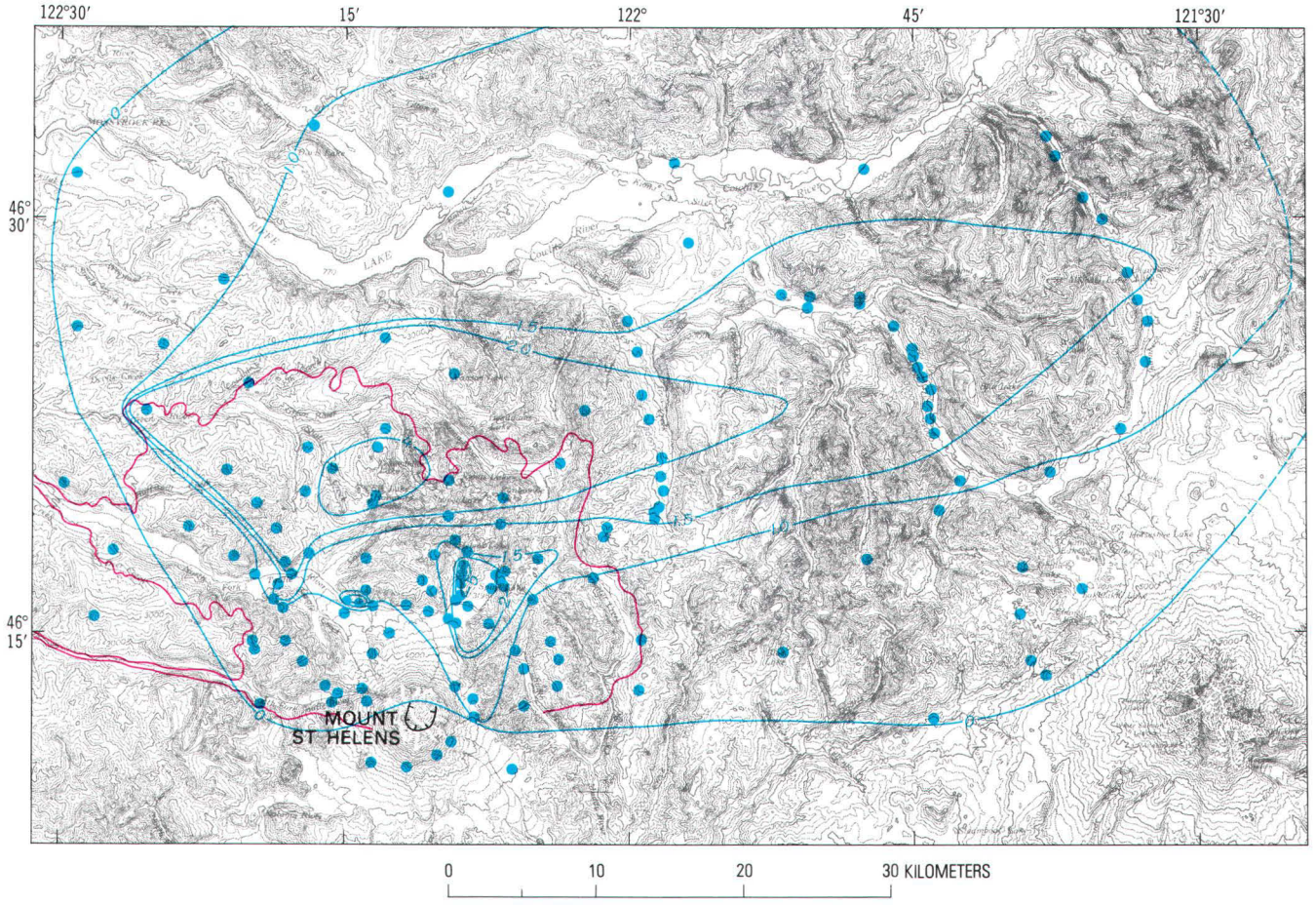

Figure 264.—Isopach map of silt facies of May 18 density-flow and air-fall deposit (layer A3), showing outline of devastated area (in red). Solid circles, sample localities. Contour values in centimeters.

distributed to relatively high altitude, whereas the materials of layers A1 and A2 were transported close to the ground. The process of distribution of layer A3 beyond the down-timber area is discussed by Waitt and Dzurisin (this volume).

SEQUENCE OF EVENTS REVEALED BY TIMBER

CONDITION OF TIMBER

The pyroclastic density flow uprooted, shattered, and carried away many of the trees as far as 12 km north of the volcano; in protected areas trunks left standing were topped and delimbed, and the fragments were transported out of the area. From 12 to 25 km timber was downed but not removed, and beyond the down-timber area is a narrow zone where standing trees are scorched (fig. 257). Although trees on ridges were felled radially outward from the volcano, trees behind some steep slopes were felled obliquely or even toward the volcano—evidence of vorticity in a density flow channeled by topography. The root balls of most felled, nontransported trees face the volcano, indicating the direction from which the density flow generally arrived. Some transported trees, however, are rotated 180°, indicating that the flow dragged some trees outward by their root balls.

Within 10 km north of the crater, timber was stripped from both the far and the near slopes of ridges, indicating that the flow followed topography, eroding timber as it flowed down into each valley and up over each succeeding transverse ridge. The near sides of ridges 10–12 km out are stripped, but not the far sides. Immediately north of very steep cirque headwalls, as at Fawn and Hanaford Lakes, trees

were blown down toward the volcano. Beyond about 12 km the front of the flow thus did not hug the ground strictly; rather it lofted as it swept over cliffs and then circled back toward the cliffs as eddies hundreds of meters in diameter. In the outer half of the down-timber zone in areas of rugged topography, fanning patterns of downed timber indicate flow divergence, whereas crossed-timber patterns indicate convergence of separated flow streams. On the east side of upper Smith Creek valley, small standing trees that are bent toward the volcano are more abraded on their far sides than on their near sides. This abrasion pattern shows that one arm of the density flow arrived first directly from the volcano; a second flow channeled down the valley, banked on the sharply concave far side of the valley, and then continued downvalley obliquely toward the volcano, abrading the far sides of the trees.

Shattered stumps within 10 km of the volcano splay upward in long splinters tilted away from the volcano (fig. 265), indicating that the trunks were pulled out end-wise while being toppled by a lateral force from the volcano. The transported logs and shattered limbs are intensely bruised by impacts with rocks or timber. At distances of 8–20 km in areas shielded from the flow by steep, north-facing slopes, many trees were snapped off midway up, some having a well-defined break and on the far side a peel scar. This pattern indicates that lateral shear by the flow was intense midway up the tree, but was small on the lower third of the tree. Floating on Spirit Lake and St. Helens Lake are splintered logs and limbs that the flow stripped from adjacent slopes. Beyond 12 km, where trees were felled or topped but not removed, Fawn, Hanaford, Venus, Boot, Meta, and Curtis Lakes are nearly free of floating timber.

The near sides of most stumps and standing delimbed trees were more abraded by projectiles than the far sides. Within 8 km of the volcano, the near sides of stumps are abraded several centimeters deep; in distal areas the near sides are roughened by sand blasting. On downed trees the near sides (former undersides) of limbs are debarked and abraded, indicating that even after the erosive phase that downed these trees, projectiles transported by the flow still had a strong lateral component. Some 10 km east-northeast of the volcano, the limbs of some downed trees are debarked on their near sides (former undersides) in a pattern that indicates that the path of maximum abrasion sloped 20° downward away from the volcano.

The near sides of standing trunks of topped trees within 15 km north of the volcano are stripped of bark, and the underlying wood is bruised and scorched. Behind sharp ridges and in distal areas, bark retained on the near sides of standing snags is dried, cracked, blistered, and partly detached from the underlying wood; but on the far sides the bark is unbaked, uncracked, and unblistered, and sap ran beneath it for months after the eruption. In the north-to-northeast sector small, limber trees that remained upright are stripped of needles and bark, and their branches are bent around the tree toward the direction that the large trees were felled. The roots of the large downed trees have their near sides (former undersides) scorched, and some roots were bent away from the volcano, toward the tops of the downed trees. These relations indicate that even at the outer edge of downed timber the wave of searing gas moving forcefully from the mountain either outlasted or entirely followed the downing of the timber.

Like the outer edge of the down-timber zone, the outer edge of the zone of scorched standing trees is sharp; in several places the base of scorching climbs through the trees from the inner edge to the outer edge of the scorch zone. The sharp outer boundaries of downing and scorching and the outward climb of scorching indicate that the flow lost energy and density and rather abruptly rose above the cooler ambient air. By 4 min or so after the beginning of the density flow, this low-level air was being drawn rapidly toward the volcano as the vertical column developed (Rosenbaum and Waitt, this volume).

Many trees lying on or even buried by the density-flow deposit burned or smoldered for weeks after the eruption. Inspection with night-vision glasses on May 29 showed the fires to be concentrated within 15 km of the volcano in the west-northwest and northeast sectors. In the west-northwest sector fires were two orders of magnitude more abundant than in the north sector, and in the northeast sector they were three orders of magnitude more abundant. These concentrations of fires reveal the path of the most lasting and hottest gas from the volcano. The northeast and west-northwest were directions to which gas preferentially escaped between the edges of the moving landslide

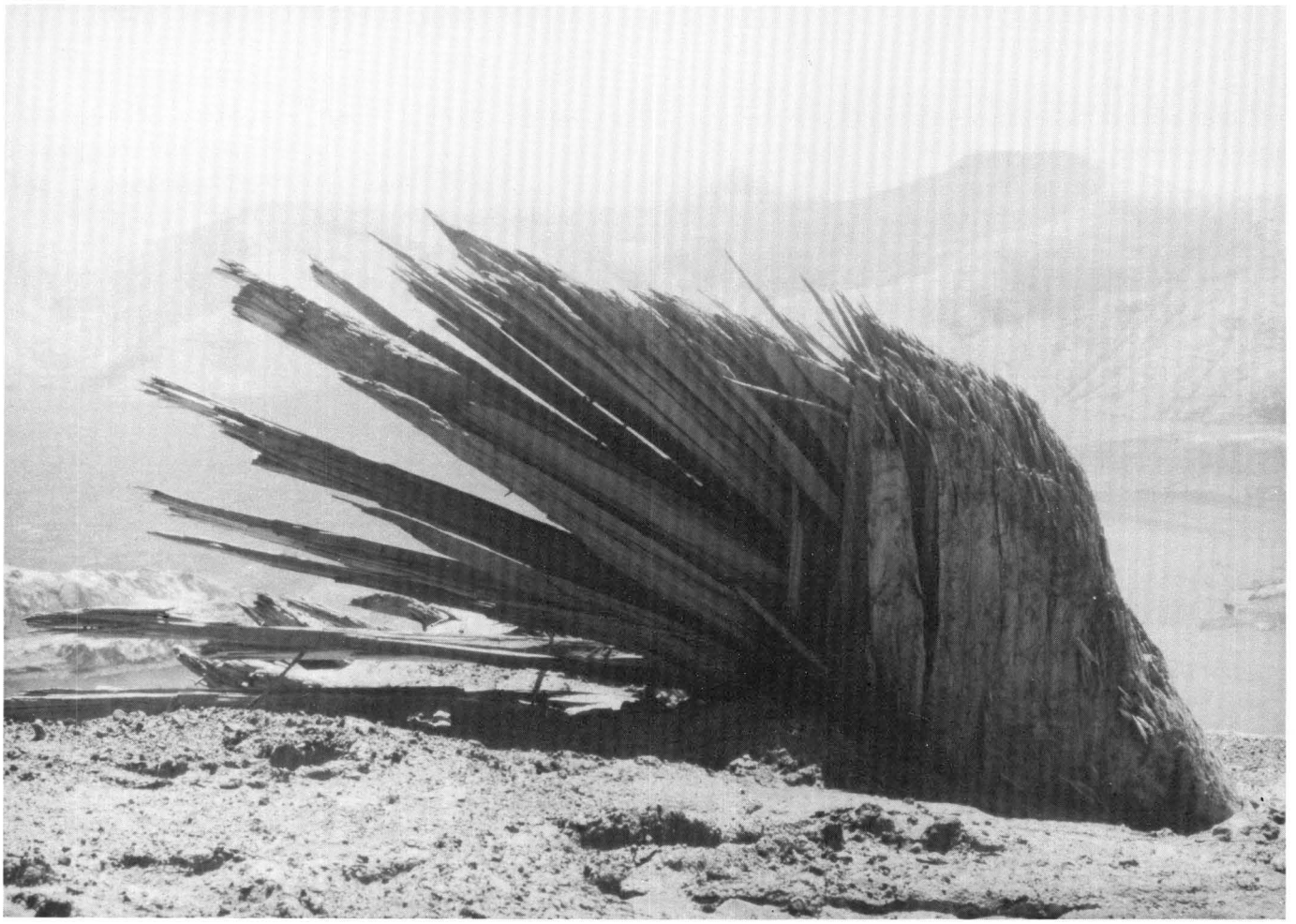

Figure 265.—Stump of fir tree 8 km north of volcano showing splinters tilted away from volcano and abrasion on side toward volcano.

and the walls of the developing theater, whereas heat within the density flow moving northward was mitigated by a greater volume of landslide material transported by the flow in that direction. Along the lateral margin of downed timber on the east flank of the volcano, trees were bent outward but not downed, and their needles were yellowed but not scorched brown or black, indicating that the lateral margin of the flow on the east was relatively cool. West of the volcano, on the other hand, the lateral margin of the downed timber is flanked by a wide scorch zone (fig. 257). On the west and southwest flanks, trees near timberline are scorched in a series of lobes along minor valleys. Small tongues of the density flow that channeled into the heads of these valleys were hot enough to scorch but not forceful enough to down timber.

STRATIGRAPHY OF DEPOSITS ON TIMBER

TIMBER WITHIN 12 KM OF CRATER

Downed timber 6–12 km north of the volcano is thickly overlain by the pyroclastic density-flow deposit. Trees that are fully down and buried by the basal A1 layer, and inclined trees protruding from the deposit, retain at least some bark on their topsides (former near sides), which are overlain by layers A1, A2, and A3 (fig. 266). Layers A1 and A2 are thin

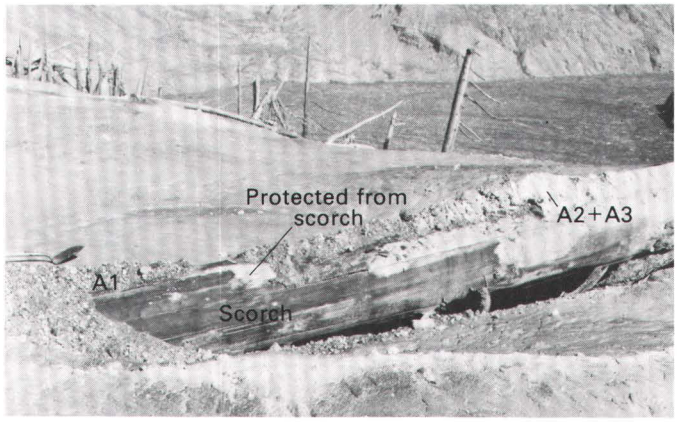

Figure 266.—Proximal downed tree projecting to left beneath coarse layer A1, in turn overlain by layers A2 and A3 at right. Trunk is darkened where tree was debarked and scorched where not protected by overlying layer A1.

because the curved surface of the trees failed to accumulate the flowing material. The fact that trees project baseward beneath layer A1 indicates that most or all of layer A1 accumulated after the trees fell; the presence of intact bark beneath A1 material indicates that abrasion by layer A1 was small on horizontal surfaces. The felled trees were thus stabilized during or before the accumulation of layer A1.

On downed trees projecting above but discontinuously veneered by the flow deposit, bark is removed and the underlying wood scorched where it had not been veneered by layer A1. This relation shows not only that layer A1 was not hot enough to scorch the large trees, but also that a flux of very hot gas moved from the volcano after layer A1 accumulated on the logs. Layer A3, on the other hand, forms a discontinuous veneer over the abraded and burned timber, showing that the abrasion and subsequent scorching preceded the arrival of layer A3.

At some places 10–12 km north of the volcano, limber trees that remained erect in the density flow are stripped of needles and are scorched. But some that were bent over and buried by the flow deposit, and were reexposed by gullying a few days later, sprang back as living trees. Similarly reexposed rocks retained living moss. The presence of green vegetation beneath layers A1 and A2 further indicates that the searing heat not only followed the leading erosive edge of the density flow, but also followed the burial of timber by layer A1.

TIMBER 15–25 KM FROM CRATER

Downed trees at Obscurity Lake, 15 km north of the volcano, are overlain by the same stratigraphic sequence that covers the ground, the base of which is layer A2 (fig. 267). The downed logs retain all their bark, whereas bark 1–20 m above the ground was stripped from the near sides of standing snags. These relations indicate that the trees were downed prior to the deposition of A2 and prior to the wave of searing gas that contributed to the stripping of exposed bark. Near the outer edge of the down-timber zone, small, limber, standing trees are stripped of needles and the remaining twig ends are abraded. But the lower branches buried by layer A2 retain blackened, brittle needles. These relations indicate that the searing heat

Figure 267.—Stratigraphic section atop distal downed tree. Layers A2 and A3 overlie bark.

both accompanied and outlasted the accumulation of layer A2.

SCORCH ZONE

In the zone of scorched standing timber 20 km north of the mountain, a very thin layer A2 forms the base of the density-flow deposit. On the near sides of trees brown-scorched branches are discontinuously coated with gray silt of layer A3. Needles covered with this silt are as scorched as those not coated (fig. 268). Thus, although the scorching may have accompanied and outlasted deposition of layer A2, it entirely preceded deposition of layer A3.

TREE FRAGMENTS IN DEPOSITS

SEQUENCE BEFORE AND DURING DEPOSITION

Tree fragments within the pyroclastic density-flow deposit inside the down-timber zone are splintered limbs and trunks of trees; beyond the devastated area they are branches and cones that had been stripped from the proximal forest, scorched, and transported outward. The upward decrease in concentration and size of wood within layer A1 reveals that most of the larger fragments traveled close to the ground and accumulated with the onset of A1 deposition.

Figure 268.—Scorched needles beneath layer A3 plastered on tree. Needles beneath layer A3 are just as scorched as those not covered.

Near the volcano bruised and scorched branch ends as long as 75 cm were deposited within the upper part of layer A2 and within and atop layer A3. Thus it appears that branches of trees shattered by the frontal part of the pyroclastic density flow were scorched and convoluted upward in the trailing cloud. Because the heavier branches could not have remained airborne for long after convection ceased, they must have settled during the ensuing minutes. Beyond the outer limit of layer A2, scorched fragments as long as 15 cm lie within layer A3 and in the base of the overlying central-column air-fall unit, showing that farther from the mountain tree fragments remained airborne for several tens of minutes.

Fir needles and small twigs are scattered throughout layers A1, A2, and A3, but in some areas on the north they are concentrated at the top of layer A3. The finer fragments stripped from the forests thus remained suspended for tens of minutes after the density flow had swept the devastated area. Most needles are brown or black regardless of their stratigraphic position, indicating that they were scorched prior to deposition. On the east flank of the volcano at the south edge of the devastated area, layers A1 and A2 contain unburned twigs and green or only yellowed needles, indicating that on this lateral fringe the density flow was forceful enough to dislodge branches and needles, but not hot enough to scorch them.

EFFECTS AFTER DEPOSITION

Wood incorporated into layer A1 near the volcano ranges from unbaked fragments to vitreous charcoal, but highly charcoalized wood occurs only in the northeast and west-northwest sectors within 10 km of the volcano. In these two areas the degree of charcoalization of small trees and wood fragments varies systematically with depth in layer A1. On ridges 8 km from the crater in both sectors, small trees standing above the density-flow deposit are bruised and scorched but not charcoalized. A few centimeters below the top of layer A1, the small trees and fragments have charred exteriors but brown and brittle interiors, while a half meter below the surface the wood is vitreous charcoal. Toward the base of the deposit, the wood is only baked brown and brittle but is not charcoal. This regular variation in degree of

charring of incorporated wood clearly resulted from baking after emplacement.

In the northwest-through-north-northeast sector, incorporated wood fragments near the base of the section are baked brown but not charcoalized, even though the thicknesses of layers A1 and A2 are similar to those in the northeast and west-northwest sectors where wood is charcoalized. In places on the north where the entire unit A accumulated a few meters deep in valleys and therefore remained fairly hot for weeks, needles in layers A1 and A2 are black, whereas those in layer A3 are only yellowed. The needles in layers A1 and A2 therefore must have been scorched only after deposition, although the general lesser degree of baking by the flow deposit in the northwest-through-northeast sector indicates that it was emplaced at lower temperature than the same deposit in the northeast and west-northwest sectors.

SEQUENCE OF EVENTS REVEALED BY MOTOR VEHICLES

EFFECTS ON VEHICLES

Vehicles and heavy logging equipment 8–20 km from the volcano were battered and scorched. Within the inner two-thirds of the down-timber zone, many vehicles were moved and some even overturned. Abrasion generally decreases outward from the volcano: vehicles within 13 km were battered, but those farther out were only sandblasted.

To the west-northwest and to the northeast, vehicles especially show the effects of heat: burned or blistered exterior paint, burned upholstery, melted exterior plastic, delaminated window glass. Even vehicles near the outer edge of the down-timber zone have melted plastic and delaminated windows in the west-northwest and northeast sectors—the same sectors in which fires in downed timber had been most concentrated.

STRATIGRAPHY OF DEPOSITS IN AND ON VEHICLES

Vehicles within 15 km of the volcano that were not overturned have inside them layers A1 through A3 in ordinary stratigraphic succession. Angular boulders as large as 30 cm were deposited inside vehicles 5 km west and 15 km north of the mountain, showing that even near the outer limits of layer A1 the density flow transported large rock fragments at least 1.5 m above the ground surface, although some may have been lobbed by uprooting timber.

An overturned truck 15 km northwest of the volcano is overlain successively by beds A2a, A2b, A2c, and layer A3—just as is the adjacent ground surface (fig. 269). The vehicle therefore overturned during an initial erosive phase of the flow and was not further disturbed during and after the accumulation of the basal flow deposit.

Material of layers A1 and A2 inside the automobile at the Coldwater I observation station was overlain by dry (dried by heat?) layer A3 containing pisolites as large as 1 cm. These materials entered the vehicle laterally through windows removed by the initial phase of the density flow. As in distal areas, layer A3 material in this proximal area fell on a sloping trajectory from the volcano.

SUMMARY OF EYEWITNESS ACCOUNTS AND PHOTOGRAPHS

Sequential photographs reveal that the pyroclastic density flow began while two great landslides descended the north flank of the volcano (Moore and Albee; Rosenbaum and Waitt; Voight and others; all this volume). Photographs show the first landslide descending to the lower flank of the mountain, then a series of spherical and partly lateral blasts emanating from the vacated area. These blasts then quickly enveloped the entire area and developed into a dense gray pyroclastic density flow whose fluted steep front advanced rapidly outward and downward off the volcano. Initially flowing northward, the density flow after several seconds also expanded off the volcano east and west as a dense ground-hugging flow from which a convoluting cloud convected upward well behind the leading edge. From photographs taken by G. D. Rosenquist and from limiting times provided by seismic signals, S. D. Malone (written commun., 1980) calculated the northward speed of the flow front at about 650 km/hr near the base of the mountain, and an average 275 km/hr from there to 5 km farther northeast. Eyewitnesses on Mount Rainier and others much closer saw a north-expanding, steep-fronted, dense cloud no more than

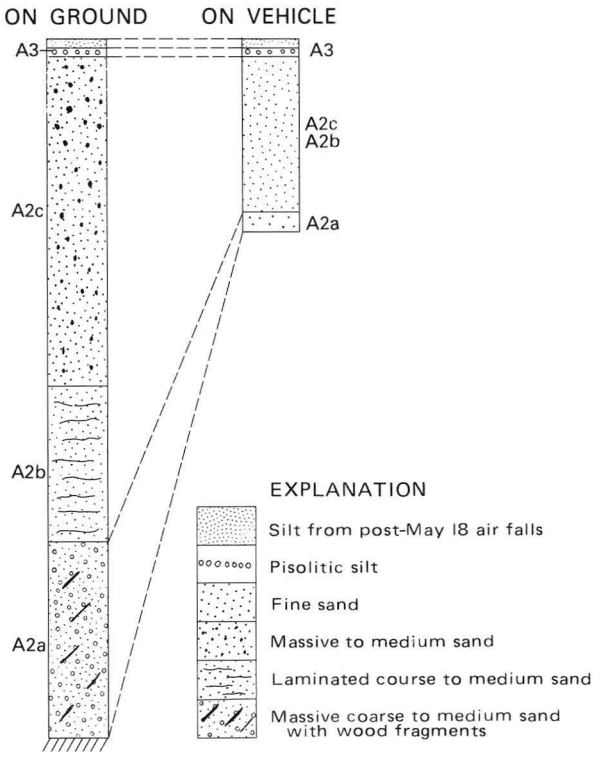

Figure 269.—Comparative stratigraphic sections on level ground and on underside of overturned vehicle near Elk Rock.

200 m thick that hugged the topography like a fluid, the front disappearing from view as it descended into valleys and reappearing as it ran up over divides (Rosenbaum and Waitt, this volume). It maintained this very steep, relatively low front as it flowed outward 20–25 km. While driving at about 100 km/hr, one party kept pace with and outran the front of the flow for several kilometers down a segment of the North Fork Toutle valley where timber afterward was leveled and overlaid by layer A2. Some trees tumbled at the front of the advancing cloud; others went down just behind the front of the cloud. One party was unscathed as the base of the density flow skipped overhead and trimmed the tops off the trees (Rosenbaum and Waitt, this volume).

Near the outer edge of the downed timber, the front of the dense, low-level initial density-flow cloud was followed seconds later by searing heat and laterally moving dust lasting 2 min or less. Then, after a brief clearing, a second cloud of choking dust descended almost vertically. Minutes after the beginning of the density flow, a dark anvil-shaped cloud associated with the formation of the vertical column expanded upward and then rapidly outward to the north and east. Starting within 15 km of the volcano at about 0850 and in distal areas at about 0900, dark-gray pisolitic mud fell from this second high-level cloud as far outward as Camp Baker on the west, the Cowlitz River valley on the north, and Mount Adams on the east. Sand-sized ash and charred tree material fell from the anvil cloud onto Mount Rainier and Mount Adams. Beyond the scorch zone there were no direct effects of the density flow; instead, rock projectiles fell from the dark anvil cloud, followed by pisolitic ash and charred branches and cones, followed for hours by dry ash and pumice lapilli.

PROCESSES OF EMPLACEMENT

The large size, angularity, and poor sorting of clasts in layer A1 and the nearly massive structure of this layer reveal that it was turbulently emplaced by a high-energy process. The normal grading within both layers A1 and A2, which successively overlie eroded materials, indicates that the velocity was highest near the front of the density flow and decreased within the trailing phases. The decrease in the velocity and competence of the flow as it expanded is shown by two trends: (1) the outward thinning and grading of the basal material from cobble gravel a meter or so thick near the mountain to medium sand a few centimeters thick in the scorch zone; and (2) the outward sequence of downed, deeply bruised, transported timber; downed, pitted, nontransported timber; and standing, nonabraded, scorched timber. A general decrease in velocity from 650 km/hr to 100 km/hr is inferred from eyewitness accounts and sequential photographs.

The flow was partly impelled by directed explosions on the mountain, but only in the initial stages. From the mountain it probably moved partly by continued gas expansion, but the heavier-than-air gas-rock mixture was generally pulled downslope by gravity. The normal grading of the density-flow deposit stratigraphically upward as well as laterally outward from the volcano indicates that the flow itself was stratified; the coarsest particles and the densest concentration were near the base and near the leading edge of the flow. The flow stratification could not have been only horizontal or only vertical, but was both (fig. 270). The poor sorting and meager stratification of layer A1 indicate that turbulence at the base of the flow near its front mixed sand- to

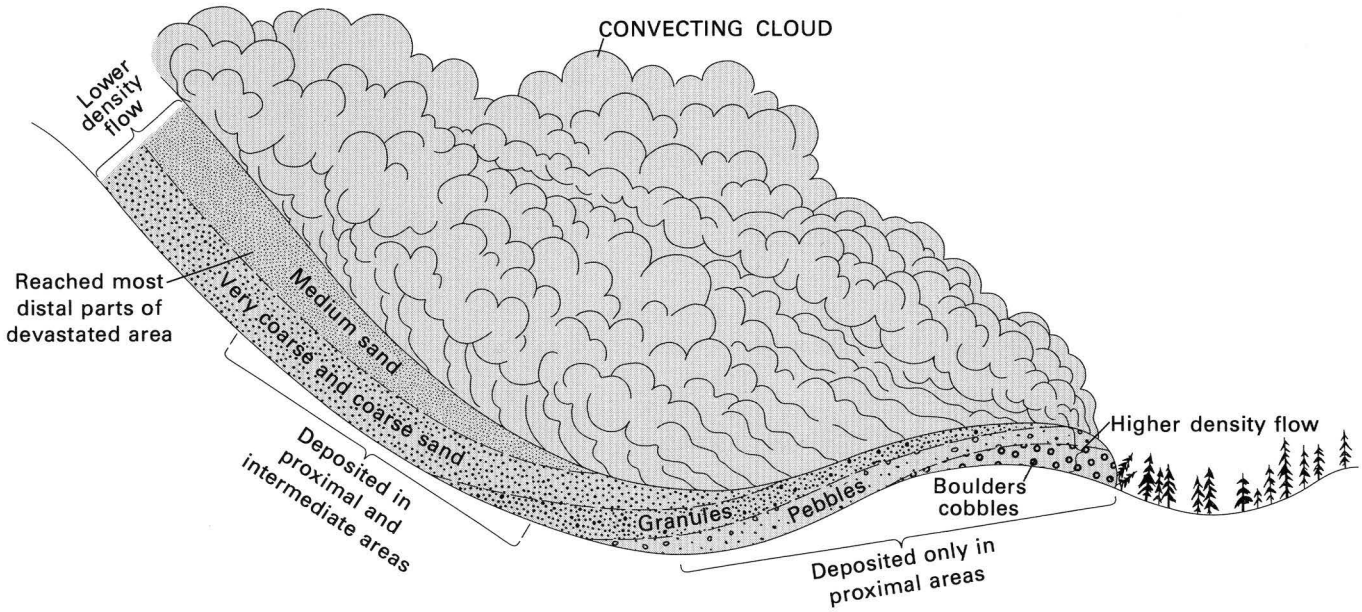

Figure 270.—Schematic diagram of pyroclastic density flow sweeping through proximal area, showing inferred maximum particle size and relative density within flow.

boulder-sized particles and deposited them rapidly enough to produce only indistinct, thick bedding. The presence of laminated sand within layer A2 suggests that shortly later the flow became laminar.

The change from the massive or weakly bedded structure in layer A1 and bed A2a to conspicuous laminations in bed A2b reveals that an *abrupt* change from turbulent to laminar flow occurred during the *gradual* decrease in velocity and competence as the surge expanded. Although scour depressions around obstacles and drifting in the lee of obstacles provide surface relief at the top of layer A1, regular wave forms developed only in layer A2. Some of these waves are developed in bed A2a and only modified by bed A2b, others are formed in bed A2b: the waves formed under the entire range of decreasing velocities that emplaced layer A2. The laminations of bed A2b are variously backset, plane, and foreset, corresponding respectively to antidune, plane, and dune bedding in water-laid sediment. Bed A2b therefore seems to have accumulated while the laminar flow passed from a higher flow regime to a lower one.

The successive outward displacement of the maximum thicknesses and inner margins of layers A1, A2, and A3 shows that the north flank of the volcano was largely bypassed by the finer materials. Layer A2 was deposited by a trailing phase of the pyroclastic density flow, whose competence and velocity on the flanks of the volcano must have been too great to permit sand-sized material to accumulate. Only after the flow front had moved out several kilometers did the internal turbulence and forward velocity of the flow decrease enough for the trailing phase to begin depositing its sandy load.

Layer A3, on the other hand, was deposited mostly from the anvil cloud, which began to develop about 4 min after the beginning of the eruption and began to deposit air-fall material about 10 min or so later. Because this cloud was impelled upward and then expanded rapidly outward, particles from it had trajectories that skipped over areas close to the volcano. Material from the anvil cloud apparently composes the pisolitic zone, which shows a systematic outward stratigraphic lowering in the northwest-through-east-northeast sector—from the top of layer A3 within 10 km of the mountain, to the middle of layer A3 at 18 km, to the base of layer A3 from 25 to 60 km. Within 10 km of the mountain, where a nonpisolitic zone underlies the pisolitic zone, layer A3 may have a dual genesis. The nonpisolitic basal silt may have fallen partly from the cloud convoluting directly off the flow, whereas the pisolitic layer fell from the anvil cloud associated with the initial vertical column. In distal areas the occurrence of nonpisolitic silt above

the pisolitic zone may simply be an effect of the lower settling velocity of nonaggregated silt compared to that of pisolites.

COMPARISON WITH OTHER PYROCLASTIC DEPOSITS AND THEIR INFERRED EMPLACEMENT PROCESSES

The sequence during the first 10 min of the May 18 eruption of Mount St. Helens is rare in the annals of observed volcanic phenomena. Despite the devastation by the pyroclastic density flow at Mount St. Helens, no comparable event has been so closely observed and photographed. The observed lateral cloud of, and devastation caused by, the initial "nuée ardente" of January 21, 1951, at Mount Lamington, Papua New Guinea (Taylor, 1958, p. 39–47, figs. 11–12 and 52–72), are similar to but less extensive than those of the pyroclastic density flow at Mount St. Helens. The resultant deposits at Mount Lamington are much thinner and finer than those at Mount St. Helens: the Mount Lamington deposit (Taylor, 1958, p. 51–53) is similar to the Mount St. Helens layers A2 and A3 but has no equivalent to layer A1. The effects of the "directed blast" at Lassen Peak in 1915 (Day and Allen, 1925, p. 19–26) are similar to but cover a much smaller area than the effects of the density flow at Mount St. Helens. But as the phenomena at Lassen Peak were not observed, Mount St. Helens better illuminates the Lassen event than vice versa. A distant analogy to the Mount St. Helens density flow may be the directed "blast" of Bezymianny volcano in Kamchatka, U.S.S.R., in 1956 (Gorshkov, 1959). This eruption similarly began with a lateral blast, resulted in a similar breach in the mountain, and moved a similar volume of material, which was similarly deposited as coarse, angular lithic debris. But there are differences. Whereas the agglomerate at Bezymianny is a valley deposit confined to a 25° sector, the deposit at Mount St. Helens is spread across ridges and valleys alike through a 180° sector around the volcano. The Bezymianny deposit is a boulder gravel even at the surface of the deposit far from the mountain, but the Mount St. Helens deposit grades outward from cobble to granule gravel and grades upward into finer material.

The theoretical and comparative literature on pyroclastic flows and surges is preoccupied with low-density sand-sized glass and pumice distributed by base surges caused by phreatomagmatic explosions or collapse of magmatic eruption columns (Fisher, 1966; Moore, 1967; Fisher and Waters, 1969, 1970; Waters and Fisher, 1971; Schmincke and others, 1973; Sparks, 1976; Sparks and Wilson, 1976; Sheridan, 1979; Wohletz and Sheridan, 1979). In grain size, sorting, internal stratification, composition, and stratigraphic position beneath ignimbrites, layer A1 of the pyroclastic-surge deposit at Mount St. Helens resembles the "co-ignimbrite lag-fall deposit" of Wright and Walker (1977). But the genesis and emplacement mechanism at Mount St. Helens altogether differ from Wright and Walker's column-collapse interpretation. Although there was collapse of the mixture of rock and gas explosively ejected a few hundred meters above the flank of Mount St. Helens, the resultant catastrophic flow off the mountain was in no sense caused by a collapsing Plinian column. And whereas the lag-fall deposit is a phase of ash-flow emplacement, at Mount St. Helens the emplacement of the density-flow deposit is unrelated to the subsequent emplacement of the ash-flow deposits.

Coarse lithic deposits similar to layer A1 at Mount St. Helens are not recognized in the tripartite division of pumiceous pyroclastic deposits (fall, surge, flow) by Sparks and Walker (1973), who contend that most such lithic deposits result from rock avalanches and are thus not truly pyroclastic. Although in its coarse grain size and general massiveness layer A1 at Mount St. Helens resembles Sparks and Walker's pyroclastic-flow deposits more closely than their surge deposits, it differs in that it was deposited across high-relief divides as well as in valleys. Layer A1 is a true pyroclastic deposit emplaced by density flow. The density flow at Mount St. Helens may reveal the emplacement process of widespread agglomerates around many other modern and ancient volcanoes.

Of layer A2 at Mount St. Helens, bed A2b most closely resembles a classic surge deposit. Yet, unlike examples from the literature, the phase of flow that deposited layer A2 followed and then outdistanced the far more energetic phase of flow responsible for layer A1. Although bed A2b seems to represent a sedimentologic environment generally similar to that of classic ground surges or base surges, the process by which this environment was produced at Mount St. Helens is different from the classic-surge processes of

column collapse or expansion from the base of a rising column. At Mount St. Helens, the "classic-surge" environment was merely a transient waning phase trailing the violent frontal part of the pyroclastic density flow.

The pyroclastic density flow at Mount St. Helens was similar to classic surges in its relatively low density and its capacity to flow over ridges with only modest regard for topography. This event differs from classic surges in its size: the potential energy of the flow as it began its descent off the mountain was much greater than that of previously described surges, and accordingly the maximum grain size and other sedimentologic parameters of its deposits represent higher energy states than ever before observed for analogous processes.

REFERENCES CITED

Crandell, D. R., and Mullineaux, D. R., 1978, Potential hazards from future eruptions of Mount St. Helens volcano, Washington: U.S. Geological Survey Bulletin 1383-C, 26 p.

Day, A. L., and Allen, E. T., 1925, The volcanic activity and hot springs of Lassen Peak: Carnegie Institute of Washington Publication 360, 190 p.

Fisher, R. V., 1966, Mechanism of deposition from pyroclastic flows: American Journal of Science, v. 264, p. 350–363.

Fisher, R. V., and Waters, A. C., 1969, Bedforms in base-surge deposits: lunar implications: Science, v. 165, p. 1349–1352.

_____1970, Base surge bed forms in maar volcanos: American Journal of Science, v. 268, p. 157–180.

Folk, R. L., 1974, Petrography of sedimentary rocks: Austin, Tex., Hemphill Publishing Co., 182 p.

Gorshkov, G. S., 1959, Gigantic eruption of the volcano Bezymianny: Bulletin Volcanologique, v. 20, p. 77–109, 39 pls.

Moore, J. G., 1967, Base surge in recent volcanic eruptions: Bulletin Volcanologique, v. 30, p. 337–363.

Mullineaux, D. R., Hyde, J. H., and Rubin, Meyer, 1975, Widespread late glacial and postglacial tephra deposits from Mount St. Helens volcano, Washington: U.S. Geological Survey Journal of Research, v. 3, p. 329–335.

Schmincke, H.-U., Fisher, R. V., and Waters, A. C., 1973, Antidune and chute and pool structures in the base surge deposits of the Laacher See area, Germany: Sedimentology, v. 20, p. 553–574.

Sheridan, M. F., 1979, Emplacement of pyroclastic flows—A review: Geological Society of America Special Paper 180, p. 125–136.

Sparks, R. S. J., 1976, Grain size variations in ignimbrites and implications for the transport of pyroclastic flows: Sedimentology, v. 23, p. 147–188.

Sparks, R. S. J., and Walker, G. P. L., 1973, The ground surge deposits: a third type of pyroclastic rock: Nature; Physical Science, v. 241, p. 62–64.

Sparks, R. S. J., and Wilson, L., 1976, A model for the formation of ignimbrites by gravitational column collapse: Geological Society of London Journal, v. 132, p. 441–451.

Taylor, G. A., 1958, The 1951 eruption of Mount Lamington, Papua: Australia Bureau of Mineral Resources, Geology and Geophysics Bulletin 38, 117 p.

Waters, A. C., and Fisher, R. V., 1971, Base surges and their deposits: Capelinhos and Taal volcanos: Journal of Geophysical Research, v. 76, p. 5596–5614.

Wohletz, K. H., and Sheridan, M. F., 1979, A model of pyroclastic surge: Geological Society of America Special Paper 180, p. 177–194.

Wright, J. V., and Walker, G. P. L., 1977, The ignimbrite source problem—Significance of a co-ignimbrite lag-fall deposit: Geology, v. 5, p. 729–732.

MUDFLOW DEPOSITS

Destructive mudflows commonly accompany pyroclastic eruptions on stratovolcanoes. Because such poorly sorted and unstratified volcaniclastic deposits typically contain abundant coarse fragments, the term lahar is commonly applied to the broad textural range of volcanic mudflows and debris flows like those that occurred at Mount St. Helens on and after May 18. Mudflow is also used as a general term for flows in which sand, silt, and clay are abundant, although the term debris flow is preferred for those that consist dominantly of coarser material.

Destructive lahars developed within minutes of the beginning of the May 18 eruption, as hot pyroclastic debris melted snow and glacial ice on upper slopes of the cone. Aerial photographs show that large areas of the above-timberline slopes of the volcano were scoured by lahars on the morning of May 18, especially on the east and west flanks. Early lahars descended the Muddy River, Pine Creek, and the South Fork Toutle River (Janda and others; Cummans). In upper reaches of these drainages, the flows appear to have originated as wet lithic avalanches, locally reaching velocities of as much as 45 m/s as determined by the geometry of cross-valley runups. As velocities decreased downvalley, these avalanches changed into mudflows.

The most voluminous mudflow originated by slumping and flowage of water-saturated deposits of the debris avalanche in the upper North Fork Toutle River valley. This mudflow did not reach peak stage until late afternoon and early evening on May 18, perhaps because of the time required to integrate flowage across the hummocky topography of the debris-avalanche deposit. This mudflow extended more than 120 km down valley, to the Cowlitz and Columbia Rivers, and caused widespread channel filling, flooding, and damage to roads, bridges, and other structures.

THE 1980 ERUPTIONS OF MOUNT ST. HELENS, WASHINGTON

LAHAR MOVEMENT, EFFECTS, AND DEPOSITS

By RICHARD J. JANDA, KEVIN M. SCOTT, K. MICHAEL NOLAN, *and* HOLLY A. MARTINSON

ABSTRACT

Lahars occurred on May 18, 1980, on nearly all streams draining the cone of Mount St. Helens and were formed in three major ways: (1) The most voluminous lahar originated by slumping and flowing of water-saturated parts of the debris avalanche in the headwaters of the North Fork Toutle River. This lahar, which had the characteristics of a mudflow, modified more than 120 km of channel, including the main Toutle River and sections of the Cowlitz and Columbia Rivers. (2) Lahars with the highest velocities originated by catastrophic ejection of mixtures of lithic debris, ash and lapilli, water, and entrapped air; most such flows were confined to the immediate vicinity of the cone, but some were transitional to or were replaced downstream by mudflows that traveled much longer distances. (3) Finally, minor lahars were formed by melting of debris-laden ice and snow, and some were triggered by the heat of pyroclastic flows and recently deposited tephra. Although the largest 1980 lahars were devastating in their impacts on channels and flood plains, the effects were less than those of some earlier Holocene lahars of Mount St. Helens.

Flow velocities ranged from less than 1.5 m/s in downstream reaches, conveying the massive mudflow that originated on the North Fork Toutle River, to more than 40 m/s for highly mobile flows, debouching from steep canyons near the cone.

Lahar deposits are generally thin compared with depths of initiating flows. Thick fill was deposited locally, however, especially by mudflows. Even where lahars caused minimal channel deposition or scour occurred, overbank deposits are commonly more than 1 m thick. Present channels are unstable and are adjusting rapidly to the altered geomorphic and hydrologic conditions. Continued erosion will release much sediment from previously stable, pre-May 18 channel and flood-plain deposits, as well as from sediment deposited on and after May 18.

INTRODUCTION

Most major streams that originate on Mount St. Helens were significantly modified by lahars during and shortly after the May 18 eruption (U.S. Geological Survey, 1980; fig. 271). The lahars included both mudflows and debris flows at ambient or slightly elevated temperatures. The timing of the lahars can be constrained by tephra chronology (Waitt, this volume; Waitt and Dzurisin, this volume), by direct observation (Cummans, this volume; Rooth, 1980; Rosenbaum and Waitt, this volume), and by time-sequential aerial photographs. The number and timing of lahars differed significantly between valleys.

Following Mullineaux and Crandell (1962), the term "lahar" is applied to the broad range of debris flows and mudflows that resulted from the volcanic activity on and subsequent to May 18. Debris flow and mudflow represent closely similar forms of rheological behavior. The term "mudflow" is commonly used to describe the flows in which the mud content (silt plus clay) is sufficient to give the deposits a cohesive matrix and a typical muddy appearance. The total mud content may, however, be only a subordinate part of the poorly sorted deposit. Debris-flow deposits are less cohesive, more granular, and generally better sorted.

By far the most extensive and destructive lahars were those formed in the headwaters of the North

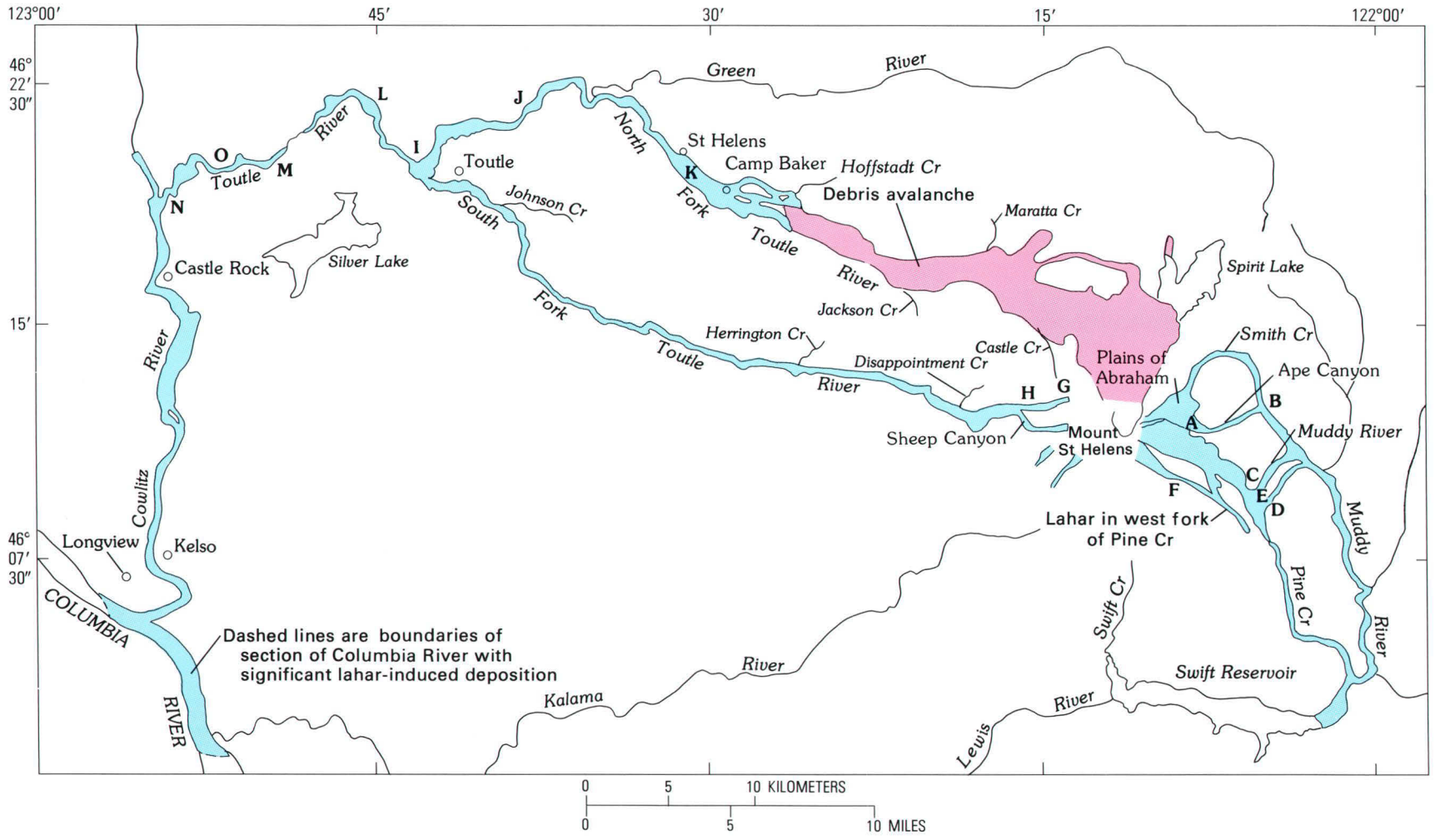

Figure 271.—Location map showing streams draining flanks of Mount St. Helens and areas impacted by lahars (shaded). Capital letters designate locations discussed in text.

Fork Toutle River; these flows ultimately deposited more than 50 million m^3 of sediment along the lower Cowlitz and Columbia Rivers (Lombard and others, 1981; Peter Haini, written commun., 1980).

Destructive lahars also swept down the South Fork Toutle River. Rapidly flowing lahars originated in the headwaters of Pine Creek and the western tributaries to Muddy River, and smaller lahars and pyroclastic flows occurred in the headwaters of Swift Creek and the Kalama River (fig. 271). The impact of these lahars on bridges, roads, and other public works is discussed by Schuster (this volume).

Cohesive, clast-studded mudflow deposits extend to the highest flow marks throughout the lahar-impacted reaches of the North Fork Toutle River and the main Toutle River, as well as the lower Muddy, South Fork Toutle, and lower Cowlitz Rivers. In contrast, the highest limits of flow along the upper Muddy and South Fork Toutle Rivers are marked by abraded rock surfaces and trees. This abrasion, together with the granular texture of deposits laid down by the peak flow, suggests that the largest lahars along the upper Muddy and South Fork Toutle Rivers were debris flows or avalanches.

The most striking lahar-induced modification of valley morphology is widespread deposition, even though the lahar deposits are commonly less than 10 percent of the depths of the peak flows. Large amounts of scour were caused by the lahars along steep narrow canyons.

The May 18 lahars were voluminous and destructive. From socio-economic perspectives they were devastating. Nonetheless, from geologic and hazard-assessment perspectives, these lahars had less impact on the landscape than did some earlier Holocene lahars of Mount St. Helens (Mullineaux and Crandell, 1962; Crandell and Mullineaux, 1973, 1978). Velocities and length-descent ratios for the May 18 lahars generally fall within the range reported for earlier lahars at Mount St. Helens and at comparable volcanoes. The long runout of the main lahar from the North Fork Toutle River, however, is somewhat anomalous.

This report summarizes initial findings on the timing and physical characteristics of lahars formed during and shortly after the May 18 eruption, and on the consequent changes in valley morphology. The lahars are described in clockwise order, starting with upper Smith Creek and ending with the North Fork Toutle River (fig. 271).

ACKNOWLEDGMENTS

Special thanks are extended to Barry Voight, Harry Glicken, and John Cummans for information and much helpful discussion. We are also grateful for enthusiastic field assistance from Martha A. Sabol, James M. Duls, Jr., Lawrence A. Freeman, and Lyn J. Topinka. Janis L. Markman helped with many logistical problems. Weyerhaeuser Company provided detailed topographic maps of the Mount St. Helens area and access to their St. Helens tree farm.

UPPER SMITH CREEK

The upper Smith Creek basin was severely impacted by the 0832 PDT (Pacific Daylight Time) May 18 directed blast and the consequent blast pyroclastic flows that developed in channels (Hoblitt and others, this volume; Moore and Sisson, this volume; Waitt, this volume). The deposits of the blast pyroclastic flow in the upper Smith Creek area are commonly more than 2 m thick; they are overlain by silty gray ash with abundant accretionary lapilli, layer A3, which in turn are overlain by coarse pumiceous air fall, unit B (stratigraphic terminology from Waitt, this volume, and from Waitt and Dzurisin, this volume). The relation between the channelized blast pyroclastic flows and the massive mudflows that moved through Smith Creek remains to be established. The lahars that occurred on May 18 in upper Smith Creek tributaries

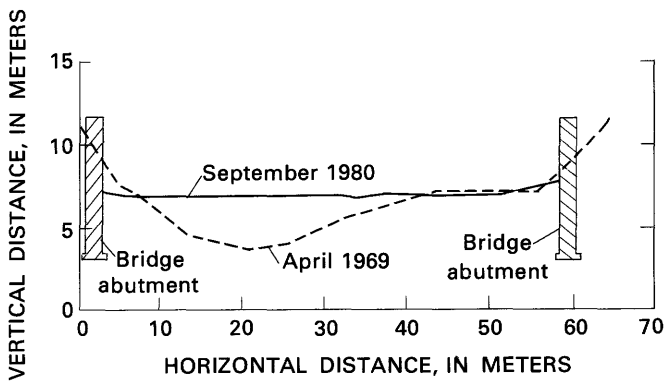

Figure 272.—Preeruption and posteruption cross-sectional profiles of the Muddy River at Muddy River bridge, 8.2 km upstream from the confluence with the Lewis River. Preeruption survey data from U.S. Forest Service site plans approved April 8, 1969.

that drain directly from the northeastern flank of Mount St. Helens were pumiceous mudflows less than 1.5 m thick. These mudflows, which overlie deposits of the blast pyroclastic flow, occurred during or shortly after the formation of unit B.

Deposits of both the blast pyroclastic flow and the later, smaller mudflows contain abundant angular-to-subangular pebbles and cobbles of a distinctive blue-gray dacite probably derived from the 1980 cryptodome that intruded the north flank of Mount St. Helens (Moore and Albee, this volume). The thin pumiceous mudflows in the upper Smith Creek tributaries that drain directly from Mount St. Helens locally reworked some of the blast pyroclastic-flow deposits from earlier eruptions.

MUDDY RIVER

Voluminous air-mobilized lithic avalanches, lithic mudflows, debris flows, and pumiceous mudflows at ambient or slightly elevated temperatures, as well as hot pumiceous pyroclastic flows, were generated in the headwaters of the western tributaries to Muddy River on May 18 (fig. 271). The lahars deposited more than 13 million m^3 of water and sediment in Swift Reservoir between 0900 and 1200 (Cummans, 1981). Thin lithic and pumiceous mudflows and debris flows apparently were also generated by rapid melting of snow and ice.

INITIAL EVENTS

The number, types, and sequence of lahars differed between tributaries. On the eastern flank of the volcano, the maximum flow was associated with enormous, highly mobile lithic debris flows and avalanches that swept down the Plains of Abraham, Ape Canyon, upper Muddy River, and some eastern tributaries to Pine Creek (fig. 271). This assemblage of flows, here informally called the upper Muddy River lahar, moved across some areas that had previously been eroded by the directed blast during the 0832 eruption. Deposits of this lahar are in turn overlain by silty gray ash with abundant accretionary lapilli, layer A3, which started to fall within minutes of the 0832 eruption. Thus, the upper Muddy River lahar was generated during the explosive phase of the 0832 eruption.

Trimlines and abrasion marks on trees suggest that the upper Muddy River lahar was 10–20 m deep. A lobe of this lahar surged across a 75-m-high hill near the head of Ape Canyon (A in fig. 271). If the kinetic energy of a frictionless, 20-m-deep flow were converted to the potential energy of the lahar deposits on the crest of this hill, the flow velocity must have exceeded 32 m/s. Similarly, the more than 80-m runup on the eastern valley wall of Smith Creek, opposite the mouth of Ape Canyon (B in fig. 271), requires velocities exceeding 40 m/s. That these velocities were attained close to the volcano is reasonable, because the deposition that began in Swift Reservoir as early as 0900 on May 18 requires an average velocity greater than 13 m/s.

Sediment deposited by the upper Muddy River lahar covers a large area, but it is commonly less than 2 m thick. The sediment consists primarily of angular blocks and lapilli of lithic debris in a fine sand or silty sand matrix, and contains less mud and pumice than do the deposits of later lahars in this same area. The intermediate diameter of the largest clasts is about 0.5 m. The blocks consist of types of andesite, dacite, and less commonly basalt from the modern volcanic cone, as well as 1980 cryptodome dacite (Moore and Albee, this volume) and hydrothermally altered dacite and andesite from ancestral Mount St. Helens (C. A. Hopson, written commun., 1980). The timing, lithology, and high velocity of the upper Muddy River lahar suggest that it was caused by the explosive ejection of a mixture of rock, ash, and water from the former summit of the volcano. The high mobility of the initial lahar may indicate that air was trapped in the ejecta as they fell back to the cone.

The upper Muddy River lahar spilled into the steep northeast-trending canyon of Muddy River (C in fig. 271), the similar unnamed canyon containing Hoo Hoo Lake (D in fig. 271), and into two forks of Pine Creek. In Pine Creek, flow was concentrated in the eastern fork. At the low hill that forms a common drainage divide for Muddy River, Hoo Hoo Lake, and Pine Creek (E in fig. 271), the upper Muddy River lahar attained less than 30 m of runup and velocities were probably less than 20 m/s. Despite significantly reduced velocity, this lahar still scoured vegetation, soil, colluvium, and older lahar deposits along all but the westernmost spillover route.

The lahar along the main southeast-trending Smith Creek–Muddy River valley below Ape Canyon

(fig. 271), here informally called the lower Muddy River lahar, destroyed two major road bridges (fig. 272) and buried 20 km of U.S. Forest Service roads on the flood plain of the Muddy River. This lahar also destroyed the Eagle Cliff bridge across the Lewis River near the head of Swift Reservoir. Peak flow was 10–20 m deep and transported cobbles and boulders near the surface. Most new deposits are less than 0.3 m thick near the margins of the inundated area and 1–2.5 m thick near former channels. Locally the channel was scoured to bedrock. The high flow-marks on riparian trees and bedrock surfaces along the lower Muddy River are formed of cohesive mud that commonly contains spherical cavities and pebbles. Many trees close to the axis of maximum flow, however, were sheared off and pushed in front of the advancing lahar. A massive logjam accumulated on the Muddy River in the tortuous, narrow canyon immediately upstream of the confluence with the Lewis River. Along the margins of the inundated areas, the riparian vegetation was toppled and abraded into long, tapering "bayonet trees."

LATER EVENTS

Several mudflow deposits as much as 2.5 m thick stratigraphically overlie deposits of a pumiceous pyroclastic flow that was observed surging down the headwaters of the Muddy River shortly before 1600 on May 18 (Rooth, 1980). Deposits of this flow consist predominantly of pebble-size pumice and fill gullies that were eroded several meters deep into the upper Muddy River lahar and pre-May 18 deposits. Where the pumice flow deposits overlie the earlier deposits, they display prominent flow ridges 0.2 m high that are parallel to its lateral margin. The overlying mudflow deposits display silt- and clay-rich matrices, dispersed cobbles and boulders of andesite, dacite, and less commonly basalt, prominent flow ridges, and varying amounts of included pumice and other surficial tephra. Relationships between these mudflow deposits and various surficial tephra layers suggest that at least one of these flows occurred during the waning phases of the May 18 eruption, that one occurred following May 18 but prior to the end of the eruption on May 25, that another occurred between May 25 and the end of the eruption on June 12, and that several thin flows of limited extent occurred later in the summer.

PINE CREEK

Sizable debris flows and mudflows occurred in the headwaters of the west fork of Pine Creek. The most voluminous of these flows occurred at about the same time as the upper Muddy River lahar with which it interfingers (fig. 271). Peak flow of the Pine Creek lahar, which had the character of a mudflow, was 10 m or less in depth near locality F (fig. 271). The resulting deposits are 0.5–2.5 m thick. The matrix of the lahar on the west fork of Pine Creek contains more mud than that of the upper Muddy River lahar. The amount of cross-valley banking of mudlines due to radial acceleration at a stream bend near locality F in figure 271 suggests that the initial lahar of May 18 on the west fork of Pine Creek had a velocity of about 31 m/s (Fink and Malin, 1980). Despite high initial velocity and volume, however, this lahar did not reach the confluence of the forks of Pine Creek. Heavily sediment-laden water that flowed out from or immediately followed this lahar nonetheless caused significant erosion and deposition along reaches of the west fork of Pine Creek not directly impacted by the mudflow.

A smaller lahar occurred after the May 18 air fall but before the May 25 air fall. This lahar was characterized by larger average grain size and apparent shear strength, but was of lower velocity than was the initial lahar (Fink and Malin, 1980). A still smaller

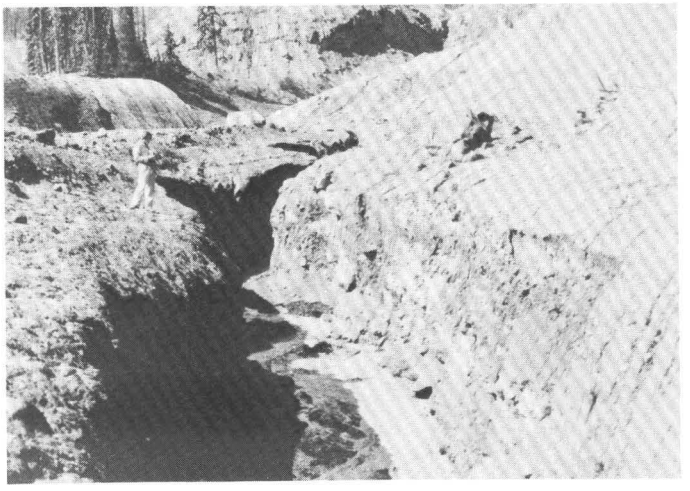

Figure 273.—Trench enlarged and deepened by water torrents at west fork of upper Pine Creek. Trench eroded through older unconsolidated lahar deposits overlain by about 0.5 m of May 18 lahar deposits.

debris flow occurred after May 25 but before mid-July. Throughout the summer and early fall, small torrents of water laden with pumice and lithic debris, similar to torrents observed in the upper Muddy River, occurred during periods of rain or intensive melting of snow and ice in the headwaters of the west fork of Pine Creek. These torrents progressively enlarged and deepened a trench eroded through the May 18 and older unconsolidated lahar deposits. By early September this trench was locally more than 6 m deep (fig. 273). As in the upper Muddy River, much of the sediment that was eroded from this area by subsequent high streamflow or lahars was derived from older lahar deposits exposed in the unstable walls of this trench.

SOUTH FORK TOUTLE RIVER

INITIAL EVENTS

The lithologic character and sequence of lahars on May 18 in the headwaters of the South Fork Toutle River were similar to those in the headwaters of Muddy River. Large volumes of water-saturated lithic debris ejected during the initial phases of the eruption flowed rapidly down most of the western flank of the volcano between Toutle Glacier and the headwaters of Sheep Canyon. Water-saturated ejecta collected in South Fork Toutle River and developed into a single, sharp-crested mudflow peak that was observed by witnesses many kilometers downstream. In the area between Disappointment Creek and Sheep Canyon, peak flow occurred within minutes of the 0832 eruption, because peak mudflow deposits rest on directed-blast deposits but underlie layer A3.

The flow down the upper South Fork Toutle River locally ran up 110 m on the precipitous north valley wall (G in fig. 271). This flow scoured preexisting soil and colluvium, and left only a scattering of clasts and a thin (less than 0.3 m), discontinuous gray veneer of debris-flow deposits on the valley wall. In the field, May 18 runup deposits are difficult to distinguish from lithologically similar, older deposits that crop out on the valley wall at that point.

On the north valley wall of the South Fork Toutle River about 1 km upstream of Sheep Canyon (locality H; figs. 271, 274), May 18 lahar-scoured surfaces and thin lag deposits occur as much as 54 m above the general depositional surface of the lahar. These deposits were not formed by cross-valley banking of mudlines due to radial acceleration around bends, or by cross-valley surging of a tributary flow; therefore, they indicate that flow of the initial South Fork Toutle River lahar was highly turbulent and was charac-

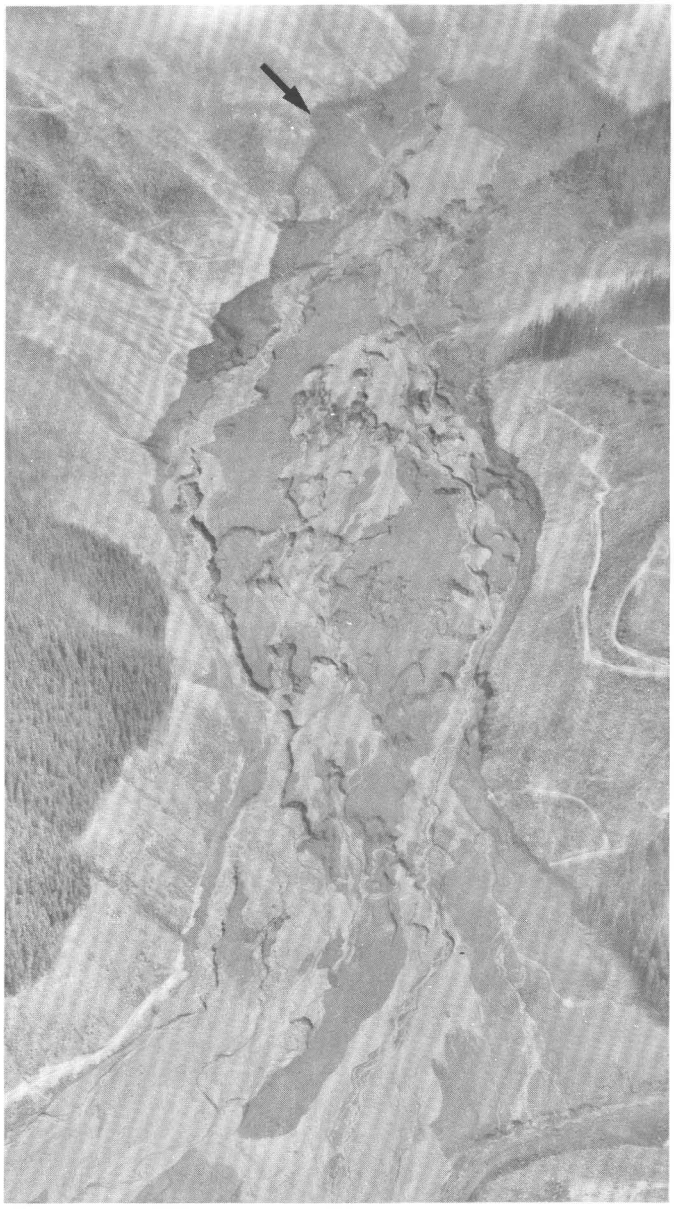

Figure 274.—Oblique aerial photograph of upper South Fork Toutle River, looking east and upstream. Arrow indicates runup of lahar on north valley side slope (see locality H in fig. 271). Initial May 18 lahar deposits appear as dark-gray areas; later May 18 pumiceous mudflow deposits appear as light-gray areas in valley bottom. Inundated valley in bottom center of photograph is 1.0 km wide. Photograph by Austin Post, May 19, 1980.

terized by considerable cross-valley sloshing. This suggestion is consistent with observations of an eyewitness 6 km downstream (Rosenbaum and Waitt, this volume).

Other eyewitness accounts, as well as the character and spacial distribution of the lahar deposits in South Fork Toutle River downstream of locality H, suggest that flow became less turbulent and slowed rapidly. One party of survivors, within 8.5 km of the summit of Mount St. Helens at the time of the eruption, drove downvalley and crossed a bridge 18.5 km from the summit 10–12 min after the eruption (R. B. Waitt, written commun., 1980); this timing suggests that the average velocity of the lahar in this reach was not more than 31 m/s. Cross-valley banking of mudlines due to radial acceleration around valley bends suggests an average velocity between 7 and 29 m/s (Wigmosta and others, 1980). Residents who observed the arrival of the South Fork Toutle River lahar near the town of Toutle described the flow front as a 2- to 3-m-high tangle of logs and other woody debris that advanced downstream at 3 to 4 m/s. Compilation of eyewitness accounts of the timing of peak stage between locality H and the confluence of the North Fork and South Fork Toutle River suggests an overall average velocity of about 7 m/s (Cummans, this volume).

Depth of the South Fork Toutle River lahar also decreased markedly in a downvalley direction. Near locality H (fig. 271) the flow was at least 15 m deep. At the stream gage immediately below the confluence of the North Fork and South Fork Toutle River, flow rose 6.4 m to a stage that exceeded the peak of 72 prior years of record by 0.3 m (Cummans, this volume). Peak discharge of that lahar at the Cowlitz River at Castle Rock (fig. 271) was marked by only a 0.98-m increase in stage. At Longview (fig. 271), passage of this peak was reportedly marked by the arrival of a large mass of floating woody debris, but by no increase in stage and little increase in turbidity.

Pronounced downvalley reductions in both velocity and depth of the South Fork Toutle River lahar are compatible with the downstream decrease in discharge computed by Wigmosta and others (1980). Dramatic downvalley changes in texture and composition of the deposits of the initial South Fork Toutle River lahar indicate changes in the nature of the flow. Near the volcano, deposits of the initial May 18 lahar are generally less than 1.5 m thick and possess a granular matrix that is transitional between typical mudflow and debris-flow deposits. The base of the May 18 lahar deposits in these areas is often difficult to recognize, except where the May 18 and older deposits are separated by a zone of roots, toppled vegetation, or partially decayed organic matter. This difficulty reflects striking lithologic similarities between the May 18 and older lahar deposits.

Between Disappointment Creek and Johnson Creek, however, deposits of the peak May 18 lahar are more typical of a mudflow, because their matrices contain abundant silt and clay. Streamlined longitudinal "whaleback" bars of subangular cobble gravel that have a locally intact framework and a silt- and clay-rich matrix occur at several different levels. Crests of the higher of these bars are within about 2 m of the high mudline; this correspondence suggests a close association of the bars with the mudflow peak. Sediment composing these bars typically displays either a nonconsistent internal variation in properties or a crude normal (upward-fining) size gradation. Gently sloping berms at levels below the peak mudflow are underlain by better sorted, less cohesive sediment that is typically associated with granular debris flow. Fine sediment in the upper parts of both bars and berms typically is better sorted and stratified than sediment in their coarse basal parts. This vertical sequence of deposits suggests that waning phases of the South Fork Toutle River lahar at any given point may have been characterized by a somewhat rapid transition between mudflow, debris flow, and heavily sediment-laden streamflow ("hyperconcentration" of Beverage and Culbertson, 1964).

The peak South Fork Toutle River lahar apparently was transformed to highly sediment-laden streamflow. Massive mudflow deposition took place between Johnson Creek and the confluence of the North Fork and South Fork Toutle River. Little mudflow deposition occurred below the confluence; downstream, the main South Fork lahar is typically represented by less than 1 m of relatively well sorted silt and fine to medium sand with weakly developed internal stratification. At the head of the constricted canyon reach below the confluence, however, this water-laid runout deposit is overlain by 2.5 m of South Fork mudflow deposits, suggesting local ponding of the mudflow phase. Water-laid deposits record passage of the lahar past the town of Tower (L in fig. 271), Tower Road bridge (M in fig. 271), and old U.S. Highway 99 (N in fig. 271). Downstream from the confluence, the South Fork Toutle River deposits rest

upon distinctively different older alluvium and lahar deposits that display larger average grain size (cobbles and boulders), greater rounding, a larger proportion of dacite and andesite from ancestral Mount St. Helens, and fewer rocks from the modern cone. Neither deposit contains large amounts of pre-Mount St. Helens (upper Eocene to Oligocene) metavolcanic rocks, even though most of the drainage basin is underlain by those rocks.

The magnitude of mudflow-induced modifications of channel geometry can be substantiated more completely throughout the Toutle River system and lower Cowlitz River valley than on the south and east flanks of the volcano, because the preeruption valley configuration is documented by numerous bridge contract plans and detailed (1:9600) topographic maps. Comparisons indicate that the initial May 18 lahar on the South Fork Toutle River substantially modified the valley and channel configuration of that river. Vegetation adjacent to the original channel was either sheared off or toppled and abraded into long, tapering "bayonet" trees. Bank erosion, as well as deposition along both the thalweg and flood plain, was readily discernible nearly everywhere. However, amounts of erosion and deposition were highly variable (fig. 275, *A* and *B*).

Most of the 0.8-km-wide valley bottom in the vicinity of Sheep Canyon and Disappointment Creek displays a veneer of May 18 lahar deposits that is generally less than 1 m thick. However, vertical-walled gullies commonly more than 4 m deep were incised into the May 18 and older lahar deposits by the waning phase of the May 18 lahar. Continued erosion of these gullies and the main river channel is an important source of downvalley sedimentation.

The surge of the South Fork Toutle River lahar through the confined canyon between Herrington Creek and Johnson Creek caused strikingly less channel modification than that in upstream and downstream alluvial reaches. The lahar scoured away soil and colluvium from the valley sides, and then deposited a thin veneer of mudflow deposits up to the peak flood mark. Flat-topped berms and "whaleback" bars rise from 2 to 5 m above the general level of the channel.

Through the broad alluvial reach between Johnson Creek and the North Fork Toutle River, fill from the May 18 lahar is from 2 to 4 m thick (fig. 275, *C* and *D*).

LATER EVENTS

A second lahar was observed in the upper reaches of the South Fork Toutle River at about 1400 on May 18. This lahar probably accounts for the anastomosing pattern of light-gray deposits seen in aerial photographs to be resting on the initial darker gray May 18 lahar deposits in areas upstream from Disappointment Creek (fig. 274). These deposits appear to have originated in the headwaters of the main South Fork Toutle River canyon, not in the unnamed tributaries and Sheep Canyon that drain the northwestern flank of the volcano. The deposits that underlie the anastomosing light-gray areas in the photographs are highly pumiceous debris-flow deposits 0.05–0.25 m thick. The pumice in these deposits is white to light gray, well rounded, and predominantly less than 0.5 cm in intermediate diameter. Nonetheless, pumice clasts as much as 3 cm in intermediate diameter are abundant. A probably correlative low berm of highly pumiceous debris-flow deposits was observed at several localities adjacent to the low-water channel in downstream reaches of the South Fork Toutle River, prior to being eroded by high streamflows in November 1980. The pumiceous debris flow was probably generated by accelerated melting of the heavily debris- and tephra-laden Toutle and Talus Glaciers, which drain directly into the main upper South Fork Toutle River canyon. Melting may have been induced by the accumulation of hot tephra or by a small pyroclastic flow during the afternoon of May 18.

Figure 275.—Preeruption and posteruption cross-sectional profiles of South Fork Toutle River. A, At site of Weyerhaeuser bridge no. 5700–1, 1.0 km downstream from Disappointment Creek. Note both erosion and deposition near thalweg. Preeruption profile from Weyerhaeuser Company. B, At site of Weyerhaeuser bridge no. 4100–3, near mouth of Herrington Creek, 8.7 km downstream from preceding section. Preeruption profile from Weyerhaeuser Company. C, Near Toutle, at site of discontinued (1957) stream-gaging station (no. 14.2410), 2.2 km upstream from confluence with North Fork Toutle River. Note channel aggradation and widening. Nearly all the indicated change occurred on May 18. Preeruption profile determined from information collected during discharge measurement. D, At Cowlitz County highway bridge, 1.2 km upstream from confluence with North Fork Toutle River. Note extensive fill. Preeruption profile from Cowlitz County Department of Public Works.

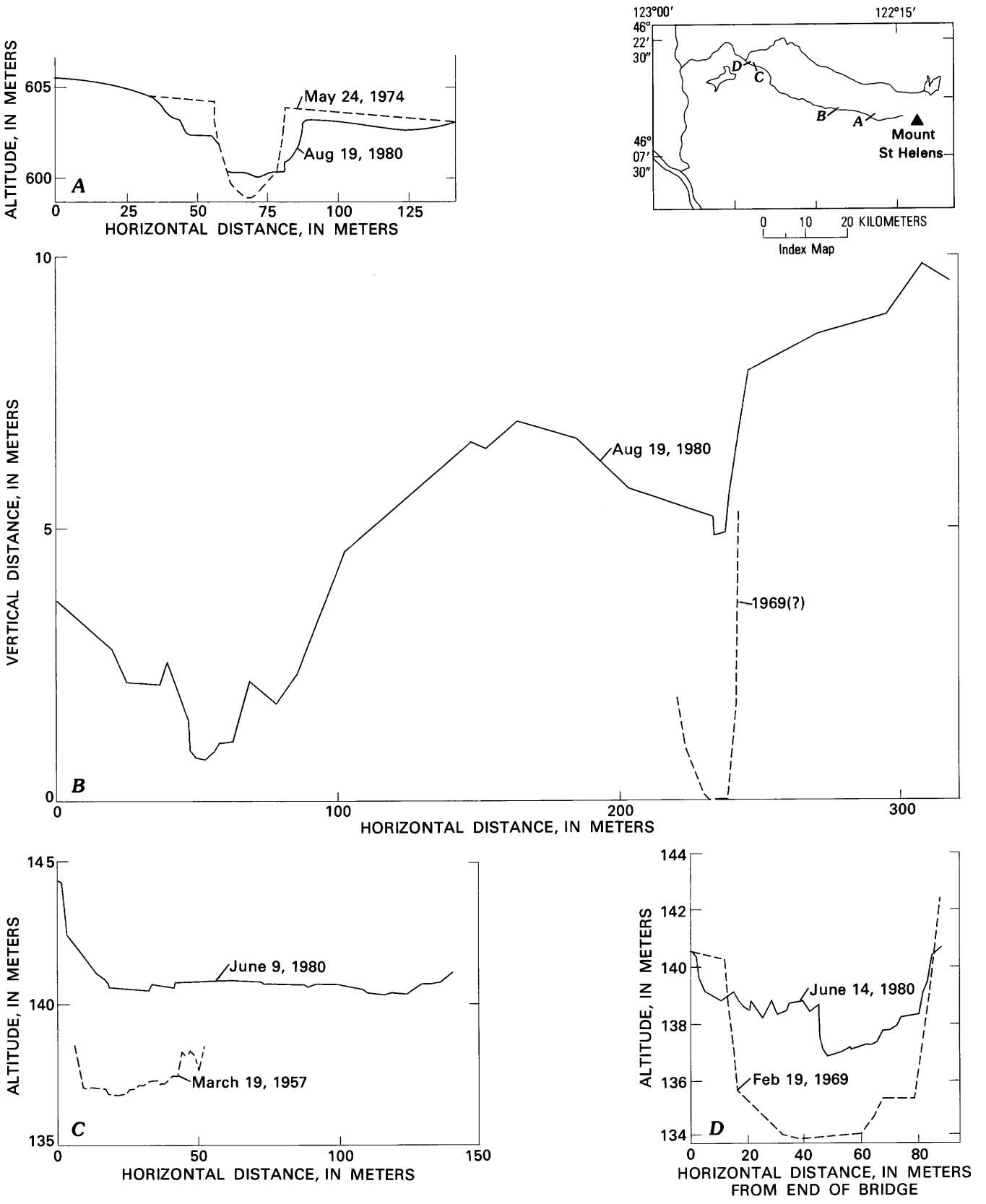
ALTITUDE, IN METERS
605
600
A
0
25
50
75
100
125
HORIZONTAL DISTANCE, IN METERS
May 24, 1974
Aug 19, 1980
123°00′
122°15′
46°
22′
30″
46°
07′
30″
D
C
B
A
Mount
St Helens
0
10
20 KILOMETERS
Index Map
VERTICAL DISTANCE, IN METERS
10
5
0
B
0
100
200
300
HORIZONTAL DISTANCE, IN METERS
Aug 19, 1980
1969(?)
ALTITUDE, IN METERS
145
140
135
C
0
50
100
150
HORIZONTAL DISTANCE, IN METERS
June 9, 1980
March 19, 1957
ALTITUDE, IN METERS
144
142
140
138
136
134
D
0
20
40
60
80
HORIZONTAL DISTANCE, IN METERS
FROM END OF BRIDGE
June 14, 1980
Feb 19, 1969

Unlike the upper Muddy River and Pine Creek areas, no extensive lahars seem to have been generated in the upper South Fork Toutle River during eruptions after May 18. However, channel incision and gullying of lahar deposits, caused by heavy rains in November and December, have contributed significant quantities of coarse sediment to downstream reaches of the South Fork Toutle River. A substantial part of this sediment was eroded from pre-May 18 lahar deposits.

NORTH FORK TOUTLE RIVER

The destructive lahar that flowed through the North Fork Toutle River during the afternoon of May 18 differed from the lahars in other valleys on that day in that it originated on water-saturated parts of the hummocky debris avalanche (Voight and others, this volume), not high on the volcano. This lahar also differed from the other lahars by its greater volume, lower velocity, more sustained flow, coarser and more poorly sorted deposits, and greater length of flow. Despite these differences, the deposits of this lahar display surface morphology, gross lithologic character, and vertical textural changes that are similar to those of other May 18 lahar deposits. An additional similarity is the thinness of the deposits in most reaches relative to the depth of the responsible flow.

Observations from helicopters and subsequent aerial photographs show that the through-flowing mudflows started predominantly on the surface of the avalanche deposit and not on the cone (pl. 1; Voight and others, this volume). Observers in rescue helicopters flying over the distal parts of the hummocky avalanche deposit during the late morning and afternoon of May 18 saw numerous grayish-brown mudflows moving over the irregular surface of the avalanche (Harry Glicken, written commun., 1980). Numerous individual flows of contrasting texture and color were observed to originate from slumping and flowing of water-saturated parts of the avalanche deposit, to pond in closed depressions, and to break out of those depressions as larger, more homogeneous flows. Unponded parts of the flows were only a few meters deep and flowed downvalley at rates of 12 to 15 m/s. The impact of this complex sequence of flows differed greatly from point to point. Some areas experienced progressive deposition; others experienced alternating erosion and deposition; and still others, particularly toward the distal end of the avalanche, experienced progressive erosion.

Back-calculated stability analysis of the 0832 landslide that started the avalanche indicates that the entire potential detachment plane must have been subjected to a pore pressure equivalent to 480 m of liquid water. Thus, most of the slide mass was probably water saturated and some parts may even have been subjected to artesian pressures (B. Voight, written commun., 1980). Additional water was provided by rapid melting of the finely pulverized portion of the 0.13 km^3 of glacial ice that was removed from the mountain and incorporated into the debris avalanche (Brugman and Meier, this volume). However, much of the melt water was released long after the lahars were started; occasional large blocks of glacial ice, which were visible in the avalanche for many weeks following emplacement, played no role in mobilizing the lahars of May 18.

The peak lahar did not leave the distal end of the avalanche deposit until about 1330. By this time, the peak of the South Fork Toutle River lahar had already passed into the Cowlitz River, and lahar-induced deposition in Swift Reservoir was almost complete (Cummans, 1981).

Leaving the avalanche deposit, the North Fork Toutle River lahar took two routes—one followed the downstream channel of Hoffstadt Creek and the other followed the main channel of the North Fork Toutle River. The timing of flows down these two routes is uncertain, but both flows converged into a single flow about 4 km above the townsite of St. Helens (fig. 276*B*). One voluminous lahar having the initial texture of a mudflow then continued downstream. It swept away bridge decks and girders, but left piers in place. A portion of this lahar flowed up the Green River and deposited mudflow deposits, coarse woody debris, and steel-bridge girders in rearing ponds of the Green River fish hatchery.

Along the alluvial reach between the distal end of the avalanche and the mouth of the Green River, the North Fork Toutle River lahar substantially modified the drainage pattern and overall valley morphology, even though most of the resulting deposits are only 1 or 2 m thick. Between the Green River and locality J (fig. 271), the lahar surged down a confined bedrock canyon but caused only minor change in overall valley morphology, even though 1–1.5 m of overbank mud-

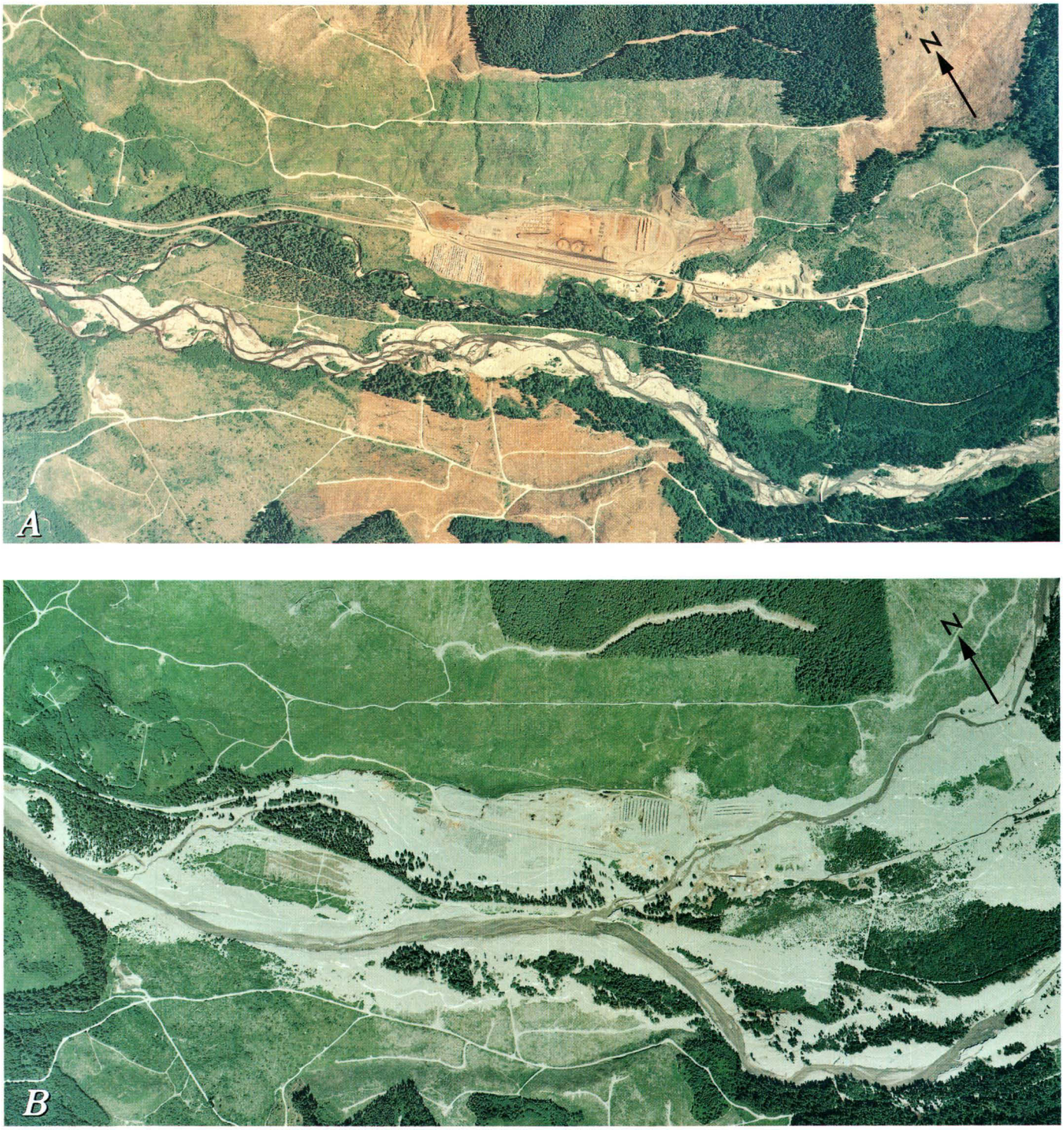

Figure 276.—Vertical aerial photographs, scale 1:24,000, showing valley of North Fork Toutle River near Camp Baker (near center of photograph). Flow from right to left. A, preeruption photograph, June 5, 1978; B, posteruption photograph, June 19, 1980. Width of mudflow inundation in center of photograph is 1.0 km. Note change in position of Hoffstadt Creek, which joins the North Fork Toutle River at Camp Baker in B. Photographs from Washington Department of Natural Resources.

flow deposits are present locally (fig. 277*A*). Between locality J (fig. 271) and the Toutle River stream-gaging station near Silver Lake (near I in fig. 271), a reach that includes the confluence of the North Fork and South Fork Toutle River, the North Fork Toutle River lahar again caused massive changes in channel pattern and valley morphology. Overbank deposits commonly are 3 m thick, and the sites of some former channels have more than 5 m of new deposits. Nonetheless, the channel in late summer was commonly incised as much as 1 m below the preeruption surface (fig. 277*B*).

In the broadly inundated areas between Camp Baker and the townsite of St. Helens (K in fig. 271), the contrast in heights of mudlines on upstream and downstream sides of standing trees suggests that flow velocities were commonly 4–5 m/s; however, close to the axes of maximum flow along both Hoffstadt Creek and the North Fork Toutle River, numerous trees were either sheared off or toppled and abraded. Increased depth of flow probably contributed to the increased damage, but local flow velocities higher than those suggested by mudlines on surviving trees may have been an additional factor.

Leaving the St. Helens area, the North Fork Toutle

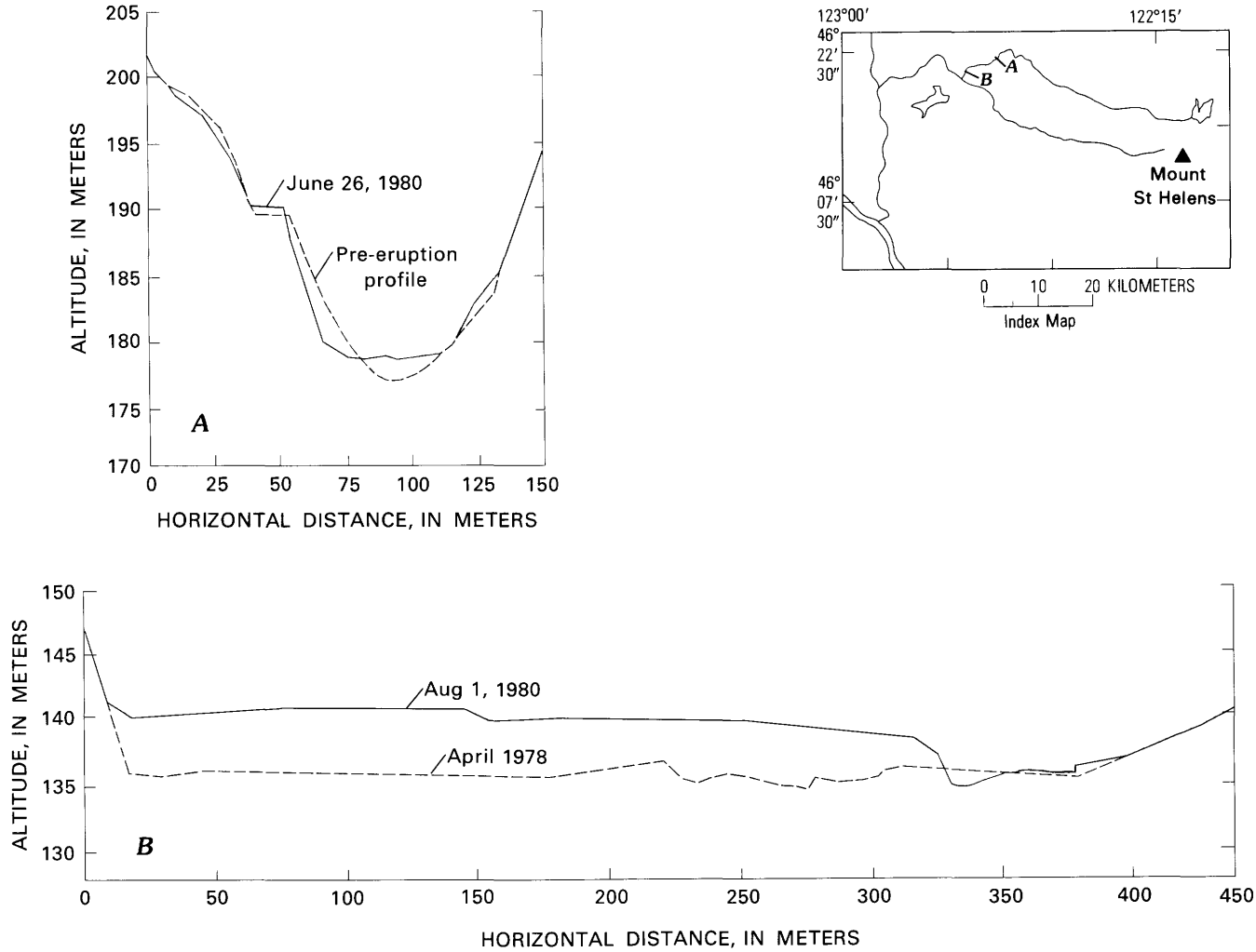

Figure 277.—Preeruption and posteruption cross-sectional profiles of the North Fork Toutle River. A, At State Highway 504 bridge near Kid Valley, 6.7 km downstream from the Green River. Little change in profile occurred. Preeruption profile from Washington State Department of Transportation. B, 0.5 km upstream from confluence with South Fork Toutle River. Note extensive fill on most of flood plain. Preeruption survey from Tudor Engineering. Observed depths of fill in adjoining areas are 1–1.5 m less than that suggested by comparison of preeruption and posteruption surveys, which appear to have used different altitude data.

River lahar flowed into a more constricted bedrock canyon. Velocities implied by cross-valley banking (superelevation) due to radial acceleration on bends suggest that immediately below the mouth of the Green River, the mean flow velocity for the peak lahar was about 12 m/s. Throughout the rest of the North Fork Toutle River, however, superelevation on stream bends and contrasting upstream and downstream mudlines on standing trees imply velocities of 6.0–8.0 m/s. Velocities at bends were computed from the formula $v = (g\,\psi \cos \delta \tan \beta)^{1/2}$ where v is mean velocity, g is the acceleration due to gravity, ψ is the radius of curvature for the stream bend, δ is the slope angle of the channel, and tan β is the presumed cross-valley slope of the flow surface (Johnson and Hampton, 1969). Similar computations have been reported by Wigmosta and others (1980) and Fink and Malin (1980), who computed velocities ranging from 7.0 to 31 m/s for the Toutle River and Pine Creek mudflows. Videotapes of television newsreels provide additional documentation of these high velocities. However, as with the lahar in South Fork Toutle River, timed visual observations suggest that downstream progression of peak stage of the lahar in the North Fork Toutle River was considerably slower than the computed at-a-point velocities. Sustained ponding of the lahar may have occurred near the confluence of the North Fork and South Fork Toutle River. This ponding may indicate restricted discharge through the constricted canyon reach below the confluence, but it may also reflect or have been augmented by a massive logjam in the same general area (Cummans, this volume).

The nature of the impact of the North Fork Toutle River lahar on flood-plain vegetation and the contrasting height of mudlines on the upstream and downstream sides of standing trees suggest that at any given cross section, the velocity of the lahars dropped markedly away from the thread of maximum flow. Sheared trees, as well as toppled and abraded trees (fig. 278), are restricted to the near-channel parts of the inundated area. Considerable splashing is commonly evident at the top of mudlines on the upstream sides of standing trees adjacent to the zone of toppled abraded trees. The difference in height between mudlines on the upstream and downstream sides of standing trees is greatest in the areas showing signs of splashing, and decreases to zero over distances of a few tens of meters transverse to the direction of flow. In areas of inundated forest that have consistent

Figure 278.—"Bayonet" trees on inundated area along North Fork Toutle River. Note sharpening of trees to points in downstream direction.

mudline elevations, partially decomposed logs from the former forest floor (fig. 279), as well as some mobile homes and small wooden-frame houses, floated passively on the mudflow; they were ultimately deposited in a relatively unmodified state on the new flood-plain surface (fig. 280).

Lahar deposits overlying the massive avalanche deposit and in the broad alluvial reach above the town of St. Helens are predominantly subangular pebble and cobble gravels with abundant silt and clay in the matrix. The deposits are mostly from 0.5 to 2 m thick and display rather flat surfaces, except where they have been incised by gullies and channel erosion. Upper surfaces of most thin lahar deposits on the avalanche are rather smooth, but some show distinct, ropy flow structures similar to those of pahoehoe lava; local relief on the flow structures is typically 7.5 cm or less. On steeply sloping channel margins, both on the avalanche and at numerous downvalley locations, veneers of cohesive mudflow deposits at and immediately below the peak flow levels show multiple recessional surge lines that are generally separated from one another by less than 0.3 m. Where the margin of the peak flow rests on a smooth, gently sloping surface, such as a road, an abrupt flow front at least 3 cm high is commonly present. Large (0.5–2 m in diameter) angular clasts of such noncohesive materials as avalanche deposits, colluvium, weathered older lahar deposits, and weathered tephra, occur commonly on the surface of the lahar

deposit and sporadically within the deposits themselves. These fragile clasts are commonly found more than 1 km from their most probable sources.

Where either expansion or contraction of a reach caused a major change in flow competence, large streamlined longitudinal "whaleback" bars of poorly sorted boulder or cobble gravel are commonly present. These features, which vary greatly in height and length, are as much as 60 m in length and 4 m in height. Height-to-length ratios are generally less than 0.05. As with similar features along the South Fork Toutle River, these large bars were apparently closely associated with the mudflow peak. The basic morphology of these bars is depositional, but localized erosion during recessional flows extensively modified some bars.

Figure 279.—"Nurse" log lying beneath mudline showing locally passive nature of mudflow near edge of flood plain. Note marks on standing tree caused by abrasion of the log as it floated up with rising stage and then lowered during falling stage.

Figure 280.—Locally passive nature of mudflow is shown by relatively intact condition of house, which apparently floated on mudflow surface to this position.

Differences in sorting and degree of admixture of old alluvium indicate that significant erosion accompanied the bar-forming phase of flow. The lower parts of the bars where viewed in cross section contain a larger proportion of rounded and subrounded cobbles and boulders, as well as sand derived from the underlying alluvium, than do the upper parts. The basal 5–15 cm of the deposits typically contain more silt and clay and are browner and more compact than the overlying deposits. Locally, a faint platy structure is evident in this basal layer.

Above the compact basal layer, the deposits typically are massive or exhibit crude normal size gradation. The gradation tends to be concentrated in the uppermost 0.2 m of the deposit and gives the appearance of a mud-rich "skin." Uncommonly, poorly defined stratification is discernible in these bars; individual strata show crude normal size gradation, are generally less than 2 m thick, and are nearly parallel to the surface of the bar. Fragile clasts of older surficial deposits and soils are present at the surface of the bars and locally within the bar deposit. Also resting on the surface or embedded only a few centimeters into the tops of the bars are rounded to subangular boulders and blocks commonly more than 1 m in diameter. The surficial boulders and blocks are composed of the same general suite of lithologies found within the deposits

and include high-density pyroxene andesite. The large clasts of low-density hydrothermally altered ancestral dacite (C. A. Hopson, written commun., 1980) and vesicular 1980 cryptodome dacite (Moore and Albee, this volume) are more abundant near the peak flow marks than elsewhere in the deposits. Compared to the South Fork Toutle River mudflow, that on the North Fork Toutle River was less commonly overridden by

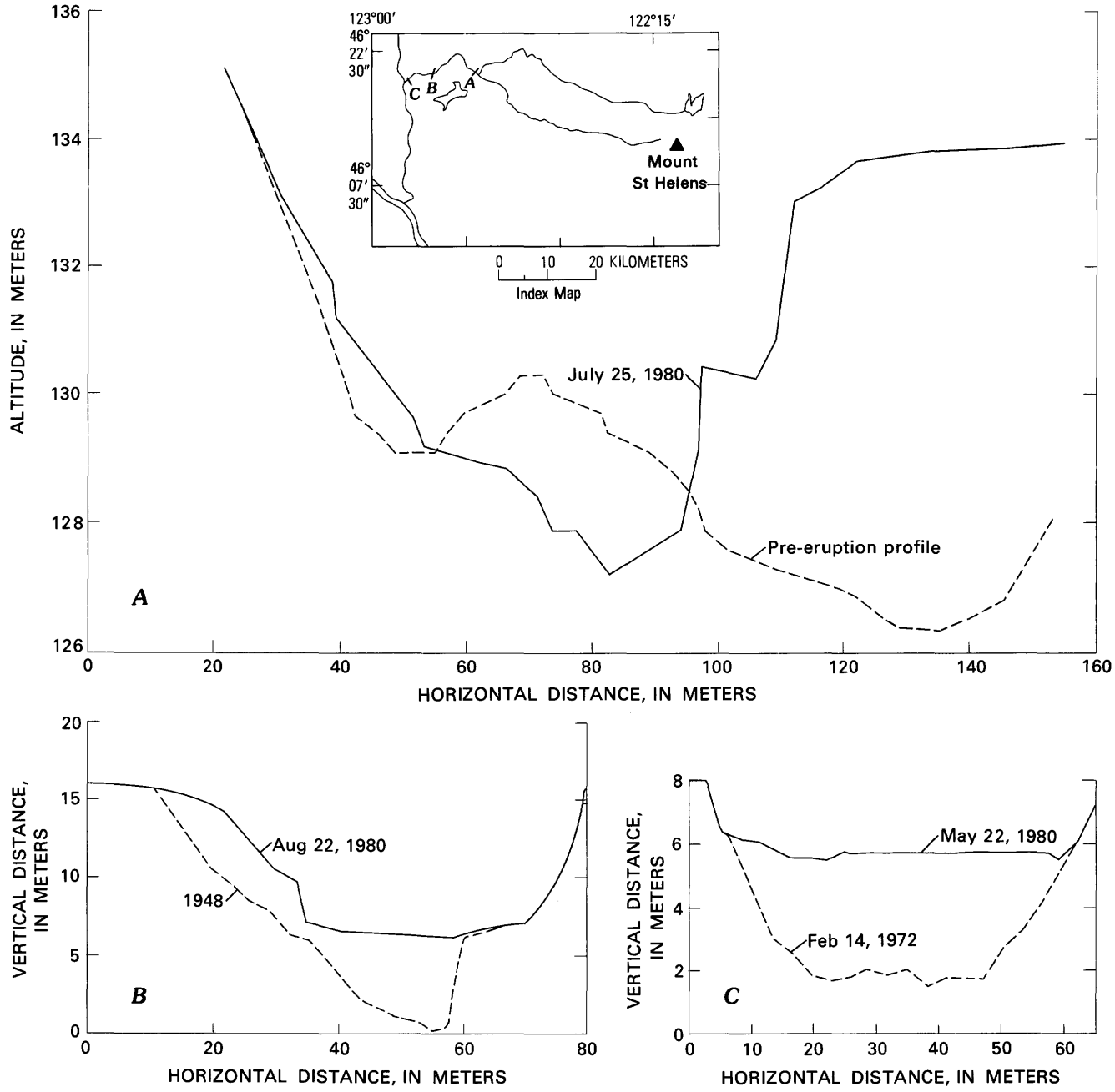

Figure 281.—Preeruption and posteruption cross-sectional profiles of Toutle River. A, At Coal Bank Bridge, State Highway 504, located near I in figure 271. Note thick accumulation of mudflow deposits on right side of profile. Preeruption profile from Washington State Department of Transportation. B, At Tower bridge, M in figure 271. Note thalweg aggradation and formation of berm on left side of profile. Preeruption profile from Cowlitz County Department of Public Works. C, At State Highway 99 bridge, N in figure 271. Preeruption and posteruption profiles, U.S. Geological Survey.

associated streamflow, but as on the South Fork Toutle River, debris-flow transport after peak mudflow is locally evidenced by low lateral berms of less cohesive sediment.

TOUTLE RIVER

Downstream from the confluence of the North Fork and South Fork Toutle River, the number and variation of flows were reduced. The deposits mainly represent the larger, more sustained flows from the North Fork Toutle River. At several localities (*I*, *L*, and *M* in fig. 271), coarse-grained but cohesive mudflow deposits from the North Fork Toutle River can be observed resting on stratified noncohesive sand and silty sand deposited by the downstream runout of heavily sediment-laden water from the initial South Fork Toutle River lahar. Along much of the Toutle River, the average thickness of May 18 lahar deposits is less than 1 m because the river flows primarily through narrow bedrock canyons. In these constricted reaches, the flows eroded considerable amounts of colluvium and alluvium, but lahar-deposited bars and berms are locally prominent (fig. 281, *A* and *B*). Large-scale lahar deposition along the lower Toutle River was concentrated in the wide alluvial reaches near the town of Tower (L in fig. 271) and immediately upstream from the Cowlitz River (figs. 271 and 281*C*).

Peak flow velocities through the lower Toutle River were apparently substantially lower than those along either the North Fork or South Fork Toutle River. Once again, computed average at-a-point velocities were substantially higher than was the average velocity at which the peak stage progresssed downstream. For example, in the Hollywood Gorge area (O in fig. 271) cross-valley banking implies average flow velocities of about 3.2 m/s, whereas timed observations suggest that the peak stage was propagated downvalley at an approximate rate of only 1.5 m/s (Cummans, this volume; written commun., December 1980).

COWLITZ RIVER

Unlike the peak South Fork Toutle River lahar, which underwent striking changes in volume and rheological character in a downstream direction, the peak mudflow associated with the North Fork Toutle River lahar underwent little change as it flowed through the Toutle and lower Cowlitz Rivers. Mudflow deposits accreting to the banks of the lower Cowlitz River and representing the peak flow are generally similar in texture to those found lateral to the channel of the Toutle River. Rocks from Holocene eruptions of Mount St. Helens constitute most of the pebble-size and larger clasts, even though those rocks underlie a small percentage of the drainage basin. A secondary mudflow berm at a level about 1–2.5 m below peak flow level occurs discontinuously along the Cowlitz River. A thin (0.1–0.5-m) layer of fine-grained water-deposited sediment occurs at the surface of this lower mudflow berm and is evidence of overriding streamflow. The uppermost mudflow deposits in the secondary berm are characterized by abundant splintered and shattered wood fragments—a significant proportion of them charred. Clasts of low-density hydrothermally altered ancestral dacite are also abundant on and near the surface of the secondary mudflow berm.

Throughout the mudflow-impacted reaches of the lower Cowlitz River, several levels of progressively better sorted debris-flow deposits occur below the earlier mudflow levels. The geometry of the debris flow and superimposed streamflow deposits suggests that both types of flow occurred simultaneously. The most prominent of the debris-flow berms on the Cowlitz River is locally overlain by texturally uniform 0.1- to 1.0-m-thick fine-grained sediment with current-produced bedding. Thus, a relatively uniform thickness of streamflow deposits was deposited before recessional incision was accomplished by either continuing debris flow or restabilized streamflow. Similar stratigraphic relations exist in other areas where both types of flow were observed to occur simultaneously. The recessional episode of debris flow was characterized by abundant immersed and partly immersed boulders as much as 0.9 m in intermediate diameter. Lower debris-flow units are generally finer grained and occur in association with sand layers that contain abundant, current-produced, internal sedimentary structures. Immersed and partly immersed boulders are much less abundant than are those in the higher units. The deposits of the lower berms thus were probably produced by flows transitional to normal streamflow.

Depths of flow at the mouth of the Toutle River were sufficiently great to allow large volumes of mud

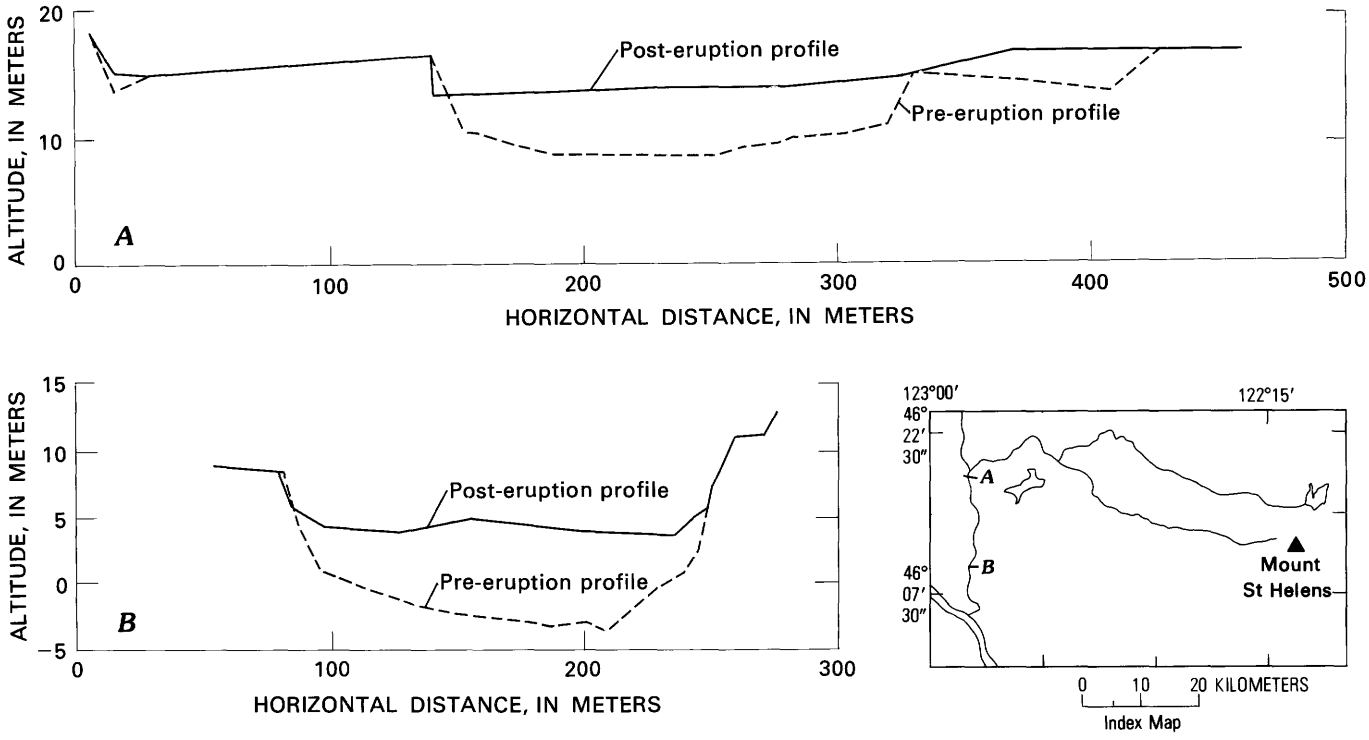

Figure 282.—Preeruption and posteruption cross-sectional profiles of the Cowlitz River. A, 1.0 km below mouth of Toutle River. Note reduced channel capacity. Preeruption profile from Tudor Engineering; posteruption profile by U.S. Geological Survey, Washington District Office. B, 11.1 km upstream from confluence with Columbia River. Note reduced channel capacity. Preeruption profile from Tudor Engineering; posteruption profile by U.S. Geological Survey.

and debris to flow upstream along the Cowlitz River for about 3 km. Effects of the lahars continued farther upstream, where meander bend pools formerly in excess of 10 m deep were reportedly filled.

The morphologic and hydraulic changes brought about by the May 18 and 19 laharic sedimentation along the Cowlitz River are discussed in detail by Lombard and others (this volume). Figure 282 provides examples of morphologic changes in this area. The timing and velocity of lahar movement through the lower Cowlitz River are discussed by Cummans (this volume).

SUMMARY AND CONCLUSIONS

Lahars affected nearly all streams draining the cone of Mount St. Helens, but to variable extents that reflect in part the directional character of the initial eruption. Extensive lahars originated in the Toutle River system and the Muddy River–Pine Creek drainages. The most voluminous flow, which originated on the debris avalanche in the headwaters of the North Fork Toutle River, modified more than 120 km of channel, including sections of the Cowlitz and Columbia Rivers.

Lahars formed in three major ways: (1) The largest lahar originated by slumping and flowing of water-saturated parts of the debris avalanche. (2) The lahars with the highest velocities originated by catastrophic ejection of mixtures of lithic debris, ash and lapilli, water, and entrapped air. These lahars were confined to the immediate vicinity of the cone, but some were transitional to mudflows that traveled much longer distances. (3) Finally, small lahars formed by accelerated melting of debris-laden ice and snow, and some were triggered by the heat of pyroclastic flows.

Although the largest 1980 lahars were devastating in their impacts on channels and flood plains, the impacts were less than those of some lahars associated with earlier eruptions. This comparison is important for future hazard assessments at Mount St. Helens and elsewhere.

Many flow features indicate highly viscous, probably non-Newtonian flow behavior. On flat surfaces

such as roads, the lateral edges of the highest lahar deposits on both the North Fork Toutle River and the lower Muddy River were marked by abrupt flow fronts at least 3 cm high. Flows of various consistencies supported cobbles and boulders at or near their surfaces. Fragile boulder-size clasts of soil and colluvium occur perfectly preserved in coarse gravel bars. These clasts and the platy structure of the thin basal layer of mudflow units suggest that vertical shear was concentrated at the base of the flow and that "plug" flow occurred at least locally. The gradual reduction in runup heights on trees with distance from the axis of maximum velocity, however, indicates a less concentrated distribution of shear in the horizontal plane.

Flow velocities ranged from less than 1.5 m/s in downstream reaches on the North Fork Toutle River to more than 40 m/s for highly mobile flows on and near the cone. Apparent discrepancies between velocities at individual points and the lower rates at which the peak stage was propagated downvalley are explained by local variations in channel configuration and slope, loss of volume through progressive deposition, and the expectable difference between rates of movement of the entire mass of a mudflow and flow near the axis of maximum velocity.

Flow characteristics of the catastrophically induced lahars, especially those in the South Fork Toutle River and Muddy River watersheds, changed strikingly downstream. Air-mobilized lithic avalanches and flows were transformed to and replaced by mudflows downvalley. In the South Fork Toutle River farther downstream, the mudflow was changed to and replaced by debris flow and normal streamflow. This contrasts with the massive lahar that originated on the North Fork Toutle River, the peak deposits of which were remarkably similar throughout the entire course of the flow to the Columbia River. Downstream changes did occur in the recessional character of this flow, particularly in the amounts and relative proportions of debris flow and normal streamflow.

The lahar deposits are generally thin compared with the depths of the initiating flows. Nonetheless, impressive amounts of fill were deposited locally, particularly by mudflows. For example, over 4 m of channel thalweg fill occurred locally on the South Fork Toutle River. Even where lahar-induced channel deposition was slight or where scour occurred in channels, overbank deposits are commonly more than 1 m thick. At some sites on the North Fork Toutle River, 3–4 m of fill occurred on the flood plain. However, the postlahar channels are commonly incised through the May 18 deposits and into older alluvium or lahar deposits.

The present channels are unstable and are adjusting rapidly to changes in geomorphic and hydrologic conditions. Continued erosion will release much sediment from previously stable pre–May 18 channel and flood-plain deposits, as well as from sediment deposited on May 18 and subsequently.

REFERENCES CITED

Beverage, J. P., and Culbertson, J. K., 1964, Hyperconcentrations of suspended sediment: Proceedings of American Society of Civil Engineers, Journal of Hydraulics, v. 90, Hy 6, p. 117–128.

Crandell, D. R., and Mullineaux, D. R., 1973, Pine Creek volcanic assemblage at Mount St. Helens, Washington: U.S. Geological Survey Bulletin 1383-A, 23 p.

_____1978, Potential hazards from future eruptions of Mount St. Helens volcano, Washington: U.S. Geological Survey Bulletin 1383-C, 26 p.

Cummans, John, 1981, Mudflows resulting from the May 18, 1980, eruption of Mount St. Helens, Washington: U.S. Geological Survey Circular 850-B, 16 p.

Fink, J., and Malin, M., 1980, Rheological properties of mudflows associated with recent eruptions of Mount St. Helens: EOS (American Geophysical Union Transactions), v. 61, no. 46, p. 1138.

Johnson, A. M., and Hampton, M. A., 1969, Subaerial and subaqueous flow of slurries: Unpublished final report to the U.S. Geological Survey; available through U.S. Geological Survey Library, Menlo Park, Calif., and Branner Library, Stanford University, Stanford, Calif.

Lombard, R. E., Miles, M. B., Nelson, L. M., Kresch, D. L, and Carpenter, P. J., 1981, Channel conditions in lower Toutle and Cowlitz Rivers resulting from mudflows of May 18, 1980: U.S. Geological Survey Circular 850-C, p.

Mullineaux, D. R., and Crandell, D. R., 1962, Recent lahars from Mount St. Helens, Washington: Geological Society of America Bulletin, v. 73, no. 7, p. 855–870.

Rooth, G. H., 1980, A personal account of a nuee ardente on Mount St. Helens during the eruption of May 18, 1980: Oregon Geology, v. 42, p. 141–144.

U.S. Geological Survey, 1980, Preliminary aerial photographic interpretive map showing features related to the May 18, 1980, eruption of Mount St. Helens, Washington: U.S. Geological Survey Miscellaneous Field Studies Map MF-1254.

Wigmosta, Mark, Fairchild, L. H., Smith, J. D., Dunne, T., and Flanagan, P., 1980, Field evidence for the dynamics of the Toutle River mudflows, May 18, 1980 [abs.]: 1980 American Geophysical Union Fall Meeting, San Francisco, p. 65.

THE 1980 ERUPTIONS OF MOUNT ST. HELENS, WASHINGTON

CHRONOLOGY OF MUDFLOWS IN THE SOUTH FORK AND NORTH FORK TOUTLE RIVER FOLLOWING THE MAY 18 ERUPTION

By JOHN CUMMANS

ABSTRACT

On May 18, 1980, Mount St. Helens, in southwestern Washington, erupted violently, setting off a chain of devastating hydrologic events. During the eruption, a massive debris avalanche that moved down the north side of Mount St. Helens was deposited in the North Fork Toutle River valley. Approximately 3 billion cubic yards of material, including rock, ash, pumice, snow, and ice was deposited directly north of the mountain in the upper 17 mi of the valley.

Following the onset of the eruption, a mudflow quickly developed in the South Fork Toutle River, and several hours later, a much larger mudflow originated from the debris avalanche deposit in the North Fork Toutle River valley. The North Fork mudflow caused widespread destruction as it moved downstream through the lower Toutle and Cowlitz Rivers.

INTRODUCTION

On May 18, 1980, following more than 8 weeks of earthquakes and minor eruptions, Mount St. Helens exploded violently, causing a massive debris avalanche that deposited approximately 3 billion cubic yards of rock, ash, pumice, snow, and ice in the upper 17 mi of the North Fork Toutle River valley (Youd and Wilson, 1980). Following the onset of the eruption, a mudflow quickly developed in the South Fork Toutle River, and, several hours later, a much larger mudflow originated from the massive debris-avalanche deposit in the North Fork Toutle River valley. Smaller mudflows developed in the Lewis and Kalama River valleys (Cummans, 1981).

Owing to the destruction of most gaging stations, the events are documented primarily by the piecing together of eyewitness accounts. Principal sources of information were radio logs of the Cowlitz County Communications Center, verbal and written reports of river-watch deputies, Weyerhaeuser Co. personnel who witnessed the scenes from a helicopter, and notes that Harry Glicken, USGS (U.S. Geological Survey), took during his interviews of D. C. Crockett. L. F. Edtl and Mr. and Mrs. Dan Calvert were interviewed by the author.

ACKNOWLEDGMENTS

Information contained in this report was compiled from numerous sources. The author gratefully acknowledges the cooperation of the many private individuals cited in the text and of the following organizations and their representatives: City of Longview, Wash., Leland F. Edtl, utilities engineer; Cowlitz County, Wash., Sheriff Les Nelson; Cowlitz County Communications Center, Al Gervenack and Brenda Hostetter; Pacific Power and Light Company, Stan DeSousa; U.S. Geological Survey, Menlo Park, Calif., Harry Glicken, Dick Janda, Mike Nolan, and Richard B. Waitt, Jr.; Washington State Department of Emergency Services, Jim Thomas; Weyerhaeuser Company of Longview, Jack Schoening and Ray Pleasant.

DESCRIPTION OF THE DRAINAGE SYSTEMS AND MUDFLOWS

DRAINAGE SYSTEM

Both the North Fork and South Fork Toutle River originate on the north to northwestern slope of Mount St. Helens (fig. 283), both streams flowing westerly to a juncture about 25 mi west of the mountain. Prior to the eruption, the two streams drained a combined area of about 15 mi^2 of mountain slope above the 4,000-ft elevation. Above their confluence, the North Fork drains 303 mi^2, of which 132 mi^2 is Green River drainage, and the South Fork drains 129 mi^2.

The Toutle River, formed by the junction of North Fork and South Fork, flows in a generally westward direction into the Cowlitz River; total drainage is 512 mi^2. The Cowlitz River flows south into the Columbia River, and several miles of its lower reach are affected by tides in the Columbia River (fig. 283).

MUDFLOWS

SOUTH FORK TOUTLE RIVER

The initial and largest mudflow on the South Fork Toutle River was first observed at 0850 PDT on May 18, by David C. Crockett, KOMO-TV News, Seattle, Wash. Crockett was on the south side of the river and about 4.5 mi west of the mountain when the eruption began. As he later recounted (to Harry Glicken, USGS), roads were quickly blocked by overbank flow, necessitating that he abandon his car and proceed on foot. He reported crossing "warm peat, or warm, fluid, brown concrete" during his escape. The approximate location of Crockett's abandoned vehicle is shown in figure 283.

Mr. Crockett also reported a second mudflow in the South Fork at about 1400. It reportedly was much smaller than the first, lasting about 20 min, but again sufficient to overflow the channel.

The first direct report on the major South Fork mudflow was at 1003 when a flood-watch deputy radioed that "a 5-ft rise of South Toutle River" was passing Weyerhaeuser's camp 12 (42.4 river miles upstream from the mouth of Cowlitz River). At 1005, the deputy stated that the flow was "knocking down trees," and at 1007, he reported that a "12-ft flash flood was moving down the South Fork below camp 12." The mudflow movement was swift, available information indicating that it traveled from the mountain to camp 12, a distance of 27 river miles, in 90 min.

At 1013, a river-watch deputy reported by radio that mud and debris were moving toward the bridge at the gaging station 1 mi west of Toutle near the mouth of the South Fork Toutle River. At 1014, the deputy described the flow as a 12-ft wall of water with logs, debris, and buildings. At 1020, the leading edge of the mudflow arrived at the South Fork's confluence with the North Fork, just upstream from State Highway 504 bridge. A deputy reported that the mudflow stage was just below the Highway 504 bridge at 1048, which was probably the approximate time of the peak stage at that location. Both the bridge west of Toutle and the Highway 504 bridge survived the South Fork mudflow.

At the Toutle River gaging station at Silver Lake (located 0.25 mi below the Highway 504 bridge), the river stage at 1020 was 2.54 ft, a normal level. By 1025, the river stage was rising. The large mudflow then quickly ruined the automatic continuous stage recorder so that the timing and stage of the peak were not recorded. At 1450 USGS personnel determined that the high-water mark at the gage was about 23.5 ft. This is the highest stage ever observed at the site, which has been maintained since 1909. The previous highest stage, 22.56 ft, occurred on December 2, 1977.

After peaking, the stage receded rapidly near the confluence. At 1112, river-watch deputies reported that the river level at the Highway 504 bridge had dropped 6 ft; at 1116, 8 ft. They also reported that the entire surface of the river was covered with floating logs for about 25 min.

At 1151, a logjam was reported to have just broken up on the Toutle River near Tower Road bridge (26.5 river miles upstream from the mouth of the Cowlitz River), as the peak passed that area. By this time, the flow was reported as "just a trickle" 10 mi upstream at the Highway 504 bridge.

By 1300, the mudflow entered the Cowlitz River, which was capable of containing the flow within its banks. At 1330, the stage at the Castle Rock bridge (Cowlitz River mile 17.3 and 2.7 mi below the mouth of the Toutle River) had risen to 13.15 ft, as recorded at the USGS gage. Prior to the approach of the mudflow, the river was at a normal stage of 10.0 ft, and it

returned to 10.0 ft at 1415. The mudflow, with its logs and debris, continued within banks down the Cowlitz River.

According to Mr. Leland F. Edtl, utilities engineer for the city of Longview, Wash., the leading edge of the mudflow, "with logs, trees, limbs, and bark," arrived at the intake of the Longview water treatment plant (Cowlitz River mile 5.2) at 1615. The peak probably occurred at about 1700 or shortly thereafter; however, Mr. Edtl observed logs in the river for 3 to 3.5 hr. During this period, Mr. Edtl observed no increase in water levels nor deterioration of the water quality. Water temperature was 51°F, and turbidity remained at its normal level of 4 Jackson turbidity units. However, the turbidity abruptly increased to 420 Jackson turbidity units between 2000 and 2030, and the treatment plant intake was closed.

On May 20, USGS personnel observed the upper reaches of the South Fork Toutle River and found clear evidence of the mudflow in the form of mudlines and other residual features. The flow had been confined within steep valley walls except for a 5- to 6-mi reach above the confluence with the North Fork Toutle River, where some overbank flow had occurred.

NORTH FORK TOUTLE RIVER

The massive debris avalanche that accompanied the May 18 eruption blocked State Highway 504 along the North Fork Toutle River with a 17-mi-long plug of rock, ash, ice, snow, and other debris. At Spirit Lake, at the upper end of the plug, the debris thickness reached 400 ft; near Elk Rock, at the lower end, about 150 ft (Youd and Wilson, 1980). The

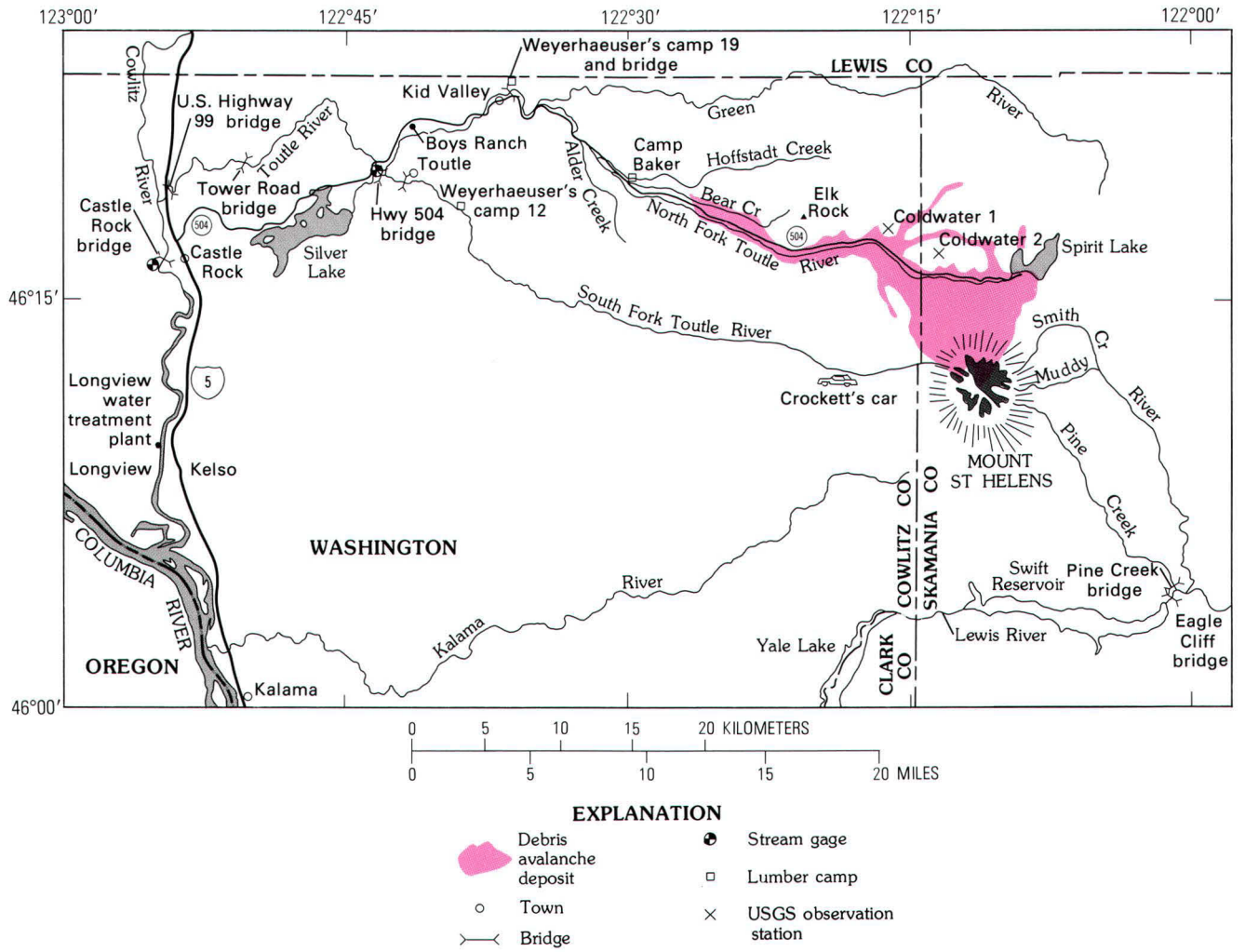

Figure 283.—Drainage system and localities at which mudflows were observed on May 18 and May 19, 1980, Mount St. Helens, Wash.

thickest debris, as much as 600 ft, was deposited about 1 mi below Spirit Lake. Large volumes of material from the debris-avalanche deposit entered Spirit Lake. High-water marks later observed above the northeast arm of the lake suggest that the lake water may have been temporarily displaced as the debris came in, subsequently flowing back over the newly deposited materials. The new lake surface is about 200 ft higher than prior to the eruption and about 200 ft lower than the surface of the massive debris deposit.

The early posteruption observations of the upper North Fork Toutle River were made by Harry Glicken of the USGS during helicopter search missions for Survey personnel at the Coldwater observation stations (fig. 283). Between 1200 and 1300, Glicken observed small plumes of ash and steam emanating from numerous mudflows on top of the debris-avalanche deposit. Below the toe of the deposit, Glicken observed downed trees, ash cover, and flowing mud; the mud was shallow and did not cover boulders 2 ft in diameter in the riverbed.

At about the same time, a Weyerhaeuser Co. team reconnoitering the area by helicopter noted that the stage of the North Fork Toutle River was low, presenting no problems at either Camp Baker or camp 19 (fig. 283). About 2 mi upstream from Camp Baker, the team noted blown-down timber across both State Highway 504 and the main Weyerhaeuser logging road. They also saw the debris deposit, and a few miles farther upstream (probably near Elk Rock), observed the surface character of the debris that filled the valley floor.

At 1300, the team headed upstream to check a report of water and debris moving down the North Fork, and observed streams of muddy water flowing down both sides of the valley on the surface of the debris-avalanche deposit. The two flows were heavy and visible for some distance as their leading edges kicked up large plumes of ash. At 1325, the mudflows arrived near Elk Rock, about 63 mi upstream from the mouth of the Cowlitz River.

Additional aerial observations of the mudflows were made by Jack Schoening, a member of the Weyerhaeuser Co. team. Mr. Schoening (oral commun., 1980) reported that the team was over Camp Baker at 1357 when the flows along the north side of the North Fork Toutle River valley were reaching the area. One minute later, the north side flow hit the camp, moving into the equipment and shop areas. The mudflow on the south side of the valley had yet to reach Camp Baker. By 1430, the camp was reported to be destroyed. The maximum flow in the area probably occurred at about 1500, when a logjam near the camp reportedly broke loose. At 1700, Mr. Schoening flew over the camp again and reported that the devastation was worse than that observed at 1430.

Some subsequent observations in the Camp Baker area are of interest. On May 18, Ray Pleasant, a pilot for Weyerhaeuser Co., observed the edge of the mudflow at one shop building. Several days later he noted that the mud covered a wider area around the building than before and was about 3 ft deeper. Another Weyerhaeuser employee who noted a "little" mud near his camp equipment at about 1800 on May 18, observed that the mud was deeper when he returned on May 19. These observations indicate that either (1) later mud flowed on top of the initial deposits, or (2) the consistency of the mudflow was so thick that flow in the center was higher than at the edges, thus requiring time for the edges to stabilize at a final higher depth.

At 1440, the Cowlitz County Communications Center received a report that the mudflow was passing Alder Creek (fig. 283). At 1501, the bridge on State Highway 504, 0.6 mi upstream from the mouth of Alder Creek, was reported destroyed by the flow; by 1530 the mudflow was passing the mouth of the Green River.

Mr. and Mrs. Dan Calvert, residents at Kid Valley, observed the mudflow at the Weyerhaeuser camp 19 bridge from about 1500 until about 1630, at which time they were rescued by the helicopter. They stated that during this period the flow kept rising and had the consistency of fresh mortar. They saw a fully loaded logging truck moving downstream submerged only to the level of the lowermost tier of logs. Mr. Calvert (oral commun., 1980) reported many buildings and ice chunks being carried along in the flow. The surface of the mudflow appeared smooth to Mr. Calvert, who did not recall seeing waves. Upon his return several days later, Mr. Calvert observed that the mudlines along the channel appeared to be higher than the stage at the time of their rescue.

At 1655, Weyerhaeuser personnel observed camp 19 by helicopter and noted that the mudflow was over the wheels of railroad cars; this level was later determined to be about the maximum height of the flow. At about 1720, they reported that the flow was

continuing and that more logs had been swept from the storage area. Based on the information furnished, the peak flow at camp 19 probably occurred at about 1700.

The Cowlitz County Communications Center received a report of the mudflow reaching the boys' ranch about 2 mi north of Toutle at about 1745. Ray Pleasant, of Weyerhaeuser Co., examined the site shortly after 1845, and reported that the mudflow depth appeared to have reached its maximum. As much as 3–4 ft of mud had been deposited in some of the buildings. The peak flow at this location probably occurred at about 1800.

The North Fork Toutle River mudflow was just upstream from the State Highway 504 bridge near Toutle at 1748. After uprooting trees at a nearby park (locally known as Harry Gardner Park), the mudflow destroyed the Highway 504 bridge, apparently between 1810 and 1815. At the USGS gage 0.25 mi downstream, the automatic radio stage transmitter was functioning at 1800, but failed to report at 1815. The peak flow at the gage is estimated to have occurred at about 1900.

River-watch deputies reported extraordinarily high stages at the confluence of the two forks until 2055, when it was reported that the stage was falling as though "something broke loose." On May 19, mudflow marks at the gaging site (fig. 284) just below the Highway 504 bridge were measured to be 53 ft above gage datum, about 30 ft higher than for the South Fork Toutle River mudflow. A surveying team then ran levels from high-water marks at the gage site to a narrow gorge 800 ft downstream. The measurements revealed only a slight downstream slope of the mud-

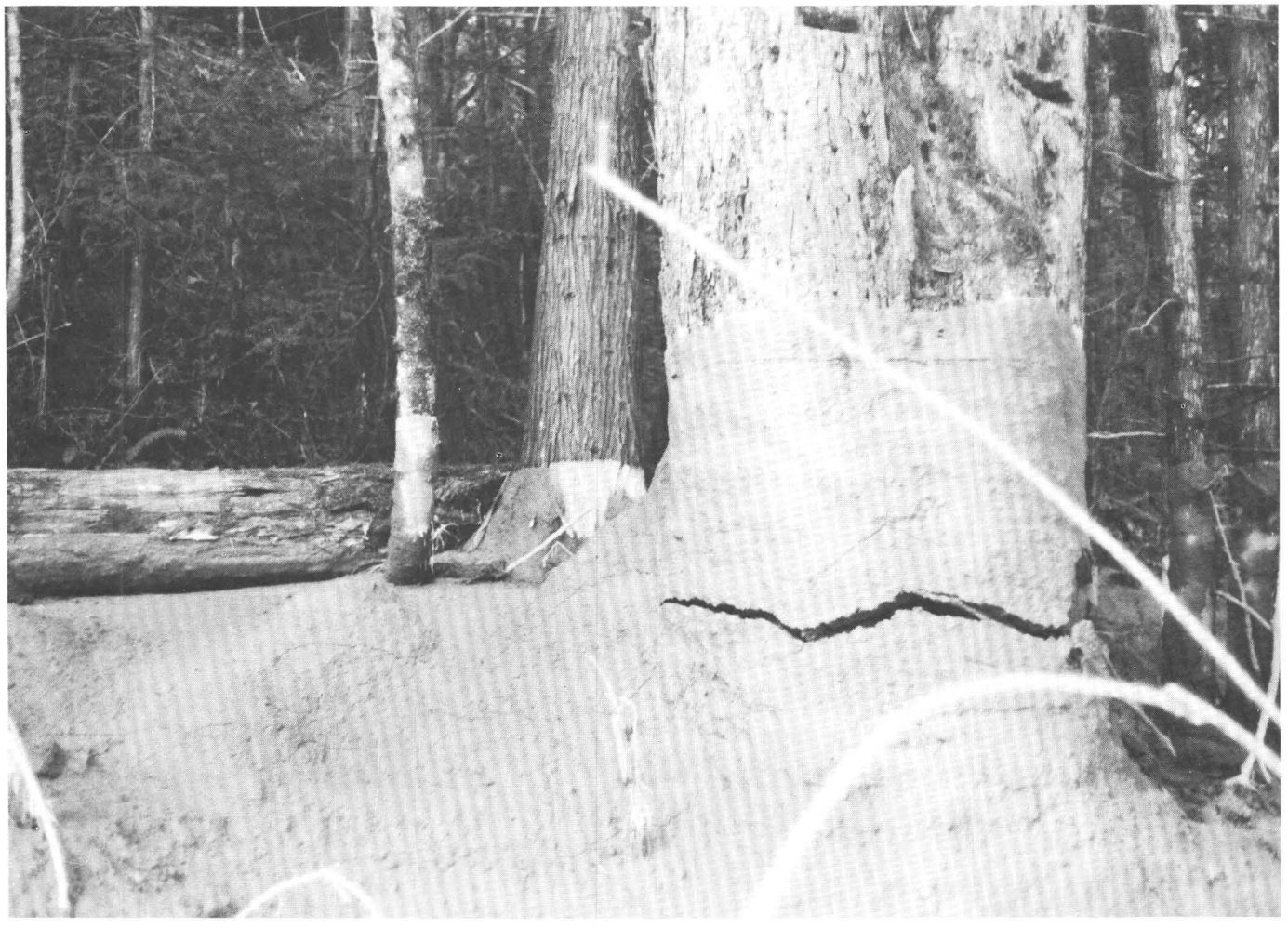

Figure 284.—Characteristic mudflow marks along the Toutle River, Wash., just downstream from State Highway 504 bridge. The material, when dry, has a coarse, abrasive texture. Photograph taken May 19, 1980.

flow surface, indicating that ponding had occurred in this reach. The ponding was largely responsible for the extraordinarily high stage in this reach, and apparently was caused by a massive logjam at the entrance to the constricting gorge, which is 0.8 mi downstream from the confluence of the North Fork and South Fork. The blockage and ponding may have been aided by debris arriving from the secondary mudflow observed by David Crockett on the upper South Fork at 1400. Figure 285 shows the resultant devastation just downstream from the confluence, in the area of the destroyed Highway 504 bridge.

At 2029, the mudflow covered the Tower Road bridge, 10.3 mi downstream from the Highway 504 bridge; at 2041, a report said the bridge had been destroyed. The peak at the Tower Road bridge probably occurred at about 2115.

The mudflow arrived at the mouth of the Toutle River at about 2030, where it was described as having a homogeneous, mortarlike consistency from bank to bank. The early part of the mudflow past this point carried logs, buildings, and a pickup truck. As the mudflow entered the Cowlitz River, the main mass moved downstream, but part moved upstream for 2.5 mi.

The mudflow continued downstream and the automatic gage at Castle Rock was quickly covered with mud and became inoperative. However, water levels were measured periodically at this site by USGS personnel. As shown in figure 286, water levels rose to a crest of 29.3 ft at midnight. Stages only 0.1–0.2 ft lower were observed from 2355 (May 18) to 0045 (May 19).

At the Castle Rock bridge, the temperature of the

Figure 285.—Flooded area at destroyed State Highway 504 bridge just below the confluence of the North Fork and South Fork Toutle River, Wash. Photograph taken May 19, 1980.

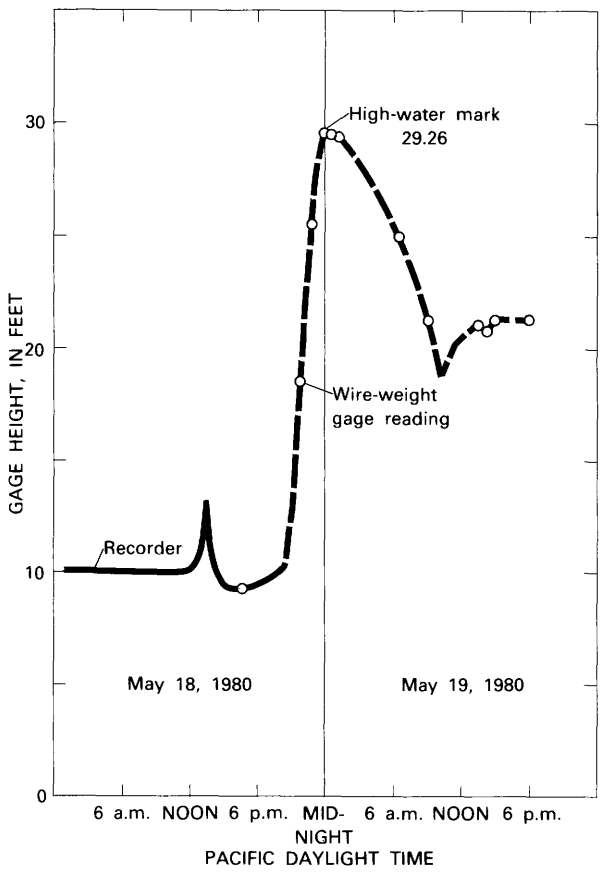

Figure 286.—Stage from recorder and wire-weight gage readings. Cowlitz River at Castle Rock, Wash., May 18–19, 1980.

mixed mudflow and Cowlitz River water was 85°F at 0115. On May 19, at 0630, the stage was down to 25.0 ft, but the temperature remained at 85°F. For comparison, at 0945, the mudflow temperature in the Toutle River at the Interstate Highway 99 bridge was 91°F.

At 0300 on May 19, the stage at the Longview water treatment plant (Cowlitz River mile 5.2) was reported to be 21 ft, which was at or near the maximum. Mr. Edtl, utilities engineer for the city of Longview, reported that the flood had receded 4 ft by 0800, when the water temperature was 90°F and turbidities were too high to be measurable.

DISCUSSION

MUDFLOW VELOCITIES

The movement of the mudflows in the North Fork and South Fork Toutle River is summarized in table 41. Travel velocities listed in the table are averages between successive locations. Velocities at any particular point between locations may have varied considerably from that listed because of local differences in channel configuration and streambed slope. The computed velocities are based upon the time-of-travel of the peak mudflow stage. The reported timing of the peak stages at the designated locations are believed to be accurate to within one-half hour, except for that of the Cowlitz River at Castle Rock.

Table 41.—Approximate time, location, and average velocity of the peak stages of the mudflows originating in the South Fork and North Fork Toutle River, Wash., May 18, 1980

[All times are Pacific Daylight time, ft/s, feet per second]

Time of peak stage	Site: Location	River miles upstream from mouth of Cowlitz River	Average velocity between locations (ft/s)
	South Fork mudflow		
0832	Eruption at source of South Fork---	69.4	
			27.4
0850	David Crockett's car----------	63.8	
			23.5
1010	Weyerhaeuser camp 12----------	42.4	
			12.3
1050	State Highway 504 bridge----------	36.8	
			15.1
1150	Tower Road bridge----------	26.5	
			8.1
1330	Castle Rock bridge (gage)----------	17.3	
			5.1
1700	Longview water treatment plant-----	5.2	
	North Fork mudflow		
0832	Eruption (dam below Spirit Lake)---	74	
1330	Elk Rock area----------	63	
			7.8
1500	Camp Baker----------	55	
			6.9
1700	Weyerhaeuser camp 19 (1900 bridge)	45.6	
			7.9
1800	Boys' ranch near Toutle----------	40.2	
			5.6
1900	Toutle River gage (0.25 mi below State Highway 504 bridge)--------	36.4	
			6.5
0915	Tower Road bridge----------	26.5	
			4.9
2400	Castle Rock bridge (gage)----------	17.3	
			4.4
0400 (May 19)	Longview water treatment plant-----	5.2	

Large differences occurred in velocities of the mudflows in the North Fork and South Fork. Above the point of confluence (near State Highway 504 bridge), the weighted average velocity for the peak stage of the North Fork mudflow is about 7 ft/s (feet per second), whereas that for the South Fork mudflow is about 22 ft/s. The threefold higher velocity in the South Fork possibly resulted from a combination of steeper streambed slopes, smaller channel capacities, and a higher water content of the mudflow.

The South Fork mudflow also moved through the

Toutle River down to the Castle Rock bridge at a greater velocity than did the North Fork mudflow. Downstream from Castle Rock, in the channel of the Cowlitz River, the velocities of the two mudflows were similar.

POST-MUDFLOW CHANNEL CHANGES

Comparison of preeruption and posteruption profiles indicates that the mudflow significantly altered the channel configuration, and hence the flow capacity of the lower Cowlitz River. Cross-sectional measurements of the Cowlitz River channels at both Kelso and Castle Rock reveal that deposits of sediment and debris raised the average elevation of the channel bottom about 15 ft at each location. Prior to the mudflows, the maximum carrying capacity of the Cowlitz River at Castle Rock (at the floodstage of 23.0 ft) was 76,000 ft^3/s. As of July 1980, the channel capacity was about 7300 ft^3/s. At that time, the river could carry less than 10 percent of its former capacity without flooding the surrounding valley.

REFERENCES CITED

Cummans, John, 1981, Mudflows resulting from the May 18, 1980, eruption of Mount St. Helens, Washington: U.S. Geological Survey Circular 850-B, 16 p.

Youd, T. L., and Wilson, R. C., 1980, Stability of Toutle River blockage, Mount St. Helens hazards investigations: U.S. Geological Survey Open-File Report 80-898, 14 p.

PUMICEOUS PYROCLASTIC-FLOW DEPOSITS

Pyroclastic flows are high-velocity surface flows of high-temperature fragmental material. Such flows potentially are very destructive because of their high temperatures and great mobility. Historic flows have been observed to travel a few kilometers from vents at velocities of up to 60 m/s, and analyses of prehistoric deposits suggest that large flows can cover distances of as much as 100 km at velocities of up to 200 m/s.

Pyroclastic flows are commonly subdivided on the basis of constituent materials and grain size into ash flows, pumice flows, lithic pyroclastic flows, block-and-ash flows, and so on. Ash flows consist chiefly of ash-sized particles of glass shards and phenocrysts; the term pumice flow is applied if pumice lapilli and blocks are dominant. Ash flows are a common type of pyroclastic flow, especially in large-volume eruptions. Block-and-ash flows contain abundant, large, little-vesiculated fragments and commonly form by explosive disruption or gravitational failure of the flank of a growing lava dome. Many pyroclastic flows are preceded by a ground-hugging hurricane-like surge cloud and accompanied by an overriding ash cloud, each of which may result in recognizable deposits.

Pumiceous pyroclastic flows of mafic dacite occurred during six major 1980 eruptions at Mount St. Helens (May 18, May 25, June 12, July 22, August 7, and October 16–18). This sequence presented exceptional opportunities to observe and photograph pyroclastic flows in motion, study their primary depositional features, measure thermal and rheological properties, relate size and sorting parameters to eruption characteristics, and monitor compositional changes. In general, time intervals between successive pyroclastic eruptions increased during 1980, and eruptive volumes, vesicularity, and degree of chemical differentiation decreased.

Pyroclastic flows were first observed shortly after noon on May 18; resulting deposits extend as much as 8 km from the vent, cover an area of about 15 km^2, and have a bulk volume of about 0.2 km^3 (Rowley and others). The deposits form a fan-like pattern of sheets, tongues, and lobes of mostly poorly sorted ash and clasts of pumice and dense dacite. Successively younger 1980 pyroclastic-flow deposits, in general, cover progressively smaller areas and have smaller volumes. The flows formed along with development of large vertical ash columns. Most pyroclastic flows originated when bulbous masses of ash, lapilli, and blocks rose only a short distance above the inner crater before spreading laterally to the north, but some flows were observed to result from gravitational collapse of parts of an accompanying vertical ash column.

Morphologic and rheologic measurements on pyroclastic-flow deposits of July 22 and August 7 indicate that the flows moved as non-Newtonian fluids, most readily modelled as Bingham plastics (Wilson and Head). Reverse grading of coarse, low-density pumice clasts in marginal levee deposits is interpreted as the consequence of briefly increased fluidization, related to interaction between the flow and surrounding air at the time of emplacement.

Petrographic and textural studies indicate that all 1980 pyroclastic-flow deposits consist mainly of juvenile dacite, containing plagioclase, hypersthene, hornblende, and Fe-Ti-oxide phenocrysts in a vesicular glassy matrix (Kuntz and others). In general, successively younger deposits show increasing modal proportions of plagioclase, hypersthene, and Fe-Ti-oxide phenocrysts, increasing average anorthite content of plagioclase, increasing phenocryst:glass ratios, and decreasing porosity. These relations suggest that successive eruptions have tapped deeper levels in a compositionally zoned magma chamber, have progressively depleted the magma of volatiles, and have been characterized by decreased amounts of vesiculation and gas thrust.

THE 1980 ERUPTIONS OF MOUNT ST. HELENS, WASHINGTON

PYROCLASTIC-FLOW DEPOSITS

By PETER D. ROWLEY, MEL A. KUNTZ, *and* NORMAN S. MACLEOD

ABSTRACT

Pyroclastic flows were produced during six major 1980 eruptions of Mount St. Helens volcano, on May 18, May 25, June 12, July 22, August 7, and October 16–18. The pyroclastic flows formed simultaneously with, or just prior to, large vertical (Plinian) ash columns. Visual observations suggest that most pyroclastic flows originated when bulbous masses of ash, lapilli, and blocks rose only a short distance above the inner crater and spread laterally northward. Some pyroclastic flows, however, were observed to result from gravitational collapse of parts of accompanying Plinian ash columns. Most of the resulting deposits are on the northern flank within 8 km of the crater, but associated ash-cloud deposits of May 18 extend several kilometers farther northward, and small pyroclastic flow deposits occur locally on the western, southern, and eastern flanks of the volcano.

Pyroclastic flows were first observed being emplaced at 1217 PDT (Pacific Daylight time) on May 18, nearly 4 hr after the start of the eruption, and successive pyroclastic flows continued to form intermittently for about 5 hr thereafter. They extended north as far as 8 km to Spirit Lake and North Fork Toutle River. The resulting deposits have a volume of at least 0.12 km^3, cover an area of about 15.5 km^2, and consist of a succession of flow units that have a maximum total thickness of at least 40 m and individual thicknesses generally of 0.25 to 10 m. Fumaroles and phreatic-explosion pits formed in the May 18 deposits, especially in the northern part of the plain.

Since May 18, the time interval between eruptions has been generally increasing, and successively younger pyroclastic-flow deposits have, in general, successively smaller volumes. The volumes of the post-May 18 pyroclastic-flow deposits are as follows: May 25, 0.001 km^3; June 12, 0.01 km^3; July 22, 0.006 km^3; August 7, 0.004 km^3; and October 16–18, 0.001 km^3. The pyroclastic flows spread 4–7.5 km from the vent and they cover areas of 1.7–8.3 km^2.

Pyroclastic-flow deposits form a fanlike pattern of sheets, tongues, and lobes of nonwelded and mostly poorly sorted ash and clasts of pumice and dense (lithic) dacite. Most tongues and lobes are less than 4 m thick and generally have marginal levees and steep distal ends. Pumice lapilli and blocks are normally highly vesiculated and show subtle lithologic, petrographic, and chemical differences from one major eruption to another. In general, successively younger deposits have higher block and lapilli to ash ratios and are slightly more mafic in composition. Ash-cloud and surge deposits are fine grained, moderately well sorted, and bedded, and they form beds or dunes within and beyond the limit of the pyroclastic-flow deposits.

INTRODUCTION

This report describes pyroclastic-flow deposits and associated deposits and features that formed during six of the seven major 1980 eruptions of Mount St. Helens volcano, Washington. The six eruptions took place on May 18, May 25, June 12, July 22, August 7, and October 16–18. The seventh eruption, on December 27–28, produced only a volcanic dome and minor amounts of air-fall ash. The study of the pyroclastic flows began with observations by numerous geologists of the May 18 eruption and deposits. Our field studies, during July through October, focused on the distribution, features, petrology, and mechanical properties of the deposits (MacLeod and others, 1980). The present report discusses eruptions, distributions, and field characteristics of the deposits; their petrology and grain-size characteristics are described by Kuntz and others (this volume), their chemistry is given by Lipman, Norton, and others (this volume), and their temperatures are reported by Banks and Hoblitt (this volume).

In the report, we use *pyroclastic flow* in the sense of Aramaki (1957, 1961) and Aramaki and Yamasaki (1963) to refer to a "surface flow of high-temperature, essential, fragmental material"; as such it is equivalent to the basal avalanche of a nuée ardente. Many pyroclastic flows are accompanied by a preceding, ground-hugging, hurricane-like surge cloud, and all have an overriding ash cloud (Sparks and others, 1973; Sheridan, 1979), each of which generally results in recognizable deposits. *Surge deposits* are planar to crossbedded, are mostly well sorted, and consist of mostly fine-grained material; they typically form dunes marginal to and at the base of pyroclastic-flow deposits (Sparks and Walker, 1973; Sparks, 1976; Sheridan, 1979; Wohletz and Sheridan, 1979). Deposits of the ground-hugging basal avalanche, or pyroclastic flow, consist of numerous *flow units* of generally poorly bedded and poorly sorted, commonly graded material. A *tongue* refers to major tonguelike accumulations, whereas *lobes* are smaller and may extend out from tongues. *Ash-cloud deposits* (Crandell and Mullineaux, 1973; Fisher, 1979) result from the cloud that rises as much as several kilometers above the advancing pyroclastic flow and may continue well beyond it. They are massive to well-bedded, commonly crossbedded, moderately well sorted, fine-grained beds and dunes that overlie or are marginal to the pyroclastic-flow deposits. Some ash-cloud deposits result from airfall, but most 1980 ash-cloud deposits at Mount St. Helens were emplaced by turbulent surges of ash similar to those described by Fisher (1979). *Phreatic-explosion pits* are large holes bored by steam explosions through pyroclastic-flow deposits and other deposits.

ACKNOWLEDGMENTS

We are grateful to many persons for sharing their observations from aircraft and the ground and for comments and suggestions during discussions on pyroclastic-flow deposits. We especially thank D. A. Swanson, R. P. Hoblitt, N. G. Banks, P. W. Lipman, J. G. Rosenbaum, J. G. Moore, R. L. Christiansen, C. D. Miller, D. R. Crandell, D. W. Peterson, D. R. Mullineaux, R. B. Waitt, Jr., M. P. Doukas, T. A. Leighley, T. J. Casadevall, R. W. Decker, Lionel Wilson, Stephen Self, T. J. Bornhorst, J. W. Vallance, and L. A. McBroome. A. M. Kaplan and L. A. McBroome assisted in some of the field studies. Exceptional helicopter pilots Michael Holtsclaw, Michael Montgomery, Robert Edwards, and Warren Fortier greatly assisted our field work. The manuscript benefited from suggestions by D. R. Crandell, P. L. Williams, and D. R. Mullineaux.

RESULTS OF EARLY ERUPTIVE ACTIVITY

During the last 2,500 yr, Mount St. Helens has erupted both lithic and pumiceous pyroclastic flows that extended at least 5 to 11 km from the vent (Crandell and others, 1975, 1979; Crandell and Mullineaux, 1978; Hoblitt and others, 1980). None of the deposits are welded and few are known to exceed the volume of those of May 18 (D. R. Crandell, oral commun., 1980).

The 1980 eruptions at Mount St. Helens began March 27, following a week of seismic activity. The material deposited between March 27 and May 18 consisted of several small mudflows and thin air-fall deposits. The major eruption, beginning at 0832 PDT on May 18, produced two principal units. The first unit consists of debris-flow deposits, locally as much as 200 m thick, that formed from landsliding of rock debris from the northern flank of the volcano into the North Fork Toutle River (Glicken and others, 1980; Voight and others, 1980). The second unit is thin lateral-blast deposits, of pulverized lithic rock debris, juvenile dacite, and vegetation from the northern flank of the volcano that were sprayed in an arc of 150° over an area 20 × 35 km (Christiansen, 1980; Kieffer, 1980; Miller and Hoblitt, 1980; Sisson and Moore, 1980; Waitt and Dzurisin, 1980; U.S. Geological Survey, 1980). Air-fall ash from the Plinian eruption column that arose within several minutes after the start of the eruption and that continued through most of the day locally thinly coats these deposits (Sarna-Wojcicki and Waitt, 1980; Sarna-Wojcicki and others, 1980).

The destruction of much of the summit and upper northern flank of Mount St. Helens during the morning left a huge open-sided north-facing "amphitheater" (fig 287). On May 19, an "inner crater," about 0.25 km in diameter and more than 50 m deep, occupied the south end of the amphitheater; it was

Figure 287.—Northern flank of Mount St. Helens, Wash., showing the rampart (R), amphitheater (A), stairsteps (S), and southern part of the pumice plain (P). View from Coldwater Ridge.


A
A
A
R
R
A
S
S
P
P

filled by volcanic domes after the eruptions of June 12, August 7, October 18, and December 27–28. A low ridge, referred to as the "rampart" and built by fallback of mostly coarse material, extends east-west between the inner crater and the northern, outer part of the amphitheater. The relatively smooth floor of the outer amphitheater, about 100 m below the top of the rampart, slopes about 5° northward until it reaches the north-sloping (15°) volcano flank, which is cut by numerous north-trending channels due mostly to erosion by pyroclastic flows. The largest of these is a canyon, the "stairsteps," that extends down the flank and has been the main path for pyroclastic flows. Its steplike floor consists of a series of cliffs and nearly flat benches. The "pumice plain" extends from the base of the northern flank of the volcano, where the stairsteps and other channels debouch, to as far north as Spirit Lake and the former valley of the North Fork Toutle River. The surface of the pumice plain slopes northward 2°–3°. Phreatic-explosion pits are abundant on the northern part of the pumice plain; the largest, about 2 km west of Spirit Lake, is referred to as the "big phreatic-explosion pit."

OBSERVATIONS ON ERUPTIONS AND DISTRIBUTION OF DEPOSITS

ERUPTION OF MAY 18

The exact time of the first pyroclastic flow is not known. The sustained vigorous Plinian column during the morning may have generated small pyroclastic flows by column collapse, but none were observed. A plume from a phreatic-explosion pit southwest of Spirit Lake was visible during the morning, but the ground surface was obscured by clouds, so pyroclastic flows are not known to have formed the pit (D. A. Swanson, oral commun., 1981). However, new magmatic material formed much of the lateral-blast deposits and apparently resulted in pumice seen falling at 0900 east of the mountain (Rosenbaum and Waitt, this volume). At about noon, the eruption cloud lightened in color from medium gray to dirty white, probably reflecting a greater magmatic component to the eruption (D. A. Swanson, oral commun., 1980). At about 1217, and periodically for the rest of the afternoon, ash clouds that accompanied pyroclastic flows could be seen (table 42), through occasional breaks in the eruptive clouds and rain clouds, to be moving laterally out from under the Plinian column. The eruption had a high discharge rate for about 9 hr, until about 1730 (Christiansen and Peterson, this volume), and then began to subside. These observational data agree with seismic data that show that harmonic tremoring, indicative of magma movement, began just before noon and continued at a high rate until about 1730 (Malone and others, this volume).

Nearly all pyroclastic flows came to rest north of the volcano. They extended as far as 8 km from the vent, to Spirit Lake and the valley of the North Fork Toutle River (fig. 288). The pyroclastic flows banked against the bedrock ridge (Coldwater Ridge) on the north side of the valley and pooled in the valley and in the Spirit Lake basin, infilling highly irregular topography left by the debris avalanche. Hills of debris-avalanche deposits locally protrude through the pyroclastic-flow deposits on the pumice plain. Some of the accompanying ash clouds traveled north across the bedrock ridge and into South Coldwater Creek, leaving thin deposits of ash.

Small pyroclastic flows came to rest high on the western, southern, and eastern flanks of the volcano (table 42; fig. 289), but few of the resulting deposits are widespread. Pyroclastic-flow deposits now are exposed at three locations on the east side of the volcano (pl. 1). One of these is above the headwaters of Ape Canyon, where pyroclastic-flow deposits as thick as 2 m thin eastward to about 0.25 m thick just west of Pumice Butte (nearly 4 km from the inner crater). South of Windy Pass, in the headwaters of a tributary to Smith Creek, the deposits are as much as 1.5 m thick and are about 3.5 km from the vent. Pyroclastic-flow deposits at least 3 m thick, exposed on the plain along and north of the headwaters of Muddy River, evidently crossed the crater rim between Ape Glacier and Shoestring Glacier and traveled about 5 km from the vent. The deposits at Muddy River in most places are overlain by a mudflow that was deposited about 2 weeks later (R. P. Hoblitt, oral commun., 1980).

Pyroclastic-flow deposits of May 18 cover an area of about 15.5 km^2. Their thickness and volume are known only approximately because their base is only locally exposed, and they are exposed in cross section only in phreatic-explosion pits. The maximum measured thickness, 38 m, is in the big phreatic-explosion pit, but even there the base of the deposits is not ex-

Table 42.—Recognized eruptive events relating to pyroclastic-flow deposits, May 18 to October 18

[PDT, Pacific Daylight time. Leaders (---), not measured or observed]

Date	Local time (PDT)	Plinian column height, in m	Location on volcano	Observer	Comments
May 18----	0832	18,000	North side--------	Dorothy and Keith Stoffel, and others.	Emplacement of debris flow and lateral blast. No pyroclastic flows seen.
Do-----	1200	---	--------do--------	D. A. Swanson----------	Plinian cloud starts to lighten in color.
Do-----	1217	---	--------do--------	----------do----------	First pyroclastic flow seen.
Do-----	?	---	West side---------	Austin Post----------	Pyroclastic flow in Toutle and Talus Glacier area; photograph taken sometime between 1100 and 1230 PDT (fig. 289).
Do-----	1230	---	--------do--------	D. A. Swanson----------	Pyroclastic flow.
Do-----	1244	---	--------do--------	----------do----------	Do.
Do-----	1255	---	West side---------	----------do----------	Do.
Do-----	1258	---	North side--------	----------do----------	Do.
Do-----	1348	---	--------do--------	J. G. Rosenbaum----------	Do.
Do-----	1440	---	--------do--------	----------do----------	Do.
Do-----	1506	---	--------do--------	----------do----------	Do.
Do-----	1527	---	West side---------	----------do----------	Do.
Do-----	1531	---	--------do--------	----------do----------	Do.
Do-----	1536	---	--------do--------	----------do----------	Do.
Do-----	1545	---	--------do--------	----------do----------	Do.
Do-----	1545-1555	---	Plains of Abraham-	----------do----------	Pyroclastic flow--probably the same one described by Rooth (1980) on the "south side" of the volcano.
Do-----	1558	---	South side--------	----------do----------	Pyroclastic flow in Swift Glacier area.
Do-----	1600	---	West side---------	----------do----------	Pyroclastic flow in Toutle and Talus Glacier area.
Do-----	1630-1930	---	North side--------	R. L. Christiansen--------	One or two pyroclastic flows seen.
May 25----	0232	14,000	--------do--------	None----------	Pyroclastic flows emplaced, probably just after 0232 PDT.
June 12---	1905	11,000	--------do--------	----------do----------	Pyroclastic flows may have been emplaced, but none seen.
Do-----	2111	15,000	--------do--------	----------do----------	Main event, producing pyroclastic flows. Eruptive activity ceased at about 0200 PDT of June 13; large volcanic dome emplaced within several days after this.
July 22---	1714	14,000	--------do--------	R. P. Hoblitt, M. P. Doukas, J. W. Vallance, and others.	Eruption lasted 6 min. Small pyroclastic flow emplaced in amphitheater.
Do-----	1825	18,000	--------do--------	----------do----------	Eruption lasted 22 min. Pyroclastic flow extended 6.5 km from vent toward Spirit Lake.
Do-----	1901	14,000	--------do--------	----------do----------	Eruption lasted 2 hr 40 min. Pyroclastic flow extended 7 km from vent to big phreatic-explosion pit.
Aug. 7----	1623	13,000	--------do--------	P. W. Lipman, R. P. Hoblitt, and others.	Pyroclastic flows extended more than 5.5 km from the vent.
Do-----	2232	11,000	--------do--------	None----------	Pyroclastic flows probably emplaced. A small dome filled part of the inner crater within a few days.
Oct. 16---	2158	13,000	--------do--------	----------do----------	Pyroclastic flows probably emplaced.
Oct. 17---	0928	14,000	--------do--------	----------do----------	Pyroclastic flows extended about 4 km to north, as recorded by a television camera.
Do-----	2112	14,000	--------do--------	----------do----------	Pyroclastic flows extended about 4 km to north.
Oct. 18---	1235	8,000	--------do--------	D. A. Swanson, T. A. Leighley, P. D. Rowley.	Small pyroclastic flows on the rampart area, probably by column collapse.
Do-----	1432	6,000	--------do--------	----------do----------	Plinian column, but no pyroclastic flows. Large dome started to form immediately, filling nearly all of inner crater within 5 hr; it was much larger by 0900 PDT the next morning.

posed. They may be thicker elsewhere in the northern part of the pumice plain. The deposits thin southward toward the base of the stairsteps. The thickness is generally less than several meters in the amphitheater and on the northern flank. The estimated volume of all pyroclastic-flow deposits of May 18 is at least 0.12 km^3, collectively an "intermediate"-sized deposit according to Aramaki (1961) and Sheridan (1979).

ERUPTION OF MAY 25

Darkness and poor weather prevented observations of the pyroclastic flows of May 25; they probably formed during the opening minutes (0232) of the eruption, when activity was at its peak. Most of the pyroclastic-flow deposits of May 25 extended north from the vent for about 4 km, where they ended in a

S

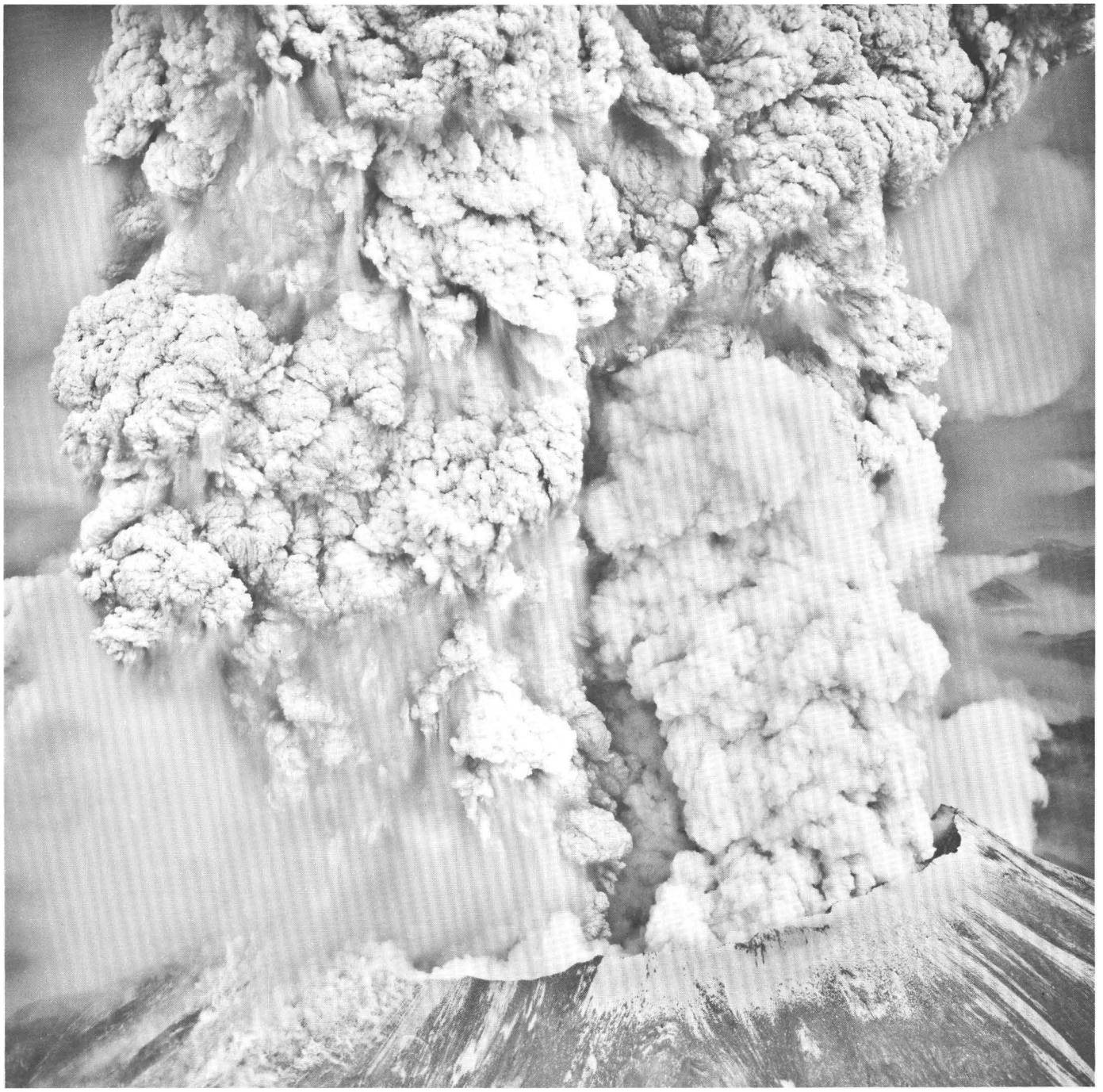

Figure 289.—West side of Mount St. Helens, Wash., showing emplacement of a May 18 pyroclastic flow (on the left) in the Toutle and Talus Glacier area by collapse of a margin of the Plinian column. Photograph by Austin Post.

Figure 288.—Pyroclastic-flow deposits of May 18, 1980, Mount St. Helens, Wash., on the western part of the pumice plain. Several phreatic-explosion pits, 5–25 m across, are visible; base of stairsteps (S) is in background.

small tongue just north of the base of the stairsteps. Small pyroclastic-flow deposits were emplaced at the 1,600- to 1,700-m level of Forsyth Glacier, on the high north-northeastern amphitheater rim (N. G. Banks, oral commun., 1980). A small tongue, as much as 2 m thick and more than 100 m long, occurs east of Forsyth Glacier and south of Windy Pass, about 3.5 km from the vent. The deposits in the tongue are lithologically distinct from the deposits of May 18, on which they rest; they may be the distal part of the deposits that occur on Forsyth Glacier. The pyroclastic flows of May 25 were small: their areal extent was about 1.7 km^2, their thickness rarely exceeds 2 m, and their estimated volume is 0.001 km^3.

ERUPTION OF JUNE 12

The pyroclastic flows of June 12 probably were all vented shortly after 2111 (table 42; fig. 290). The resulting deposits consist of two main tongues, one extending about 7.5 km north to the south edge of Spirit Lake, and another about 7 km to the north-northwest, where it pooled in the bottom of the big phreatic-explosion pit (fig. 291). Areal extent of the deposits of June 12 is about 8.3 km^2. Maximum thickness of the deposits is about 5 m, except where they accumulated to about 8 m in the big phreatic-explosion pit. They are estimated to be 2–3 m thick at the base of the stairsteps, and their total estimated volume is 0.01 km^3.

ERUPTION OF JULY 22

Most pyroclastic-flow deposits of July 22 were emplaced just after 1825, when tongues extended 6.5 km toward Spirit Lake (fig. 292), and just after 1901 when tongues spread nearly 7 km into the southeastern part of the big phreatic-explosion pit

Figure 290.—Pyroclastic-flow deposits of June 12, 1980, Mount St. Helens, Wash., showing a tongue, nearly 1 km long, and its lobes. The deposits overlie an older thin tongue of June 12 deposits. Pyroclastic-flow deposits (light gray) and debris-avalanche deposits (dark gray) of May 18 can be seen at upper left. View looking northwest from southeast side of pumice plain. Photograph taken July 13, 1980.

(table 42; R. P. Hoblitt, written commun., 1980). These pyroclastic flow deposits have an areal extent of about 4.8 km^2, a maximum thickness of about 4 m in the big phreatic-explosion pit and of 2–4 m elsewhere, and an estimated volume of 0.006 km^3.

ERUPTION OF AUGUST 7

Most pyroclastic-flow deposits of August 7 were emplaced just after 1623 (fig. 293), when tongues extended more than 5.5 km from the vent, and just after 2232, when tongues extended more than 4 km to north of the stairsteps (table 42; R. P. Hoblitt, written commun., 1980). Areal extent of the pyroclastic flow deposits of August 7 is about 3.6 km^2, their maximum thickness is about 5 m on the pumice plain, and they have an estimated volume of 0.004 km^3.

ERUPTION OF OCTOBER 16–18

Pyroclastic-flow deposits probably were emplaced just after 2158 on October 16. Fog prevented helicopters from leaving Vancouver in time to witness a morning eruption on October 17, but records made by a remote television camera (Miller and Hoblitt, this volume) showed that pyroclastic flows emplaced shortly after 0928 extended north for 4 km along the west side of the amphitheater floor to north of the base of the stairsteps. Three pyroclastic-flow tongues, each 100–200 m long, also came to rest on the lower western wall of the amphitheater. They moved east, downslope, toward the inner crater, but stopped before they reached it. They were almost entirely covered by air-fall material later the same day. Pyroclastic-flow deposits formed at about 2112 on the

Figure 291.—The big phreatic-explosion pit, from the east, Mount St. Helens, Wash. Pyroclastic-flow deposits of June 12, 1980, have pooled in the base of the pit; tongues of pyroclastic-flow deposits of July 22 have entered east (near) side. Hills of debris-avalanche deposits occur around pit, and part of Coldwater Ridge is in upper right corner. Photograph taken October 6, 1980.

same day have almost exactly the same size and distribution as those of the morning eruption, and they just barely covered the earlier units (fig. 294). An eruption at 1235 on October 18 produced only small pyroclastic-flow tongues that barely moved over the rampart (table 42). Maximum thickness of the deposits of the October 16–18 eruption is about 4 m at the base of the stairsteps and 2 m elsewhere. The total area of the deposits is about 2.3 km^2, and their volume is about 0.001 km^3

PYROCLASTIC-FLOW DEPOSITS

Pyroclastic-flow deposits of the 1980 eruptions consist of variable proportions of ash shards and ash-, lapilli-, and block-sized clasts of pumice and dense lithic material. The maximum temperatures recorded for newly deposited pyroclastic flows range from 300°C in flow units of May 18 to more than 700°C in flow units of October 17 (Banks and Hoblitt, this volume). When initially deposited, the resulting deposits had the consistency of flour in which innumerable pumice balls were floating. They were extremely dusty and treacherous to walk on; a person could sink up to his ankles or deeper unless he stepped on concentrations of pumice. A large rock thrown into an ash-rich part produced small subdued splashes and waves and caused tiny jets of air to escape to the surface. Ash from the youngest pyroclastic-flow deposits of July 22 and October 17 seemed to have less bearing strength than older ones of the same days. Absorbed rainwater and settling compacts the ash, increases surface tension, and

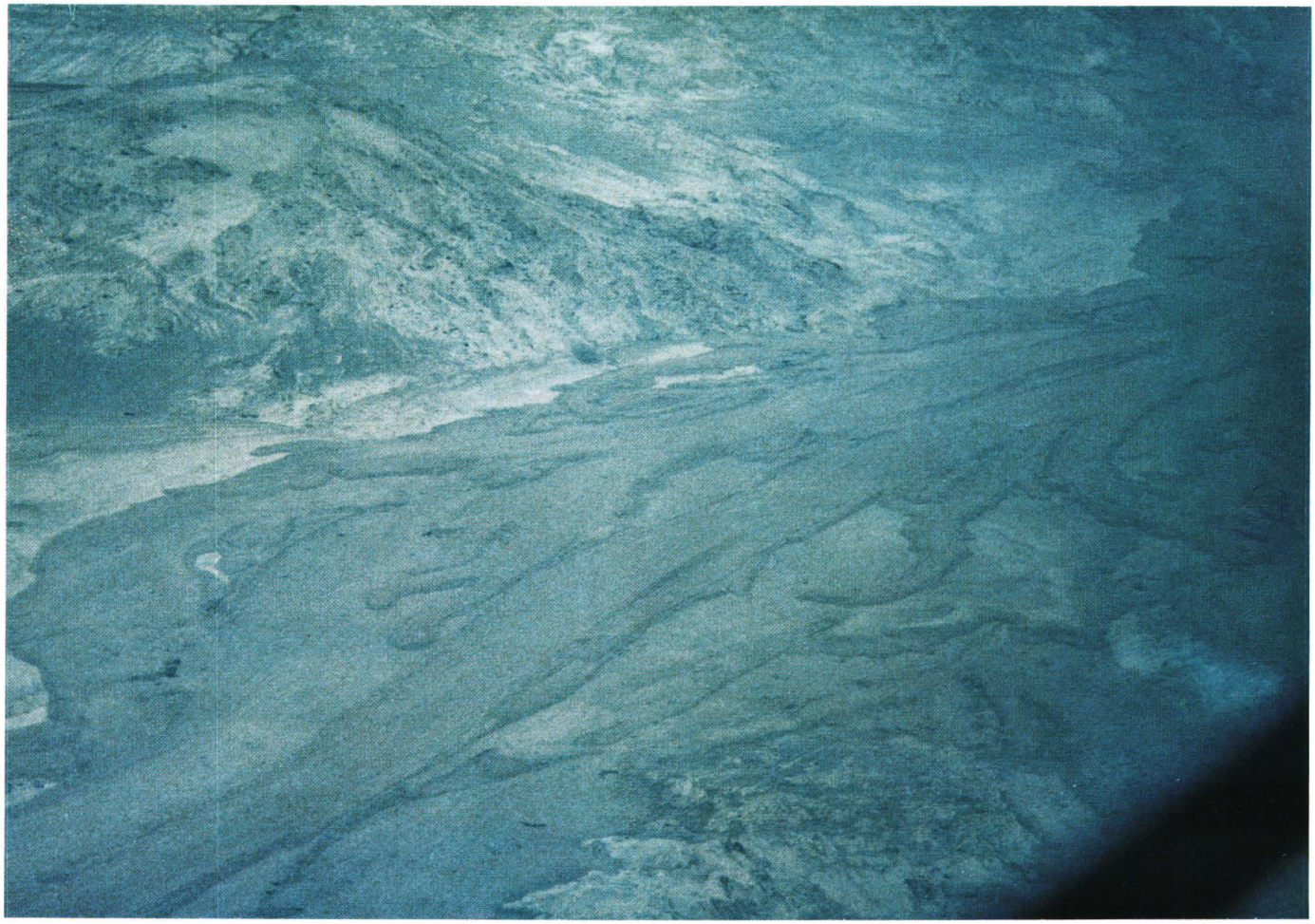

Figure 292.—Tongues of pyroclastic-flow deposits of July 22, 1980, Mount St. Helens, Wash. View of southeast side of pumice plain looking south-southeast. Pyroclastic flows moved from right to left; distance from upper right to lower left is about 1.5 km. Photograph taken August 5, 1980.

hardens the surface. June through August, 1980, however, were dry months in the Mount St. Helens area. In this near absence of rain, the temperature (Banks and Hoblitt, this volume) and fluidity of the top one-half meter of each pyroclastic flow remained high for as long as 2 mo.

SURFACE FEATURES

Deposits of individual pyroclastic flows range from sheetlike masses (fig. 288) to narrow, elongate tongues and lobes (figs. 292, 294, 295). Deposits generally have a distributary depositional pattern, wherein small lobes commonly extend out from larger tongues (fig. 290). The depositional form is controlled by the relative proportion of block-sized pumice, the volume of the pyroclastic flow, and the shape of the underlying surface. Those pyroclastic-flow deposits with abundant pumice blocks apparently had less mobility and velocity; they formed long narrow tongues or lobes that have high, steep margins.

Sheets and tongues generally followed depressions, but momentum carried some upslope. Successive pyroclastic-flow deposits are piled one on another at the south edge of the pumice plain, where a change in slope caused velocity to decrease. Pyroclastic-flow deposits of May 18 formed a fan 500 m wide, 1,500 m long, and 30 m high on the east side of the plain immediately below a sinuous channel on the flank down which the flows traveled. Small lobes radiate away from the fan. Successive pyroclastic flows of May 18 formed similar fans northwest of the base of the stairsteps. Overlapping bulbous lobes of June 12 pyroclastic-flow deposits, each 10–50 m long and having steep fronts about 1 m high, were arranged in steplike fashion at the east side of the big phreatic-explosion pit, indicating that final emplacement there occurred as gushes of material of progressively decreasing volume. Preceding flows of the same eruption produced a flat floor in the bottom of the pit.

Perhaps the most conspicuous pyroclastic-flow tongues were formed during the July 22 eruption (fig. 292). The main tongue on the pumice plain is about 1,800 m long by 100–400 m wide and consists of a series of anastomosing leveed lobes that are 15–75 m wide. Farther west, the main body of the July 22 pyroclastic-flow deposits forms an 800-m-wide sheetlike deposit that has many distributary channelways, some extending as far as the big phreatic-explosion pit (fig. 291).

Pyroclastic-flow sheets and tongues are commonly 1–4 m thick near their margins, but locally are probably thicker than 10 m in their interior parts. The heights of lobes in May 18 deposits are less than 2 m, due largely to their lower block to ash ratio, whereas lobes in younger deposits are as much as 5 m thick. Many pyroclastic-flow lobes of May 18 show a fine, almost lacy appearance in plan view. The lacy appearance is due to swashes of pumice that form long, curved ribs 5–25 cm high.

In cross section, sheetlike deposits are commonly lens-shaped and have tapered margins and distal ends. Tongues and lobes, however, vary in shape depending upon location (fig. 296). Distal ends generally have a convex-upward profile, in which the center is higher than the end or sides. In contrast, lateral profiles of the lobes farther upslope are convex downward, and have marginal levees that stand above the axial part of the lobe. The change in shape of the lobes results largely from drainout of ash and pumice down the axis of the lobe, leaving high levees and producing thick, bulbous distal ends. Pyroclastic-flow deposits with these morphological features are common both in the amphitheater and on the pumice plain.

Marginal levees have heights above the adjacent interior of as much as 1 m in pyroclastic-flow deposits of May 18, and as much as 2 m in deposits of younger eruptions. Levees consist mostly of pumice blocks; ash shards and ash- and lapilli-sized pumice fill in around the clasts but are not visible at the surface. Levees appear to form when coarser material at the edges of tongues or lobes lagged behind and was deposited, whereas fluidized finer grained material and air with entrained coarser lapilli and blocks continued down the axis of the tongue or lobe. The levees remained stationary and continued to build while the interior of the lobe continued moving. Locally, material from lobe interiors overtopped the levees and formed small lobes at a high angle, commonly 90°, to the edge of the main tongue. Levees also are higher than the rest of the lobe because they contain less ash and deflate less after emplacement.

Longitudinal ridges that have a height of as much as 2 m, a width of as much as 5 m, and a length locally exceeding 100 m lie parallel to the direction of flow on the surface of some long narrow tongues; they seem to be due to differential flow rates or pulses within the tongue. Transverse ridges, perpendicular

Figure 293.—Development of pyroclastic flow during 1623 PDT (Pacific Daylight time) eruption on August 7, 1980, viewed from Coldwater Ridge about 8 km north of Mount St. Helens, Wash. Photographs by Peter W. Lipman. A, Initiation of main eruption at about 1626 PDT. Lower-level easterly winds have pushed light-gray fume cloud to west side of amphitheater, and dark-gray ash-rich eruptive fountains, only a few hundred meters high, are visible within crater. B, Development of pyroclastic flow at about 1627 PDT, as dense ash-rich eruptive material spills out to north from amphitheater before vertical Plinian column is well developed. C, Fully developed pyroclastic flow at about 1629 PDT,

to the direction of flow, occur locally at the distal end. These ridges result when gushes with block-rich fronts ramp up behind each other as they come to rest.

Pyroclastic-flow deposits of June 12 locally have formed a bench topography created by postemplacement downslope remobilization, leaving arcuate scarps or embayments. The original depositional surface stands 1–2 m above the surface of the remobilized material. The time at which the material slumped and remobilized is unknown, but it was probably just before the pyroclastic flows came to rest or, at the most, soon after they came to rest; N. G. Banks (oral commun., 1981) noted the scarps about 11 hr after the eruptions. Similar breakaway scarps in May 18 deposits have much gentler slopes (commonly about 15°), and, in places, are much higher (locally more than 10 m). Lobes of remobilized material extend outward from the scarps. Remobilization of these pyroclastic-flow deposits must have occurred within minutes or a few hours after deposition because some scarps are draped with tongues and lobes of pyroclastic-flow deposits formed on the same day.

The amount of deflation (compaction due mainly to release of air and other gas) of pyroclastic-flow deposits after they came to rest is poorly known, but most of it occurred within a day, and probably within hours, of deposition. The distal end of the eastern

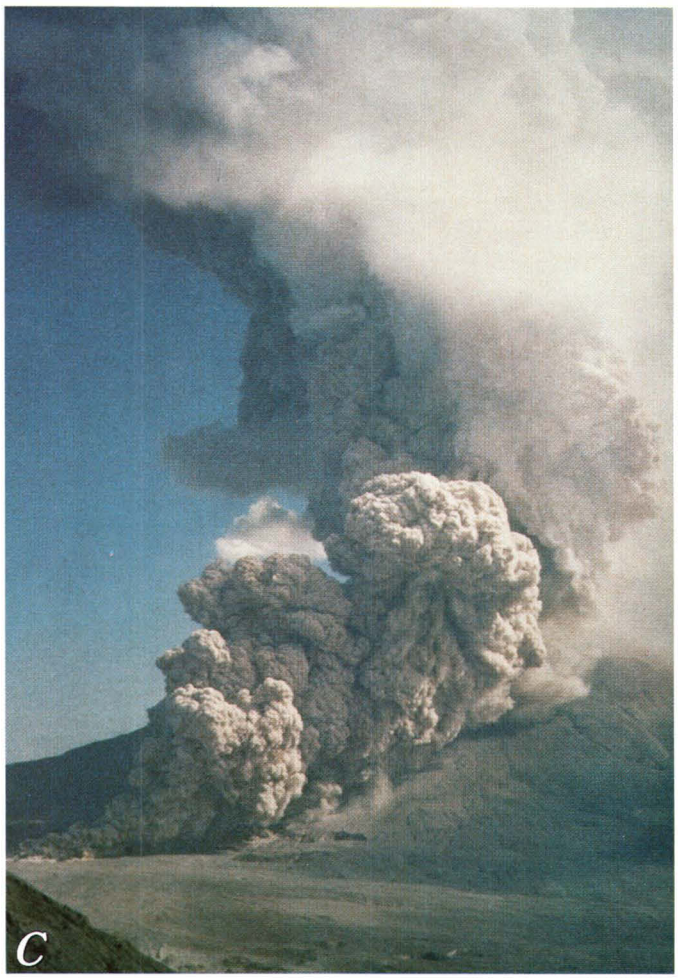

moving across the flank and pumice plain north of the volcano. Flow speeds in excess of 100 km/hr were measured from carefully timed 35-mm still photographs and from 16-mm motion pictures (Hoblitt, 1980). Ash cloud rises above the basal pyroclastic flow; main Plinian column is the higher, more diffuse cloud in background. D, After motion of pyroclastic flow has ceased, at about 1631 PDT, associated ash cloud billows toward viewpoint, and impending fallout from it and the Plinian column necessitated departure of observers.

tongue of the July 22 deposits, estimated to be about 2 m high when visited within one-half hour after it was emplaced, had deflated to about half this thickness a day later (D. A. Swanson, oral commun., 1980). In contrast, steel rods driven on August 8 into pyroclastic-flow lobes of the preceding day showed deflation of 0–5 mm during the next 8 days. The surface of the deposits of June 12 in the big phreatic-explosion pit sagged as much as 1 m (in the center of the pit) by August 1980, according to measurements by N. G. Banks (oral commun., 1981). In most places, deflation does not seem to have been great. Concentrations of pumice blocks would not occur at the surface of flow units if pyroclastic flows were significantly expanded (Wilson and Head, this volume). Furthermore, large, dense lithic blocks did not depress surfaces of lobes on which they lay, nor is there any obvious draping due to differential compaction over large buried blocks.

Welding has been observed only on the rampart, where pink and light-green pyroclastic-flow material, and perhaps some air-fall material, of either June 12 or July 22 welded by high temperatures near the vent (N. G. Banks, oral commun., 1980). Pyroclastic-flow material also may be welded at depth within the inner crater. Banks and Hoblitt (this volume) noted a general progressive increase in maximum temperatures for pyroclastic flows of successively younger

eruptions. Pyroclastic-flow deposits of May 18 apparently were too cool to weld, whereas those of younger eruptions evidently were too thin to weld even though they were hotter. Obvious temperature effects in the pyroclastic-flow deposits are limited to a slight color change upward from gray to pink in some post-May 18 deposits, to poorly developed joints in some units of May 18 and younger eruptions, and to pink oxidation of glass in shards and in pumice. A pink 2- to 5-cm-thick layer formed at the top of June 12 deposits in the big phreatic-explosion pit about 1 day after emplacement, and this layer thickened to 1.5 m by late August 1980 (N. G. Banks, oral commun., 1981). Cooling joints in pyroclastic-flow deposits of many eruptions have been especially prominent on the floor of the amphitheater (D. A. Swanson, oral commun., 1981).

INTERNAL STRUCTURES

During the summer and fall of 1980, vertical exposures through pyroclastic-flow deposits were limited almost exclusively to the walls of phreatic-explosion pits. Such outcrops of May 18 deposits in the northern part of the pumice plain reveal numerous light-tan flow units (fig. 297). The south side of the big phreatic-explosion pit, above the level of the infilling deposits of June 12, is formed of four flow units that dip several degrees to the north and that have thicknesses, from base to top, of 2.3, 2.6, 1.2, and 19.2 m. Laterally, most divide into additional separate flow units. The 19.2-m unit, for example, thickens northward, and most of it is exposed on the northern wall of the pit, where it may be locally separated into five more flow units that have thicknesses

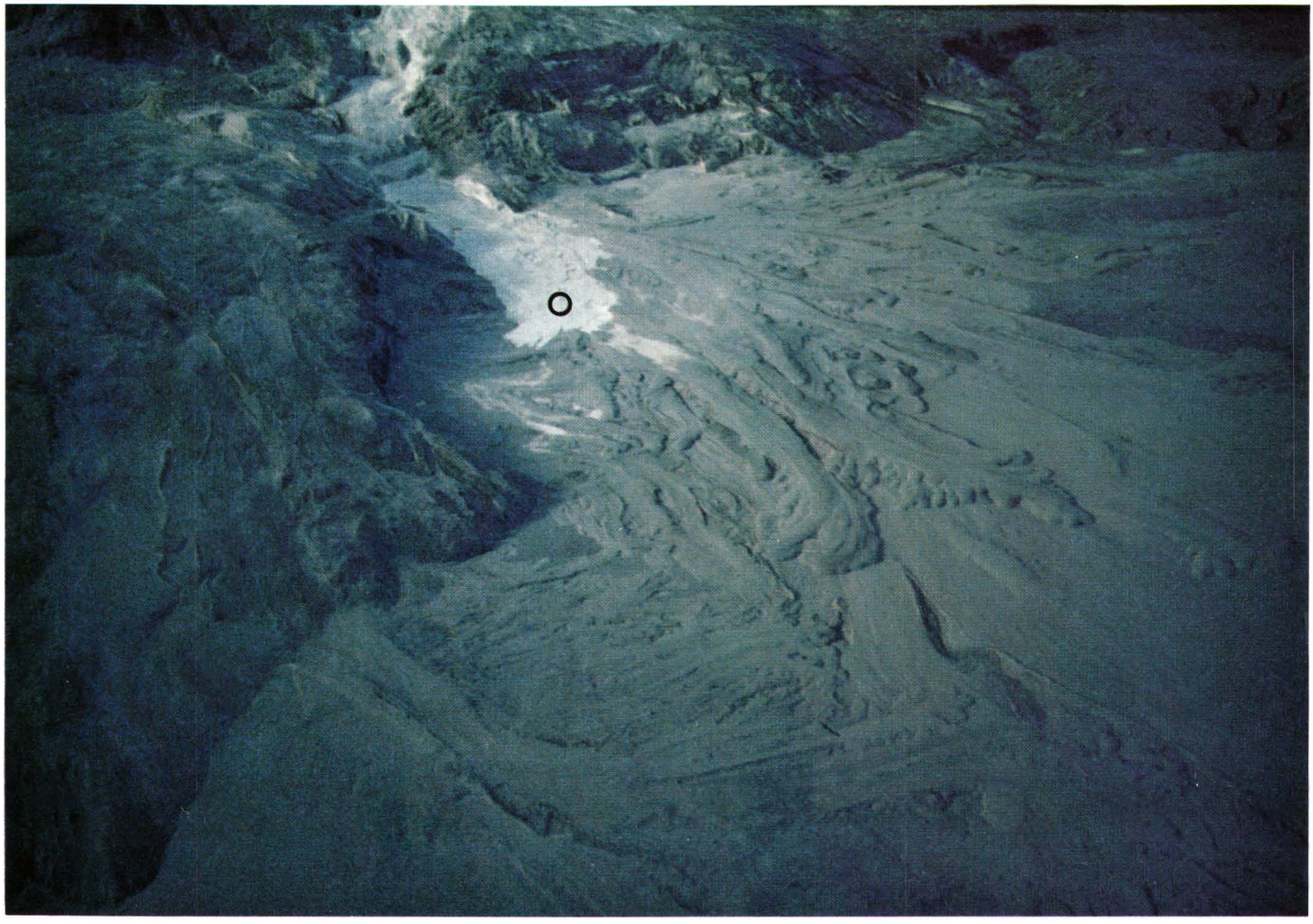

Figure 294.—Distal end of pyroclastic-flow deposits (light gray) of the night of October 17, 1980 (O), just north of base of stairsteps, Mount St. Helens, Wash. Well-developed tongues and lobes beyond (north of) these deposits were emplaced on August 7, as were most of the deposits in foreground. View looking south-southwest, October 18, 1980.

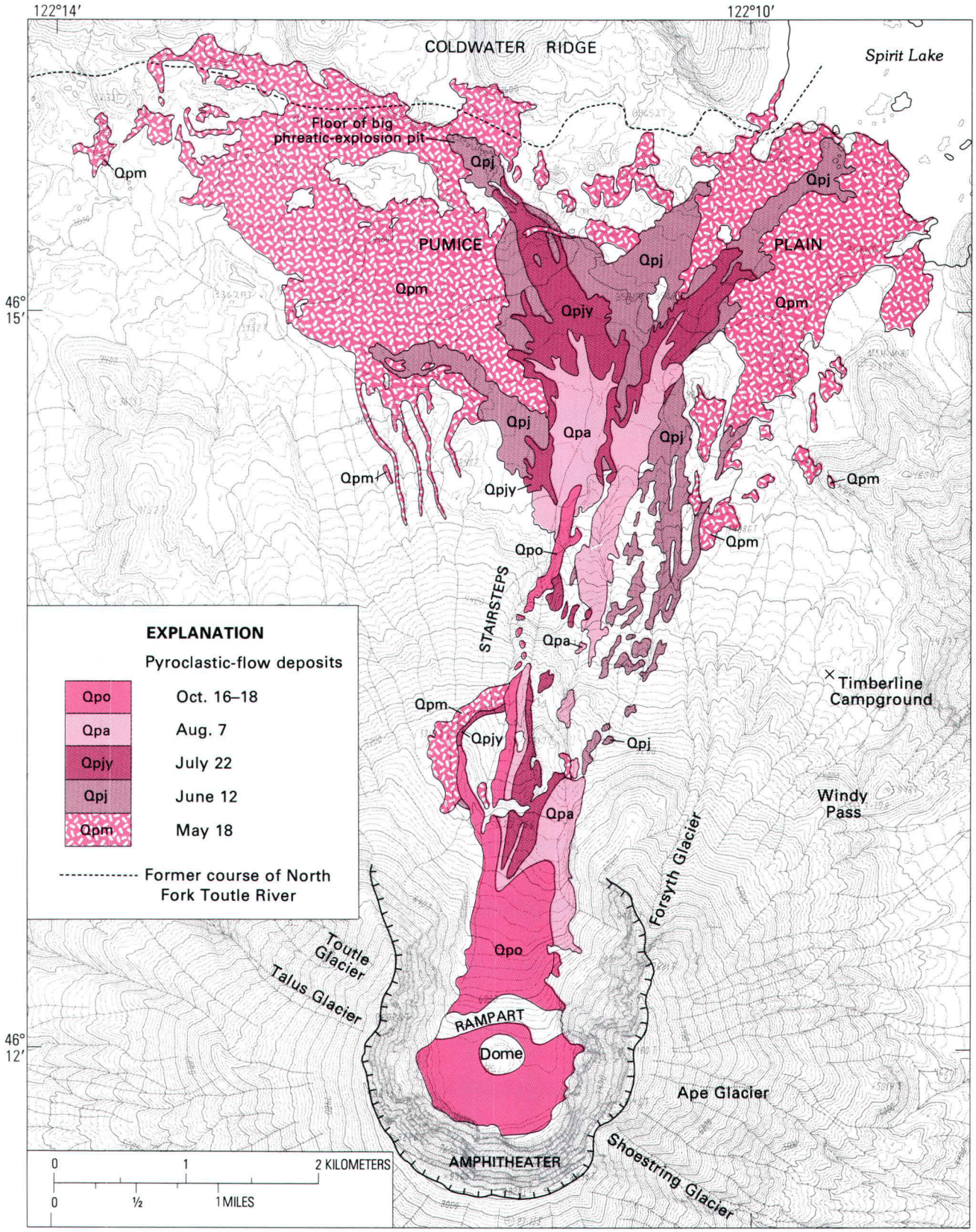

Figure 295.—Geologic map of pyroclastic-flow deposits on northern flank of Mount St. Helens.

Figure 296.—Distal end of a lobe of pyroclastic-flow deposits formed during the night of October 17, 1980, just north of the base of the stairsteps. View to southwest, October 18, 1980.

of 2.7 (base not exposed), 3.8, 2, 3.5, and 16 m. Flow units less than 1 m thick are common in the walls of other pits.

Each flow unit consists of poorly sorted shards, pumice fragments, and lithic fragments that are generally, but not everywhere, normally graded with respect to dense lithic clasts and reversely graded with respect to light pumice clasts (layer 2b of Sparks and others, 1973). Locally, a thin (several centimeters or less) fine-grained ash layer, reversely graded with respect to pumice, occurs at the base of flow units; it corresponds to layer 2a of Sparks and others (1973). Fumarole pipes are visible in some vertical sections. Flow units are more abundant, are thinner, and are better sorted and bedded on the north side of the pumice plain than they are toward the volcano.

LITHOLOGY

Ash-sized juvenile material, light gray to light tan, makes up most of the volume of nearly all pyroclastic-flow deposits. The material consists of shards, pumice, and broken phenocrysts. Fragments of foreign lithic material are a ubiquitous component of the ash-sized fraction.

Lapilli- to block-sized material consists of juvenile pumice and lesser amounts of foreign lithic material.

Figure 297.—Flow units of pyroclastic-flow deposits of May 18, 1980, in northern wall of the big phreatic-explosion pit.

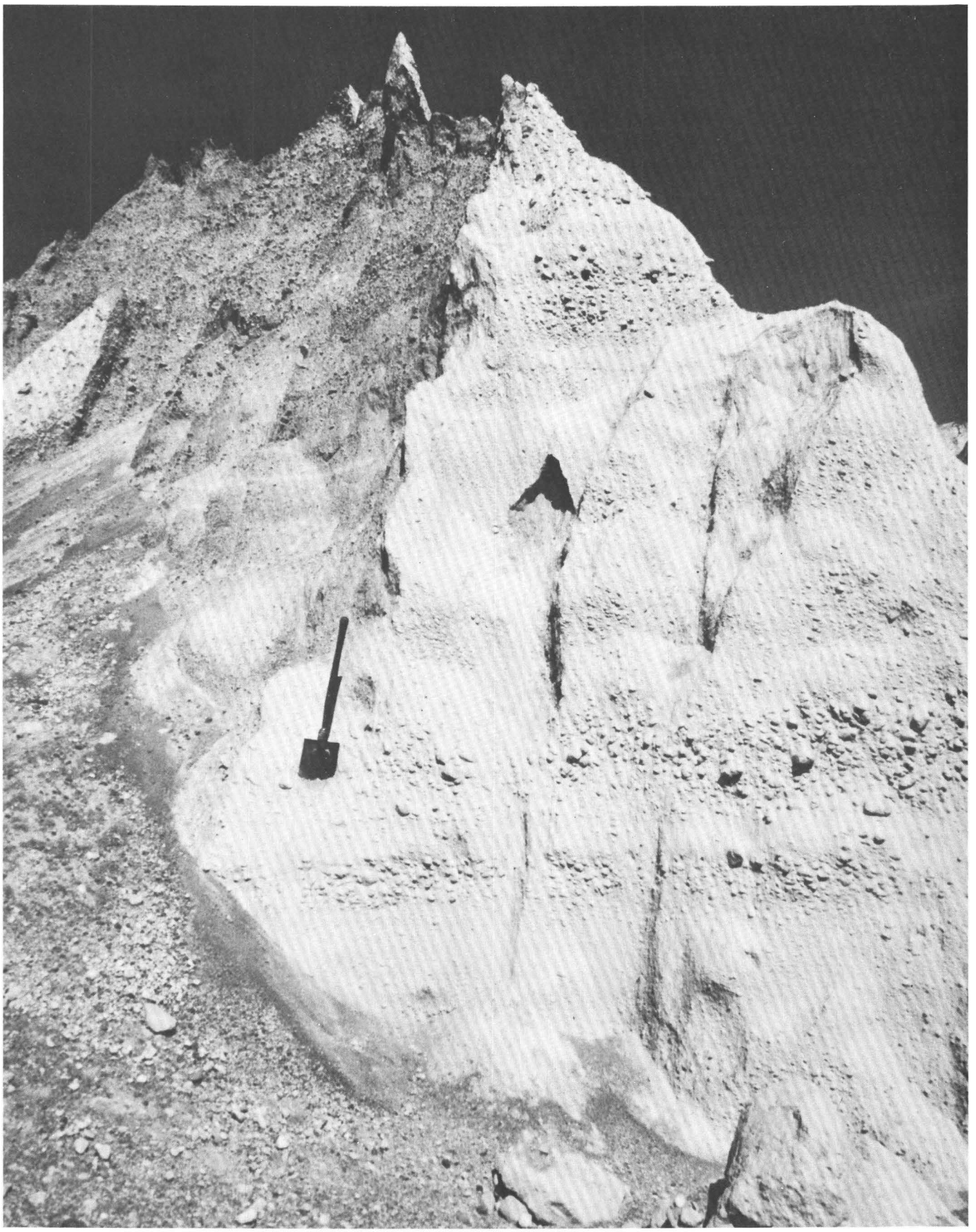

Most lapilli and blocks are subequant; the long axes of the sparse elongated blocks commonly parallel the flow direction. Charred, scorched, and carbonized wood fragments, as long as 0.5 m, occur locally within and on the surface of pyroclastic-flow deposits of May 18 and June 12. Just south of Spirit Lake, largely uncharred wood fragments and logs are abundant between flow units; flow units here were deposited in a fan at the lake edge on top of floating wood or floating wood swashed back on top of newly deposited flow units.

Most lithic clasts in the pyroclastic-flow deposits are from three sources: (1) plucked from the ground surface during erosion of the volcano flanks by the pyroclastic flows, (2) torn from the sides of the vent during eruption, and (3) incorporated from the disrupted dome and vent-filling material. Some lithic clasts, however, are metamorphic rocks, mostly amphibolite, derived from great depth. Lithic clasts are most abundant in pyroclastic-flow deposits of May 18 and June 12. One lithic block deposited at the base of the stairsteps by pyroclastic flows of July 22 was about 5 m in maximum diameter, and others deposited at the southern rim of the big phreatic-explosion pit by pyroclastic flows of June 12 are about 3 m long, but most lithic clasts are less than 0.25 m long.

Pumice lapilli and blocks in pyroclastic-flow deposits are rounded or subrounded; in contrast, pumice in associated air-fall deposits is angular. Most pumice is well vesiculated, and has a density of less than 1; pumice of each younger eruption generally is progressively denser (Kuntz and others, this volume). There does not appear to be a significant change in size of pumice blocks away from the vent. Deposits of the six major pyroclastic-flow eruptions (May 18 to October 16–18) have progressively higher proportions of lapilli and block-sized pumice to ash-sized pumice and shards. Additionally, the youngest pyroclastic flow deposits of each eruption generally have a higher lapilli and block to ash ratio than do deposits emplaced earlier in that eruption. These youngest pyroclastic-flow deposits show more pronounced surface features, but generally do not extend as far from the vent, in part because they were less mobile than were the older, more ash rich pyroclastic flows.

Differences in lithology of pumice clasts are helpful in distinguishing the deposits of the six major pyroclastic-flow eruptions. Pumice of May 18 is highly vesiculated and light tan; the interiors of most large pumice blocks are oxidized pink and orange, and progressively larger blocks have darker shades of color inside. Most pumice clasts of May 18 are less than 10 cm long, but blocks as large as 1 m occur rarely. The largest pumice clasts are generally smaller than the largest lithic clasts in deposits of May 18, whereas the reverse is true in younger pyroclastic-flow deposits. Pumice of May 25 consists of two types—a light-gray to light-tan, highly vesiculated rock and a denser, light- to medium-gray rock that locally contains layers of similar chemical composition (Lipman, Norton, and others, this volume) but of different color and density. Large blocks are much more common than in the deposits of May 18.

Pumice of June 12 ranges from highly vesiculated, tan clasts to moderately vesiculated or dense, light- to medium-gray clasts. Clasts are as long as 1 m but most are less than 0.5 m. The gray pumice commonly contains layers, from several millimeters to 15 cm wide, of different density and of different shades of gray. Contacts between layers are generally sharp, whereas contacts in pumice of May 25 are generally gradational and layers are thicker. Some of the distinctive clasts of June 12 were picked up from the surface and incorporated into younger pyroclastic-flow deposits.

Pumice of July 22 consists of light-tan, pinkish-tan, and light-greenish-gray, highly vesiculated clasts as much as 1 m long. Breadcrust bombs (that is, pumice clasts with breadcrust-like surfaces), as large as 1.5 m long but generally less than 0.25 m long, are common especially in the deposits of the youngest (1901 PDT) eruption. Fragmented crystals of hornblende and plagioclase, as long as 3 cm, are common as inclusions in pumice. These crystals occur in large cavities in the pumice as broken fragments that were pulled apart by gas expansion of the pumiceous matrix. Metamorphic amphibolite inclusions have been similarly stretched and pulled apart; some occur as thin, discontinuous coatings on the interior of elongated gas cavities as long as 0.25 m.

Pumice of August 7 consists of light-gray to tan clasts as much as 1 m long. Breadcrust bombs as long as 1 m are sparse within the deposit, and some may have been picked up from the deposits of July 22. Inclusions include amphibolite as large as 3 cm, and hornblende and plagioclase crystals as large as 1 cm.

Pumice blocks of October 16–18 are off-white and are as much as 1 m long. They resemble those of July 22 and August 7 in being highly vesiculated and in containing sparse expanded phenocrysts and inclu-

sions. Breadcrust bombs were distributed outside the inner crater after several of the eruptions, but were not seen within pyroclastic-flow deposits themselves.

Pumice clasts of all eruptions contain phenocrysts of plagioclase, hornblende, orthopyroxene, iron-titanium oxides, and traces of clinopyroxene. Slightly different ratios of these minerals appear to distinguish each eruption (Kuntz and others, this volume). Chemical analyses of pumices show that they all are dacite and of similar composition, but that they become progressively, though slightly, more mafic with successive eruptions (Lipman, Norton, and others, this volume).

LAG DEPOSITS

Pyroclastic-flow lag deposits consist of a surface pavement of relatively large pumice and lithic blocks and only minor amounts of ash or lapilli. Generally the deposits are only one block thick, and considerable space separates the blocks. The pumice blocks in lag deposits are commonly denser than most pumice of associated flows. Lag deposits are particularly associated with pyroclastic-flow deposits of June 12, perhaps because these deposits contain relatively dense pumice and abundant large lithic blocks.

Lag or laglike deposits occur in several settings:

1. Lag deposits near or on steep slopes on the pumice plain. For instance, June 12 pyroclastic flows that spilled down over the steep southeast end of the big phreatic-explosion pit left an extensive lag deposit on both the steep slope and the gently sloping rim south of it. Blocks in the lag are as long as 3 m. Dense blocks that would normally remain in the flow came to rest because the viscosity and density of the flow decreased as the velocity increased, and the flow inflated as it ramped over the lip.
2. Lag deposits along the margins of pyroclastic-flow deposits. This type of deposit is common at places where the surface near the pyroclastic-flow deposit slopes gently toward the flow, as in a channel. The pyroclastic flow climbed or "swashed" a short distance up the side of the channel during movement and left a lag of blocks on the sloping surface. Lag deposits of this kind were recognized in channels on the volcano flank and on the pumice plain.
3. Laglike deposits at distal ends of pyroclastic-flow deposits, where the main body of the deposit grades downstream into a laglike deposit. A good example occurs at the end of the June 12 pyroclastic-flow deposit that extends to Spirit Lake. The lag is in part due to the greater momentum of larger blocks, which rolled beyond the end of the main body of the flow.
4. Lag deposits in depressions on steep slopes and on hills. Lag deposits in depressions occur on the northern flank of the volcano near the stairsteps, where pyroclastic flows moved at their greatest velocity but left only minor material. Here, deposits range from ash that is relatively depleted in pumice and lithic lapilli and blocks to moderately well sorted pumice and lithic blocks. Likewise, a sparse lag remains on the sides and crests of irregular hills of debris-avalanche deposits, such as just west of Spirit Lake, that were overridden by pyroclastic flows of May 18.
5. Laglike accumulations of huge blocks within pyroclastic-flow deposits. The best examples of this type occur on the south end of the pumice plain just below the stairsteps, in pyroclastic-flow deposits of June 12 and July 22. The flow velocity decreased markedly as the flows reached the gentle slope of the pumice plain. Huge blocks, some of which probably had rolled down the flank, could no longer remained entrained in the pyroclastic flow and came to rest before the finer material that surrounded them.
6. Lag-fall deposits of very coarse material deposited near the vent. Much of the material on the rampart and within the amphitheater south of it represents coarse lag-fall deposits (Wright and Walker, 1977) associated with the pyroclastic flows.

ASH-CLOUD AND SURGE DEPOSITS

Bedded, fine-grained deposits of ash and small, sparse pumice and lithic lapilli occur at the northern part of the pumice plain and are scattered elsewhere around the margins of many pyroclastic flows. Most of these deposits resulted from the ash cloud that rose above the basal ground-hugging pyroclastic flow, but some resulted from ground surge associated with the pyroclastic flow itself. The two types are distinguished by bedding forms, grain-size analyses (Kuntz

and others, this volume), stratigraphic position, and distribution. Only a brief summary of these deposits is given here.

The surfaces of ash-cloud deposits range from planar to those that have dunes. The dunes are irregular in shape, are commonly oriented transverse to the direction of movement of the cloud, and typically are 3–10 m long, 1–4 m wide, and 0.5–1.5 m high. Slopes on stoss sides (15°–25°) are steeper than are opposing slopes on lee sides (2°–10°). Bedding within the dunes commonly parallels the surface, but many beds are discontinuous or show stoss- or lee-side thickening. The most extensive and thickest ash-cloud deposits, associated with the May 18 pyroclastic flows, occur in a broad zone that extends from Spirit Lake westward to beyond the big phreatic-explosion pit and northward to South Coldwater Creek. They rest both on debris-avalanche deposits that ramped up and over a 300-m-high saddle in Coldwater Ridge and on overlying lateral-blast deposits. They are as much as 10 m thick at the base of the ridge and thin generally northward up the ramp to about 25 cm at the saddle on the ridge. Dunes on gently sloping surfaces in this area become smaller in wavelength and amplitude northward up the ramp, and the grain size also decreases. Ash-cloud deposits of probable June 12 age occur in one small area, about 30 m across, against Coldwater Ridge just east of, and one-third the distance up, the debris-avalanche ramp. The May 18 and June 12 deposits formed when the turbulent ash clouds rolled forward until they reached the steep bedrock slope, where their forward motion slowed and where they deposited much of their suspended load. Similar ash deposits occur around the margins of the May 18 pyroclastic-flow deposits, particularly on the lower and middle northeastern flank of the volcano (west of the former site of Timberline Campground).

Dune forms and pinch-and-swell bedding indicate that most of the ash-cloud deposits did not originate by subvertical fallout, but in large part were formed from subhorizontal transport of ash. Erosion of the surface by turbulent winds is indicated by the fact that accretionary lapilli and dacite fragments from the underlying lateral-blast deposits were swept up and incorporated into the deposits. As the deposits formed, they probably had the consistency of flour and had extremely low yield strengths, for where deposited on relatively steep slopes they immediately slumped and flowed. Some ash-cloud dunes on the northern flank of the volcano may be related to surges rather than to pyroclastic flows.

Ash-cloud deposits also form thin coatings of ash on the surfaces and margins of pyroclastic-flow deposits. These coatings are several centimeters thick on and adjacent to June 12 pyroclastic-flow deposits, where they commonly had dune forms (N. G. Banks, oral commun., 1981). These deposits are rapidly eroded and may not be preserved for more than a few weeks.

Pyroclastic surge deposits related to May 18 pyroclastic flows cover a broad area on the northern flank of the volcano that extends northeastward from the edge of the amphitheater (below Sugar Bowl dome, east of the stairsteps). The surface is marked by dunes 0.5–2 m high that generally have steep stoss sides and gently sloping lee sides. Many larger dunes have crescent to V shapes whose convex sides point toward the amphitheater. The surfaces of small surge dunes resemble those of dunes in the ash-cloud deposits, but in cross section most dunes are shown to be antidunes that migrated toward the amphitheater as they grew. The antidunes are similar to those formed around large phreatic-explosion pits (see next section). Surge dunes are well bedded, and individual beds range from well sorted to poorly sorted. Beds on stoss sides vary considerably in thickness and commonly form lens-shaped accumulations, whereas bedding on lee sides is rudely planar and parallels the surface of the dune.

Surge deposits may occur as thin (as thin as 5 cm) aprons that extend a few tens of meters beyond the lateral margins and distal ends of some pyroclastic-flow tongues. They were also observed as beds at the bases of some flow units exposed in phreatic-explosion pits and in breakaway scarps. Most of these beds are thin (10–50 cm), but in some localities are as much as 2 m thick. Internally they are well bedded and show antidune structures similar to those described by Sparks and Walker (1973) and by Sparks (1976).

Surge deposits locally overlie a May 18 pumice-fall deposit; surge deposits likely were deposited at the same time as the pyroclastic flows. Surge deposits may have formed by several mechanisms: (1) by relatively low-concentration, high-velocity density flows (surges); (2) by phreatic activity in the crater; (3) by surges at and beyond the leading edge of pyroclastic flows; and (4) by lofting into the air of pyroclastic flows as they traveled outward from the amphi-

theater and crossed the steep flank of the volcano.

Extremely large dunes, as much as 3–4 m high and 10–30 m long, occur near surge deposits in or adjacent to large channels on relatively steep but irregular slopes east of the stairsteps. Although the dunes are moderately well bedded, individual beds in them are very poorly sorted and resemble pyroclastic-flow deposits. The dunes show nearly planar unconformities on their stoss sides that dip gently toward the amphitheater. These large dunes appear to be the result of deposition by pyroclastic flows that traveled down channels; farther downslope they appear to grade into typical May 18 pyroclastic-flow deposits. The velocity probably was extremely high as a result of the steep slope, and particle concentration was low as a result of turbulence from ramping over steep breaks in slope, so that dunes formed rather than the more massive, laminar-flow-deposited pyroclastic-flow deposits.

PHREATIC-EXPLOSION PITS

Phreatic activity of two types occurred either continuously or sporadically for several weeks or months after deposition of most pyroclastic flows. The first type created fumaroles, which occur in all pyroclastic-flow deposits and which are the most common means of venting air, steam, and other gases from the cooling deposit. They form small (as much as 2 m) circular vents either scattered in an irregular pattern or along straight lines. Less commonly, fumaroles are concentrated in areas as large as several hundred square meters. Some fumaroles were rooted in underlying lateral-blast deposits.

The second and most spectacular type of phreatic activity produced phreatic-explosion pits. These craters occur in pyroclastic-flow deposits and debris-avalanche deposits of May 18 and rarely in pyroclastic-flow deposits of June 12. Most pits are circular in plan, 5–100 m in diameter and 1–20 m deep. The largest is the big phreatic-explosion pit, which is 0.7 km long (east-west) and 0.3 km wide (north-south). It originally was about 38 m deep, but was partly filled by pyroclastic-flow deposits of June 12. Crater walls in debris-avalanche material are steep and craters are shaped like inverted cones. Except for pits near Spirit Lake that contain water, pit walls in pyroclastic material have gentle slopes because the deposits have such low strengths that they continually sloughed, thus enlarging the crater for distances of as much as 50 m and locally forming flat pit floors.

Phreatic-explosion pits started to form on May 18 when hot pyroclastic flows and debris flows covered water in streams, ponds, and springs; the water flashed to steam, and the upward-directed steam explosions reamed holes in the overlying deposits. Some large pits, including the big phreatic-explosion pit, resulted from migrating phreatic vents and from coalescence of multiple pits. All large phreatic-explosion pits are on the north edge of the pumice plain, along the south side of Spirit Lake, and along or near the former North Fork Toutle River west of Spirit Lake. Most of the reaming of the pits occurred within several days after the May 18 and June 12 eruptions. Some that formed in pyroclastic-flow or debris-avalanche deposits on May 18 were partly filled by pyroclastic-flow deposits that date to later in the day. Pits as much as several meters in diameter also formed during the winter of 1980–1981 in deposits of June 12 on the floor of the big phreatic-explosion pit after rainwater pooled there (D. A. Swanson, oral commun., 1981).

The phreatic explosions deposited beds of ejected debris as much as 4 m thick as aprons around the pits. Bedding in these deposits consist of planar and sand-wave forms, including dunes. Dunes, which occur only around some large pits within pyroclastic-flow deposits, are as much as 3 m long, 1.5 m wide, and 1 m high. The dunes, rudely oriented with crests parallel to the edge of the pit, are of progressively smaller amplitude and wavelength with greater distance away from the pit. Trenches dug through many dunes demonstrate that most or all are antidunes; that is, most deposition was on the stoss side. Depositional mechanisms consist of surge for sand-wave and some planar beds, and of air fall for other planar beds. Bomb sags and steep dips on stoss sides of dunes suggest that in many places the beds were wet and cohesive when formed.

EROSION BY PYROCLASTIC FLOWS

The northern flank of Mount St. Helens, for a width of more than 4 km, and the amphitheater floor contain north-trending grooves and channels due in large part to erosion by pyroclastic flows. They are incised in older 1980 pyroclastic flows and in pre-1980 volcanic rocks, which consist largely of moderately

well consolidated breccias and much subordinate lava flows and tuff. Grooves are several meters wide, 0.2–2 m deep, and 20–100 m long. Channels are considerably larger, as much as 50 m wide, 40 m deep, and more than 1 km long. The most spectacular channel, which forms the stairsteps, has been the main path for pyroclastic flows down the flank of the volcano. A second major channel, about 0.5 km to the east, also has a steplike floor and also has been a major path for pyroclastic flows. Both these channels, as well as some smaller channels, largely coincide with stream channels that existed before the eruption of May 18. Pyroclastic flows thus were partly directed down preexisting ravines and enlarged them. Gently sloping surfaces, such as the treads of the stairsteps and much of the amphitheater floor, are covered by pyroclastic-flow deposits. With each major eruption, a new pyroclastic flow flushed out most earlier deposits and left a thin cover of new deposits. Erosion dominated over deposition on the volcano flank, whereas deposition dominated on the pumice plain. The presence of channels and grooves in bedrock and the presence of remnants of pyroclastic-flow deposits of different ages demonstrates that pyroclastic flows of May 18 poured northward over the entire northern flank of the volcano, whereas those of June 12 and July 22 were restricted to an area less than 2 km wide. Those of August 7 were confined to an area about 0.5 km wide, and those of May 25 and October 16–18 were funneled largely down the stairsteps.

Prior to the eruption of August 7, we drove vertical rows of 16-cm-long iron nails flush with the bedrock (breccia) wall in the stairsteps as high as 10 m above the floor. After passage of pyroclastic flows, the upper part of the stairsteps showed erosion of 4 cm or more, irrespective of height above the floor; thus, erosion was not confined to low parts of the stairsteps. All nails from the stations near the base of the stairsteps were removed by the flow and the configuration of the channel differed from that before the eruption. The parts of other channels low on the volcano flank also are deeper and wider with respect to the pre-May 18 stream valleys than those parts higher on the flank. Erosion was greatest where the pyroclastic flows traveled at their greatest speed near the base of the steep flank; there the flows abraded and scoured most parts of the bedrock channel to depths measured in meters. Furthermore, preliminary topographic contours suggest that pyroclastic flows of May 18 may have gouged out the base of the stairsteps more than 35 m below the pre-May 18 surface. During the eruption of October 16–18, the walls of the stairsteps were further modified by local removal of more than several meters of bedrock. For example, a nearly vertical, 10-m-high bedrock (breccia) cliff between the second and third step down from the top of the stairsteps became a gently sloping, 3-m-wide gully.

ERUPTIVE PROCESSES

The eruptive mechanisms of the 1980 pyroclastic flows on the northern flank of Mount St. Helens appear to differ somewhat from those reported for many other historic pyroclastic flows, where collapse of Plinian columns or avalanches of debris from domes or spines has been observed to be the main source. Specifically, most of the Mount St. Helens pyroclastic flows formed when bulbous masses of inflated ash, lapilli, and blocks erupted a few hundred meters or less above the inner crater and then collapsed and spilled over the constraining rampart. Such rapid accumulation took place during or before pulses of maximum upward acceleration (that is, gas thrust) of the Plinian column. After material spilled over the rampart, it moved relatively slowly down the gently sloping floor of the ampitheater, then accelerated (to as much as 100 km/hr; Hoblitt, 1980) as it plunged down the northern flank of the volcano. Dense, cauliflower-shaped ash clouds evolved from and rose hundreds of meters above the ground-hugging pyroclastic flows.

The eruptions of July 22, August 7, and October 17–18 (table 42) were the best observed, and they clearly show this avalanche-type emplacement of pyroclastic flows, commonly preceded by fountains of pyroclastic material erupting from the vent (fig. 293; Hoblitt, 1980). The larger pyroclastic flows of May 18, which more closely resemble preserved prehistoric welded ash-flow tuffs in their volume and grain size, could have had different emplacement mechanisms, but the size of the eruptive clouds and bad weather during the eruption made visual observations difficult. Several pyroclastic flows that were seen on the northern flank, however, suggest the same mechanisms as were documented for the pyroclastic flows of the July 22, August 7, and October 17 eruptions (D. A. Swanson and J. G. Rosenbaum, oral communs., 1980).

Rosenbaum likened one of the few visible eruptions in the afternoon of May 18 to a "pot boiling over." Further evidence that most 1980 pyroclastic flows on the north resulted from upwelling of material is that no erosion of the rampart or inner amphitheater was seen after any major eruption. Such erosion might be expected if column collapse were significant, for then the pyroclastic flows would be expected to have a high velocity within the amphitheater, something not observed so far. R. L. Christiansen (oral commun., 1980), however, concluded that column collapse contributed significantly to, if not produced, a pyroclastic flow that he saw form between about 1630 and 1930 on May 18.

In contrast to the mechanism that led to the pyroclastic flows on the north, the small pyroclastic flows emplaced on the western, southern, and eastern flanks (fig. 289) of Mount St. Helens were formed by Plinian column collapse of the St. Vincent type (Hay, 1959), in which part of the edge of the Plinian column lost upward momentum and gravitationally collapsed onto the outer slope of the volcano (Rooth, 1980). Most of these pyroclastic flows took place on May 18, but at least one occurred on May 25. Deposits on the amphitheater walls near the inner crater from the morning eruption of October 17, and from the 1235 eruption of October 18 were also caused by column collapse.

CHANGES WITH TIME

About 85 percent of the volume of the 1980 pyroclastic-flow deposits was erupted on May 18. Since then, with the exception of the small deposits of May 25, each successive eruption has produced a smaller volume pyroclastic-flow deposit. The eruption of December 27–28 produced only a large dome and small amounts of air-fall ash. The interval between successive eruptions has also increased, with the exception of the relatively short interval between the eruptions of July 22 and August 7. The block and lapilli to ash ratios are generally higher in successively younger deposits, and petrographic and chemical data from pumice (Kuntz and others, this volume; Lipman, Norton, and others, this volume) suggest a subtle trend toward slightly more mafic magma with time. The maximum measured postemplacement temperature also has been greater for successively younger deposits (Banks and Hoblitt, this volume).

These temporal changes suggest that, unless a new body of magma is emplaced under Mount St. Helens, the amount of magma in the chamber that has a composition likely capable of producing pyroclastic flows is being rapidly depleted. If this is true, there likely will continue to be progressively longer intervals between future eruptions, and these eruptions will produce either domes or hotter pyroclastic-flow deposits that contain relatively more lapilli and block pumice and that have increasingly mafic compositions. Geologic history indicates (Crandell and others, 1975, 1979; Crandell and Mullineaux, 1978; Hoblitt and others, 1980) that this trend may terminate by eruption of andesitic lava flows and perhaps also by dacite domes.

REFERENCES CITED

Aramaki, Shigeo, 1957, The 1783 activity of Asama volcano—Part II: Japanese Journal of Geology and Geography, v. 28, no. 1-3, p. 11-33.

_____1961, Classification of pyroclastic flows: International Geology Review, v. 3, p. S18-S24.

Aramaki, Shigeo, and Yamasaki, Masao, 1963, Pyroclastic flows in Japan: Bulletin Volcanologique, v. 26, p. 89-99.

Christiansen, R. L., 1980, Eruption of Mt. St. Helens—Volcanology: Nature, v. 285, no. 5766, p. 531-533.

Crandell, D. R., and Mullineaux, D. R., 1973, Pine Creek volcanic assemblage at Mount St. Helens, Washington: U.S. Geological Survey Bulletin 1383-A, 23 p.

_____1978, Potential hazards from future eruptions of Mount St. Helens volcano, Washington: U.S. Geological Survey Bulletin 1383-C, 26 p.

Crandell, D. R., Mullineaux, D. R., and Rubin, Meyer, 1975, Mount St. Helens volcano—Recent and future behavior: Science, v. 187, no. 4175, p. 438-441

Crandell, D. R., Mullineaux, D. R., and Miller, C. D., 1979, Volcanic hazards studies in the Cascade Range of the western United States, *in* Sheets, P. D., and Grayson, D. K., eds., Volcanic activity and human ecology: New York, Academic Press, p. 195-219.

Fisher, R. V., 1979, Models for pyroclastic surges and pyroclastic flows: Journal of Volcanology and Geothermal Research, v. 6, p. 305-318.

Glicken, H., Janda, R., and Voight, B., 1980, Catastrophic landslide/debris avalanche of May 18, 1980, Mount St. Helens volcano [abs.]: EOS, v. 61, no. 46, p. 1135.

Hay, R. L., 1959, Formation of the crystal-rich glowing avalanche deposits of St. Vincent, B.W.I.: Journal of Geology, v. 67, p. 540-562.

Hoblitt, R. P., 1980, Observations of pyroclastic flows of July 22 and August 7, 1980, Mount St. Helens, Washington [abs.]: EOS, v. 61, no. 46, p. 1137.

Hoblitt, R. P., Crandell, D. R., and Mullineaux, D. R., 1980, Mount St. Helens eruptive behaviour during the past 1,500 yr: Geology, v. 8, no. 11, p. 555–559.

Kieffer, S. W., 1980, The May 18 lateral "blast" at Mt. St. Helens: Preliminary mapping of effects in the devastated area and a model for multiphase fluid flow [abs.]: Geological Society of America Abstracts with Programs, v. 12, no. 7, p. 462.

MacLeod, N. S., Kuntz, M. A., Rowley, P. D., and Hoblitt, R. P., 1980, Pyroclastic flows of the 1980 eruptions of Mount St. Helens, Washington [abs.]: EOS, v. 61, no. 46, p. 1137.

Miller, C. D., and Hoblitt, R. P., 1980, Stratigraphy of deposits produced by the May 18, 1980, lateral blast at Mount St. Helens, Washington [abs.]: EOS, v. 61, no. 46, p. 1135.

Rooth, G. H., 1980, A personal account of a nuée ardente on Mount St. Helens during the eruptions of May 18, 1980: Oregon Geology, v. 42, no. 8, p. 141–144.

Sarna-Wojcicki, A. M., and Waitt, R. B., 1980, Areal distribution, thickness, and composition of volcanic ash erupted from Mount St. Helens on May 18, 1980 [abs.]: Geological Society of America Abstracts with Programs, v. 12, no. 7, p. 515.

Sarna-Wojcicki, A. M., Shipley, Susan, Waitt, R. B., Dzurisin, Daniel, Hays, W. H., Davis, J. O., Wood, S. H., and Bateridge, Thomas, 1980, Areal distribution, thickness, and volume of downwind ash from the May 18, 1980 eruption of Mount St. Helens: U.S. Geological Survey Open-File Report 80–1078, 7 p.

Sheridan, M. F., 1979, Emplacement of pyroclastic flows—A review, *in* Chapin, C. E., and Elston, W. E., eds., Ash-flow tuffs: Geological Society of America Special Paper 180, p. 125–136.

Sisson, T. W., and Moore, J. G., 1980, Deposits and effects of the May 18, 1980 Mount St. Helens pyroclastic surge [abs]: EOS, v. 61, no. 46, p. 1135.

Sparks, R. S. J., 1976, Grain size variations in ignimbrites and implications for the transport of pyroclastic flows: Sedimentology, v. 23, p. 147–188.

Sparks, R. S. J., and Walker, G. P. L., 1973, The ground surge deposit—A third type of pyroclastic rock: Nature, Physical Science, v. 241, p. 62–64.

Sparks, R. S. J., Self, S., and Walker, G. P. L., 1973, Products of ignimbrite eruptions: Geology, v. 1, no. 3, p. 115–118.

U.S. Geological Survey, 1980, Preliminary aerial photographic interpretive map showing features related to the May 18, 1980 eruption of Mount St. Helens, Washington: U.S. Geological Survey Miscellaneous Field Studies Map MF-1254.

Voight, B., Janda, R., Glicken, H., Douglass, P. M., Nolan, M., and Hoblitt, R., 1980, Catastrophic rockslide-avalanche of May 18, 1980, Mount St. Helens volcano, Washington [abs.]: Geological Society of America Abstracts with Programs, v. 12, no. 7, p. 542.

Waitt, R. B., Jr., and Dzurisin, Daniel, 1980, Stratigraphic framework of the 18 May 1980 eruption of Mount St. Helens [abs.]: Geological Society of America Abstracts with Programs, v. 12, no. 7, p. 543.

Wohletz, K. H., and Sheridan, M. F., 1979, A model of pyroclastic surge, *in* Chapin, C. E., and Elston, W. E., eds., Ash-flow tuffs: Geological Society of America Special Paper 180, p. 177–194.

Wright, J. V., and Walker, G. P. L., 1977, The ignimbrite source problem—Significance of a co-ignimbrite lag-fall deposit: Geology, v. 5, p. 729–732.

THE 1980 ERUPTIONS OF MOUNT ST. HELENS, WASHINGTON

MORPHOLOGY AND RHEOLOGY OF PYROCLASTIC FLOWS AND THEIR DEPOSITS, AND GUIDELINES FOR FUTURE OBSERVATIONS

By LIONEL WILSON[1 2] *and* JAMES W. HEAD[1]

ABSTRACT

Morphological and rheological measurements were made on some of the deposits of the pyroclastic flows of July 22 and August 7. Evidence indicates that the flows moved as non-Newtonian fluids most readily modeled as Bingham fluids.

Values are given for yield strengths of the flows: at the time of emplacement, after a few days, and after a few weeks. Average values are about 600, 1,500, and 10,000 N/m^2, respectively. Corresponding estimates of effective viscosities are 4, 1,000, and 1,500 Pa s (pascal seconds), respectively.

Extensive reverse grading of coarse, low-density pumice clasts in the levee deposits was the result of interaction between the flow and the atmosphere, which increased the degree of fluidization of the levees at the time of their emplacement.

An attempt is made to catalog the kinds of observations that should routinely be made on pyroclastic flows, their deposits, and the eruptions which form them.

INTRODUCTION

Pyroclastic flows are potentially the most destructive products of volcanic eruptions, due essentially to their high temperature and great mobility. Historic flows have been observed to move as far as a few kilometers from the vent at speeds as great as 60 m/s (meters per second) (Moore and Melson, 1969; Nairn and Self, 1978), but field measurements on prehistoric flow deposits (Williams, 1942; Koch and McLean, 1975; Yokoyama, 1974; Miller and Smith, 1977; Rose and others, 1979) and theoretical analyses (Sparks and Wilson, 1976; Sparks and others, 1978) suggest that the larger flows have moved as far as 100 km from the vent at average speeds of as much as 200 m/s. The 1980 eruptions at Mount St. Helens produced one substantial pyroclastic-flow sequence on May 18, and a number of smaller ones on June 12, July 22, August 7, and October 16–18 (Rowley and others, this volume). In this report, we use the term "pyroclastic flow" to refer to the moving body of pyroclastic material and the term "pyroclastic-flow deposit" to refer to the topographic feature and the rock body after it comes to rest.

The smaller pyroclastic flows are particularly interesting because some detailed visual and television records of their motion were made (Hoblitt, 1980). The flow deposits are small enough so that representative measurements of flow geometry and grain-size properties can be made with minimal effort. The deposits were emplaced on gently sloping ground, so mapping their topography was relatively easy. In this study, values of flow-deposit thickness, grain size, clast density, and postemplacement rheology are used to constrain the dynamic processes that occurred while the flows were moving. The measurements

[1]Department of Geological Sciences, Brown University, Providence, Rhode Island 02912.

[2]Lunar and Planetary Unit, Department of Environmental Sciences, University of Lancaster, Lancaster, LA1 4YQ, United Kingdom.

were made on August 12 on deposits emplaced on July 22 and August 7.

ACKNOWLEDGMENTS

We thank R. P. Hoblitt, W. I. Rose, and helicopter pilot Michael Montgomery for invaluable assistance in the field. R. W. Nichols loaned the shear vane used for yield-strength measurements. The penetrometer was loaned by the Division of Engineering, Brown University. Norman MacLeod provided aerial photographs used to plan the fieldwork. We acknowledge numerous valuable discussions with R. P. Hoblitt, C. D. Miller, Norman MacLeod, W. I. Rose, and Harry Pinkerton on various aspects of the study. The USGS (U.S. Geological Survey) provided logistic support in the field; other travel and laboratory expenses were supported by the Department of Geological Sciences of Brown University, the Marlar Foundation, and the Planetary Geology Program of the U.S. National Aeronautics and Space Administration.

MORPHOLOGIC AND GRANULOMETRIC STUDIES OF FLOW DEPOSITS

Two flow lobes of the July 22 pyroclastic-flow deposits (fig. 298, *A* and *B*) and one lobe of the August 7 deposits (fig. 298*C*) were examined. These lobes were typical of the July 22 and August 7 deposits in width, length, and thickness, and were studied mainly because they were accessible. The lobes generally had a very well defined and constant width and depth along their lengths (fig. 299). The widths of the lobes studied ranged from about 5 to 20 m, and maximum thicknesses ranged from about 0.5 to 1.5 m; lobe lengths were much more variable, ranging from 80 to 600 m. Identifiable flow lobes formed parts of larger, branching systems.

All of the lobes studied have a well-defined levee-channel structure (fig. 300). The levees consist of slightly raised banks of fairly uniform width along both sides of each lobe and generally have a combined width equal to about 30 percent of the total lobe width. The thickness of material in the central channel was typically about 90 percent of the levee thickness, though on locally steep slopes the central channel fill was sometimes as small as about 50 percent of the levee thickness. This thinner central channel fill commonly became overthickened in the adjacent downslope region where the steepness of the slope decreased, giving the impression of postemplacement drainage or slumping of channel fill on the locally steep slopes.

The bulk of the material forming the flow deposits is rounded, light-toned, fairly vesicular pumice; most of the grains in the mass are 1 mm in diameter or smaller, though clasts as large as several hundred millimeters in length are found at the surface of channel deposits (fig. 300). A detailed grain-size analysis of the channel deposits has not yet been done, but partial excavation of a channel indicated that a wide range of grain sizes is present throughout the vertical profile. The bulk density of a sample of channel material, taken with as little disturbance as possible from a depth of about 200 mm, was found to be 1450 kg/m^3.

The levee deposits, in contrast, show a strong concentration of 30- to 200-mm pumice clasts in an outer surface layer that is commonly 2–4 clast diameters thick (fig. 301). Below this layer, particles less than 1 mm in size form the bulk of the deposit. Bulk densities of a sample of the 30 largest pumice clasts taken from an area of about 0.2 mm^2 at the top of a levee range from 550 to 1,050 kg/m^3, and have a mean of 880 kg/m^3. There is no significant correlation between bulk density and size.

A volumetrically small (perhaps 1 percent), but morphologically striking, component of both levee and channel deposits consists of pumice clasts, commonly larger than 100 m, which have an angular, fractured, breadcrust-textured outer skin (fig. 302). The skin is less vesicular than the interior; the relative surface areas of skin plates and bounding fractures indicate a volume expansion of the interior of about 15 percent after skin formation.

RHEOLOGICAL MEASUREMENTS MADE ON PYROCLASTIC-FLOW DEPOSITS

For several weeks after their emplacement, the central channels of the pyroclastic-flow deposits showed striking deformation when attempts were made to walk on them. Pressure of about half or more of the weight of an adult on one foot (that is, 10,000 N/m^2) caused the ash to deform easily with a low viscosity. In contrast, a lower pressure of about 1,000–2,000 N/m^2

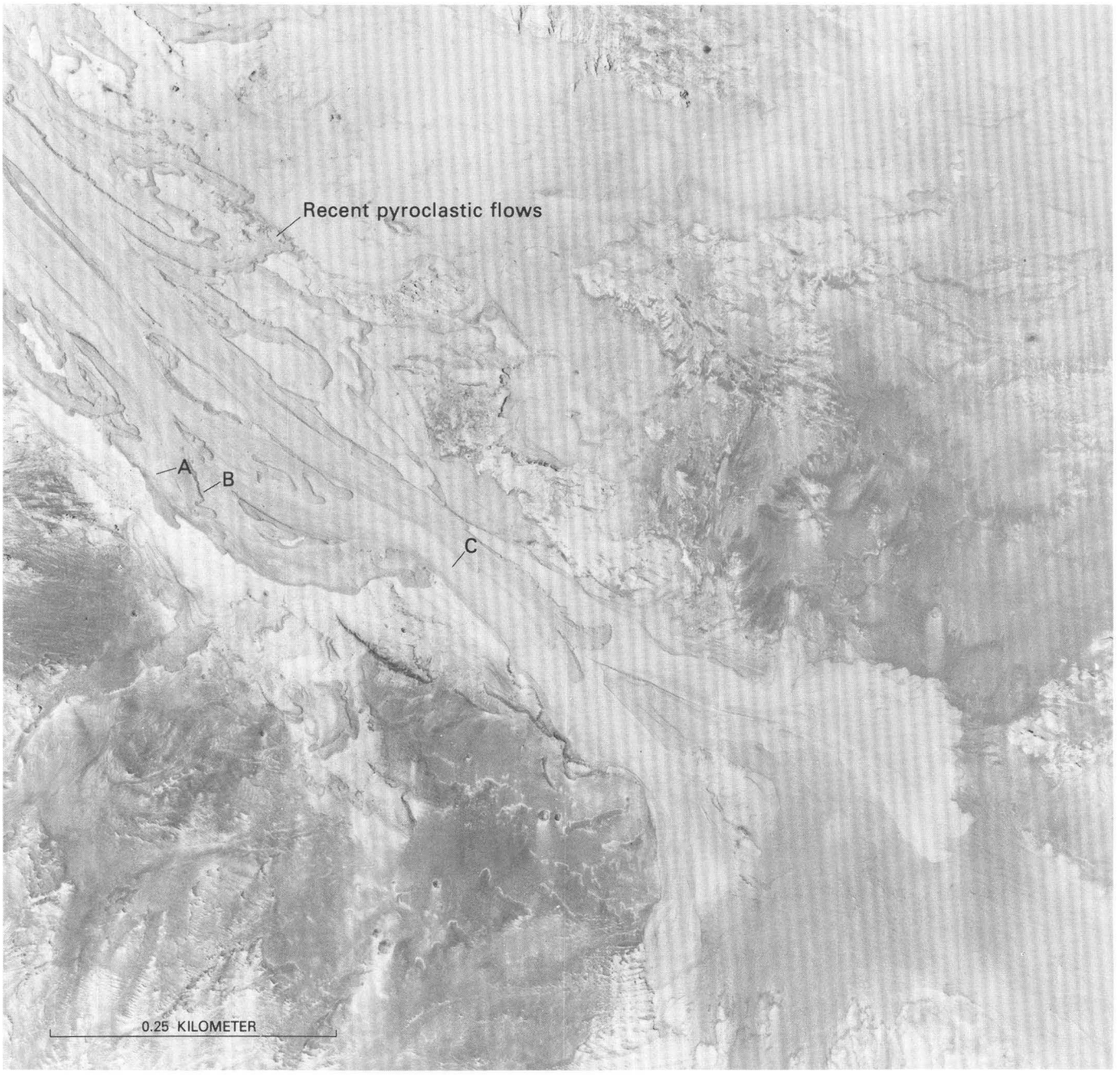

Figure 298.—Recent Mount St. Helens and C where pyroclastic flows, flow lobes examined, and stations A, B, measurements were made. Photograph taken July 31, 1980.

could be supported, and caused the ash to release gas (sometimes in small jets) for a few seconds over an area several times larger than that of the applied load. By the end of these few seconds, the deposit had become much stronger within the degassed area, and easily supported the weight of an adult on one foot (about 20,000 N/m^2). This characteristic of the flow deposits indicates that they were acting as plastic materials having time-dependent rheological properties. The most important of these properties is the yield strength, a measure of the stress that must be applied to initiate deformation. (A fuller discussion of these rheological properties is given in the next section of this report.) An estimate of the yield strength can be gained from the above bearing strengths (10,000 and 1,000–2,000 N/m^2). A plastic having a yield strength

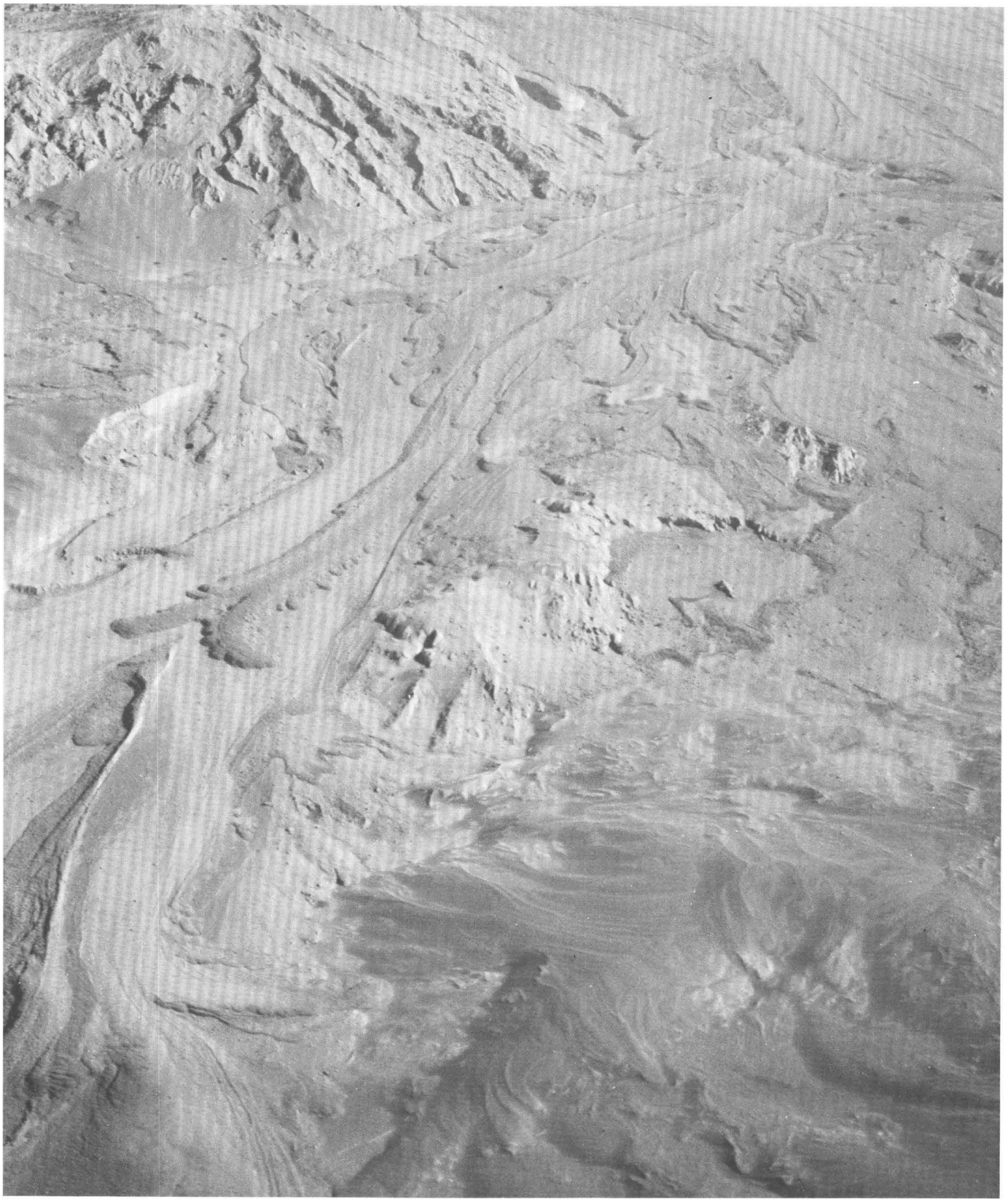

Figure 299.—Oblique view of lobes of pyroclastic-flow deposits of July 22 and August 7 eruptions showing generally constant width and thickness of deposits. Same area as shown in figure 298.

Figure 300.—Perspective view of a single lobe of deposits from July 22 eruption showing slightly raised levees and central channel. Persons are standing at edge of channel just inside levees. Dashed line marks approximate crest of levees. Lobe turns to right just behind persons. Photograph taken at station B (fig. 298).

S_y will support a surface load of as much as $(2+\pi)S_y$, that is, about $5S_y$ (Johnson, 1970). Applying this expression to each of the above stresses shows that the yield strengths of the channel deposits were between about 300 and 2,000 N/m².

The above observations were supplemented by measurements with a shear vane and a penetrometer. The shear vane consisted of a pair of thin metal blades, each having an area of about 500 mm², mounted symmetrically at right angles to one another, at one end of a rod about 0.5 m long. At the other end of the rod was a calibrated dial gauge giving shear strength readings directly in the range of 300 to 30,000 N/m². The vanes and rod were inserted into the flow deposit to a chosen depth, and the gauge was rotated until the rod began to turn. A slipping clutch mechanism preserved the dial gauge reading at the moment that the deposit failed in shear. The shear strength so recorded was numerically equal to the yield strength of the material (see the section on "Theoretical rheological considerations"). The values observed, ranging from 400 to 18,000 N/m², are shown in table 43.

The penetrometer consisted of a cylindrical barrel containing a spring. Rods of known cross-sectional area and various lengths could be screwed into the lower end of the barrel. A handle on the end of a shaft fitted through a hole in the upper end of the barrel could be used to apply force to the spring. The force was measured by the amount of compression of the spring and was read on a scale, calibrated from 10 to 300 N, on the shaft. The instrument was used in two modes, to measure the compressive strength of the pyroclastic-flow deposits, or to measure their effective viscosity. To measure compressive strength, a steadily increasing force was applied vertically to the deposit through a rod of suitable cross-sectional area (found by trial and error) until the ash surface failed

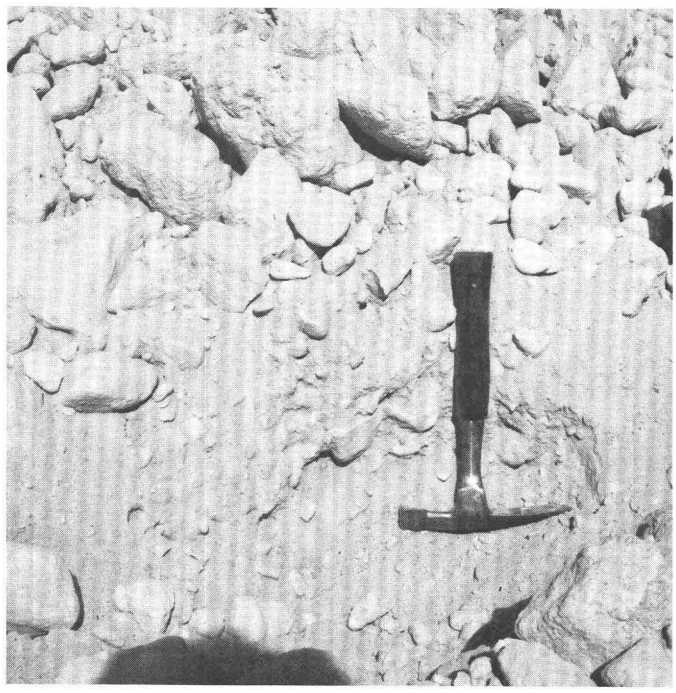

Figure 301.—Concentration of large pumice clasts in the uppermost part of a levee. Hammer head is 160 mm long. Photograph taken at station B (fig. 298).

Table 43.—Rheological observations on certain pyroclastic flows on Mount St. Helens

[Leaders (---), no measurement made]

Station	Location[1]	Compressive strength of degassed, compacted matrix (N/m^2)	Yield strength of uncompacted matrix (N/m^2)	Apparent viscosity, η (Pa s)
A	Interior of levee beneath top layer of coarse pumice.	200,000-500,000	---	---
A	Center of channel in excavated hole 0.2 m deep.	---	6,000-15,000	---
A	Center of channel on fresh surface.	---	2,000-18,000	1,200 before compaction, 13,000 after compaction.
B	10 m from flow front---	---	4,000	---
B	2.5 m from front-------	---	6,000-7,000	---
C	Levee------------------	$2x10^6$	9,000-16,000	---
C	Channel----------------	---	800-4,800	2,000
D	Channel, 3 m from levee edge.	---	2,000-5,000	---
D	Channel, 6 m from levee edge.	---	2,000	---
D	Channel, 9 m from levee edge.	---	900	30-2,000
E	Channel----------------	100,000-200,000	400-1,500	600-2,000
F	Channel----------------	200,000-250,000	600-3,200	700-2,000

[1]Locations of stations A, B, and C are shown on figure 298. Stations D and E are on upper parts of the July 22 flows. Station F is on flow probably formed August 7.

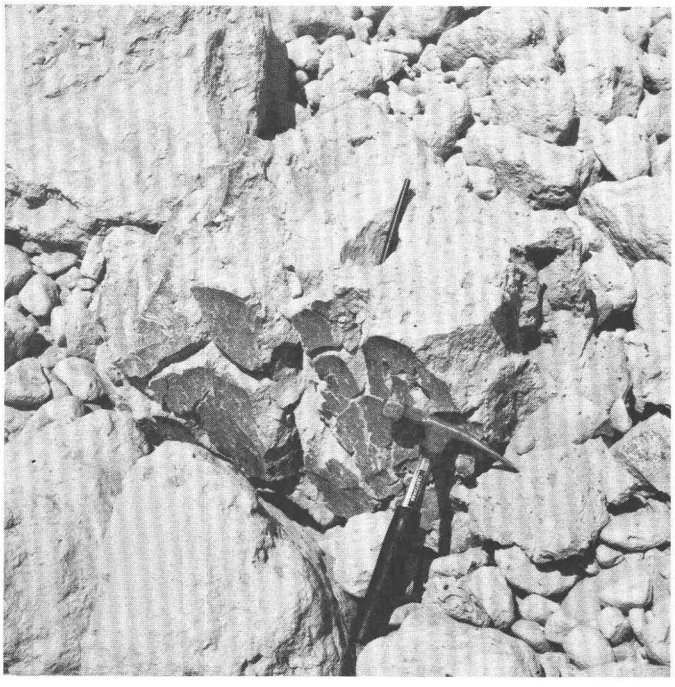

Figure 302.—Pumice clast showing breadcrust texture of surface layer. Pen lies within a large vesiclelike structure, and additional similar features are just above hammer head. Hammer head is 160 mm long.

and penetration began. The applied force per unit area of the end of the rod was a measure of the compressive strength (table 43). The values, ranging from 100,000 to 250,000 N/m^2 for the channels, are greater than those deduced from the experiments involving walking on the flows, because the method used, the application of a steadily increasing force to the penetrometer, tended to maximize the amount of degassing of the flow.

To measure the effective viscosity of the flow deposits, a sudden and, as nearly as possible, constant force, F, was applied to the penetrometer through a rod of small enough radius, r, that the compressive strength was exceeded. The rate of penetration of the rod, u, was estimated by eye, and the apparent viscosity of the deposit, η (table 43), was obtained from

$$\eta = \frac{F}{6\pi r u}.$$

The values found are in the range of 30 to 13,000 Pa s. The above formula is not the one most often used to calculate viscosities in penetrometer experiments

(Lamb, 1932; Kelley and others, 1964). Commonly, the penetrometer rod is inserted gently into the deposit, prior to the application of the force, to a depth, L, greater than about $15r$, and the viscosity value is obtained from a formula such as

$$\eta = \frac{F(\log_e [L/r] - 0.72)}{2\pi(L + L_e)u}$$

where L_e is an empirical correction obtained by calibration (Pinkerton, 1978). Useful results for the pyroclastic-flow deposits were difficult to obtain in this way because, once the compressive strength was exceeded, the rate of penetration of the rod was so great that a meaningful average value of L could not be assigned. The viscosities obtained are probably no more accurate than a factor of two, based on repeated measurements made within a small area.

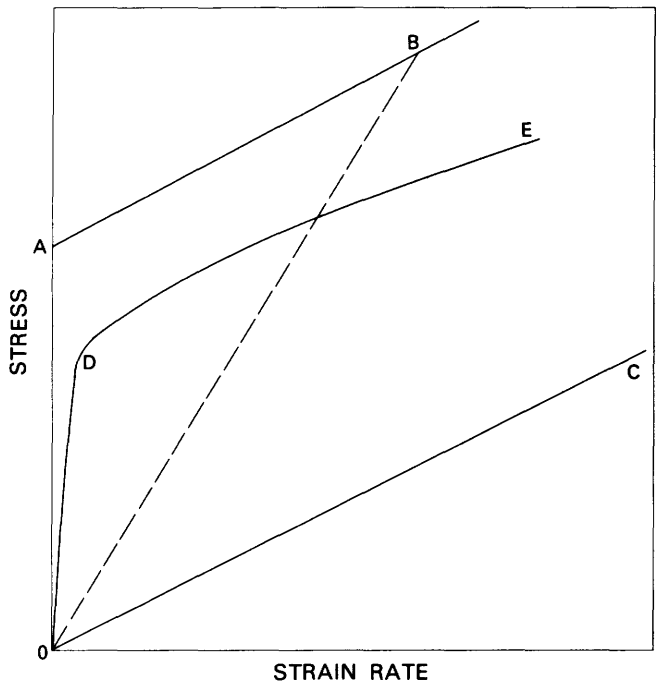

Figure 303.—Relationship of stress to strain rate for various materials. OC, simple Newtonian fluid; OAB, ideal Bingham fluid; ODE, real Bingham fluid. Slope of line OB would give apparent viscosity of ideal Bingham fluid.

THEORETICAL RHEOLOGICAL CONSIDERATIONS

The simplest general rheological response curve of a fluid is that of a Bingham fluid, line OAB in figure 303. For such a material, a finite stress (OA) must be applied to cause any deformation; the corresponding strength being overcome is called the yield strength, S_y. Once the fluid deforms (that is, flows), it responds linearly, and the slope of the line AB is its plastic viscosity. A fluid having $S_y = 0$ is called a Newtonian fluid (OC, fig. 303). Most real fluids have rather more complex curves like ODE, which approximate the Bingham fluid curve. Basaltic lava flows give curves of this type (Pinkerton and Sparks, 1978), because of the interactions between the completely liquid matrix and the included phenocrysts and bubbles.

The rheological properties of pyroclastic flows are expected to be more complex. The fluid matrix of the flow consists of fine ash and gas. The gas is probably magmatic gas exsolving while the flow is in motion, and is a mixture of magmatic gas and entrained air after the flow has come to rest. The fine ash and gas stay locked together as a compound fluid as long as the ash particles are small enough that their terminal fall velocity through the gas is much less than the overall velocity of the gas relative to the ground surface. The large pumice clasts have the same effect on pyroclastic flows as the phenocrysts have on lava flows. The boundary size of clasts that should be regarded as part of the fluid matrix and clasts that should be regarded as inclusions is not a constant, even for a fixed distribution of grain sizes; it depends also on the bulk density of the gas-clast mixture and, more importantly, on the rate at which stresses are applied.

An important distinction between Newtonian and non-Newtonian fluids is emphasized by their motion when flowing. On an inclined plane, Newtonian fluids spread indefinitely both laterally and downslope; on a flat surface, they spread out and become thinner until limited by surface-tension forces. Fluids having a finite yield strength, however, spread only to a well-defined limiting width and depth on a given slope and, also, do not spread indefinitely on a flat plane.

The field measurements made on the flow deposits described earlier, which indicated finite yield

strengths and relatively low effective viscosities, together with the morphological measurements of finite widths and thicknesses of the pyroclastic-flow deposits, are clearly consistent with the idea that the deposits acted as non-Newtonian fluids at the time they were emplaced, and also at the time they were examined, as much as 20 days later.

PROPERTIES OF THE PYROCLASTIC FLOWS IN MOTION

The yield strength of the material at the base of a levee determines the vertical thickness of the levee at the moment of emplacement; if the thickness is T, the bulk density of the flow material is ρ, the acceleration due to gravity is g, and the levee forms on a slope δ, then the yield strength, S_y, is (Johnson, 1970):

$$S_y = T\rho g \sin \delta.$$

We measured $\delta = 3$ and T in the range of 0.5 to 1.5 m for several of the July 22 flow lobes, and the deposit bulk density of $\rho = 1{,}450$ kg/m^3 was measured for one of these lobes. We show later in the report that the bulk density of the flow in motion cannot have been much less than this. Thus, S_y must equal 400–1,100 N/m^2. This range of values should be compared with the values in table 43, which range from 400 to 18,000 N/m^2 for the central-channel deposits when examined. The implication is that, at the time they were examined, the more fluid of the fresh flow deposits had shear strengths very similar to those of the flows at the moment of levee emplacement.

We noted above that the densities of the larger pumice blocks collected from the top of a levee range from 550 to 1,050 kg/m^3, and have a mean of 880 kg/m^3. The only two detailed mechanisms which have been proposed to explain the upward migration of coarse clasts (Johnson, 1970) are grain dispersive forces (that is, collisions) as described by Bagnold (1968), or flotation in the fluidized matrix as a result of the density contrast between the clasts and the matrix. The relative importance of these two processes could be checked by measuring the sizes and densities of any large clasts still present in the fine-grained matrix in the region below the coarse surface layer. If most of these large clasts are more dense than those in the surface layer, and especially if there is a normally graded basal layer of dense, large clasts, then flotation must have been the dominant means of upward migration. If, however, collisions produced the upward migration, the surface layer should contain all large clasts, irrespective of density. No large, high-density clasts were observed on the tops of the levees examined, but the high temperatures of the deposits prevented us from examining the bases of levees for such clasts. However, normal grading of dense clasts was observed in the deposits of the May 18 pyroclastic flow (Kuntz and others, this volume). These facts make it very probable that flotation of pumice is the dominant process in the formation of levees. The observation that all of the coarse pumice densities are less than 1,100 kg/m^3, which is, in turn, less than the bulk density of the matrix (1,450 kg/m^3 in its postemplacement state), indicates that the matrix was only slightly expanded from its postemplacement state at the time of levee emplacement. If the matrix were expanded by a factor of as little as 2, the coarse pumice clasts would not float in it.

Some detailed ideas on the extent of clast motion within the moving flows can be gained by calculating the terminal fall (or rise) velocity, U_T, of large pumice clasts in the gas-fines matrix. (Sparks and others, 1978, gave some examples for thick, low-density pyroclastic flows.) U_T can be found from (Lionel Wilson, T. C. Huang, and G. P. L. Walker, unpub. data):

$$U_T = 0.5\left\{\sqrt{\left(\frac{34.45\eta}{D\alpha}\right)^2 + \frac{3.372\Delta\sigma\, g\, D}{\alpha}} - \frac{34.45}{D\alpha}\right\},$$

where η is the fluid viscosity, α the fluid density, D the maximum diameter of the clast, g the acceleration due to gravity, and $\Delta\sigma$ the difference between the densities of the clast and fluid. $\Delta\sigma$ is always treated as positive, but if the clast is lighter than the fluid, U_T is a terminal rise velocity, not a fall velocity. The numerical constants are mean values derived from many measurements on pumice clast shapes.

Consider first the conditions we have deduced for the flotation of coarse pumice clasts in levees, for example, a matrix density, α, of 1,100 kg/m^3, and a clast density of 900 kg/m^3, so that $\Delta\sigma = 200$ kg/m^3. The effective viscosity, η, of the gas-fines mixture will be larger than that of the gas alone, η_o, which is equal to about 3×10^{-5} Pa s at temperatures of about 1,000K. The Einstein correction formula (Landau and Lifshitz, 1959) is

$$\eta = \eta_o (1 + \tfrac{5}{2}\phi),$$

where ϕ is the volume of silicate fines divided by the total volume of the gas-fines mixture, approximately 0.5 in this example. The formula does not apply strictly as ϕ approaches unity, but, nonetheless, an increase in viscosity by a factor of 2 is clearly likely. Table 44 gives the U_T values, which range from 0.1 to 0.7 m/s for pumice clasts of 10 to 300 mm diameter. Thus, in an unexpanded flow as thick as the final deposits, the sorting of most of the coarse clasts into a layer on top of the levees would take as long as 1–2 s (actually somewhat longer because the clasts do not reach terminal velocity instantaneously). Examination of the interiors of the levees (fig. 301) shows that coarse-clast separation is well advanced but not complete, and so we infer that whatever the process that resulted in the slight expansion of the levees and the pumice flotation, it was in operation for no longer than a few seconds.

In the above formula for terminal rise velocities of pumice clasts, motion is assumed to take place in a Newtonian fluid. However, the finite levee and channel thicknesses indicate that the materials forming them had yield strengths ranging from 400 to 1,100 N/m² at the moment of deposition. A yield strength can prevent pumice flotation under certain circumstances. Johnson (1970) found that a pumice clast will not rise at all unless its density contrast with the surrounding matrix exceeds a threshold value corresponding to the condition

$$\Delta\sigma > \frac{8S_y}{gD}.$$

If we adopt a conservative value of $S_y = 500$ N/m², $\Delta\sigma$ must then exceed 400 kg/m³ to float a meter-size pumice fragment, a condition that is easily satisfied by the matrix and pumice densities measured, but $\Delta\sigma$ must exceed 4,000 kg/m³ to float a 10-cm diameter pumice fragment, a condition that is quite impossible. Yet pumice fragments of this size are strongly reversely graded in the levee deposits and, in contrast, are almost ungraded in the central channel deposits.

The above facts strongly suggest that the process that modified the levees for a few seconds to permit pumice flotation did not affect the central channels and involved a marked reduction in levee yield strength. The only model that we have yet devised to fit these circumstances is one in which the levees are considered to be the products of a strong, transient interaction between the main body of the moving pyroclastic flow and the surrounding air. The interaction would most probably take place at the front of the flow. We envision the flow front overrunning and trapping air, which is heated and passes up through the body of the flow while it expands. In moving through the flow, the air fluidizes the solids; that is, it supports the weight of the solids for a short time. Clast-to-clast contact is greatly reduced, and the yield strength of the flow decreases by several orders of magnitude, allowing pumice and lithic-fragment grading to begin. The fluidized body has essentially no strength and is easily penetrated by the advancing main body of the flow. As the fluidized mass is pushed to either side, the air completes its escape, taking with it a significant fraction of the finer grain sizes to form a billowing cloud over the main flow; fluidization and clast grading cease, and the remaining mass forms the levees.

Table 44.—Sorting velocities of pumice fragments in pyroclastic flows on Mount St. Helens

[Values are given for terminal rise velocities of pumice fragments having a density of 900 kg/m³ in a matrix, bulk density of 1,100 kg/m³, and effective viscosity 6×10^{-5} Pa s]

Maximum pumice diameter (m)	Terminal rise velocity in gas-fines matrix (m/s)
0.3	0.70
.1	.41
.03	.22
.01	.13

The relationships between the levee width, central-channel width, levee thickness, and degree of grading would, therefore, be functions of the two main time scales of the interactions involved: the time scale for overrunning air at the front of the flow (dependent, among other things, on the pyroclastic-flow velocity) and the time scale for heating and loss of the air (dependent on the grain-size distribution and thickness of the central-channel material). Further examination of the products of pyroclastic flows having wide ranges of velocity and thickness will be needed to permit the development of a detailed model.

If, as the lack of strong pumice grading suggests, the central channels were never strongly fluidized (by air or exsolved magmatic gas), most of the channel fill

must have moved, without internal shear, as a rigid body; shear took place only in a basal zone and at the edges next to the levees. Verification of this concept of rigid-body flow would require the measurement of the size and density of the largest clasts observed to be supported at the channel surface. Johnson (1970) gave a formula from which a minimum value of the yield strength can be approximated:

$$S_y = \frac{dg}{8}(\rho_b - q\rho),$$

where d is the total vertical height of an ellipsoidal block of density ρ_b resting in a flow deposit of density ρ, and q is the fraction of d by which the block is submerged in the flow. We were not able to remove any large blocks of this sort that we observed or to obtain samples for density measurements, but this could be done at any future time. As an order-of-magnitude estimate, we recorded the presence of blocks with $d \cong 0.8$ m and $q \cong 0.5$. We noted previously in this section that $\rho \cong 1{,}450$ kg/m^3, and we found large pumice blocks on levees having $\rho_b \cong 900$ kg/m^3; these values indicate that $S_y \cong 200$ N/m^3 is a lower limit. Although we may have underestimated q and ρ_b, this value is not too much smaller than the values of 400 to 1,100 N/m^3, which were deduced from levee heights.

We can obtain an estimate of the effective viscosity of the pyroclastic flow in motion using formulas developed by Johnson (1970) for debris flows. Let b be the depth and a the half-width of a channel of material of density ρ moving down a slope δ at speed v, and having an effective viscosity η. Define k^* and w^* by:

$$k^* = \frac{S_y}{b\rho\, g \sin\delta} \qquad w^* = \frac{\eta v}{b\, \rho g \sin\delta}.$$

Johnson (1970) showed w^* as a function of k^* and a/b. Parameters for one of the flows we examined (fig. 298, loc. C) are, roughly, $S_y = 900$ N/m^2 (from levee height), $b = 1.5$ m, $\rho = 1{,}450$ kg/m^3, and $\delta \cong 3°$. Therefore, $k^* = 0.8$. For this flow, $a \cong 5$ m, and so $a/b \cong 3.3$. For these values of k^* and a/b, $w^* = 0.03$, and so $\eta v = 50$ kg/s^2. Hoblitt (1980) has inferred velocities in the range of 15 to 20 m/s on the shallower slopes of the volcano for the pyroclastic flows of August 7, and velocities of 30–40 m/s were attained on the steeper, upper slopes. The deposit at location C was probably produced by a flow near the end of its travel, having $v = 10$–15 m/s, which indicates that $\eta \cong 4$ Pa s. This value is very approximate because the values of S_y and v used are, themselves, approximations, and because Johnson's model was developed for flow of a plastic material in a rigid-walled channel rather than between levees.

SUMMARY

A number of constraints can be placed on processes occurring during the motion of the pyroclastic flows of July 22 and August 7 and during the emplacement of the deposits they formed.

1. The existence of a levee-channel structure in the deposits implies that the pyroclastic flows moved as non-Newtonian (Bingham) fluids while in motion, at least near the end of their travel where substantial deposits were formed.

2. The sizes of the largest clasts seen at the surface in the essentially ungraded central-channel deposits indicate channel yield strengths of about 200 N/m^2. Levee heights indicate rather larger yield strengths of 400–1,100 N/m^2 during levee emplacement. Inferred velocities of the moving flows indicate a viscosity of about 4 Pa s. A large error (at least a factor of 2) must be attached to the viscosity estimate.

3. Field measurements of rheological properties of the flow deposits give yield strengths of 400–3,200 N/m^2 and viscosities of 700–2,000 Pa s for channel deposits a few days after emplacement (table 43, stations D, E, and F); corresponding values are 2,000–18,000 N/m^2 and 100–2,000 Pa s after a few weeks (table 43, stations A, B, and C). The changes are presumably the result of slow loss of gas from within the deposits and changes in the packing of the clasts.

4. The well-advanced but incomplete reverse grading of low-density pumice fragments in levee deposits indicates that some process reduced the yield strength of the levee matrix for a few seconds just before it came to rest. We infer that this process was the passage of engulfed atmospheric air through the levee during its formation from the advancing flow front.

Table 45.—Recommended observations to be made on pyroclastic flows and pyroclastic-flow deposits

[Observations will give information about: A, Large-scale rheology of pyroclastic flow during emplacement; B, Rheology of pyroclastic-flow materials under various strain rates: C, Small-scale mechanisms occurring during the generation and emplacement of pyroclastic flow; D, Relationship between eruption mechanisms in vent and pyroclastic-flow initiation]

General observations
1. Where do levees start in relation to the vent? (D)
2. Is there any evidence of deposition in the area between the vent and where levees begin? (D)
3. What is the slope of the substrate and does it change along the flow deposit? (A)
4. Are levee width and channel width variable? What is the relationship as a function of down-flow distance? (A)
5. Do breakouts occur in levees? What is their distribution? (A, B)
6. Do younger flows deform earlier channels and levees when they cross over them, and, if so, is the amount of deformation related to the time interval between the events (excavate to determine)? (A)
7. What is the relation of the shape and direction of the flow deposit to topographic obstacles? (A)

Field observations at flows
1. What is the relationship of the flow deposits to the substrate? (A, B)
2. Is there any sign of deformation of the substrate from load of flow? (B)
3. Is there any evidence of fine material having been expelled from the side of the levee? (C)
4. What is the nature of the substrate? (A)
5. What is the slope of the substrate? (A)

Levee and snout
1. Determine heights and cross-sectional profiles (by surveying or measuring suitably oriented photographs). (A)
2. Determine size distribution of surface materials. (A)
3. Determine grain-size distribution and variation with depth (if possible, excavate and sample several levels through entire thickness of flow). (A)
4. Determine particle roundness and angularity. (C)

Channel
1. What is the relation of the channel surface to levees (lower, same level, higher)? How much lower or higher, if any? (A)
2. Does this relation change with distance along the flow deposit? Is it a function of local slope? (A)
3. Are there any surface structures (ripples, longitudinal ridges, or other structures)? (A)
4. Are there any large clasts on the channel surface? (B) What is their size (estimate 3 mutually perpendicular axis lengths)? What percentage is exposed, and how high above the flow surface? What percentage is covered, and how deep below the flow surface? What is the bulk density of the clasts?

Channel--Continued
5. What is the grain-size distribution of channel materials as a function of depth (excavate and sample the flow)? (A) What are particle angularity and roundness relations? (C)
6. What is the gas composition of hot (greater than 100°C) materials at depth as a function of the distance from the front of the flow? (A, B)
7. What is the temperature of the flow at depth (measure complete profile if possible)? (A, C)
8. How does the channel surface respond when stepped on? Count the number of little gas jets formed and estimate the area in which they form; estimate the diameter of holes through which gas escapes, and estimate the largest ash fragment blown out of each hole and the height to which it rises. (B)

Other general field observations
1. Are there any breadcrust clasts? (C)
2. What percentage of the clasts are breadcrusted? (C)
3. Are any clasts only partly breadcrusted? (C)
4. What is their size distribution? (C)
5. Where do they occur (levee, channel)? (C)
6. Large breadcrusted clasts are often partly buried. Is crusting equally well developed on the buried side? (C)
7. Do breadcrusted clasts occur at depth within channels and levees? (C)
8. What is the thickness of the crust? (C)
9. What is the width of the intercrustal area? (C)

Photography of flows during emplacement
1. There are two major objectives in photographing active pyroclastic flows: (1) to determine flow velocity, and (2) to obtain detailed images of the motion of the front of the flow. Although both objectives are of high priority, flow-velocity determinations are the more useful of the two. If possible, a second camera should be used for detailed photography of the flow front if it has a long focal length lens; otherwise, the growth of the turbulent cloud over the main body of the flow should be photographed.
2. Observe the flow from right angles to the direction of movement.
3. Note location of photographer as accurately as possible.
4. To determine flow velocities, recognizable topographic features must appear in the background of the photograph.
5. Determine the time between frames--for a still camera, take frames at regular intervals and determine the interval by counting seconds.

SUGGESTIONS FOR FUTURE RESEARCH

Some critical observations still need to be made on existing flow deposits and on the motions of future flows to answer the following questions:

1. Is the billowing cloud of gas and ash that is always observed over the moving flows produced only from the head and levees or is an appreciable part produced also from the central channel of each flow? High-resolution photography might resolve this question; the information would help determine the extent to which air was incorporated into moving flows.

2. When one flow lobe crosses another within a short time interval (as happened at least once with the July 22 flows), is the lower lobe grossly deformed or swept away? The deposits could be excavated to check. The answer to this question would give information on the rate at which the rheological properties of the deposits changed with time after emplacement.

3. Is the total grain-size distribution of channel deposits the same as that in levees, apart from the

Table 46.—Recommended observations to be made on eruption clouds

[These observations would aid the calculation of discharge rates from the vent and exsolved magmatic-gas content of the eruption products]

Discrete explosions spaced by many seconds and forming discrete clouds
Determine the height of each cloud (can be done photographically from a long distance if ground features are included for scale). Determine the geometry of the cloud as it rises.
Discrete explosions closely spaced and individual bursts coalescing into a single cloud
Determine the height of the cloud as a function of time, and the number of bursts in a given time interval.
Steady or nearly steady eruption
Record height and geometry of the cloud both as it grows and after it reaches maximum height. (This is best done photographically. It is vital to have pictures from both upwind of the cloud and from right angles to the wind direction. If possible, take several tens of seconds of motion-picture film, especially of the base of the cloud. In all photographs, include the top of the mountain for scale.)

high concentration of coarse pumice clasts in the top of the levees? The grain-size distribution should be measured as a function of vertical position in both channel and levees at many locations along a lobe. These measurements would permit an estimate to be made of the amount of small grain-size material elutriated from the levees during their formation.

4. Are pumice fragments equally rounded, and are breadcrust bombs equally common at all positions along a flow? Are breadcrust bombs present in channel and levee deposit interiors? This knowledge would provide information on the extent of internal motion within the moving flows.

5. Do larger scale pyroclastic-flow deposits from earlier in the eruption have well-defined levees? It is important to establish the relationship between the width and height of levees and the width, thickness, and velocity of advance of the main part of the moving flow.

A list of observations that should be made, both on moving flows and on flow deposits, is given in table 45. A list of observations that should be made on eruption columns is given in table 46.

REFERENCES CITED

Bagnold, R. A., 1968, Deposition in the process of hydraulic transport: Sedimentology, v. 10, p. 45–50.

Hoblitt, R. P., 1980, Observations of pyroclastic flows of July 22 and August 7, 1980, Mount St. Helens, Washington [abs.]: EOS, v. 61, no. 46, p. 1137–1188.

Johnson, A. M., 1970, Physical processes in geology: San Francisco, Freeman, Cooper, and Co., 577 p.

Kelley, J. E., Roberts, T. D., and Harris, H. M., 1964, A penetrometer for measuring the absolute viscosity of glass: U.S. Bureau of Mines Report of Investigations 6358, 11 p.

Koch, A. J., and McLean, Hugh, 1975, Pleistocene tephra and ash-flow deposits in the volcanic highlands of Guatemala: Geological Society of America Bulletin, v. 86, no. 4, p. 529–541.

Lamb, H., 1932, Hydrodynamics: Cambridge, Cambridge University Press, 738 p.

Landau, L. D., and Lifshitz, E. M., 1959, Fluid mechanics: London, Pergamon Press, 536 p.

Miller, T. P., and Smith, R. L., 1977, Spectacular mobility of ash flows around Aniakchak and Fisher calderas, Alaska: Geology, v. 5, no. 3, p. 173–176.

Moore, J. G., and Melson, W. G., 1969, Nuées ardentes of the 1968 eruption of Mayon Volcano, Philippines: Bulletin Volcanologique, v. 33, ser. 2, p. 600–620.

Nairn, I., and Self, S., 1978, Explosive eruptions and pyroclastic avalanches from Ngauruhoe in February 1975: Journal of Volcanology and Geothermal Research, v. 3, no. 1/2, p. 39–60.

Pinkerton, Harry, 1978, Methods of measuring the rheological properties of lava: United Kingdom, University of Lancaster Ph. D. thesis, 435 p.

Pinkerton, Harry, and Sparks, R. S. J., 1978, Field measurements of the rheology of lava: Nature, v. 276, p. 383–385.

Rose, W. I., Grant, N. K., and Easter, John, 1979, Geochemistry of the Los Chocoyos ash, Quezaltenango valley, Guatemala: Geological Society of America Special Paper 180, p. 87–99.

Sparks, R. S. J., and Wilson, L., 1976, A model for the formation of ignimbrite by gravitational column collapse: Geological Society of London Journal, v. 132, p. 441–451.

Sparks, R. S. J., Wilson, L., and Hulme, G., 1978, Theoretical modelling of the generation, movement and emplacement of pyroclastic flows by column collapse: Journal of Geophysical Research, v. 83, no. B-4, p. 1727–1739.

Williams, Howell, 1942, The geology of Crater Lake National Park, Oregon, with a reconnaissance of the Cascade Range southward to Mount Shasta: Carnegie Institution of Washington Publication 540, 162 p.

Yokoyama, S., 1974, Flow and emplacement mechanisms of the Ito pyroclastic flow in southern Kyushu, Japan: Tokyo Kyoiku Daigaku Science Reports, sec. C, v. 12, p. 17–62.

THE 1980 ERUPTIONS OF MOUNT ST. HELENS, WASHINGTON

PETROGRAPHY AND PARTICLE-SIZE DISTRIBUTION OF PYROCLASTIC-FLOW, ASH-CLOUD, AND SURGE DEPOSITS

By MEL A. KUNTZ, PETER D. ROWLEY, NORMAN S. MACLEOD, RICHARD L. REYNOLDS, LISA A. MCBROOME, ALLAN M. KAPLAN, *and* DAVID J. LIDKE

ABSTRACT

Pumice lapilli and blocks in pyroclastic-flow deposits of May 18, May 25, June 12, July 22, August 7, and October 16–18, and gray dacite in the May 18 lateral-blast deposit contain variable amounts of plagioclase, orthopyroxene, amphibole, and iron-titanium oxide phenocrysts, which are set in a vesicular, glassy matrix. The composition and proportion of phenocrysts found in pumice fragments of successively younger pyroclastic-flow deposits show the following general trends: an increase in the anorthite content of plagioclase from An_{41} for the May 18 pyroclastic-flow deposits to An_{44} for the October 16–18 pyroclastic-flow deposits; an increase in the modal proportions of plagioclase, orthopyroxene, and iron-titanium oxide minerals; an increase in the ratio of total phenocrysts to total phenocrysts plus glass; a decrease in the ratio of amphibole to amphibole plus orthopyroxene; and a decrease in vesicularity of pumice fragments.

The median grain size increases and the sorting is poorer for successively younger pyroclastic-flow deposits erupted from May 18 to August 7. Conversely, the median grain size is smaller and the sorting better for pyroclastic-flow deposits of October 16–18 than for the earlier deposits. Ash-cloud and surge deposits associated with the May 18 eruption are appreciably finer grained and better sorted than any of the pyroclastic-flow deposits.

Data in this report and elsewhere in this volume, as interpreted in light of published experimental studies, suggest that each successive eruption has tapped a deeper level in a thermally and compositionally zoned magma chamber, that the magma had a fairly high water content, that successive eruptions have largely depleted the magma of its volatiles, and that successive eruptions have been characterized by decreased vesiculation and gas thrust.

INTRODUCTION

The petrography, petrology, density, and particle-size distribution of pyroclastic-flow, ash-cloud, and surge deposits of the 1980 eruptions were studied to augment field investigations of the same deposits (Rowley and others, this volume). Presented here are preliminary data obtained in a 2-mo period following completion of field studies. Future studies will focus in more detail on mineralogical and compositional variations and on vertical and lateral variations in particle-size distributions in products of the eruptive sequence.

Laboratory work included the examination of about 125 thin sections of pumice samples taken from pyroclastic-flow deposits. Modal analyses were made by counting 1,000 or more points for each thin section. The universal stage was used to make positive identification of untwinned and unzoned feldspar and to measure optic axial angles, angles between optical directions and crystallographic axes, and the optical orientation for orthopyroxene, clinopyroxene, and amphibole. The iron-titanium oxide minerals in pumice samples from pyroclastic-flow deposits of May 18, May 25, June 12, July 22, and August 7, were examined using polished grain mounts submersed in oil under reflected light. Thermomagnetic analysis

was used to complement the petrographic identification of magnetic iron-titanium oxide minerals and to provide crude estimates of their compositions.

The bulk density and grain density of pumice samples from pyroclastic-flow deposits were determined by a method utilizing the Archimedes principle. Particle-size distributions were determined by sieving and settling methods; the components in each size class for each sample were identified using a binocular microscope.

The samples used for the mineralogical, density, and particle-size distribution studies were collected in the field without any strict, systematic sampling design. This lack of system was due to the limited time available for our field work, which was constrained by helicopter, weather, and safety restrictions and by the unavailability of suitable base maps. This sampling problem places limitations on the applicability of statistical analyses to these samples. Nevertheless, we present our preliminary results with the full realization that additional studies using more systematic sampling designs may modify our conclusions. Sample locality information may be obtained from the authors.

ACKNOWLEDGMENTS

Many coworkers in the U.S. Geological Survey contributed to this study. In particular, we thank Peter W. Lipman, Donald A. Swanson, and Richard P. Hoblitt for pumice samples of the May 25 pyroclastic-flow deposits. Gordon Johnson provided equipment and advice for making density determinations. Donald M. Cheney provided advice and assistance in determining particle-size distributions.

PETROGRAPHY OF PUMICE

The mineralogy and petrology of pumice samples from pyroclastic-flow deposits are rather simple. All samples have a glassy matrix and contain phenocrysts of plagioclase, orthopyroxene, amphibole, and iron-titanium oxide minerals that are typically 0.5–2 mm in longest dimension. Clinopyroxene has been identified in small amounts (much less than 1 percent) in some thin sections. Neither quartz, tridymite, alkali feldspar, nor biotite have been observed in any thin section, although traces of cristobalite were observed in a few thin sections. Apatite is present in the matrix of all samples as tiny crystals. The mineral descriptions that follow apply generally to all deposits; significant variations are noted where appropriate.

The plagioclase, orthopyroxene, amphibole, and iron-titanium oxide minerals occur (1) as crystals that were in equilibrium with and crystallizing from the melt at the time that it was vesiculated and quenched, and (2) as crystals that were not in equilibrium and either show evidence of resorption in their cores and along their margins or have reaction rims. Some of the latter crystals may represent products of an earlier period of crystallization of the same magma under different pressure, temperature, and water-content conditions, whereas others may be foreign to the magma. Many of the crystals that may be considered foreign to the magma appear texturally similar to those in amphibolite xenoliths. We refer to all crystals that were not in equilibrium with the melt as "xenocrysts" because the origins of many individual crystals are not clearly indicated in thin section. Further mineralogic studies utilizing electron microprobe analysis may clarify the origin of the "xenocrysts."

PLAGIOCLASE

Most plagioclase phenocrysts are dominantly 0.2–1.5 mm long, but some are as long as 3 mm. They grade down to microlites less than 0.05 mm long in some samples. Most plagioclase is euhedral; equant and lath shapes predominate over triangular shapes. Many crystals are composites of several smaller crystals that adjoin on (010) faces; some have irregular, embayed margins.

Many large plagioclase crystals have spongy cores containing roughly equal proportions of plagioclase and glass inclusions, which are surrounded by an outer rind that is devoid of inclusions. The glass inclusions consist of irregular-shaped, oblong, vermicular, or nearly spherical pale-lavender blebs. Many of these blebs in turn contain fluid and solid inclusions. The blebs form an interconnected network in most crystals, but in others they are separated from one another. Some glass inclusions are arranged in thin layers parallel to compositional zone boundaries near crystal edges. A few crystals appear to be skeletal and are filled with pumiceous glass that contains opaque minerals. This type of glass is identical to and continuous with the glass in the matrix that surrounds the crystal.

Nearly all plagioclase crystals are twinned on the Carlsbad-albite and albite twin laws; twinning on (001) composition planes is less common. The plagioclase crystals are zoned to some degree, and some crystals are strikingly zoned. Zoning is typically normal, but oscillatory and reversed zonings are also present.

Plagioclase compositions were determined by universal stage measurement of the extinction angle Y∧[100]/(010) on albite twins, using the curves of Slemmons (1962). Compositions of 7 to 14 crystals were determined in each of five thin sections from pumice samples from pyroclastic-flow deposits of May 18, May 25, June 12, July 22, August 7, and October 16–18, and compositions of 10 to 12 crystals were determined in each of three thin sections of dense, gray dacite from the May 18 lateral-blast deposit (table 47). The total range of compositions determined is An_{30} to An_{50}; thus all crystals are andesine. A general trend toward more calcic plagioclase occurs in successively younger deposits (table 47), but the trend is not statistically significant, as the mean plagioclase compositions of the deposits are well within one standard deviation of each other.

A few plagioclase crystals in some thin sections occur as clots of several smaller crystals that have various orientations. Irregular, non-crystal-face boundaries occur in clots of plagioclase and amphibole. The plagioclase crystals in both varieties of clots may be xenocrysts(?).

Each thin section contains some plagioclase crystals that are not obviously twinned or zoned when viewed on a flat stage. Tilting of these crystals to high angles on the universal stage, however, shows that most of them have at least a hint of plagioclase-type twinning and zoning. However, a few plagioclase crystals are indeed untwinned and not obviously zoned; all such crystals are tabulated as plagioclase in the modal analyses.

Table 47.—Summary statistical data for plagioclase composition of pumice samples from 1980 lateral-blast and pyroclastic-flow deposits, Mount St. Helens, Washington

[Data expressed as percent anorthite]

Type of deposit	Number of determinations	Mean	S.D.[1]	Range	Maximum single-crystal variation
Lateral blast, May 18	35	42	3	37-49	7
Pyroclastic flow					
May 18	47	41	4	30-48	n.d.[2]
May 25	38	42	4	32-49	12
June 12	54	41	3	36-47	8
July 22	56	43	2	37-47	9
August 7	57	43	3	36-49	9
October 16-18	57	44	2	40-50	8

[1] Standard deviation (1 sigma).
[2] Not determined.

ORTHOPYROXENE

Orthopyroxene occurs as elongate, prismatic crystals, typically 0.5 mm long and about 0.05 mm wide. Most have well-developed (100), (010), (110), and (101) faces. Nearly all orthopyroxene contains opaque inclusions. Some crystals occur in clots of 3 or 4 anhedral crystals or in clots that also contain clinopyroxene, hornblende, plagioclase, and opaque minerals. Both varieties of clots may be xenocrysts(?).

The optical properties and pleochroism of the orthopyroxene indicate it is hypersthene (about En_{60}): $n_Z \cong 1.72$, $2V_X = 54°-66°$, birefringence is 0.013–0.016, and pleochroic colors are X = light tan, Y = honey brown, and Z = light greenish yellow.

CLINOPYROXENE

Clinopyroxene is a sparse constituent of the 1980 Mount St. Helens rocks. A few crystals appear in some thin sections from pumice samples of all deposits, but when present total less than 0.1 percent. Clinopyroxene crystals are invariably anhedral, rounded, and less than 0.5 mm long. They do not have reaction rims, but the shape of the clinopyroxene crystals suggests that they crystallized earlier from the melt at higher temperature and pressure and were not in equilibrium with the melt at the time of eruption and quenching, or they may be xenocrysts(?). Some crystals occur in xenocrystic(?), coarse-grained clots with orthopyroxene, amphibole, plagioclase, and opaque minerals. The amount of clinopyroxene appears to increase in successively younger deposits, but we cannot confirm this observation with modal data because of the very small amount present.

Limited optical data suggest that the clinopyroxene is augite. Birefringence is about 0.031, $2V_Z \cong 32°$, Z ∧c $\cong 28°$, the optic axial plane is parallel to (010), and most crystals are twinned on (100).

AMPHIBOLE

Amphibole crystals occur in all thin sections, but pumice samples of the May 18 lateral-blast deposit contain significantly more amphibole than do pumice samples from younger deposits.

Amphibole crystals show considerable variation in size and shape, both within a single thin section and between sections. In any one thin section, crystals are typically either subhedral or anhedral; less commonly both types occur together. The anhedral crystals may represent an earlier crystallization under higher pressure and temperature conditions and they have been subsequently resorbed. The more euhedral crystals may reflect crystallization at lower temperature and pressure conditions shortly before eruption after the melt had ascended to near the surface. Most crystals are roughly equant and range from 0.2 to 1.0 mm long. A few crystals are very elongate, with lengths of 1.6 mm and widths of 0.2 mm. In a few crystals in each thin section, (100) and (110) faces are recognizable on subhedral crystals. Some anhedral crystals are skeletal or spongy; they contain vermicular, interconnected voids filled with vesicular, opaque-charged glass that is continuous with the surrounding glassy matrix. Lamellar twinning on (100) is common to most crystals in all thin sections examined.

Amphibole in some samples from all pyroclastic-flow deposits has thin reaction rims, less than 0.01 mm thick, that consist of plagioclase, opaque minerals, and orthopyroxene. All crystals in the reaction rims are less than 0.002 mm. The reaction rims become thicker and more coarse grained in pumice samples from successively younger pyroclastic-flow deposits, suggesting that progressive changes within the magma, probably loss of water, have made the amphibole increasingly unstable. The anhedral, roughly equant, and skeletal amphibole crystals may reflect earlier crystallization under higher temperature and pressure conditions. These crystals may have been subsequently partially resorbed under conditions of lower temperature, lower confining pressure, and lower water content that accompanied the rise of the magma. The more euhedral and (or) elongate amphibole crystals may reflect crystallization shortly before eruption when the magma had risen to a higher crustal level.

Preliminary optical data on the amphibole suggest that it is hornblende. Pleochroic colors are Z = brownish green, Y = light green, and X = pale honey brown; Z $\wedge c$ is about 25–30°; and $2V_X$ is about 65°.

IRON-TITANIUM OXIDE MINERALS

Iron-titanium oxide minerals occur in all pumice samples from the pyroclastic-flow deposits of May 18, May 25, June 12, July 22, and August 7. They consist dominantly of species of the ulvospinel-magnetite (Usp-Mt_{SS}) and ilmenite-hematite (Ilm-Ht_{SS}) solid solution series. Two distinct populations of iron-titanium oxides of different origins and thermal histories are present in each sample in each pyroclastic-flow deposit. One population consists of Usp-Mt_{SS} and Ilm-Ht_{SS} grains that are optically homogeneous or nearly so. The other population of grains exhibits complex intergrowths of iron- and titanium-bearing oxides that resulted from moderate to extensive high-temperature oxidation of the Usp-Mt_{SS} or Ilm-Ht_{SS} host. The optically homogeneous grains crystallized apparently as primary constituents in the magma and were rapidly cooled during outgassing and eruption. In contrast, grains with complex intergrowths either occur as xenocrysts(?) with extensive marginal alteration to fine-grained hematite and a TiO_2 phase or they occur in altered xenoliths.

The relative abundance of the primary, optically homogeneous iron-titanium oxide minerals and of the highly oxidized contaminant grains varies between and within some pyroclastic-flow deposits. The percentage of iron-titanium oxide grains that show alteration ranges from 50 percent or more in the basal pyroclastic-flow deposits of the May 18 eruption to about 2 percent in the uppermost pyroclastic-flow deposits of the May 18 eruption. Contaminant grains are even more scarce (less than about 1 percent of the iron-titanium oxide suite) in samples of pumice of the May 25, June 12, and August 7 eruptions, but they constitute as much as 10 percent in July 22 pyroclastic-flow deposits.

The primary Usp-Mt_{SS} (titanomagnetite) grains in all pyroclastic-flow deposits are similar in texture and distribution. They are subequant to equant, range in longest dimensions from less than 1 μm to about 250 μm, and occur in and adjacent to silicate phenocrysts in the glassy groundmass and in reaction rims around hornblende phenocrysts. Nearly all Usp-Mt_{SS} grains appear to be compositionally homogeneous,

except that they contain small inclusions of silicate and sulfide minerals. About 1 percent or less of Usp-Mt_{SS} grains in the June 12, July 22, and August 7 pyroclastic-flow deposits, however, exhibit incipient development of ilmenite lamellae in a trellis pattern along (111) planes in the titanomagnetite host. These grains have unaltered margins and occur in unaltered silicate phenocrysts and in the groundmass or, rarely, within reaction rims around hornblende; they thus are distinguished from the metatitanomagnetite grains that occur as xenocrysts(?) or in extensively altered xenoliths.

The primary Ilm-Ht_{SS} grains display a wide range in size (from about 4 to 200 μm across) and occur, as do the Usp-Mt_{SS} grains, in and adjacent to silicate phenocrysts and in the groundmass. No systematic petrographic differences were observed among the primary Ilm-Ht_{SS} grains in the different pyroclastic-flow deposits.

In addition to the extremely rare trellis-type intergrowths, ilmenite is intergrown with titanomagnetite in composite (ilmenite typically external) and sandwich textures (see Haggerty, 1976). In some examples, ilmenite extends beyond the titanomagnetite to form graphic intergrowths with silicate phenocrysts, indicating that the ilmenite originated directly from the melt rather than by later oxidation of Usp-Mt_{SS}.

Thermomagnetic curves (saturation magnetization versus temperature) of magnetic separates from pumice samples of the May 18, June 12, July 22, August 7, and October 16–18 pyroclastic-flow deposits are reversible and show dominantly a single curie temperature at about 375° ± 10°C. The overwhelming abundance of optically homogeneous Usp-Mt_{SS} grains in the analyzed magnetic separates and the very limited range of curie temperatures indicate that titanomagnetite with a rather uniform composition of about $\frac{1}{3}\ Fe_2TiO_4 \cdot \frac{2}{3}\ Fe_3O_4$ is the dominant magnetic iron-titanium oxide. An identical result was found for magnetic oxides in the June 1980 dacite dome (Olhoeft and others, this volume).

Ilm-Ht_{SS} species of approximately 65 mol percent Fe_2O_3 would also have a curie temperature of about 375°C. However, in the magnetic separates the absence of Ilm-Ht_{SS} grains unattached to either Usp-Mt_{SS} or to fragments containing Usp-Mt_{SS} grains argues against the presence of ferrimagnetic Ilm-Ht_{SS}, at least in any significant amounts. This conclusion is also supported by the extreme improbability that Usp-Mt_{SS} and Ilm-Ht_{SS} species in these pumice samples would have nearly identical curie temperatures.

MATRIX

The matrix of all thin sections studied is formed of pumiceous glass and microlitic crystals of plagioclase and opaque minerals, and a few small crystals of orthopyroxene and amphibole typically with a trachytic texture. The glass is colorless or pale yellow; orange and reddish-orange glass is present as coatings on vesicle walls in a few sections. The glass is generally charged with very fine grained opaque material, but in some thin sections it contains little or none. In thin section, vesicles are mostly round in outline and about 0.03 mm in diameter. Smaller vesicles range down to about 0.01 mm. Irregular-shaped and elongate vesicles as much as several centimeters long occur in some pumice specimens from all pyroclastic-flow deposits.

Vesicle walls range from about 0.005 to 0.05 mm in thickness. Some larger vesicles are surrounded by smaller vesicles that have length-to-width ratios of 100:1 or more. The marginal vesicles were apparently flattened and stretched as the larger, adjacent vesicles expanded.

MODAL ANALYSES

METHODS

Because pumice represents clots of quenched vesiculated magma, variations in its modal composition reflect compositional variation in the source magma. Modal analyses, consisting of 1,000 or more points, were made on gray dacite from the lateral-blast deposit of May 18 and on pumice samples from pyroclastic-flow deposits. Components counted included plagioclase, orthopyroxene, amphibole, and iron-titanium oxide phenocrysts and glass plus vesicles. We found it extremely difficult to discriminate between vesicles and glass in thin section, so they were counted together. The total proportion of vesicles (volume percent) was determined from bulk-density and grain-density data described

later. The vesicle percent figure was subtracted from the total of the modal analyses, and the analyses were recalculated to 100 percent (table 48). Accessory minerals and clinopyroxene total less than 0.1 percent in all modal analyses and they are not listed in table 48.

MODAL VARIATION

Pumice samples from the individual pyroclastic-flow deposits and dacite from the lateral-blast deposits show considerable modal variation. Nevertheless the average modes of successive eruptions (table 48, figure 304) show slight but significant trends. In general, the percentage of phenocrysts increases in successively younger deposits. However, emplacement temperatures have been generally higher in younger pyroclastic flows (Banks and Hoblitt, this volume) and, assuming that these higher emplacement temperatures reflect increasing magma temperatures, phenocryst content would be expected to be lower in younger pumice, if all other conditions were the same. Apparently a decrease in the water content (reflected by decreases in vesicularity and amphibole content), coupled with systematic changes in the magma composition, more than compensated for the increase in temperature and caused the liquidus to be shifted to higher temperatures. Thus more of the magma crystallized even though magma temperatures apparently increased in successive eruptions.

Plagioclase, orthopyroxene, and iron-titanium oxide minerals generally increase in abundance in successively younger deposits, whereas amphibole and the ratio of amphibole to amphibole plus orthopyroxene generally decrease (table 48). This decrease in apparent stability of amphibole likely reflects decreasing water content in the magma.

The change in the proportion of phenocrysts is compared to the change in the proportion of glass in figure 304. Plagioclase, orthopyroxene, and iron-titanium oxide minerals generally increase as glass decreases, but the increase is not strictly age dependent. This lack of age dependence may reflect either the heterogeneity of individual units or the insufficiency of our samples to represent the units. The fewest modes were determined on the two units that plot out of age order (May 25 and Oct. 16–18); their averages might plot in age order if more modal analyses had been made. The decrease in amphibole content with decrease in glass suggests that some or all of the amphibole crystals may be unstable and not on the liquidus.

DENSITY MEASUREMENTS

Pumice lapilli were selected for density measurements from samples of the pyroclastic-flow deposits so as to represent the observed range in megascopic textures, colors, and densities. Dry bulk densities were determined using a method described by Chleborad and others (1975) that employs the Archimedes principle. Lapilli were weighed after heating at about 95°C to drive off excess moisture. The lapilli were then saturated in water under a vacuum, both to approximate a saturated, surface-dry condition and to increase their masses so that the lapilli would sink when subjected to the Archimedes process. The

Table 48.—Modal analyses of 1980 lateral-blast and pyroclastic-flow deposits of Mount St. Helens
[Recalculated vesicle-free to 100 percent]

Type of deposit	Number of determinations	Glass	Plagioclase	Orthopyroxene	Amphibole	Iron-titanium oxides	Percent vesicles[1]	Percent phenocrysts	$\frac{\text{Amphibole}}{\text{Amphibole + Orthopyroxene}}$	$\frac{\text{Crystals}}{\text{Crystals + Glass}}$
Lateral-blast, May 18	3	66.7	25.1	3.3	3.7	1.2	36	33.3	0.53	0.33
Pyroclastic flows										
May 18	11	62.1	30.0	4.2	2.5	1.2	71	37.9	.37	.38
May 25	7	59.5	32.8	4.1	2.3	1.3	63	40.5	.36	.41
June 12	18	60.5	31.1	4.9	2.3	1.1	57	39.5	.32	.40
July 22	11	57.1	35.3	4.5	1.9	1.2	65	42.9	.30	.43
August 7	12	51.3	39.7	5.3	2.1	1.5	61	48.1	.28	.49
October 16-18	7	54.8	35.8	5.8	2.1	1.4	58	45.2	.27	.45

[1]Determined from bulk density and grain density data (table 49).

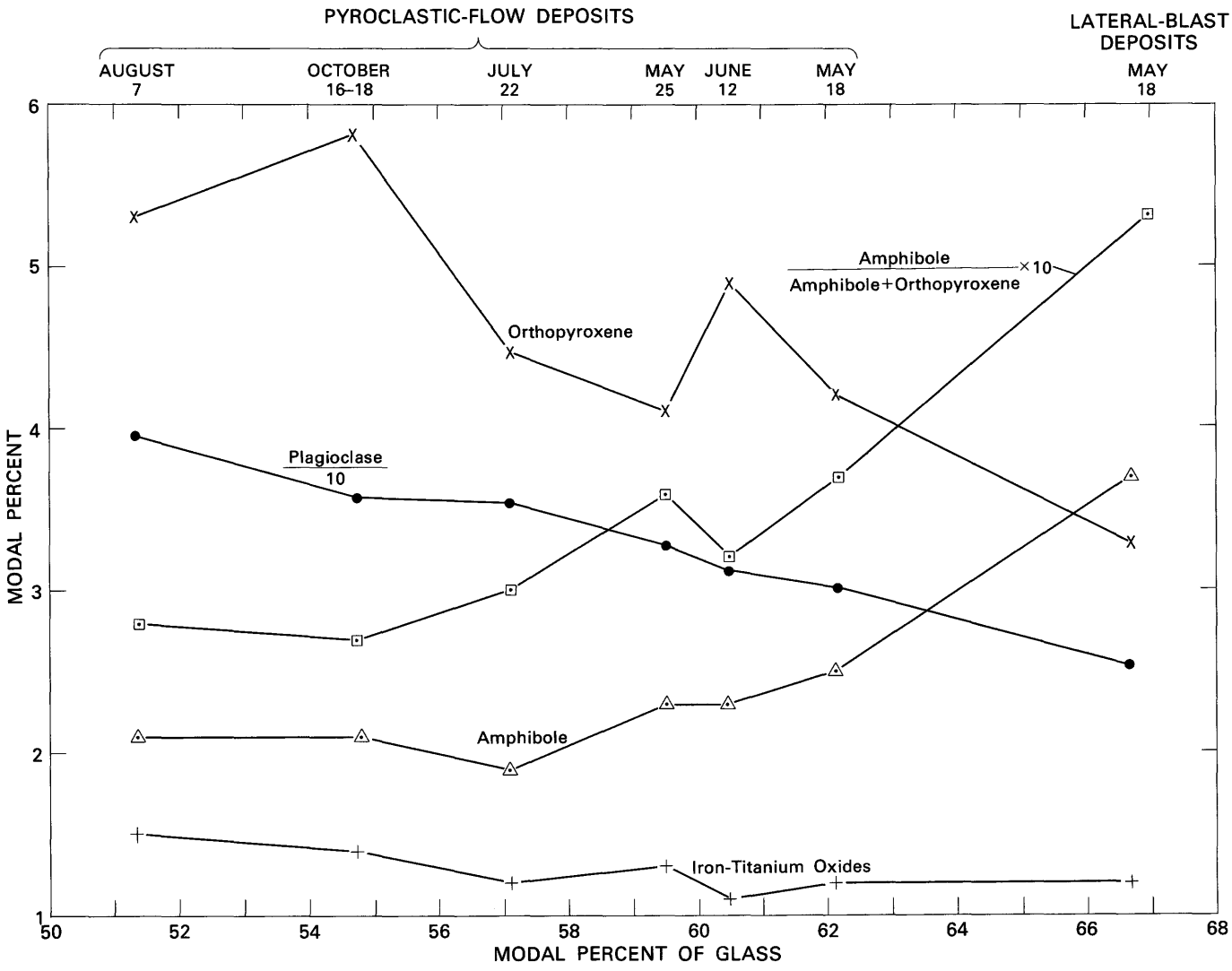

Figure 304.—Modal percent of phenocrysts and ratio of amphibole to amphibole plus orthopyroxene, plotted against modal percent of glass for gray dacite from lateral-blast deposit and pumice from pyroclastic-flow deposits.

volumes of the lapilli were measured three times, and the average volume was used to compute the density.

Grain densities (glass plus phenocrysts) of selected lapilli samples were measured by use of a helium-air pycnometer. The measurements are based on a comparison of the pressure-volume relationship of the sample with that of a standard, nonporous volume. Samples were crushed and weighed, their volumes were determined, and their densities were calculated by the method described by Johnson (1979).

Average values for bulk density and grain density for pumice samples from the lateral-blast deposit and the pyroclastic-flow deposits are given in table 49. The data show a general increase in both bulk density and grain density of pumice samples in successively younger pyroclastic-flow deposits. The average total porosity (a measure of total vesicle volume) was determined for pumice samples from the lateral-blast deposit and the pyroclastic-flow deposits by the relation

$$Pt = 100\left(1 - \frac{Db}{Dg}\right)$$

where Pt = total porosity,
Db = bulk density, and
Dg = grain density (Daly and others, 1966).

The high bulk density and low total porosity of gray dacite from the lateral-blast deposit appear consistent with the conclusion that the pumice of that

Table 49.—Average values for bulk density, grain density, and total pore space of gray dacite from the lateral-blast deposits and of pumice lapilli from pyroclastic-flow deposits of Mount St. Helens

Type of deposit	Bulk density		Grain density		Total pore space (percent)
	Mean (g/cm^3)	No.[1]	Mean (g/cm^3)	No.[1]	
Lateral blast,					
May 18--------	[2]1.66	262	2.52	3	36
Pyroclastic flow,					
May 18-------	.74	8	2.55	3	71
May 25-------	.95	2	([3])	0	[3]63
June 12------	1.08	10	2.53	3	57
July 22------	.88	11	2.55	1	65
August 7-----	1.02	12	2.61	3	61
October 16-18	1.12	12	2.65	5	58

[1] Number of determinations.
[2] Data from Hoblitt and others (this volume).
[3] Grain density (Dg) not determined; total pore space calculated using Dg=2.60.

deposit represents magma that had crystallized in the edifice of Mount St. Helens before the May 18 eruptions (Lipman, Norton, and others, this volume).

PARTICLE SIZE ANALYSES

METHODS

Individual deposits at Mount St. Helens show significant variation in particle size, and thus many size analyses are necessary to characterize both individual deposits and all deposits of a single eruption. The particle size varies greatly even in single pyroclastic-flow units. Vertical sections through deposits of May 18, for instance, show reverse grading (fine to coarse upward) of light pumice lapilli and normal grading (coarse to fine upward) of heavy lithic fragments. Additionally, large pumice lapilli and blocks are concentrated relative to the fine ash matrix at the margins of levees, channels, and lobes of pyroclastic-flow deposits of all ages. Exposed vertical sections are rare in the pyroclastic-flow deposits. Multiple samples of each flow unit were collected, however, from vertical sections in phreatic pits in the deposits of May 18 and from slump scarps in the deposits of June 12 and May 18. Inasmuch as holes in the post-June 12 deposits do not maintain vertical walls, it was difficult to sample more than 0.5 m below the surface. For post-June 12 deposits, the upper 10–20 cm of the surface was scraped away to remove air-fall deposits and the surficial layer in which pumice lapilli and blocks are concentrated, and bulk samples that typically weighed 4–7 kg were collected. More representative samples that reflect vertical and horizontal variation in particle size may be obtained later when younger deposits become more consolidated and have been dissected by streams.

Samples were dried, weighed, and then split into particle-size fractions of greater and less than 32 mm. The diameters of pumice fragments greater than 32 mm were measured by hand, and the samples in each phi size class (Krumbein, 1934) were weighed on a pan balance. The fraction less than 32 mm was split with a sample splitter to obtain a subsample of 500–700 g. The subsample was then sieved gently by hand for about 5 min in a set of sieves with a size range of 16 to $\frac{1}{2}$ mm at 1-phi intervals. The $<\frac{1}{2}$ -mm fraction was transferred into a $\frac{1}{2}$ to $\frac{1}{16}$ mm sieve set (1-phi intervals), which was placed on a sieve vibrator and vibrated at the lowest possible frequency and intensity and for the minimum time required for particle separation (5 min or less) so as to minimize particle abrasion. Fractions in each size class were then weighed on a pan balance. Weight fractions in size classes less than $\frac{1}{16}$ mm were determined for ash-cloud deposits by a settling-velocity hydrophotometer method. Estimates of the volume percent of pumice, lithic clasts, crystals, and glass shards were made for each size class by visual examination with a binocular microscope.

COMPONENTS AND SIZE CLASSES

Walker (1971) classified the components of pyroclastic deposits into five groups: lithic fragments, pumice fragments, dense glass fragments, crystals, and vitric ash shards. All these components form significant proportions of Mount St. Helens deposits, except glass fragments.

Lithic fragments are dark-gray, black, deep-reddish-brown, and brown foreign rock particles derived mainly from the conduit walls and expelled during eruptions. They are typically about 10 to 30 mm in diameter, but holocrystalline clots of crystals as small as 1 mm are also found in thin sections. Most megascopic lithic fragments are andesite and basalt, and microscopic xenocrysts and xenoliths

resemble amphibolite and gabbro texturally and mineralogically.

Almost all of the pumice fragments are larger than 1/8 mm. Some have flow bands of contrasting vesicularity and shades of gray. The bands are several millimeters to several centimeters thick. Light-gray bands are more vesicular than the darker bands, and the differing vesicularity is apparently the only reason for the difference in color, as the two bands have the same mineralogical composition.

The crystal components are phenocrysts that were largely freed from their glassy matrix by vesiculation and by fragmentation and abrasion of pumice fragments. These crystals, like the phenocrysts in the pumice, are plagioclase, orthopyroxene, and amphibole. The crystals are mostly less than 1 mm across, as are the phenocrysts in the pumice fragments. Films of glass and parts of vesicle walls occur on the surfaces of many crystals.

Irregularly shaped glass shards with concave indentations that represent ruptured vesicle walls and wall junctions are the chief component of the material less than 1/8 mm.

STATISTICAL AND GRAPHICAL ANALYSES

Particle-size frequency distributions were determined for samples of pyroclastic-flow, ash-cloud, and surge deposits (Rowley and others, this volume). Cumulative weight percentages were plotted versus phi (ϕ) size class intervals on arithmetic graph paper (Murai, 1960) to obtain a graphical analysis of each size distribution and to easily compare cumulative curves of samples of deposits of different ages and modes of origin. Statistics that characterize each cumulative curve were used for numerical comparisons and for graphical purposes. Statistics calculated from quartile measurements from cumulative curves are quartile mean size and quartile skewness; we also determined the median phi size and calculated kurtosis and the Inman deviation.[1] Cumulative curves and statistics distinguish various types and ages of volcanic deposits. Plots of the Inman deviation versus median grain size (ϕ_{50}) are used to compare deposits of different mode of origin and pyroclastic-flow deposits of different ages (fig. 305).

[1]Quartile mean size $=(\phi_{75}+\phi_{25})/2$; quartile skewness $=[(\phi_{75}+\phi_{25})/2]-\phi_{50}$; kurtosis $=(\phi_{75}-\phi_{25})/[2(\phi_{90}-\phi_{10})]$; Inman deviation $=(\phi_{84}-\phi_{16})/2$; median phi size $=\phi_{50}$.

PYROCLASTIC-FLOW DEPOSITS

The size distributions of samples from pyroclastic-flow deposits of Mount St. Helens occupy a broad area in figure 305. Both the median grain size and the deviation increase in successively younger pyroclastic-flow deposits from May 18 through August 7. The median grain size and deviation for the pyroclastic-flow deposits of October 16–18, however, do not represent a continuation of this trend; instead, they are nearly the same as those of the pyroclastic-flow deposits of July 22.

May 18.—As is obvious in the field, pyroclastic-flow deposits of May 18 have finer grain sizes (fig. 306; table 50) and higher proportions of lithic fragments than succeeding pyroclastic-flow deposits. The median grain size is about 1/2 mm and the range in median grain sizes is about 1.5 phi units (1/3–1 mm; see tables 50 and 51). Seven of the nine samples have bimodal or trimodal particle-size distributions, with the single or double minor modes occurring in the coarse tail. The main modes all occur in the 1/4–1/2 mm size range (table 51). The low deviation values and the relatively small average median grain sizes both indicate that the vesiculation and disruption process of the May 18 eruption was greater than that of succeeding eruptions.

June 12.—The median grain sizes of samples from the pyroclastic-flow deposits of June 12 span more than three phi size classes, 0.5–4 mm (fig. 305, table 52). The average deviations of the grain-size distributions also span about three phi size classes. These deposits are more poorly sorted than pyroclastic-flow deposits of May 18 but somewhat better sorted than pyroclastic-flow deposits formed after June 12 (table 50). The pyroclastic-flow deposits of June 12 have the most negative average skewness of all the pyroclastic-flow deposits (table 50), indicating that they have more pronounced coarse-tail grading than the other pyroclastic-flow deposits. The coarse-tail grading may be due to the extremely high preemplacement and postemplacement mobility of the June 12 pyroclastic-flow deposits. Some samples may represent deposits that contain lag materials or, alternatively, samples taken near the surface may have been depleted of fine matrix by elutriation of ash during flowage or by postemplacement sifting. Thus, our samples may be biased toward the coarser sizes. The particle-size distributions of three of the six

Table 50.—Average values and ranges of statistics for the particle-size distributions of 1980 volcanic deposits of Mount St. Helens

Type of deposit	Number of samples	Median phi size		Inman deviation		Quartile skewness		Kurtosis	
		Mean	Range	Mean	Range	Mean	Range	Mean	Range
Surge, May 18----	6	2.58	2.08 to 3.28	1.52	1.38 to 2.00	0.01	-0.09 to 0.16	0.26	0.23 to 0.30
Ash-cloud, May 18	6	4.32	3.87 to 4.68	2.03	1.60 to 2.27	-.10	.01 to -.34	.29	.23 to .33
Pyroclastic flow,									
May 18 ------	9	.72	.07 to 1.60	2.69	1.40 to 3.43	-.48	-.02 to -.82	.29	.23 to .38
June 12------	6	.26	1.15 to -2.01	3.42	1.69 to 4.66	-.81	-.30 to -1.70	.33	.24 to .48
July 22 -----	6	-.14	1.20 to -3.68	3.91	2.78 to 4.94	-.42	-.40 to 1.83	.31	.24 to .36
August 7-----	4	-1.40	-.10 to -3.15	4.32	3.73 to 4.68	-.52	.67 to -1.81	.39	.34 to .41
October 16-18	6	.10	-1.06 to 1.91	3.96	3.44 to 4.52	-.62-	.08 to -1.59	.29	.16 to .35

samples are bimodal, with the major modes falling in the coarsest size fractions, from 32 to greater than 64 mm (table 52). This distribution reflects the abundance and relatively high density of coarse pumice fragments in the June 12 pyroclastic-flow deposits.

July 22.—Pyroclastic-flow deposits of July 22 have intermediate median grain sizes but the greatest ranges of all the pyroclastic-flow deposits, spanning about 5 phi units (fig. 305, tables 50 and 53). One sample (80R-186a) shows the coarsest median grain size (about 12 mm) of all the samples of pyroclastic-flow deposits (table 53). The large range in median grain sizes probably reflects the broad range in grain sizes present in the prominent levees, lobes, and chan-

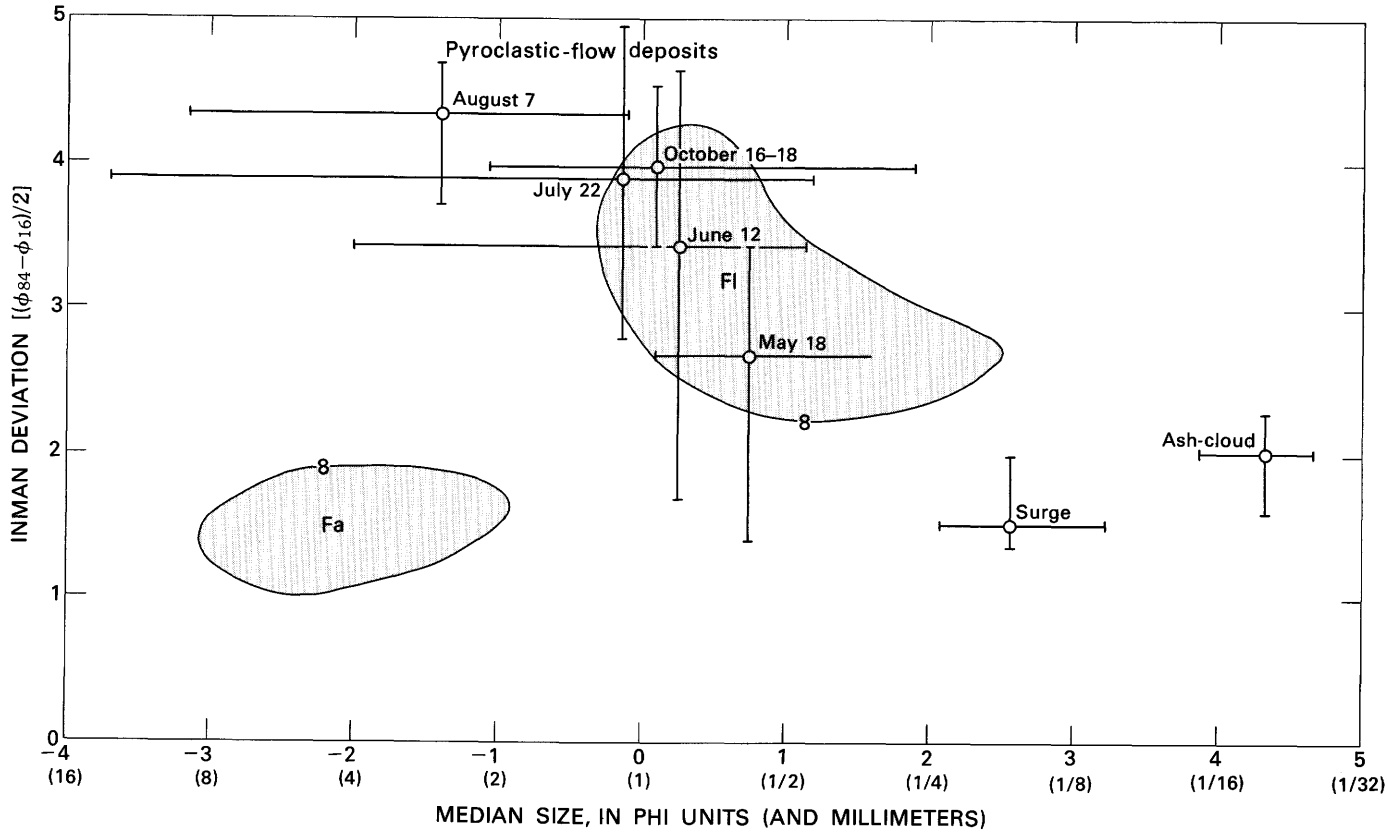

Figure 305.—Inman deviation versus median phi size of pyroclastic-flow, surge, and ash-cloud deposits. Symbols with error bars show average values and range in values for samples of a single type and date. The 8-percent contour lines outline major concentrations of values for pyroclastic-flow (Fl) and pyroclastic-fall (Fa) deposits as reported by Walker (1971).

Table 51.—Particle-size distributions and statistics for pyroclastic-flow deposits of the May 18, 1980, eruption of Mount St. Helens

Size-class limits		Sample number								
phi	mm	K80-39	K80-21	80R-225	80R-223	80R-183d	K80-71	80R-237	80R-232b	80R-232c
		Weight percent of total sample								
-6	64------	0	0	0.3	1.8	4.1	0	0	8.3	5.0
-5	32------	0	0	7.4	7.4	2.9	7.3	1.9	10.9	9.0
-4	16------	0	2.0	7.1	9.2	8.0	5.4	8.8	9.4	9.2
-3	8------	2.5	7.2	8.1	8.7	7.7	7.7	11.6	7.2	10.3
-2	4------	8.0	11.7	9.5	8.9	8.2	8.8	10.7	7.0	8.0
-1	2------	9.4	12.4	9.9	9.0	8.4	8.6	9.0	6.7	7.2
0	1------									
1	1/2-----	14.7	16.4	12.3	12.1	11.6	11.8	12.3	10.2	10.8
2	1/4-----	27.6	22.5	17.1	16.8	15.6	18.7	19.7	16.4	17.0
3	1/8-----	18.0	15.6	14.0	12.9	14.2	15.1	13.7	12.5	12.8
4	1/16----	15.9	9.1	7.3	7.0	8.1	10.4	5.2	5.4	5.7
		4.0	3.2	6.9	6.3	11.2	6.2	7.1	6.1	5.0
		Statistics								
Median phi size--		1.60	0.98	0.68	0.48	0.95	1.02	0.68	0.10	0.07
Quartile mean----		1.58	.78	.06	-.06	.44	.49	.13	-.72	-.46
Inman deviation--		1.40	2.01	2.78	2.98	3.08	2.84	2.65	3.43	3.06
Quartile skewness		-.02	-.21	-.63	-.54	-.51	-.54	-.56	-.82	-.53
Kurtosis---------		.23	.27	.25	.30	.27	.27	.30	.38	.31

nels of the July 22 pyroclastic flow deposits (Rowley and others, this volume); the coarsest particles are concentrated at levee crests and lobe margins, and the finest particles are concentrated in the center of channels. The July 22 deposits are more poorly sorted (higher deviation) than any earlier pyroclastic-flow deposit, but later pyroclastic-flow deposits are even more poorly sorted.

August 7.—Samples of pyroclastic-flow deposits of August 7 have the largest average median grain size of all the pyroclastic-flow deposits (fig. 305, tables 50 and 54). This greater coarseness apparently results from the lower degree of vesiculation in the August samples; it is also possible that some of these deposits originally had a more regular size distribution and that fine-grained particles were winnowed out. The August samples have the highest average deviation (poorest sorting) but the lowest range in total deviation (tables 50 and 54). Thus, the August 7 pyroclastic-flow deposits are the most poorly sorted of all 1980 pyroclastic-flow deposits.

The particle-size distributions of all four samples from the August 7 pyroclastic-flow deposits are strongly bimodal, with the major mode occurring in the coarsest size fraction (32 to larger than 64 mm).

Table 52.—Particle-size distributions and statistics for pyroclastic-flow deposits of the June 12, 1980, eruption of Mount St. Helens

[Underlined statistics are estimates calculated from extrapolations of cumulative curves]

Size-class limits		Sample number					
phi	mm	K80-72	K80-62	80R-184a	80R-183c	K80-23	80R-186c
		Weight percent of total sample					
-6	64----	0	0	0	0	0	26.7
-5	32----	0	0	3.5	16.7	26.7	3.2
-4	16----	0	0	6.4	9.0	1.0	3.9
-3	8----	2.0	4.9	4.3	5.8	5.0	9.0
-2	4----	3.1	8.9	5.8	4.2	5.4	6.9
-1	2----	9.2	10.3	7.2	4.3	6.4	6.8
0	1----	18.1	10.4	8.5	4.6	18.7	6.8
1	1/2---	21.9	13.5	13.4	7.2	10.2	9.3
2	1/4---	23.5	17.4	18.3	10.3	12.9	10.5
3	1/8---	11.9	16.5	14.9	10.61	10.3	7.9
4	1/16---	7.1	13.7	8.2	10.0	6.6	5.0
		3.4	4.5	9.4	17.0	6.9	3.9
		Statistics					
Median phi size--		.83	1.15	1.05	0.80	-0.29	-2.01
Quartile mean----		.17	.85	.57	-.45	-1.66	-2.51
Inman deviation--		1.69	2.45	2.93	4.66	4.21	4.35
Quartile skewness		-.66	-.30	-.48	-1.25	-1.37	-.50
Kurtosis---------		.24	.29	.24	.35	.38	.38

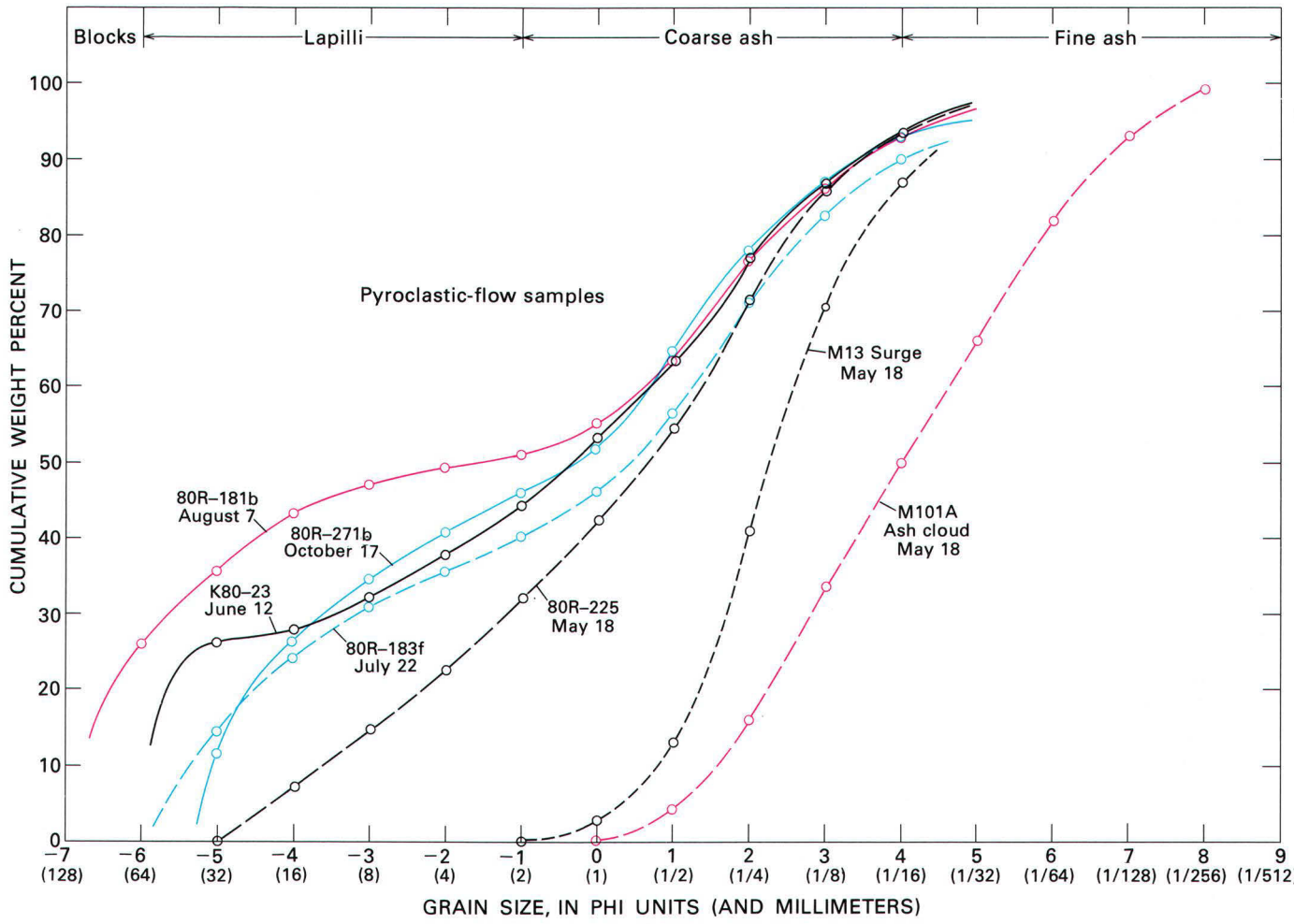

Figure 306.—Cumulative percent curves for grain sizes of representative samples of pyroclastic-flow deposits from eruptions of May 18, June 12, July 22, August 7, and October 16–18, and surge and ash-cloud deposits of the eruption of May 18.

The minor mode occurs in the 1/2–1/4 mm size class in all four samples (table 54).

October 16–18.—The particle size distributions of pyroclastic-flow deposits of October 16–18 are similar to those of the July 22 eruption in terms of median grain size and deviation (tables 50 and 55). All six samples have bimodal particle size distributions, with one mode in the largest size class in two of the samples and in the next to largest size class in the other four samples. The other mode occurs in the 1/2–1/4 mm size range in all samples.

ASH-CLOUD DEPOSITS

Ash-cloud deposits (Rowley and others, this volume) were formed during all major pyroclastic-flow eruptions but accumulated in significant volume only during the May 18 eruption. Table 56 lists the particle size distributions and statistics of six representative samples of the May 18 ash-cloud deposits. The distinctive field of the ash-cloud deposits in terms of median phi size and Inman deviation is shown in figure 305. Ash-cloud deposits are characterized by the smallest median grain size (about 1/25 mm) of all the deposits of the 1980 eruptions (tables 50 and 56). The low values of the weight percents in the 1/16–1/32 mm size class (table 56) may be spurious and simply reflect the change in size determination technique for particle sizes less than 1/16 mm.

Ash-cloud deposits consist dominantly of glass shards and broken crystals; crystals are more abundant in size fractions above 1/16 mm than they are in

Table 53.—Particle-size distributions and statistics for pyroclastic-flow deposits of the July 22, 1980, eruption of Mount St. Helens

[Underlined statistics are calculated from extrapolations of cumulative curves]

Size-class limits		Sample number					
phi	mm	80R-183	80R-188a	80R-183f	K80-60	80R-182a	80R 186a
		Weight percent of total sample					
-6	64----	0	0	0	0	15.0	23.0
-5	32----	3.8	12.7	14.4	0	7.5	13.4
-4	16----	4.0	10.0	8.7	1.2	1.9	12.1
-3	8----	5.6	3.3	7.8	16.7	4.8	4.5
-2	4----	6.4	3.6	4.2	11.0	5.6	1.1
-1	2----	6.4	5.0	5.3	9.0	5.5	1.3
0	1----	7.2	6.4	6.1	9.0	7.3	2.1
1	1/2---	12.7	12.5	10.5	14.5	12.2	6.2
2	1/4---	17.5	15.0	14.3	16.8	13.5	10.0
3	1/8---	14.0	9.8	11.4	11.7	10.9	7.9
4	1/16---	8.9	9.5	7.1	8.8	7.0	6.1
		13.5	12.3	10.4	1.5	9.0	12.3
		Statistics					
Median phi size--		1.20	0.79	0.43	0.15	0.25	-3.68
Quartile mean----		.80	-.34	-.78	-.31	-.88	-1.86
Inman deviation--		3.08	4.21	3.98	2.78	4.46	4.94
Quartile skewness		-.40	-1.13	-1.21	-.46	-1.13	1.83
Kurtosis---------		.24	.32	.32	.32	.30	.36

finer size fractions. The ash-cloud deposits include pumice and lithic fragments as large as 8 mm (table 56); these are probably contaminants incorporated into the ash-cloud deposits as a result of erosion of the upper surface of underlying deposits by the turbulent ash-cloud winds. The ash-cloud deposits locally include accretionary lapilli and dacite fragments like those in lateral-blast deposits that in places underlie them. The size distribution of the ash-cloud deposits is consistent with transport by turbulent clouds above the basal avalanche of the pyroclastic flow; such clouds would be expected to carry only fine-grained material elutriated from the basal avalanche.

SURGE DEPOSITS

Surge deposits are planar to crossbedded dune deposits that consist of mostly fine-grained particles. They formed during all eruptions but accumulated in significant volume only during the May 18 and June 12 eruptions (Rowley and others, this volume). Table 57 lists the particle size distributions and statistics of six representative samples of the May 18 surge deposits. The distinctive field of the surge deposits in terms of median phi size and Inman deviation is shown in figure 305. The particle size distibutions of the surge deposits are characterized by variable positive and negative skewness and median grain size of about 1/4 mm (table 57). Surge deposits are coarser grained than ash-cloud deposits but finer grained than pyroclastic-flow deposits (table 50, fig. 305).

Particles larger than about 2 mm are mainly lithic and pumice fragments, crystals and minor amounts of glass fragments occur in the 1/4–1 mm size range, and glass fragments are the main component of particles smaller than 1/4 mm. With respect to pyroclastic-flow deposits, the surge deposits have a higher lithic fragment-to-pumice ratio in the larger size classes and a higher glass-to-crystal ratio in the smaller size classes. The lithic fragment-to-pumice ratio may be higher because erosion of the upper surface of underlying deposits leaves a lag of lithic fragments that are subsequently surrounded by the ash. The high glass-to-crystal ratio may be a consequence of the relative terminal fall velocities of the two components in the turbulent surge clouds. Crystals settle out of the clouds faster than the less dense glass fragments.

Table 54.—Particle-size distributions and statistics for pyroclastic-flow deposits of the August 7, 1980, eruption of Mount St. Helens

[Underlined statistics are calculated from extrapolations of cumulative curves]

Size-class limits		Sample number			
phi	mm	80R-181c	80R-181a	80R-181b	80R-181e
		Weight percent of total sample			
-6	64----	0	31.9	26.1	19.2
-5	32----	14.2	6.6	9.4	16.4
-4	16----	11.9	7.8	7.8	3.5
-3	8----	10.4	4.0	3.8	2.6
-2	4----	6.7	3.6	2.1	2.2
-1	2----	5.5	3.9	2.4	2.7
0	1----	5.7	4.7	3.6	3.7
1	1/2---	10.3	7.6	9.0	9.7
2	1/4---	13.1	10.9	12.1	12.0
3	1/8---	9.7	8.5	9.6	9.6
4	1/16---	5.8	5.5	6.9	7.5
		6.7	5.1	7.2	11.0
		Statistics			
Median phi size--		-0.63	-3.15	-1.71	-0.10
Quartile mean----		-1.16	-2.48	-2.10	-1.79
Inman deviation--		3.73	4.21	4.65	4.68
Quartile skewness		-.53	-.67	-.39	-1.81
Kurtosis---------		.34	.40	.41	.40

Table 55.—Particle-size distributions and statistics for pyroclastic-flow deposits of the October 16–18, 1980, eruption of Mount St. Helens

[Underlined statistics are calculated from extrapolations of cumulative curves]

Size-class limits		Sample number					
phi	mm	80R-271a	80R-271b	80R-271c	80R-275	80R-247c	80R 247d
		Weight percent of total sample					
-6	64----	6.4	0	0	0	7.7	9.0
-5	32----	13.4	11.1	7.2	10.0	6.4	11.5
-4	16----	9.7	15.5	20.9	3.3	2.1	5.6
-3	8----	8.8	8.0	11.2	2.4	2.1	4.2
-2	4----	6.3	6.3	5.9	3.6	1.2	2.7
-1	2----	5.0	5.4	5.3	3.8	2.0	2.8
0	1----	5.3	5.5	5.6	4.7	3.7	3.9
1	1/2---	10.5	11.9	11.2	8.6	11.5	10.8
2	1/4---	12.0	13.2	11.7	15.5	18.4	16.5
3	1/8---	7.4	8.6	6.6	18.5	16.0	12.4
4	1/16---	8.7	6.5	9.6	14.4	11.1	8.2
		6.4	8.1	5.0	15.3	17.7	12.6
		Statistics					
Median phi size--		-0.91	-0.28	-1.06	1.91	1.71	-0.79
Quartile mean----		-1.35	-1.15	-1.26	1.38	1.64	-.80
Inman deviation--		4.09	3.80	3.70	3.44	4.21	4.52
Quartile skewness		-.44	-.87	-.20	-.53	-.08	-1.59
Kurtosis---------		.33	.34	.35	-.20	.16	.35

Table 56.—Particle-size distributions and statistics for ash-cloud deposits of the May 18, 1980, eruption of Mount St. Helens

Size-class limits		Sample number					
phi	mm	M104B	M110B	M106	M100D	M101A	M115
		Weight percent of total sample					
-3	8----	1.3	0	0	0	0	1.2
-2	4----	3.2	.2	0	0	0	.1
-1	2----	2.9	.3	.2	.1	.1	.3
0	1----	1.6	.6	.4	.3	.7	.6
1	1/2---	2.2	2.3	2.6	2.0	3.7	1.6
2	1/4---	6.6	8.7	10.1	9.5	12.0	8.5
3	1/8---	11.0	14.9	15.8	17.5	17.3	17.6
4	1/16---	14.5	17.2	15.8	18.1	16.2	23.1
5	1/32---	10.3	10.8	12.2	8.9	16.1	22.5
6	1/64---	23.6	21.5	20.5	20.8	15.7	14.5
7	1/12---	14.5	14.9	16.9	17.2	11.4	8.2
8	1/25---	7.5	7.6	5.0	4.9	5.9	1.9
		.5	.7	.8	.8	.7	.3
		Statistics					
Median phi size--		4.68	4.61	4.38	4.36	4.00	3.87
Quartile mean----		4.34	4.39	4.34	4.37	4.00	3.87
Inman deviation--		2.27	2.07	2.10	2.02	2.09	1.60
Quartile skewness		-.34	-.22	-.04	.01	0	0
Kurtosis---------		.23	.30	.32	.33	.29	.26

INTERPRETATION OF DATA

The textures and shapes of plagioclase, orthopyroxene, amphibole, and iron-titanium oxide phenocrysts suggest that these minerals crystallized both early and late in the crystallization history of the magma. Early crystals formed under higher temperature and pressure conditions and were probably not in equilibrium with the melt under later conditions of lower temperature and pressure, as evidenced by resorption and reaction rims on some of the crystals of each of four phenocryst phases. Later crystals of each of the four phenocryst phases are more euhedral, suggesting that they were in equilibrium with and crystallizing from the magma at the time of eruption and quenching. The progressively thicker and more coarse grained reaction rims on amphibole crystals in pumice samples from successively younger pyroclastic-flow deposits suggest that amphibole became increasingly unstable as water content in the magma declined.

Experimental studies at 2 kbar total pressure indicate that hornblende in dacite from Crater Lake, Oreg., crystallizes from the melt only if the water content is above about 5 weight percent and if the temperature is less than 975°C (Ritchey and Eggler, 1978). The phenocryst assemblage of the 1980 Mount St. Helens pumice, which includes amphibole but very little clinopyroxene, suggests that the magma had a fairly high water content. The experimental studies suggest that hornblende in the Crater Lake dacite formed by reaction of the liquid with earlier formed minerals; however, the textures and shapes of amphibole in pumice from Mount St. Helens indicate clearly that some of the amphibole was crystallizing at the time of eruption. The reaction rims on some of the amphibole crystals and the shape of the amphibole stability curve presented by Ritchey and Eggler indicate that loss of water pressure was probably a significant factor that affected the stability of amphibole and the other phenocryst phases.

The plagioclase composition and modal data of this report and the bulk chemical composition data of Lipman, Norton, and others (this volume) suggest that each successive eruption tapped a deeper level in a thermally and compositionally zoned magma source, in which plagioclase became more calcic and the amounts of orthopyroxene, hypersthene, and iron-titanium oxide minerals increased with depth.

Successively younger pyroclastic flows are generally characterized by progressively smaller volumes (Rowley and others, this volume) and, in most cases,

Table 57.—Particle-size distributions and statistics for surge deposits of the May 18, 1980, eruption of Mount St. Helens

Size-class limits		Sample number					
phi	mm	K80-47	K80-57	80R-2406	M13	M5	M11
		Weight percent of total sample					
-3	8----	1.1	0.1	4.5	0	0.9	0
-2	4----	.6	1.4	1.2	0	4.2	.3
-1	2----	.8	1.1	.8	.2	4.1	.8
0	1----	1.2	1.9	1.4	2.2	6.3	3.0
1	1/2---	4.0	6.6	5.4	11.0	13.0	12.9
2	1/4---	14.3	18.3	15.5	27.6	19.5	29.8
3	1/8---	22.8	21.6	24.8	29.5	20.3	28.3
4	1/16---	25.2	26.2	24.1	16.7	14.9	14.1
		30.0	22.7	22.4	12.8	16.9	10.8
		Statistics					
Median phi size--		3.23	2.95	2.90	2.25	2.09	2.08
Quartile mean----		3.15	2.86	2.85	2.41	2.08	2.21
Inman deviation--		1.45	1.47	1.58	1.30	2.00	1.30
Quartile skewness		-.08	-.09	-.06	.16	-.01	.13
Kurtosis---------		.30	.30	.23	.24	.24	.23

poorer sorting, larger particle sizes, and lower porosity in pumice fragments. These factors suggest that successive eruptions and emissions of gas between eruptions have strongly depleted the magma of its volatile components. As a consequence, successive pyroclastic flows show progressively smaller amounts of vesiculation and gas thrust. If no new magma is added to the magma reservoir, future eruptions may be less violent and likely will produce viscous domes, and (or) lava flows of more mafic composition, and (or) smaller volumes of pyroclastic-flow deposits.

REFERENCES CITED

Chleborad, A. F., Powers, P. S., and Farrow, R. A., 1975, A technique for measuring bulk volume of rock materials: Association of Engineering Geologists Bulletin, v. 12, no. 4, p. 317–322.

Daly, R. A., Manger, G. E., and Clark, S. P., Jr., 1966, Density of rocks, *in* Clark, S. P., Jr., ed., Handbook of physical constants, (revised edition): Geological Society of America Memoir 97, p. 20–26.

Haggerty, S. E., 1976, Oxidation of opaque mineral oxides in basalts *in* Rumble, D., III, ed., Oxide Minerals: Mineralogical Society of America, Short Course Notes, v. 3, 100 p.

Johnson, G. R., 1979, Textural properties, *in* Initial report of the petrophysics laboratory: U.S. Geological Survey Circular 789, p. 70–71.

Krumbein, W. C., 1934, Size frequency distributions of sediments: Journal of Sedimentary Petrology, v. 4, p. 65–77.

Murai, I., 1960, Pumice-flow deposits of Komogatake: Tokyo University Earthquake Research Institute Bulletin, v. 38, p. 451–466.

Ritchey, J. L. and Eggler, D. H., 1978, Amphibole stability in a differentiated magma chamber; an experimental investigation: Carnegie Institution of Washington Yearbook 77, p. 790–793.

Slemmons, D. B., 1962, Determination of volcanic and plutonic plagioclases using a three- or four-axis universal stage—Revision of Turner method: Geological Society of America Special Paper 69, 64 p.

Walker, G. P. L., 1971, Grain size characteristics of pyroclastic deposits: Journal of Geology, v. 79, p. 696–714.

LAVA DOMES

Extrusions of steep-sided domical masses of viscous silicic lava commonly follow discharge of more fluid gas-rich magma as pyroclastic material. At least half a dozen dacitic domes have formed at Mount St. Helens in the past few thousand years, including the large summit dome that capped the volcano prior to the 1980 eruptions; accordingly, the appearance of a lava dome within the crater formed on May 18 was anticipated. Detailed observations were made on rates, shapes, and compositions of successive phases of growth of the ensuing composite dacitic dome that grew later during 1980. Many prehistoric domes, at Mount St. Helens and at other similar volcanoes, probably evolved by similarly complex growth patterns that generally could not, however, be deduced from the resulting final deposit.

Rise of magma to a shallow level beneath the new crater was indicated in early June by increased SO_2 gas emission and by a central warm area detected by airborne radiometers. The first dome, of dacitic composition similar to associated pyroclastic material, grew for at least 7 days following the June 12 explosive activity (Moore, Lipman, and others), eventually reaching about 365 m in diameter and 45 m in height. The central part of this dome was blown out during the July eruption, and the resulting inner crater was largely filled by a second smaller dome that grew for about a day following explosive eruptions on August 7. A somewhat more mafic dome of silicic andesite, intermediate in size between the June and August domes, formed at the same site in about half a day following the Oct. 16–18 pyroclastic eruptions. Between December 27 and January 3, two dacitic dome lobes were erupted from flanks of the October dome without significant premonitory pyroclastic activity. All the 1980 dome units were subcircular in plan and developed apical sags or collapse pits during late stages of growth, due either to lateral spreading, degassing, or to withdrawal of magma from below. Further growth of the composite dome of 1980 was anticipated, and beginning on February 12, 1981, another extrusion occurred from the crest of the October dome.

Physical, electric, and thermomagnetic properties of samples of the June 1980 dome, determined under laboratory conditions, suggest atypically low oxygen and sulfur activities in the magma, probably due to effective degassing prior to extrusion of the dome (Olhoeft and others). The thermal energy of the June dome, calculated from laboratory determinations of physical properties, was used to calibrate energy estimates for other phases of the 1980 eruptions (Friedman, Olhoeft, and others). The total energy yield of the eruptions through October 1980 is estimated at 1.33×10^{25} ergs, similar in yield to the eruption of Mauna Loa (Hawaii) in 1950 but only half as great as the directed-blast eruption of Bezymianny (Kamchatka) in 1956.

THE 1980 ERUPTIONS OF MOUNT ST. HELENS, WASHINGTON

GROWTH OF LAVA DOMES IN THE CRATER, JUNE 1980–JANUARY 1981

By JAMES G. MOORE, PETER W. LIPMAN, DONALD A. SWANSON, *and* TAU RHO ALPHA

ABSTRACT

Five episodes of explosive magmatic activity have occurred between May 25, 1980, and early January 1981, within the May 18 crater beneath the pre-May 18 summit of the volcano. After explosions waned in three of these episodes (June 12, August 7, and October 16–18), a dacite or andesite lava dome rose within the small explosion crater. In late December and early January 1981, extrusion of lava tripled the volume of the preexisting October dome.

The dacitic June dome grew for at least 7 days following the June 12 explosive activity, and by June 28–29 was dormant and possibly slightly collapsing. It grew to 365 m in diameter and 45 m in height, with a volume of about 4.7×10^6 m^3. The dome was partly destroyed and covered with tephra during the July 22 eruption.

The dacitic to andesitic August dome grew for slightly more than a day following the August 7 explosive activity. It was emplaced within the July 22 crater to a height of about 60 m, with a surface diameter of about 120 m and a volume of 0.7×10^6 m^3.

The andesitic October dome grew rapidly for only about one-half day following the October 16–18 explosive activity that blasted out the August dome and probably part of the remaining June dome. For several days following this rapid growth, the dome sagged at the summit and continued to spread outward. At the end of October the dome was about 225 m in diameter and 37 m high and had a volume of about 1.5×10^6 m^3.

The December composite dome grew by enlargement of the October dome from about December 27, 1980, to January 2–4, 1981. The eruption added two subcircular dacite lobes to the October dome by slow extrusion of lava beneath a solidified carapace. The southeast lobe is about 200 m in diameter and 90 m high, and the northwest lobe is about 75 m in diameter and 40 m high. The resulting composite dome has a volume of about 5×10^6 m^3, of which about 3.5×10^6 m^3 was erupted during the end-of-the-year event.

INTRODUCTION

Following the great eruption of May 18, five episodes of moderate explosive activity occurred in 1980: May 25, June 12, July 22, August 7, and October 16–18. After explosions waned in three of these episodes (June, August, and October), stiff, viscous dacite or andesite lava domes rose within and, in two cases, overflowed the inner explosion crater. Beginning in late December, nonexplosive extrusion enlarged the October dome. All of the domes appear to have been fed from the same conduit, which lies 1 km beneath the previous summit area of the mountain and beneath the center of the pre-May 18 explosion crater. The domes are compared in table 58.

Detailed maps of the domes have not yet been made from aerial photographs. In this report the domes are shown in a series of oblique physiographic drawings (fig. 307), based in part on the topographic map made from July 1 aerial photographs. Details of the domes are based on vertical and oblique photographs and on reports from observers. Calculated volumes of the domes include only the visible part

and do not consider that part in buried craters or within the feeding conduit.

ACKNOWLEDGMENTS

Michael Holtsclaw, Terry Leighley, Donald Peterson, and Peter Rowley made important observations of dome growth.

THE JUNE DOME

The first dome of the 1980 eruptions grew in the crater following the explosive eruption during the night of June 12. Weather conditions prevented direct observations until the morning of June 15, and at this time the dome was a symmetrical circular mass, tan to light gray, with an estimated diameter of 200 m and height of 30–40 m.

Several features suggest that an intrusive dome may have been close to the surface before and during the June 12 eruption. On June 11, a crescent-shaped lake about 300–400 m long and 50–75 m wide occupied much of the south side of the crater floor (fig. 307*A*). This lake partly surrounded a tephra-covered mound centered where the dome later emerged. This mound probably resulted from an early subsurface rise of the June dome, although possibly it reflected an earlier cryptodome emplaced at the end of the May 25 activity. The character of the pyroclastic flows erupted on June 12 also suggests the presence of a cryptodome at shallow depth. The deposits of June 12 contain abundant blocks of dense gray dacite as much as 2 m in diameter, which contrast with the highly vesicular pumiceous ash flows erupted on May 18. The June 12 deposits are similar, in some ways, to block-and-ash flows emplaced as a result of dome collapse and perhaps originated, in part, from fragmentation of the solidified margin of a growing, subsurface dome. The small pyroclastic flows of May 25 were transitional in fragment size and vesicularity between those of May 18 and June 12, and were probably representative of the evolving shallow magma body that eventually reached the surface as a dome. All subsequent ash flows contain such relatively dense, breadcrusted blocks, which were presumably derived from preexisting domes or cryptodomes.

Observations made during the latter half of June revealed a slow growth in the height and diameter of the dome. The cracked, breadcrust-like surface remained similar in appearance but became somewhat grayer in color, because of increased ash cover, and local accumulations of yellowish sulfur and iron hydroxides appeared. Eruptions of tephra occurred locally from areas of gas emissions at the margin of the dome in late June. Between June 15 and 28, the crater walls and floor were devoid of running or standing water, but by June 28 a small pond had formed on the southwest side of the crater. Aerial photographs taken July 1 indicate that the dome was about 365 m in diameter, 45 m high, and precisely centered beneath the previous phreatic crater that had formed at the summit of the volcano between March 27 and May 18 (fig. 307*B*).

Measurements of dome size were started on June 15, using helicopter altimetry, and on June 19, using theodolite-angle measurements; but observations were repeatedly hampered by limited visibility due to clouds, fume, and wind-blown ash. The helicopter altimetry observations of changes in dome height were based on the lowest helicopter elevation at which the top of the dome could be observed across the top of a tephra rampart 200 m north of the dome summit. While measurements were taken, the helicopter hovered over a landmark 2 km north of the rampart until the dome crest came into view above the rampart. Although the helicopter altimeter readings are considered accurate only to about 15 m, the geometry of the line of sight permitted recognition of changes in dome height greater than 1.5–2 m. Repeated helicopter measurements indicated upward growth of the dome at 2–3 m per day from June 15

Table 58.—Comparison of dome dimensions, altitudes, volume, compositions, and dates of emplacement

[~, about]

	June dome	August dome	October dome	December[1] composite dome
Diameter (in meters)	365	120	225	SE lobe ~200 NW lobe ~75
Height (in meters)--	45	~60	37	SE lobe ~90 NW lobe ~40
Altitude of top (in meters).	1896	~1880	1952	~2000
Growth period-------	June 12–19.	Aug. 8–9.	Oct. 18–19.	From about Dec. 27 to Jan. 2–4.
Volume (in 10^6 m^3)--	4.7	0.7	1.5	[2] ~5
Silica content (in weight percent)[3].	63.6	63.0	61.5	63.2

[1]Rough, preliminary estimates.

[2]Total volume of October plus December-January dome material. Net volume increase is roughly 3.5×10^6 m^3.

[3]Compositions from Lipman, Norton, and others, this volume.

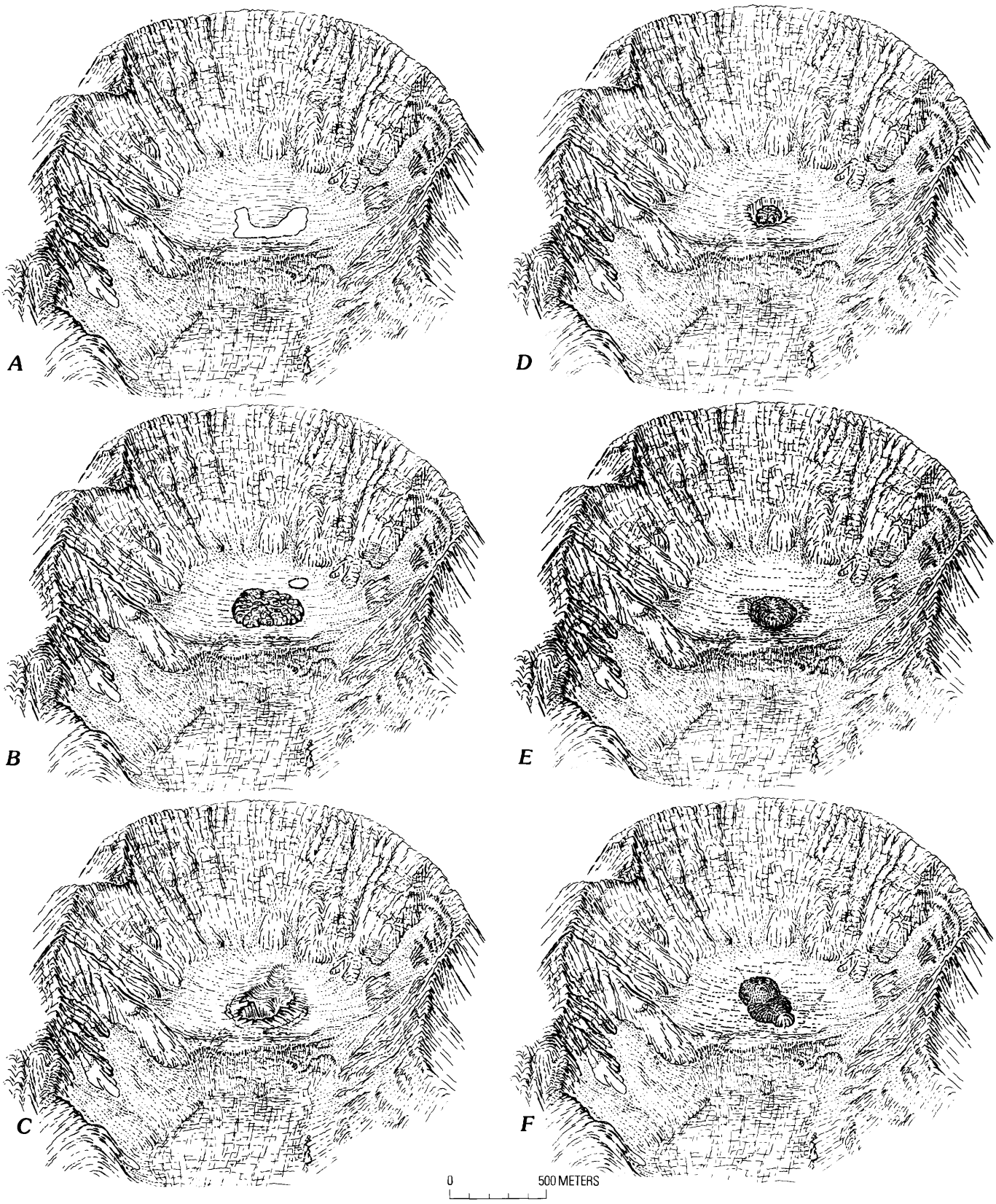

Figure 307.—View of the summit and amphitheater of Mount St. Helens from the north, at an angle of 30° above the horizon. No vertical exaggeration. A, June 11, 1980, showing crescent-shaped lake. B, July 1, 1980, showing the June dome. C, August 1, 1980, showing the crater formed July 22. D, August 10, 1980, showing the August dome. E, October 22, 1980, showing the October dome. F, January 10, 1981, showing the December dome.

through the late afternoon of June 19. No observations were made June 20–27 because of poor weather, but measurements of June 28–29 indicated no further dome growth, and possibly a slight subsidence.

Theodolite measurements were possible on June 19, 29, 30, and July 1, from a ridge 8.5 km north of the dome. They indicate that the dome was dormant and possibly collapsed about 2.5 ± 1 m between June 19 and July 1. These measurements suggest that the dome grew actively for at least 7 days (June 12–19), after which extrusion stopped and the dome collapsed slightly under its own weight. The volume of the dome at the end of June was about 4.7×10^6 m^3. It is composed of a relatively dense plagioclase-hypersthene-hornblende-augite dacite that is chemically similar (63.3–64.0 percent SiO_2) to pumice erupted June 12 (Lipman, Norton, and others, this volume).

THE AUGUST DOME

The explosive eruption of July 22 formed a new elongate crater (250×600 m), removed more than half of the June dome, and covered the remainder of the June dome with 5–10 m of tephra (fig. 307*C*). This crater exposed cross sections of the June dome in its east, north, and west walls. Deep vertical joints in the dome remained incandescent for more than a month. The south part of the crater extended, as a narrow trench, several hundred meters beyond the southern limit of the dome. The reason for this departure from the circular shape of other post-May 18 craters and domes is not known.

During the afternoon and night of August 7, relatively small explosive eruptions from the deep, northern part of the July crater ejected ash and fed a small pumiceous pyroclastic flow that swept north, part way to Spirit Lake. A dome began to rise in the vent crater during the morning of August 8. By the end of the day, the dome had filled the lower half of the 90-m-deep crater. The dome rose another 20 m by the morning of August 9, as determined by helicopter altimetry, and during that day reached to within 30 m vertically of the July crater rim. The height of the dome remained stable from August 10 through the morning of August 15, but helicopter measurements on August 17 indicated subsidence of 6–7 m, which may have occurred during a small eruption on the afternoon of August 15. A large cavern, about 10–20 m in diameter and depth, developed in the west base of the dome during the August 15 event. Dull incandescence was visible in this cavern and in deep summit cracks through August and much of September. The August dome was about 120 m in diameter (fig. 307*D*) and had a volume of about 0.7×10^6 m^3. No samples were collected in place from this dome; however, blocks apparently blown from it are generally similar, though slightly more mafic (63.0 percent SiO_2) than samples from the June dome.

THE OCTOBER DOME

A series of explosive eruptions that fed several pyroclastic flows began the evening of October 16, blowing out the small August dome completely, as well as most of the surrounding remnants of the June dome. The final eruption at 1428, October 18, threw a plume of pyroclastic material to a height of 6 km, leaving a shallow saucer-shaped depression about 250 m in diameter at the site of the former crater. As visibility improved at about 1520, a new dome, about 5 m high and 25 m across, was visible in this depression. An hour later the dome was about 10 m high and 40 m wide, and at 1830 it was 20–25 m high and 50–70 m wide. As the dome grew, slabs spalled off and rolled down the flanks, revealing the bright incandescent interior. Small trickles of orange-red, viscous lava oozed from several points on the west and east sides; the eastern streams fed a small pond in the moat between the dome and crater wall. Orange flame flickered from several holes in the side of the dome.

At 0925 on October 19, the dome covered most of the crater floor and was subcircular in plan, with a diameter of about 185 m. The height of the dome was about 50 m, as determined by helicopter altimeter and confirmed later in the morning by theodolite measurements from a ridge 8.5 km to the north. The surface of the dome was convex upward and was cut by deep cracks with incandescent walls. Several spires reached a few meters above the general surface. The sides of the dome were nearly vertical and frequently sloughed off, creating small talus cones (breches d'ecroulement). Noisy emission of gas occurred from various fumaroles around the base of the dome; several of these remained active until the December activity.

Theodolite measurements initiated at 1030 on October 19, documented changes in shape and dimen-

sions of the dome over the next several days. The dome subsided more than 18 m and widened more than 15 m (in some places more than 19 m) between October 19 and 27. These changes took place at a rate of as much as 2.1 m/hr on October 19 but had nearly stopped by October 27. During this period, the shape of the dome changed markedly and finally acquired a nearly flat top with a small depression near its center. Large cracks, as deep as 5–7 m, radiated from this depression like spokes on a wheel. A single spire rose 3–4 m above the general surface. The initiation of subsidence probably reflects the cessation of extrusion and the stagnation of the magma column. This apparently occurred during the night of October 18–19, and the dome then spread and sagged under its own weight.

The final diameter of the subcircular dome was about 225 m (fig. 307*E*), and the altitude of the upper surface was about 1,952 m; these figures were calculated from horizontal and vertical angles and checked by photogrammetry. The altitude of the October dome was more than 50 m higher than that of the June dome because of the tephra that had accumulated on the crater floor during the July, August, and October pyroclastic events. The height of the October dome above the floor of the explosion crater was about 37 m, as determined by hand leveling and vertical angles. The volume was about 1.5×10^6 m^3, assuming a cylindrical shape; the actual volume of extruded lava was probably somewhat greater, because the calculated volume did not consider the concave nature of the crater floor or the curved shape of the top of the dome.

Samples of the dome are silicic andesite with 60.8–61.5 weight percent SiO_2 (Lipman, Norton and others, this volume). This dome is more mafic, and hence less viscous than the previous domes, which accounts for its more rapid growth and relatively smoother surface. Small scattered inclusions of vesicular basalt with indistinct margins occur in the October dome and associated pumice. They suggest the possible mixing of a fluid basalt magma with the dominant silicic melt.

THE DECEMBER COMPOSITE DOME

The October dome was enlarged and strongly modified by an eruption between about December 27, 1980, and January 2–4, 1981. The eruption was preceded by several days of marked seismicity, increased radial cracking of the crater floor surrounding the dome, and sporadic ejection of vesicular tephra from vents on the dome. The eruption itself consisted wholly of slow extrusion of lava beneath a solidified carapace; no Plinian column or other significant tephra ejection occurred. The resulting enlarged composite dome, which includes most of the material of the October dome plus that erupted in late December 1980 and early January 1981, is here referred to as the December composite dome (fig. 307*F*).

Precise times at which the eruption began and ended are not known. The first observation of dome enlargement was from a fixed-wing aircraft at about 0900 on December 28, but poor visibility prevented observers from seeing into the crater for the previous day and a half. Visibility was good during the remainder of the eruption, but the rate of extrusion was so slow that the time of cessation could only be approximated at sometime between January 2 and 4.

The eruption added two subcircular lobes to the October dome. The larger of the two, the southeast lobe (fig. 308), was erupted from the southeast sector of the dome, from a wedge-shaped hole that had formed during an explosion on December 13. This lobe moved mainly toward the southeast, beyond the former margin of the dome. It was the first lobe to begin forming, and by 1500 on December 28 it was an estimated 50 m high and 60–80 m in east-west diameter. The southeast lobe grew slowly throughout the eruption. After extrusion had stopped, its height was estimated by helicopter altimetry at about 100 m, although collapse later reduced its height to about 90 m, and its paced east-west diameter was about 200 m. Precise dimensions are yet to be measured, but this lobe is clearly larger and higher than the October dome (fig. 308).

The smaller northwest lobe was not present on December 28 but had reached nearly its final size when first observed at 0830 on December 31. This lobe was erupted from a vent within the existing October dome, perhaps along a large crack that had slowly widened in November and December. The lobe spread a short distance north-northwestward beyond the former margin of the dome, barely overtopping the crest of the tephra rampart. Its final estimated width is about 75 m and its height about 40 m; precise measurements have not yet been made.

Both lobes are petrographically similar to one another and to previous dome rocks. Each has a scoriaceous carapace and a relatively nonvesicular in-

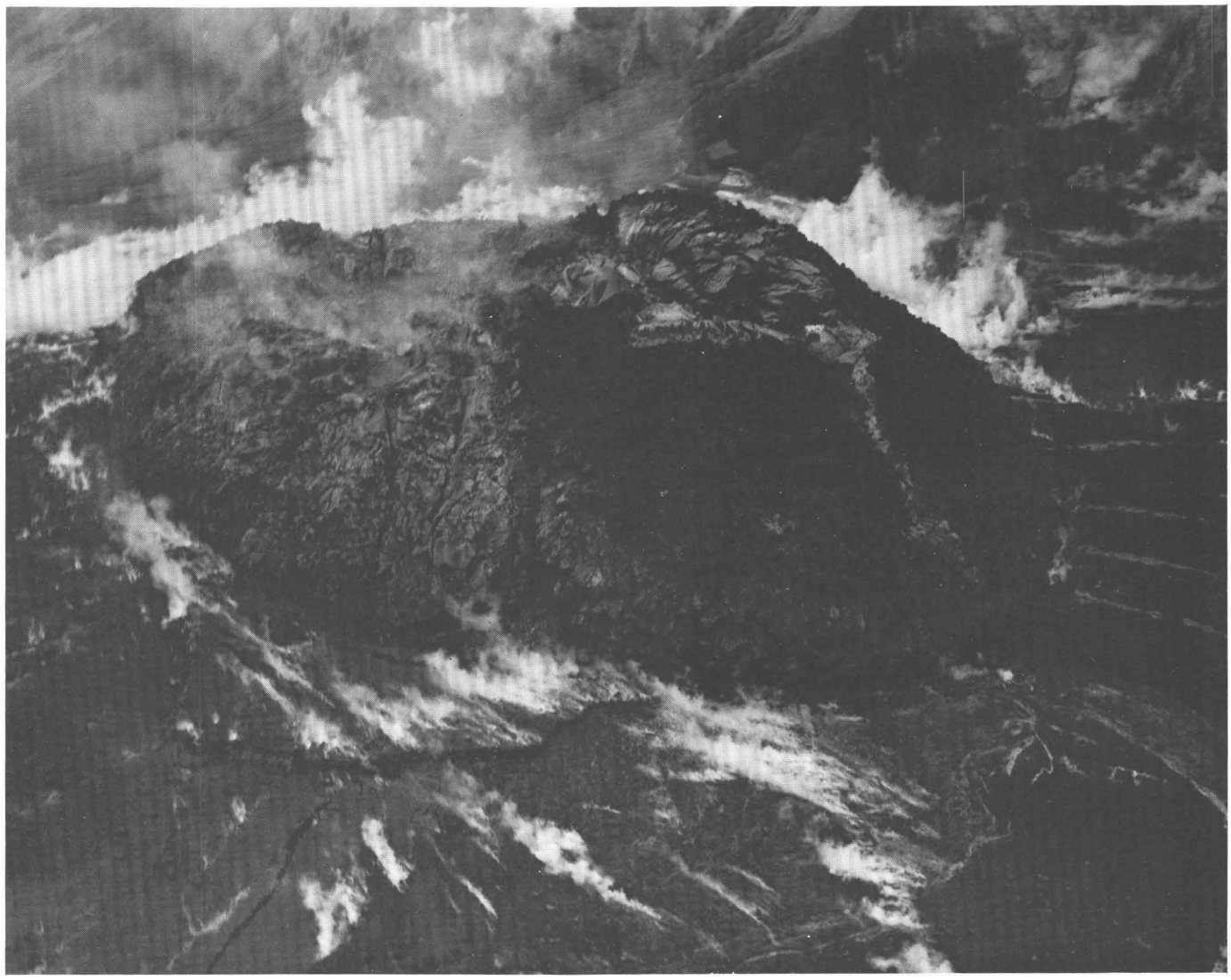

Figure 308.—The December composite dome from the south. On the right is the scoriaceous southeast lobe, erupted starting about December 28; it is about 200 m across and 90 m high. The smoother surfaced October dome, on left, has a pit at its crest that formed by subsidence during the December activity. Photograph by Terry Leighley, January 7, 1981.

terior, as indicated by talus blocks. Both lobes have an irregular, jagged crestal area resulting from a collapse following the end of extrusion. Large smooth-walled cracks radiated from a central zone; these cracks were present during extrusion but became more prominent after the eruption had ended and collapse began. Each lobe contains an estimated 2–3 percent inclusions, including plutonic rocks, amphibolite, hornfels, metavolcanic rocks, and rare white quartzite. An analyzed sample from the southeast lobe contains 63.2 percent SiO_2, compositionally similar to the August dome but more silicic than the October dome (table 58).

The existing October dome was deformed during December. On December 28, the surface of the October dome was uplifted 10–15 m from its former height. A spire towered 10–15 m above this surface at midday on December 28 but collapsed at 1545, leaving only a stump. The whole crestal area collapsed in early January, after most extrusion had stopped, creating a pit in the top of the October dome. The pit, an estimated 10–15 m deep and 30–40 m in diameter, is floored by rubble shed from the walls. Apparently the October dome had inflated as new magma rose and spread outward in the two new lobes. As the eruption ended, magma possibly withdrew into the

conduit, located directly below the uplifted area, and the surface of the dome subsided. Preliminary volume calculations indicate that the southeast lobe contains about 3×10^6 m^3 and the northwest lobe contains about 0.6×10^6 m^3. About 0.1×10^6 m^3 of magma moved out of the October dome, resulting in the summit collapse pit. The net volume addition to the October dome is about 3.5×10^6 m^3 and the volume of the December composite dome is about 5×10^6 m^3 (table 58).

THE 1980 ERUPTIONS OF MOUNT ST. HELENS, WASHINGTON

PHYSICAL PROPERTIES OF THE JUNE 1980 DACITE DOME

By G. R. OLHOEFT, R. L. REYNOLDS, J. D. FRIEDMAN, G. R. JOHNSON, *and* G. R. HUNT[1]

ABSTRACT

Physical properties of specimens of the June 1980 lava dome have been measured and compared with other volcanic products. The dome samples are medium-gray, crystal-rich dacite vitrophyres with 55:15:30 ratio of glass (including microlites) to vesicles to phenocrysts (mainly plagioclase). Reflection and transmission spectra, bulk density, and specific gravity are characteristic of dacite compositions. Electrical properties, volatile outgassing in vacuum, and thermomagnetic properties all suggest low oxygen and sulfur activities in the magma. The very low water and sulfur contents may have resulted from devolatilization of the magma prior to extrusion of the dome. Electrical measurements indicate extreme disequilibrium in the material as a result of rapid cooling and also extreme surface chemical reactivity as a result of emplacement of the upper levels of the dome under nearly anhydrous conditions.

INTRODUCTION

The presence of a protodome at shallow depths was suggested at least as early as June 8, 1980, when a large, hot area on the crater floor appeared on an infrared image obtained at 2128 PDT (Friedman, Frank, and Kieffer, this volume). The subsurface growth of this protodome was also suggested by the presence of a broad, low topographic feature in the center of the crater, which coincided with the location of the subsequently exposed dome (Moore and others, this volume). The character of the June 12 pyroclastic ejecta also suggested a protodome at shallow depth, perhaps blocking the vent at that time. The deposits of June 12 contained abundant blocks of dense gray dacite, similar to block-and-ash deposits ejected during dome collapse at other volcanoes. These blocks may have been derived from the solidified margins of the evolving dome prior to its emergence at the crater surface (Moore and others, this volume). The surface of the lava dome was cracked, ragged, and shattered, with ejected fragments and blocks spilled down its sides (fig. 309). For a description and history of this dome, see Moore and others (this volume) and Friedman, Frank, and Kieffer (this volume).

Several fragments ejected from the dome or protodome onto the tephra of the June 12 eruption were collected on the rampart north of the dome on June 29 (fig. 310). Sample JDF-6-29-80-1 is more vesicular than sample JDF-6-29-80-2, which has sulfurous sublimates on its surface and is more cracked (bread-crusted) on one side. Both samples are medium-gray crystal-rich dacite vitrophyre and are similar in mineral assemblage. Preliminary petrographic examination of JDF-6-29-80-1 (Ray Wilcox, written commun., 1980) indicated that the vesicular glassy matrix is crowded with pyroxene and feldspar microlites. The refractive index of the glass is 1.491–1.492, in contrast to the refractive index of 1.495–1.497 of most of the glass in the May 18 downwind tephra. The phenocrysts consist of zoned plagioclase (about An_{45-55}), orthopyroxene, hornblende (many grains with reaction rims), opaque oxide, and rare clinopyroxene (fig. 311). Approximate proportions are as follows:

[1]Deceased, March 26, 1981.

glass (including microlites)	55 volume percent
vesicles	15 volume percent
phenocrysts	30 volume percent
plagioclase	20 percent as tablets as large as 2 mm
orthopyroxene	5 percent as prisms as large as 1 mm
hornblende	4 percent as corroded prisms as large as 0.8 mm
opaque oxides	1 percent as cubes and octahedra as large as 0.18 mm (titanomagnetite and ilmenite)
clinopyroxene	trace as corroded crystals

Table 59.—Chemical analysis of June dacite (JDF-6-29-80-2)

[X-ray fluorescence analysis by J. Carr and A. Sarna-Wojcicki. Leaders (---) indicate no determination made]

Chemical	Percent
SiO_2	61.95
Al_2O_3	17.43
Fe_2O_3	5.05
MgO	1.89
CaO	5.28
Na_2O	4.25
K_2O	1.36
TiO_2	.67
P_2O_5	.14
MnO	.072
ZrO_2	---
Cr_2O_3	.03
NiO	.006
BaO	.064
SrO	.093
Total	98.25

One inclusion of calcic plagioclase and clinopyroxene about 8 mm long was also noted. In chemical composition, sample JDF-6-29- 80-2 is a low-silica dacite (table 59), similar to many analyzed samples of 1980 deposits (Lipman, Norton, and others, this volume). SiO_2 is somewhat low, in comparison with otherwise similar analyses of 1980 samples.

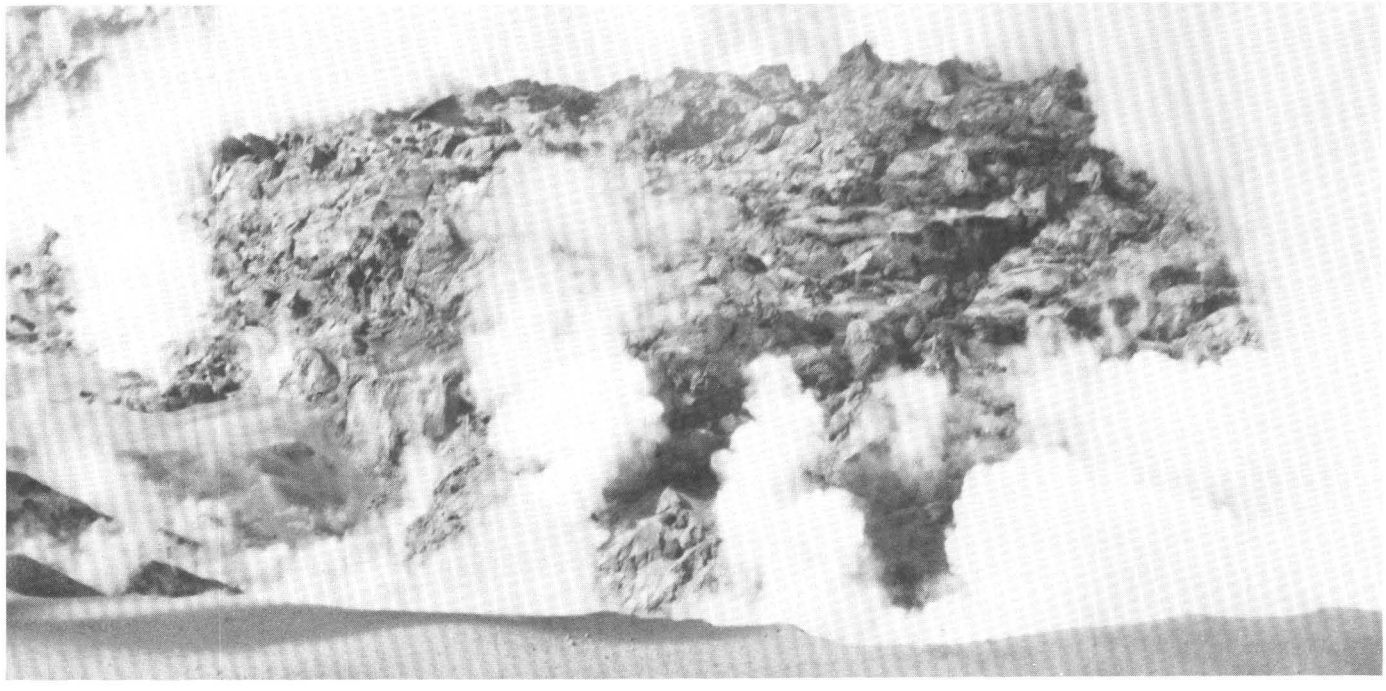

Figure 309.—Dacite dome from near ground level, looking south, June 29. Photograph by Jules Friedman from helicopter above point at which fragments were collected. Fracture in surface of dome is visible at upper right. Dome height is 65 m and east-west diameter is about 325 m, part of which is obscured by circumferential fumarole emanations.

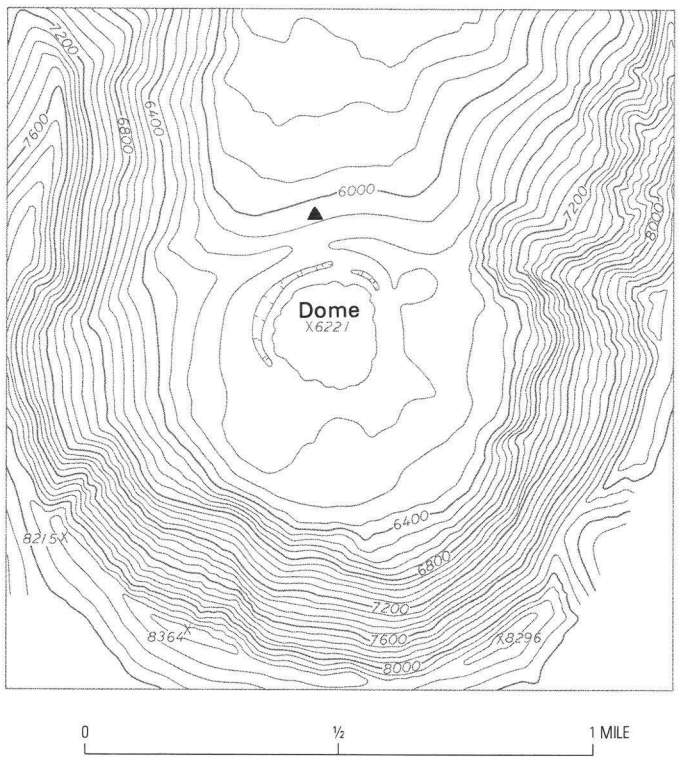

Figure 310.—Location of samples JDF-6-29-80-1 and -2 (shown by triangle); collected June 29, 1980.

The location of the collected fragments near the dome and on thick June 12 tephra deposits, the lack of alteration of the glass and microvesicularity of these specimens, and their chemical and petrographic similarity to other 1980 Mount St. Helens specimens suggest that the collected fragments were ejected from the dome (or protodome) during a degassing and chilling episode between June 12 and 29, 1980. Thus, many of the physical properties of the June dome, which was subsequently partly destroyed in the July 22 eruption, can be determined from these fragments.

SPECTROSCOPIC PROPERTIES

Spectral properties of rocks provide information on their mineral and chemical compositions and are also important for interpretation of thermal and other remote sensing images. The infrared reflection spectrum from 0.3 to 2.5 μm was recorded from the surface of powdered June dome sample JDF-6-29-80-2, and the transmission spectrum from 2.5 to 30 μm was recorded for the same sample embedded in a KBr matrix (Hunt, 1979).

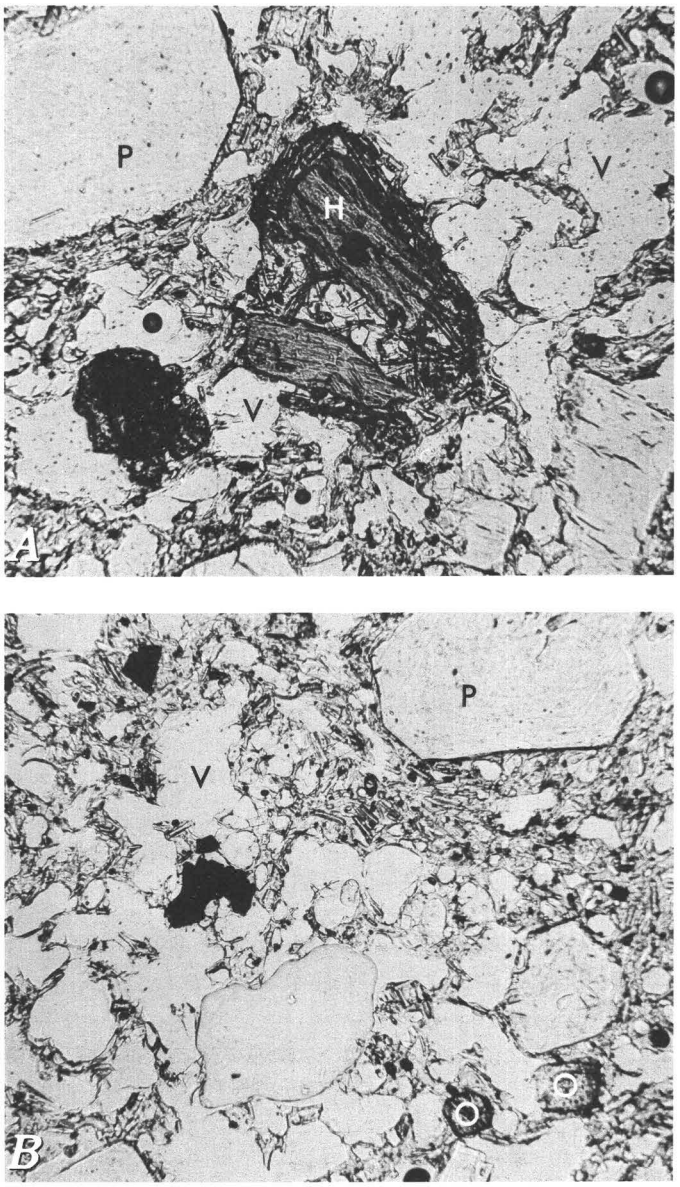

Figure 311.—Photomicrographs of dacite vitrophyre. Plane-polarized light; top edge of each photomicrograph is 1.0 mm. A, Sample JDF-6-29-80-1. Typical flow-banding expressed by pyroxene and plagioclase microlites in glass matrix between plagioclase (P) and hornblende (H) phenocrysts and between vesicles (V). Opaque oxides (black), chiefly titanomagnetite, occur within a hornblende phenocryst and in the adjacent reaction rim. B, Sample JDF-6-29-80-2. Pyroxene and plagioclase microlites strewn through a glassy matrix. The remainder of the section consists of vesicles (V) and orthopyroxene (O), plagioclase (P), and opaque oxide (black) phenocrysts.

Comparison of the infrared spectrum (determined by the bulk structure of the material) with those of other minerals and rocks (Hunt and Salisbury, 1974)

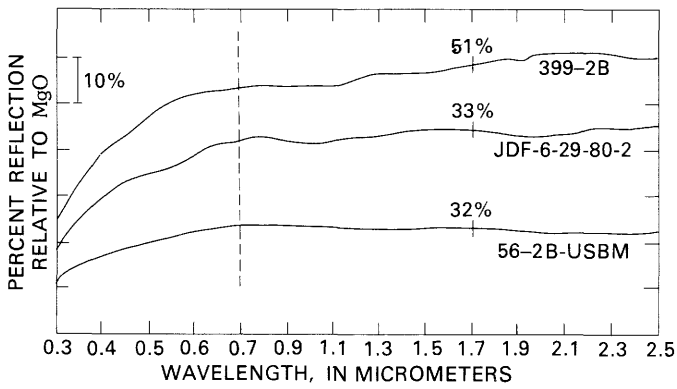

Figure 312.—Reflection spectra of Mount St. Helens dacite sample JDF-6-29-80-2 compared to two other dacites. Note scale change at 0.7 μm.

indicates that the spectral characteristics of the June dome resemble those of other dacites (fig. 312). Consequently, the spectra for sample JDF-6-29-80-2 are shown in figure 312 between those of two other dacite samples: sample 56-2B-USBM is composed mostly of sodic feldspar phenocrysts in a glassy matrix containing microcrystalline plagioclase laths, and sample 399-2B bears phenocrysts of quartz and magnetite in a glassy flow-banded matrix rich in microscopic feldspar laths.

The reflection spectra covering the ultraviolet, visible, and near-infrared ranges (fig. 312) are all quite nondescript, displaying only extremely weak specific absorption bands (inflections in curves near 0.55, 1.0, and 1.9–2.0 μm) and a decrease in reflectivity from 0.7 to 0.3 μm. This decrease is typical of materials containing even small amounts of iron. The sharper weak band near 1.9 μm in sample 399 is due to a minor amount of water, and the feature near 1.0 μm is due to iron. In the June dome sample, the two weak, broad bands at 1.0 μm and 1.95 μm suggest the presence of pyroxene. The low overall reflection values for the June dome sample and 56-USBM dacite suggest the presence of small amounts of magnetite or an equivalent oxide.

The segment of the infrared transmission spectrum (6–30 μm) which displays the most important features for silicates is shown in figure 313. The intense bands shown here are caused mostly by the fundamental O-Si-O stretching at 8–12 μm; the Si-O-Si stretching at 12–15 μm (which differs for different feldspars); Si,Al-O-Al,Si stretching at 15–20 μm (which is the same for all feldspars); and Si-O-Si stretching in quartz with bending and deformation lattice modes at 20–30 μm.

The spectrum of the June dacite displays the same overall shape as the spectra of the other two dacites, but differs from each in details. The feature near 16 μm (which appears as a shoulder in the June dome and the sample 399-2B dacite spectra) is resolved as an independent band. The spectrum of sample 399-2B differs from the June dome spectrum in that fine sharp features indicating quartz or quartz distortions of the feldspar bands are apparent at 12.5, 12.8, 14.4, and 26.7 μm (for sample 399-2B). For comparison of dacite spectra in general with those of other types, see Hunt (1979).

TEXTURAL PROPERTIES

Hydraulic conductivity (permeability), specific gravity (grain density), bulk density, specific surface area, and pore-size distribution of lava dome speci-

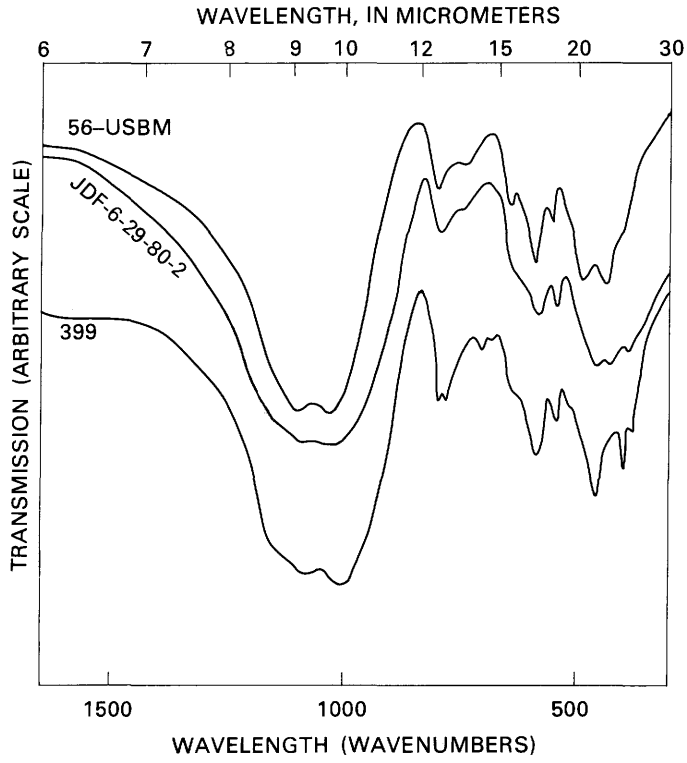

Figure 313.—Transmission spectra of Mount St. Helens dacite sample JDF-6-29-80-2 in KBr matrix compared to two other dacites.

Table 60.—Textural properties and magnetic susceptibility of Mount St. Helens samples, 1980

[DBD, dry bulk density using calipered volume and vacuum dry weight; DBA, dry bulk density using volume determined from Archimedes principle; DBM, mercury intrusion zero-pressure bulk density; SGA, specific gravity (grain density) using grain volume determined from Archimedes principle; SGH, specific gravity using grain volume obtained by helium pycnometry; SGG, specific gravity of crushed rocks using helium pycnometry; SGM, specific gravity using mercury porosimetry (69 MPa maximum pressure of penetration); WAP, water accessible porosity, derived by formula 100(1-DBA/SGA); HAP, helium accessible porosity, derived by formula 100(1-DBD/SGH); TOP, total porosity, derived by formula 100(1-DBD/SGG); SSA, specific surface area from mercury penetration porosimetry; mD, millidarcy; Mg/m^3, megagrams per cubic meter; *, sample destroyed; leaders (---), no data]

Sample No.	Hydraulic conductivity (mD)	DBD (Mg/m^3)	DBA (Mg/m^3)	DBM (Mg/m^3)	SGA	SGH	SGG	SGM	WAP	HAP	TOP	SSA (m^2/g)	Magnetic susceptibility (c.g.s./cm^3)	Additional physical properties
JDF 6-29-80-1														
a.	67.4	1.610	1.631	---	2.380	2.387	---	---	31.47	32.55	38.55	---	8.81×10^{-4}	Elec. prop.* (figs. 315 to 317).
b.	---	1.545	1.579	---	2.387	2.380	---	---	33.85	35.08	41.03	---	8.33×10^{-4}	---
d.	---	1.481	1.505	1.62	2.388	2.455	2.620	2.59	36.98	39.67	43.47	1.87	---	Mercury porosimetry* (fig. 314).
e.	92.1	1.527	1.544	---	2.383	2.398	---	---	35.21	36.32	41.72	---	---	Streaming potential.
JDF 6-29-80-2														
a.	---	1.545	1.558	1.61	2.239	2.247	---	2.56	30.42	31.24	40.00	4.51	9.32×10^{-4}	Mercury porosimetry* (figs. 312, 314).
b.	---	1.579	1.584	---	2.235	2.253	2.575	---	29.13	29.92	38.68	---	9.21×10^{-4}	Mag. prop.* (figs. 312, 318).
d.	---	---	---	---	---	---	---	---	---	---	---	---	---	Thermal prop.* (fig. 312; Taylor and Groot, 1980).
JDF 8-20-80-3														
a.	---	0.611	0.656	---	1.822	1.856	---	---	64.00	67.08	76.82	---	3.79×10^{-4}	---
b.	---	0.610	0.652	---	1.768	1.876	2.636	---	63.12	67.48	76.86	---	3.59×10^{-4}	---
c.	---	0.570	0.615	---	1.792	1.906	---	---	65.68	70.09	78.38	---	3.30×10^{-4}	---
JDF 8-20-80-4														
a.	---	1.955	1.982	---	2.451	2.479	2.565	---	19.14	21.14	23.78	---	1.13×10^{-3}	---
b.	---	1.925	1.952	---	2.442	2.454	---	---	20.07	21.56	24.95	---	1.09×10^{-3}	---

SAMPLE DESCRIPTIONS

JDF 6-29-80-1	Frothy rind of piece ejected from June dome (found near rampart, overlying tephra of June 12).
JDF 6-29-80-2	Pyroclastic fragment of dome or protodome from same location as JDF 6-29-80-1.
JDF 8-20-80-3	Pyroclastic-flow deposit of August 7 (pumice) from pumice plain at edge of pyroclastic flow.
JDF 8-20-80-4	Pyroclastic fragment or bomb, probably from May 18 eruption from Northwest Dome.

mens were determined by methods as described in Johnson (1979). Table 60 summarizes the results for the June dome samples, a pumice fragment from the August 7 pyroclastic-flow deposit, and a May 18 bomb fragment.

The samples exhibit typical density and specific gravity ranges for volcanic materials, but exhibit greater than normal surface areas, related to the microvesicularity. Figure 314 illustrates the pore-size distribution for two June dome samples.

ELECTRICAL PROPERTIES

The electrical properties were measured by methods described in Olhoeft (1979, 1980). Figures 315–317 illustrate the DC resistivity versus temperature as measured in a vacuum while simultaneously monitoring volatile outgassing (fig. 316). Despite significant isolated porosity (ranging from 4 to 6 percent), the dome sample outgassed less volatiles by two orders of magnitude than subaerial glossy Hawaiian tholeiite and only slightly more than most lunar basalt samples. No appreciable water or sulfur was outgassed, even upon melting. In contrast, even terrestrial granites outgas significant amounts of water upon melting (Olhoeft, 1981).

The solid line in figure 315 is described by the following equation:

$$p^{-1} = 2\times10^{-10}e^{-0.07/kT} + 0.9\,e^{-0.95/kT} + 3\times10^{14}e^{-4/kT}$$

where p = DC resistivity in ohm-m,
k = Boltzmann's constant
= 8.61735×10^{-5} eV/K, and
T = absolute temperature in kelvins.

Between 400° and 700°C, the data do not fit the equation well because the sample was reequilibrating rapidly. Nonlinear, complex resistivity measurements

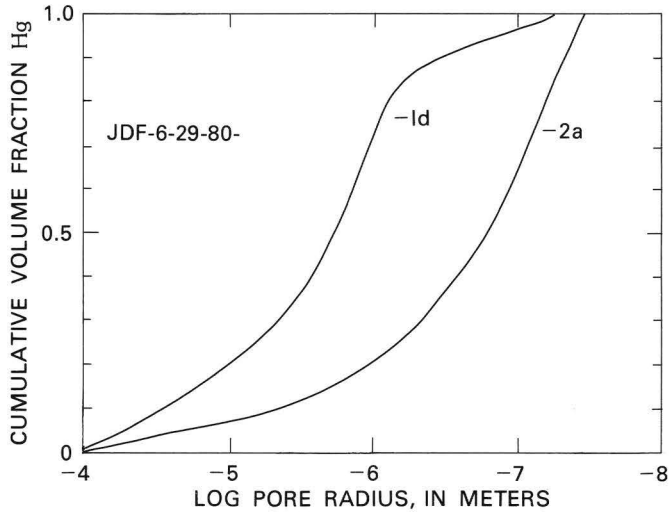

Figure 314.—Cumulative volume fraction of mercury intruded into sample plotted against log pore radius, samples JDF-6-29-80-1d and JDF-6-29-80-2a. Both samples have the same 37.2 percent mercury-accessible porosity.

(Olhoeft, 1979) were used to monitor this reequilibration. In this region, strong oxidation-reduction reactions were observed near 550°C followed by electrochemical signatures characteristic of ion-exchange processes near 700°C. Although the activation energy

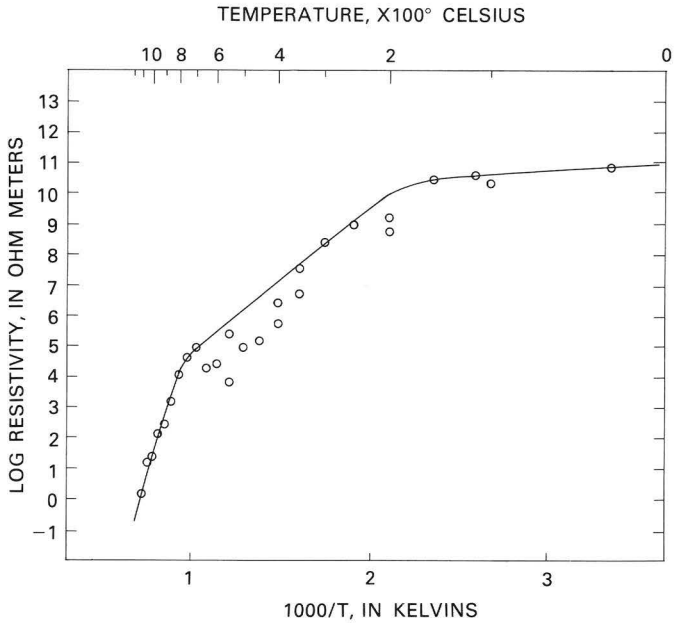

Figure 315.—Log DC electrical resistivity versus reciprocal temperature for June dome sample JDF-6-29-80-1a. The solid line is the plot of equation 1.

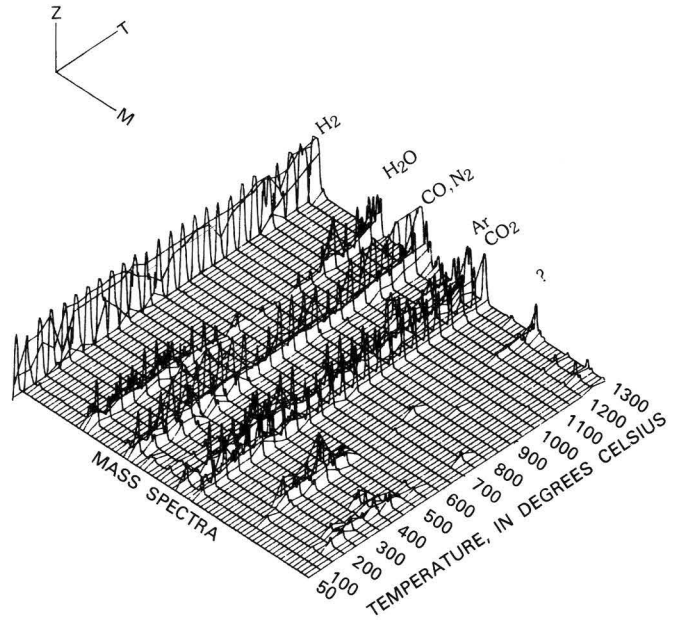

Figure 316.—Volatile outgassing shown as mass spectra versus temperature for sample JDF-6-29-80-1a. Note that H_2, CO, N_2, and Ar peaks are reduced in amplitude by a factor of 10 for clarity. Query indicates unknown material.

of the DC conduction process is 0.95 eV between 200° and 700°C, the activation energy of the relaxation time constant associated with the 500°–700°C reequilibration is 1.3 eV. The ion exchange processes and return of the DC resistivity to stable behavior at

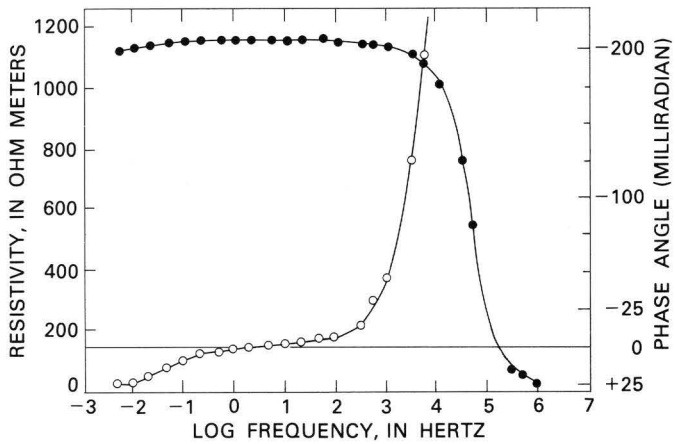

Figure 317.—Complex resistivity spectra for 0.001-m KCl-saturated sample JDF-6-29-80-1a. The reversal in sign of the phase angle below 5 Hz is indicative of a highly reactive surface chemistry in an anhydrous silicate. Solid dot, resistivity; open circles, phase angle.

700°C indicated the beginning of melting although full melting was not observed until 1050°C. Ion exchange would also be expected if the glass began to behave as a Bingham solid or polymeric silicate.

The complex resistivity spectra at 22°C from 10^{-3} to 10^{6} Hz for a June dome sample saturated with 0.001 m KCl (fig. 317) shows a strong reversal in the sign of the phase angle below 5 Hz, with a maximum negative induced polarization of +25 mrad that is characteristic of water-rock interaction due to highly reactive anhydrous surfaces. This high surface reactivity was further confirmed by the measured streaming potential coefficient of 973 mV/bar, nearly 100 times that found in most rocks.

MAGNETIC PROPERTIES

Magnetic properties of the dacite vitrophyre of the June dome were studied by alternating field demagnetization of the natural remanent magnetization in an arbitrarily oriented core, by petrographic examination of magnetic grains, and by thermomagnetic analysis (Watson, 1979). Large changes (as much as 25°) in the apparent remanent direction occurred commonly after each step of progressive demagnetization in peak fields of 50 to 800 Oe (oersteds), suggesting the presence of a magnetically unstable component carrying viscous remanent magnetization. The intensity of magnetization versus demagnetization field is characterized by substantial decay of magnetization after cleaning in low, alternating fields (median demagnetizing field was 65 Oe).

The magnetic fraction in the sample consists of species of the ulvospinel-magnetite solid-solution series (Usp-Mt_{ss}). The Usp-Mt_{ss} grains are subequant to equant and display a wide range in size from about 1 μm to 180 μm across; about 80 percent of the grains, however, are larger than 20 μm (fig. 311). Usp-Mt_{ss} phenocrysts occur in the groundmass, and within and marginal to plagioclase, pyroxene, and hornblende phenocrysts. In addition, small (1–10 μm) Usp-Mt_{ss} grains are concentrated within reaction rims that surround some hornblende phenocrysts (fig. 312). Most Usp-Mt_{ss} grains are optically homogeneous; rarely, these grains contain small inclusions of iron sulfide and silicate minerals (about 2–6 μm across). Composite ilmenite (typically external) is associated with about 10 percent of the Usp-Mt_{ss} grains. The large size of the Usp-Mt_{ss} grains, coupled with the paucity of their observable subdivision by exsolution or oxidation intergrowths, indicates that a substantial proportion of the magnetic grains are multidomain.

Thermomagnetic curves of saturation magnetization versus temperature (fig. 318) of the whole rock and of magnetic separates are reversible and indicate curie temperatures of 375° ± 5°C. Thermomagnetic analysis in conjunction with petrographic observations identify the magnetic carrier as titanomagnetite with an approximate composition 1/3 Fe_2TiO_4·2/3 Fe_3O_4. Large, multidomain-size titanomagnetite probably accounts for the observed magnetic instability of the sample.

DISCUSSION

The physical-properties measurements characterize the June dome as being of dacitic composition with normal density and porosity, with anhydrous

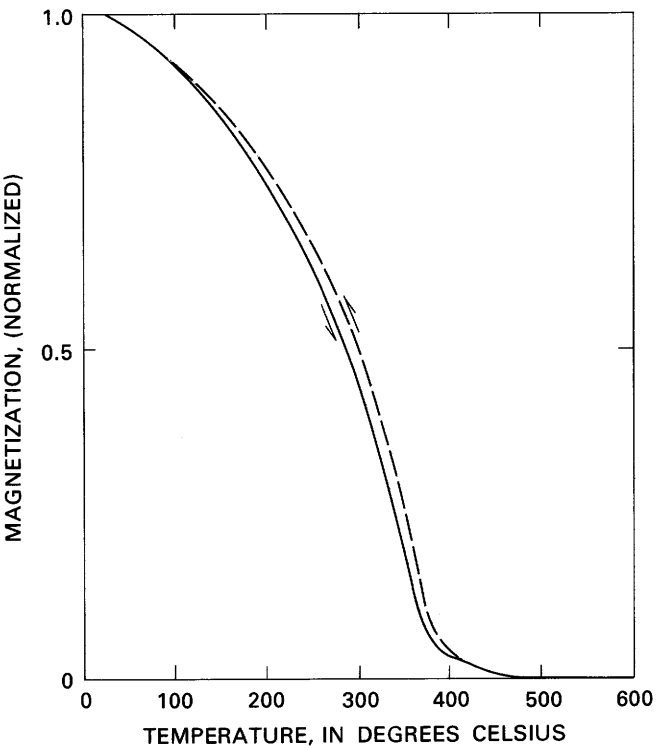

Figure 318.—Normalized saturation magnetization (J_T/J_O) versus temperature curve for sample JDF-6-29-80-2b. Experiment carried out in air using a 5-kG (kilogauss) field. Solid and dashed lines represent heating and cooling paths, respectively.

emplacement following an earlier devolatilization episode, and having rapid thermal cooling.

Absence of ilmenite lamellae within titanomagnetite grains reflects lack of intense high-temperature oxidation of these grains, and is consistent with the volatile outgassing results, which indicate low water content at the time of emplacement of the dome. This suggests low oxygen fugacities in the magma prior to extrusion and cooling of the lava dome. Similarly, the paucity of sulfide minerals within the iron-titanium oxide minerals reflects low sulfur content in the lava dome, also consistent with the volatile outgassing.

High glass content (55 percent) and the rapid 500°–700°C re-equilibration noted during the electrical-properties measurements indicate a very rapid thermal cooling from magmatic melt to about 500°C.

The extremely small amount of water observed in occluded pore spaces, along with the extremely high streaming-potential coefficient, and negative induced-polarization response, indicate an extremely high surface chemical reactivity due to anhydrous emplacement of the lava dome. The microvesicularity and resultant high surface area are indicative of high surface tension in the melt due to lack of water.

REFERENCES CITED

Hunt, G. R., 1979, Spectroscopic properties, *in* Hunt, G. R., Johnson, G. R., Olhoeft, G. R., Watson, D. E., and Watson, Kenneth, Initial report of the Petrophysics Laboratory: U.S. Geological Survey Circular 789, p. 49–67.

Hunt, G. R., and Salisbury, J. W., 1974, Mid-infrared spectral behavior of igneous rocks: AFCRL-TR-74-0625, Environmental Research Paper 496.

Johnson, G. R., 1979, Textural properties, *in* Hunt, G. R., Johnson, G. R., Olhoeft, G. R., Watson, D. E., and Watson, Kenneth, Initial report of the Petrophysics Laboratory: U.S. Geological Survey Circular 789, p. 67–74.

Olhoeft, G. R., 1979, Electrical properties, *in* Hunt, G. R., Johnson, G. R., Olhoeft, G. R., Watson, D. E., and Watson, Kenneth, Initial report of the Petrophysics Laboratory: U.S. Geological Survey Circular 789, p. 1–26.

———1980, Initial report of the Petrophysics Laboratory—1977–1980 Addendum: U.S. Geological Survey Open-File Report 80-522, 9 p.

———1981, Electrical properties of granite with implications for the lower crust: Journal of Geophysical Research, v. 86, p. 931–936.

Taylor, R. E., and Groot, H., 1980, Thermophysical properties of Mount St. Helens Sample, TPRL-237: Thermophysical Properties Research Laboratory, Purdue University, 11 p.

Watson, D. E., 1979, Magnetic properties, *in* Hunt, G. R., Johnson, G. R., Olhoeft, G. R., Watson, D. E., and Watson, Kenneth, Initial report of the Petrophysics Laboratory: U.S. Geological Survey Circular 789, p. 26–49.

HEAT CONTENT AND THERMAL ENERGY OF THE JUNE DACITE DOME IN RELATION TO TOTAL ENERGY YIELD, MAY-OCTOBER 1980

By JULES D. FRIEDMAN, GARY R. OLHOEFT, GORDON R. JOHNSON, *and* DAVID FRANK

ABSTRACT

The heat content of the dacite dome of June 1980 is estimated from laboratory measurements of thermophysical properties, supplemented by published data on latent heat of fusion. A crystallization temperature of 970°–990° C was inferred from melting experiments and Fe-Ti-oxide geothermometry (Melson and Hopson, this volume). The volume of the visible dome was estimated to be 4.6×10^6 m^3 from vertical aerial photographs. The thermal energy of the visible dacite dome is 1.5×10^{16} J (Joule), calculated from data on volume, crystallization temperature, bulk density (2.2 g/cm^3), specific heat (1.059 J/g/K), latent heat of fusion (350 J/g), and heat content (1,385 J/g for solid dacite and 140 J/g for associated volatiles). Including inferred subsurface dome material above the conduit, the total energy would be approximately 3.4×10^{16} J. Eruption of the dome was comparable to an eruption of intermediate magnitude, intensity III+ on the Tsuya scale, or intensity IV+ on the Hedervári scale. The total thermal energy released at Mount St. Helens between May and October 1980 is estimated conservatively at 1.2×10^{18} J, about 93 percent of the total energy released during this period.

INTRODUCTION

In this report, we calculate the thermal energy and total energy of the June dacite dome from the estimated volume of the dome and determinations of thermophysical properties of the dacite, including thermal conductivity, thermal diffusivity, specific heat, and thermal inertia. Additional physical properties are given in the preceding companion paper (Olhoeft and others, this volume). Using volume and mass data for the ejecta from May through October 1980 from other reports in this volume, we compare the energy yield of the June dome with estimated yields of the other eruptive events, infer the total energy yield, and make comparisons with other historic eruptions.

GROWTH OF DOME AND INFERRED FORM

The near-surface presence of the dome was evident as early as June 8 from infrared images, topographic evidence, and the character of the pyroclastic blocks ejected on June 12 (Moore and others, this volume; Friedman, Frank, and others, this volume). The dome was first observed on June 15, when it was about 200 m in diameter and 40 m high. From June 15 to 19, the dome rose about 2.5 m/day, reaching its maximum height of 52–53 m above the crater floor on June 19. Measurements on vertical aerial photographs of July 1 indicate the average diameter of the dome was about 330 m; its form was somewhat polygonal (fig. 175*A*). The dome grew largely by expansion from within, and the ratio of diameter to visible height remained about 6:1. We infer that the dome was funnel-shaped in section, with a narrow conduit and a floor dipping

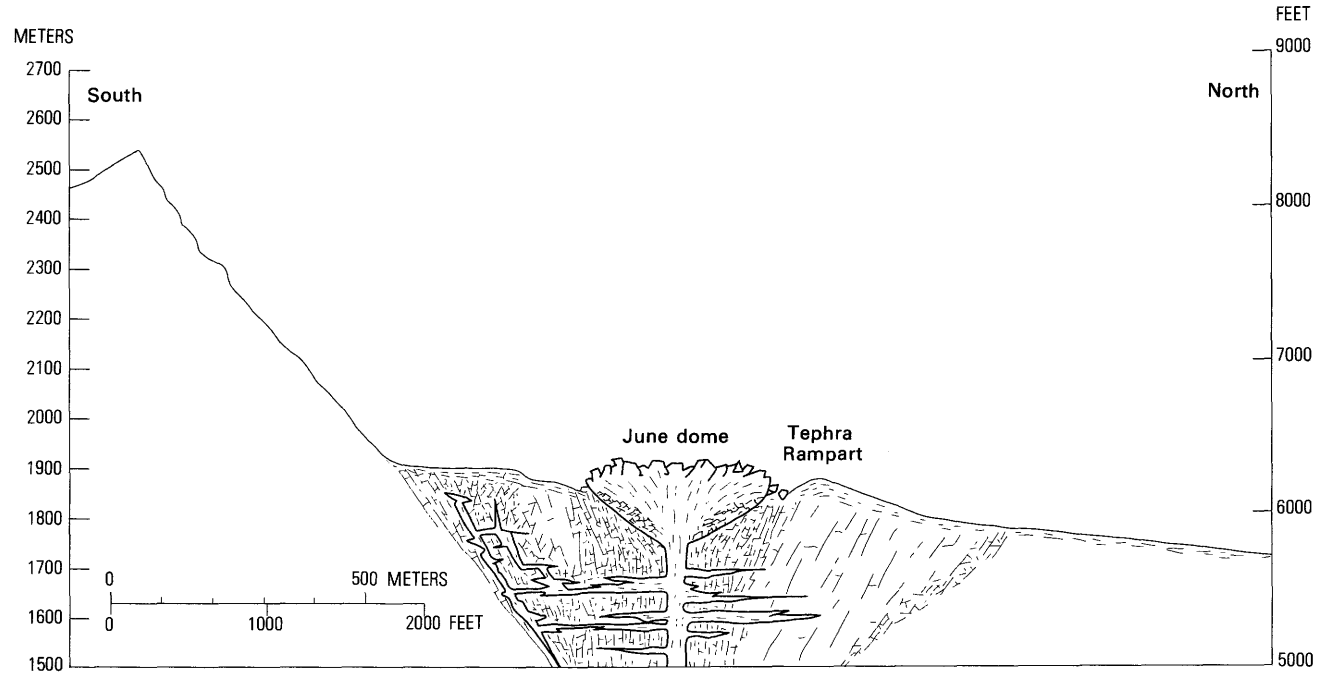

Figure 319.—North-south schematic section through the crater and dome in late June. The dome is inferred to cap a 30-m-wide magma column and fill a 100-m-deep, funnel-shaped crater. The dome fans out on top of vent-filling breccia and tephra from previous eruptions and, in some areas, lies upon its own breccia.

slightly inward (fig. 319). The volume of the visible dome is about 4.6×10^6 m^3 (0.0046 km^3). If the funnel shape inferred in figure 319 is valid, the total volume of the dome would be a little less than 10^7 m^3. From the volume of the visible dome on June 19, we estimate its rate of growth after June 15 as 0.7×10^6 m^3/day or 8 m^3/s. If the dome emerged at the surface on June 12, its growth rate was 0.6×10^6 m^3/day or 7 m^3/s.

THERMAL ENERGY OF THE JUNE DOME

The thermal energy of solid eruptive products is calculated from the relationship (Yokoyama, 1956)

$$E_{th} = V\sigma (Tc + B) \qquad (1)$$

where V is the volume in cm^3, σ is bulk density in g/cm^3; T is the crystallization temperature in °C, c is specific heat, and B is latent heat of fusion.

We use an average bulk density of 2.2 g/cm^3, based on measured densities and porosities (Olhoeft and others, this volume). An average crystallization temperature of 980°C is based on Fe-Ti-oxide geothermometry on similar June dome fragments (Melson and Hopson, this volume), supplemented by a dry-melt liquidus temperature of 1050°C determined on dome fragments (Olhoeft and others, this volume); $980° \pm 50°$C is the estimated crystallization temperature, if we assume 3 percent water content. Near-surface temperatures of about 850°C, measured by thermocouple in incandescent cracks on the crater floor (R. P. Hoblitt, oral commun., 1980), are minimum limits on the solidus temperature of the dacite.

The thermophysical properties of the dacite are temperature dependent (table 61, figs. 320, 321). Specific heat values (c) range from 0.730 J/g/K to 1.226 J/g/K over the cooling range of the dacite (fig. 321), with an integrated specific heat value of 1.059 J/g/K. This integrated value is compatible with a published value of 1.03 J/g/K for volcanic rocks (Desai and others, 1974, p. 43, 201).

Latent heat of fusion (B) of the dacite can be estimated from modal data (from R. E. Wilcox, in Olhoeft and others, this volume), in which plagioclase, An_{45-55}, hypersthene, and hornblende are the dominant crystallized minerals. Recently determined latent heats of fusion are 487.3 J/g for anorthite and 207.4 J/g for albite (Weill and others, 1980, p. 95; D.

Table 61.—Temperature dependence of thermophysical properties of Mount St. Helens dacite, based on June dome fragment 6-29-80-2

[Bulk density was measured at 1.4956 g/cm before heating and 1.4917 g/cm after heating; 1.496 g/cm was used for the above calculations]

Temperature (°C)	Thermal conductivity (k) [1](watt/cm/K)	Thermal diffusivity (α) [1](cm²/s x 10^{-2})	Specific heat (c) [1](J/kg/K)	Thermal inertia (β)[3] (J/m²/s$^{1/2}$)
23	0.537	0.492	730.	765.8
100	.558	.447	835.	834.9
200	.572	.411	930.	892.1
300	.600	.394	1,018.	955.9
400	.624	.390	1,070.	1,000.2
500	.640	.386	1,109.	1,030.4
600	.686	.400	1,147.	1,084.9
700	.738	.421	1,172.	1,137.5
800	.804	.450	1,195.	1,198.9
900	.876	.483	[2]1,213.	1,260.8
1000	.965	.526	[2]1,226.	1,330.3

[1]Taylor and Groot (1980).
[2]Extrapolated.
[3]Thermal inertia (β) calculated from the relationship $\beta = \sqrt{K\rho c}$.

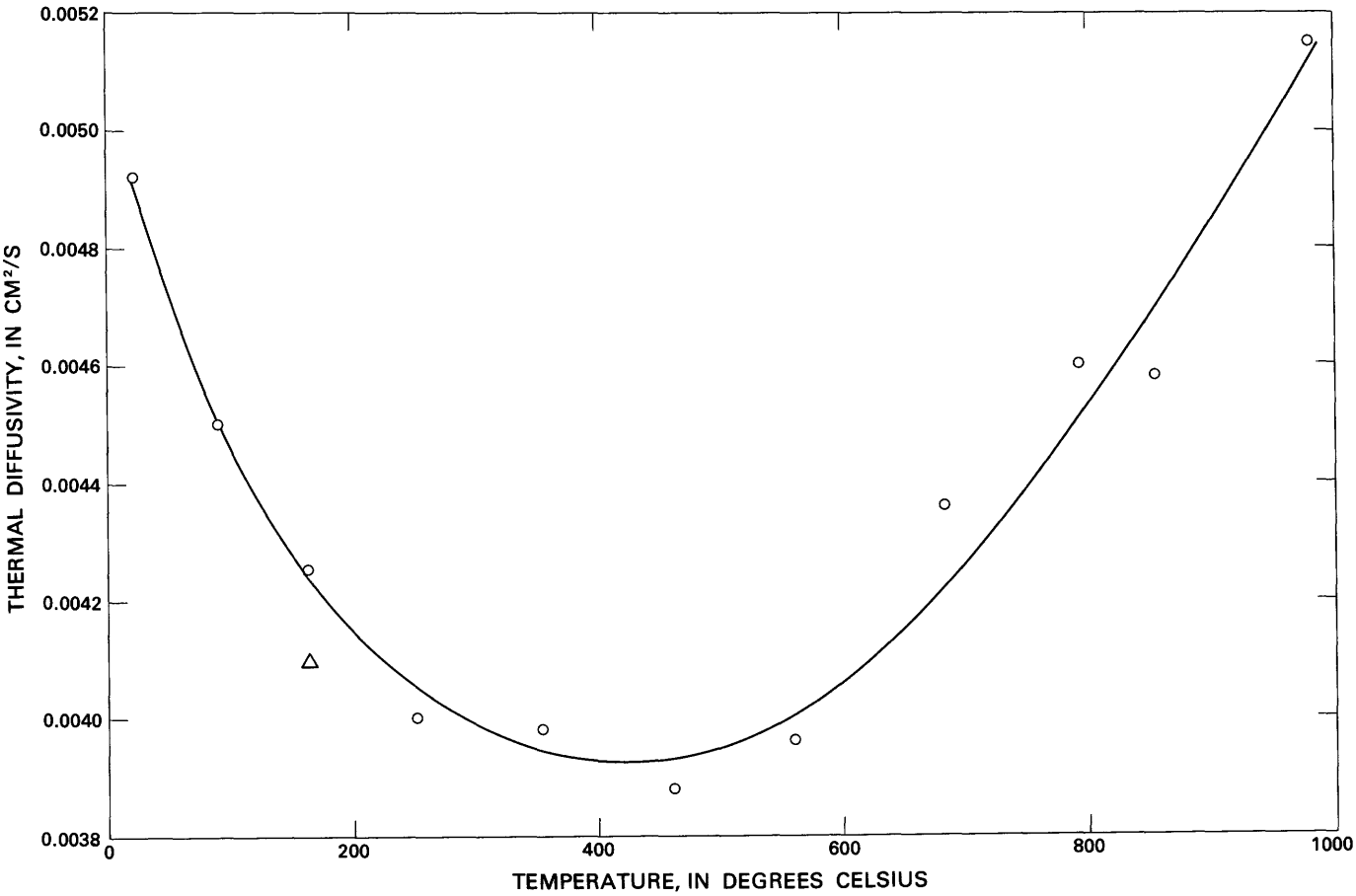

Figure 320.—Thermal diffusivity of sample of June dacite dome (sample No. JDF 6-29-80; Olhoeft and others, this volume). Circle, value obtained upon heating sample in laboratory; triangle, value upon cooling sample in laboratory.

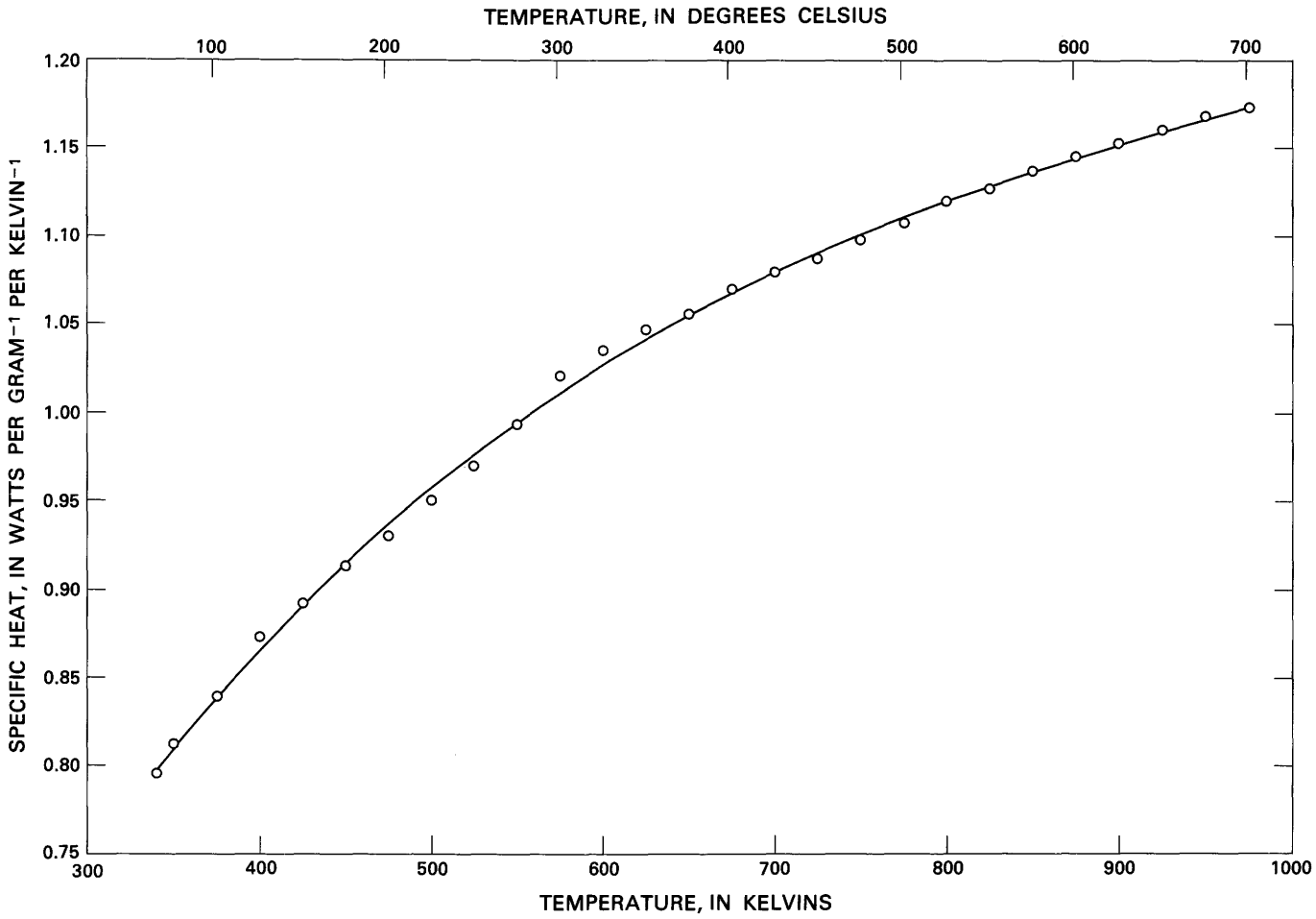

Figure 321.—Specific heat of dacite from June dome.

F. Weill, written commun., 1980). Values for hornblende and orthopyroxene are somewhat higher, from 365 to 625 J/g (Robie and Waldbaum, 1968). Accordingly, we estimate the latent heat of fusion of Mount St. Helens dacite at about 350 J/g, exclusive of the heat content of associated volatiles. This value is based on some residual glass in the dacite, as in the sample used for laboratory measurements. To the degree that the interior of the dome devitrifies completely, as seems likely, the latent heat of fusion would increase accordingly. The dacite value estimated here also agrees with enthalpy-temperature data for other volcanic rock melts (Stout and Piwinskii, 1980, p. 8).

From the preceding discussion, we estimate the heat content of the June dacite at 1,375 J/g at an estimated 6–8 percent early subsolidus porosity. This value is comparable to published energy equivalents of 1,254–1,507 J/g for volcanic products (Imbó, 1965, p. 38; Yokoyama, 1972, p. 165; Blackwell, 1978, p. 182).

Based on the enthalpy of steam, the ancillary heat content of the volatiles contained in the June dacite, at 3 percent water vapor and 980°C, is about 140 J/g (Keenan and Keyes, 1936). The combined heat content of the dacite lava and the enthalpy of 3 percent water vapor associated with the magma is thus 1,527 J/g.

From the estimated heat contents of the dacite and associated volatiles and the mass of the visible dome, the thermal energy is 1.5×10^{16} J. Assuming a funnel shape for the subsurface dome (fig. 319), the total energy may approach 3.4×10^{16} J.

If the visible dome emerged on June 12, the rate of thermal energy yield can be estimated from its growth rate from June 12–19 (7 m^3/s) and June 15–19

(8 m^3/s). Using equation 1, and including the enthalpy of 3 percent water vapor, the thermal energy yield was 2.4×10^{10} J/s from June 12–19; and 2.7×10^{10} J/s from June 15–19, approaching 3×10^4 MW.

POTENTIAL ENERGY EXPENDED IN EXTRUSION OF DOME

The potential energy (E_{pot}) in ergs expended in extruding the dome may be approximated by

$$E_{pot} = m_1 Hg \quad (2)$$

where m_1 = mass of lava extruded (g),
H = vertical distance lifted (cm)
g = acceleration of gravity (980.665 dyne/cm)

The minimum E_{pot} is thus that energy expended in extruding the dome from a depth of 2 km (approximate locus of preeruptive seismic hypocenters, Endo and others, this volume) to its maximum height of 53 m. Here, $E_{pot} = 2.5 \times 10^{21}$ ergs, about 1 percent of the thermal energy yield of the visible dome.

ESTIMATED TOTAL ENERGY YIELD BETWEEN MAY AND OCTOBER 1980

THERMAL ENERGY

Using the thermophysical properties determined for the June dacite and volume, mass, and density data for the magmatic tephra and pyroclastic flows erupted between May and October (table 62), we can calculate the thermal energy released using equation 1. As for the June dacite, we estimate a 3 percent volatile content, largely water vapor, at 980°C. From this we infer the heat loss via volatiles for solid magmatic products to be 140 J/g.

To estimate the thermal energy (E_{th_1}) released by the debris avalanche of May 18, we conservatively infer an average temperature of 80°C for the entire debris avalanche and blast deposits based on measurements of approximately 70°–100°C made soon after emplacement (Banks and Hoblitt, this volume). These temperatures are probably low for the entire mass of debris, considering the presence of secondary fumaroles. The volume of the debris avalanche is taken as 2.61 km^3 at 2.6 g/cm, equivalent to the volumetric loss from the volcano, measured from topographic data (Moore and Albee, this volume), minus the lithic material included in tephra. The heat content of the debris avalanche is based on a specific heat of 1.06 g/cm. The thermal energy (E_{th_1}) of these deposits (5.19×10^{17} J) and of the magmatic tephra (E_{th_2}) and pyroclastic-flow deposits (E_{th_3}) of May 18 and 25, June 12, and July 22 are given in table 63. The mass and thermal energy equivalent volume of a hypothetical magmatic component of the debris avalance would be 0.11 km^3 (table 62).

KINETIC ENERGY

The kinetic energy released by ejection of 2.63 km^3 of the debris avalanche and associated deposits (E_{k_1}), the total magmatic and nonmagmatic tephra (E_{k_2}), and the pyroclastic-flow deposits (E_{k_3}) is estimated from:

$$E_k = 1/2\, mV_0^2 \quad (3)$$

where m is mass and V_0 is the initial velocity of solid ejecta (Yokoyama, 1957). If we neglect air resistance and thereby obtain lower boundary values, the initial velocity of ejecta V_0 is given by Gorshkov (1959, p. 107) and others as

$$V_0 = rg \quad (4)$$

where r is the lateral distance (cm) reached by the center of mass of the ejected material, and g is the acceleration of gravity (dynes/cm).

For the vertical ejection of pyroclastics, neglecting atmospheric drag and other factors, Imbó (1965, p. 24) and others give

$$V_0 = 2gh \quad (5)$$

where h is the height reached by the pyroclastics. In this study, h is taken as the height reached by eruption columns during the *gas-thrust stage only*.

The kinetic energy yield of the debris avalanche and associated deposits is conservatively estimated from the following considerations: (1) the mass (m) of

Table 62.—Volumes of volcanic deposits, Mount St. Helens, May-June 1980

Magmatic volume of tephra

Date	Mass[1] (g)	[1]Equivalent volume (km^3) at density 2.6 g/cm^3	[2]Equivalent volume of magma (km^3)
May 18	4.88×10^{14}	0.20	0.0845
May 25	$.42 \times 10^{14}$	.016	.0070
June 12	$.45 \times 10^{14}$	.017	.0078
July 22	$.04 \times 10^{14}$	.001	.00045
Total--	5.79×10^{14}	.222	0.10

Magmatic volume of pyroclastic flows

Date	[3]Volume (km^3) [4](at bulk density 0.63 g/cm^3)	Equivalent volume (km^3) at density 2.6 g/cm^3	Percent magmatic[3]	Mass of magmatic component of pyroclastic flows (g)	Equivalent volume of magma (km^3)
May 18	0.200	0.048	75	9.45×10^{13}	0.036
May 25	.003	.001	90	1.70×10^{12}	.001
June 12	.012	.003	90	6.80×10^{12}	.003
July 22	.016	.004	90	9.09×10^{12}	.003
Total--	.231	0.056		1.12×10^{14}	0.043

Volume of nonmagmatic component of debris avalanche and other deposits of May 18

Volume (km^3)	Density (g/cm^3)	Mass (g)
2.63	2.6	6.76×10^{15}

Total volume of magmatic deposits at density 2.6 g/cm^3 (km^3)

Equivalent volume of magmatic component of debris-avalanche and blast deposits (volume of cryptodome)	0.12
Equivalent volume of magmatic tephra	.10
Equivalent volume of pyroclastic flows	.04
Volume of lava domes (through October 1980)	.01
Total magmatic deposits	0.27

Total volume of volcanic ejecta scaled to density 2.6 g/cm^3 (km^3)

Magmatic deposits	0.27
Nonmagmatic component of debris avalanche and other deposits	2.63
Total ejecta	2.90

[1] From Sarna-Wojcicki, Shipley and others, this volume.
[2] 45 percent of total volume (Andrei Sarna-Wojcicki, oral commun., 1980).
[3] Volume of pyroclastic flows (estimated from data provided 11/80, by N. Macleod, oral commun., 1980).
[4] Bulk density of pyroclastic flows (Olhoeft and others, this volume).

the old lithic components is approximated by the 2.73 km^3 of material lost from the volcanic edifice minus 0.1 km^3, the lithic component of the May 18 tephra and pyroclastic flow deposits (Sarna-Wojcicki, Shipley, and others, this volume; Rowley and others, this volume); (2) the velocity of ejection, V_0, is taken as 150 m/s, probably a lower limit.

The ejection velocity at 0832 PDT on May 18 is still problematic, but the following evidence provides reasonable limits. The velocity of the lateral eruption

Table 63.—Mount St. Helens energy yield, May-October 1980, in ergs

[>, greater than; N.A., not applicable]

Energy category		Prior to May 18	May 18	May 25	June 12	July 22	Aug. 7-14	Oct. 1-18	Totals
Thermal (E_{th})	E_{th_1} debris flow	0	5.36×10^{24}	0	0	0	0	0	5.36×10^{24}
	E_{th_2} magmatic tephra	0	3.64×10^{24}	3.05×10^{23}	3.24×10^{23}	1.91×10^{22}	Negligible	Negligible	4.29×10^{24}
	E_{th_3} pyroclastic flow deposits	0	1.47×10^{24}	2.64×10^{22}	1.06×10^{23}	1.41×10^{23}	Low	Negligible	1.74×10^{24}
	E_{th_4} lava domes	0	0	0	3.4×10^{23}	0	Estimated 3.4×10^{22}.	Estimated 3.4×19^{23}.	$.71 \times 10^{24}$
Kinetic (E_k)	E_{k_1} debris flow	0	$>2.6 \times 10^{23}$	0	0	0	0	0	2.6×10^{23}
	E_{k_2} tephra	Negligible	$3.0 \times I0^{23}$	1.89×10^{22}	2.02×10^{22}	1.80×10^{21}	Negligible	Negligible	3.41×10^{23}
	E_{k_3} pyroclastic flow deposits	0	$.77 \times 10^{23}$	0.85×10^{21}	3.40×10^{21}	4.54×10^{21}	Negligible	Negligible	$.86 \times 10^{23}$
Potential (E_p)		Unknown	3.5×10^{23}	Negligible	2.5×10^{21}	Negligible	Estimated 2.5×10^{20}.	Estimated 2.5×10^{21}.	3.55×10^{23}
Baric (acoustic) wave (E_{bw})		0	[a] $2.1 \times 10^{23} \pm$	0	0	0	0	0	$2.1 \times 10^{23} \pm$
Elastic strain (E_e)		Negligible	6.6×10^{18}	N.A.	N.A.	1.4×10^{16}	N.A.	1.4×10^{16}	6.6×10^{18}
Seismic (E_s)		[b] 1.8×10^{20}	---	Low	Low	Low	Low	Low	1.8×10^{20}
Total		1.167×10^{25}		3.51×10^{23}	8.24×10^{23}	1.66×10^{23}	$.34 \times 10^{23}$	3.43×10^{23}	[c] $>1.34 \times 10^{25}$

[a] From J. W. Reed (1980).

[b] Endo and others (this volume), includes May 18.

[c] Estimates and totals are limited in reliability to two significant figures.

cloud, probably a lower limit for ejection velocity, reached 150–200 m/s, from photographic and seismic-station evidence (Voight, this volume). For an upper limit of ejection velocity as manifested by the vertical eruption column we apply equation 5. The height (h) reached by the gas-thrust stage only is considered; the total eruption column height of May 18 and the larger eruption columns of succeeding months also have a convective-rise stage. The smaller eruption columns of August, rising to 7,000 m, may represent largely the gas-thrust phase (David Harris, oral commun., 1980). If we apply this height to equation 5 (minus the altitude of the crater rim) for the May 18 and later eruption columns, the ejection velocity is 375 m/s, as an upper limit.

Velocities of 316 m/s (comparable to our upper limit) were observed for the leading edge and 199 m/s for the trailing edge of an ionospheric system of magnetic perturbations that traveled across North America on May 18 (Fougere and Tsacoyeanes, 1980, p. 1209). These perturbations, traveling radially outward from the blast of 0832 PDT, were associated with the acoustic or infrasonic wave created by the atmospheric pressure pulse.

The same average ejection velocity, 260 m/s, is obtained from both sets of boundary conditions: (1) velocities of the lateral eruption cloud and the vertical eruption column, and (2) the atmospheric infrasonic-wave velocities. Following Gorshkov (1959, p. 108) and Minikami (1950), the pressure at the moment of explosion can be estimated if the Bernoulli law remains essentially valid for pressure and velocity of the ejected material. If so,

$$P = \frac{\rho V_0^2}{2}$$

where P is pressure, ρ is density of the material, and V_0 is initial velocity. For an ejection velocity of 260 m/s, the pressure is 880 atm.

Using a different approach (C. W. Burnham, in Yoder, 1979), based on dacitic composition (about 63 percent SiO_2), porosities obtained in this study, 970°C melting temperature, and 3 percent water content, the overpressure at the onset of the May 18 eruption would have been about 650 atm and the initial velocity 225 m/s.

The average velocity between our limits gives an estimated E_{k_1} energy yield for magmatic tephra of 3.0×10^{23} ergs and an E_{k_3} of the pyroclastic-flow deposits of 0.77×10^{23} ergs.

POTENTIAL ENERGY

The potential energy (E_{pot}), representing change of level of magma in the volcanic vent during eruption, was estimated conservatively as 2.5×10^{21} ergs for the June dome, several orders of magnitude lower than other forms of energy expended. Similar E_{pot} estimates are included in table 63 for the August and October domes. In part, the E_{pot} for May 18 is part of the decompression energy associated with the devolatilization or so-called "phreato-magmatic" event and is not calculated here; to raise the volume of magma erupted on May 18, about 0.38 km^3, from a depth of 2 km to the present crater floor would have expended about 3.4×10^{23} ergs.

BARIC-WAVE ENERGY

The acoustic or baric-wave energy (E_{bw}), expended in the blast of May 18 was reported as 0.2 to 2.1×10^{23} ergs (Reed, 1980; Mitchell, 1980, p. 120–121). Gorshkov (1959) reported that air-wave energy was equivalent to 50 percent of the total kinetic energy for the eruption and isobaric wave at Bezymianny. If conditions were similar at Mount St. Helens, the baric-wave energy estimated suggests that the kinetic energy (E_k) estimated in the previous section is correct within an order of magnitude.

SEISMIC ENERGY

The seismic energy (E_s), before and during the eruption of May 18, is reported as 1.8×10^{20} ergs (Endo and others, this volume); the subsequent seismic energy yield during 1980 was considerably smaller (Weaver and others, this volume) and is not shown in table 63.

ELASTIC STRAIN ENERGY

Energy expended in fracturing the volcano is equivalent to the elastic strain energy (E_e) contained in the edifice before it disintegrated on May 18, given by

$$E_e = \tfrac{1}{2}\, \gamma e^2\, V \qquad (6)$$

where γ represents Young's modulus, 5×10^{11} dyne/cm^2, according to Birch and others (1942, p. 73); e, the ultimate shearing strength of rock is approximated by the numeric 10^{-1} (Tsuboi, 1933, p. 276); and V is the volume of the disintegrated mass of the volcano, 2.63 km^3. The elastic strain energy expended is thus only about 6.6×10^{18} ergs, including effects of pre-May 18 fracturing.

CONCLUSIONS

The total energy yield of the Mount St. Helens eruptions from May through October 1980 is estimated at 1.34×10^{25} ergs (table 63), between intensity VII and VIII on the Tsuya volumetric scale (Tsuya, 1955) and between VI and VII on the Hédervári energy-yield scale (table 64). These estimates are conservative and omit several energy components: (1) decompression energy of the massive devolatilization on May 18[1], and (2) the thermal and kinetic energy yield of magmatic tephra that were ejected into the upper atmosphere. Of the total estimated, 1.23×10^{25} ergs or 93 percent represents thermal energy. The thermal energy of the June dome, 4.8×10^{23} ergs, represents less than 4 percent of the volcanic energy expended between May and October.

The thermal energy released within the debris avalanche and associated deposits, 5.2×10^{24} ergs, exceeds by an order of magnitude the combined kinetic and

[1]The decompression energy (see Kieffer, this volume) includes the following energy components, some estimated here and others not: (1) to lift the magma (potential energy), (2) to produce tephra from the magma (not calculated), (3) to distribute the tephra (largely kinetic energy (E_k), (4) to generate atmospheric pressure and acoustic waves (included), (5) some elements of seismic energy (included), and (6) to open the conduit or eruption channel (partly included in the estimated elastic-strain energy (E_e)).

Table 64.—Thermal energy yield of selected volcanic eruptions

Hédervári intensity scale	Volcano and year of eruption	Volume of volcanic ejecta (km^3)	Thermal energy yield (ergs)	References
0-I	Halemaumau, Hawaii, 1928-----	<0.00001	$<3.7 \times 10^{20}$	Hédervári (1963, table 3, p. 377-380).
II	Sakura-zima, Japan, 1955-----	.00005	4.22×10^{20}	Do.
III	Réunion, Indian Ocean, 1956--	.0002	6.3×10^{21}	Do.
	Halemaumau, Hawaii, 1924-----	.00024	8.8×10^{21}	Do.
	Mugogo, Congo, 1957----------	.00075	2.4×10^{22}	Do.
	Sakura-zima, Japan, 1973-74--		[a] 2.5×10^{22}	Friedman and others (1976, p. 326).
IV	Etna, Sicily, 1955----------	.00371	1.4×10^{23}	Hédervári (1963, table 3, p. 377-380).
	Halemaumau, Hawaii, 1954-----	.006	2.2×10^{23}	Do.
	Kilauea, Hawaii, 1921--------	.0067	2.5×10^{23}	Do.
V	Lemongan, Java, 1887---------	.010	2.9×10^{23}	Do.
	June lava dome, Mount St. Helens, Wash., 1980.	.005	$(1.5\text{-}3.4) \times 10^{23}$	
	Tenerife Canary Islands, 1909	.015	4.7×10^{23}	Hédervári (1963, table 3, p. 377-380).
	Paricutin, Mexico, 1952------	.015	5.5×10^{23}	Do.
	Kilauea-Iki, Hawaii, 1959----	.05	1.8×10^{24}	Do.
	Mauna Loa, Hawaii, 1942------	.08	2.5×10^{24}	Do.
VI	Vesuvius, Italy, 1906--------	.4	1.8×10^{24}	Do.
	Sakura-zima, Japan, 1946-----	.1	2.9×10^{24}	Do.
	Kilauea-Iki, Hawaii, 1960----	.2	5.9×10^{24}	Do.
	Hekla, Iceland, 1970---------	.2	7.3×10^{24}	Friedman and others (1976, p. 326).
	Mount St. Helens, Wash., May-Oct. 1980.	.3	1.3×10^{25}	
	Mauna Loa, Hawaii, 1950------	.5	1.5×10^{25}	Hédervári (1963, table 3, p. 377-380).
	Taal, Luzon, 1911------------	.5	4.8×10^{24}	Do.
	Ambrym, New Hebrides, 1950-51	.8	7.7×10^{24}	Do.
	Dyngjufjöll (Askja), Iceland, 1875.	.4	2.0×10^{25}	Hedervari (1963, table 3, p. 377-380), Sigurur Thorarinson, oral commun., 1970).
	Bezymianny, U.S.S.R., 1956---	1.0	2.2×10^{25}	Gorshkov (1959, p. 108).
	Hekla, Iceland, 1845---------	.9	2.5×10^{25}	J. D. Friedman (unpub. data, based on Thorarinsson, 1967).
	Hekla, Iceland, 1947-48------	1.0	3.1×10^{25}	Do.
VI	Paricutin, Mexico, 1943-51---	1.4	2.6×10^{25}	Hédervári (1963, table 3, p. 377-380).
	Etna, Sicily, 1669-----------	1.0	3.4×10^{25}	Do.
	Surtsey, Iceland, 1963-67----		3.8×10^{25}	J. D. Friedman (unpub. data, based on Thorarinsson, 1967).
	Sakura-zima, Japan, 1914-----	2.1	4.6×10^{25}	Matuzawa (in Rittmann, 1963, p. 423).
	Lansarote, Canary Island, 1730-36.	1.5	4.7×10^{25}	Hedervari (1963, table 3, p. 377-380).
	Santa Maria, Guatemala, 1902-	5.5	5.3×10^{25}	Do.
	Kliuchevskaya Sopka, Kamchatka, 1829.	3.7	1.1×10^{26}	Do.
VIII	Oraefajökull, Iceland, 1362	10.0	9.6×10^{25}	Do.
	Krakatoa, Sunda, 1883--------	18.0	1.7×10^{26}	Do.
	Laki, Iceland, 1783----------	30.0	8.7×10^{26}	Do.
	Coseguina, Nicaragua, 1835---	50.0	4.8×10^{26}	Do.
	Mount Mazama, Oregon, 7000 B.P.	71.0	6.8×10^{26}	Do.
IX	Tambora, Sumbawa, 1815-------	[b] 30.0	2.88×10^{26} to 1.4×10^{27}	Do.

[a] Kinetic energy yield.

[b] Unpublished data, revision of Hédervári value by Friedman, based on lowest volumetric output of the 1815 Tamboro eruption in the volcanologic literature.

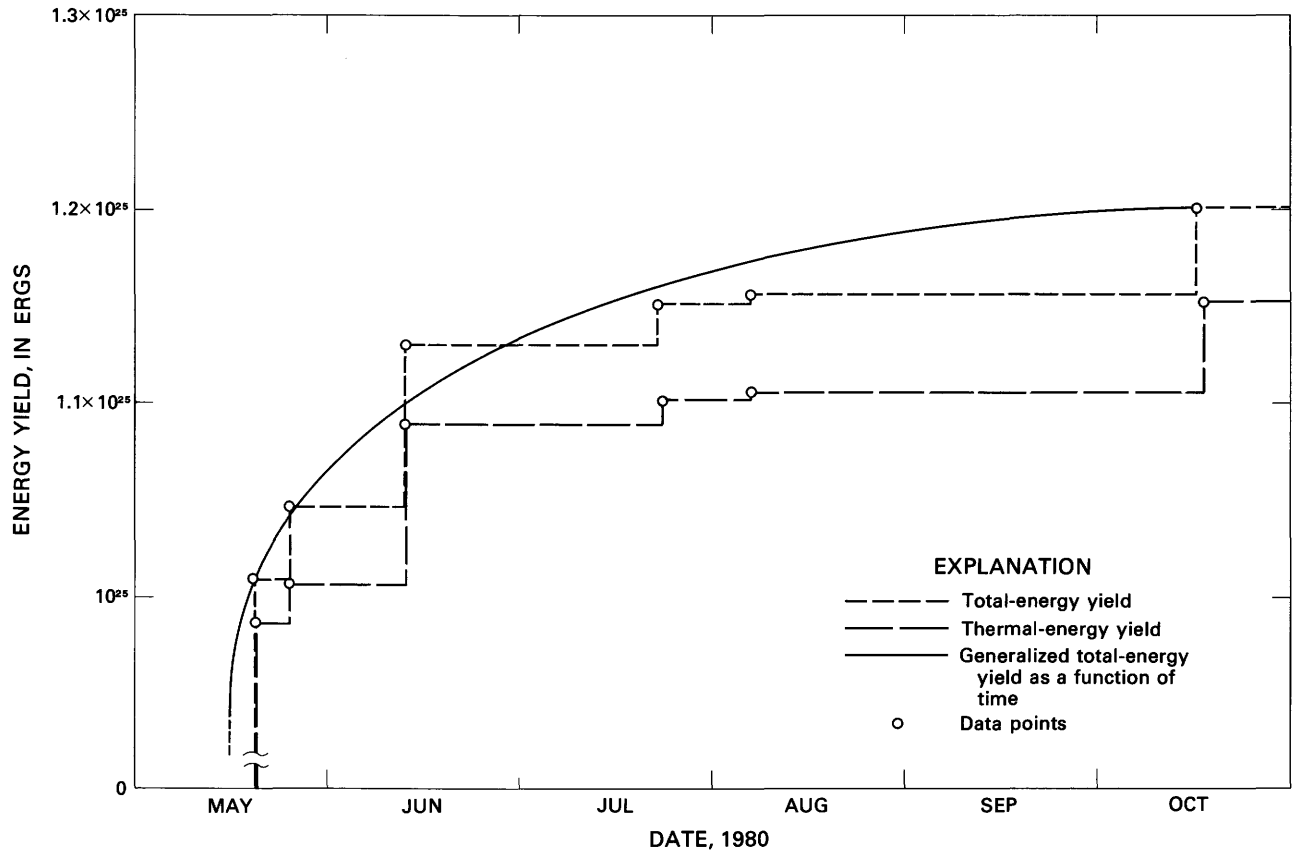

Figure 322.—Cumulative thermal energy expended in relation to total energy yield at Mount St. Helens between May and October 1980.

potential energy ($>6.5\times10^{23}$ ergs) expended in ejecting 2.73 km³ of lithic components from the old volcano. It follows, then, that the heat of the debris avalanche and associated deposits and fumarolic activity are probably derived directly from a magmatic component, rather than from transformation of kinetic energy. If so, the debris-avalanche and blast deposits contain the thermal equivalent of about 0.11 km³, or 4 percent, magmatic material, compatible with the inferred presence of a pre-May 18 cryptodome (Moore and Albee, this volume). The overall thermal energy yield of the eruption sequence is equivalent to the ejection of at least 0.38 km³ of magmatic material.

Approximately 85 percent (or more) of the energy released during the Mount St. Helens eruption sequence through October 1980 was expended in the eruption of May 18 at a maximum rate greater than 1.3×10^{20} erg/s or 10^7 MW. The rate of energy output (fig. 322) declined significantly from May through October.

In terms of energy released through October 1980, and, hence, in magnitude of eruption, the Mount St. Helens sequence is comparable to the Mauna Loa eruption of 1950 (table 64). This similarity is to be expected because of the great volume of basaltic lava with its huge thermal energy content extruded from Mauna Loa. In comparison to the 1956 eruption of Bezymianny, Kamchatka (Gorshkov, 1959), our conservative estimate of energy yield at Mount St. Helens equals 60 percent of the total energy expended at Bezymianny.

REFERENCES CITED

Birch, F., Schairer, J. F., and Spicer, H. C., 1942, Handbook of physical constants: Geological Society America of Special Paper 36, 325 p.

Blackwell, D. D., 1978, Heat flow and energy loss in the western United States, chapter 8 in Smith, R. B., and Eaton, G. P., eds., Cenozoic tectonics and regional geophysics of the

western Cordillera: Geological Society of America Memoir 152, p. 175–208.

Burnham, C. W., *in* Yoder, H. S. Jr., 1979: The Evolution of the Igneous Rocks Fiftieth Anniversary Perspectives, Chapt. 16, Volatile Constituents: Princeton University Press, p. 439–482.

Day, A. L., and Allen, E. T., 1925, The volcanic activity and hot springs of Lassen Peak: Carnegie Institute of Washington, no. 360, 186 p.

Desai, P. D., Navarro, R. A., Hasan, S. E., Ho, C. Y., DeWitt, D. P., and West, T. R., 1974, Thermophysical properties of selected rocks: Center for Information and Numerical Data Analysis and Synthesis, CINDAS Report 23, 256 p.

Fougere, P. F., and Tsacoyeanes, 1980, AFGL Magnetometer observations of Mount St. Helens eruption: American Geophysical Union, EOS, v. 61, no. 50, p. 1209.

Friedman, J. D., and Frank, David, 1980, Infrared surveys, radiant flux, and total heat discharge at Mount Baker volcano, Washington, between 1970 and 1975: U.S. Geological Survey Professional Paper 1022-D, 33 p.

Friedman, J. D., Heiken, Grant, Randerson, D., and McKay, D. S., 1976, Observations of eruption clouds from Sakurazima volcano, Kyushu, Japan from Skylab 4: Journal of Volcanology and Geothermal Research, v. 1, p. 305–329.

Gorshkov, G. S., 1959, Gigantic eruption of the volcano Bezymianny: Bulletin Volcanologique, ser. 2, v. 20, p. 77–112.

Hédervári, P., 1963, On the energy and magnitude of volcanic eruptions: Bulletin Volcanologique, v. 25, p. 373–385.

Imbó, Giuseppe, 1965, Eruptive energies: Annali dell' Osservatario Vesuviano, Serie VI, p. 1–43.

Keenan, J. H., and Keyes, F. G., 1936, Thermodynamic properties of steam: New York, John Wiley and Sons, Inc., 89 p.

Minikami, T., 1950, On explosive activities of andesitic volcanoes and their forerunning phenomena: Bulletin Volcanologique, Ser. II, tome X.

Mitchell, J. M., 1980, Mt. St. Helens, a climate change: Weatherwise, American Meteorological Society, v. 33, p. 120–121.

Reed, J. W., 1980, Barograph records of Mount St. Helens eruption of May 18, 1980: Sandia National Laboratories, Environmental Research Division 4533, Report 6/9/80.

Rittmann, Alfred, 1963, Les volcans et leur activite: Edition Francaise, Masson et Cie, Editeurs, Paris, Vie.

Robie, R. B., and Waldbaum, D. R., 1968, Thermodynamic properties of minerals and related substances at 298.15K * * * and one atmosphere * * * and at higher temperatures: U.S. Geological Survey Bulletin 1259, 256 p.

Stout, N. D., and Piwinskii, A. J., 1980, The enthalpy (H_T - H_{298}) of anhydrous silicate melts from 1520 to 2600 K: Lawrence Livermore Laboratory UCRL-52918, 53 p.

Taylor, R. E., and Groot, H., 1980, Thermophysical properties of Mount St. Helens sample: Thermophysical Properties Research Laboratory, TPRL 237, 11 p.

Thorarinsson, Sigurdur, 1967, The eruptions of Hekla in historical times, *in* The eruption of Hekla 1947–1948: Reykjavík, Vísindafélag Islendinga, Society Scientiarum Islandica, 182 p.

Tsuboi, Chuji, 1933, Notes on the mechanical strength of the earth's crust: Tokyo University Earthquake Research Institute Bulletin, v. 11, pt. 2, p. 275–277.

Tsuya, Hiromichi, 1955, On the 1707 eruption of volcano Fuji: Tokyo University Earthquake Research Institute Bulletin, v. 33, p. 341–383.

Weill, D. F., Stebbins, J. R., Hon, R., and Carmichael, I. S. E., 1980, The enthalpy of fusion of anorthite: Contributions to Mineralogy and Petrology, v. 74, p. 95–102.

Yokoyama, Izumi, 1956, Energetics in active volcanoes, 1st paper (Activities of volcano Mihara, Ooshima Island during the period 1953–53): Tokyo University Earthquake Research Institute Bulletin, v. 34, p. 185–196.

_____1957, Energetics and active volcanoes: Tokyo University Earthquake Research Institute Bulletin, v. 35, pt. 1, p. 75–97.

_____1972, Heat and mass transfer through volcanoes: Revista Italiana Geofisica, v. 21, p. 165–169.

AIR-FALL DEPOSITS

Ash falls accompanied every major eruption in 1980, as well as the steam-blast eruptions prior to May 18. The resulting air-fall ash stratigraphy is complex but is resolvable because observations were made after each major eruption. The data collected permit correlations and comparisons between the individual air-fall deposits and variations in eruptive behavior, changing composition and volume of erupted magma, direction and velocity of upper winds, effects of eolian fractionation, and with earlier ash deposits from Mount St. Helens and other similar volcanoes.

During the early steam-blast activity from March 27 to May 14, the volume of ash erupted and the area covered were small, and the total bulk volume was only about 8×10^5 m^3 (Sarna-Wojcicki, Waitt, and others). The ash consisted entirely of angular lithic and crystal grains that originated by abrasion and brecciation of preexisting rocks from the conduit and vent. The volume of ash erupted is less, by an order of magnitude, than the volume of the crater formed during the same time interval, mainly because the volume of the new crater resulted partly from deformation and partly from melting of ice in the preexisting summit crater.

Air-fall deposits of the May 18 eruption display a complex stratigraphy reflecting the multiple eruptive events. Deposits within a few tens of kilometers of the volcano contain four principal units (Waitt and Dzurisin): (1) basal gray lithic ash that contains much organic material and is related to the directed blast, (2) tan pumice and lithic lapilli deposited from the plume of the vertical eruptive column, (3) pale-brown vitric ash interpreted as related to ash clouds generated by pyroclastic flows on the north slope and to large steam explosions near Spirit Lake, and (4) fine gray ash that resulted from the waning of the the eruption late on May 18 and settling out of fines still in the atmosphere from earlier activity. Such a sequence, deposited within 12 hr on May 18, demonstrates that multiple stratigraphic units can be deposited rapidly during a single eruptive sequence.

More distant ash-fall deposits show fewer units, as coarser and denser lithic and crystal fragments preferentially settled out, resulting in deposition of a single bed of fine vitric ash at distances of more than a few hundred kilometers from the vent (Sarna-Wojcicki, Shipley, and others). Ash fall was visible at least 1,500 km to the east. Mapped distributions of the ash-fall deposits differ from radar and satellite locations of the airborne ash cloud, reflecting different wind directions and velocities at different altitudes and times. Thickness and volume of the combined tephra of May 18 are similar to those of the major 19th-century air-fall deposit (tephra layer T), but are an order of magnitude less than the largest prehistoric tephra units from Mount St. Helens.

Air-fall deposits of the explosive eruptions from May 25 through Oct. 16–18 are much smaller than those of May 18, and they generally decreased in volume with time (Waitt and others). These deposits trend in varying azimuths away from the volcano, reflecting differing wind directions. Each shows offsets in thickness and grain-size axes, which resulted from differing directions and velocities of high- and low-level winds, and each shows a local increase of thickness far downwind from the volcano.

THE 1980 ERUPTIONS OF MOUNT ST. HELENS, WASHINGTON

PREMAGMATIC ASH ERUPTED FROM MARCH 27 THROUGH MAY 14, 1980–EXTENT, MASS, VOLUME, AND COMPOSITION

By ANDREI M. SARNA-WOJCICKI, RICHARD B. WAITT, JR., MARTA J. WOODWARD, SUSAN SHIPLEY, *and* JOSE RIVERA

ABSTRACT

During the early period of activity from March 27 until May 14, the volume of ash erupted and the area blanketed by the ash were small. Much of this early ash alternated with snow accumulations, and as a result, a detailed stratigraphy of ash and snow was briefly preserved. We estimate the total mass of early ash erupted to be about 10^{12} g, and to have a total bulk volume of about 8×10^5 m^3 (assuming a bulk density between 1.2 and 1.6 g/cm^3). Assuming the ash to have come from rock having a density of 2.6 g/cm^3, this corresponds to a volume of 4×10^5 m^3 of solid rock, an order of magnitude less than the 7.5×10^6 m^3 volume of the crater in mid-April. The discrepancy in volume is due to (1) the amount of ash erupted being underestimated on the flanks and summit area of the volcano and in far-distal areas, (2) the volume of the summit crater that had been glacial ice, and (3) the volume of the crater caused by crustal distention.

Ash erupted during the early period consisted of angular lithic and crystal grains nearly identical in mineralogy and chemical composition to coarse lithic ejecta at the summit of the volcano. These ejecta probably originated by abrasion and brecciation of preexisting rocks within the vent during gas explosions. Juvenile material was not found in this early ash.

Lithic-crystal ash of this type may be mistaken for clastic detritus in sedimentary strata. As at Mount St. Helens and other similar volcanoes when such ash can be identified, it may serve as a precursor to future major magmatic eruptive episodes.

INTRODUCTION

From March 27 through May 14, small nonmagmatic eruptions ejected ash as high as 2.5 km above the summit crater. Ash was carried by wind in every direction within a radius of about 50 km; dustings were reported from as far as Bend, Oreg., 250 km to the south, and 120 km to the north at Tacoma, Wash.

ASH AND SNOW STRATIGRAPHY OF EARLY NONMAGMATIC ERUPTIONS

Beginning March 27, Mount St. Helens was monitored and photographed such that not only were many times and durations of venting events recorded, but the azimuths of many airborne plumes and air-fall lobes were routinely recorded.

Much of the ash erupted during the nonmagmatic phase was deposited on snow, particularly at higher elevations near the volcano, during late March and

early April. During these eruptions ash falls were often interspersed with snowfalls, and on occasion snow and ash fell together. This stratigraphy made it possible to identify ash layers from individual small eruptions and to sample ash uncontaminated by ground detritus (fig. 323). Uncontaminated samples could also be collected from natural sediment traps such as leaves.

In late April and early May much of the snow cover had melted and ash was deposited directly on the ground, as it had been at lower elevations farther from the volcano throughout the early activity. As the top layer of snow melted, the younger layers of ash became superposed on earlier ones below, until the entire sequence was telescoped into a single layer. Ash layers exposed at the surface and underlain by snow rapidly developed a small-curd texture apparently caused by wetting of the ash with melting of underlying snow, and accretion of the wet ash owing to surface tension (fig. 324). In most places, where the ash cover was uneven or patchy, the ash melted the underlying snow faster than the adjoining ash-free snow melted, because ash has a lower albedo than snow and absorbs more heat from insolation during the day (see Driedger, this volume). The wet ash layer became progressively uneven if not discontinuous, and formed a diffuse base owing to the downward transposition of fine ash particles into the melting snow. In melted areas, the remnant composite ash layer was patchy even where ash fall had been relatively heavy. Where ash fall had been light, the ash so blended into the groundcover that it was not a recognizable, discrete layer. The ejecta from relatively energetic eruptions were much coarser and thicker in the summit area than on the lower flanks of the volcano; the smaller eruptions deposited virtually all their ejecta on the upper flanks. Some of the denser eruptive clouds produced slope-hugging cold

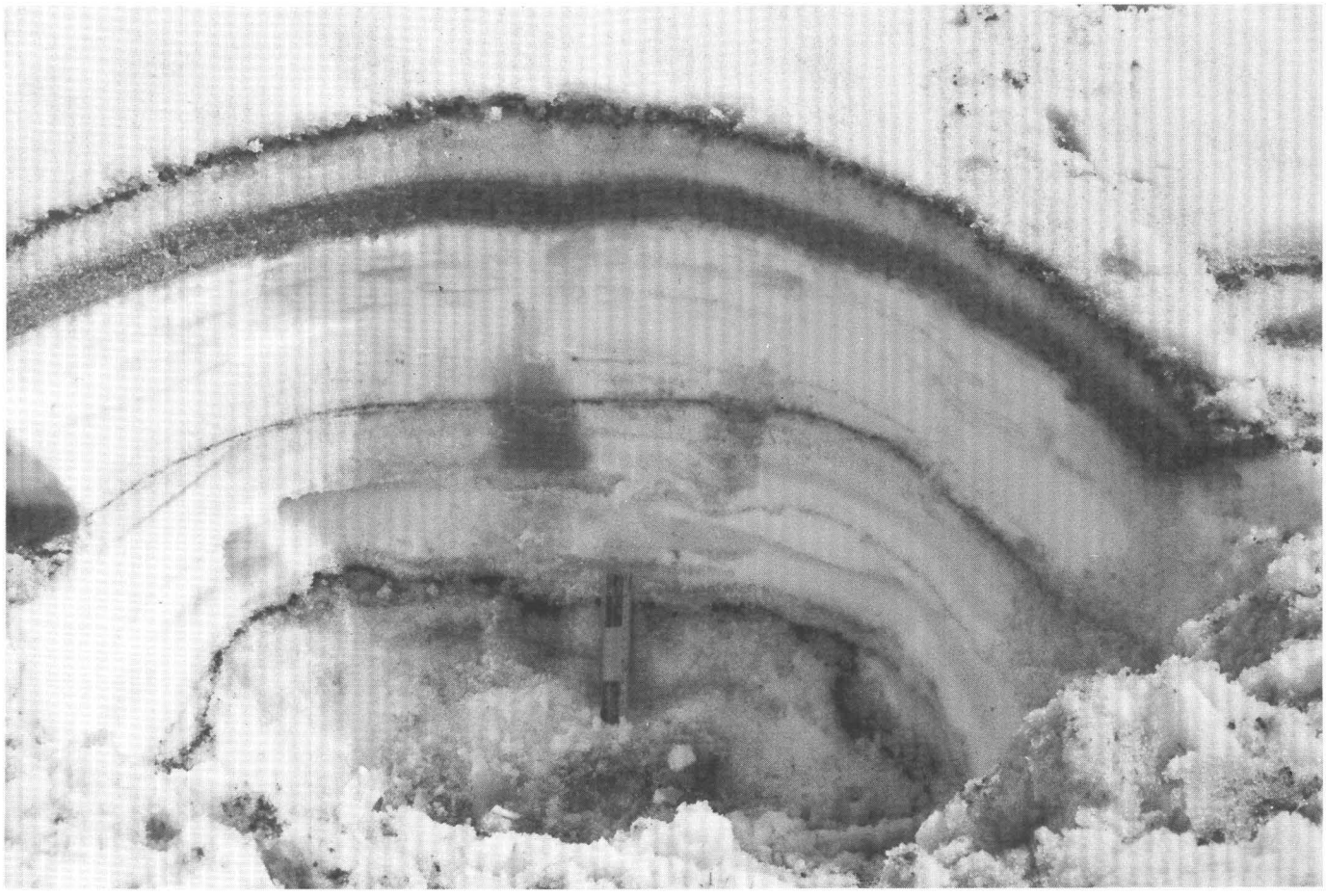

Figure 323.—Stratigraphy of ash and snow at Timberline parking lot, north flank of Mount St. Helens, April 11, 1980. Scale, 15 cm.

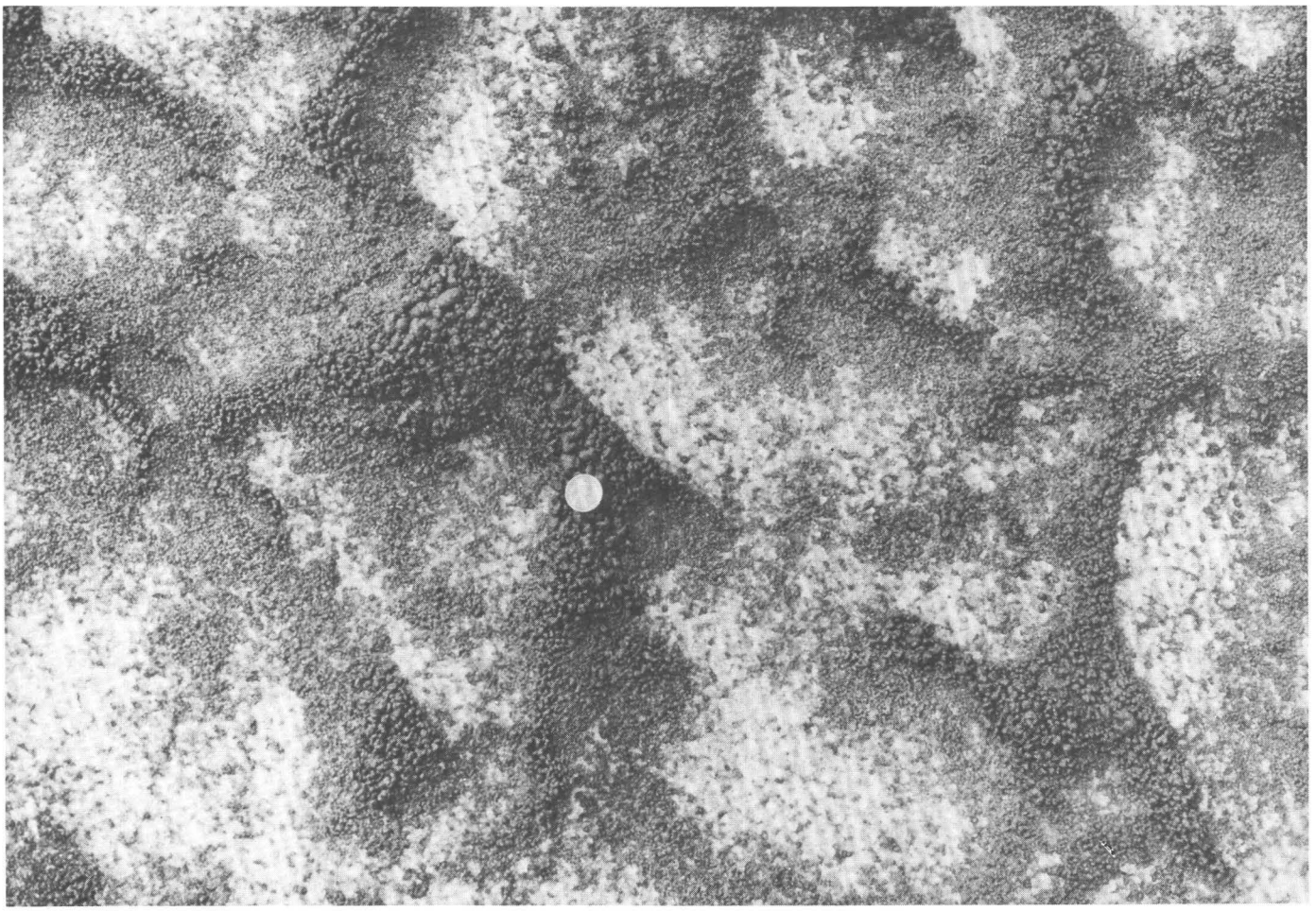

Figure 324.—Snow having surface layer of ash with curd texture. Sample collected east of Mount St. Helens in Smith Creek, March 29, 1980.

flows of ash clouds down the downwind flank of the volcano. The flows would separate from the surface about halfway down the mountain, leaving a very sharp margin of the deposit (fig. 325).

From March 27 until April 1 the bases of ash columns from the volcano were dark gray and even black at the base, as was the color of newly fallen ash on snow, indicating that the ash was erupted and fell wet. After April 1 some of the ash plumes were gray to light gray, also the color of ash-fall lobes on the mountain. These colors indicate that some ash was erupted and fell relatively dry. On April 4, for example, 9 km northwest of the crater a sample was collected dry as the ash fell through clouds on a generally rainy day—indicating that the ash was erupted dry and warm enough to remain dry in transit despite the wet clouds.

MASS AND VOLUME OF EARLY NONMAGMATIC ASH

Estimates of minimum mass and volume of material erupted prior to April 16 were made from samples collected during April 14 through 16. Direct measurements of ash thickness were unreliable because of the diffuse and uneven snow-ash boundaries.

Samples for mass measurements were collected from about 30 sites within a 40-km radius of the volcano, although the upper flanks of the volcano where the deposit was decimeters or meters thick was not measured. We collected the samples from 30 × 30-cm or larger areas where snow was still on the ground, which isolated the ash from ground detritus. The collected ash was separated from thawed snow

Figure 325.—Sharp lobate margin of flow-emplaced ash on north flank of mountain (right), April 2, 1980. At extreme right just below lobe margin is Goat Rocks. View is to west-southwest.

water by suction filtering, then dried and weighed. An isomass (mass per unit area) map obtained by contouring the resultant values shows a multi-lobe pattern of deposition that reflects winds during the different eruptions (fig. 326). To estimate the mass of material erupted, areas within each isomass contour were measured by planimetry, and the areas multiplied by their respective mass increments. The total estimated mass is about 8×10^{11} g. This estimate does not include the mass of ash produced during minor nonmagmatic eruptions that followed our volumetric sampling. If included, deposits of eruptions between April 17 and 22 and between May 7 and 14 would increase our estimate by no more than one third, to a total of 11×10^{11} g. Even with this adjustment, the mass estimate is minimal. Neither the thick ejecta on the high flanks and summit of the volcano nor distal areas sprinkled by ash are accurately represented. Assuming a bulk density between 1.2 and 1.6 g/cm^3 for the uncompacted ash, the total ash blanket from the early nonmagmatic eruptions would amount to a volume of $7–9 \times 10^5$ m^3. Assuming a rock density of about 2.6 g/cm^3 for the summit-crater rock prior to eruption (somewhat lower than the 2.8 g/cm^3 typical of solid dacite to allow for fracture porosity, voids, and ice in the summit rocks), the estimated mass would be equivalent to 4×10^5 m^3 of solid rock, more than an order of magnitude less than the estimated 7.5×10^6 m^3 of material missing from the crater that had formed before May 18 (Moore and Albee, this volume). This discrepancy can be attributed to (1) the volume of the summit crater that had been glacial ice rather than rock, (2) our estimate of nonmagmatic-eruption mass underrepresenting the coarse ejecta

thickly deposited near the summit of the volcano and the fines deposited downwind, and (3) the volume of the crater that was caused by structural collapse rather than by explosive excavation.

COMPOSITION OF PREMAGMATIC ASH AND COARSE EJECTA

The tephra produced during the premagmatic phase of eruption originated by abrasion of rock within the crater and vent. The ash consists of moderately sorted to very poorly sorted euhedral to anhedral crystals, crystal fragments, and lithic grains, but contains no juvenile material such as volcanic glass or pumice. Some lithic fragments, however, have a vitric groundmass. Scanning-electron-microscope photographs of the ash show rounded edges, conchoidal fractures, and impact pits, probably caused by abrasion in the vent (figs. 327, 328). Dominant phyric minerals are calcic plagioclase and hypersthene, with subordinate amounts of clinopyroxene and hornblende and minor iron-titanium oxides. No phyric quartz was observed in the samples, although a pure-silica phase was detected under the electron microscope by energy-dispersive X-ray fluorescence spectrometry. The silica is in the form of cocoon-like coatings on some grains (fig. 329), probably opal or crystobalite formed by hydrothermal activity in the vent. Petrography of thin sections of lithic ejecta from the nonmagmatic events collected at the former summit crater indicates that the mineralogy of proximal lithic fragments is nearly identical to that of the more distal ash. Energy-dispersive X-ray fluorescence spectra of some minor and trace elements of lithic ejecta and coarse ash collected at the former summit (table 65) indicate that summit ash and lithic ejecta are nearly identical in chemical composition, further indicating that the ash originated as rock that was pulverized within the volcanic vent.

There is a systematic change in composition of ash that accumulated progressively farther downwind (fig. 330; table 65), probably because fine lithic fragments and the finer grained matrix were winnowed from the coarser lithic and crystal fraction. From

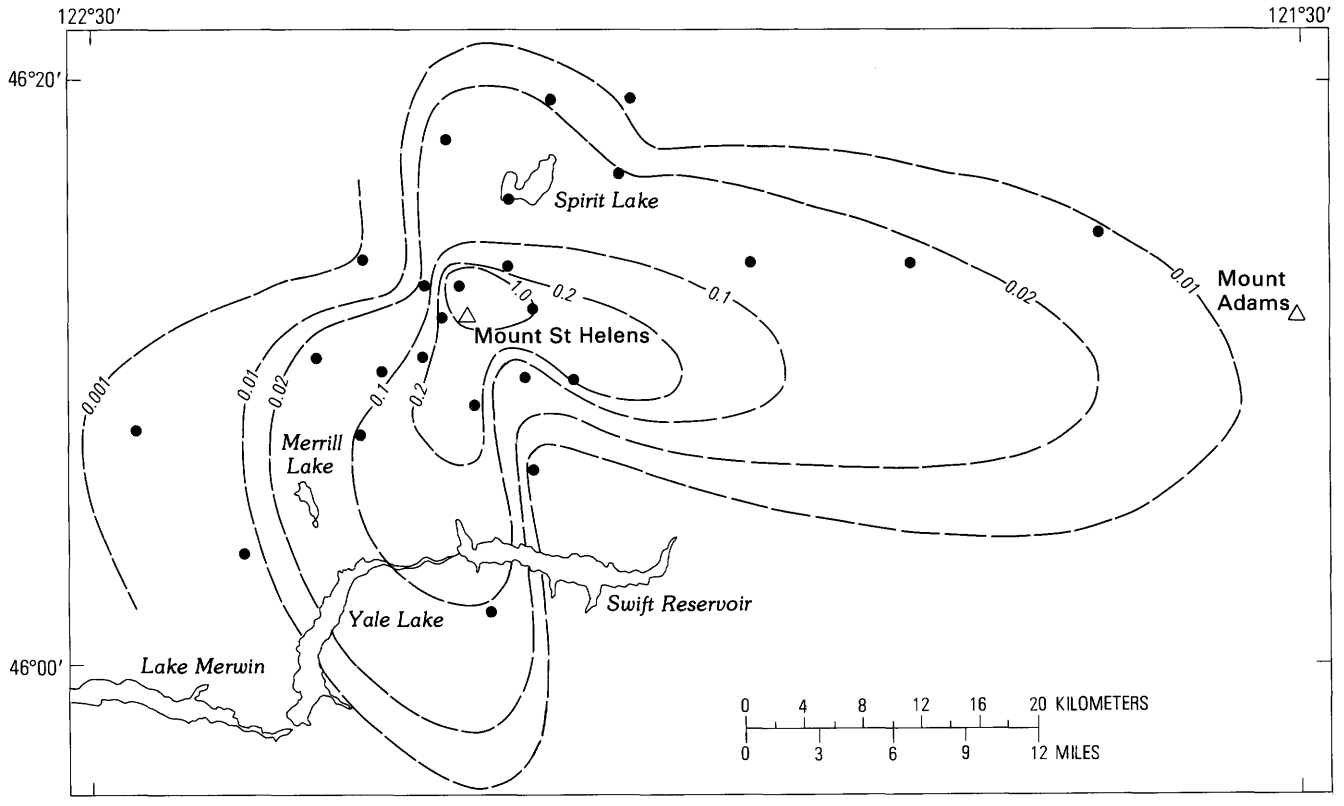

Figure 326.—Isomass map of early nonmagmatic ash erupted from Mount St. Helens between March 27 and April 17. Isolines represent mass per unit of area in g/cm². Sample locality sites indicated by solid circles.

Table 65.—Energy-dispersive X-ray fluorescence analysis of bulk samples of Mount St. Helens ash and lithic ejecta

[Values given are ratios of integrated, normalized peak intensities to total counts in the spectral region (window) studied. USGS rock standard G-1 (granite) is given for comparison. M. Woodward, analyst]

Sample	K	Ca	Ti	Mn	Fe	Cu	Zn	Rb	Sr	Y	Zr	Nb	Date collected	Site[1]	Weight (g)	Sample type
DSH-1	107	104	171	96	1,017	29	52	347	4,216	313	2,057	292	03/29	DW	0.50	Ash.
DSH-2a	95	94	172	99	1,029	25	47	341	4,237	314	2,005	314	03/29	DW	.49	Do.
DSH-2b	96	97	172	97	1,026	26	48	351	4,245	321	2,053	298	03/29	DW	.50	Do.
DSH-2c	94	96	174	99	1,028	26	47	340	4,223	307	2,068	318	03/29	DW	.50	Do.
DSH-4	91	89	169	100	1,033	25	45	330	4,260	310	2,014	304	03/30	DW	.50	Do.
SH-8a	110	97	171	95	1,022	31	49	366	4,141	329	2,119	291	04/04	SC	.50	Do.
SH-8b	123	102	171	99	1,021	31	50	374	4,204	314	2,063	290	04/04	SC	.50	Do.
DSH-13	117	107	163	97	1,012	32	49	380	4,315	297	1,958	301	04/04	DW	.50	Do.
8033A	96	95	167	102	1,024	24	49	362	4,337	303	1,936	306	04/11	DW	.50	Do.
8033B	102	100	171	97	1,028	23	49	332	4,345	285	1,965	304	04/11	DW	.50	Do.
8036	91	96	170	103	1,035	22	48	323	4,402	284	1,894	289	04/11	DW	.50	Do.
SH-9	119	99	165	100	1,026	30	50	408	4,122	322	1,964	306	04/11	SC	.50	Do.
STA-10	119	102	166	96	1,014	32	50	391	4,087	335	2,051	314	04/16	SC	.50	Do.
STA-10.5	115	99	162	99	1,036	30	49	385	4,188	313	2,079	289	04/16	SC	.50	Do.
STA-10A	132	98	159	101	1,016	30	52	403	4,154	324	2,055	290	04/16	SC	.50	Rock.
STA-10B	123	99	158	100	1,022	28	52	381	4,118	327	2,045	285	04/16	SC	.50	Do.
STA-10C	126	99	164	98	1,023	30	51	404	4,105	348	2,059	300	04/16	SC	.50	Do.
G-1	994	73	219	89	819	50	114	1,506	1,960	502	2,485	453				
	943	69	226	91	863	48	115	1,532	1,994	497	2,517	392				

[1]DW, downwind ash, SC, summit or crater rim sample.

the former summit crater downwind to 20 km, the ash was enriched with the heavier and coarser crystals of feldspar and ferromagnesian minerals together with coarser lithic fragments, while fine lithic fragments and fine-grained matrix minerals probably were winnowed out and carried downwind beyond the sampled zone. The higher proportion of crystals is reflected in the enrichment of strontium relative to rubidium in the proximal downwind samples. The strontium, like calcium, is concentrated in the more coarsely crystalline, early crystallizing phyric minerals, whereas the rubidium most likely resides in the fine-grained, late crystallizing fraction that makes up the matrix of the rock. Ejecta near the vent are

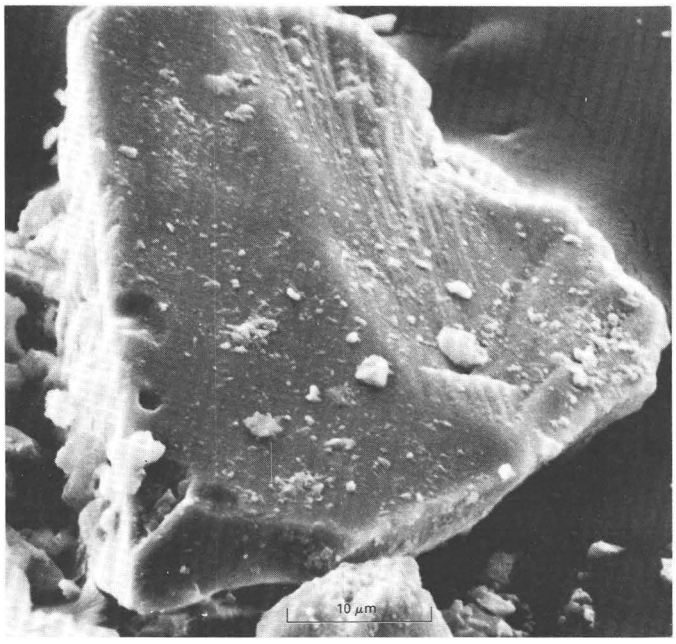

Figure 327.—Hypersthene crystal showing effects of abrasion. Photograph by Robert Oscarson, using scanning-electron microscope.

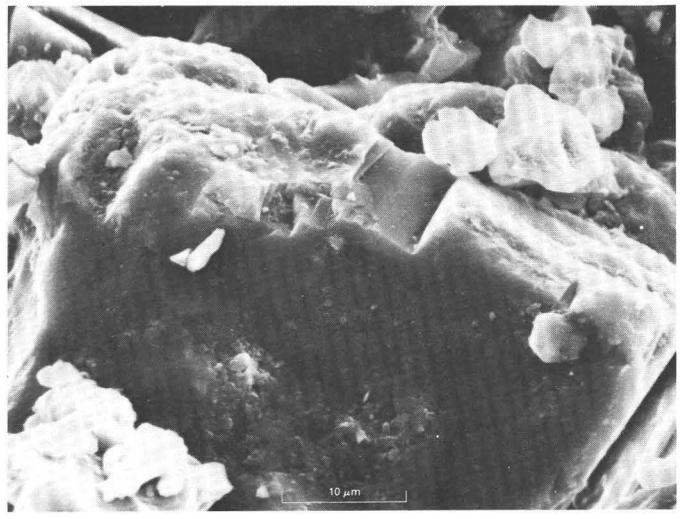

Figure 328.—Plagioclase feldspar crystal showing effects of abrasion and chipping along cleavages. Photograph by Robert Oscarson, using scanning-electron microscope.

coarse and dominantly lithic. Downwind near the volcano, the coarser lithic and phyric fragments tend to settle out, while finer grains remain suspended. At distal sites, the proportion of fine-grained matrix crystals and fine-grained lithic fragments tends to increase relative to other components.

NONMAGMATIC LITHIC-CRYSTAL ASH IN THE STRATIGRAPHIC RECORD AS PRECURSOR TO MAGMATIC ERUPTION

The type of premagmatic ash erupted from Mount St. Helens between March 27 and May 14 could easily be overlooked within clastic sedimentary strata—especially in volcanic terrane where such ash is petrographically similar to clastic detritus. Identified by texture, mineralogy, and chemistry, such tephra layers may constitute marker beds for stratigraphic correlation. Eruptions of lithic-crystal tephra at Mount St. Helens presaged the magmatic eruption of May 18. We are currently studying similar lithic-crystal tephra layers in the stratigraphic section at Mount St. Helens to determine their temporal relations to older pumiceous tephra units and thereby to determine their usefulness as precursors to older major magmatic eruptions.

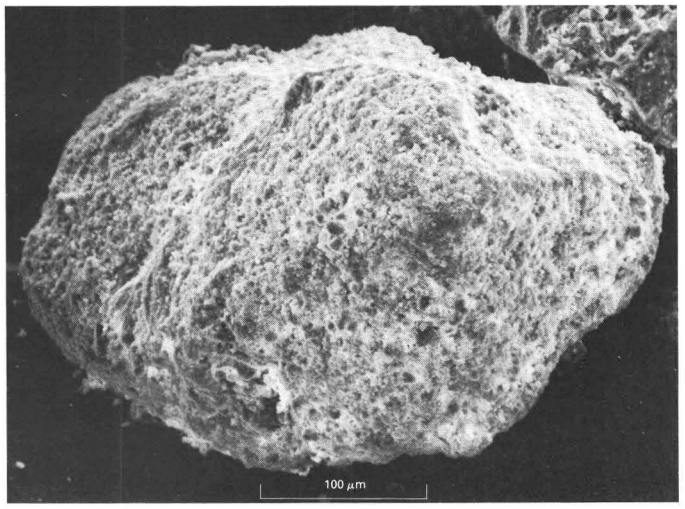

Figure 329.—Coating of a pure silica phase (crystobalite or amorphous silica) on a plagioclase feldspar grain. Photograph by Robert Oscarson, using scanning-electron microscope with energy-dispersive X-ray fluorescence spectrometer.

REFERENCE CITED

Crandell, D. R., and Mullineaux, D. R., 1978, Potential hazards from future eruptions of Mount St. Helens volcano, Washington: U.S. Geological Survey Bulletin 1383-C, 26 p.

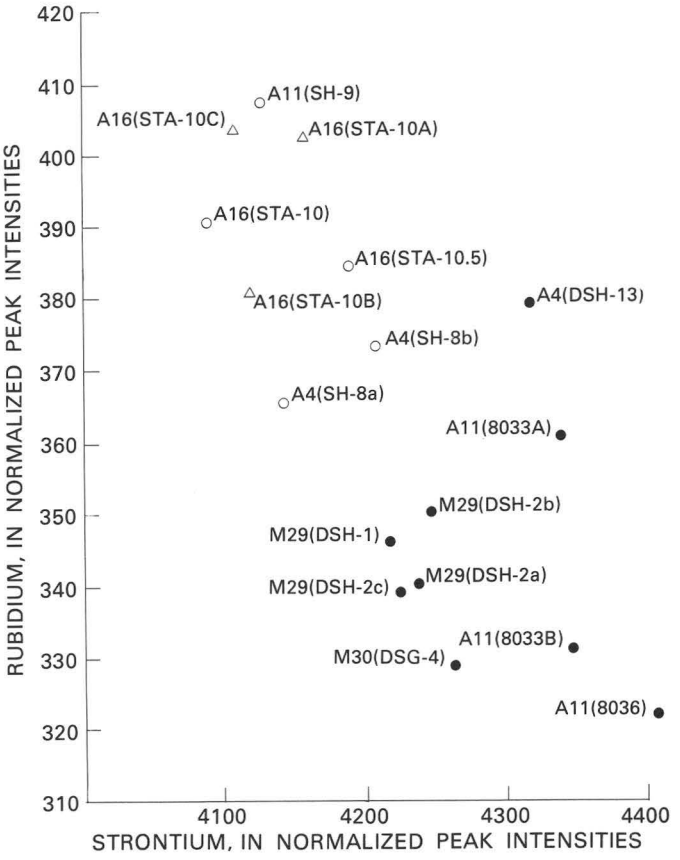

Figure 330.—Ratios of integrated, normalized peak intensities to total counts within each of two spectral regions (windows), for rubidium and strontium, determined by energy-dispersive X-ray fluorescence analyses of whole-rock ash and lithic ejecta erupted from Mount St. Helens, March-April, 1980. Solid circle, downwind ash sample collected ≥ 3 km from vent; open circle, ash at summit or crater rim; open triangle, lithic fragments from summit or crater rim. Sample number includes month and day sample was collected; M, March; A, April. All downwind ash was collected wet except sample DSH-13. All summit or crater rim ash was collected relatively dry.

THE 1980 ERUPTIONS OF MOUNT ST. HELENS, WASHINGTON

AREAL DISTRIBUTION, THICKNESS, MASS, VOLUME, AND GRAIN SIZE OF AIR-FALL ASH FROM THE SIX MAJOR ERUPTIONS OF 1980

By ANDREI M. SARNA-WOJCICKI, SUSAN SHIPLEY, RICHARD B. WAITT, JR., DANIEL DZURISIN, *and* SPENCER H. WOOD[1]

ABSTRACT

The airborne-ash plume front from the Mount St. Helens eruption of May 18 advanced rapidly to the northeast at an average velocity of about 250 km/hr during the first 13 min after eruption. It then traveled to the east-northeast within a high-velocity wind layer at altitudes of 10–13 km at an average velocity of about 100 km/hr over the first 1,000 km. Beyond about 60 km, the thickest ash fall was east of the volcano in Washington, northern Idaho, and western Montana. A distal thickness maximum near Ritzville, Wash., is due to a combination of factors: (1) crude sorting within the vertical eruptive column, (2) eruption of finer ash above the high-velocity wind layer at altitudes of 10–13 km, and (3) settling of ash through and below that layer. Isopach maps for the May 25, June 12, August 7, and October 16–18 eruptions show distal thickness maximums similar to that of May 18.

A four-unit tephra stratigraphy formed by the May 18 air fall within proximal areas east of the volcano changes to three units, two units, and one unit at progressively greater distances downwind. Much of the deposit beyond 200 km from the volcano has two units. A lower thin dark lithic ash is inferred to represent products that disintegrated from the volcano's summit in the initial part of the eruption and early juvenile pumice and glass. An upper, thicker, light-gray ash rich in pumice and volcanic-glass shards represents the later voluminous eruption of juvenile magma. The axis of the dark-ash lobe in eastern Washington and northern Idaho is south of the axis of the light-gray ash lobe because the high-velocity wind layer shifted northward during the eruption. The areal distribution of ash on the ground is offset to the north relative to the mapped position of the airborne-ash plume, because the winds below the high-velocity wind layer were more northward.

Except for the distal thickness near Ritzville, Wash., mass per area, thickness, and bulk density of the May 18 ash decrease downwind, because larger grains and heavier lithic and crystal grains settled out closer to the volcano than did the lighter pumice and glass shards. A minimum volume of 1.1 km^3 of uncompacted tephra is estimated for the May 18 eruption; this volume is equivalent to about 0.20–0.25 km^3 of solid rock, assuming an average density of between 2.0 and 2.6 g/cm^3 for magma and summit rocks. The estimated total mass from the May 18 eruption is 4.9×10^{14} g, and the average uncompacted bulk density for downwind ash is 0.45 g/cm^3. Masses and volumes for the May 25 and June 12 eruptions are an order of magnitude smaller than those of May 18, but average bulk densities are higher (about 1.00 and 1.25), owing to compaction by rain that fell during or shortly after the two eruptions. Volume and mass of the July 22 eruption are two orders of magnitude smaller than those of May 18, and those of the August 7 and October 16–18 eruptions are three orders of magnitude smaller. The eruption of May 18, however, is smaller than five of the last major eruptions of Mount St. Helens in terms of volume of air-fall tephra produced, but probably is intermediate if the directed-blast deposit is included with the air-fall tephra.

INTRODUCTION

The eruption of Mount St. Helens on May 18, 1980, and the succeeding major eruptions present an excellent opportunity to study dispersal patterns and

[1]Boise State University, Boise, Idaho, 83725.

depositional characteristics of windborne ash. Many large historic volcanic eruptions have occurred on islands or peninsulas adjacent to oceanic areas or in areas of difficult access. Where volcanoes have been accessible to direct observation, most downwind ash plumes have been carried across ocean areas, and the areal extent, thickness, grain size, and mass of ash could not be fully documented. Specific eruptions in point are Tamboro (1815), Krakatoa (1883), Katmai (1912), Hekla (1974), and Bezymianny (1956). Quizapú volcano (1932), however, is a notable exception. The May 18 eruption of Mount St. Helens occurred on land, and the ash plume was carried eastward across accessible areas where observations could be readily made on the ground. In addition, owing to technological developments within recent years, satellite imagery was available to track the areal extent and progress of an airborne-ash plume.

We mapped the areal distribution of an airborne-ash plume, charted its downwind progress, and compared its airborne distribution with the distribution of the ash lobe on the ground. Several geologists sampled across the ash lobe shortly after the ash had fallen; therefore, various characteristics were documented before the ash was disrupted by wind or rain. Because each geologist conducted a traverse completely across the fallen-ash lobe, using the same methods and observational criteria, a coherent, compatible data base was provided.

ACKNOWLEDGMENTS

This report is the result of a large cooperative effort by many individuals who contributed observations, samples, and other help and information. We are particularly grateful to T. E. Bateridge, J. O. Davis, W. H. Hays, M. P. Doukas, James Beget, Evelyn Newman, Robert Mark, Carol Price, Daniel May, Albert Eggars, Carolyn Driedger, Harry Glicken, Michael Ryan, M. W. Brugman, David Sawyer, and C. C. Helicker for conducting sampling traverses across tephra lobes.

We are also grateful to R. P. Hoblitt, P. L. Weis, Barry Voight, Thor Kiilsgaard, C. F. Kienle, Jr., Sandra Embrey, Edwin Olson, Gregory Hahn, J. A. Barker, Brian Atwater, Kenneth Fox, F. K. Miller, J. W. Nichols, Mrs. David Mahre, W. P. Nash, Bruce Cochran, C. R. Knowles, Lynn Disbrow, Lester Zeiheu, Glen Izett, Carl Rice, Edwin Danielson, Robert Courson, Robert Quinn, Michael Folsom, Daisuke Shimozuru, E. F. Hubbard, Steve Frenzel, Marv Fretwell, David Frank, D. P. Dethier, Norman Banks, R. R. Hooper, T. A. Cahill, R. E. Wilcox, James Bailey, John Strong, and D. B. Mitchell for providing samples, observational data, or other information.

We are grateful to Gail McCoy, who helped to compile thickness data and helped with grain-size analyses, and to Graig McHendrie, who helped with computer processing of grain-size data.

VERTICAL GROWTH AND DOWNWIND PROGRESS OF THE ASH PLUME FROM THE MAY 18 ERUPTION

A few minutes after the start of the eruption at 0832 PDT (Pacific Daylight time) on May 18, a vertical column of hot, ash-charged gas shot vertically from the volcano and grew rapidly to altitudes of 23 km or more. According to an airborne eyewitness, the vertical plume rose to an altitude of 7.6 km at 0838, to 10.7 km at 0840, and to about 18 km at 0842 (Rosenbaum and Waitt, this volume). The column expanded rapidly into a mushroom shape 10 min after the start of the eruption. By 0845, the time of the first satellite images after the start of the eruption, the ash plume had expanded to an ovoid lens about 80 km long in an east-west direction, 45 km wide in the north-south direction, and about 9–14 km in thickness (figs. 331, 332). At 0845 the top of the ash plume had risen to 23 km, and by 0900, to perhaps as much as 27 km (Carl Rice, oral commun., 1980). The average vertical rate of ascent of the column between 0838 and 0842 is 44 m/s, or about 160 km/hr (fig. 333). By 1012 the column had subsided to an altitude of about 13 km, but the eruption continued into the late afternoon.

The prevailing westerly wind swept the ash plume east-northeast. From a sequence of NOAA satellite photographs taken from stationary orbit at half-hour intervals between 0845 and 1816 on May 18 (fig. 332), we compiled an isochron map of the airborne-ash plume front. By 0945 the widening plume front passed over Yakima, Wash., 135 km downwind, and by about 1200, over Spokane, Wash., and Moscow, Idaho, about 400 km east of Mount St. Helens. By

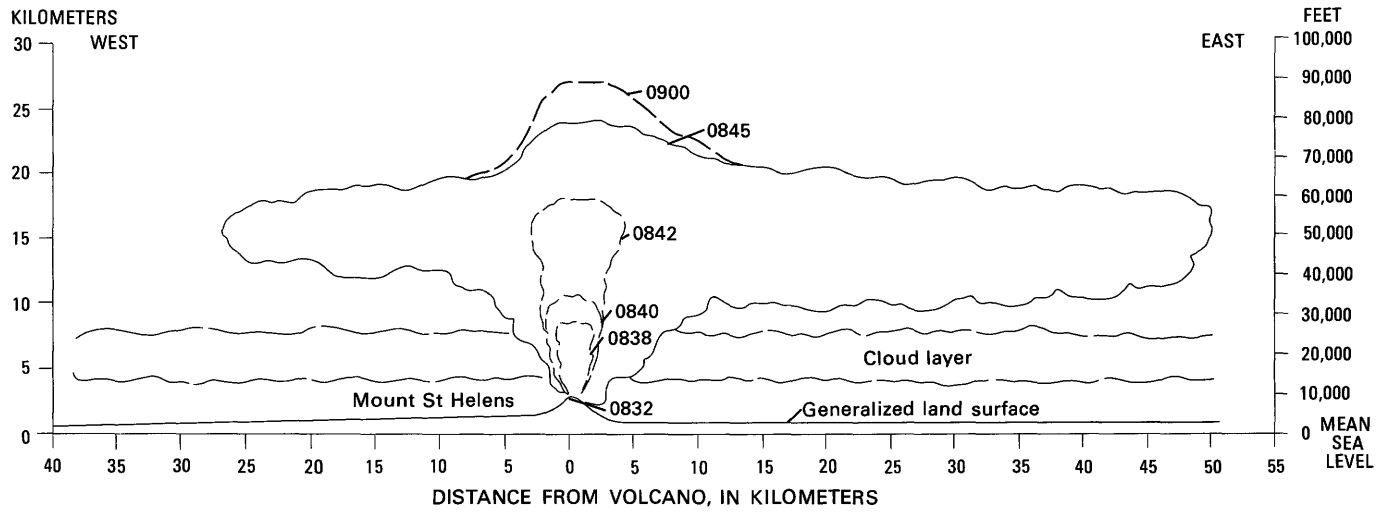

Figure 331.—Diagrammatic east-west profile showing early vertical growth and lateral expansion of plume from the May 18 eruption. Altitudes between 0838 and 0842 are from Rosenbaum and Waitt (this volume) and those between 0845 and 0900 are from Carl Rice (oral commun., 1980). Horizontal extent for 0845 is from NOAA satellite photograph taken at 0845 PDT, sector KB7.

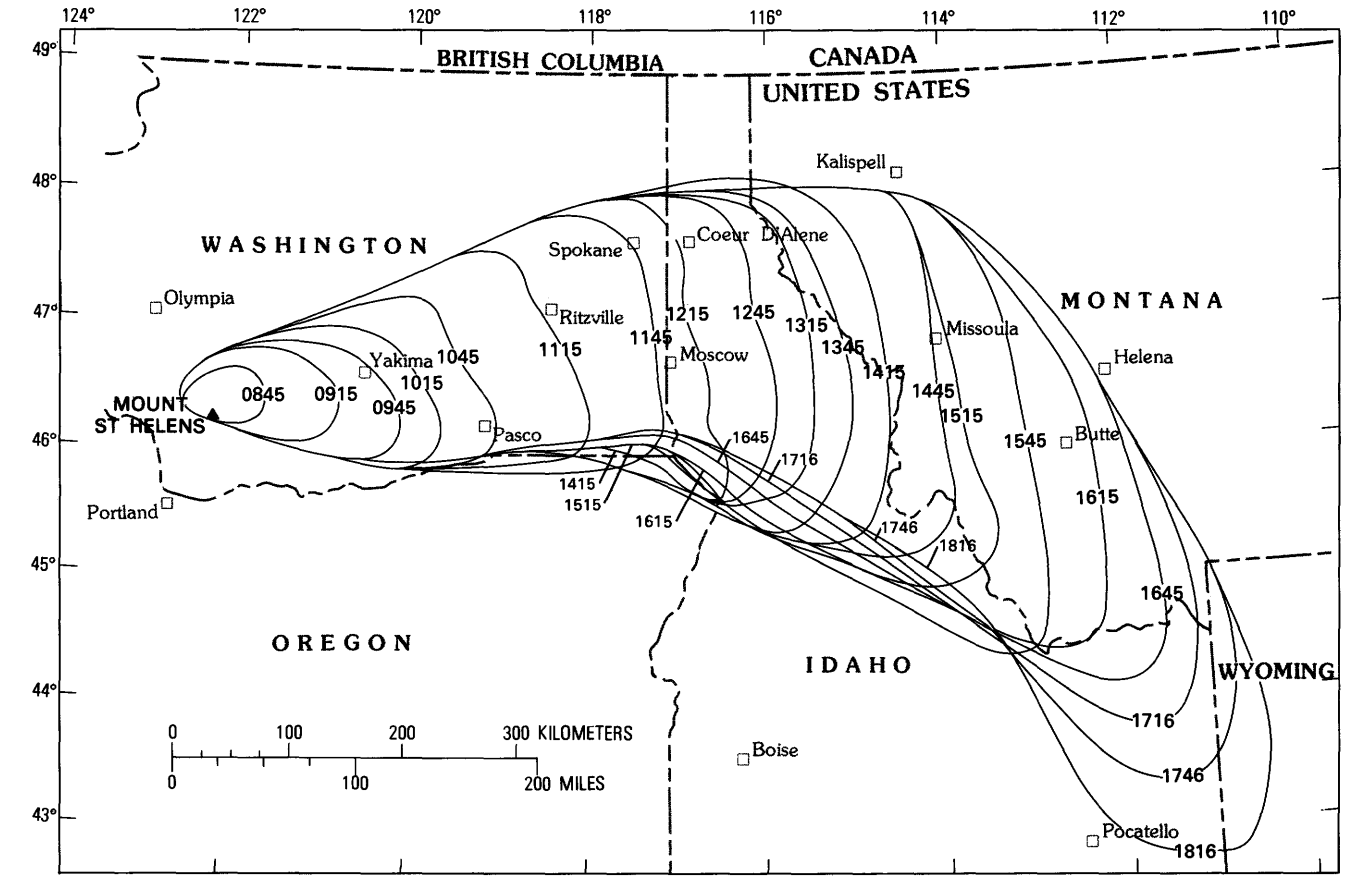

Figure 332.—Isochron map showing maximum downwind extent of ash from airborne-ash plume erupted from Mount St. Helens on May 18 and carried by fastest moving wind layer, as observed on satellite photographs. Map is compiled from NOAA satellite photographs (sectors KB7 and SA40) taken at half-hour intervals between 0845 and 1816 PDT. Plot of plume position relative to ground was visually corrected for zenith angle. Probable error in position of plume boundaries is ±10 km in the north-south direction, and ±5 km in the east-west direction.

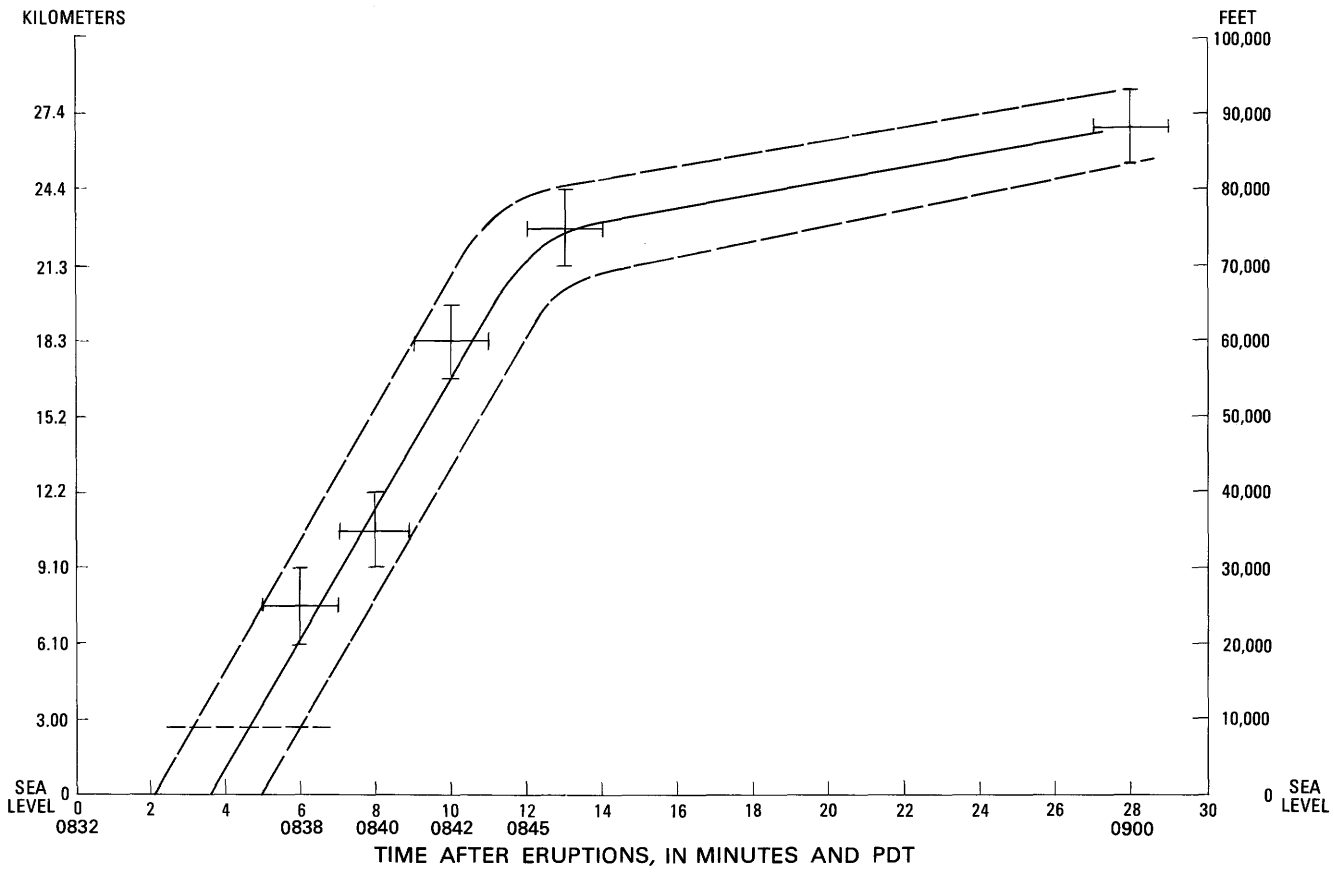

Figure 333.—Rate of ascent of vertical plume from eruption of May 18. Lower three data points are from eyewitness reports (Rosenbaum and Waitt, this volume). Upper two data points are from satellite observation (Carl Rice, oral commun., 1980). Bars indicate possible errors in time and altitude.

about 1500 the plume front had passed over Missoula, Mont., where changing wind directions swung the front to the southeast. By about 1800, the plume front had passed into northwestern Wyoming. After nightfall on May 18, the plume could not be monitored with visible-spectrum photographs, and infrared imagery was insufficient to define plume boundaries. By the morning of May 19, the ash plume had passed into the midcontinent, where its margins became so diffuse and mixed with clouds that its boundaries could not be accurately detected. The densest part of the ash plume, however, was tracked across the plains to the East-Central United States, where it swung northeast over New England, Maritime Provinces of Canada, and out over the North Atlantic Ocean. Traveling eastward, the ash plume returned over the West Coast of North America in early June after circling the globe (Danielson, 1980). Although high-velocity winds at altitudes of 10–13 km carried the main body of ash eastward, higher stratospheric winds carrying some fine ash looped over the Northwestern United States, then veered westward and carried the finest ash over the North Pacific Ocean (Danielson, 1980).

The heaviest ash fall from the plume east of Mount St. Helens was observed in Washington, northern Idaho, and western Montana; lighter ash fall was reported in Wyoming, western South Dakota, western Nebraska, Colorado, and northern New Mexico. Light dustings were sporadically reported farther east and northeast. The finest ash, which remains suspended in the atmosphere, has circled the Earth many times; on the basis of the effects from historic eruptions such as Krakatoa in 1883 (G. J. Symons, 1888), it is likely to remain suspended in the atmosphere for years.

We derived a traveltime curve (fig. 334) for the front part of the plume from figure 332 by plotting the time the plume traveled since the start of the eruption against the maximum horizontal distance it traveled between each satellite photograph. Plume-front velocities calculated from satellite imagery give

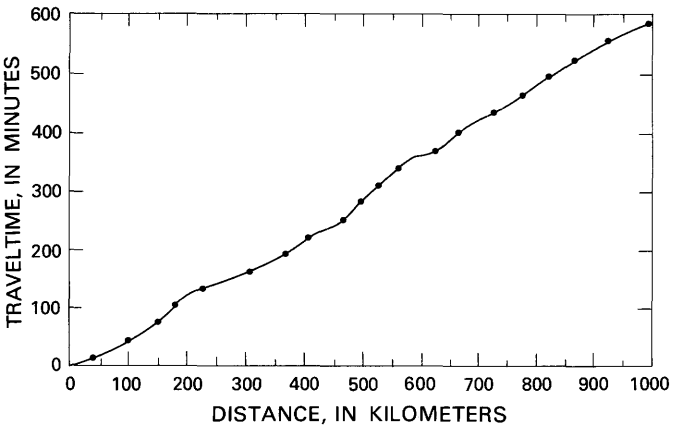

Figure 334.—Traveltime versus distance from the volcano for airborne-ash plume from the May 18 eruption. Traveltimes were calculated from a trajectory at approximately maximum distances from the volcano, as determined from NOAA satellite photographs (fig. 332).

estimates of the horizontal component of velocity only. An average horizontal component of velocity of the tephra plume front for the first 13 min is about 250 km/hr. The average azimuth of maximum velocity 13 min from the start of the eruption is about 040° from the volcano. This azimuth is intermediate between the predominantly northward direction of the initial directed blast and the 058° azimuth of the axis of the air-fall lobe that was determined from subsequent thickness measurements on the ground. This relation suggests that the initial directed-blast cloud was rapidly swept toward a more easterly direction by the prevailing wind. Because the 250-km/hr velocity represents an average over the first 13 min, and because the plume-front velocity decreased after the first 13 min, velocities of the expanding ash cloud in the first few minutes of the eruption must have been much greater. Average velocities of the ash-plume front over the first 13 min, as calculated from satellite photographs, were only about 220 km/hr in the direction of the prevailing wind, about 185 km/hr northward, about 150 km/hr northwestward, and zero to the south and southwest. The velocity of the plume front averaged about 100 km/hr as it traveled east-northeast over the first 1,000 km. Fine ash erupted above the level of high-velocity winds (above 13 km altitude) was carried at lower velocities along different trajectories (Danielson, 1980).

We do not have accurate altitude control for the ash-plume front as it traveled east-northeast. The base of the leading edge of the plume was reported to be at about 11.9–12.2 km, which corresponds to the high-velocity air layer along much of its observed route in the Western States, but diffuse parts of the downwind plume were observed to altitudes of about 21.3 km (Edwin Danielson, NASA-Ames, oral commun., 1980). Typical wind profiles at Spokane, Wash., for the period 1600 on May 17 to 0400 on May 19 (fig. 335), show velocity maximums at altitudes of 10.7–12.2 km. Low-level winds were more northward than were the high-level winds (fig. 335), which offset the ash lobe on the ground to the north relative to the position of the airborne cloud.

AREAL EXTENT AND THICKNESS OF ASH FROM THE MAY 18 ERUPTION

During traverses across the ash lobe, uncompacted thickness of ash was measured, and samples were collected from measured areas to determine the mass per area. Samples were collected from surfaces that were generally free of ground litter or dust prior to the eruption—from vehicles, shed roofs, and other artificial surfaces away from heavily traveled roads. The initial uncompacted thicknesses were measured before the first rain on May 21. Because most of the traverse through Ritzville, Wash., was made on May 21 and 22 after rain had begun, thickness values there were lower than those made before rain had started. We have adjusted the thickness values along this traverse by using associated mass-per-area values, and by comparing these values to mass-per-area values and associated uncompacted thicknesses along adjacent traverses that were measured before rain had started. Adjusted initial thicknesses for the Ritzville, Wash., traverse are on the average twice those measured after the rainfall.

The "saddle" near Vantage, Wash., and the distal thickness maximum near Ritzville, Wash. (figs. 336, 337), are unusual. This type of distribution has been documented only once—for the 1932 eruption of Quizapu (Larsson, 1937). Isopach maps for eruptions of May 25, June 12, August 7, and October 16–18 show similar distal thickness; thus, such features may be fairly common. Because these distal thickness highs were formed on fair days as well as rainy, they cannot be attributed to scavenging of ash by rain, a mechanism suggested for anomalous distributions of downwind thickness by Wilcox (1959).

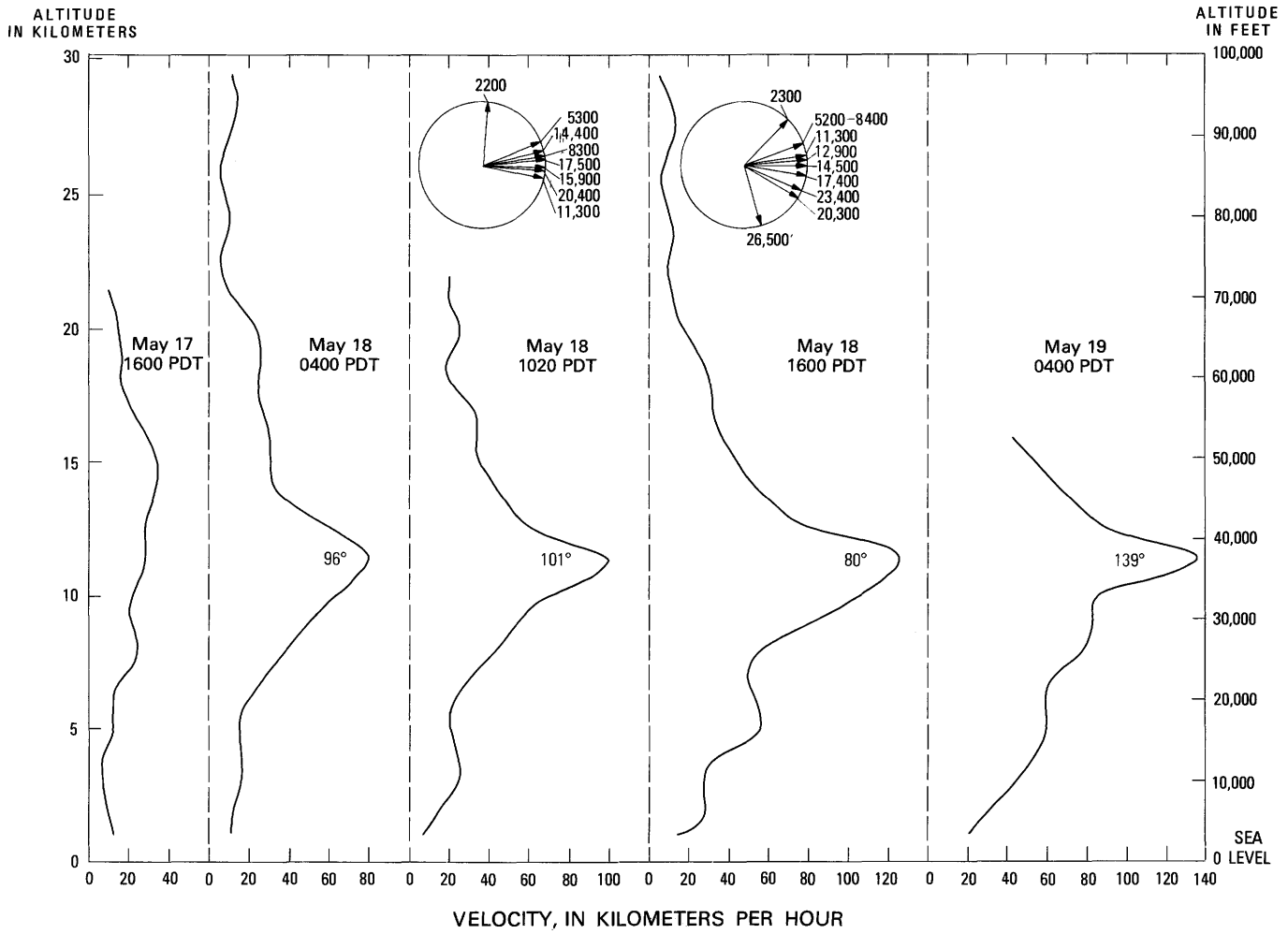

Figure 335.—Average wind-speed profiles from measurements at Spokane, Wash., between May 17 and May 19, by the U.S. National Meteorological Service. Data were averaged for intervals of about 1,500 m (5,000 ft). Average direction toward which the wind was blowing is shown in degrees, adjacent to the high-velocity wind layer. Circular wind diagrams show average directions toward which the wind was blowing at different altitudes, at 1020 and 1600 PDT on May 18 at Spokane, Wash.

We do not understand how the distal thickness maximum near Ritzville, Wash., formed. Major factors controlling downwind distribution of tephra in an eruption such as that of May 18 are the height of the vertical eruptive column, the size range and distribution of ejecta, the velocities and directions of wind at different altitudes above the volcano and downwind, and the manner in which these factors vary with time. The vertical eruption column, which extended above the high-velocity wind layer for much of the day, probably acted as a crude sorting mechanism. J. G. Moore (written commum., 1980) suggested that the distal thickness maximum near Ritzville, Wash., formed from fallout of ash that was erupted above the high-velocity wind layer; the thickness low near Yakima, Wash., formed from ash injected into the high-velocity layer; and the primary areas of maximum thickness near the volcano formed from ejecta erupted below the high-velocity layer.

Along the easternmost traverse through Missoula, Mont., ash was too thin in most places to measure directly. Thicknesses for this traverse were estimated by comparing an average of three uncompacted thicknesses in Missoula, where the ash was thick enough to measure, with the average of associated masses per area. Thicknesses at other sampled sites in

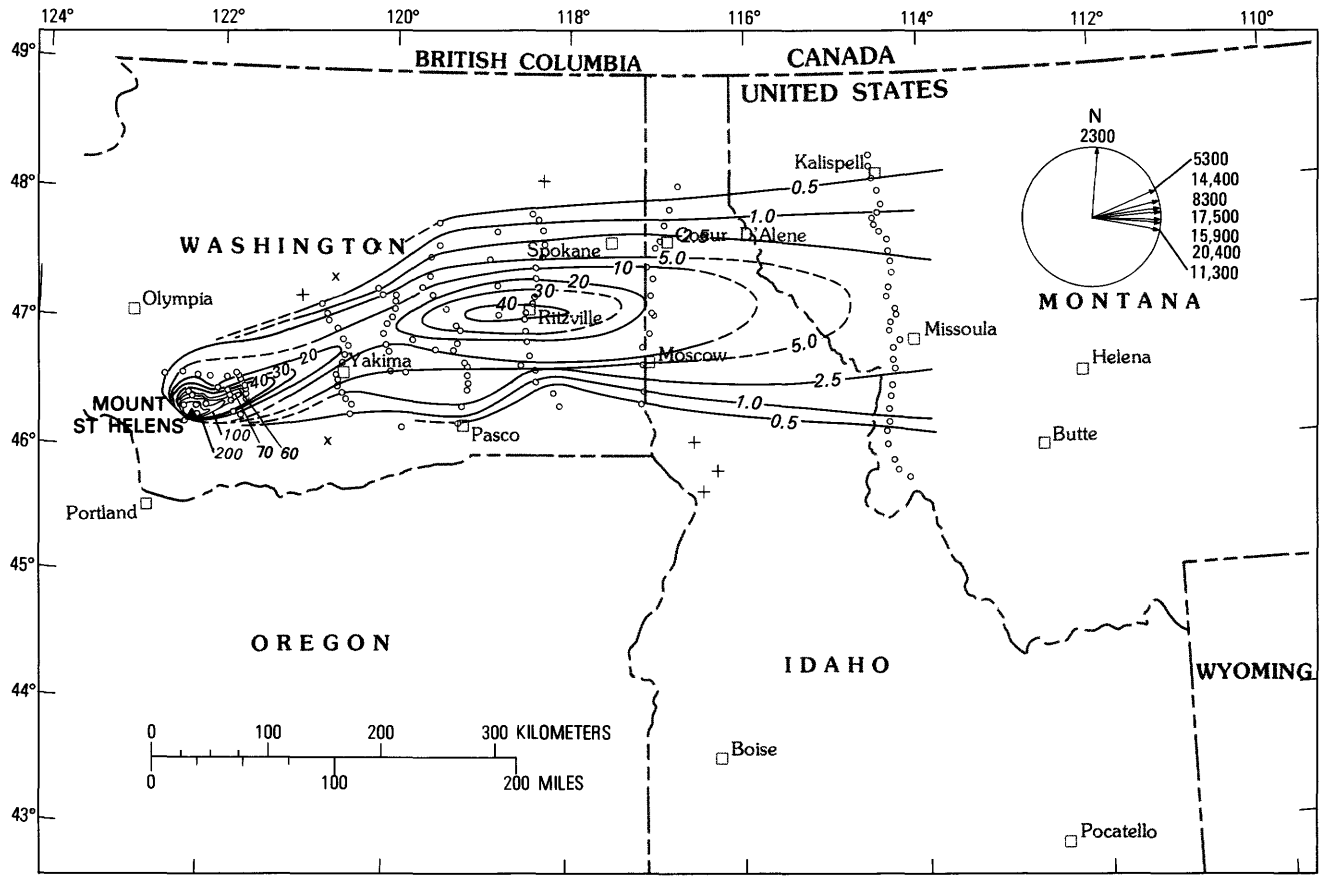

Figure 336.—Isopach map of air-fall ejecta on May 18. Lines represent uncompacted thickness, in millimeters. +, light dusting of ash; x, no ash observed; circles, observation sites. Circular diagram shows average directions toward which wind was blowing, for different altitudes, at 1020 PDT on May 18, at Spokane, Wash. Data from U.S. National Meteorological Service. Thicknesses along north-south traverse through Ritzville and at four observation sites about 30–50 km to the west have been adjusted for postdepositional compaction due to rain. Ash along north-south traverse through Missoula was too thin to measure directly, and thicknesses have been calculated from mass per area, using thickness and associated mass per unit area measured near Missoula. Data on north-south traverse through Ritzville and four sites 30–50 km to the west from J. O. Davis. Data on north-south traverse through Missoula from Thomas Bateridge. Data in vicinity of Spokane from Paul Weis.

this traverse were calculated by applying this ratio to the known mass per area at each site.

Sampling traverses were not made east of western Montana, though spot thicknesses were reported farther east and southeast in Montana and Wyoming. Only a light "dusting" of ash fell farther downwind than Wyoming. Some reports of thicknesses within our map area by other observers were much higher than those stated in this report; for example, maximum thicknesses more than two times those reported in this study were observed by USGS personnel about 54 km north of Moscow, Idaho, near the axis of the May 18 ash plume (fig. 336) (Ernest F. Hubbard, oral commun., 1980). Hooper and others (1980) reported ash 1.25 cm thick in Moscow, Idaho, whereas we measured 0.4 cm on May 20 and 21. There are several possible reasons for these discrepancies: First, where observations were made prior to ours, initial uncompacted thicknesses may have been greater owing to greater initial cohesion between ash particles. Second, some observers may have reported maximum rather than average thicknesses. Thicknesses shown in figure 336 are the same as or lower than those reported by others. Our measurements are internally consistent and agree with isomass data that are based on independent measurements. Because some compaction

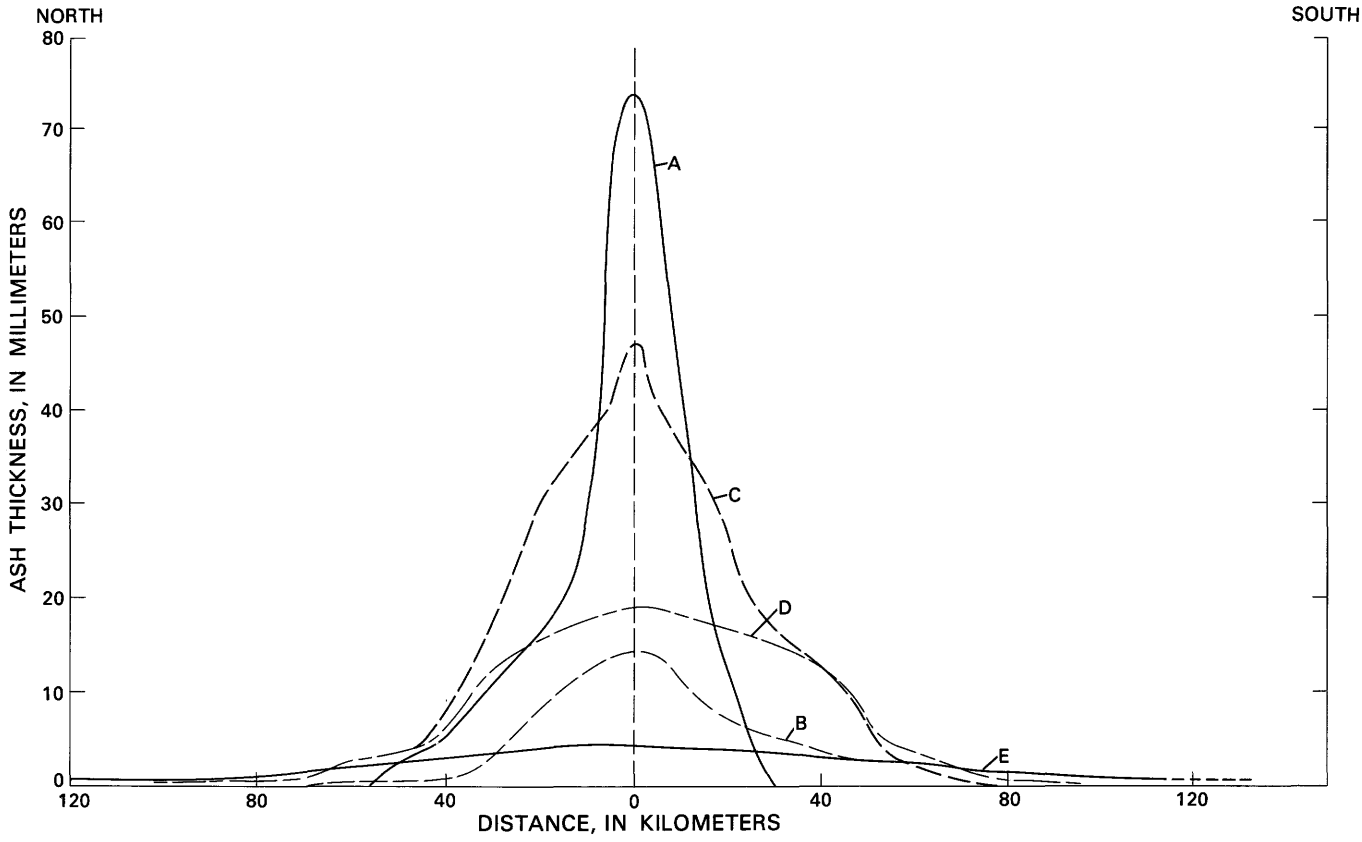

Figure 337.—Profiles across tephra lobe, normal to plume axis. Profiles are centered on axis at the following distances downwind from the eruption: A, 40 km; B, 170 km; C, 315 km (secondary thickness maximum near Ritzville); D, 415 km; E, 630 km.

undoubtedly occurred before some ash was measured, our estimate of initial bulk volume is a minimum. Initial uncompacted thickness is an ephemeral parameter that is not easily measured; consequently, it is not as reliable as isomass or compacted thickness.

MASS AND BULK DENSITY OF FALLEN ASH FROM THE MAY 18 ERUPTION

Compaction due to loading, wind, rain, or time will not affect measurements of mass, because mass per area is unchanged by compaction. Samples collected from measured areas were weighed, and mass per unit area was contoured (fig. 338). The shape of the isomass map is generally the same as that of the isopach map (fig. 336).

We estimated uncompacted bulk densities for individual observation sites by dividing the uncompacted thickness into the the mass per unit area. Thickness, mass, bulk density, and mean grain size generally decrease with distance from the volcano (figs. 339, 342). The decrease in bulk density reflects the depletion of crystal and lithic grains and the relative enrichment of the lighter pumice and glass shards downwind. This effect has been documented in other studies (Larsson, 1937). Packing of grains also plays a large if not dominant role in the decrease of bulk density downwind. Compaction by rain alone commonly effects a twofold increase in bulk density, indicating that newly fallen ash was very loosely packed. The angular and irregular glass and pumice shards that compose a progressively greater portion of low-density downwind ash are more loosely packed than are the denser, more equant crystal and lithic grains. The average bulk density calculated for Missoula, Mont., is very low (0.11 g/cm^3), although the data on uncompacted thickness there are sparse, and the error in measuring the very thin layer of ash is significant.

STRATIGRAPHY, GRAIN SIZE, AND AREAL DISTRIBUTION OF DOWNWIND ASH

Proximal stratigraphy of the May 18 air-fall deposits northeast of the volcano, along the axis of the downwind lobe, consists of four units referred to as units A through D (Waitt and Dzurisin, this volume). This stratigraphy changes progressively with distance downwind. Unit D can be traced only locally in proximal areas, and pinches out some distance west of Yakima, Wash., 135 km east-northeast of Mount St. Helens (fig. 339, *A*). The three layers observed 130 km downwind along the lobe axis north of Yakima are a basal, 1-mm-thick, gray silt-size ash (unit 1); an overlying, 1-mm-thick, "salt-and-pepper"-colored fine sand-size ash composed of lithic and crystal fragments and fine pumice shards (unit 2); and an uppermost, 17-mm-thick, fine sand- to silt-size light-gray to tan ash composed of pumice and glass shards, crystals, and minor lithic fragments (unit 3) (fig. 339). Unit 1 is the distal equivalent of proximal layer A3. Unit 2 is the distal equivalent of layer B1, a coarse "salt-and-pepper"-colored layer that contains abundant angular lithic fragments, small pumice lapilli, and crystals (Waitt and Dzurisin, this volume). Unit 3 is most probably a distal facies of layers B2 and B4, the thickest proximal layers that contain most of the coarse pumice (fig. 339). Unit 3 may also contain late-settling, fine low-density particles from the other proximal units A through D.

About 200–250 km downwind from Mount St. Helens along the lobe axis, unit 2 pinches out or merges with the basal unit. From Moses Lake, some

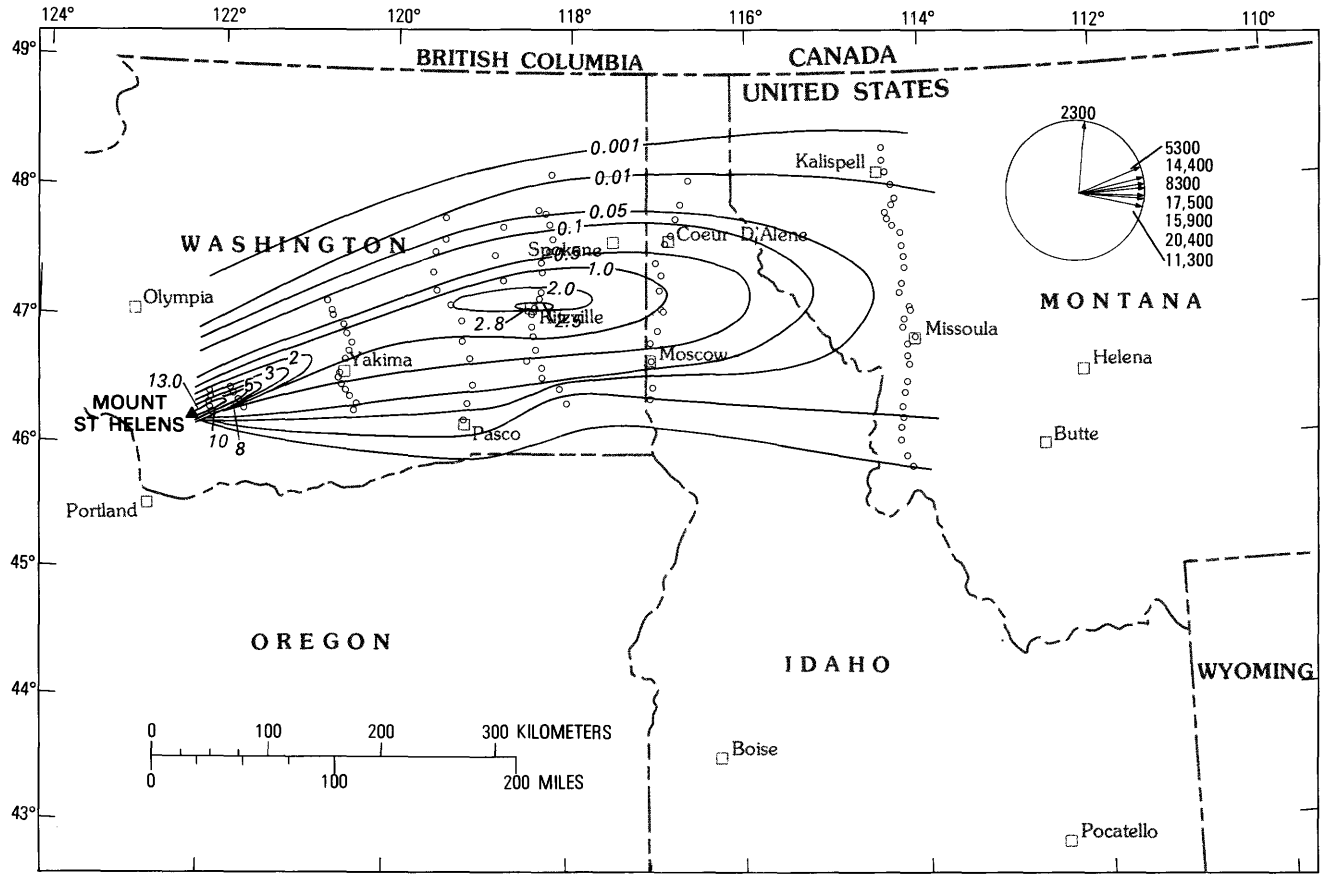

Figure 338.—Isomass map of ash erupted from Mount St. Helens on May 18. Lines represent mass of ash per area, in g/cm². Open circles represent observation stations. Circular diagram shows average directions toward which wind was blowing for different altitudes at 1020 PDT on May 18, at Spokane, Wash. Data from U.S. National Meteorological Service. Samples of ash were collected from measured, essentially horizontal surfaces, oven dried at 60°C for 12 hr, and weighed. Data on north-south traverse through Ritzville, Wash., and three sites 40–50 km to the west, from J. O. Davis. Data on north-south traverse through Missoula, Mont., from Thomas Bateridge.

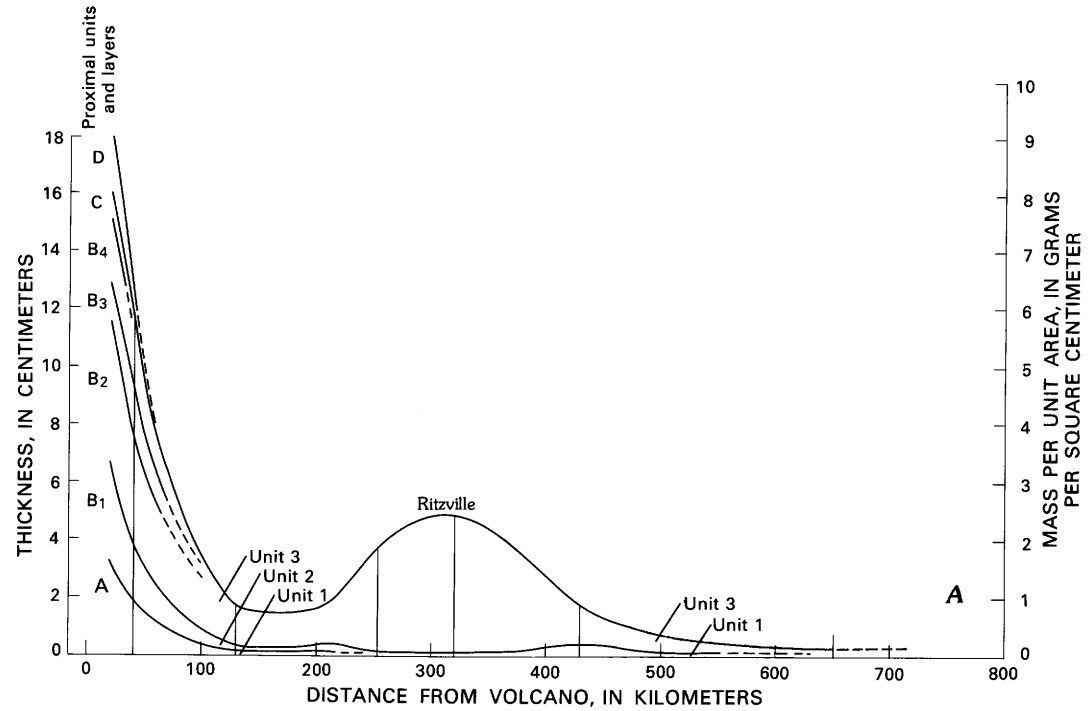
Proximal units and layers
D
C
B4
B3
B2
B1
A
Unit 3
Unit 2
Unit 1
Ritzville
Unit 3
Unit 1
A
THICKNESS, IN CENTIMETERS
MASS PER UNIT AREA, IN GRAMS PER SQUARE CENTIMETER
DISTANCE FROM VOLCANO, IN KILOMETERS

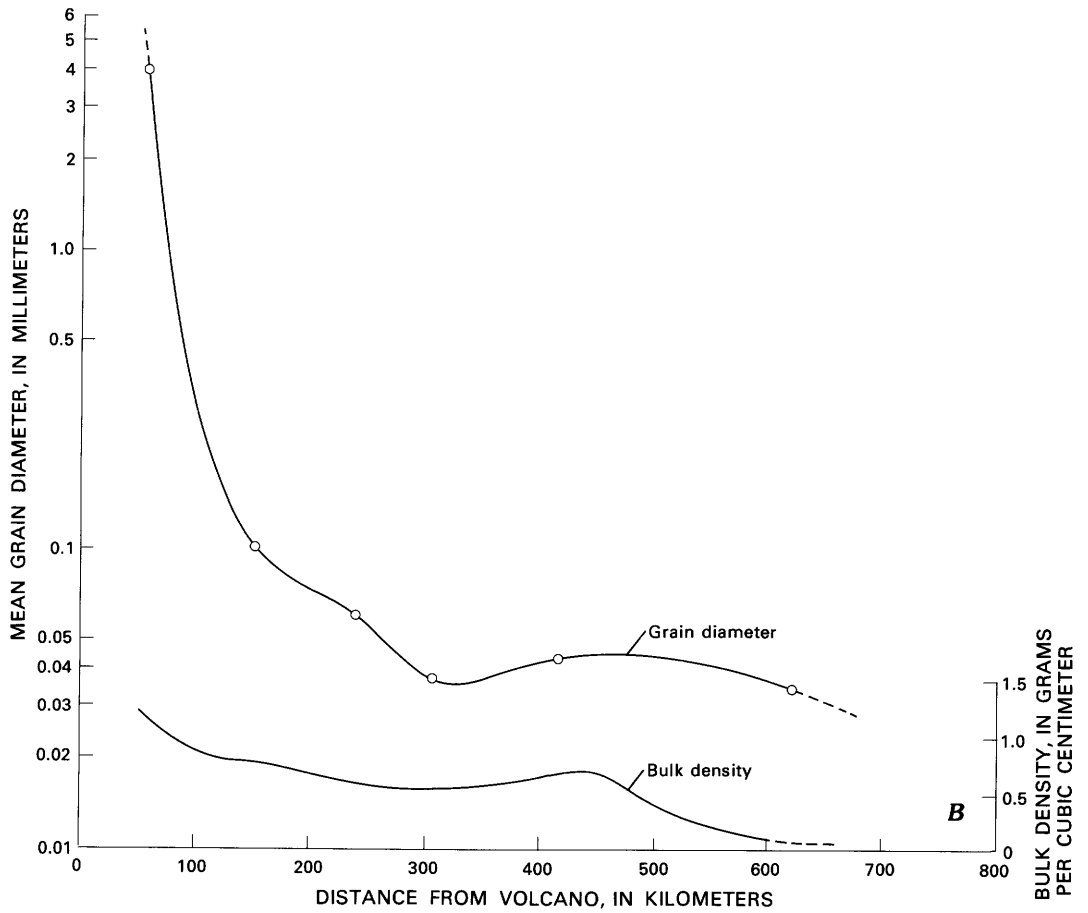
Grain diameter
Bulk density
B
MEAN GRAIN DIAMETER, IN MILLIMETERS
BULK DENSITY, IN GRAMS PER CUBIC CENTIMETER
DISTANCE FROM VOLCANO, IN KILOMETERS

250 km east of Mount St. Helens, to the western border of Idaho and to some undetermined distance beyond, the ash blanket consists of unit 1 and the thicker unit 3. Farther downwind, in western Montana, only a single light-gray layer was deposited. The basal unit may have pinched out or, more likely, the two layers have merged owing to mixing downwind.

The pronounced distal thickening of ash in the vicinity of Ritzville, Wash. (figs. 336, 339), is caused by the thickening of unit 3. Unit 1 also may have a distal thickness maximum between 400 and 500 km downwind along the lobe axis. This distal thickening of unit 1 may correlate with a high in bulk density and mean-grain diameter (fig. 339) at about the same distance.

The dark ash (unit 1) began to fall considerably before the light-colored ash (unit 3). At Spokane, Wash., the advancing ash cloud became visible about 1400, ash started falling about 1543, and daylight was noticeably obscured about 1545 (Paul Weis, written commun., 1980). Satellite photographs, however, indicate that the ash front passed over Spokane about 2 hr before the cloud was visible to the ground observer, except for a sun halo that appeared about 1215. This time difference suggests that the front of the ash cloud was diffuse. Similarly, dark ash fell at Pullman, Wash., from about 1400 until about 1615, when light-colored ash began to fall. The light-colored ash continued to fall until about 0200 on May 19 (Hooper and others, 1980). On the north-south traverse through Moscow, Idaho, the axis of the dark layer is about 40 km south of the axis of the light-colored layer (fig. 340); this difference suggests that deposition for each layer occurred under somewhat different wind conditions. At Missoula, Mont., ash fall began about 2000–2030, some $3\frac{1}{4}$ to $3\frac{3}{4}$ hr after the front passed, but near the north end of the traverse, ash fall began between 2100 and 2200, about $3\frac{1}{2}$ to $4\frac{1}{2}$ hr after the front passed. Both in eastern Washington and in western Montana, 2 hr or more elapsed between the passage of the ash-cloud front and the start of ash fall on the ground. The delay was greater on the north side of the plume than on the south side.

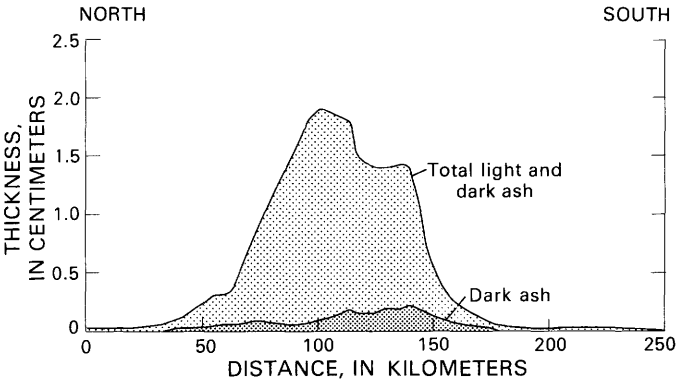

Figure 340.—Thickness of dark- and light-colored ash layers along the north-south traverse through Moscow, Idaho (see fig. 336 for location of traverse).

We compared the isochron map, which shows the approximate shape and areal dimensions of the airborne-ash plume, with the isomass map, which shows the minimum areal and mass distribution of the ash on the ground (fig. 341). The ash lobe on the ground is offset to the north relative to the position of the airborne plume. This northward shift of the air-fall lobe relative to the position of the airborne plume is a result of different wind directions with altitude. Much of the ash deposited from central Washington to western Montana was probably carried in the high-velocity (60–125 km/hr) wind layer at altitudes of about 10–13 km (fig. 335). This layer was transporting ash towards azimuths 093°–101° (1020 PDT at Spokane according to U.S. National Meteorological Service). By 1600, these high-velocity winds had shifted northeastward, toward azimuths 079°–087° (fig. 335). This shift in wind direction apparently is the cause of the axis of the earlier, dark ash being offset to the south of the axis of the later, light-colored ash (fig. 340). During late morning and afternoon of May 18, however, the slower low-level wind was consistently more northeastward than was the high-level wind. At Spokane, velocities of low-level winds at altitudes 2,250–5,300 m were 30–60 km/hr. At 1020 they were toward azimuth 005°–070°, and at 1600 toward azimuth 048°–070°. These vectors 10°–90° north of the high-level wind vectors explain why the ash fell on the ground north of the observed airborne-ash plume.

Figure 339.—Stratigraphy of May 18 air-fall deposits northeast of volcano, along axis of downwind lobe. A, Variation in stratigraphic units and thickness. B, Variation in mean grain size and uncompacted bulk density. Bulk-density profile was derived by dividing thickness curve into mass-per-area at corresponding distances from volcano. Contours dashed where uncertain.

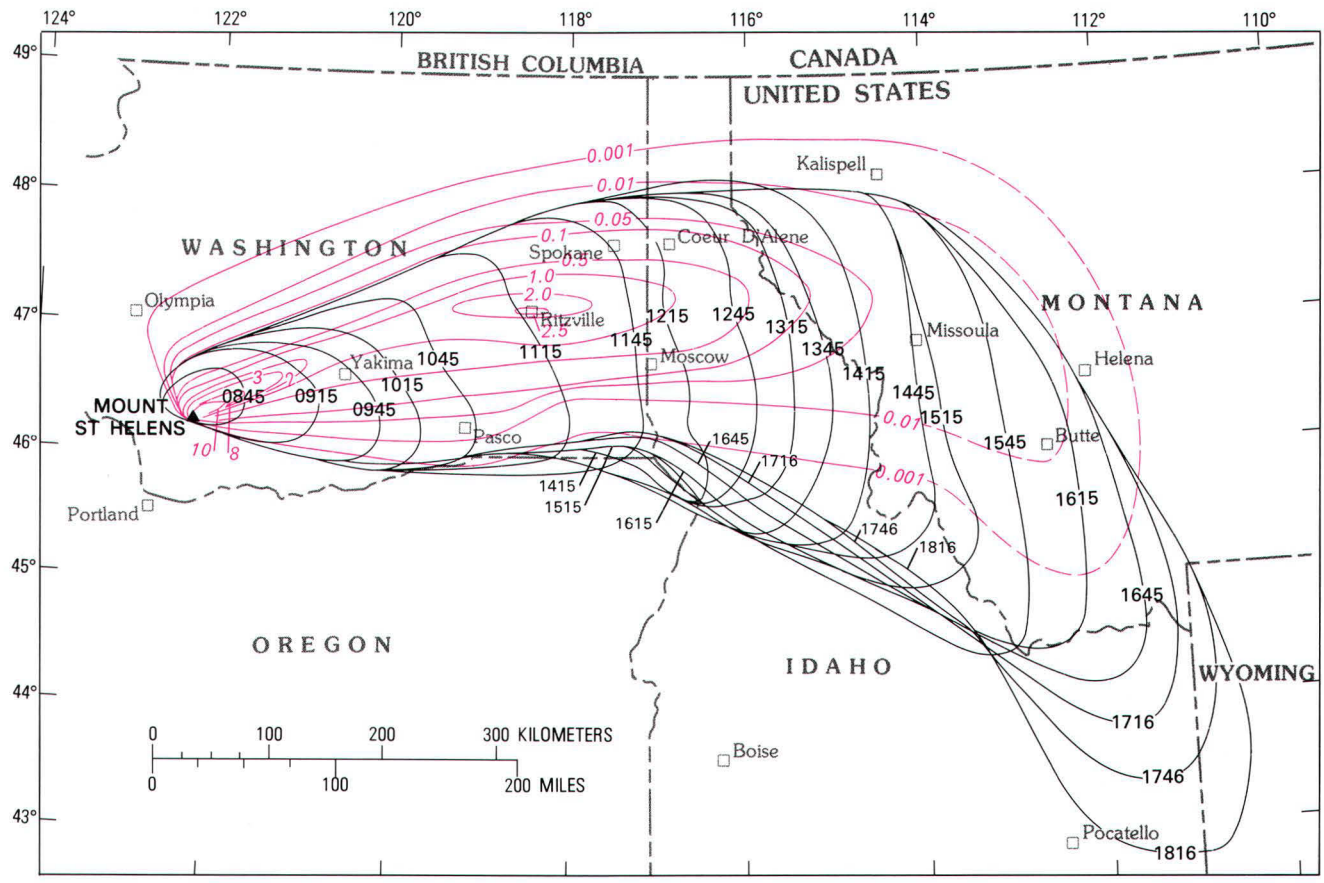

Figure 341.—Isochron and isomass maps compared. Black lines, isochrons of airborne-ash plume; red lines, isomass of fallen-ash lobe; and red dashed lines, inferred positions of isomass lines extended beyond area of control. Time in PDT. See figures 332, 338, and text for further explanation.

Winnowing of fine ash from the main body of the plume caused dusting and reduced visibility for tens of kilometers north of the northern boundaries of our isopach and isomass maps. The southern plume boundary, however, was quite sharp in south-central Washington. Within 50 km of Mount St. Helens, the southern margin of the air-fall lobe is marked by coarse, scattered pumice lapilli, but it contains no fine ash. Downwind in central Washington, eyewitnesses reported a sharp southern boundary to the falling ash, which was coarse- to medium-sand size. The fine ash was winnowed northward toward the axis of the air-fall lobe. Size analysis of ash samples confirms eyewitness observations. In Washington and northern Idaho, mean grain sizes on the south side of the downwind lobe are greater and size gradients are steeper than those on the north side (figs. 336, 342).

TOTAL VOLUME, MASS, AND AVERAGE BULK DENSITY FOR DOWNWIND ASH FROM THE MAY 18 ERUPTION

We estimated total, uncompacted bulk volume of downwind ash by measuring areas within each isopach contour of figure 336 using a planimeter. Each thickness increment was multiplied by its area, and volumes were summed. The total volume was multiplied by a correction factor[2] to compensate for unmeasured small volumes between the stepped increments and the curved surface of the ash lobe. The

[2]Total volume and mass values for the May 18 eruption (Sarna-Wojcicki and others, 1980) did not include this correction factor, which is calculated to be 1.33.

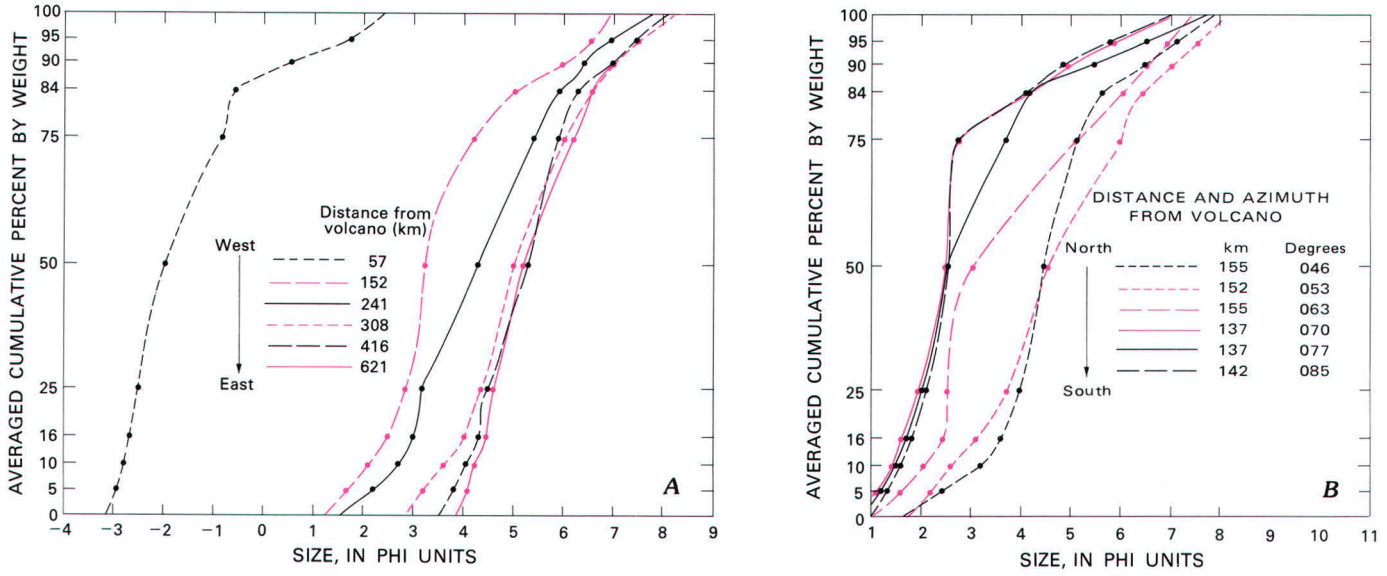

Figure 342.—Cumulative weight-percent curves of downwind ash at increasing distances from Mount St. Helens. A, Averaged curves. The curve representing the size distribution at 57 km downwind is from a single composite sample containing units A through D (Waitt and Dzurisin, this volume). The five curves representing greater downwind distances are averages of several samples from each of the five downwind traverses normal to the lobe axis (fig. 336). B, Cumulative weight-percent curves of downwind ash along a north-south traverse through Yakima, Wash.

estimated minimum total bulk volume of uncompacted downwind air-fall material (within the 0.5-mm isopach) is 1.1 km^3. This estimate is a minimum, because some of our thickness measurements were made after compaction.

We estimated the total mass of downwind ash in a similar way from figure 338. Total mass was between 4.9×10^{14} g and 5.5×10^{14} g. The greatest mass of air-fall ash fell in rather small areas, 4,000–40,000 km^2 (fig. 343); progressively smaller amounts fell in larger areas. The unmeasured mass beyond the 0.001 g/cm^2 isomass contour (fig. 343) is probably small. Part of the total mass, however, remained suspended and was transported beyond our study area; some of the finest dust and aerosol will remain suspended for several years (Symons, 1888). Our mass estimate is consequently a minimum. On the basis of analogy with previous eruptions and of graphic estimates of total air-fall volumes, Rose and Hoffman (1980) suggested that as much as 75 percent of the air-fall volume and 40 percent of the mass are outside the 2.5-mm isopach (fig. 336). An average bulk density of 0.45 g/cm^3 for the downwind lobe was calculated by dividing the total mass by the total uncompacted volume. If our initial uncompacted thicknesses are low, this value would be a maximum estimate of average initial uncompacted density.

We have calculated a range of solid-rock volumes that correspond to the mass of downwind ash. Although the density of solid unfractured dacite of the former volcano summit would have been about 2.8 g/cm^3, the material probably consisted of fractured and partly vesiculated rock as well as magma. We consequently assume that if the density of rock and magma before eruption is between 2.0 and 2.6 g/cm^3, then the equivalent in-place rock volume is between 0.20 and 0.25 km^3. The volume missing from the mountain after the eruption of May 18, calculated from preeruption and posteruption topographic maps, is 2.7 km^3 (Moore and Albee, this volume). Most of the missing volume must be in the debris avalanche, mudflows, and directed-blast deposits, whereas only a small fraction was erupted into and deposited by the downwind plume.

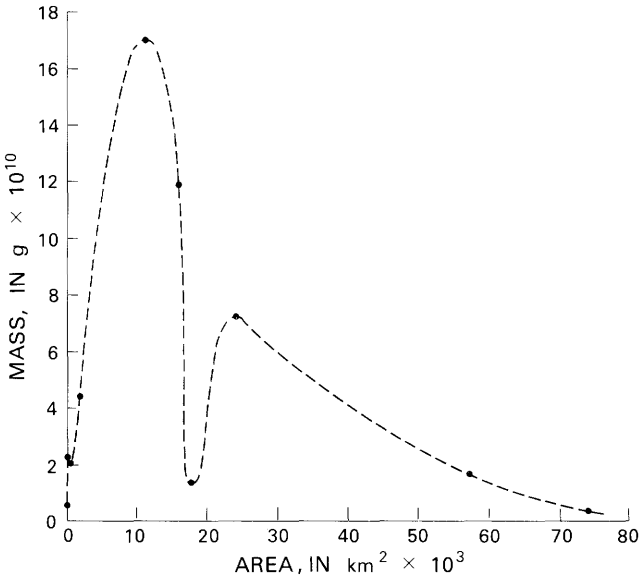

Figure 343.—Mass of downwind ash as a function of the size of the area covered. Areas bounded by isomass lines in figures 338 and 341 were planimetered, and the mass associated with each area increment plotted against the corresponding associated measured area increment.

AREAL DISTRIBUTION, THICKNESS, AND MASS OF ASH FROM THE FIVE MAJOR ERUPTIONS AFTER MAY 18

Eruptions from Mount St. Helens on May 25, June 12, July 22, August 7, and October 16–18 were considerably smaller in mass and volume than that of May 18. Distribution patterns from those eruptions, together with that of May 18, are instructive for anticipating areal extent of ash from future eruptions and for interpreting transport and dispersal patterns of ancient volcanic ashes.

Beyond 20 km from the volcano, the air-fall ash from the May 25 eruption was distributed over a 140° sector from the volcano, from azimuths 180°–320° (fig. 344). This wide distribution is a consequence of divergent wind directions at different altitudes above the volcano. The fast, higher level winds between altitudes 5,500 and 15,000 m blew toward the northwest (fig. 344). A layer of ash about 0.3–0.5 mm thick covered Aberdeen, Wash., about 150 km to the northwest. Traces of fine dusting were reported throughout much of the Olympic Peninsula, to distances of as much as 240 km to the northwest. The slower, lower level winds carried ash to the west, southwest, and south. Longview, Wash., 55 km west of the volcano, received 1–2 mm of ash, and Vancouver, Wash., about 75 km to the southwest, about 0.3 mm of ash. A distal thickness maximum similar to that near Ritzville, Wash., during the May 18 eruption appears 70–80 km northwest of Mount St. Helens (fig. 344).

Bulk volume for the May 25 eruption is 0.03 km^3 and total mass is 0.42×10^{14} g, giving an uncompacted average bulk density of 1.03. The equivalent in-place rock volume prior to eruption is between 0.016 and 0.022 km^3, or about 0.08 that of the May 18 eruption.

The air-fall ash distribution of the June 12 eruption is complicated, and probably is an effect of different wind directions at different altitudes (fig. 345). Wind vectors on June 12 were within a 90° arc, toward azimuth 150°–240° (fig. 345, inset). Thickness and mass were measured as far southwest as Vancouver, but farther downwind only thickness was measured. Data from nearby sites were used to estimate mass at sites where only thicknesses were measured. Airborne observers at an altitude of 5,000 m noted that ash was transported to the south, southwest, and west from the volcano. Ash distribution on the ground (fig. 345), however, indicates that low-level winds within 50 km of the volcano carried ash within a wide sector between azimuth 120° and 220°. Higher level winds at altitudes of about 7,500–12,000 m transported ash toward the southwest within a sector between azimuth 225° and 240°. Massive fallout from this cloud formed a distal thickness maximum about 45 km southwest of Mount St. Helens. Fine ash, which remained suspended at lower altitudes near St. Helens, Oreg., is inferred to have been transported to the south and southeast by lower level winds apparently localized along the Columbia River. Fine dusting, however, was reported farther south. The mass of material erupted on June 12 was about the same as that erupted on May 25 (table 66).

Thickness measurements of ash from the eruptions of May 25 and June 12 were of wet ash; consequently, thicknesses were less than if the ash had been dry. Average initial uncompacted bulk densities calculated from total volume and mass are 1.03 and 1.25 g/cm^3, respectively, for the two eruptions.

The eruption of July 22, like that of May 18, occurred on a fair day, and ash was carried to the northeast. Data for areal distribution and thickness of this ash are sparse beyond 135 km northeast of Mount St. Helens. Beyond several tens of kilometers from the

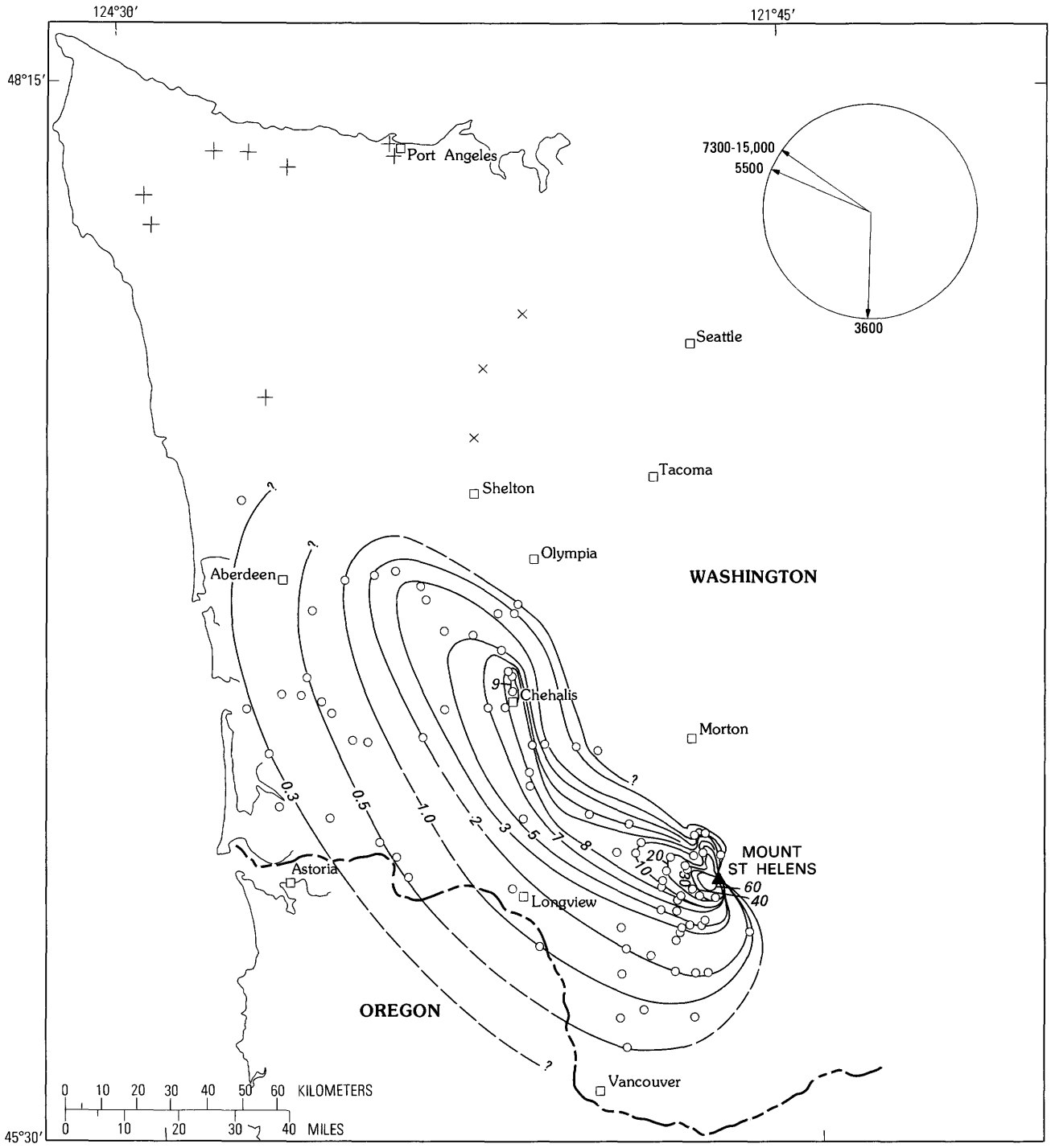

Figure 344.—Isopach map of air-fall ash of May 25. Ash thickness in millimeters. Circle, measureable amount of ash observed; +, light dusting or trace amount of ash observed; x, no ash was observed. Contour dashed where beyond control area. Circular diagram shows predicted wind directions for selected altitudes (in meters) near Mount St. Helens. Arrows point in the direction wind blew. Data are from U.S. National Weather Service. Data north and west of Chehalis, Wash., from James Beget.

Table 66.—Mass, volume, bulk density, and area covered by the 0.1-g/cm² isomass contour for downwind ash erupted from Mount St. Helens, March 27 through October 18.

	Early phase[1]	May 18	May 25	June 12	July 22	August 7	October 16–18
Total mass, x 10^{14} g	0.008	4.88	0.42	0.45	0.04	0.01	0.007
Volume, uncompacted, bulk km^3	[2].0006	1.10	.031	.027	[3].004	.0008	.0005
Volume, in-place rock, km^3 using density 2.6 g/cm^3	.0003	.20	.016	.017	.001	.0005	.00025
Calculated average uncompacted bulk density, g/cm^3	[2]1.25	.45	1.03	1.25	[3].50	1.25	1.29
Area covered within the 0.1-g/cm^2 isomass contour, in km^2	340	57,372	6,751	14,190	513	17.7	5.8

[1]Early premagmatic eruptions, March 27–April 17. Does not include some minor eruptive activity between April 17 and 22 and May 7–14.

[2]Thickness measurements were not reliable, or ash layers were too thin. Uncompacted density of 1.25 g/cm^3 was used, comparable to wet-ash values of June 12 eruption (see text).

[3]Ash too thin to measure at most sites. Uncompacted density of 0.5 g/cm^3 was used, comparable to dry-ash values of May 18 eruption (see text).

volcano, the ash was too thin to measure, and measurements only for mass per area were made (fig. 346). Near the volcano, the axis of the air-fall ash lobe trended about 060°, almost directly atop the May 18 axis, but whereas the axis of the May 18 lobe turned more eastward near Yakima, Wash., the July 22 air-fall lobe swung more northward. Mass values beyond Yakima are scattered and cannot be contoured reliably. Mass measurements near the Idaho-Canada border, about 490 km to the northeast, were higher than values in intervening areas. These variations in thickness may result from strong low-level winds that blew throughout the day and disturbed the ash, or the higher values downwind may represent distal thickness maximums similar to those described for the previous three eruptions.

As occurred in the earlier eruptions, the lobe deposited on July 22 had a pronounced asymmetry, which probably resulted from divergent wind directions at different altitudes. Faster, high-level winds were directed toward a sector from azimuth 043°–055°, but lower level winds were directed to about 068° (fig. 346, inset). Thus the northwest boundary of the plume was fairly sharp and the mass gradient was fairly steep for proximal areas, but the southeastern boundary was more diffuse and the mass gradient tailed off gradually. We estimate a mass of 4×10^{12} g for the July 22 eruption, assuming a configuration for the 0.0004-g/cm^3 isomass contour as shown in figure 347. The air-fall mass estimated for the July 22 eruption was about 122 times smaller than that for the May 18 eruption. If we assume an uncompacted bulk density of about 0.50 g/cm^3 for ash from this eruption, which is similar to that of the May 18 eruption which also occurred on a fair day, then the uncompacted bulk volume of ash from this eruption is about 0.004 km^3, and the equivalent in-place rock volume prior to eruption is about 0.001 km^3 (fig. 347, table 66).

Distribution patterns for the eruptions of August 7 and October 16–18 (figs. 348, 349) are multilobed, which most likely reflects shifts in wind directions between successive eruptive pulses. Three major pulses, for instance, were recorded during the August 7 eruption, which may correspond to the three lobes observed in the ash-distribution pattern. Distal thickness maximums are also observed for both the August and the October eruptions. Four distal maximums are observed for the eruption of October 16–18, in which five separate eruptive pulses were noted. Analyses of ash-distribution patterns and their correlation with wind direction and altitude for the later eruptions are still in progress.

Erupted mass and volume for the six major eruptions of 1980 from Mount St. Helens declined roughly exponentially with time and leveled off somewhat between the last two eruptions (fig. 350). Differences in mass and volume between the first and last eruption are three orders of magnitude.

VOLUME OF DOWNWIND ASH FROM THE MAY 18 ERUPTION COMPARED WITH VOLUMES FROM PREVIOUS ERUPTIONS OF MOUNT ST. HELENS

One way to compare the magnitude of the May 18 eruption with magnitudes of previous eruptions of Mount St. Helens is to compare the volumes of their respective tephra deposits. Evidence for many of the older tephra layers from Mount St. Helens, however, is fragmentary and volumes cannot be accurately measured. Both thickness data and volume estimates for several historic eruptions from other volcanoes, however, are available. We have plotted curves of maximum air-fall thickness against distance for each of these historic eruptions. At distances of about 25–100 km downwind, the slopes of these curves are roughly parallel, and thickness increases directly with volume. Next, we plotted the maximum thicknesses of the historic tephra layers (at arbitrarily chosen distances of 50 and 100 km from their vents) against the volume of each eruption (fig. 351). Using thick-

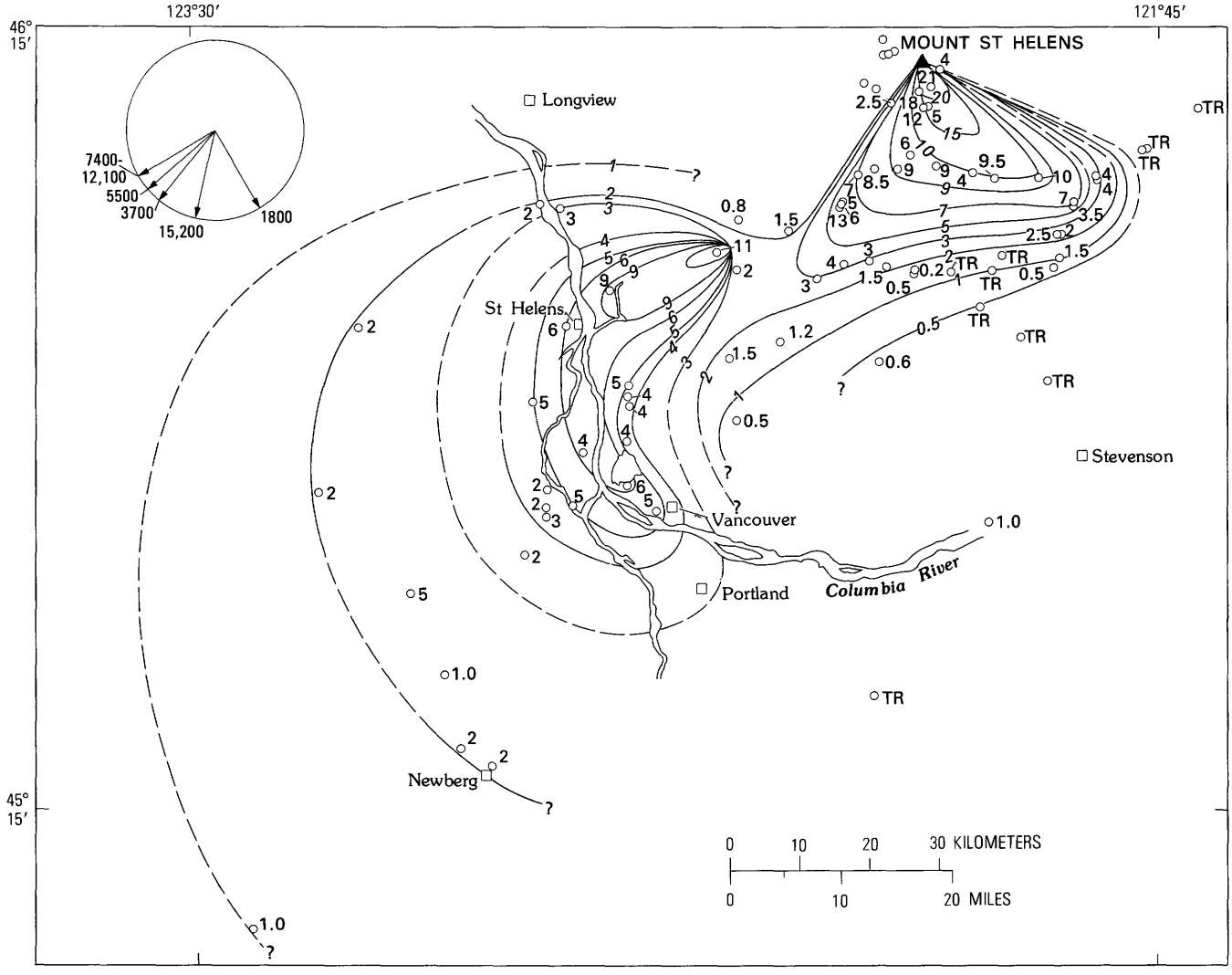

Figure 345.—Isopach map of air-fall ash of June 12. Ash thickness in millimeters. Circle, observation site with measured thickness (these are given because thickness values are scattered, and some appear anomalous); TR, trace; dashed lines, beyond control area. Circular diagram shows predicted wind directions for selected altitudes (in meters) near Mount St. Helens. Arrows point in the direction wind blew. Data are from U.S. National Weather Service. Data from sites southwest of Columbia River, from C.F. Kienle. Data for some stations south of Mount St. Helens, from Carolyn Driedger and Jerry Kendall.

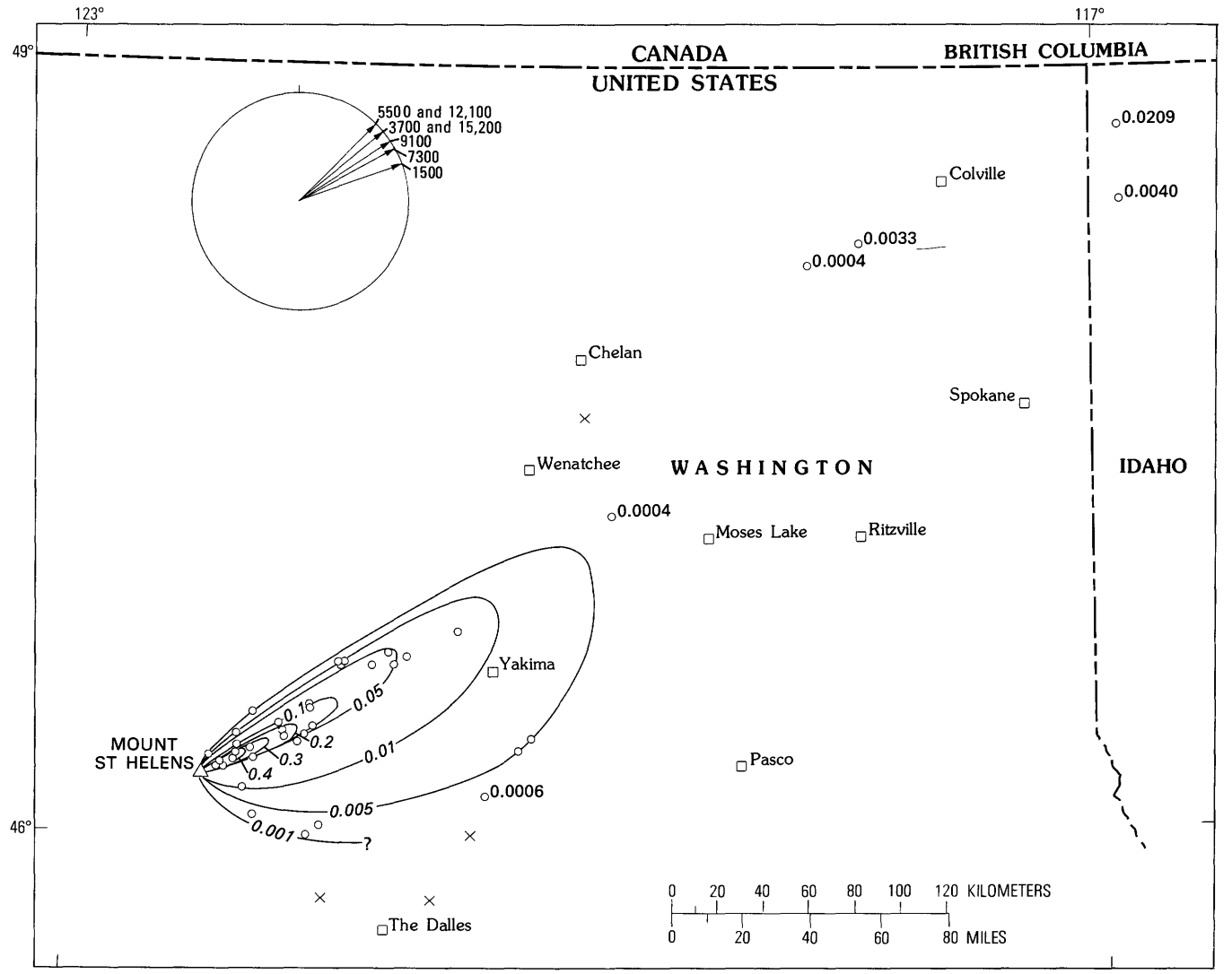

Figure 346.—Isomass map (mass per unit area, in g/cm²) map of air-fall ash of July 22. Circle observation site; x, no ash observed. For sites beyond the contoured area numbers represent mass in g/cm². Circular diagram represents predicted wind directions for selected altitudes, in meters, in the vicinity of Mount St. Helens. Arrows point in the direction toward which the wind blew. Data are from the U.S. National Weather Service. Data for distal sites in central Washington from M. P. Doukas. Data for sites in vicinity of Colville, Wash., from Brian Atwater and Kenneth Fox. Data from northwestern Idaho, from Fred Miller.

ness data for some of the previous eruptions of Mount St. Helens (Crandell and Mullineaux, 1978) and curves from figure 351, we estimate that the 1842 layer of Mount St. Helens had a volume of about 0.03 km³, that layer T (erupted about A.D. 1800) had a volume of between 0.3 and 0.4 km³, and that layer Yn (erupted about 4,000 B.P.) had a volume of about 4.5–5 km³, compared to the 1.1 km³ volume of the May 18 eruption. In this method of comparison, volumes of broad, diffuse lobes or of lobes with distal maximums such as that of May 18 will be underestimated, but volumes of sharp, narrow lobes will be overestimated; consequently, these estimates are rough, probably within a factor of two of the actual

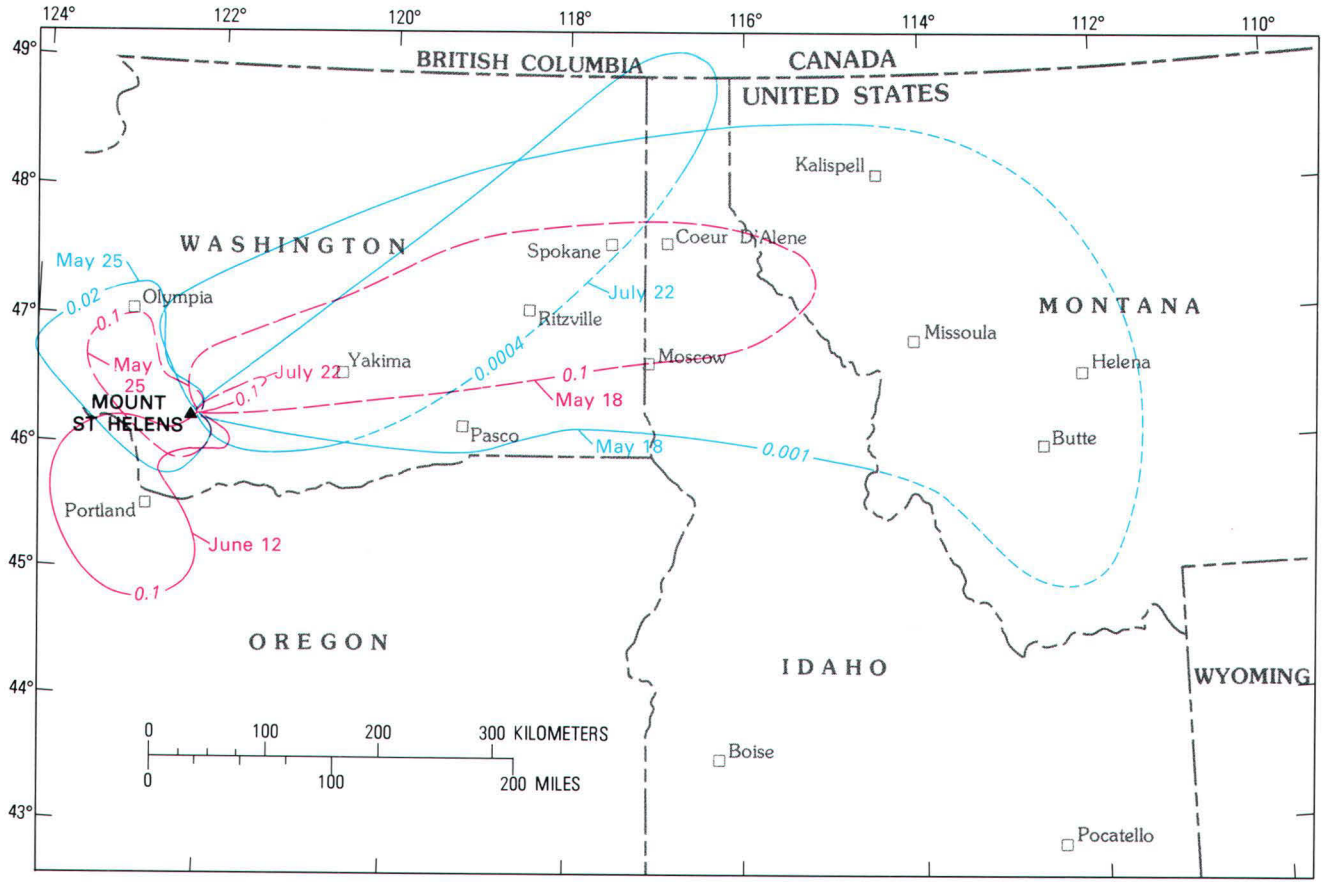

Figure 347.—Comparison of isomass maps for the first four eruptions of 1980. Numbers on contours represent mass-per-unit area, in g/cm². The 0.1-g/cm² contour is shown for each of the four eruptions. One contour is shown for the June 12 eruption; two contours are shown for the May 18, May 25, and July 22 eruptions.

volumes.

Another method of estimating the relative magnitude of the May 18 eruption is to compare the area covered by a certain isopach with the areas of the same isopach of previous eruptions. The 20-cm isopachs for air-fall ejecta of five previous eruptions of Mount St. Helens (Crandell and Mullineaux, 1978) are compared with the 20-cm isopach of air-fall deposits of the May 18 eruption (fig. 352). We have also estimated the minimal volumes within the 20-cm isopach contours of each of these eruptions by multiplying the measured areas by 20 cm (table 67). The area covered by 20 cm or more of air-fall tephra from the May 18 eruption is very small, about 16.2 km² (dark pattern of fig. 352), compared to previous large tephra eruptions of Mount St. Helens. In this comparison, however, another factor needs to be considered in addition to errors resulting from differences in shapes of different lobes: the magnitude of the May 18 eruption cannot be assessed on the basis of volume of air-fall tephra alone, because much of the energy of the eruption was spent on the initial directed blast. The blast contained much fragmented older rock that had made up the volcanic edifice, together with lesser amounts of other pumice and juvenile rock. Consequently, much of the initial energy of the eruption was expended on moving dense, solid rock laterally, rather than propelling light pumice and ash vertically. Volume of air-fall tephra might have been considerably greater if the north slope of the mountain had not failed and triggered the directed blast. If the blast deposit and air-fall-ash areas are considered together,

Table 67.—Area and volume of air-fall ash of the May 18 eruption compared with those of five older eruptions from Mount St. Helens.

[Data for older eruptions from Crandell and Mullineaux, 1978; see fig. 352]

	May 18 (air fall)	May 18 (total)[1]	Layer T	Layer Wn	Layer We	Layer Yn	Layer Ye
Area within the 20-cm isopach, km^2	16.2	276	108	534	138	1698	120
Minimal volume within 20-cm isopach, km^3	0.003	0.06	0.02	0.11	0.03	0.34	0.02
Relative volume, if May 18 (air fall)=1	1	20	6.7	37	10	113	6.7

[1]Includes directed-blast deposit (units A_1 and A_2) as well as air-fall tephra. Does not include debris-avalanche or mudflow deposits.

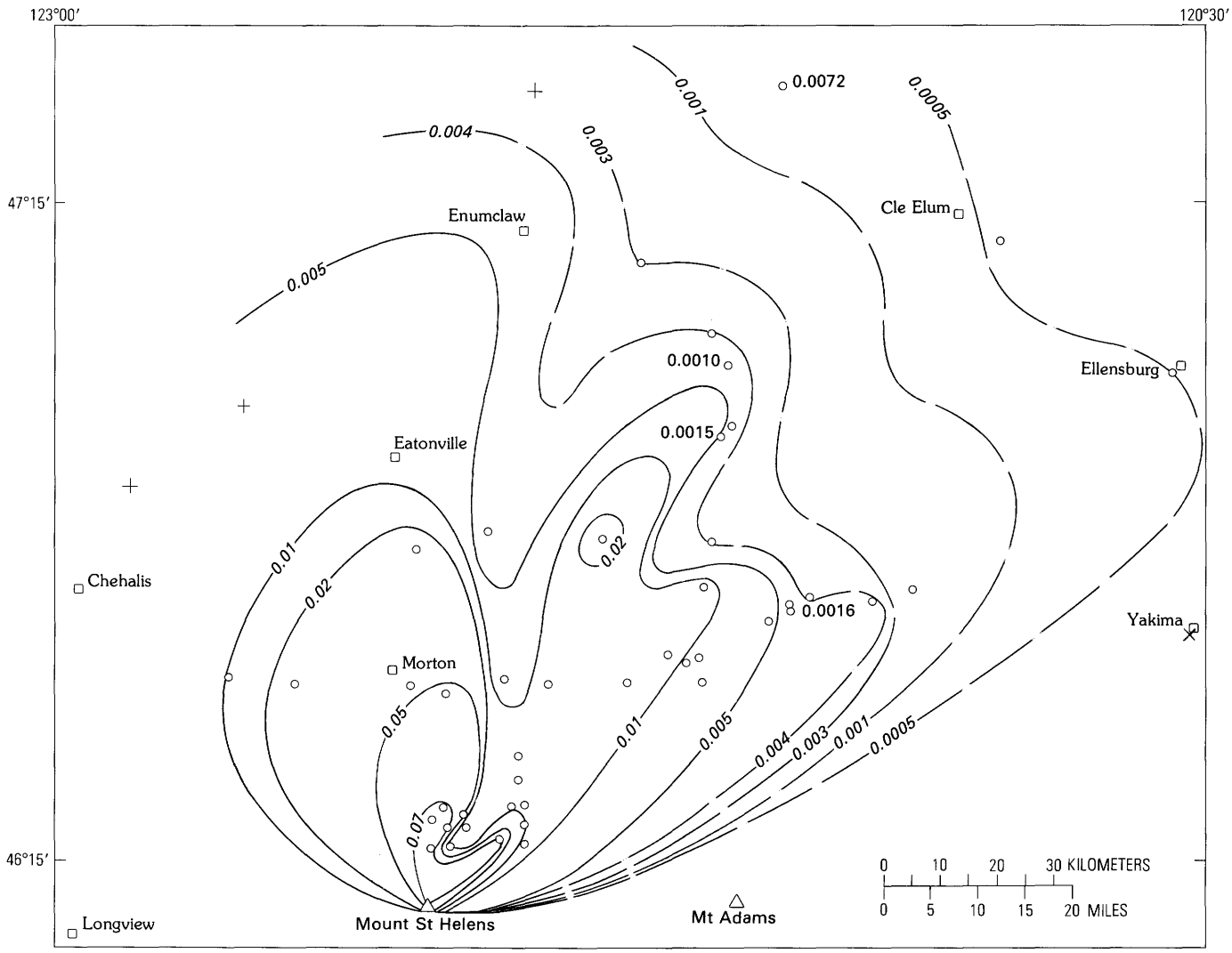

Figure 348.—Isomass map (mass per unit area, in g/cm²) of air-fall ash of August 7. Numbers adjacent to individual sites are mass-per-area values, which are anomalously high or low relative to adjacent contours. Circle, observation site; +, light dusting of ash; x, no ash observed. Contour dashed where inferred beyond control area. Samples collected by M. P. Doukas, R. B. Waitt, Jr., and J. A. Barker.

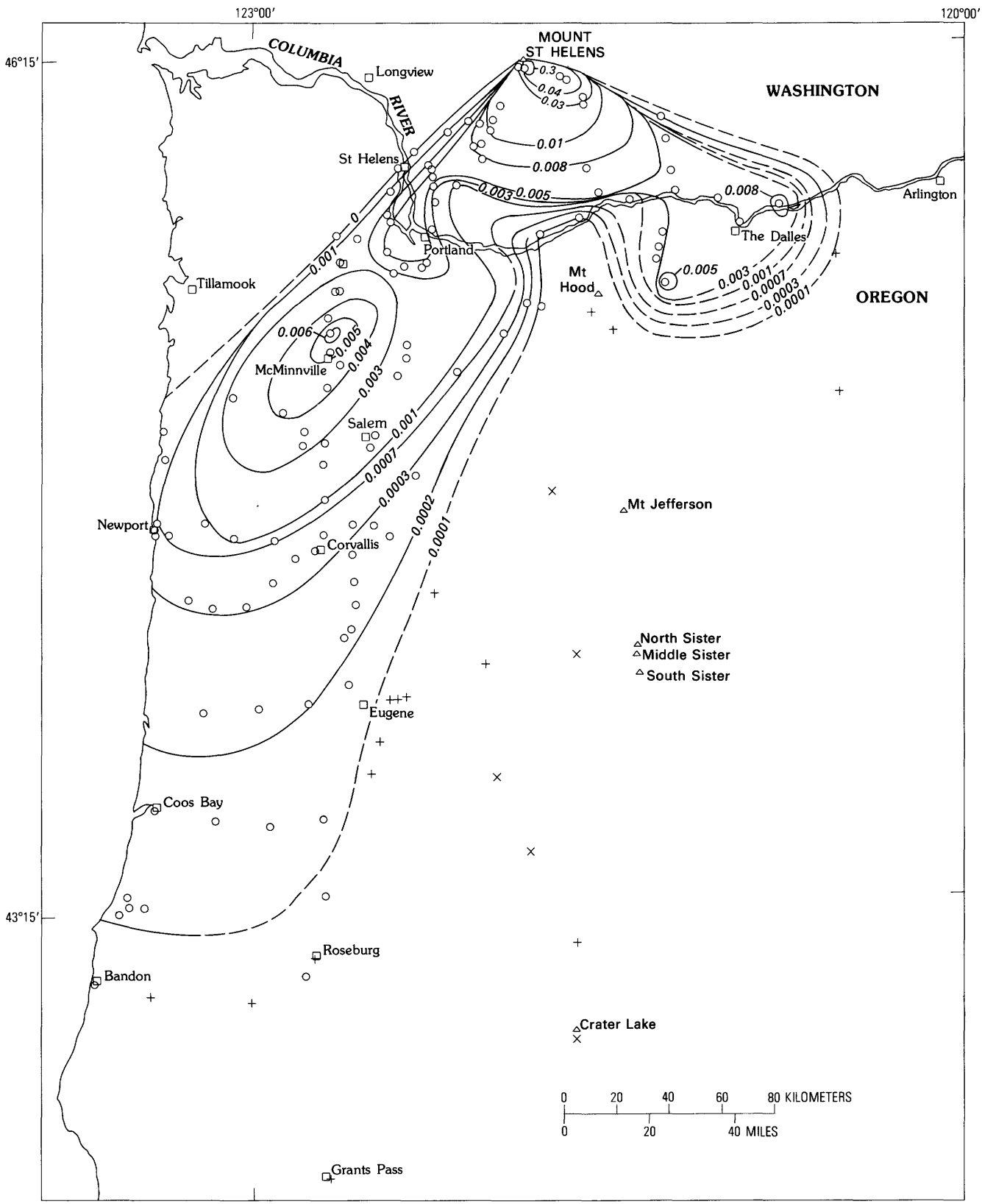

Figure 349.—Isomass map (mass per unit area, in g/cm²) of air-fall ash of October 16–18. Circle, observation site; +, light dusting of ash; x, no ash observed. Contour dashed where inferred beyond control area. Samples collected by Evelyn Newman, Robert Mark, Carol Price, and Susan Shipley.

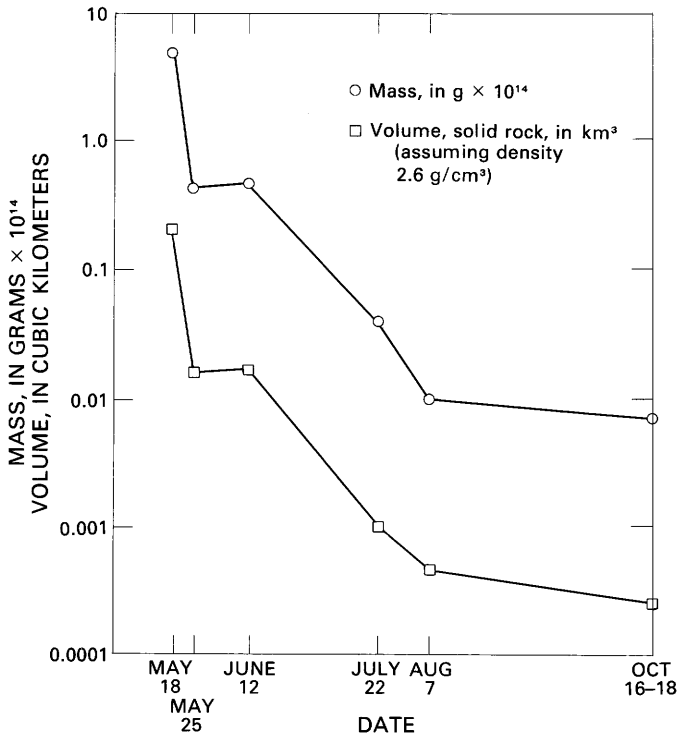

Figure 350.—Mass and volume of air-fall ash from six 1980 eruptions of Mount St. Helens.

however, the area covered by the 20-cm isopach is larger (light pattern of fig. 352), and the minimal volume within that isopach is about 0.06 km³ (table 67). Thus, if we rank the eruption of May 18 on the basis of air-fall volume alone, it would be smaller than five of the most recent large tephra eruptions of Mount St. Helens (table 67); but if the directed-blast deposit as well as air-fall tephra is considered in the comparison, the May 18 eruption would be equal to or somewhat greater than the eruptions that produced layers T, We, and Ye, but smaller than the eruptions that produced layers Wn and Yn (table 67).

SUMMARY

During the current episode of activity the eruption of May 18 produced by far the largest volume of material and covered the largest area (table 66); it accounted for about 84 percent of the total mass of ash erupted since activity started, 83 percent of the estimated volume, and about 93 percent of the uncompacted bulk volume. The eruption of May 18 covered 72 percent of the total area blanketed by the 1980 eruptions if the 0.1-g/cm² isomass contour is used as a basis of comparison (fig. 347). Total volume, mass, and area covered by each of the six magmatic eruptions have decreased markedly and, with the exception of the May 25 eruption, systematically with time. The volume of air-fall tephra erupted on May 18 is the smallest when compared to the volumes of previous major eruptions from Mount St. Helens, but the volume is intermediate if the directed-blast deposit is included with the air-fall tephra.

None of the ash lobes produced by the six magmatic eruptions of 1980 is truly symmetrical; some of them, like those of May 25, June 12, August 7, and October 16–18, have complicated distribution patterns. These characteristics of ash distribution are effects of variations in wind velocity and direction with altitude, combined with characteristics of the vertical eruptive column. Similar factors probably have affected distribution of ancient ashes. Increase in thickness downwind toward distal thickness maxima could be misinterpreted in the stratigraphic record as thickening toward a source. The observed ash distributions for these modern eruptions not only represent a predictive tool for determining possible distribution patterns for future eruptions of active volcanoes, but also are models for interpreting dispersal patterns of ancient ashes.

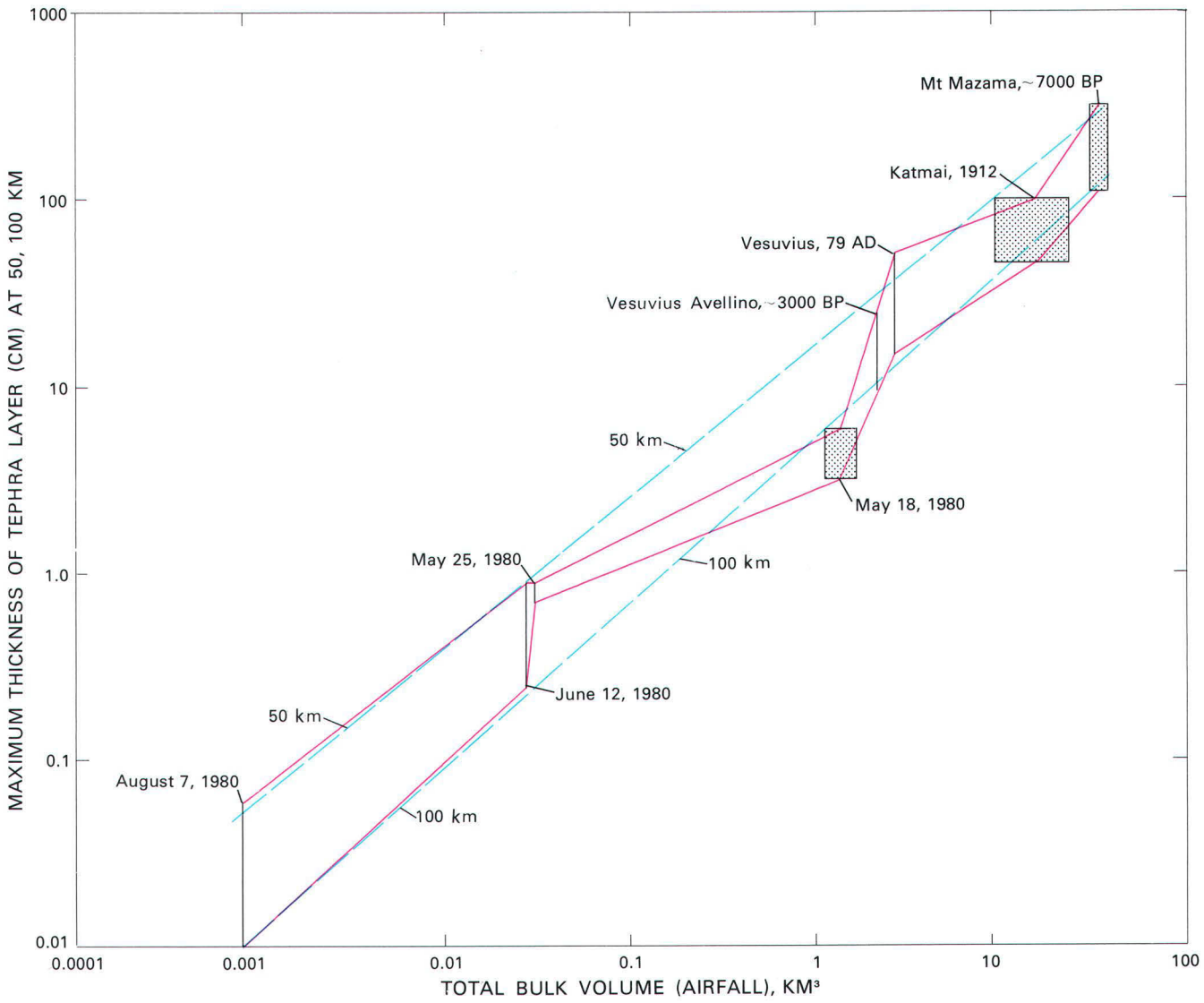

Figure 351.—Maximum thicknesses of air-fall tephra layers at distances of 50 and 100 km from the volcano (vertical black lines), plotted against estimated volumes of erupted tephra for Mount St. Helens, Mount Mazama (Williams, 1942; Williams and Goles, 1968), Katmai (Wilcox, 1959; Curtis, 1968), Vesuvius A.D. 79 (Lirer and others, 1973), and Vesuvius Avellino (Lirer and others, 1973) (red lines). Blue lines are visually averaged through the data points. Shaded areas indicate volume-to-thickness ratio uncertainties.

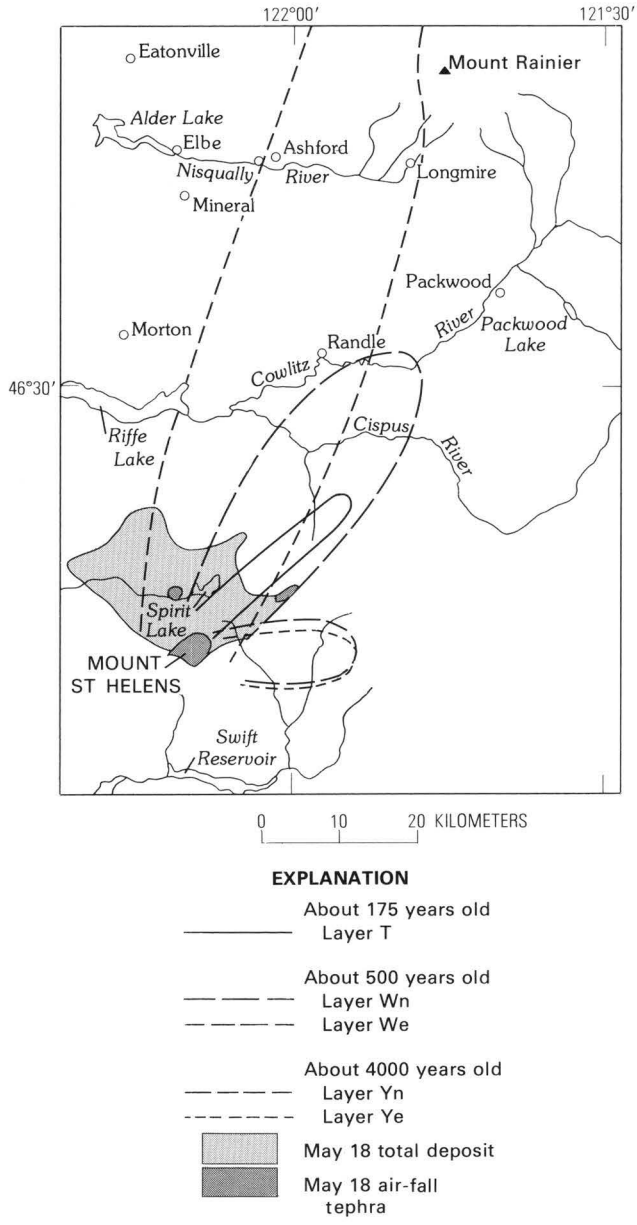

Figure 352.—Areas covered by 20 cm or more of tephra during five relatively large pre-1980 tephra eruptions, compared with air-fall tephra of the May 18 eruption and total deposits of 20 cm or more from May 18 eruption excluding debris avalanche, mudflows, and pyroclastic pumice-ash flow. Figure modified from Crandell and Mullineaux (1978, fig. 2).

REFERENCES CITED

Crandell, D. R., and Mullineaux, D. R., 1978, Potential hazards from future eruptions of Mount St. Helens Volcano, Washington: U.S. Geological Survey Bulletin 1383-C, 26 p.

Curtis, G. H., 1968, Stratigraphy of ejecta from the 1912 eruption of Mount Katmai and Novarupta, Alaska, *in* Coats, R. R., Hay, R. L., and Anderson, C. A., eds., Studies in volcanology: Geological Society of America Memoir 116, p. 153-210.

Danielson, Edwin, 1980, Mount St. Helens plume dispersion based on trajectory analysis [abs.]: NASA Symposium on Mount St. Helens Eruption, 1980, Washington, D.C., Abstract Digest, p. 21.

Hooper, P. R., Merrick, I. W., and Laskowski, E. R., 1980, Composition of the Mount St. Helens ashfall in the Moscow-Pullman area on May 18, 1980: Science, v. 209, no. 4461, p. 1125–1126.

Larsson, Walter, 1937, Vulkanische Asche vom Ausbruch des chilenischen Vulkans Quizapú (1932) in Argentina gesammelt—Eine Studie über äolische Differentiation: Uppsala University Geological Institution Bulletin, v. 26, p. 27–52.

Lirer, L., Pescatore, T., Booth, B., and Walker, G. P. L., 1973, Two Plinian pumice-fall deposits from Somma-Vesuvius, Italy: Geological Society of America Bulletin, v. 84, p. 759–772.

Rose, W. I., Jr., and Hoffman, M. F., 1980, Distal ashes of the May 18, 1980, eruption of Mount St. Helens [abs.]: EOS (Transactions American Geophysical Union), v. 61, no. 46, p. V28.

Sarna-Wojcicki, A. M., Shipley, Susan, Waitt, R. B., Jr., Dzurisin, Daniel, Hays, W. H., Davis, J. O., Wood, S. H., and Bateridge, Thomas, 1980, Areal distribution, thickness, and volume of downwind ash from the May 18, 1980, eruption of Mount St. Helens: U.S. Geological Survey Open-File Report 80–1078, 11 p.

Symons, G. J., F. R. S., ed., 1888, The eruption of Krakatoa and subsequent phenomena, Report of the Royal Society: London, Harrison and Co., 494 p.

Wilcox, R. E., 1959, Some effects of recent volcanic ash falls with especial reference to Alaska: U.S. Geological Survey Bulletin 1028–N, p. 409–476.

Williams, Howel, 1942, Geology of Crater Lake National Park, Oregon: Carnegie Institution of Washington Publication 540, 162 p.

Williams, Howel, and Goles, Gordon, 1968, Volume of Mazama ash-fall and the origin of Crater Lake caldera: Oregon Department of Geology and Mineral Industries Bulletin 62, p. 37–41.

THE 1980 ERUPTIONS OF MOUNT ST. HELENS, WASHINGTON

PROXIMAL AIR-FALL DEPOSITS FROM THE MAY 18 ERUPTION—STRATIGRAPHY AND FIELD SEDIMENTOLOGY

By RICHARD B. WAITT, JR., *and* DANIEL DZURISIN

ABSTRACT

Proximal air-fall deposits of the May 18 eruption of Mount St. Helens comprise four principal stratigraphic units. In upward succession they are: gray sandy silt (part of unit A), pumice and lithic gravel (unit B), pale-brown sand and silt (unit C), and gray silt (unit D). From 20 to 60 km east-northeast of the mountain the entire air-fall lobe and the lobes of each unit thicken exponentially toward areas near the volcano. Layer A3, the air-fall component of unit A, thickens toward an apparent source area 15 km north of the volcano. Its content of vesicular gray dacite and scorched tree fragments shows that it is related to the directed blast (pyroclastic density flow) that began at 0833 PDT. Unit B thickens toward the central vent and clearly is the primary deposit of the plume from the central eruptive column. Four layers composing this unit are attributed to fluctuations in the height of the eruptive column in the morning and afternoon. Unit C thickens toward the ash-flow deposits west of Spirit Lake and is largely the deposit from ash clouds that rolled outward from and convected upward off ash flows on the north flank during the afternoon. It is also partly a distal air-fall deposit from phreatic vents that redistributed ash-flow material as secondary eruptive columns. Unit D, which thickens toward the central vent, resulted from the waning central column in the evening. This four-unit stratigraphy comprising more than 10 distinctive layers accumulated within 12 hr. Ancient multi-layered deposits from Mount St. Helens and other volcanoes may represent similar sets of discrete but nearly simultaneous events.

At distances of 10–100 km from the volcano, the entire May 18 air-fall lobe is similar in thickness to ancient pumice layer T (A.D. 1800), the thickest air-fall deposit of the early 19th-century eruptive episode of Mount St. Helens. Unit B of the May 18 air-fall lobe is half to one-fourth as thick as pumice layer T. Unit D, an order of magnitude thinner than pumice layer T, is similar in thickness to the A.D. 1842–43 lobe, the thickest deposit of the mid-19th-century activity. The May 18 unit-B deposit is an order of magnitude both thinner and finer grained than the thickest and coarsest Quaternary air-fall deposits from Mount St. Helens and other Cascade Range volcanoes.

INTRODUCTION

The eruption of Mount St. Helens on May 18, 1980, had several phases. Moments after the great north-side landslide at 0832 PDT, a directed blast (pyroclastic density flow) swept off the volcano and within minutes spread across and devastated a 500-km^2 area to the north (fig. 353). Between 4 and 10 min after the beginning of the blast (Rosenbaum and Waitt, this volume), a vertical eruptive column developed as high as 20 km and alternately waxed and waned throughout the morning and afternoon. From ash flows that descended the north flank during the afternoon, convecting clouds of elutriated ash drifted downwind. By late afternoon secondary phreatic vents that developed in the ash-flow deposits 7 km north of the central vent redistributed some of the ash-flow material by means of secondary vertical columns. By evening the central column had greatly subsided but continued to emit ash. During each of these phases of the eruption, ejected material was carried east-northeast and winnowed by the prevailing windstream.

Within a few days after the eruption, we had categorized the air-fall deposits 20–60 km downwind

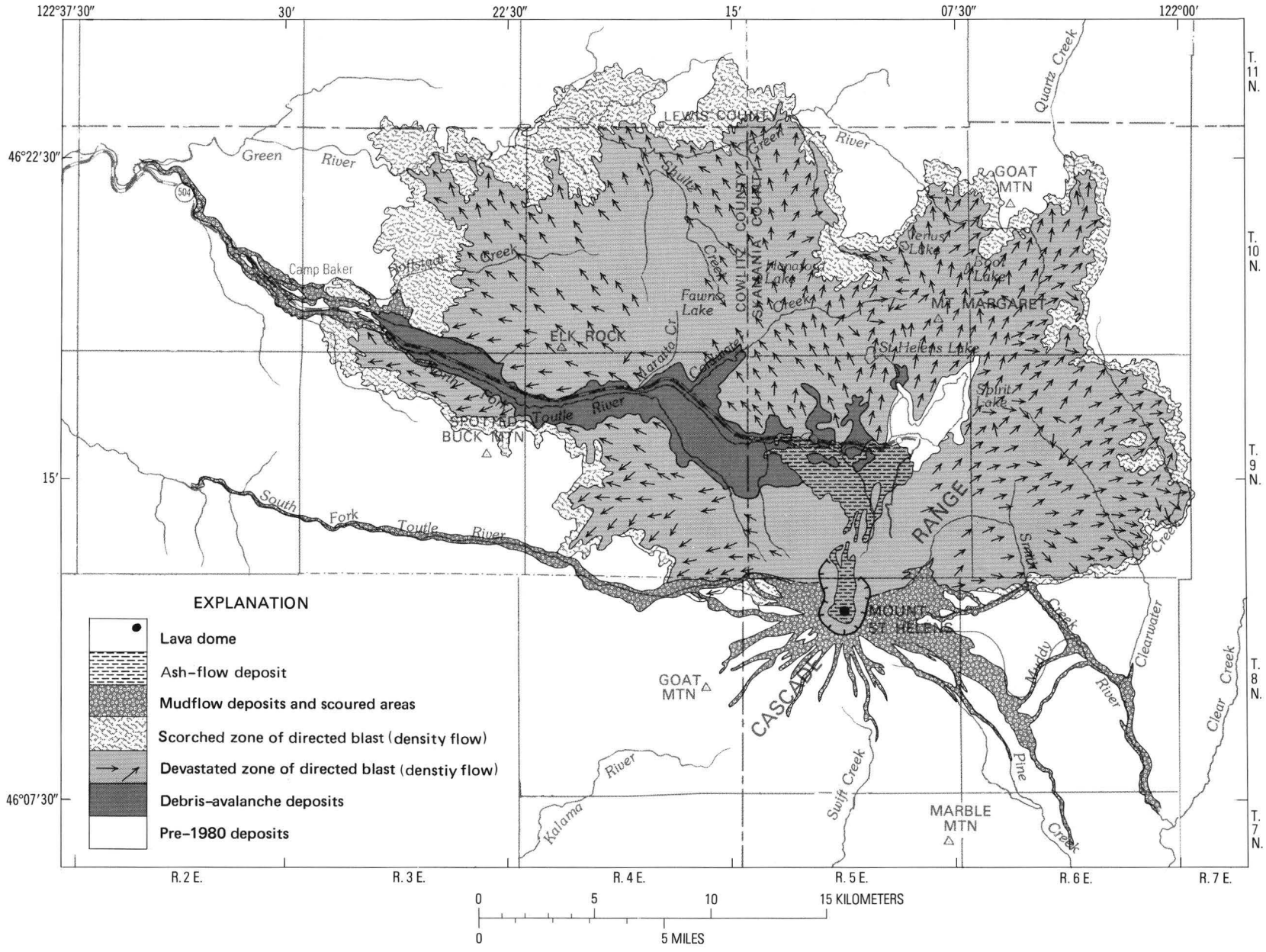

Figure 353.—Index map of Mount St. Helens area showing deposits and features of the 1980 eruptions. Geology modified from plate 1.

of the volcano into four units, designated from bottom to top as unit A (dark-gray sandy silt[1]), unit B (pumice and lithic gravel[1]), unit C (pale-brown sand to silt), and unit D (gray silt) (fig. 354*A*)[2]. This stratigraphy was followed toward the volcano, where between late May and late September these units were subdivided and developed into a comprehensive stratigraphy (fig. 354*B*). We report here on the stratigraphy and origin of air-fall deposits within 60 km of the volcano ("proximal area"). Sarna-Wojcicki, Shipley, and others (this volume) provide a comprehensive regional treatment of the air-fall deposits.

ACKNOWLEDGMENTS

This work has benefited from collaboration with colleagues in the U.S. Geological Survey. Judy A. Barker, Michael P. Doukas, and Susan Shipley assisted in the field in August and September. A few of the field data on the east and southeast were collected by Andrei Sarna-Wojcicki and Spencer Wood. Vicki L. Hansen collated numerical data from field notes and drafted the preliminary figures. Discussions with Andrei M. Sarna-Wojcicki and Susan Shipley, who have reduced regional data on the airborne plume, air-fall deposit, and geochemistry, have aided our understanding of the proximal air-fall deposits.

STRATIGRAPHY

The relatively straightforward four-unit stratigraphy of the broad area 20–60 km downwind of the volcano (fig. 354*A*) thickens considerably and becomes more complex closer to the volcano. At a distance of 20 km along the axis of the air-fall lobe, unit B is readily divisible into three layers. Closer to the volcano units A, B, and C are each similarly divisible into several layers. The composite proximal stratigraphic column (fig. 354*B*) shows the most complete stratigraphic sequence.

Isopach maps of air-fall units are based on about

[1]Standard Wentworth (1922) sediment-size terms are used to provide a distinct designation for each grain-size interval. Unit designations like "granule gravel," taken from Folk (1974), designate only median grain size of the deposit, and not rounding, sorting, or genesis of particles. Fuller explanation appears in Waitt (this volume).

[2]Units B and C of May 18 are not to be confused with tephra sets B and C that Mullineaux and Crandell (this volume) have designated in the ancient stratigraphy of the volcano.

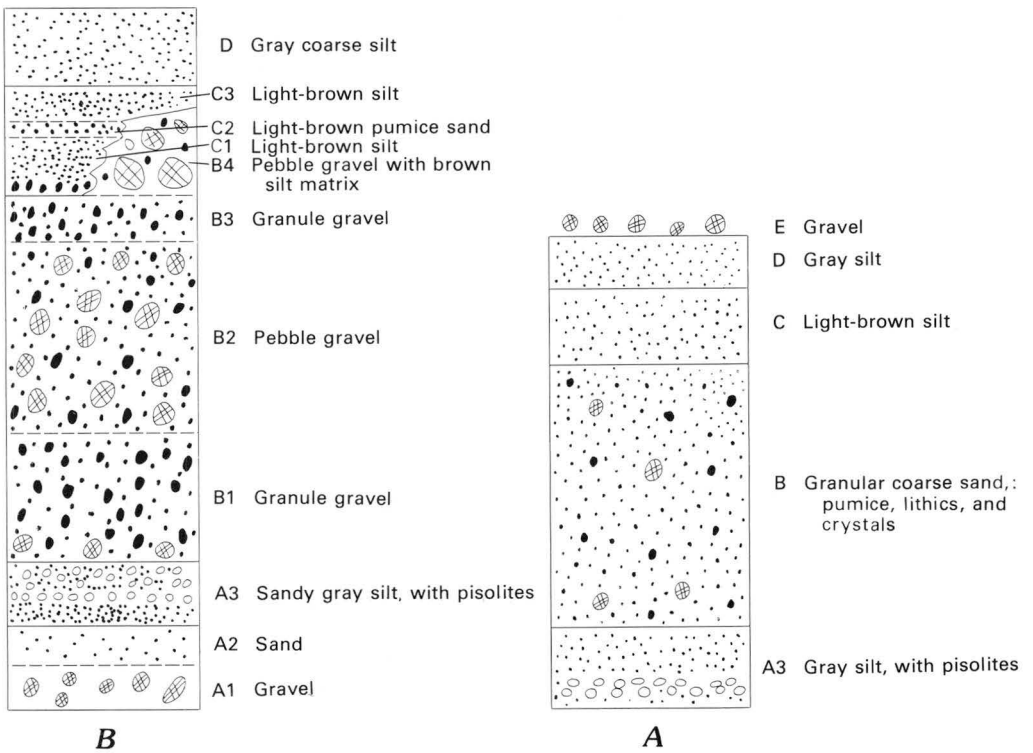

Figure 354.—Schematic stratigraphic columns of air-fall deposits from the May 18 eruption. A, column 40 km from volcano, differentiation by units (except for layer A3). B, composite column within 10 km of volcano, all distinct layers shown.

250 excavations scattered east to northwest of the volcano (fig. 353). The total-thickness isopach map of May 18 units shows a broad northward lobe and a sharp east-northeast lobe (fig. 355). These lobes are the deposit from two principal events of May 18: (1) a directed blast (pyroclastic density flow) that catastrophically swept 10–25 km to the north, northwest, and northeast and an attendant air fall extending another 30 km outward (Waitt, this volume); and (2) the vertical eruptive column and other events that ejected material high enough to enter the east-northeast windstream. All but roughly 2 cm (layer A3) of the northward lobe is the direct deposit of the blast (density-flow) event (layers A1 and A2) (figs. 258, 262 and 263). The east-northeast lobe comprises four overlapping air-fall units, mostly coarse air-fall pumice and lithic fragments from the central eruptive column (unit B). But the four units do not all emanate from exactly the same source area.

Beyond 5 km from the volcano, there is little local variation in thickness of the primary air-fall units within or among nontimbered areas. Near the trunks of living conifers, however, air-fall material is somewhat thinner because of outward shedding by the limbs overhead.

DEPOSITS OF THE DIRECTED BLAST (PYROCLASTIC DENSITY FLOW) AND OF ATTENDANT AIR FALL (UNIT A)

STRATIGRAPHY

Gravel and sand layers (layers A1 and A2).—The stratigraphic unit at the base of the air-fall sequence, which beyond 20 km is a sandy silt only millimeters thick, thickens and coarsens to gravel and sand more than 1 m thick on the north flank of the volcano. Near the volcano a basal gravel (layer A1) decimeters

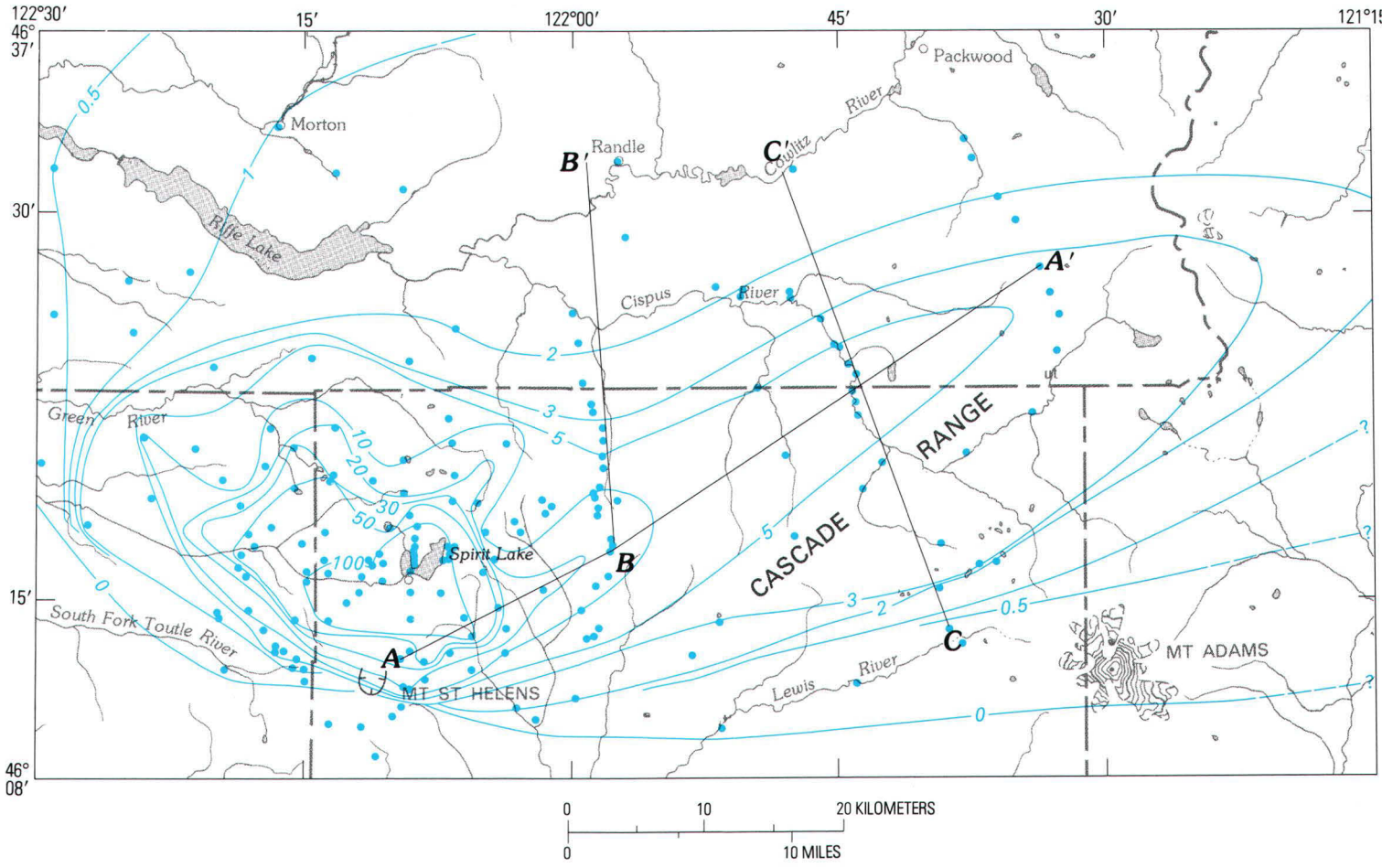

Figure 355.—Isopach map of total May 18 directed-blast (pyroclastic density flow) and air-fall deposits. Contour values in centimeters; thickness measured at sites indicated by blue dots.

thick is overlain by gray sand (layer A2) several centimeters thick.

Silt layer (layer A3).—Overlying layers A1 and A2 is a layer millimeters thick of moderately sorted dark-olive-gray[3] sandy silt (layer A3) characterized by pisolites (accretionary lapilli) (fig. 354*B*). Layer A3 is the only material of unit A distributed broadly beyond 20 km from the volcano. Within 15 km of the volcano on the north, the lower part of layer A3 does not contain pisolites, the upper part does; from 15 to 40 km north and out to 60 km east of the volcano, however, the basal part of layer A3 contains pisolites, whereas the upper part of the layer does not. The nonpisolitic phase of layer A3 composes the entire unit A beyond the outer limits of pisolites. At the base of this layer 20 km to the east, rare inconspicuous wisps of gray crystal-lithic ash probably accumulated during premagmatic eruptions from late March to mid-May (Sarna-Wojcicki, Waitt, and others, this volume). Layer A3 forms at least part of the basal unit of the distal air-fall sequence (Sarna-Wojcicki, Shipley, and others, this volume). Part of layer A3 fell wet and preferentially accumulated on limbs on the near side of coniferous trees. In the area of the directed blast (pyroclastic density flow) and broadly north to the Cowlitz valley and east to beyond Mount Adams, scorched branches, needles, and cones of conifers accumulated at the base of, within, or atop layer A3, although some are in the basal part of unit B.

[3]Colors measured moist from Munsell Soil Color Chart.

LATERAL VARIATIONS

Layers A1 and A2, which become thinner and finer grained away from the volcano, are restricted to the area of the downed and scorched timber (Waitt, this volume). The attendant layer A3 becomes gradually thinner away from the volcano, but rather abruptly pinches out on the volcano flanks (fig. 356).

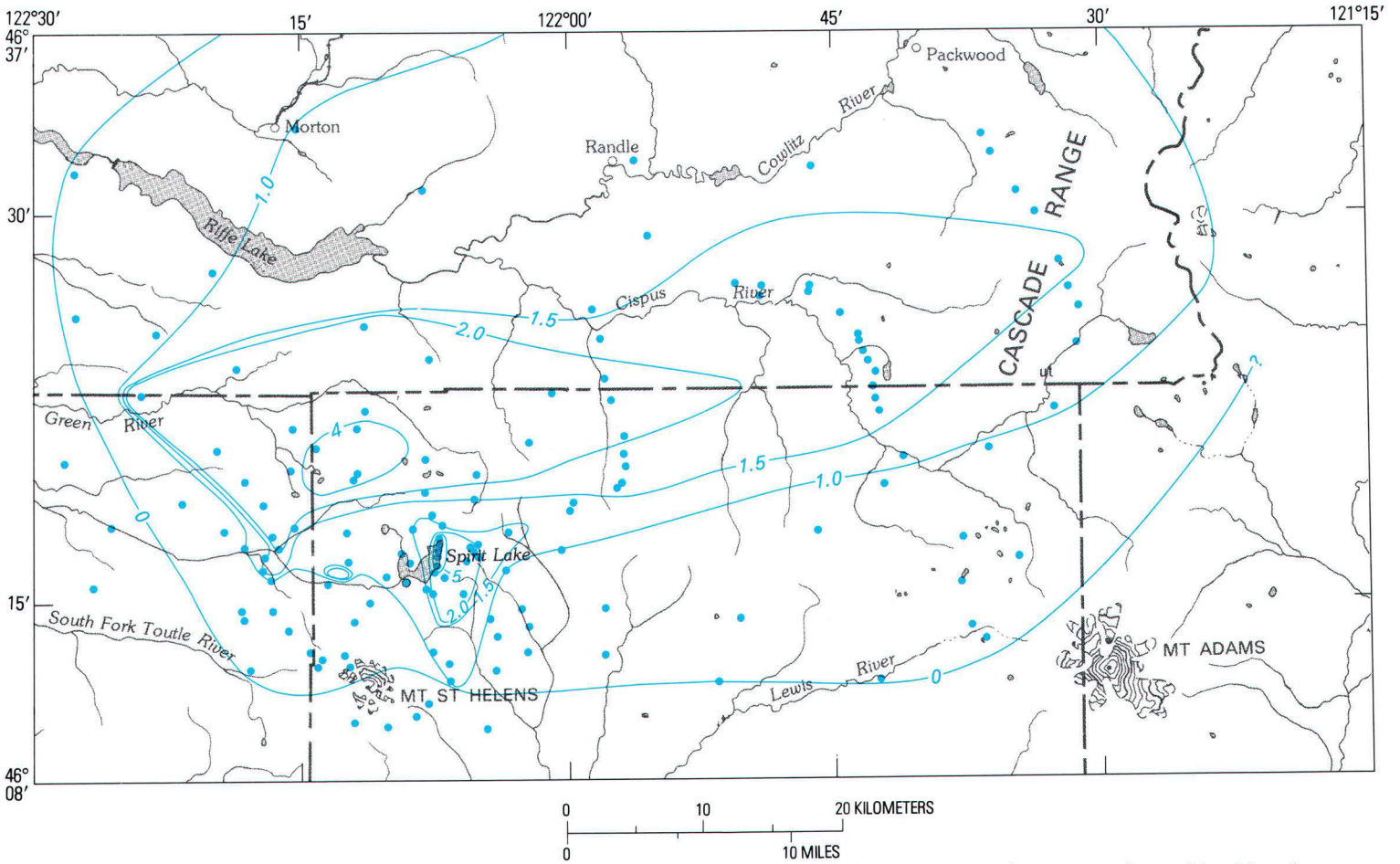

Figure 356.—Isopach map of layer A3. Contour values in centimeters; thickness measured at sites indicated by blue dots.

ORIGIN AND TIMING

Layers A1 and A2, confined to the area of devastation within 20 km of the crater on the west, north, and east, are the products of the directed blast (pyroclastic density flow) that began at 0833 PDT. Description and stratigraphy of layers A1 and A2 and discussion of the event appear in Waitt (this volume), Moore and Sisson (this volume), and Hoblitt and others (this volume).

Layer A3 extends some 50 km to the north and hundreds of kilometers to the east-northeast. Its basal stratigraphic position, content of juvenile dacite and scorched tree fragments, and other attributes (Waitt, this volume) relate this unit to the directed blast (density-flow). Unlike the materials of layers A1 and A2 that were directly deposited by the flow traveling close to the surface, the material of layer A3 drifted far downwind. The pisolites characterizing parts of this unit show that the silt rose high or fast enough to condense water. Eyewitnesses beyond the area of the ground-hugging blast (density-flow) cloud first experienced air fall as pisolites from a dark cloud that swept a few kilometers overhead. The downwind axis of thickness of layer A3 emanates from the area of maximum thickness of layer A3 that is 15 km north of the mountain— probably the area of dominant trajectory of A3 material ejected upward and northward from the mountain (Waitt, this volume).

The branches and cones deposited within layer A3 had been eroded by the blast on the flanks of Mount St. Helens. The tree fragments that fell on Mount Adams and other distal localities apparently were drawn up by the initial vertical column. The enormous updraft attending the rapid growth of the vertical column minutes after the beginning of the eruption developed a strong wind toward the volcano (Rosenbaum and Waitt, this volume). The cloud that had enveloped the flanks of the volcano was thus drawn up, and spread quickly to the north and east as a dark anvil-shaped cloud. Just after the base of this cloud passed over the Cowlitz valley, Mount Adams, and areas closer to the volcano, scorched tree fragments and pisolites began to fall (Rosenbaum and Waitt, this volume). The close stratigraphic association of scorched tree fragments with layer A3 far downwind independently corroborates the sequence assembled from the eyewitness reports. The material of layer A3 fell from about 0850 to 0930 PDT within 25 km of the mountain, and from about 0900 to 1000 PDT 30–70 km away (Rosenbaum and Waitt, this volume).

PUMICE-LITHIC AIR-FALL UNIT (UNIT B)

STRATIGRAPHY

At distances of 50–100 km along the axis of the air-fall plume and at closer distances along the margins of the plume, a single layer of pumice-lithic granule gravel to sand overlies unit A (fig. 354*A*). In proximal areas broadly distributed along the axis of the lobe, the unit thickens and coarsens toward the volcano and is divisible into two to four layers (figs. 354*B*, 357).

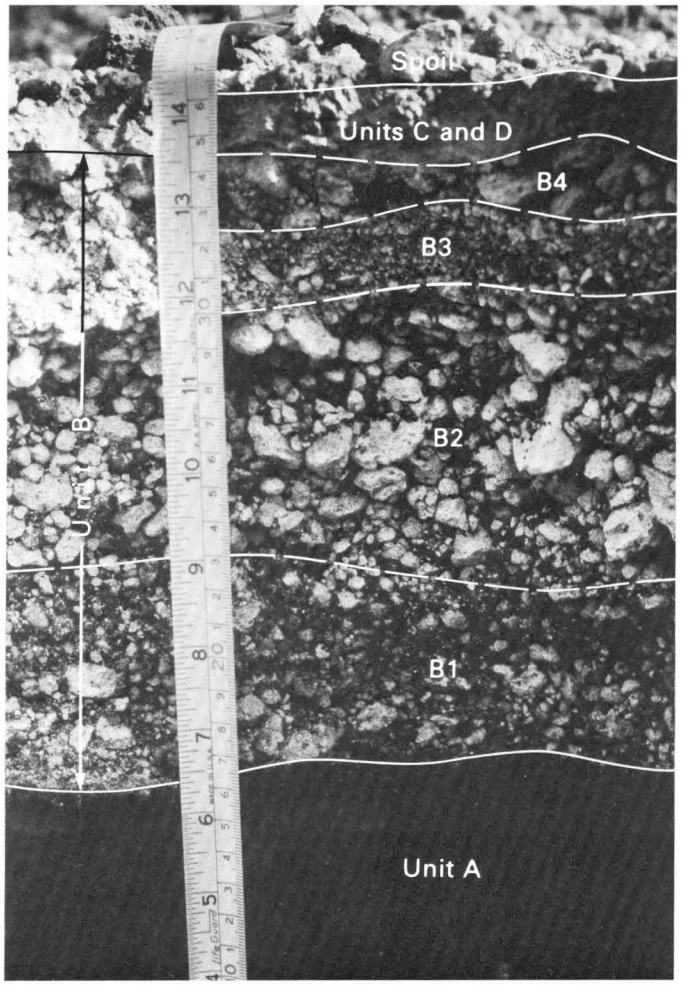

Figure 357.—Section view of units A, B, C, and D, showing divisions of unit B (layers B1, B2, B3, and B4). Right side of scale is graduated in centimeters; left side is in inches.

Basal lithic-rich layer (layer B1).—More than 50 percent by volume of the basal layer of unit B consists of lithic fragments and crystals; the remainder consists of pumice. The minor fraction of pumice in the layer extends to the base and is embedded in the top of layer A3. Near the volcano and along the axis of the lobe as far away as 25 km, layer B1 is lithic-pumice granule gravel; in more distal areas and along the margins of the lobe, it is a crystal-lithic-pumice sand. At some sites along the axis of the lobe 6–20 km from the vent, the base of layer B1 consists of scattered pumice pebbles or of a pumice-pebble zone 1–2 cm thick (fig. 357).

Lower pumice-rich layer (layer B2).—Layer B1 is overlain by a coarser layer B2 that contains 60–75 percent pumice by volume, the remainder being lithics and crystals. Near the volcano layer B2 is a pebble gravel that is generally reversely graded (fig. 357); along the margins at distances of from 20 to 50 km, it thins and fines to granule gravel, and in distal areas downwind fines to sand. This layer is about two phi-intervals coarser grained than the underlying layer B1: layer B1 consists of granule gravel where layer B2 is pebble gravel, or of medium sand where B2 is very coarse sand (fig. 357).

Upper lithic-rich layer (layer B3).—Along the axis of the lobe 10–25 km from the crater, layer B2 is overlain by a finer grained layer richer in lithic fragments and crystals, layer B3. This layer is recognized only at a few sites, and elsewhere it is obscured by the enclosing thicker and coarser layers B2 and B4.

Upper pumice-rich layer (layer B4).—Overlying layer B2 or layer B3 (where present) with a sharp contact is a coarse pale-brown layer containing 75 percent or more pumice by volume, the remainder lithic fragments and crystals (figs. 354*B* and 357). Unlike layers B1, B2, and B3, layer B4 has a conspicuous matrix of light-brown silt that also coats the pumice fragments. The mean and maximum sizes of pumice fragments in this layer are generally coarser than even those at the top of layer B2, although the layer is everywhere thinner than layer B2.

Toward the northern margin of the lobe of unit B near the volcano, layer B4 apparently thins to the point where it consists of scattered pumice granules and pebbles enclosed by unit C. Beyond 30 km from the volcano along this margin, layer B4 becomes sparser and finer grained, and the distinction between this layer and the light-brown unit C grows arbitrary. The merging of layer B4 with unit C, which in some places along the north margin of unit B both overlies and underlies pumice pebbles of unit B, indicates that layer B4 accumulated contemporaneously with part or all of unit C.

Sections near volcano with obscure stratigraphy.—On the east flank of the volcano, unit B does not show the internal stratification that exists only a few kilometers farther downwind but consists of a relatively thin, reversely graded layer of pumice and lithic fragments. Pumice blocks as large as 30 cm at the top of these sections protrude conspicuously through the overlying unit D. The generally finer lower part probably correlates with layer B1, and the coarser pumice at the top with layers B2 and B4, but contacts between these phases are obscure.

Large pumice fragments at and near the top of unit B on the east flank of the volcano have a pale-red interior that grades outward to a pale-orange rind 1.5 cm thick that in turn grades outward abruptly to a white rind 1.5 cm thick. The larger blocks thus apparently remained hot enough after they fell to oxidize.

LATERAL VARIATIONS

Within 5 km of the volcano, the air-fall section is notably thinner on the leeward (east) side of standing tree trunks than on the windward side, indicating an eastward component of fall. The 16-cm-thick section of units A, B, and D on the east flank of the volcano thickens to 20 cm against the windward side of a standing trunk but is only 3 cm thick against the leeward side. A lateral component to unit-B air fall is also shown by a 40-cm pumice block wedged from the west between two trunks.

The isopach map of unit B (fig. 358) shows that the axis of maximum thickness is alined with the central vent. The maximum thickness is some 15 km east-northeast of the crater, and the unit thins both downwind and toward the volcano. Isopleths of maximum pumice size, which splay broadly across the lobe of maximum thickness (fig. 358), illustrate the downwind and lateral decrease in particle size. The axis of coarseness is slightly clockwise of the axis of maximum thickness.

A stratigraphic cross section along the axis of the May 18 air-fall lobe illustrates downwind changes (fig. 359*A*). Unit B forms some 60–90 percent of the total thickness and therefore determines most of the

variation in total thickness. From its maximal thickness 15 km downwind, unit B is thinner and coarser grained upwind, and thinner and finer grained downwind. As unit B becomes finer grained downwind, the internal stratigraphy progressively disappears, so that beyond about 50 km only a single layer represents layers B1, B2, B3, and B4.

Stratigraphic cross sections across the main air-fall lobe (fig. 359*B* and 359*C*) illustrate lateral variations in the lobe. From its axis of maximal thickness at 25 km from the volcano to the margin of the lobe only 10 km north, unit B decreases in median grain size from granule gravel to sand, and its four internal layers merge into a single layer (fig. 359*B*).

ORIGIN AND TIMING

The alinement of the axes of coarseness and thickness with the central vent clearly identifies unit B as the deposit of the vertical column from the central vent. The column rose to 14 km or higher at least four times—twice in morning and twice in afternoon (Harris, Rose, and others, this volume; Rosenbaum and Waitt, this volume).

Layer B1.—The relatively low pumice content and fine grain size indicate a relatively low-energy eruptive column. Pumice occurs at the base of the unit, indicating that the initial vertical eruptive column, which within 30 min began depositing material downwind, carried juvenile pumice. The coarse pumice at the base of layer B1 in some places suggests a brief strong pulse at the beginning of the vertical eruption. Layer B1 probably formed from the initial to mid-morning eruption column.

Layer B2.—The coarser grain size and higher pumice content of layer B2 compared to layer B1 indicate that the vertical column itself became generally

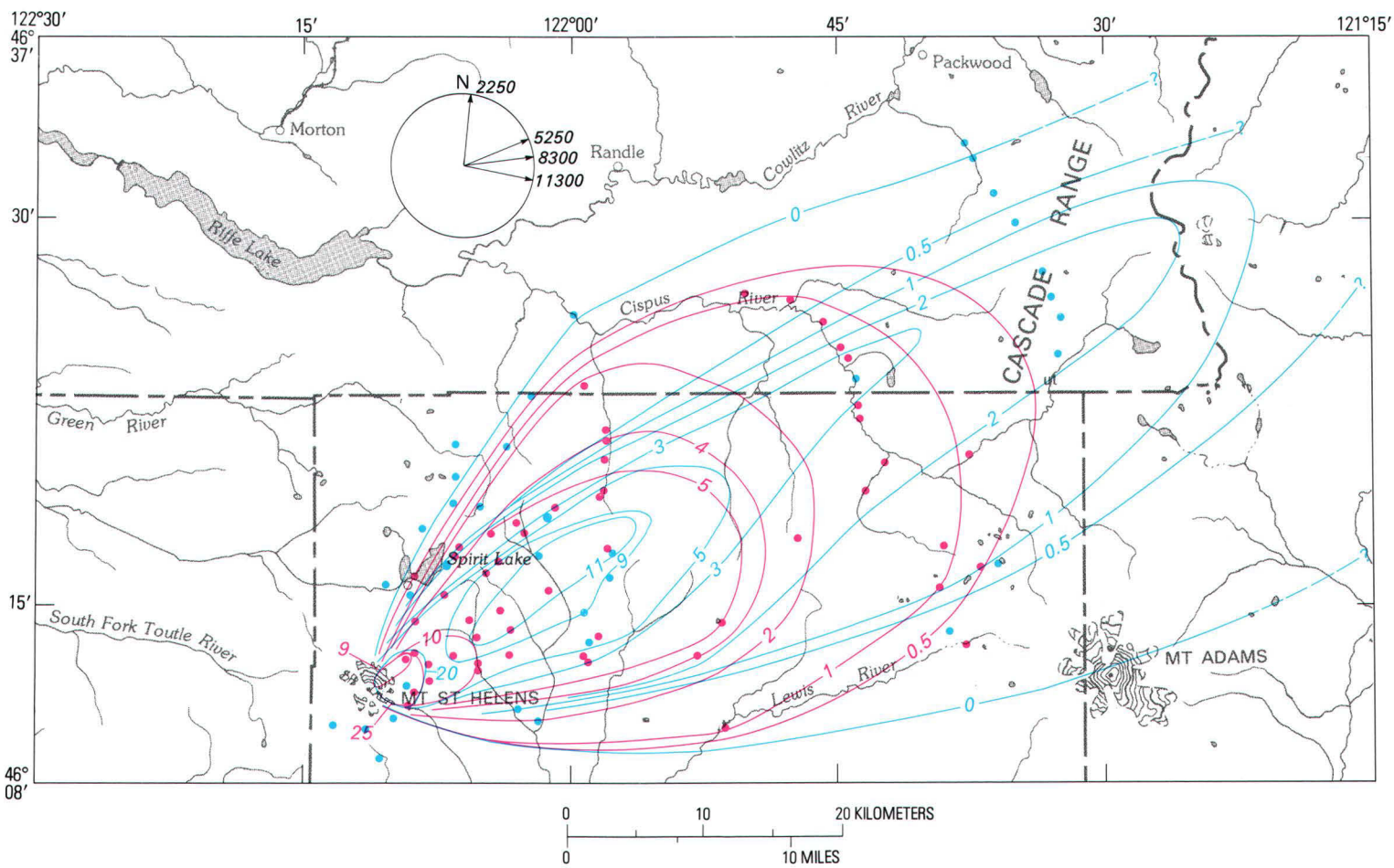

Figure 358.—Isopachs (blue lines and data points) and isopleths of maximum pumice size (red lines and data points) of unit B. Contour values in centimeters. Circular diagram shows approximate wind direction at various altitudes (in meters), from data supplied by U.S. National Meteorological Service.

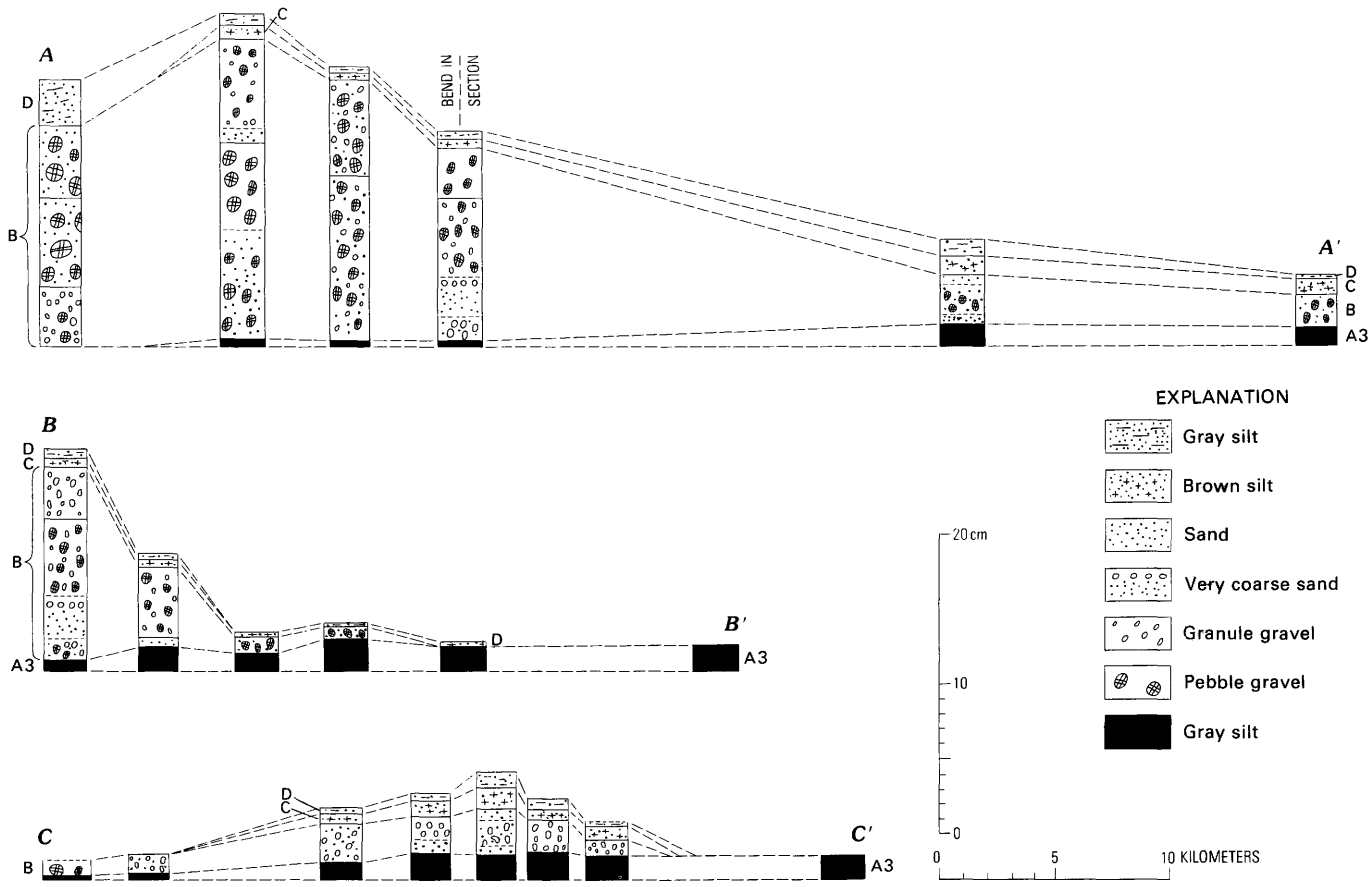

Figure 359.—Stratigraphic cross sections (see fig. 355 for locations). Section A-A', along axis of unit B lobe. Section B-B', across air-fall lobe about 25 km from volcano. Section C-C', across air-fall lobe about 40 km from volcano. Dashed lines indicate correlation of units A, B, C, and D.

more pumiceous, probably reflecting an increased rate of eruption of gas and pumice. The generally abrupt contact with layer B1 suggests that this change was abrupt. The general reverse grading of pumice fragments within layer B2 indicates that a trend toward higher altitude pumice ejection continued for some time. The lack of a pale-brown matrix suggests that this layer preceded the first ash flow. Layer B2 probably is the deposit of a relatively high column in late morning.

Layer B3.—The thin and sparsely recognized layer B3 records a fairly brief interval of a lower vertical column between the times of higher column represented by layers B2 and B4. The absence of a brown matrix indicates that this layer also preceded the first ash flow.

Layer B4.—The coarseness of layer B4 compared to layer B2 indicates a very gaseous pulse of the column; its relative thinness suggests that it accumulated during a shorter time interval than did layer B2 or from a less dense eruptive column. The abrupt appearance of the pale-brown silty matrix indicates an abrupt change in the vertical eruptive column. The matrix is similar in grain size and identical in color to the matrix of ash-flow deposits on the north flank of the mountain. Eruptions began to generate ash flows down the north flank at about 1217 PDT, (Rowley and others, this volume, table 42) when the eruptive column distinctly lightened in color (D. A. Swanson, oral commun., 1980). The abrupt appearance of a brown matrix in the air-fall deposit probably records this change. During magmatic eruptions in July and August, part of the pale-brown cloud convecting off north-flowing ash flows was drawn up into the vertical column simultaneously developing over the central vent (aerial-oblique photographs by R. P. Hoblitt, J. E. Vallance, and M. P. Doukas). The brown color of layer B4 probably resulted from a vertical eruptive column on May 18 that either similarly drew up part of the cloud convected off the ash flows,

or simply incorporated this fine material that was being generated by the ash-flow-producing explosions at the crater. Layer B4 thus originated from afternoon eruptions.

Variations in thickness and coarseness within unit B.—The maximum thickness of unit B some 15 km downwind from the volcano probably is due to the dominant trajectory of coarse particles. Ejected in the central column to a certain mean altitude, the coarse particles then drifted laterally in the prevailing windstream. Pumice fragments were produced in sizes ranging from 3-m blocks to micrometer-sized shards. The vertical column carried the fine fragments above the high-velocity windstream (above 13 km), from where they were transported laterally far downwind to form the white silt ash dominating the distal air-fall deposits (Sarna-Wojcicki, Shipley, and others, this volume). Few of the very coarsest fragments, on the other hand, even cleared the crater rim. The largest pumice block found on the lower east flank of the volcano is 40 cm in diameter. In the ash-flow deposits, however, 1-m pumice blocks are common and some are even larger. Such large fragments apparently remain low enough in the eruptive column that they can be transported from the crater area only by relatively dense ash flows. Of the coarse fragments thrust upward by the vertical column, a zone of maximum concentration develops at some altitude range. By the time this mode of coarse pumice and lithics has fallen to the ground, it has been translocated many kilometers downwind. Coarser fragments, not ejected as high and less influenced by the prevailing windstream than finer fragments, fall closer to the volcano. Having less volume, these coarser fragments produce a thinner layer.

The axis of maximum thickness is slightly counterclockwise of the axis of maximum coarseness (fig. 358). The low-level wind on May 18 was northward of the east-northeastward high-level wind that carried the plume. As material fell from the high-level plume, the lower level winds winnowed the finer material from the south to the north side of the plume. This pattern in unit B on May 18 resembles the pattern in more recent air-fall lobes, in each of which the axis of maximum thickness is displaced from the axis of maximum pumice size in the direction of the low-level winds (Waitt and others, this volume).

The May 18 unit B lobe, however, differs from the later air-fall lobes in that, in addition to coarse pumice at the southern margin of the lobe, some coarse pumice also lies sparsely along the northern margin. The main cause of this complication is that the isopleth map is of the entire unit B, which includes three relatively coarse layers that probably fell during three discrete episodes of high eruptive column between early morning and mid-afternoon of May 18. Between morning and late afternoon low-level winds had shifted northward. Many of the largest pumice fragments on the north half of the lobe are brownish and lie within unit C, and probably belong to layer B4, whereas coarse pumice near the southern margin is not brown and probably belongs to layer B2 or B1. The isopleth map thus mixes the results of sublobes influenced by gradually changing wind directions. The apparent northward displacement of the axis of thickness of layer B4 from the axis of layer B2 and the broad splay of the isopleth contours seem to reveal a gradual counterclockwise rotation of the axis of fallout during May 18--the abundant coarse pumice on the south having fallen from morning eruptions, the sparse coarse pumice on the north from afternoon eruptions.

PALE-BROWN SAND AND SILT (UNIT C)

STRATIGRAPHY

In the north-through-northeast sector a layer of pale-brown to light-brownish-gray silt to sand (unit C) overlies layer A3 and unit B. At a distance of 20 km along the axis of the air-fall lobe, the unit is a silty, medium to fine sand about 2 cm thick; it thins northward, southward, and downwind (to the east-northeast) to silt only a few millimeters or less in thickness. Where the material is fine sand or coarser, it probably contains the distal facies of layer B4. South and east of Spirit Lake rare pumice pebbles, probably of layer B4, are embedded near the top of unit C. Unit C thickens to several decimeters thick just north of the ash-flow deposits. Near Spirit Lake unit C comprises three layers—a coarser pumiceous layer divides a lower fine layer from an upper fine layer (figs. 354*B*, 360).

Lower silt (layer C1).—The lower layer (C1) is massive pale-brown silt to fine sand 0.5–2 cm thick. On the spur between the arms of Spirit Lake, this layer consists partly of pale-brown pisolites as much as 8 mm in diameter, but on the east side of the lake in Harmony Falls basin pisolites occur only in a rela-

tively thin zone near the base of the layer. Some of the pisolites have spherical cores of gray silt, which are pisolites reworked from the underlying layer A3. The basal contact with layer A3 is sharp, and at the spur between the arms of the lake it is channeled a few millimeters into layer A3. In places there are loading structures caused by layer C1 deforming the upper surface of layer A3 (fig. 360). The upper contact of layer C1 with layer C2 ranges from sharp to gradational.

Pumice sand (layer C2).—The middle layer of unit C, 0.2–0.5 cm thick near Spirit Lake, is of white pumice and lithic coarse to medium sand with a meager pale-brown silt matrix. Its upper contact with layer C3 is sharp. On the ridgecrest just southeast of Spirit Lake, where there are only two layers of unit C, layer C2 forms the basal coarse sand that is overlain by massive silt (layer C3).

Upper silt (layer C3).—The upper layer of unit C is massive pale-brown silt 2–3 cm thick that is similar to layer C1 but does not contain pisolites.

LATERAL VARIATIONS

Unit C is confined to the north half of the total air-fall lobe. The isopach map clearly shows that unit C thickens not toward the central crater, but toward the lower slope of the volcano about 8 km north of the crater (fig. 361). This is not only the area of ash-flow emplacement, but is also where one or more explosive secondary phreatic vents were active in late afternoon of May 18.

Unit C appears complex in figure 359*A* partly because the line of section is across the south half of the lobe of unit C, is oblique to the axis of unit C, and close to the volcano misses the lobe altogether. Unit C generally thins and fines to the east-northeast, and becomes stratigraphically less complicated. The stratigraphic relation of unit C to layer B4 in the northern part of the air-fall lobe becomes ambiguous beyond 20 km from the volcano. The pale-brown silt and sand beyond 30 km from the volcano probably is both unit C and layer B4, which seem to have resulted from different but contemporaneous events.

ORIGIN AND TIMING

Unit C, which thickens westward toward the ash-flow deposits just west of Spirit Lake some 8 km north of the crater, clearly originated from the north-side ash flows. On Coldwater Ridge, just north of the ash-flow plain, unit C is absent on steep slopes but thickens to many decimeters in adjacent flat areas or depressions. The ash deposited there originated by elutriation from the ash flows and was carried beyond the flows as turbulent clouds (Rowley and others, this

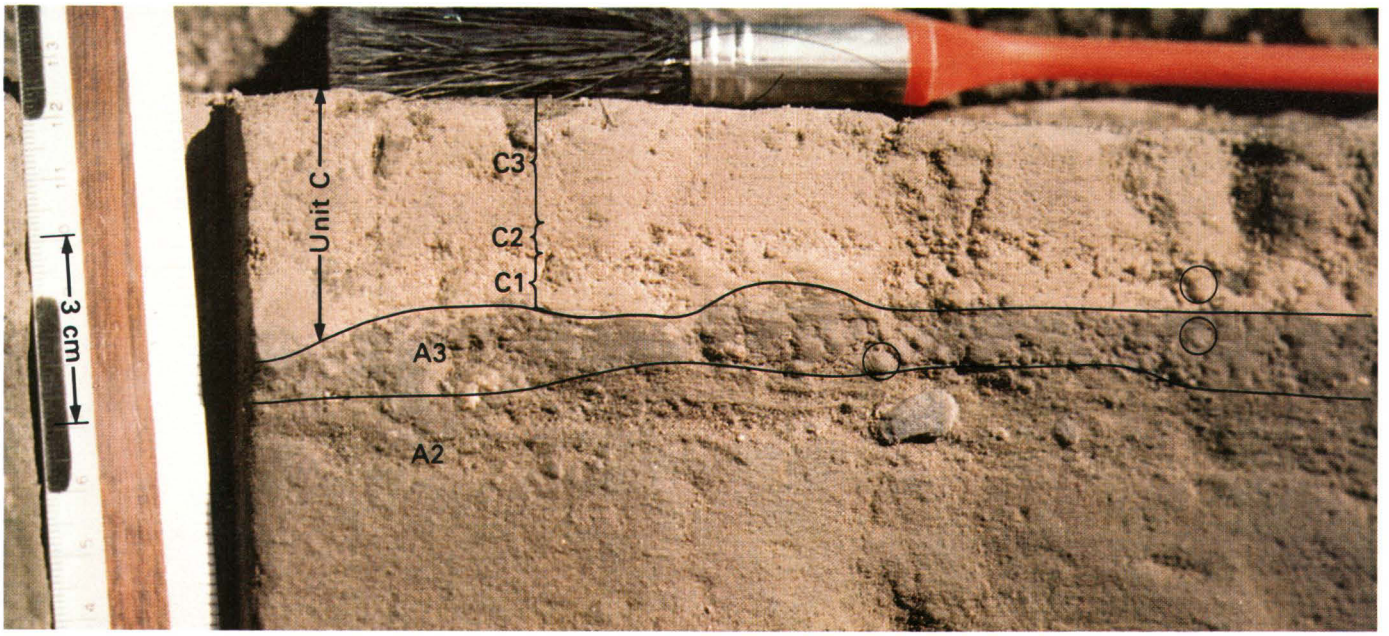

Figure 360.—Photograph taken near Spirit Lake showing layers of unit C and disconformable contact with layer A3. Pisolites, some of which are circled, can be seen in layers A3 and C1.

volume). Being fine grained, hot and dry, the ash deposited on steep slopes by the turbulent ash clouds subsequently flowed downslope to more level sites. These thick deposits gradually thin to only a few centimeters many kilometers to the north and east (fig. 361), where their relatively uniform thickness indicates air-fall deposition.

The sequence of three layers near Spirit Lake records a sequence of events related to the ash flows. The basal layer C1 lies disconformably on layer A3. Some of the 2- to 4-mm gray pisolites eroded from layer A3 were rolled into larger pisolites concentrically layered with pale-brown silt. Most of the large pisolites, however, are entirely of the pale-brown silt indigenous to unit C. The pisolitic layer is thickest, and the relief on its contact with layer A3 greatest, from 10 to 100 m above the new lake surface on the spur between the arms of the lake (figs. 353, 360); sparser pisolites occur at the northeastern margin of the lake. The pisolites indicate that water condensed on the ash particles, causing them to adhere to one another. These characteristics suggest that layer C1 originated as the distal edge of the largest ash flows that swept into the southern margin of the lake. The turbulent clouds rolling beyond the ash flows, being less dense than water, continued across the lake. Acquiring moisture from the lake surface, the ash particles formed pisolites that were swept along by the laterally moving cloud and upslope on the far side of the lake. Layer C1 is absent on the ridge crest just southeast of Spirit Lake because the momentum of the turbulent, denser-than-air ash cloud carried the

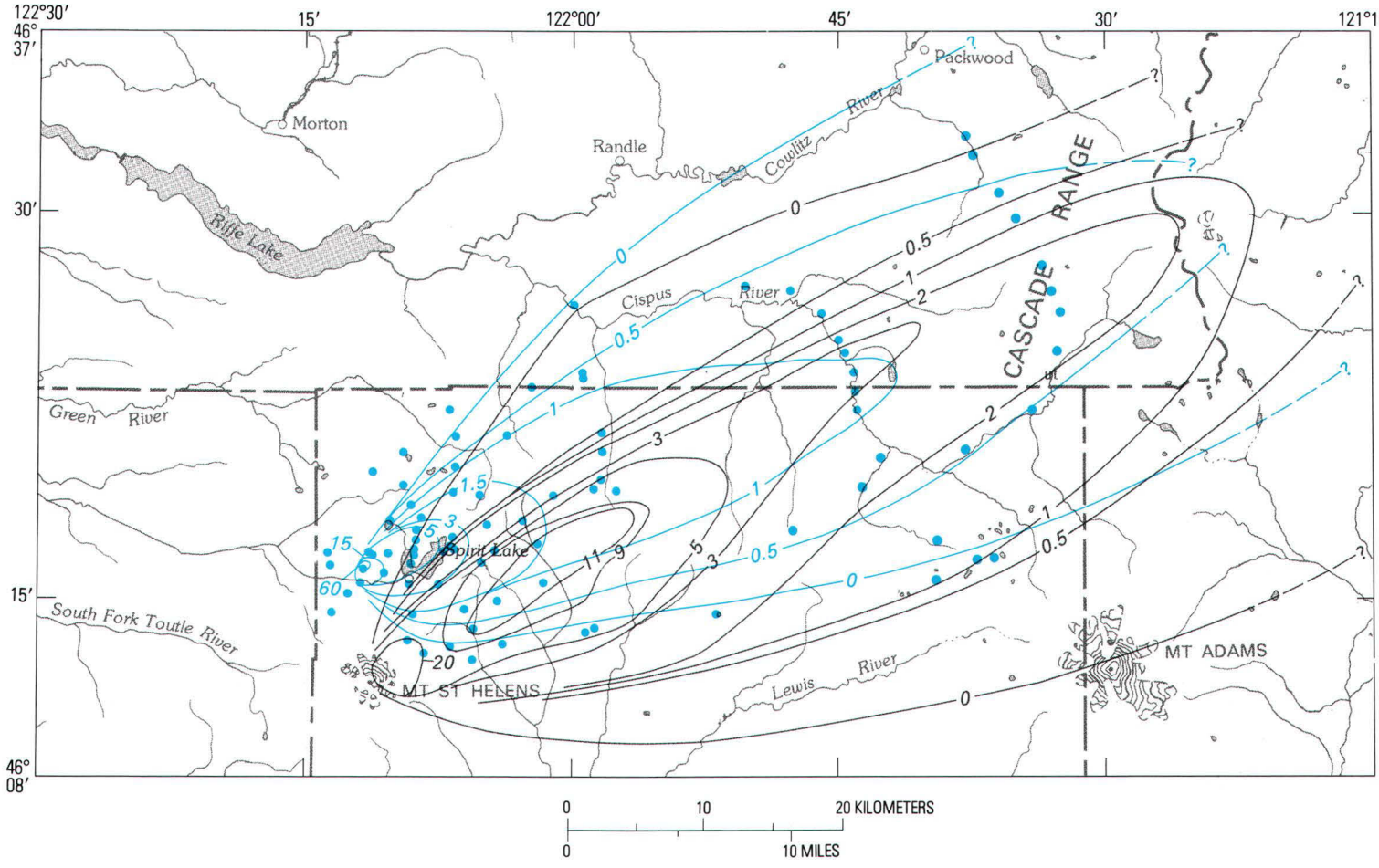

Figure 361.—Isopach map of units B (screened gray) and C (blue contours and data points). Contour values in centimeters. Thickness of unit C measured at sites indicated by blue dots; see figure 358 for data points where thickness of unit B was measured.

cloud northward at low levels. The bulk of layer C1, however, probably is air-fall material of a cloud that merely convected off the ash flows.

Layer C2 represents an event energetic enough to propel coarse sand- to gravel-sized pumice high enough into the windstream to be partly winnowed of the pale-brown silt. This layer may record the initiation of the secondary phreatic column that reworked ash-flow material from late afternoon until at least 2045 PDT. The principal secondary column was only 1 km upwind from the west margin of Spirit Lake.

Layer C3, which lacks pisolites, seems to be mainly fallout from the cloud convected off the ash flows; it probably also is air-fall silt from the plume of the secondary phreatic columns as they became smaller. This unit overlies layer C2, attributed to the most energetic phase of the phreatic columns. Layer C3 therefore must date from late afternoon and evening.

During most of the afternoon of May 18, the cloud convecting up from the north-side ash flows rose 2 km or more; the plume of the phreatic eruption that reworked newly accumulated ash-flow material rose to altitude 3 km in late afternoon and evening. Beyond 15 km east-northeast of the ash-flow plain, the single unit of silt to fine sand of unit C probably is material that drifted downwind from three sources: turbulent clouds propelled laterally off the ash flows, clouds convecting upward from them, and plumes from phreatic eruptions reworking the hot ash-flow deposits.

UPPER GRAY SILT (UNIT D)

DESCRIPTION

Northeast and east-northeast of the volcano, the May 18 air-fall deposits are capped by a layer of gray silt a few centimeters thick close to the volcano but only millimeters thick beyond 20 km (figs. 354, 357). Unit D is texturally similar to the pale-brown silt of unit C, but when wet is sharply distinguished from unit C by its gray color. Unlike layer A3, unit D is well sorted and does not contain tree fragments.

LATERAL VARIATIONS

On the lower east flank of the volcano, the windward sides of trees are notably plastered with gray silt. As unit A is nearly absent here, this silt must be from unit D, showing that even the latest air fall on May 18 fell with a lateral component of movement. Unit D decreases only slightly in grain size downwind.

Unit D is thickest on the flank of the volcano but also has an amplified thickness some 40 km from the vent (fig. 362). This amplified thickness probably was caused by the common trajectory of the most abundant particles in the eruptive column. The maximum-thickness axis of unit D is displaced slightly northward from the maximum-thickness axis of unit B.

ORIGIN AND TIMING

The axis of maximum thickness of unit D is alined with the central crater, and the unit overlies both units B and C and interfingers with neither. Unit D therefore must have accumulated from the plume from the vertical column after 1900 PDT, when the top of the column had declined to below altitude 5.5 km but continued to be dark with emitted ash. The amplified thickness 40 km from the mountain is similar to the amplified thickness in fine air-fall deposits of May 18, May 25, and June 12, amplified thicknesses that formed 40–250 km downwind of central eruptive columns ejected to altitudes of from 12 to 18 km (figs. 336, 344, and 345). The amplified thickness of unit D probably resulted from the downwind trajectory of fine particles that had been ejected roughly to altitude 4–5 km during the waning phase of the May 18 eruption. Low-level winds were counterclockwise of the high-level winds throughout May 18. The material of unit D, ejected to comparatively low altitude, was moved from the vent by a windstream that was northward of the high-altitude windstream that carried most of the material of unit B.

SURFICIAL PUMICE (UNIT E)

DESCRIPTION

In the coniferous forest beyond the devastated area but broadly along the axis of unit B, scattered pumice pebbles overlie unit D (fig. 363). This layer is present only beneath the branches of living trees. It is absent in the area of downed timber, in natural clearings within the forest, and along roads and other man-made clearings.

ORIGIN AND TIMING

For many days after May 18, coarse pumice fell from the branches of living conifers, where it had been selectively trapped on May 18. Because of their delayed arrival at the ground surface, these pumice fragments were deposited not with unit B where they stratigraphically belong, but upon the surface of unit D, which had become coherent because of rain. The pumice overlying unit D 40 km east of the volcano has a median size of about 7 mm, whereas that of the primary air fall (unit B) is only 1.5 mm. Yet clearly the two layers were part of a single population delivered simultaneously to the area of their separate accumulation.

This delayed pumice fall was followed by air-fall pumice on July 22, whose distribution corresponded closely to that of the May 18 air-fall lobe (Waitt and others, this volume). The scattered pumice of May 18 unit E and of July 22 mingled to constitute the single discontinuous layer that overlies unit D.

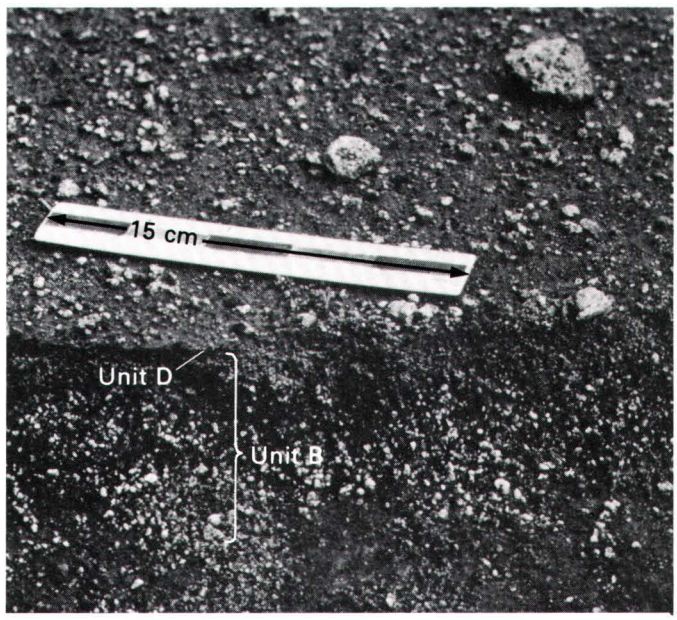

Figure 363.—Scattered pumice of unit E, found only in coniferous forest, overlying unit D.

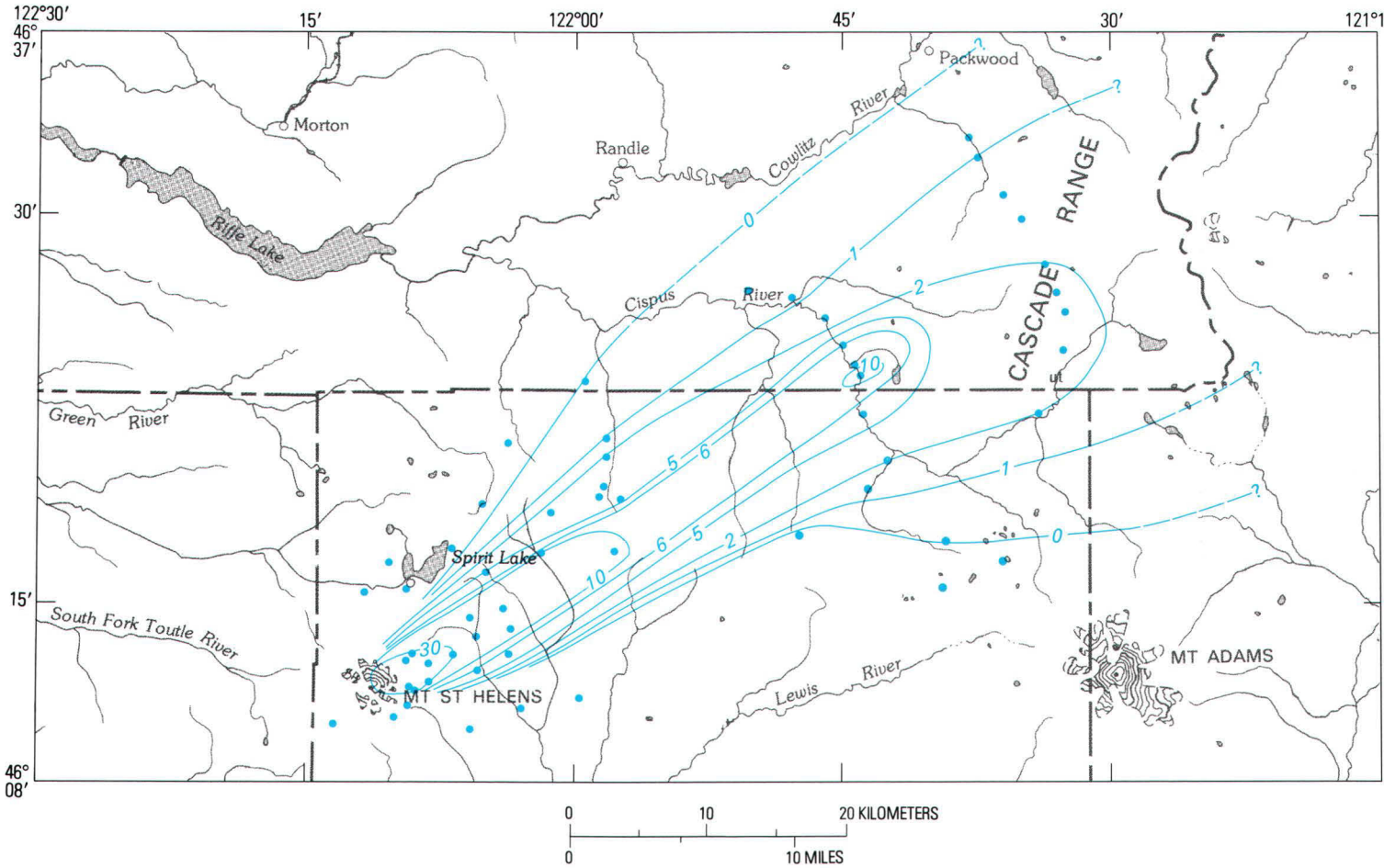

Figure 362.—Isopach map of unit D. Contour values in millimeters. Thickness measured at sites indicated by blue dots.

INTERPRETATION OF STRATIGRAPHY OF ANCIENT AIR-FALL DEPOSITS

Because the units and layers of the May 18 deposits can be traced to thicker deposits that are easily exposed by shallow excavation, and because many of these units and layers can be logically attributed to events that were observed on May 18, the origin of these deposits is relatively clear. The sequence of 10 distinguishable air-fall layers all deposited as a consequence of the May 18 eruption is an example to aid interpretation of stratigraphic sections of ancient tephra. Viewed from the future, the sharp boundaries in texture or color between units A, B, C, and D, or between layers A2 and A3 or layers C2 and C3, could be taken as evidence of separate events spanning considerable time. Yet these units are all products of a single day's activity at Mount St. Helens. The layer of fir needles in some areas concentrated atop layer A3 also could be taken to imply a time break during which nearby standing trees casually shed debris onto the new surface; whereas they are needles eroded from trees only an hour or so earlier. A future ^{14}C date obtained for this layer will not only be a maximum-limiting age for the overlying layer and a minimum-limiting age for the underlying layer, but will also closely date both layers.

RELATIVE MAGNITUDE OF ERUPTION

Whereas the thickest proximal accumulation of May 18 unit B is about 25 cm, on the north-through-northeast sector, ancient air-fall pumice accumulations—layers Yn (3400 B.P.), Wn (450 B.P.), and T (A.D. 1800) (Crandell and Mullineaux, 1978, figs. 2, 9)—are as thick as 1 m. In proximal areas the coarse air-fall material of May 18 was thus quite thin compared to three major air-fall lobes from the volcano. East of the Cascade Range, however, the fine air-fall deposit of May 18 forms a continuous layer almost a half-centimeter thick along the axis of the lobe. In unplowed areas this layer probably will remain as a permanent white-ash layer comparably thick to some of the ancient Mount St. Helens ash lobes in eastern Washington (Waitt, 1980, fig. 11*A*).

In the proximal area the thickness of each air-fall unit decreases exponentially downwind from the vent (fig. 364). The magnitude of the May 18 eruption relative to other eruptions of Mount St. Helens and other Cascade Range volcanoes can be compared by plotting thickness of air-fall lobes as a function of distance from the vent. The unit B lobe is generally one-half to one-fourth as thick as pumice layer T, the thickest air-fall deposit of the early 19th-century eruptive episode. The unit B lobe is 4 or 5 times thicker than the 1842–43 lobe, the largest air fall during the mid-19th-century episode (Harris, 1976, p. 178–181). The 1842–43 lobe is similar in thickness to unit D, the final low-energy central-column deposit of May 18.

Beyond 10 km from the volcano, the thickness of the entire May 18 lobe—units A, B, C, and D together—is similar to the thickness of ancient pumice layer T (fig. 364), which is also similar to other lobes

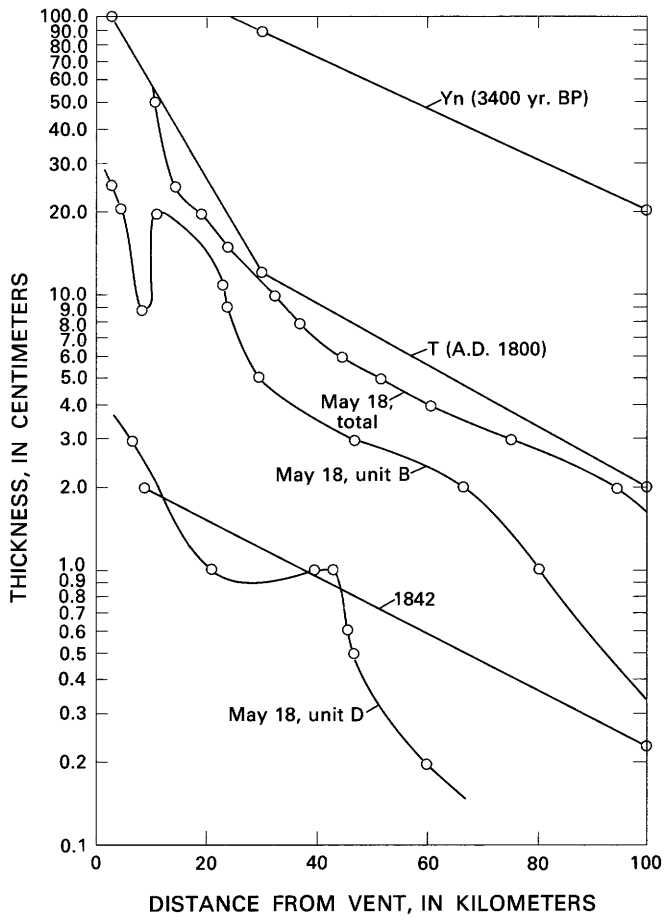

Figure 364.—Plot of thickness of air-fall lobes from Mount St. Helens as a function of distance downwind of volcano. Data from pre-1980 eruptions from Crandell and Mullineaux (1978, figs. 2, 9). Open circles, data points.

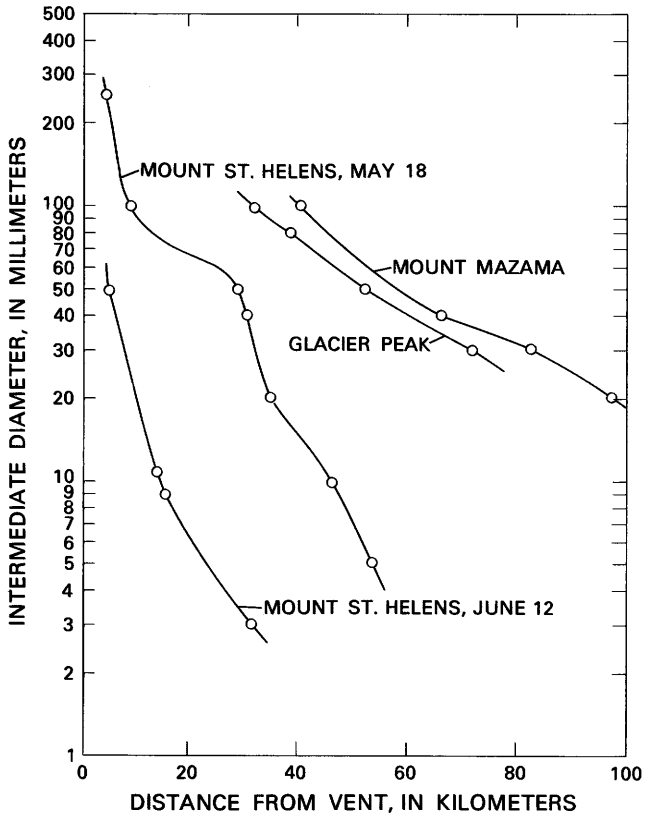

Figure 365.—Plot of intermediate diameter of largest pumice fragments as a function of distance downwind from volcano. Data from Glacier Peak and Mount Mazama from Porter (1978, fig. 8). Open circles, data points.

during each of two earlier highly explosive episodes—layers We and Ye (Crandell and Mullineaux, 1978). Except near the volcano, these lobes and the total May 18, 1980, lobe were each roughly 5 times thinner than Mount St. Helens lobe Wn (450 yr B.P.), and 10 times thinner than lobe Yn (3400 yr B.P.) and than the two thickest lobes from the eruptions of Glacier Peak 11,250–13,000 yr B.P. (fig. 364).

Maximum particle size in air-fall deposits, a measure of the transportational competence of the eruptive column and the prevailing windstream, also decreases exponentially with distance downwind from the vent (fig. 365). Maximum pumice size of the Mount St. Helens May 18 unit B is 5–10 times larger than that of post-May 18 eruptions from Mount St. Helens (fig. 376). But maximum pumice size of unit B is 5–10 times smaller than that from large ancient eruptions of the Cascade volcanoes Glacier Peak and Mount Mazama (fig. 365).

REFERENCES CITED

Crandell, D. R., and Mullineaux, D. R, 1978, Potential hazards from future eruptions of Mount St. Helens volcano, Washington: U.S. Geological Survey Bulletin 1383-C, 26 p.

Folk, R. L., 1974, Petrography of sedimentary rocks: Austin, Texas, Hemphill Publishing Co., 182 p.

Harris, S. L., 1976, Fire and ice—The Cascade volcanoes: Seattle, The Mountaineers, 316 p.

Hoblitt, R. P., Crandell, D. R., and Mullineaux, D. R., 1980, Mount St. Helens eruptive behavior during the past 1,500 years: Geology, v. 8, no. 11, p. 555–559.

Mullineaux, D. R., Hyde, J. H., and Rubin, Meyer, 1975, Widespread late glacial and postglacial tephra deposits from Mount St. Helens volcano, Washington: U.S. Geological Survey, Journal of Research, v. 3, p. 329–335.

Porter, S. C., 1978, Glacier Peak tephra in the North Cascade Range, Washington: stratigraphy, distribution, and relationship to late-glacial events: Quaternary Research, v. 10, p. 30–41.

Waitt, R. B., Jr., 1980, About forty late-glacial Lake Missoula Jokulhlaups through southern Washington: Journal of Geology, v. 88, p 653–679.

Wentworth, C. K., 1922, A scale of grade and class terms for clastic sediments: Journal of Geology, v. 30, p. 377–392.

THE 1980 ERUPTIONS OF MOUNT ST. HELENS, WASHINGTON

PROXIMAL AIR-FALL DEPOSITS OF ERUPTIONS BETWEEN MAY 24 AND AUGUST 7, 1980—STRATIGRAPHY AND FIELD SEDIMENTOLOGY

By RICHARD B. WAITT, JR., VICKI L. HANSEN, ANDREI M. SARNA-WOJCICKI, *and* SPENCER H. WOOD[1]

ABSTRACT

During each of the magmatic eruptions of Mount St. Helens on May 25, June 12, July 22, and August 7, a vertical eruptive column rose intermittently to altitudes of 12–15 km, from which pumice, lithic fragments, and crystals settled downwind in lobes that generally become thinner and finer away from the volcano. Each ejecta lobe is asymmetric according to several criteria, including (1) the axes of maximum thickness and of maximum pumice size are not midway between the two margins of the lobe, (2) the axis of maximum pumice size does not correspond to the axis of thickness, and (3) the median size of particles grades through several grain-size intervals from one lateral margin to the other. The fining in grain size across the lobe is due to the rotation of wind directions with altitude, so material falling from a high-level airborne plume is winnowed as it falls through transverse low-level winds. Wind directions that rotate clockwise with increasing altitude effect an air-fall lobe whose axis of maximum coarseness is clockwise of the axis of maximum thickness; wind directions that rotate counterclockwise with increasing altitude effect an air-fall lobe whose trend of maximum coarseness is counterclockwise of the axis of maximum thickness.

The thickness of air-fall deposits from eruptions on May 25 through August 7 range variously from one-third to one-fortieth that of the May 18 air-fall deposit at a given distance from the volcano. The post-May 18 deposits are an order of magnitude thinner than Mount St. Helens pumice layer T (A.D. 1800) and two orders of magnitude thinner than Mount St. Helens pumice layer Yn (3400 yr B.P.), which is similar in thickness to the most voluminous air-fall deposits of other Cascade Range volcanoes. The maximum size of pumice within the May 18 air-fall lobe is 5–10 times that of the post-May 18 lobes. The overlapping air-fall lobes of May 25, June 12, July 22, and August 7 form a stratigraphic layer that in most places is indivisible into deposits of the separate eruptions.

INTRODUCTION

After the May 18, 1980, eruption of Mount St. Helens, smaller magmatic eruptions occurred on May 25, June 12, July 22, August 7, and October 16–18. None of these repeated the devastating events of May 18, but each eruption produced a vertical column over 10 km tall from which ash drifted downwind, and also produced ash flows down the north flank from which a convected cloud drifted downwind. This report analyzes the air-fall deposits in areas within 60 km of the crater. The distal plumes and air-fall deposits are discussed by Sarna-Wojcicki, Shipley, and others (this volume) and the ash-flow deposits by Rowley and others (this volume).

ACKNOWLEDGMENTS

M. P. Doukas and J. A. Barker collected some of the field data for the July 22 and August 7 eruptions. From wind data supplied by the U.S. National

[1]Present address: Boise State University, Boise, Idaho 83725.

Meteorological Service, Susan Shipley constructed wind-direction diagrams that accompany the deposit maps.

DISTRIBUTION OF AIR-FALL DEPOSITS

The limits and field characteristics of air-fall deposits of the first five magmatic eruptions (fig. 366) were determined within a few days of each eruption, but additional data were gathered for weeks afterward. Air-fall materials of eruptions of May 25 and later are generally distinguishable from May 18 material because the upper part of the May 18 air-fall deposit is silt (Waitt and Dzurisin, this volume) that had been wetted and dried and had thus become somewhat coherent before being overlaid by the younger materials.

THICKNESS, GRAIN SIZE, AND COMPOSITION OF AIR-FALL DEPOSITS

TOTAL DEPOSIT

The total thickness of air-fall deposits (fig. 367) is dominated by those of the May 18 eruption—the directed-blast (pyroclastic density-flow) deposits impelled to the north (Waitt; Moore and Sisson; Hoblitt and others; this volume), and air-fall deposits from the central column that drifted east-northeast (Waitt and Dzurisin, this volume). The lobe southeast of the volcano apparently resulted mostly from a nonmagmatic eruption on May 24, the lobe to the northwest by the magmatic eruption on May 25, and that to the south by magmatic eruptions on May 25 and June 12. The July 22 air-fall deposit, which accumulated atop

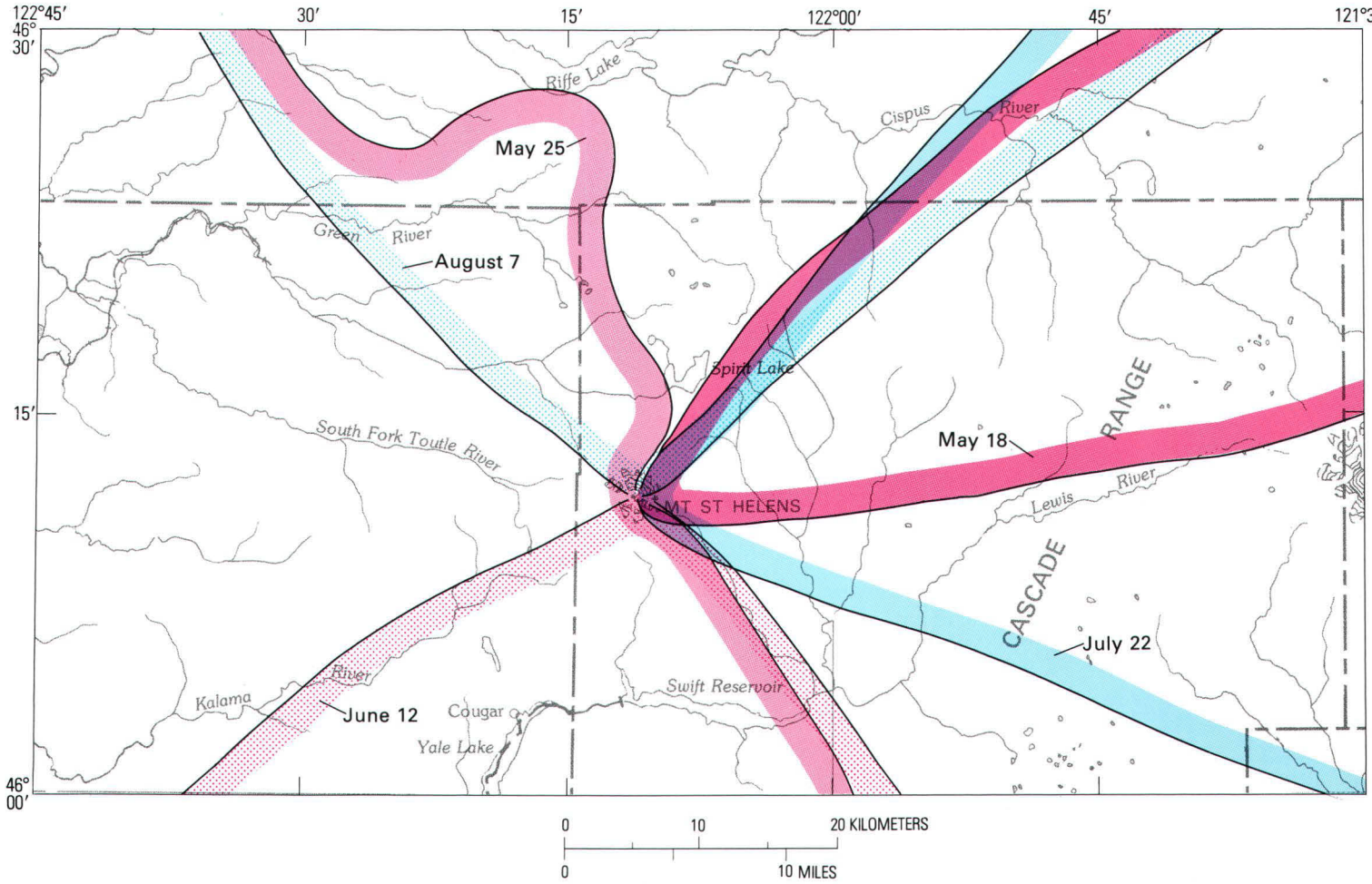

Figure 366.—Index map showing discernible limits of air-fall lobes of eruptions from May 18 through August 7, 1980.

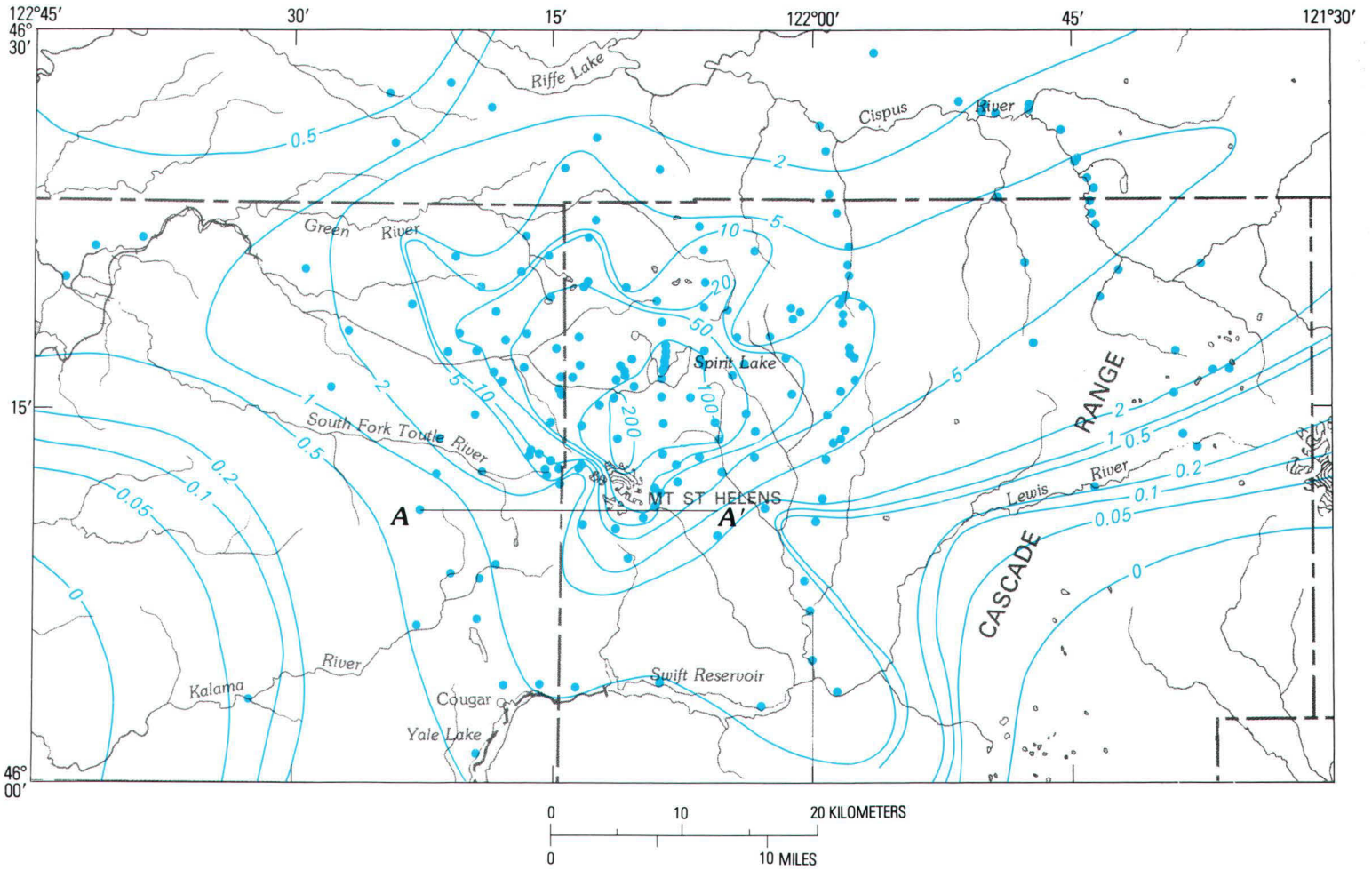

Figure 367.—Isopach maps of air-fall deposits through July 22, 1980. Contour values in centimeters; thickness measured at sites indicated by blue dots. Cross section A–A′ is shown in figure 374.

the May 18 air-fall lobe to the east-northeast, scarcely altered the total-thickness isopachs. The August 7 and October 16–18 air-fall deposits are not included on the total-thickness isopach map (fig. 367), but they were even thinner than the deposits of July 22. Of several minor nonmagmatic ash plumes between the magmatic eruptions, only the narrow lobe attributed to May 24 is thick enough to affect the isopach contours.

MAY 24 DEPOSIT

An ash deposit noted on the southeast flank of the volcano on May 30 is dark-gray lithic-crystal fine sand.[2] This deposit, sharply defined 15 km southeast of the crater, composes most of the southeastern lobe in the total-thickness isopach map (fig. 367). The lobe is south of the margin of the air-fall lobe of May 18 and is largely east of the margins of May 25 and June 12 air-fall deposits. Although its age is not absolutely certain, it probably resulted from a dense nonmagmatic ash plume on May 24 that for several hours drifted southeast (David A. Gibney, oral commun., 1980).

MAY 25 DEPOSIT

The May 25 air-fall deposit consists of small-pebble gravel to very coarse sand near the volcano on the northwest-through-southwest sector, and grades to medium to very fine sand to the west and northwest away from the volcano (fig. 368). About an arc 30 km from the volcano the median grain size also grades laterally across the deposit from medium sand at the

[2]Standard Wentworth sediment-size terms are used to provide a distinct designation for each grain-size interval. Unit designations like "granule gravel," taken from Folk (1974), designate only median grain size of deposits, and not rounding, sorting, or genesis of particles. Fuller explanation appears in Waitt (this volume).

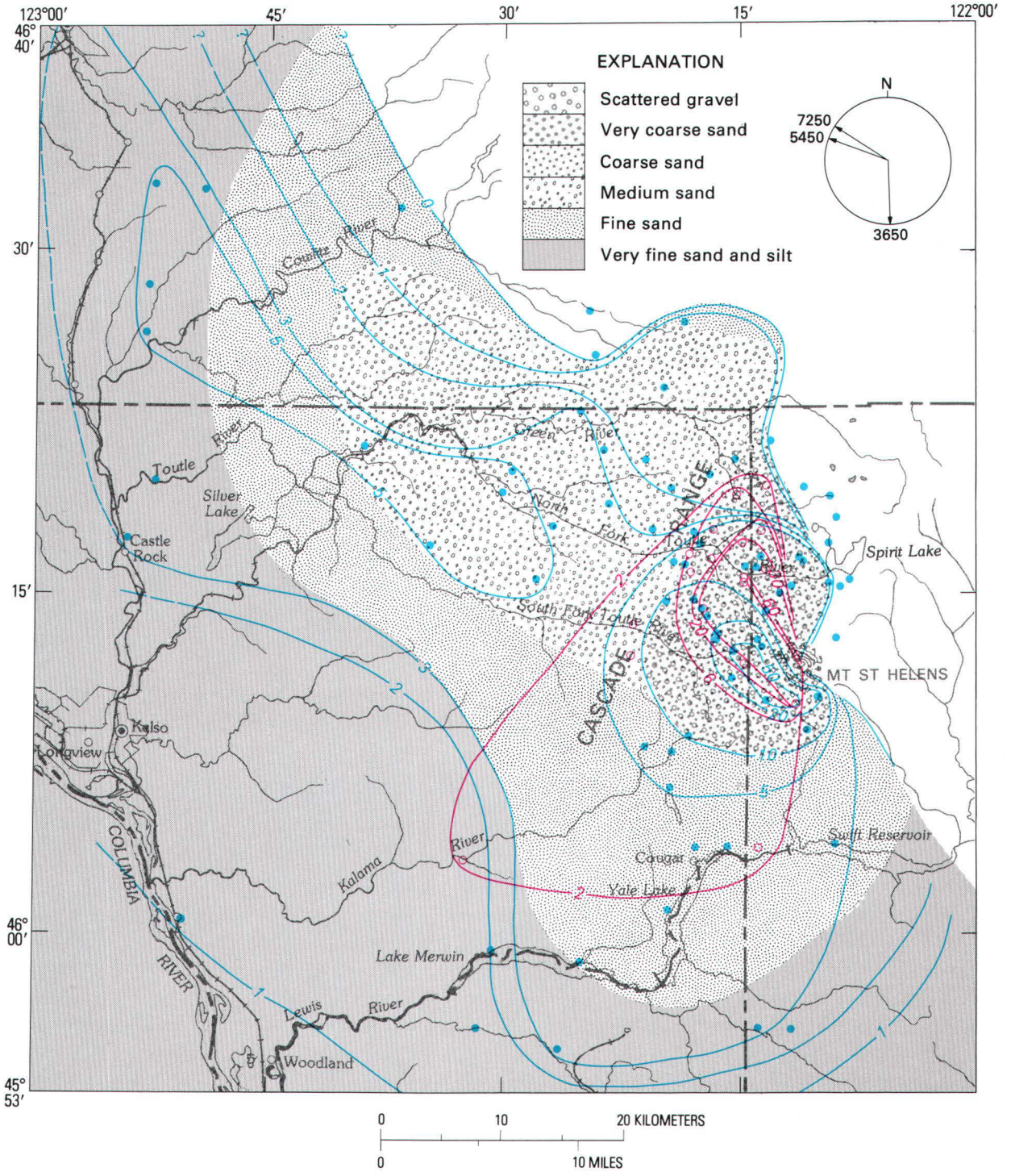

Figure 368.—Map of May 25 air-fall deposit showing isopachs (blue lines), median grain size (patterned areas), and isopleths of intermediate diameter of largest pumice fragment (red lines). All contour values are in millimeters. Wind directions shown for altitudes below 7,500 m. Blue dot, thickness measured at site; red open circle, pumice diameter measured at site. Median grain size determined at about half of the data points.

north margin to silt at the south margin.

Unlike the other air-fall lobes of 1980, each of which is spread through an arc of 90° or less, the May 25 air-fall deposit spread through a 180° arc from south-southeast to north-northwest. The wide arc resulted from a great variance in the wind directions on May 25, which rotated clockwise (in plan view) with altitude: material ejected to altitudes below 4 km drifted south, while that ejected to 5–6 km drifted northwest (fig. 368). The material accumulated thickest to the northwest. The axis of maximum pumice size trends clockwise of the axis of maximum thickness, consistent with the southwardly decrease in median grain size laterally across the lobe. Of the material ejected to high altitude, the finer grained was winnowed to the south by the low-level winds.

The May 25 air-fall deposit contains frothy white pumice like that of the May 18 air-fall deposit (Waitt and Dzurisin, this volume), and also up to 25 percent dense gray pumice similar to a minor component of the May 25 ash-flow deposits (P. W. Lipman, oral commun., 1980). Whereas the May 18 eruption segregated vesicular gray dacite in the directed-blast (pyroclastic density-flow) deposit from the frothy white pumice in the air-fall and ash-flow deposits, the May 25 eruption mixed both rock types into both the air-fall and ash-flow deposits.

JUNE 12 DEPOSIT

The June 12 air-fall lobe is spread broadly southward from the volcano (fig. 369). Although data on maximum pumice size are sparse, gravel-sized pumice fragments fell on the southwest flank of the volcano and other sites near the western margin of the air-fall lobe (fig. 370). The axis of maximum pumice size is clockwise of the axis of maximum thickness. The median grain size grades laterally across the lobe, from scattered pumice gravel and coarse sand at the northwestern margin to fine sand and silt at the eastern margin. Up to an altitude of 12 km, the wind on June 12 rotated clockwise with altitude: material carried west-southwest by high-altitude wind descended through winds toward the southwest, south, and southeast that winnowed the fines from the west side of the plume.

The June 12 air-fall and ash-flow deposits, like those of May 25, contain dense gray pumice sparsely mixed with white frothy pumice. In distal areas like Vancouver, Wash., the ash near the western margin was a pumice-crystal-lithic sand.

The June 12 air-fall deposit includes a mantle of pale-brown sand and silt that overlay and subdued the microtopography of the May 18 ash-flow deposits just east of the margin of the June 12 ash-flow deposits. The mantle was the same pale-brown color as air-fall unit C of May 18 (Waitt and Dzurisin, this volume). The silt that was convected from the June 12 ash flows accumulated millimeters thick downwind to the east and southeast. Whereas the ash flows were channeled by and ponded in topographic lows, this pale-brown silt to the east accumulated nearly evenly on minor topographic highs and lows alike, including areas higher than the top of the ash flows.

JULY 22 DEPOSIT

The July 22 eruptive plume drifted east-northeast, approximately the same direction as the May 18 plume. The air-fall deposit resulted from an eruption comprising three discrete events.

The air-fall deposit is a pebble gravel near the volcano north of the axis of the lobe and grades outward along the axis to coarse sand (fig. 371). From the east-northeast-trending plume the fallout was blown southeastward by winds below altitude 5 km (R. P. Hoblitt and J. E. Vallance, unpub. aerial-oblique photographs). The low-altitude wind thus winnowed fines from the north toward the south margin of the plume. The effects in the field are conspicuous, for the north margin of the lobe near the volcano is sharp and is characterized by scattered cobble- to granule-sized pumice (fig. 372), while the south half of the lobe is a continuous layer of gray sand and silt that tapers to a diffuse ill-defined margin. The axis of maximum pumice size consequently lies counterclockwise of the axis of maximum thickness (fig. 371)—the opposite of the patterns of May 25 and June 12 (figs. 368, 369).

The material at the north side of the lobe comprises 70 percent white pumice, 20 percent gray pumice, and 10 percent lithics and crystals. The gray pumice is lighter in color and less distinct from the white pumice than in the May 25 and June 12 air-fall deposits.

The July 22 ash flows were small compared to those of June 12, and there is no recognizable downwind deposit of the ash-flow cloud. Much of the plume that

convected from the ash flows was drawn up into the vertical eruptive column (J. E. Vallance, unpub. aerial-oblique photographs), a process that the southward low-level winds of July 22 probably aided.

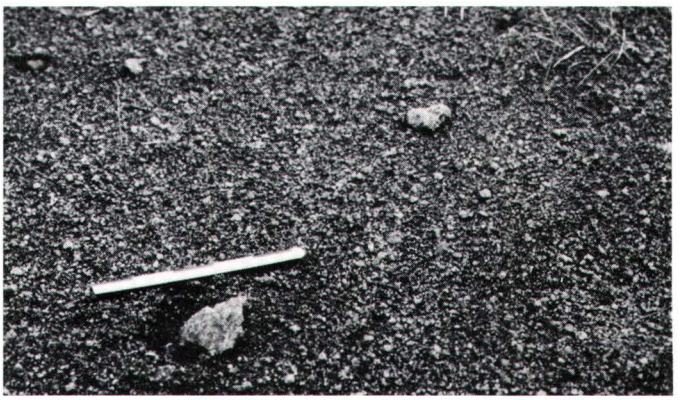

Figure 370.—Coarse pumice (from June 12 eruption) that formed impact pits in the finer but much thicker May 25 air fall at Butte Camp, on southwest flank of volcano. Scale is 15 cm long.

AUGUST 7 DEPOSIT

The August 7 eruption comprised several plumes; downwind the ash fell during at least two distinct intervals spaced hours apart. Within 25 km of the volcano, sparse pumice granules accumulated in a sector on the north that had not received air-fall material since May 18. The material grades downwind to the north into medium and fine sand, which at Randle and Ellensburg, Wash., fell partly as ac-

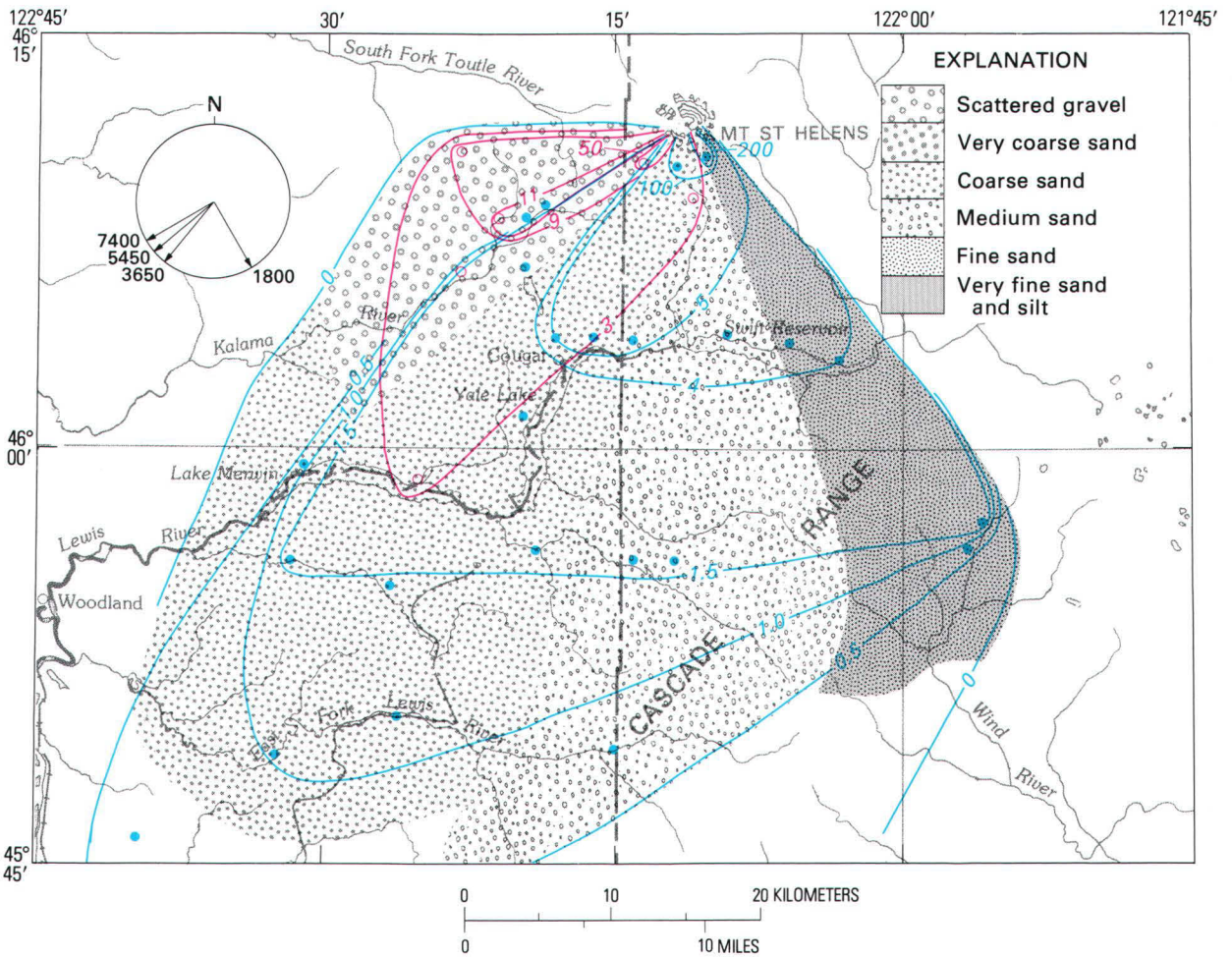

Figure 369.—Map of June 12 air-fall deposits showing isopachs (blue lines), median grain size (patterned areas), and isopleths of intermediate diameter of largest pumice fragment (red lines). All contour values are in millimeters. Wind directions shown for altitudes below 7,500 m. Blue dot, thickness measured at site; red open circle, pumice diameters measured at site. Median grain size determined at about half of the data points.

creted pellets that quickly disintegrated into sand. Almost everywhere this deposit was too thin (less than 0.5 mm) to be measured, but along U.S. Highway 12 in the Cowlitz River valley it was thickest (1 mm) north-northeast of the volcano (fig. 373). The material was thinner and sparser than that of the July 22 eruption, which had been the thinnest magmatic air-fall deposit. The distinction between white and gray pumice had all but disappeared.

The deposit along the eastern margin of the lobe 20 km from the vent consists of scattered small pebbles to granules of pumice and lithic fragments, whereas along the western margin at a similar distance from the volcano, the deposit was a nearly continuous veneer of medium to fine sand (fig. 373). Although data on maximum pumice diameter are sparse, the axis of maximum pumice size is clockwise of the trend of maximum thickness, as it was on May 25 and June 12. The observed wind below 6 km altitude was counterclockwise of the upper level winds, and consequently the fines tended to be winnowed westward across the plume.

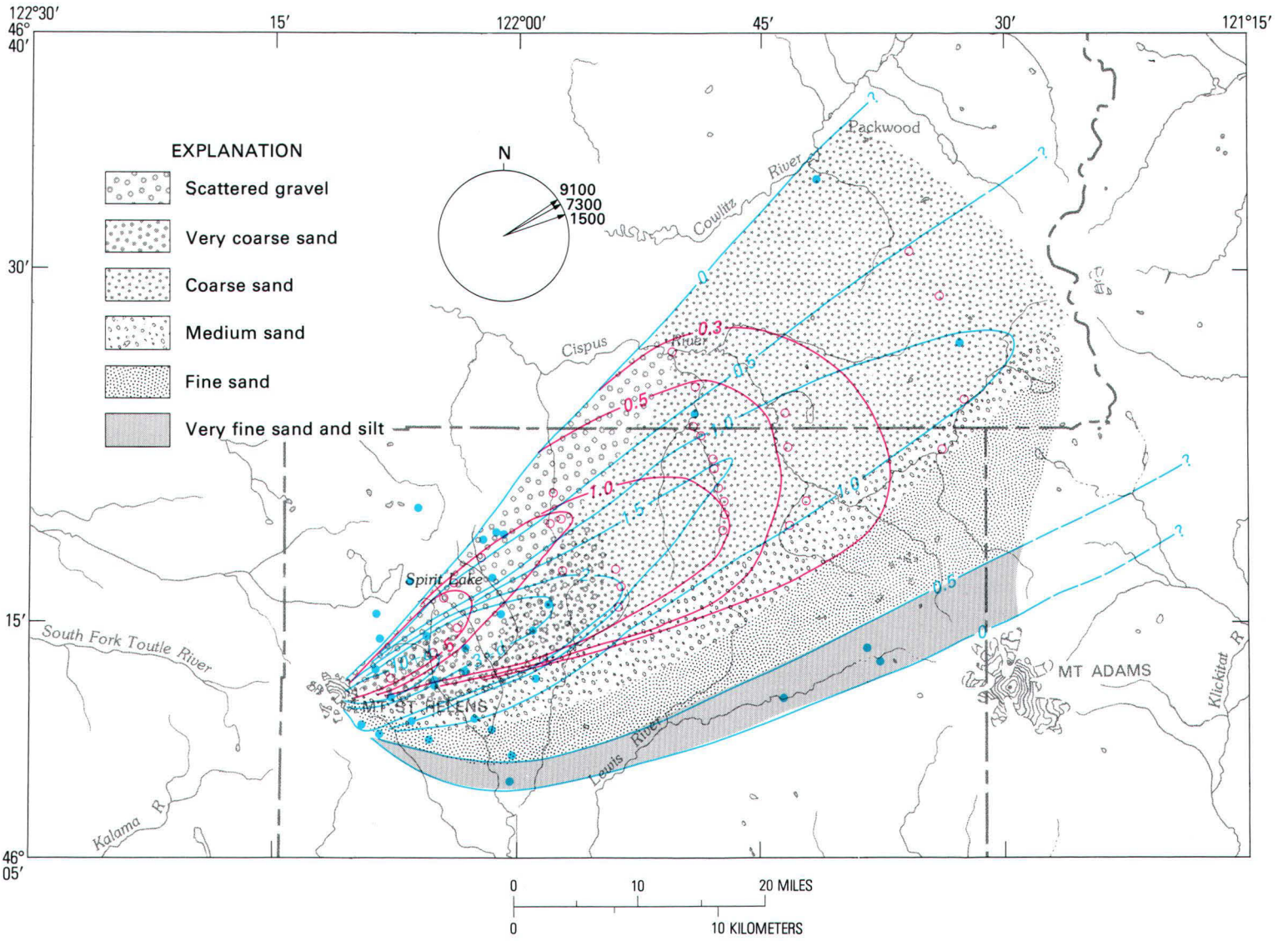

Figure 371.—Map of July 22 air-fall deposit showing isopachs (blue lines), median grain size (patterned areas), and isopleths of intermediate diameter of largest pumice fragment (red lines). All contour values are in millimeters. Wind directions shown for altitudes below 9,500 m. Blue dot, thickness measured at site; red open circle, pumice diameters measured at site. Median grain size determined at about half of the data points.

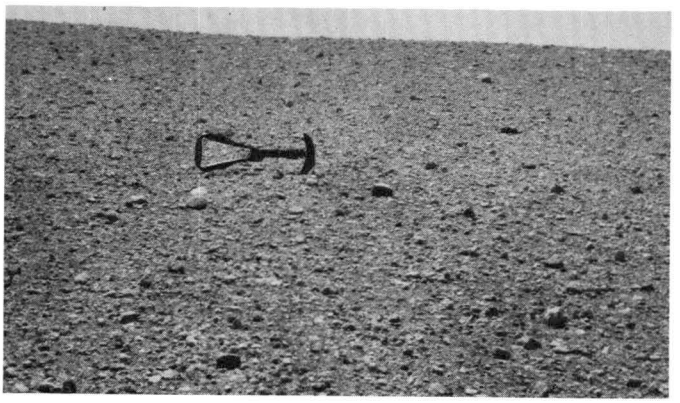

Figure 372.—Coarse pumice of July 22 eruption overlying coherent surface of silt at top of May 18 air-fall deposit. Shovel handle is about 30 cm long.

MINOR NONMAGMATIC DEPOSITS

Several relatively minor eruptions occurred between the magmatic eruptions. A brief plume on August 15, for example, shot to 4.5 km altitude, from which lithic-crystal sand and silt fell sparsely as far as 50 km to the southeast, where it settled onto the surficial layer of May 24 and June 12 material. The deposits of such nonmagmatic eruptions generally cannot be distinguished from the much thicker and coarser deposits of previous magmatic eruptions.

STRATIGRAPHY OF AIR-FALL LAYERS

Where a thin or scattered coarse air-fall deposit accumulates in an area that previously received thin or scattered coarse air-fall material but subsequently was not overlaid by finer material, the two deposits blend into a single layer. Most of the May 18 air-fall deposit is stratigraphically isolated from various overlying younger air-fall products by the intervening May 18 silt of layer A3 or units C or D (Waitt and Dzurisin, this volume). Materials of May 25 and later that overlie this fine-grained May 18 surface have not been similarly mantled.

The coarse July 22 air-fall deposit is readily distinguished from the coarse May 18 air-fall deposit in most of the area of mutual fallout because of the intervening May 18 silt deposits. At the south margin of the May 18 lobe, however, where May 18 units C and D are absent and layer A3 is less than 1 mm thick, the July 22 air-fall deposit is stratigraphically indistinguishable from May 18 material. The two are rudely distinguishable by the grading across both lobes: scattered pumice and lithic gravel fell on the south side of the May 18 lobe, whereas the south margin of the July 22 lobe tapered to a continuous layer of fine sand to silt. Thus, in the east-to-east-southeast sector, scattered coarse May 18 pumice and lithic fragments mingle with fine sand and silt of July 22 that merely settled among the coarse May 18 fragments. Within the coniferous forest east of the area devastated on May 18, air-fall pumice selectively trapped by the trees on May 18 eventually accumulated on the surface of May 18 layer D (Waitt and Dzurisin, this volume), later to mingle with the July 22 air-fall deposit in a single layer.

Northeast of the volcano it was difficult even on August 8 to distinguish the coarse August 7 air-fall deposit from the coarse July 22 air-fall deposit where the two overlapped. But on vehicles, swept roads, and the May 18 silt surface specifically cleared between July 24 and August 6, the scattered pumice and lithic fragments of August 7 could be distinguished from the similar but much coarser and more abundant July 22 material. On unprepared natural surfaces, the two air-fall deposits constitute an indivisible stratigraphic layer. Similarly on the northwest, the August 7 air-fall deposit is indistinguishable from the May 25 air-fall deposit.

The southwest flank of the volcano received coarse pumice and lithic fragments on May 25 and again on June 12. The pebble-size scattered fragments of the June 12 deposit are distinguishable from the continuous layer of much finer May 25 material because observations just before, during, and just after the June 12 eruption recorded the changes. For the stratigraphic record, however, the two deposits now constitute a layer barely distinguishable into two deposits (figs. 370, 374). From Butte Camp on the lower southwest flank of the volcano, the coarse scattered pumice of June 12 thickens into a continuous but finer layer on the south flank, where the underlying layer of May 25 thins and becomes even finer (fig. 374); from Butte Camp the coarse surficial June 12 pumice becomes progressively sparser and finer on the west flank, where the underlying May 25 layer becomes much thicker, and the two layers are thus partly distinguishable (fig. 374).

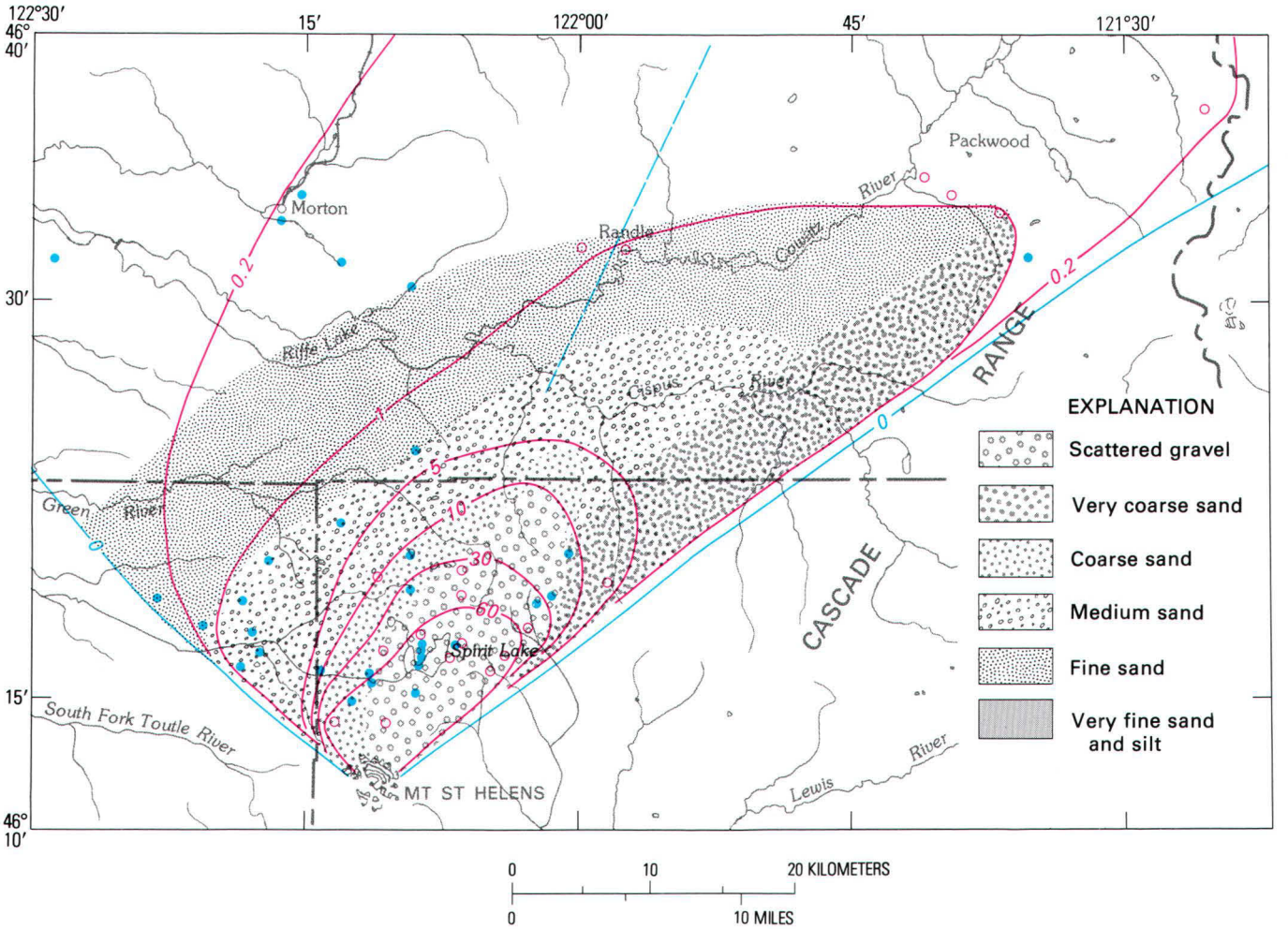

Figure 373.—Map of August 7 air-fall deposit showing median grain size (patterned areas), isopleths of intermediate diameter of largest pumice fragment (red lines), and axis of maximum thickness (blue dashed line). High-level wind was toward northeast; low-level wind toward northwest. All contour values are in millimeters. Blue dot, thickness measured at site; red open circle, pumice diameter measured at site. Median grain size was determined at about half of the data points.

Most of the air-fall material overlying the coherent silt surface of the May 18 deposits is thus a single stratigraphic layer consisting of five overlapping air-fall lobes. From the southwest clockwise to the east they are June 12, May 25, August 7, May 18 (late fall from trees), and July 22.

Except for the relatively thick lobe of May 24, air-fall deposits from relatively minor nonmagmatic eruptions cannot be distinguished from the deposits of the major magmatic eruptions. These minor additions do not affect the field thicknesses or the isopach or isopleth maps, but they do constitute a contaminant to the finer fractions of the magmatic deposits with which they mix.

RELATIVE MAGNITUDE OF ERUPTIONS

Magmatic eruptions of May 25 through August 7 may be compared to each other and to the May 18 eruption by the relative thicknesses of lobes. The maximum thickness of each lobe decreases roughly exponentially with distance from the vent, although the rate of decrease is somewhat irregular, especially in the May 25 deposit (fig. 375). The eruptions became generally less voluminous with time, the August 7 lobe being thinner by an order of magnitude than the May 25 lobe. At distances of 20–60 km from the volcano, the May 18 lobe is 3–10 times thicker

than the May 25 and June 12 lobes, 20 times thicker than the July 22 lobe, and 40 times thicker than the August 7 lobe. The individual thicknesses of the post-May 18 lobes are of the same order of magnitude as that of unit D of May 18, which resulted from only the final wane of the eruptive column (fig. 375; Waitt and Dzurisin, this volume). The thicknesses of the May 25 through August 7 lobes may also be compared to pre-20th century air-fall lobes from Mount St. Helens (Crandell and Mullineaux, 1978, table 2; Hoblitt and others, 1980). The May 25 and June 12 lobes are similar in thickness to the thickest lobe (A.D. 1842–43) of the mid-19th-century eruptive episode (fig. 375).

The largest pumice fragments at a given distance from the volcano are a measure of the transportational competence of the central eruptive column and of the wind velocity. The maximum pumice diameter decreases roughly exponentially with distance from the volcano, although the rate is variable (fig. 376). At distances of 25 km from the vent, the largest pumice fragments of the post-May 18 lobes, taken as a group, show that these eruptive columns were 3–10 times less competent than the May 18 eruptive column, if the wind velocities were roughly the same. The post-May 18 columns were roughly 50 times less competent than two ancient plumes from highly explosive eruptions of Cascade Range volcanoes Glacier Peak (11,250–13,000 yr B.P.) and Mount Mazama (6,700 yr B.P.) (fig. 376).

DISCUSSION OF ASYMMETRY OF LOBES

Each of the air-fall lobes of magmatic eruptions from Mount St. Helens on May 25 through August 7 is asymmetric in five ways: (1) the axis of maximum thickness is not midway between the two margins of the lobe; (2) the axis of maximum pumice diameter is not centered between the lateral boundaries; (3) the axis of maximum pumice size does not correspond to the axis of maximum thickness; (4) the median size of particles grades through several grain-size intervals from one lateral margin to the other, and (5) the boundary defining the coarse side of the lobe is sharp but the opposite boundary is diffuse. This asymmetry is caused by rotation in wind direction with altitude, so the material falling from a high-level plume is winnowed by transverse low-level winds.

Because coarse fragments are less affected by transverse winds than are fine particles, they fall more nearly vertically, causing the sharp outer boundary of coarse material on the windward side of the lobe. The axis of maximum pumice size therefore more closely approximates the path of the high-level plume than does any other single depositional characteristic. Winnowing by transverse low-level winds shifts the zone of maximum thickness downwind from the path of the high-level plume. The arc defined by the entire lobe, the arc between the axes of maximum pumice size and of maximum thickness,

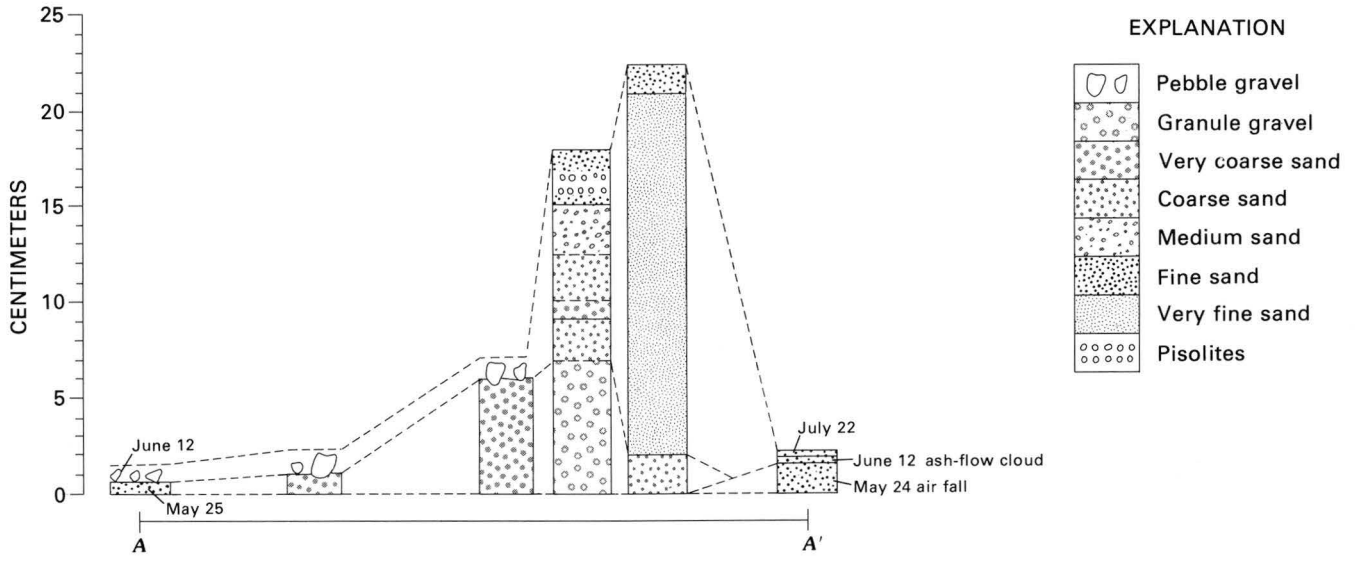

Figure 374.—Stratigraphic cross section A–A' (see figure 367 for location) of air-fall deposits on west and south flanks of Mount St. Helens; data through July 20, 1980. Dashed lines show correlation of air-fall deposits.

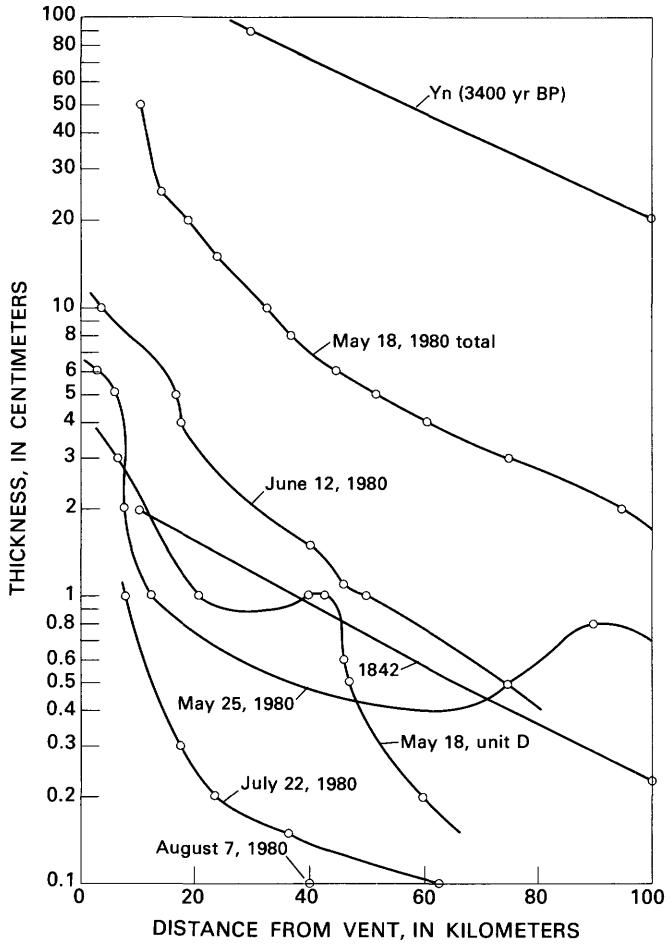

Figure 375.—Maximal thickness of air-fall lobes from Mount St. Helens plotted as function of distance downwind from volcano. Data for pre-1980 Mount St. Helens eruptions from Crandell and Mullineaux (1978, fig. 9). Open circles, data points.

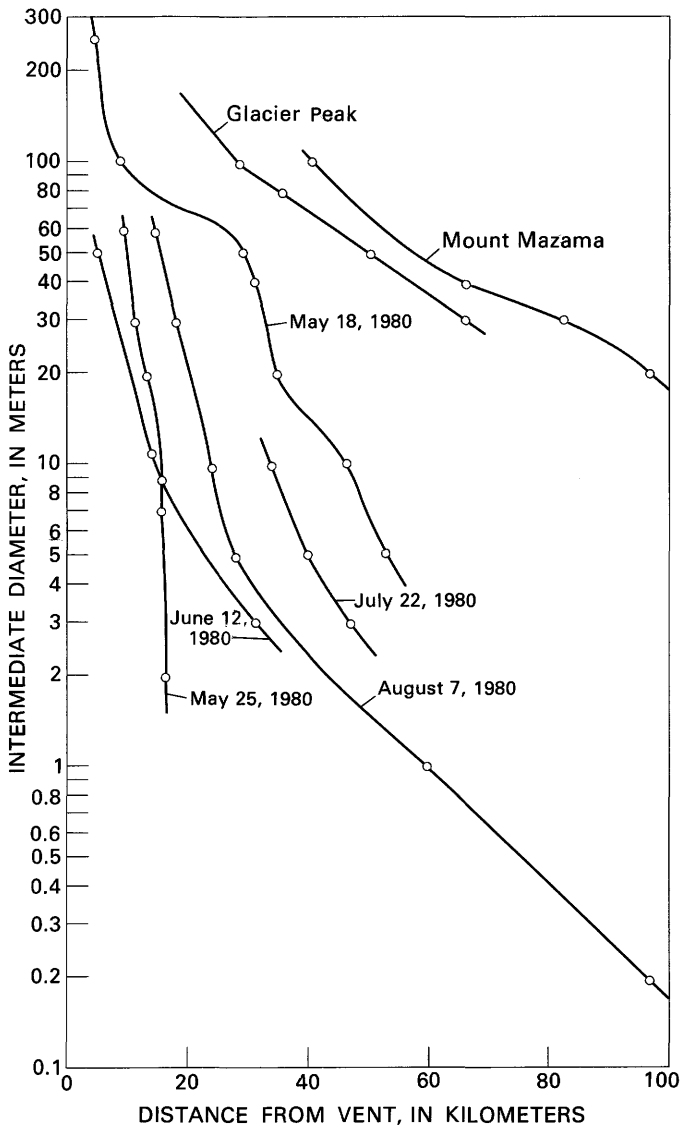

Figure 376.—Intermediate diameter of largest pumice fragment plotted as a function of distance downwind from Mount St. Helens volcano. Data from Glacier Peak and Mount Mazama volcanoes are from Porter (1978, fig. 8). Open circles, data points.

and the lateral spread between the fallout zones of coarse and fine particles must vary directly with the magnitude of shear between the high-level and low-level wind vectors.

Most of the important variables that affected air-fall distribution—rotation in wind direction with altitude, and duration, height, and qualitative density of eruption column—are known for the May 25 through August 7 eruptions. All of these variables and the measured parameters of the consequent air-fall distribution can be written as a mathematical equation by which a computerized "model" could relate these variables to each other. The materials of each air-fall lobe reflect the rotation in wind direction with altitude. The maps presented herein may be used to calibrate such a model, one that will predict air-fall distribution and grain size for future eruptions of similar magnitude. For a hypothetical eruption column of a certain density ejected to a certain height for a certain duration, it should be possible to predict with some accuracy the distribution, thickness, and grain-size pattern of fallout influenced by each future-day's projected wind vectors.

Some studies of ancient air-fall lobes suggest that the axis of maximum thickness coincides with the axis

of maximum pumice size (for example, Porter, 1978, figs. 3, 4). The small post-May 18 lobes from Mount St. Helens suggest that these axes do not necessarily coincide. Nor does median size necessarily decrease toward both margins of the lobe from an axis of maximum coarseness along the middle. Because a rotation of wind direction with altitude displaces the axis of maximum thickness from the axis of maximum pumice size and causes a grading of median size across the lobe, the general structure of the wind column at the time of an ancient eruption may be deduced from these parameters in ancient volcanic air-fall lobes.

REFERENCES CITED

Crandell, D. R., and Mullineaux, D. R., 1978, Potential hazards from future eruptions of Mount St. Helens volcano, Washington: U.S. Geological Survey Bulletin 1383-C, 26 p.

Folk, R. L., 1974, Petrography of sedimentary rocks: Austin, Texas, Hemphill Publishing Co., 182 p.

Hoblitt, R. P., Crandell, D. R., and Mullineaux, D. R., 1980, Mount St. Helens eruptive behavior during the past 1,500 years: Geology, v. 8, p. 555–559.

Porter, S. C., 1978, Glacier Peak tephra in the North Cascade Range, Washington—stratigraphy, distribution, and relationship to late-glacial events: Quaternary Research, v. 10, p. 30–41.

GEOCHEMISTRY OF THE DEPOSITS

It is difficult to reconstruct magmatic compositional variations from chemical analyses of eruptive products, especially pyroclastic deposits. In addition to extensive separation of volatile phases during eruption, quenched porous glassy volcanic materials are unstable under atmospheric conditions and rapidly tend to hydrate, oxidize, and otherwise alter. For prehistoric deposits, timing of eruption and deposition is difficult or impossible to determine precisely. Accordingly, petrologic study of volcanic materials that have been collected immediately after eruption at known times—commonly at Mount St. Helens while still hot—can be especially rewarding, even when the total compositional variation is not large in comparison to the total compositional range in eruptive products from the volcano.

Precise major-oxide analyses show small but significant variations in compositions of 1980 eruptive products (Lipman, Norton, and others). With time, compositions of erupted magma generally became more mafic, and volumes decreased, both during the day on May 18 and during subseqeuent explosive eruptions from May 25 to October 16–18. All compositions are mafic dacite, transitional to andesite. These changes are thought to represent different compositions at progressively deeper levels in a compositionally zoned or stratified magma body, similar to progressions in silicic volcanic sequences elsewhere. Volumes of magma decreased in successive pyroclastic eruptions in 1980, and the proportions erupted relatively quiescently as lava domes increased. The total volume of magma erupted in 1980 was 0.24 km^3, considerably less than that of some previous pyroclastic eruptions of Mount St. Helens.

Electron-probe analyses of coexisting ilmenite and magnetite in the 1980 eruptive products indicate crystallization temperatures of about 990°C and oxygen fugacities of about -9.7 (log_{10}), showing no distinct trends with time (Melson and Hopson). Both mineral and bulk chemical compositions are similar to 16th–19th century eruptive products but less differentiated than some earlier prehistoric pyroclastic deposits. Dark- and light-gray banded layers, relatively common in 1980 pumice blocks, contain compositionally varying mineral phases and indicate mixing of different parts of the same magma chamber or of magma from different bodies.

Alteration of the 1980 volcanic deposits was studied to increase knowledge of hydrothermal processes within active volcanoes and to aid interpretation of alteration patterns in older volcanic deposits (Dethier and others). Active alteration of new deposits is indicated by the chemistry of fumarole encrustations and of surface thermal waters, ash-leaching experiments, and scanning electron microscope studies of mineral and glass surfaces. Calculated stability relations indicate that kaolinite and smectite should be stable alteration phases, but, with the exception of the fumarole encrustations, new secondary minerals were not found in the 1980 deposits, indicating that rates of crystallization are slow.

Chemical compositions of the airfall ash erupted on May 18 reflect varying mixtures of magmatic constitutents and of old rock from the volcano, as well as winnowing of light particles and settling out of dense particles downwind from the volcano (Sarna-Wojcicki, Meyer, and others). Phenocrysts and lithic fragments are concentrated in near-source deposits, and glass shards become more abundant downwind, yielding chemical trends similar to those of magmatic crystal-liquid fractionation processes. Such physical mixing and sorting processes obscure any systematic compositional trends in ash from the post-May 18 eruptions.

New X-ray fluorescence techniques for major elements and induction-coupled-plasma techniques for minor elements, developed to provide rapid accurate chemical analyses, were extensively used in analyses of Mount St. Helens eruptive products (Taggart and others), as well as conventional wet-chemical analyses of major elements and neutron-activation determinations of minor elements.

THE 1980 ERUPTIONS OF MOUNT ST. HELENS, WASHINGTON

COMPOSITIONAL VARIATIONS IN 1980 MAGMATIC DEPOSITS

By PETER W. LIPMAN, DANIEL R. NORTON, JOSEPH E. TAGGART, JR., ELAINE L. BRANDT, *and* EDYTHE E. ENGLEMAN

ABSTRACT

Major-oxide chemical analyses of quenched glassy rocks by modified wet-chemical and X-ray fluorescence methods demonstrate small but significant compositional variations (SiO_2 = 64.4–60.3 percent) in magmatic materials erupted from Mount St. Helens in 1980. Compositions of erupted magma generally became more mafic and volumes decreased with time, both during the sequence of catastrophic eruptions on May 18 and also during the subsequent series of eruptions from May 25 through December 28. Most of the analyzed rocks are reasonably classed as mafic dacites, but the lava dome erupted on October 17–18 is a silicic andesite. These changes are interpreted as representing samples of successively deeper levels in a compositionally zoned or stratified magma body, similar to progressions in many other silicic eruptive sequences. The most silicic liquid portion of this magma body was largely exhausted by May 25. A plot of time of eruption in 1980 versus cumulative volume defines an asymptotic curve, suggesting that only a small volume of explosively eruptible magma remains at high levels within the volcano. Extensive preeruption crystallization of the 1980 magmas and compositional similarities to eruptive products of the past few hundred years at Mount St. Helens suggest that a long-lived high-level magma chamber may have erupted recurrently. The compositional trends also suggest that eruption of even more mafic magma, perhaps as andesitic lava flows, may occur in the near future.

INTRODUCTION

Determination of magmatic compositions and compositional ranges for erupted volcanic materials can provide insights into the volume, depth, and physical state of subvolcanic magma chambers. For the 1980 Mount St. Helens activity (table 68), initial determinations by rapid X-ray fluorescence (XRF) methods (Hoblitt and others, 1980; Wozniak and others, 1980) had demonstrated that a variety of volcanic products from the May and June eruptions were similar in composition. Accordingly, although we have continued to use the rapid and relatively inexpensive XRF analyses to monitor for major compositional changes, we have also made more precise analyses for major oxides on a suite of samples that represent all magmatic eruptions up through the activity of October 1980, using the long-established wet-chemical methods of the U.S. Geological Survey. Only XRF analyses are currently available for ejecta of the December activity. Most analyses were on individual large blocks of glassy pumice and scoria, some collected while still hot, that should provide close approximations of magmatic compositions. Too few samples have been analyzed thus far to characterize the full range of compositional variation, either within single eruptive episodes or during the sequence of 1980 events. Nevertheless, the changes are sufficiently systematic that they are confidently considered to document small but significant compositional variations as a function of date of activity and eruptive volume. Compositions became less evolved (more mafic) and volumes generally decreased with time, both during the sequence of catastrophic eruptions on May 18, and also during the subsequent series of eruptions from May 25 through December 28.

Table 68.—Summary of magmatic eruptions, 1980 activity of Mount St. Helens, Wash.
[km³, cubic kilometers; XRF, X-ray fluorescence; hr, hour; d, day. Leaders (---) indicate no data]

Phase	Date	Eruptive type	Duration	Estimated volume of magma[1] (km^3)			SiO_2 content	
				Pyroclastic flows and surge	Tephra falls	Dome	Wet chemical[2]	XRF[3]
1	May 18 (morning).	Lateral blast and surge eruption, largely phreatic, of hot subsolidus crystalline dacite, interpreted as quenched top and margins of magma body.	3 hr	0.048	0.04	---	64.4	---
1	May 18 (afternoon).	Plinian eruption of liquid dacite as pumice and ash falls and pyroclastic flows, representing interior of magma body.	5 hr	.041	.06	---	63.0-63.9	---
2	May 25----------	Small Plinian eruptions, producing tephra falls and pyroclastic flows.	~3 hr	.0004	.016	---	64.3-64.4	---
3	June 12---------	Plinian eruptions, producing tephra falls and pyroclastic flows.	3 hr	.003	.017	---	63.3-64.0	---
3	June 12-19------	Growth of June lava dome within crater----------	~7 d			0.005	---	[4]63.6
4	July 22---------	Plinian eruption, producing tephra falls and pyroclastic flows.	5 hr	.002	.001	---	63.3	60.3-64.0
5	Aug. 7----------	Small Plinian eruption, producing tephra falls and pyroclastic flows.	6 hr	.001	.0005	---	62.5	63.0
5	Aug. 7-9--------	Growth of August lava dome within crater----------	~3 d			.001	---	63.0
6	Oct. 16-18------	Several small Plinian eruptions, producing tephra falls and pyroclastic flows.	2 d	.0005	.0005	---	---	62.8-63.0
6	Oct. 18-19------	Growth of October lava dome within crater----------	~1 d			.002	---	61.5
7	Dec. 28, 1980 to Jan. 1-2, 1981.	Growth of December dome lobes on flanks of October dome.	5-7 d			.003	---	63.2
		Total--------		0.096	0.135	0.011		

[1]Modified from: Moore and Sisson (this volume); Moore and others (this volume); Rowley and others (this volume); Sarna-Wojcicki and others (this volume). Magmatic volumes taken as one-third depositional volumes of pyroclastic flows.
[2]From table 69.
[3]From table 70.
[4]From Hoblitt and others, 1980 (table 2, analysis p).

ACKNOWLEDGMENTS

We thank Richard Hoblitt, Terry Leighley, C. Dan Miller, Peter Rowley, and Donald Swanson for providing some of the samples that were analyzed. Phenocryst modes listed in table 69 were determined by Lisa McBroome and Mel Kuntz. Finally, we dedicate this paper to the memory of David Johnston, our friend and colleague, whose fascination with and skillful study of geochemical problems of arc volcanism will serve as a worthy model for all of us in the future.

ANALYTICAL METHODS

Chemical analyses reported in table 69 were made by long-established gravimetric and volumetric wet-chemical techniques, supplemented by spectrometric and electrometric methods capable of the high accuracy and precision required for this study. SiO_2, Al_2O_3, Fe_2O_3, FeO, MgO, CaO, H_2O^+ (combined), H_2O^- (moisture), TiO_2, P_2O_5, and MnO were determined by the methods of Peck (1964). Na_2O and K_2O were analyzed by a flame-photometric method, utilizing sample fusion with lithium borate and measurement by an Instrumentation Laboratory model 343 flame photometer.

Carbon dioxide was determined by a coulometric method (Huffman, 1977): carbon dioxide released from the sample with perchloric acid is reacted with a partially aqueous solution of monoethanolamine, and the resulting strong acid is titrated with a coulometrically generated base to a photometric end point. A Coulometric model 5010 coulometer and model 5030 carbonate-carbon apparatus were used.

Sulfur was determined by direct combustion and iodate titration (American Society for Testing and Materials, 1966). In this method, sulfur oxides are released from the sample contained in a crucible, using a vanadium pentoxide oxidizer and a copper accelerator. A Leco induction furnace and model 532 automatic sulfur titrator were used. Chlorine was determined by the volumetric method of Peck and Tomasi (1959). Fluorine was determined by a selective-ion electrode method: samples are fused with sodium hydroxide, dissolved in ammonium citrate, and the potentials of the solutions are read with a fluoride electrode. An Orion Ionalyzer model 801A was used to measure potentials.

The methods used for determination of Na_2O, K_2O, CO_2, S, and F were checked against those of

Table 69.—Wet chemical analyses (weight percent) of juvenile eruptive products from Mount St. Helens, Wash., May 18–October 1980

[Analyses by E. L. Brandt and E. E. Engleman. Leaders (---) indicate no data]

Sample No.---	1	2	3	4	5	6	7	8	9	10	11	12
Eruption date		May 18, 1980			May 25, 1980		June 12, 1980		July 22, 1980	Aug. 7, 1980	Oct. 16–18	
Unit---------	Blast dacite	Pumice fall	Pyroclastic flow, lower	Pyroclastic flow, upper	Pyroclastic flow, pumice	Pyroclastic flow, banded scoria	Pyroclastic flow, pumice	Pyroclastic flow, dense scoria	Pyroclastic flow, pumice	Pyroclastic flow, pumice	Pyroclastic flow, pumice	Lava dome
Field No.----	SH21	SH51	SH23	SH24	SH22A	SH22B	SH52A	SH52B	SH71	SH72	80R-240A	SH116
Lab No.------	D227 200	D227 207	D227 203	D227 204	D227 201	D227 202	D227 205	D227 206	D228 844	D228 845	D231107	D231112
SiO_2---------	64.39	63.66	63.87	63.03	64.29	64.41	63.29	64.01	63.29	62.52	63.22	61.54
Al_2O_3--------	17.39	17.45	17.39	17.51	17.40	17.41	17.65	17.55	17.82	18.07	17.69	17.93
Fe_2O_3--------	1.51	1.50	1.44	1.82	1.55	1.47	1.63	1.57	1.55	1.74	1.52	1.61
FeO----------	2.70	2.75	2.29	2.66	2.70	2.66	2.86	2.64	3.02	2.92	3.06	3.69
MgO----------	1.87	1.93	1.90	2.10	1.86	1.84	2.07	1.90	2.14	2.24	2.17	2.57
CaO----------	4.93	5.03	5.00	5.20	4.92	4.94	5.17	4.98	5.25	5.54	5.33	5.85
Na_2O---------	4.61	4.57	43.50	4.59	4.66	4.61	4.58	4.59	4.55	4.48	4.59	4.37
K_2O---------	1.32	1.30	1.27	1.29	1.32	1.32	1.27	1.29	1.19	1.14	1.25	1.10
H_2O^+---------	.15	.35	.48	.49	.08	.15	.31	.24	.07	.05	.04	.00
H_2O^----------	.07	.14	.07	.04	.06	.10	.05	.08	.05	.03	.06	.02
TiO_2---------	.60	.64	.60	.64	.60	.58	.65	.61	.65	.66	.66	.79
P_2O_5---------	.13	.09	.13	.14	.13	.13	.08	.08	.13	.13	.14	.15
MnO----------	.07	.07	.07	.08	.07	.07	.08	.07	.08	.08	.08	.09
CO_2---------	.00	.01	.00	.00	.00	.00	.01	.01	.01	.00	.01	.00
S----------	.01	.07	.04	.06	.01	.01	.04	.02	.01	.01	---	---
Cl----------	.03	.02	.05	.02	.04	.03	.02	.02	.03	.04	.03	.03
F----------	.02	.03	.02	.06	.02	.02	.01	.01	.02	.03	.02	.02
	99.80	99.61	99.62	99.73	99.71	99.75	99.77	99.67	99.86	99.68	99.87	99.76
Less O------	.03	.05	.04	.05	.03	.03	.03	.02	.03	.03	.03	.03
Total---	99.77	99.56	99.58	99.68	99.68	99.72	99.74	99.65	99.83	99.65	99.84	99.73

SAMPLE DESCRIPTIONS

[Abbreviations for modes (volume percent): m, matrix (glass and vesicles); pl, plagioclase; opx, orthopyroxene; hbl, hornblende; opq, opaque oxides; o, others]

1. Block of dense gray dacite, collected by P. W. Lipman at "Castle" geodetic station: lat 46° 15.5′ N., long 122° 14.7′ W. Mode: m 84.4, pl 12.1, opx 1.9, hbl 1.2, opq 0.4.
2. Aggregate sample of 2- to 5-cm-diameter pumice fragments, collected by P. W. Lipman along Smith Creek: lat 46° 13.8′ N., long 122° 6.1′ W. Mode: m 88.4, pl 8.7, opx 1.4, hbl 0.9, opq 0.6.
3. Aggregate sample of 5- to 10-cm-diameter pumice lumps, collected by D. A. Swanson at base of wall of large phreatic-explosion pit ("Pumice Pond"): lat 46° 15.6′ N., long 122° 17.9′ W.
4. Aggregate sample of 5- to 10-cm-diameter pumice lumps, collected at top of wall of large phreatic explosion pit by D. A. Swanson: same locality as 3 but 30 m higher in section.
5. Vesicular tan pumice block, collected by P. W. Lipman near base of "stair-steps": lat 46° 14.2′ N., long 122° 17.7′ W. Mode: m 84.5, pl 11.4, opx 1.9, hbl 1.0, opq 1.0.
6. Banded dense gray scoria block, collected by P. W. Lipman near base of "stair-steps" at same locality as 5. Mode: m 85.2, pl 12.2, opx 1.6, hbl 0.6, opq 0.4.
7. Vesicular tan pumice block, collected by P. W. Lipman near large phreatic-explosion pit ("Pumice Pond"): lat 46° 15.8′ N., long 122° 17.8′ W. Mode: m 89.9, pl 8.5, opx 1.0, hbl 0.5, opq 0.1.
8. Dense gray scoria block, collected by P. W. Lipman near large phreatic-explosion pit ("Pumice Pond"), nearly same locality as 7. Mode: m 80.1, pl 15.6, opx 2.6, hbl 1.0, opq 0.7.
9. Vesicular gray pumice block, collected by P. W. Lipman near large phreatic-explosion pit ("Pumice Pond"), nearly same locality as 7. Mode: m 91.7, pl 7.0, opx 0.6, hbl 0.6, opq 0.1.
10. Vesicular gray pumice block, collected by P. W. Lipman in amphitheater of crater: lat 46° 12.6′ N., long 122° 11.4′ W. Mode: m 85.0, pl 12.4, opx 1.7, hbl 0.6, opq 0.2, o 0.1.
11. Breadcrust dense gray block, collected by T. Leighley at north edge of inner crater: lat 46° 12.0′ N., long 122° 11.5′ W.
12. Scoriaceous margin of southeast dome lobe collected by T. Leighley and D. A. Swanson on Dec. 28, 1980, at west margin: lat 46° 12.0′ N., long 122° 11.4′ W.

Peck (1964) and Peck and Smith (1964), in order to provide continuity with accurate, precise time-honored methods.

X-ray fluorescence analyses (table 70) were made by a method in which samples are fused with lithium tetraborate and the resultant discs are analyzed with a Phillips PW1600 wavelength-dispersive simultaneous X-ray spectrometer (Taggart and others, 1980; Taggart and others, this volume). The method has been tested, with good agreement, against silicate rock standards and the wet-chemical analyses reported in table 68 (Taggart and others, this volume). Although the XRF and wet-chemical results show good agreement, XRF analyses cannot duplicate the accuracy and precision of the time-tested wet-chemical methods described above. Because of the relatively limited variation in samples collected from the 1980 Mount St. Helens deposits, the determinations by XRF show more scatter than do those by the classical techniques.

ERUPTIVE SEQUENCE AND RELATED COMPOSITIONAL CHANGES

The eruptions that occurred from March 27 until the paroxysmal eruption of May 18 appear to have been entirely phreatic steam blasts, and the ejecta consisted of pulverized material blown from the old volcanic cone. Characteristics of the juvenile material erupted on May 18 and subsequently are summarized in table 68.

The large-volume lateral explosions that began at about 0832 PDT (Pacific Daylight time) on May 18 and that were also largely hydrothermal in character (Christiansen and Peterson, this volume) contained large proportions (in places more than 50 percent by volume) of distinctive, partly devitrified gray dacite. The dacite occurs as dense blocks, as much as 0.5 m in diameter, characterized by low contents of vesicles and groundmass glass in comparison to the later-erupted frothy pumice and ash. Blocks of this dacite locally display crude polygonal cooling joints, which may represent weakly developed breadcrust textures, and which shatter readily when tapped with a hammer. These textural and structural features indicate that this abundant rock type was erupted as hot but partly devitrified material at near-solidus temperatures (Moore and Sisson, this volume; Hoblitt and others, this volume). Measured temperatures in deposits containing abundant fragments of the gray dacite were as high as 277°C (Banks and Hoblitt, this volume).

We interpret the gray dacite as representing the quenched upper part of the magma body that was the source of juvenile liquid dacite erupted later on May 18. Analyzed blocks of the gray dacite (table 69, sample 1; Hoblitt and others, 1980, table 1, analysis k) are the most silicic and otherwise compositionally evolved magmatic material that was erupted in 1980. The near-source lateral-blast deposits accordingly consist of approximately equal proportions of juvenile and older material (Moore and Sisson, this volume; Hoblitt and others, this volume). The voluminous downwind fine-grained tephra that are correlative with the blast deposits (unit A: Waitt and Dzurisin, this volume; Sarna-Wojcicki, Shipley, and others, this volume) thus must also constitute a mix of juvenile and older material; for the volume estimates in table 68, the same proportions have been assumed as for the close-in blast deposits.

Falls of light-colored pumice were observed east of the volcano as early as 0915 on the morning of May 18 (Rosenbaum and Waitt, this volume), just after the eruptive column reached its maximum height of more than 24 km, indicating that gas-rich liquid was erupted soon after the initial explosion. Variations in height of the Plinian column and in the level of harmonic tremor later during the day (Christiansen and Peterson, this volume; Endo and others, this volume) indicate significant variations in intensity of the eruption before it diminished at about 1700 PDT; pyroclastic flows appear to have been erupted episodically during this interval. Samples of pumice from the tephra-fall deposits and from the lowest exposed pyroclastic-flow materials (table 69, samples 2, 3) are similar in composition and are slightly less silicic than the dense gray dacite from the preceding lateral-blast deposits. A sample of pumice from one of the latest pyroclastic flows erupted on May 18 (table 69, sample 4), collected from about 35 m higher in the same section as the lower pyroclastic-flow sample, is less silicic and less evolved in other major elements than any analyzed material erupted earlier during the day. Although the compositional range of the four May 18 samples is small for all elements (only about 1.4 percent SiO_2), compositions of juvenile material appear to have become progressively less evolved during the sequence of May 18 eruptions (fig. 377*A*).

On the morning of May 25, a relatively brief magmatic event produced a widespread ash fall to the

Table 70.—X-ray fluorescence analyses, in weight percent, of juvenile eruptive products from Mount St. Helens, Wash., July 1980–January 1981

[Analyses by J. E. Taggart, Jr., A. J. Bartel, and J. S. Walberger; nm, no meaningful change]

Sample No.---	1	2	3	4	5	6	7	8	9	10	11
Eruption date	July 22			Aug. 7	Aug. 7-9	Oct. 17 (morning)		Oct. 17 (afternoon)	Oct. 16-18		Dec. 28, 1980-Jan. 4, 1981
Unit---------	Pyroclastic flows, pumice			Pyroclastic flow, pumice	lava dome(?)	Pumice fall	Pyroclastic flow, pumice	Pyroclastic flow, pumice	Lava dome	Lava dome(?)	Lava dome
Field No.----	SH CHEM 9	SH CHEM 10	SH CHEM 11	SH CHEM 12	SH 114	80R 242	80R 240A	80R 246	SH 116	SH 115	CSH 52
Lab No.------	D229590	D229591	D229592	D229593	D231110	D231108	D231107	D231109	D231112	D231111	QV-70-231226
SiO_2---------	64.0	60.3	61.5	62.5	63.0	63.0	62.8	63.0	61.5	60.8	63.2
Al_2O_3--------	17.5	18.7	18.2	17.7	17.7	17.8	17.6	17.5	18.0	18.3	18.0
Fe_2O_3TOT[1]----	4.94	5.52	5.35	5.14	5.04	4.98	4.92	4.97	5.73	5.53	5.10
MgO----------	2.1	2.5	2.4	2.3	2.31	2.30	2.26	2.22	2.62	2.69	2.28
CaO----------	5.13	6.11	5.77	5.30	5.45	5.48	5.32	5.27	5.96	6.01	5.46
Na_2----------	4.5	4.5	4.5	4.5	4.55	4.55	4.45	4.54	4.35	4.50	4.52
K_2O----------	1.33	1.0	1.12	1.25	1.24	1.25	1.26	1.26	1.11	1.06	1.27
TiO_2---------	.66	.67	.67	.67	.67	.67	.64	.65	.79	.71	.68
P_2O_5---------	.2	.2	.1	.1	.13	.17	.14	.15	.18	.13	.12
MnO----------	.07	.11	.08	.07	.07	.07	.07	.07	.08	.08	.07
LOI[2]---------	.39	.19	.11	.14	.25	.21	.24	.41	.12	.30	nm
Total--------	100.82	99.80	99.80	99.67	100.41	100.48	99.70	100.04	100.44	100.11	100.70

[1]Total iron reported as Fe_2O_3; much of the total iron is actually present as FeO (table 69).

[2]Loss on ignition at 920°C for 1 hr.

SAMPLE DESCRIPTIONS

1. Pumice block from upper series of pyroclastic flows, collected by C. D. Miller: Approximate center S1/2 sec. 28, T. 9 N., R. 5 E.
2. Pumice block from upper series of pyroclastic flows, collected by R. P. Hoblitt: SW1/2 sec. 22, T. 9 N., R. 5 E.
3. Pumice block from lower series of pyroclastic flows, collected by R. P. Hoblitt: SW1/2 sec. 22, T. 9 N., R. 5 E.
4. Pumice block from pyroclastic flow, collected by R. P. Hoblitt: Approximate center S1/2 sec. 28, T. 9 N., R. 5 E.
5. Breadcrust dense gray block, collected by R. P. Hoblitt from crater rampart: lat 42° 12.1′ N., long 122° 11.0′ W.
6. Aggregate sample of 2- to 5-cm-diameter pumice lumps, collected by P. D. Rowley east of June Lake: lat 46° 8.7′ N., long 122° 9.0′ W.
7. Vesicular gray pumice block, collected by P. D. Rowley 100 m north of base of "stair-steps": lat 46° 14.3′ N., long 122° 11.0′ W.
8. Vesicular gray pumice block, collected by P. D. Rowley north of west end of crater amphitheater: lat 46° 12.7′ N., long 122° 11.3′ W.
9. Dense gray block, collected by T. Leighley and D. A. Swanson at north margin of dome: lat 46° 12.0′ N., long 122° 11.4′ W.
10. Breadcrust dense gray block, collected by T. Leighley at north edge of inner crater: lat 46° 12.0′ N., long 122° 11.5′ W.
11. Scoriaceous margin of southeast dome lobe, collected by T. Leighley and D. A. Swanson on December 19, 1980, at west margin: lat 46° 12.0′ N., long 122° 11.4′ W.

west of Mount St. Helens and a small pyroclastic-flow deposit on the north slope, well within the area of the May 18 deposits (Rowley and others, this volume). In comparison to the dominantly fine-grained ash-flow deposits of May 18, the May 25 pyroclastic-flow deposits contained much coarser material: tan pumice blocks, as much as 1 m in diameter, were accompanied by gray dense blocks of scoria and by conspicuously flow-layered blocks that were texturally transitional between pumice and scoria. Surprisingly, analyses of a sample of each textural type (table 69, samples 4, 5) vary little in composition and are chemically about as silicic as the most evolved material erupted on May 18—the gray dacite blocks in the initial lateral-blast deposit (table 69, sample 1).

A third magmatic eruption occurred in bad weather during the evening of June 12, and, accordingly, it is less well documented. Ash and pumice falls were distributed widely around the southwest side of the volcano, and pyroclastic flows on the north slope extended over a larger area than on May 25, although still entirely within the area covered by pyroclastic flows on May 18. The flow deposits generally resemble those of May 25: the proportion of coarse material is large, and the blocks are texturally diverse. Textural types include tan frothy pumice, denser gray scoria, flow-layered intermediate types, and virtually nonvesicular blocks of gray dacite as much as 2 m in diameter. Two analyses suggest a significant compositional range among erupted material; the sample of dense scoria is more evolved than the frothy pumice (table 69, samples 7, 8). A possible interpretation is that the dense material represents largely solidified margins of the evolved upper part of the magma body that had been mostly exhausted by the eruptions of May 18 and 25, whereas the pumice represents the remaining less differentiated liquid

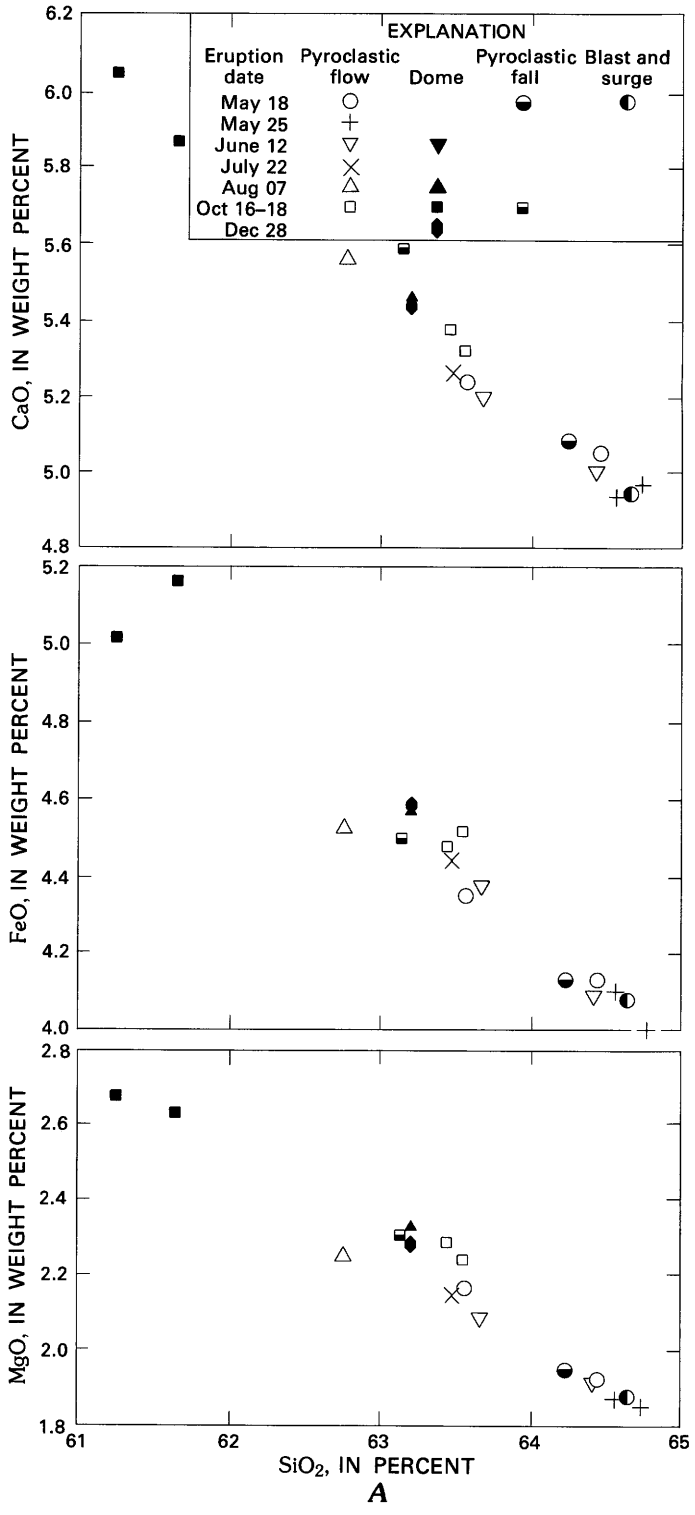

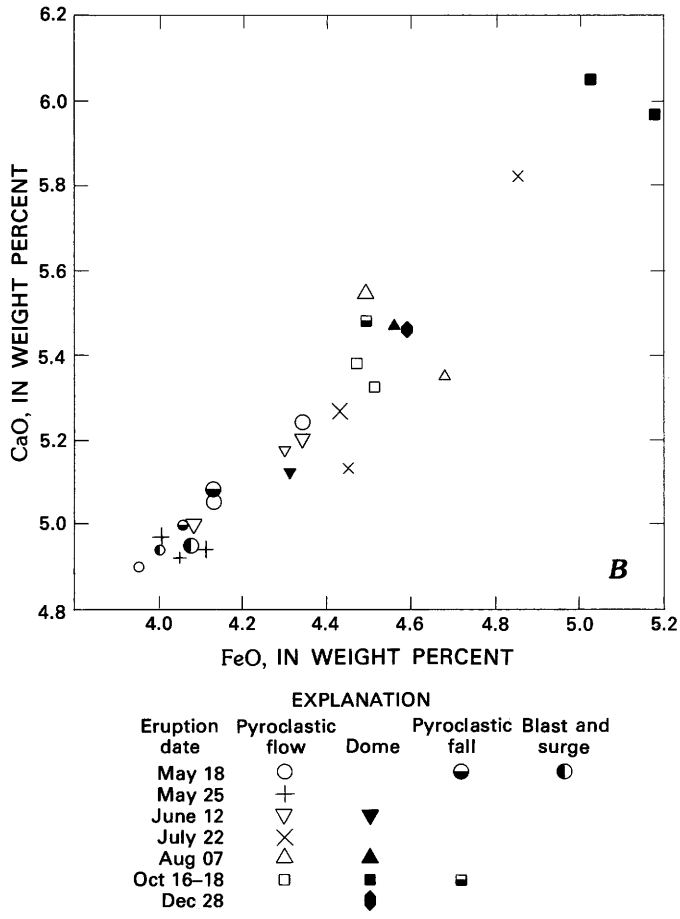

Figure 377.—Variation diagrams for selected major oxides, magmatic samples from 1980 eruptions of Mount St. Helens, Wash. Large symbols, wet-chemical analyses from table 69; small symbols, XRF (X-ray fluorescence) analyses from table 70. A, SiO_2 variation diagrams. In addition to the oxides plotted, as SiO_2 increases, Al_2O_3, TiO_2, and P_2O_5 decrease, and K_2O increases. Plotted analyses were recalculated to 100 percent on a volatile-free basis. XRF analyses (small symbols) tend to be less reliable and about 0.1–0.3 percent higher in SiO_2 content than the wet-chemical analyses, at similar contents of CaO, MgO, and FeO_{tot}. Accordingly, XRF data were not plotted for pumices from the July and August eruptions (table 70, samples 1–4), for which wet-chemical analyses were available. B, CaO versus FeO_{tot}. In addition to all data from tables 69 and 70, six XRF analyses from Hoblitt and others (1980, table 1) of May and June deposits are also plotted; these analyses scatter too greatly in SiO_2 compositions to be plotted usefully on figure 377A.

from deeper within the body.

Poor weather conditions prevented access to the central crater area for several days after the June 12 eruption, but by June 15 a large lava dome was present. The dome continued to grow slowly through June 19 but had stagnated when next visible on June 29 (Moore, and others, this volume). The composition of the June dome, as determined by XRF analysis

(Hoblitt and others, 1980, table 69, analysis p), is identical within analytical limits to that of samples of the June 12 pumice (table 69, sample 8; Hoblitt and others, 1980, table 69, analysis o).

A 40-day repose interval ended on July 22 in a renewed sequence of pyroclastic eruptions that blew out the core of the June dome and deposited a sequence of pyroclastic flows of areal extent and volume slightly smaller than that of the June 12 activity. Pumice blocks from the July pyroclastic flows are relatively uniform in field appearance: flow-layered or dense blocks are rare, although sparse breadcrusted blocks are as much as 1 m in diameter. Our one analyzed pumice sample (table 69, sample 9) is compositionally similar to the less evolved sample from the June eruption (table 69, sample 8), but three XRF analyses indicate that the July eruptive products were compositionally heterogeneous and include material as mafic as about 60.3 percent SiO_2 (table 70, samples 1–3). These samples thus are transitional between mafic dacite and silicic andesite, taking 63 percent SiO_2 as an arbitrary boundary (Ewart, 1979).

On the afternoon and evening of August 7, after several hours of premonitory seismic activity that provided an opportunity to position observers in suitable locations, a sequence of Plinian eruptions produced two small pyroclastic flows. These deposits are lithologically similar to those of July 22. Both wet-chemical and XRF analyses of pumice blocks are silicic andesite (table 69, sample 10; table 70, sample 4), within the compositional range of the July activity. A small lava dome had begun to grow within the crater, as observed on the morning of August 8, but ceased moving upward by August 9 (Moore and others, this volume). A large block of dense gray breadcrusted dacite (table 70, sample 5), which was blown out on August 7 and which probably represents a sample of the new lava dome, is compositionally little different from the analyzed August 7 pumice (table 69, sample 10).

On October 16–18, several pyroclastic flows and tephra falls were produced by a series of explosive magmatic eruptions. Samples of pumice from the initial tephra fall, from a pyroclastic flow erupted on the morning of October 17, and from a later pyroclastic flow on the afternoon of the same day (table 69, sample 11; table 70, samples 6–8) are virtually indistinguishable from each other in composition and are similar to both pyroclastic and dome material erupted in August.

The August dome was blown out by the October eruptions, but within an hour of the last Plinian eruption on the afternoon of October 17, a new lava dome began to grow within the inner crater. It continued to move upward and outward until the next morning, but thereafter upward movement ceased, although lateral spreading continued for several days, and a central sag developed (Moore and others, this volume). The final size of this dome was intermediate between the June and August domes (table 68). Both a sample collected directly from the October dome and a large breadcrusted block, blown out during the pyroclastic eruptions on October 17 and thought to represent a sample of the evolving dome, contain less than 62 percent SiO_2 (table 69, sample 12; table 70, samples 9, 10). These compositions, reasonably classed as silicic andesite (Ewart, 1979), document a further continuation of the progression toward more mafic magma at Mount St. Helens in 1980. The mafic composition of the October dome is in accord with its relatively flat profile and smoother surface textures that suggest a lower viscosity than the first two domes (Moore and others, this volume).

In late December 1980, after a few days of increased seismicity but without any precursory pyroclastic activity, viscous scoriaceous lava oozed out, first from the southeast flank, and then on the northwest side of the October dome. The December dome lobes were initially observed on December 28, and appeared to have completed growth by January 3, 1981. Scoriaceous marginal material from the southeast lobe is mafic dacite (table 70, sample 11), similar in composition to analyzed samples of the August dome and October pumice blocks, but distinctly more silicic than material from the October dome.

DISCUSSION

The analyses of juvenile magmatic material presented here document small but significant compositional variations. Chemical compositions became generally less silicic and thus less evolved, both during the sequence of catastrophic eruptions on May 18 and also during subsequent eruptions from May 25 through the end of December. Modal phenocryst proportions and the compositions of some phenocryst phases, especially the hornblende-pyroxene ratio and the composition of plagioclase, also change systematically with time of eruption (Kuntz and others, this

volume). We interpret these changes as representing samples of successively deeper levels in a compositionally zoned or stratified magma body; the changes are also similar to progressions recognized in many other silicic eruptive sequences (Smith, 1979).

After the sequential eruption of progressively less evolved material on May 18, the renewed eruption of a small volume of more evolved magma on May 25 (fig. 378*A*) suggests that the geometry of the magma body was complex or that the eruptive process on May 18 had been relatively inefficient. Probably the May 18 eruption tapped lower levels in the differentiated magma chamber without exhausting the evolved upper parts. No known differentiation process seems capable of having regenerated such evolved material in a single week. Accordingly, the material erupted on May 25 must have sampled a pocket of evolved magma that failed to erupt on May 18. No similarly evolved material has been erupted since, indicating that the upper part of the original magma body was largely exhausted by the May 25 eruption.

The subsequent eruptions in June, July, August, October, and December show a general progression toward more mafic compositions, although analyses of multiple samples document compositional diversity within single eruptions. Our data show a significant range in compositions for the June 12 eruption (table 69, samples 7, 8), and an even greater range, about 3 percent SiO_2, for the July 22 eruption (table 69, sample 9; table 70, samples 1–3). In general, however, as the analyzed materials become less evolved, the volumes decrease, both for May 18 and for the later eruptions (table 68; fig. 378*B*). The sample of the December dome lobe is more silicic than those of the October dome, but similar to samples of the August dome and of October pyroclastic material (table 69); we interpret this slight reversal in trend as reflecting recovery from eruptive draw-down in the magma chamber in October, similar to the recovery between the May 18 and May 25 eruptions. Accordingly, the December dome material would represent dacite left in the upper part of the magma chamber that failed to erupt in October, rather than any new addition of more silicic magma.

Consideration of the volume relationships, composition of magma, and time of eruption suggests that the 1980 eruptions have thus far sampled a relatively small magma body that was in an advanced state of crystallization. More than half the total volume of magmatic material erupted through October 1980 is represented by the lateral eruption of gray dacite on the morning of May 18 (fig. 378*C*) at hot but near-solidus temperatures. The most evolved liquid portion of this magma body was completely erupted by May 25. Later eruptions included large proportions of relatively viscous degassed liquids and some near-solidus materials, as represented by abundant dense blocks of dacite in many of the pyroclastic flows and the emplacement of successive lava domes in June, August, and October. In addition, both the frequency of eruptions and the volumes of erupted magma decreased with time and define an asymptotic curve that has an upper limit of less than 0.3 km^3 in cumulative volume (fig. 378*C*). This relationship suggests that the volume of eruptible dacite magma remaining within the shallow magma body is probably small. Although the volume estimates (table 68) on which these interpretations depend are relatively imprecise, the uncertainties are too small to modify significantly the general time-volume relationships shown in figure 378. As the erupted volumes decreased and the lapse times between eruptions increased, the degree of explosivity also decreased. Volume proportions of pyroclastic fall and flow material decrease with time (table 69), and the proportion of magma erupted as lava domes increased. By December, dome material was extruded without a preceding pyroclastic eruption.

The phase mineralogy of the 1980 dacite has not yet been studied in detail, but the bulk-rock compositions determined here define trends that extend toward compositions of the glassy matrix of the dacite, as analyzed by electron-microprobe techniques (Melson and others, 1980; Sarna-Wojcicki, Meyer, and others, this volume, table 85, no. 1). This relationship indicates that the observed bulk-rock compositional variations could have formed by fractional crystallization of observed phenocryst phases (mainly plagioclase, hornblende, hypersthene, and opaque oxides) in modal proportions. Alternatively, the linear compositional trends are compatible with an origin by mixing of compositionally distinct mafic and silicic magmas prior to eruption; such a hypothesis is supported by preliminary microprobe data that indicates the presence of two distinct chemical populations of some phenocrysts, especially plagioclase and hornblende (Raedeke and others, 1980).

These time-volume-compositional relationships also suggest that the magma erupted during 1980 may

be related to an older magma body that had erupted several times at Mount St. Helens in the last few hundred years (Hoblitt and others, 1980). The most silicic material erupted in May is more evolved in composition than any eruptive products from Mount St. Helens in the past few hundred years, but most of the

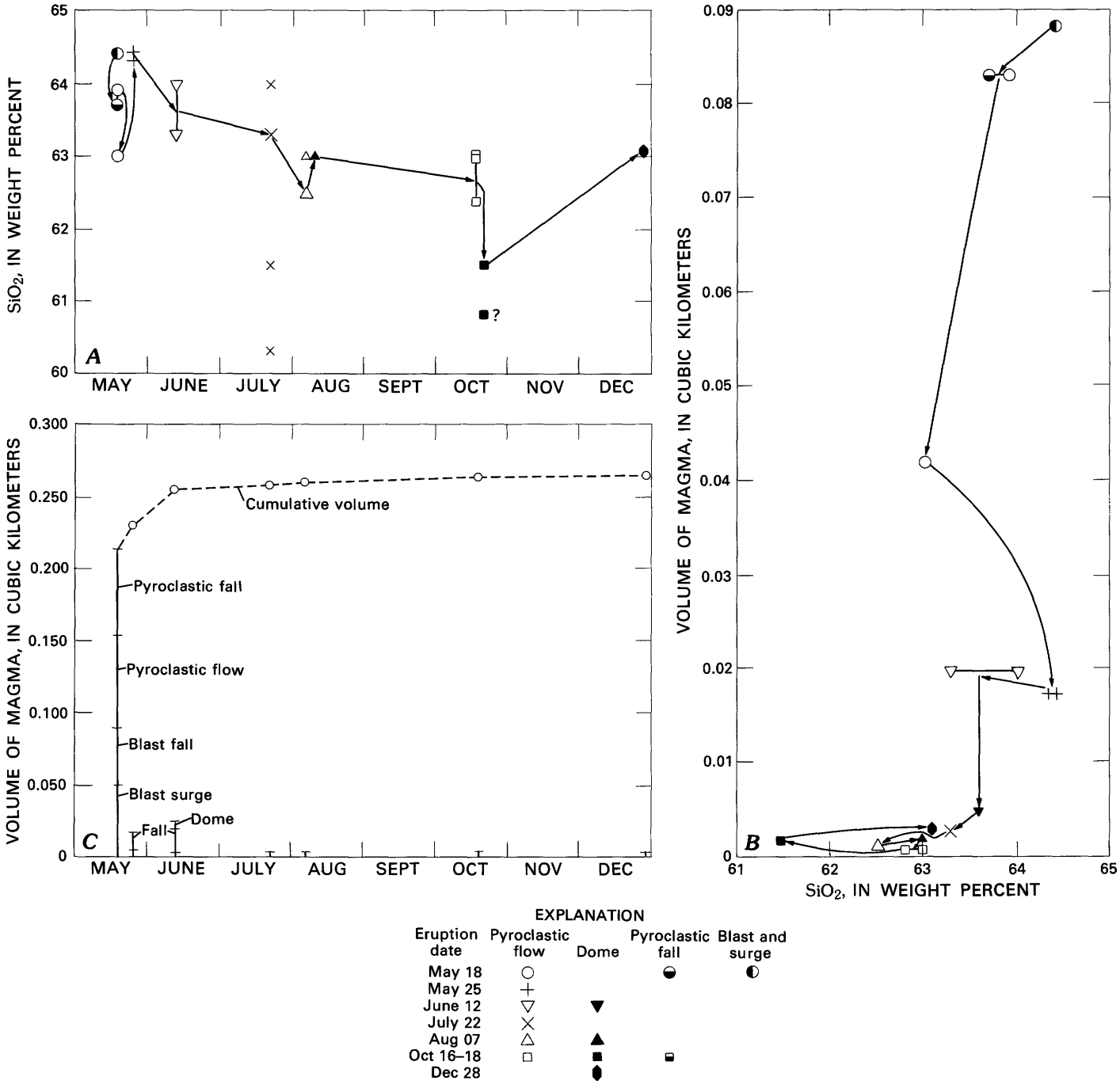

Figure 378.—Summary diagrams showing interpreted relationships between composition, volume, and time of eruption for 1980 Mount St. Helens, Wash., magmas. Volume data are from table 68; compositions are from tables 69 and 70. Large symbols in A and B, wet-chemical analyses from table 69; small symbols, X-ray fluorescence analyses from table 70. Tielines in A and B are drawn only through wet-chemical analyses of table 69 because SiO_2 values are more precise than data of table 70. A, SiO_2 versus time; B, volume versus SiO_2; C, volume versus time.

magma erupted in 1980 is similar in composition to deposits such as the Goat Rocks lava dome emplaced in the early 19th century and the summit lava dome emplaced in the 17th century (Hoblitt and others, 1980, table 1, analyses g, h, j). Could the magma erupted during 1980 thus represent further differentiation of the same body of magma that had previously been tapped in the 17th and 19th centuries?

Finally, the 1980 magmatic deposits are both much smaller in volume and less chemically evolved than many earlier prehistoric eruptions at Mount St. Helens (Hoblitt and others, 1980). No significant volume of such evolved dacite appears to be present now at shallow depth beneath the cone and available for large-volume explosive eruption in the next few years. An intriguing possibility, that we at present are unable to evaluate adequately, is that the 1980 eruptions of dacite may have been energized by upward movement of more mafic magma, similar to the basalts and andesites that have alternated with dacite at Mount St. Helens in the past (Verhoogen, 1937; Hopson and Melson, 1980). Such andesite or basalt could possibly reach the surface as relatively fluid lava during the present sequence of eruptions.

REFERENCES CITED

American Society for Testing and Materials, 1966, Sulfur by the direct combustion-iodate titration method: 1966 Book of ASTM Standards, pt. 32, p. 94–95.

Ewart, A., 1979, A review of the mineralogy and chemistry of Tertiary-Recent dacitic, latitic, rhyolitic, and related salic volcanic rocks, *in* Barker, F., ed.; Trondhjemites, dacites, and related rocks: New York, Amsterdam, Elsevier, p. 13–121.

Hoblitt, R. P., Crandell, D. R., and Mullineaux, D. R., 1980, Mount St. Helens eruptive behavior during the past 1,500 yr: Geology, v. 8, p. 555–559.

Hopson, C. A., and Melson, W. G., 1980, Mount St. Helens eruptive cycles since 100 A.D. [abs.]: EOS, v. 61, p. 1132.

Huffman, E. W., Jr., 1977, Performance of a new automatic carbon-dioxide coulometer: Microchemical Journal, v. 22, p. 567–573.

Melson, W. G., Hopson, C. A., and Kienle, C. F., 1980, Petrology of tephra from the 1980 eruption of Mount St. Helens [abs.]: Geological Society of America Abstracts with Programs, v. 12, p. 482.

Peck, L. C., 1964, Systematic analysis of silicates: U.S. Geological Survey Bulletin 1170, 89 p.

Peck, L. C., and Tomasi, E. J., 1959, Determination of chlorine in silicate rocks: Analytical Chemistry, v. 31, p. 2024–2026.

Peck, L. C., and Smith, V. C., 1964, Spectrophotometric determination of fluorine in silicate rocks: Talanta, v. 11, p. 1343–1347.

Raedeke, L. D., Mathez, E. A., and Irving, A. J., 1980, Mount St. Helens lava dome; petrography and chemistry [abs.]: EOS, v. 61, p. 1138.

Smith, R. L., 1979, Ash-flow magmatism: Geological Society of America Special Paper 180, p. 5–27.

Taggart, J. E., Jr., Wahlberg, J. S., and Taylor, H. E., 1980, X-ray spectrometric major-element analyses of tephra samples from the May 18, 1980 eruption of Mount St. Helens—Samples collected from Washington, Idaho, and Montana: U.S. Geological Survey Open-File Report 80-1130, 13 p.

Verhoogen, Jean, 1937, Mount St. Helens, a recent Cascade volcano: California University Department of Geological Sciences Bulletin, v. 24, p. 263–302.

Wozniak, K. C., Hughes, S. S., and Taylor, E. M., 1980, Chemical analyses of Mount St. Helens pumice and ash: Oregon Geology, v. 42, p. 130.

THE 1980 ERUPTIONS OF MOUNT ST. HELENS, WASHINGTON

PREERUPTION TEMPERATURES AND OXYGEN FUGACITIES IN THE 1980 ERUPTIVE SEQUENCE

By WILLIAM G. MELSON[1] *and* CLIFFORD A. HOPSON[2]

ABSTRACT

Ilmenite and magnetite coexist in all the 1980 eruptive rocks of Mount St. Helens, which are all dacite. Electron microprobe analyses reveal that these minerals show no significant change in composition with time. Experimental results give an average temperature of 990°C and an average oxygen fugacity of -9.7 bars (expressed as log to the base 10) for the 1980 eruptive sequence. Analyses of the ca. A.D. 1800 air-fall pumice (pumice of layer T) give similar values, whereas those of ca. A.D. 1500 pumice (pumice of set W) give lower values (average of 840°C at log $f_{O_2} = -12.5$ bars). A clearcut trend of temperature and oxygen fugacity with time is not apparent in the eruptive sequence. Magma mixing, which is revealed by banded dark and light dacite, is common in the 1980 eruptive sequence. Calculated temperature and oxygen-fugacity differences between these bands suggest that mixing of magma in different parts of the same magma chamber or of magma from different magma chambers has occurred.

INTRODUCTION

The ongoing eruption of Mount St. Helens has provided a time sequence of tephra and dome rocks from a complex composite volcano (Verhoogen, 1937; Hopson, 1971; Mullineaux and others, 1975; Crandell and others, 1975). Explosive eruptions of dacitic magma have been followed by the rise of small dacitic domes and vent fillings that do not project above the vent. As of November 11, 1980, six major explosive sequences have occurred: May 18, May 25, June 12, July 22, August 7, and October 16–18. As part of an ongoing study of ejecta from these events, the results of electron microprobe analyses of coexisting ilmenite and magnetite are presented, and from these data we infer preeruption temperatures and oxygen fugacities using the experimental results of Lindsley (1976, 1977). For comparison, samples from pumice of layer T and set W (Mullineaux and Crandell, this volume) were also studied. This is the first of several petrologic studies that we are doing on the 1980 eruptive sequence. Studies nearing completion include major-element, petrographic, and melt-inclusion variations with time of eruption.

The rapid extrusion and cooling of the dacitic liquids to form pumice ideally should preserve the preeruption oxide compositions (Buddington and Lindsley, 1964). Therefore, posteruption oxidation and exsolution due to slow cooling, features which complicate iron-titanium oxides in lava flows and domes (Haggerty, 1976), should be minimal. Lipman (1971) has shown the usefulness of using the composition of ilmenite and magnetite to trace the temperature and f_{O_2} changes in studies of compositionally zoned magma bodies.

[1]Department of Mineral Sciences, Smithsonian Institution, Washington, D.C. 20560.

[2]Department of Geological Sciences, University of California, Santa Barbara, Calif. 93106.

Table 71.—Average temperatures and oxygen fugacities for the 1980 eruptive sequence

[Pumice of pre-1980 tephras, layer T and set W, given for comparison. Oxygen-fugacity (f_{O_2}) values are expressed as log to the base 10. Temperature (T) and f_{O_2} calculated from data of Lindsley (1977). SDT is two standard deviations of temperature variations. Names in parentheses in comments column are those who provided samples. AF, air-fall tephra; PF, pyroclastic-flow tephra; BD, blast deposits; EB, ejected block collected from ramparts; D, sample directly from dome; ---, not determined]

Determination No.	Sample date and No.	T (°C)	f_{O_2} (bars)	SDT	No. of ilmenite analyses	No. of magnetite analyses	Comments
	May 18:						
1	115379-34---	1010	-9.3	60	9	12	"Blast facies" (D. A. Swanson), BD.
2	115230------	1002	-9.4	83	4	11	White pumice (C. R. Kienle), AF.
3	115379-8-1--	990	-9.5	35	5	5	White pumice (W. G. Melson), AF.
	May 25:						
4	115331A-----	1006	-9.2	54	8	9	White pumice (C. R. Kienle), AF.
5	115379-31-1-	992	-9.2	117	10	11	Dark lapilli (D. A. Swanson), AF.
6	115379-32-4-	990	-9.5	86	12	10	Light lapilli (D. A. Swanson), AF.
	June 12:						
7	115335B-----	976	-9.2	165	6	11	White pumice (C. R. Kienle), AF.
8	115379-30-1-	918	-11.0	169	10	10	White part of mixed magma block (D. A. Swanson), PF.
9	115379-30-2-	1003	-9.6	105	10	10	Dark portion of above.
10	115379-30-2-	1030	-9.3	---	2	1	Megacryst of above.
	Post-June 12:						
11	115341------	1022	-9.5	61	7	13	Meissner dome sample, D.
12	SH1592-2----	992	-9.6	148	7	8	Dacite from post-June 12 dome (C. A. Hopson), EB.
13	SH1507-2----	990	-9.5	61	10	10	Do.
14	115379-40---	1012	-9.3	120	12	10	Probable dome sample (D. A. Swanson), EB.
	July 22:						
15	115377-1-3--	972	-10.1	108	20	22	White pumice (W. G. Melson), PF.
	August 7:						
16	115413------	967	-10.4	138	10	10	Gray pumiceous dacite (C. A. Hopson), density >1, PF.
17	115415------	1002	-9.7	52	10	11	Do.
	Post-August 7:						
18	115417------	972	-10.1	57	10	10	Dacite from vent filling (C. A. Hopson), EB.
	Pumice, layer T:						
1a	SH257-1-----	1006	-9.2	91	10	10	(C. A. Hopson) AF.
	Pumice, set W:						
2a	SH1405-2----	848	-12.0	38	10	11	(C. A. Hopson) AF.
3a	SH221-1A----	827	-12.7	40	4	7	Do.
4a	SH221-1A----	847	-12.7	---	2	2	Megacrysts in above.
5a	Several-----	805	-13.3	55	20	20	Data from D. R. Smith (1980), AF.

ACKNOWLEDGMENTS

Samples for this study were provided by several individuals whose names are listed in parentheses in table 71. The assistance of D. A. Swanson and of C. F. Kienle (Foundation Sciences, Inc.) in obtaining samples is particularly acknowledged. Thin sections were prepared by R. D. Johnson and F. E. Walkup, and electron-microprobe laboratory maintenance and assistance were provided by Eugene Jarosewich, J. A. Nelen, and C. R. Obermeyer. D. R. Smith, who completed an M.A. thesis on the pre-1980 tephras of Mount St. Helens under the guidance of W. P. Leeman, Rice University, provided a copy of the thesis and made useful comments on the approach used here.

The U.S. Geological Survey and the Pacific General Electric Company provided helicopter support during our field studies. We gratefully acknowledge the technical reviews of the manuscript by A. T. Anderson, University of Chicago, and R. F. Fudali, Smithsonian Institution.

SAMPLING THE ERUPTIVE SEQUENCE

The cataclysmic lateral blast from the north side of Mount St. Helens on the morning of May 18 resulted in overlapping directed-blast deposits that extend more than 20 km from the mountain (Miller and Hoblitt, 1980; Sisson and Moore, 1980). The basal unit of the blast deposits is a coarse proximal facies consisting of lithic lapilli and blocks. About one-half of the heterolithologic block assemblage within the coarse basal facies is composed of a distinctive gray, glassy, microvesicular hornblende-hypersthene dacite; ubiquitous subradial jointing of the dacite indicates quick cooling from a high-temperature state. This dacite is believed to be the explosively fragmented remnants of a cryptodome, which formed from new magma that rose into the cone of Mount St. Helens during the period March 20 to May 18, 1980 (Miller and Hoblitt, this volume; Moore and Sisson, this volume). In our present study, magnetite and ilmenite are analyzed from one specimen (115379-34, table 71) of this juvenile "blast dacite."

During the late morning and afternoon of May 18, a Plinian-type eruption column that rose to more than 20 km (Christiansen and Peterson, 1980) deposited white hornblende-hypersthene dacite pumice in the form of widespread air falls and local pyroclastic flows as a result of column collapse. Samples 115230 and 115379-8-1 (table 71) are from air-fall pumice of this phase.

Eruptions on May 25 and June 12 also produced pumiceous pyroclastic flows, as well as air-fall pumice and ash. White pumice and ash are the chief products, but both eruptions also ejected mixed (banded) light and dark pumiceous dacite. Samples of the May 25 ejecta (table 71) are from air-fall deposits; they include white pumice (115331A) and also denser (subpumiceous), light- and dark-gray mixed dacite (115379-31-1, 115379-32-4). June 12 samples (table 71) include white air-fall pumice (115335B) and a block of mixed white and dark dacite from a pyroclastic flow (115379-30-1 and 2).

The low dome of augite-hornblende-hypersthene dacite that rose into the crater after the June 12 eruption is represented in our suite of samples by a fragment from the dome margin (115341) and by locally ejected blocks collected from the crater rampart immediately adjacent to the dome (SH1592-2, SH1507-2, 115379-40). All four samples are similar petrographically and appear to have come from the dome.

The eruptions of July 22 and August 7 ejected pumice as pyroclastic flows (Hoblitt, 1980), and fine ash as airborne tephra. Samples from July 22 (115377-1-3) and August 7 (115413, 115415) represent pumice from pyroclastic flows (table 71).

The low, vent-filling protodome that rose into the crater after August 7 is represented by a single sample (115417) collected from an ejected block on the crater lip. This augite-hornblende-hypersthene dacite is much denser (less microvesicular) than the post-June 12 dome rock and also differs in petrographic details.

The May 18 cataclysmic explosion is characteristic of the onset of some previous eruptive cycles of Mount St. Helens. These typically are dacites, which eventually are followed by domes and then by andesite lava flows (Melson and Hopson, 1980).

PETROGRAPHY

Modal analyses show that opaques make up less than 1 to about 2 volume percent of the 1980 eruptives. This abundance and the presence of both phases—magnetite and ilmenite—in all the examined samples allow these phases to be used to reconstruct T-f_{O_2} (temperature-oxygen fugacity) conditions for the magmas in which they crystallized. The value of this approach for the historic and prehistoric eruptives of Mount St. Helens was pointed out by D. R. Smith (1980).

Ilmenite and magnetite occur in minute, rounded to euhedral grains less than 5 μm (micrometers) across to rounded to euhedral phenocrysts more than 500 μm across. Rarely are grains of ilmenite and magnetite in contact. Such coexisting grains were sought as evidence of contemporaneous crystallization, and thus possibly a greater likelihood of thermal and oxygen-fugacity equilibration. Ilmenite and magnetite commonly have roundish edges, which may indicate some re-solution or may be a result of their growth habit.

Samples of tephra from the May 25, June 12, and August 7 eruptions consist of more than one type of dacite. In one sample, dark (115379-30-2) and white

Table 72.—Average composition of ilmenite in the 1980 eruptive sequence, May 18 through August 7

[Nos. 1-18 correspond to determination numbers in table 71. Fe and TiO end-members are from method of Anderson (1968); ---, not determined]

Determination No.--	1	2	3	4	5	6	7	8	9	10	11	12	13	14	15	16	17	18
Electron microprobe analyses in weight-percent oxides																		
SiO_2------	---	0.05	0.01	0.09	0.05	0.07	0.09	0.11	0.10	0.08	0.17	0.11	0.17	0.04	0.07	0.01	0.02	0.08
Al_2O_3-----	.31	.41	.32	.40	.20	.21	.25	.18	.08	.16	.33	.19	.17	.26	.24	.11	.25	.12
FeO*------	52.56	53.16	51.58	51.61	51.51	51.78	51.72	50.48	52.97	52.82	51.99	51.56	51.59	52.80	51.11	50.61	51.24	50.91
MgO-------	2.35	2.60	3.03	2.93	2.28	2.67	2.19	2.11	1.93	2.19	2.53	2.00	2.77	2.45	2.42	2.02	2.32	2.48
CaO-------	.11	.22	.10	.15	.11	.12	.05	.15	.12	.03	.14	.10	.09	.09	.08	.13	.11	.09
TiO_2------	40.21	41.47	41.34	39.53	41.03	40.63	40.88	41.95	40.72	41.22	40.76	40.16	40.52	40.75	42.20	42.84	41.32	42.32
MnO-------	.53	.51	.50	.46	.59	.52	.51	.67	.55	.49	.57	.53	.46	.50	.57	.64	.57	.58
Total----	96.07	98.42	96.88	95.17	95.77	96.00	95.69	95.65	96.47	96.99	96.49	94.65	95.77	96.89	96.69	96.36	95.83	96.58
Number of cations per three oxygens																		
Si--------	---	---	---	---	---	---	---	---	---	---	---	---	---	---	---	---	---	---
Al--------	.01	.01	.01	.01	.01	.01	.01	.01	---	---	.01	.01	.01	.01	.01	---	.01	---
Fe^{++}------	1.17	1.15	1.12	1.15	1.14	1.14	1.15	1.11	1.17	1.16	1.14	1.16	1.14	1.16	1.11	1.10	1.13	1.11
Mg--------	.09	.10	.12	.12	.09	.11	.09	.08	.08	.09	.10	.08	.11	.10	.09	.08	.09	.10
Ca--------	---	.01	---	---	---	---	---	---	---	---	---	---	---	---	---	---	---	---
Ti--------	.86	.86	.86	.85	.87	.86	.87	.89	.86	.87	.86	.87	.86	.86	.88	.90	.87	.88
Mn--------	.01	.01	.01	.01	.01	.01	.01	.01	.01	.01	.01	.01	.01	.01	.01	.01	.01	.01
Total----	2.14	2.13	2.13	2.14	2.13	2.14	2.12	2.11	2.13	2.13	2.13	2.13	2.13	2.14	2.11	2.10	2.12	2.11
Ilmenite-	.78	.79	.79	.77	.80	.79	.80	.83	.80	.80	.79	.80	.79	.79	.82	.84	.81	.82
Hematite-	.22	.21	.21	.23	.20	.21	.20	.17	.20	.20	.21	.20	.21	.21	.18	.16	.19	.18

*Total iron reported as FeO.

(115379-30-1) dacite are mixed at the hand-specimen level. The dark component of the mixed dacitic rocks generally is denser, is richer in hornblende, lacks augite, and resembles the "blast dacite" of May 18 (morning), whereas the white component of the lower density dacite contains minor amounts of augite and is more like the main volume of the May 25 and June 12 ejecta. Where the light and dark components were observed, thin sections of each of the different lithologies were prepared and separate analyses of their coexisting oxides were performed. Obviously different magma types (various types of dacite) have erupted in each episode through and including October 16-18.

ANALYTICAL METHODS

Initial analyses revealed only slight compositional differences between the coexisting iron-titanium oxides from the various eruptions. Thus, each set of analyses was normalized to an internal standard, USNM96189 ilmenite (Jarosewich and others, 1979), which improves the precision of analyses on different days. The probes were run at 15-kV accelerating voltage at a beam current of 0.15 μA (microamps).

Precision for ilmenite analyses at FeO (total Fe calculated as FeO) = 46.50 is $2\sigma = 0.69$; at $TiO_2 = 45.50$ is $2\sigma = 0.71$, and at MnO = 4.77 is $2\sigma = 0.13$ for 18 repeated analyses of the ilmenite standard in nine probe runs.

CALCULATION OF TEMPERATURES AND OXYGEN FUGACITIES

Data used here to calculate T and f_{O_2} for the 1980 eruptive sequence (table 71) are from Lindsley's (1977) most recent experimental parameters for determining T and f_{O_2} from the composition of coexisting ilmenite and magnetite. The computer program of Lindsley (1977) also was used. The analyses for each sample are not included here but are available by a written request to one of the authors. A total of 208 analyses of ilmenite and 234 analyses of magnetite are given in these tables, along with petrographic comments on each analyzed crystal. The average compositions for ilmenite and magnetite in the eruptive sequence are given in tables 72 and 73, respectively. Analyses of ilmenite and magnetite in pumice of layer T and set W are given in tables 74 and 75, respec-

Table 73.—Average composition of magnetite in the 1980 eruptive sequence, May 18 through August 7

[Nos. 1-18 correspond to determination numbers in table 71. Fe and TiO end-members are from method of Anderson (1968); ---, not determined]

Determination No.	1	2	3	4	5	6	7	8	9	10	11	12	13	14	15	16	17	18
Electron microprobe analyses in weight-percent oxides																		
SiO_2-----	0.02	0.16	0.04	0.10	0.11	0.14	0.12	0.14	0.16	0.09	0.22	0.17	0.19	0.13	0.10	0.10	0.04	0.15
Al_2O_3-----	2.80	2.61	3.08	2.95	2.62	2.73	2.26	2.65	2.33	3.69	2.41	2.18	2.25	2.38	2.28	1.66	2.23	2.01
FeO*-----	78.15	79.70	78.28	77.44	78.35	78.21	78.44	79.18	79.07	77.63	78.12	77.74	78.69	79.59	77.66	77.48	77.38	77.52
MgO-------	1.67	1.48	1.86	1.86	1.29	1.84	1.26	1.19	1.20	1.56	1.69	1.18	1.75	1.55	1.51	1.16	1.46	1.60
CaO-------	.09	.12	.09	.04	.09	.16	.04	.06	.08	.03	.07	.07	.07	.05	.08	.07	.06	.07
TiO_2------	9.44	9.89	9.59	8.94	9.69	9.42	9.69	9.33	10.09	11.11	10.54	9.82	9.77	10.26	10.71	11.73	11.03	10.99
MnO-------	.50	.49	.45	.42	.51	.47	.49	.52	.52	.47	.54	.48	.45	.49	.51	.54	.52	.52
Total----	92.67	94.45	93.39	91.75	92.66	92.97	92.30	93.07	93.45	94.58	93.59	91.64	93.17	94.45	92.85	92.74	92.72	92.86
Number of cations per four oxygens																		
Si--------	---	.01	---	---	---	.01	.01	.01	.01	---	.01	.01	.01	.01	---	---	---	.01
Al--------	.15	.14	.16	.16	.14	.14	.12	.14	.12	.19	.13	.12	.12	.12	.12	.09	.12	.11
Fe^{++}-----	2.95	2.96	2.92	2.95	2.96	2.94	2.99	2.99	2.97	2.82	2.90	2.98	2.96	2.95	2.91	2.91	2.90	2.90
Mg--------	.11	.10	.12	.13	.09	.12	.09	.08	.08	.10	.11	.08	.12	.10	.10	.08	.10	.11
Ca--------	---	.01	---	---	---	.01	---	---	---	---	---	---	---	---	---	---	---	---
Ti--------	.34	.35	.34	.33	.35	.34	.35	.34	.36	.39	.38	.36	.35	.36	.39	.42	.40	.40
Mn--------	.02	.02	.02	.02	.02	.02	.02	.02	.02	.02	.02	.02	.02	.02	.02	.02	.02	.02
Total----	3.59	3.57	3.58	3.59	3.58	3.58	3.58	3.59	3.57	3.52	3.55	3.57	3.58	3.57	3.55	3.53	3.54	3.55
Ulvospinel	.28	.29	.28	.26	.30	.28	.29	.29	.31	.34	.31	.30	.28	.30	.32	.36	.33	.32
Magnetite-	.72	.71	.72	.74	.70	.72	.71	.71	.69	.66	.69	.70	.72	.70	.68	.64	.67	.68

*Total iron reported as FeO.

tively. The ulvospinel component of magnetite and the end-member ilmenite in ilmenite, parameters used to calculate T and f_{O_2}, were determined using the method outlined by Anderson (1968).

Average T and f_{O_2} can be calculated from: (1) the average composition of ilmenite and magnetite and (2) the average of all possible T and f_{O_2} for all possible pairs of ilmenite and magnetite in a given sample. Therefore, if there are 20 analyses for each ilmenite and each magnetite in a given sample, then 400 possible $T$and f_{O_2} values can be calculated; the average T and f_{O_2} calculated using these methods are similar. Two standard deviations (STD) of T in table 71 are calculated using the second method; average T and f_{O_2} in table 71 are calculated using the first method.

Temperatures range from 967°C (Aug. 7 pumiceous dacite sample 115413) to 1022°C (post-June 12 dome sample 115341). Megacrysts of ilmenite and magnetite in the June 12 dacite (115379-30-2 from a pyroclastic flow) give the highest T yet calculated, 1030°C. The calculated analytical precision of these determinations is about 40°C for samples run on different days and about 30°C for samples within a given analytical setup. Temperatures inferred from phase equilibria among silicate minerals were estimated at about 950°C for the May 18 white pumice (Melson and Hopson, 1980), which is about 50° lower than the temperature indicated by coexisting magnetite and ilmenite (1002°C; table 71, sample 115230).

In regard to the redox state of the eruptives, the data in T-f_{O_2} space (fig. 379) give a trend about 1 log unit above the trend for the nickel-nickel oxide buffer. These values are almost 1 log unit lower than the f_{O_2} values obtained by Carmichael (1967) for salic rocks in the area of Lassen Peak, Calif.

TEMPERATURE AND OXYGEN-FUGACITY RANGE WITHIN SINGLE THIN SECTIONS

Some of the samples in table 71 have a wide range of inferred T and f_{O_2} values. Analytical precision accounts for ± 30°C of the variation of T in a section analyzed in a single probe. This variation is exceeded in all the samples examined so far, but is closely approached in May 18 sample 115379-8-1 ($2\sigma = 35$) and in sample SH-1405-2 from pumice of set W ($2\sigma = 38$).

Table 74.—Average composition of ilmenite in pumice of layer T and set W

[Nos. 1a–5a correspond to those for pumice (layer T and set W) in table 71. Fe and TiO end-members are from method of Anderson (1968); ---, not determined]

Determination No.--	1a	2a	3a	4a	5a
Electron microprobe analyses in weight-percent oxides					
SiO_2--------	0.02	0.09	0.06	0.06	0.19
Al_2O_3-------	.25	.09	.11	.10	.01
FeO*--------	52.35	49.70	49.07	50.32	49.28
MgO---------	2.48	2.42	2.23	2.08	1.58
CaO---------	.11	.09	.08	.03	---
TiO_2--------	39.16	44.21	44.77	45.03	44.51
MnO---------	.49	.62	.63	.65	.49
Total------	94.86	97.22	96.95	98.27	96.06
Number of cations per three oxygens					
Si----------	---	---	---	---	---
Al----------	.01	---	---	---	---
Fe^{++}--------	1.18	1.06	1.05	1.07	1.07
Mg----------	.10	.09	.09	.08	.06
Ca----------	---	---	---	---	---
Ti----------	.85	.91	.92	.92	.93
Mn----------	.01	.01	.01	.01	.01
Total------	2.15	2.09	2.08	2.08	2.07
Ilmenite---	.77	.86	.88	.87	.89
Hematite---	.23	.14	.12	.13	.11

*Total iron reported as FeO.

Table 75.—Average composition of magnetite in pumice of layer T and set W

[Nos. 1a–5a correspond to those for pumice (layer T and set W) in table 71. Fe and TiO end-members are from method of Anderson (1968); ---, not determined]

Determination No.--	1a	2a	3a	4a	5a
Electron microprobe analyses in weight-percent oxides					
SiO_2--------	0.04	0.19	0.13	0.12	.24
Al_2O_3-------	2.38	2.08	2.44	2.50	2.26
FeO*--------	78.06	79.19	78.78	79.58	79.59
MgO---------	1.52	1.25	1.13	1.13	1.32
CaO---------	.10	.09	.06	.06	----
TiO_2--------	8.72	9.65	9.57	10.09	9.60
MnO---------	.48	.48	.45	.47	.35
Total------	91.30	92.93	92.56	93.95	93.36
Number of cations per four oxygens					
Si----------	----	.01	.01	.01	.01
Al----------	.13	.11	.13	.13	.12
Fe^{++}--------	3.02	3.00	3.00	2.97	3.00
Mg----------	.10	.08	.08	.08	.09
Ca----------	----	----	----	----	----
Ti----------	.32	.35	.35	.36	.35
Mn----------	.02	.02	.02	.02	.01
Total------	3.61	3.59	3.58	3.57	3.58
Ulvospinel-	.26	.29	.30	.31	.29
Magnetite--	.74	.71	.70	.69	.71

*Total iron reported as FeO.

Variation is a maximum ($2\sigma = 169$) in the white portion of the mixed magma block erupted June 12 (115379-30-1).

Ideally, only magnetite and ilmenite that can be definitely shown to have crystallized simultaneously will give meaningful T and f_{O_2} values. Petrographic evidence of such simultaneity of growth can be represented by intergrown oxides and, less commonly, by oxides in contact. Intergrown oxides are rare in the samples thus far studied, but oxides in contact do occur in most sections, albeit only two to five per about 5 cm² of section area. Another approach involves the assumption that the smallest groundmass grains crystallized simultaneously just prior to eruption. These various approaches can be applied, for example, to the most diverse oxide compositions found so far—the white portion of the June 12 mixed-magma block (115379-30-1, table 71):

	T(°C)		f_{O_2} (bars)
Grains in contact:			
Pair 1 ----------	871		−11.9
Pair 2 ----------	989		−9.7
Groundmass grains:			
(5 magnetite, 7 ilmenite) -----	898		−11.1
2σ of T and f_{O_2} ---------- 187		2.8	

Note: The f_{O_2} values are expressed as log to the base 10.

For the in-contact pairs the T difference, 118°C, is smaller than that for the sample as a whole, but is still large. The 2σ variation for the groundmass grains is slightly larger (187) than the 2σ variation for all possible T values for the sample (169). In conclusion, we are apparently seeing crystals that probably formed at different $T$and f_{O_2} values, possibly at T intervals in excess of 100°C.

CONCLUSIONS

1. Preeruption average temperatures range from 1006°C to 976°C for air-fall tephra from the May 18 through August 7 eruptive sequence. For all samples analyzed, average T is 990°C and average f_{O_2} is -9.7 bars at log to the base 10. An average temperature of 1010°C for the blast dacite intruded into the mountain prior to May 18 is in the upper part of this range. On the basis of data presented here, a discernible systematic secular change of T and f_{O_2} in this sequence is not apparent.

2. White and dark portions of a mixed-magma block erupted June 12 and collected from a pyro-

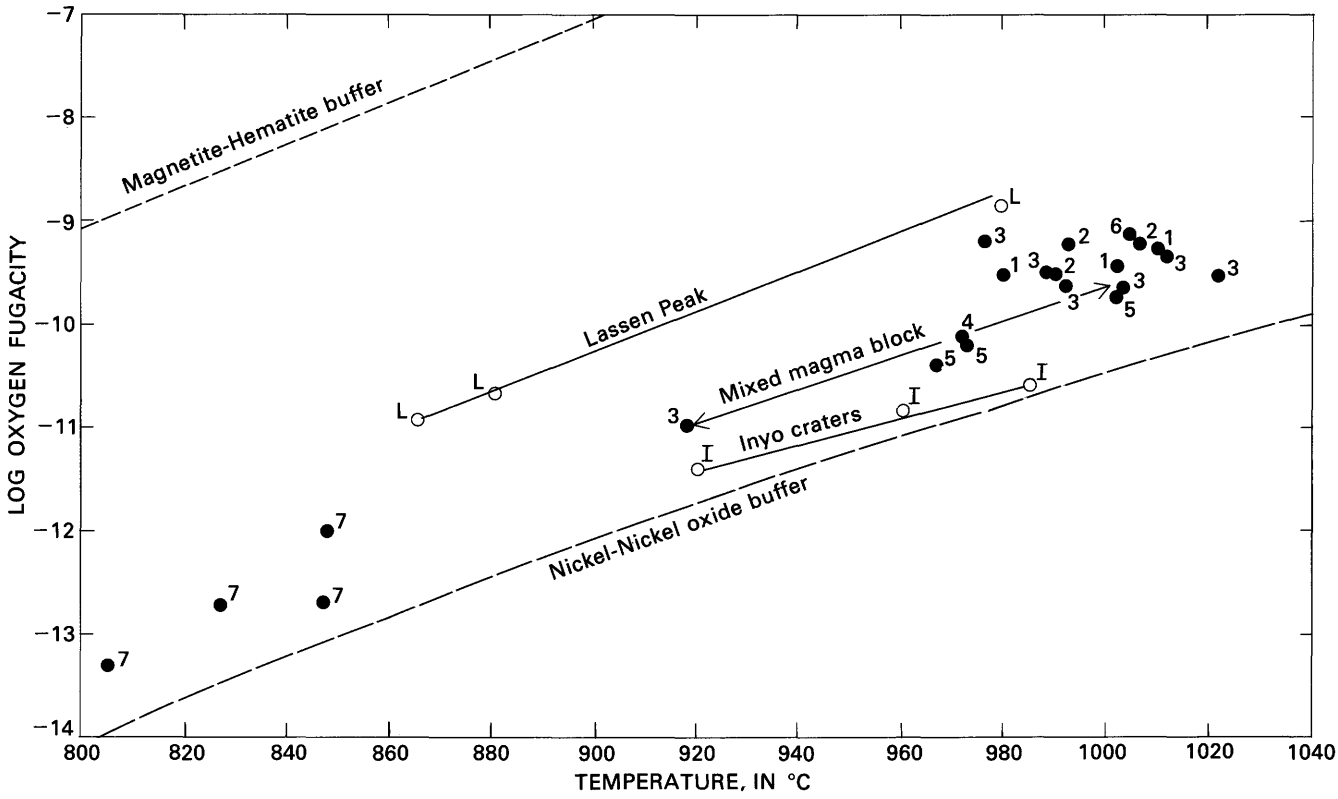

Figure 379.—Temperature and oxygen fugacity for the 1980 eruptive sequence (solid circles). 1, May 18; 2, May 25; 3, June 12 and post-June 12 dome; 4, July 22; 5, August 7 and post-August 7 dome; 6, pumice of layer T; 7, pumice of set W. Carmichael (1967) data for Lassen Peak area (L) and Inyo Craters (I) are included for comparison (open circles).

clastic flow give average temperatures respectively of 918° and 1003°C, a range greater than the entire range for air-fall tephra. The dark dacite component resembles the dacite from the May 18 blast and may represent a remnant of that magma remaining in the conduit. Magma mixing is inferred to have taken place in the conduit during eruption either of a thermally zoned single dacitic magma body or of separate magma bodies of different thermal histories.

3. T and f_{O_2} values for the pumice of layer T (ca. A.D. 1800) are similar to those of the 1980 pumice sequence.

4. The pumice of set W (ca. A.D. 1500) has inferred preeruption average temperatures of around 840°C, more than 100°C cooler than those inferred for the 1980 sequence.

5. Average temperatures reported in table 71 should not be inferred to indicate a single temperature or a narrow temperature range for crystallization of the iron-titanium oxides. In some samples, it does indeed appear that the T and f_{O_2} crystallization interval of the oxides has been small (for example, May 18 pumice sample 115379-8-1), but in others (for example, June 12 mixed-magma bomb sample 115379-30-1), the T interval of crystallization may be in excess of 100°C.

6. The f_{O_2} gives a trend about 1 log unit above the trend for the nickel-nickel oxide buffer, which is about 1 log unit below a trend defined for salic rocks of the Lassen Peak, Calif., area (Carmichael, 1967).

REFERENCES CITED

Anderson, A. T., 1968, The oxygen fugacity of alkaline basalt and related magmas, Tristan da Cunha: American Journal of Science, v. 266, p. 704-727.

Buddington, A. F., and Lindsley, D. H., 1964, Iron-titanium oxide minerals and synthetic equivalents: Journal of Petrology, v. 5, p. 310-357.

Carmichael, I. S. E., 1967, Iron-titanium oxides of salic volcanic rocks and their associated ferromagnesium silicates: Contributions to Mineralogy and Petrology, v. 14, p. 45.

Christiansen, R. L., and Peterson, D. W., 1980, Chronology of the 1980 eruptive activity of Mount St. Helens, Washington:

EOS (American Geophysical Union), v. 61, no. 46, p. 1133.
Crandell, D. R., Mullineaux, D. R., and Rubin, Meyer, 1975, Mount St. Helens volcano—recent and future behavior: Science, v. 187, no. 4175, p. 438–441.
Haggarty, S. E., 1976, Opaque mineral oxides in terrestrial igneous oxides, *in* Oxide minerals: Mineralogical Society of America Short Course Notes, v. 3, p. 101–169.
Hoblitt, R. P., 1980, Observations of pyroclastic flows of July 22 and August 7, 1980, Mount St. Helens, Washington: EOS (American Geophysical Union), v. 61, no. 46, p. 1137.
Hopson, C. A., 1971, Eruptive sequence at Mount St. Helens, Washington: Geological Society of America Abstracts with Program, v. 3, no. 2, p. 138.
Jarosewich, E., Nelen, J. A. and Norberg, J. A., 1979, Electron microprobe reference samples for mineral analyses: Smithsonian Contributions to Earth Sciences, no. 22, p. 68–70.
Lindsley, D. H., 1976, Experimental studies of oxide minerals, *in* Oxide minerals: Mineralogical Society of America Short Course Notes, v. 3, p. 61–84.
_____1977, Thermodynamic solution model for coexisting Ti-magnetite plus ilmenite: EOS (American Geophysical Union), v. 58, p. 519.
Lipman, P. W., 1971, Iron-titanium oxide phenocrysts in compositionally zoned ash-flow sheets from southern Nevada: Journal of Geology, v. 79, p. 438.
Melson, W. G. and Hopson, C. A., 1980, Petrology of tephra from the 1980 eruption of Mount St. Helens: Geological Society of America Abstracts with Programs, v. 12, no. 7, p. 482.
Miller, C. D., and Hoblitt, R. P., 1980, Stratigraphy of the deposits produced by the May 18 lateral blast at Mount St. Helens, Washington: EOS (American Geophysical Union), v. 61, no. 46, p. 1135.
Mullineaux, D. R., Hyde, J. H., and Rubin, Meyer, 1975, Widespread late glacial and postglacial tephra deposits from Mount St. Helens volcano, Washington: U.S. Geological Survey Journal of Research, v. 3, p. 329–335.
Sisson, T. W., and Moore, J. G., 1980, Deposits and effects of the May 18, 1980 Mount St. Helens pyroclastic surge: EOS (American Geophysical Union), v. 61, no. 46, p. 1135.
Smith, D. R., 1980, The mineralogy and phase chemistry of silicic tephras erupted from Mount St. Helens volcano, Washington: Rice University, M.A. thesis, 161 p.
Verhoogen, J., 1937, Mount St. Helens—a recent Cascade volcano: University of California Publications in Geological Sciences, p. 263–302.

THE 1980 ERUPTIONS OF MOUNT ST. HELENS, WASHINGTON

ALTERATION OF NEW VOLCANIC DEPOSITS

By DAVID P. DETHIER, DAVID R. PEVEAR, *and* DAVID FRANK

ABSTRACT

Sulfate-rich minerals in crusts around rootless fumaroles gave the best mineralogic evidence for alteration of the new deposits at Mount St. Helens 150 days after the May 18 eruptions. Tephra and flowage deposits erupted in 1980 are dominated by plagioclase, glass, and ferromagnesian minerals in the bulk materials; trioctahedral smectite, cristobalite, and finely comminuted glass and plagioclase dominate the < 2-micrometer fraction. Ash-leaching experiments, the chemistry of surface waters, and scanning electron microscope studies of mineral surfaces all suggest that alteration is taking place as surfaces react with H_2SO_4 and HCl. Comparison of surface-water and tephra compositions suggests that amorphous residues rich in silicon, aluminum, and iron must be forming as the result of alteration processes.

Stability relations calculated from chemical data indicate that kaolinite is stable in most surface water sampled on Mount St. Helens deposits, except for warm ponds on the debris-avalanche deposits, where smectite is predicted. However, no newly formed kaolinite or smectite has been recognized in the deposits. Abundant smectite in material blasted from the old cone is a result of pervasive, low-temperature alteration under neutral to basic conditions. The lack of opal, kaolinite, and alunite in all deposits studied indicates that acid-sulfate alteration, if present, could not have been widespread in the old cone. Either halloysite or kaolinite may form in the new deposits, along with smectite, within a few hundred to a few thousand years under cool, humid conditions, as cations and silica are leached from surface layers of the deposits during soil formation.

INTRODUCTION

The type and degree of alteration of volcanic deposits is often used as evidence for the timing of alteration and, by inference, the nature of the process. Alteration, as it is used here, includes chemical weathering and hydrothermal processes. Clastic volcanic rocks may be hydrothermally altered before they are erupted or during the cooling process after emplacement. Alteration may also result from soil-forming (Ugolini and Zasoski, 1979) or diagenetic (Davies and others, 1979) processes during the centuries or millennia that follow an eruption. In the vicinity of active geothermal systems, alteration may occur in deposits genetically related to present activity (Sorey, Lewis, and Olmsted, 1978) or in older, unrelated rocks (Goff and others, 1977). Detailed studies of mineral alteration and the chemistry of water associated with modern hydrothermal systems (see, for instance, Schoen and others, 1974; Keith and Muffler, 1978) have provided abundant information on temperature, reaction pathways, neoformed minerals, water residence time, and other variables. These studies and many others concerned with pyroclastic and associated deposits (Smith, 1960) help to explain alteration patterns commonly observed in volcanic deposits. However, many questions related to the timing and mechanism of alteration remain unanswered, and their answers may be vital to the proper interpretation of past volcanic processes from the often sketchy geologic evidence.

One characteristic of altered deposits—the relative abundances of the various alteration products they contain—has been used successfully to determine the origin of lahars from certain Cascade Range volcanoes. Crandell (1971) used the abundance of

montmorillonite as strong evidence of hydrothermal alteration when he reinterpreted the Holocene Osceola Mudflow, previously thought to be a till, as a lahar derived from the summit area of Mount Rainier. The abundance of kaolinite and opal in certain tephra and mudflow deposits from Mount Baker indicates that they originated in the acid-sulfate altered areas of Sherman Crater (Frank, 1981). Older, clay-rich mudflows from Mount St. Helens (Hyde, 1975) and Glacier Peak (Beget, 1980) may imply similar patterns of alteration in thermal areas and subsequent flowage following slope failure. Chlorite, smectite, and mica associated with the Mazama tephra (Dudas and Harward, 1975a) and chlorite contained in the Mount St. Helens "Yn" tephra (Mullineaux, 1974) have previously been interpreted as pedogenic minerals (Zachara, 1979). Yet it is possible that these minerals are accessory ejecta (Dudas and Harward, 1975b) and represent fragments of altered vent areas that were erupted during the initial stages of large magmatic events. Thus it may be possible to glean additional information on eruptive activity and the nature of hydrothermal alteration within a volcano from mineralogic studies of the eruptive products.

Mineral alteration by hydrothermal or weathering processes generally consists of the reaction of primary minerals or glass, in the presence of hydronium, hydroxyl, and other ions, to form secondary phases and dissolved solids. The course of alteration can be studied by examining changes in the primary phases, the nature of the secondary phases, the chemistry of water in contact with the minerals, or changes in the bulk chemistry of the volcanic deposit.

The violent eruption of tephra and flowage deposits at Mount St. Helens in 1980 provides an excellent opportunity to study the initial stages of alteration in volcanic rocks. In our preliminary work, we have emphasized mineralogic studies of the new volcanic deposits. We have also sampled thermal waters warmed by contact with the hot deposits, and encrustations at rootless fumaroles, which resulted from boiling of shallow ground water within the deposits. The chemistry of the thermal waters provides additional evidence for reaction pathways suggested by the mineralogic studies. In addition, we report the concentrations of certain trace elements (such as As, B, Fe, Li, and Mn) and other substances in surface waters that may affect biological recovery of the devastated area or that might contaminate downstream waters in the future. These studies contribute to our understanding of the timing and mechanism of alteration in clastic volcanic rocks and will aid the interpretation of alteration found in older volcanic deposits.

ACKNOWLEDGMENTS

This study has benefited from the critical comments of T. E. C. Keith and D. E. Marchand of the U.S. Geological Survey. J. M. Klein, of the Survey's district office in Tacoma, Wash., provided field instrumentation and chemical analyses of water samples. T. J. Casadevall, D. A. Johnston, and M. P. Doukas, all USGS, provided several lake-water and tephra samples, and J. K. Hartley of Western Washington University greatly aided with sample preparation and analyses. We also gratefully acknowledge the helicopter transportation provided by D. J. Easterbrook of Western Washington University, Bellingham, Wash., for part of our sampling efforts.

PREVIOUS WORK

The existing literature on the geology of Mount St. Helens provides extensive information on the age, stratigraphic relationships, and mineralogy of the bedrock and surficial deposits (Mullineaux and Crandell, this volume). Although no studies have specifically emphasized hydrothermal alteration or the mineralogy of the clay fraction, some evidence of past alteration has been reported. Mullineaux and Crandell (1962) noted alpha-cristobalite, feldspar, quartz, and halloysite in the clay fraction of a mudflow assemblage exposed near Silver Lake, dated at about 2000 years B.P. Verhoogen (1937) noted the presence of opal in crusts, a reddish alteration in the interiors of andesite fragments in the summit area, and the abundance of cristobalite in the groundmass of many lavas. Phillips (1941) mentioned the presence of brightly colored minerals at the historically active fumarole area on The Boot (fig. 380), north of the summit.

Observations of surficial alteration by Verhoogen (1937) and Phillips (1941) refer to localities associated with the old summit dome. Extensive areas of purple, brown, red, pink, and yellow hues on the surface of the dome, particularly near its lower margin, were

Figure 380.—Northwest slope of Mount St. Helens, September 30, 1975. Hydrothermal alteration in the summit and Goat Rocks domes is indicated by a faint pink to purple discoloration near the dome margin. Arrows note the historically active hydrothermal areas at The Boot (A) and the southwest slope (B); these two areas occur near the contact of the summit dome and underlying lavas and pyroclastic material. Photograph by W. G. Sikonia.

visible in pre-1980 summer views (fig. 380). These areas were probably affected by pervasive fumarolic activity that accompanied dome emplacement and cooling. Similar discoloration was also conspicuous at the Goat Rocks dome (fig. 380). Observations in April 1980 demonstrated that such alteration extended well below the surface. Extensive red and brown hues were visible in the interior of Goat Rocks where it was freshly exposed by small rock avalanches, and on the inner west wall of the newly formed summit crater within the old summit dome. Active hydrothermal alteration was noted on The Boot by Phillips (1941), and Friedman and Frank (1977) examined a small thermal zone on the southwest slope. Both of these areas were probably thermally active since the last eruptions of the mid-1800's.

DEPOSITS ERUPTED IN 1980

The 1980 eruptive activity at Mount St. Helens can be divided into three phases: (1) phreatic explosions and bulging of the north flank from March 27 to May 17, (2) a catastrophic avalanche followed by hydrothermal-magmatic explosions and pyroclastic flows on May 18, and (3) voluminous fumarolic emission, magmatic explosions, pyroclastic flows, and related dome construction and destruction from May 18 through late fall, 1980. Deposits emplaced in 1980 include: (1) a blanket of *lithic* (including partly altered rock, glass fragments, and crystals) and *vitric air-fall tephra* concentrated to the east-northeast of the mountain but extending to other quadrants as

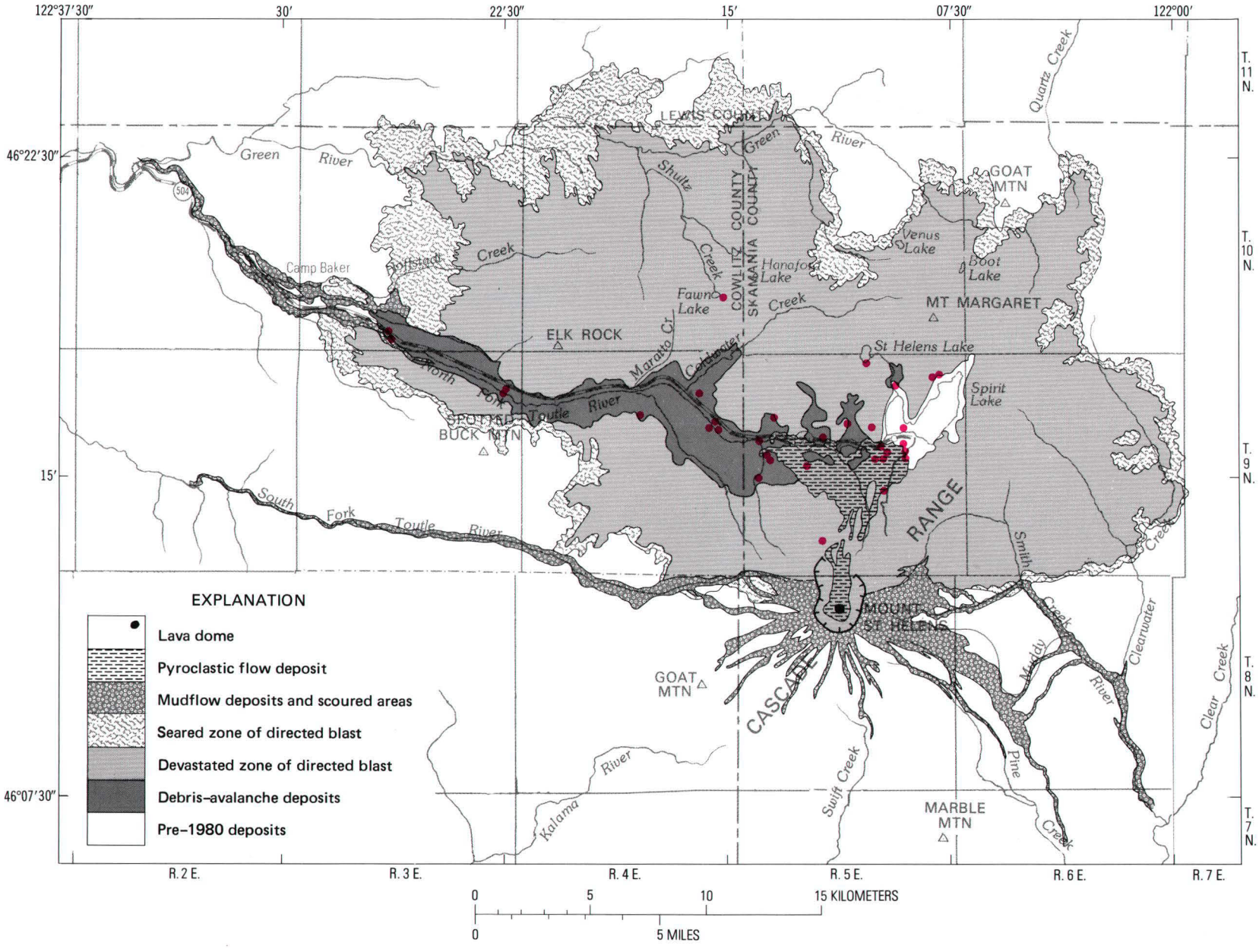

Figure 381.—Distribution of deposits, except air-fall tephra, erupted from Mount St. Helens in 1980 and locations of sample sites in red.

well (Sarna-Wojcicki, Waitt, and others, this volume); (2) a *debris-avalanche deposit*, which fills the upper North Fork Toutle River valley (Voight and others, this volume); (3) *large mudflows* along the North and South Fork Toutle Rivers, along the Cowlitz and Muddy Rivers, and along Pine Creek (Janda and others, this volume); (4) *smaller mudflows* in all other drainages on the south slopes of Mount St. Helens; (5) organic-rich lithic debris emplaced by a laterally directed *blast* (Hoblitt and others; Moore and Sisson; Waitt, all this volume); and (6) *pyroclastic flows* (Rowley and others, this volume) and associated ash-cloud deposits, which extend north from the crater to Spirit Lake.

Portions of the debris avalanche, the blast deposits, and the pyroclastic flows were hot when emplaced (Hoblitt and others, 1980), resulting in large phreatic explosions near Spirit Lake and many ephemeral fumaroles and thermal ponds west and south of the lake. The blast deposits and most of the hot blocks in the debris avalanche cooled to near-ambient temperatures within a few months, but the interors of pyroclastic flows remained well above 100°C at depth at the end of 1980. Finally, several domes have been emplaced in the center of the crater since mid-June; the margins of these domes are marked by profuse fumarolic activity, as is the interior margin of the crater.

METHODS

Our analysis of alteration in the new deposits relies heavily on X-ray diffraction (XRD) and scanning electron microscope (SEM) studies on the < 2-μm fraction of the deposits, and on the chemistry of thermal waters in contact with the eruptive products. We began sampling air-fall tephra in late March 1980 and continued through April and early May. After the May 18 eruption, we sampled and analyzed air-fall tephra from localities in Washington and other western States. In early June we collected water, dry sediment, and suspended-sediment samples from about 20 sites in the new deposits at the volcano, and in October we collected additional samples from the pyroclastic flows. To supplement these samples, we collected encrustations and measured temperatures at about 10 rootless fumaroles and analyzed samples of rock from the pre-May 18 summit crater, from the June dome, and from a variety of locations on the slopes of the volcano. Sample localities are shown on figure 381; detailed descriptions of sample sites are given in Dethier and others (1981).

Sediment samples were air-dried and the < 2-μm fraction was separated by centrifugation. Oriented < 2-μm samples on ceramic tiles and bulk, randomly oriented samples were treated by standard methods (Jackson, 1973) and were analyzed by X-ray diffraction techniques on a General Electric XRD-5 diffractometer and by SEM methods using an AMR-1200 equipped with an energy-dispersive analyzer. Selected samples were treated with dimethyl sulfoxide (DMSO) to check for kaolinite (Abdel-Kader and others, 1978). Grain mounts and thin sections were examined by standard petrographic techniques.

Water temperature, pH, and specific conductance were measured in the field and upon return to the laboratory, where about 1 L of each sample was filtered through a 0.45-μm cellulose filter. Filtered and unfiltered samples were submitted to the USGS central laboratory in Denver by the Tacoma district office and were analyzed by standard methods (Skougstad and others, 1978) for about 75 constituents.

DATA

The mineralogy and chemistry of material erupted from Mount St. Helens, particularly the air-fall tephra, has been extensively analyzed (Fruchter and others, 1980; Hooper, Herrick, Laskowski, and Knowles, 1980). The effect of the eruption on surface-water chemistry has been investigated in the Toutle and Cowlitz River systems, and at lakes in the blast zone (Klein and Taylor, 1980). We have reported reconnaissance mineralogic and water-chemistry data (Dethier and others, 1981) for samples collected through early June 1980. We summarize these data below, report the results of additional sampling, and reproduce data from other sources to aid in the discussion and interpretation of our results.

Table 76 lists the minerals present in the coarse and < 2-μm fraction of material erupted in 1980, including suspended sediment from the thermal waters and encrustations collected at rootless fumaroles. Samples for mineralogical analyses from the debris-avalanche, lithic air-fall tephra, and blast deposits represent material derived mostly from the upper kilometer and north side of the cone. We analyzed only 14 samples

Table 76.—Mineralogic compositions of deposits erupted from Mount St. Helens in 1980

Type of deposit	Number of samples	Major minerals		Comments
		In bulk sample	In <2-μm fraction[1]	
Pumiceous pyroclastic flows and vitric air-fall tephra.	35	Glass, plagioclase, hypersthene, hornblende, magnetite, and ilmenite.	([1])----------	Magmatic material erupted May 18 and afterwards. Pumiceous clasts carefully cleaned to remove pervasive lithic contaminants.
Lithic air-fall tephra.	20	Plagioclase, devitrified microlite-rich glass, hypersthene, hornblende, magnetite, cristobalite[2], tridymite, and quartz.	Smectite, mixed-layer chlorite-smectite, chlorite, and mica.	Nonmagmatic material erupted before May 18.
Debris-avalanche, blast, and mudflow deposits.	[3]44	Plagioclase, hypersthene, hornblende, glass, quartz, magnetite, ilmenite, chabazite, and phillipsite.	Smectite, mixed-layer chlorite-smectite, and chlorite.	Contains abundant charred organic matter at many locations.
Encrustations and minerals in pumice at fumaroles.	14	Alunite ($K_xNa_{1-x}Al_3(SO_4)_2(OH)_6$), amorphous material, glauberite ($Na_2Ca(SO_4)_4.22H_2O$), gypsum, halite, halotrichite ($FeAl_2(SO_4)_4.22H_2O$), hematite, thenardite (Na_2SO_4), and zeolites (analcime, clinoptilolite, erionite(?), and mordenite(?)).	([1])----------	Collected at temperatures from 80° to 260°C.

[1]Minor amounts of all minerals present in bulk samples occur in the <2-μm fraction.
[2]Also present in the June dome and, with tridymite, in three samples of the old summit dome collected in April 1980.
[3]30 from debris avalanche, 8 from blast deposit, and 6 from mudflow.

of the blast and mudflow deposits, but their mineralogy appears similar to that of the lithic air-fall tephra and the debris-avalanche deposit. Analyzed samples from the heterogeneous debris-avalanche deposit include fine-grained facies, material from steam vents and thermal ponds, and samples of the large, brightly colored (red, green, and white) blocks common in the deposit in areas east of Coldwater Creek. The encrustations and vesicle-filling minerals listed in table 76 were collected in early June from pyroclastic flows, and in early October from the surface and warm interior of flows emplaced 100 to 150 days earlier.

Chemical analyses of tephra are reported by Fruchter and others (1980), Hooper, Herrick, Laskowski, and Knowles (1980), and Sarna-Wojcicki, Meyer, and others (this volume). Korosec and others (1980) reported that lithic material erupted in 1980 consists largely of plagioclase (An_{30-50}); 5 to 15 percent pyroxene, amphibole, and altered glass; and minor amounts of magnetite and other minerals. Hooper, Herrick, and Laskowski (1980) reported that newly deposited ash collected in Pullman, Wash., on May 18 contained about 70 percent plagioclase (An_{50}), "lithic" fragments composed primarily of a brown glass full of microlites, 5–10 percent opaque oxides, and small proportions of basaltic hornblende and orthopyroxene. Vitric tephra contains abundant fresh glass and plagioclase (An_{50}?) in varying proportions, and less than 10 percent ferromagnesian and opaque minerals (Korosec and others, 1980). Studies by Fruchter and others (1980), Hooper, Herrick, Laskowski, and Knowles (1980), and ourselves tend to confirm these general conclusions.

SEM study of the mineral and glass fragments (fig. 382) suggest that most were mechanically abraded during eruption and transport, but surfaces generally appear fresh. Some of the hypersthene crystals and glass shards from the pyroclastic flows and rootless fumaroles display pitting, etching, and other solution features, and many of the finest particles undoubtedly dissolved after a short period of contact with acidic solutions. Plagioclase crystals and crystals of neoformed minerals like gypsum, sulfur, and halotrichite from these environments appear fresh. Euhedral crystals of preexisting minerals, such as cristobalite, tridymite, and smectite, are present in some samples (fig. 383), and the zeolites phillipsite

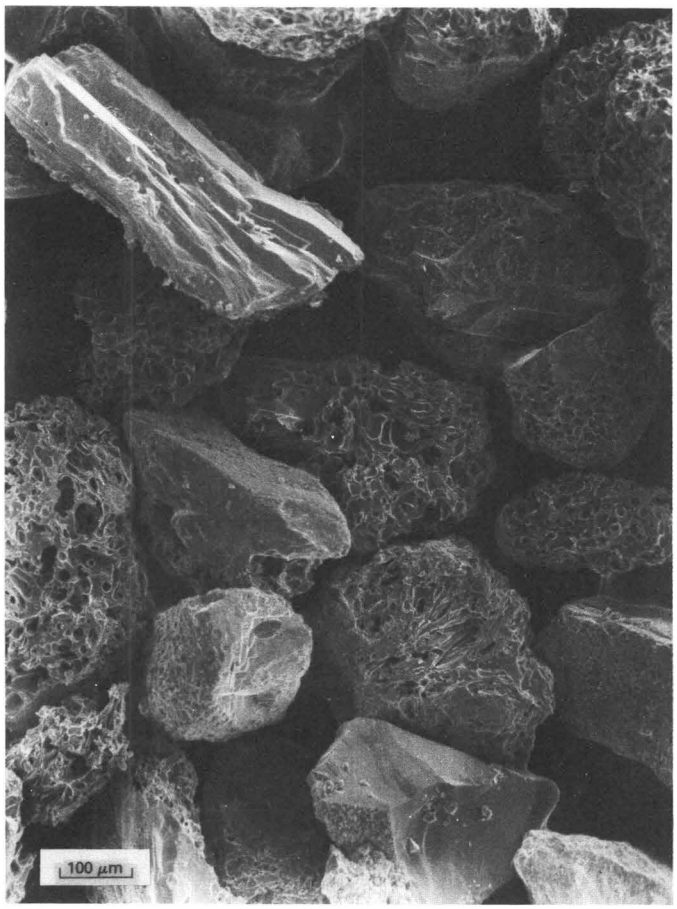

Figure 382.—SEM image of abraded pumiceous shards and feldspar in tephra from the May 18 eruption. Sample collected in Yakima, Wash.

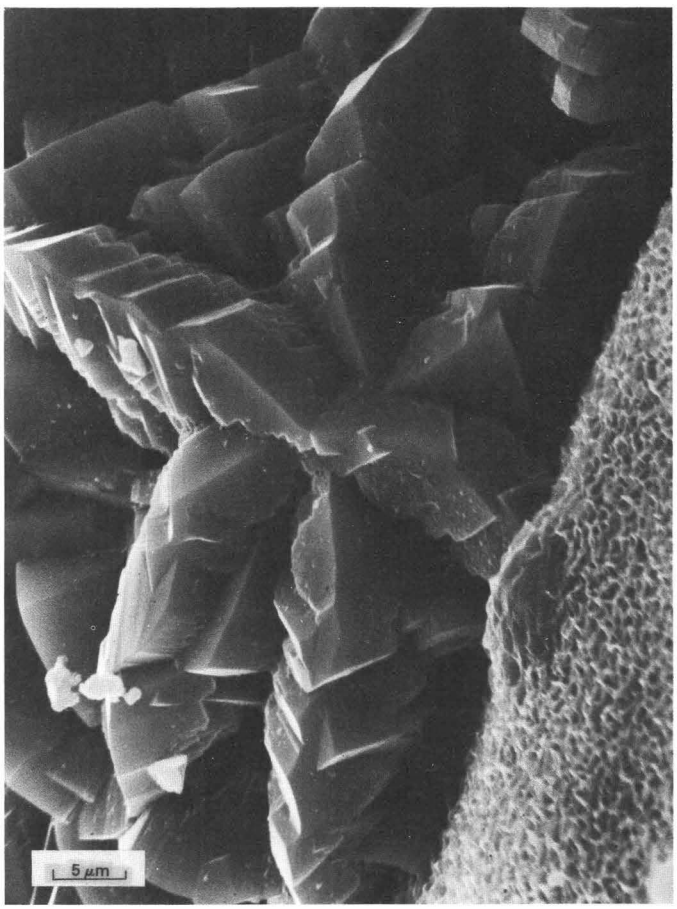

Figure 383.—SEM image of chabazite and smectite (magnesium-iron saponite) in an altered clast collected from the debris-avalanche deposit.

and chabazite are commonly present as vesicle fillings in old clasts transported by the debris avalanche. The smectite and zeolites appear to have formed by precipitation, probably during hydrothermal alteration of the old cone. The zeolite minerals in fig. 384 were found in the interior of a pumiceous clast collected 60 cm below the surface at a 260°C fumarole. They are probably neoformed minerals, but the clast could be older material transported by the pyroclastic flow. Figure 385 compares an unidentified, fibrous neoformed mineral in a vesicle (fig. 385*B*) to empty vesicles in similar material from the May 18 eruption (fig. 385*A*).

The chemistry of thermal ponds, Spirit Lake, and surface waters flowing through hot deposits is summarized in table 77; detailed analyses are given in Dethier and others (1981). Analyses included 16 trace elements in addition to those listed, but the dissolved and suspended levels of these elements were generally less than 15 μg/L and were below detection limits in most cases. In general, the analyses show $Na > Ca > K = Mg$, $SO_4 > Cl > HCO_3 > > F$, and $Mn > > Sr = B > Li > Ba$; other trace elements display irregular patterns at lower concentrations.

Fruchter and others (1980) and Hinkley and others (1980) have reported the results of simple ash-leaching experiments using air-fall tephra collected in Washington, Idaho, and Montana. (See table 78.) Samples were collected before any rain fell. The sample from Tieton, Wash., contained considerable sand and was composed largely of lithic material, whereas the Montana samples were glass-rich medium and fine silt. Table 78 shows the amount of each element removed from the ash by distilled water. Fruchter and others (1980) agitated 10:1 (by weight) water-ash mixtures and allowed them to stand for an hour before analysis, while Hinkley and others (1980) soaked 1:1.72 (by weight) mixtures in columns for 4 hr,

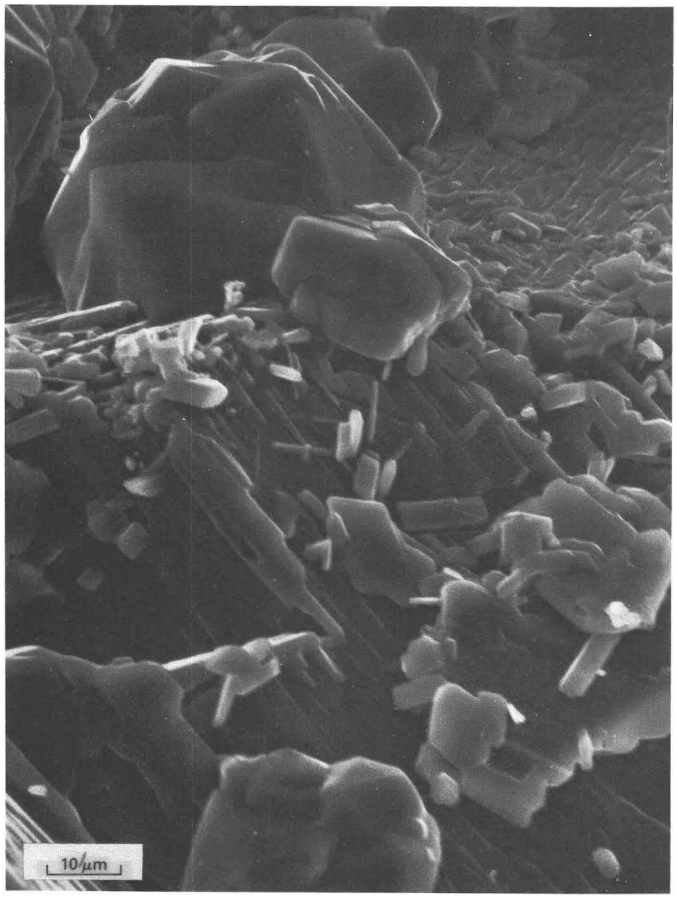

Figure 384.—SEM image of the interior of a pumice clast collected at a depth of 60 cm in a May pyroclastic flow. Temperature of sample when collected on Oct. 15, 1980, was 260°C. Image shows a deeply etched plagioclase grain with rounded, silica-coated crystals of analcime(?) and smaller, euhedral crystals of an unidentified aluminosilicate.

leached them with 100 mL of water, and then repeated the procedure twice (Charles Collier, written commun., May 30, 1980). Significant quantities of chloride, sulfate, boron, calcium, and manganese were removed from most samples, particularly from the finest fractions, while iron and silica were nearly immobile. Although the analytical procedures are not exactly comparable, these data suggest the changes in water chemistry that could be expected during the initial stages of mineral alteration.

DISCUSSION

Material derived from the eruption of Mount St. Helens in 1980 includes large volumes of hydrothermally altered rock and fresh, glassy deposits. Both the altered and fresh materials are unstable under surface conditions, but the alteration of existing minerals and glass and the crystallization of new minerals are relatively slow processes. Alteration of the new deposits can be described from (1) mineralogic changes in the fine fraction; (2) etching, pitting, and solution of surfaces visible in SEM studies; (3) the composition of encrustations and vesicle fillings at the rootless fumaroles; and (4) the chemistry of the mineralized solutions. The mineralogy of the altered rock erupted from the cone reflects hydrothermal processes that characterized the volcano between eruptions and suggests alteration pathways that may be followed by the new deposits. Because alteration in the newly deposited rocks occurs most rapidly in the still-warm pyroclastic flows and in warm areas of the debris-avalanche deposit, the following discussion emphasizes those areas.

Old and new volcanic rocks at Mount St. Helens contain abundant dacitic glass and sodium-calcium plagioclase, minor hypersthene and hornblende, and accessory titanomagnetite as primary phases. Some primary minerals, including quartz, ilmenite, and clinopyroxene, are also present in minor amounts, and we ignore them in this discussion. Trioctahedral smectite, cristobalite, tridymite, hematite, mixed-layer chlorite-smectite, and chlorite are common as alteration or devitrification products in older rocks at Mount St. Helens (contributing to lithic tephras and the debris avalanche). Acid-sulfate alteration of the type observed at other Cascade volcanoes, such as Mount Baker, has not been found in older Mount St. Helens deposits or in lithic components of the new deposits. Given the simple suite of solid reactants at Mount St. Helens, the secondary phases shown in table 79 can be predicted for alteration under acid or neutral conditions (Lovering, 1957; Narebski and Paulo, 1973; Keith and Muffler, 1978).

ALTERATION REACTIONS

Mineralogic evidence for alteration reactions includes (1) sulfate and chloride-rich encrustations at fumaroles, (2) neoformed(?) zeolites in warm pyroclastic deposits, and (3) possible neoformed smectite, mixed-layer (ML) chlorite-smectite, and chlorite in debris-avalanche ponds and steam vents. Because glass dissolution is suggested by SEM studies and should be expected according to other studies (Aomine and Wada, 1962; Saigusa and others, 1978;

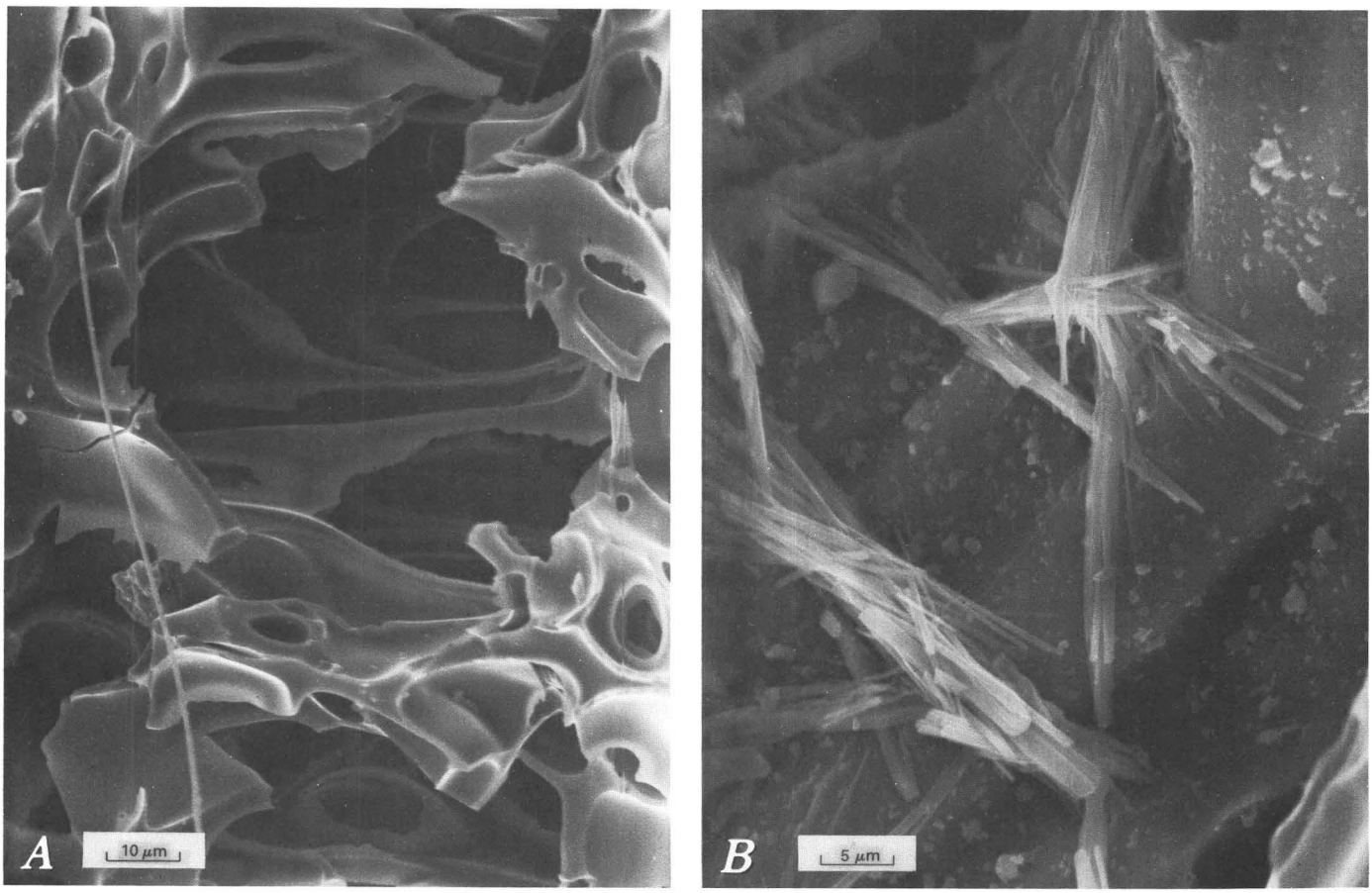

Figure 385.—SEM images of pumiceous material from the May 18, 1980, eruption. A, Interior of pumice clast collected in Yakima, Wash., on May 18. B, Interior of pumice clast collected at a depth of 60 cm in a May pyroclastic flow on Oct. 15, 1980. Temperature of sample when collected was 260°C. Unidentified acicular mineral contains sodium and magnesium.

Zachara, 1979), it is likely that amorphous aluminosilicate complexes (or allophane) are present in the new Mount St. Helens deposits, causing a high background in some XRD patterns that is similar to that described by Wada (1977). It is also likely that calcic portions of the plagioclase (Busenberg, 1978) are altering to smectite or allophane, but there is no positive evidence for either reaction. Trioctahedral smectite is pervasive in all the deposits, and ML chlorite-smectite and chlorite are present in many samples but are most abundant in warm areas of the debris-avalanche deposit. These observations suggest the transformation series smectite / ML chlorite-smectite / chlorite, which is common in slightly alkaline environments. Alteration of ferromagnesian minerals to smectite or chlorite and iron oxhydroxides, and the precipitation of smectite from solution are also likely in such environments. However, smectite, chlorite-smectite, and chlorite pervaded the pre-May 18 cone, and so we cannot be certain that their abundance in warm ponds and steam vents indicates alteration and precipitation there. The absence of alunite, opal, or other acid-sulfate minerals in the debris-avalanche deposits provides strong evidence that areas of acid-altered rock must have been very limited in the old cone, if they were present at all.

The concentration of the hydronium (H_3O^+) ion affects both the nature and the rate of the initial alteration reactions and remains an important variable in all weathering processes. Many eruption products could have supplied H_3O^+ to the deposits: Sulfuric (H_2SO_4), hydrochloric (HCl), and nitric (HNO_3) acid droplets were noted as condensates on the surfaces of ash particles from the May 18 eruptive plume (Fruchter and others, 1980), and sulfur dioxide (SO_2) emission rates averaged more than 1,000 t (metric tons) per day from June to October, with higher rates noted during eruptions (Casadevall and others, 1980). In addition, hydrogen sulfide (H_2S), which has been measured at rootless fumaroles south of Spirit Lake

Table 77.—Dissolved constituents, pH, and temperature of surface waters collected at Mount St. Helens in early June 1980

Constituent	Snowmelt under hot blast deposit (1 sample)	Inflow to SE. corner Spirit Lake (1 sample)	Ponds in pyroclastic deposits (3 samples)		Spirit Lake (6 samples)			Ponds in debris-avalanche deposit (3 samples)[2]	
			Mean	Range	Mean	SD[1]	Range	Mean	Range
	Data in milligrams per liter								
Ca^{+2}------	22	6.7	27.7	22-31	73.7	1.1	72-75	193	100-250
Mg^{+2}------	3.0	.5	3.7	2.8-4.1	12.3	.5	12-13	45	18-67
Na^{+}-------	19.0	16.0	34.3	23-40	68.4	1.7	67-71	235	85-350
K^{+}--------	3.4	2.0	5.9	4.1-6.9	15.0	0	---	25	11-33
SO_4^{-2}-----	58.0	23.0	76.0	76-94	160	6.3	150-170	663	310-950
Cl^{-} ------	30.0	11.0	32.7	19-40	86.2	.7	85-87	270	110-340
[3]HCO_3^{-} ---	19.5	22.0	29.3	25.6-31.7	150	6.3	146-159	159	63-244
F^{-} -------	0	.3	.3	0.2-0.3	.2	0	---	.8	0.5-1.2
SiO_2------	6.8	21.0	14.0	12-16	46.1	.7	45-47	34	22-53
	Data in micrograms per liter								
Al--------	100	60	17	10-30	60	35	0-90	10	---
As--------	1	1	1	---	11	.5	11-12	8	2-15
Ba--------	20	6	16	10-20	50	0	---	53	30-100
B---------	7	3	70	30-90	373	65	300-480	817	380-1,200
Fe--------	290	<10	<10	---	2,700	994	1,300-3,600	<17	<10-31
Li--------	16	14	16	12-18	58	3	56-63	100	63-140
Mn--------	450	23	530	340-630	4,886	90	4,700-5,200	2 800	1,400-6,400
Sr--------	100	29	123	120-140	320	0	---	623	400-1,000
pH--------	[4]6.1	[4]7.2	7.1	6.9-7.3	[4]6.5	.1	6.4-6.5	7.6	7.5-8.3
Temp. (^{0}C)	.5	7.5	23.0	21.0-24.0	26.5	.8	25.5-27.0	23.4	21.5-26.8

[1]Standard deviation.

[2]Two debris-avalanche samples were collected on July 30, 1980, by J. M. Klein, USGS, Tacoma, Wash.

[3]Calculated from alkalinity measurements, so includes carbonate species and dissolved organic acids, particularly in Spirit Lake.

[4]Field values were 0.5 pH units lower.

(Casadevall and others, this volume), reacts with water in an oxygenated environment by a series of reactions (Schoen and others, 1974):

$$H_2S + \tfrac{1}{2}O_2 = H_2O + S^0$$
$$S^0 + O_2 = SO_2$$
$$SO_2 + \tfrac{1}{2}O_2 = SO_3$$
$$SO_3 + H_2O = H_2SO_4.$$

Native sulfur is present in the crater and at some of the rootless fumaroles, and many of the encrustations are sulfates. Droplets of sulfuric acid and lesser amounts of hydrochloric acid were probably present on the surfaces of all tephra erupted at Mount St. Helens after April 1980, and they are common in the crater and at rootless fumaroles in the pyroclastic flows. Increased SO_2 emissions at the volcano may be a significant source of acidity for precipitation that falls downwind, but precipitation pH at the mountain reflects upwind sources of industrial pollution and atmospheric mixing. Acid-sulfate alteration is likely to be strongest in the surface zone of fumaroles.

The pH of ash leachates (Fruchter and others, 1980) and surface waters in the devastated area (table 77) range from slightly acidic to slightly basic, and the leachate and surface waters contain high concentrations of SO_4^{-2}, Cl^-, and, in some cases, HCO_3^-. The relatively high pH values indicate that mineral acidity

Table 78.—Percentages of elements removed from Mount St. Helens tephra by leaching with distilled water

[Calculated as $\frac{\text{mass removed in leachate}}{\text{mass in unleached sample}} \times 100$; leaders (—), not determined]

Element	Tieton, Wash.[1]	Missoula, Mont.[1]	Helena, Mont.[2]
Ca	0.5	1.3	2.0
Mg	.1	.4	.7
Na	.4	.6	.9
K	.3	.4	--
S	24	39	64
Cl	29	47	80
SiO_2	.001	.002	.008
Ba	--	--	.03
B	2.5	1.1	2.5
Fe	.0002	.002	.001
Mn	.5	1.0	1.6
Sr	--	--	.6

[1]Calculated from data of Fruchter and others (1980). 10:1 water-ash mixtures were shaken and allowed to stand 1 hr before analysis.

[2]Leachate data for sample from Helena (Charles Collier, written commun., May 30, 1980) compared with bulk composition for sample from Missoula (Fruchter and others, 1980). Helena samples were leached three successive times with 100 mL water after standing in a 1:1.72 water-ash mixture for 4 hr each time.

(Stumm and Morgan, 1970) supplied by H_2SO_4 and HCl is neutralized as hydronium ions dissolve very fine particles and react with fresh mineral and glass surfaces, releasing cations such as Na^+ and Ca^{+2} into solution. As the pH rises, the buffered carbonic acid (H_2CO_3) system becomes the principal source of hydrogen, and cation-exchange reactions and precipitation of secondary phases become more important.

CHEMISTRY OF SURFACE WATERS

The composition of surface waters sampled in June reflects (1) alteration and dissolution of minerals and glass, including surface coatings, (2) leaching of elements from organic matter, particularly in Spirit Lake, and (3) precipitation of secondary products. Tephra and water-sample compositions, plotted in figure 386, suggest that potassium is relatively immobile, and that the Ca-Na ratio in surface water may reflect the composition of the materials in contact with the water. The relative mobility of elements in the tephra can be calculated from the leachate data presented in table 78 as the ratio ((concentration in leachate/concentration in unleached tephra) × 100) for each element. Those data show

$$Cl > SO_4 > > B > Ca = Mn > Na > Mg = K = Sr > > Ba > > SiO_2 > Fe.$$

Surface-water compositions display similar patterns, except Ca and Na change positions in the index. Silica, aluminum (not included in table 78), and iron are highly immobile; chloride and sulfate are highly mobile; and boron, calcium, and manganese are the most mobile of the remaining elements. Two inferences can be drawn from these results: (1) the highly mobile elements from the tephra existed as liquid or readily soluble coatings on grain surfaces, much as they did in encrustations around fumaroles, and (2) immobile elements, such as silica and

Table 79.—Secondary phases that may result from alteration of minerals or glass in a near-surface environment

[Based on Keith and Muffler, 1978; Schoen, White, and Hemley, 1974]

Primary phases[1]	Secondary phases	
	Neutral or basic environment	Acid environment
Dacitic or rhyolite glass; plagioclase; hypersthene and hornblende; titanomagnetite; trioctahedral smectite; chlorite; cristobalite and tridymite.	Smectite; sodic or potassic feldspar[2]; cristobalite or opal; zeolites; mixed-layer chlorite-smectite and chlorite; hematite, goethite, and iron oxyhydroxides; calcite.	Amorphous material; allophane and imogolite; opal or cristobalite; kaolinite or halloysite; pyrite; alunite and other sulfates; hematite; vermiculite or mixed-layer phases; gibbsite.

[1]Includes altered material from the old summit dome.

[2]Most common at depth in hydrothermal systems, but may form during glass devitrification.

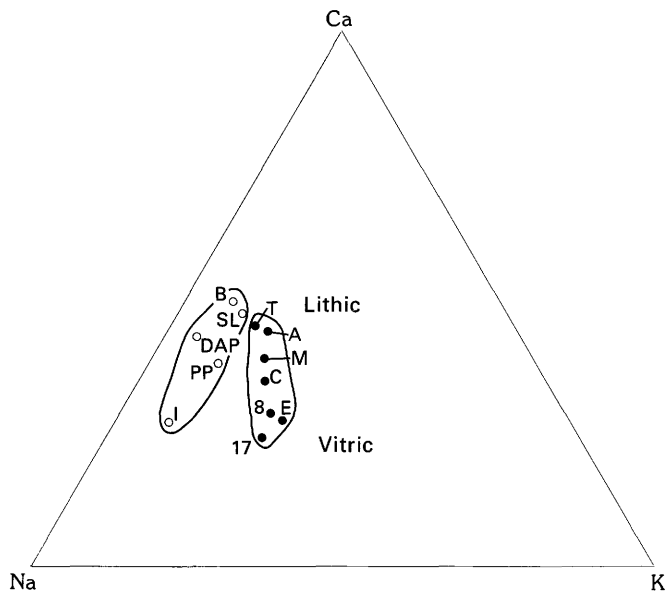

Figure 386.—Ternary diagram showing the proportions of calcium, sodium, and potassium in tephra and surface-water samples. Surface-water samples (open circles) include the following: B, snowmelt in hot blast deposit; DAP, pond in debris-avalanche deposit; I, inflow to Spirit Lake; PP, pond on pyroclastic flow; and SL, Spirit Lake. Tephra samples (solid circles) include the following: A, C, and E from Pullman, Wash., area (Hooper, Herrick, Laskowski, and Knowles, 1980); M from Missoula, Mont., and T from Tieton, Wash. (Fruchter and others, 1980); and 8 and 17 from table 80 of Sarna-Wojcicki, Meyer, and others (this volume).

aluminum, must dominate the residue formed by dissolution of the surface layers of glass, feldspar, and ferromagnesian minerals. The relative mobility of Ca and Mn suggests that these elements either were concentrated in soluble form at grain surfaces or occupied exchange sites. However, sodium is present in higher concentrations than calcium in most surface waters at Mount St. Helens, particularly in those on pyroclastic flows. The lower levels of calcium in surface waters may reflect selective removal to exchange sites on allophane (Wada, 1977), or high calcium levels in the leaching experiments may have resulted from solution of gypsum coatings on mineral and glass surfaces.

Concentrations of most trace metals in surface waters from Mount St. Helens are low compared to those in other thermal waters. (See Wollenberg and others, 1979.) Manganese concentrations are high in all samples, and dissolved iron levels were high in Spirit Lake in June 1980. The relatively low levels of iron in other surface waters and a reported decrease of iron concentrations in Spirit Lake since June (T. J. Casadevall, written commun., 1980) probably result from the precipitation of an iron oxide or sulfide phase. Oxidation and precipitation rates of manganese are retarded in neutral or acidic organic-rich water (Stumm and Morgan, 1970); the rates are slower than rates for iron in most waters, which may explain the high manganese concentrations.

The stoichiometry of weathering solutions may be used, in relatively simple systems, to suggest the nature and rates of weathering reactions (Stumm and Morgan, 1970). For instance, the weathering of andesine feldspar to kaolinite may be written thus (Stumm and Morgan, 1970):

$$Ca_{0.5}Na_{0.5}Al_{1.5}Si_{2.5}O_8 + 1.5H + 2.75\,H_2O \rightarrow 0.75Al_2Si_2O_5(OH)_4 + 0.5Ca + 0.5Na + H_4SiO_4.$$

The molar ratios of $Ca:Na:H_4SiO_4$ in weathering solutions for this reaction should be 1:1:2, but the measured values for the Spirit Lake inflow and the mean of the pyroclastic-flow ponds give 1:4.2:1.3 and 1:2.3:0.24, respectively. These discrepancies suggest that congruent alteration of plagioclase does not control solution composition. If the dissolution of the glassy fraction of the pumice is a controlling factor, the Ca-Na ratio in solution should be near 0.34 (as reported for separated glass samples, this volume, table 80, analyses 8 and 17), even if silica and aluminum are conserved. Weathering of deposits rich in lithic material or organic matter should result in higher Ca-Na ratios, but all postulated weathering systems are complicated by the tendency of divalent cations such as Ca^{+2} and Mg^{+2} to preferentially occupy exchange sites in crystalline or amorphous material. Chemical data from the leaching experiments, the Spirit Lake inflow, and the pyroclastic-flow ponds give Ca-Na ratios, respectively, of 0.91, 0.24, and 0.43. Water from the pyroclastic flows thus gives ratios that bracket the predicted values. Stoichiometric data suggest that the composition of water in contact with the pyroclastic material reflects the dissolution of glass rather than the alteration of andesine to kaolinite, but laboratory experiments are required to substantiate the conclusion.

STABILITY DIAGRAMS

Equilibrium thermodynamics provides an additional method for examining mineral stability and water chemistry. Figure 387 is a plot of stability relations in the gibbsite-kaolinite-amorphous silica-smectite system. The compositions of water from ponds on the pyroclastic flows, from the inflow to Spirit Lake, and from Spirit Lake plot in the kaolinite stability field, but the data suggest ponds in the debris avalanche are saturated with calcium smectite. The stability field drawn for calcium smectite should be regarded as approximate because of uncertainties in extrapolating thermodynamic data to the composition of specific smectites. Metastable reaction products may also persist at relatively low temperatures. We have sketched lines on the stability diagram to show the progressive change in chemistry from rainwater to the surface waters. If data for dissolved sodium and sodium smectite are used (Tardy, 1971), the debris-avalanche pond waters still plot in the smectite field, and the other waters remain in the kaolinite field. Stability fields for chlorite, magnesium smectite, or other minerals could be plotted by using additional axes. However, figure 387 is the simplest diagram that includes the principal dissolved cations and silica.

REACTION RATES

Stability diagrams and data from the literature for soil-forming processes and hydrothermal alteration suggest that kaolinite (or halloysite) and smectite should be forming in the new deposits at Mount St. Helens. We have not positively identified neoformed smectite or kaolinite; the high levels of sulfur, iron, calcium, and sodium in encrustations at fumaroles and the presence of zeolites in the warm pyroclastic flows provide the strongest evidence for neoformed minerals. Mixed-layer chlorite-smectite and chlorite that are present in some thermal waters may be neoformed, in part.

However, the chemistry of surface waters, leaching experiments, and the appearance of glass and mineral surfaces under high magnification suggest that dissolution and alteration are occurring at present. The lack of evidence for crystalline aluminosilicates such as kaolinite suggests the presence of amorphous or nearly amorphous material, but we have not chemically analyzed this phase. Many investigators (see Ugolini and Zasoski, 1979) report rapid neoformation of minerals in ash-rich deposits. The absence of neoformed crystalline silicates in deposits from Mount St. Helens after 150 days of alteration may reflect either slow rates of dissolution or sluggish recrystallization of amorphous material, perhaps inhibited by the abundance of sulfate, chloride, and cations.

Despite the ambiguities in interpreting the leachate and surface-water chemistry in terms of mineral weathering, it is apparent that two interrelated proc-

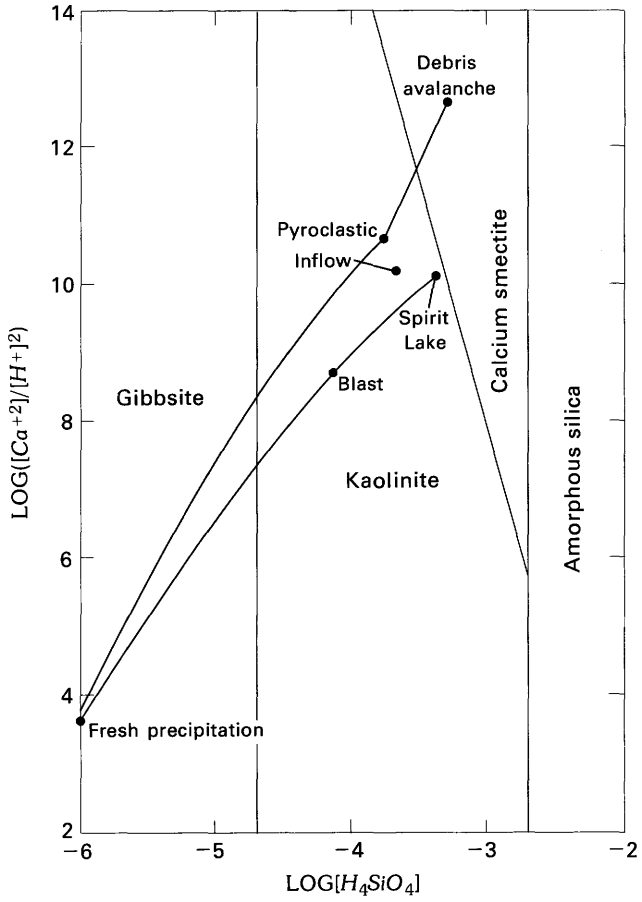

Figure 387.—Stability relations of gibbsite, kaolinite, calcium smectite, and amorphous silica at 25°C. Surface-water activities calculated from compositional data shown in table 77; precipitation activity value calculated from data of Dethier (1979). Thermodynamic data from Helgeson (1969).

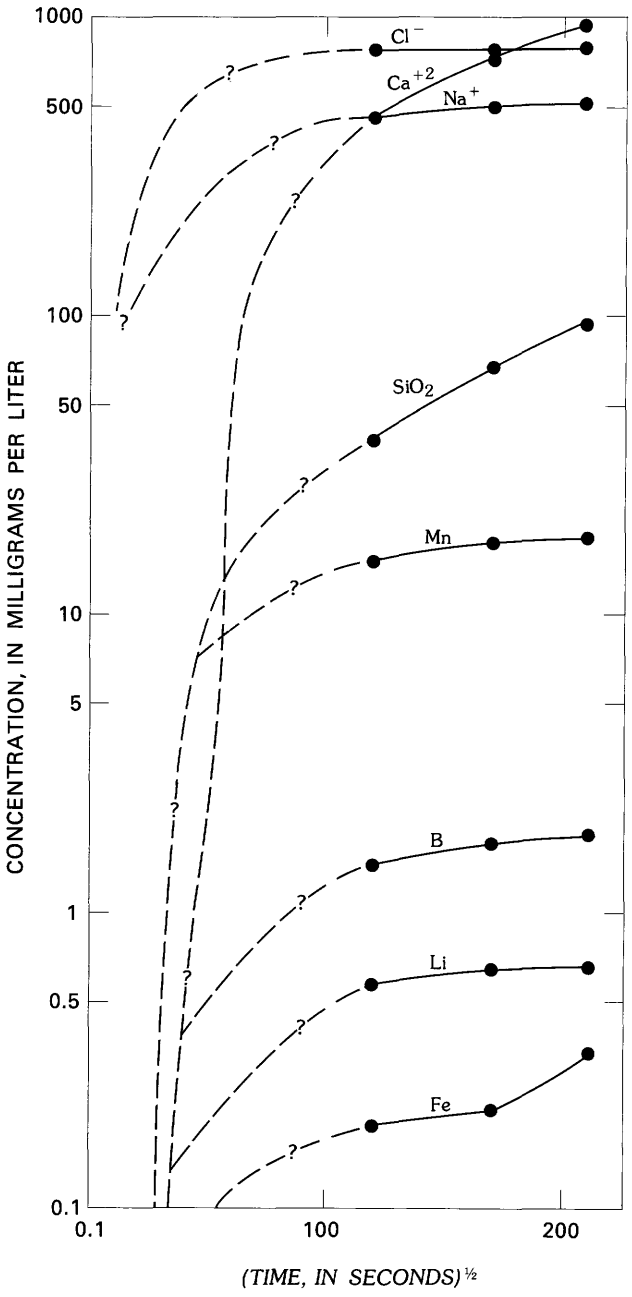

Figure 388.—Rate of mineral solution suggested by leaching of vitric ash with distilled water (Charles Collier, written commun., May 30, 1980).

esses occur during the initial phases of alteration. Rapid surface reactions (fig. 388) and the dissolution of the finest particles apparently dominate the first seconds to hours (Busenberg and Clemency, 1976; Holdren and Berner, 1979) of rock-water contact. Then slower reaction rates occur as mineral-surface sites are filled by more stable ions, the pH of the solution rises, and the kinetics of diffusion processes becomes important. In general, these initial, rapid reactions follow simple, first-order kinetics (White and Claasen, 1980), while long-term alteration is controlled by slower, diffusion-controlled reactions of the general form

$$C_i = k_i t^n$$

where C_i = dissolved activity of species i at time t,
k_i = rate constant for species i,
t = reaction time, usually expressed in seconds,
and
n = exponent dependent on reaction, generally $0 < n < 1$.

We arbitrarily set $n = ½$ in plotting figure 388. Concentrations and times in figure 388 are approximate, but it is apparent that silica is released to solution at a rapid rate, chloride ion is not released after the initial stage of leaching, and the other constituents show initially rapid releases followed by slower rates. An extensive literature examines the causes of these slower rates (see, for instance, Petrović, 1976; and Siever and Woodford, 1979); it is possible that control is exercised by surface reactions at lattice defects (see Berner, 1978; Berner and Holdren, 1979) or by the rate of diffusion through a patchy, amorphous aluminosilicate layer (Paces, 1973) that is slowly dissolving.

In closed systems, C_i eventually approaches an upper value determined by equilibrium (Helgeson, 1972), but in the open systems that characterize most surface waters, "equilibrium" is a somewhat misleading concept, and C_i is likely to reflect reaction kinetics and water contact time. More extensive interpretation of reaction rates from surface-water chemistry requires laboratory study of glass dissolution and a better understanding of contact time, flow pathways, and other hydrologic factors.

FORMATION OF SECONDARY MINERALS

The amorphous alumina and silica-rich residue predicted by elemental mobility, reaction rates, and other factors noted above should crystallize to kaolinite or halloysite. In the presence of higher pH and a greater H_4SiO_4 concentration, neoformation may result in smectite. The pervasive smectite in the

debris avalanche and in other deposits probably formed in the cone of Mount St. Helens over the past few hundred to few thousand years through hydrothermal action at relatively low temperatures. It may have been concentrated in fracture systems associated with domes, particularly the summit dome and Goat Rocks. Smectite, ML chlorite-smectite, and chlorite could be forming now in the debris avalanche, and perhaps in Spirit Lake as well. Sulfur, alunite, gypsum, and other products of acid-sulfate alteration have formed within 30 cm of the surface in the oxidized zone of some rootless fumaroles, and neoformed(?) zeolite minerals are present, without acid-sulfate species, at greater depths in these fumaroles. This mineral assemblage is similar to that described by Lovering (1957) for the Valley of Ten Thousand Smokes in Alaska, and, on a minute scale, to the mineral assemblage at the active geothermal system at Steamboat Springs, Nev. (Schoen and others, 1974). There is no evidence that kaolinite-group minerals or other crystalline silicates had formed after about 150 days. Rodrique and others (1973) showed that kaolinite can be produced at ~200°C from solution in only a few weeks. However, the absence of kaolinite in the thermal ponds at Mount St. Helens (~25°C) is not surprising, as Hem and Lind (1974) have shown that crystallization of kaolinite takes several months to years at these temperatures. Furthermore, crystallization may be inhibited by the Si-Al ratio in solution by high-alkali concentrations (see Eberl and Hower, 1975), by the presence of certain forms of organic matter, or by high concentrations of sulfate and chloride ions. Subsurface temperatures at several sample sites in the pyroclastic flows remain above 200°C at present, so crystallization could be inhibited by one of the nonthermal factors.

Sparse data from older Mount St. Helens deposits and studies of alteration in other volcanic deposits permit us to speculate about mineral alteration that will occur in the new deposits. Halloysite noted by Mullineaux and Crandell (1962) in a mudflow dating to 2,000 yr B.P. may reflect acid-sulfate alteration in the cone, crystallization from allophane in the moist, acidic-weathering environment near Mount St. Helens, or possibly both. Because Ugolini and Zasoski (1979) report that halloysite forms rapidly from volcanic ash in moist environments, and there is no evidence that the halloysite was a hydrothermal mineral, we assume that the older halloysite is a product of soil-forming processes. We infer that halloysite is likely to form in the weathering zone of the 1980 deposits within a few hundred to a few thousand years. Other likely minerals include kaolinite, cristobalite or opal, and possibly vermiculite, in addition to smectite. These minerals can be expected to form in leached zones beneath organic matter that is already beginning to accumulate in some of the deposits; deeper, less weathered portions of the deposits are likely to continue to reflect the mineralogy of the parent material or its alteration products (ML chlorite-smectite and chlorite). Ferromagnesian minerals will probably weather most rapidly, followed by glass or plagioclase. (See Jackson, 1964.) Many of the highly colored encrustations present in the pyroclastic flows are quite soluble and thus ephemeral, with the exceptions of hematite and zeolites at depth, which may provide lasting mineralogic evidence of fumarolic activity. (See Lovering, 1957; Narebski and Paulo, 1973.) We would expect the most rapid mineralogic changes in the cooling portions of the pyroclastic flows, where glass devitrification will result in the formation of a feldspar and cristobalite or tridymite mixture perhaps accompanied by halloysite or kaolinite. Finally, neutral or slightly alkaline pH levels in the debris-avalanche, blast, and mudflow deposits could promote the formation of additional smectite and zeolites. However, as silica and cations are leached by the abundant precipitation of the area, clay mineralogy of the deposits will probably come to resemble that of the Silver Lake mudflow reported by Mullineaux and Crandell (1962).

SUMMARY

The mineralogy of encrustations at fumaroles, chemistry of surface water, and solution features observed by SEM study suggest that the deposits emplaced in 1980 are undergoing alteration as they cool and react with surface waters. The chemistry of waters warmed by the deposits and the results of ash-leaching experiments indicate that water reacts quite rapidly with glass, ferromagnesian minerals, and plagioclase, leaving amorphous residues rich in silicon, aluminum, and iron. With the exception of minerals at fumaroles and possibly smectite, ML chlorite-smectite, and chlorite at some warm ponds, neoformed minerals could not be detected in deposits after 150 days of alteration. Crystallization of the amorphous residue apparently proceeds slowly, even in deposits at 200°C, and may be inhibited by an ex-

cess of one or more cations, improper Si-Al ratios, abundant sulfate or chloride, or other factors.

Kaolinite formation in the new deposits is predicted by stability relations calculated for most surface waters on those deposits, while smectite stability is suggested for thermal ponds in the debris-avalanche deposit. The prevalence of trioctahedral smectite in the < 2-μm fraction of material that composed the old cone suggests that alteration occurred there at neutral to slightly alkaline pH and at temperatures of a few hundred degrees or less, perhaps localized around and in the summit and Goat Rocks domes. Opal, kaolinite, and halloysite were not found in any of the new deposits, including the debris avalanche, so areas of acid-sulfate alteration in the old cone must have had limited extent if they were present at all. However, as silica and cations are leached from the newly formed deposits during soil-forming processes, and as the pyroclastic flows undergo thermal alteration, halloysite or kaolinite will probably form. The presence of halloysite in an approximately 2,000-yr-old mudflow, noted by Mullineaux and Crandell (1962), suggests that this mineral will probably form in the new deposits within the next few hundred to few thousand years.

REFERENCES CITED

Abdel-Kader, F. H., Jackson, M. L., and Lee, G. B., 1978, Soil kaolinite, vermiculite, and chlorite identification by an improved lithium DMSO X-ray diffraction test: Soil Science Society of America Journal, v. 42, no. 1, p. 163–167.

Aomine, S., and Wada, K., 1962, Differential weathering of volcanic ash and pumice resulting in formation of hydrated halloysite: American Mineralogist, v. 47, p. 1024–1048.

Beget, J. E., 1980, Eruptive history of Glacier Peak volcano, Washington State: Geological Society of America Abstracts with Programs, v. 12, no. 7, p. 384.

Berner, R. A., 1978, Rate control of mineral dissolution under earth surface conditions: American Journal of Science, v. 278, p. 1235–1252.

Berner, R. A., and Holdren, G. R., 1979, Mechanism of feldspar weathering—II. Observations of feldspar from soils: Geochimica et Cosmochimica Acta, v. 43, p. 1173–1186.

Busenberg, Eurybiades, 1978, The products of the interaction of feldspars with aqueous solutions at 25°C: Geochimica et Cosmochimica Acta, v. 42, p. 1679–1686.

Busenberg, Eurybiades, and Clemency, C. V., 1976, The dissolution kinetics of feldspars at 25°C and 1 atm CO_2 partial pressure: Geochimica et Cosmochimica Acta, v. 40, p. 41–50.

Casadevall, T. J., Johnston, D. A., Stoiber, R. E., and Williams, S. N., 1980, SO_2 monitoring at Mount Saint Helens: Geological Society of America Abstracts with Programs, v. 12, no. 7, p. 399.

Crandell, D. R. 1971, Postglacial lahars from Mount Rainier volcano, Washington: U.S. Geological Survey Professional Paper 667, 75 p.

Crandell, D. R., and Mullineaux, D. R., 1978, Potential hazards from future eruptions of Mount St. Helens volcano, Washington: U.S. Geological Survey Bulletin 1383-C, 26 p.

Crandell, D. R., Mullineaux, D. R., and Rubin, Meyer, 1975, Mount St. Helens volcano; recent and future behavior: Science, v. 187, no. 4175, p. 438–441.

Davies, D. K., Almon, W. R., Bonis, S. B., and Hunter, B. E., 1979, Deposition and diagenesis of Tertiary-Holocene volcaniclastics, Guatemala: Society of Economic Paleontologists and Mineralogists Special Publication no. 26, p. 281–306.

Dethier, D. P., 1979, Atmospheric contributions to streamwater chemistry in the North Cascade Range, Washington: Water Resources Research, v. 15, no. 4, p. 787–794.

Dethier, D. P., Frank, David, and Pevear, D. R., 1981, Chemistry of thermal waters and mineralogy of the new deposits at Mount St. Helens—A preliminary report: U.S. Geological Survey Open-File Report 81-80, 24 p.

Dudas, M. J., and Harward, M. E., 1975a, Phyllosilicates in soils developed from Mazama ash: Soil Science Society of America Proceedings, v. 39, p. 572–577.

_____1975b, Weathering and authigenic halloysite in soil developed in Mazama ash: Soil Science Society of America Proceedings, v. 39, p. 561–571.

Eberl, Dennis, and Hower, John, 1975, Kaolinite synthesis—The role of the SiAl and (alkali)/(H^+) ratios in hydrothermal systems: Clays and Clay Minerals, v. 23, no. 4, p. 301–309.

Frank, David, 1981, Origin, distribution, and rapid removal of hydrothermally formed clay at Mount Baker, Washington: U.S. Geological Survey Professional Paper, in press.

Friedman, J. D., and Frank, David, 1977, Heat discharge from Mount St. Helens, Washington: U.S. Geological Survey Open-File Report 77-541, 29 p.

Fruchter, J. S., and others, 1980, Mount St. Helens ash from the 18 May 1980 eruption—Chemical, physical, mineralogical, and biological properties: Science, v. 209, no. 4461, p. 1116–1125.

Goff, F. E., Donnelly, J. M., Thompson, J. M., and Hearn, B. C., Jr., 1977, Geothermal prospecting in the Geysers-Clear Lake area, northern California: Geology, v. 5, p. 509–515.

Helgeson, H. C., 1969, Thermodynamics of hydrothermal systems at elevated temperatures and pressures: American Journal of Science, v. 267, p. 729–804

Helgeson, H. C., 1972, Kinetics of mass transfer among silicates and aqueous solutions; correction and clarification: Geochimica et Cosmochimica Acta, v. 36, p. 1067–1070.

Hem, J. D., and Lind, C. J., 1974, Kaolinite synthesis at 25°C: Science, v. 184, p. 1171–1173.

Hinkley, Todd, Lichte, F. E., Taylor, H. E., and Smith, K. S., 1980, Composition of ash and its leachates from Mount St. Helens: Geological Society of America Abstracts with Pro-

grams, v. 12, no. 7, p. 447.
Hoblitt, R. P., Banks, N. G., Ryan, M. P., Rosenbaum, J. G., and Davis, M. J., 1980, Emplacement temperatures of Mt. St. Helens eruptive products: Geological Society of America Abstracts and Programs, v. 12, no. 7, p. 447.
Holdren, G. R., Jr., and Berner, R. A., 1979, Mechanism of feldspar weathering—I. Experimental studies: Geochimica et Cosmochimica Acta, v. 43, p. 1161–1171.
Hooper, P. R., Herrick, I. W., and Laskowski, E. R., 1980, Mount St. Helen's ashfall on Pullman, WA, May 18–19, 1980: Geological Society of America Abstracts with Programs, v. 12, no. 7, p. 450.
Hooper, P. R., Herrick, I. W., Laskowski, E. R., and Knowles, C. R., 1980, Composition of the Mount St. Helens ashfall in the Moscow-Pullman area on 18 May 1980: Science, v. 209, p. 1125–1126.
Hyde, J. H., 1975, Upper Pleistocene pyroclastic-flow deposits and lahars south of Mount St. Helens volcano, Washington: U.S. Geological Survey Bulletin 1383-B, p. B1–B20.
Jackson, M. L., 1964, Chemical composition of soils, *in* Bear, F. E., ed., Chemistry of the soil: New York, Reinhold Publishing Corp., p. 71–141.
_____1973, Soil chemical analysis—Advanced course [2d rev. ed.]: Madison, Wis. [published by the author], 895 p.
Keith, T. E. C., and Muffler, L. J. P., 1978, Minerals produced during cooling and hydrothermal alteration of ash flow tuff from Yellowstone drill hole Y-5: Journal of Volcanology and Geothermal Research, v. 3, p. 373–402.
Klein, J. M., and Taylor, H. E., 1980, Mount St. Helens, Washington, 1980 volcanic eruption, part II, Chemical variations in surface waters affected by volcanic activity: EOS, American Geophysical Union Transactions, v. 61, no. 46, p. 956.
Korosec, M. A., Rigby, J. G., and Stoffel, K. L., 1980, The 1980 eruption of Mount St. Helens, Washington—Part 1, March 20–May 19, 1980: Washington Division of Geology and Earth Resources Information Circular no. 71, 27 p.
Lovering, T. S., 1957, Halogen-acid alteration of ash at Fumarole No. 1, Valley of Ten Thousand Smokes, Alaska: Geological Society of America Bulletin, v. 68, p. 1585–1604.
Mullineaux, D. R., 1974, Pumice and other pyroclastic deposits in Mount Rainier National Park, Washington: U.S. Geological Survey Bulletin 1326, 83 p.
Mullineaux, D. R., and Crandell, D. R., 1962, Recent lahars from Mount St. Helens, Washington: Geological Society of America Bulletin, v. 73, no. 7, p. 855–870.
Mullineaux, D. R., Hyde, J. H., and Rubin, Meyer, 1975, Widespread late glacial and postglacial tephra deposits from Mount St. Helens volcano, Washington: U.S. Geological Survey Journal of Research, v. 3, p. 329–335.
Narebski, Wojcieche, and Paulo, Andrzej, 1973, Solfataric alteration products of andesitic lavas in the crater of Cotopaxi volcano, Ecuador: Mineralogia Polonica, v. 4, p. 67–80.
Paces, Tomas, 1973, Steady state kinetics and equilibrium between ground water and granitic rock: Geochimica et Cosmochimica Acta, v. 37, p. 2641–2663.
Petrovic, Radomir, 1976, Rate control in feldspar dissolution—II., The protective effect of precipitates: Geochimica et Cosmochimica Acta, v. 40, p. 1509–1522.
Phillips, K. N., 1941, Fumaroles of Mount St. Helens and Mount Adams: Mazama, v. 23, p. 37–42.
Rodrique, L., Poncelet, G., and Herbillon, A., 1973, Importance of the silica subtraction process during hydrothermal kaolinitization of amorphous silico-aluminas: International Clay Conference, 4th, Madrid 1972, Proceedings: Madrid, Division de Ciencias C.S.I.C., p. 187–198.
Saigusa, Masahiko, Shoji, Sadao, and Kato, Tatsuto, 1978, Origin and nature of halloysite in Ando soils from Towada tephra, Japan: Geoderma, v. 20, p. 115–129.
Sarna-Wojcicki, A. M., and Waitt, R. B., Jr., 1980, Areal distribution, thickness, and composition of volcanic ash erupted from Mount St. Helens on May 18, 1980: Geological Society of America Abstracts with Programs, v. 12, no. 7, p. 515.
Schoen, Robert, White, D. E., and Hemley, J. J., 1974, Argillization by descending acid at Steamboat Springs, Nevada: Clays and Clay Minerals, v. 22, p. 1–22.
Siever, Raymond, and Woodford, Norma, 1979, Dissolution kinetics and the weathering of mafic minerals: Geochimica et Cosmochimica Acta, v. 43, p. 717–724.
Skougstad, M. W., Fishman, M. J., Friedman, L. C., Erdmann, D. E., and Duncan, S. S., eds., 1978, Methods for analysis of inorganic substances in water and fluvial sediments: U.S. Geological Survey Open-File Report 78–679, 1006 p.
Smith, R. L., 1960, Ash flows: Geological Society of America Bulletin, v. 71, p. 795–842.
Sorey, M. L., Lewis, R. E., and Olmsted, F. H., 1978, The hydrothermal system of Long Valley caldera, California: U.S. Geological Survey Professional Paper 1044-A, 60 p.
Stumm, Werner, and Morgan, J. J., 1970, Aquatic chemistry—An introduction emphasizing chemical equilibria in natural waters: New York and London, Wiley-Interscience, 583 p.
Tardy, Yves, 1971, Characterization of the principal weathering types by the geochemistry of waters from some European and African crystalline massifs: Chemical Geology, v. 7, p. 253–271.
Ugolini, F. C., and Zasoski, R. J., 1979, Soils derived from tephra, *in* Sheets, P. D., and Grayson, D. K., eds., Volcanic activity and human ecology: New York, Academic Press, p. 83–124.
Verhoogen, Jean, 1937, Mount St. Helens, a recent Cascade volcano: California University Department of Geological Science Bulletin, v. 24, no. 9, p. 263–302.
Wada, Koji, 1977, Allophane and imogolite, *in* Dixon, J. B., and Weed, S. B., eds., Minerals in soil environments: Madison, Wis., Soil Science Society of America, p. 603–638.
White, A. F., and Claassen, H. C., 1980, Kinetic model for the short-term dissolution of a rhyolitic glass: Chemical Geology, v. 28, p. 91–109.
Wollenberg, H. A., Bowen, R. E., Bowman, H. R., and Strisower, B., 1979, Chemical studies of rocks, water, and gases at Mt. Hood, Oregon: Oregon Department of Geology and Mineral Industries Open-File Report 0-79-2, 57 p.
Zachara, John, 1979, Clay genesis and alteration in two tephritic subalpine podzols of the central Cascades, Washington: Seattle, University of Washington College of Forest Resources M.S. thesis, 81 p.

THE 1980 ERUPTIONS OF MOUNT ST. HELENS, WASHINGTON

COMPOSITION OF AIR-FALL ASH ERUPTED ON MAY 18, MAY 25, JUNE 12, JULY 22, AND AUGUST 7

By ANDREI M. SARNA-WOJCICKI, CHARLES E. MEYER, MARTA J. WOODWARD, *and* PAUL J. LAMOTHE

ABSTRACT

A high content of heterogeneous lithic fragments at proximal sites in the basal layer (layer A3) of air-fall ash from the May 18 eruption of Mount St. Helens supports the hypothesis that this layer was largely derived from disintegration of older rocks that formed the upper part of the pre-1980 volcano. Poorly vesiculated pumice and sparse white pumice lapilli in this unit mark the first appearance of juvenile material. Abundant coarse pumice in the overlying unit B correlates with the appearance of abundant juvenile material in the vertical eruptive column. The basal part of unit B (layer B1) is the least silicic, while the uppermost part (layer B4) is the most silicic of the proximal tephra. At distal downwind areas, a basal, thin, dark ash (unit 1) correlates with the basal layer A3 of proximal sites, while an overlying thicker, light-colored layer (unit 2) correlates with unit B, based on petrographic characteristics and chemistry. Downwind, the bulk chemical composition of air-fall ash increases in silica, potassium, rubidium, and zirconium and decreases in aluminum, calcium, and titanium, apparently because the denser, coarser lithic and crystal clasts settle out close to the volcano, leading to a relative enrichment of pumice and glass shards farther downwind.

The bulk chemical compositions of air-fall ash from the first five magmatic eruptions of 1980 are similar and do not show any obvious trends. Furthermore, there is no obvious difference in composition between the May 18 air-fall pumice and that of several previous major eruptions of Mount St. Helens. Glass composition of pumice from the May 18 eruption is most similar to that of layer T (the youngest of the major pre-1980 silicic tephra deposits of Mount St. Helens): both have more iron, manganese, calcium, and titanium and less silica and potassium than is found in older tephra beds. The major-, minor-, and trace-element compositions of glass from each of the major eruptive episodes of Mount St. Helens are distinctive, making it possible to distinguish between them on the basis of glass chemistry.

Compared to average crustal composition, proximal and distal tephra from the first four magmatic eruptions of 1980 are enriched in silica, aluminum, sodium, chlorine, scandium, gallium, and cesium; concentrations of all other elements analyzed are similar to or below the average values.

INTRODUCTION

The eruptions of May 18, May 25, June 12, July 22, and August 7, 1980, have provided us with an outstanding opportunity to study the chemical variability of air-fall ash deposits as a function of emplacement time and distance from the source. Air-fall tephra from these eruptions is made up of three main components—pumice, lithic fragments, and mineral grains—at both proximal and distal sites, although the proportions of these components vary widely. Each component may be drawn from two different sources: juvenile material, solidified from molten magma erupted from the volcano, and accidental material derived through disintegration of older rocks that previously formed part of the mountain. The pumice fraction (with its associated glass shards) is predominantly juvenile; a small proportion of this component in some of the air-fall ash deposits (especially basal layer A3), however, may originate in older pumice layers. The lithic fragments are largely

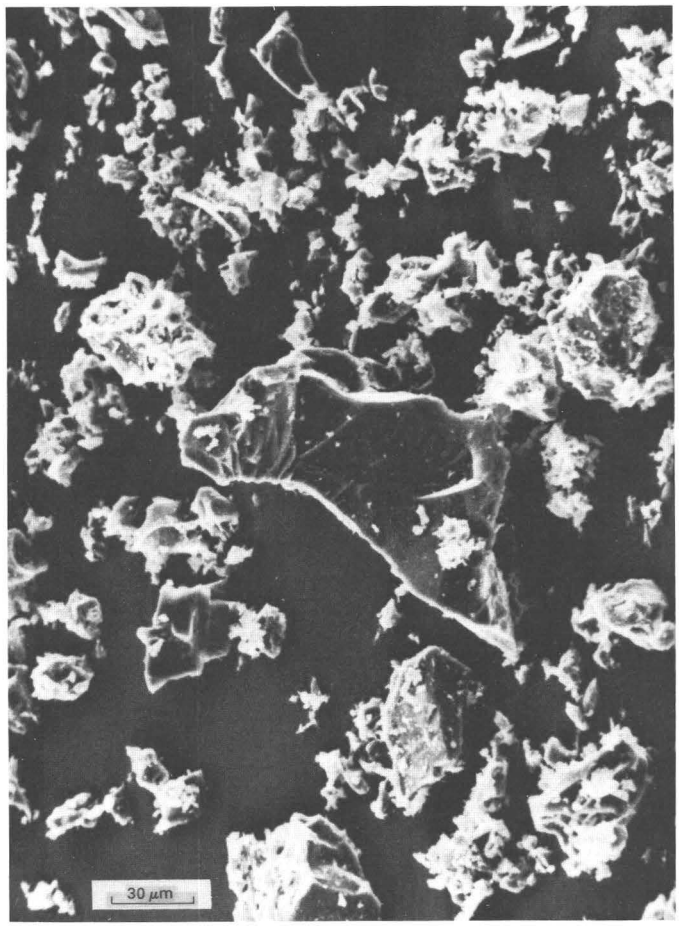

Figure 389.—Unsized May 18 ash collected at Moscow, Idaho. SEM photograph by Robert Oscarson.

Figure 390.—Portion of a glass shard in unsized May 18 ash, showing broken vesicle wall and adhering fine material. Many fragments are less than 1 μm across. SEM photograph by Robert Oscarson.

accidental; some may have been derived, however, from the crystallizing outer margin of the magma chamber or cryptodome intruded into the volcano before eruption (Moore and Albee, this volume). Unattached crystals and mineral fragments have been derived both from the older rocks and from the crystallizing magma; consequently, they are both magmatic and accidental in origin.

The proportions of these three main components, their respective particle sizes, and the ash stratigraphy formed at any particular downwind site result from the complex interaction of several physical-temporal variables. Most significant among these variables are (1) the composition of the magma, (2) the explosiveness of the eruption, (3) the nature of the rock making up the volcanic edifice, and (4) the wind speeds and directions at different altitudes above the volcano and the surrounding terrain. Actual deposition is controlled by these variables, by the way they change with time, and by the distance downwind from the volcano at which the ash falls out. Because of these factors, the relative proportions of the three components differ considerably from site to site. Because these components have different chemical compositions and because the composition of an individual component may change with time during the eruption, the chemical compositions of bulk ash samples vary considerably with location and with stratigraphy at each site.

ACKNOWLEDGMENTS

We appreciate the efforts of many people in the U.S. Geological Survey and in several other organiza-

tions, which have made this report possible. Some of the samples and (or) sample data were provided by S. H. Wood (Boise State Univ.), J. O. Davis (Desert Research Inst., Univ. Nevada), Thomas Bateridge (Geoservices West, Missoula, Mont.), James Beget (Univ. Washington), and P. R. Hooper (Washington State Univ.). Instrumental neutron activation analyses (table 82) were performed by Frank Asaro and Helen Michael (Lawrence Berkeley Laboratory).

Those within the USGS who provided samples or information about Mount St. Helens tephra include D. R. Mullineaux, R. B. Waitt, Jr., Daniel Dzurisin, M. P. Doukas, R. P. Hoblitt, and F. K. Miller. Tephra analyses were made by V. G. Mossotti, T. W. Holmes, S. D. Ramage, J. F. Carr, T. L. Fries, and Chris Heropoulos, all USGS. Robert Oscarson made SEM photos of the ash, and Jose Rivera made density separations. Susan Shipley helped with preparation of the manuscript, and Jane Pike and Wendell Duffield improved the manuscript through many helpful suggestions.

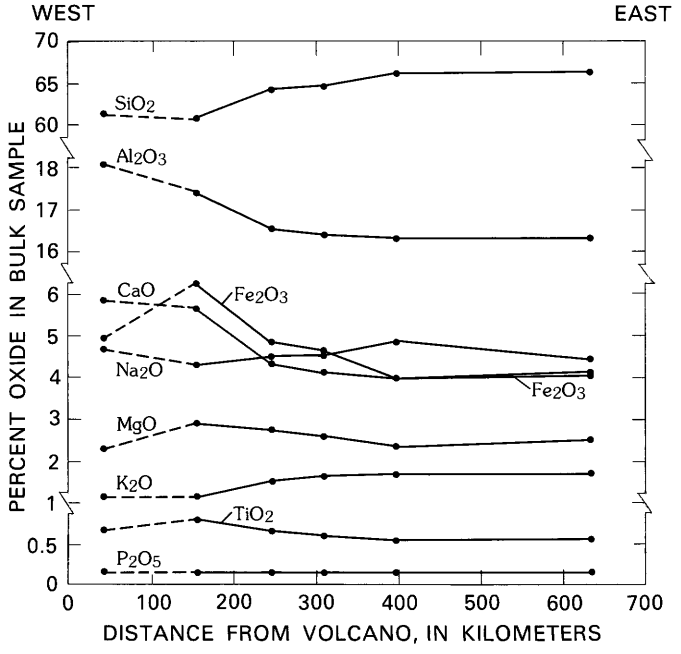

Figure 391.—Downwind variation in composition of bulk samples of air-fall ash. Dashed lines, trends based on weighted average for four samples from most proximal site. Wavelength-dispersive X-ray fluorescence analyses by V. G. Mossotti, Chris Heropoulos, and J. F. Carr.

ERUPTION OF MAY 18

PROXIMAL TEPHRA

The major air-fall ash units within the proximal area (units A through D; Waitt and Dzurisin, this volume, figs. 354, 357, and 359) differ from each other in petrography and bulk chemical composition. Samples of layer A3 and units B and D (stratigraphic terminology of Waitt and Dzurisin, this volume, figs. 354, 357, and 359) were examined under binocular and petrographic microscopes to determine the proportions of their components. We had difficulty in making modal counts because of the large size variation in each unit. Small particles, for instance, would adhere to larger ones, making grain identifications difficult or impossible. Samples were sieved through a 40-μm mesh, and the coarser fraction was separated in liquids with densities of 2.5 and 2.8 g/cm^3. The resulting three separates of the coarser fraction were

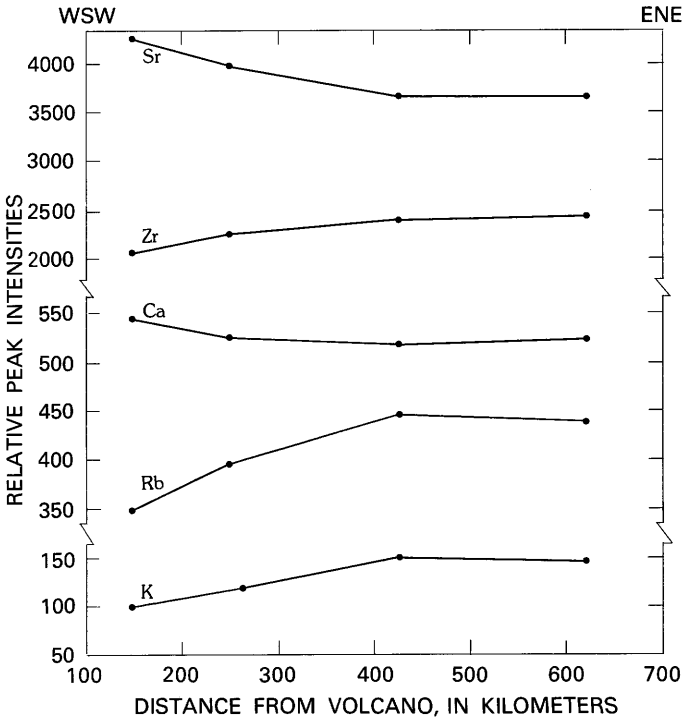

Figure 392.—Downwind variation of selected elements in bulk samples of air-fall ash. Relative peak intensity based on ratio of counts at peak energy level for each element compared to total counts in spectral region (window) studied. Each dot represents average value for several samples at an average distance from volcano. Energy-dispersive X-ray fluorescence analyses by M. J. Woodward.

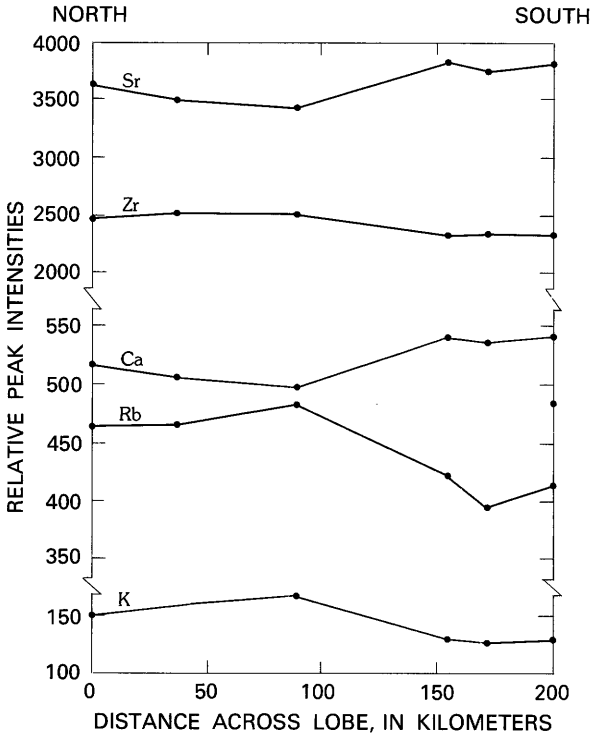

Figure 393.—Bulk compositional variation for selected elements across ash lobe along north-south traverse through Missoula, Mont. Relative peak intensity based on ratio of counts at peak energy level for each element compared to total counts in spectral region (window) studied. Energy-dispersive X-ray fluorescence analyses by M. J. Woodward.

then examined and visual estimates of the major components were made. The amounts of glass and pumice shards, crystals, and crystal fragments, which make up the bulk of material finer than 40 μm, are probably underestimated, but the estimates are roughly representative of the physical composition of each unit.

At proximal downwind sites northeast of the volcano (Waitt and Dzurisin, this volume, figs. 354, 357, and 359), the lowermost layer (layer A3), is generally silt to medium sand sized and dark gray in color. This layer, texturally an accretionary lapilli ash, composes about 10 to 15 percent of the total thickness of air-fall material and has a bulk density of about 1.1 to 1.2 g/cm³. Amounts of the following components were estimated by visual inspection of the coarse (> 40-μm) fraction:

Component	Percent
Density less than 2.5 g/cm³	
Bluish-gray, poorly vesiculated, porphyritic dacitic pumice	12
White to grayish-white, moderately well vesiculated pumice	5
Black, glassy scoria, light-gray lithic fragments, and minor carbonized or charred wood and plant fragments	6
Density 2.5 to 2.8 g/cm³	
Lithic fragments of various types of volcanic rocks, from light gray (dacitic?) to dark gray, brown, or black (andesitic and basaltic?)	42
Plagioclase feldspar crystals and crystal fragments	28
Density greater than 2.8 g/cm³	
Denser dark-brown to black lithic fragments (basaltic?)	2
Mafic crystals and crystal fragments, dominantly hypersthene, hornblende, ilmenite, magnetite, minor limonite(?), and clinopyroxene	6

In proximal areas, unit B, the next youngest, consists of pumice lapilli, lithic lapilli, and crystals. The lower part of this unit (layer B1) is rich in coarse lithic fragments associated with finer pumice lapilli; the mixture of darker lithic fragments and light-gray to white pumice lapilli gives it a "salt-and-pepper" appearance. Upwards in this unit (layers B2, B3, and B4 of Waitt and Dzurisin, this volume, figs. 354, 357, and 359), pumice lapilli coarsen and increase in abundance, while lithic fragments decrease in size and abundance. Layers B2 and B3 are light grayish white, whereas layer B4 is light brown or tan, owing to a coating of fine, tan to light-brown glass on the larger grains. Within a few tens of kilometers downwind from the volcano, the upper layers of unit B (layers B2, B3, and B4) merge, and only a twofold unit is recognized (fig. 339). This unit comprises about 60 to 70 percent of the total thickness of air-fall material and has a bulk density of about 0.9 to 1.0 g/cm³. About 42 km downwind to the northeast, the lower part of unit B (dominantly layers B1 and B2) consists of the following components (estimated by visual inspection of the > 40-μm fraction):

Component	Percent
Density less than 2.5 g/cm³	
Coarse, white to light-grayish-white, poorly to moderately well vesiculated, porphyritic pumice	28
Density 2.5 to 2.8 g/cm³	
Lithic fragments of various types of volcanic rocks, as in layer A3	32
Plagioclase feldspar crystals and crystal fragments	32
Density greater than 2.8	
Denser dark-brown to black lithic fragments	4
Mafic crystals and crystal fragments, as in layer A3	4

This lower part is overlain by layer B4 and a thin coating of unit C; the following composition is for these upper layers combined:

Component	Percent
Density less than 2.5 g/cm³	
Light-brown to tan, moderately well to well vesiculated pumice lapilli	19
Density 2.5 to 2.8 g/cm³	
Light to dark lithic fragments, as in layer A3	25
Plagioclase feldspar crystals and crystal fragments	42
Density greater than 2.8 g/cm³	
Dark-brown to black lithic fragments	7
Mafic crystals and crystal fragments, as in layer A3	7

Unit C, the next-to-highest unit in the air-fall layer, like the uppermost unit D, is thin and is present only within about 50 to 100 km downwind of the volcano (figs. 354, 357, and 359; fig. 339). Unit C, a silt- to medium-sand-sized ash, consists of glass and pumice shards, together with fine lithic fragments and crystals. This unit is light brown to tan in color. It makes up only about 3–5 percent of total air-fall material. Beyond several tens of kilometers downwind, unit C merges with unit B and cannot be distinguished as a separate layer. No separate analyses of unit C were made.

Unit D, the uppermost air-fall layer erupted on May 18, is a fine, gray, silt- to medium-sand-sized ash. It constitutes about 10–12 percent of the total thickness of air-fall tephra in the proximal downwind areas and has a density of about 1.1 to 1.2 g/cm³. It has the following components (estimated by visual inspection of the coarse (> 40-μm) fraction):

Component	Percent
Density less than 2.5 g/cm³	
Fine pumice and glass shards, clear to microlitic or microporphyritic; some orange glass; a few large pumice shards 1 to 2 mm in diameter	25
Density 2.5 to 2.8 g/cm³	
Lithic fragments, as in layer A3; reddish-brown, altered lithic fragments	25
Plagioclase feldspar crystals and crystal fragments	42
Density greater than 2.8 g/cm³	
Dark-brown to black lithic fragments; altered, dense, red to reddish-brown lithic fragments	1
Mafic crystals and crystal fragments, as in layer A3	7

The chemical composition of layer A3 (table 80, sample 1) is like that of the basic dacite or silicic andesite that formed the former summit dome (table 83, sample 9). The abundance of lithic fragments (42 percent) and plagioclase feldspar crystals (28 percent) supports the suggestion that unit A3 is largely composed of accidental material from the disintegration of older rocks that made up the upper part of the volcano. The poorly vesiculated, bluish-gray pumice (12 percent) in the lighter fraction, however, probably represents juvenile material from the preeruption

Table 80.—Chemical analyses of tephra of the

[Data in percent. Analysis No. 7 is of a pumice clast, and Nos. 8 and 17 are analyses of separated volcanic glass; all other analyses are of total bulk fluorescence, V. G. Mossotti, T. W. Holmes,

No.	Description	Distance (km) and direction from volcano	Locality	Collector
		Proximal tephra		
1	Thin, basal lithic-crystal ash (layer A3)	42 NE.	23 km SSW. of Packwood, Wash.	R. B. Waitt, Jr.
2	Thick, coarse, pumice-lithic-crystal ash (layers B1 and B2 combined).	42 NE.	-----do----------	---do----------
3	Medium-grained pumice-lithic-crystal ash (B4, with small amount of unit C).	42 NE.	-----do----------	---do----------
4	Thin, uppermost, fine lithic-crystal-vitric ash (unit D).	42 NE.	-----do----------	---do----------
5	Average of 1-4, weighted according to relative thickness and density.	42 NE.	-----do----------	---do----------
6	Thin, fine, lithic-crystal ash----------	52 E.	Mount Adams----------	Hikers----------
7	Pumice clast from coarse pumice-lithic-crystal ash (unit B2)----------	18 NE.	16 km S. of Cispus River-----	R. B. Waitt, Jr.
8	Glass from sample 7----------	18 NE.	-----do----------	---do----------
		Distal tephra		
9	Ash from axis of downwind lobe----------	154 ENE.	27 km NE. of Yakima, Wash.---	Daniel Dzurisin
10	Ash from near axis of downwind lobe------	248 ENE.	16 km SE. of Moses Lake, Wash.	---do----------
11	Ash, 38 km S. of lobe axis----------	305 ENE.	38 km S. of Ritzville, Wash.-	J. O. Davis-----
12	Ash, 8 km S. of lobe axis----------	308 ENE.	8 km S. of Ritzville, Wash.--	---do----------
13	Ash, 14 km N. of lobe axis----------	320 ENE.	14 km NE. of Ritzville, Wash.	---do----------
14	Ash, 54 km S. of lobe axis----------	400 E.	Moscow, Idaho----------	S. H. Wood------
15	Ash, 10 km S. of lobe axis----------	420 ENE.	47 km N. of Moscow, Idaho----	---do----------
16	Ash from axis of downwind lobe---------	632 E.	23 km N. of Missoula, Mont---	Thomas Bateridge
17	Glass from sample 14----------	400 E.	Moscow, Idaho----------	S. H. Wood------

cryptodome (Moore and Albee, this volume). This material is uniform in color, texture, and density, so it probably is not accidental older rock. The light-colored pumice in layer A3 (5 percent) marks the first appearance of moderately well vesiculated juvenile pumice—this material matches the composition and physical appearance of juvenile pumice in unit B, as determined by energy-dispersive X-ray fluorescence analysis (M. J. Woodward, oral commun., 1981).

A thin, fine, lithic-crystal-vitric ash collected on Mount Adams by hikers shortly after the beginning of the May 18 eruption (table 80, sample 6) is identical to layer A3 (sample 1) and undoubtedly represents the same unit. Both samples contain charred pine and fir needles and other fine plant particles. These were derived from the destruction of vegetation during the initial lateral blast and subsequently were incorporated into the vertical plume by convection. The analyses of these two samples have lower totals than those of other proximal samples, perhaps reflecting a higher carbon content.

The lowest occurrence of pumice lapilli in unit B, which overlies layer A3, correlates with the first appearance of large amounts of juvenile pumice in the eruptive column. Although the pumice constitutes about 50 percent of the sample by volume, it accounts for only 28 percent of the total by weight. The large percentages of lithic fragments (32 percent) and plagioclase feldspar (32 percent) may be the cause of the more mafic, andesitic composition of the bulk sample (table 80, sample 2). Juvenile material in unit B is more silicic than the bulk composition; an analysis of a pumice clast from unit B (table 80, sample 7) indicates it is dacitic in composition. Glass separated from the pumice (table 80, sample 8) is the most silicic component of the juvenile ash; it also has the highest potassium content but is depleted in the other major and minor elements.

The bulk composition of layer B4 (including a small amount of unit C; table 80, sample 3) is the most silicic of all the proximal-sample compositions. Layer B4 and unit C both have high proportions of fine glass

May 18, 1980, eruption of Mount St. Helens

sample. Nos. 8 and 17 were analyzed by electron microprobe, C. E. Meyer, analyst; all other analyses were by wavelength-dispersive X-ray and S. D. Ramage, analysts; ---, not determined]

SiO_2	Al_2O_3	Fe_2O_3	MgO	CaO	Na_2O	K_2O	TiO_2	P_2O_5	MnO	Cl	ZrO_2	Cr_2O_3	NiO	BaO	SrO	Total
							Proximal tephra									
61.53	17.18	5.46	2.44	5.41	4.67	1.39	0.74	0.20	0.07	---	---	---	---	---	---	99.10
59.69	19.54	4.60	2.33	6.60	4.83	1.02	.64	.13	.06	---	---	---	---	---	---	99.46
64.17	17.07	4.68	2.21	5.12	4.33	1.06	.64	.13	.06	---	---	---	---	---	---	99.50
62.11	17.57	5.05	2.14	5.40	4.74	1.35	.73	.18	.07	---	---	---	---	---	---	99.34
60.39	18.89	4.77	2.31	6.24	4.78	1.11	.67	.15	.06	---	---	---	---	---	---	99.37
61.75	17.18	5.39	2.42	5.38	4.64	1.37	.75	.18	.07	---	---	---	---	---	---	99.13
62.56	18.12	4.57	2.02	5.41	4.68	1.23	.62	.13	.06	---	---	---	---	---	---	99.43
71.37	15.09	2.57	.49	2.76	4.30	1.94	.44	---	.06	.10	---	---	---	---	---	98.98
							Distal tephra									
60.96	17.48	6.28	2.90	5.68	4.32	1.18	0.82	0.17	0.09	---	0.019	<0.002	0.002	0.025	0.062	99.99
65.21	16.52	4.87	1.79	4.39	4.47	1.55	.68	.16	.07	---	.022	< .002	<.001	.036	.050	99.82
65.27	16.65	4.64	1.86	4.47	4.49	1.59	.66	.16	.06	---	.021	< .002	.002	.036	.050	99.94
65.97	16.12	4.14	1.48	3.99	4.82	1.66	.58	.15	.06	---	.021	< .002	<.001	.039	.047	99.07
65.94	16.43	4.16	1.48	4.04	4.45	1.67	.59	.15	.07	---	.021	< .002	<.001	.038	.048	99.08
65.83	16.43	4.02	1.35	4.07	5.13	1.68	.56	.15	.06	---	---	---	---	---	---	99.28
66.72	16.23	3.96	1.40	3.95	4.63	1.72	.55	.14	.06	---	.022	< .002	<.001	.039	.046	99.46
66.45	16.34	4.05	1.55	4.13	4.42	1.68	.56	.16	.06	---	.024	< .002	.0015	.040	.046	99.51
71.47	14.99	2.48	.52	2.32	4.68	2.03	.37	---	.05	.09	---	---	---	---	---	99.00

and pumice shards, not reflected in the modal estimates given above for the coarse fraction, which may explain why they have higher silica contents than the lower part of unit B.

Unit D, the uppermost layer (table 80, sample 4) is most similar in bulk composition to layer A3 (table 80, sample 1) and to pumice from the lower part of unit B (table 80, sample 7). This unit has a high percentage of fine glass and pumice shards, but also a high percentage of crystal fragments, both plagioclase feldspar and mafic minerals. This layer represents the waning period of the May 18 eruption.

DISTAL TEPHRA

Samples of downwind ash were examined by means of a petrographic microscope, a scanning electron microscope with an attached EDAX energy-dispersive X-ray spectrometer, and an X-ray diffractometer.

A typical distal ash sample from the May 18 eruption (collected at Moscow, Idaho) consisted of a dark basal layer about 1 mm thick (unit 1) and a thicker, light-gray to tan upper layer (unit 3) about 3 mm thick (Sarna-Wojcicki, Shipley, and others, this volume). In order of decreasing abundance, the dark ash was composed of fine glass and pumice shards, plagioclase feldspar grains, colorless lithic grains containing microphenocrysts in a glassy groundmass, brownish dusty to nearly opaque lithic grains, hypersthene, hornblende, brown glass, isotropic orange to yellow grains (altered glass?), opaque grains (titanomagnetite and ilmenite, according to electron microprobe analyses), rare clinopyroxene, and charred or carbonized plant fragments. The upper ash layer, again in order of decreasing abundance, was composed of clear glass in the form of bubble-wall and bubble-wall-junction shards, plagioclase feldspar fragments and cleavage flakes, colorless pumiceous shards with spindle-shaped or tubular vesicles (figs. 389, 390), microlitic lithic fragments with glassy groundmass (like

Table 81.—Compositions of May 18 volcanic glass samples, showing variation downwind, compared to compositions of May 18 bulk ash, older glass samples from Mount St. Helens, and standard granite

[Analyses by energy-dispersive X-ray fluorescence, Marta J. Woodward, analyst. Values given are integrated peak intensities divided by total counts in each of two spectral regions (windows)]

No.	Description	Distance from volcano (km)	$K_{k\alpha}$	$Ca_{k\alpha}$	$Ca_{k\beta}$	$Ti_{k\alpha}$	$Mn_{k\alpha}$	$Fe_{k\alpha}$	$Fe_{k\beta}$	$Rb_{k\alpha}$	$Sr_{k\alpha}$	$Y_{k\alpha}$	$Zr_{k\alpha}$
						May 18 glass samples							
1	Glass from sample 10, table 80	248	239	444	80	177	115	6,188	1,000	590	2,694	406	2,701
2	Glass from sample 11, table 80	305	236	439	80	169	112	6,115	981	622	2,702	413	2,722
3	Glass from sample 12, table 80	308	233	441	83	180	114	6,198	994	574	2,816	399	2,697
4	Glass from sample 13, table 80	320	233	448	78	177	114	6,182	998	602	2,711	419	2,625
5	Glass from sample 15, table 80	420	234	438	79	173	114	6,191	1,003	597	2,785	421	2,730
6	Glass from sample 14, table 80	400	234	438	77	173	111	6,211	999	605	2,826	411	2,850
7	Glass from sample 16, table 80	632	239	441	77	171	111	6,116	991	601	2,652	427	2,707
8	Glass from sample 7, table 80	18	234	437	77	173	113	6,195	1,011	600	2,831	410	2,834
	Average		235	441	79	174	113	6,175	997	599	2,752	413	2,733
	Sample standard deviation		±2	±4	±2	±4	±2	±37	±9	±14	±70	±9	,±74
						Comparative compositions							
9	Layer T glass (~180 years old)[1]	8	174	427	76	170	121	6,320	1,016	541	2,813	412	2,422
10	Layer Pm glass (~2,400-3,000 years old)[1]	8	391	523	92	168	140	5,859	954	682	2,875	400	2,562
11	Bulk ash from dark basal layer (table 80, sample 14)	400	132	542	95	176	95	6,286	1,023	393	3,789	355	2,342
12	Bulk ash from light upper layer (table 80, sample 14)	400	175	494	86	172	103	6,265	1,017	489	3,464	358	2,583
13	Granite; USGS standard rock G-1 (Flanagan, 1973)		1,040	440	73	211	86	5,264	836	1 527	2,043	513	2,429

[1]From pumice-lapilli-lithic ash collected by D. R. Mullineaux, A. M. Sarna-Wojcicki, and R. B. Waitt, Jr., 1977.

those observed in the dark ash layer but not as abundant), hypersthene, light-green to brown hornblende, opaque minerals (again, titanomagnetite and ilmenite), oxyhornblende, and clinopyroxene. No porphyritic crystalline silica phase was detected under the electron microscope, although small amounts of quartz were detected by X-ray diffraction. Glass and pumice shards composed perhaps 60–70 percent of the sample in the upper layer (unit 3), but were much less abundant, perhaps about 30–40 percent, in the lower layer (unit 1). We made density separations of both the dark- (unit 1) and light- (unit 3) colored ash using samples collected at Pullman, Wash., by P. R. Hooper. We centrifuged ash samples in liquids with densities of 2.5 and 2.8 g/cm³. The dark ash contained 26 percent material lighter than 2.5 g/cm³ (dominantly volcanic glass shards), 67 percent material between 2.5 and 2.8 g/cm³ (dominantly plagioclase feldspar and lithic grains), and 7 percent material heavier than 2.8 g/cm³ (mafic minerals and lithic fragments). By comparison, these fractions in the light-colored ash were 80, 16, and 4 percent, respectively.

At downwind locations 200 km or more east-northeast of Mount St. Helens, only the two layers of ash are distinguished, and at distances of about 600 km or more, only a single thin layer (Sarna-Wojcicki, Shipley, and others, this volume). The lower layer (unit 1) at distal locations is less silicic than the upper layer (unit 3) (Hooper and others, 1980). The lower layer also contains less potassium, rubidium, and zirconium but more strontium than the upper layer (table 81, samples 11 and 12).

Unit 1 is correlated with proximal layer A3, though it contains some early-settling coarser lithic fragments from layer B1. Samples of the lower layer have a bimodal grain-size distribution, with a secondary mode representing coarser lithic fragments and feldspar grains probably derived from B1. Unit 3 is correlated with unit B, though it has some fine material from units C and D, and possibly layer A3 as well

(Sarna-Wojcicki, Shipley, and others, this volume, fig. 339).

The ash at distal, downwind areas was fine grained and poorly sorted (fig. 389). For instance, at Moscow, Idaho, maximum grain diameters were in the 120–150 μm range. (See also Sarna-Wojcicki, Shipley, and others, this volume.) There was an abundance of finer material as small as a fraction of a micrometer, but most grains finer than about 1–2 μm were adhering to the larger grains (fig. 390). All grains larger than about one-quarter of a micrometer (the smallest observed) were angular and anhedral.

VARIATIONS IN DISTAL TEPHRA COMPOSITION

To facilitate comparison of the proximal ash with finer, inseparable distal ash samples, we calculated a representative average composition of the air-fall ash at the locality 42 km northeast of Mount St. Helens,

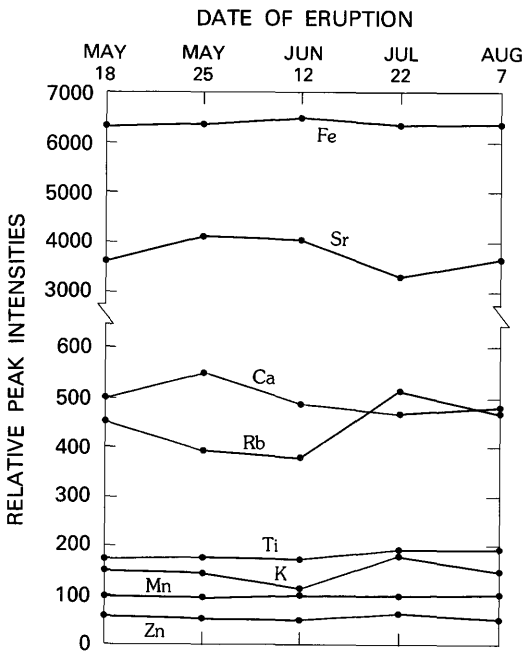

Figure 394.—Compositional variation for selected elements in bulk air-fall ash of the major eruptions of May 18, May 25, June 12, July 22, and August 7. Relative peak intensity based on ratio of counts at peak energy level for each element compared to total counts in spectral region (window) studied. Energy-dispersive X-ray fluorescence analyses by M. J. Woodward.

Table 82.—Instrumental neutron activation analyses for a number of major, minor, and trace elements in glass and bulk samples of May 18 air-fall ash

[Analyses by Frank Asaro and Helen Michael, Lawrence Berkeley Laboratory. ---, not calculated]

Element	May 18 air-fall deposits				Average analytical error	Average for crustal rock[3]
	Glass		Bulk ash[2]			
	Proximal[1]	Distal[2]	Split 1	Split 2		
	Data in percent					
Na	3.86	3.80	3.81	3.77	±0.08	2.83
Al	7.75	7.29	8.87	8.45	±.13	8.13
Cl	.16	<.34	.13	.14	±.05	.02
K	1.49	1.71	.96	1.31	±.24	2.59
Ca	1.9	1.6	3.3	3.1	±:6	3.63
Ti	.17	.15	.36	.46	±.05	.44
Fe	1.77	1.67	2.84	2.75	±.04	5.00
	Data in parts per million					
Sc	5.24	4.97	8.30	8.25	±0.07	5
V	38	41	98	64	±19	110
Cr	<1.3	<1.3	9.8	9.3	±.7	200
Mn	405	389	519	516	±9	1,000
Co	4.2	4.0	9.4	9.1	±.2	23
Ni	<8	<8	<11	14	±6	80
Zn	38	33	38	35	±3	65
As	<3.3	<5	<6	<5	---	2
Rb	54	50	49	49	±4	120
Mo	<1.3	1.5	<3.0	<2.7	±.4	1
Cs	2.36	2.23	1.72	1.93	±.09	1
Ba	446	427	402	404	±18	400
La	15.6	13.6	12.8	12.4	±.5	18
Ce	34.0	33.4	31.9	32.7	±.6	46
Nd	16.2	15.3	18.6	16.6	±.8	24
Sm	2.86	2.71	2.72	2.73	±.02	7
Eu	.76	.73	.95	.93	±.01	1
Tb	.38	.38	.41	.42	±.02	.9
Dy	2.3	2.0	2.5	2.7	±.1	5
Yb	1.34	1.28	1.40	1.37	±.02	3
Lu	.21	.19	.21	.22	±.01	.8
Hf	4.82	4.44	4.17	4.31	±.06	5
Ta	.381	.364	.419	.409	±.004	2
W	2.0	<1.3	<.84	<.49	±.5	1
Ir	<.002	<.003	<.002	<.002	---	.001
Au	<.012	<.014	<.031	<.021	---	.005
Th	4.01	3.68	3.27	3.31	±.04	10
U	1.52	1.48	1.21	1.18	±.03	2

[1]From proximal sample of May 18 air-fall pumice collected 42 km NE. of Mount St. Helens by R. B. Waitt, Jr.

[2]From distal sample of May 18 air-fall ash collected at Moscow, Idaho, by S. H. Wood.

[3]From Mason (1958).

where layer A3 and units B through D were sampled. We first calculated the bulk density of compacted samples from each of the four units by weighing equal volumes of each, then multiplied each by the thickness of the layer. The resulting values were normalized and used as weighting factors in calculating an average composition of proximal air-fall ash (table 80, No. 5).

The proportion of fine pumice and glass shards in-

Table 83.—Chemical analyses of tephra of May 18, May 25, June 12, and July 22 eruptions compared

[Samples 1-7, wavelength-dispersive X-ray fluorescence analyses by V. G. Mossotti, J. F. Carr, and T. W. Holmes. Samples 8 and 9 by wet-

No.	Description	Distance (km) and direction from volcano	Locality	Collector	SiO_2
1	Weighted average of proximal May 18 air-fall ash (table 80, No. 5).	42 NE.	23 km SSW. of Packwood, Wash.	R. B. Waitt, Jr.	60.39
2	Most silicic distal May 18 ash sample (table 80, No. 15).	420 ENE.	47 km N. of Moscow, Idaho----	S. H. Wood------	66.72
3	May 25 proximal air-fall ash-------	8.7 N.	1.5 km W. of Spirit Lake-----	R. B. Waitt, Jr.	62.85
4	May 25 distal air-fall ash---------	82 NW.	3 km S. of Centralia, Wash---	James Beget-----	62.60
5	June 12 distal air-fall ash--------	75 SW.	Vancouver, Wash--------------	R. B. Waitt, Jr.	62.33
6	July 22 distal air-fall ash--------	78 SE.	Bingen, Wash-----------------	M. P. Doukas----	62.58
7	-----do----------	530 NW.	Upper Priest Lake, Idaho-----	F. K. Miller----	67.66
8	Pre-1980 tuff (ash?)---------------	3 E.	Eastern base of cone---------	([1])	62.66
9	Pyroxene andesite (dacite?)--------	0	Former summit dome-----------	([1])	62.86
10	Weighted average lithosphere[2]----------				59.18

[1]Analyses reported by Verhoogen (1937, p. 293).
[2]Calculated by Clarke and Washington (1924, p. 32).
[3]FeO recalculated to Fe_2O_3, and oxides recalculated to 100 percent.

creased downwind, relative to lithic fragments and crystal grains, owing to settling of the heavier particles close to the source while the lighter ones continued downwind. The downwind enrichment in pumice fragments (table 80, sample 7) and especially glass shards (table 80, sample 8) resulted in higher silica and potash contents in distal samples but lower contents of other major and minor elements (fig. 391). This process is similar to that described by Larrson (1937) for the 1932 eruption of Quizapú volcano, Chile. The high iron content in ash at Yakima, Wash. (table 80, sample 9), is anomalous and may result from sample contamination. Rubidium and zirconium also are enriched downwind, while strontium is depleted (fig. 392). These trends suggest that zirconium and rubidium are enriched in the glass fraction and that zircon did not crystallize; further, these inferences are supported by microscopic examination of the ash samples. Strontium, which substitutes for calcium in the major crystalline phases (plagioclase feldspar, the pyroxenes and hornblende) tends to be depleted downwind, as the heavier crystal grains and lithic fragments fall closer to the source.

A sequence of samples taken across the plume axis along a north-south traverse through Missoula, Mont. (fig. 393), shows a compositional asymmetry which corresponds to the asymmetry in the downwind lobe (Sarna-Wojcicki, Shipley, and others, this volume, figs. 336, 339). Calcium and strontium decrease from south to north, while zirconium, rubidium, and potassium increase. These variations reflect a greater proportion of lithic and crystal fragments in the south half of the lobe, and higher proportions of fine pumice and glass shards in the north half. This segregation results from two wind effects: First, the upper-level winds shifted slightly during the May 18 eruption, and so products from the latter part of the eruption followed a more northerly course. Second, northward surface winds winnowed finer particles out of the ash as it descended, leading to the progressive fining of deposits northward across the lobe. (See Sarna-Wojcicki, Shipley, and others, this volume.)

Glass separated from ash at distal localities is essentially identical in chemical composition to that at proximal localities (compare samples 8 and 17, table 80). Energy-dispersive X-ray fluorescence data on several major and minor elements in the volcanic glass (table 82) indicate that the glass composition from this eruption is virtually the same no matter where the ash was sampled; consequently, the liquid phase of the magma must have been quite homogeneous. These observations provide important confirmation of a basic assumption made in the chemical identification ("fingerprinting") of volcanic glass for purposes of temporal correlation: that the glass of individual widespread tephra units has essentially the same composition no matter where it is sampled.

ERUPTIONS OF MAY 25, JUNE 12, JULY 22, AND AUGUST 7

The major- and minor-element compositions of bulk ash samples from the eruptions of May 25, June 12, July 22, and August 7 vary little from that of the

with analyses of pre-1980 ash and summit-dome rock and estimate of average composition of lithosphere
chemical methods, from Verhoogen (1937). Analysis No. 10, estimate of average composition of lithosphere from Clarke and Washington (1924)]

Al_2O_3	Fe_2O_3	MgO	CaO	Na_2O	K_2O	TiO_2	P_2O_5	MnO	ZrO_2	Cr_2O_3	NiO	BaO	SrO	H_2O	Total
18.89	4.77	2.31	6.24	4.78	1.11	0.67	0.15	0.06	---	---	---	---	---	---	99.37
16.23	3.96	1.40	3.95	4.63	1.72	.55	.14	.06	0.022	<0.002	<0.001	0.039	0.046	---	99.46
17.27	4.59	2.00	4.95	4.58	1.35	.61	.14	.06	.013	<.002	<.001	.032	.056	---	98.50
17.17	4.95	2.15	5.16	4.72	1.41	.71	.16	.07	.018	<.002	.002	.033	.056	---	99.21
16.89	5.96	2.65	5.15	4.65	1.36	.79	.18	.08	.016	<.002	.002	.030	.054	---	100.14
17.72	4.97	2.15	5.37	4.53	1.28	.65	.15	.07	.018	<.002	.001	.030	.060	---	99.57
15.83	4.04	1.30	3.58	4.65	1.79	.60	.15	.06	.022	<.002	<.001	.040	.040	---	99.76
17.45	[3]4.52	1.96	4.64	4.07	1.24	.54	.16	Trace	---	---	---	.060	---	2.72	[3]100.02
18.13	[3]5.04	2.29	5.22	4.04	1.15	.54	.14	Trace	---	---	---	.05	.04	.50	[3]100.00
15.25	[3]7.23	3.46	5.11	3.72	3.12	1.03	.30	.11	.04	.05	.03	.05	.02	1.30	[3]100.00

May 18 air-fall ash. (Compare proximal air-fall ash samples 1, 2, 5, and 6, table 83.) No obvious, systematic, time-related trends appear in a plot of bulk chemistry for the first five eruptions of 1980 (fig. 394). The increase in silica and potassium concentration and the depletion of the other major and minor elements downwind are evident between samples 6 and 7 (table 83) from the eruption of July 22, but not between samples 3 and 4 (table 83) from the eruption of May 25. This disparity may be due to the lesser distance separating the latter two samples or to the complicated ash distribution pattern for the May 25 eruption (Sarna-Wojcicki, Shipley, and others, this volume). We have only one analysis of air-fall bulk ash from the eruption of June 12; further analyses are being run on bulk samples and separated components to determine the chemical variations within and between these air-fall ashes.

BULK COMPOSITIONS OF THE AIR-FALL ASHES OF MAY 18, MAY 25, JUNE 12, AND JULY 22 COMPARED TO AVERAGE CRUSTAL ABUNDANCES

Compared to the average composition of continental crustal rocks (Clarke and Washington, 1924; table 83, No. 10), both proximal and distal ash samples from the four current eruptions of Mount St. Helens are enriched in silica, aluminum, and sodium; contain about the same amount of calcium; and are depleted in all other major and minor elements. With respect to other minor and trace elements (tables 82, 84), bulk air-fall ash samples from the 1980 eruptions of Mount St. Helens are enriched in chlorine, scandium, gallium, and cesium and are depleted or about the same for the remaining elements compared to average crustal abundances (tables 82, 84; from Mason, 1958).

MAY 18 ASH SAMPLES COMPARED TO OLDER ASHES ERUPTED FROM MOUNT ST. HELENS

Because air-fall ash is a mechanical mixture of several components, no two bulk chemical analyses of the same ash from two different sites are likely to match chemically. To compare compositions of ash of different ages, we need to compare some fairly homogeneous component. Analyses of pumice from each eruption would represent the entire juvenile component, excluding gases. We do not have a sufficient number of analyses of pumice for comparison, and variations in the amount of crystalline material included present a sampling problem that causes scatter in the chemical data on replication. In fact, this latter phenomenon disguises much of the variation distinguishing the past and present pumices of Mount St. Helens (fig. 395). However, we do have an adequate number of glass analyses to use as a basis of comparison, and volcanic glasses not only represent the bulk of juvenile material ejected during most eruptions, they also tend to be relatively homogeneous.

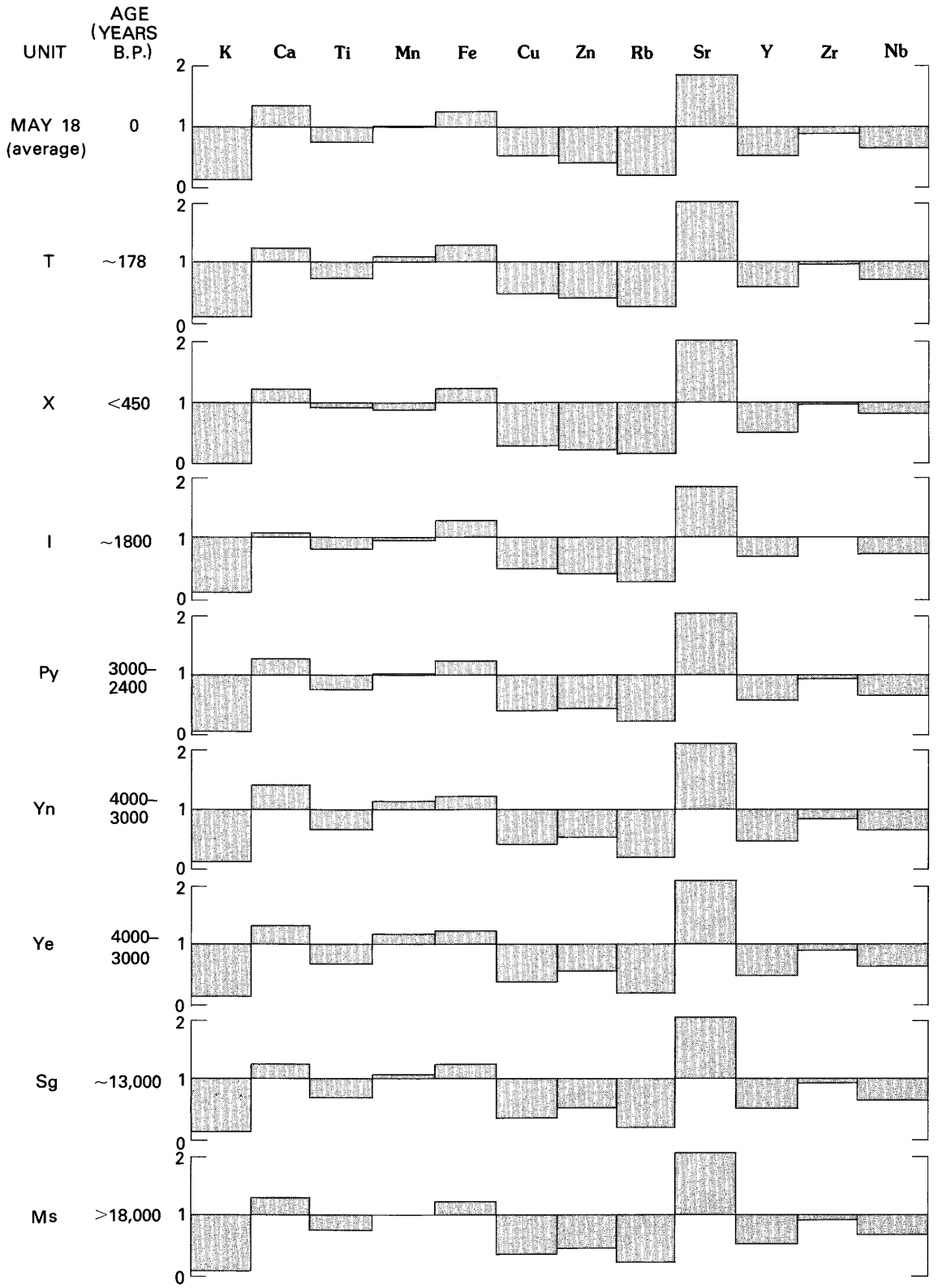

Figure 395.—Minor- and trace-element content in pumice of May 18 air-fall ash compared to that of previous eruptions, expressed as ratios to USGS standard granite G-1 (Flanagan, 1973). Energy-dispersive X-ray fluorescence analyses by M. J. Woodward. Tephra-unit designations and ages from Mullineaux and others (1975, 1978).

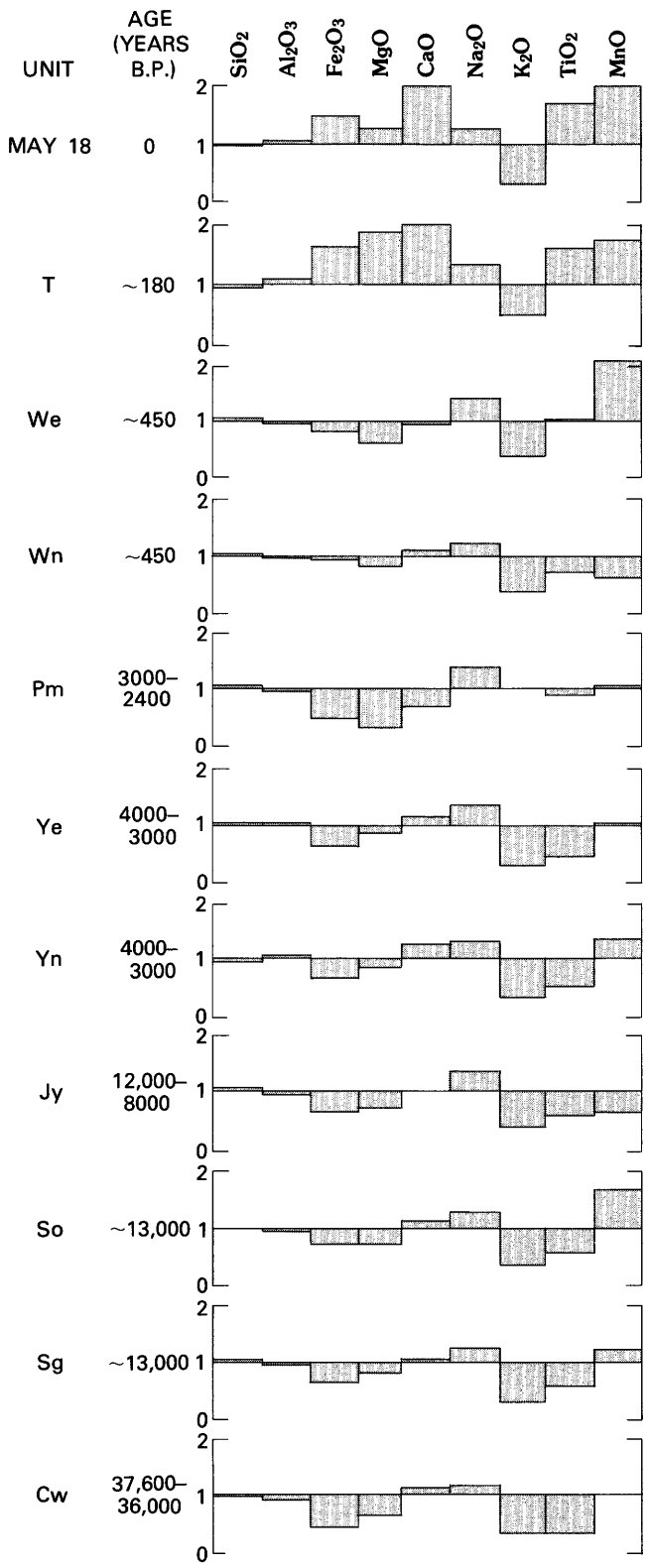

Figure 396.—Major- and minor-element content in glass of May 18 air-fall ash compared to that of previous eruptions, expressed as ratios to USGS standard granite G-1 (Flanagan, 1973). See table 85 for analyses. C. E. Meyer, analyst. Tephra-unit designations and ages from Mullineaux and others (1975, 1978).

Glass from the May 18 eruption is most similar to layer T—the most recent widespread pre-1980 air-fall ash, erupted about A.D. 1800 (Mullineaux and Crandell, this volume). Electron microprobe analyses of layer T show it to be the least silicic of all the glasses we have analyzed from previous major eruptions (table 85; fig. 396); it also has the highest concentration of aluminum, magnesium, iron, manganese, calcium, and titanium. Indeed, there appears to be a rough enrichment trend with time for the lighter transition elements in glasses of the major eruptions of Mount St. Helens. Sodium, potassium, and chlorine concentrations for both the May 18 and layer T ash are within the ranges of glass compositions of the older ashes. Energy-dispersive X-ray fluorescence data further indicate that layer T has less rubidium and zirconium than the May 18 ash, but more strontium.

The REE (rare-earth-element) concentrations in glass of May 18 ash are within the range determined for glasses of older major tephra units erupted from Mount St. Helens (fig. 397). The chondrite-normalized REE patterns for glass of the May 18 eruption and older Mount St. Helens glasses are similar to those of widespread silicic ashes erupted from other Quaternary Cascade Range sources, but the actual concentrations of the elements differ.

CONCLUSIONS

The major May 18 air-fall ash units within the proximal area differ from each other in petrography and bulk chemistry. The basal layer A3 contains a high proportion of lithic fragments, presumably older rocks derived from explosive disintegration of the former summit of the volcano. This layer is correlated with unit 1 of distal downwind ash, as the two units have similar chemistry and petrography and both contain charred plant fragments derived from the initial lateral pyroclastic surge. Proximal unit B is correlated with unit 3 of the downwind areas (Sarna-Wojcicki, Shipley, and others, this volume, fig. 339), although the rapid-settling, larger lithic grains and crystals of layer B1 may form the upper part of unit 1. In contrast to silicic tephra of most previous major eruptions from Mount St. Helens, tephra from the May 18 eruption contains abundant lithic and crystal fragments, attesting to the explosiveness of this eruption. Bulk ash samples of the May 18 eruption at distal downwind sites had higher silica and potassium contents, but lower iron, calcium, magnesium, titanium, and manganese concentrations than the

Table 84.—Minor- and trace-element concentrations in tephra erupted during the early, nonmagmatic phase of activity and on May 18, May 25, and June 12, 1980

[Direct-reading quantitative emission spectroscopic analysis. Lower limits of determination for some elements in some of the samples were determined by 6-step semiquantitative spectroscopy. P. J. Lamothe, T. L. Fries, and Chris Heropoulos, analysts. Values are in parts per million; —, not determined]

Element	Pre-magmatic ash[1]	May 18 tephra[2]								May 25 tephra[3]		June 12 tephra[4]	Average in crustal rocks[5]
		1	2	3	4	5	6	7	14	3	4		
Li	<100	<50	<50	<50	<50	<50	<50	<50	<50	<50	<50	<50	30
Be	2	1.3	<1.0	<1.0	1.5	~1.0	1.2	1.2	2.4	1.5	1.7	1.7	2
B	10	<10	<10	<10	<10	<10	<10	<10	<10	<10	<10	<10	3
Sc	15	10	<10	<10	10	<10	10	<10	<10	<10	<10	10	5
V	70	82	85	67	85	82	84	59	53	61	75	89	110
Cr	7	21	15	12	17	17	23	24	11	10	13	14	200
Mn	700	580	570	510	550	560	560	480	500	540	600	720	1000
Co	20	12	11	10	12	11	12	8.5	6	8.8	11	13	23
Ni	10	20	14	13	18	16	20	8.9	11	9.6	16	18	80
Cu	30	40	30	32	39	35	50	24	37	27	35	39	45
Zn	100	69	55	64	70	63	61	52	50	51	70	59	65
Ga	30	18	19	16	17	18	16	16	21	19	21	19	15
As	2	<1	<1	<1	4	~1	<1	2	3	1	2	1	2
Se	---	<5	<5	<5	<5	<5	<5	<5	<5	<1	<1	<1	0.09
Sr	500	460	580	470	470	510	450	480	360	460	440	420	450
Y	15	17	13	13	17	15	16	13	16	11	16	15	40
Zr	150	320	130	160	280	220	310	140	290	140	150	150	160
Nb	<7	<25	<25	<25	<25	<25	<25	<25	<25	<25	<25	<25	24
Mo	<2	<10	<10	<10	<10	<10	<10	<10	<10	<10	<10	<10	1
Ag	<.2	<1.0	<1.0	<1.0	<1.0	<1.0	<1.0	<1.0	<1.0	<1.0	<1.0	<1.0	.1
Cd	<.2	<.2	<.2	<.2	<.2	<.2	<.2	<.2	<.2	<.2	<.2	<.2	.2
Sn	2	<10	<10	<10	<10	<10	<10	<10	<10	<10	<10	<10	3
Sb	<1	<1	<1	<1	<1	<1	<1	<1	<1	<1	<1	<1	.2
Te	<1	<50	<50	<50	<50	<50	<50	<50	<1	<1	<1	<1	.002
Ba	300	350	280	300	350	320	350	340	440	320	330	300	400
La	20	<20	<20	<20	<20	<20	<20	<20	<20	<20	<20	<20	18
Ce	<50	<100	<100	<100	<100	<100	<100	<100	<100	<100	<100	<100	46
W	<10	<100	<100	<100	<100	<100	<100	<100	<100	<100	<100	<100	1
Re	<7	<50	<50	<50	<50	<50	<50	<50	<15	<50	<50	<50	.001
Au	<.2	<.2	<.2	<.2	<.2	<.2	<.2	<.2	<.2	<.2	<.2	<.2	.005
Hg	---	<1	<1	<1	<1	<1	<1	<1	<1	<5	<5	<5	.5
Tl	<1	<1	<1	<1	<1	<1	<1	<1	<1	<1	<1	<1	1
Pb	10	10	7	10	10	9	10	15	20	5	7	5	15
Bi	<.2	<.2	<.2	<.2	<.2	<.2	<.2	<.2	<.2	<.2	<.2	<.2	.2

[1]Lithic-crystal ash-breccia of early nonmagmatic eruptions, former summit of Mount St. Helens. Collected April 16, 1980, by A. M. Sarna-Wojcicki and R. P. Hoblitt.
[2]Sample Nos. same as in table 80.
[3]Sample Nos. same as in table 83.
[4]Same as sample 5 in table 83.
[5]From Mason (1958).

proximal tephra, reflecting downwind depletion of lithic and crystal grains relative to glass and pumice shards. The composition of glass, however, was essentially the same regardless of where the tephra was sampled.

Bulk compositions of ash erupted on May 18, May 25, June 12, July 22, and August 7 are about the same. Compared to average crustal abundances, tephra erupted from Mount St. Helens is enriched in silica, aluminum, sodium, chlorine, scandium, gallium, and cesium and depleted or about the same for the remaining major, minor, and trace elements analyzed.

Glass from the eruption of May 18 is most similar to that of layer T, erupted about A.D. 1800

Table 85.—Chemical analyses of volcanic glass from May 18 ash compared with analyses of glass from older ashes erupted by Mount St. Helens

[Electron microprobe analyses by C. E. Meyer. Tephra-unit designations and ages from Mullineaux and others (1975, 1978). n.a., not applicable]

No.	Unit	Age (years B.P.)	SiO_2	Al_2O_3	Fe_2O_3[1]	MgO	CaO	Na_2O	K_2O	TiO_2	MnO	Cl	Total
1	May 18	0	71.4	15.1	2.6	0.49	2.76	4.30	1.94	0.44	0.06	0.10	99.19
2	T	180	70.4	15.7	2.9	.72	2.82	4.48	2.50	.42	.05	.13	99.92
3	We	450	74.3	13.5	1.5	.25	1.35	4.59	2.33	.26	.06	.08	98.22
4	Wn	450	74.0	14.0	1.7	.31	1.60	3.99	2.25	.19	.02	.10	98.16
5	Pm	3,000-2,400	74.9	13.2	.9	.15	.98	4.59	2.10	.23	.03	.06	97.14
6	Ye	4,000-3,000	72.8	14.0	1.2	.33	1.62	4.10	1.98	.13	.03	.10	96.29
7	Yn	4,000-3,000	72.3	14.4	1.2	.33	1.73	4.23	1.99	.14	.04	.09	96.45
8	Jy	12,000-8,000	74.7	13.6	1.2	.27	1.40	4.43	2.23	.16	.02	.09	98.10
9	So	13,000	76.9	13.9	1.4	.30	1.59	4.20	2.22	.16	.05	.10	100.82
10	Sg	13,000	73.0	13.8	1.2	.31	1.48	4.06	2.09	.16	.03	.07	96.20
11	Cw	37,600-36,000	72.3	12.8	.8	.24	1.59	3.87	2.17	.10	.03	.06	93.96
Average (3-11)----------			73.9	13.7	1.2	.28	1.48	4.23	2.15	.17	.03	.08	n.a.
Sample standard deviation			±1.5	±.5	±.3	±.06	±.22	±.26	±.12	±.05	±.01	±.02	n.a.

[1]Total Fe calculated as Fe_2O_3.

from Mount St. Helens. Both glasses are enriched in some light transition elements and in magnesium and calcium relative to glasses of previous eruptions, and both are depleted in silica and potassium. Glasses from successive eruptive episodes of Mount St. Helens can be distinguished on the basis of their chemical composition.

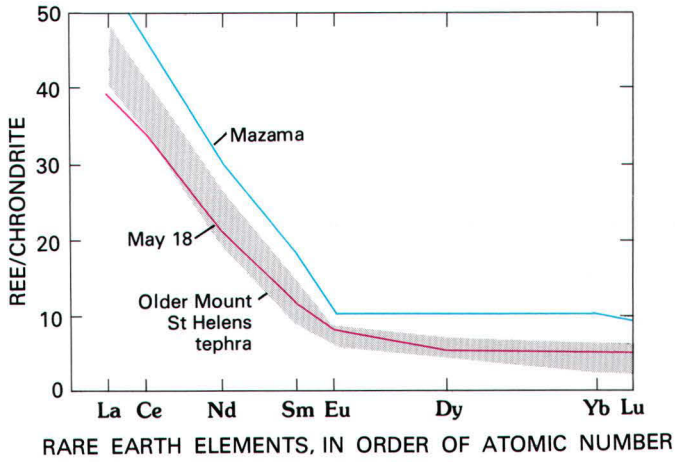

Figure 397.—Rare-earth-element (REE) content in glass from May 18 ash (red), compared to the range for glass from several older ashes (stippled), relative to content of corresponding elements in chondrite (Leedy's chondrite, Masuda and others, 1973). REE content in glass of ash from Mount Mazama (blue) shown for comparison. Analyses by Frank Asaro, Helen Michael, and Harry Bowman, Lawrence Berkeley Laboratory.

REFERENCES CITED

Clarke, F. W., and Washington, H. S., 1924, The composition of the earth's crust: U.S. Geological Survey Professional Paper 127, 117 p.

Flanagan, F. J., 1973, 1972 values for international geochemical reference samples: Geochimica et Cosmochimica Acta, v. 37, p. 1189-1200.

Hoblitt, R. P., Crandell, D. R., and Mullineaux, D. R., 1980, Mount St. Helens eruptive behavior during the past 1500 yr: Geology, v. 8, p. 555-559.

Hooper, P. R., Merrick, I. W., Laskowski, E. R., and Knowles, C. R., 1980, Composition of the Mount St. Helens ashfall in the Moscow-Pullman area on 18 May 1980: Science, v. 209, no. 4461, p. 1125-1126.

Larrson, Walter, 1937, Vulkanische Asche vom Ausbruch des chilenischen Vulkans Quizapú (1932) in Argentina gesammelt—Eine Studie über äolische Differentiation: Uppsala University Geological Institution Bulletin, v. 26, p. 27-52.

Mason, Brian, 1958, Principles of geochemistry: New York, John Wiley and Sons, Inc., 310 p.

Masuda, Akimasa, Nakamura, Noboru, and Tanaka, Tsuyoshi, 1973, Fine structures of mutually normalized rare-earth patterns of chondrites: Geochimica et Cosmochimica Acta, v. 37, p. 239-248.

Mullineaux, D. R., Hyde, J. H., and Rubin, Meyer, 1975, Widespread late glacial and postglacial tephra deposits from Mount St. Helens volcano, Washington: U.S. Geological Survey Journal of Research, v. 3, no. 3, p. 329-335.

Mullineaux, D. R., Wilcox, R. E., Ebaughaugh, W. F., Fryxell, R., and Rubin, Meyer, 1978, Age of the last major scabland flood of the Columbia Plateau in eastern Washington: Quaternary Research, v. 10, no. 2, p. 171-180.

Verhoogen, Jean, 1937, Mount St. Helens, a recent Cascade volcano: California University Department of Geological Sciences Bulletin, v. 24, no. 9, p. 263-302.

METHODS OF ANALYSIS OF SAMPLES USING X-RAY FLUORESCENCE AND INDUCTION-COUPLED PLASMA SPECTROSCOPY

By JOSEPH E. TAGGART, JR., FREDERICK E. LICHTE, *and* JAMES S. WAHLBERG

ABSTRACT

Methods for major element analysis using a Phillips PW1600 wavelength-dispersive simultaneous X-ray spectrometer, and trace element analysis on a Jarrell-Ash Model 1160 direct-reading polychrometer using inductively coupled argon plasma excitation are described. These state-of-the-art instrumental methods have been used to great advantage for the rapid release of quality analytical data on samples from the recent eruptions of Mount St. Helens. Analyses of geological reference materials are presented.

INTRODUCTION

As part of a continuing program to provide accurate, rapid chemical analyses, USGS (U.S. Geological Survey) laboratories investigate new techniques and instrumentation, from which methods are then developed for analyzing geologic materials. Two multielement automated instrumental methods were brought online during 1977–80.

Major element analysis has been developed on a Phillips PW1600 wavelength-dispersive simultaneous X-ray spectrometer, and trace element analysis has been developed on a Jarrell-Ash Model 1160 direct-reading polychrometer using inductively coupled argon plasma excitation (Lichte and others, 1980).

These state-of-the-art instrumental methods have performed well during many of the USGS research projects on Mount St. Helens. Although the analytical quality had been established prior to the eruption of May 18,1980, the fast turnaround times and large sample capacities of the methods were not fully appreciated until tested by the immediacy required by this catastrophic event.

The methods have been used to great advantage for the rapid release of quality analytical data for samples from the recent eruptions of Mount St. Helens. Analyses of the May 18 eruptive material were released by September (Taggart and others, 1980) and again by November (Hoblitt and others, 1980; Taylor and Lichte, 1980). Turnaround time on select samples has allowed close monitoring of changes in chemistry of magma from one eruptive event to another in 1980 (Lipman and others, this volume), because analyses of newly erupted rock could be provided within a few days after eruption.

X-RAY SPECTROMETRIC MAJOR-ELEMENT ANALYSIS

SAMPLE PREPARATION

An 0.8-g powdered (< 100 mesh) portion of each sample was weighed into an ignited, tared, platinum-

Table 86.—Instrument parameters for Phillips PW1600 X-ray spectrometer

[μm, micrometers; TLAP, thallium hydrogen phthalate; PE, pentaecrythritol tetrakis (hyroxymethyl) methane; GE, germanium (111); LiF, lithium fluoride; P10 gas, 90 percent argon + 10 percent methane]

Element	Line	Crystal	Detector-gas	Window
Na	Kα	Semifocused TLAP---	Flowcounter, P10	1 μm polypropylene.
Mg	Kα	-----do----------	-----do---------	Do.
Al	Kα	Semifocused PE-----	-----do---------	Do.
Si	Kα	-----do----------	-----do---------	Do.
P	Kα	Semifocused GE-----	-----do---------	Do.
K	Kα	Semifocused PE-----	-----do---------	Do.
Ca	Kα	Semifocused LiF 200	Sealed argon----	50 μm beryllium.
Ti	Kα	-----do----------	-----do---------	Do.
Mn	Kα	-----do----------	-----do---------	Do.
Fe	Kα	-----do----------	-----do---------	Do.

gold (95:5) crucible. The samples were then ignited for 20 min in a muffle furnace at 925°C, cooled in a desiccator, and reweighed. The weight loss is reported as percent loss on ignition (LOI).

In order to eliminate particle-size effects and to decrease matrix effects, samples were presented to the X-ray spectrometer as a lithium tetraborate glass-disc fusion product. An 8-g charge of lithium tetraborate was added to each crucible and mixed with the ignited sample. Four drops of concentrated hydrobromic acid were added to the contents of each crucible to serve as a nonwetting agent; this addition prevents the finished disc from sticking to the mold. Seven crucibles with sample, and seven empty molds (Taggart and Wahlberg, 1979) were loaded into an automatic fluxer (Taggart and Wahlberg, 1980) which was then placed in a muffle furnace at 1120°C for 17 min. During this time, the tilting action of the fluxer homogenizes the molten sample-flux mixture. After the mixing phase of the fusion is completed, the crucibles are inverted; thus, the fused mixture is poured into the molds. The fluxer is then removed from the muffle furnace and cooled to near room temperature. The hardened glass discs are removed from the molds, labeled, and stored in individual plastic boxes—all without touching the analytical surface of the disc.

INSTRUMENT CONDITIONS

The sample discs are analyzed with a Phillips PW1600 wavelength-dispersive simultaneous X-ray spectrometer. The samples are loaded into the instrument, care being taken to avoid touching the analytical surface of the glass disc. Each sample is

Table 87.—Analyses of seven igneous rock standards (expressed in percent) by X-ray fluorescence spectroscopy using a Phillips PW1600 simultaneous spectrometer

[XRF, analysis by X-ray fluorescence; Abbey, values from Abbey (1978)]

	SiO_2	Al_2O_3	[1]Fe_2O_3	MgO	CaO	Na_2O	K_2O	TiO_2	P_2O_5	MnO
Andesite, AGV-1:										
XRF----------	59.9	17.2	6.88	1.57	5.11	4.25	2.99	1.08	0.52	0.08
Abbey----------	59.72	17.22	6.84	1.55	5.00	4.31	2.93	1.05	0.50	0.10
Dunite, DTS-1:										
XRF----------	40.6	0.18	8.84	49.8	0.11	<0.2	<0.05	<0.02	<0.05	0.11
Abbey----------	40.68	0.29	8.60	49.83	0.13	0.01	0.00	0.01	0.00	0.11
Granite, G-2:										
XRF----------	69.9	15.6	2.73	0.81	1.98	3.94	4.54	0.49	0.13	0.02
Abbey----------	69.19	15.35	2.67	0.77	1.98	4.06	4.52	0.50	0.14	0.04
Granodiorite, GSP-1:										
XRF----------	67.2	15.2	4.32	1.01	2.04	2.61	5.51	0.66	0.29	0.02
Abbey----------	67.31	15.19	4.33	0.96	2.02	2.80	5.53	0.66	0.28	0.04
Basalt, BRN:										
XRF----------	38.4	10.2	13.0	13.3	14.0	2.91	1.38	2.70	1.10	0.18
Abbey----------	38.39	10.25	12.9	13.35	13.87	3.07	1.41	2.61	1.05	0.20
Granite, GSN:										
XRF----------	66.4	15.0	3.73	2.28	2.55	3.61	4.69	0.67	0.28	0.04
Abbey----------	65.98	14.71	3.75	2.31	2.51	3.78	4.64	0.68	0.28	0.06
Lujavarite, NIM-SARM-3-L:										
XRF----------	52.1	13.6	9.97	0.32	3.18	8.23	5.38	0.48	0.05	0.74
Abbey----------	52.45	13.59	9.96	0.28	3.24	8.30	5.46	0.49	0.06	0.76

[1]Total Fe as Fe_2O_3.

irradiated by a rhodium target end-window tube operating at 35 kilovolts and 60 milliamps. The spectrometer chamber is kept under a vacuum of less than 0.2 mm of mercury. Table 86 shows the instrument parameters for each element.

Each sample is counted for 100 s. Because of the stability of the PW1600, use of what is variously known as an updater, monitor pellet, or drift pellet is unnecessary. Experience has shown that the "drift" of the instrument over an 8-hr period is commonly less than the counting statistics of many of the channels involved in "updating" with a monitor pellet. To substantiate that drift has not occurred, a test pellet of known composition is recounted every tenth sample. In the event that drift has occurred since the last time the test pellet was measured, the results for the intervening unknowns are discarded. Surprisingly, samples usually can be run for an 8-hr shift with less than the acceptable cutoff of 0.5-percent drift (1-percent drift for sodium is due largely to poor counting statistics). When drift does occur, or after a period during which the instrument has not been used, the slope of the calibration curves are restandardized and recalculated rather than just "updating" to a single monitor pellet.

The instrument is controlled and all calculations are carried out with a dedicated Digital Equipment Corporation (DEC) PDP 11/04 computer. Because of the computer automation of the instrument, a restandardization routine takes only 12 min longer than updating (unattended "machine" time), and generally yields better results.

To diminish the effects of blank contribution, flux is homogenized in 15-lb batches by rolling it in a large carboy. Batches are numbered and glass blanks are prepared from each batch. Using the DEC PDP 11/04, recalibration of the intercept of the calibration curves with glass blanks eliminates relatively small blank contributions in less than 15 min.

Interelement matrix effects are corrected with de Jongh's matrix model (de Jongh, 1973). Alpha influence coefficients for the de Jongh model are

Table 88.—Comparison between conventional wet chemical analyses (classic) and X-ray fluorescence (XRF) analyses for 10 samples from Mount St. Helens

	Classic	XRF	Classic	XRF	Classic	XRF	Classic	XRF	Classic	XRF
Sample No.--	200		201		202		203		204	
SiO_2	64.39	64.5	64.29	64.0	64.41	64.4	63.87	63.4	63.03	62.5
Al_2O_3	17.39	17.5	17.40	17.4	17.41	17.5	17.39	17.5	17.51	17.5
$^1Fe_2O_3$	4.51	4.55	4.55	4.53	4.43	4.50	4.54	4.61	4.78	4.84
MgO	1.87	1.96	1.86	1.92	1.84.	1.91	1.90	1.99	2.10	2.16
CaO	4.93	5.02	4.92	5.02	4.94	5.04	5.00	5.05	5.20	5.22
Na_2O	4.61	4.69	4.66	4.61	4.61	4.56	4.50	4.58	4.59	4.52
K_2O	1.32	1.33	1.32	1.31	1.32	1.32	1.27	1.29	1.29	1.27
TiO_2	.60	.60	.60	.61	.58	.59	.60	.61	.64	.64
P_2O_5	.13	.13	.13	.13	.13	.14	.13	.13	.14	.14
MnO	.07	.06	.07	.06	.07	.06	.07	.06	.08	.07
Sample No.--	205		206		207		844		845	
SiO_2	63.29	63.1	64.01	64.0	63.66	63.3	63.29	63.3	62.52	62.4
Al_2O_3	17.60	17.6	17.50	17.6	17.40	17.4	17.82	17.8	18.07	18.0
$^1Fe_2O_3$	4..81	4.86	4.50	4.55	4.56	4.61	4.91	4.96	4.99	4.99
MgO	2.07	2.12	1.90	1.93	1.93	2.00	2.14	2.18	2.24	2.25
CaO	5.17	5.23	4.98	5.05	5.03	5.14	5.25	5.36	5.54	5.64
Na_2O	4.58	4.65	4.59	4.56	4.57	4.53	4.55	4.61	4.48	4.55
K_2O	1.27	1.27	1.29	1.30	1.30	1.29	1.19	1.25	1.14	1.20
TiO_2	.65	.65	.61	.60	.64	.63	.65	.65	.66	.67
P_2O_5	.13	.13	.13	.13	.14	.14	.13	.15	.13	.16
MnO	.08	.07	.07	.07	.07	.07	.08	.07	.08	.07

[1]Total iron as Fe_2O_3. For classic rock total iron, FeO had to be recalculated as Fe_2O_3 and that number added to the Fe_2O_3 determination.

Table 89.—Element selection and detection limits for Jarrell-Ash induction-coupled argon plasma emission spectrometer

[nm, nanometers; detection limit in micrograms per gram except *, percent; leaders (---) indicate elements that are not compatible with the digestion procedure]

Element	Wavelength (nm)	Detection limit	Element	Wavelength (nm)	Detection limit	Element	Wavelength (nm)	Detection limit
Ag	328.0	10	Ge	265.1	---	Sc	424.6	2
Al	309.2	*.05	Hf	291.6	---	Se	196.0	---
As	193.6	15	Ho	345.6	2	Si	251.6	---
Au	242.9	10	K	766.4	*.001	Sm	442.4	5
B	249.7	---	La	398.8	5	Sn	189.9	5
Ba	455.4	1	Li	670.7	5	Sr	421.5	5
Be	313.0	1	Lu	261.5	5	Ta	240.0	10
Bi	223.0	20	Mg	279.5	*.001	Tb	367.6	5
Ca	317.9	*.01	Mn	257.6	2	Te	238.5	---
Cd	226.5	1	Mo	202.0	2	Th	401.9	5
Ce	418.6	10	Na	588.9	*.001	Ti	334.9	*.001
Cr	267.7	2	Nb	413.7	5	Tm	313.1	5
Cu	324.7	2	Nd	430.3	5	U	409.0	50
Dy	340.7	5	Ni	231.6	2	V	292.4	2
Er	369.2	5	P	213.6	*.01	W	207.9	10
Eu	397.1	5	Pb	220.3	10	Y	321.6	5
Fe	259.9	*.01	Pr	422.2	15	Yb	328.9	1
Ga	294.3	5	Sb	217.5	---	Zn	213.8	2
						Zr	339.1	---

calculated from fundamental parameters using the program ALPHAS on an IBM 360/75 computer. Alphas suitable for a 1:10 sample to lithium tetraborate dilution of geologic materials were determined by Lobeek (1976). Extensive tests were conducted to determine the relationship between theoretically determined alphas and experimentally observed interelement effects. Seven elements were selected that had a range of characteristic X-ray energies. In all tests, the theoretically determined influence coefficients agreed with those determined experimentally. In addition, the difficulty encountered with count rates on the sodium channel pointed out the advantages of using theoretical alphas. The instrument was calibrated using 30 international geologic standards from various agencies. Table 87 shows the results obtained on a variety of standards that were not involved in the calibration of the instrument. These analyses were performed on a one sample disc-one analysis basis. Further tests of accuracy were made by participation in round-robin analyses of standard materials (Govindaraju, 1980).

Ten samples of Mount St. Helens material that were analyzed by conventional wet chemical techniques (Lipman and others, this volume) were reanalyzed by X-ray fluorescence. The results for these analyses are shown in table 88, and show good agreement. Routine redeterminations on seven Mount St. Helens glass discs were performed before each new Mount St. Helens job to ensure high precision between jobs.

INDUCTION-COUPLED ARGON PLASMA EMISSION SPECTROMETRIC ANALYSIS

SAMPLE PREPARATION

The inductively coupled argon plasma (ICP) is noted for its high sensitivity for most elements (Fassel and Kniesley, 1974; Scott and Kokot, 1975). One of its requirements is that samples must first be in solution. For solid samples such as volcanic ash, this means that they must be dissolved using appropriate reagents.

Preparation of the ash and rock samples was accomplished by dissolution using a combination of acids (HF, HNO_3, $HClO_4$). Typically, 0.5 g of ash was digested on a hotplate in Teflon crucibles and diluted to 50 mL using 3-percent HCl. This digestion

Table 90.—Analysis of U.S. Geological Survey reference standard G-2 by inductively coupled argon plasma (ICP) emission spectroscopy

[All values are in micrograms per gram. Reference values are from Abbey (1980)]

Element	Concentration on two runs by ICP		Reference value
Ba	1850	1870	1900
Be	1.8	2.0	2.4
Cd	<1	<1	.04
Ce	162	151	160
Co	5	4	5
Cr	12	13	8.0
Cu	10	11	10
Li	36	33	35
Mn	250	253	260
Mo	2	2	1.
Nb	8	2	13
Ni	4	2	3.6
Pb	28	34	30
Sc	4	4	3.5
Sr	470	474	480
V	36	36	36
Y	10	10	11
Yb	.8	.5	.9
Zn	85	86	85

volatilizes silica, and other elements as noted in table 89, and only partially attacks the mineral zircon, but offers a fairly complete digestion of other minerals in the ash and rock samples.

INSTRUMENTAL CONDITIONS

The solutions from the acid digestion were analyzed for 60 elements. Of the 60 elements, only about 40 elements were at high enough concentrations to be detected by ICP using the described sample preparation. The elements, wavelengths, and detection limits are listed in table 89.

Each sample requires about 90 s of instrument time for analysis. Integration time for on-peak and background intensity measurement is 24 s; the remainder of the time is required for equilibration of the sample in the nebulizer spray chamber.

As noted in table 89, the major elements were also quantified using the inductively coupled plasma-atomic emission spectroscopy technique. The precision of the technique was approximated at ±5 percent relative standard deviations. The technique does not offer the precision found in the X-ray technique. The analysis for the major elements was necessary, however, to mathematically correct for spectral interferences of these elements on the wavelengths of interest for minor and trace elements.

To verify the accuracy of the methods, the U.S. Geological Survey standard G-2 was analyzed at the beginning and end of the analysis of each group of samples. The analysis of this standard is given in table 90. The data shown in table 91 for the analysis of ash samples collected at Yakima, Wash., and Moscow, Idaho, after the onset of the May 18 eruption demonstrate the usefulness of the technique in differentiating subtle changes in concentration for the minor and trace elements.

Table 91.—Minor- and trace-element analysis (in micrograms per gram) of volcanic ash by inductively coupled plasma emission spectroscopy

	Yakima, Wash.	Moscow, Idaho		Yakima, Wash.	Moscow, Idaho
Ba	247	344	Nb	<3	<3
Be	<1	<1	Ni	17	8
Cd	<1	<1	Pb	<10	11
Ce	26	33	Sc	13	7
Co	18	8	Sr	553	345
Cr	13	3	V	94	52
Cu	46	37	Y	13	13
Li	25	29	Yb	1.3	1.3
Mn	847	453	Zn	87	53
Mo	<1	2			

REFERENCES CITED

Abbey, Sydney, 1978, Studies in "standard samples" for use in the general analysis of silicate rocks and minerals; Part 5—1977 Edition of "usable" values: Reprinted in X-Ray Spectrometry, v. 7, no. 2, p. 99-121.

_____1980, Studies in "standard samples" for the use of the general analysis of silicate rocks and minerals; Part 6—1979 Edition of "usable" values: Canadian Geological Survey Paper 80-14.

de Jongh, W. K., 1973, X-ray fluorescence analysis applying theoretical matrix correction—Stainless steel: X-Ray Spectrometry, v. 2, no. 4, p. 151-158.

Fassel, V. A., and Kniesley, R. N., 1974, Inductively coupled plasma optical or emission spectroscopy: Analytical Chemistry, v. 46, p. 1110a-1120a.

Govindaraju, K., 1980, Report (1980) on three GIT-IWG rock reference samples—Anorthosite from Greenland, AN-G; basalte d'Essey-la-Côte, BE-N; granite de Beauvoir, MA-N: Geostandards Newsletter, v. 4, no. 1., p. 49-138.

Hoblitt, R. P., Crandell, D. R., and Mullineaux, D. R., 1980, Mount St. Helens eruptive behavior during the past 1,500 yr: Geology, v. 8, p. 555-559.

Lichte, F. E., Sutton, A. L., Crock, J. G., and Layman, L. R., 1980, Analysis of geologic samples with a 63 element inductively coupled plasma emission spectrometer [abs. no. 054.]: Pittsburgh Conference on Analytical Chemistry, March 10, Atlantic City, New Jersey.

Lobeek, G. W., 1976, Table of influence coefficients 76.08.31.02: Eindhoven, The Netherlands, N. V. Phillips, 9 p.

Scott, R. H., and Kokot, M. L., 1975, Application of inductively coupled plasma to the analysis of geochemical samples: Analytical Chimica Acta, v. 75, p. 257-270.

Taggart, J. E., Jr., and Wahlberg, J. S., 1979, New mold design for casting fused samples: Advances in X-Ray Analysis, v. 23, p. 257-261.

Taggart, J. E., Jr., and Wahlberg, J. S., 1980, A new in-muffle automatic fluxer design for casting glass discs for X-ray fluorescence analysis [abs. 327a]: Federation of analytical chemists and spectroscopy societies conference, Sept. 19, 1980, Philadelphia, Pa.

Taggart, J. E., Jr., Wahlberg, J. S., and Taylor, H. E., 1980, X-ray spectrometric major-element analyses of tephra samples from the May 18, 1980 eruption of Mount St. Helens—Samples collected from Washington, Idaho, and Montana: U.S. Geological Survey Open File Report 80-1130, 13 p.

Taylor, Howard E., and Lichte, F. E., 1980, Chemical composition of Mount St. Helens volcanic ash: Geophysical Research Letters, v. 7, no. 11, p. 949-952.

EFFECTS OF THE 1980 ERUPTIONS

EFFECTS OF THE 1980 ERUPTIONS

The effects of the May 18 eruption were cataclysmic in some places near the volcano, especially in the North Fork Toutle River. About 60 people were killed or are missing, mostly in the 600-km² devastated area. Whereas many effects of the eruption were anticipated, others were not; thus, the eruption illustrated some advantages and limitations of volcanic-hazards assessments based on the past eruptive record.

Along the North Fork Toutle River, the debris avalanche covered the floor of the upper part of the valley. Along several other streams, mudflows raised valley floors and diverted streams into new positions. Farther downvalley mudflows and floods spread over valley floors, raised channel beds, and destroyed or damaged countless civil works. Downwind from the volcano, ash fall produced darkness during daylight hours, halted highway traffic, and damaged machinery, especially internal combustion engines. Ash-fall deposits also affected snowmelt and changed stream and lake-water chemistry. On the other hand, the ash added fresh material to the soil over vast tracts of agricultural land. The far-reaching effects of the 1980 eruptions are the subject of evaluations by many Federal, State, and local government agencies as well as private interests; only a few aspects are treated in this volume.

On May 18, mudflows and floods that raced down almost all valleys that head on the volcano were especially destructive along the Toutle and Cowlitz Rivers. Near the confluence of the Toutle and Cowlitz Rivers, mudflows and floods left deposits as much as 3 m thick on parts of the flood plain, and nearly 5 m thick in preexisting channels (Lombard and others). Deposits that reduced channels to as little as 10 percent of their preeruption capacities created a potential for unusually high floods, even from normal winter-season precipitation.

Destruction or damage to civil works was extensive, both near and far from the volcano (Schuster). Most roads, bridges, and buildings immediately north of the volcano and in the upper reaches of the North Fork Toutle River valley were destroyed on May 18. Mudflows resulted in extensive property loss along the South Fork Toutle and North Fork Toutle Rivers, and lesser damage along the lower Cowlitz River and tributaries of the Lewis River that head on Mount St. Helens. At the mouth of the Cowlitz River, mudflow deposits raised the bed of the Columbia River ship channel enough to block passage of large vessels. In addition, ash fall in eastern Washington, northern Idaho, and Montana severely hampered transportation and other public utility systems, and required removal and disposal of large amounts of ash. Ash from the May 25 and June 12 eruptions had similar effects on southwestern Washington and in the Portland, Oreg., area.

Eruptive products affected water quality in streams, causing marked increases in several inorganic and organic compounds, and total iron, manganese, and aluminum (Klein). The changes measured were short lived in streams affected only by ash fall, and increases were less as distance increased from the volcano. Effects were more persistent, however, in streams that drain areas containing blast, debris-avalanche, and mudflow deposits.

In order to judge toxicity of ash in lakes, leachates that had been passed through ash from near Richland and near Moses Lake in Washington were tested on a blue-green alga common in nearby lakes (McKnight and others). At expectable concentrations for such lakes, leachate from the Richland ash sample was toxic to the alga but leachate from the Moses Lake ash was not. The toxicity is attributed to concentrations of dissolved organic carbon compounds or metal-organic complexes. Studies reported earlier in this volume show that the ash at Richland consists of a higher proportion of the oldest ash bed of May 18, which is relatively rich in organic material, than does the ash near Moses Lake.

At Ritzville, where ash as much as 50 mm thick covers wide tracts of agricultural land, investigations were begun immediately to determine its effects on soils and plants (Gough and others). Samples of soil and of parts of wheat plants taken along a transect directly across the ash lobe disclosed changes in both soil layers and plants. Four weeks after May 18, rain had leached measurable amounts of some compounds from the ash into the soil, and some changes in soil pH had resulted. Variation in concentrations of several metallic elements in soil and in wheat suggest a need for future tests to determine the effects of elevated levels of metallic elements on future crops.

On the volcano, the May 18 and subsequent major

eruptions radically changed the ice and snow cover, and ash affected snowmelt in downwind areas. The landslides and eruption of May 18 completely removed two glaciers from the north flank of the volcano and beheaded most others (Brugman and Meier). Seventy percent of the glacier volume that had existed before May 18 was removed, and the remainder was blanketed with new detritus. Loss of accumulation area and probably reduction in subglacial water pressure caused the beheaded Shoestring Glacier to decrease in velocity. Swift Glacier, in contrast, was not beheaded and maintained constant velocity through the summer of 1980. Ash thicker than about 24 mm should decrease the rate of melting of ice and snow, and lesser thicknesses increase it (Driedger); the maximum enhancement of melting would be expected under an ash cover about 3 mm thick.

THE IMPACT OF MUDFLOWS OF MAY 18 ON THE LOWER TOUTLE AND COWLITZ RIVERS

By R. E. LOMBARD, M. B. MILES, L. M. NELSON,
D. L. KRESH, *and* P. J. CARPENTER

ABSTRACT

The volcanic eruptions of Mount St. Helens on May 18, 1980, triggered mudflows on the South Fork and North Fork Toutle River that deposited as much as 15 ft of sediment in the channels of the Toutle and lower Cowlitz Rivers. The thickness of the sediment deposited on the flood plains ranged from almost none just upstream from Kelso to about 10 ft near Castle Rock and the mouth of the Toutle River. Levees in Castle Rock, Kelso, and Longview contained the mudflows and prevented flooding of those communities. Mudflow deposits reduced the within-channel flow capacity of the lower Toutle and Cowlitz Rivers to about one-tenth of former capacity, except at Kelso and Longview where deposition was minor. The potential exists for unusually high flood levels, as much as 10 ft higher than normal, from autumn and winter precipitation.

INTRODUCTION

The explosive volcanic eruption of Mount St. Helens on May 18, 1980, triggered mudflows in several streams that head on the flanks of the volcano. Mudflows that originated in the North Fork and South Fork Toutle River were especially significant because of their immense magnitudes and consequent destruction. These two mudflows deposited large volumes of sediment in the North Fork and South Fork Toutle River; and in the Toutle, lower Cowlitz, and Columbia Rivers. In the lower Toutle and Cowlitz River valleys, as much as 15 ft of mud and debris were deposited in the river channels, and as much as 10 ft on the adjacent flood plains (fig. 398). These deposits destroyed houses, covered productive bottomland, and killed extensive tracts of trees. They also created a potential for further accumulation of sediment and future flood hazards to life and property.

This report describes changes caused by the mudflows in the channels and flood plains of the lower Toutle and Cowlitz Rivers. The data used to compute the morphologic changes were obtained from field measurements and observations made during May and early June 1980.

ACKNOWLEDGMENTS

Appreciation is expressed to the U.S. Army Corps of Engineers, Portland District, Oreg.; Tudor Engineering Company, Seattle, Wash.; and Towill, Inc., San Francisco, Calif., who furnished cross-sectional data, aerial photographs, and other useful information.

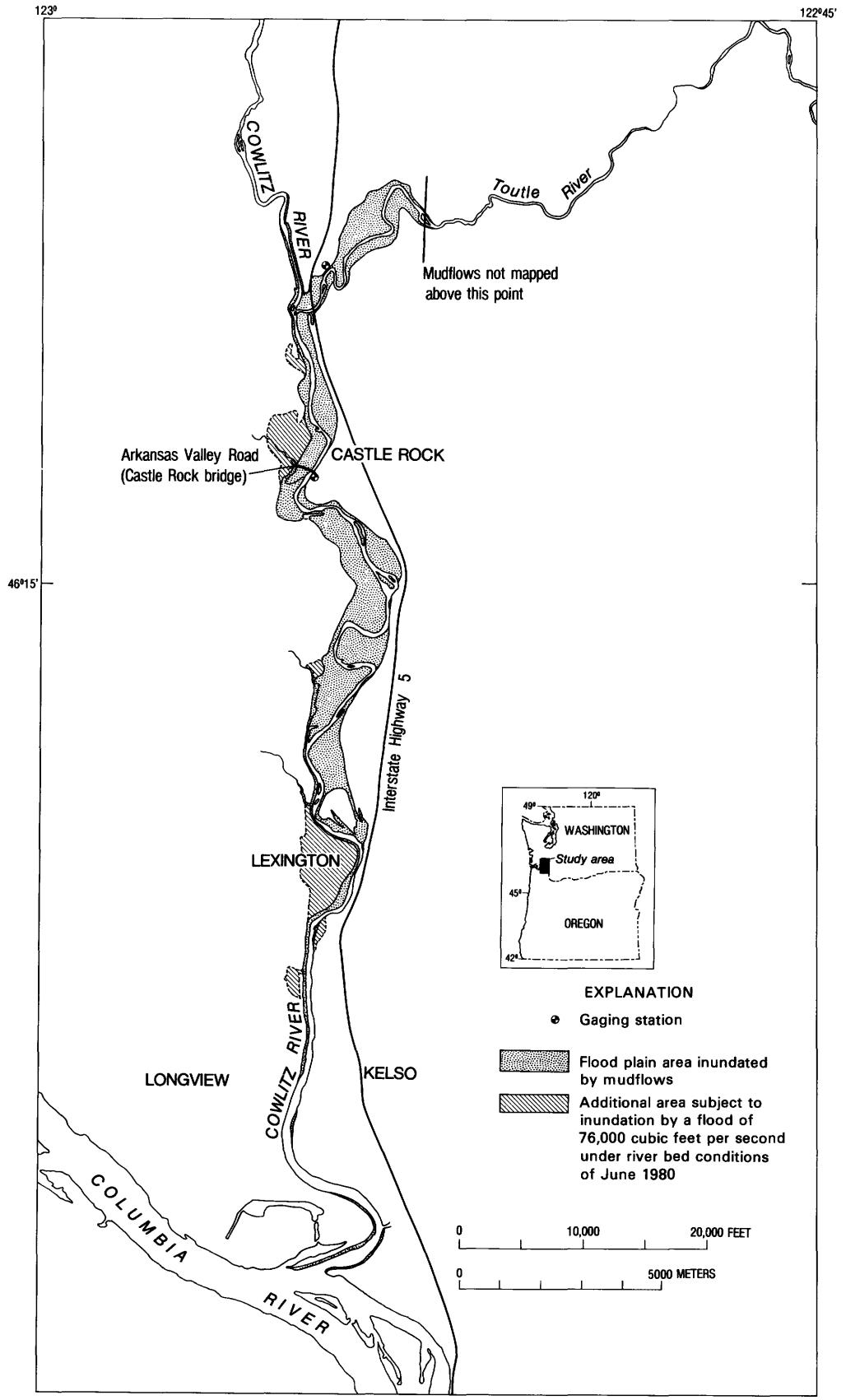

Figure 398.—Extent of inundation by mudflows of May 18, 1980, along the lower Toutle and Cowlitz Rivers, Wash.

THE MUDFLOWS

Cummans (this volume) has described the chronology and velocities of the mudflows that originated in the South Fork and North Fork Toutle River after the onset of the May 18 eruption. Figure 399 shows the timing of the mudflows in the Cowlitz River at Castle Rock, Wash. At noon on May 18, the river stage at the Castle Rock bridge was 30.2 ft. The peak stage of the South Fork Toutle River mudflow occurred at about 1330 PDT (Pacific Daylight time) when the stage reached 33.4 ft. The

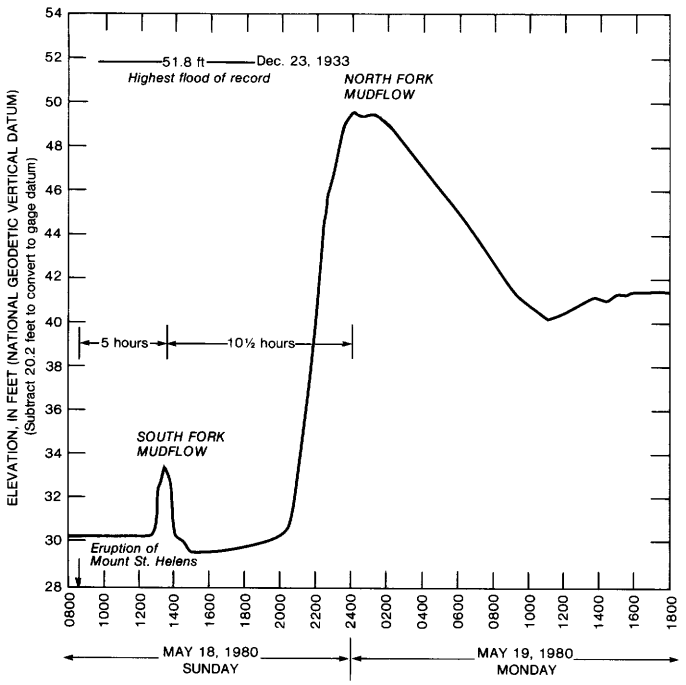

Figure 399.—River stage, Cowlitz River at Castle Rock, Wash., May 18–19, 1980.

level then quickly dropped, returning to 30.2 ft by 1415. The South Fork Toutle River mudflow was confined entirely within the channel of the Cowlitz River, but the associated deposition is unkown, because channel conditions were soon altered by the larger North Fork Toutle River mudflow.

At about the same time (1330 on May 18) that the first mudflow peaked at Castle Rock, a second larger mudflow was developing on the massive debris-avalanche deposit in the devastated upper part of the North Fork Toutle River valley (Cummans, this volume). This massive and highly destructive

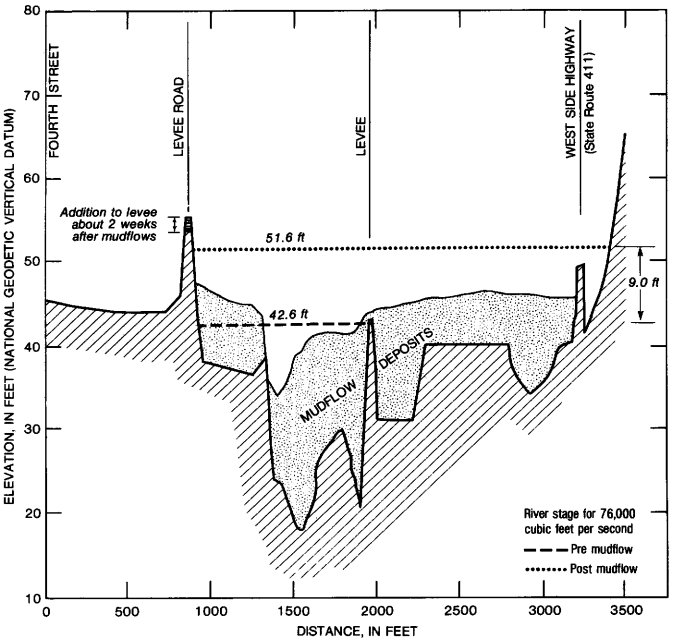

Figure 400.—Channel and valley conditions of the Cowlitz River near Castle Rock, Wash., prior to and after the mudflows of May 18, 1980. The cross section is located 1,400 ft downstream from the Castle Rock bridge.

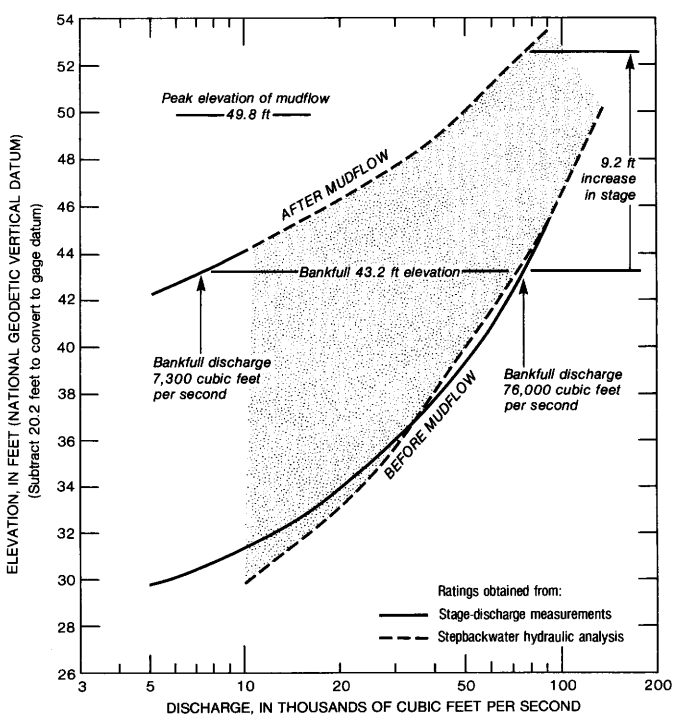

Figure 401.—Relation between river stage and discharge prior to and after the mudflows of May 18, 1980, Cowlitz River at Castle Rock, Wash.

mudflow moved more slowly than the South Fork mudflow, with the peak stage at Castle Rock (fig. 399) occurring at about midnight on May 18. The peak stage of the second mudflow was 49.5 ft, 16.1 ft higher than the first mudflow. The North Fork mudflow spilled over the lower Cowlitz River flood plain, leaving deep deposits of sand, volcanic ash, and gravel-sized pumice on the flood plain and in the channel. The areal extent of the inundation is shown in figure 398.

In figure 399, the shape of the hydrograph beginning at about 1100 on May 19 is indicative of the massive sediment deposition that occurred in the channel during the North Fork Toutle River mudflow. The deposition raised the riverbed, and reduced the capacity of the channel to convey water. For example, at 0800 on May 18, a flow of 6,160 ft^3/s (cubic feet per second) occurred at a river stage of 30.1 ft. In contrast, at 0800 on May 20 (not shown), a similar flow of 6,140 ft^3/s occurred at a river stage of 42.4 ft—12.3 ft higher than before the mudflow.

EFFECT OF MUDFLOWS ON CHANNEL AND FLOOD PLAIN

Prior to the mudflows, the lower Toutle and Cowlitz Rivers had well-defined channels, confined in places by artificial levees. Figure 400 compares the

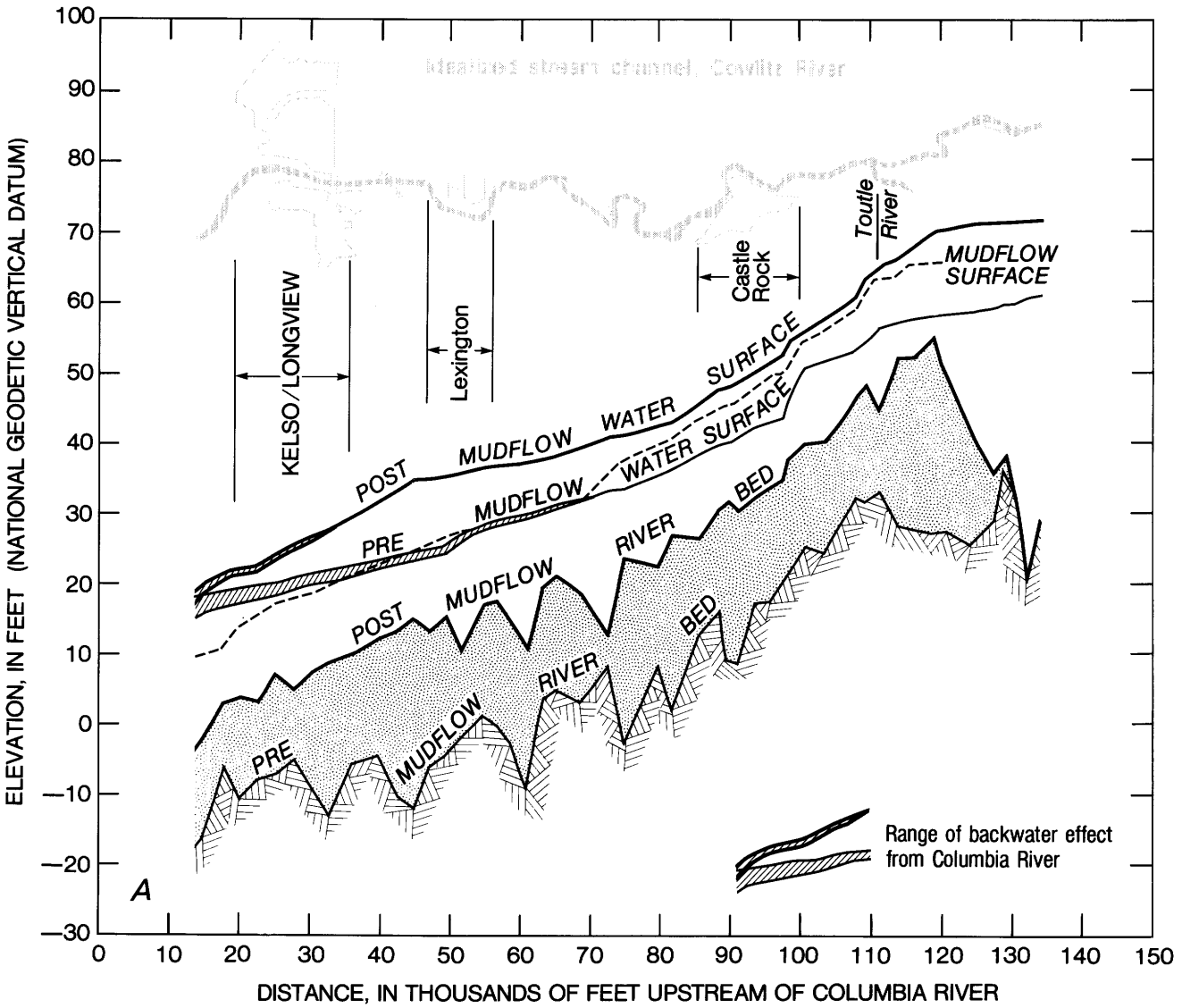

Figure 402.—Channel bottom and water-surface elevation prior to and after

pre- and post-mudflow character of a cross section through the Cowlitz River and flood plain, 1,400 ft downstream from the Castle Rock bridge. At this location, the North Fork Toutle River mudflow was contained by the east bank (left-hand side) levee, but overtopped the west side levee, leaving thick deposits of sediment between the levee and the West Side Highway. Particularly evident in the cross section are (1) the great thickness of deposits within the channel, and (2) the smoothing of the overbank profile on the west bank. The average depth of sediment deposited over the entire cross section was 9.3 ft. Within the channel (levee to levee), deposition raised the low point (thalweg) by 16.3 ft.

In the Castle Rock area, the North Fork Toutle River mudflow failed to top the 1.5-mi-long east bank levee that was built to protect the city; in places, however, the flow came within inches of the top. At many other locations along the Toutle and lower Cowlitz Rivers, the mudflows were not contained by levees or roads and, hence, overflowed and left widespread deposits on the flood plain (fig. 398). In general, the thickness of the overbank deposits decreased in a downstream direction.

Downstream from Lexington, few overbank deposits occurred, and in the vicinity of Kelso and Longview (fig. 398), levees completely confined the mudflows to the channel. Part of the North Fork Toutle

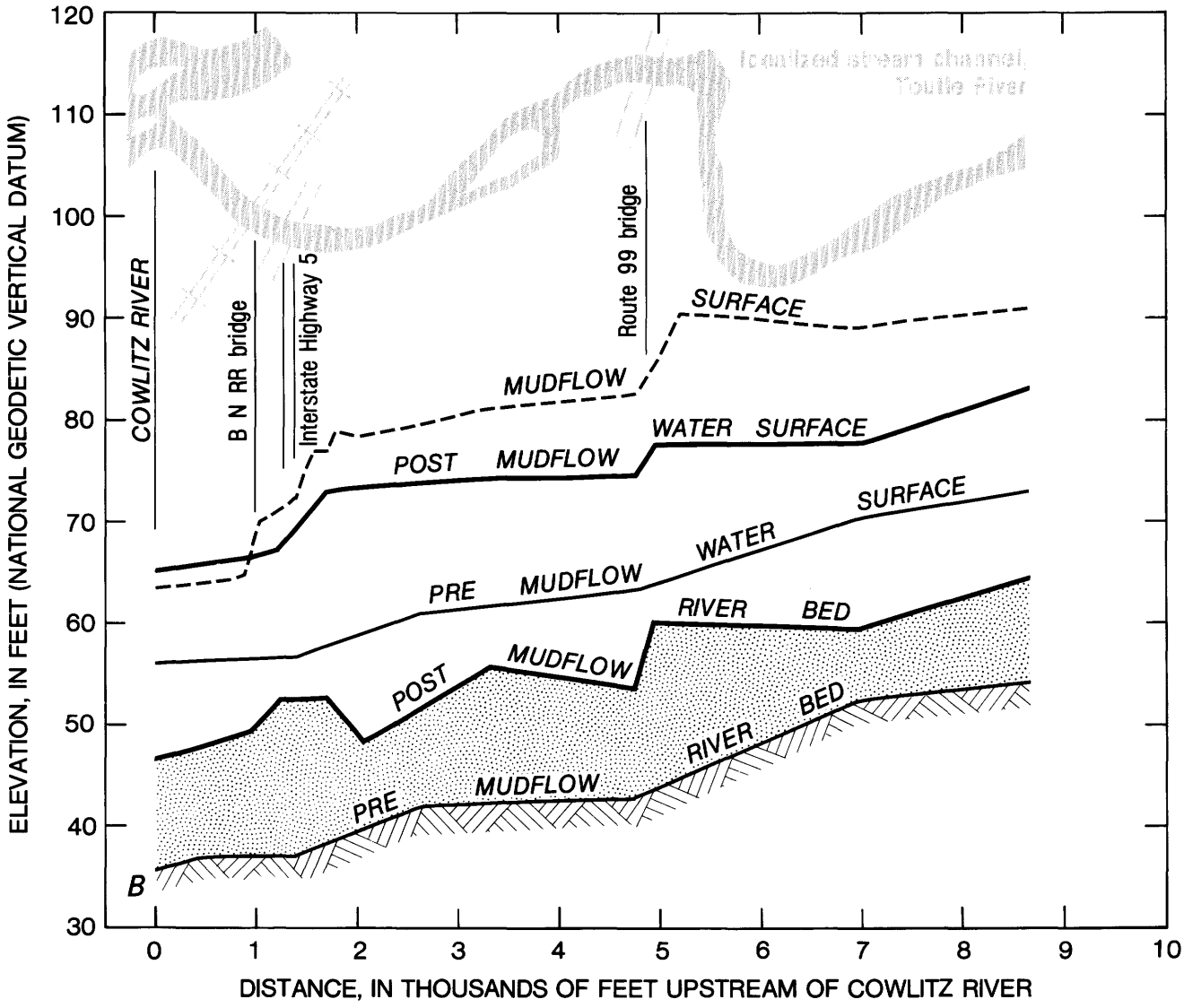

the mudflows of May 18, 1980. A, lower Cowlitz River; B, lower Toutle River.

River mudflow also moved about 2.5 mi upstream in the Cowlitz River above the Toutle River confluence, but overbank deposits were not extensive.

EFFECT OF MUDFLOWS ON FLOOD ELEVATIONS

Hydraulic characteristics of the lower Toutle and Cowlitz Rivers were analyzed to compute flood stages on both rivers before and after the mudflows. The water-surface elevations were computed with the aid of the U.S. Geological Survey's step-backwater computer program (Shearman, 1976).

Cross-sectional data for the backwater analyses were obtained from several sources. Step-backwater analyses for the rivers before the mudflows were based on data provided by U.S. Army Corps of Engineers (written commun., 1980), Tudor Engineering Company (written commun., 1980), and Towill, Inc. (written commun., 1980). Step-backwater analyses for the rivers after the mudflows were based on detailed surveys of the channels and flood plains by the U.S. Geological Survey and the U.S. Army Corps of Engineers on June 19, 1980, and on two channel surveys by the U.S. Geological Survey between May 19 and June 18, 1980.

Prior to the eruption and subsequent mudflows, flood stage on the Cowlitz River at the Castle Rock gage was 43.2 ft (fig. 401) with a corresponding flow of 76,000 ft^3/s (National Weather Service, oral commun., 1980). Floodstage at the U.S. Geological Survey gage at Castle Rock after the mudflows remained about the same as before, but the capacity of the channel to convey water was reduced to about one-tenth of the preeruption level. A flow of 76,000 ft^3/s occurring after the mudflows would produce a stage 9.2 ft higher at the gaging station at Castle Rock (fig. 401), and a stage 9.0 ft higher at the cross section 1,400 ft downstream (fig. 400). In the vicinity of Castle Rock, a post-mudflow discharge of 76,000 ft^3/s would be contained by the levee on the east bank but would inundate the valley to the west.

Increases in stage along both the lower Toutle and lower Cowlitz Rivers as a result of mudflow deposits are shown in figure 402. These stage profiles were computed for a flow of 76,000 ft^3/s in the Cowlitz River, and for proportional flow of 38,000 ft^3/s in the Toutle River and in the Cowlitz River above the Toutle River. The latter discharge was determined to be an appropriate proportional discharge in the Toutle River for a flow of 76,000 ft^3/s in the Cowlitz River at Castle Rock. The posteruption increases in the stage profiles in figure 402 are based on channel conditions during June 1980, and do not reflect subsequent channel changes that have resulted from fill, scour, dredging, or alteration of levees.

Elevations of the mudflows along the lower Toutle and Cowlitz Rivers, as determined from mudlines, are also shown in figure 402. The peak elevation of the North Fork Toutle River mudflows at the Castle Rock gage was 49.8 ft (fig. 401). For comparison, table 92 gives the discharges and stages for recorded floods exceeding 76,000 ft^3/s at this gage. (Compiled from:

Table 92.—Peak discharges exceeding 76,000 cubic feet per second and corresponding river stage (from highest to lowest) of Cowlitz River at Castle Rock, Wash., during period of record 1927-78

[ft^3/s, cubic feet per second]

Date of peak	Discharge (ft^3/s)	River stage (ft)[1]
Dec. 23, 1933-----	139,000	51.8
Dec. 4, 1975-----	[2]86,700	44.73
Dec. 2, 1977-----	[2]86,400	44.68
Dec. 13, 1946-----	85,100	44.60
Dec. 23, 1964-----	[3]83,900	44.61
Jan. 20, 1972-----	[2]81,600	44.00

[1]Subtract 20.2 ft to convert to gage datum.

[2]Flow regulated by Mayfield Reservoir and Riffe Lake. Total usable capacity, 1,318,800 acre-ft.

[3]Flow regulated by Mayfield Reservoir. Usable capacity, 21,380 acre-ft.

U.S. Geological Survey, 1958, 1963, 1971, 1972, [1972–75], [1976–79].)

SUMMARY

This report documents some depositional and flood impacts of mudflows on the lower Toutle and Cowlitz Rivers after the onset of the May 18, 1980, eruption of Mount St. Helens. Deposits of as much as 15 ft of sediment reduced flow capacity in the lower Cowlitz to about one-tenth of the preeruption capacity, thereby creating a high potential for severe flooding during the autumn and winter high-flow season.

REFERENCES CITED

Shearman, J. O., 1976, Computer applications for step-backwater and floodway analyses, User's manual: U.S. Geological Survey Open-File Report 76–499, 103 p.

U.S. Geological Survey, 1958, 1963, 1971, 1972, Surface water supply of the United States—Part 14, Pacific slope basins in Oregon and lower Columbia River basin: U.S. Geological Survey Water-Supply Papers 1318, 1738, 1935, 2135. [Titles vary slightly.]

_____[1972–75], Water resources data for Washington—Part 1, Surface water records: U.S. Geological Survey. [Records for years 1971, 1972, 1973, 1974.]

_____[1976–79], Water resources data for Washington—Water year [years 1975, 1976, 1977, 1978]: U.S. Geological Survey Water-Data Reports WA–75–1, WA–76–1, WA–77–1, WA–78–1.

THE 1980 ERUPTIONS OF MOUNT ST. HELENS, WASHINGTON

EFFECTS OF THE ERUPTIONS ON CIVIL WORKS AND OPERATIONS IN THE PACIFIC NORTHWEST

By ROBERT L. SCHUSTER

ABSTRACT

Civil works and operations immediately north of Mount St. Helens and in the upper reaches of the North Fork Toutle River were almost completely destroyed by the lateral blast and debris avalanche from the May 18 eruption. Mudflows caused by the same eruption caused severe damage on the remainder of the Toutle River and lesser damage on the lower Cowlitz River and along parts of the Lewis River. Sedimentation had a severe impact on the lower Columbia River. In addition, ash deposited over eastern Washington, northern Idaho, and western Montana by the May 18 eruption hampered transportation and municipal operations. Ash from the eruptions of May 25 and June 12 had a similar, but lesser, effect on southwestern Washington and the Portland, Oreg., area.

INTRODUCTION

Civil works such as highways, railways, waterways, airports, bridges, buildings, dams and reservoirs, and water-supply, sewage-disposal, drainage, and flood-control systems are all vital to the populace of any developed area. All these kinds of works and their attendant operations were directly affected by the Mount St. Helens eruptions. Most of the outright destruction of public and private civil works occurred either in the immediate vicinity of Mount St. Helens or in the Toutle River drainage; however, considerable damage to facilities and interruption of operations also occurred farther downstream along the Cowlitz and Columbia Rivers (fig. 403). In addition, civil works and operations in eastern Washington, northern Idaho, and even western Montana were disrupted by ash fall from the May 18 eruption; the May 25 and June 12 eruptions similarly affected western Washington and the Portland area of Oregon, respectively, but to a lesser degree than the May 18 eruption.

This report discusses damages to civil works and disruption of civil operations in both public and private sectors. Transportation facilities and operations were the most intensely affected. The State of Washington, the U.S. Forest Service, the Weyerhaeuser Company, and Cowlitz County sustained considerable loss to transportation facilities and operations in the vicinity of Mount St. Helens. The movement of ship traffic on the Columbia River to and from the Port of Portland was severely disrupted by sediment deposited in the Columbia at the mouth of the Cowlitz River. Removal and disposal of ash from roads and highways required substantial efforts in widespread areas farther from the mountain; these operations were conducted primarily by State, county, and local governmental agencies, by private companies, and by individuals.

Flood control on the Toutle and Cowlitz Rivers, which is under the jurisdiction of the U.S. Army Corps of Engineers, was completely disrupted by

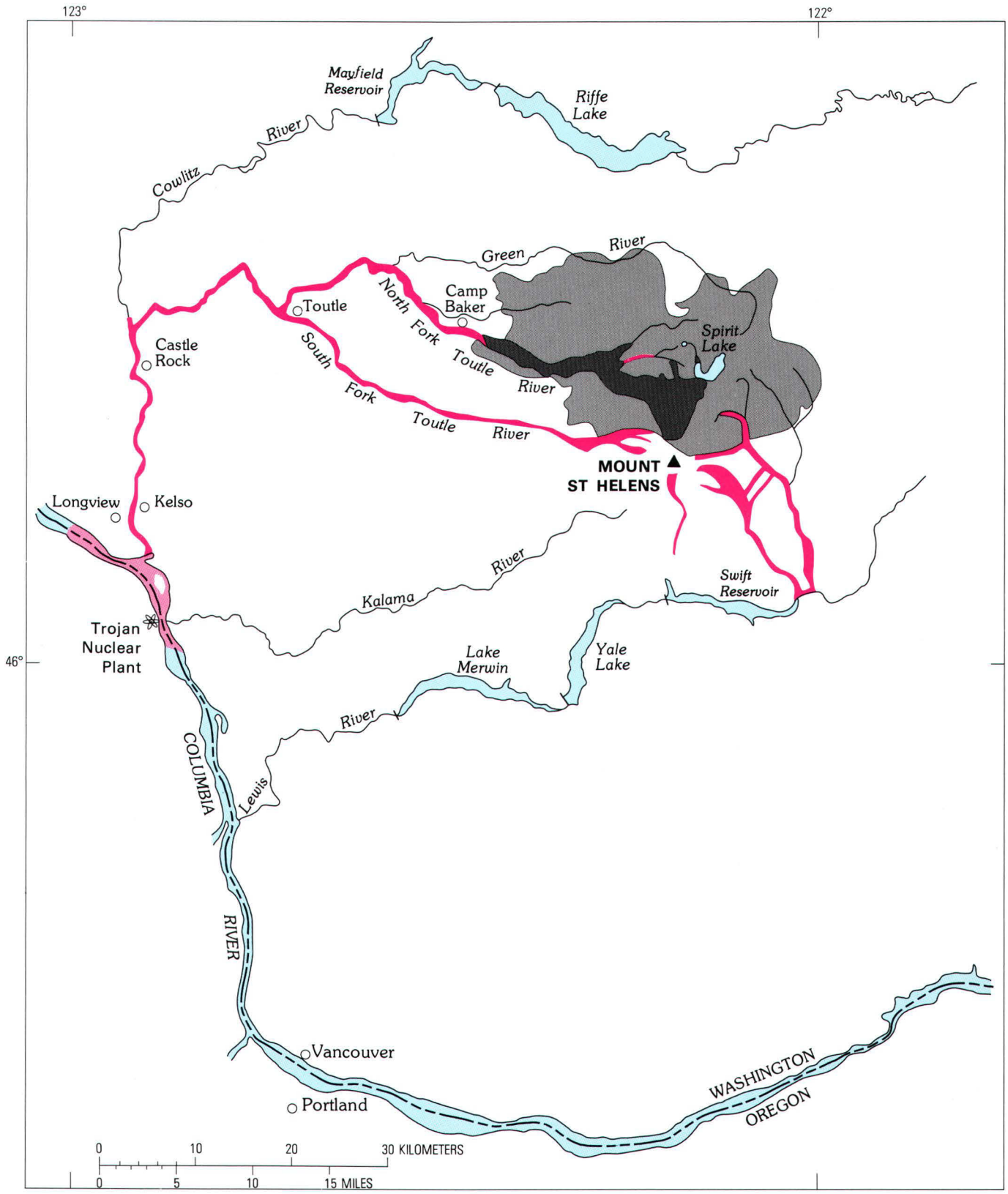

Figure 403.—Location map of area near Mount St. Helens directly affected by the May 18 eruption. Debris avalanche, dark gray; area devastated by blast, light gray; mudflows, light red; area of major sedimentation, dark red.

sediment deposited in these rivers. In addition, mudflows and sedimentation caused damage to water-supply systems in municipalities along the Toutle and Cowlitz Rivers, and ash fall disrupted municipal sewage-disposal and storm-drain systems in eastern Washington. Damage to dams, reservoirs, and power-supply systems was minor.

This report describes the damage and losses to civil works and operations due to lateral blast, debris avalanche, mudflows, flooding and sedimentation, and ash fall.

EFFECTS OF THE LATERAL BLAST

Destruction of civil works and operations immediately north of Mount St. Helens due to the May 18 eruption was sudden and total. The lateral blast from the eruption consisted of shock wave, thermal effect, and massive amounts of airborne pyroclastic debris, some of which was hot (Hoblitt and others, this volume; Moore and Sisson, this volume). The blast affected an area that extends generally northward through an arc of approximately 120° from northwest to east-northeast (fig. 403). Within this arc, destruction was essentially total within a radial distance of 13 km (8 mi) from the crater of Mount St. Helens; all vegetation and most of the soil were removed from slopes that face the volcano (Watershed Rehabilitation Team, 1980). Because this zone was principally a recreation and timber-producing area, its civil works consisted primarily of roads and bridges, recreational buildings, campgrounds, and timber-harvesting facilities.

Beyond the zone of total devastation, in an area extending to about 18 km (12 mi) east-northeast and 22–24 km (14–15 mi) north and northwest from the crater of Mount St. Helens, old-growth timber was blown down and lesser vegetation was killed by the blast, buried by airborne debris, or both (pl. 1). In this zone, falling trees caused extensive damage to recreational and logging roads and operations; however, much of this damage has since been repaired.

Surrounding this blowdown zone was a halo as much as 2–3 km (1–2 mi) wide within which the thermal effect of the blast killed the vegetation; damage from the blast itself to civil works within this zone was minimal.

EFFECTS OF THE DEBRIS AVALANCHE

Following the collapse of the upper northern portion of the cone of Mount St. Helens, a debris avalanche consisting of about 2.5 km^3 (0.6 mi^3) of material, which ranged from fine ash to boulder-size rocks, completely buried the remaining northern slope of the mountain and the south shoreline of Spirit Lake; it cascaded northward into Spirit Lake itself and extended about 24 km (15 mi) down the valley of the North Fork Toutle River from the mountain (Glicken and others, 1980). In that valley the debris avalanche terminated only 3 km (2 mi) east of Camp Baker, a large operational facility for logging in the area. Camp Baker was the upstream terminus for a logging railroad and the main hub for timber-haul roads in the area.

The debris avalanche had the following direct effects on civil works and operations:

1. Public and private buildings and attendant facilities on the shore of Spirit Lake were obliterated. Nearly all these properties were related to recreation on the lake and in the surrounding area.

2. State Highway 504 was permanently buried from timberline on Mount St. Helens to the end of the debris avalanche in the valley of the North Fork Toutle River, a length of some 32 km (20 mi). Two of the seven bridges the State lost in the valley were in this section of highway (fig. 404). In addition, many kilometers of private logging roads and five private and two U.S. Forest Service bridges were destroyed.

No "major" structures such as dams and reservoirs, powerplants, or large buildings were in the area devastated by the debris avalanche. Had the debris avalanche gone to the south, it might have inundated Swift Reservoir (fig. 403) and caused flooding of the lower valley of the Lewis River.

The destruction of existing civil works by the debris avalanche was not related to the designs of structures and facilities. The only way that destruction of civil works could have been avoided in the area would have been by land-use planning that prevented development in that area. However, nearly all the development occurred before Crandell and Mullineaux (1978) identified and publicized the

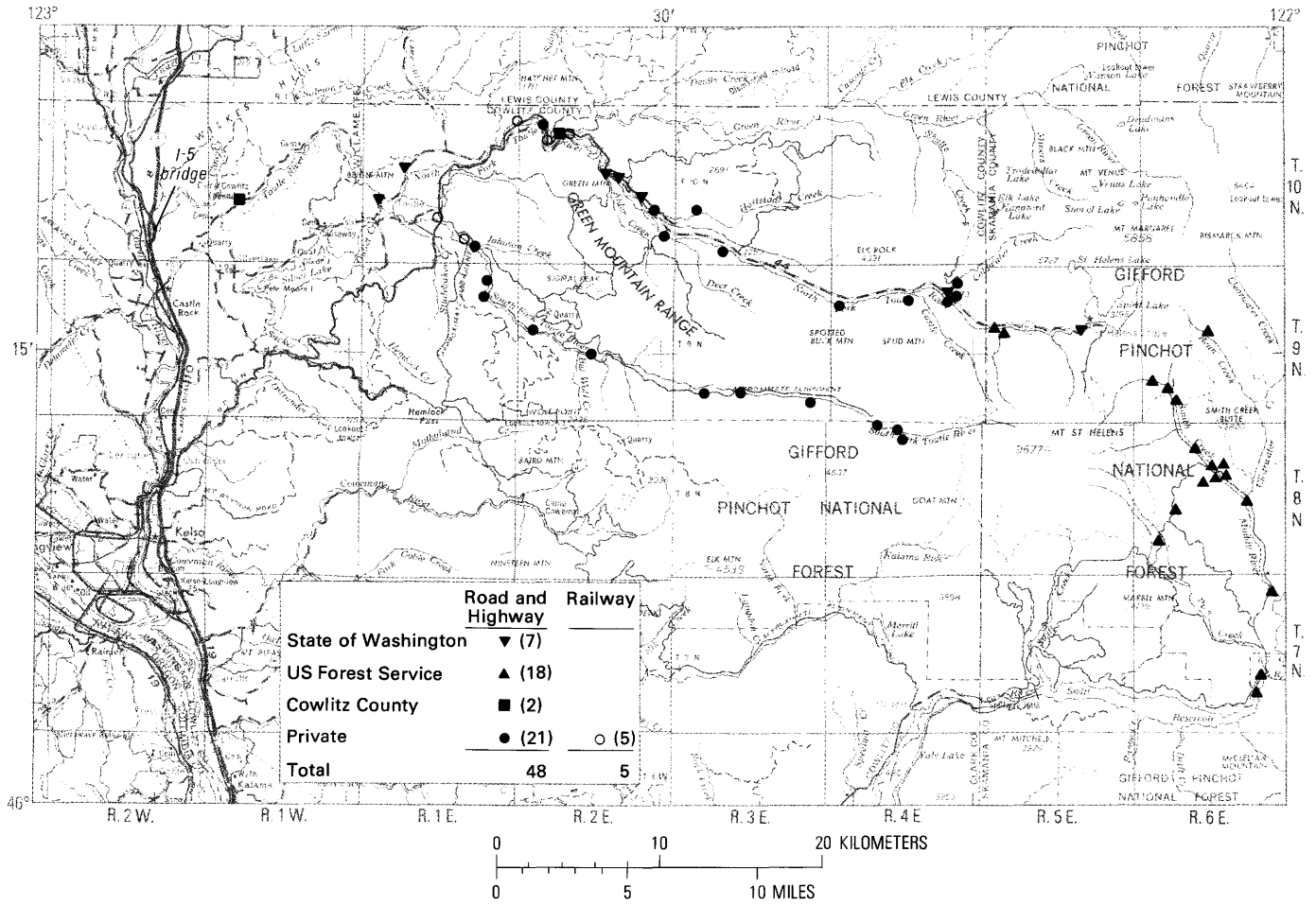

Figure 404.—Locations of bridges destroyed or heavily damaged by the debris avalanche and mudflows resulting from the May 18, 1980, eruption. Note location of the critical Interstate 5 bridge, which survived the mudflow on the Toutle River.

potential hazards from Mount St. Helens. The lessons learned here should not be forgotten; restrictions on future development in this area should be carefully considered in relation to possible future eruptions.

Even without further major eruptions, the debris avalanche poses a major threat to civil works and developments downstream in two ways (Lombard and others, this volume; Voight and others, this volume):

1. Until the surface of the debris avalanche has been covered by vegetation, it will be extremely susceptible to erosion, and the eroded material will wash downstream. If the volume is large enough, it could further clog the already reduced channels of the posteruption Toutle and Cowlitz Rivers, and thus flood low-lying parts of the river valleys. To reduce the volume of sedimentation downstream, the U.S. Army Corps of Engineers in the summer and fall of 1980 spread grass seed on the lower part of the debris avalanche to develop an erosion-resistant cover of grass before the heavy fall-to-spring runoffs, and constructed a pervious embankment dam 1,300 m (4,200 ft) long and 12 m (40 ft) high at the spillway. This embankment dam will serve as a "debris restraining" structure; water will pass through it, but sediment will be deposited in the reservoir. The entrapped sediment will then be dredged from the reservoir and piled in windrows protected from erosion by waste logs.
2. The debris avalanche dammed several tributaries to the North Fork Toutle River, including the outlet from Spirit Lake (Jennings and others, this volume). Each of the lakes formed in this manner may eventually cause its immediate "dam"

to fail either due to landsliding or due to overtopping, perhaps followed by rapid downward erosion. Water released by such failures could cause major flooding downstream. One of the purposes of the Corps of Engineers debris-restraining dam mentioned above is to impede at least partially any flooding that occurs in this manner.

EFFECTS OF MUDFLOWS

As a direct result of the May 18 eruption, mud and associated debris flowed down several of the valleys that radiated from the mountain (fig. 403). The largest and most destructive mudflows occurred in the valleys of the North Fork and South Fork Toutle River and in the Cowlitz River downstream of its confluence with the Toutle; however, mudflows in tributaries of the Lewis River on the southeast and east sides of the mountain were large enough to destroy forest roads and bridges and to flow into Swift Reservoir (Janda and others, this volume).

TOUTLE RIVER MUDFLOWS

The mudflow in the North Fork Toutle River was formed primarily by remobilization of material in the debris avalanche, and thus affected the valley floor only downstream from the terminus of the debris avalanche. Conversely, the mudflow in the valley of the South Fork Toutle River began on the slopes of the mountain and thus affected the entire length of the valley.

In addition to destroying or heavily damaging about 200 homes in the Toutle River valley, the mudflows had the following effects on civil works:

1. Buried about half of State Highway 504 from Camp Baker to the town of Toutle under as much as 2 m (6 ft) of sediment (fig. 405), many kilometers of private logging roads and railway, and several kilometers of Cowlitz County roads. The length of private and county roads buried by mudflows is a significant percentage of the total losses in these categories shown in table 93, and mudflows destroyed all 27 km (18 mi) of railway shown.
2. Destroyed or badly damaged 27 bridges in the valley, including 5 of the 7 bridges lost on State Highway 504 (examples, figs. 406 and 407), 15 highway and 5 railway bridges privately owned and used to transport logs to downvalley lumber mills, and 2 highway bridges owned by Cowlitz County. Most of these were modern concrete and (or) steel structures, the largest being the 160-m (525-ft) steel-girder Coal Bank bridge that spanned the Toutle River on State Highway 504 near the town of Toutle. This bridge was destroyed by a mudflow that carried timber debris (fig. 407). With the exception of one log-stringer bridge, the private logging highway bridges on both the North Fork and South Fork Toutle River were modern concrete structures built between 1972 and 1979, and the railway bridges were major steel structures over the North Fork and South Fork.

Only four bridges spanning the Toutle River, North Fork and South Fork were not destroyed or seriously damaged by the mudflows. Three of these were high enough that they received only minor, nonstructural damage from buffeting by timber debris carried by the mudflows; the fourth, the Kid Valley bridge on State Highway 504, had sufficient clearance that it was not touched. Of these four bridges, the most crucial to the transportation system of western Washington were the Interstate 5 bridge and the Burlington Northern railway bridge, which span the Toutle River where it empties into the Cowlitz River (fig. 408). Because these bridges carry nearly all the highway and railway traffic between Portland and Seattle, their destruction would have severely affected interstate commerce. Interstate 5 traffic was detoured for 12 hr

Table 93.—Length in kilometers of highways, roads, and railways destroyed or extensively damaged as a direct result of the May 18 eruption

	Highways and roads (km)	Railways (km)
State of Washington	48	0
U.S. Forest Service	38	0
Cowlitz County-----	16	0
Private----------	198	27
Total---	300	27

while the highway bridge was in immediate danger from the mudflow, flooding, and debris, and the railway bridge was closed for repairs for 24 hr; but the overall disruption of western Washington's transportation system fortuitously was minor compared to the possible effect of the destruction of these bridges.

3. Partially submerged and heavily damaged three large logging camps (two on the North Fork Toutle River and one on the South Fork). These camps were used primarily as maintenance and storage facilities for logging operations. The largest and most heavily damaged of the three was Camp Baker, which was buried by as much as 2 m (6 ft) of sediment. Figure 409 illustrates typical destruction of transportation equipment at Camp Baker. These logging camps were dug out and restored to full operation within a few months of the eruption.
4. Destroyed water-supply and sewage-disposal systems owned by residents, private companies, and local governments. For example, the water-supply plant for the town of Toutle, which obtained water from the South Fork Toutle River, was buried by 2 m (6 ft) of sediment.

EFFECTS OF ORIGINAL PLANNING AND DESIGN OF STRUCTURES

Because the potential hazard from Mount St. Helens was not publicized until 1978, roads, railroads, and bridges on the Toutle River and its forks were designed to be safe from potential floods, not from mudflows. In April 1980, D. R. Crandell (oral commun.) noted that State Highway 504 locally was situated as little as 2 m (6 ft) above river level and that bridges on this highway had clearances of only about 5–6 m (15–20 ft); an exception was the Kid Valley bridge, which survived the May 18 eruption because

Figure 405.—Mudflow deposit covering State Highway 504 near the town of Toutle to a depth of 2 m (6 ft).

its clearance was approximately 12 m (40 ft). Obviously, these structures could not survive mudflows that had measured local depths (based on mud marks on trees) of as much as 17 m (55 ft), nor would it have been economically feasible to design and build roads and bridges that would not be inundated by these mudflows. It certainly would not have been practical to design all bridges for mudflows equivalent to some prehistoric mudflows that had combined thicknesses measured in this valley of as much as about 20 m (65 ft) (D. R. Crandell, oral commun., 1980).

RECONSTRUCTION

In spite of the large amounts of damage to civil works in the valleys of the Toutle River and its forks, reconstruction of much of the damaged works proceeded rapidly, particularly of facilities related to recovering timber from the area. For example, the three logging camps mentioned above were dug out and restored to full operation during the summer of 1980. Highways and roads that provide access to the area by homeowners and timber workers also were generally in usable condition by the end of the summer. Many kilometers of roadway were restored to service by road crews using front-end loaders or similar equipment to remove sediment. Most highway bridges were replaced by temporary spans by the end of the summer; for example, the Coal Bank bridge on State Highway 504 was replaced by a shorter steel Bailey bridge that was placed at a narrower reach of river a few hundred meters downstream.

The logging railway that extended downstream from Camp Baker did not fare so well. The mudflows destroyed the railway's five bridges and tore up several kilometers of track. An economic decision was made to restore only the two bridges on the South Fork and to terminate the railway near the town of Toutle; thus, the upper 21 km (13 mi) section of railroad was abandoned, and its function was taken over by conventional haul roads. The two railway bridges on the South Fork were replaced by temporary structures within a few weeks, and construction quickly was begun on permanent steel and concrete replacements.

The minor damage to the railway bridge on the main Portland-Seattle route (fig. 408) was quickly repaired to allow resumption of full rail traffic between those cities. However, because the channel for the Toutle River was considerably constricted by sediments remaining from the mudflow, this railway bridge and the adjacent Interstate 5 bridge still were threatened by possible flooding during the 1980–81 winter-spring runoff. To lessen the danger to these essential structures, the Corps of Engineers dredged sediment from the Toutle River for a distance of 1½ km (1 mi) upstream from the bridges (Bechly, 1980).

COWLITZ RIVER MUDFLOWS

Mudflows from the tributary Toutle River issued into the Cowlitz River late in the evening of May 18. Although the mass of sediment and water was considerably diluted by mixing with the large volume of water in the Cowlitz, it still can be classified as a mudflow while passing down the Cowlitz (Janda and others, this volume). The hydrologic aspects of this mudflow and associated flooding are discussed by Lombard and others (this volume). However, the mudflows, flooding, and accompanying debris that occurred along the Cowlitz River as a result of the May 18 eruption drastically affected operations of municipal water-supply services for Longview and Kelso, and both water-supply and sewage-disposal services for Castle Rock.

The city of Longview (population 30,000) takes its water from the Cowlitz River, 21 km (13 mi) downstream from its confluence with the Toutle River; this water is pumped through a raw-water plant to a nearby filtration treatment plant (Edtl, 1980). The first flood and debris reached Longview late on the afternoon of May 18; by late that evening the flood had passed, but turbidity of water entering the treatment plant increased, at first to 10 JTU (Jackson turbidity units), then to 20, 40, 120, and, by the end of the day, to 420 JTU. By 0300 on May 19, the Cowlitz River, which was clogged by debris and mud, had risen 4 m (13 ft) and had swept away the plant's water-supply intake structure shearboom. By 0800 the flood had partially receded, but left behind a 3½-m (12-ft) deposit of mud and silt that clogged the plant's intake, pumps, and screens, and partially filled its sedimentation basins (fig. 410); no permanent damage was done, but it took weeks before the system was completely unclogged and back in full service. On May 19 the raw-water temperature in the Cowlitz River, which normally is about 7°C (45°F) at this time of year, had risen to 32°C (90°F), and turbidity levels were an almost unmeasurable 50,000–77,000 JTU; thus, the

Figure 406.—The 75-m (247-ft) St. Helens bridge on State Highway 504. A, Before May 18, Photograph by D. R. Crandell. B, After May 18 when it was washed out by the mudflow on the North Fork Toutle River, This steel structure was carried about ½ km (¼ mi) downstream and was partially buried by the mudflow.

raw water was virtually untreatable even had the treatment system been operable.

Two weeks before the eruption, the city of Kelso (Longview's sister city, population 12,000) had installed a new collector system to pump water from gravels permeated by the Cowlitz River (G. Wilder, Kelso City Engineer, oral commun., 1980). This system was temporarily put out of action by electrical and mechanical problems due to flooding and sedimentation. A longer range problem was caused by sediment clogging the river gravels, which reduced their permeability and their potential as a water-supply source; as a direct result, the collector system, which has a rated production of 19,000 m^3/day (5 million gal/day), was able to produce only 5,700 m^3/day (1.5 million gal/day) more than a month after the eruption.

The city of Castle Rock (population 2,000) is on the low flood plain of the Cowlitz River, only 3 km (2 mi) downstream from the mouth of the Toutle River. The Castle Rock fairgrounds were covered by river sediment to a depth of as much as 1–1½ m (3–5 ft) (Hawkins and others, 1981). The city lost its water intake in the May 18 flood and, until repairs were made, had to truck water from the small town of Vader, about 14 km (9 mi) to the north. In addition, the outfall for the city-sewage treatment plant was washed away, and storm sewers, which were completely silted in, had to be cleaned before they were usable.

The mudflow and flood deposited more than 38 million m^3 (50 million yd^3) of sediment in the Cowlitz River, downstream from the mouth of the Toutle River (Bechly, 1980); this was nearly enough to fill the original Cowlitz River channel. To restore the original channel and thus minimize future flooding, the Corps of Engineers as of December 1980 had dredged approximately 27 million m^3 (35 million yd^3) of sediment from

the river (J. Bechly, U.S. Army Corps of Engineers, oral commun., 1980). Dredging of the Cowlitz is expected to continue for several more years as new sediment is washed downstream from the Toutle River. Estimated costs are about $300 million through 1985. Nearly all the spoil material is being placed in low, marshy areas along the river; in general, this action is expected to increase property values, particularly for formerly flood-prone areas that have potential as industrial sites.

MUDFLOWS ON THE LEWIS RIVER AND ITS TRIBUTARIES

As shown in figure 403, as a result of the May 18 eruption, mudflows occurred in tributaries of the Lewis River on the south, southeast, and east sides of the mountain (Janda and others, this volume). These mudflows buried several kilometers of U.S. Forest Service recreational and timber-haul roads and destroyed 16 bridges on these roads. The bridges were concrete, steel, and log-stringer structures ranging in length from 17 to 104 m (55 to 340 ft).

Potentially the most serious hazard from mudflows on the upper Lewis River and its tributaries is to Swift Reservoir and dam, which lie about 15 km (10 mi) south and southeast of Mount St. Helens (fig. 403). Swift dam is an earthfill dam that has a crest length of 640 m (2,100 ft) and a height of 156 m (512 ft); it impounds a reservoir that has a gross capacity of about 920 million m^3 (755,000 acre-ft) for hydroelectric power generation and recreation. Crandell and Mullineaux (1978) noted that a mudflow of large volume flowing into Swift Reservoir could raise the level of the reservoir faster than the water could be discharged safely. In addition, if such a flow entered the full reservoir rapidly, it could create a wave that might overtop the dam. Either of these events could result in downstream flooding that would endanger Yale Lake and Lake Merwin reservoirs and residents of the lower Lewis River valley, particularly those in the town of Woodland.

Crandell and Mullineaux (1978) estimated that the

Figure 407.—The 160-m (525-ft) steel-girder Coal Bank bridge on State Highway 504 near the town of Toutle. A, Before May 18. Photograph by D. R. Crandell. B, Being destroyed by mudflow carrying debris in the Toutle River valley. Note puffs of dust coming from the ends of the span at the exact moment of failure. Copyrighted photograph by R. Werth, The Daily News, Longview, Wash., published with permission. Large girders from this structure were carried about 2 km (1¼ mi) downstream by the mudflow.

largest single mudflow that might be expected to enter Swift Reservoir from Mount St. Helens would have a volume of no more than 125 million m^3 (roughly 100,000 acre-ft). On the basis of this estimate and of the recognition of potential for a large mudflow due to volcanic activity, the reservoir was drawn down 7 m (23 ft) below the normal maximum operating level between March 24 and 28, 1980; this reduction left a vacant storage volume of about 125 million m^3 (100,000 acre-ft) (Pacific Power & Light Company, 1980).

The May 18 eruption sent mudflows down Pine Creek and Muddy River into the Lewis River at the head of Swift Reservoir (fig. 403); inflow of over 13.5 million m^3 (11,000 acre-ft) of water, sediment, and debris into the reservoir raised the water level about 3/4 m (2½ ft) (Pacific Power & Light Company, 1980). A water-level recorder at the dam indicated that a wave about ½ m (1½ ft) high occurred there. The only consequence to the reservoir was a loss of storage capacity due to the sediment; however, because only about 545 million m^3 (447,000 acre-ft) of the original reservoir consisted of usable capacity, and because most of the sediment flowed toward the bottom of the reservoir into the zone of "dead storage," the resulting loss in power-production capacity was insignificant.

Realizing that a potential hazard to Swift Reservoir from future mudflows still exists, Pacific Power & Light Company has sponsored a study to determine potential effects of future mudflows on the reservoir (Pacific Power & Light Company, 1980). In that

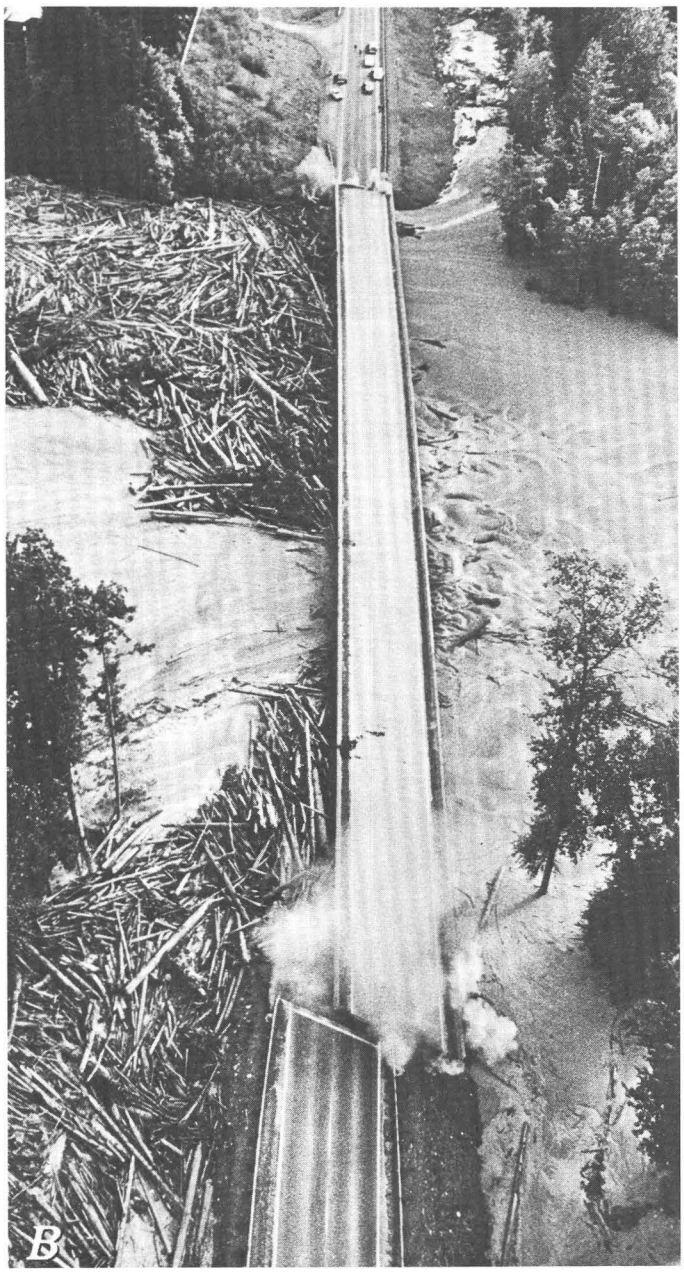

study, model "mudflows," consisting of bentonite, barite, and water, were released into a 1:500-scale model of the reservoir and its entering streams at different rates and at different reservoir levels. The effects on the reservoir were determined by wave-height measurements. Application of the results of these studies will enable better prediction of the necessary drawdown if future activity of Mount St. Helens results in a strong possibility of mudflows into Swift Reservoir.

EFFECTS OF SEDIMENTATION IN THE COLUMBIA RIVER

The Cowlitz River mudflow and floods caused by the May 18 eruption deposited about 34 million m^3 (45 million yd^3) of sediment in the Columbia River from 100 to 120 km (63 to 75 mi) upstream from its mouth (Bechly, 1980). This material consisted mainly of pumiceous sands and gravels, because most clay and silt-size materials were distributed farther downriver or carried into the Pacific Ocean. As illustrated in figure 411, most of the sediment was deposited upstream from the mouth of the Cowlitz River; apparently, the first sediment that issued from the Cowlitz partially dammed the Columbia, thus deflecting later sediment upstream.

Prior to the May 18 eruption, almost a dozen ocean-going freighters came up the Columbia River to the Port of Portland daily; each ship is the equivalent of three to five railway freight trains in terms of cargo capacity. An immediate effect of deposition of the sediment was the blocking of the Columbia River navigation channel to that shipping. By June 1 the Corps of Engineers had three hopper dredges working to clear the Columbia River channel and had contracted for six pipeline dredges, which began work during the summer. The Corps of Engineers has removed some 11.5 million m^3 (15 million yd^3) of sediment in dredging a new channel approximately 12 m (40 ft) deep and 180 m (600 ft) wide (J. Bechly, U.S. Army Corps of Engineers, oral commun., 1980). Costs of excavating this channel and maintaining it are estimated at $45 million through 1982.

As for the Cowlitz River, location of dredge spoil areas along the Columbia River has not been as great a problem as anticipated. In the early stages of Columbia River dredging, the material was disposed of in shallow water along the edge of the river immediately south of the dredged channel. Later, much of the material was placed in low shoreline areas that were subject to annual flooding and therefore of marginal value for agricultural, residential, or industrial use. The raising of the surface level of some of this marginal land actually may have increased its commercial value.

The Trojan Nuclear Plant is probably the most important civil works structure along the segment of the Columbia River affected by sedimentation. This plant, which has a rated electrical production of 1.13 million kW, is on the Oregon shore of the

Columbia River 8 km (5 mi) upstream from the mouth of the Cowlitz River, directly opposite the mouth of the Kalama River, and 18 km (11 mi) downstream from the mouth of the Lewis River (fig. 403). Water for cooling the plant is obtained from the Columbia River. Soundings performed by the Corps of Engineers on May 24 showed that the river channel in front of the plant, which originally had a depth of as much as 36 m (120 ft), had partially infilled to a maximum deposition of 12 m (40 ft) (J. Bechly, oral commun., 1980). This deposition of material was confined to the deeper parts of the river channel and did not affect the plant's water intake structure (Portland General Electric Company, 1980).

However, as a result of the deposition of this sediment, Portland General Electric Company, which owns the Trojan Nuclear Plant, was asked by the U.S. Nuclear Regulatory Commission what sedimentation effects would be expected if an eruption, similar to the May 18 event, occurred on the west or south flanks of Mount St. Helens and poured debris flows or mudflows into the Kalama or Lewis Rivers (Portland General Electric Company, 1980). Studies sponsored by Portland General Electric Company predicted maximum sediment deposition from such an event of 3½ m (12 ft) at the mouth of the Kalama

Figure 408.—The Interstate 5 bridge and Burlington Northern railway bridge over the Toutle River at its mouth on May 19. These bridges sustained minor damage by flooding, sediment, and debris as a result of the May 18 mudflow. Note water vapor rising from the water, and timber debris being removed from the deck of the railroad bridge. Photograph by W. Guderian, The (Portland) Oregonian, published with permission.

River and 7½ m (25 ft) at the mouth of the Lewis River. The deposition from the Lewis River would extend downstream in the Columbia River for about 8 km (5 mi), and thus would not affect the nuclear plant. Because the post-May 18 channel in front of the plant's water intake structure has a minimum depth of about 10½ m (35 ft), the additional deposition from the Kalama River would not reach the intake structure, which is at a depth of 3 m (10 ft).

EFFECTS OF ASH FALL FROM THE MAY 18 ERUPTION

The May 18 eruption of Mount St. Helens ejected some 3.67×10^8 t (metric tons)(4.05×10^8 short tons) of tephra, nearly all consisting of ash which, within a few hours, fell in a broad band across eastern Washington, northern Idaho, and western Montana (Sarna-Wojcicki and others, 1980). This heavy ash fall, which had an estimated volume of about 0.73 km^3 (0.18 mi^3), greatly affected civil works and operations in the areas of deposition. The bulk of the ash fell in Yakima, Grant, Adams, Whitman, and Spokane Counties of eastern Washington, where depths reached as much as 10 cm (4 in.); however, depths sufficient to require ash removal by mechanical equipment or jetting also occurred in northern Idaho and western Montana.

IMMEDIATE EFFECTS ON TRANSPORTATION OPERATIONS

The ash fall immediately paralyzed transportation in the area. Within hours of the eruption, 2,900 km (1,800 mi) of State highways were closed in eastern Washington (Anderson, 1980) due to ash accumulation. Interstate 90, which crosses the State from Seattle to Spokane, was closed for a week. Many thousands of kilometers of county roads, municipal

Figure 409.—Weyerhaeuser Company employee bus heavily damaged and partially buried by mudflow on the North Fork Toutle River near Camp Baker. Bus was unoccupied when hit by the mudflow.

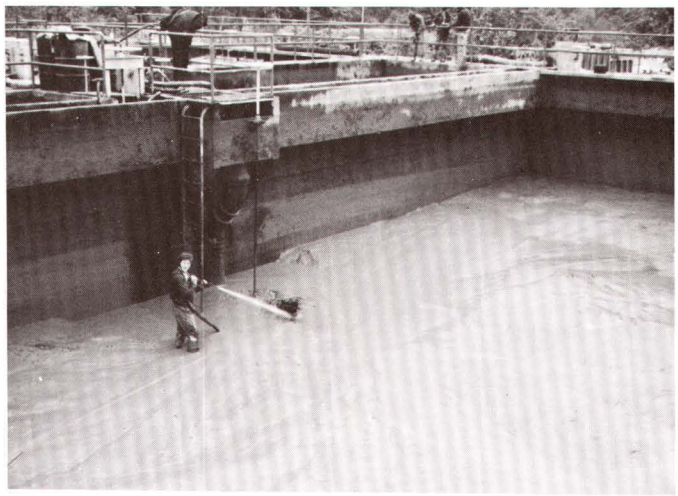

Figure 410.—Cleaning the Longview, Wash., water-supply filtration plant sedimentation basin, May 29. Photograph by L. F. Edtl, City of Longview. Reprinted from OpFlow, v. 6, no. 7 (July 1980), by permission. Copyright 1980, American Water Works Association.

streets, and irrigation district service roads also were closed, some for only a few hours, some for weeks.

Air transportation in the area was directly impeded by the ash cloud itself, but it was more lastingly affected by ash accumulation on airport runways, taxiways, and aprons, which curtailed air operations until it was removed. Table 94 denotes periods of shutdown and loss of scheduled air traffic for commercial airports in eastern Washington due to ash from the May 18 eruption.

Rail transportation in the area fared much better than either automobile or air transport. Except for slowdowns and equipment problems for a couple of days, rail traffic was nearly normal, and the railway companies did not have ash-removal problems as serious as those on highway and airport pavements.

Table 94.—Days of shutdown and numbers of commercial operations canceled due to ash accumulation at eastern Washington airports from May 18 eruption

Airport	Days of shutdown	Commercial operations canceled
Spokane International--------	3	576
Yakima----------	7	160
Pullman-Moscow----------	7	117
Tri-Cities (Pasco, Kennewick, Richland).	0	97
Grant County----------	15	[1]80

[1] In addition, Japan Air Lines training operations at Grant County Airport were shut down for a total of 28 days during which 1,386 flights were canceled.

EFFECTS ON SEWAGE-DISPOSAL SYSTEMS

Almost all municipalities in the area of thick ash accumulation experienced severe problems due to clogging of storm sewers, and several had plugged sanitary sewage-disposal systems. Particularly hard hit were Moses Lake (population 12,000) and Yakima (population 50,000) in eastern Washington. The storm drain system for Moses Lake, consisting of 380 catch basins, was solidly plugged by the 5–7 cm (2–3 in.) of ash

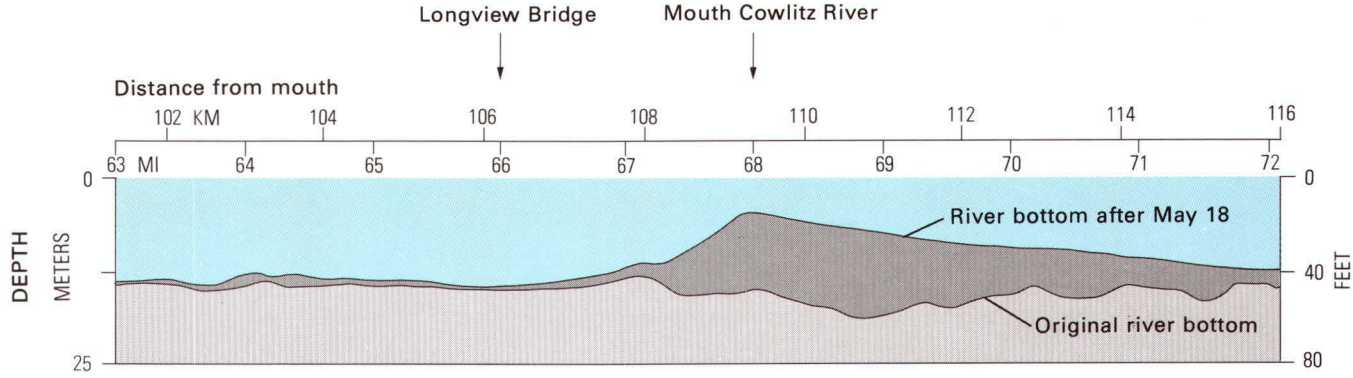

Figure 411.—Longitudinal profile of the bottom of the Columbia River where sediment resulting from the May 18 eruption entered from the Cowlitz River. Note that most of the sediment was deflected upstream. (Modified from Bechly, 1980.)

washed from the streets during cleanup. In addition, Moses Lake's entire sewage-disposal plant, consisting of four clarifiers, two trickling filters, and two digesters, was plugged by a jellylike mixture of sewage and ash. The system was out of operation for 5 weeks.

Yakima, which had about 1–2 cm (½–¾ in.) of ash on the ground, had similar problems. From May 21–25 the Yakima wastewater-treatment plant was out of operation due to plugging and damage to pumps, filters, clarifiers, and so forth; during this period the system was bypassed, and all sewage was divested directly to the Yakima River. Direct damage costs to the system were estimated as follows: treatment plant, $700,000; sanitary collection system, $290,000, and storm-sewer system, $90,000 (White, 1980).

In Spokane (population 175,000), which received about ½ cm (¼ in.) of ash, the 1½-year-old sewage-treatment plant did not plug up, even though some 13,600 t (15,000 short tons) of ash had to be flushed out of the plant. However, all 13,000 catch basins in the storm drain system were filled and had to be cleaned (Yake, 1980). Other smaller cities in eastern Washington and northern Idaho had similar problems, but on a lesser scale.

Cities in eastern Washington rely primarily on deep wells for water supply, and most storage is in enclosed reservoirs or tanks. For these reasons, the ash caused only minor problems to municipal water-supply systems.

ASH REMOVAL

Because of the great volume of material involved, removal of ash from highways, roads, streets, sidewalks, buildings, and airports was the greatest overall problem faced by public and private entities in the area. For example, the Washington State Highway Department estimated that it removed 540,000 t (600,000 short tons) of ash from State highways after the May 18 and May 25 eruptions (fig. 412); the Highway Department was still removing ash from median strips, ditches, and gutters on Interstate 90 in eastern Washington as late as October 1980. As another example, the East Columbia Basin Irrigation District estimates that its maintenance forces removed some 350,000 m^3 (450,000 yd^3) of ash from its 2,250 km (1,400 mi) of roads along irrigation canals in Adams and adjacent counties.

Figure 412.—Removal of ash from the May 18 eruption, Interstate 90, eastern Washington. Photograph by Washington State Highway Department.

Some of the most serious ash-removal problems occurred in municipalities in eastern Washington. For example, at Moses Lake, where the average ash depth was about 6 cm (2½ in.), approximately 230,000 m^3 (300,000 yd^3) of ash was measured in its post-cleanup disposal piles (M. G. McLanahan, Assistant Public Works Director, City of Moses Lake, oral commun., 1980). Ritzville (population 2,000), the county seat of Adams County, was covered with about 8–10 cm (3–4 in.) of ash; 115,000 m^3 (150,000 yds^3) of ash was deposited in an old quarry outside town (Gary Miller, Public Works Director, Adams County, oral commun., 1980). Figure 413 shows a temporary spoil pile of Ritzville ash.

Airports in eastern Washington also experienced major problems in ash removal. Twenty thousand tons of ash was removed from runways, taxiways, and aprons at the Yakima Airport. Approximately 45,000 m^3 (60,000 yd^3) of ash was removed from the Grant County Airport, which serves as a training facility for airlines; Japan Air Lines shut down its training operations from this airport for 28 days due to ash. Some 6,500 m^3 (8,500 yd^3) of ash was removed from the Spokane International Airport, although the thickness there was only about ½–1 cm (¼–½ in.).

Figure 413.—Spoil site, 8,000 m² (2 acres), Ritzville, Wash., normally reserved for surplus snow; contains 10,000 m³ (13,000 yd³) of ash from the May 18 eruption. Depth of spoil is 1–1½ m (3–5 ft). Photograph by G. B. McLucas, State of Washington, Division of Geology and Earth Resources.

EFFECTS OF POST–MAY 18 ASH FALLS

Although the eruptions of May 25 and June 12 were much smaller than that of May 18, they did produce significant ash falls (Sarna-Wojcicki and others, this volume). During those eruptions, however, the winds were generally from the east. The May 25 event deposited a blanket of ash as much as 1 cm (½ in.) thick in western Washington northwest of Mount St. Helens as far as the Pacific Ocean, causing major transportation and ash-removal problems on the highway system and in several small cities; hardest hit were Centralia (population 11,000) and Chehalis (population 6,000). The June 12 eruption spread a thinner ash cover to the southwest. Although Portland, Oreg. (population 400,000), received only about ¼ cm (⅛ in.) of ash, 5,300 m³ (7,000 yd³) was removed from the 2,400 km (1,500 mi) of city streets (Lang, 1980).

SUMMARY AND CONCLUSIONS

Civil works and operations in the vicinity of and downstream from Mount St. Helens were heavily impacted by the lateral blast, debris avalanche, mudflows, floods, and sedimentation from the May 18 eruption of Mount St. Helens. This same eruption resulted in ash fall in eastern Washington, northern Idaho, and western Montana, which severely dis-

rupted transportation, shut down sewage disposal systems, and caused massive problems of ash removal and disposal. Table 95 summarizes the relationships between the various eruptive processes and products of Mount St. Helens and the types of civil works and operations impacted.

The growth of communities and development of other land uses in areas downvalley and downwind from Mount St. Helens occurred almost entirely after 1857, the time of the last eruption prior to 1980. During the following 123 yr of volcano inactivity, communities, highways, bridges, hydroelectric dams and reservoirs, railroads, and airports were constructed in the region, but the possible effects of future eruptions on these developments was given little or no thought. This disregard for volcanic eruptions in planning new developments has not been unique to the Mount St. Helens region, but has characterized the entire Cascade Range with its many inactive but potentially dangerous volcanoes (Crandell and others, 1979).

This report has described examples of the effects of various kinds of volcanic events on structures and on other developments that are vital to the economic wellbeing of an entire region. Many of these effects were specifically predicted in volcanic-hazards assessments of Mount St. Helens and other volcanoes (for example, Crandell, 1976; Crandell and Mullineaux, 1978). Now that these events have occurred and are within the experience of engineers, planners, and public officials, the potential hazards from volcanic eruptions probably will no longer be disregarded. It is hoped that the examples described herein will help to guide future land-use planning around other volcanoes, and will show that a conscious choice should be made between acceptance of the possibility of increased costs due to changes in design or locations of structures, and acceptance of the possible costs of an eruption. Judgments as to which alternative is preferable surely will vary from one kind of development to another, and from one volcano to another; they should be based on social and economic factors as well as on scientific appraisals of the potential hazards at each volcano.

Table 95.—Types of civil works and operations affected by eruptive processes and products from Mount St. Helens

	Lateral blast	Debris avalanche	Mudflows	Flooding and sedimentation	Ash fall
Transportation:					
Highways and roads--	X	X	X	X	X
Railways----------			X		X
Bridges----------		X	X		
Air transport-------					X
Water supply:					
Water treatment-----			X	X	X
Equipment----------			X	X	X
Waste disposal:					
Treatment plants----				X	X
Storm sewers--------				X	X
Streets/roads-------		X	X	X	X
Dredge spoils-------		X	X	X	
Flood control---------		X	X	X	
Reservoirs----------			X		
Powerplants and transmission facilities.				X	X

REFERENCES CITED

Anderson, D. A., 1980, The eruption of Mount Saint Helens: Maintenance and Operations Newsletter, Washington State Department of Transportation, v. 62, April-June, 8 p.

Bechly, J. F., 1980, Mt. Saint Helens eruption—restoration of Columbia and Cowlitz River channels: Texas A&M University Dredging Seminar, College Station, Tex., Nov. 6, 52 p.

Crandell, D. R., 1976, Preliminary assessment of potential hazards from future eruptions in Washington: U.S. Geological Survey Miscellaneous Field Studies Map MF-774.

Crandell, D. R., and Mullineaux, D. R., 1978, Potential hazards from future eruptions of Mount St. Helens volcano, Washington: U.S. Geological Survey Bulletin 1383-C, 26 p.

Crandell, D. R., Mullineaux, D. R., and Miller, C. D., 1979, Volcanic-hazards studies in the Cascade Range of the Western United States, *in* Sheets, P. D., and Grayson, D. K., eds., Volcanic activity and human ecology: New York, Academic Press, p. 195–219.

Edtl, L. F., 1980, Cowlitz River carries water supply problems: OpFlow, American Water Works Association, v. 6, no. 7, July, p. 4–5.

Glicken, H., Janda, R., and Voight, B., 1980, Catastrophic landslide/debris avalanche of May 18, 1980, Mount St. Helens volcano [abs.]: American Geophysical Union, Transactions, v. 61, no. 46, Nov. 11, p. 1135.

Hawkins, N. M., Schroeder, W. L., Murdock, W. G., and Mar, B. W., 1981, The Mount St. Helens eruption of May 1980—assessment of engineering and related impacts: Report to the National Research Council (in press).

Lang, John, 1980, Report on volcanic ash cleanup of city streets: Report to Mayor Connie McCready, City of Portland, Oreg., July 15, 6 p.

Pacific Power & Light Company, 1980, Study of effects of potential volcanic activity on Lewis River projects: Board of Consultants Report, September, 91 p.

Portland General Electric Company, 1980, Response to Nuclear Regulatory Commission in reply to July 25, 1980, questions regarding volcanic activity at Mt. St. Helens and its relation to the Trojan Nuclear Plant: September, 8 p.

Sarna-Wojcicki, A. M., Shipley, Susan, Waitt, R. B., Dzurisin, Daniel, Hays, W. H., Davis, J. O., Wood, S. H., and Bateridge, Thomas, 1980, Areal distribution, thickness, and volume of downwind ash from the May 18, 1980, eruption of Mount St. Helens: U.S. Geological Survey Open-File Report 80–1078, 11 p.

Watershed Rehabilitation Team, 1980, Mount St. Helens emergency watershed rehabilitation report: U.S. Forest Service, Pacific Northwest Region, Portland, Oreg., 243 p.

White, W. T., 1980, Mt. St. Helens volcanic ash versus Yakima wastewater treatment facility: Newsletter, Institute for Water Resources of the American Public Works Association, v. 6, no. 2, p. 4–8.

Yake, G. A., 1980, A brief resume on the effects of the Mount St. Helens eruption fallout: City of Spokane report to the Governor's Recovery Team, State of Washington, Yakima, Wash., May 27, 4 p.

THE 1980 ERUPTIONS OF MOUNT ST. HELENS, WASHINGTON

SOME EFFECTS OF THE MAY 18 ERUPTION OF MOUNT ST. HELENS ON RIVER-WATER QUALITY

By JOHN M. KLEIN

ABSTRACT

The May 18 eruption of Mount St. Helens had a pronounced effect on the water quality in rivers draining areas affected by the blast, debris avalanche, mudflows, and ash. Comparison of preeruption and posteruption data shows marked increases in selected rivers of the levels of sulfate, chloride, turbidity, total nitrogen, total organic nitrogen, and total iron, manganese, and aluminum.

In streams affected solely by ash, the changes were short lived, and the intensity of change decreased with distance from Mount St. Helens. In contrast, the effects were more persistent in streams that drain the areas affected by the blast and mudflows.

INTRODUCTION

After 100 yr of dormancy, Mount St. Helens, in southwestern Washington, erupted on March 27, 1980; and ash and steam were emitted. Eruptions of ash and steam continued during March and April, and continual seismic activity was recorded.

On May 18, at 0832 PDT, Mount St. Helens erupted violently. Following an explosive north-trending lateral blast, ash and steam were shot vertically to more than 15 km. Immediately north of the volcano, a once-productive forest was pyrolyzed and destroyed. At a greater distance from the mountain, trees were uprooted and stripped of bark, branches, needles, and leaves.

Airborne ash was carried eastward and dispersed over eastern Washington and other States farther downwind (fig. 414). Watersheds just east of the volcano received heavy ash fall. However, streams draining to the south tributary to the Columbia River (fig. 415) received only traces of ash.

At the beginning of the eruption, part of the north flank of the volcano collapsed, depositing a massive debris avalanche of rock, ash, pumice, and ice in the upper 25 km of the North Fork Toutle River valley (fig. 415). A mudflow quickly developed in the South Fork Toutle River, and several hours later, a much larger mudflow, originating from the massive debris-avalanche deposit, flowed down the North Fork Toutle River. The North Fork mudflow moved downstream through the lower Toutle and Cowlitz Rivers, and a considerable part of the sediment was conveyed through the Cowlitz into the Columbia River.

The massive alterations caused by the eruption could be expected to have marked effects on river-water quality. This report describes some of the effects caused by ash deposition in rivers east of the volcano, and the effects of massive debris-avalanche and mudflow deposits in rivers draining to the west and south.

ASH COMPOSITION

Fruchter and others (1980) have reported some general compositional trends of the volcanic ash at various distances from the volcano. Silica content in-

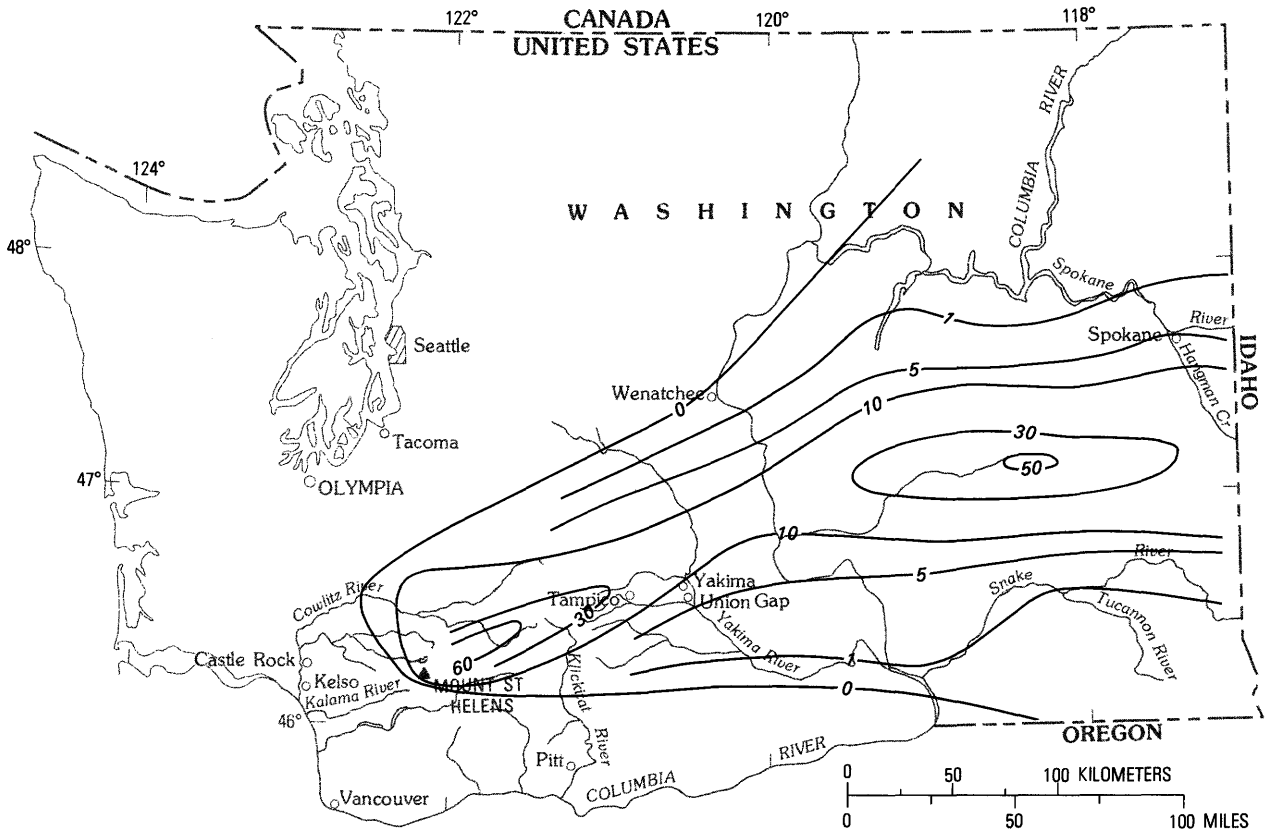

Figure 414.—Thickness of ash deposit erupted from Mount St. Helens on May 18. Contour values in millimeters. Isopach data modified from Sarna-Wojcicki, Shipley, and others (this volume).

creased with distance, whereas iron, magnesium, calcium, and manganese decreased. Potassium and sodium showed little variability.

Taylor and Lichte (1980) analyzed volcanic-ash samples for major, minor, and trace-element composition. They also observed variations in chemical composition of ash with distance from Mount St. Helens, and related these to changes in the physical characteristics of the ash. In addition, Taylor and Lichte reported water-soluble components after column leaching the ash with known volumes of distilled water. A summary of some of the major, minor, and trace soluble-constituent concentrations of the ash at specified locations is in table 96.

From these analyses alone, one might expect that a major impact on river-water quality would be an increase, from preeruption levels, in the concentrations of certain soluble constituents, especially chloride and sulfate. The timing of such compositional changes with respect to the eruption would depend on whether the ash fell on land or water, and the occurrence and intensity of precipitation on ash that was deposited on land. If ash fell on water, the soluble constituents would dissolve rapidly and be observed

Table 96.—Major, minor, and trace constituents dissolved from volcanic ash from the May 18, 1980, eruption of Mount St. Helens

[Values are in micrograms per gram of dry ash, from Taylor and Lichte (1980). <, less than]

Constituent	Tampico, Wash.	Ft. Simcoe, Wash.	Moses Lake, Wash.	Potlatch, Idaho
Calcium-----	89	190	151	190
Magnesium---	13	42	27	30
Sodium------	87	209	143	164
Potassium---	1.7	41	20	23
Ammonium----	<.07	.90	1.2	.75
Chloride----	134	319	178	369
Fluoride----	.81	2.4	1.3	3.7
Sulfate-----	297	744	534	524
Silica------	8.1	16	19	13
Nitrate-----	1.8	7.0	2.8	1.0
Boron-------	.28	.74	.58	.47
Iron--------	.013	.013	.024	.013
Manganese---	2.0	7.3	2.0	5.8
Zinc--------	.024	.062	.012	.240

in analyses of samples collected soon after deposition. Heavy precipitation on land-deposited ash might wash large quantities of soluble constituents into streams, whereas light precipitation would leach those constituents into the soil where they would react with soil materials. In the latter case, changes in stream-water composition might not be measurable. Moreover, changes would occur after sufficient water had leached through the soil and eventually entered the water course.

Calcium and bicarbonate are normally the predominant dissolved constituents in streams of the Pacific Northwest. Variations in concentrations are small, occur slowly, and are correlated with stream discharge. A major geologic event such as this eruption and subsequent ash fall might be expected to produce noticeable changes in the chemical composition of waters.

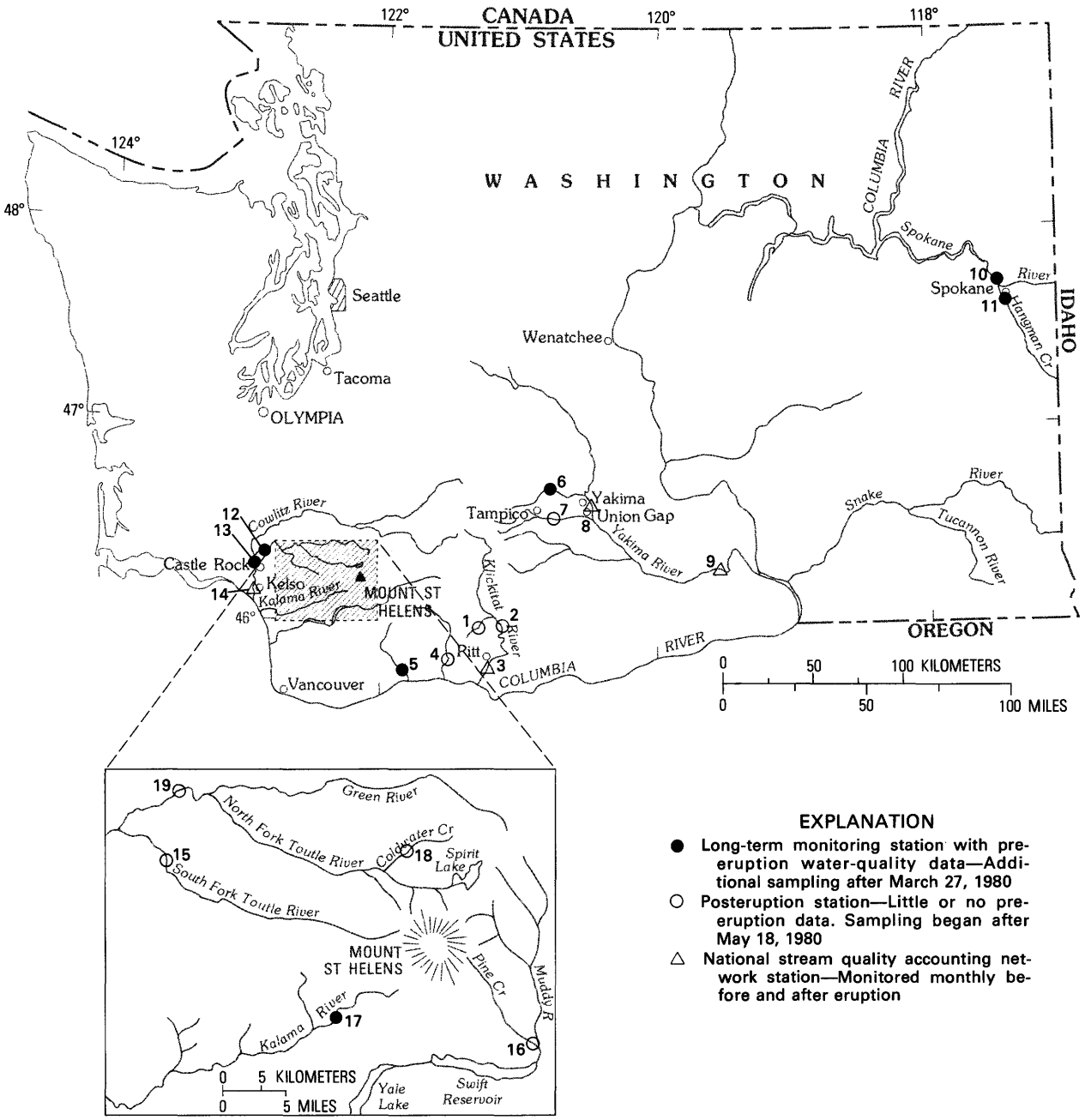

Figure 415.—Location of water-quality sampling stations.

DATA COLLECTION

Following the eruption of March 27, a program of water-quality data collection was initiated at selected stream sites surrounding Mount St. Helens (fig. 415). Measurements at these stations supplemented data collected monthly at several USGS National Stream Quality Accounting Network Stations[1] and at other sites sampled periodically.

Following the May 18 eruption, additional measuring stations (fig. 415) were established. Initially, samples were collected daily at some of the sites that received heavy ash fall or were affected by the debris avalanche or mudflows. After several days, the sampling frequency was decreased to weekly until the end of June. Since then, samples have been collected monthly.

All water samples were collected from river cross sections using depth-integrating samplers and

[1]The NASQAN consists of more than 500 surface-water monitoring stations at which water-quality measurements of the Nation's streams and rivers are made monthly or bimonthly.

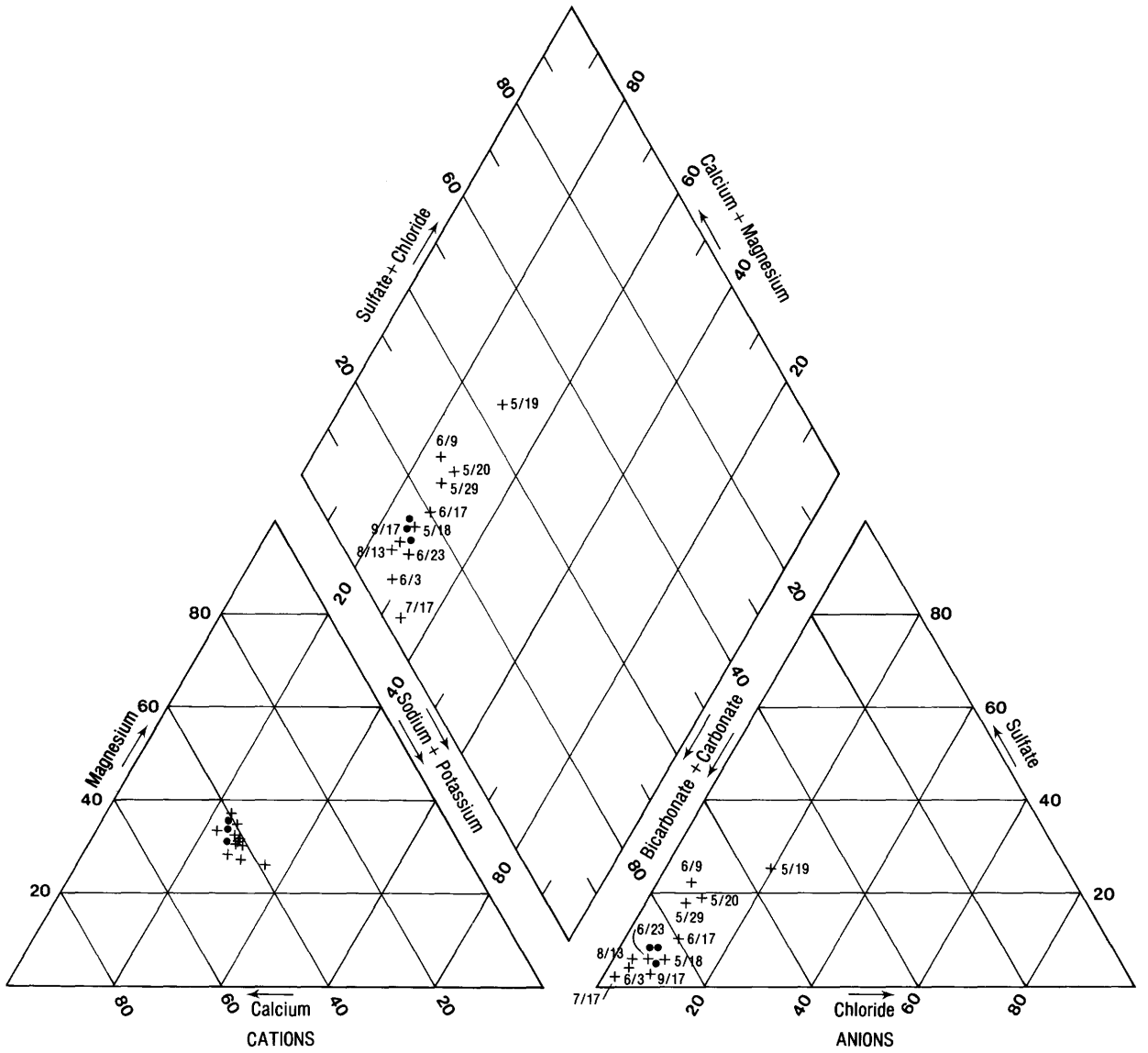

Figure 416.—Percentage composition of water from the Klickitat River near Pitt, Wash. (fig. 415, station 3). Dots represent data collected before May 18; plus signs represent data collected on date shown (during or after May 18 eruption). (Variation in cation composition was relatively minor, precluding the need for accompanying dates.)

methods (Guy and Norman, 1970). Samples to be analyzed for dissolved trace elements and major chemical constituents were filtered through 0.45-μm (micrometer) membrane filters, placed in acid-washed polyethylene bottles, and acidified with double-distilled, analytical-grade nitric acid to prevent absorption and chemical precipitation. Unfiltered samples were analyzed for total trace-element concentrations. Samples for analysis of nitrogen and phosphorus were chilled at the time of collection and during shipment to the USGS laboratory in Arvada, Colo. Constituents were analyzed by methods described by Skougstad and others (1979). Data from only some of the stations in the overall sampling network are used in this preliminary report.

RESULTS AND DISCUSSION

The following discussion is supplemented with several figures to illustrate the basic findings. Variation in chemical composition is shown for several sites by use of trilinear diagrams (for example, fig. 416). Within each triangle and the center quadrangle, the percentage of the cations (calcium, magnesium, sodium, and potassium) and the anions (bicarbonate, carbonate, chloride, and sulfate) totals 100 thus, changes in the relative amounts of these constituents are shown concisely. Variation in the levels of sulfate, chloride, total nitrogen, total organic nitrogen, and turbidity[2] are shown in time-series plots for selected sites (for example, fig. 417). For each parameter, the same scale is used for all sites to facilitate comparison of the relative magnitudes of change.

EFFECTS OF ASH ON RIVER-WATER QUALITY

As expected from the distribution of ash fall (fig. 414), streams to the south of the volcano, tributary to the Columbia River (fig. 415, stations 4 and 5), were unaffected. A small tributary to the Klickitat River (fig. 415, station 1) was also unaffected.

East of Mount St. Helens, the magnitude of the observed effects of ash deposition was a function of the pattern of ash depths and the relative volumes of water draining from heavily and slightly affected areas down to the sampling sites. In general, the magnitude of the observed effects ranged from pronounced in streams close to the volcano to slight in streams in eastern Washington. In the following sections, the effects are described in streams located progressively eastward from the volcano.

KLICKITAT RIVER

Samples from the Klickitat River near Glenwood (fig. 415, station 2) and near Pitt (fig. 415, station 3) showed that ash deposition had a pronounced effect on water composition. The changes at the Pitt station downstream were not as pronounced as those at the Glenwood station, near the headwaters, owing to dilution from tributary drainages that received very light ash fall. However, the length of the historic record of measurements at the Pitt station makes it the better location for discerning the ash-fall effects.

The shift in chemical composition of the water from May 18 until several days later is illustrated in a trilinear diagram (fig. 416). The sample taken on May 18 showed no effects of ash fall, but the sample collected the following day showed much higher percentages of chloride and sulfate, which suggests the addition of soluble chloride and sulfate compounds from the ash. By May 20, the anion composition had shifted back toward the normal preeruption percent-

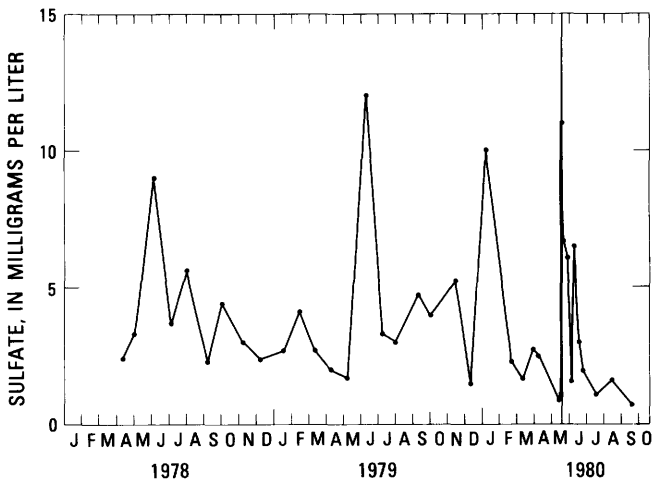

Figure 417.—Time-series plot of sulfate concentration in the Klickitat River near Pitt, Wash. (fig. 415, station 3). Vertical line indicates May 18 eruption.

[2]Turbidity, an optical phenomenon, was determined as the nephelometric turbidity unit (NTU), which refers to the amount of light scattered at 90° when the turbidimeter is calibrated with formazin.

ages, and subsequent samples confirmed that the composition had returned to the normal range. The cation composition did not vary to any measurable extent, probably because the percentage of soluble cations in the ash (table 96) was not substantially different from that of the native waters.

Changes in the anion concentrations in the Klickitat River at Pitt were extremely short lived, as illustrated by the time-series plots of sulfate and chloride (figs. 417 and 418). Samples collected just after May 18 showed increases in the concentration of these constituents. The increase in sulfate, although significant, did not exceed previous high concentrations. The chloride increase noted in the May 19 sample was notably greater than in preeruption and other posteruption samples. By the end of June, the concentrations of both sulfate and chloride had returned to within the preeruption ranges of values.

The most dramatic effects of the ash fall on water quality in the Klickitat are illustrated in the time-series plots of total nitrogen, total organic nitrogen, and turbidity (figs. 419 and 420). Samples collected just after May 18 contained levels of these three parameters well above the highest observed during the previous 2 yr. Because the nitrogen analyses were performed on unfiltered samples, the correspondence between the peaks in nitrogen and turbidity suggests that the nitrogen was closely associated with the particulate material. The peaks observed on June 17 are probably related to ash fall from the eruption of June 12.

The high nitrogen concentrations cannot be as easily correlated to the ash as were the high sulfate and chloride concentrations because the ash was not analyzed for organic nitrogen. However, the increase in nitrogen corresponding to the time of ash deposition is not surprising. The major blast on May 18

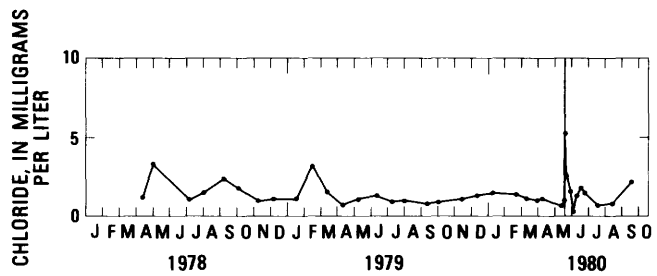

Figure 418.—Time-series plot of chloride concentration in the Klickitat River near Pitt, Wash. (fig. 415, station 3). Vertical line indicates May 18 eruption.

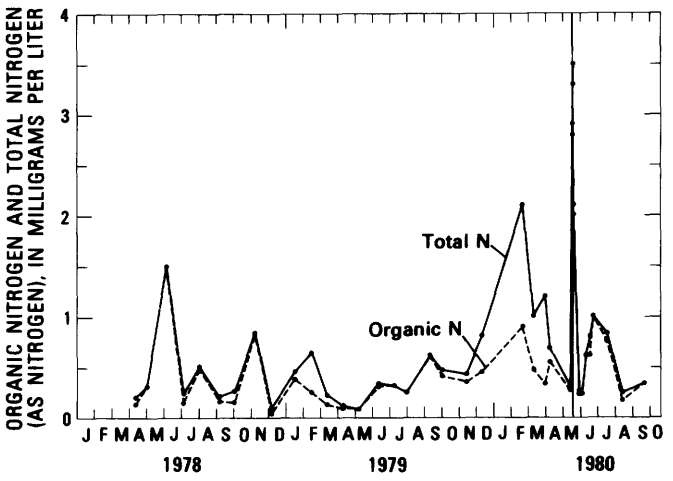

Figure 419.—Time-series plot of total organic nitrogen (dashed) and total nitrogen (solid line) concentrations (as nitrogen) in the Klickitat River near Pitt, Wash. (fig. 415, station 3). Vertical line indicates May 18 eruption.

denuded the nearby environment, destroying the forest and other vegetation. Pyrolysis (a major chemical change due to intense heat) of the forest may have resulted in vaporization of much forest organic material, which included a large quantity of nitrogen. The vaporized organic material probably condensed, attached to the ash particles, and was transported in the ash plume. For a short time, organic nitrogen conveyed by ash into water would stay attached to the ash particles. After some time, dissolution, mineralization, and nitrification of this nitrogen would result in increased amounts of dissolved nitrate. The effects of ash fall on the nitrogen concentrations and turbidity were short lived. By July, the variations had returned to within the normal range.

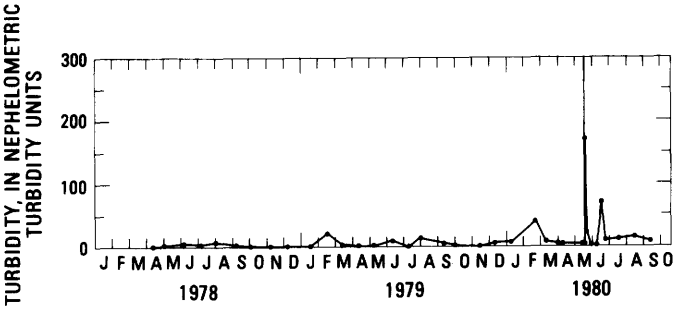

Figure 420.—Time-series plot of turbidity in the Klickitat River near Pitt, Wash. (fig. 415, station 3). Vertical line indicates May 18 eruption.

AHTANUM CREEK

In streams farther east of the volcano, such as the North Fork and South Fork Ahtanum Creek (fig. 415, stations 6 and 7), variations in element content and turbidity were similar to those in the Klickitat River. Data from the North Fork Ahtanum Creek site near Tampico (fig. 415, station 6) show the similarity (fig. 421).

Higher percentages of sulfate and chloride were observed in the sample taken May 18, rather than in the sample taken on May 19, when the change was seen in the Klickitat River. The time difference is probably the result of the proximity of Ahtanum Creek to the heaviest ash-fall area (fig. 414), and a shorter travel time of water from within the watershed to the sampling site. The degree of change in composition over normal values was also greater, because the entire drainage received substantial ash.

YAKIMA RIVER

In streams and rivers still farther east of the volcano, the effects of ash fall on surface-water quality

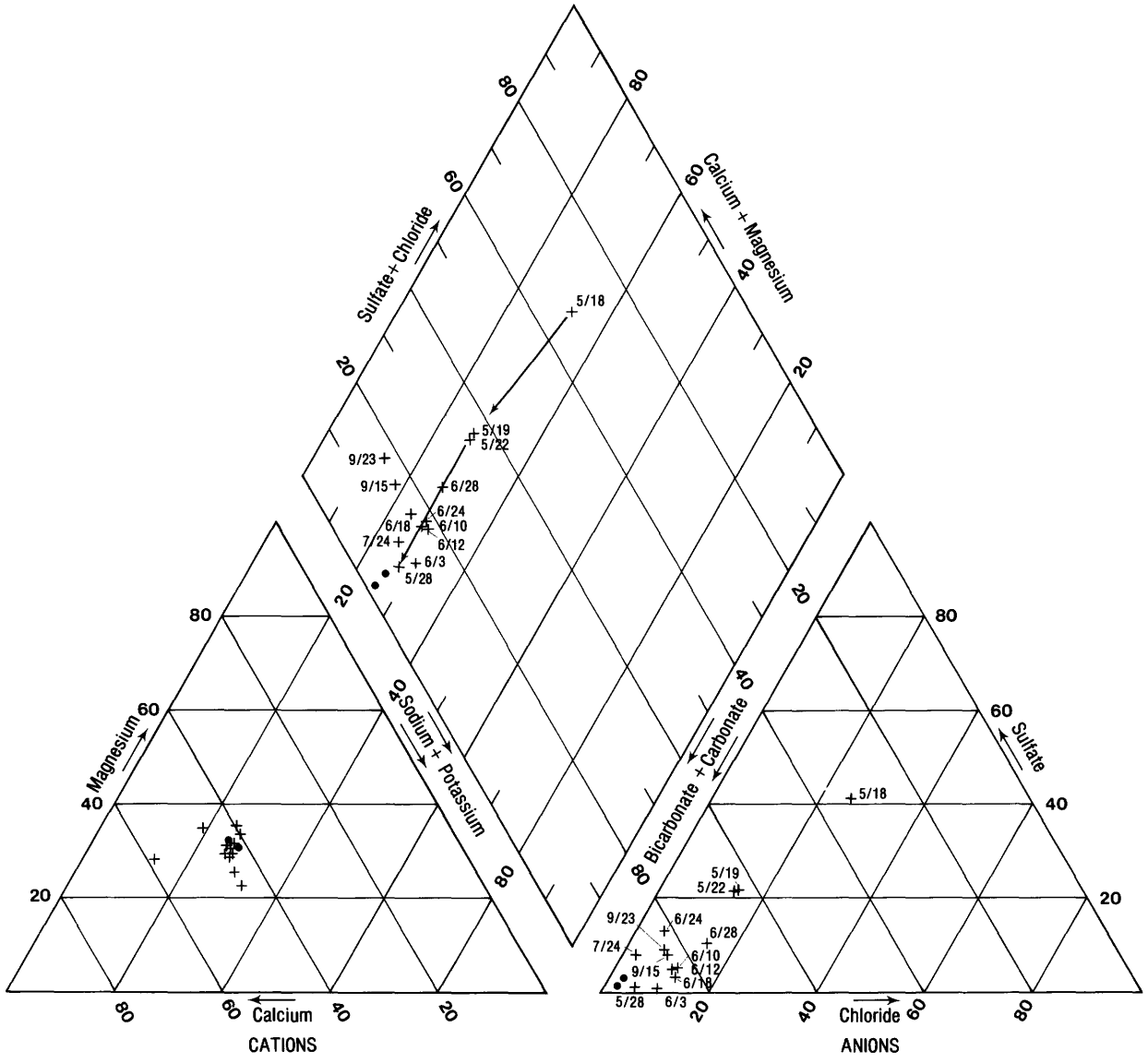

Figure 421.—Percentage composition of water from North Fork Ahtanum Creek near Tampico, Wash. (fig. 415, station 6). Dots represent data collected before May 18; plus signs represent data collected on date shown (during or after May 18 eruption). (Variation in cation composition was relatively minor, precluding the need for accompanying dates.)

were much less apparent than in the Klickitat River and Ahtanum Creek. Besides the Columbia River, the Yakima River is the major river draining central Washington, and much of the land it drains received significant ash fall. Of the two stations on the Yakima having long historical water-quality records (fig. 415, stations 8 and 9), data from station 8 near Union Gap best illustrate the water-quality changes observed following the eruption.

At the Union Gap station, sulfate and chloride concentrations in samples varied sharply over a brief period following the major ash fall of May 18 (figs. 422, 423) and subsequent eruptive events, but the magnitudes of change were small relative to pre-eruption variations. Indeed, it is difficult to decide whether the short-term fluctuations were due to the ash fall, or were merely artifacts of increased sampling frequency. The much lower effect on water quality in the Yakima than in the Klickitat River and Ahtanum Creek probably resulted from dilution of water in tributaries that received much ash by water from tributaries that received little or no ash.

In contrast to the undramatic changes in sulfate and chloride, the levels of total organic nitrogen, total nitrogen, and turbidity increased abruptly shortly after the May 18 ash fall to values well above the highest values observed during the previous year (figs. 424, 425). Also, the increase in total nitrogen amount was due largely to total organic nitrogen, which, in the preceding year's samples, had accounted for only about 50 percent of the total nitrogen concentrations.

As at the stations on the Klickitat River and Ahtanum Creek, the increases in nitrogen and turbidity were short lived. By July, the variations were within the range of those observed during the previous year.

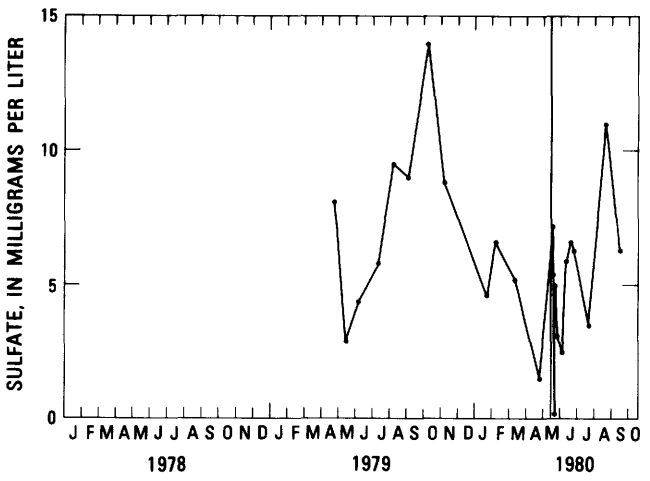

Figure 422.—Time-series plot of sulfate concentration in the Yakima River near Union Gap, Wash. (fig. 415, station 8). Vertical line indicates May 18 eruption.

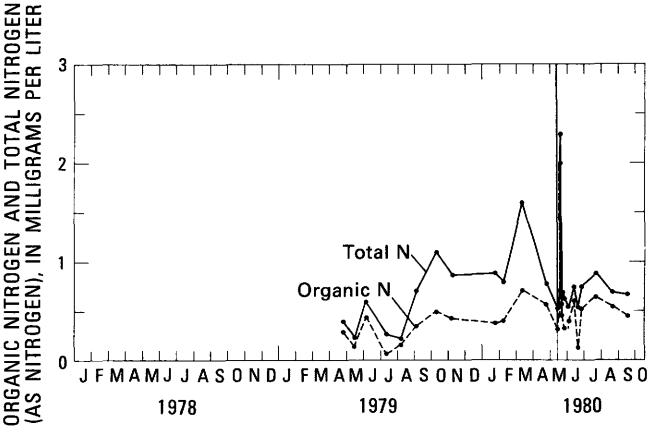

Figure 424.—Time-series plot of total organic nitrogen (dashed line) and total nitrogen (solid line) concentrations (as nitrogen) in the Yakima River near Union Gap, Wash. (fig. 415, station 8). Vertical line indicates May 18 eruption.

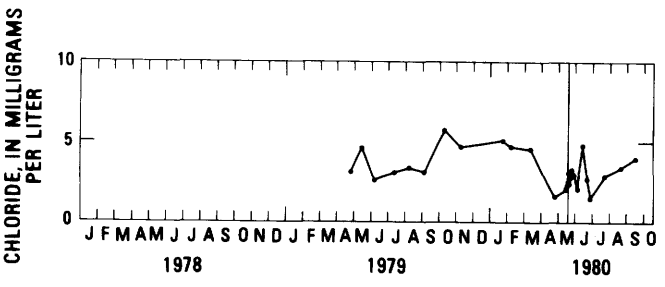

Figure 423.—Time-series plot of chloride concentration in the Yakima River near Union Gap, Wash. (fig. 415, station 8). Vertical line indicates May 18 eruption.

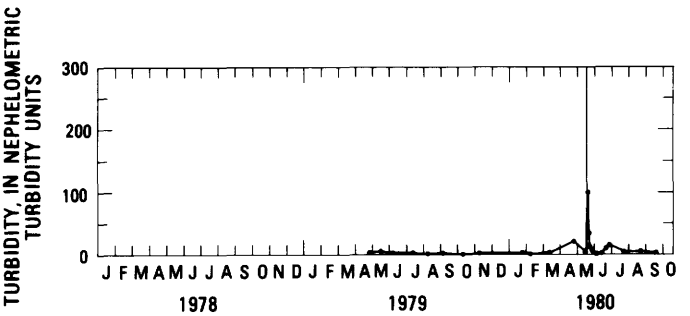

Figure 425.—Time-series plot of turbidity in the Yakima River near Union Gap, Wash. (fig. 415, station 8). Vertical line indicates May 18 eruption.

SPOKANE RIVER

Still farther east, the effects of ash fall on water quality were much less apparent than those at the Yakima River near Union Gap. In eastern Washington, the Spokane River drains an area of northwestern Idaho and eastern Washington that received substantial ash fall; effects of ash deposition on the river were evaluated using data from one site on the Spokane River near Riverside State Park in Spokane (fig. 415, station 10) and Hangman Creek (fig. 415, station 11).

At both stations, the percentages of sulfate and chloride in samples collected after ash fall were small and well below the highest values observed during the previous 2 yr. Here again, an increase in turbidity was accompanied by increases in total organic nitrogen and total nitrogen, with organic nitrogen accounting for most of the increase. The increases occurred on May 27, during and following a major storm.

EFFECTS OF VOLCANIC DEBRIS AND MUDFLOWS ON RIVER-WATER QUALITY

The Toutle River headwater drainages were strongly altered by debris-avalanche deposits and pyroclastic-flow and mudflow deposits from the May 18 eruption. The downstream reaches of the Toutle River and the lower Cowlitz River below its confluence with the Toutle were devastated by massive mudflows and flooding. Water samples collected regularly since the eruption from the Toutle and Cowlitz Rivers show that these events have had a pronounced and persistent effect on the surface-water quality.

A water sample collected from the Toutle River near Castle Rock (fig. 415, station 12) on March 29, before the major eruption, contained calcium and bicarbonate as the predominant dissolved chemical constituents (fig. 426). The sample collected on May 20 showed higher percentages of sulfate and chloride. Samples collected at this station through July showed continuing high sulfate and chloride concentrations, indicating that these constituents continued to leach from the ash, debris, and mudflow deposits. The mudflows on May 18 prohibited collection of satisfactory water-quality samples. On May 19, the specific conductance in the Toutle River near Castle Rock was 1,200 μmhos (micromhos), compared with normal values of about 90 μmhos. On May 20, when the first samples could be collected, the specific conductance was 560 μmhos. These values indicate dissolved-solids concentrations of about 6 to 12 times above normal for the Toutle River.

Following the major eruption, sampling frequency was increased in the Cowlitz River at Castle Rock (fig. 415, station 13) to determine the effects of inflow from the Toutle River drainage. Starting on May 30, samples were also routinely collected at Kelso (fig. 415, station 14) to monitor changes in quality between the two sites and to document the quality of water flowing into the Columbia River.

The compositional variations in the Cowlitz River at Castle Rock were similar to those observed in the Toutle River; however, the overall effect was reduced because of dilution by flow from the upper Cowlitz. The variability of the composition of water at the Castle Rock station was and is being determined by the character and magnitude of discharge from the devastated Toutle River system, by upstream dredging activities in the Cowlitz and Toutle, and by dilution effects of discharge from the upper Cowlitz.

In the Cowlitz River at Kelso (fig. 415, station 14), high concentrations of sulfate and chloride were measured in late May and early June, although maximum values for both parameters were below those in samples collected monthly during the previous 2 yr. However, the mudflow deposits had a dramatic effect on the levels of total organic nitrogen, total nitrogen, and turbidity (figs. 427, 428). Samples collected in late May and early June at Kelso showed turbidity values well above the previous maximum value observed at this station. Again, turbidity increases were accompanied by dramatic increases in the total nitrogen concentration, with most of the increases due to total organic nitrogen.

Figure 429 shows the major ion composition of water samples collected before and after the eruption at miscellaneous stations close to the volcano. In the South Fork Toutle River (fig. 429, station 15), a major increase occurred in chloride concentration, the increase in sulfate was negligible, and only minor cation changes were observed. Similar changes were observed in Pine Creek at its confluence with the Lewis River (fig. 429, station 16). Samples collected before the major eruption indicated that the water was characterized by sodium and bicarbonate, but posteruption changes resulting from mudflows in

Pine Creek showed a higher percentage of chloride.

The Kalama River (fig. 429, station 17) was relatively unaffected by the May 18 eruption, but received ash deposits from the May 25 event. Only minor increases in sulfate and chloride were observed.

Posteruption water-chemistry data from Coldwater Creek (fig. 429, station 18) and the Toutle River near Kid Valley (fig. 429, station 19) showed nearly equal percentages of the major dissolved-chemical constituents. These stations had greater percentages of sulfate and chloride than all other sites, indicating a greater chemical effect of the eruption on streams whose headwaters are within the area of the blast and debris-avalanche deposits.

OCCURRENCE OF TRACE METALS

Analysis of the ash (table 96) showed the presence of iron, manganese, and several other metals which, in the investigated streams and rivers, normally occur in very low concentrations. To determine the effects

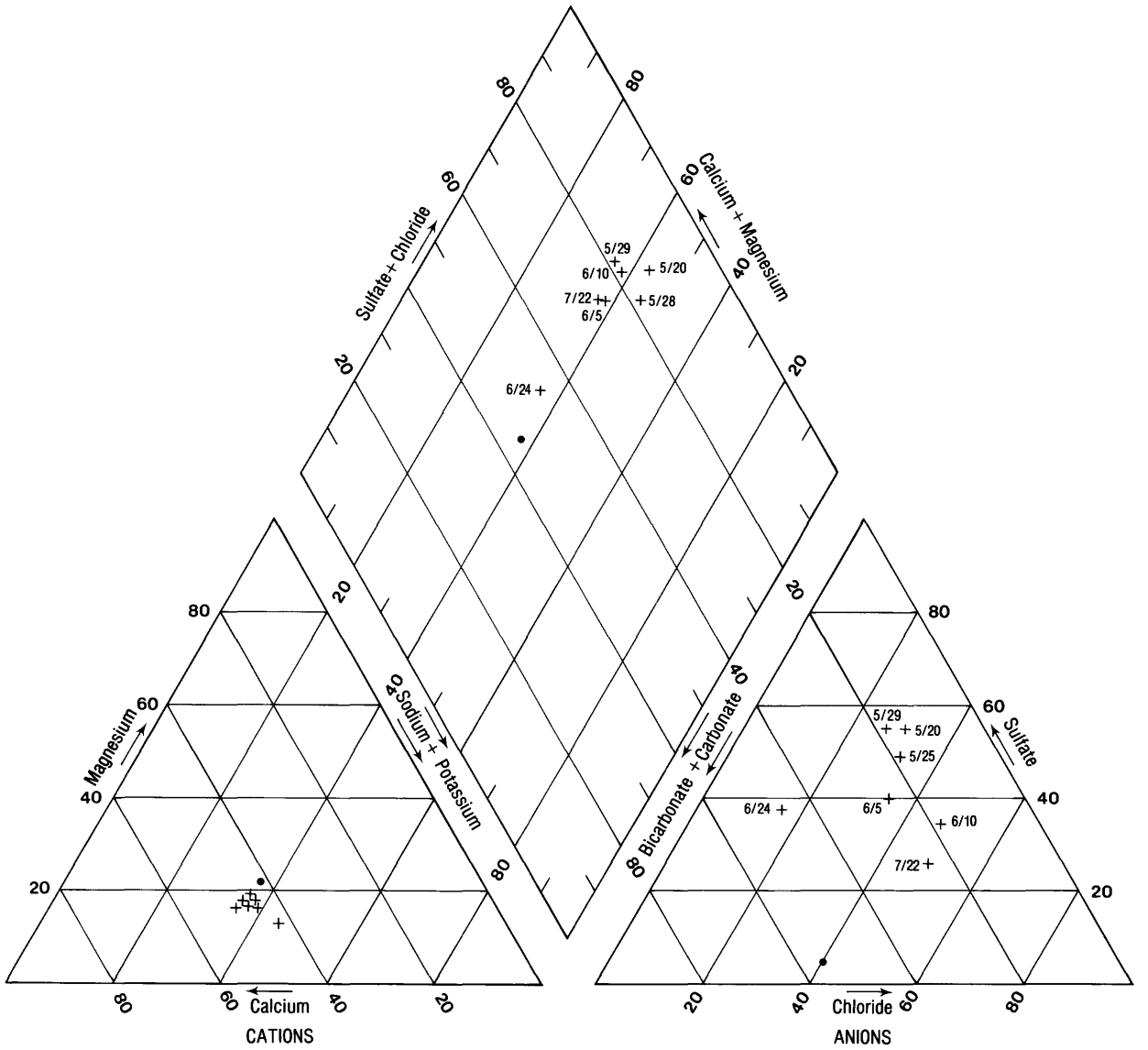

Figure 426.—Percentage composition of water from the Toutle River near Castle Rock, Wash. (fig. 415, station 12). Dots represent data collected before May 18; plus signs represent data collected on date shown (after May 18 eruption). (Variation in cation composition was relatively minor, precluding the need for accompanying dates.)

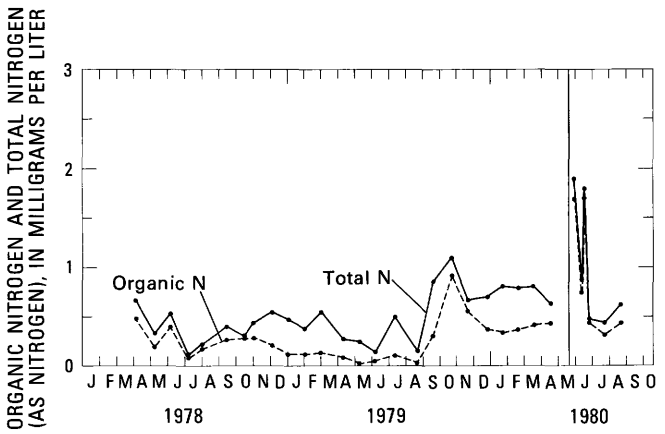

Figure 427.—Time-series plot of total organic nitrogen and total nitrogen concentrations (as nitrogen) in the Cowlitz River at Kelso, Wash. (fig. 415, station 14). Vertical line indicates May 18 eruption. Data points not connected between April and June because sampling was not frequent enough to show probable peaks resulting from May 18 eruption and associated debris avalanche and mudflows.

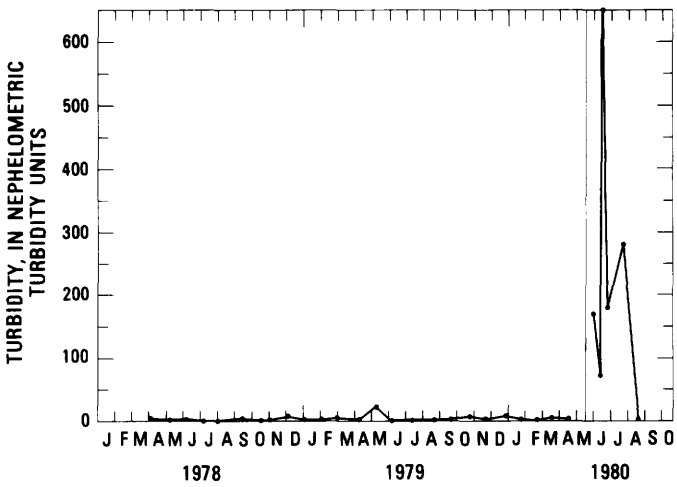

Figure 428.—Time-series plot of turbidity in the Cowlitz River at Kelso, Wash. (fig. 415, station 14). Vertical line indicates May 18 eruption. Data points not connected between April and June because sampling was not frequent enough to show probable peak resulting from May 18 eruption and associated debris avalanche and mudflows.

of ash fall on concentrations of these trace metals, both filtered and unfiltered samples were analyzed to measure the dissolved and total metal concentrations. The difference between the two values represents the concentration in the suspended sediments.

Concentrations of suspended sediments were high in most of the samples, and most of the trace metals determined were associated with these sediments. The dissolved-metal concentrations (table 97) were generally much lower than the suspended-sediment metal concentrations, and were only slightly higher than preeruption levels in those streams affected solely by ash depostion. In the Toutle and Cowlitz Rivers, posteruption concentrations of dissolved iron, manganese, and aluminum increased and persisted, owing to continued leaching from the debris-avalanche and mudflow deposits.

Total concentrations of iron, manganese, and aluminum increased greatly over preeruption levels (table 97). Total concentrations of these metals at the Toutle and Cowlitz stations increased 100 to 500 times over preeruption values, whereas the concentrations increased only about 5 to 50 times at the ash-affected stations on the Klickitat River and the North Fork Ahtanum Creek. There was also a marked difference between the mudflow- and ash-affected stations in the duration of total metal-concentration increases. At the Klickitat and North Fork Ahtanum stations, the increases in total metal concentrations were short lived. In contrast, increases at the Toutle and Cowlitz River stations persisted at least through June, owing to the continuing influx of suspended sediment.

Concentrations of other trace metals of inter-

Table 97.—Variation in trace-metal content of surface water at selected stations in Washington

[Values in micrograms per liter. Leaders (---), no data]

Station	Date	Iron		Manganese		Aluminum	
		Dissolved	Total	Dissolved	Total	Dissolved	Total
Klickitat River near Pitt (station 3).	5/13	60	850	3	20	40	620
	5/18	80	680	20	40	40	500
	5/19	70	4,200	10	90	70	3,100
	5/20	60	1,100	7	30	40	820
	5/29	47	500	3	3	30	640
North Fork----- Ahtanum Creek near Tampico (station 6).	3/30	170	600	7	20	140	470
	5/18	50	17,000	70	360	60	16,000
	5/19	60	4,600	10	80	110	2,200
	5/28	85	920	10	20	50	400
Toutle River--- near Castle Rock (station 12).	3/29	70	230	20	20	40	200
	5/20	95	22,000	1,000	1,300	310	20,000
	5/22	21	76,000	1,200	2,200	700	55,000
	5/25	160	50,000	350	1,400	540	33,000
	5/27	110	78,000	490	2,000	250	57,000
	5/29	65	41,000	400	1,300	270	34,000
	6/5	110	32,000	380	1,100	110	65,000
	6/10	140	40,000	320	1,100	100	85,000
	6/19	240	33,000	290	290	40	20,000
	6/24	210	19,000	290	680	140	100,000
Cowlitz River-- at Kelso (station 14).	4/16	50	400	5	10	---	---
	5/30	24	12,000	110	350	120	29,000
	6/12	90	10,000	90	290	80	10,000
	6/17	70	45,000	110	900	20	39,000
	6/25	80	8,000	70	230	60	10,000

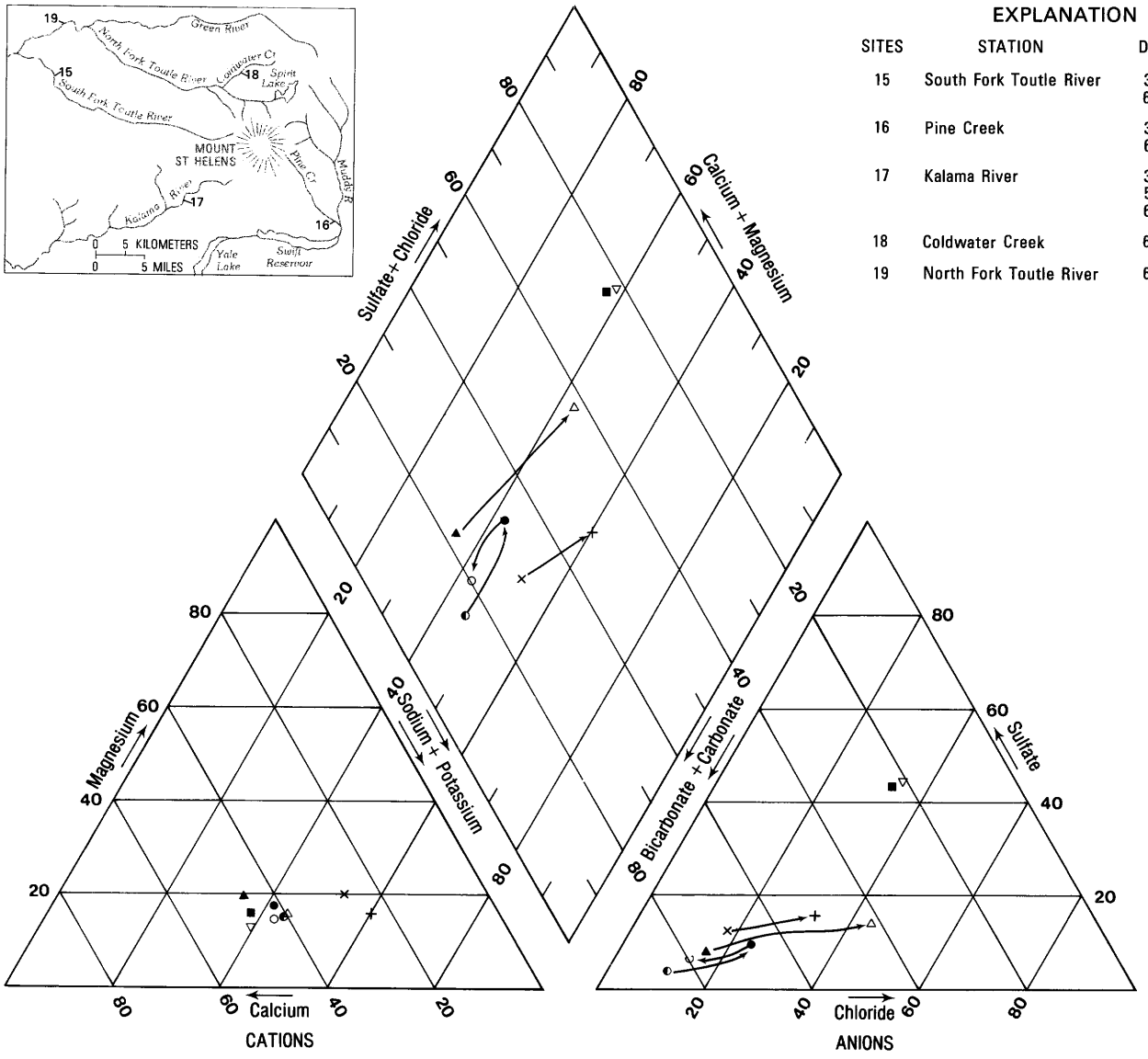

Figure 429.—Percentage composition of water from miscellaneous sampling sites near Mount St. Helens, showing changes resulting from May 18 eruption.

est—arsenic, cadmium, chromium, and cobalt—were not noticeably higher than levels before the ash fall in either the filtered or unfiltered samples.

SUMMARY

The May 18 eruption of Mount St. Helens in southwestern Washington had a pronounced effect on river-water quality. The effects were greatest in the Toutle River system, which was devastated by the blast, a massive debris-avalanche deposit, and mudflows. The Cowlitz River, into which the Toutle drains, was also affected severely. Relatively small but still marked changes in water quality were observed in drainage basins affected by ash east of the volcano.

The major changes in water quality associated with the eruptive events included increases in the levels of sulfate, chloride, total nitrogen, total organic nitrogen, turbidity, iron, manganese, and aluminum. In the ash-affected basins east of Mount St. Helens, the observed water-quality changes were short lived and, in general, decreased in magnitude with distance from the volcano. Changes in water quality in the Toutle and Cowlitz Rivers persisted longer, owing to

continuing influx and leaching of sediment in the devastated headwater areas.

Total concentrations of iron, manganese, and aluminum increased greatly over preeruption levels to as much as 100 to 500 times in the Toutle and Cowlitz Rivers, compared to 5 to 50 times at the reported sites east of the volcano. At all sampled sites, the dissolved metal concentrations were generally much lower than the suspended metal concentrations.

It is especially interesting that high concentrations of total nitrogen and total organic nitrogen were observed in posteruption water samples. In all samples, the high nitrogen concentrations were associated with high levels of turbidity, and the greater proportion of the nitrogen was organic. The high concentrations of organic nitrogen probably resulted from pyrolysis of forest material within the blast zone. The vaporized organic products may have immediately become attached to volcanic-ash particles and then were transported to the point of deposition.

REFERENCES CITED

Fruchter, J. S., and others, 1980, Mount St. Helens ash from the 18 May 1980 eruption— chemical, physical, mineralogical, and biological properties: Science, v. 209, no. 4461, p. 1116–1125.

Guy, H. P., and Norman, V. W., 1970, Field methods for measurement of fluvial sediment: U.S. Geological Survey Techniques of Water-Resources Investigations, Book 3, Chap. C2, 59 p.

Skougstad, M. W., Fishman, M. J., Friedman, L. C., Erdmann, D. E., and Duncan, S. S., eds., 1979, Methods for determination of inorganic substances in water and fluvial sediments: U.S. Geological Survey Techniques of Water Resources Investigations, Book 5, Chap. A1, 626 p.

Taylor, H. E., and Lichte, F. G., 1980, Chemical composition of Mount St. Helens volcanic ash: Geophysical Research Letters, v. 7, no. 11, p. 949–953.

EFFECTS ON A BLUE-GREEN ALGA OF LEACHATES OF ASH FROM THE MAY 18 ERUPTION

By DIANE M. MCKNIGHT, GERALD L. FEDER, *and* ERIC A. STILES

ABSTRACT

Bioassays using leachate from volcanic ash of the May 18 eruption of Mount St. Helens indicate that leachate from ash collected at Richland, Wash., is toxic to the blue-green alga *Anabaena flos-aquae*, and leachate from ash collected at Moses Lake, Wash., is not. The difference in the toxicity of the two ash leachates can be attributed to the differences in concentration of cationic-exchangeable, dissolved organic carbon compounds. In the Richland ash leachate, 17 percent of the dissolved organic carbon was retained on a cation-exchange column, whereas only 7 percent of the dissolved organic carbon from the Moses Lake ash leachate was retained. *Anabaena flos-aquae* cultures spiked with leachate from Richland volcanic ash diluted to 1:250 showed toxic effects, whereas cultures spiked with leachate from Moses Lake volcanic ash diluted to 1:25 showed no toxic effects.

Preliminary data indicate that the toxic components include one or more of the following substances: (1) cationic organic compounds such as amines; (2) highly hydrophobic (sparingly soluble) organic compounds such as phenols that interact with and are retained by a cation-exchange resin; or (3) metal-organic complexes that are retained by interaction of the metal with a cation-exchange resin. The toxic components of the volcanic ash are not uniformly present in the ash-fall area.

INTRODUCTION

In order to determine the possible effects of volcanic ash from the May 18, 1980, eruption of Mount St. Helens on lake-water quality and ecology, ash samples were collected from several locations (fig. 430) for chemical analysis of their distilled-water leachates, and the leachates were tested on a common blue-green alga (*Anabaena flos-aquae*). The chemical analyses indicate that, relative to natural surface waters in the affected area, the leachates contain high concentrations of several potentially toxic trace elements, specifically manganese, zinc, copper, and cadmium (table 98).

In addition, the leachates contain large concentrations of important algal nutrients (phosphate, nitrate, and ammonia) and as much as 200 mg/L (milligrams per liter) of dissolved organic carbon (Taylor and Lichte, 1980). Chemical analyses of the organic compounds in volcanic ash from Richland, Wash., indicate that many of the identified components (for example, dicarboxylic acids, n-alkanes, 4-Methoxybenzaldehyde, and trimethylphenanthrene) could have originated as breakdown products of pyrolized plant material (Pereira and others, 1980). These organic products may have formed during the eruption as a lateral blast of superheated gases and hot ash flattened nearly 500 km^2 of coniferous forest. J. A. Leenheer (oral commun., 1980) of the USGS reported that the concentration of organic compounds in ash leachates varied with location, with higher concentrations near the periphery of the May 18 ash-fall area than toward its center. Richland is near the south edge of the ash fall, about 230 km east of Mount St. Helens (fig. 430).

The objectives of this study were to (1) determine whether trace elements, organic compounds, or both, are the components responsible for toxicity found in a

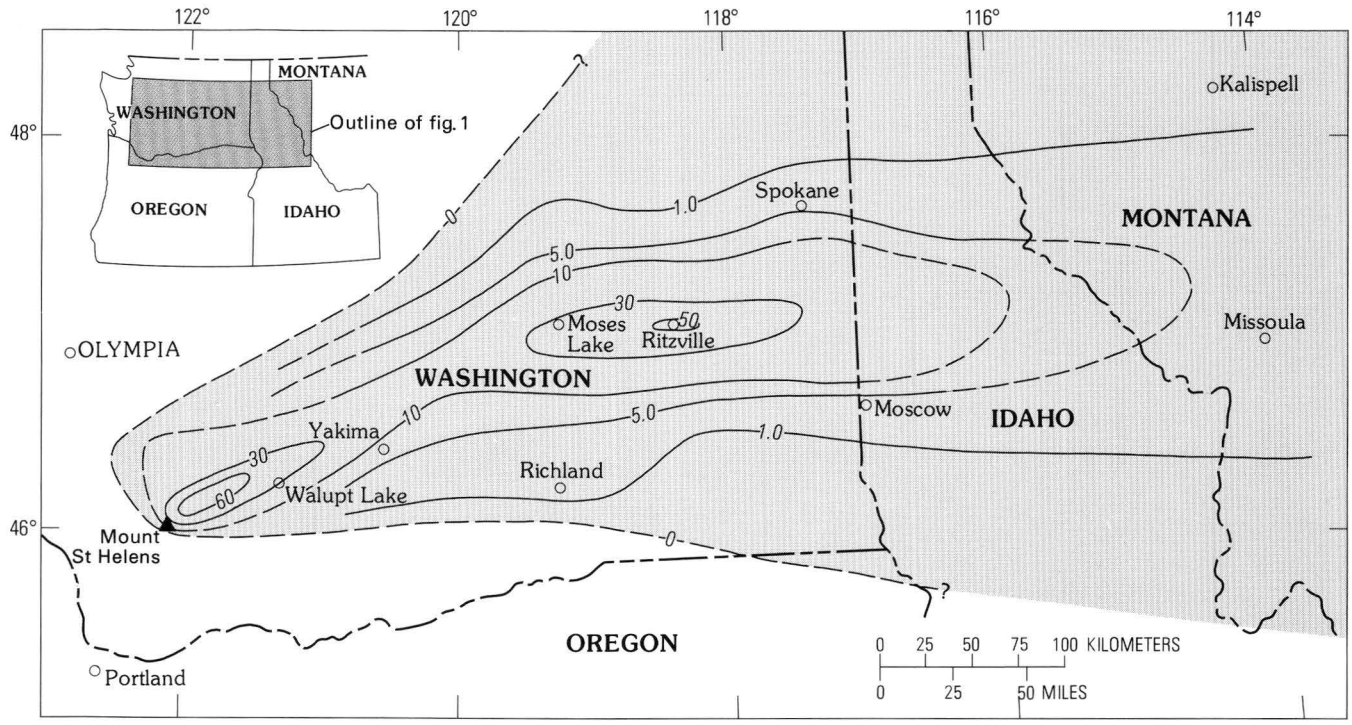

Figure 430.—Isopach map of ash erupted from Mount St. Helens on May 18, 1980. Isopach lines represent uncompacted thickness of ash in millimeters (modified from Sarna-Wojcicki, Shipley, and others, this volume). Lake Lenore and Warden Lake are close to Moses Lake and are not shown separately.

preliminary study (McKnight and others, 1981) of volcanic-ash leachate from Richland; (2) isolate and identify the trace minerals or organic compounds causing the toxicity, and (3) determine if leachate from volcanic ash from a central area of the ash fall (Moses Lake) is also toxic to blue-green algae. The Moses Lake region has many lakes and received relatively thick ash deposits (fig. 430). The site was also chosen to test the hypothesis that the observed areal variations in organic and inorganic composition of the ash (J. A. Leenheer, oral commun., 1980) result in corresponding variations in toxicity of volcanic-ash leachates.

METHODS

BACKGROUND

This study included several simultaneous bioassay experiments that used different chemical fractions of the volcanic-ash leachates to determine the chemical characteristics of the toxic constituents. The flow chart in figure 431 shows the experimental design used in the experiments with ash from Richland and Moses Lake. Essentially, the experiment consisted of: (1) testing the toxicity of the unfractionated leachate, (2) passing the leachate through a cation-exchange resin, and (3) testing the toxicity of the effluent and of trace metals like those removed by the cation-exchange resin.

CULTURE OF *ANABAENA FLOS-AQUAE*

Anabaena flos-aquae UTEX 1444 was grown in 250 mL (milliliters) of synthetic freshwater culture medium (WC medium) in 500-mL polycarbonate Erlenmeyer flasks at 23°C under continuous light. This synthetic culture medium provides more optimal conditions than most natural water, permitting *Anabaena* to grow faster, and providing for more reproducible and controlled experiments. Other reasons for using the synthetic culture medium are the large variations in chemistry of lake water in the study area (table 98) and the difficulty in transporting and preserving natural water for laboratory study. Growth was monitored by measurement of the concentration of chlorophyll *a* in the cultures every other day and by microscopic examination of the cultures.

Table 98.—Composition of four lakes in ash-fall area in central Washington, synthetic freshwater medium, and leachate from volcanic ash from Richland and Moses Lake, Wash.

[ND, not determined; < ,less than; leaders (---), not applicable]

	Walupt Lake[1]	Warden lake[1]	Moses Lake[1]	Lake Lenore[1]	Synthetic freshwater medium	Richland volcanic ash		Moses Lake volcanic ash	
	(mg/L)				(mg/L)	Concentration in leachate (mg/L)	Amount leached per gram ash (mg/g)	Concentration in leachate (mg/L)	Amount leached per gram ash (mg/g)
Major cations									
Na	1.0	29	11	200	30	167	0.17	251	0.19
Ca	1.6	6.3	12	2.9	13	182	.21	234	.19
Mg	.2	9.4	6.6	5.3	5	39	.43	48	.037
Sr	.009	.07	.09	.02	(2)	1.2	.001	1.0	.001
K	ND	ND	ND	ND	[3]4	ND	ND	ND	ND
Major anions									
Cl	2.7	19	7.6	130	[3]18	ND	ND	ND	ND
SO_4	3.2	58	27	210	[3]14.5	ND	ND	ND	ND
F	.2	.8	.5	2.5	(2)	ND	ND	ND	ND
NO_3+NO_2-N	.06	.33	.04	.01	[3]14	ND	ND	ND	ND
PO_4-P	ND	ND	ND	ND	[3]1.5	ND	ND	ND	ND
Dissolved organic carbon	0.8	5.7	4.3	13.2	[3] [4]1	69	0.086	52	0.045
pH	ND	7.5	6.5	8.7	8.0	7.1	---	7.4	---
Alkalinity (milli-equivalents/L)	.3	4.0	2.8	16.8	.3	---	---	---	---

	Walupt Lake[1]	Warden lake[1]	Moses Lake[1]	Lake Lenore[1]	Synthetic freshwater medium	Richland volcanic ash		Moses Lake volcanic ash	
	(µg/L)				(µg/L)	Concentration in leachate (µg/L)	Amount leached per gram ash (µg/g)	Concentration in leachate (µg/L)	Amount leached per gram ash (µg/g)
Trace metals									
Mn	2	2	1	<1	1.3	4,910	6.14	3,170	2.77
Zn	<3	<3	<3	<3	2.6	303	.38	18	.016
Li	<4	5	5	11	(2)	176	.22	246	.21
Cu	<10	<10	<10	<10	.6	103	.13	30	.026
Ba	7	10	20	10	(2)	87	.11	80	.070
Fe	<10	<10	<10	<10	56	65	.081	24	.021
Co	<3	<3	<3	<3	.15	29	.036	4	.003
Cd	<1	<1	<2	<1	(2)	17	.020	9	.008
Mo	<10	<10	<10	<10	.14	8	.010	31	.027
Chlorophyll a	0.31	1.9	78.6	9.5	---	---	---	---	---

[1]Walupt Lake is near Mount St. Helens, and Warden lake and Lake Lenore are near Moses Lake in central Washington (fig. 430); lakes were sampled on July 17 and 18, 1980. Warden lake is 8 km west of Warden, Wash.

[2]Constituent was not included in preparation of synthetic freshwater medium.

[3]Concentrations were not measured but were calculated from dilution of stock solutions in preparation of synthetic freshwater medium.

[4]1 mg/L dissolved organic carbon obtained by adding Biscayned fulvic acid (F. M. Thurman and Ronald Malcolm, USGS, written commun., 1980).

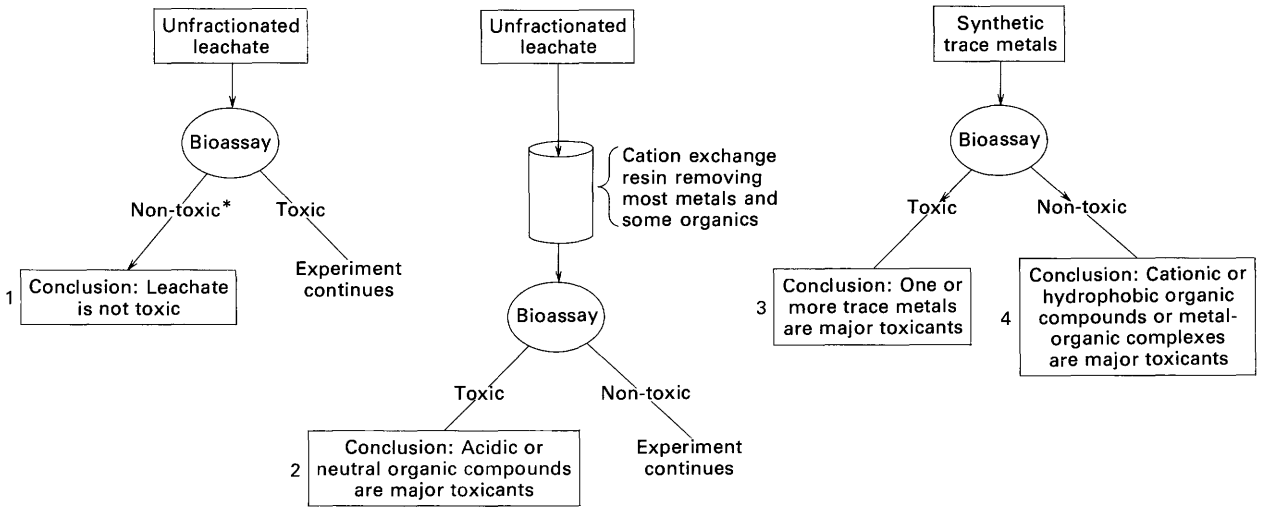

*Fractional continues to compare fractionation with toxic leachates and to determine if any fraction stimulates growth.

Figure 431.—Generalized flow chart showing experimental design used to determine the general character of toxicants in volcanic-ash leachates.

LEACHING OF VOLCANIC ASH

In the experiment using the Richland volcanic ash, 100 mL of leachate was obtained from a column packed with 80 g (grams) of ash and saturated for 14 hr at 23°C with 100 mL of WC medium (without trace metals or fulvic acid added). In the experiment using Moses Lake volcanic ash, 150 mL of leachate was obtained from a column packed with 172 g of ash, saturated for 12 hr at 23°C with 150 mL of WC medium. In both leaching experiments, more WC medium was added to prevent the columns from becoming dry. The difference in the amount of ash used for the Richland and Moses Lake experiments was governed by the amount of ash available for study. A Millipore HA 0.45 μm (micrometer) filter, previously leached in WC medium, was placed at the bottom of the column to retain particulate material. The leachates were stored in glass containers at 4°C.

The chemical composition of unaltered WC medium and Richland and Moses Lake volcanic-ash leachates are compared in table 98 with the composition of four lakes in the ash-fall area (fig. 430). The amounts of trace metals and organic material leached are also shown. The analysis for major cations and trace metals was done by inductively coupled plasma emission spectroscopy, and the dissolved organic carbon was determined using a Beckman 915 carbon analyser. Several of the measured constituents in the leachates (manganese, copper, zinc, cadmium, and organic carbon) were present in concentrations high enough to be possibly toxic to algae (Hutchinson, 1957; Bartlett and others, 1974). Both leachates had high concentrations of copper, cadmium, and zinc. Almost twice as much organic carbon was leached per gram of ash from the Richland sample as from the Moses Lake sample, which is in accord with the trend reported by J. A. Leenheer (oral commun., 1980), that samples from the periphery of the ash-fall area contain higher amounts of organic compounds.

FRACTIONATION OF VOLCANIC-ASH LEACHATE

In order to remove cationic trace metals and organic compounds, the Richland and Moses Lake volcanic-ash leachates were passed through a 30-mL column of sodium-saturated cation-exchange resin from which possible contaminants had been previously extracted with methanol. Because of the different amounts of leachate available from the ash-leaching step, different volumes were fractionated for the Richland and Moses Lake samples.

A 25-mL sample of the Richland leachate was passed through the column, followed by distilled water, and a 50-mL volume of leachate and distilled water was collected in a volumetric flask. Only 67 percent of the organic carbon in the leachate was recovered in the first 50 mL. Another 50 mL of distilled water was passed through the column, bringing the total recovery of dissolved organic carbon to 83 percent; 17 percent was retained on the column (table 99). These two 50-mL effluent fractions were combined, resulting in a fourfold dilution of the leachate. As shown in table 99, most of the trace metals were retained by the cation-exchange resin.

Table 99.—Composition of leachate of volcanic ash from Richland and Moses Lake, Wash., after passing through cation-exchange resin

[<, less than]

	Richland leachage (1:4 dilution)[1]		Moses Lake leachate (1:2 dilution)[2]	
pH----------	7.0		6.2	
Major cations	Concentration (mg/L)	Percent change of initial concentration caused by exchange column	Concentration (mg/L)	Percent change of initial concentration caused by exchange column
Na----------	150	[3]300	352	[3]172
Ca----------	.04	[4]99	.01	[4]100
Mg----------	<.04	[4]100	<.04	[4]100
Sr----------	.06	[3]100	<.04	[4]100
Dissolved organic carbon----	14.3	[4]17	24.3	[4]7
Trace metals	Concentration (µg/L)	Percent decrease of initial concentration caused by exchange column	Concentration (µg/L)	Percent decrease of initial concentration caused by exchange column
Mn----------	<1	100	<1	100
Zn----------	5.9	92	.5	94
Li----------	<4	100	<4	100
Cu----------	<10	100	1.9	87
Ba----------	2.3	89	2.6	93
Fe----------	<10	100	<10	100
Co----------	<3	100	<3	100
Cd----------	1.3	69	.1	98
Mo---------	<10	100	<10	100

[1]1:4 dilution was obtained by flushing cation-exchange column with 75 mL of distilled, deionized water after passing 25 mL of leachate through the column.

[2]1:2 dilution was obtained by flushing cation-exchange column with 50 mL of distilled, deionized water after passing 50 mL of leachate through the column.

[3]Increase.

[4]Decrease.

A 50-mL sample of the Moses Lake leachate was processed in the same way, and 100 mL was collected. The recovery of dissolved organic carbon in the effluent was 93 percent, a much higher amount than was recovered from the Richland leachate; only 7 percent was left on the column (table 99). Most of the trace metals in the Moses Lake leachate were also retained by the cation-exchange resin.

ADDITION OF LEACHATE FRACTIONS TO ALGAL CULTURES

The volcanic-ash leachate fractions were filter sterilized and were added to duplicate flasks of culture medium before inoculation with *Anabaena flos-aquae*. Because the Moses Lake ash leachate has a lower concentration of dissolved organic carbon, the added amounts of leachate were scaled to approximate the concentrations of dissolved organic carbon from the Richland ash that were toxic in the preliminary experiment (McKnight and others, 1981). In both experiments, a concentration of 2 mg/L dissolved organic carbon was used to correspond to the leachate diluted to 1:50 that completely inhibited growth in the preliminary experiment, and a concentration of 0.2 mg/L dissolved organic carbon was used to correspond to the 1:500 dilution that caused abnormal cell morphologies but did not inhibit growth.

Table 100 presents the concentrations of trace metals and dissolved organic carbon obtained in the culture media by adding different volumes of unmodified volcanic-ash leachate, cation-exchanged leachate, and synthetic trace metals. The synthetic trace-metal solutions were formulated to reproduce concentrations of trace metals in the leachates that might be toxic to algae at 1:100 dilution. Manganese was highest in concentration of the trace metals in both leachates. However, even at the 1:25 dilution, the concentrations of manganese approximated those in natural waters of the affected area (compare table 100 to table 98).

RESULTS

RICHLAND VOLCANIC-ASH LEACHATE

Figure 432 shows the growth curves for the experiment with Richland volcanic-ash leachate. The

Table 100.—Concentration of trace metals and dissolved organic carbon in cultures of Anabaena flos-aquae *used for bioassay experiments*

[Values are in μg/L, except dissolved organic carbon, mg/L; ND, not detected; leaders (---), not applicable]

	Richland volcanic-ash leachate					Moses Lake volcanic-ash leachate				
	Concentration, unfractionated leachate added[1]		Concentration, cation-exchange leachate added[2]		Concentration, synthetic metal solution added	Concentration, unfractionated leachate added[3]		Concentration, cation-exchange leachate added[4]		Concentration, synthetic metal solution added
Dilution-----	1:35	1:250	1:35	1:350	---	1:25	1:250	1:25	1:250	---
Dissolved organic carbon-----	2.0	0.27	1.5	0.15	---	2.0	0.21	1.8	0.19	---
Manganese----	139	19.6	ND	ND	150	122	12.6	ND	ND	122
Zinc---------	8.6	1.2	.6	.06	8.6	.7	.07	.04	.004	([5])
Lithium------	5.0	.7	ND	ND	10.5	9.5	.98	ND	ND	9.5
Copper-------	2.9	.4	ND	ND	3.1	1.1	.12	.14	.02	1.1
Barium-------	2.5	.4	.2	.03	([5])	3.1	.32	.19	.02	([5])
Iron---------	1.8	.3	ND	ND	([5])	.9	.10	ND	ND	([5])
Cobalt-------	.8	.12	ND	ND	([5])	.15	.02	ND	ND	([5])
Cadmium------	.5	.07	.14	.01	1.1	.3	.04	.01	.001	.3
Molybdenum---	.23	.03	ND	ND	.57	1.2	.12	ND	ND	1.2

[1]The 1:35 dilution was obtained by adding 7.3 mL of unfractionated leachate to 250 mL of culture medium. The 1:250 dilution was obtained by adding 1 mL of unfractionated leachate to 250 mL of culture medium.

[2]The 1:35 dilution was obtained by adding 29.2 mL of previously diluted (1:4) cation-exchanged leachate to 250 mL of culture medium. The 1:350 dilution was obtained by adding 2.9 mL of previously diluted (1:4) cation-exchanged leachate to 250 mL of culture medium.

[3]The 1:25 dilution was obtained by adding 10 mL of unfractionated leachate to 250 mL of culture medium. The 1:250 dilution was obtained by adding 1 mL of unfractionated leachate to 250 mL of culture medium.

[4]The 1:25 dilution was obtained by adding 20 mL of previously diluted (1:2) cation-exchanged leachate to 250 mL of culture medium. The 1:250 dilution was obtained by adding 2 mL of previously diluted (1:2) cation-exchanged leachate to 250 mL of culture medium.

[5]Constituent was not included in preparation of synthetic freshwater medium.

graphs show similar growth rates for the control, cation-exchanged leachate, and synthetic trace-metal cultures (0.64, 0.62, and 0.58 per day, calculated from increases in chlorophyll *a* concentration with time, table 101). As in the preliminary experiment, the unfractionated leachate had a lethal effect on *Anabaena flos-aquae* at a concentration of 2 mg/L dissolved organic carbon. The cultures exposed to the unfractionated leachate at a concentration of 0.27 mg/L dissolved organic carbon had a 7-day period of no net growth (lag phase) prior to an exponential growth phase of 0.51 to 0.69 per day. In comparison, a 2-day lag phase had been observed using a concentration of 0.20 mg/L dissolved organic carbon in leachate (1:500 dilution) in the preliminary experiment.

The results of this experiment using Richland ash leachate correspond to the fourth conclusion depicted in figure 431, wherein the leachate is toxic, but the cation-exchanged leachate and the synthetic trace metals are not. The most likely conclusion is that the toxicants are part of the 17 percent of organic carbon that was retained by the cation-exchange column. Several types of organic compounds could be retained: (1) cationic organic compounds such as amines; (2) strongly hydrophobic (sparingly soluble) organic compounds such as phenols that interact with and are retained by the resin; or (3) metal-organic complexes that are retained by interaction of the metal with the cation-exchange resin.

Anabaena flos-aquae filaments from the experiments with Richland volcanic ash are shown in figure 433. Filaments from the cultures inoculated with cation-exchanged leachate and synthetic trace

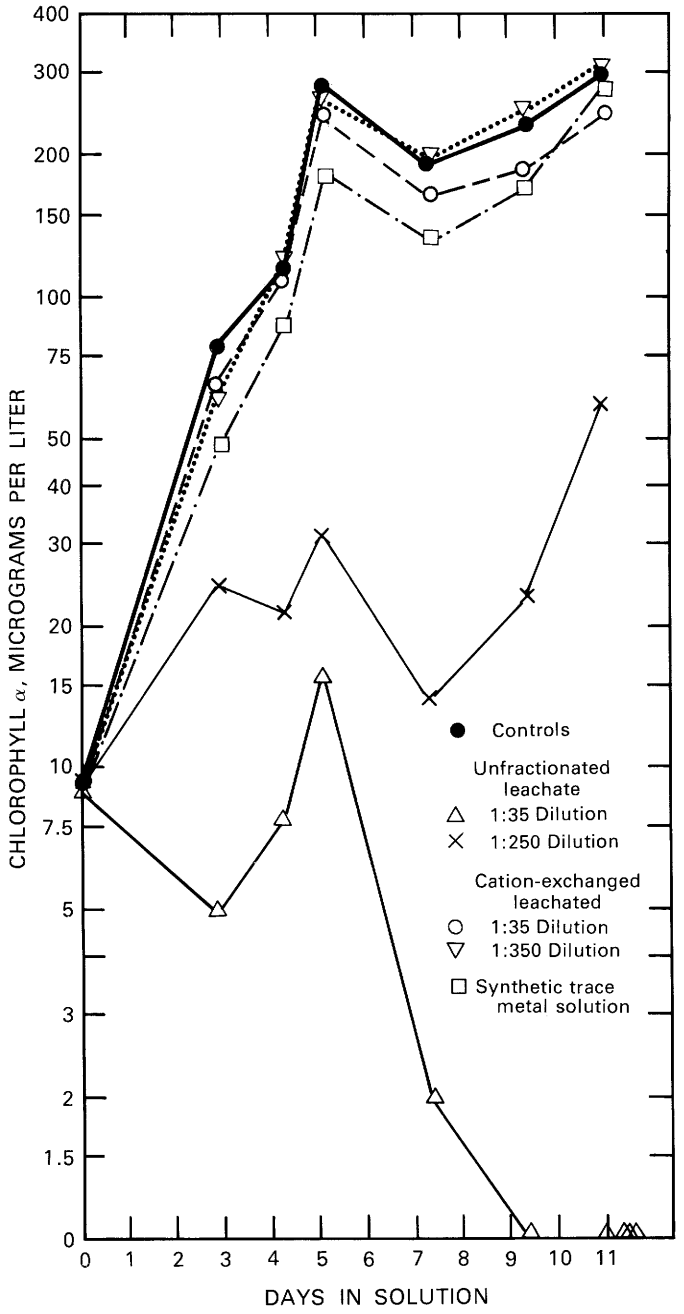

Figure 432.—Growth of Anabaena flos-aquae *as indicated by increase of chlorophyll* a *exposed to different fractions of Richland volcanic-ash leachate.*

metals were similar in appearance to those in the control cultures. In the cultures containing the higher concentration of unfractionated leachate, where no growth occurred, only short filaments (fewer than five cells per chain) having an aberrated morphology were observed. In the cultures containing the lower concentration of unfractionated leachate, which grew after a 7-day lag phase, the filaments were longer (more than 20 cells per chain), but still had an aberrated morphology. These abnormal cells were also observed in the cultures exposed to unfractionated Richland ash leachate in the preliminary experiment (McKnight and others, 1981); they are characterized by greater width in the direction perpendicular to the filament and by a grainier appearance than normal cells have. Heterocysts, the enlarged cells where nitrogen fixation occurs in filamentous blue-green algae, were observed in all cultures except those exposed to the unfractionated volcanic-ash leachate.

Table 101.—Growth rates of duplicate Anabaena flos-aquae *cultures exposed to different fractions of leachates of volcanic ash from Richland and Moses Lake, Wash.*

[Growth rates calculated from increases of chloropyll *a* with time. Table 100 shows content of dissolved organic carbon and selected trace metals in each culture. NG, no growth]

Experiment with Richland ash leachate	Growth rate per day, computed from day 0 to day 5.1	
	Culture	Duplicate culture
Control	0.64	0.64
Unfractionated leachate, 1:35 dilution	NG	NG
Unfractionated leachate, 1:250 dilution	[1].51	[1].69
Cation-exchanged leachate, 1:35 dilution	.62	.62
Cation-exchanged leachate, 1:350 dilution	.62	.67
Synthetic trace metals	.58	.58

Experiment with Moses Lake ash leachate	Growth rate per day, computed from day 2 to day 4.4	
	Culture	Duplicate culture
Control	0.71	0.83
Unfractionated leachate, 1:25 dilution	.69	.74
Unfractionated leachate, 1:250 dilution	.71	.69
Cation-exchanged leachate, 1:25 dilution	.69	.69
Cation-exchanged leachate, 1:250 dilution	.74	.71
Synthetic trace metals	.67	.69

[1]Growth rate after 7-day lag phase.

Duplicate flasks of fresh, untreated WC medium were inoculated with abnormal *Anabaena flos-aquae* cells from the Richland ash experimental cultures. The cultures inoculated with *A. flos-aquae* cells initially exposed to the lower concentration of leachate grew within a week, whereas the cultures inoculated with cells exposed to the higher leachate concentration grew after 3 weeks. No abnormal cells were observed in the cultures at the end of the experiment, which indicates that the effects of the toxicants on the morphology of the blue-green algal cells are reversible.

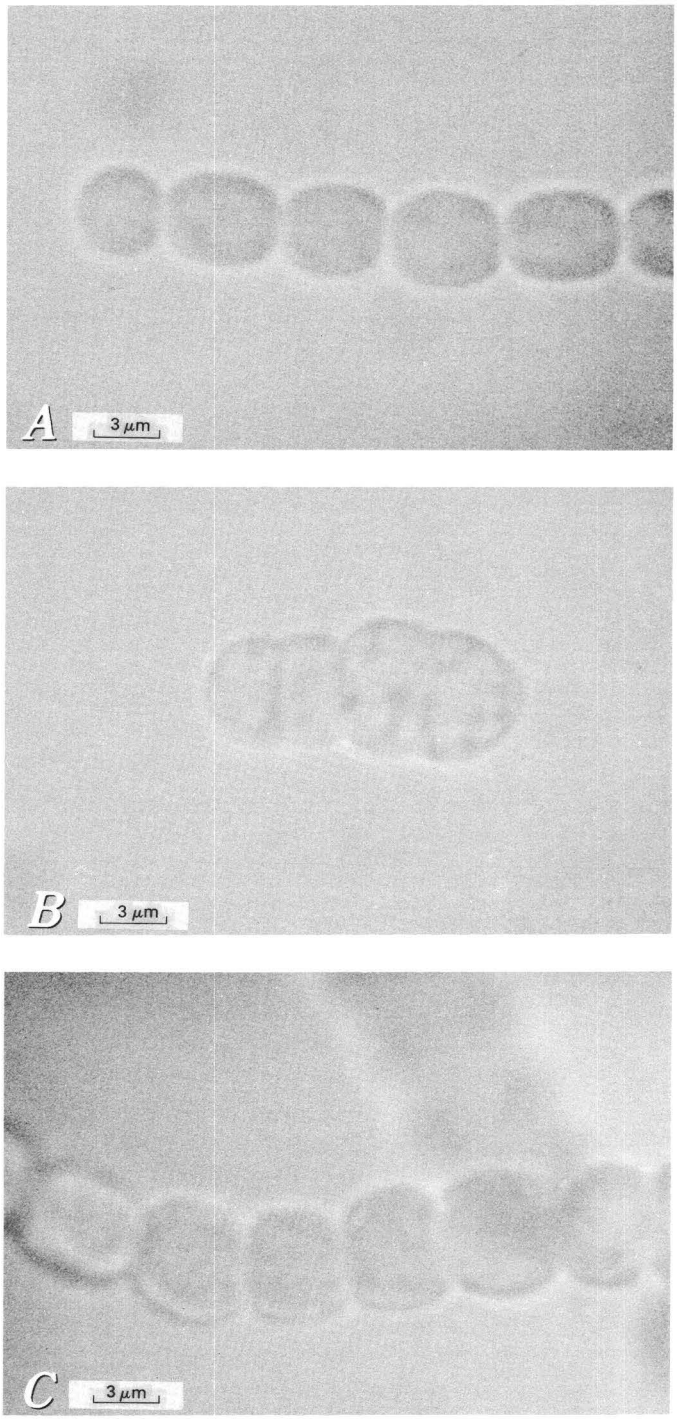

Figure 433.—Photomicrographs showing morphological differences between Anabaena flos-aquae *grown in cultures exposed to various concentrations of unfractionated Richland volcanic-ash leachate. Enlargements of photomicrographs taken of unpreserved cultures with light microscope; × 3600. A, control culture; B, culture exposed to 1:35 dilution; C, culture exposed to 1:250 dilution.*

MOSES LAKE VOLCANIC-ASH LEACHATE

Growth curves from the experiment in which different fractions of Moses Lake ash leachate were added to *Anabaena flos-aquae* cultures are shown in figure 434. None of the leachate additions had significant effects on growth or final biomass, nor did they cause changes in cell morphology. The data in table 101 show no significant differences in growth rate computed from day 2 to day 4.4 among the various cultures.

Lack of any toxic effect of the Moses Lake ash leachate on algal growth is not surprising because the toxicants in the Richland ash leachate were apparently part of the 17 percent of the dissolved organic carbon retained by the cation-exchange column, and this fraction contributed only 7 percent of the total dissolved organic carbon to the Moses Lake leachate. The toxicants simply may not be present in the Moses Lake leachate or else they may occur in much lower concentrations.

SUMMARY AND CONCLUSIONS

The data reported here confirm that leachate of volcanic ash that fell at Richland is toxic to *Anabaena flos-aquae*, even at large dilutions. In addition, the results indicate that the toxic substances are probably organic compounds retained on a cation-exchange resin, rather than uncomplexed trace metals such as manganese, zinc, copper, and cadmium; or acidic or neutral organic compounds that would have passed through the cation-exchange resin. The toxic constituents retained on the cation-exchange resin could be one or more of the following types: (1) cationic organic compounds such as amines; (2) strongly hydrophobic (sparingly soluble) organic compounds, such as phenols, that interact with and are retained by the resin; or (3) metal-organic complexes that are retained by interaction of metals with the cation-exchange resin.

Results indicate that the leachate from Moses Lake ash has neither an inhibitory nor stimulatory effect on the growth of *Anabaena flos-aquae*. This finding is consistent with the contrasting results from the Richland volcanic-ash leachate, because the fraction of

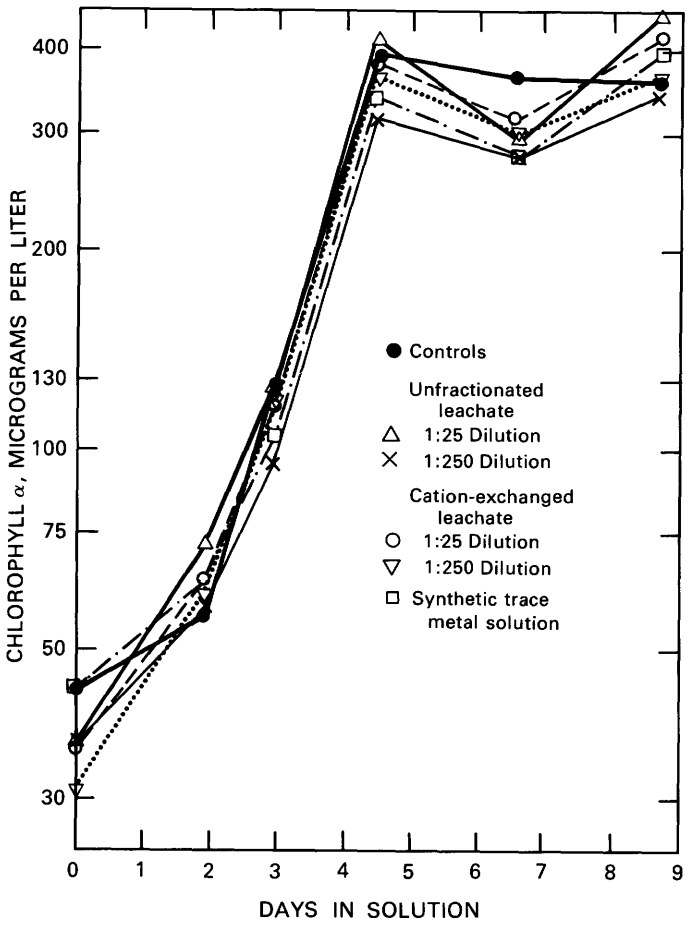

Figure 434.—Growth of Anabaena flos-aquae *as indicated by increase of chlorophyll* a *exposed to different fractions of Moses Lake volcanic-ash leachate.*

that leachate found to be toxic occurs at a much lower concentration in the Moses Lake leachate.

The lack of toxicity shown by laboratory experiments with Moses Lake volcanic-ash leachate is consistent with field observations of algal populations in several lakes from the area. Soap Lake and Lake Lenore, northwest of the town of Moses Lake, have been studied for several decades, and their summer phytoplankton assemblages during 1980 were similar to those in previous years (Walker, 1975; W. T. Edmondson, University of Washington, oral commun., 1980). Moses Lake, itself, had its usual dense, blue-green algal bloom. In Warden lake, 8 km west of Warden, Wash., the 1980 phytoplankton assemblage was dominated by diatoms and chysophytes, the same as reported (Dion and others, 1978) for previous years.

REFERENCES CITED

Bartlett, Larry, Rabe, F. W., and Funk, W. H., 1974, Effects of copper, zinc, and cadmium on *Selanastrum capricornutum:* Water Research, v. 8, p. 179–185.

Dion, N. P., Bortleson, G. C., and Innes, J. K., 1978, Data on selected lakes in Washington: Washington State Department of Ecology, Water-Supply Bulletin 42, pt. 6, 125 p.

Hutchinson, G. E., 1957, Geography, physics, and chemistry, V. 1 *of* A treatise on limnology: New York, John Wiley, 1014 p.

McKnight, D. M., Feder, G. L., and Stiles, E. A., 1981, Toxicity of volcanic ash leachate to a blue-green alga—Results of a preliminary bioassay experiment: Journal of Environmental Science and Technology, v. 15, no. 3, p. 362–364.

Pereira, W. E., Rostad, C. E., and Taylor, H. E., 1980, Mt. St. Helens, Washington, 1980 volcanic eruption—characterization of organic compounds in ash samples: Geophysical Research Letters, v. 7, no. 11, p. 953–954.

Taylor, H. E., and Lichte, F. E., 1980, Chemical composition of Mount St. Helens volcanic ash: Geophysical Research Letters, v. 7, no. 11, p. 949–952.

Walker, K. F., 1975, The seasonal phytoplankton cycles of two saline lakes in central Washington: Limnology and Oceanography, v. 20, p. 40–53.

THE 1980 ERUPTIONS OF MOUNT ST. HELENS, WASHINGTON

RESPONSE OF GLACIERS TO THE ERUPTIONS OF MOUNT ST. HELENS

By MELINDA M. BRUGMAN *and* MARK F. MEIER

ABSTRACT

Eruptive activity beginning March 27 initially covered the 5 km^2 of glaciers on Mount St. Helens with thin layers of ash, and large areas on some glaciers were deeply fractured by the bulging volcano. Blast and landslide suddenly removed 70 percent of the glacier ice volume (0.1 km^3) on May 18. Melting of snow and ice by hot ash flows, erosion of glaciers by avalanches and mudflows, and deposition of thick ash deposits on that day drastically affected the mass balance of all the glacier ice remaining on the volcano. Response of Shoestring Glacier to sudden loss of its accumulation area and to 6-m decrease in thickness was a progressive decrease in velocity along the entire remaining length of the glacier, which began within a few weeks of the eruption and continued throughout the summer. The observed velocity trend of summer 1980 was dramatically different from that of the previous year. Deceleration throughout the 1980 summer may have been caused by reduction in subglacial water pressure, which affects glacier sliding. Swift Glacier, which was covered with a thick ash layer but not beheaded, had virtually constant velocity throughout the 1980 summer. The recent eruptions of Mount St. Helens offer an unprecedented opportunity to study transient-flow dynamics of glaciers with drastically changed geometries and mass balances, in addition to providing a framework for future hazard evaluation of the glaciers that cover this and other Cascade Range volcanoes.

INTRODUCTION

Prior to the May 18 eruption, there were 11 named glaciers[1] and many small perennial snow and ice masses on the slopes of Mount St. Helens (fig. 435). The May 18 eruption removed 70 percent of the glacier ice on the volcano. Melting glacier snow and ice added to the lubrication of mudflows, one of the most destructive effects of the volcanic eruption for people living downvalley. Many glaciers remained on the volcano after May 18; some glaciers were beheaded and thinned, whereas others were barely affected.

An excellent opportunity to study the effects of drastic changes in glacier geometry on glacier motion was created, particularly on Shoestring Glacier, where the flow behavior had been studied during the summer of 1979. The flow response and sliding behavior of glaciers on Mount St. Helens should be of considerable interest not only for hazard analysis, but also for providing better insight into glacier flow mechanics and response theory, applicable to many other glaciers.

In this report general characteristics of the glaciers before and after the 1980 eruptions are compared. The highly affected Shoestring Glacier is contrasted with the virtually unaffected Swift Glacier. The impacts of the eruption on mass balance and glacier flow behavior are discussed, and these results are inter-

[1]The most recent U.S.Geological Survey 15-minute topographic quadrangle of Mount St. Helens (1958) names only four of them: Wishbone, Forsyth, Ape, and Shoestring Glaciers. Five of the other seven glaciers (Nelson, Swift, Dryer, Talus, and Toutle Glaciers) are labeled on the posteruption 1:100,000-scale map of Mount St. Helens and vicinity (U.S. Geological Survey and others, 1980). Loowit and Leschi Glaciers are shown on the map entitled Mount St. Helens—Spirit Lake (U.S. Forest Service, 1973).

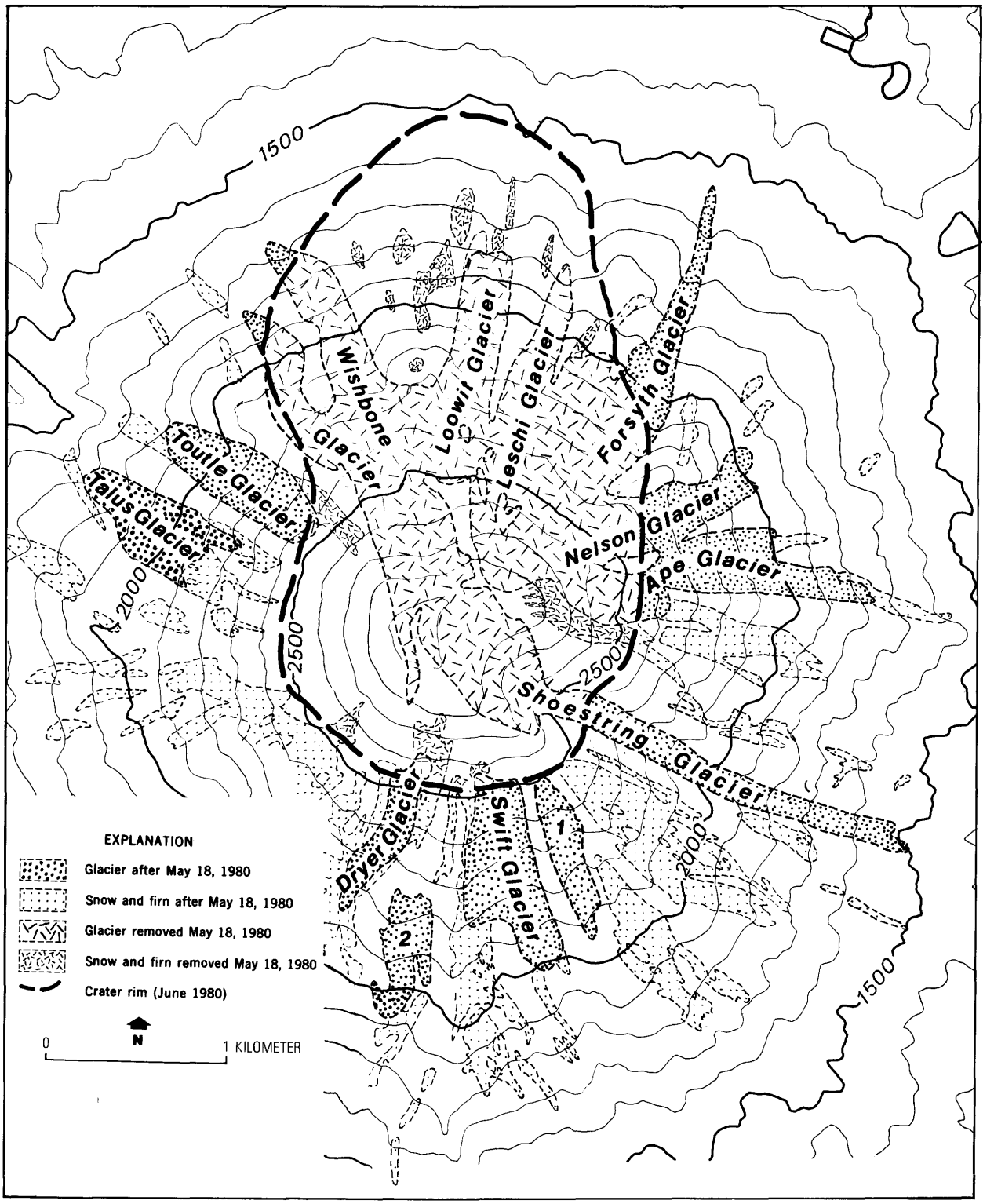

Figure 435.—Glaciers on Mount St. Helens before and after May 18 eruption. Unnamed glaciers (1 and 2) are shown in table 102. Contours show preeruption topography; contour interval 100 m.

preted in terms of existing knowledge of glacier physics. Glacier-covered volcanoes pose special potential hazards associated with the presence of snow and ice, and these are described to assist in hazard evaluation for the future at Mount St. Helens and other Cascade Range volcanoes.

ACKNOWLEDGMENTS

The assistance, advice, and support of many people have made this research and report possible, in particular Keith Echelmeyer, Barclay Kamb, Robert Krimmel, and Dr. and Mrs. Brugman. Field assistance at various times under difficult and sometimes dangerous conditions by Carolyn Driedger, Suzanne Brown, Bruce Furakowa, Dave VanAlstein, Eugene Miya, Steve Snowden, Emily Chase, Bill Brugman, Neil Cochran, Dan May, and Sharon Dahl is gratefully acknowledged, as is the skillful flying by several pilots, especially Michael Montgomery and Bob Edwards, and the logistical support of Jan Markman, Patrice Luker, Doloris Oakes, and other USGS personnel in Tacoma and Vancouver. Reviews by Barclay Kamb, Keith Echelmeyer, Bob Sharp, and Kerry Sieh have also been of great help to this report.

GENERAL CHARACTERISTICS OF THE GLACIERS BEFORE THE 1980 ERUPTIONS

Prior to the May 18 eruption, approximately 5 km^2 of the area of Mount St. Helens was covered with glacier ice, representing a volume of approximately 0.18 km^3. Most of the ice was concentrated on the northern flank of the volcano above 1,650 m altitude, but glaciers and snowfields existed on all sides of the mountain (fig. 435). Deep winter snowfall, extensive avalanche and wind transport of snow to low-lying areas, and frequent insulation of the ice and snow by dust and rockfall deposits allowed glaciers to survive at relatively low altitudes on the slopes of the volcano.

The glaciers on Mount St. Helens had few recent moraines, contained abundant englacial debris, and produced very little surface runoff but many small outburst floods. They were generally thin (20–60 m) and flowed over steep slopes (averaging 25°) of loose volcanic debris. Glacier thicknesses varied seasonally by as much as 10 m (more than 10 percent of the glacier depth) due to seasonal melting and avalanches of rock, snow, and ice. Several glaciers had made recent advances. Many of the unusual characteristics of the glaciers on Mount St. Helens should also be common to glaciers on other Cascade Range volcanoes, particularly those which have highly permeable deposits underlying the ice cover.

CHARACTERISTICS OF SHOESTRING GLACIER

A study of Shoestring Glacier, on the east side of Mount St. Helens (figs. 436, 437), was begun in 1979 to test current hypotheses on the basal sliding of glaciers. Marker poles were emplaced along the length of Shoestring Glacier in June 1979 and June 1980. Selection of marker sites was based on surface characteristics of the glacier, visibility of markers from the survey points, and potential hazard in establishing and maintaining the markers. Markers were relocated whenever necessary to keep them in sight from the survey points. Coordinates of the markers were measured from the survey points several times each month during the summers, and also in late February and early May 1980, using K&E Laser Ranger III and Kern theodolite. During the 1980 summer, Ranger III was replaced by HP-3808 and Leitz Red I electronic distance measurers. Measurements are accurate to within a few millimeters.

The unusual permeability of the debris bed of Shoestring Glacier was expected to affect the subglacial water pressure and thus the basal sliding, so that the relation of water pressure to velocity could be more fully understood. Just prior to the May 18 eruption, Shoestring Glacier was advancing strongly, almost overriding glacier deposits from a major advance in the late 1930's.

Direct measurement of ablation rates during the summer of 1979 on Shoestring Glacier indicated rates of about 6 cm/day (water equivalent) on snow and

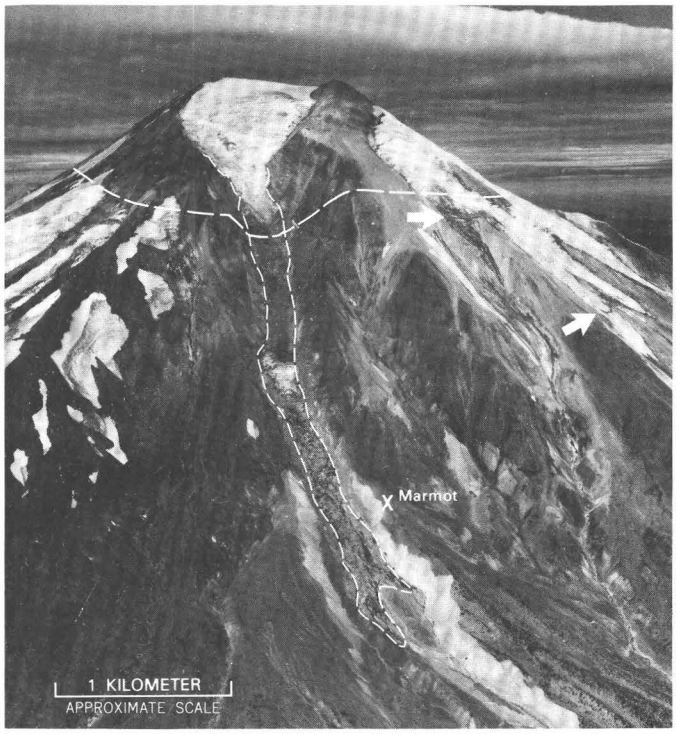

Figure 436.—Eastern slope of Mount St. Helens showing Shoestring Glacier as it appeared on September 29, 1979. Rock-covered surface of Shoestring Glacier is outlined by a thin dashed line. Swift Glacier can be seen just below left skyline on south slope of volcano. Conspicuous debris layers (angular, unsorted rock debris, about 1 m thick, embedded in ice) on Ape and Nelson Glaciers are shown by white arrows; debris layer on Shoestring Glacier is concealed by surface rock debris. Survey point Marmot is shown with a white X. Approximate crater rim following May 18 eruption is shown by heavy dashed line. Photograph by Austin Post (USGS 79 L4-16).

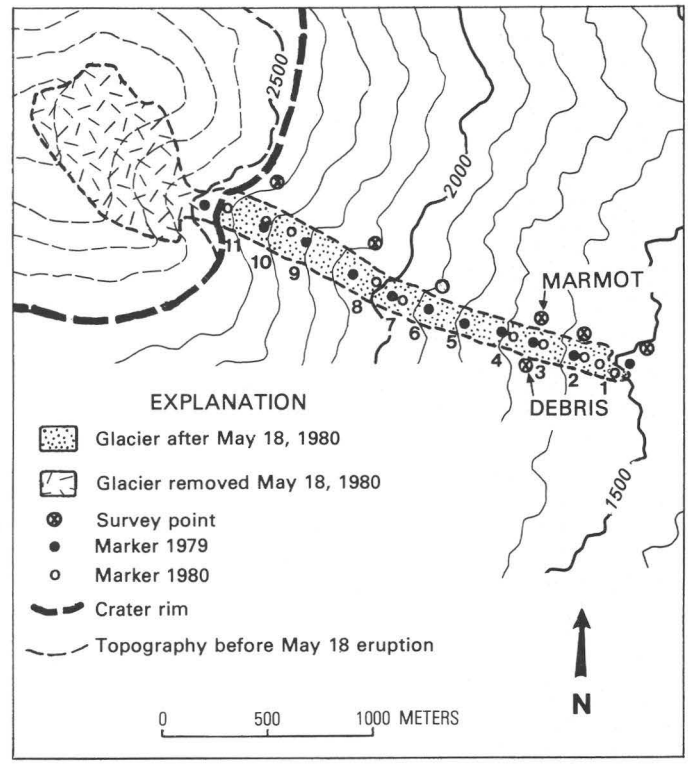

Figure 437.—Map of Shoestring Glacier showing regions on glacier where marker coordinates were surveyed (numbers) and approximate distribution of markers and survey points used in 1979 and 1980. Contour interval 100 m.

less than 1 cm/day on glacier ice covered with surface moraine and rockfall debris. The highest ablation rates (as much as 10 cm/day) occurred on dirty avalanche snow. The average streamflow from Shoestring Glacier during the 1979 summer can be estimated from ablation measurements to be about 0.54 m^3/s; net evaporation and condensation were probably negligible. Yet less than half this amount was measured in the stream below the terminus in July 1979 (0.23 m^3/s). Perhaps the balance of the runoff was accounted for by ground-water flow.

Outburst floods commonly occurred during the summer on Shoestring Glacier prior to 1980, and probably also on other glaciers around the volcano. Floods were especially common in August and September, and they appeared to originate high on the glacier, most often in region 8 (fig. 437). These floods may have been caused by water accumulating in crevasses or in caverns in the glacier. No evidence of volcanic heating beneath the glacier was found.

Early summer crevasse patterns on Shoestring and other glaciers on Mount St. Helens showed narrow marginal zones about 10 m wide of closely spaced, en echelon crevasses (fig. 438). Measurements on Shoestring Glacier showed that the crevasse zones corresponded to the margins of a central region of "plug flow," in which the velocity was almost constant across the glacier (fig. 439). The narrow zone of strong deformation appeared to be associated with an englacial debris layer (fig. 439). Layers similar to those on Shoestring Glacier could be discerned on the Ape, Nelson, Toutle, Loowit, Swift, and possibly other glaciers (figs. 435, 436), but they have not been documented elsewhere in the Cascade Range. Debris layers may originate from rock and snow avalanches,

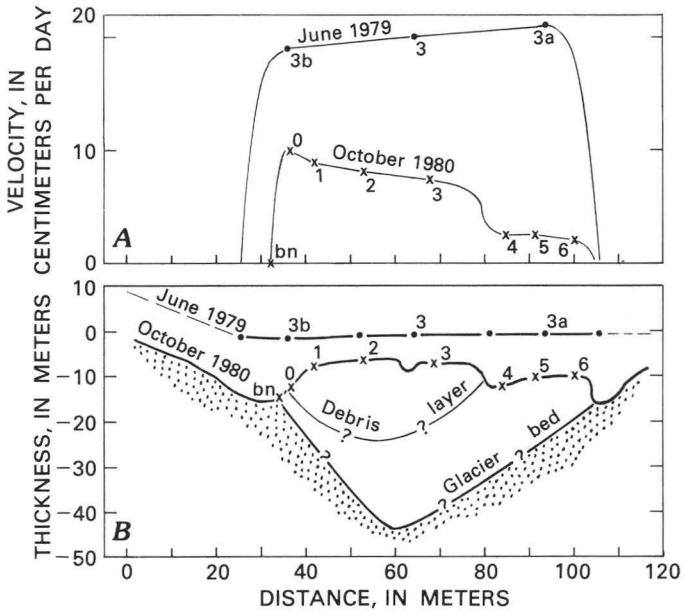

Figure 439.—Diagrammatic cross sections in region 3 of Shoestring Glacier (see fig. 437) comparing velocity and thickness in June 1979 and October 1980. Marker "bn" is "base nail" emplaced in ice a few centimeters above glacier bed. A, velocity. Note that velocities are almost constant across glacier except where deformation occurs in vicinity of englacial debris layer and at glacier margin. B, thickness. Note that profiles were measured in June 1979 (before summer snowmelt) and October 1980 (after eruption removed previous winter's snowfall and firn accumulation); thickness changed very little during summer of 1980. The Debris survey point is located at the origin (on left).

small mud flows, or volcanic activity; however, little is known about them, how they are formed, and how they behave.

Longitudinal profiles of velocity in June and August 1979 showed velocities of approximately 20 cm/day over the lowest 300 m of glacier, increasing to 30–40 cm/day upglacier from region 5 (fig. 440). Velocity was relatively constant over the lowest 300 m but increased markedly during the summer far-

Figure 438.—Lower part of Shoestring Glacier as it appeared on May 17, showing narrow zones of marginal crevasses. Location of survey point Marmot indicated with black X. The approximate crater rim after May 18 is shown by dashed line. Surface of volcano was recently covered with ash. Regions where ash was dry appear light (highly reflective) compared to dark areas where ash was damp due to melting of underlying snow. Photograph by R. M. Krimmel (USGS 80S3–100).

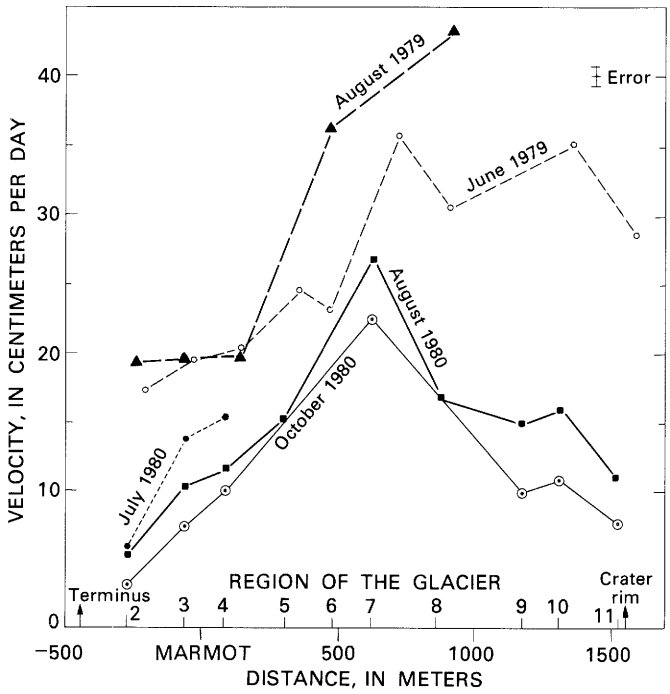

Figure 440.—Diagrammatic longitudinal profiles of Shoestring Glacier showing velocity during 1979 and 1980. Origin of distance scale is located at survey point Marmot. Note dramatic decrease in 1980 velocities along entire length of glacier compared to velocities measured in 1979, especially for markers closest to crater rim.

ther upglacier. This suggests that basal sliding may have been negligible near the terminus but was a major component of the motion upglacier.

The outburst floods on Shoestring Glacier in 1979 occurred in the same regions as the increased late-summer ice velocities above region 5 (fig. 440). This may indicate that late-summer buildup of water pressure increased the local sliding rate of the glacier above region 5. Spatial and temporal variations in ice velocities during the 1979 summer may have been due to varying water pressure beneath the glacier caused by spatial differences in bed permeability and temporal variations in water drainage. Additional evidence of late-summer increase in ice velocity high on the glaciers of Mount St. Helens, and a probable relation to basal sliding, is provided by seismic events observed by Weaver and Malone (1979), which they relate to "stick-slip" motion along glacier beds. The frequency of the events was observed to increase during August (S. D. Malone, written commun., 1980).

GENERAL EFFECTS OF THE 1980 ERUPTIONS

Growth of the prominent volcanic bulge on the mountain from March 27 through May 17, 1980, affected portions of Forsyth, Loowit, Leschi, Wishbone, Nelson, and Shoestring Glaciers. Deformation, earthquakes, and oversteepening caused intricate crevassing and ice avalanching on the bulge. However, the bulge did not appear to affect the terminus portions of the glaciers. Ice velocities measured on the lower part of Shoestring Glacier (region 3) from February 23 to May 16, 1980, showed no major changes from preeruptive velocities of 18–20 cm/day. Ash deposited on the mountain from March 27 to May 17 generally ranged in thickness from a trace to 3 cm, and was interbedded with snow; effect of the deposited ash on the rate of glacier flow was probably negligible.

The explosion of Mount St. Helens on May 18 changed the glaciers dramatically (fig. 435). The changes in each glacier resulting from the May 18 eruption are summarized in table 102. Seventy percent of the ice on the volcano, including large parts of Wishbone, Forsyth, Nelson, Ape, and Shoestring Glaciers, and all of Loowit and Leschi Glaciers, was blasted away, melted, or displaced as shattered blocks. Nelson, Forsyth, Ape, and Shoestring Glaciers (fig. 436) were beheaded. Pyroclastic flows melted and eroded about 6 m of snow and ice from Shoestring Glacier and similar amounts from Nelson and Ape Glaciers, generating large mudflows that swept down the valleys of Smith Creek, Muddy River, and Pine Creek. Partial melting of Toutle and Talus Glaciers generated a large mudflow that swept down South Fork Toutle River. Subsequent air-fall and mudflow deposits as much as 3 m thick covered the remaining glaciers on the volcano.

During the summer of 1980, deep rills and channels were cut in the ash-covered surfaces of the remaining glaciers by small streams, which may have been generated by rainfall, outburst floods, abnormal surface melt caused by warm ash flows, or normal daily melt from exposed snow and ice.

Beheaded and ash-covered glaciers similar to those on Mount St. Helens have been observed on other volcanoes such as Katmai (Muller and Coulter,

Table 102.—Changes in glacier area, depth, and volume as a result of the May 18 eruption

Glacier	Area			Depth (estimated average)		Volume		
	Before (km^2)	Removed (km^2)	Percent removed	Before (m)	After (m)	Before (km^3)	Removed (km^3)	Percent removed
Forsyth----	0.87	0.65	75	45	20	0.039	0.035	90
Wishbone---	.83	.79	95	45	5	.037	.037	[1]99
Shoestring-	.64	.43	68	40	30	.026	.020	77
Ape--------	.45	.11	24	35	30	.016	.006	37
Loowit-----	.43	.11	100	30	0	.013	.013	100
Swift------	.36	.03	7	25	25	.009	.001	11
Nelson-----	.29	.12	41	35	30	.010	.005	50
Toutle-----	.28	.02	4	30	15	.008	.004	50
Leschi-----	.26	.26	100	30	0	.008	.008	100
Talus------	.23	0	0	30	15	.007	.003	43
Unnamed (1)	.16	0	0	20	20	.003	0	0
Dryer------	.14	.02	14	15	15	.002	0	0
Unnamed (2)	.08	0	0	15	15	.001	0	0
Total--	5.02	2.86				0.179	0.132	

[1]A few small parts of Wishbone Glacier remain, but their volumes total less than 0.001 km^3.

1957b) and Bezymianny (Gorshkov, 1959). The effects of the May 18 eruption of Mount St. Helens have permanently altered the state of balance and dynamics of all the glaciers on the volcano.

EFFECTS ON MASS BALANCE

The difference between accumulation and ablation on a glacier surface over a particular time interval (usually a year) is called the glacier mass balance. If the mass balance changes, the glacier will generally respond by a change in ice thickness, velocity, and terminus position.

ACCUMULATION

An immediate effect of the May 18 eruption was a dramatic change in the geometry of the accumulation areas of most of the glaciers. The eruption removed large portions of the accumulation areas of Shoestring, Forsyth, Nelson, and Ape Glaciers (fig. 435). Only minor changes occurred to the accumulation areas of Swift, Toutle, and Talus Glaciers, but the accumulation in some of these areas will in some cases be significantly affected by the destruction of surrounding slopes that formerly contributed large amounts of snow to glacier areas by avalanche and wind transfer.

Avalanche snow and ice failed to accumulate on lower Shoestring Glacier in summer 1980, contrary to what had been observed during the previous summer. In July and August 1979, avalanche deposits as much as 3 m thick were observed at the 2,000-m level on this glacier; the deposits came from steep upper slopes that have since been destroyed during the May 18 eruption. Reduction of avalanche deposits and windblown snow will cause a general decrease in the net accumulation on all the remaining glaciers. Also, the glacier accumulation areas may be further altered if the crater continues to enlarge.

Snow, rime, and avalanche deposits in the central amphitheater crater may remain throughout the year if the volcano cools. Deep shade and insulation due to dust layers may allow the snow to persist despite the low elevation of the crater floor, in much the same way that a glacier has developed in the Katmai caldera following the 1912 eruption (Muller and Coulter, 1957a). Alternatively—or in addition—a

lake might form from melt water derived from the snow and ice.

ABLATION

Ablation caused by hot ash flows moving over snow and glacial ice during the major eruptions generated mudflows, some of which may have melted or eroded additional snow and glacial ice. Comparison of survey measurements on the remaining portion of Shoestring Glacier in 1979 and 1980 indicated that the amount of glacier thickness removed by the May 18 eruption depended upon location. The average apparent loss over the lower part of this glacier was 6 m. This loss was due in part to erosion by mudflows and avalanches, as indicated by the removal and redistribution of old surficial rock debris; just off glacier margin, erosion was indicated by recession of rock cliffs and steep, loose slopes bordering the glaciers and destruction of some bench marks placed near the glacier prior to the eruption. Although no preeruption survey data are available, the May 18 melt and erosion loss to Toutle and Talus Glaciers appears to be 10–15 m of snow and ice.

Ash deposits, which averaged 1 m in thickness on Shoestring and Swift Glaciers, almost totally insulated the snow and ice from melting during the summer of 1980. About 90 percent of the posteruption glacier area on the volcano continued to be covered with thick ash deposits during late September. Slowly cooling volcanic deposits on Shoestring, Toutle, Talus, and lower Forsyth Glaciers continued to cause some additional melting throughout the summer. Mudflows and gullying caused glacier ice to be exposed to solar radiation, causing further ablation.

The surface-lowering of ash-covered snow can be caused by compaction of ash or snow, deflation, erosion or redeposition of ash or other debris, melting of snow and ice, or the flow of underlying glacial ice. Ash thicknesses averaged 130 cm at seven measured locations on Swift Glacier. Ash compaction rates or deflation rates averaged only 0.15 cm/day from July 26 to October 6, 1980. The snow surface lowered an additional 0.25 cm/day from July 26 to August 3, 1980, and 0.71 cm/day from August 3 to October 6, 1980. Snow underlying the ash showed an increase in grain size and a decrease in pore volume, which might account for most of the observed surface-lowering through summer 1980.

Ash thicknesses greater than 2.4 cm have been observed to decrease the melting of underlying snow (Driedger, this volume). Thus most of the observed surface-lowering of the snow was probably due to compaction and flow caused by the weight of the overlying ash. Ablation measurements on Shoestring Glacier showed that almost no melting of snow and ice occurred on glacier surfaces that were buried by more than a few centimeters of ash.

SUMMARY OF MASS BALANCE EFFECTS

The glaciers that remained on the south slopes of Mount St. Helens had unusually positive mass balances in 1980, owing to the insulating effect of thick ash deposits, which virtually stopped ablation after May 18. The glaciers remaining on the east and west slopes had unusually large negative mass balances in 1980, owing to accelerated melting on May 18 and loss of accumulation areas. Changes in avalanche and wind-drift accumulation patterns and removal of accumulation areas (caused by the destruction of the summit region) will cause generally negative mass balances during the years to come. With time and sufficient cooling of the volcano, the central amphitheater may support snow and glacier growth.

Mudflows caused by unstable layers of water-saturated material in the lower portion of the ash deposits have already modified ash thickness patterns on some glaciers. Steep glacier surfaces may gradually become clear of insulating ash layers, but less steep regions may become more deeply covered with ash and mudflow deposits. Windblown ash and additional ash fall and rockfall will cause reduced ablation on the glaciers of Mount St. Helens for many years to come. Because of the reduced ablation, ash-covered glacier ice may remain for decades in spite of generally negative mass balances, as is the case at the Knife Creek Glaciers on Katmai (Muller and Coulter, 1957b).

EFFECTS ON GLACIER FLOW

The eruptions greatly modified either the geometry or the surface mass balance, or both, of all the

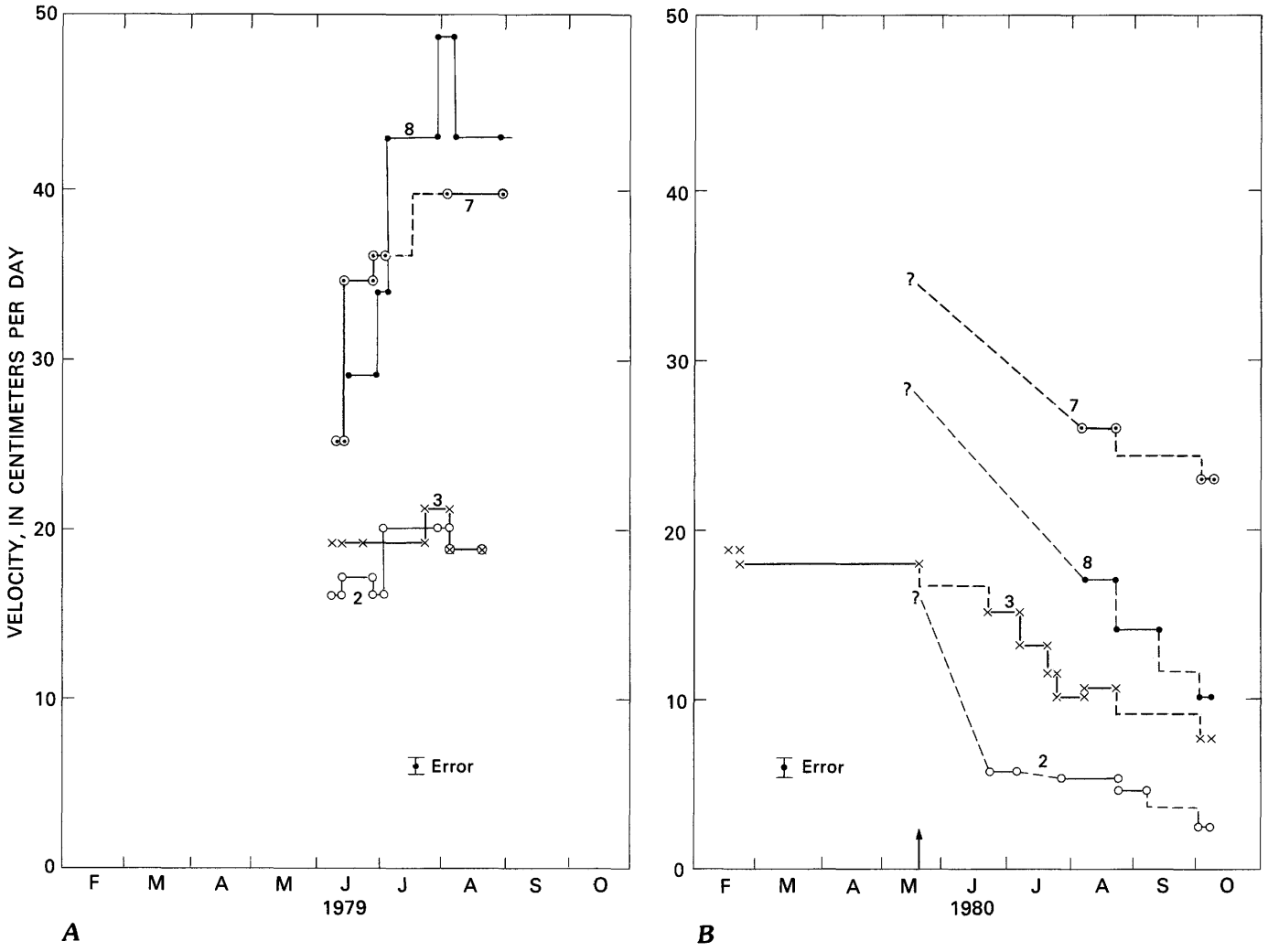

Figure 441.—Seasonal variations in velocity of Shoestring Glacier in regions 7 and 8, typical of upper part, and in regions 2 and 3, typical of lower part. (See fig. 437 for region locations.) A, 1979. Note that large variations in velocity occurred on upper part of glacier, while only slight variations occurred on lower part. B, 1980. Decrease in velocity after eruption on May 18 (shown by heavy arrow) was noted at all locations. Queries indicate velocities extrapolated backward from data obtained later in 1980.

glaciers. Therefore, the stresses and the velocity characteristics of all the glaciers have been affected. The sudden changes in geometry produced by the May 18 explosion would be expected to have large and immediate effects on glacier flow. The changes in surface mass balance would be expected to consist of an immediate adjustment to the modified 1980 mass balance, followed by a long-term adjustment to continuing balance changes caused by the newly imposed geometry and environment. The modification of glacier flow regimes can be illustrated by comparing the transient flow regimes of Shoestring Glacier, which had large changes in geometry, to those of Swift Glacier, which had no changes in geometry, but had an altered surface balance.

FLOW OF SHOESTRING GLACIER

Prior to May 18, the velocity of lower Shoestring Glacier did not change markedly with time, but the velocity of the upper glacier showed large seasonal fluctuations. After May 18, all velocities decreased. Figures 441*A* and *B* show the rate of movement of

regions 2 and 3, and 7 and 8, which typify the velocity characteristics of the lower and upper parts of the glacier, respectively. (The locations of these markers are shown in fig. 437.) Before the eruption of May 18, markers in regions 2 and 3 showed a very slight seasonal variation in velocity around average values of about 19 cm/day. Markers in region 8, on the other hand, showed variations of more than 15 cm/day around an average value of 30 cm/day. By the end of June 1980, the average velocity in region 3 had decreased to 15 cm/day, and by early October it had decreased further to 8 cm/day. Velocities in regions 7 and 8 also showed major decreases from June to October 1980.

The deceleration from June 20 to August 5, 1980, in region 3 appears to have been almost constant at about 0.15 cm/day/day. If it is valid to assume that deceleration was constant, and we extrapolate backward in time from June 20, we can conclude that the deceleration began in region 3 about 20 days after the eruption of May 18, 1980. In contrast to the possible delayed response in region 3, a very rapid reduction in glacier velocity of more than 60 percent appeared to occur very soon after the May 18 eruption in region 2, located near the glacier terminus. Unfortunately, the difficulty of making observations immediately after May 18 makes it impossible to determine the start of deceleration at most velocity markers.

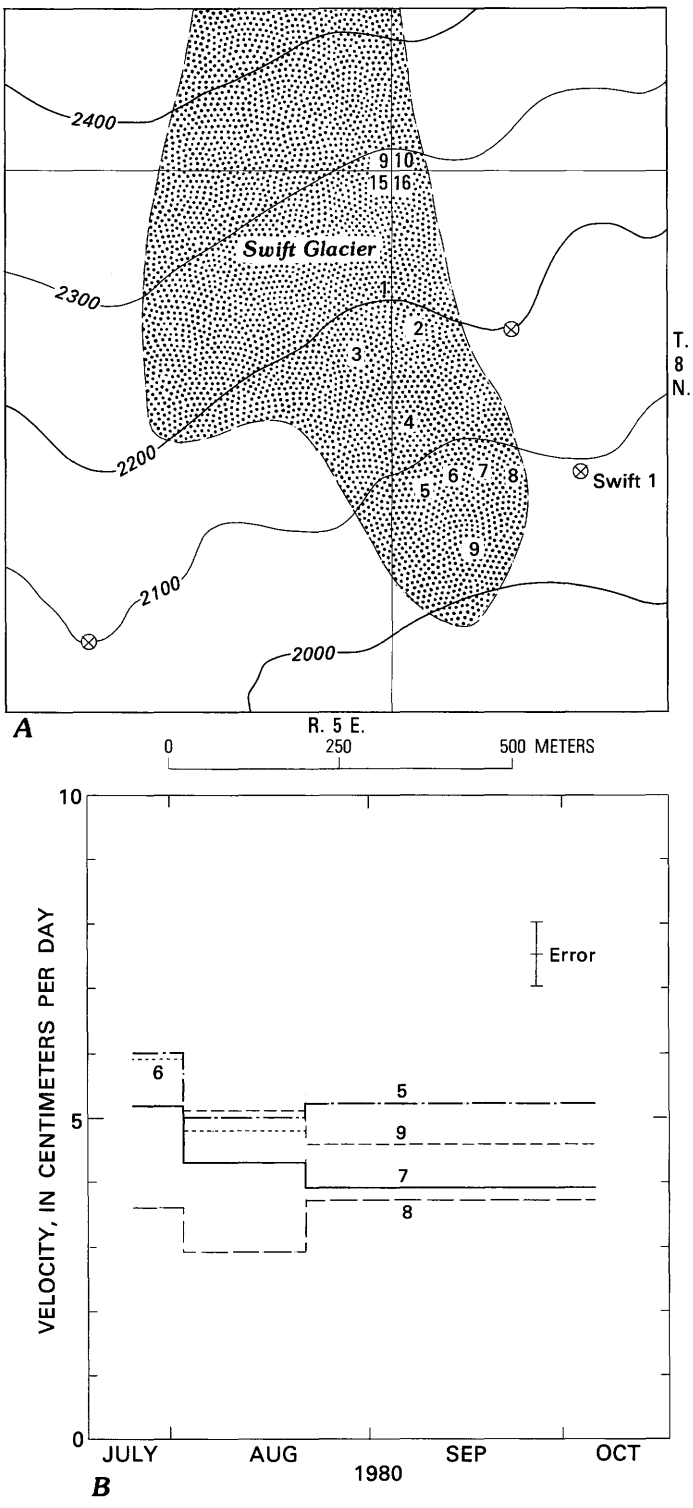

FLOW OF SWIFT GLACIER

Swift Glacier on the south side of Mount St. Helens displayed velocities that were relatively constant throughout the summer of 1980 (fig. 442). Nine markers were surveyed through the period July 26 to October 6, 1980; the data for five markers are shown on figure 442. (The remaining data have yet to be analyzed.) All the markers showed velocities between 3 and 6 cm/day with little if any significant deceleration. (Velocities on Swift Glacier had not been measured prior to 1980; thus preeruptive velocity

Figure 442.—Velocities calculated for selected markers located on Swift Glacier, on south flank of Mount St. Helens. A, Map of Swift Glacier showing location of markers (numbers) and survey points (x's). Data for markers 1–4 not yet reduced. Topographic contour 100 m. B, Velocities calculated from coordinates measured on July 26, August 3, August 22, and October 10, 1980. Marker 6 was destroyed after August 22 measurement. Note low velocities, relatively large error, and insignificant deceleration compared to that observed on Shoestring Glacier (fig. 441B). Variations in velocities for each marker are considered insignificant because they fall within the range of error.

comparisons cannot be made.) The 5-m-thick deposits of 1979–80 winter snow that survived over most of the glacier throughout the summer of 1980 appear to have kept the thickness and thus possibly the velocity relatively constant. Melting occurred in gullies that dissected the glacier surface during the late 1980 summer, which might account for some of the observed changes in velocities.

Transverse profiles of velocity (fig. 443) showed that velocity was almost constant across the glacier; note, however, the sharp decrease in velocity at the glacier margin. More studies will be needed to determine if the marginal zone of high deformation is related to an englacial debris layer, as is the case for the lower Shoestring Glacier.

INTERPRETATION OF CHANGES IN FLOW

Study of the change in flow regime resulting from the sudden and drastic changes to the glaciers should lend insight into the physics of glacier flow and basal sliding. The principal change observed on Shoestring Glacier was flow deceleration, possibly simultaneous throughout the length of the glacier, which began either immediately or soon after the May 18 eruption and continued at least until October 1980. Thickness change due to ablation and surface erosion on May 18

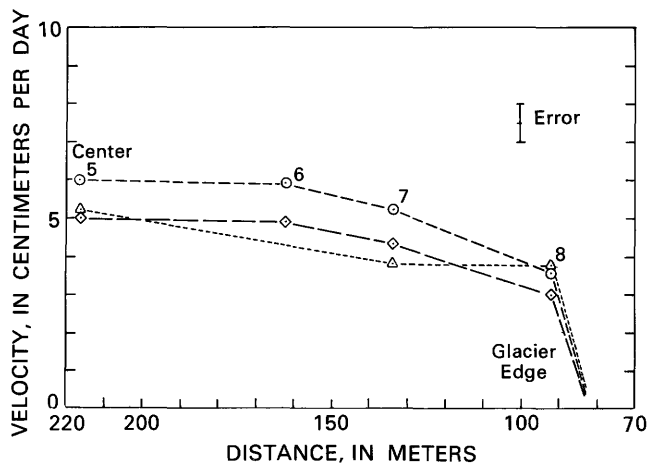

Figure 443.—Diagrammatic cross sections of Swift Glacier showing velocities during summer of 1980. Short-dashed line, velocity between July 26 and August 3; long-dashed line, velocity between August 3 and 22; dotted line, velocity between August 22 and October 10, 1980. Origin of x-axis is survey point Swift 1 (see fig. 442A).

was also significant, but it would only account for part of the observed deceleration; the sudden beheading probably affected the upper part of the glacier more, and sooner, than it did the lower part, but inaccessibility to the glacier and safety considerations prevented data collection that might have tested this assumption.

Removal of snow, rock debris, and ice from the surface of Shoestring Glacier could cause an essentially instantaneous decrease in ice velocity. An average decrease of about 10 percent in glacier thickness appears to have occurred; flow adjustment to such a thickness change could account for an immediate decrease of 30–50 percent in ice velocities. Changes in velocity of this amount eventually occurred at some locations along the length of the glacier. Major shear deformation or sliding appears to be occurring in the vicinity of the thick englacial debris layer (fig. 439). Response to thickness changes may involve the sliding properties of the debris layer and the basal zone. Unfortunately, the characteristics of the debris layer are not yet fully understood, and the thickness of ice overlying the layer is known only in deep gullies or on glacier margins, making analysis difficult.

Another difficulty in attributing the velocity decrease to thickness change is the fact that very little velocity change was observed on the lower glacier in 1979, in spite of a seasonal thickness change of about the same magnitude.

The beheading of upper Shoestring Glacier could have resulted in an immediate reduction in longitudinal stress gradients within about 1 km of the location of severance (Budd, 1968). Observations on Shoestring Glacier indicate that the largest reduction of velocities that cannot be directly attributed to thickness changes occurred along the upper glacier within about 1 km of the crater rim (fig. 440), which agrees well with theoretical predictions.

Subsequent adjustment of glacier flow to changes in local slope and thickness has been studied in terms of kinematic wave theory (Nye, 1963). Decrease in glacial thickness or changes in longitudinal stress gradients may lead to the development of kinematic waves, which are perturbations in ice velocity, thickness, and (or) discharge that travel along the length of the glacier. The speed of the waves can be estimated to be in the range of 40–120 cm/day on Shoestring Glacier. The velocity data (figs. 440, 441) show no evidence of wave propagation. However, wave velocities as slow as 120 cm/day would not be

easily detectable on Shoestring Glacier during the 1980 summer; they may possibly be observed in future years.

The gradual decrease in velocities which occurred on Shoestring Glacier throughout the summer of 1980 cannot be attributed to simple flow theory involving kinematic waves. Nor does it appear possible to attribute the gradual decrease to continuing thinning caused by surface ablation. Ablation rates of less than 1 cm/day were measured on the ash-covered areas of both Swift and Shoestring Glaciers, and maximum rates of only 2 cm/day on surfaces where ice was locally visible under surface debris. Possible errors in using these values as area-averaged ablation rates arise from the additional melting that occurred in the deep gullies that incised the glacier surfaces during 1980, and from irregularities in ablation patterns caused by erosion and deposition by local mudflows and outburst floods. Ablation rates would have to be as high as 8–20 cm/day averaged across the glacier to account for the observed deceleration of Shoestring Glacier in region 8 in 1980. Such ablation rates are highly unlikely. Thus, the relatively continuous decrease in glacier velocities of 0.1–0.2 cm/day/day on Shoestring Glacier does not appear to be controlled by continuous melting on the glacier surface.

In order to explain the behavior of Shoestring Glacier during the summer of 1980 and the gradual slowdown in ice velocities, additional physical factors controlling the glacier motion must be considered. The role of water pressure on glacier flow should be included, particularly since differential basal and englacial sliding appear to be important. Summertime increases in glacier velocity of Nisqually Glacier on Mount Rainier have been attributed to increases in water pressure at the base of the glacier (Hodge, 1974). Surging glaciers such as Variegated Glacier in Alaska also display marked increases in ice velocity associated with increases in subglacial water pressure. The occurrence of large outburst floods in August 1979 from upper Shoestring Glacier in region 8 and pronounced seasonal variations in velocity (fig. 441*A*) could indicate an increase in basal water pressure in that region in late summer, leading to high rates of basal sliding.

The change in flow regime following the eruption may be related to changes in subglacial water pressure. Instantaneous measurements of streamflow from Shoestring Glacier gave values in 1980 similar to those observed during the previous year. Measurements[2] in July 1979 averaged 0.23 ± 0.07 m^3/s, and in July 1980 (after the volume of the glacier was reduced by about 75 percent) measurements averaged 0.18 ± 0.07 m^3/s. Also, the average July ablation rates in 1979 summed over the glacier area were far larger than the measured streamflow, and it is likely that very little of this water was lost by evaporation. Therefore, much of the melt water from the upper glacier must have been discharged through ground-water flow. Late-summer increases in water pressure underneath upper Shoestring Glacier may be expected to disappear or sharply diminish because the water source provided by the accumulation basin was removed in 1980.

Reductions in subglacial water pressure due to the removal of glacial source areas may affect not only the glaciers whose accumulation area has been removed, but also all other glaciers, because all glaciers influence and are influenced by the water-table regime of the volcano. Although the influence of water pressure on the motion of the glaciers on Mount St. Helens is not fully understood, it remains a possible explanation for much of the seasonal variation in velocity observed prior to 1980 and for some of the gradual deceleration observed on Shoestring Glacier during the summer of 1980.

POTENTIAL HAZARDS

The thick volcanic deposits overlying the glaciers of Mount St. Helens can be considered to be a large mass of well-lubricated, unstable debris which, if triggered, may slide off the glacier surface, generating mudflows downvalley. These deposits are especially thick on the south side, at the headwaters of streams leading to Swift Reservoir. Numerous small mudflows occurred throughout the summer of 1980. In addition, large mudflows may be generated by the movement of pyroclastic or lava flows over seasonal snow-cover, firn, and glacier surfaces; the opening of a fumarole under a glacier; or the release of a glacier outburst flood. The potential hazard for flooding downvalley will increase in winter months as snow and rime accumulate on the volcano.

[2]Error given refers only to error of discharge measurements; no continuous record could be obtained. Stream discharge may have reached 1.5 m^3 or higher during short, unmeasured periods of heavy rain or outburst flooding, as indicated by a series of movie pictures taken during the summer of 1980.

If heat output in the crater diminishes, a new glacier may form there. The presence of this snow and ice would add to the danger of flooding and phreatic eruptions if the volcano becomes active again.

Changes in the existing snow and glacier ice may be premonitory of changing activity in the volcano. Unusual crevasse patterns, stream discharge, ice deformation, or thickness changes may give some indication of increased heat flux or distortion in the volcano beneath the glaciers. Excessive melting at the base of a glacier on the volcano would most likely result in a recognizable collapse feature on the glacier surface. This might be accompanied by increased water pressures within the glacier and increased sliding rates.

The glaciers that remain on Mount St. Helens are not expected to melt away in the near future unless subjected to unusual volcanic heating. Therefore, the glacial ice and snowfields retain an undetermined potential for generating mudflows or other hazards for the foreseeable future. Similar but more disastrous effects from volcanic eruptions are possible from many other volcanoes in the Cascade Range that harbor far larger masses of ice, such as Mounts Rainier, Hood, Baker, and Shasta.

SUMMARY

The eruptions of Mount St. Helens during 1980 have dramatically changed the areal extent, thickness, volume, mass balance, and velocity patterns of most of the glaciers on the volcano. The glaciers contributed about 0.1 km^3 of glacial snow and ice to the lubrication of the May 18 debris avalanche and mudflows. Ice and snowmelt also contributed to other mudflows that radiated outward from the volcano on May 18. Later eruptions had less effect on the glaciers that remained. All the remaining glaciers have been insulated to some extent by blankets of volcanic ash, bombs, or mudflow debris; some of the glaciers were insulated from any major melt of the previous winter snow. The overall mass balances of the glaciers are expected to be negative in the future due to the removal of the summit region, which was the source of snow transported to lower areas by avalanching or wind action. Except for Dryer and Swift Glaciers and the numerous small snowfields on the southeast to southwest portions of the volcano, all the glaciers were somewhat thinned and melted by hot ash flows that moved over their surfaces during the May 18 eruption. Most of the melting, however, affected only the seasonal snow and firn that overlie the glacier ice.

Flow response of the beheaded Shoestring Glacier to the eruption of May 18 was an immediate and continuous deceleration throughout the summer, markedly different from the velocity trend measured during the previous summer. Swift Glacier, which was not beheaded to any significant degree, did not experience such a dramatic change in ice velocities. Thinning of Shoestring Glacier might explain some of the reduction in glacier velocities but does not account for the gradual deceleration. Removal of the upper area of Shoestring Glacier could have caused or contributed to the initial deceleration of the ice, but a change in the water-pressure regime within and under the glacier is needed to explain the gradual slowdown throughout the 1980 summer. The effects of the transmission of longitudinal stress along the length of a glacier and changes in subglacial water pressure are important but relatively unknown characteristics of glaciers on Mount St. Helens. The cause of the progressive decrease in velocity of Shoestring Glacier and its implications for other glaciers on Mount St. Helens will not be fully understood until it is seen how the glaciers continue to respond to effects of the May 18 eruption during the coming years.

Results from investigation of the glaciers on Mount St. Helens will not only provide important and interesting insights into the sliding and transient-flow dynamics of glaciers lying over volcanic terrain but will also be of great assistance in evaluating changes that may occur on other potentially active ice-mantled volcanoes.

SELECTED REFERENCES

Budd, W. F., 1968, The longitudinal velocity profile of large ice masses: Commission of Snow and Ice, Reports and Discussions, General Assembly of Bern, Sept./Oct. 1967, International Association of Scientific Hydrology Publication No. 79, p. 58–77.

Gorshkov, G. S., 1959, Gigantic eruption of the volcano Bezymianny: Bulletin Volcanologique, v. 20, p. 77–109.

Hodge, S. M., 1974, Variations in the sliding of a temperate glacier: Journal of Glaciology, v. 13, no. 69, p. 349–369.

Iken, A., 1973, Schwankungen der Oberflächengeschwindigkeit des White Glacier, Axel Heiberg Island: Zeitschrift für Gletscherkunde u. Glazialgeol., v. 9, p. 207–219.

Kamb, B., 1970, Sliding motion of glaciers: theory and observation: Review of Geophysics and Space Physics, v. 8, no. 4, p. 673–728.

Kamb, B., Engelhardt, H., Harrison, W. D., and Raymond, C. F., 1980, Waves of accelerated motion in a glacier approaching surge: A.G.W. Fall Meeting Program, 1980, p. 66.

Muller, E. H., and Coulter, H. W., 1957a, Incipient glacier development within Katmai caldera, Alaska: Journal of Glaciology, v. 3, no. 21, p. 13–17.

_____1957b, The Knife Creek Glaciers of Katmai National Monument, Alaska: Journal of Glaciology, v. 3, no. 22, p. 116–122.

Nye, J. F., 1963, On the theory of the advance and retreat of glaciers: Geophysical Journal of the Royal Astronomical Society, v. 7, no. 4, p. 431–456.

U.S. Forest Service, 1973, Mount St. Helens and Spirit Lake: U.S. Forest Service map, scale 1:62,500.

U.S. Geological Survey, U.S. Forest Service, and Washington State Department of Natural Resources, 1980, Mount St. Helens and vicinity, Washington—Oregon: U.S. Geological Survey map, scale 1:100,000.

Weaver, C. S., and Malone, S. D., 1979, Seismic evidence for discrete glacier motion at the rock-ice interface: Journal of Glaciology, v. 23, no. 89, p. 171–184.

THE 1980 ERUPTIONS OF MOUNT ST. HELENS, WASHINGTON

EFFECT OF ASH THICKNESS ON SNOW ABLATION

By CAROLYN L. DRIEDGER

ABSTRACT

Eruptions of Mount St. Helens have deposited ash over snow-covered ground in several northwestern States. To determine the effect of ash on the snow ablation rate, surface lowering was measured on plots of ash of different thickness and compared with the ablation of nearby, artificially cleared clean snow. Ash of a thickness greater than 24 mm deters ablation, whereas lesser thicknesses aid ablation. Maximum enhancement of ablation occurs where ash is 3 mm thick. This is, conservatively, an increase of 90 percent over ash-free conditions.

INTRODUCTION

Thickness of ash deposited from the May 18, 1980, eruption of Mount St. Helens ranged from a trace to several centimeters over snow-covered ground in several northwestern States, and to many meters on the mountain. It has long been known that the darkening of a snow surface will change its ablation rate. Because much of the water supply of the Pacific Northwest originates as snow, Federal and local agencies place great emphasis on prediction of the annual volume of snowmelt runoff, and the processes governing its release.

The purpose of this study was to establish the relationship between ash thickness and snowpack ablation, which in turn would aid in understanding the impact of future volcanic ash eruptions on snowmelt runoff, flood probability, water supply, and hydroelectric power production. Although no previous study has been made to determine the effect of different ash thicknesses on snow ablation, considerable work has been done to determine the effect of surface debris on ablation, using sand (M. Yoshida and K. Higuchi, written commun. to M. F. Meier, U.S. Geological Survey, 1980), coal dust (Bazhev, 1975), and morainal material (Fujii, 1977; Loomis, 1971), for example.

Fujii (1977) found, on the Khumbu Glacier of Mount Everest in Nepal, that supraglacial debris causes greatest enhancement of snow ablation at a thickness of 5 mm, whereas ablation was deterred at thicknesses greater than 15 mm. Higuchi and Nagoshi (1977) found, in the Tateyama Mountains of Japan, that the maximum increase in summer snow ablation due to sand cover also occurred where the sand was 5 mm thick. Sand became a deterrent to ablation at a thickness of 20 mm.

In the present study, emphasis was placed on examining ash of relatively small thickness, because thin ash deposits are more likely to occur over large areas. Furthermore, the previous studies of ablation where sand and morainal material covered ice or snow suggest that thin ash (5–15 mm) may create a greater hazard of rapid runoff than will ash of greater thickness. All ash plots shared the same meteorological environment, and no attempt was made to relate these results to snow roughness, to slope, or to meteorological conditions.

ACKNOWLEDGMENTS

The author wishes to express gratitude to Dr. Steven M. Hodge, Robert M. Krimmel, and Dee Molenaar for their valuable discussion and comments.

PROCEDURES

Initial measurements of snow-surface lowering[1] were made in naturally ash-covered areas near Mount St. Helens. From May through July 1980, the surface lowering of naturally ash-covered snow was compared to that of a nearby, artificially cleared snow plot. Surface lowering was measured relative to about 20 points marked on a nylon string suspended between two wooden stakes. However, owing to difficulties involved with maintaining controls using this method of comparison, establishment of artificial ash-covered plots in an ash-free environment was deemed to be more feasible.

In August 1980, ash was collected from near Takhlakh Lake, about 50 km east-northeast of Mount St. Helens, and was taken to South Cascade Glacier, 250 km north of Mount St. Helens, near Darrington, in the northern Cascade Range of Washington. Ash plots were established end to end in two parallel rows; the plots were 1 m apart and the rows were 10 m apart. All plots were about 1 by 5 m in size, on an approximately north-facing slope of 2.3°.

[1]Surface lowering is used to describe these direct measurements. Although ablation best describes the processes by which snow and ice are lost from a glacier, it is measured in terms of water equivalency.

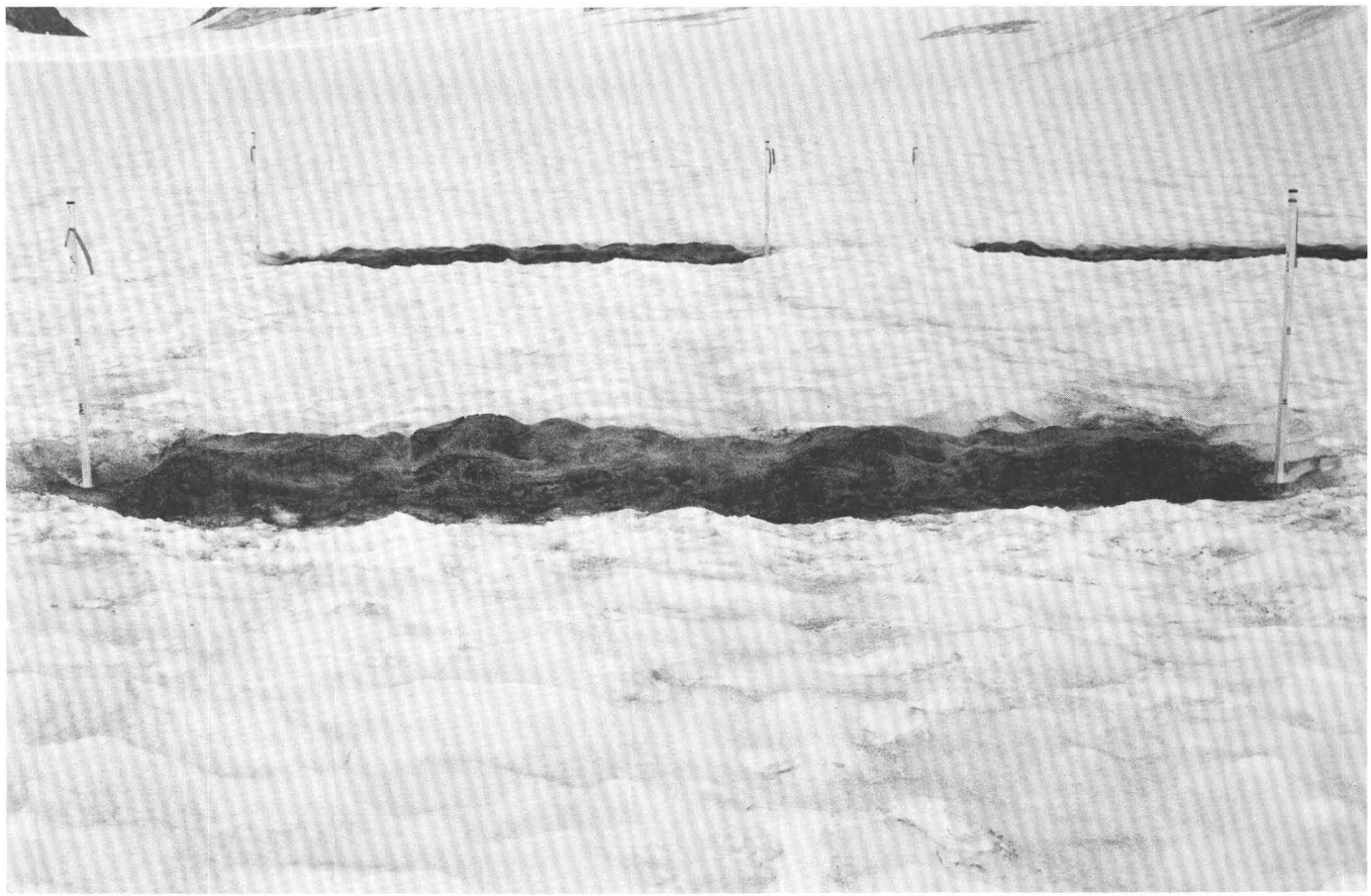

Figure 444.—A 20-mm-thick ash plot 7 days after ash was spread on snow surface, South Cascade Glacier, Wash. Distance between poles is about 5 m; each plot is about 1 m wide.

Six plots were established by spreading ash to thicknesses of 30, 20, 15, 10, 5, and 2 mm (fig. 444). The ash was sprinkled onto the plots through a large-mesh wire screen. A seventh plot was established on which a trace amount (0.75 mm) of ash was sprinkled. An eighth plot was left in its natural state—covered by nonerupted windblown particles and a fine dusting of ash (about 0.25 mm thick) from the August 7 eruption. A ninth plot was cleared of all visible particles. Surface lowering was measured, relative to about 20 points on a nylon string between stakes, once a day between August 18 and August 26.

Snow density was measured at three localities in the vicinity of the plots before ash was spread, to distinguish between the effects of compaction and ablation. A dry-sieve analysis of the ash was completed in the laboratory to determine grain size. A solarimeter was used to measure ash albedo at an ash plot 6 m in diameter on South Cascade Glacier. These measurements were completed so that results can be applied to ash falls of future volcanic eruptions.

DISCUSSION OF OBSERVATIONS

In a preliminary 1-week investigation near Mount St. Helens, ash about 1 mm thick increased surface lowering by 23 percent. At Takhlakh Lake, where ash erupted from the volcano was deposited to a thickness of 26 mm, surface lowering was decreased 18 percent less than under ash-free conditions. These results differ from those of the later study on South Cascade Glacier because of the difficulty in maintaining an ash-free plot, of varying radiation conditions in adjacent study areas, and of the difference in seasonal snow types.

Figure 445 shows the amount of surface lowering of the artificially ash covered plots relative to the ash-free plot in the study at South Cascade Glacier. During the 8-day duration of the study shown on the graph (fig. 445), weather conditions were representative of those in the northern Cascade Range in summer. The sky was partly cloudy and there were intermittent rain showers. Maximum enhancement of ablation occurred on the plots with 2- and 5-mm ash thickness. Ash deterred ablation at depths greater than about 24 mm and aided ablation at lesser depths.

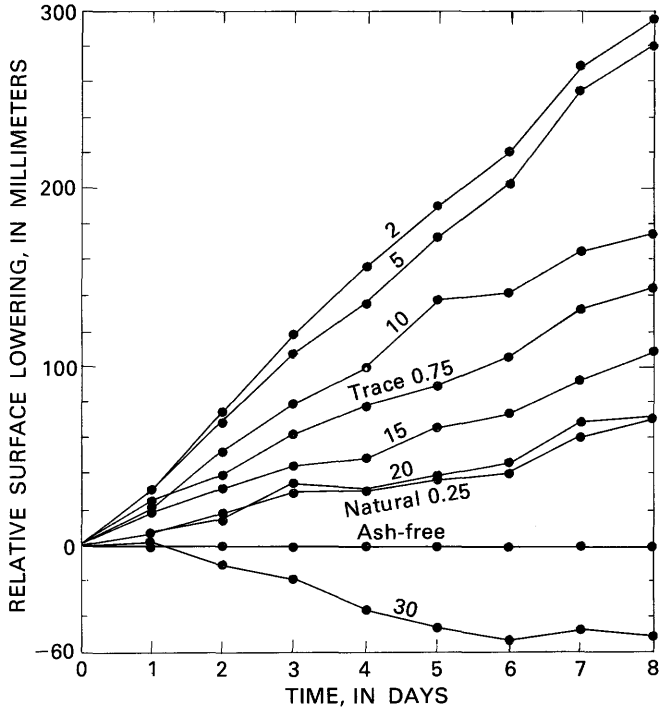

Figure 445.—Amount of surface lowering at nine plots on summer snow in August 1980, at South Cascade Glacier, Wash. One plot was ash free. Thickness of ash on other plots is shown in millimeters (mm). Ash was sprinkled on seven plots to thickness indicated. Natural represents plot with original thickness of ash; no ash was added to this plot.

Where deposited in a thickness of 20 mm, ash had the same effect on snow ablation as did the natural particle covering. Estimated measurement error, on the order of 8 mm, is within the dots on the graph. Anomalies on the graph may be due to the settling of stakes, to rain, to local redistribution of ash as a result of changes in roughness, and to human errors in measuring.

Figure 446 shows the relationship between ash thickness and the difference in ablation rate relative to ash-free conditions, determined by making a least-squares fit to figure 445. Maximum enhancement of ablation is estimated to occur when ash is about 3 mm thick; conservatively, an increase of at least 90 percent over ash-free conditions. These conclusions are consistent with observations made at Trident Volcano in Alaska by Muller and Coulter (1957) in 1953, indicating that loosely compacted ash at a thickness of "somewhat less than one inch" is sufficient to retard melting of

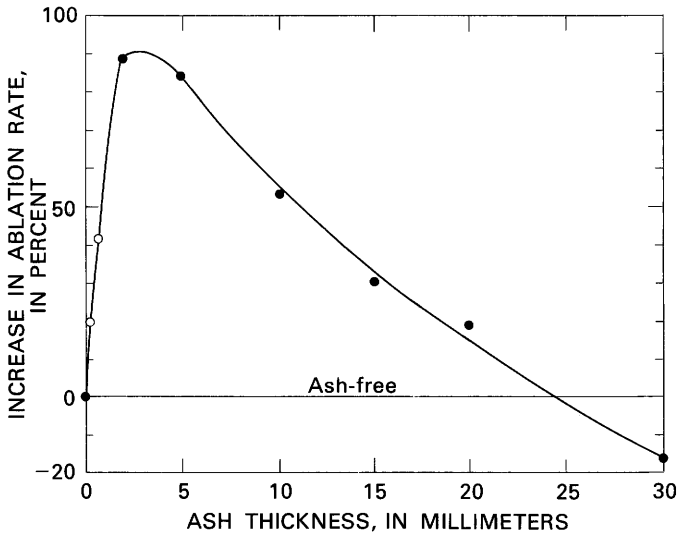

Figure 446.—Change in ablation rate of different ash thicknesses at plots on South Cascade Glacier, Wash., August 1980. An analysis of ash thickness between 2 and 5 mm may determine that the curve peak is higher than indicated. Solid circles indicate measured ash thickness; open circles indicate estimated ash thickness.

underlying snow (Muller and Coulter, 1957, p. 120).

This phenomenon is a balance between increased absorption of shortwave radiation, due to decreased albedo, and conduction of heat through the ash to melt the underlying snow. In ash thicker than 24 mm, conduction of heat becomes so slow that it more than offsets the increased temperature caused by decreased albedo. Ash layers less than about 24 mm thick allow the conduction of heat through the ash to increase the ablation rate.

Dry-sieve analysis established that 91 percent of the ash particles were between 0.25 and 1.0 mm in diameter. Fifty-five percent of the total sample were greater than 0.5 mm in diameter. When deposited, the bulk ash absorbed moisture immediately. The albedo of this wet ash was about 0.16. The density of the snow was 0.5 g/cm^3 (grams per cubic centimeter) throughout the study.

CONCLUSIONS

Maximum enhancement of ablation, conservatively 90 percent over ash-free conditions, is estimated to occur when ash is 3 mm thick, and is due to a lower albedo that allows greater absorption of heat. Ash deters ablation at thicknesses greater than 24 mm. These effects will have an impact on the rate of snowmelt runoff and, therefore, water-dependent facilities. Continued work is planned to lead to a better understanding of snowpack ablation due to the effects of different snow surfaces, ash sizes, slopes, and meteorological conditions.

REFERENCES CITED

Bazhev, A. B., 1975, Artificial augmentation of snow melting in a firn basin of a mountain glacier with the aim of increasing runoff, *in* Snow and ice, Proceedings of the Moscow symposium, August 1971: International Association of Hydrological Sciences Publication 104, p. 211–218.

Fujii, Y., 1977, Field experiment on glacier ablation under a layer of debris cover: Journal of the Japanese Society of Snow and Ice, 39, Special Issue, p. 20–21.

Higuchi, K., and Nagoshi, A., 1977, Effect of particulate matter in surface snow layers on the albedo of perennial snow patches,*in* Isotopes and impurities in snow and ice, Proceedings of the Grenoble symposium, August/September 1975: International Association of Hydrological Sciences Publication 118, p. 95–97.

Loomis, S. R., 1971, Morphology and ablation processes on glacier ice, Ice-Field Range Research Project—Scientific Results 2: American Geographical Society and Arctic Institute of North America, p. 27–31.

Muller, E. H., and Coulter, H. W., 1957, The Knife Creek Glaciers of Katmai National Monument, Alaska: Journal of Glaciology, v. 3, no. 22, p. 116–122.

THE 1980 ERUPTIONS OF MOUNT ST. HELENS, WASHINGTON

ASH-FALL EFFECTS ON THE CHEMISTRY OF WHEAT AND THE RITZVILLE SOIL SERIES, EASTERN WASHINGTON

By L. P. GOUGH, R. C. SEVERSON, F. E. LICHTE, J. L. PEARD, M. L. TUTTLE, C. S. E. PAPP, T. F. HARMS, *and* K. S. SMITH

ABSTRACT

Four weeks after the May 18, 1980, eruption of Mount St. Helens, samples of the following materials were collected along a 75-km transect south of Ritzville, Wash.: (1) soft, white club wheat—immature grain heads and stems and leaves; (2) soils—Ap1-, Ap2-, and B-horizons; (3) volcanic ash; and (4) a mixture of ash and the Ap horizons. In addition, mature whole grains were sampled at the same sites about 8 weeks following the eruption. Sampling sites were edaphically, lithologically, and vegetationally similar but differed in the depth of their ash deposits, which ranged from 40 mm to less than 0.1 mm.

Ash and soil chloride levels and specific conductances indicate that precipitation, received by the sites between the time of ash deposition and the time of sampling, percolated to a depth of about 25 cm. Leaching of chloride and sulfate from the ash into the soil was measured. DTPA-NH_4CO_3 (diethylene triamine pantaacetic acid-ammonium bicarbonate) extractable levels of cadmium, iron, manganese, nickel, and zinc were much lower in the ash than in the Ap soil horizons directly below the ash. These differences are due to naturally higher levels in soil and not to ash leaching. Exchangeable calcium, magnesium, and potassium concentrations are lower, and sodium is higher, in ash than in soil Ap horizons. Leaching of fresh ash had little effect on the exchange status of soils. At sites having significant ash accumulation, the pH of the ash was higher than that of soil horizons directly below the ash; however, at the site where less than 0.1 mm of ash was measured, soil pH was higher than the pH of either soil or ash at sites having more ash. The Ap1- and Ap2- horizons of soil had the lowest pH where the ash fall was greatest. The pH of these horizons (especially the Ap2) increased as ash-fall amounts decreased.

The concentrations of 25 elements in plant material were examined for trends related to ash deposition. Elevated sulfur levels in mature grain and in immature grain heads were noted in samples from sites having 20 mm or more of ash. Cadmium in wheat was not found to be related to the ash fall; however, cadmium in the whole grain occurred in greater concentrations (2.9 ppm) than either in the grain heads (0.5 ppm) or in the stems and leaves (0.6 ppm). The elevated levels of many DTPA-extractable elements measured in soils, especially at the sites of greatest ash fall, may alter the levels of these metals in subsequent wheat crops; therefore, analyses of wheat element content should be repeated for at least another growing season.

INTRODUCTION

Varying amounts of ash were deposited over the Palouse region of east-central Washington from the May 18, 1980, eruption of Mount St. Helens. A large ash fall occurred at Ritzville, Wash., for reasons discussed elsewhere in this volume. Figure 447 shows isopleths of uncompacted-ash thickness in the area surrounding Ritzville (Sarna-Wojcicki and others, 1980). The effects of the ash on the soils and wheat quality are largely unknown. The grayish-white surface of the ash should have had the immediate effect

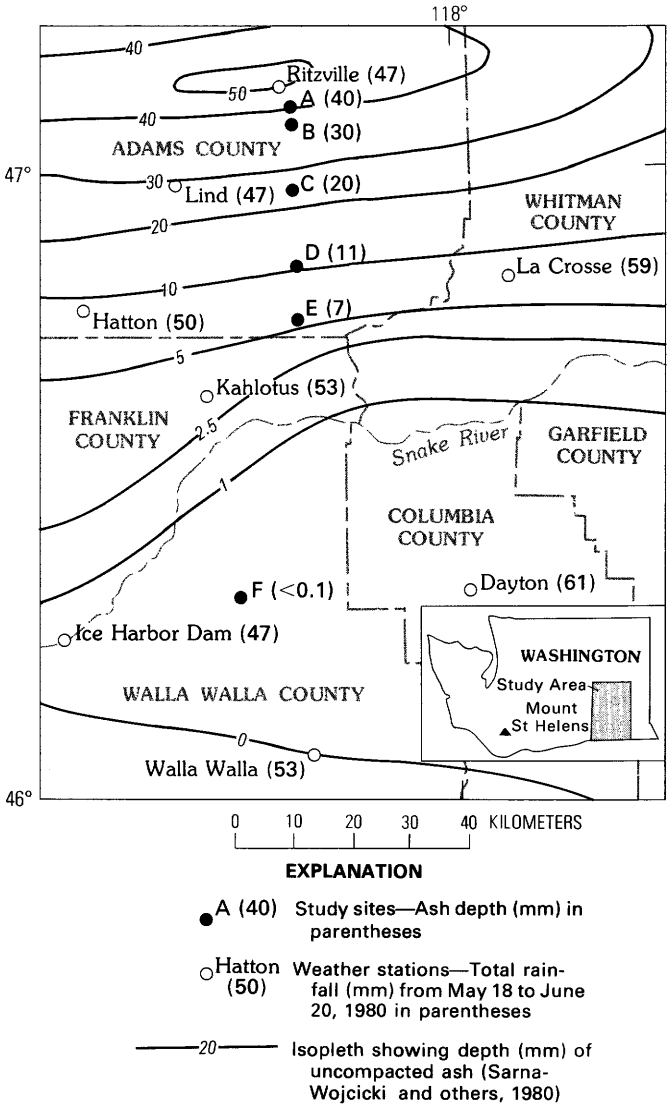

Figure 447.—Index map of eastern Washington showing sample-site localities south of Ritzville and volcanic-ash deposition isopleths.

of increasing the albedo of the soil and reducing soil temperatures from those normally attained during the summer. The lower soil temperatures, the increased moisture regime, and the chemical character of the ash may have temporarily affected the rates of chemical, physical, and microbiological processes in the soil and thereby have altered soil element availability and plant element uptake.

ACKNOWLEDGMENTS

The authors acknowledge the support of the wheat farmers whose fields we sampled in Adams and Walla Walla Counties and the cooperation of Mr. B. Heineman of the Washington Association of Wheat Growers, Ritzville. The Grain Inspection Branch, Grain Division of the Agricultural Marketing Service, U.S. Department of Agriculture, kindly allowed us the use of their dockage tester for cleaning chaff from the whole-grain wheat samples. Samples of wheat and soil were prepared and analyzed in the Denver laboratories of the U.S. Geological Survey by the authors and the following individuals: J. G. Crock, D. B. Hatfield, and G. O. Riddle.

METHODS

SAMPLE-SITE SELECTION

The Ritzville soil series is agriculturally valuable and is widely distributed in Adams and Walla Walla Counties. These counties are in the Palouse hills and grasslands of the Columbia Plateaus province where the vegetation is composed of the *Agropyron spicatum-Festuca idahoensis* association (Franklin and Dyrness, 1969); however, 90 percent or more of the land area is now under cultivation. Sites were selected along a 75-km transect from Ritzville south toward Walla Walla, Wash. (fig. 447). At all sites the soil series and crop were the same, but the volcanic ash thickness varied.

SAMPLING AND ANALYSIS OF SOILS

The Ritzville soil series is classified as a Calciorthidic Haploxeroll. It is developed in deep loess. At all sampling sites in this study, the Ap-horizon was from 18 to 20 cm thick, and the B-horizon was 70 to 80 cm thick. Carbonates (used as the indicator for the B-C horizon boundary) were first found at depths of 90 to 100 cm. At locations A, C, D, and F (fig. 447), samples were collected of the ash layer, the upper half of the Ap-horizon (Ap1), the lower half of the Ap-horizon (Ap2), and the upper 30 cm of the B-horizon. In addition, a sample of the ash and the Ap-horizon from these locations were mixed in proportion to their thickness in order to simulate effects of plowing. At locations B and E (fig. 447), the soil was similarly sampled; however, no samples of the B-horizon were collected. At locations A, C, D, and F, two sites separated by a distance of about 50 m were sampled; at locations B and E only a single site was sampled.

All soil and ash samples were dried in the laboratory at ambient temperature and disaggregated to pass a 2-mm sieve. For all samples, 100 percent of the material passed the sieve. Particle-size distribution was determined by the hydrometer method (Day, 1965; Grigal, 1974). Organic-matter content was determined by combustion at 550°C (Dean, 1974). Exchangeable cations, and cations and anions in a saturation extract, were determined by standard methods with minor modifications as described in Crock and Severson (1980). Concentrations of trace metals were determined in a DTPA-NH_4HCO_3 (diethylene triamine pentaacetic acid-ammonium bicarbonate) extract (Soltanpour and Schwab, 1977), using the techniques described for DTPA in Crock and Severson (1980); however, the determinations were made by ICP-OES (inductively coupled argon plasma-optical emission spectroscopy).

SAMPLING AND ANALYSIS OF WHEAT

The agriculture of southeastern Washington is dominated by the production of soft, white winter wheat (Leonard and Martin, 1963). Although the preference for certain wheat varieties changes, for the past several years most of the fields south of Ritzville in Adams County have been planted with cultivars of soft, white club wheat (*Triticum compactum*). In 1978, 51 percent of the soft, white wheat production of Adams County was composed of white club varieties, and, in turn, 98 percent of the white club wheat was composed of the cultivars Moro and Paha (Pacific Northwest Crop Improvement Association, 1979).

Between June 16 and 20, 1980 (one month after the major Mount St. Helens eruption), we collected four samples of club wheat grain heads (tops), and wheat stems (culms) and leaves, at each of locations A, C, D, and F (fig. 447). These four samples were composed of replicates collected at two sites approximately 50 m apart within the same field (location). The analytical results of the replicates were subsequently averaged to give two data points per location. At locations B and E, only one sample of each of these materials was collected; therefore, the data from these locations do not represent replicate averages. In all cases, the material for each sample consisted of a composite of numerous individual plants collected over about a 5-m^2 area. Information from farmers indicates that our samples are composed mostly of the cultivar Paha.

The levels of both major and minor (trace) essential elements vary in a given plant tissue as it matures; therefore, we took our samples over as brief a period of time as possible. Nevertheless, the stage of maturity of the wheat increased from north to south along the transect. In general, the more northerly sites were in the late-bloom stage, whereas further south the material was mostly in the milk stage.

Because we were also interested in the possible alteration of the element composition of the mature whole grain (kernel or caryopsis), a second sampling of the transect was conducted on July 14 to 16. In general, the wheat tops at this time were dry and the kernels mature (some samples from the more northerly sites were still in the dough stage). The general harvest by area farmers did not begin until the fourth week of July.

Field inspection of the grain heads collected in June showed the possible presence of volcanic ash and soil dust lodged within the flower parts (glumes, lemmas, and paleas). Figures 448 and 449 are scanning electron photomicrographs[1] of part of the rachis of an unwashed grain head collected at location A-1. The bristles at the base of the lemmas in figure 448 clearly show a microtopography conducive to the entrapment of airborne particles. Figure 449 shows a cluster of several volcanic-ash particles (all less than 20 μm in size) among the lemma bristles.

Because of the obvious presence of contamination, the grain heads were cleaned prior to chemical analysis. The cleaning procedure consisted of submerging the heads in a beaker of tap water and subjecting them to energy from an ultrasonic probe for about 2 min. This procedure was performed three times with changes of tap water, followed by an ultrasonic rinsing in distilled water. The stage of maturity of the heads (late bloom to milk) made this procedure possible—had they been fully mature the kernels would have separated from the heads. The samples of stem and leaf material were judged not to be extensively contaminated and were not cleaned.

The July collections of mature heads were handled in the laboratory as follows: (1) the heads were oven dried at 40°C for 48 hr; (2) the grain was separated

[1]The photomicrographs were taken using a Cambridge Stereoscan 180 scanning electron microscope at an accelerating voltage of 30 kV (kilovolts). The specimens were plated with a gold layer estimated to be several hundred angstroms thick.

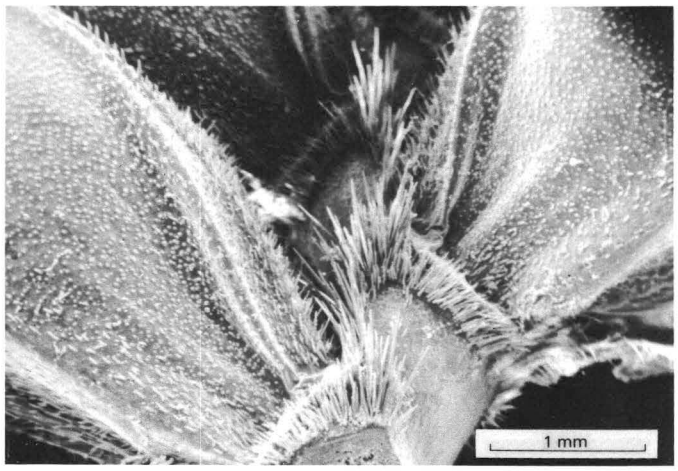

Figure 448.—Scanning electron photomicrograph of the bristles on part of an unwashed wheat-head rachis, location A-1, eastern Washington.

from the heads by gently grinding the heads in a mortar until most of the kernels had been released; and (3) the chaff was separated from the kernels by passing the samples twice through a dockage tester.

The wheat grain heads and stems and leaves were dried in an oven at 35°C and then ground to pass a 1.3-mm screen. The whole-grain samples were also ground. A weighed portion of the ground material was ashed in a muffle furnace in which the heat was increased 50°C/hr to a temperature of 550°C; this temperature was held for 14 hr. The ashed material was then reweighed to determine the ash yield.

The methods of analysis used for the elements in plant ash were as follows: atomic-absorption spectroscopy for cadmium, calcium, cobalt, copper, magnesium, potassium, sodium, and zinc; colorimetry for phosphorus; fluorimetry for uranium; and ICP-OES for aluminum, barium, chromium, iron, lanthanum, lead, lithium, manganese, nickel, strontium, titanium, vanadium, and yttrium. The analytical methods used for the volatile elements in the dry plant material were: flameless atomic-absorption spectroscopy for arsenic and mercury; selective ion electrode for fluorine; fluorometry for selenium; and turbidimetry for total sulfur. Voucher specimens of *T. compactiom* are stored in the herbarium of the U.S. Geological Survey, Denver.

STATISTICAL METHODS

Approximately 10 percent of the wheat, soil, and ash samples were split and analyzed in duplicate to provide a means of segregating natural sample variation from analytical variation. The duplicate samples, plus all other samples, were analyzed in a sequence that was randomized with respect to geographic location.

Analysis-of-variance was used to estimate the natural and analytical variation components. Large analytical variation (relative to natural variation) will obscure the natural variation, and any interpretations must be cautiously made. Natural variation in the element content of wheat is expressed as three components: among six locations, between paired sites within a location, and between paired samples within sites. Natural variation for soils and ash is expressed as two components: among six locations for samples of a given soil horizon or ash, and between paired sample sites at a location. If variation among locations and between paired sites is not statistically significant for a given parameter, then uniformity in the materials sampled is established. If variation among locations and between sites is statistically significant, then this significance may be due either to nonuniformity in wheat and soils or to the differing effects of the ash-fall amounts. The coefficient of variation was also computed, based on total variation, in order to provide a means of making comparisons between soil horizons and ash, and among soil constituents.

Analyses for elements present in trace quantities result in some values being reported as "less than" or "not detected." Because statistical tests require

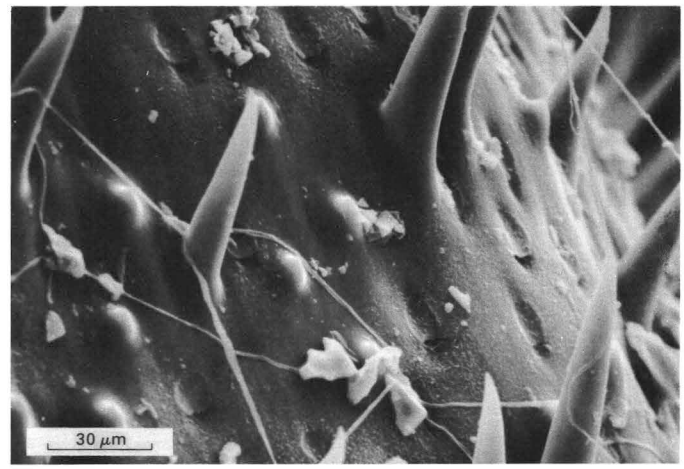

Figure 449.—Scanning electron photomicrograph of volcanic ash on the unwashed surface of a wheat-head floret, location A-1, eastern Washington.

completely numeric data sets, these "less than" values were replaced by small arbitrary values equal to 0.7 times the LLD (lower limit of determination). Such a replacement is justified because the small number of replaced values (values labeled as "less than" in tables 104–107, 109, and 110) would not materially alter the interpretations of the statistical tests. Concentrations of arsenic, cobalt, lithium, and mercury are not given for plants because more than 50 percent of the values reported by the analyst were below the LLD (0.05 ppm, 1.0 ppm, 4.0 ppm, and 0.01 ppm, respectively).

RESULTS AND DISCUSSION

ANALYTICAL VARIATION

Analytical variation estimates the cumulative errors inherent in the procedural steps necessary to provide a determination of a constituent's concentration in a sample. These steps include sample preparation, extraction (soils and ash), instrumental analysis, calculations, and recording of data. A few constituents measured in wheat, ash, and various soil horizons show an excessive "between analyses within samples" component of variation (tables 103 and 109). If this analytical variation is large relative to the natural variation, then interpretations based on natural variation for that constituent must be made with caution. However, where estimates of analytical variation are high, the estimates of total variance are generally small. For many samples, the relatively high analytical variation may represent duplicate analyses differing by only a fraction of a part per million. These small deviations between duplicate determinations are, however, statistically significant where only very small differences were measured between locations or between samples at a location (table 104).

PRECIPITATION AFTER ASH FALL

Between May 18 (when the ash fall occurred) and June 20 (when the sampling was completed), about 50 mm of precipitation was received in the area between Ritzville and Walla Walla, Wash. (U.S. Department of Commerce, 1980a, 1980b). Cumulative amounts of precipitation for this time period are shown at various recording stations in figure 447. The precipitation occurred mainly on May 22 (6 mm), May 26 to 28 (28 mm), and June 12 to 15 (17 mm). Therefore, all samples of ash had been leached. Lenfesty (1967, table 5) and Harrison and others (1964, table 5) reported that the available water-holding capacity for the Ritzville silt loam soil type is about 0.17 to 0.20 cm/cm. In these reports, available water-holding capacity is defined as the amount of water, in excess of the wilting coefficient, held in soil against the force of gravity. Using a simplistic approach, and ignoring antecedent moisture, evaporation, and transpiration, 50 mm of precipitation should percolate at least 25 cm into the Ritzville soil.

TRANSECT UNIFORMITY IN SOILS

Concentrations of DTPA-extractable metals (table 104), exchangeable cations and pH (table 105), constituents measured in a water-saturation extract (table 106), and particle size and organic matter (table 107) in ash and soil, are given for each transect location that was sampled. Particle-size data indicate that these materials, including ash, are uniformly of a silt loam texture (table 107). The sand, silt, and clay contents are uniform with depth at each sampling location; however, sand content decreases and silt content increases slightly with distance (both north and south) from the Snake River (fig. 447 and table 107). This gradation probably reflects patterns of loess deposition rather than physical or chemical weathering of the soils during their formation. Organic-matter content of the various horizons is also very uniform with depth in each soil, and among sampling locations (table 107). Therefore, these data suggest uniformity in soils with depth and uniformity from site to site for both particle size (reflecting soil parent material) and organic-matter accumulations (reflecting soil-formation processes).

Data for variance analyses of chemical and physical properties of ash and soil among sampling locations and between sampling sites within each location (table 103) does not give as clear an indication of uniformity as does the particle-size and organic-matter data. Significant differences in silt and sand content among locations are shown for all horizons sampled (table 103). However, the observed range in the data (table 107) and the coefficients of variation (table 103) for sand and silt can be considered small

Table 103.—Variance analysis of constituents measured in samples of Mount St. Helens ash and various horizons of the Ritzville soil series, eastern Washington

[Leaders (---), not determined; *, variance component significantly different from zero at the 0.05 probability level]

Constituent and sample description	Total variance	Percentage of total variance			Coefficient of variation
		Between locations	Between samples within locations	Between analyses within samples	
BASED ON DTPA EXTRACT					
Cd:					
Ash----------	0.0283	2.5	0	97.5	312
Apl-horizon---	.000548	38.4	0	61.6	34
B-horizon-----	.000110	0	0	100	36
Cu:					
Ash----------	.0237	5.1	73.9	21.0	6
Apl-horizon---	.0319	0	*88.2	11.8	9
B-horizon-----	.0841	*45.7	37.9	16.4	13
Fe:					
Ash----------	3.39	45.9	44.2	9.9	12
Apl-horizon---	141	*75.4	12.6	12.0	47
B-horizon-----	23.7	27.5	*68.2	4.3	35
Mn:					
Ash----------	.183	*84.1	13.2	2.7	16
Apl-horizon---	22.0	65.0	*35.0	0	53
B-horizon-----	1.60	36.6	*60.2	3.2	57
Ni:					
Ash----------	.0164	*31.3	0	68.7	72
Apl-horizon---	.0532	73.0	*24.7	2.3	32
B-horizon-----	.0321	41.5	0	58.5	24
Zn:					
Ash----------	.00522	20.1	47.9	32.0	23
Apl-horizon---	.0697	*87.5	5.4	7.1	26
B-horizon-----	.0156	0	*92.0	8.0	44
BASED ON EXCHANGEABLE CATIONS					
Ca:					
Ash----------	0.0596	*84.6	12.6	2.8	15
Apl-horizon---	2.25	*77.3	*22.5	.2	22
B-horizon-----	1.95	0	74.2	25.8	17
Mg:					
Ash----------	.00384	13.2	0	86.8	23
Apl-horizon---	.0925	0	*97.3	2.7	129
B-horizon-----	.312	*72.1	1.8	26.1	165
K:					
Ash----------	.0213	21.8	31.3	46.9	17
Apl-horizon---	.0544	0	65.5	34.5	11
B-horizon-----	.101	30.3	4.3	65.4	19
Na:					
Ash----------	.0950	68.4	31.6	0	36
Apl-horizon---	.0452	*53.0	36.0	11.0	44
B-horizon-----	.130	4.1	39.0	56.9	19
BASED ON WATER-SATURATION EXTRACT					
SC[1]:					
Ash----------	0.211	72.8	*27.1	0.1	34
Apl-horizon---	.0881	*71.7	1.5	26.8	42
B-horizon-----	.0121	.1	0	99.9	46
Ca:					
Ash----------	8.82	63.5	*33.1	3.4	41
Apl-horizon---	.303	2.6	*92.1	5.3	24
B-horizon-----	.102	*49.7	33.1	17.2	32
Mg:					
Ash----------	.370	*56.7	25.3	18.0	39
Apl-horizon---	.210	0	*92.9	7.1	33
B-horizon-----	.0391	45.7	0	54.3	26
K:					
Ash----------	.144	5.3	0	94.7	117
Apl-horizon---	.242	20.4	12.4	67.2	33
B-horizon-----	.131	22.5	0	77.5	66
Na:					
Ash----------	4.67	*89.9	6.9	3.2	47
Apl-horizon---	1.02	*53.8	0	46.2	89
B-horizon-----	.132	41.2	*55.0	1.8	82

Table 103.—Variance analysis of constituents measured in samples of Mount St. Helens ash and various horizons of the Ritzville soil series, eastern Washington—Continued

Constituent and sample description	Total variance	Percentage of total variance: Between locations	Between samples within locations	Between analyses within samples	Coefficient of variation
BASED ON WATER-SATURATION EXTRACT—Continued					
Cl:					
Ash----------	6.12	*93.2	*6.4	.4	78
Apl-horizon---	1.34	30.6	*68.4	1.0	66
B-horizon-----	.0569	0	58.2	41.8	38
SO_4:					
Ash----------	41.5	0	*93.6	6.4	55
Apl-horizon---	3.39	*90.5	6.9	2.6	58
B-horizon-----	.0494	0	67.1	32.9	42
BASED ON COMBUSTION AT 550° C					
OM[2]:					
Ash----------	0.00290	50.9	49.1	---	12
Apl-horizon---	.0599	0	100	---	8
B-horizon-----	.126	78.0	22.0	---	12
BASED ON SELECTIVE-ION ELECTRODE					
pH:					
Ash----------	0.0261	10.6	76.7	12.7	2
Apl-horizon---	.673	*90.2	*9.5	.3	13
B-horizon-----	.0678	17.0	*79.3	3.7	4
BASED ON PHYSICAL PROPERTIES					
Sand:					
Ash----------	13.9	*98.2	1.8	---	18
Apl-horizon---	52.3	*96.9	3.1	---	38
B-horizon-----	35.8	*96.1	3.9	---	33
Silt:					
Ash----------	4.78	*73.2	12.8	---	3
Apl-horizon---	30.2	*96.4	6.6	---	9
B-horizon-----	41.5	*85.6	14.4	---	10
Clay:					
Ash----------	3.64	55.4	44.6	---	12
Apl-horizon---	6.89	32.3	67.7	---	14
B-horizon-----	10.6	*73.6	26.4	---	18

[1]Specific conductance
[2]Organic matter

from location to location and can probably be discounted at the scale of generalization used in this study.

If significant variation among locations and between sites for many other constituents in table 103 cannot be explained by other factors, uniformity among locations and between sites cannot be confirmed, and the influence of varying amounts of ash fall on soil chemistry cannot be assessed. We feel, however, that these significant variation components may reflect factors other than nonuniformity of soils between locations, and may be explained in two ways. First, only a few samples were split and analyzed in duplicate. If a single analysis of an unsplit sample is in error, its variation will not be reflected as analytical error (between analyses within samples level in table 103), but will be included at some other level of the sampling design (between locations or between samples). Also, for many constituents showing significant variation, the total variance and the coefficient of variability are very small, indicating uniformity rather than nonuniformity of soils among locations or between sites at a location. Second, the samples of ash and soil were collected during early to mid-June, or about 4 weeks after the ash fall had occurred. The variability among locations may reflect actual differences in soil chemistry due to the leaching of the varying amounts of ash at each location.

Table 104.—Concentrations of metals in DTPA-NH_4HCO_3 extracts of Mount St. Helens ash and various horizons of the Ritzville soil series, eastern Washington

[Values in parts per million; ---, not data available; <, less than]

Sites at locations (fig. 1)----- Sample description	A-1	A-2	B	C-1	C-2	D-1	D-2	E	F-1	F-2
					CADMIUM					
Ash----------	<0.02	<0.02	<0.02	0.03	<0.02	0.28	0.02	<0.02	---	---
Ash + Ap-horizon----------	.08	.08	.06	.08	.07	.13	.07	.05	---	---
Ap1-horizon----------	.09	.09	[1].07	.08	.08	.05	.06	[1].07	0.07	0.04
Ap2-horizon----------	.09	.08	---	.07	.08	.06	.07	---	.02	.04
B-horizon----------	.03	.03	---	.03	.04	.03	<.02	---	.04	.03
					COPPER					
Ash----------	2.8	2.5	2.6	2.5	2.7	2.8	2.7	2.9	---	---
Ash + Ap-horizon----------	2.4	2.3	2.1	2.3	2.2	1.9	2.3	1.8	---	---
Ap1-horizon----------	2.2	2.0	[1]2.0	2.2	1.8	1.9	2.0	[1]1.8	1.9	2.1
Ap2-horizon----------	2.2	2.2	---	2.0	2.0	1.9	2.5	---	2.1	2.2
B-horizon----------	2.4	2.5	---	2.3	2.6	1.8	2.2	---	2.4	2.4
					IRON					
Ash----------	17	15	13	13	14	16	18	17	---	---
Ash + Ap-horizon----------	40	32	36	20	25	24	31	26	---	---
Ap1-horizon----------	44	29	[1]34	22	24	28	27	[1]27	8.6	12
Ap2-horizon----------	52	37	---	30	28	33	24	---	16	16
B-horizon----------	11	21	---	18	19	13	16	---	7.0	12
					MANGANESE					
Ash----------	3.2	3.3	3.1	2.3	2.4	2.5	2.8	2.8	---	---
Ash + Ap-horizon----------	16	10	13	7.0	23	8.1	14	9.4	---	---
Ap1-horizon----------	17	9.6	[1]11	6.8	8.6	10	8.2	[1]9.5	2.8	3.1
Ap2-horizon----------	27	11	---	5.3	5.8	8.9	5.0	---	2.7	4.2
B-horizon----------	1.3	2.1	---	1.9	3.8	4.2	2.3	---	1.1	1.4
					NICKEL					
Ash----------	<0.2	<0.2	<0.2	<0.2	<0.2	0.3	0.3	0.2	---	---
Ash + Ap-horizon----------	.9	.8	.7	.7	.7	.8	1.0	.6	---	---
Ap1-horizon----------	1.0	1.0	[1] .9	.7	.8	.7	.8	[1] .6	0.3	0.6
Ap2-horizon----------	1.0	.9	---	.8	.8	.9	1.1	---	.4	.5
B-horizon----------	.8	.9	---	.8	.7	.8	1.0	---	.6	.5
					ZINC					
Ash----------	0.4	0.3	0.3	0.2	0.3	0.3	0.4	0.4	---	---
Ash + Ap-horizon----------	1.1	1.0	1.1	1.1	1.1	.9	.9	1.2	---	---
Ap1-horizon----------	1.1	1.0	[1]1.3	1.3	1.1	.9	.9	[1]1.2	0.6	0.7
Ap2-horizon----------	1.1	.9	---	1.1	1.0	.8	.8	---	.5	.7
B-horizon----------	.2	.5	---	.3	.3	.4	.2	---	.2	.3

[1]Value from a composite sample of the Ap1- and Ap2-horizons.

Table 105.—Exchangeable cations and pH measured on samples of Mount St. Helens ash and various horizons of the Ritzville soil series, eastern Washington

[Values in milliequivalents per 100 g, except pH which is reported in standard units; ---, no data available; <, less than]

Sites at locations (fig. 1)------ Sample description	A-1	A-2	B	C-1	C-2	D-1	D-2	E	F-1	F-2
				CALCIUM						
Ash----------	1.9	1.7	1.6	1.7	1.8	1.4	1.4	1.3	---	---
Ash + Ap-horizon----------	5.6	5.9	5.6	5.6	5.8	6.3	7.3	6.3	---	---
Ap1-horizon----------	5.8	6.6	[1]6.1	6.1	6.5	6.2	7.5	[1]6.3	9.8	8.6
Ap2-horizon----------	5.8	6.3	---	6.2	6.4	5.7	7.9	---	9.2	8.4
B-horizon----------	7.4	7.9	---	8.3	8.5	6.9	10	---	9.7	8.1
				MAGNESIUM						
Ash----------	0.3	0.3	0.3	0.3	0.2	0.3	0.3	0.3	---	---
Ash + Ap-horizon----------	2.0	2.3	2.1	2.1	2.2	2.8	2.4	2.1	---	---
Ap1-horizon----------	2.1	2.7	[1]2.3	2.4	2.5	2.7	2.5	[1]2.1	2.6	2.6
Ap2-horizon----------	2.1	2.5	---	2.4	2.5	2.5	2.7	---	2.5	2.6
B-horizon----------	3.0	3.1	---	3.4	2.8	4.2	4.1	---	3.3	2.9
				POTASSIUM						
Ash----------	1.1	0.8	1.1	0.8	0.8	0.9	0.7	0.8	---	---
Ash + Ap-horizon----------	2.1	2.0	2.7	2.4	2.3	1.8	1.8	1.7	---	---
Ap1-horizon----------	2.1	2.6	[1]2.5	2.4	2.5	2.2	1.9	[1]2.0	2.1	2.3
Ap2-horizon----------	2.0	2.1	---	2.3	2.3	1.2	1.2	---	1.8	2.2
B-horizon----------	1.5	1.5	---	1.8	2.0	1.7	2.2	---	1.3	1.6
				SODIUM						
Ash----------	1.0	1.3	1.3	0.8	0.8	0.5	0.8	0.5	---	---
Ash + Ap-horizon----------	<.3	.5	.5	.5	.5	.3	.5	.3	---	---
Ap1-horizon----------	.9	.5	[1] .3	.5	.5	.5	.5	[1] .3	.3	.3
Ap2-horizon----------	.3	.3	---	.5	.3	.3	<.3	---	.3	.3
B-horizon----------	.6	.3	---	.3	.3	1.2	.3	---	.6	.3
				pH						
Ash----------	7.2	6.8	6.9	6.8	6.9	6.8	6.8	6.7	---	---
Ash + Ap-horizon----------	5.5	5.8	5.6	6.1	5.9	6.0	5.8	5.6	---	---
Ap1-horizon----------	5.3	5.9	[1]5.5	6.1	6.1	6.0	6.0	[1]6.6	7.6	7.2
Ap2-horizon----------	4.9	5.6	---	5.8	5.9	5.7	5.9	---	6.9	6.9
B-horizon----------	7.0	6.4	---	6.8	6.6	6.8	6.6	---	7.2	7.0

[1]Value from a composite sample of the Ap1- and Ap2-horizons.

COMPOSITION OF ASH AND SOIL-ASH MIXTURES

Concentrations of DTPA-extractable metals in ash are relatively uniform from location to location and between sites at any one location (table 104). DTPA-extractable metals from samples of ash from Yakima, Moses Lake, and Spokane, Wash., and Moscow, Idaho (H. F. Mayland, U.S. Department of Agriculture, Kimberly, Idaho, written commun.,

Table 106.—Concentrations of constituents measured in water-saturation extracts of Mount St. Helens ash and various horizons of the Ritzville soil series, eastern Washington

[Values in milliequivalents per liter of extract, except for specific conductance, which is reported as millimhos per centimeter of extract; ---, not determined]

Sites at locations (fig. 1)------ Sample description	A-1	A-2	B	C-1	C-2	D-1	D-2	E	F-1	F-2
					CALCIUM					
Ash----------	11	9.7	10	6.7	7.1	3.1	7.4	4.5	---	---
Ash + Ap-horizon----------	3.7	4.5	2.9	2.5	3.6	1.7	2.2	2.6	---	---
Ap1-horizon----------	2.2	3.4	2.9	2.1	2.9	2.0	1.6	3.2	2.1	2.0
Ap2-horizon----------	3.4	2.9	---	1.7	2.7	2.3	1.8	---	1.5	1.5
B-horizon----------	1.1	.9	---	.8	1.3	.6	.8	---	1.4	1.2
					MAGNESIUM					
Ash----------	2.3	2.1	2.1	1.1	1.2	1.0	1.9	1.2	---	---
Ash + Ap-horizon----------	2.1	3.1	1.8	1.7	2.3	1.3	1.2	1.6	---	---
Ap1-horizon----------	1.3	2.3	1.8	1.4	1.9	1.5	.9	1.8	0.8	1.0
Ap2-horizon----------	1.9	1.9	---	1.1	1.8	1.7	1.0	---	1.0	.9
B-horizon----------	.8	.7	---	.6	.8	.7	.5	---	1.0	1.0
					POTASSIUM					
Ash----------	1.3	0.9	1.1	0.8	1.1	0.9	1.0	1.4	---	---
Ash + Ap-horizon----------	1.7	2.4	2.5	2.0	2.1	1.1	.8	1.6	---	---
Ap1-horizon----------	1.5	2.0	2.2	1.6	1.6	1.8	.8	1.6	0.9	1.1
Ap2-horizon----------	1.4	2.5	---	1.2	1.9	1.6	.8	---	.6	.9
B-horizon----------	.3	.7	---	.7	.9	.8	.6	---	.3	.5
					SODIUM					
Ash----------	6.3	7.8	7.6	3.1	3.0	3.1	3.5	3.4	---	---
Ash + Ap-horizon----------	2.1	.3	1.9	1.7	1.8	1.0	.8	.8	---	---
Ap1-horizon----------	1.9	2.2	.9	1.9	1.6	.6	.8	.5	0.4	0.5
Ap2-horizon----------	.8	.9	---	1.6	.6	.8	.7	---	.4	.6
B-horizon----------	.3	.4	---	.2	.2	1.2	.4	---	.4	.3
					CHLORIDE					
Ash----------	4.9	5.5	7.9	1.8	1.7	1.3	2.7	1.1	---	---
Ash + Ap-horizon----------	3.4	4.6	4.2	3.4	4.0	1.7	1.0	1.9	---	---
Ap1-horizon----------	1.8	4.6	3.9	1.7	2.6	1.4	.8	1.2	0.6	1.2
Ap2-horizon----------	4.6	5.6	---	1.9	5.1	3.9	2.5	---	.5	.8
B-horizon----------	.4	1.0	---	.7	.8	.9	.7	---	.5	.4
					SULFATE					
Ash----------	16	16	19	15	1.6	4.9	13	8.5	---	---
Ash + Ap-horizon----------	5.1	4.9	3.7	4.0	4.6	2.4	3.9	1.9	---	---
Ap1-horizon----------	5.3	5.0	2.2	4.0	5.3	3.5	2.8	1.6	0.8	1.0
Ap2-horizon----------	3.0	1.0	---	1.6	2.1	1.8	1.8	---	.5	.8
B-horizon----------	.5	.7	---	.5	1.0	.8	.4	---	.3	.4
					SPECIFIC CONDUCTANCE					
Ash----------	1.8	1.8	2.0	1.2	1.2	0.8	1.4	1.1	---	---
Ash + Ap-horizon----------	1.2	1.4	1.0	.9	1.0	.5	.6	.7	---	---
Ap1-horizon----------	.9	1.2	1.0	.8	1.0	.5	.5	.8	0.4	0.5
Ap2-horizon----------	.9	.9	---	.5	.9	.7	.5	---	.4	.3
B-horizon----------	.2	.3	---	.2	.3	.4	.2	---	.2	.2

[1]Value from a composite sample of the Ap1- and Ap2-horizons.

Table 107.—Loss on ignition (organic-matter estimate) and particle-size distribution measured on samples of Mount St. Helens ash and various horizons of the Ritzville soil series, eastern Washington

[Values reported as percent in sample; ---, no data available]

Sites at locations (fig. 1)----- Sample description	A-1	A-2	B	C-1	C-2	D-1	D-2	E	F-1	F-2
				LOSS ON IGNITION AT 550°C						
Ash----------	0.5	0.4	0.5	0.4	0.4	0.5	0.5	0.5	---	---
Ash + Ap-horizon----------	2.7	2.9	3.2	3.0	3.1	2.9	2.9	3.3	---	---
Ap1-horizon----------	3.2	3.5	[4]3.2	3.3	3.2	2.9	3.2	[4]3.1	2.9	3.4
Ap2-horizon----------	3.1	3.3	---	2.8	3.2	2.7	3.1	---	2.8	3.1
B-horizon----------	3.2	3.5	---	2.9	2.5	2.7	2.8	---	2.5	2.6
				SAND[1]						
Ash----------	16.2	16.7	16.7	21.6	21.4	23.7	23.7	25.1	---	---
Ash + Ap-horizon----------	13.7	12.5	12.0	17.5	15.2	24.8	23.9	32.5	---	---
Ap1-horizon----------	11.9	12.5	[4]11.5	13.5	14.4	25.6	25.1	[4]27.9	25.9	22.5
Ap2-horizon----------	12.6	11.7	---	15.4	17.2	26.5	25.9	---	21.6	18.8
B-horizon----------	11.3	14.0	---	16.2	14.9	26.5	25.3	---	19.1	19.9
				SILT[2]						
Ash----------	65.8	64.3	65.3	62.4	64.3	62.0	61.9	60.6	---	---
Ash + Ap-horizon----------	67.0	68.2	71.0	61.8	63.5	53.9	58.4	50.2	---	---
Ap1-horizon----------	67.1	69.8	[4]68.1	65.2	67.9	56.7	57.9	[4]54.1	60.4	60.2
Ap2-horizon----------	68.8	69.0	---	65.2	62.1	59.1	53.4	---	61.4	63.2
B-horizon----------	68.0	65.3	---	64.4	69.1	52.8	57.0	---	66.5	67.4
				CLAY[3]						
Ash----------	18.0	19.0	18.0	16.0	14.3	14.3	14.3	14.3	---	---
Ash + Ap-horizon----------	19.3	19.3	17.0	20.7	21.3	21.3	17.7	17.3	---	---
Ap1-horizon----------	21.0	17.7	[4]20.3	21.3	17.7	17.7	17.0	[4]18.0	13.7	17.3
Ap2-horizon----------	18.7	19.3	---	19.3	20.7	14.3	20.7	---	17.0	18.0
B-horizon----------	20.7	20.7	---	19.3	16.0	20.7	17.7	---	14.3	12.7

[1]Greater than 0.05 mm.
[2]From 0.002 to 0.05 mm.
[3]Less than 0.002 mm.
[4]Value from a composite sample of the Ap1- and Ap2-horizons.

November, 1980), are slightly higher than those of samples reported here (table 104) for manganese and zinc, and similar for iron and copper; the range reported for copper is 1.7 to 2.3 ppm, for iron 12 to 24 ppm, for manganese 6 to 12 ppm, and for zinc 0.6 to 3.6 ppm. A notable discrepancy in the concentrations of the metals in the Ap-horizons was found between the locations having measurable ash fall (locations A–E) and the location where less than 0.1 mm of ash was observed (location F, which is referred to as the zero-ash site). In general, lower metal concentrations were measured in the Ap-horizons at location F than at locations A–E. This difference may simply reflect a natural trend, or, more probably, the leaching of ash at locations A–E has, by some mechanism, altered the metal composition of the Ap-horizons.

Mixing of ash with the Ap1- and Ap2-horizons at locations A-E resulted in metal concentrations similar to those measured in the unmixed Ap1- and Ap2-horizons. The expected decrease in concentration in the mixed samples, due to dilution of the Ap-horizon with ash of low metal content, was not evident. This lack of decrease is most obvious at location A where a 4-cm depth of ash was mixed with a 20-cm depth of soil.

Exchangeable calcium, magnesium, potassium, and sodium in ash show a small range among locations (table 105). Calcium, magnesium, and potassium are

lower in ash than in soil, whereas sodium is higher. When ash and soil are mixed (table 105), however, the amounts of exchangeable cations are similar to the amounts measured in the Ap1 and Ap2 soil horizons. The expected decrease in exchangeable calcium, magnesium, and potassium due to dilution, and the expected increase in sodium due to concentration, were not observed, even at the high-ash location. The soil and ash were mixed in the field when the samples were collected, and a period of about 1 mo elapsed before the samples were analyzed. It seems unlikely that this incubation period would be sufficient for soil organisms to react with the ash and thus alter the ash to mimic the exchangeable-cation status of soil; however, no other explanation is apparent.

Ash pH was higher than that of the Ap soil horizons by about one or two units, except at the zero-ash site (F). The pH of the Ap1-horizon at F was about one-half unit higher, and that of the Ap2-horizon was about equal to the pH of the ash. Mixing of ash and soil changed the pH of the soil Ap-horizon very little (table 105). Apparently, soil is much more highly buffered than ash, and the addition of ash, even at the high-ash site, increased soil pH by 0.2 unit or less.

Most water-soluble constituents in ash show a fairly wide range in concentration from location to location and between sites at any one location (table 106). In general, the concentrations of water-soluble constituents decreased as ash thickness decreased. This effect could be associated either with differences in ash composition from location to location or, more probably, with the effect of leaching of the different thicknesses of ash by varying amounts of precipitation at each location. All water-soluble constituents were higher in ash at all locations (A–E) than in the Ap-horizons at the zero-ash location (F). At each location, the mixture of ash and the Ap-horizons resulted in slightly higher calcium, magnesium, potassium, sodium, chloride, and sulfate amounts, and conductance, compared to the mean of the Ap-horizons; and these mixtures at locations A–E were much higher than the mean of the Ap-horizons at location F.

CHANGES IN SOIL COMPOSITION

Water (precipitation) percolated through the ash layer and into the soil between the time of the ash fall (May 18) and the collection of samples (June 16–20). The differences in chloride, sulfate, and specific conductance (table 106) between locations A–E and F suggest that this precipitation percolated at least to the bottom of the Ap2-horizon (20 cm) and probably into the upper part of the B-horizon. At the zero-ash location (F), chloride is relatively low in concentration, and it decreases with depth. Pre-ash-fall chloride at the other locations should have been similar in concentration in each horizon to location F, based on the assumption that the soils collected at all locations are relatively uniform. The maximum chloride levels measured in the Ap2-horizon, and the slight increase in the 30-cm composite of the B-horizon, suggest that leaching moved a large amount of water-soluble chloride from the ash into the Ap2-horizon and probably into the upper few centimeters of the B-horizon. Mobility of chloride and its resistance to retention by adsorption or exchange reactions in soil is well documented. The amounts of water-soluble chloride in fresh ash are certainly sufficient to account for the increases measured. T. K. Hinkley (U.S. Geological Survey, unpub. data, 1980) has shown that fresh ash from Richland, Wash., released 770, 7.4, and 2.4 mg/L of chloride in successive pore-volume leaches with water.

Comparing the levels of calcium, magnesium, potassium, sodium, and sulfate in locations A–E with location F shows that these constituents were also leached into the Ap2-horizon. Adsorption and exchange reactions certainly affect the movement of these constituents more than chloride, and it can be shown from the data in table 106 that, although increased levels were measured in the Ap2-horizon, most of these water-soluble constituents were retained in the Ap1-horizon. Specific conductance also illustrates this effect for the major cations and sulfate (table 106). T. K. Hinkley's data (U.S. Geological Survey, unpub. data, 1980) for three successive pore-volume water leaches of fresh ash show calcium as 380, 160, and 70 mg/L; magnesium as 83, 5.4, and 1.7 mg/L; sodium as 280, 13, and 8 mg/L; sulfate as 1,200, 450, and 180 mg/L; and potassium as 250 mg/L (only the first pore volume of water was analyzed for potassium). These values are certainly great enough to account for the increases measured in the soils of this study.

Exchangeable cations do not show the same trends as the water-soluble cations. This difference seems reasonable because exchangeable cation amounts were lower in the ash than in the soil, and percolating

water should alter only slightly the exchange status of soils.

At location F, where less than 0.1 mm of ash was observed, the pH of all soil horizons was near neutral (table 105). At locations A–E, the Ap1- and Ap2-horizons had their lowest pH where ash fall was greatest, and the pH of these horizons increased as ash-fall decreased (table 105). This trend is most pronounced for the Ap2-horizon but can also be observed reasonably well for the Ap1-horizon. In the Ap1-horizon, and especially in the Ap2, an inverse relation between ash-fall thickness and pH is apparent (table 105). The Ap2-horizon has a pH at location A (highest ash-fall site) of about 5, this increases at locations C and D to about 6 (intermediate ash-fall sites), and it is about 7 at location F (zero ash fall). The pH of the B-horizon is fairly uniform between locations A–E, but is about one-half unit higher at location F. Whether this difference in pH of B soil horizons is due to nonuniformity between the sites north and south of the Snake River or to ash-fall differences is unclear.

A direct relation between ash-fall thickness and concentration of DTPA-extractable metals is apparent (table 104). Ratios between the average metal concentration measured in the Ap2-horizon at the zero ash-fall location (F), the intermediate ash-fall locations (C and D), and the high ash-fall location (A) are as follows: cadmium and iron 1:2:3, copper 1:1:1, manganese 1:2:5, and nickel and zinc 1:2:2. The trends for the Ap1- and B-horizons are similar, although the differences in ratios between zero and high ash-fall sites are not as large. Correlation coefficients between DTPA-extractable metals in the Ap1-, Ap2-, and B-horizons and pH are as follows: cadmium −0.67, copper 0.13, iron −0.94, manganese −0.84, nickel −0.70, and zinc −0.76. The correlation coefficients between pH of the Ap1-, Ap2-, and B-horizons and ash-fall thickness is −0.57. Correlations between pH and DTPA-extractable metals, except copper, and between pH and ash-fall thickness are statistically significant at the 0.001 probability level.

The explanation for this decrease in soil pH, presumably related to ash-fall thickness, is not apparent from the data presented here. The samples of ash are basic or near neutral (table 105). Water-saturation extracts of unweathered ash also show a near-neutral pH (Fruchter and others, 1980, table 4). Leaching of constituents in ash is apparently not the cause of this change in soil pH. In this study, the discrepancy between the decreased soil pH and the basic or near-neutral ash, plus the many reports that the ash was initially mildly corrosive (Fruchter and others, 1980), needs to be resolved. Perhaps the rainfall that occurred subsequent to the ash fall was acidic, and the data reported here reflect the composition of the precipitation rather than that of the ash fall.

ELEMENT CONTENT OF CLUB WHEAT

Table 108 lists the concentration of 25 elements (and plant-material ash yield) in the three types of wheat samples collected at sites along the transect. The whole-grain samples were not analyzed by ICP–OES; therefore, we report concentrations in all three plant materials for only about half of the elements.

Examination of the transect data for each element and each plant material revealed few strong ash-deposition-related trends. The fact that the pH of the A-horizon plus ash, Ap1, and Ap2 samples may have been affected by the ash fall (noted earlier) means that some impact on the availability (and root uptake) of cations such as aluminum, cadmium, copper, iron, manganese, and zinc can be expected. Also, it seems reasonable to assume that trace constituents such as arsenic, boron, cadmium, chloride, fluoride, and sulfate may be in forms available for direct foliar absorption, because these constituents are reported to be substantially higher in ash than soil and are apparently easily leached from the ash with water (Fruchter and others, 1980; Engibous, 1980; and T. K. Hinkley, U.S. Geological Survey, unpub. data, 1980).

Table 109 shows which levels, in the analysis-of-variance design, possessed a significant proportion (expressed as a percentage) of the total variance in the element content of wheat. Most of the variability for a majority of elements in the various wheat materials is found in the "between site" level or below. This means that wheat samples are likely to differ, in their element composition, as much within a field (location) or between replicate samples at a site as they are between locations that received varying amounts of volcanic-ash deposition. About one-fourth of all analytical determinations showed 50 percent or more of the variability in the data to be the result of error introduced by the laboratory procedures. In these instances, any natural variability in the data is ef-

Table 108.—Average concentration of elements in replicate samples of club wheat at sites having varying depths in volcanic ash south of Ritzville, Wash.

[Concentrations are on an ash weight basis except where noted; ppm, parts per million; mm, millimeters; <, less than]

Sites at locations (fig. 1)------	A-1,	A-2,	[1]B,	C-1,	C-2,	D-1,	D-2,	[1]E,	F-1	F-2
Ash depth (mm)------------------	40	40	30	20	20	11	11	7	<0.1	<0.1
Sample description										
PLANT-MATERIAL ASH YIELD (PERCENT)										
Whole grain----------	1.9	2.1	1.8	1.6	1.8	1.6	1.6	1.6	1.9	1.8
Grain head----------	5.5	6.0	6.1	5.6	5.8	5.9	5.4	5.7	5.6	5.2
Stems and leaves----------	7.3	7.6	6.1	7.4	6.4	6.2	6.0	7.7	7.2	6.3
ALUMINUM (PERCENT)										
Grain head----------	0.41	0.48	0.69	0.80	0.58	0.80	0.60	0.65	0.78	0.78
Stems and leaves----------	.64	1.2	1.1	1.6	1.7	1.4	.89	.61	.72	.66
BARIUM (PPM)										
Grain head----------	180	200	190	240	260	260	260	270	200	200
Stems and leaves----------	300	390	350	520	630	580	580	330	500	550
CADMIUM (PPM)										
Whole grain----------	4.0	3.0	3.0	4.1	1.8	5.0	2.8	3.1	2.6	1.7
Grain head----------	.50	.40	.40	.34	.44	.34	.50	.28	.94	.44
Stems and leaves----------	2.0	.40	.80	.50	.28	.28	.50	.80	.28	.28
CALCIUM (PERCENT)										
Whole grain----------	1.8	1.2	2.0	1.8	1.8	2.1	2.1	2.2	2.0	1.8
Grain head----------	1.6	1.2	1.4	.90	1.0	1.2	1.0	1.8	1.0	.95
Stems and leaves----------	2.8	1.9	2.9	2.2	2.4	2.0	2.0	3.2	2.5	2.6
CHROMIUM (PPM)										
Grain head----------	3.5	3.5	3.5	3.5	3.5	3.5	3.5	3.5	3.5	6.5
Stems and leaves----------	3.5	6.1	3.5	3.5	6.4	3.5	4.8	3.5	6.5	5.2
COPPER (PPM)										
Whole grain----------	200	160	240	190	140	200	190	200	170	180
Grain head----------	80	78	60	85	52	65	70	70	60	50
Stems and leaves----------	40	18	40	21	16	15	13	40	16	10
[2]FLUORINE (PPM)										
Whole grain----------	3.0	3.0	3	3.0	3.0	4.0	4.0	3	3.0	3.0
Grain head----------	4.0	3.0	3	3.0	4.0	3.0	3.0	3	5.0	4.0
Stems and leaves----------	4.0	4.0	5	6.0	5.0	3.0	4.0	4	3.0	4.0
IRON (PERCENT)										
Grain head----------	0.56	0.49	0.68	0.68	0.54	0.66	0.56	0.72	0.65	0.66
Stems and leaves----------	.84	.98	1.0	1.2	1.2	1.1	.90	.92	.90	.91

Table 108.—Average concentration of elements in replicate samples of club wheat at sites having varying depths of volcanic ash south of Ritzville, Wash.—Continued

Sites at locations (fig. 1)	A-1,	A-2,	[1]B,	C-1,	C-2,	D-1,	D-2,	[1]E,	F-1	F-2
Ash depth (mm)	40	40	30	20	20	11	11	7	<0.1	<0.1
Sample description										
LANTHANUM (PPM)										
Grain head	4.0	1.4	1.4	1.4	2.0	4.2	2.1	1.4	2.6	2.6
Stems and leaves	1.4	2.9	2.2	3.4	4.0	2.6	2.8	1.4	3.0	3.2
LEAD (PPM)										
Grain head	9.0	9.0	7.0	22	11	7.0	7.0	48	7.0	7.0
Stems and leaves	32	15	7.0	9.0	11	8.5	7.0	67	7.0	10
MAGNESIUM (PERCENT)										
Whole grain	5.8	4.3	6.4	5.5	5.3	6.6	6.3	7.1	6.8	5.9
Grain head	1.8	1.6	1.6	1.8	1.5	1.6	1.8	1.9	1.8	1.8
Stems and leaves	1.7	1.2	1.6	1.4	1.1	1.4	1.2	1.5	1.6	1.4
MANGANESE (PPM)										
Grain head	830	760	610	860	680	730	780	720	540	600
Stems and leaves	940	860	560	860	840	860	900	590	300	420
MOLYBDENUM (PPM)										
Grain head	1.9	2.8	3.1	2.4	4.4	2.7	3.0	1.5	11	8.8
Stems and leaves	1.1	2.1	3.1	.70	2.0	4.0	1.0	.70	7.8	5.6
NICKEL (PPM)										
Grain head	18	26	8.9	17	15	36	20	11	13	13
Stems and leaves	6.6	8.1	7.9	6.6	12	11	5.4	5.4	4.2	4.6
PHOSPHORUS (PERCENT)										
Whole grain	11	10	11	13	12	11	11	12	14	13
Grain head	4.2	3.9	3.2	4.2	3.6	3.7	3.8	3.3	3.8	3.8
Stems and leaves	1.4	1.0	1.2	1.0	.92	.85	.82	1.3	.90	.60
POTASSIUM (PERCENT)										
Whole grain	26	22	26	24	24	28	26	27	28	22
Grain head	13	12	10	11	8.5	8.3	10	12	10	9.0
Stems and leaves	20	14	18	15	12	12	14	20	12	12
[2]SELENIUM (PPM)										
Whole grain	0.020	0.020	0.04	0.020	0.050	0.015	0.015	0.05	0.040	0.070
Grain head	.020	.040	.02	.020	.050	.020	.010	.02	.030	.050
Stems and leaves	.015	.020	.02	.015	.030	.010	.0085	.01	.020	.030

Table 108.—Average concentration of elements in replicate samples of club wheat at sites having varying depths of volcanic ash south of Ritzville, Wash.—Continued

Sites at locations (fig. 1)------	A-1,	A-2,	[1]B,	C-1,	C-2,	D-1,	D-2,	[1]E,	F-1	F-2
Ash depth (mm)----------	40	40	30	20	20	11	11	7	<0.1	<0.1
Sample description										
SODIUM (PERCENT)										
Whole grain----------	0.32	0.14	0.28	0.24	0.27	0.19	0.20	0.19	0.18	0.22
Grain head----------	.22	.23	.26	.26	.24	.22	.18	.17	.24	.20
Stems and leaves----------	.24	.34	.32	.38	.40	.39	.27	.18	.19	.18
STRONTIUM (PPM)										
Grain head----------	120	100	130	110	92	100	86	120	95	96
Stems and leaves----------	180	190	200	200	200	200	160	200	170	180
[2]SULFUR (PERCENT)										
Whole grain----------	0.14	0.12	0.15	0.11	0.095	0.12	0.10	0.12	0.10	0.10
Grain head----------	.14	.14	.16	.13	.11	.12	.12	.15	.10	.095
Stems and leaves----------	.14	.080	.15	.092	.040	.065	.060	.18	.048	.032
TITANIUM (PPM)										
Grain head----------	200	200	290	400	280	400	300	340	410	400
Stems and leaves----------	270	540	470	740	800	660	420	290	400	400
URANIUM (PPM)										
Whole grain----------	0.035	0.042	0.065	0.035	0.035	0.035	0.035	0.035	0.042	0.048
Grain head----------	.45	.48	.80	.45	.68	.70	.52	.70	.40	.40
Stems and leaves----------	.075	.052	.035	.042	.048	.035	.042	.035	.035	.042
VANADIUM (PPM)										
Grain head----------	3.0	2.3	5.4	6.0	5.0	7.9	5.6	4.5	6.4	7.4
Stems and leaves----------	3.6	7.9	7.6	14	16	12	7.0	4.8	8.3	7.4
YTTRIUM (PPM)										
Grain head----------	2.4	1.4	1.3	2.1	1.3	1.8	1.2	3.0	1.7	1.2
Stems and leaves----------	1.3	3.2	2.7	3.0	3.0	2.8	2.3	.70	1.7	2.6
ZINC (PPM)										
Whole grain----------	800	740	1,000	880	650	780	830	720	650	760
Grain head----------	440	360	400	420	280	330	330	440	220	280
Stems and leaves----------	100	65	110	190	80	88	60	180	42	38

[1]Value reported by the analyst for a single sample--not a replicate average.
[2]Concentrations expressed on a dry-weight basis.

fectively masked, and interpretations of variance-component significance cannot be made.

If there was an ash-deposition influence on the element composition of the wheat sampled, we expected the following criteria to be met: (1) a significant "between locations" variance component; (2) a small analytical-error variance term; (3) a small amount of data censoring (less than 30 percent of the concentra-

tion values in plant material reported as below the LLD); (4) a significant (0.05 probability level) simple correlation coefficient between ash depth and the element composition of wheat; and (5) a reasonably large total variance term, indicating spread in the data points.

Sulfur in wheat whole grain and grain heads are examples (tables 108, 109) that best fit these criteria. Sulfur in whole grain has a large but nonsignificant proportion of the total variance in the data that occurs between locations and a correlation coefficient (r) of 0.65 with ash depth. Figure 450 is a triaxial plot showing the positive relation between sulfur in whole grain and ash depth and the inverse relation between sulfur and A-horizon soil pH. Sulfur in grain heads has a significant proportion of the total variance occurring between locations and r (sulfur to ash depth) equal to 0.65. Figure 453 illustrates this relationship between ash deposition, soil pH, and the sulfur content of grain heads. Sulfur in wheat stems and leaves does not possess a significant between-location component, nor is the relation between plant sulfur and ash depth as strong (r equals 0.40). Figure 452 illustrates this weaker relationship. In general, therefore, sulfur in wheat does appear to be related to the ash

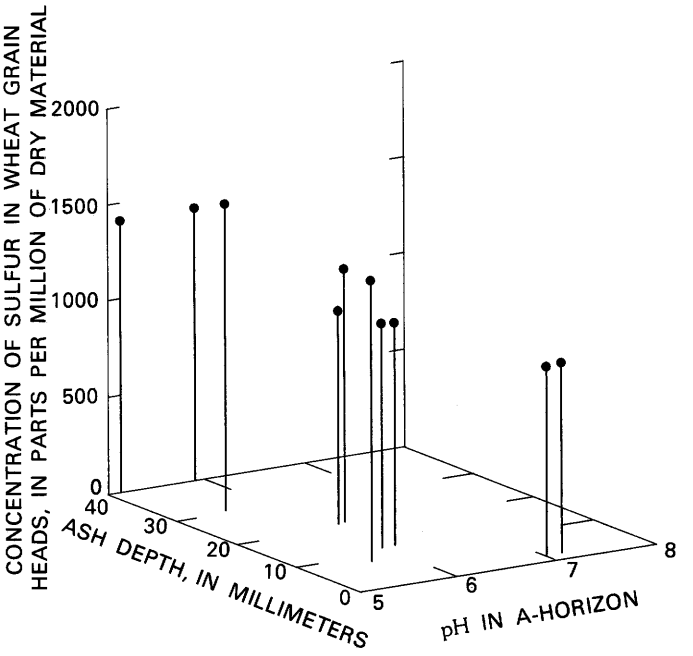

Figure 451.—Triaxial plot of the relationship between the sulfur concentration of wheat heads (tops), A-horizon soil pH, and volcanic-ash depth, from an area in eastern Washington.

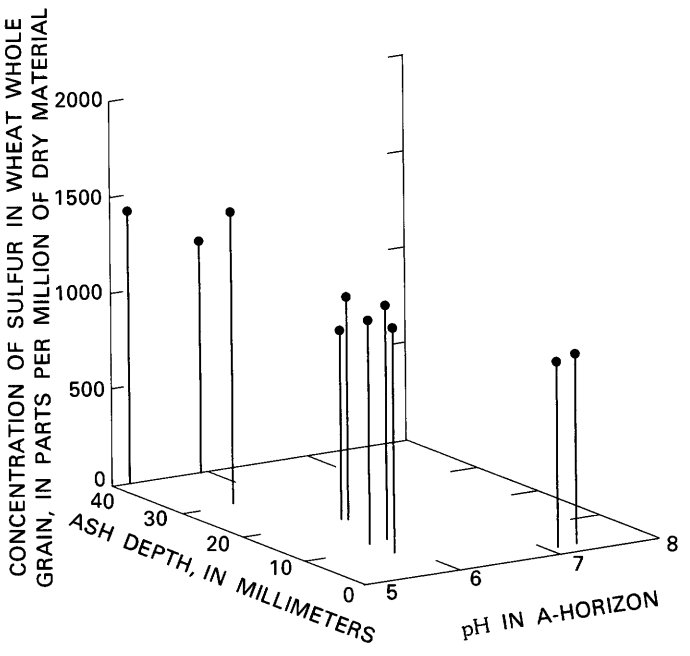

Figure 450.—Triaxial plot of the relationship between the sulfur concentration of wheat whole grain, A-horizon soil pH, and volcanic-ash depth, from an area in eastern Washington.

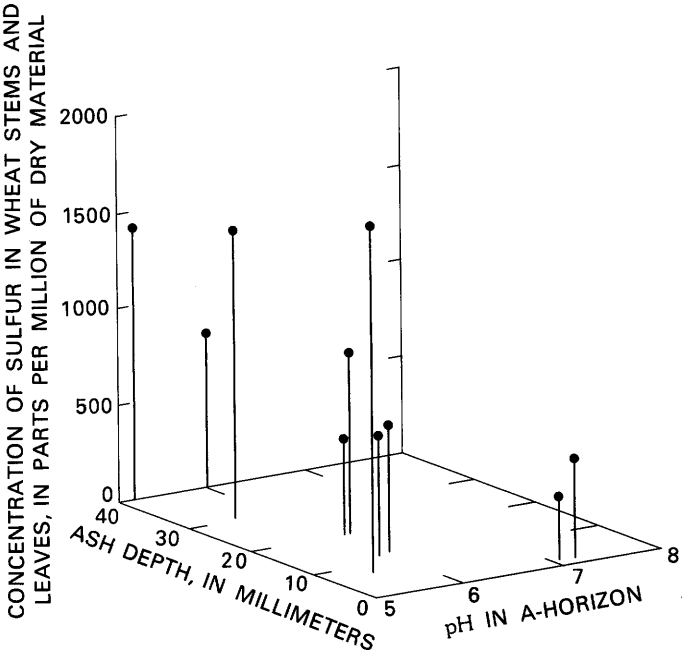

Figure 452.—Triaxial plot of the relationship between the sulfur concentration of wheat stems and leaves, A-horizon soil pH, and volcanic-ash depth, from an area in eastern Washington.

Table 109.—Variation in the element concentrations in ash of soft, white club wheat collected south of Ritzville, Wash.

[Variance analysis was performed on the ash base concentrations except where noted; ratio, the proportion of the analyses having values above the lower limit of determination of the total number of analyses; *, component of variance was tested as significant at the 0.05 probability level]

Element or ash	Ratio	Analysis of variance: Total $\log_{10}$ variance	Percent of total variance between: Locations	Sites within locations	Samples within sites	Analyses within samples
Ash yield:						
Wheat grain-------	20:20	0.00300	*64	<1	*28	7.9
Grain head--------	18:18	.00286	<1	<1	*95	4.2
Stems and leaves--	18:18	.00213	22	10	*62	5.0
Aluminum:						
Grain head--------	18:18	.0231	48	13	*38	1.2
Stems and leaves--	18:18	.0319	61	20	*14	4.3
Barium:						
Grain head--------	18:18	.00554	*77	*13	3.2	7.4
Stems and leaves--	18:18	.0129	*84	6.3	6.2	3.2
Cadmium:						
Wheat grain-------	20:20	.0315	<1	*64	1.9	34
Grain head--------	12:18	.0522	<1	<1	<1	100
Stems and leaves--	10:18	.0821	24	*53	<1	23
Calcium:						
Wheat grain-------	20:20	.00586	23	37	25	14
Grain head--------	18:18	.00778	22	*40	<1	37
Stems and leaves--	18:18	.0232	9.6	2.5	<1	88
Chromium:						
Grain head--------	1:18	.0170	<1	*44	<1	56
Stems and leaves--	6:18	.0503	<1	32	18	50
Copper:						
Wheat grain-------	20:20	.00572	5.0	*64	7.0	24
Grain head--------	18:18	.00982	15	15	*68	2.4
Stems and leaves--	18:18	.0364	42	25	*26	6.6
Fluorine[1]:						
Wheat grain-------	20:20	.0159	*24	<1	<1	76
Grain head--------	18:18	.0227	<1	45	7.4	47
Stems and leaves--	18:18	.0229	19	<1	23	58
Iron:						
Grain head--------	18:18	.00399	16	*46	*35	3.1
Stems and leaves--	18:18	.00520	*55	<1	*35	10
Lanthanum:						
Grain head--------	8:18	.0713	<1	25	<1	75
Stems and leaves--	9:18	.0970	2.5	<1	20	77
Lead:						
Grain head--------	5:18	.0468	*27	<1	<1	73
Stems and leaves--	8:18	.0759	5.3	<1	*66	29
Magnesium:						
Wheat grain-------	20:20	.00572	47	23	20	10
Grain head--------	18:18	.00477	2.7	4.4	<1	93
Stems and leaves--	18:18	.00512	13	11	67	8.4
Manganese:						
Grain head--------	18:18	.00490	65	*24	6.0	5.6
Stems and leaves--	18:18	.0416	*90	6.7	2.5	<1
Molybdenum:						
Grain head--------	18:18	.124	*71	3.4	*18	8.0
Stems and leaves--	11:18	.146	42	6.7	23	28

Table 109.—Variation in the element concentrations in ash of soft, white club wheat collected south of Ritzville, Wash.—Continued

Element or ash	Ratio	Analysis of variance: Total $\log_{10}$ variance	Percent of total variance between: Locations	Sites within locations	Samples within sites	Analyses within samples
Nickel:						
Grain head--------	18:18	.0500	13	<1	*68	19
Stems and leaves--	18:18	.0435	25	<1	28	47
Phosphorus:						
Wheat grain-------	20:20	.00362	19	<1	*70	11
Grain head--------	18:18	.00592	<1	<1	*93	6.6
Stems and leaves--	18:18	.0201	43	<1	*53	3.7
Potassium:						
Wheat grain-------	20:20	.00152	<1	*67	<1	33
Grain head--------	18:18	.0465	14	3.6	<1	82
Stems and leaves--	18:18	.0259	26	<1	<1	74
Selenium[1]:						
Wheat grain-------	20:20	.0596	45	*33	<1	22
Grain head--------	18:18	.0645	24	*62	15	<1
Stems and leaves--	17:18	.0458	*53	<1	*34	12
Sodium:						
Wheat grain-------	20:20	.0286	<1	25	43	32
Grain head--------	18:18	.00588	<1	20	<1	80
Stems and leaves--	18:18	.0234	*72	10	*14	4.0
Strontium:						
Grain head--------	18:18	.00312	<1	*62	*35	3.0
Stems and leaves--	18:18	.00244	34	5.0	29	32
Sulfur[1]:						
Wheat grain-------	20:20	.00478	44	*38	11	7.2
Grain head--------	18:18	.00479	*78	*13	3.1	5.4
Stems and leaves--	18:18	.0463	40	*53	5.7	<1
Titanium:						
Grain head--------	18:18	.0279	63	9.1	*24	3.5
Stems and leaves--	18:18	.0285	54	*25	*14	7.3
Uranium:						
Wheat grain-------	5:20	.0133	*63	<1	8.9	28
Grain head--------	18:18	.0122	31	7.3	*56	5.0
Stems and leaves--	7:18	.0194	18	<1	18	64
Vanadium:						
Grain head--------	18:18	.0612	*67	<1	21	12
Stems and leaves--	18:18	.0432	56	15	*19	9.8
Yttrium:						
Grain head--------	15:18	.0488	<1	14	10	76
Stems and leaves--	14:18	.104	<1	<1	*74	25
Zinc:						
Wheat grain-------	20:20	.00470	37	18	*39	5.5
Grain head--------	18:18	.0122	32	1.8	*51	15
Stems and leaves--	18:18	.0567	8.6	<1	53	38

[1]Variance components determined on the element concentrations in wheat dry material.

fall in a positive way. The soils data show that sulfur as sulfate is related positively to ash depth and apparently is being absorbed by the wheat. This evidence suggests that the sulfur in wheat was absorbed through the roots; however, foliar absorption may also have occurred.

A significant proportion of the variability in the concentration of molybdenum in grain heads occurs between locations; however, r (molybdenum in wheat to ash depth) equals -0.60 (large but not significant), which means that there exists an inverse relation between ash depth and molybdenum in wheat. The increase in molybdenum absorption by wheat from north to south is explained as reflecting the increase in A-horizon soil pH in the same direction. It is well documented that molybdate (MoO_4^{2-}) is the form most easily absorbed by plants and is mobilized in soils that are slightly alkaline. A direct cause-and-effect relationship between molybdenum levels in wheat and ash depth, however, cannot be made.

Other observations concerning the wheat samples collected near Ritzville are: (1) In general, concentrations of the micronutrients copper and zinc and of the macronutrients phosphorus and potassium increase from stem and leaf to grain head to whole-grain material. This trend suggests that these elements are translocated from the stems and leaves and accumulate in the grain. The importance of possible foliar absorption in this process cannot be assessed here. (2) A very unusual and dramatic uptake trend for uranium was observed, where an order-of-magnitude greater difference in grain-head material was noted over stem and leaf or whole-grain material. This implies that uranium is translocated to the grain head where it accumulates—it does not, however, translocate easily from the head to the grain. (3) A fivefold increase in cadmium in wheat stems and leaves in two samples at one of the high-deposition sites cannot be attributed to the ash fall because none of the other samples showed a similar response (table 108). It is interesting to note, however, that the ash of whole grain contained an order-of-magnitude more cadmium than the ash of either the grain heads or the stems and leaves. Although cadmium occurs in greater concentrations in the kernel, the levels found in the samples near Ritzville compare very well with levels reported by Erdman and Gough (1979) for hard, red wheat collected from throughout the Northern Great Plains (table 110) and therefore do not appear to be unusual.

Although genetically different types of wheat from widely separate geographic regions are given in table 110, the data are useful in making gross comparisons. For example, very similar geometric deviations indicate that about the same degree of variability was noted for a given element in samples from both

Table 110.—Comparison of the element content (ash-weight basis) of soft, white winter wheat from eastern Washington and hard, red winter wheat from the Northern Great Plains

[ppm, parts per million; <, less than; n, number of samples; leaders (--), do data]

Element or ash	Soft, white wheat (n=20)			[1]Hard, red wheat (n=17)		
	Geometric mean	Geometric deviation	Observed range	Geometric mean	Geometric deviation	Observed range
Ash (percent)	1.8	1.12	1.5-2.2	1.5	1.11	1.3-1.8
Cadmium (ppm)	2.9	1.47	1.5-5.4	2.3	1.47	1.0-3.5
Calcium (percent)	1.8	1.19	1.1-2.3	1.9	1.15	1.4-2.4
Copper (ppm)	180	1.19	120-250	260	1.17	190-330
Fluorine[2] (ppm)	2.8	1.30	2-4	<1	--	<1-1
Magnesium (percent)	5.9	1.17	4.2-7.4	9.3	1.09	8.0-11
Phosphorus (percent)	12	1.13	8.4-15	17	1.18	12-21
Potassium (percent)	25	1.10	21-29	25	1.14	20-33
Selenium[2] (ppm)	.029	1.80	.01-.08	.44	1.63	.15-1.0
Sodium[2] (percent)	.21	1.40	.12-.50	--	--	--
Sulfur[2] (total) (percent)	.11	1.16	.090-.15	.15	1.11	.13-.19
Uranium[3] (ppm)	<.070	--	<.035-.070	<.47	--	<.33-.47
Zinc (ppm)	780	1.16	590-1,100	1,800	1.22	1,300-2,500

[1]From Erdman and Gough (1979). The geometric mean and observe range are estimated from data originally reported on a dry weight basis.
[2]Summary statistics are on a dry-weight basis.
[3]Changes in analytical methodology explain the order of magnitude difference in the lower limit of determination of the two data sets.

regions. Also, except for concentrations of selenium and uranium (and perhaps zinc), the element composition of the grain from these two regions is remarkably similar. (The Northern Great Plains has long been recognized as having seleniferous and uraniferous areas.) These data further suggest that the impact of the Mount St. Helens eruption on the element content of the wheat in the Ritzville area was of no real significance this growing season.

SUMMARY

1. Samples of the following materials were collected at six locations, 4 weeks after the major Mount St. Helens eruption, along a 75-km transect south of Ritzville, Wash.: (1) soft, white club wheat—immature grain heads and stems and leaves; (2) soils—Ap1-horizon, Ap2-horizon, and B-horizon; (3) volcanic ash; and (4) a mixture of volcanic ash and the Ap-horizons. In addition, mature whole grain was sampled at the same sites about 8 weeks following the eruption. The locations were edaphically, lithologically, and vegetationally similar but differed in their ash deposition as follows (in mm): 40, 30, 20, 11, 7, and less than 0.1.

2. About 50 mm of precipitation between the May 18 eruption and the mid-June sampling altered the chemical composition of soil extracts so that pre-ashfall soil chemical uniformity could not be definitely established. This amount of precipitation was estimated to replenish available water in the Ritzville soil series to a depth of about 25 cm. Data for water-soluble chloride in fresh ash and in the soil horizons of this study confirmed that water penetrated the Ap1- and Ap2-horizons (about 20 cm) and probably the upper few centimeters of the B-horizon.

3. DTPA-extractable cadmium, iron, manganese, nickel, and zinc were much lower, and copper slightly higher, in the ash than in Ap soil horizons directly below the ash accumulation. However, at a site where ash fall was minimal (less than 0.1 mm), these metals were lower in the Ap-horizon than at the sites where ash fall was measurable. Leaching of ash has, by some mechanism, altered the metal composition of the Ap-horizons. Exchangeable calcium, magnesium, and potassium are lower in ash than in soil Ap-horizons, and sodium is higher. Leaching of fresh ash had little effect on the exchange status of soils. At sites where ash accumulated, the pH of the ash was higher than in soil horizons directly below the ash accumulation; however, at the site where less than 0.1 mm of ash was measured, soil pH was higher than the pH of either soil or ash at sites where ash accumulation was measured. The relation between ashfall thickness and change in soil pH is not easily explained by leaching of ash, because the ash is basic or near neutral rather than acidic.

4. The Ap1- and Ap2-horizons of soil showed their lowest pH where the ash fall was greatest. The pH of these horizons (especially the Ap2) increased as ash fall decreased. DTPA-extractable metals show an inverse relation with pH and a direct relation with ashfall thickness. The explanation for these relations between pH, ash thickness, and DTPA-extractable metals is obscure. Ash is basic or near neutral rather than acidic, and water-saturation extracts of fresh ash are reported to be near neutral in pH; however, the ash was reported to be mildly corrosive when it fell. The discrepancies between the measured neutral to basic reaction of the ash, the reports that freshly fallen ash was mildly corrosive, and the measured increased acidity of soils need to be resolved.

5. Examination of the transect data for 25 elements in plant materials revealed two strong trends related to ash deposition, as shown by an elevation of sulfur in wheat whole-grain and grain-head material at sites having 20 mm of ash or more. Concentrations of molybdenum in grain heads appear inversely related to ash deposition; however, the natural increase in Ap-horizon pH from north to south along the transect explains this trend—not the decrease in ash deposition in the same direction. The elevated levels of many DTPA-extractable elements measured in soils, especially at the sites of greatest ash fall, may alter the levels of these metals in subsequent wheat crops; therefore, analyses of wheat element content should be repeated at these same sites for at least another growing season.

6. Cadmium was not found to be related to the ash fall; however, cadmium in the whole grain occurred in greater concentrations (2.9 ppm) than either in the grain heads or in the stems and leaves.

7. Most of the variability in the element-content data for wheat materials was found at the "between sites within location" level or below. The lack of a strong variance component at the "between locations" level is further evidence that the chemistry of the aerial parts of club wheat was not appreciably affected this growing season by the ash fall.

REFERENCES CITED

Crock, J. G., and Severson, R. C., 1980, Four reference soil and rock samples for measuring element availability in the western energy regions: U.S. Geological Survey Circular 841, 16 p.

Day, P. R., Particle fractionation and particle-size analysis, *in* Methods of soil analysis—Part 1, Physical and mineralogical properties, including statistics of measurement and sampling: Madison, Wisconsin, American Society of Agronomy (Agronomy, no. 9), p. 545–566.

Dean, W. E., Jr., 1974, Determination of carbonate and organic matter in calcareous sediments and sedimentary rocks by loss on ignition—comparison with other methods: Journal of Sedimentary Petrology, v. 44, no. 1, p. 242–248.

Engibous, James, 1980, Results of research and analysis of volcanic ash from Mt. St. Helens: Washington State University, Conference on the aftermath of Mt. St. Helens, July 1980, Pullman, Wash., Proceedings, p. 9.

Erdman, J. A., and Gough, L. P., 1979, Mineral composition of wheat from coal-mine spoils and farms in the northern Great Plains, USA, *in* Wali, M. K., ed., Ecology and coal resource development: New York, Pergamon Press, p. 878–886.

Franklin, J. F., and Dyrness, C. T., 1969, Vegetation of Oregon and Washington: U.S. Department of Agriculture Forest Service Research Paper PNW–80, 216 p.

Fruchter, J. S., Robertson, D. E., Evans, J. C., Olsen, K. B., Lepel, E. A., Laul, J. C., Abel, K. H., Sanders, R. W., Jackson, P. O., Wogman, N. S., Perkins, R. W., Van Tuyl, H. H., Beauchamp, R. H., Shade, J. W., Daniel, J. L., Erikson, R. L., Sehmel, G. A., Lee, R. N., Robinson, A. V., Moss, O. R., Briant, J. K., and Cannon, W. C., 1980, Mount St. Helens ash from the 18 May 1980 eruption—chemical, physical, mineralogical, and biological properties: Science, v. 209, no. 4461, p. 1116–1125.

Grigal, D. F., 1974, Note on the hydrometer method of particle-size analysis: Minnesota Forestry Research Notes, no. 245, 4 p.

Harrison, E. T., Donaldson, N. C., McCreary, F. R., Ness, A. O., and Krashevski, Stephen, 1964, Soil survey of Walla Walla County, Washington: U.S. Department of Agriculture, Soil Conservation Service, Series 1957, no. 16, 138 p.

Lenfesty, C. D., 1967, Soil Survey of Adams County, Washington: U.S. Department of Agriculture, Soil Conservation Service, 110 p.

Leonard, W. H., and Martin, J. H., 1963, Cereal crops: New York and London, MacMillan Co., 824 p.

Pacific Northwest Crop Improvement Association, 1979, 1978 wheat production estimates by varieties in certain Pacific Northwest counties: Ritzville, Washington Association of Wheat Growers, 30 p., mimeographed publication.

Sarna-Wojcicki, A. M., Shipley, Susan, Waitt, R. B., Dzurisin, Daniel, Hays, W. H., Davis, J. O., Wood, S. H., and Bateridge, Thomas, 1980, Areal distribution, thickness, and volume of downwind ash from the May 18, 1980 eruption of Mount St. Helens: U.S. Geological Survey Open-File Report 80–1078, 14 p.

Soltanpour, P. N., and Schwab, A. P., 1977, A new test for simultaneous extraction of macro- and micro-nutrients in alkaline soils: Communications in Soil Science and Plant Analysis, v. 8, p. 195–207.

U.S. Department of Commerce, 1980a, May 1980 climatological data, Washington: U.S. National Oceanic and Atmospheric Administration, National Climatic Center, v. 84, no. 5, 20 p.

_____1980b, June 1980 climatological data, Washington: National Oceanic and Atmospheric Administration, National Climatic Center, v. 84, no. 6, 21 p.

ANALYSIS OF POTENTIAL HAZARDS

ANALYSIS OF POTENTIAL HAZARDS

Predictions of potential eruptions and assessments of volcanic hazards, based on the past activity of various volcanoes in the Cascade Range, have been made over about the past 15 yr for long-range land-use planning. These assessments postulate kinds, locations, severity, frequency, and effects of future eruptions and suggest some possible responses. Such an assessment for Mount St. Helens was completed in the mid-1970's and the report published in 1978. Because such assessments are for long-range planning, they differ from day-to-day hazard assessments, which in addition to past activity consider current information provided by monitoring. A skeleton array of seismometers, recently emplaced, picked up the initial earthquakes associated with the 1980 eruptions, and was expanded to monitor seismic activity through the rest of the year. Thus, the eruptions tested predictions of potential eruptions and their associated hazards, and also the efficacy of seismic monitoring for a Cascade Range volcano.

After May 18, the new potential hazard created by debris-avalanche deposits that raised Spirit Lake and dammed several streams tributary to the North Fork Toutle River led to stability analysis of the debris-avalanche and computer-aided analyses of floods that could result from its overtopping.

Initial USGS recommendations in response to the increase in earthquakes at Mount St. Helens (Miller and others) were based entirely on past eruptive activity at the volcano. Access to the volcano was restricted first because of danger from snow avalanches on the cone itself. As seismic activity increased, access to the area around Mount St. Helens was restricted because of the likelihood of eruptions. After the first eruption, recommendations regarding hazards and appropriate responses were based not only on the record of past activity, but also on day-to-day visual and instrumental monitoring. USGS hazards-analysis coordinators described ranges of expectable eruptions, possible responses, and expectable warnings to government officials, private interests, and the public. Hazards forecasts were generally accurate, but the magnitude of the massive landslide and laterally directed blast of May 18 exceeded expectations. Experiences during the 1980 eruptions emphasized the need for a hazards assessment before an eruption occurs, an extensive monitoring network, an onsite agency capable of handling emergency situations, and hazards-assessment personnel familiar with local geography and land use as well as the eruptive record.

Some seismometers were in place at and near the volcano when the March activity began, and the network was immediately expanded when a swarm of earthquakes followed that of March 20 (Malone and others). After March 25 frequency and magnitude of earthquakes leveled off, however, and no further changes signaled the cataclysmic eruption of May 18. After May 18, a relatively low background of seismic activity allowed changes to be more readily recognized; the eruptions of June 12 and August 7 were preceded by increases in level of harmonic tremor, and eruptions of July 22 and October 16 were preceded by increased numbers of shallow volcanic earthquakes. For each of these, the precursors were recognized and warnings issued at least 2 hr before the eruption began.

A review of eruption forecasting on a probabilistic basis, using both evidence from past events and monitoring, is encouraging (Decker). Two approaches are fruitful—the documentation of past eruptive history to provide evidence of long-term potential kinds and frequencies of eruptions, and monitoring to provide information about eruption potential on a short-term basis. Some predictions of Mount St. Helens eruptive events and effects were very successful, including those for most events of May 18, and of forthcoming eruptions in June, July, August, October, and December. Eight significant eruptions in 1980 were preceded by multiple phenomena over periods of months to hours; false alarms that occurred generally were based on occurrence of only one precursory-type phenomenon. Significant improvements are still needed in judging extents, magnitudes, times, and locations of coming eruptive events, especially when seismic activity is high. Gas studies show promise of predicting times of forthcoming eruptions, and ground-deformation studies and thermal monitoring have detected some changes that could be useful for anticipating specific events.

After the May 18 eruption, the huge debris avalanche in the North Fork Toutle River valley raised the level of Spirit Lake by about 60 m. The debris was known to contain abundant water and hydrother-

mally altered material from the volcano. A stability analysis, however (Youd and others), determined that the blockage should be stable against slope failure due to gravitational or earthquake forces of the worst reasonably postulated conditions, including saturation of the deposit. The analysis also shows that the blockage is safe against piping failure. The debris avalanche also dammed several valleys tributary to the North Fork Toutle River, creating the threat of flooding from overtopping by smaller lakes in tributary valleys as well as Spirit Lake. Immediate analyses of potential flooding aided by computer modeling provided estimates of flood volumes and heights that could be expected from overtopping and breaching (Jennings and others). One dam failed shortly after the analysis, and the resulting floods were comparable to those predicted by the computer model.

THE 1980 ERUPTIONS OF MOUNT ST. HELENS, WASHINGTON

HAZARDS ASSESSMENTS AT MOUNT ST. HELENS

By C. DAN MILLER, DONAL R. MULLINEAUX, *and* DWIGHT R. CRANDELL

ABSTRACT

Activity of Mount St. Helens that started in March 1980 prompted the U.S. Geological Survey to assume its mandated responsibility for short-term volcanic-hazards assessments and for monitoring the volcano and observing eruptions. Our assessments of potential hazards were based on the geologically recent eruptive behavior of the volcano and on day-to-day observations and interpretations of the results of monitoring. These assessments were given to various governmental officials who had to make land-use and land-access decisions, and to other concerned groups, news representatives, and the public. Our long-and short-term forecasts were generally accurate, although the magnitude of the catastrophic and unprecedented landslide and lateral blast of May 18 greatly exceeded our expectations. Our experiences as volcanic-hazards coordinators from late March to late October 1980, have shown the need for (1) hazards assessments to be completed and available before volcanoes erupt, (2) an extensive monitoring network around the volcano to provide seismic, deformation, and other kinds of data useful in day-to-day hazards appraisals, (3) an onsite agency, such as the U.S. Forest Service, to provide logistic and communication support to scientists and other groups at the outset of an eruption, and (4) one or more geologists to serve as hazards coordinators, who are intimately familiar with the eruptive history, local physical geography, and land-use patterns around the volcano.

INTRODUCTION

On Friday, March 21, 1980, and on the following Monday and Tuesday, U.S. Forest Service (USFS) officials of the Gifford Pinchot National Forest in Vancouver, Wash., and geophysicists of the University of Washington/U.S. Geological Survey (USGS) seismic research group in Seattle contacted members of the Volcanic Hazards Project of the USGS in Denver, Colo., to report that frequent earthquakes at Mount St. Helens beginning on March 20 might be precursors to a volcanic eruption. The USFS and other agencies needed immediate advice about possible events and their effects in order to help them decide about closure or evacuation of threatened areas.

We were contacted because we had recently studied the eruptive behavior of the volcano (Crandell and others, 1975; Hoblitt and others, 1980) and had considered the likelihood and potential effects of future eruptions there and elsewhere (Crandell and Mullineaux, 1978; Miller, 1980). None of us had previous experience in appraising short-term hazards at an active volcano, but we did have extensive knowledge about past eruptions of Mount St. Helens and could forecast possible kinds and extents of volcanic hazards. Consequently, we assumed the responsibility of identifying the probable kinds of future eruptions, the probable consequences of various events, and some appropriate short-term responses to future eruptions. This report summarizes how the long-range volcanic-hazards assessment for Mount St. Helens was made and how that information was applied to the 1980 events. The report also describes how hazards-related information was provided to governmental agencies and the public, some problems encountered, and the effectiveness of the assessments.

ACKNOWLEDGMENTS

We thank the personnel of the Gifford Pinchot National Forest, USFS, for providing personnel, space, and equipment to the USGS during the 1980 eruptions. Special thanks are extended to R. D. Tokarczyk, P. R. Stenkamp, E. C. Osmond, J. L. Unterwegner, G. J. Theisen, and Michael Lowry. Establishment of the USFS Emergency Coordination Center in Vancouver and organization of USFS-USGS press conferences were instrumental in making USGS hazards information available to other governmental agencies and to the public, and the contributions of experienced USFS personnel and USFS logistic support added immeasurably to the USGS hazards-response capability.

METHOD OF ASSESSING LONG-RANGE HAZARDS AT CASCADE RANGE VOLCANOES

Hazards assessments by the USGS of volcanoes in the Cascade Range have been based on historic and geologically recent records of eruptions, on the premise that the record of past activity provides the best basis for anticipating probable future eruptive behavior. The prehistoric activity of each volcano is reconstructed by examining rocks and unconsolidated deposits on and around that volcano to determine their origin, age, and extent. The distribution of various kinds of future volcanic events and their possible frequency and consequences are then predicted from these data. This method of hazard assessment has some obvious limitations. Not taken into account are events that are possible but have not happened before at the volcano being studied, or events of much greater magnitude than those in the past. Nevertheless, the method allows an objective hazards assessment to be made for each volcano, based on its own eruptive history, and we believe this approach is valid for the purpose of long-range land-use planning.

The volcanic-hazards assessment for Mount St. Helens by Crandell and Mullineaux (1978) was based chiefly on about 5 yr of investigations supplemented by information from Hyde (1975) and C. A. Hopson (unpub. mapping, 1974). The 1978 report describes the kinds of eruptions expected in the future and identifies areas that could be affected by various kinds of volcanic events. Although that report was designed to be used primarily as a basis for long-range planning, it also discusses ways in which impending eruptions can be recognized, recommends actions to be taken before an eruption, and suggests ways to mitigate the effects.

The immediate need for scientific background information when precursory activity begins at a volcano was well illustrated at Mount St. Helens in late March 1980. Such information obviously should be acquired before an emergency arises because it typically requires several years to gather. Inasmuch as each volcano seems to have a behavior pattern that differs in detail, hazards assessments of all potentially dangerous volcanoes should be completed as soon as possible and should be reassessed periodically to provide up-to-date data for hazards mitigation when eruptions occur. Prompt assessments are justified even if no eruption occurs in the near future, because their principal objective is to guide the development of areas close to and adjoining volcanoes.

RESPONSE TO PRECURSORY EARTHQUAKES AND EARLY ERUPTIONS

OBJECTIVES

Our chief objective in responding to the initial volcanic activity in late March 1980, was basically the same as that for long-range planning—to appraise hazards that could result if Mount St. Helens were to erupt. We anticipated that some people would deny the existence of significant danger from the volcano and would criticize or resist efforts to protect lives and property. Nevertheless, we believed Mount St. Helens to be dangerous, that the risk was high close to the volcano, and that lesser but significant risk extended far beyond the immediate vicinity. We also thought it necessary to explain some limits of risk; for example, in answer to questions from the public, we responded that eruptions of Mount St. Helens would not destroy the countryside from northern California to British Columbia with fast-moving lava flows, pyroclastic flows, or toxic gases. Thus, we not only discussed the dangers we believed were real, but also attempted to dispel public concern over dangers that did not exist.

A second objective was to explain the nature of volcanic activity and resulting hazards in plain lan-

guage, both to officials who were required to make decisions and to representatives of the news media and the general public, to help them understand the risk and the efforts being made to mitigate it.

We intended to provide information useful for anticipating the possible effects of eruptions but did not attempt to predict the specific time of eruptions. That position was difficult for many to accept, because they believed we could and should make such predictions, and because such predictions were being made by others. Although scientific predictions of eruptions could be made in probabilistic terms, we believed it was not possible to reliably predict specifically the kinds and times of eruptive events.[1]

We assumed responsibility for providing information to aid officials in making decisions about responses to the threat of eruption, including access to and closure of the region around the volcano, but we deliberately avoided making such decisions ourselves. This policy was not always understood or favorably received, and we had requests to make decisions both for public agencies and private companies. The limit we placed on our responsibility was based on the realization that many factors besides potential hazards must be considered for land-access decisions. Other considerations include such things as political boundaries, land ownerships, land-management responsibilities, condition of access and evacuation routes, manpower and financial limitations, and adverse consequences of closing areas to the general public and to landowners and people dependent on access for their livelihood. For these reasons, land-access restrictions often did not closely match forecast volcanic-hazard zones (for example, see fig. 454).

SPECIFIC ACTIVITIES

We first learned of the onset of events at Mount St. Helens on Friday, March 21, through a telephone call from Charles Tonn of the Gifford Pinchot National Forest. An earthquake had been felt at the volcano on the previous day, apparently a single event whose epicenter was reported by the USGS National Earthquake Information Service as about 10 km northeast of the base of Mount St. Helens. By March 24 frequent earthquakes were being felt and instrumentally recorded. On the 24th we talked repeatedly by telephone with USFS officials, geophysicists in Seattle, and other colleagues in and outside the USGS. We discussed the significance of the seismic activity, the types of eruptions that were considered likely, planning for a possible eruption, and agency responsibilities. One conversation with USFS personnel, for example, included a discussion of the safety of USFS facilities at Spirit Lake and near the east end of Swift Reservoir and the need to close the upper slopes of the volcano because of snow-avalanche danger.

Telephone conferences continued on March 25, and that evening Mullineaux arrived in Vancouver to provide the same kinds of information at the site where decisions were to be made. Facilities of the USFS in Vancouver became the focus of response efforts; USGS, USFS, other concerned agencies, and representatives of the private sector met there to coordinate contingency plans. An ECC (Emergency Coordination Center) was set up to receive and evaluate all information regarding the volcano and to disseminate information and warnings.

On March 26, the possible kinds of eruptions at Mount St. Helens and the possible kinds and extents of danger that could result were described by Mullineaux at a meeting in Vancouver of representatives of governmental agencies and private industry. As one result of the meeting, the USFS and county administrations extended closures beyond the immediate flanks of the volcano. Also on March 26, Mullineaux described the general nature of potential volcanic activity and hazards at a joint USFS/USGS press conference.

During the week of March 24–30, we arranged with the U.S. National Weather Service and the U.S. National Oceanic and Atmospheric Administration Air Resources Laboratories to receive upper air data from which potential ash-fall areas downwind from the volcano could be predicted and plotted daily by computer (Smith, 1980; fig. 453). These wind data, especially the graphic plots, showed the predicted paths of ash at various times and altitudes on an outline map of the northwestern United States. They provided a ready means of illustrating probable hazard zones from wind-carried ash during eruptions, and they were used to plan day-to-day operations around the volcano by the USGS and by various other agencies and private industries.

[1]Most significant eruptions since May 18 have been preceded by minutes or hours of seismicity (Malone and others, this volume), allowing warnings of possible activity to be issued to the public prior to onset of the eruptions. The specific kind, magnitude, and timing of eruptions, however, have not yet been predicted.

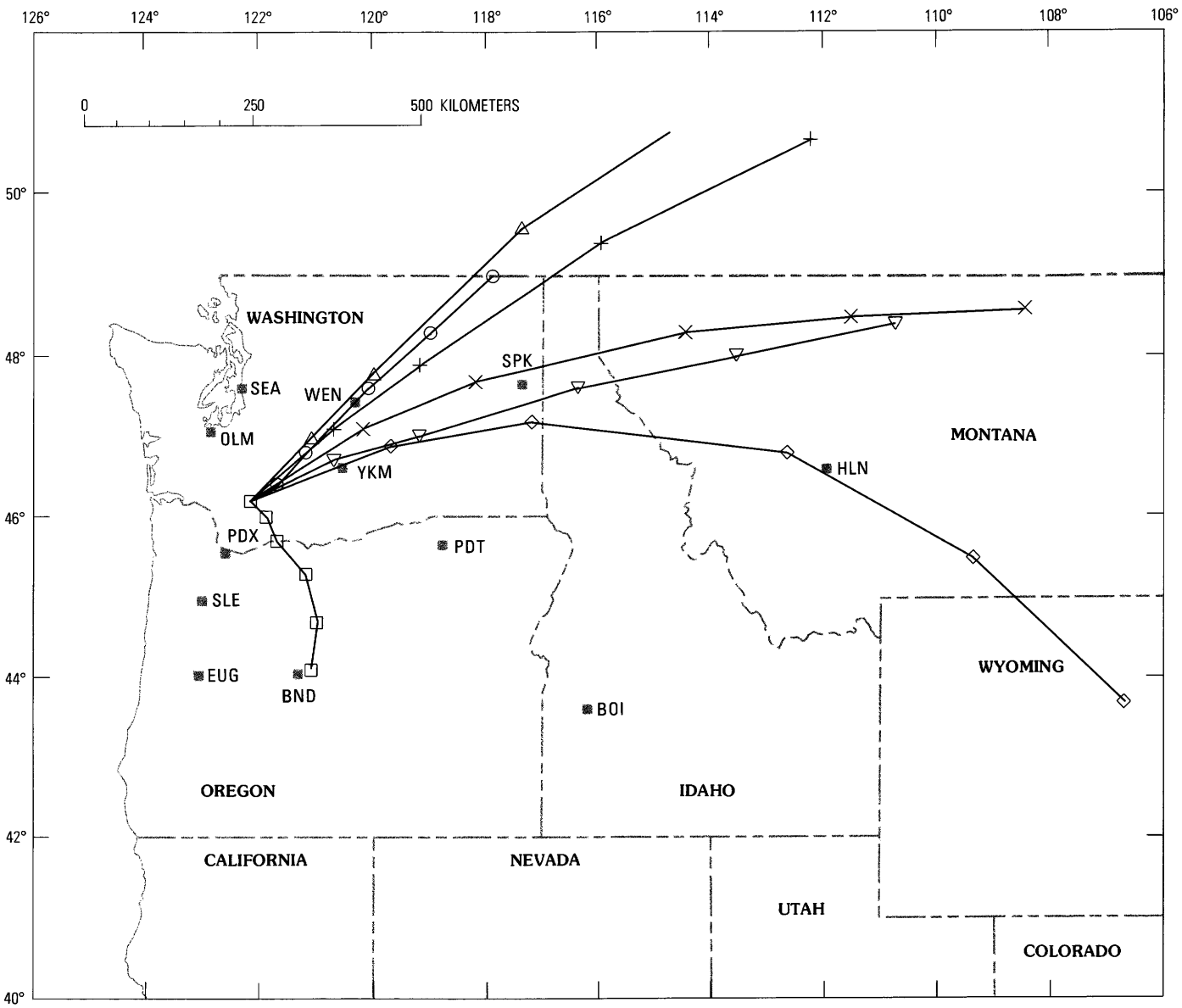

EXPLANATION

SEA	Seattle
OLM	Olympia
PDX	Portland
SLE	Salem
EUG	Eugene
WEN	Wenatchee
YKM	Yakima
PDT	Pendleton
BND	Bend
SPK	Spokane
BOI	Boise
HLN	Helena

ALTITUDE		
	FEET	Km
□	5000	1.5
○	10,000	3
△	18,000	5.5
+	23,000	7
×	30,000	9
◇	39,000	12
▽	52,000	16

Figure 453.—Computer plot of predicted movement of ash at seven different altitudes, erupted at 1100 PDT on May 18, 1980. The first two symbols on each altitude track show positions of airborne ash 3 hr apart; symbols farther along each track show 6-hr intervals.

The first eruption on March 27 produced a small, new crater within the old summit crater and, across the summit of the volcano, a set of curved fractures that extended down the northeast and northwest flanks. Aerial surveys by several observers on March 27 after the eruption showed that the block north of the fractures had dropped and that the fractured north flank showed possible outward extension. Austin Post of the USGS suggested that the north side of the volcano might have slumped. All these observations led to the view that much of the north side of the volcano had become unstable, and a large landslide on the north slope was identified thereafter as a potential hazard.

On April 1, potential hazards from an eruption of Mount St. Helens were summarized in a USGS press release (see text of press release at end of report). On the same day, a volcanic-hazards zonation map (fig. 454), newly prepared on a large-scale USFS map, was shown to agencies and companies responsible for the land surrounding the volcano. The map showed pyroclastic-flow, mudflow, and ash-fall hazards and their possible extents at three different magnitudes: (1) the largest known from the geologic record at Mount St. Helens, (2) the relatively small but most likely events, and (3) events of intermediate scale. That map was used as the primary base for oral hazards-assessment statements during April and the first half of May.

On April 14, at a meeting with representatives of the USFS, and the Washington State Department of Transportation, Highway Department, and State Patrol, Crandell described the character of a possible massive avalanche from the north side of the volcano and its importance to road closures along the North Fork Toutle River, pointing out that it could move into the Spirit Lake area and possibly extend down the North Fork Toutle River valley. Crandell also explained that such a landslide or a large earthquake could trigger a magmatic eruption. The magmatic eruption was expected to be like those of the past, however, the chief dangers being voluminous airborne ash and pyroclastic flows. These potential events and their consequences were described to other groups on April 23, and on the same date the possibility of a large landslide was stated in a letter from Crandell to the Forest Supervisor of Gifford Pinchot National Forest.

No magma was erupted from March 27 to May 18. Rock debris erupted during that period consisted of older volcanic rock that had been pulverized by steam explosions. Nevertheless, the continuing possibility of a magmatic eruption was recognized because of the continuing deformation of the north flank of the volcano, caused, presumably, by the injection of molten rock into the cone. However, we could neither predict the kind, scale, and time of a magma eruption, nor could we be sure that one would occur. Historical records show that some volcanoes in the world have undergone precursory activity like that at Mount St. Helens in March, April, and early May, without having later erupted magma.

After the climactic May 18 eruption, the dacitic composition of the magma involved was known, and the potential for further explosive eruptions was clear. A new assessment of potential hazards, therefore, was made on May 26, and another hazards map was prepared (fig. 455). Because the geologic record of past activity suggested that another eruption of equal or even greater magnitude than that of May 18 was possible, the map showed hazard zones for the maximum expectable extents of pyroclastic flows, routes of mudflows, and potential ash thicknesses at various distances from the volcano. In addition, because the large new crater was open to the north, a wedge-shaped area north of the vent was identified as a zone of high risk from lateral blasts and pyroclastic flows.

Reassessments of volcanic hazards on July 1 and September 1 included minor revisions of the May 26 assessment as a result of changes in the activity of the volcano. For example, domes that formed in the crater after the June 12 and August 7 eruptions raised the possibility of lateral blasts with little or no warning. Both domes were, in fact, destroyed by later explosive eruptions, and heavy rock fragments were thrown many kilometers.

After the May 18 eruption, overall seismic activity was much lower than before (Weaver and others, this volume), and small increases in seismic activity prior to eruptions could be identified. Such precursory earthquakes were recognized by the seismic research group in Seattle several hours before eruptions on June 12, July 22, August 7, and October 16. (For example, see "Log of events on July 22, 1980," at end of report.)

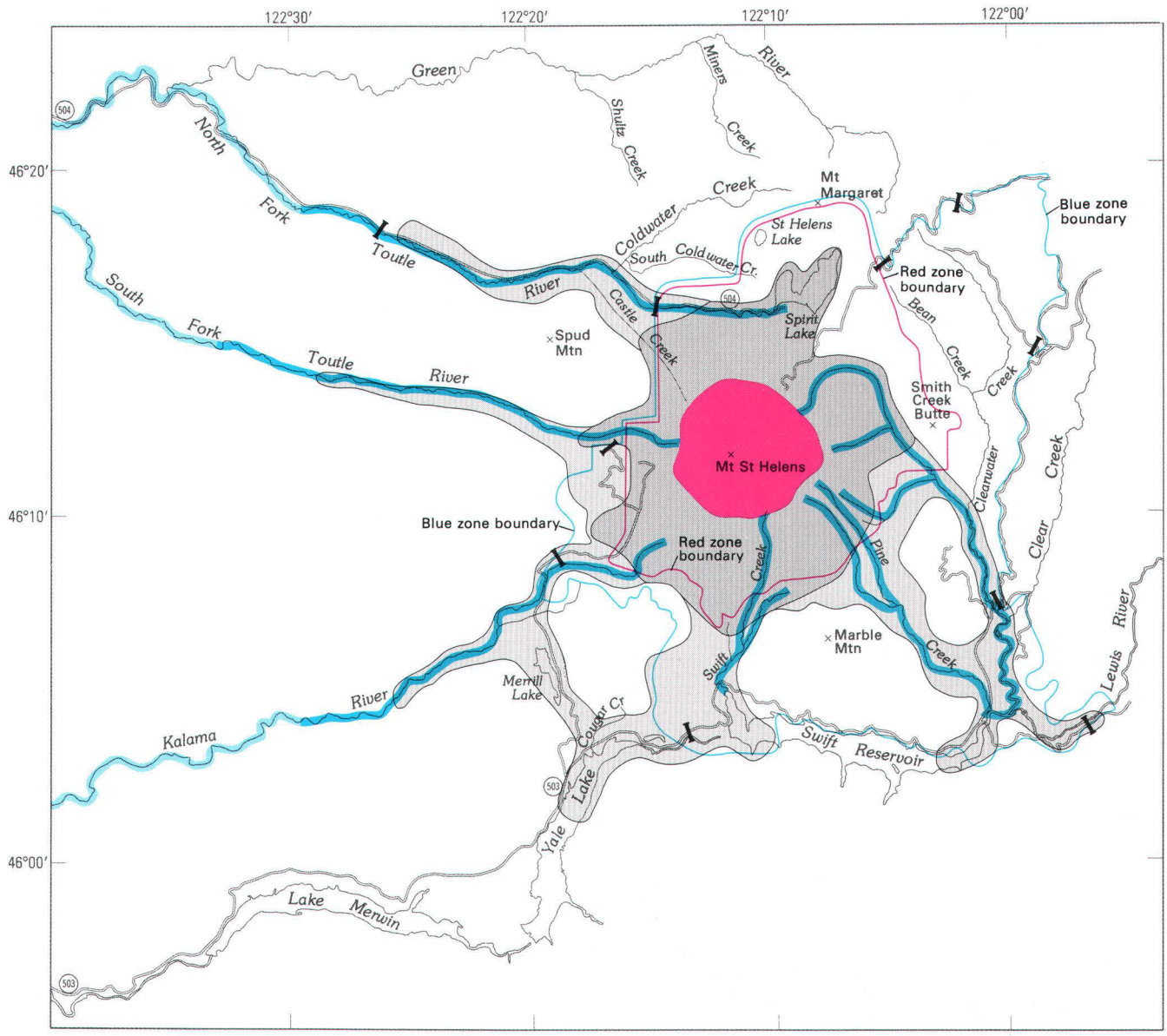

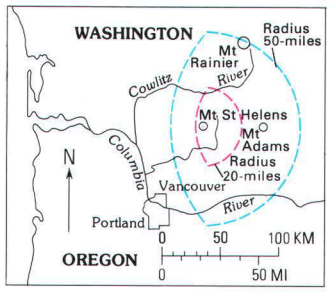

EXPLANATION

TYPE OF EVENT

MAGNITUDE OF EVENT	Pyroclastic flow	Mudflow	Maximum ashfall thickness (Inches)	
			At 20 miles	At 50 miles
Large			39	12
Medium			4	3
Small			1	<1

I - Road block effective on May 18, 1980

DISSEMINATION OF HAZARDS-RELATED INFORMATION

The main channels for distributing hazards-related information were through the ECC at the USFS offices in Vancouver, and at meetings and press conferences. The ECC was staffed on a 24-hr basis by the USFS and during critical times by the USGS and representatives of the Washington Department of Emergency Services, county sheriffs and other governmental agencies, and by several private companies. The ECC functioned as a central point for gathering and interpreting observational and monitoring data from the volcano. It was the point from which warning information could be rapidly distributed to authorities and the public.

Volcanic-hazards information also was distributed by briefings of (1) single agencies and groups of agencies; (2) individual companies; (3) individuals and groups of citizens; and (4) specific Federal, State, and local officials, and (5) by release of information through news media.

At the ECC and other USFS facilities in Vancouver, the USGS hazards coordinator discussed potential hazards at frequent meetings with various Federal, State, and local representatives. Participants in these meetings included Federal agencies such as the USFS, Federal Aviation Administration, Federal Energy Regulatory Commission, and Air Force; State agencies such as Department of Emergency Services, Department of Natural Resources, and Departments of Transportation, Highways, Game and Fisheries, and State Patrol; and commissioners and sheriffs of Cowlitz, Skamania, Lewis, and Clark Counties. Private companies included Pacific Power and Light Co., Portland General Electric, Burlington Northern, International Paper, and Weyerhaeuser Co. Information provided in these meetings was one factor used to establish boundaries of restricted areas, to determine access policies, and to plan for and mitigate the effects of eruptions.

On many occasions, the hazards coordinator provided hazards information, at the request of concerned citizens, at public meetings in various communities to help them deal with eruptions and to dispel unwarranted fears and concerns.

On still other occasions, the coordinator presented summaries concerning the current state of the volcano, potential hazards, and the long-term outlook for further eruptive activity to representatives of congressional committees, Senators and Congressmen and their staffs, to the Governors of Washington and Oregon, and on two occasions to the President of the United States.

Hazards information was made available to the general public chiefly through press conferences, as many as three in a single day, held initially in conjunction with the USFS in Vancouver and later in conjunction with the Federal Emergency Management Administration. Hazards information we presented at these conferences consisted chiefly of the current activity of the volcano and potential dangers. Information at press conferences, however, often included explanations of volcanism in general and the possible effects of eruptions on areas well beyond the vicinity of Mount St. Helens. These kinds of information were also distributed through interviews in person and by telephone for live and taped television and radio presentations and so-called "talk programs." For additional information on the volcano, the USGS released a daily update, written by the coordinator of the monitoring program at the volcano. These updates described eruptions and earthquake activity, monitoring and observational data, and other noteworthy events during the preceding 24 hr.

Figure 454.—Volcanic-hazards zones, originally drawn on USFS map (approximately 1/2 in. = 1 mi), April 1, 1980. This map shows kinds and extents of hazards for eruptions of three different magnitudes and was used for hazards briefings during April and early May. Also shown are Washington State red and blue closure zones around the mountain, and road blocks effective April 30. The red zone was closed to everyone except administrative personnel of government agencies, scientists, law-enforcement personnel, and search-and-rescue personnel, and the blue zone was also closed to everyone except those described above, although access was allowed from 0800 to 1700 by landowners or controllers with a permit. Inset shows boundaries of two ash-fall-hazard zones that reach 20 (red) and 50 (blue) mi north, east, and south of the volcano.

SOME PROBLEMS

One problem we faced was conflicting judgments as to the likelihood and magnitude of eruptions. Public officials needed scientific information and advice from the outset so that decisions could be made to protect lives and property, and differences of opinion in regard to that information and advice had to be expected. For its own credibility, however, the scientific community should attempt to provide advice through a single, authoritative source rather than through many sources of diverse background and knowledge. At Mount St. Helens, we were not the only persons capable of providing competent

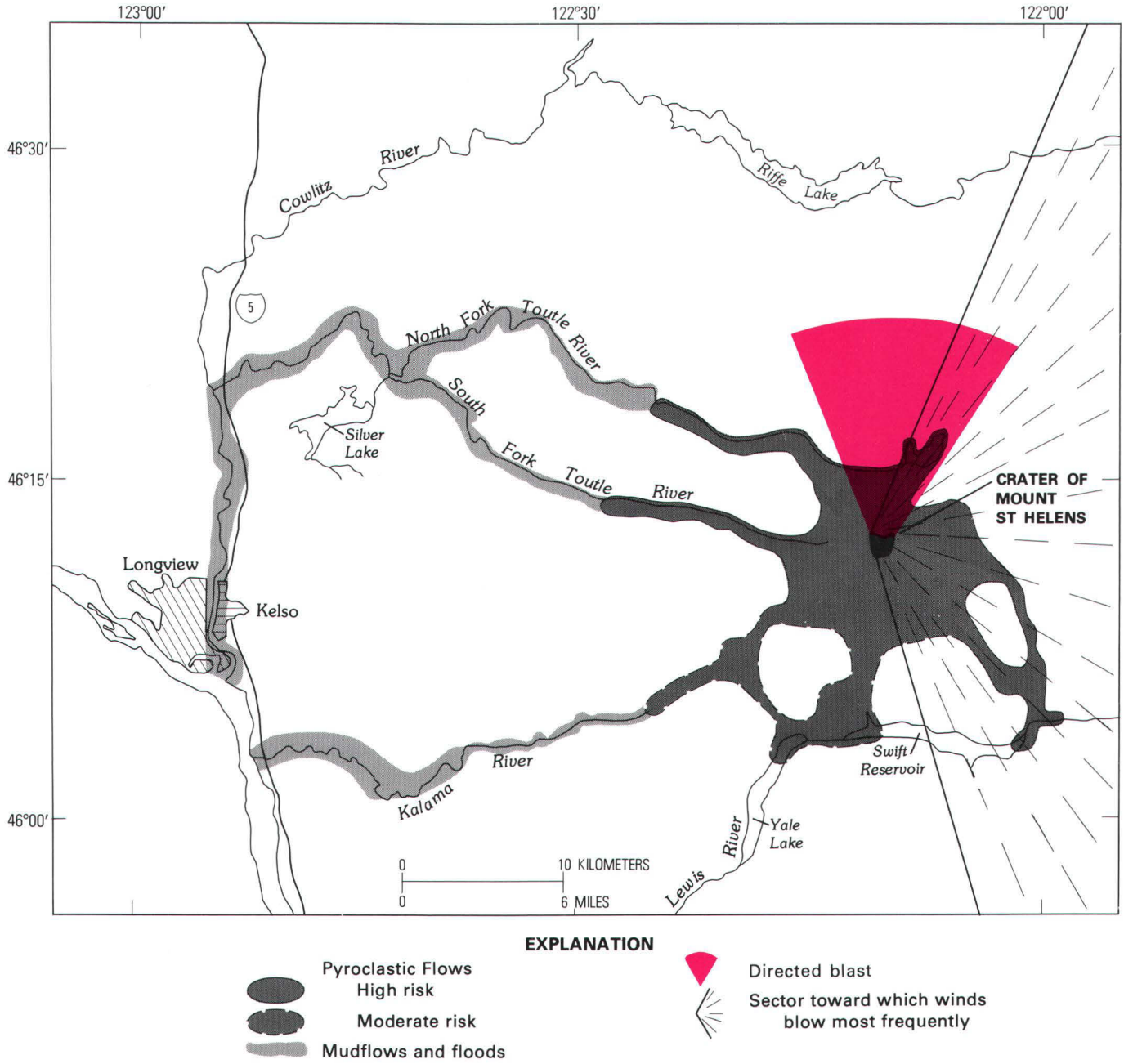

Figure 455.—Hazards zones as drawn May 26, 1980, after May 18 dacitic magmatic eruption. Map shows maximum expectable extents of pyroclastic flows, mudflows and floods, and directed blasts, and sector into which winds were most likely to blow ash. Maximum expectable ash-fall thicknesses versus distance were also calculated

scientific advice, but we did have the advantages of possessing relatively complete information on the past history of the volcano and of being in a position to receive data gathered by instrumental monitoring of the volcano. Some other scientists contacted USGS personnel at Vancouver to resolve differences of opinion, but a few officials occasionally received advice or warnings that conflicted with ours. When aware of a conflict, we attempted to determine the source of the statement or warning, to contact the source, and to resolve the differences. Resolution of such differences is important because it is difficult for public officials to evaluate conflicting scientific advice; loss of credibility for all scientists is likely if such problems cannot be resolved by the scientists themselves.

Some State agencies and private companies utilized scientific advice from sources other than the USGS, partly because those organizations needed specific advice for their special problems. The scientists involved usually coordinated their hazards assessments with the USGS, and conflicts in advice were minimal.

A second problem was related to public perception of risk and understanding the concept of gradational risk, and the meaning of lines drawn around volcanic hazards zones on a map. Ideally, risk would be equal everywhere within any one zone. Actually, risk generally increases progressively toward the volcano within any one zone and from one zone to another. Zone boundaries attempt to show points of equal risk. Theoretically, however, to represent degree of risk correctly, an infinite number of lines would have to be drawn, each of which would mark successive small increases of risk as the volcano is approached. In practice, hazard-zone boundaries are seldom more than rough approximations. The lines drawn on our hazards maps, both before and after May 18, represented our best judgment of risk based on models developed from past events, on monitoring data as they became available, and on many assumptions. The locations of these lines have a factual basis, but they do not indicate absolute differences, or even large differences of risk from one side to another. Moreover, some degree of risk must exist even beyond the outer boundaries of the outermost hazards zones.

A third problem was that of informing the public quickly and accurately of our information and opinions. The most effective way of doing this was through newspapers, radio, and television. However, significant errors occasionally were introduced by the media into information released to the public, usually by the omission of qualifying words or phrases. These changes may have been unintentional, and perhaps were made because the qualifications seemed unimportant.

Still another problem was the need to reply to and deny rumors. Exaggerations and misinformation both caused needless anxiety for officials and public alike. For example, many times before May 18, lava was reported to be flowing down the flanks of Mount St. Helens, and glows were reported above the volcano at night, implying the existence of molten rock within the crater. At one time, a so-called "eyewitness" even reported that Mount Rainier was erupting. One persistent rumor that appeared after May 18, with no basis in fact, was that the south flank of the volcano was bulging. Had this been true, there would have been concern over the possibility of another massive landslide, but repeated aerial observations found no evidence of a bulge, and ground-deformation measurements showed no sign of large-scale displacement on the south flank of the volcano. The existence of a south-side bulge was repeatedly denied at meetings and press conferences, but the rumor persisted for many weeks.

Finally, assessment of potential hazards on a day-to-day or hour-to-hour basis at an active volcano must take a multitude of factors into consideration; it requires full-time attention during eruptions and periods of frequent activity. These periods of crisis are also accompanied by a very large increase in requests for information from news representatives, governmental officials, and other individuals. Demands on our time thus were greatest when we most needed to assimilate and evaluate monitoring and observational data, discuss the implications of these data with other scientists, and make judgments concerning potential hazards. Although the presence of more than one volcanic-hazards coordinator helped, this was a continuing problem for which we never found an ideal answer.

EFFECTIVENESS OF VOLCANIC-HAZARDS ASSESSMENTS

Eruptions from March 27 through May 17 were generally small and their effects were adequately anticipated by Crandell and Mullineaux (1978). During the May 18 eruption, the distribution and effects of

airborne ash, pyroclastic flows, mudflows, and floods generally followed published forecasts and hazards information released during April and early May. Ash was carried mostly eastward from the volcano, and pyroclastic flows were restricted to areas on or near its flanks. The extents and effects of mudflows on highways, bridges, and other structures were generally as predicted. The largest mudflow (about 14 million m^3) to reach Swift Reservoir was easily contained; the reservoir had been lowered by Pacific Power and Light Co. to accommodate a volume of as much as 125 million m^3, as advised by Crandell and Mullineaux (1978, p. C15–C16). Aggradation by mudflows and floods along rivers was generally as forecast, although the shallowing of the bed of the Columbia River, which blocked the ship channel near the mouth of the Cowlitz River, was not anticipated. The potential for a north-flank landslide, not anticipated by Crandell and Mullineaux (1978), had been recognized by USGS scientists because of deformation of the north flank of the volcano (Lipman, Moore, and Swanson, this volume), and had been repeatedly publicized prior to the May 18 eruption. The actual slide on May 18, however, was much larger than expected. The subsequent cataclysmic lateral blast extended about three times farther from the volcano than the largest known previous blast at Mount St. Helens, and it devastated an area that probably is 10–15 times larger.

The May 18 eruption of Mount St. Helens showed that catastrophic events can exceed any known precedent at the same volcano. The possibility of such unprecedented events raises a question as to the validity of volcanic-hazards assessments like those prepared for some other Cascade Range volcanoes (Mount Rainier—Crandell, 1973; Mount Baker—Hyde and Crandell, 1978; Mount Hood—Crandell, 1980; Mount Shasta—Miller, 1980). To what extent should events at one or more volcanoes be used as models to portray hazards at another? For example, although the landslide and lateral blast of May 18 were on a scale unprecedented in the previous history of Mount St. Helens, very large slides have occurred during historic time at some volcanoes in the world (Bandai-san, Japan—Sekiya and Kikuchi, 1889), and very large lateral blasts have occurred at others (Bezymianny, U.S.S.R.—Gorshkov, 1959; Shiveluch, U.S.S.R.—Gorshkov and Dubik, 1970).

As an extreme response, a volcanic-hazards assessment of a specific volcano could be based on the largest known eruption at any similar volcano. This approach is not practical for purposes of land-use planning, however, because restrictions that would fully anticipate such events would require major changes in land use over very large areas and would be very costly (Crandell and Mullineaux, 1975). We believe that a more practical approach for the purpose of land-use planning is to base a hazards assessment on the documented history of the volcano being studied. After precursory or eruptive activity has begun, however, day-to-day and week-to-week hazards assessments should take into consideration not only the past behavior of the volcano, but also past events at other similar volcanoes that seem to be possible, based on ongoing observations and monitoring.

There still would be the problem, however, of determining boundaries of hazard zones for unprecedented events. There is the danger of losing credibility even for the warnings and hazard zones based on events known to have occurred before; at Mount St. Helens, there was considerable opposition to closures of areas that were severely affected by prehistoric eruptions. If boundaries based on eruptions at other volcanoes were placed far enough from a volcano to rule out any significant risk, much public criticism could be anticipated—criticism that would intensify if the predicted event did not take place, inasmuch as great inconvenience and economic loss probably would have resulted. If less conservative boundaries were drawn closer to the volcano, severe criticism could also be expected if the catastrophic event did occur and lives were lost. The dilemma has no easy solution. The most appropriate solution probably should be sought through a consensus of earth scientists, social scientists, economists, and officials responsible for public safety. The result would be a judgment of balance between predicted range of risk and amount of risk acceptable to society.

Eruptions of May 25, June 12, July 22, August 7, and October 16–18 were small compared to those of May 18, and the types and distribution of the resulting deposits were well within limits forecast by the respective hazards assessments that preceded them. Each of the eruptions produced pyroclastic flows that moved out from the crater onto the broad apron to the north. Small volumes of airborne ash also were erupted.

Ash-fall extents predicted in Crandell and Mullineaux (1978) were based on the distribution of ash-fall deposits of the past, and on average wind directions from the approximate altitude of the summit of the volcano to the highest expected altitudes of strong

winds. These factors led to the conclusion that significant amounts of ash would usually fall along relatively narrow sectors from north-northeast clockwise to south-southeast from the volcano. During the May 25 and June 12 eruptions, however, winds in different directions at different altitudes spread small volumes of ash over relatively wide sectors and affected many communities in western Washington and northwestern Oregon. Furthermore, the small amounts of ash that fell were very troublesome and had significant economic consequences (Schuster, this volume), even though they did not seriously endanger human life or health. Thus, the directions of prevailing winds should not lead investigators to overlook the possible effects of ash falls in areas that are usually upwind from the volcano.

CONCLUSIONS

The explosive eruptions of Mount St. Helens created an emergency for which the public and local governmental officials had no previous experience. A general lack of knowledge concerning volcanic processes and related hazards resulted in an immediate need for information and advice from qualified scientists. Our response to this need was greatly facilitated by a hazards assessment that had been completed and published prior to the beginning of eruptive activity (Crandell and Mullineaux, 1978).

An extensive monitoring network around Mount St. Helens provided abundant information useful in day-to-day hazard appraisals. Quantitative data from deformation monitoring of movements on the north flank of the volcano were used as a justification in keeping the Spirit Lake area closed to the public before the eruption of May 18. After May 18, the seismic monitoring network around Mount St. Helens provided warnings of possible activity as much as several hours in advance of eruptions (Malone and others, this volume).

We were able to disseminate hazards information quickly to the public and to agencies and companies responsible for safety around the volcano chiefly because the USFS had capable persons available to coordinate with other agencies; these were experienced people who had previously handled emergencies such as forest fires. The USFS provided space and logistical services for USGS personnel and set up the ECC to distribute hazards information, advisories, and warnings. The role played by the USFS contributed immeasurably to the quality of our response to the emergency.

Our experiences showed the need, in an emergency such as this, for volcanic-hazards coordinators who are familiar with the eruptive history of the volcano, with the techniques of assessing volcanic hazards, and with details of the local physical geography and such features as highways, communities, and various other kinds of land use around the volcano. These kinds of knowledge give a hazards coordinator a broad perspective of the problems caused by eruptions, and also help establish the coordinator's credibility in the eyes of the public and officials responsible for coping with the emergency.

REFERENCES CITED

Crandell, D. R., 1973 [1974], Map showing potential hazards from future eruptions of Mount Rainier, Washington: U.S. Geological Survey Miscellaneous Geological Investigations Map I-836, scale 1:250,000.

———1980, Recent eruptive history of Mount Hood, Oregon, and potential hazards from future eruptions: U.S. Geological Survey Bulletin 1492, 81 p.

Crandell, D. R., and Mullineaux, D. R., 1975, Technique and rationale of volcanic-hazards appraisals in the Cascade Range, northwestern United States: Environmental Geology, v. 1, no. 1, p. 23–32.

———1978, Potential hazards from future eruptions of Mount St. Helens volcano, Washington: U.S. Geological Survey Bulletin 1383-C, 26 p.

Crandell, D. R., Mullineaux, D. R., and Rubin, Meyer, 1975, Mount St. Helens volcano; recent and future behavior: Science, v. 187, no. 4175, p. 438–441.

Gorshkov, G. S., 1959, Gigantic eruption of the volcano Bezymianny: Bulletin Volcanologique, ser. 2, v. 20, p. 77–109.

Gorshkov, G. S., and Dubik, Y. M., 1970, Gigantic directed blast at Shiveluch Volcano (Kamchatka): Bulletin Volcanologique, v. 34, no. 1, p. 261–288.

Hoblitt, R. P., Crandell, D. R., and Mullineaux, D. R., 1980, Mount St. Helens eruptive behavior during the last 1,500 years: Geology, v. 8, no. 11, p. 555– 559.

Hyde, J. H., 1975, Upper Pleistocene pyroclastic-flow deposits and lahars south of Mount St. Helens volcano, Washington: U.S. Geological Survey Bulletin 1383-B, 20 p.

Hyde, J. H., and Crandell, D. R., 1978, Postglacial volcanic deposits at Mount Baker, Washington, and potential hazards from future eruptions: U.S. Geological Survey Professional Paper 1022-C, p. C1–C17.

Miller, C. D., 1980, Potential hazards from future eruptions in the vicinity of Mount Shasta volcano, northern California: U.S. Geological Survey Bulletin 1503, 43 p.

Sekiya, S., and Kikuchi, Y., 1889, The eruption of Bandai-San: Imperial University of Japan College Science Journal, v. 3, pt. 2, p. 91–172.

Smith, W. K., 1980, A plotting program for producing ashfall prediction maps from output of the NOAA forecast trajectory program—Application to and examples from the 1980 Mount St. Helens eruptions: U.S. Geological Survey Open-File Report 80-2005, 33 p.

TEXT OF U.S. GEOLOGICAL SURVEY PRESS RELEASE (prepared 1800 PST. April 1, 1980)

PAST EFFECTS OF MOUNT ST. HELENS VOLCANO

(Statement prepared by the U.S. Geological Survey at the request of State and local officials to describe the kind and scale of eruptive and related activity that occurred in the past at Mount St. Helens volcano.)

Should the present minor activity at Mount St. Helens volcano develop into a major eruptive phase, the following observations are given to aid local officials and the general public. These observations are condensed and paraphrased from information published in 1978 in U.S. Geological Survey Bulletin 1383-C, "Potential Hazards from Future Eruptions of Mount St. Helens Volcano, Washington," and are based on the eruptive effects of previous Mount St. Helens eruptions.

Major eruptive activity could result in the deposition of significant amounts of ash anywhere from north clockwise to a direction south-southwest of the volcano. It is unlikely with continuation of current activity that more than 1 inch of ash will fall beyond a radius of 20 miles from the summit of the volcano. Because winds at the altitudes reached by strong ash eruptions blow predominantly during any period of one or a few days in directions within this 200-degree sector, there is little likelihood that appreciable amounts of ash will fall northwest of the volcano.

The present level of activity probably presents no danger to the lives or health of people in areas more than 20 miles north, east, and south of the volcano, or more than 10 miles west of the volcano. In the past when very large eruptions have occurred, the most dangerous event has been the ejection of ash, rock, and light-weight pumice that can rise tens of thousands of feet above the volcano and be carried downwind. A few eruptions of Mount St. Helens have deposited as much as 3 feet of pumice at a distance of 20 miles, 8 inches at 60 miles, and 2 inches at 125 miles. Over these distances, the maximum size of individual pumice fragments decreases away from the volcano from several inches in diameter to the size of sand. If a similar eruption occurred, pumice would fall over a sector downwind from the volcano that could be at least 10 miles wide at a distance of 50 miles. The direction taken by the pumice would depend on wind directions at the time of the eruption.

Past experiences with other volcanic eruptions indicates that ashfall does not pose a serious threat to human health if care is taken to avoid prolonged exposure to ash-laden air and, in areas of greatest accumulation (for example, deeper than 5 or 6 inches), if ash is not allowed to accumulate on roofs that might collapse beneath the burden. Brief exposure to ash may cause minor irritation to eyes, nasal passages, and skin, but generally is not a threat to people in sound health.

Areas downwind may be cast into darkness for a short time by ashfall and may experience temporary loss of television, radio, and telephone communication. During falls of ash, people should remain indoors and avoid prolonged breathing of ash-laden air. Under extreme conditions, a period of heavy ashfall could last a few days, but it would not be expected to last more than one day at any one place.

Although the odor of sulfur may be detected at some distance from the volcano, there generally is no hazard from toxic gases beyond the immediate vicinity of the volcano, except for persons especially susceptible to fumes that contain sulfur and other gases.

Property and machinery may be damaged by exposure to abrasive ash, which may be especially hazardous to aircraft, and to mildly acidic rainfall, which may accompany ashfall. Property damage can be minimized by removing ash from metal and painted surfaces as soon as possible. The fall of even a thin layer of ash can harm agricultural crops as well as other kinds of vegetation, but ash, in many cases, can be removed from leaves by spraying with water.

Potential hazards from the fall of pumice decrease rapidly in severity downwind, so that beyond a distance of 20 miles pumice from most eruptions is most likely to cause maintenance and cleanup problems than to present a direct hazard to human life or property. However, if small amounts of pumice fell for a period of days or weeks, they could have serious cumulative effects on health and economic welfare.

In the past, the fall of large amounts of pumice on the flanks of Mount St. Helens has caused hot pumice to flow down valley floors for distances of as much as about 15 miles. In eruptions elsewhere in the world such pumice flows have been observed to travel at speeds of 30 to more than 90 miles per hour. Either

the fall of pumice on the flanks of the volcano or hot pumice flows could melt snow and cause floods and mudflows to move down the floor of valleys that head on the volcano. In the past, mudflows have extended at least 50 miles down valleys that head on the north and west sides of the volcano, and are estimated to have traveled at speeds as much as 30 miles per hour. The potential for damage from these mudflows decreases with distance from the volcano, but during a mudflow, people should move to locations above valley floors.

LOG OF EVENTS ON JULY 22, 1980

Time	Events or responses
1040	Telephone ("hotline") call to USGS from seismic research group in Seattle advising that small earthquakes ($M < 2$) began occurring that morning within or at the base of the cone and that the events constituted "a definite change in the pattern of seismic activity since May 18."

Notified the following of increase in seismic activity and to be alert for the possibility of changes in volcanic activity at the mountain:

1042	USGS field parties.[2]
1044	USFS field personnel.[1]
1045	Personnel of Washington Department of Emergency Services and Federal Emergency Management Agency.[1,2]
1047	Pacific Power and Light Co. and Cowlitz County Sheriff's Office.[1]
1055	Weyerhaeuser Co., International Paper, Washington National Guard, and Seattle U.S. Federal Aviation Administration.[1]
1102	A nongovernment radio dispatcher and scientific ground party at Mount St. Helens.[1]
1058–1114	Randle, Packwood, Mt. Adams, Wind River, and St. Helens Ranger Districts.[1]
1114	By this time, all USFS ground parties within Red Zone had been notified of the alert except one.[1]
1115	USGS geologist reports from the mountain that one survey point on the rampart within the crater has apparently moved to the north at an accelerated rate compared to the previous several weeks.
1230	Telephone conversation between USGS and seismic research group in Seattle regarding seismicity.
1252	Discussed with FAA in Seattle seismic activity at mountain.[2]
1420	Telephone conversation between USGS and seismic research group in Seattle regarding continuing seismic activity.
1515	Weyerhaeuser Co. informed of details of increased seismic activity.[2]
1525	Telephone conversation with the University of Washington. Shallow earthquakes continuing and increasing in number. Earthquakes thought to be caused by avalanches are more frequent, and there may be very low level tremor.
1545–1549	Second notification about increased seismic activity issued to USFS and USGS field parties via radio and to Department of Emergency Services, Federal Emergency Management Agency, and Sheriff's departments.[1,2]
1553	Alerted all aircraft in vicinity of Mount St. Helens by radio of seismic activity.[1]
1604	Advised Washington State Division of Geology and Earth Resources of increased seismic activity.[1]
1714	Beginning of eruption. Observers in USFS observation plane report ash column has risen to 16,000 ft.
1714	USGS helicopters report details of eruption.
1715	Department of Emergency Services, county Sheriffs, and Federal Emergency Management Agency representatives notified of eruption in progress.[1,2]
1715–1744	Notification to the following agencies of an eruption in progress: Portland General Electric; Portland Water Bureau; Pacific Power and Light; FAA, Seattle; National Warning System; Burlington Northern; Army Corps of Engineers; Bureau of Indian Affairs; Weyerhaeuser; Portland Weather Bureau; U.S. Coast Guard; all Gifford Pinchot National Forest Ranger Districts; Washington State Department of Transportation; Washington Department of Natural Resources; International Paper; and Disaster Information Center.[1]
1716	USFS observation plane reports eruption plume climbing through 30,000 ft.
1718	All USFS field parties advised of eruption by radio and ordered to leave vicinity of Mount St. Helens.[1]
1720	Portland Weather Service reports that radar showed top of plume reached 45,000 ft, but is now down below 40,000 ft.
1720	Strong eruptive activity ended, plume dying down.

[1]Carried out by U.S. Forest Service.

[2]Carried out by U.S. Geological Survey.

1731 Observation plane reports that plume now consists of a white column to 16,000–17,000 ft.

1825 Observation plane reports beginning of new eruptive activity. Harmonic tremor recorded on USGS seismographs at ECC.

1831 Observation plane reports top of plume to 30,000 ft.

1835 Portland Weather Service reports that eruptive column reached 60,000 ft on radar.

1847 Observation plane reports top of plume down to 18,000 ft and that strong eruptive activity is over.

1901 Observation plane reports beginning of new eruptive event. This event coincides with harmonic tremor on USGS seismographs.

1905 USGS geologists in helicopter report pyroclastic flow moving out of the north side of the crater.

1907 Portland Weather Service reports maximum plume height of 45,000 ft on radar.

1910 Suggestion made to Cowlitz and Skamania County Sheriff's Departments that evacuation of Cougar should be considered, due to the increasing intensity of the three eruptive pulses and the nature of the harmonic tremor reported by the seismologists in Seattle.[1,2]

1911–2141 Eruptive activity continues with varying intensity until about 2141.

THE 1980 ERUPTIONS OF MOUNT ST. HELENS, WASHINGTON

SEISMIC MONITORING FOR ERUPTION PREDICTION

By STEPHEN D. MALONE[1], ELLIOT T. ENDO, CRAIG S. WEAVER, *and* JAMES W. RAMEY[1]

ABSTRACT

Two months of intense earthquake activity preceded the cataclysmic eruption of May 18, 1980. There was no unusual seismic activity preceding this eruption by hours or days. Five subsequent major eruptions had recognizable seismic precursors. These eruptions and their precursors were recorded by a seismic network rapidly installed around the mountain beginning on March 20. The eruptions of May 25, June 12, and August 7 were preceded by increases in the level of harmonic tremor, whereas the eruptions of July 22 and October 16 were preceded by increasing numbers of shallow volcanic earthquakes. For the latter four eruptions the precursors were recognized and warnings issued at least 2 hr before the eruption began.

INTRODUCTION

The seismic monitoring of the Mount St. Helens eruptions provided data for evaluating potential seismic precursors to eruptions. Whereas the eruption of May 18 had no seismic precursors that could be identified within hours or days before the event, subsequent eruptions had clear seismic precursors that, in later cases, led to specific warnings of the impending eruption. In this report we follow the seismic history of 1980 using only the data and methods of analysis that existed at the time. Two companion reports in this volume (Endo and others; Weaver and others) present details of the seismicity and include additional analysis that was not done at the time the data were collected. In this report, additional analysis of the data is not considered; rather, only the data that were available at the time for use in hazard analysis are evaluated. Looking at precursors or predictors in retrospect is considerably different from doing it as the events occur. We hope to give a feeling for what data and interpretations existed at the time and to capture the essence of seismic monitoring for hazard warning.

[1]Geophysics Program AK-50, University of Washington, Seattle, Wash. 98195

ACKNOWLEDGMENTS

Numerous individuals have volunteered much of their time and effort to support the seismic monitoring at Mount St. Helens. We wish to thank those staff and students who have spent long hours both in the laboratory and the field assisting with this research. Specifically we thank A. B. Adams, Ely Baker, Alex Bittenbinder, Christina Boyko, Steve Bryant, Bob Crosson, Wendy Grant, Duane Hesser, Jim Hudsput, Don Leaver, Caryl Michaelson, Bob Noris, Linda Noson, Dave Pekcham, John Taber, Judy Terreberry, Steve Walters, Ed Wildermuth, and Tom Yelin. Personnel with the USGS have helped with discussions and descriptions of activity at the volcano as well as assisting in helicopter access to the mountain and in station maintenance. Specifically we thank John Dvorak, Bruce Furokawa, Arnold Okamura, John Coakley and Ed Criley.

This work has been sponsored in part by USGS contract 14-08-0001-19126 and U.S. Department of Energy contract EY-76-S-06-2225.

THE MOUNT ST. HELENS SEISMIC NETWORK

In 1969 two small permanent networks of seismic stations were set up in Washington: one in eastern Washington, the other in western Washington. Both of these networks have been gradually expanded until by March 1980, the networks consisted of 58 telemetry stations; of these 36 were in eastern Washington and on the east flank of the Cascades, and 22 were in western Washington, primarily in and around the Puget Sound lowlands (Noson and Crosson, 1980). These stations are typical telemetered stations using a 1-Hz short-period vertical seismometer, a high-gain and low-noise amplifier-VCO, low-power VHF radio and (or) telephone telemetry such that as many as eight signals can be multiplexed on one communications channel (Noson and Crosson, 1980). The station SHW was operating on the west flank of Mount St. Helens at 1,423 m elevation, having been installed in 1972 as part of a USGS volcano-monitoring program (Endo and others, 1974). The next nearest station was LMW, a comparatively low gain station, located 54 km due north of the mountain.

During the early phases of the preeruptive earthquake sequence, many stations were hurriedly installed on and around the volcano. Within 28 hr of the first earthquake in the sequence that began on March 20, four new stations had been sited near the mountain; three of these were portable tape-recording units supplied by the USGS for a previously planned field program in the southern Cascades. One was a telemetry station located 30 km north-northwest of the mountain. Figure 456 is a map of the area showing the locations of the seismic stations and their dates of operation. By March 30, 11 seismic stations were operating within 35 km of the mountain, 10 of them newly installed. Later in the sequence five additional telemetry stations were added, including one located at 2,317 m elevation on the northeast flank of the peak at the Dogs Head. Three telemetry stations and three portable stations were lost in the May 18 eruption, although one of them, the telemetry station ELK, was repaired. Additional stations have been added since May 18 to reestablish a balanced network. The portable tape-recorder stations were removed in early July leaving a total of 11 stations operating as of October.

The entire telemetry network was recorded on a computer system at the University of Washington. The portable stations were recorded onsite on magnetic tape, which required data retrieval every 5 days and time-consuming digitization of selected periods back in the laboratory. The computerized recording system is modeled on the CEDAR computer system at the California Institute of Technology (Johnson, 1979), which records on digital tape only when a transient seismic signal is present on more than a few stations at the same time. This triggered online digital recording system had been started by about the first of the year in a test mode, and was fairly stable by the first of March. Our system was recording all 58 telemetry stations of the regional network at a digitizing rate of 100 samples/s by March 20 with only rare interruptions. It was easily expanded to accommodate new stations as they were added.

During the day-to-day observations of seismic activity, four visual drum recorders were used to monitor four diagnostic stations. From these records, lists of daily activity were updated on computer files and plots made of rate of activity versus time. The techniques for picking arrival times and hypocenter determination have changed rapidly during 1980. The online data-acquisition system was functioning well by early March, but it was not until July that even a crude offline computer-assisted analysis package was developed. The details of hypocenter determination techniques are covered in reports by Endo and others and Weaver and others (this volume).

MARCH 20–MAY 18 EARTHQUAKE SEQUENCE

The first earthquake in the Mount St. Helens eruption sequence that received particular attention occurred on Thursday, March 20, at 1547 local time (PST). Within an hour of its occurrence, the earthquake, estimated to be magnitude $M_{coda} = 4$ and location lat 46°13.36′ N., long 122°14.20′ W., had been evaluated by the record analysts at the university. It was the largest earthquake to occur near a Pacific Northwest volcano since a magnitude-4.8 event in 1974 near Mount Rainier (Crosson and Lin, 1975). The USGS and the USFS (U.S. Forest Service) were

advised of this earthquake and plans were made to mount a field program if aftershocks were to occur. On reviewing the Develocorder film records in detail, several much smaller earthquakes ($M < 1$) were discovered to have been recorded several days before the March 20 earthquake, the first possibly being as early as March 16.

By the following morning, March 21, it became obvious that aftershocks were taking place and that the deployment of additional seismic stations merited the effort. By Saturday, March 22, the earthquake activity had increased. Another magnitude–4 event occurred at 1422 Saturday afternoon. That evening the USFS was advised of the continuing activity and the possibility that the earthquakes represented the beginning of a volcanic event. As the activity continued and increased in intensity over the next several days, our interpretation changed from a main shock–aftershock sequence to an earthquake swarm with possible volcanic origin. On Monday, March 24, the volcanic hazards project of the USGS was informed of the situation as well as other local USGS personnel, USFS personnel and scientists in other institutions. The news media became aware of the activity, and by midmorning our phone lines were constantly ringing and our ability to perform needed analysis was impaired by the insistent inquiries for information and interpretations of what was happening. The arrival of a USGS volcanic hazards specialist, Donal Mullineaux, at the USFS offices in Vancouver that even-

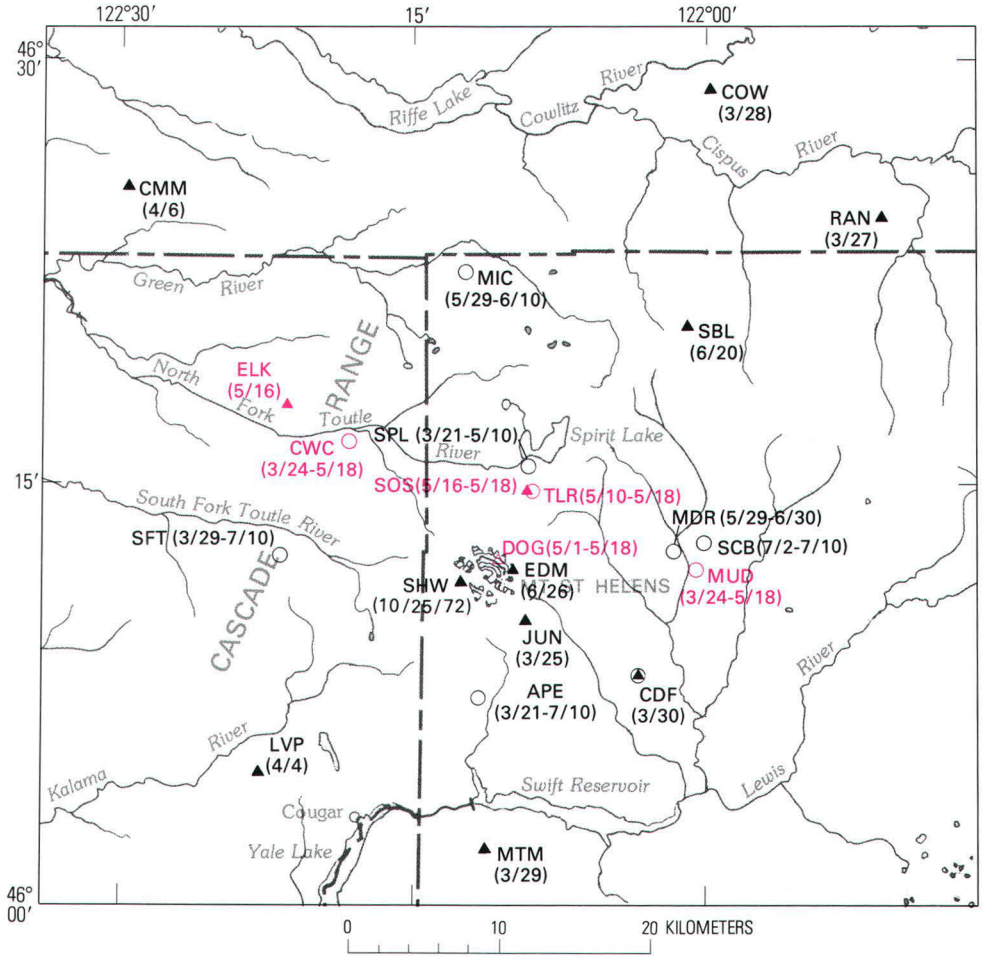

Figure 456.—Seismic stations in the Mount St. Helens network, with station codes and dates of operation; where only one date is shown, station still in use (1980). Solid triangles, operating telemetered stations; circles, portable tape recorder stations. Red symbols, stations destroyed in May 18 eruption.

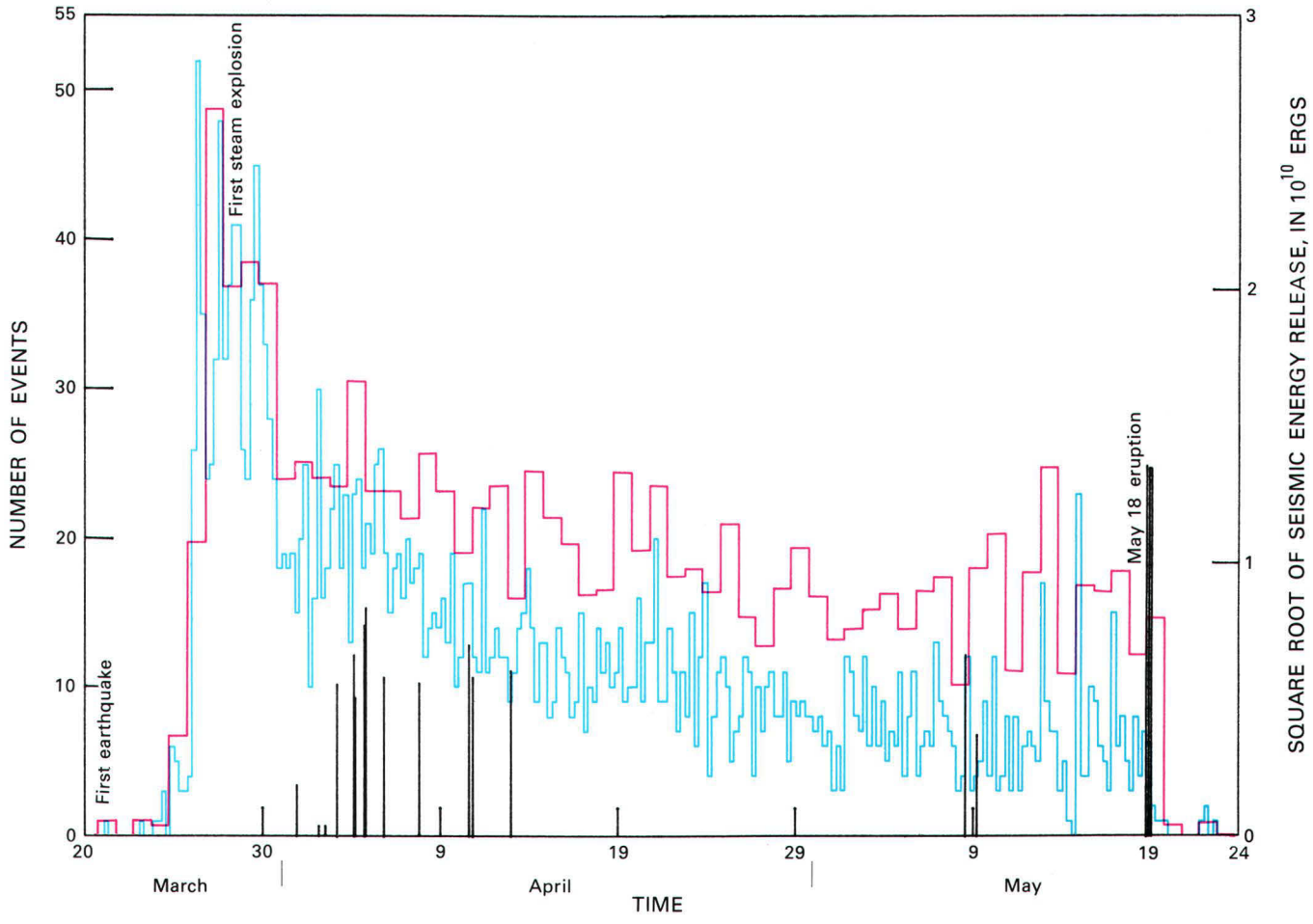

Figure 457.—Earthquake rate (blue line), square root of energy release (red line), and tremor periods (vertical black lines) from seismic data, reduced at time of recording. Energy is calculated from coda-duration magnitudes determined using the western Washington coda-duration-magnitude relation. Only earthquakes with coda duration longer than 100 s ($M = 3.2$) were used. Heights of black lines are proportional to length of tremor period.

ing helped considerably from our point of view. There was now someone for questions to be directed to about the volcanic activity that might occur.

The following day, Tuesday, March 25, the seismic activity increased dramatically. The use of the close-in station SHW for hourly counts of earthquake activity had to be abandoned because the seismograms from this station were becoming saturated (recording numerous events that overlapped). Station RAN, 30 km to the northwest was used to produce the earthquake counts, and only events with a coda duration of greater than 100 s ($M > 3.2$) were counted. The number of events was so great that smaller events were easy to miss, as they were buried in the codas of larger events. By that evening, magnitude–4 earthquakes were occurring at a rate in excess of three per hour. We did not see how this activity could continue without something dramatic happening. It was impossible to analyze in detail any significant number of these earthquakes. This intense activity continued through the night but was somewhat reduced by the next day. By Thursday, March 27, the rate of activity, while still quite high, had declined from the previous 2 days. The decline suggested that perhaps the mountain would not erupt. But at 1232 PST that afternoon, calls from several different observers indicated that an ash eruption from the summit had just occurred. This was the first of numerous steam eruptions that continued for the next several weeks.

The peak in the seismic activity had been reached on March 25, 2 days before the first eruption

(fig. 457). From then on the earthquake rate continued to decline gradually over the following 2 mo. A continuous record of number and size of earthquakes was kept on a computer file, and updated daily. This was used to look for trends in the seismicity which might give insight into future activity. We noticed that, while the number of earthquakes per unit time was decreasing, the energy release in these earthquakes was staying relatively constant, or at least was not declining as rapidly as the earthquake rate. At that time, it appeared from these data that the peak energy release occurred around the time of the first steam explosion and had declined to half that amount by mid-May, while the earthquake incidence rate peaked 2 days before the first explosion and was down to only one quarter of the peak by the middle of May. Subsequent analysis, consisting of careful and consistent rereading of all the major earthquakes, shows that the change in rate of activity, particularly the change in energy release was not as large as we first thought (Endo and others, this volume).

Evaluating the data from the rapidly expanding network was an impossible task. Only a fraction of the events recorded could be timed and located within even a week of the time they were recorded. Locations for earthquakes near the beginning of the sequence seem to scatter over a fairly large area around the mountain, although most were in the same area as the original event. There were a number of problems with the locations as they were determined early in the sequence. The network was still quite sparse, we did not have much knowledge about the local velocity structure, and reading errors were easily introduced due to the peculiar and complex waveforms of the events. Arrival times from different data sources had to be combined. The telemetry data were recorded by the computer system, but adequate software was not available to help pick these records and they had to be painstakingly analyzed by hand. By late April, the location information thus far obtained indicated that most of the events were occurring at shallow depth (less than 5 km) under the north flank of the mountain. This information, as well as the early evidence of slope failure and the expanding bulge in this region (Lipman, Moore, and Swanson, this volume), indicated that potential hazards from eruptions were higher to the north, in the Spirit Lake area, than to the south (Miller and others, this volume).

Changes in the character of individual earthquakes were observed during the 2-mo period, March 20–May 18. A distinct difference between high-frequency events and low-frequency events was noticed and noted in the computer log but no interpretation or trend in these events was made at that time (fig. 458). Magnitude-4 earthquakes were routinely occurring at a rate of several per day. At this high rate we were not sure of what changes might be an immediate precursor to a major eruption. We were on alert for major changes such as a significant increase or decrease in the earthquake rate or an unusually large event. However, because we had seen a very high earthquake rate on March 25 without a major eruption following, we were not certain how to interpret such an observation. A decrease in earthquake rate could be, of course, a sign that the sequence was drawing to a close as well as a precursor to an impending eruption.

HARMONIC TREMOR

Fourteen individual periods of strong harmonic tremor were observed on stations as far as 110 km from the mountain. The first occurred at 1217 PST on March 31 and lasted 2 min. This period of tremor was not recognized as such until the next day when a 3-min period of stronger tremor occurred at 1930 PST. This tremor saturated the seismic stations located on the mountain and was well recorded on stations all across southwestern Washington. Early the following morning there was another 3-min tremor period, and the following evening at 1935 PST a very strong tremor lasting for 15 min was observed. Figure 458 illustrates the seismic record for a portion of tremor along with typical earthquakes. The intensity of this tremor led us to speculate that the mountain might actually be in eruption at that time; however, reports from airborne visual observers indicated nothing unusual taking place. In fact, at no time during the following weeks did harmonic tremor periods obviously correlate with any visual phenomena at the mountain. We were always alert to the periods of tremor and would inform the USGS and USFS in Vancouver as soon as it was recognized, but on no occasion did these periods of tremor lead to any visibly alarming phenomena on the mountain. Attempts at correlating any of the seismic activity with observable volcanic emissions were failures. The earthquake activity seemed to be completely independent of the phreatic eruptions. After the May 18 eruption, however, this pattern changed considerably.

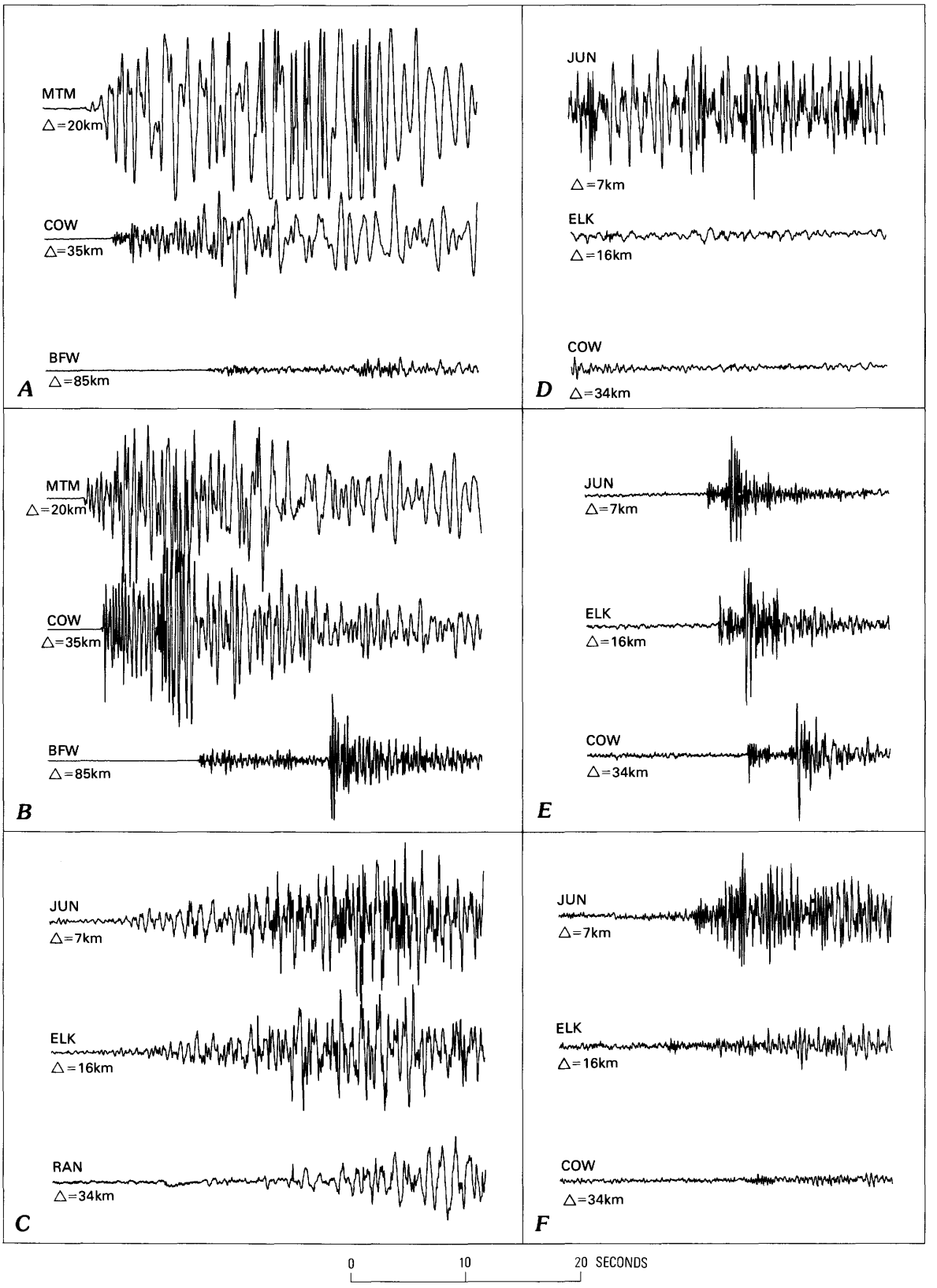

Figure 458.—Sample seismograms recorded at different relative gains, as noted, for six different kinds of seismic events, each recorded at three distances (in kilometers) from the event. Station codes are noted on each sample (see fig. 456 for location). A, low-frequency volcanic earthquake (M=3.3), relative gain, 1; B, high-frequency volcanic earthquake (M=3.2), relative gain, 1; C, eruption event on July 22, relative gain ½; D, harmonic tremor during eruption of May 25, relative gain, ½; E, posteruptive high-frequency earthquake at 11-km depth, relative gain, ¼; and F, large rock avalanche, relative gain, 1/10.

THE MAY 18 ERUPTION

On a time scale of hours, there was no apparent seismic precursor to the major eruption of Mount St. Helens on Sunday morning, May 18. During the previous day there had been 41 earthquakes greater than magnitude 3, about average for the previous few weeks. The eruption began as a large earthquake that triggered a massive landslide that culminated in a violent lateral explosion. From examination of photographs, this earthquake (estimated local magnitude of 5.1, location lat 46°12.8'N., long 122°11.6'W., depth 1.3 km, origin time 0832:11.4 PDT) is inferred to have shaken loose the unstable upper slopes of the north flank of the mountain, the area of the bulge. Approximately 0.5 km^3 of rock, ice, and snow was involved in the initial avalanche. In the following several minutes additional avalanches occurred along with a strong lateral blast. This blast was likely due to the sudden decompression of hot water-saturated rock from beneath the landslide area being blown out by the water flashing to steam. As the newly exposed rock was blown apart by the hot water and gases contained in it, more rock was exposed, which then was also blown out. The water near the surface flashing to steam produced a back pressure on the underlying rock preventing the entire mountain from exploding at once. Instead, the initial eruption was prolonged over as much as 10 min as the explosion worked its way back into the core of the mountain. A second large earthquake occurred about 2 min after the first, and strong ground shaking continued for 10–12 min after the initial event. We believed this seismic signature represented a continued lateral eruption occurring at the same time as additional landslides. During this 10-min period, the majority of the damage near to the mountain and most of the casualties occurred.

After the first 10 min the eruption changed character. The seismic signals declined, and while small earthquakes occurred at a high rate, there was no strong harmonic tremor for the next 3 hr. The volcano had probably lost its upper 300 m by then and much of the upper north flank was gone. During the following 3 hr the center of the volcano was reamed out by a continuous vertical eruption. At about 1140 PDT, harmonic tremor began. By 1230 the tremor was very strong and had a pulsating nature. The tremor continued to increase in intensity until, by 1530, it was so strong that it virtually saturated the records from all seismic stations within 150 km. It was strongly recorded on all stations in Washington and southern British Columbia and was well recorded in Missoula, Mont. (Gary Rogers, Pacific Geoscience Center, Victoria, B.C., and Tony Qamar, oral commun., 1980). At about 1730 PDT, the tremor diminished markedly but continued at lower levels for many days.

We believe that the period of strong tremor from approximately noon until 1730 represented the major magmatic portion of the eruption. The eruption column changed color from a dark gray to a lighter gray at about 1217, and shortly after this the first of many pyroclastic flows came down the north flank (D. A. Swanson, David Frank, oral commun., 1980). All subsequent major eruptions of the mountain have been accompanied by strong harmonic tremor but none was as strong as in midafternoon on May 18.

LATER MAJOR ERUPTIONS

Since May 18 there have been five additional major magmatic eruption periods with vertical columns rising to at least 10 km. Each of these eruptions had some seismic precursor that could be recognized before the eruption began. For all eruptions excluding the first on May 25, the precursor was recognized before the event and this information passed on to the volcano-watch headquarters at the USFS in Vancouver. Each of the precursors had a slightly different character and fell into two general classes: harmonic-tremor precursors and shallow-earthquake precursors.

May 25.—This eruption began at about 0228 PDT on Sunday, May 25, nearly a week after the cataclysmic eruption of May 18. Harmonic tremor had been observed continuously during the preceding week at varying intensity levels. During eruptions the tremor was strong enough to saturate the records from station SHW, and between these eruptions it varied from a barely detectable level to a moderate level of 10–15 mm on the record. Large shallow earthquakes, which had been occurring prior to May 18, had virtually ceased. Smaller earthquakes continued to occur but essentially all of these were either deep events below the volcano or earthquakes located either north or south of the volcano and had an obviously different character from the pre-May 18 volcanic earthquakes (Weaver and others, this volume).

No changes in the earthquake frequency or type occurred immediately before the May 25 eruption; however, in retrospect a change in the harmonic tremor-level can be seen. Figure 459 illustrates this change along with the earthquake occurrences during the 2 days around this eruption. Note that for the May 25 eruption there was a gradually increasing tremor amplitude up to 3 hr before the eruption began, at which time the tremor amplitude decreased dramatically. Whereas there had been variations in

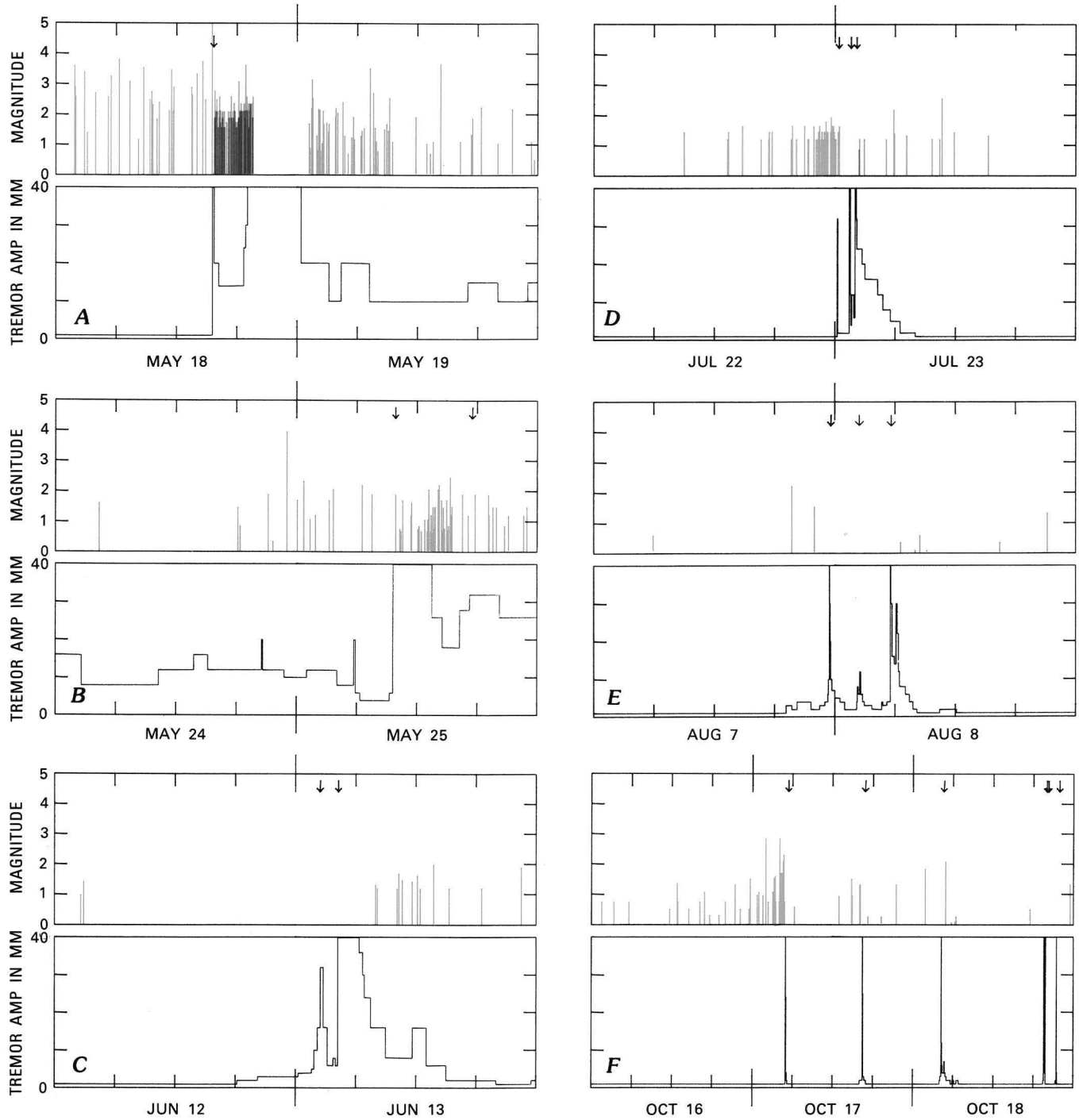

Figure 459.—Time plots of high-frequency (red lines) and low-frequency (blue lines) earthquakes occurring within 2 days of the major eruptions; the amplitude of harmonic tremor, in millimeters on records from station SHW, attenuated at 6 db, is shown on lower part of each figure (black). Arrows indicate major eruptions. Amplitudes shown as 40 mm indicate the record was saturated. Time scale shown in universal time (UTC). A, May 18–19; B, May 24–25; C, June 12–13; D, July 22–23; E, August 7–8; and F, October 16–18.

tremor amplitude during the previous week, none were as large or as abrupt as those occurring in the hours before this eruption. These tremor amplitude variations were not recognized at the time, partly because we were still somewhat preoccupied with the events of the previous week. Even if we had been more attuned to subtle changes in tremor level, we would probably not have recognized this change as a precursor to another eruption. We had seen many occurrences of harmonic tremor before May 18 that had led to no eruption. Harmonic tremor accompanying the May 25 eruption appeared to have two major pulses separated by about 6 hr. Soon after the eruption was underway, an increase in the high-frequency deep earthquakes occurred. Like the May 18 eruption, these events seemed to be triggered by the eruption and decreased in number many hours after the eruption.

June 12.—Harmonic tremor continued sporadically after the May 25 eruption for more than a week. On June 3 there was a repeat of the pattern observed on May 25, that is, an increase in harmonic-tremor amplitude followed by a sudden quiet period. The USGS in Vancouver was alerted to this observation; however, there was no eruption.

By June 8 the harmonic tremor had died out completely. Small earthquakes occurred from time to time, but no obvious harmonic tremor had occurred for days. In mid-afternoon on June 12, harmonic tremor was again observed at low level. By late afternoon its amplitude was increasing and the USGS in Vancouver was informed of this observation, although we did not predict that Mount St. Helens would necessarily erupt. About 1900 that evening there was a large increase in tremor amplitude that lasted for at least 40 min, followed by a very quiet period. This pattern was dramatic enough to cause us to call the USGS in Vancouver and the State Department of Emergency Services and suggest that we thought an eruption was likely. At 2109 a major eruption began. We were informed later that a smaller eruption had occurred shortly after 1900, about the time of the sudden increase in tremor amplitude.

Our confidence in being able to recognize harmonic tremor precursors to eruptions increased after the June 12 eruption. We remained particularly sensitive to the detection of harmonic tremor, alerting all of our staff to its subtle character and how to distinguish it from wind noise on the seismograms. Wind typically has a higher frequency than harmonic tremor and has a stronger effect on certain stations than does tremor. The key station for discriminating harmonic tremor from other seismic signals was SHW, which was fairly immune to wind noise but was quite sensitive to tremor.

July 22.—Almost 6 weeks elapsed between the June 12 eruption and that of July 22. The seismic activity during this period consisted mostly of small, isolated earthquakes occurring in the region around the mountain rather than under it. There were a few short periods of weak harmonic tremor in late June, but none of these caused us to feel that an eruption was impending.

On the morning of July 22, we noticed two earthquakes that had the low-frequency emergent character of many of the pre-May 18 low-frequency events. Preliminary locations for these events placed them directly under the north flank of the mountain, and at shallow depths. This was the same area that was so active prior to May 18 and that had been devoid of events since then. At 1030 PDT, the USGS in Vancouver was informed of these observations and our attention was concentrated on keeping alert to additional events. By midafternoon the rate of these events was obviously increasing. While we thought that these events probably represented a precursor to an eruption, we had no idea about how soon the eruption might occur. By 1600 when the rate of activity was greater than 20 events/hr, we felt that an eruption would likely occur that evening but had lingering doubts as this was not a precursor pattern that we had seen before. These doubts arose when we considered that there had been a full week of very intense earthquake activity preceding the first steam and ash eruption of March 27, and 2 mo of activity preceding the May 18 eruption. At 1713 the eruption began without any premonitory harmonic tremor. The eruption in this case came in three distinct bursts, the first two having a seismic signature that lasted only a few minutes. The third burst at 1900 was followed by gradually diminishing harmonic tremor for the next several hours. Once this last burst had started, small high-frequency deep earthquakes began to occur, much as had taken place after previous eruptions.

August 7.—At 1217 on August 7 harmonic tremor began quite abruptly; it was recorded at a moderate amplitude of 4 mm on SHW. This was immediately recognized as a possible eruption precursor. By 1330 an eruption alert was issued because the tremor was

continuing with slight increases from time to time. Two small low-frequency earthquakes occurred at 1529 and 1554, but the harmonic tremor was considered to be the significant activity. The eruption began at 1626 and again consisted of several discrete pulses. The last pulse again was followed by a few high-frequency deep earthquakes.

October 16–18.—From August 7 until mid-October there had been little unusual seismic activity. During late September several brief periods of very low level harmonic tremor had been observed, and several seismic noise bursts had been associated with large steam emissions. Possibly the first of the seismic precursors to the October eruption was a moderate-sized low-frequency earthquake on October 4. This event was not followed by additional events at a rate suggesting an eruption was imminent. Over the next 11 days, 16 more shallow volcanic earthquakes occurred. It was not until about noon of October 16 that it was suspected that a precursor sequence might be under way. By late afternoon when the records were examined in detail our suspicions were aroused enough to voice them to the USGS in Vancouver. By 1900 the rate of activity was up to 2 events/hr, and then up to 6 and 20/hr in the next 2 hr, respectively. At 1900 the largest event of the sequence took place (magnitude 2.8), which convinced us that indeed an eruption was on the way and an alert was issued.

The eruption began at 2158 with an eruption column to 12 km height, but died away within a few minutes. No harmonic tremor followed it and the earthquakes virtually ceased. Because previous eruptions had always ended with a period of harmonic tremor that gradually declined and also a few high-frequency deep earthquakes, we thought that this eruption was not complete. Even after almost 12 hr we considered the possibility of further eruptions to be high, and indeed the next morning at 0927 another eruption burst took place. Again there was not the typical ending to the sequence, thus further eruptions seemed likely. Eruptive bursts occurred again that evening at 2112 PDT and again the following afternoon at 1234 and 1245. The last eruption of this sequence occurred on the afternoon of October 18 at 1428. More harmonic tremor was observed during this period than in the preceding few days but still there were no high-frequency deep earthquakes. Consequently, we were not sure that this eruptive sequence was over. By the next day when the growth of a new lava dome was reported to have ceased and no additional eruptions had occurred, we thought that perhaps now it was indeed over. This eruption had not ended in the same way that all the others had, but it had been stretched over a longer period than the other eruptions.

DISCUSSION

Each of the major eruptions of Mount St. Helens had a distinctive pattern of seismicity, yet in each case there was an obvious seismic precursor. The precursor to the major eruption of May 18 was the 2 mo of intense earthquake activity that showed no change in the hours or days before the eruption. If the interpretation of this eruption being triggered by a massive landslide which in turn was triggered by an earthquake is correct, then no shorter term seismic precursor would be expected. The 2 mo of earthquakes, steam eruptions, and flank deformation had provided ample warning of a hazardous condition, and this warning was well heeded by the closing of a large area around the mountain to public access.

Each of the five subsequent eruptions did have recognizable seismic precursors that were observable on a time scale appropriate for immediate warnings and evacuations. It is still much too early in the analysis of these events to begin to understand the physical processes that led to the observable precursors or indeed to the eruptions themselves. We have only been able to recognize changes in the seismicity and draw conclusions from analogy with earlier eruptions to anticipate future ones. Thus any change in seismicity which has similarities to previous preeruption periods is used as a predictor. For no eruption was the prediction specific as to time; "during the next several hours" was the predominant judgment once it became obvious that something unusual was happening. Until more is known about the basic physical process generating the precursors, it is doubtful that more time-specific predictions can be made.

Some interesting observations are worth mentioning, and they may help with the interpretation of future preeruption sequences in both the short and long term. There have been two distinctly different kinds of seismic precursors, each of which has occurred under different initial conditions. When shallow earthquakes have been the seismic precursor, a visible lava dome has always been present. When

harmonic tremor was the precursor, the vent appeared to be open with no visible dome. Before May 18 there was no open vent; the mountain had obviously been plugged since the last eruption in the mid-19th century. The frequent phreatic eruptions from March to May probably did not represent a direct path to the magmatic source. The many shallow earthquakes at this time probably represented the fracturing of the preexisting volcano by magmatic intrusion. The "bulge" was the upper part of this old volcano being forced up and out by movement below. After May 18 the vent remained open through the May 25 and June 12 eruptions, both of which had harmonic tremor-type precursors. A lava dome grew and stabilized shortly after the June 12 eruption. This dome was destroyed in the July 22 eruption after shallow earthquakes again were the precursor. The next dome did not appear until after the August 7 eruption, which had only harmonic tremor as a precursor. The October 16 eruption destroyed this dome, again after shallow precursory earthquakes. We might, therefore, expect to see shallow earthquakes precede future eruptions when a lava dome is present.

A qualitative relation seems to exist between the duration and strength of the seismic precursor and the time since the previous eruption. This observation includes the long, intense seismic precursor to the May 18 eruption of 2 mo after more than 100 yr of no recorded eruptions. At the other end of the time scale, weak harmonic tremors of only a few minutes preceded each of the individual eruption bursts on October 17 and 18, in which the inter-eruption time was only 12 hr. At an intermediate time scale, the July 22 eruption had a precursor time of around 12 hr after an inter-eruption period of 40 days.

A key element in obtaining and interpreting reliable predictors is careful observational seismology, that is, recognizing the significance of a seismic signal by its character. Many sources for seismic signals exist on and around Mount St. Helens that can cause interpretational problems when the evaluation must be done quickly. If one had sufficient time to thoroughly analyze all seismic data received from the mountain, to locate every earthquake, and to compare each event at all stations, then the recognition of eruption precursors would be far easier. In reality, with limited personnel, limited recording facilities, and most of all limited time, the reliable recognition of precursors is dependent on experienced personnel who are familiar with the character of seismic signals from each station in the monitoring network. Rapid discrimination between wind noise and harmonic tremor on certain stations is frequently difficult. Low-frequency volcanic earthquakes can be easily confused with avalanche or ice-movement noises as was discovered in previous studies (Weaver and Malone, 1976). On more than one occasion excitement was generated over what appeared to be harmonic tremor that turned out to be a teleseism. We think a very important part of our monitoring effort is continuity of personnel familiar with the variety of signals that the seismic network detects. We are confident that if future eruptions have seismic precursors that are as clear as the ones prior to the past few eruptions, we will be able to recognize them in time to provide a useful hazard warning.

REFERENCES CITED

Crosson, R. S., and Lin, J., 1975, A note on the Mt. Rainier earthquake of April 20, 1974: Seismological Society of America Bulletin, v. 65, p. 549–552.

Johnson, C., 1979, CEDAR—an approach to the computer automation of short-period local seismic networks: California Institute of Technology Ph. D. dissertation.

Noson, L. L., and Crosson, R. S., 1980, Compilation of earthquake hypocenters in western Washington—1978: State of Washington Department of Natural Resources information circular 72, 18 p.

Weaver, C. S., and Malone, S. D., 1976, Mount St. Helens seismic events—volcanic earthquakes or glacial noises?: Geophysical Research Letters 3, p. 197.

THE 1980 ACTIVITY—A CASE STUDY IN FORECASTING VOLCANIC ERUPTIONS

By ROBERT W. DECKER

ABSTRACT

Forecasting volcanic eruptions on a probabilistic basis appears encouraging. In general, the forecasts of the 1980 eruptions of Mount St. Helens were accurate, saving thousands of lives. However, in more specific terms of forecasting the timing, nature, and scale of eruptions, much needs to be learned. Eight significant eruptions of Mount St. Helens were preceded by multiple geological, geochemical, and geophysical phenomena that occurred from months to hours before the eruptions. Eight false alarms also occurred, but in almost all of these only one potential precursory phenomenon was observed.

INTRODUCTION

Forecasting the time, location, nature, and scale of volcanic eruptions is one of the most urgent aspects of applied volcanology. It is not a precise science, but it can be done on a probabilistic basis. Although only a few of the world's active volcanoes are being carefully studied, eruption forecasting attempts have been encouraging (Decker, 1978). These studies on active volcanoes involve two distinct but complementary approaches: (1) Documentation of the past eruptive activity of specific volcanoes by historic records, geologic mapping, stratigraphic studies, and radiometric dating techniques. This has been the rationale of the volcanic-hazard studies by Crandell and Mullineaux (1975). (2) Monitoring the changes in geophysical and geochemical data from volcanoes before, during, and after their eruptions. This is the major approach of the USGS Hawaiian Volcano Observatory to eruption forecasting (Tilling, 1977). The combination of these two approaches, historical record and data monitoring, is a logical basis for anticipating the future activity of specific volcanoes.

Some physical processes, such as celestial mechanics, are so regular that their histories can be extrapolated with near certainty into the future. Predictions of the onset times, durations, and locations of solar eclipses can thus be done on a deterministic basis. Other physical phenomena, such as volcanic eruptions, are much more variable in nature. Extrapolating their histories and current processes into the future can only be done on a probabilistic basis. In the science of probabilistic forecasting, there are no sure predictions, only statistical gains over predictions based only on historical averages. Pasteur said it well, "Chance favors the prepared mind."

Experience and insight are important in the interpretations of highly variable phenomena such as human nature, and they should not be discounted in the interpretation of highly complex and variable physical phenomena. However, what is needed in the science of probabilistic forecasting are objective criteria for interpreting the historical and monitoring data, and more basic research into the processes of volcanism so that the precursor events of eruptions can be interpreted in terms of their physical and chemical meanings. This should lead to better predictions of the nature, time, location, and magnitude of eruptive events.

The 1980 eruptions of Mount St. Helens make available a case study showing where eruption forecasting stands today and the directions it may take in the near future. In general, the forecasting of the Mount St. Helens activity was accurate and may have saved thousands of lives. In terms of the exact timing, nature, and scale of the huge May 18 eruption and avalanche, it was not accurate enough. Experience was painfully gained at the cost of 62 lives.

ACKNOWLEDGMENTS

This summary report could not have been written without the data and discussions generously provided by many persons who have studied the recent activity of Mount St. Helens. Much of the data is published in separate chapters in this volume. More specific credit goes to the following persons who, unless otherwise noted, are members of the USGS: Elliot Endo, Stephen Malone (University of Washington), and Craig Weaver, who provided seismic data; John Dvorak, Peter Lipman, James Moore, Arnold Okamura, and Donald Swanson, who provided deformation data; Jules Friedman and Hugh Kieffer, who provided thermal data; Thomas Casadevall, David Harris, William Rose (Michigan Technological University), and Richard Stoiber (Dartmouth College), who provided volcanic gas-emission data; Robert Christiansen, Willie Kinoshita, and Donald Peterson, who provided eruption data; and Barry Voight (Pennsylvania State University), who provided data on the potential avalanche and eruption hazards. The research on Mount St. Helens has been a joint effort of many scientists and institutions working under difficult conditions. Their cooperation and generous exchange of data are gratefully acknowledged.

PAST ERUPTIVE ACTIVITY OF MOUNT ST. HELENS

Historic records indicate that eruptions occurred during 1831 to 1857, but aside from identifying Mount St. Helens as an active volcano, the records are too few to have any statistical meaning. Geologic studies and dating (Mullineaux and Crandell, this volume) have identified several eruptive periods having diverse deposits in the last 4,500 years and have established some important patterns. Dormant intervals are of two lengths, 100–300 yr and 600–700 yr; the last two intervals prior to 1800 were the short variety. The eruptive products also show that pyroclastic explosions were common, and that prehistoric eruptions of Mount St. Helens affected large areas. This type of analysis led to Crandell and Mullineaux's forecast (1978, p. C1–C2) that Mount St. Helens was especially dangerous and likely to erupt within the next hundred years. Their words were prophetic:

> Mount St. Helens has been more active and more explosive during the last 4,500 years than any other volcano in the conterminous United States. In the future, Mount St. Helens probably will erupt violently and intermittently * * * and will affect human life and health, property, agriculture, and general economic welfare over a broad area. The volcano's behavior pattern suggests that the current quiet interval will not last as long as a thousand years; instead, an eruption is more likely to occur within the next hundred years, and perhaps even before the end of this century.

The hazards report by Crandell and Mullineaux (1978) was accurate in predicting the areas affected by the May 18 eruption with regard to pyroclastic flows, air-fall ash, mudflows, and floods. The areas affected by the avalanche and directed blast are beyond the limits of any recognized prehistoric eruption of the same kind at the volcano and, therefore, were unprecedented in scale in the 4,500-yr history upon which the hazards report was based.

Careful geologic mapping during several field seasons in the Mount St. Helens area gave Crandell and Mullineaux an additional benefit in dealing with hazard warning problems. They had become well acquainted with the operations of the U.S. Forest Service, lumber industry, and utilities in the area, and this knowledge led to much better credibility for their warnings during the phase of small eruptions prior to the May 18 catastrophe.

MONITORING THE ACTIVITY AT MOUNT ST. HELENS AND OTHER VOLCANOES

Geophysical and geochemical techniques are currently being used to monitor some active volcanoes in various parts of the world (UNESCO, 1971). However, most of the world's active volcanoes are not monitored. Current techniques include monitoring the following phenomena: seismicity, ground-surface

deformation, temperature, electric and magnetic fields, gas emissions, and the chemistry and mineralogy of erupted lavas or pyroclastic materials. All of these techniques have been used during the recent activity at Mount St. Helens. Some techniques have worked better than others at forecasting, but all have yielded important data from the standpoint of obtaining a basic understanding of explosive volcanism.

PRECURSORY ACTIVITY AND ERUPTION POSSIBILITIES CONSIDERED

The first small phreatic eruption at Mount St. Helens occurred on March 27 at 1230 PST (Pacific Standard time). It was followed by hundreds of small steam and ash eruptions during March 27 to April 21 and May 7 to 14. The onset of these eruptions was preceded by 7 days of intense local seismic activity, including a period of exponential increase in seismic energy release on March 25. This seismic activity clearly signaled the high probability of the first eruption.

The May 18 eruption occurred at 0832 PDT without any distinct short-term warnings. However, the longer term precursory events were numerous and dramatic. The seismic swarm had continued with high and nearly constant energy release for 60 days. Short bursts of harmonic tremor began on March 31 and continued intermittently through April 5. Tremor recurred on April 12 and May 8.

Major visible deformation was first seen on March 27 and was monitored directly after April 23. The very large rates of deformation—1.5–2.5 m/day in an area of 1.5x2.0 km on the high north flank of Mount St. Helens—were of major concern. The close connection in time and space between the earthquake foci and the bulging area led most of the scientists studying the volcano to conclude that a shallow intrusion was taking place beneath an area just north of the summit. The possibility of a major avalanche and a lateral explosion were considered. Reports on the lateral explosions of Lassen Peak (Day and Allen, 1925), Bandai-san (Kuno, 1962), Bezymianny volcano (Gorshkov, 1959), Shiveluch volcano (Gorshkov and Dubik, 1970), and Mount Lamington (Taylor, 1958) were being reread by Mount St. Helens workers in late April and early May.

POSSIBLE ANALOGOUS ERUPTIONS

At Lassen Peak, Calif., after nearly a year of small steam explosions, a major eruption in 1915 formed an ash cloud that rose to an altitude of about 10 km, and an avalanche of hot debris destroyed an area 2x6 km on the east flank (Day and Allen, 1925). Bandai volcano in Japan erupted violently in 1888; the eruption was preceded only by a few felt earthquakes. An apparent hydrothermal explosion destroyed the summit, and formed a large horseshoe-shaped crater and a massive debris avalanche that covered 70 km^2 and killed more than 460 people (Kuno, 1962). The gigantic explosion of Bezymianny, Kamchatka, in 1956 occurred after 5 mo of smaller eruptions. It destroyed the top of the volcano, formed an ash cloud 45 km high, and devastated 500 km^2 in a huge lateral blast (Gorshkov, 1959). A similar but smaller lateral explosion at Shiveluch, Kamchatka, in 1964 destroyed the volcano's summit and devastated 98 km^2. No minor eruptions preceded the major blast, but recorded earthquakes had increased during the 10 mo prior to the explosion (Gorshkov and Dubik, 1970). Mount Lamington in Papua, New Guinea, erupted suddenly and violently in 1951. After only 6 days of felt earthquakes, landslides, and minor ash eruptions, a major pyroclastic flow devastated 176 km^2 surrounding the volcano and killed 3,000 people (Taylor, 1958).

The possibility that a lava dome might extrude at Mount St. Helens without much accompanying damage, as happened at Syowa-Sinzan in Japan in 1944–45 (Kuno, 1962), was also considered, as well as the possibility that the apparent intrusion at Mount St. Helens might cease before it caused any major avalanche or eruption. One of the most perceptive possibilities suggested between March 27 and May 18 was by Barry Voight of Pennsylvania State University. He compared Mount St. Helens to the areas of large historic avalanches, at Gros Ventre, Wyo., in 1925, and Madison Canyon, Mont., in 1959, and decided that a potential failure of the north flank of Mount St. Helens could generate an avalanche of 1–3 km^3. Voight (written commun., May 1, 1980) noted that:

> A catastrophic event of the kind observed at Bandai-san—in which an explosively motivated fragmental flow devastated an area of more than 70 km^2—must be regarded as a legitimate possibility, particularly in view of the enhanced hydraulic pressure conditions implied by frequent summit steam explosions and the relatively high level of released seismic energy.

On the more prosaic side, a bulging slope associated with rock creep (increased tilt) may lead to an increase of rockfall hazards from exposed rock areas such as Goat Rocks, increased snow avalanche hazard, and increased risk of glacier falls.

In general, for most natural catastrophes, the larger the event, the more rarely it occurs. Therefore, most of the scientists studying Mount St. Helens in early May considered that a significant avalanche and eruption were distinctly possible, but that extremely large events were not very probable. Even so, the possibility of danger was clearly evident from prehistoric eruptions of Mount St. Helens, historic eruptions at other volcanoes, and the ongoing high rate of seismicity and deformation. These factors were considered by authorities responsible for land management around the volcano in their decision to continue restricting access to the volcano, even in the face of mounting public pressure to open the Spirit Lake recreation area.

PRECURSORY ACTIVITY AFTER MAY 18

Smaller but significant eruptions after May 18 were also preceded by geological, geochemical, and geophysical signals. The May 25 eruption at 0228 PDT was preceded by 7 days of harmonic tremor and by smaller eruptions as much as 10 hr in advance. Harmonic tremor for 9 hr and a smaller eruption 2 hr in advance also preceded the June 12 eruption at 2110 PDT.

No tremor preceded the July 22 eruption, but the eruption was marked by increasing local seismicity for 8 hr before, as well as by several centimeters of outward deformation of the crater rampart during July 18–22. A pattern of decreasing CO_2 emission and CO_2/SO_2 ratios for 9 days was also observed prior to July 22.

Harmonic tremor for 4½ hr preceded the August 7 eruption at 1624 PDT. The CO_2 emission and CO_2/SO_2 ratios also showed a decrease for 5 days prior to August 7.

The October 16 eruptions, which began at 2158 PDT, were preceded by more than 30 hr of increased local seismicity, 12 days of small northward displacements of the crater rampart, and a decrease of CO_2 emission and CO_2/SO_2 ratios between October 9 and 15.

On December 13–14, a small sector of the lava dome was apparently blown out. Because of bad weather, this eruption was not witnessed. Local seismicity began to increase on December 25 and reached a maximum by December 26–27, and the

Table 111.—Geological, geochemical, and geophysical changes that occurred before significant eruptions of Mount St. Helens

[hr, hours; leaders (---), phenomenon did not occur or was not detected]

Eruptions	Onset of changes before eruptions					
	Seismicity	Tremor	Deformation	Thermal anomaly	Gas emission	Small eruptions
Mar. 27, 1230 PST.	7 days	---	---	---	---	---
May 18, 0832 PDT.	60 days	49 days[1]	53 days	53 days	---	53 days[1]
May 25, 0228 PDT.	---	7 days	---	---	---	10 hr
June 12, 2110 PDT.	---	9 hr	---	---	---	2 hr
July 22, 1714 PDT.	8 hr	---	4 days	---	9 days	---
Aug. 7, 1624 PDT.	---	4 1/2 hr	---	---	5 days	---
Oct. 16, 2158 PDT.	30 hr	---	12 days	---	7 days	6 days
Dec. 27-28	2 days	---	14 days	---	---	14 days

[1]Intermittent.

crater rampart moved tens of centimeters northward. On December 28, renewed growth of the lava dome was observed. This growth continued through January 2–4, 1981, doubling the volume of the dome.

The summary of eruptions in table 111 shows that more than one precursory phenomenon was evident before the beginning of each eruption. Most of the precursors were clearly recognized and were reported before the eruptions. The pattern of tremor before the May 25 eruption and the pattern of gas emissions before the July 22 eruption were recognized as apparent precursors after the eruption had occurred. Even though there was no short-term warning of the May 18 eruption, five different, long-term phenomena indicated the possibility of a future eruption.

Precursory events not followed by eruptions (false alarms) did occur, and these probably are inevitable in any probabilistic forecasting system. Table 112 lists eight occurrences of precursory-type events that were not followed by significant eruptions. Only before August 15 was there more than one potential precursory event.

Although there is ample evidence that several phenomena, which can be observed and measured, give warnings of impending eruptions for hours to months in advance, no single pattern has clearly repeated itself before all or even most of the eruptions. Basic scientific research, as well as human experience and judgment, are still needed in large measure.

THE FUTURE

The major eruptions of Mount St. Helens in 1980 not only indicate that science and technology can partially anticipate and ameliorate volcanic hazards, but also give some indication of priorities for future investigations. These are as follows: (1) carry out geologic mapping, stratigraphic studies, and radiometric dating to establish the geologic history of each potentially active volcanic center or area; (2) install limited networks of seismometers to monitor these volcanic centers or areas; (3) make baseline geophysical and geochemical measurements on these volcanic centers or areas for comparison with future changes; (4) install additional seismometers and other continuous monitoring devices at volcanic centers or areas when increased seismicity or other changes suggest that increasing activity is occurring.

Because of the generally long repose intervals between eruptive periods of explosive volcanoes, several volcanic centers or areas should be studied and monitored from one observatory. Most important of all, the geologic, geophysical, and geochemical studies on several volcanoes should be done by a group of scientists at one headquarters. Volcanology is such a broad field of research that many of its problems can only be solved by scientists from different disciplines—geology, chemistry, physics, and mathematics—working closely together.

Table 112.—Precursory phenomena that were not followed by significant eruptions at Mount St. Helens

[Leaders (---), phenomenon did not occur or was not detected]

Date	Type and duration					
	Seismicity	Tremor	Deformation	Thermal anomaly	Gas emission	Small eruptions
June 3	---	Several hours.	---	---	---	---
June 26	---	--do---	---	---	---	---
July 28	---	---	---	---	---	20 min.
Aug. 15	---	---	---	---	2 days	Several minutes.
Aug. 25	---	---	---	---	4 days	---
Sept. 24	---	---	---	---	---	4 hr.
Oct. 1--	---	---	---	---	---	Duration unknown.
Nov. 18-19.	---	---	---	---	---	Do.

REFERENCES CITED

Crandell, D. R., and Mullineaux, D. R., 1975, Technique and rationale of volcanic-hazards appraisals in the Cascade Range, northwestern United States: Environmental Geology, v. 1, no. 1, p. 23-32.

_____1978, Potential hazards from future eruptions of Mount St. Helens Volcano, Washington: U.S. Geological Survey Bulletin 1383-C, 26 p.

Day, A. L., and Allen, E. T., 1925, The volcanic activity and hot springs of Lassen Peak: Carnegie Institute of Washington Publication 360, 190 p.

Decker, R. W., 1978, State of the art in volcano forecasting, *in* Geophysical predictions: Washington, D.C., National Academy of Sciences, Studies in Geophysics, p. 47-57.

Gorshkov, G. S., 1959, Gigantic eruption of the volcano Bezymianny: Bulletin Volcanologique, ser. 2, v. 20, p. 77-112.

Gorshkov, G. S., and Dubik, Y. M., 1970, Gigantic directed blast at Shiveluch Volcano (Kamchatka): Bulletin Volcanologique, v. 34, no. 1, p. 261-288.

Kuno, Hisashi, 1962, Catalogue of the active volcanoes of the world, including solfatara fields, Part XI, Japan, Taiwan and Marianas: Rome, Italy, International Association of Volcanology, 332 p.

Taylor, G. A. M., 1958, The 1951 eruption of Mount Lamington, Papua: Australia Bureau of Mineral Resources Bulletin 38, 117 p.

Tilling, R. I., 1977, Monitoring active volcanoes, *in* U.S. Geological Survey Yearbook, Fiscal Year 1977, p. 36-40.

UNESCO, 1971, The surveillance and prediction of volcanic activity: Paris, United Nations Educational, Scientific and Cultural Organization, Earth Sciences series, no. 8, 166 p.

STABILITY OF BLOCKAGE IN NORTH FORK TOUTLE RIVER

By T. LESLIE YOUD, RAYMOND C. WILSON, *and* ROBERT L. SCHUSTER

ABSTRACT

During the May 18, 1980, eruption of Mount St. Helens, a massive rock-debris avalanche descended the mountain and came to rest in the North Fork Toutle River. The avalanche blocked the river valley with debris deposits as much as 170 m thick, raised the level of Spirit Lake 60 m, and presented a threat of flooding and siltation to downstream residents (in addition to the flooding that occurred the day of the eruption) should the blockage give way or breach. This study investigated the stability of the main blockage impounding Spirit Lake. Components of the study included field inspections, field and laboratory tests, and standard engineering calculations, which indicate that the blockage is stable against slope failure due to gravitational or earthquake forces, and that it should resist piping failure both under 1980 and probably future hydrological conditions.

INTRODUCTION

At the time of the May 18 eruption of Mount St. Helens, a massive rock-debris avalanche with a volume of about 2.5 km^3 blocked the North Fork Toutle River at Spirit Lake (Glicken and others, 1980). This event raised the water level in Spirit Lake about 60 m, due to the blockage of the lake's drainage and partial filling of the lake with debris. The slope failure and debris-emplacement processes are described by Voight and others (this volume). The extent of the debris avalanche is plotted in figure 460, and the general character of the surface of the blockage is shown in figures 214 and 461.

Immediately following emplacement of the debris avalanche, a flood of water and sediment swept down the North Fork Toutle River below the debris-avalanche blockage, causing considerable damage and sedimentation along downstream rivers as far as Longview, Wash. (Janda and others, this volume; Lombard and others, this volume; Schuster, this volume). The debris-avalanche blockage in the North Fork Toutle River posed an even greater hazard of flooding and debris inundation should the blockage give way or breach and release a torrent of water from Spirit Lake. The purpose of this investigation was to evaluate the stability of the debris blockage of the North Fork Toutle River and the potential for catastrophic breach of that blockage.

A preliminary evaluation of the stability of the blockage was made shortly after the May 18 eruption by Youd and Wilson (1980). That evaluation was based on preliminary topographic data and assumed material properties. This report contains a reevaluation of the stability of the blockage based on updated topography and measured material properties.

Failure of the North Fork Toutle River debris-avalanche blockage could occur by any one or a combination of three possible processes: (1) The debris blockage could become unstable due to gravitational forces or possible earthquake forces and slip or flow downstream, releasing a torrent of water from Spirit Lake. (2) Water seeping through the de-

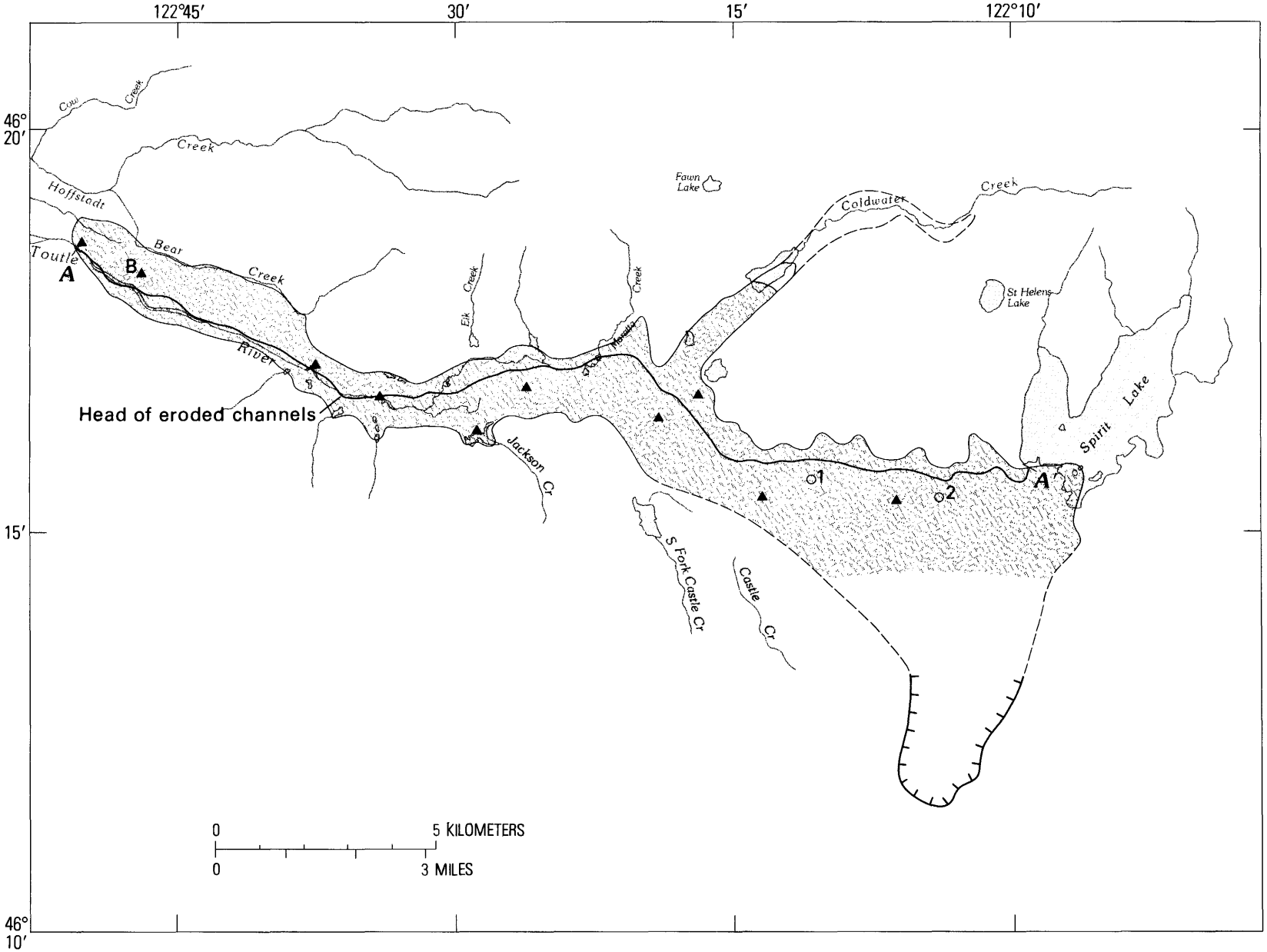

Figure 460.—Extent and source area of Mount St. Helens debris-avalanche deposits, and location of Spirit Lake. Cross section A–A′ shown on fig. 465, and B, point from which fig. 461 was photographed. Localities 1 and 2 discussed in text. Sampling sites indicated by triangles.

bris blockage from the impounded lake could cause headward erosion of a tube or channel breaching the blockage, a process called "piping." (3) Water level in the lake could rise, overtop the blockage, rapidly cut a channel through easily erodible debris, and release a flood of water from Spirit Lake. The possibility of failure by each of these modes is considered here.

FIELD AND LABORATORY INVESTIGATIONS

On the morning of May 23, 1980, Wilson and Youd, in company with Barry Voight, Pennsylvania State University, flew up the North Fork Toutle River by helicopter to inspect the debris blockage and surrounding area. Pertinent observations from that flight are as follows:

Flow in the river immediately below the blockage was relatively low (estimated to be about 1.5 m^3/s). Considerable erosion of channels into the downstream tail of the blockage (figs. 460, 465) had occurred during flooding that immediately followed the debris emplacement. Erosion, however, had virtually ceased by the time of our visit.

The surface of the blockage was highly irregular, exhibiting many hummocks, depressions, and pits. Maximum relief on the hummocks and depressions was about 60 m. Some pits and other depressions contained ponded water. Perceptible flow or seepage could not be seen entering or leaving any of these ponds. Many scarps and fissures cut the ground surface. Most of these scarps and fissures were caused by local slumping near steep slopes. We saw no systematic set of ground cracks indicative of

Figure 461.—View to east of debris avalanche from distal margin. Figure 460 shows location from which photograph was taken.

postdepositional, downstream mass movement of any part of the blockage.

We landed on the debris avalanche (fig. 460, loc. 1) to inspect materials exposed by erosion of hummocks and in pit walls. The upper few tenths of a meter of accumulated debris was fine sand-sized ash, which had been reworked by water in topographically lower areas. Beneath the ash, the debris consisted of a heterogeneous mixture of silt, sand, pebbles, cobbles, and boulders, with sporadically distributed large blocks of ice. The color, texture, and mineral composition of the coarse-grained matrix varied greatly from place to place. However, the material was consistently well graded (poorly sorted), ranged in size from silt to large boulders, and was loosely packed. The heterogeneous material beneath the ash was debris-avalanche material from the massive rock slide that occurred on the north side of Mount St. Helens at the time of the May 18 eruption. The hummocky nature of the ground surface and the nature of the materials exposed in many outcrops indicate that the bulk of the North Fork Toutle River blockage is debris-avalanche material covered by a thin veneer of volcanic ash.

After flying over the crest of the blockage, we flew over and around Spirit Lake. The lake was covered with floating, dust-covered logs. Jagged mounds of broken rock formed islands at several locations, indicating that a considerable amount of rock debris had entered the lake and was responsible in large part for the approximate 60-m rise in lake level. Spouts of boiling water marked locations of hot rocks on the lake bottom and indicated that water temperatures, and hence evaporation rates, were high. Many small streams and rivulets were flowing into the lake, the largest of which was estimated to be carrying less than 0.6 m^3/s. We estimated total flow into the lake to be between 1.1 and 2.8 m^3/s. Shoreline beaches and a set of markers left by a previous field party showed that lake level had declined slightly, about 0.15 m in the preceding 2 days (May 21–23).

We measured the altitude at lake level with the helicopter altimeter and measured the altitude of the lowest point on the crest of the blockage (fig. 460, loc. 2) in a similar manner. The difference between the two measurements was 60 m ± about 3 m. At the crest of the blockage, the surface was covered by a meter or so of ash. The surface was hummocky, however, and a few exposures revealed coarse-grained

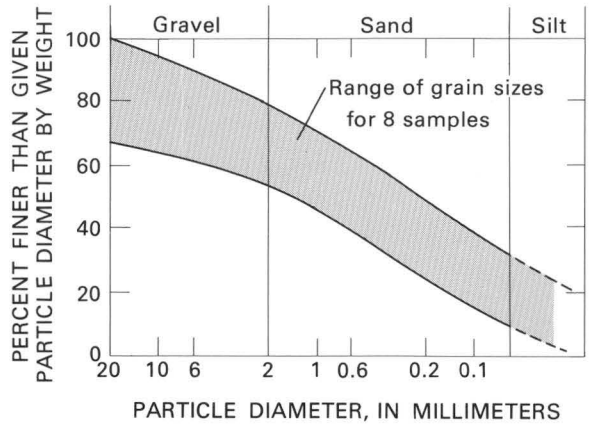

Figure 462.—Range of grain sizes for samples taken from eight widespread localities on the debris avalanche.

Figure 463.—Photomicrograph of typical sand-sized grains from the debris avalanche, showing subangular to angular shapes.

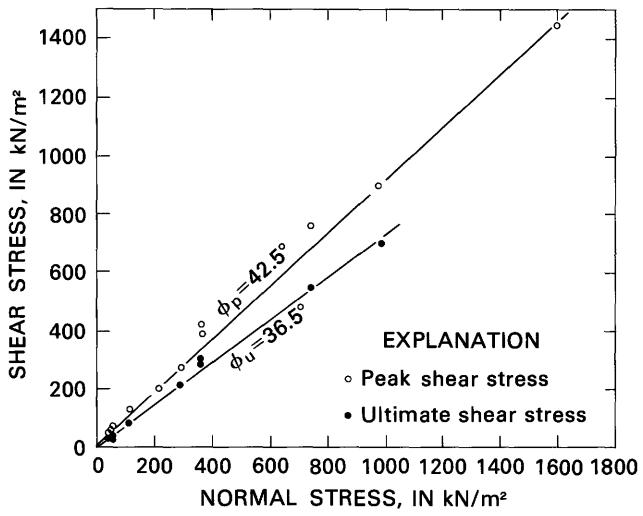

Figure 464.—Results of direct shear tests on avalanche material finer than 2 mm in diameter recompacted to a density of 1.82 g/cm³ showing conservative estimates of 42.5° and 36.5° for the peak and ultimate angles of internal friction, respectively.

material beneath the ash, indicating that the bulk of the deposit is avalanche debris.

Between September 15 and 22, 1980, Schuster and Youd, in company with Harry Glicken, University of California at Santa Barbara, conducted in-place density tests and took bag samples from selected locations (fig. 460) on the debris blockage for evaluation of material properties. Tests on bag samples were run in the laboratory for grain-size distribution, grain shape, specific gravity, and shear strength. Eleven measurements of density of avalanche material yielded dry densities ranging from 1.71 to 1.94 g/cm³ with an average of 1.82 g/cm³. Pycnometer tests yielded an average specific gravity of 2.66 for the debris grains. Based on these values, average porosity and void ratio are 32 percent and 46 percent, respectively. Grain-size distributions for eight bag samples from a variety of locations plot within a rather narrow range, as shown in figure 462. Coefficients of uniformity for these eight samples average about 50. (The coefficient of uniformity is defined as the ratio of the particle diameter for which 60 percent of material by weight is finer grained to the particle diameter for which 10 percent of the material is finer grained.) Microscopic examination revealed that the sand-and silt-sized particles are subangular to angular (fig. 463). Eleven direct shear tests were run on debris material finer than 2 mm in diameter recompacted to a density of 1.82 g/cm³ ± 0.03 g/cm³. The shear test results (plotted in fig. 464) yield estimates of 42.5° and 36.5° for peak and ultimate angles of internal friction, respectively, with essentially no cohesive strength. To be conservative, we used the ultimate angle of internal friction in the stability calculations given in the next section of this report.

From a comparison of preeruption and posteruption topographic maps, we plotted the profile of the debris blockage, shown in figure 465. The length of blockage from Spirit Lake to the head of the eroded channels is about 18 km. The debris is as much as about 170 m deep with an average depth of about 90 m. General slopes on the blockage range from about 3.0 percent on the long downstream tail of the avalanche deposit to about 5.5 percent on both sides of the crest. Locally, near hummocks and depressions, slopes are much steeper.

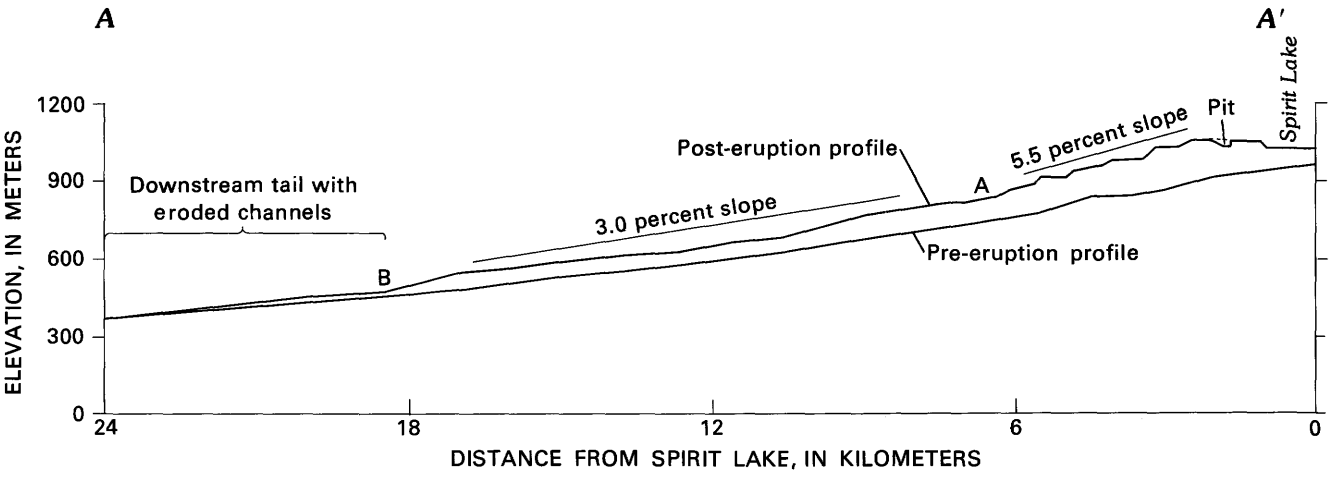

Figure 465.—Profile of debris avalanche between Spirit Lake and the toe of the avalanche. Vertical exaggeration × 5.

EVALUATION OF FAILURE POTENTIAL

FAILURE BY SLIPPAGE OR LIQUEFIED FLOW

During the field investigations, we found no evidence of postdepositional massive slope movements in the debris avalanche. Scarps and fissures marked locations of local slumping on steep hummock or pit slopes. These local failures reflect random local motions and thus do not affect the overall stability of the blockage. Our field observations indicated that the overall avalanche deposit was safe against slope instability caused by gravitational forces.

To check this conclusion and evaluate the stability of the slope under several possible conditions, analyses were made using standard engineering calculations. For these analyses, the 18-km-long debris-avalanche blockage was modeled as an infinite slope with seepage flowing parallel to the surface. The factor of safety, F, against slope failure for this case is (Skempton and Hutchinson, 1969):

$$F = \frac{(c' + z\cos^2\beta\,(\rho_d - m\,\rho_w)\,g\tan\phi')}{(\rho_d g z\cos\beta\sin\beta),} \qquad (1)$$

where c' is the effective cohesion, z is depth to the failure plane, β is the slope of the failure surface, ρ_d is the bulk density of the debris, ρ_w is the density of water, g is the acceleration of gravity, m is the ratio of the depth of water-saturated sediments above the failure plane to the depth of the failure plane, and ϕ' is the effective angle of internal friction. The measured effective cohesion for the debris is zero; inserting this value, equation 1 reduces to:

$$F = ((1 - m\rho_w/\rho_d)\tan\phi')/\tan\beta. \qquad (2)$$

In our calculations we use the ultimate angle of internal friction ϕ_u', which gives a conservative estimate of the factor of safety. We also conservatively assume that the debris is dry above the phreatic ground-water surface and saturated below that surface. Calculated factors of safety for several possible ground-water conditions in the debris blockage are listed in table 113.

Table 113.—Factors of safety against slope failure for various ground-water conditions

Ground-water condition	Factor of safety	
	Slope 5.5 pct	Slope 3.0 pct
No lateral seepage, m = 0.	13.0	25.0
Lateral seepage through half of slope above failure plane, m = 0.5.	10.0	18.0
Lateral seepage through entire slope, m = 1.0.	7.1	13.0

Immediately after the eruption, the debris contained considerable ice and water; however, it is doubtful that a continuous regime of lateral seepage through the debris avalanche was established at that time. For this initial condition (no lateral seepage through the debris avalanche), $m = 0$, which also makes the factor of safety independent of bulk density. The calculation for this condition yields a factor of safety of 25 for the 3.0 percent average general slope on the long downstream tail of the blockage, and 13 for the 5.5 percent maximum general slope behind the crest of the blockage (table 113).

To estimate the factor of safety under probable steady-state seepage conditions (after a lateral seepage regime is fully established), we set the depth to the saturated zone equal to half the depth to the potential failure plane ($m = 0.5$) and assumed half the voids in the material to be filled with water (average $\rho_d = 1.93$ g/cm^3). For the 3.0 percent average general slope, the factor of safety against slope failure is 18, and for the maximum general slope of 5.5 percent, the factor of safety is 10.

For a worst case condition, we assumed seepage parallel to the slope throughout the debris blockage and saturated debris material ($m = 1.0$, $\rho_d = 2.14$ g/cm^3). This condition would essentially require that lake level be at the crest of the blockage and that precipitation infiltrate the slope. For the average general slope of 3.0 percent, the factor of safety is 13, and for the maximum general slope of 5.5 percent, the factor of safety is 7.1.

These calculations indicate that the blockage impounding Spirit Lake is not subject to slope failure under any probable hydrologic conditions. Because the angle of internal friction measured in this study (36.5°) is greater than the angle (26°) assumed by Youd and Wilson in their preliminary study, the bet-

ter estimates of factors of safety given here are all greater than those previously reported (Youd and Wilson, 1980, p. 6–7).

In the event of a nearby earthquake of magnitude 5 or greater, some settlement of the debris-avalanche blockage could occur due to compaction. In a large event, settlement could be as much as a couple of meters. Lateral spreading of parts of the blockage could also occur, but lateral displacement of the entire mass would not be likely to exceed a few meters even in a large event. These displacements would not reduce the ability of the blockage to hold back the water in Spirit Lake unless water in the lake were at the critical overtopping level. Locally, ground displacements could be much greater during an earthquake but those displacements would not affect the overall stability of the blockage. Consideration was given to the possibility of liquefaction and massive downstream flow failure of the blockage. Past experience indicates that such flows do not develop on slopes less than 5 percent (Youd, 1978, p. 48). The slope of the North Fork Toutle River valley is about 2.5 percent and the average general slope on the blockage is about 3.0 percent. These gentle slopes effectively eliminate potential for flow failure under all but the most severe hydrologic conditions. If the blockage were to become completely saturated, flow failure might be possible on the steeper slopes near the crest of the blockage. Again, flow failure would be possible on some steeper local slopes.

FAILURE BY PIPING

We saw no evidence of rapid erosion or substantial flow from the toe or downstream tail of the debris avalanche during our field investigations in May and September 1980. These processes are integral parts of the piping mechanism. Hence, no threat of failure due to piping existed immediately after the eruption.

To confirm this conclusion, calculations were made to check the safety of the blockage against piping. A standard engineering analysis for safety of embankments against piping compares the hydraulic gradient at the point of seepage exit from an embankment to the critical gradient, that is, the gradient at which the material becomes quick (Taylor, 1948, p. 550). The critical gradient is calculated from the equation:

$$i_c = (G-1)/(1-e), \quad (3)$$

Table 114.—Calculated exit gradients at points A and B (fig. 465), assuming homogeneous permeability, and two-dimensional flow

[1 m = 3.28 ft]

Lake elevation (m)	Exit gradient	
	Point A	Point B
1035	0.047	0.031
1080	.055	.038

where G is the specific gravity of the material and e is the void ratio. Inserting the values of $G = 2.66$ and $e = 0.46$, determined from field and laboratory tests, the calculated critical gradient for the material in the blockage is 1.14. The exit gradient is determined from a flow net. It was beyond the scope of this study to construct a flow net for the debris blockage. However, assuming a homogeneous material and a two-dimensional flow regime, exit gradients can be estimated from the head loss across the shortest flow path to possible exit points. Exit gradients calculated using these assumptions and the cross section in figure 465 do not exceed 0.055 (table 114) and are only a small fraction of the critical gradient of 1.14. Inhomogeneities in the material, flow constrictions in the lateral direction caused by obstructions in the embankment, or lateral flow toward eroded channels could increase these exit gradients; but in our judgment the increase would not be nearly enough to generate piping through the debris blockage in its 1980 configuration. We did not analyze potential for piping through subsections of the material impounding smaller lakes and ponds on or adjacent to the main blockage.

In our preliminary study of the safety of the debris blockage (Youd and Wilson, 1980, p. 7–9), we used an alternative engineering calculation to evaluate piping potential (Terzaghi and Peck, 1967, p. 612–618). Those analyses also indicated that the debris-avalanche blockage is safe against piping.

FAILURE BY OVERTOPPING

With the level of Spirit Lake 60 m below the crest of the blockage and falling, no immediate threat of water overtopping and eroding a breach through the blockage existed immediately after or during the summer following the May 18, 1980, eruption. During

future periods of high runoff, it may be possible for the lake to fill and flow over the blockage. (It is also possible that sufficient water will seep through the embankment to prevent overtopping.) Further studies are necessary to determine the possibility of future overtopping and the consequences of such an event.

CONCLUSIONS

At the 1,036-m level of Spirit Lake, the blockage in the North Fork Toutle River is stable against failure due to (1) slope instability either from gravitational or earthquake forces and (2) piping or erosion by seepage through the blockage, both under 1980 and probable future hydrologic conditions. In addition, with the lake at this level, it has approximately 60 m of freeboard; thus overtopping is not a factor at this time (October 1980).

Our calculations indicate that the debris avalanche impounding Spirit Lake is also safe against slope failure and piping even if lake level should rise to the crest of the embankment. (Overtopping of the embankment could produce erosion and perhaps other serious problems.) Nevertheless, we recommend that the blockage be monitored for signs of piping or distress as the lake fills.

REFERENCES CITED

Glicken, H., Janda, R., and Voight, B., 1980, Catastrophic landslide debris avalanche of May 18, 1980, Mount St. Helens volcano [abs.]: American Geophysical Union, Transactions, v. 61, no. 46, November 11, p. 1135.

Skempton, A. W., and Hutchinson, J. N., 1969, Stability of natural slopes and embankment foundations: International Conference on Soil Mechanics and Foundation Engineering, 7th, Mexico City, State of the Art Volume, Proceedings, p. 291-340.

Taylor, D. W., 1948, Fundamentals of Soil Mechanics: New York, John Wiley, 691 p.

Terzaghi, Karl, and Peck, R. B., 1967, Soil Mechanics in engineering practice, 2nd ed.: New York, John Wiley, 729 p.

Youd, T. L., 1978, Major cause of earthquake damage is ground failure: Civil Engineering, April 1978, p. 47-51.

Youd, T. L., and Wilson, R. C., 1980, Stability of Toutle River blockage—Mt. St. Helens hazards investigations: U.S. Geological Survey Open-File Report 80-898, 14 p.

COMPUTER ASSESSMENTS OF POTENTIAL FLOOD HAZARDS FROM BREACHING OF TWO DEBRIS DAMS, TOUTLE RIVER AND COWLITZ RIVER SYSTEMS

By M. E. JENNINGS, V. R. SCHNEIDER, *and* P. E. SMITH

ABSTRACT

Flood hazards in the Toutle River and Cowlitz River systems posed by the possible breaching of two debris dams formed during the May 18, 1980, eruption of Mount St. Helens were analyzed and evaluated. The dams investigated include the one that impounds Spirit Lake and a plug dam at Elk Rock on the North Fork Toutle River. Two computer models were used in the study—one that simulates dam-break floods and another that simulates unsteady stream flow.

The Elk Rock dam breached after the assessment was made. Peak-discharge values computed from the assessment were approximately the same as those measured or estimated during and after the breach.

The studies illustrate that useful dam-break and flood-hazard estimates are possible with existing computer models, even though data may be only approximate and incomplete.

INTRODUCTION

Mount St. Helens, in southwestern Washington, erupted at 0832 PDT (Pacific Daylight time), on May 18, 1980; the north side of the cone was removed by landslides and a powerful lateral blast. A huge volume of airborne and avalanche debris buried land and water features in the drainage area immediately north and northwest of the mountain. Major geomorphic and hydrologic changes extended downstream along the valleys of the Toutle and Cowlitz Rivers, and mudflows and hydraulic effects occurred as far as the Columbia River (fig. 466). Details of these events are described in other reports of this volume.

The present report describes flood hazards created by the massive debris-avalanche deposit in the North Fork Toutle River valley and by downstream sediment deposition. The debris deposit is as much as 600 ft thick; it formed a dam about 500 ft high at the outlet of Spirit Lake, creating a set of conditions that might lead to overtopping, breaching, and subsequent downstream flooding. To date (January 1981), these events have not occurred. However, U.S. Geological Survey (USGS) hydrologists witnessed and recorded the overtopping and breaching of a similar but smaller dam on the North Fork Toutle River near Elk Rock. A flood-hazard assessment made the day before the breakout proved to be reasonably accurate and useful for the choice of advance protective measures.

This report contains a brief description of the computer models used to make the dam-break and flood-hazard analyses, analyses of the dam-break potential at Spirit Lake and at Elk Rock, and downstream flood routings from both of these sites.

DAM-BREAK COMPUTER MODELS

Land (1980) described and evaluated available dam-break, flood-wave computer models and concluded that the model developed by Fread (1980) was the most generally applicable. Land's modified version, the Dam Break Flood Forecast (DBFF) model, was used for

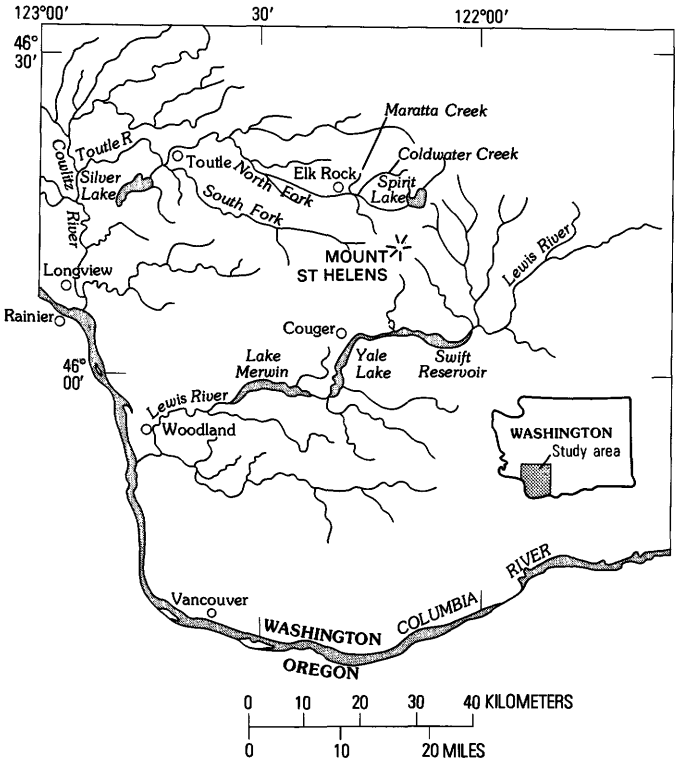

Figure 466.—Drainage system in the vicinity of Mount St. Helens, Wash.

the Mount St. Helens dam-break hazard calculations.

The DBFF modification of Fread's model uses the current understanding of dam-failure mechanics and hydrodynamic flow theory to predict the formation of a dam-break wave and its downstream movement. The modified model is a practical tool that has wide applicability. It can function with input that ranges from complete and accurate data to estimates of input data. The model is economical to run, as it requires only nominal amounts of time on large computers.

The DBFF model has three functional parts (Fread, 1980; Land, 1980): (1) description of the mode of dam failure; that is, the temporal and geometric description of the breach; (2) computation of the hydrograph of outflow through the developing breach as governed by the physical and hydraulic features of the reservoir, mainly rates of inflow to the reservoir and its storage characteristics; and (3) routing of the outflow hydrograph through the downstream valley to determine discharge-hydrograph changes resulting from downstream variations in valley storage capacity and from frictional resistance to flow.

The DBFF model permits adoption of a variety of breach-formation characteristics to simulate either overtopping or piping failure. The user specifies the failure-time interval and the final size and shape of the fully developed breach. During model operation, the breach formation begins when the water-surface elevation (h) of the reservoir exceeds a critical input stage (h_f). An overtopping failure is simulated when (h_f) is set to a value such that a sufficient amount of water is flowing over the crest of the dam to cause failure. A piping failure is simulated when (h_f) is set to a value less than that of the height of the dam. Overtopping failure modes were assumed for the North Fork Toutle River calculations. The mode of breach failure selected influences the results significantly.

DBFF computes the outflow from the breached dam as the summation of breach flow and flow through spillway outlets. The total outflow hydrograph is a function of water-surface elevation and outlet geometry and is related to depletion of reservoir-storage volume. The reservoir routing in DBFF uses either (1) a hydrologic-storage routing technique based on the law of conservation of mass, or (2) a hydraulic technique based on the law of conservation of mass and momentum. The hydrologic-storage routing technique was used for all reservoir routings described in this report.

After the outflow hydrograph from a breached dam is determined (expressed in terms of stage and discharge by the model), the hydrograph must be routed through the downstream river valley. The DBFF model uses a hydraulic-routing method based on the two differential equations that govern one-dimensional unsteady flow—the equations of continuity and momentum. A nonlinear implicit finite-difference algorithm was used to solve the equations. The computational procedure is capable of simulating both subcritical and supercritical flows.

According to Fread (1980), a distinguishing feature of flood waves generated by dam breaks is the great magnitude of the peak discharge compared to the magnitude of flood waves generated by runoff. A dam-break flood is usually many times greater than the runoff flood of record. For example, the largest flood estimated for a Spirit Lake debris-dam failure was about 25 times the maximum flood observed on the Toutle River during a 54-yr period. The time span from the first rise to the peak of the discharge hydrograph generally is short. This feature can cause

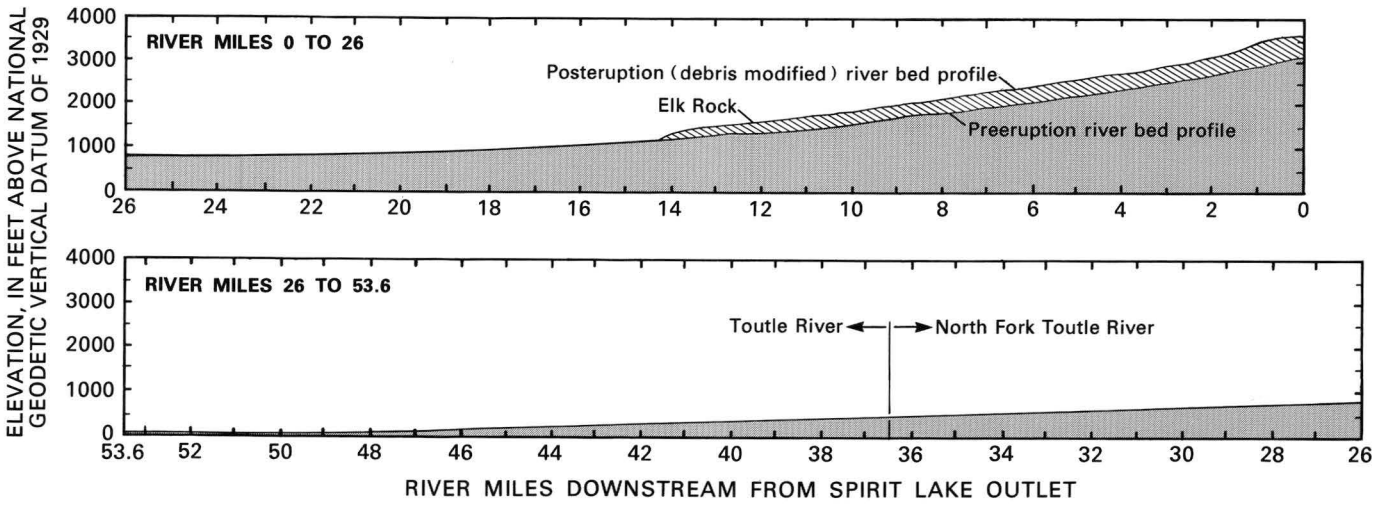

Figure 467.—Approximate preeruption and posteruption bed profiles of the North Fork Toutle and Toutle Rivers. Spirit Lake outlet is at river mi 0. Modified from Youd and Wilson (1980, fig. 2).

serious computational difficulties. In the process of routing dam-break flood hydrographs down the North Fork Toutle and the Toutle Rivers, considerable time was spent eliminating computational problems that were introduced by the rapid rise in stage.

A model that simulates unsteady streamflow, J879, documented by Land (1978) was used to route flood hydrographs down the North Fork Toutle and Toutle Rivers, and then down the Cowlitz River to its juncture with the Columbia River. Model J879 is a computer program for simulating one-dimensional subcritical, gradually varied unsteady flow. It does not perform dam-break calculations. The program solves the differential equations for unsteady flow using a linear implicit finite-difference algorithm as the computational method. A report by Land (1978) details the J879 computational scheme. Model J879 was used because the DBFF model did not include the option that would accommodate the correct downstream boundary condition at the Columbia River.

SPIRIT LAKE DAM-BREAK HAZARD

Immediately after the onset of the eruption of Mount St. Helens on May 18, 1980, many uncertainties arose concerning the extent of hazards, both geologic and hydrologic. The massive debris blockage—estimated to be 3–4 billion yd^3 (cubic yards) (Youd and Wilson, 1980)—was known to block the outlet of Spirit Lake. However, due to limited visibility from aircraft and to the dangers of onsite observation, only limited information was available about the size of the posteruption lake and the stability of the debris dam.

On May 19, USGS hydrologists visited the Spirit Lake area and determined that the elevation of the lake surface had been raised about 200 ft by the events of May 18. The lake was judged to represent a possible flood hazard, and the USGS thus began to estimate the downstream flow peaks that would occur if the debris dam was breached. The estimates were to be completed within 2 days, and, therefore, were based largely on initial onsite observations of water and land conditions. These data were fragmentary and approximate, particularly for characteristics of lake storage and of the debris dam.

A comparison of an approximate debris-modified bed profile of the North Fork Toutle River with the original bed profile is shown in figure 467. Representative channel cross sections constructed from topographic maps and used to model the Toutle and North Fork Toutle Rivers are shown in figure 468. Although preeruption cross-sectional configurations were used in the absence of posteruption information, vertical elevations of cross sections in the first 14.5 river mi downstream from the lake outlet were raised in accordance with early estimates of the debris-modified bed profile. The elevations used are somewhat lower than those given by Youd and Wilson (1980, fig. 2).

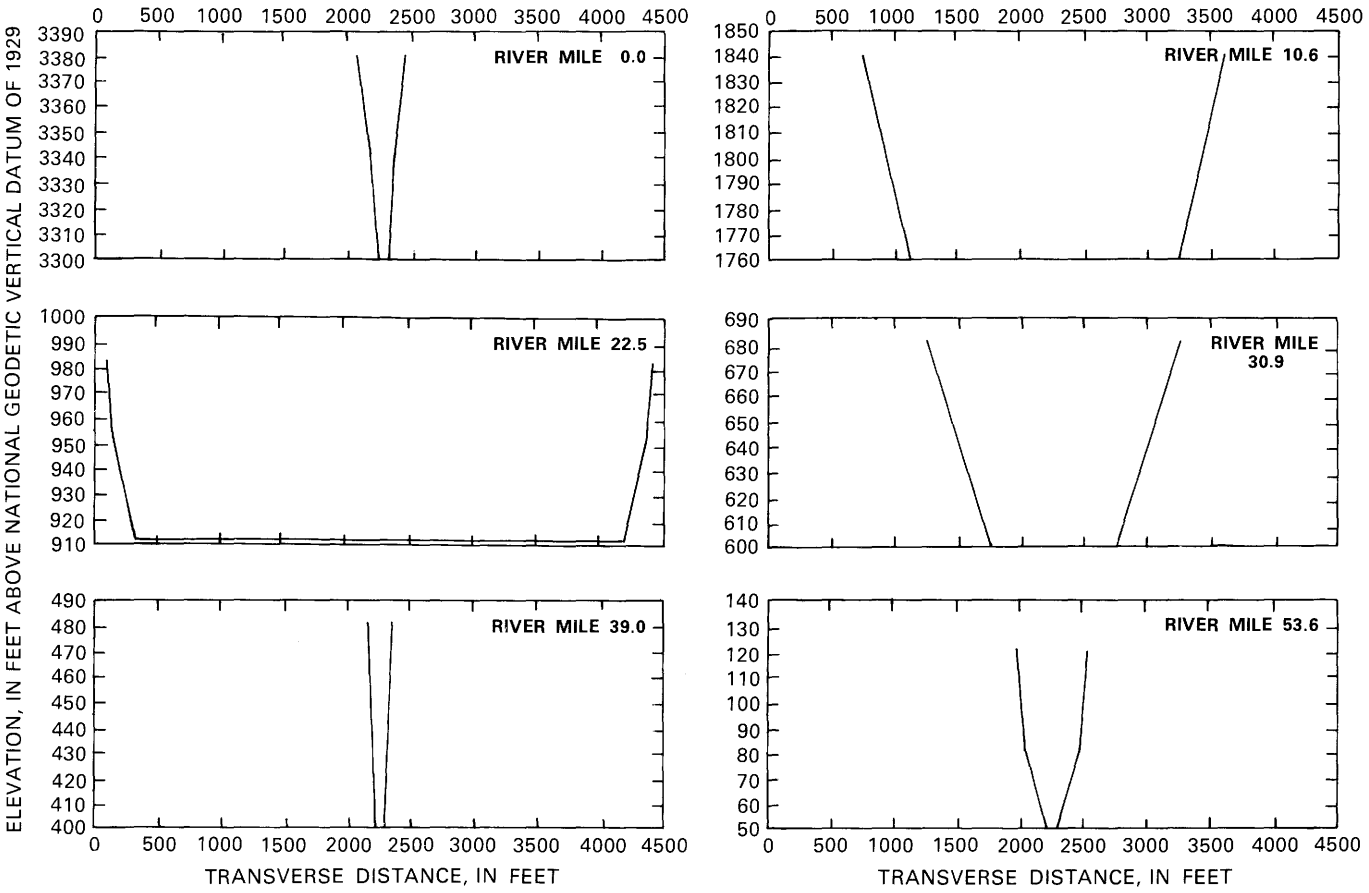

Figure 468.—Selected cross sections of the North Fork Toutle River and Toutle River channels used in modeling studies.

The use of approximate cross-sectional information from small-scale maps was to prove a hindrance in achieving acceptable computational results by creating numerical model instabilities. To eliminate model instabilities, it was necessary to make many runs with the DBFF model, trying different combinations of time steps and reach lengths.

One of the many difficulties encountered in evaluating the Spirit Lake flood hazard was to determine the most probable mode of failure of the Spirit Lake blockage (Youd and Wilson, 1980). In addition to the stability of the debris material forming the dam, the probable mode of failure was dependent upon the height and the lateral width of the blockage, the size and the volume of the lake impoundment, and the height of water behind the blockage. Onsite information was minimal. Attempts to treat the debris blockage as a dam proved to be only partly useful. The final decision was to conceptualize the Spirit Lake hazard as an overtopping failure, rather than as a piping failure or other possible form of breach. Because of the great downstream extent of the debris blockage (14.5 river mi), piping or other forms of failure were considered unlikely.

Overtopping and subsequent breaching conceivably could result from mudflows entering the lake, from runoff of melted snow and ice, or from a combination of these events. Water discharged by an overtopping failure was hypothesized as flowing over the debris blockage and down channels that were carved in the debris mass by mudflows that flowed across it later in the day on May 18.

Working from this hypothesis of the mode of failure, calculations were made for overtopping and failure of the Spirit Lake dam throughout the estimated 53.6-mi reach from Spirit Lake (river mi 0) to the mouth of the Toutle River (river mi 53.6). A trapezoidal breach was assumed as the most probable

geometric profile, and side slopes of two vertical to one horizontal also were assumed. Three cases were investigated; different sizes and duration of breach development were assumed for each:

Assumption	Case I	Case II	Case III
Duration of breach development (hr)	1	1	3
Final breach depth (ft)	150	100	50
Maximum breach width (ft)	200	200	200
Discharge at dam (cubic feet per second).	1,130,000	613,000	174,000

The discharges in each case were computed based on the estimated reservoir stage and the assumed breach dimensions.

Results of calculations for the three cases are presented in table 115 and in figure 469. The computed range in downstream discharge was variable and convergence of profiles at the mouth was only moderate, indicating little attenuation of the flood wave. Thus, uncertainty in the prediction of potential failure characteristics resulted in corresponding

Table 115.—Summary of peak discharges and elevations along the North Fork Toutle and Toutle Rivers, Wash., for three assumed cases of Spirit Lake dam failure (computed using the Dam-Break Flood Forecast model)

[ft, feet; ft³/s, cubic feet per second; hr, hour]

River miles downstream from Spirit Lake	Case I[1] Discharge (ft³/s)	Case I[1] Elevation[4] (ft)	Case II[2] Discharge (ft³/s)	Case II[2] Elevation[4] (ft)	Case III[3] Discharge (ft³/s)	Case III[3] Elevation[4] (ft)
0.0	1,130,000	3,376	613,000	3,358	174,000	3,330
17.0	1,010,000	1,214	546,000	1,209	158,000	1,204
39.0	475,000	482	296,000	466	128,000	444
[5]53.6	474,000	98	295,000	89	127,000	77

[1]Case I--Duration of breach development, 1 hr, final breach depth, 150 ft; maximum breach width, 200 ft.
[2]Case II--Duration of breach development, 1 hr; final breach depth, 100 ft; maximum breach width, 200 ft.
[3]Case III--Duration of breach development, 3 hrs; final breach depth, 50 ft, maximum width of breach, 200 ft.
[4]Elevations are referenced to National Geodetic Vertical Datum of 1929.
[5]River mile 53.6 is the mouth of the Toutle River.

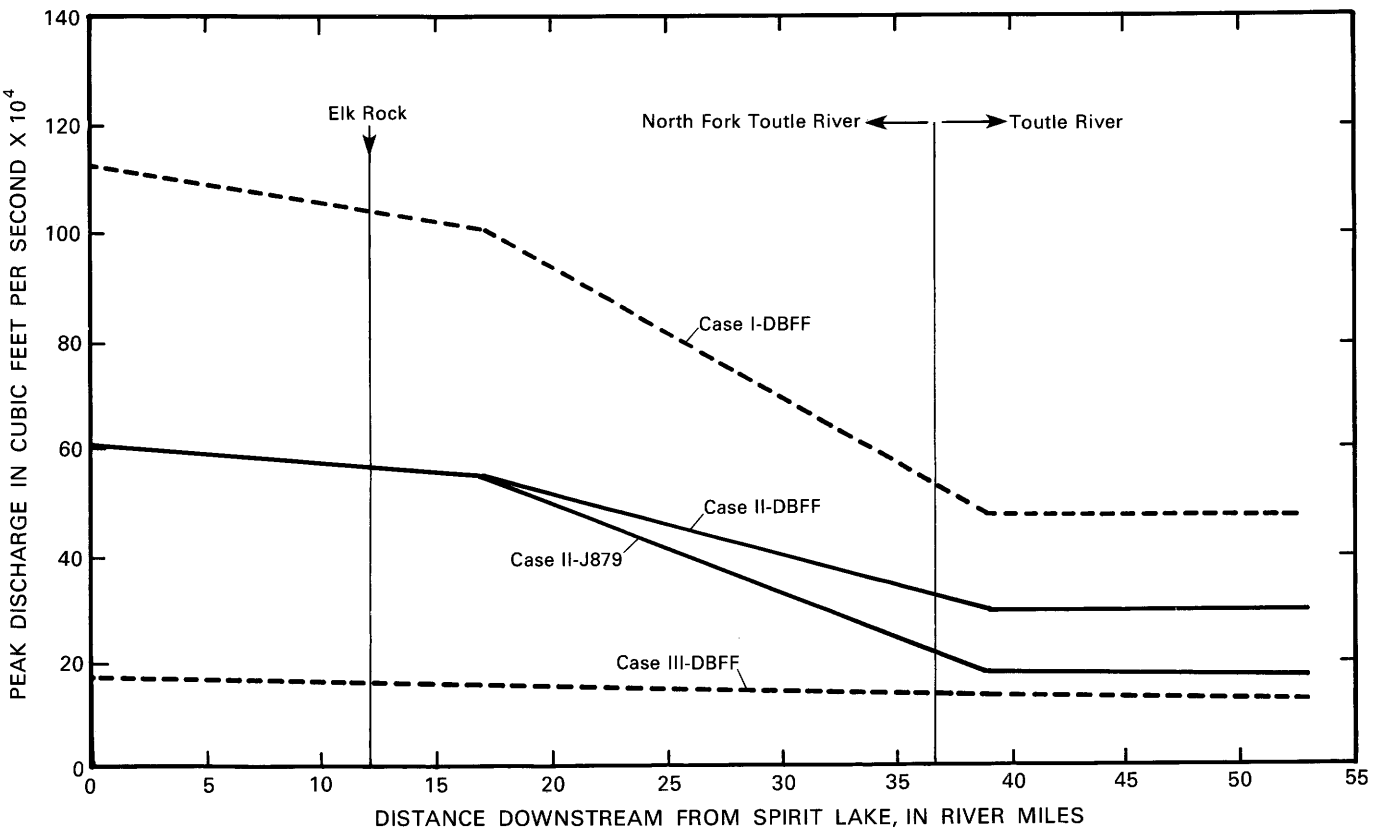

Figure 469.—Simulated profiles of peak discharge along the North Fork Toutle and Toutle Rivers, Wash., using computer models DBFF and J879.

uncertainty in the dam-break flood-hazard estimates.

The Case II results shown in table 115 were reported to USGS headquarters in Reston, Va., as the basis for emergency planning. Subsequently, calculations were made for Case II conditions in the Cowlitz River using the flood-routing program J879. A special river-mileage system was adopted for the Cowlitz River flood-routing exercise, and the calculations were based on the computed channel cross sections shown in figure 470. Preeruption configurations also were used for the Cowlitz River because no post-eruption data were available. In addition, assumptions were made of a constant flow of 9,000 ft³/s from the upper Cowlitz River and a constant Columbia River stage elevation at river mi 73.1 (mouth of Cowlitz River) of 5.5 ft above the National Geodetic

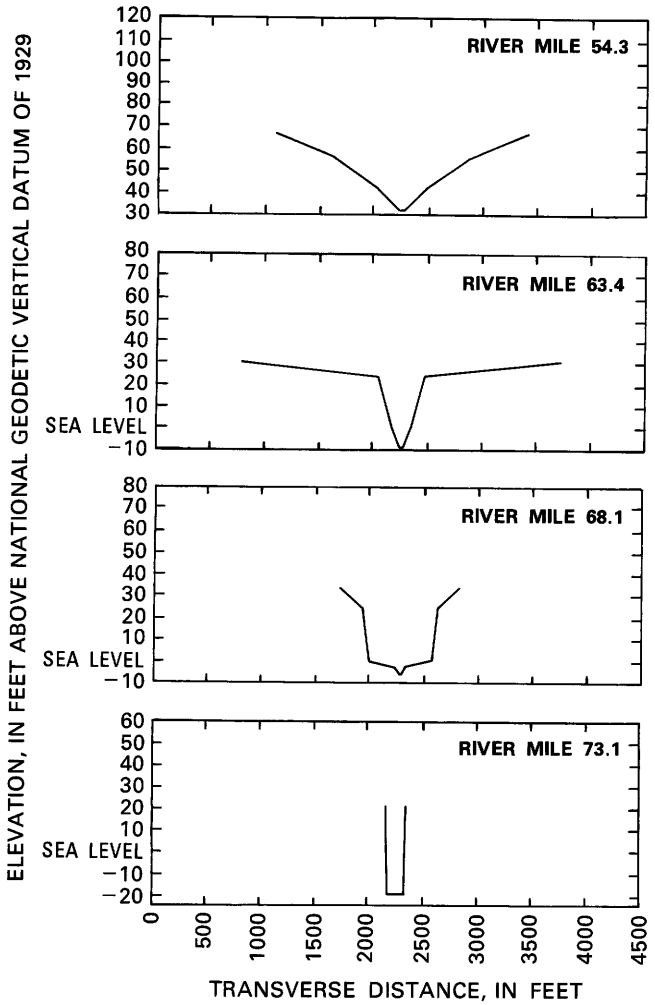

Figure 470.—Selected cross sections of the Cowlitz River channel used in modeling studies.

Table 116.—Summary of peak discharges and elevations along the North Fork Toutle, Toutle, and Cowlitz Rivers, Wash., for the Case II Spirit Lake dam failure (computed using the J879 model)

[ft³/s, cubic feet per second]

River miles downstream from Spirit Lake	CASE II	
	Discharge (ft³/s)	Elevation[1] (feet)
17.0	557,000	1,209
39.0	176,000	450
53.6	174,000	85
[2]54.3	[3]183,000	65
63.4	138,000	36
[4]73.1	72,500	5.5

[1]Elevations are referenced to National Geodetic Vertical Datum of 1929.
[2]River mi 54.3 is first cross section on Cowlitz River (fig. 470).
[3]A constant flow of 9,000 ft³/s was assumed to come from the upper reach of the Cowlitz River.
[4]River mi 73.1 is the mouth of the Cowlitz River. The downstream boundary condition adopted was a constant water-surface elevation of 5.5 ft.

Vertical Datum of 1929 (NGVD). The Columbia River at this location is affected significantly by tides, but for simplification the average elevation was used.

The results of the calculations for Case II, using program J879, from river mi 17.0 downstream from Spirit Lake to river mi 73.1 at the mouth of the Cowlitz River are given in table 116. The discharge estimate of 138,000 ft³/s at river mi 63.4 can be used as a point of reference. This discharge corresponds to about a 500-yr flood for an unsilted Cowlitz River channel. Sedimentation after the mudflows of May 18–19 markedly decreased the channel capacity of the lower Cowlitz River.

A comparison of results obtained using the DBFF and J879 models was possible downstream from river mi 17.0 on the North Fork Toutle River. The flood-routing technique, J879 model, resulted in considerably more attenuation than did the dam-break technique, DBFF model (fig. 469). The explanation for this difference in attenuation is not obvious and requires further research. Program J879 may contain, at least for large, steep-fronted flood waves, some artificial numerical attenuation, especially when reach sizes and time steps are large. The attenuation may be the result of using the linear implicit finite-difference

algorithm. The attenuation of the flood wave simulated by the DBFF model was so small that it is questionable, especially in reaches of the Toutle River downstream from the confluence of the North Fork Toutle and South Fork Toutle Rivers.

ELK ROCK PLUG-DAM HAZARD

The surface of the debris blockage in the North Fork Toutle River was hummocky, and had many depressions and pits, some of which contained water. The debris dammed the mouth of several tributaries to the North Fork, including Maratta and Coldwater Creeks. During July and early August, 1980, a small lake impounded at the mouth of Maratta Creek (fig. 466) broke through its dam as a result of saturation of the dam material and of overtopping. The lake water flowed downstream a short distance where it became trapped behind an earthen obstruction (plug) on the hummocky surface of the debris deposit. The plug soon failed and the water moved 4 mi farther downstream, where it collected behind another plug and formed a 250-acre-ft lake near Elk Rock.

The new lake presented a flood hazard, and the USGS made a series of dam-break calculations using the DBFF model and input data obtained from onsite observations. The downstream face of the plug dam was 112 ft high and 215 ft wide. The ponded water was 30 ft deep, and the base of the pond was 82 ft above the base of the dam.

The model computations were made on August 26. The next day, the plug failed after a rainstorm. For several hours after the failure, USGS personnel observed the breaching of the dam (which took about 40 min) and the downstream movement of the flood wave. Visual estimates of flood discharge were made at several localities by USGS and U.S. Army Corps of Engineers personnel, and discharge was measured at two gage sites. A comparison of the computed peak discharge with the estimated and measured peak discharges at various localities is presented in table 117. The computed discharge at the plug dam was based on the assumed formation of a near-vertical 30-ft slot (100-percent breach) in the 112-ft-high and 215-ft-wide plug within a period of 6 min. Calculations were made and results were averaged using hypothetical failure widths of 60, 80, and 100 ft. The actual failure occurred progressively but erratically during a 40-min period, and resulted in an irregular opening about 52 ft high. Considering the hypothetical assumptions on which the model calculations were based, the comparison between the simulated and the estimated-measured discharges is considered to be good.

Table 117.—Comparison of discharge simulated by computer models with measured or estimated peak discharges on the North Fork Toutle and Toutle Rivers, Wash., for the Elk Rock plug-dam failure

[ft³/s, cubic feet per second; leaders (---) indicate no data]

River miles downstream from Elk Rock	Simulated discharge (ft^3/s)	Discharge (ft^3/s)	
		U.S. Geological Survey	U.S. Army Corps of Engineers
0.0	[1]20,000	[2]16,000	[2]16,000
5.6	10,400	[2]8,000	[2]8,500
[3]26.4	---	[5]2,660	---
[4]41.6	1,500	[5]1,400	---

[1]Average of discharges computed using hypothetical failure widths of 60, 80, and 100 ft.
[2]Visual estimate.
[3]Toutle River at Silver Lake gage.
[4]Toutle River at U.S. Highway 99 gage.
[5]Measured.

The Elk Rock plug-dam failure resulted in damage to heavy channel-maintenance equipment in the North Fork Toutle River, but in no injuries or deaths. The relative accuracy of the pre-failure prediction underscores the utility of computer-based models for estimating flood hazards resulting from dam breaks.

CONCLUSIONS

Flood hazards posed by potential dam failures were evaluated. Investigations included the debris dam impounding Spirit Lake and the plug dam at Elk Rock. The DBFF model was used to evaluate hypothetical failures and to route flows to the Cowlitz River. A second model (J879) was used to route flow down the Cowlitz to the Columbia River. For both models, differences of data accuracy and completeness hampered computation of reliable hazard estimates.

The Elk Rock plug dam failed the day after the theoretical failure analysis had been made, providing an opportunity to compare hypothetical and actual results. The comparison between the simulated and estimated discharge is good, indicating that computer models can be useful in the assessment of dam-break flood hazards even though input data are approximate and incomplete.

REFERENCES CITED

Fread, D. L., 1976, Flood routing in meandering rivers with flood plains: Annual American Society of Civil Engineers, 3d, Rivers '76, Symposium of Waterways, Harbors and Coastal Engineering Division, August, Proceedings, v. 1, p. 16–35.

_____1980, DAMBRK—The NWS dam-break flood forecasting model: Silver Spring, Md., Office of Hydrology, National Weather Service (NWS) Report, 37 p.

Land, L. F., 1978, Unsteady streamflow simulation using a linear implicit finite-difference model: U.S. Geological Survey Water-Resources Investigations 78–59, 59 p.

_____1980, Evaluation of selected dam-break flood-wave models by using field data: U.S. Geological Survey Water-Resources Investigations 80–44, 60 p.

Youd, T. L., and Wilson, Raymond, 1980, Stability of Toutle River blockage, Mount St. Helens hazard investigation: U.S. Geological Survey Open-File Report 80–898, 14 p.

INDEX

[Italic page numbers indicate major references. Unless otherwise indicated, entries refer to events of May 18, 1980]

U

V

W

Y

Z

☆ U.S. GOVERNMENT PRINTING OFFICE: 1982—576-486